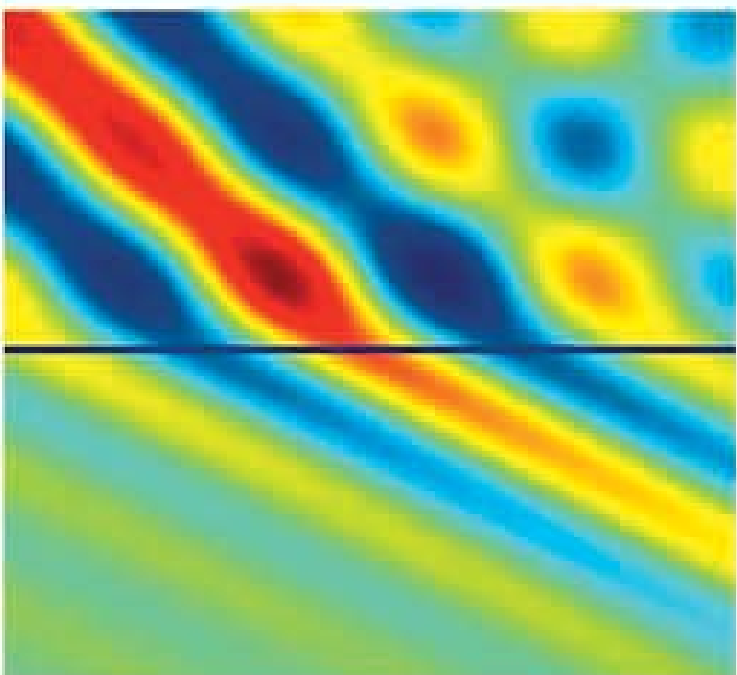


THEORY AND COMPUTATION OF ELECTROMAGNETIC FIELDS



JIAN-MING JIN

 WILEY

 IEEE
IEEE PRESS

*THEORY AND
COMPUTATION OF
ELECTROMAGNETIC
FIELDS*

THEORY AND COMPUTATION OF ELECTROMAGNETIC FIELDS

JIAN-MING JIN

University of Illinois



A JOHN WILEY & SONS, INC., PUBLICATION

Copyright © 2010 by John Wiley & Sons, Inc. All rights reserved

Published by John Wiley & Sons, Inc., Hoboken, New Jersey

Published simultaneously in Canada

No part of this publication may be reproduced, stored in a retrieval system, or transmitted in any form or by any means, electronic, mechanical, photocopying, recording, scanning, or otherwise, except as permitted under Section 107 or 108 of the 1976 United States Copyright Act, without either the prior written permission of the Publisher, or authorization through payment of the appropriate per-copy fee to the Copyright Clearance Center, Inc., 222 Rosewood Drive, Danvers, MA 01923, (978) 750-8400, fax (978) 750-4470, or on the web at www.copyright.com. Requests to the Publisher for permission should be addressed to the Permissions Department, John Wiley & Sons, Inc., 111 River Street, Hoboken, NJ 07030, (201) 748-6011, fax (201) 748-6008, or online at <http://www.wiley.com/go/permission>.

Limit of Liability/Disclaimer of Warranty: While the publisher and author have used their best efforts in preparing this book, they make no representations or warranties with respect to the accuracy or completeness of the contents of this book and specifically disclaim any implied warranties of merchantability or fitness for a particular purpose. No warranty may be created or extended by sales representatives or written sales materials. The advice and strategies contained herein may not be suitable for your situation. You should consult with a professional where appropriate. Neither the publisher nor author shall be liable for any loss of profit or any other commercial damages, including but not limited to special, incidental, consequential, or other damages.

For general information on our other products and services or for technical support, please contact our Customer Care Department within the United States at (800) 762-2974, outside the United States at (317) 572-3993 or fax (317) 572-4002.

Wiley also publishes its books in a variety of electronic formats. Some content that appears in print may not be available in electronic formats. For more information about Wiley products, visit our web site at www.wiley.com.

Library of Congress Cataloging-in-Publication Data

Jin, Jian-Ming, 1962-

Theory and Computation of Electromagnetic Fields / Jian-Ming Jin.

p. cm.

ISBN 978-0-470-53359-8 (cloth)

1. Electromagnetic fields—Mathematics—Textbooks. I. Title.

QC665.E4J56 2010

530.14'1—dc22

2010008436

Printed in the United States of America

10 9 8 7 6 5 4 3 2 1

CONTENTS

<i>PREFACE</i>	xii
<i>ACKNOWLEDGMENTS</i>	xv
PART I ELECTROMAGNETIC FIELD THEORY	
CHAPTER 1 BASIC ELECTROMAGNETIC THEORY	3
1.1 Review of Vector Analysis	3
1.1.1 Vector Operations and Integral Theorems	3
1.1.2 Symbolic Vector Method	6
1.1.3 Helmholtz Decomposition Theorem	8
1.1.4 Green's Theorems	9
1.2 Maxwell's Equations in Terms of Total Charges and Currents	9
1.2.1 Maxwell's Equations in Integral Form	11
1.2.2 Maxwell's Equations in Differential Form	14
1.2.3 Current Continuity Equation	14
1.2.4 The Lorentz Force Law	15
1.3 Constitutive Relations	15
1.3.1 Electric Polarization	15
1.3.2 Magnetization	17
1.3.3 Electric Conduction	19
1.3.4 Classification of Media	19
1.4 Maxwell's Equations in Terms of Free Charges and Currents	22
1.5 Boundary Conditions	24
1.6 Energy, Power, and Poynting's Theorem	26
1.7 Time-Harmonic Fields	29
1.7.1 Time-Harmonic Fields	29
1.7.2 Fourier Transforms	30
1.7.3 Complex Power	32
1.7.4 Complex Permittivity and Permeability	36
Notes	37
References	37
Problems	37
CHAPTER 2 ELECTROMAGNETIC RADIATION IN FREE SPACE	43
2.1 Scalar and Vector Potentials	43
2.1.1 Static Fields	44
2.1.2 Time-Harmonic Fields and the Lorenz Gauge Condition	45
2.2 Solution of Vector Potentials in Free Space	47
2.2.1 Delta Function and Green's Function	48
2.2.2 Green's Function in Free Space	49
2.2.3 Field-Source Relations in Free Space	50
2.2.4 Why Use Auxiliary Potential Functions	51
2.2.5 Free-Space Dyadic Green's Functions	52
2.3 Electromagnetic Radiation in Free Space	55
2.3.1 Infinitesimal Electric Dipole	55
2.3.2 Finite Electric Dipole	57
2.3.3 Far-Field Approximation and the Sommerfeld Radiation Condition	59
2.3.4 Circular Current Loop and Magnetic Dipole	61
2.4 Radiation by Surface Currents and Phased Arrays	63
2.4.1 Radiation by a Surface Current	63
2.4.2 Radiation by a Phased Array	65
Notes	69
References	69
Problems	69
CHAPTER 3 ELECTROMAGNETIC THEOREMS AND PRINCIPLES	73
3.1 Uniqueness Theorem	73
3.2 Image Theory	75
3.2.1 Basic Image Theory	76
3.2.2 Half-Space Field-Source Relations	80
3.3 Reciprocity Theorems	82
3.3.1 General Reciprocity Theorem	82
3.3.2 Lorentz Reciprocity Theorem	83
3.3.3 Rayleigh-Carson Reciprocity Theorem	83
3.4 Equivalence Principles	85
3.4.1 Surface Equivalence Principle	85

3.4.2	Application to Scattering by a Conducting Object	87
3.4.3	Application to Scattering by a Dielectric Object	90
3.4.4	Volume Equivalence Principle	92
3.5	Duality Principle	94
3.6	Aperture Radiation and Scattering	95
3.6.1	Equivalent Problems	96
3.6.2	Babinet's Principle	99
3.6.3	Complementary Antennas	101
References		102
Problems		103

CHAPTER 4	TRANSMISSION LINES AND PLANE WAVES	107
4.1	Transmission Line Theory	107
4.1.1	Governing Differential Equations and General Solutions	107
4.1.2	Reflection and Transmission	110
4.1.3	Green's Function and Eigenfunction Expansion	111
4.2	Wave Equations and General Solutions	115
4.2.1	Wave Equations and Solution by Separation of Variables	116
4.2.2	Characteristics of a Plane Wave	117
4.2.3	Wave Velocities and Attenuation	119
4.2.4	Linear, Circular, and Elliptical Polarizations	121
4.2.5	Wave Propagation in Metamaterials	124
4.3	Plane Waves Generated by A Current Sheet	125
4.4	Reflection and Transmission	127
4.4.1	Reflection and Transmission at Normal Incidence	127
4.4.2	Reflection and Transmission at Oblique Incidence	129
4.4.3	Total Transmission and Total Reflection	132
4.4.4	Transmission into a Left-Handed Medium	135
4.4.5	Plane Waves versus Transmission Lines	137
4.5	Plane Waves in Anisotropic and Bi-Isotropic Media	137
4.5.1	Plane Waves in Uniaxial Media	137
4.5.2	Plane Waves in Gyrotropic Media	142
4.5.3	Plane Waves in Chiral Media	145
References		147
Problems		147

CHAPTER 5 FIELDS AND WAVES IN RECTANGULAR COORDINATES 152

5.1	Uniform Waveguides	152
5.1.1	General Analysis	152
5.1.2	General Characteristics	156
5.1.3	Uniform Rectangular Waveguide	160
5.1.4	Losses in Waveguides and Attenuation Constant	167
5.2	Uniform Cavities	170
5.2.1	General Theory	171
5.2.2	Rectangular Cavity	173
5.2.3	Material and Geometry Perturbations	175
5.3	Partially Filled Waveguides and Dielectric Slab Waveguides	178
5.3.1	General Theory	178
5.3.2	Partially Filled Rectangular Waveguide	180
5.3.3	Dielectric Slab Waveguide on a Ground Plane	183
5.4	Field Excitation in Waveguides	187
5.4.1	Excitation by Planar Surface Currents	187
5.4.2	Excitation by General Volumetric Currents	189
5.5	Fields in Planar Layered Media	191
5.5.1	Spectral Green's Function and Sommerfeld Identity	191
5.5.2	Vertical Electric Dipole above a Layered Medium	192
5.5.3	Horizontal Electric Dipole above a Layered Medium	194
5.5.4	Dipoles on a Grounded Dielectric Slab	196

Note 197

References 198

Problems 198

CHAPTER 6 FIELDS AND WAVES IN CYLINDRICAL COORDINATES 200

6.1	Solution of Wave Equation	200
6.1.1	Solution by Separation of Variables	200
6.1.2	Cylindrical Wave Functions	203
6.2	Circular and Coaxial Waveguides and Cavities	204
6.2.1	Circular Waveguide	205
6.2.2	Coaxial Waveguide	208
6.2.3	Cylindrical Cavity	212
6.3	Circular Dielectric Waveguide	213
6.3.1	Analysis of Hybrid Modes	214

<p>6.3.2 Characteristics of Hybrid Modes 217</p> <p>6.4 Wave Transformation and Scattering Analysis 222</p> <ul style="list-style-type: none"> 6.4.1 Wave Transformation 223 6.4.2 Scattering by a Circular Conducting Cylinder 224 6.4.3 Scattering by a Circular Dielectric Cylinder 227 6.4.4 Scattering by a Circular Multilayer Dielectric Cylinder 230 <p>6.5 Radiation by Infinitely Long Currents 234</p> <ul style="list-style-type: none"> 6.5.1 Line Current Radiation in Free Space 234 6.5.2 Radiation by a Cylindrical Surface Current 236 6.5.3 Radiation in the Presence of a Circular Conducting Cylinder 238 6.5.4 Radiation in the Presence of a Conducting Wedge 241 6.5.5 Radiation by a Finite Current 243 <p>References 245</p> <p>Problems 245</p>	<p>7.5.4 Radiation in the Presence of a Conducting Cone 288</p> <p>References 291</p> <p>Problems 292</p>
PART II ELECTROMAGNETIC FIELD COMPUTATION	
CHAPTER 8 THE FINITE DIFFERENCE METHOD 297	
<hr/>	
<p>8.1 Finite Differencing Formulas 298</p> <p>8.2 One-Dimensional Analysis 300</p> <ul style="list-style-type: none"> 8.2.1 Solution of the Diffusion Equation 300 8.2.2 Solution of the Wave Equation 302 8.2.3 Stability Analysis 302 8.2.4 Numerical Dispersion Analysis 305 <p>8.3 Two-Dimensional Analysis 306</p> <ul style="list-style-type: none"> 8.3.1 Analysis in the Time Domain 306 8.3.2 Analysis in the Frequency Domain 308 <p>8.4 Yee's FDTD Scheme 309</p> <ul style="list-style-type: none"> 8.4.1 Two-Dimensional Analysis 309 8.4.2 Three-Dimensional Analysis 311 <p>8.5 Absorbing Boundary Conditions 314</p> <ul style="list-style-type: none"> 8.5.1 One-Dimensional ABC 314 8.5.2 Two-Dimensional ABCs 316 8.5.3 Perfectly Matched Layers 318 <p>8.6 Modeling of Dispersive Media 329</p> <ul style="list-style-type: none"> 8.6.1 Recursive Convolution Approach 329 8.6.2 Auxiliary Differential Equation Approach 331 <p>8.7 Wave Excitation and Far-Field Calculation 333</p> <ul style="list-style-type: none"> 8.7.1 Modeling of Wave Excitation 334 8.7.2 Near-to-Far Field Transformation 337 <p>8.8 Summary 338</p> <p>References 339</p> <p>Problems 340</p>	
CHAPTER 9 THE FINITE ELEMENT METHOD 342	
<hr/>	
<p>9.1 Introduction to the Finite Element Method 343</p> <ul style="list-style-type: none"> 9.1.1 The General Principle 343 9.1.2 One-Dimensional Example 344 <p>9.2 Finite Element Analysis of Scalar Fields 347</p> <ul style="list-style-type: none"> 9.2.1 The Boundary-Value Problem 347 9.2.2 Finite Element Formulation 348 9.2.3 Application Examples 354 	

9.3	Finite Element Analysis of Vector Fields	359	10.5	Analysis of Microstrip Antennas and Circuits	443
9.3.1	The Boundary-Value Problem	359	10.5.1	Formulation of Integral Equations	443
9.3.2	Finite Element Formulation	360	10.5.2	The Moment-Method Solution	446
9.3.3	Application Examples	364	10.5.3	Evaluation of Green's Functions	446
9.4	Finite Element Analysis in the Time Domain	372	10.5.4	Far-Field Calculation and Application Examples	451
9.4.1	The Boundary-Value Problem	373	10.6	The Moment Method in the Time Domain	452
9.4.2	Finite Element Formulation	374	10.6.1	Time-Domain Integral Equations	453
9.4.3	Application Examples	378	10.6.2	Marching-On-in-Time Solution	454
9.5	Absorbing Boundary Conditions	379	10.7	Summary	458
9.5.1	Two-Dimensional ABCs	380	References	458	
9.5.2	Three-Dimensional ABCs	383	Problems	460	
9.5.3	Perfectly Matched Layers	386			
9.6	Some Numerical Aspects	390			
9.6.1	Mesh Generation	391			
9.6.2	Matrix Solvers	391			
9.6.3	Higher-Order Elements	392			
9.6.4	Curvilinear Elements	393			
9.6.5	Adaptive Finite Element Analysis	393			
9.7	Summary	393			
References	394				
Problems	395				

CHAPTER 10 THE METHOD OF MOMENTS 399

10.1	Introduction to the Method of Moments	399
10.2	Two-Dimensional Analysis	404
10.2.1	Formulation of Integral Equations	404
10.2.2	Scattering by a Conducting Cylinder	407
10.2.3	Scattering by a Conducting Strip	411
10.2.4	Scattering by a Homogeneous Dielectric Cylinder	415
10.3	Three-Dimensional Analysis	416
10.3.1	Formulation of Integral Equations	416
10.3.2	Scattering and Radiation by a Conducting Wire	421
10.3.3	Scattering by a Conducting Body	425
10.3.4	Scattering by a Homogeneous Dielectric Body	430
10.3.5	Scattering by an Inhomogeneous Dielectric Body	433
10.4	Analysis of Periodic Structures	436
10.4.1	Scattering by a Planar Periodic Conducting Patch Array	436
10.4.2	Scattering by a Discrete Body-of-Revolution Object	441

CHAPTER 11 FAST ALGORITHMS AND HYBRID TECHNIQUES 463

11.1	Introduction to Fast Algorithms	463
11.2	Conjugate Gradient-FFT Method	465
11.2.1	Scattering by a Conducting Strip or Wire	466
11.2.2	Scattering by a Conducting Plate	466
11.2.3	Scattering by a Dielectric Object	472
11.3	Adaptive Integral Method	478
11.3.1	Planar Structures	478
11.3.2	Three-Dimensional Objects	482
11.4	Fast Multipole Method	487
11.4.1	Two-Dimensional Analysis	487
11.4.2	Three-Dimensional Analysis	492
11.4.3	Multilevel Fast Multipole Algorithm	495
11.5	Adaptive Cross-Approximation Algorithm	500
11.5.1	Low-Rank Matrix	500
11.5.2	Adaptive Cross-Approximation	502
11.5.3	Application to the Moment-Method Solution	504
11.6	Introduction to Hybrid Techniques	508
11.7	Hybrid Finite Difference-Finite Element Method	509
11.7.1	Relation between FETD and FDTD	510
11.7.2	Hybridization of FETD and FDTD	512
11.7.3	Application Example	514
11.8	Hybrid Finite Element-Boundary Integral Method	515
11.8.1	Traditional Formulation	517

11.8.2 Symmetric Formulation	520	12.1.4 Time-Domain Simulation Methods	538
11.8.3 Numerical Examples	523	12.1.5 Hybrid Techniques	540
11.9 Summary	526	12.2 Applications of Computational Electromagnetics	540
Notes	527	12.3 Challenges in Computational Electromagnetics	551
References	527	References	552
Problems	531		
CHAPTER 12 CONCLUDING REMARKS ON COMPUTATIONAL ELECTROMAGNETICS 533			
12.1 Overview of Computational Electromagnetics	533	APPENDIX	559
12.1.1 Frequency- versus Time-Domain Analysis	533	Vector Identities	559
12.1.2 High-Frequency Asymptotic Techniques	534	Integral Theorems	559
12.1.3 First-Principle Numerical Methods	536	Coordinate Transformation	560
		INDEX	561

PREFACE

As is implicit in its title, this book consists of two parts. Part 1 is on the theory of electromagnetic fields and is intended to serve as a textbook for an entry-level graduate course on electromagnetics. Part 2 is on the computation of electromagnetic fields and is intended for an advanced-level graduate course on computational electromagnetics. Whereas there are several textbooks available for the entry-level graduate electromagnetics course, no textbook is available for the advanced course on computational electromagnetics. This book is intended to fill this void and present the electromagnetic theory in a systematic manner so that students can advance from the first course to the second without much difficulty.

Even though the first part of the book covers the standard basic electromagnetic theory, the coverage is different from that of existing textbooks, mainly because of the undergraduate curriculum reform that has happened during the past two decades. Many universities have reduced the number of required courses in order to give students more freedom to design their own portfolios. As a result, only one electromagnetics course is required for undergraduate students in most electrical engineering departments in the country. New graduate students come to take the graduate electromagnetics course with significant differences in their knowledge of the basic electromagnetic theory. To meet the challenge to benefit all students of different levels, our course contents cover both fundamental theories (such as vector analysis, Maxwell's equations and boundary conditions, and transmission-line theory) and advanced topics (such as wave transformation, addition theorems, and scattering by a layered sphere).

When writing the first part of this book, the author has kept the following in mind. First, this book is not intended to be an extensive reference book on electromagnetic theory. It should cover only the fundamental components that electrical engineering graduate students need to know so that they have the foundation to learn more advanced topics in the future, and all the material can be taught within one semester. Therefore, we have to be very selective in choosing topics to be covered. Second, the style of the book should fit classroom teaching and self-learning, rather than use as a reference book. For example, it would be desirable for a reference book to have a chapter to present a complete theory of Green's functions. However, for classroom teaching it would be better to introduce new ideas and concepts piece by piece as needed. Third, the writing and teaching should adhere to the central theme that the entire electromagnetic theory is developed based on Maxwell's equations using mathematics as a tool. The treatment of every subject should start with Maxwell's equations or something based on Maxwell's equations directly.

The second part of the book covers a few major computational methods for numerical analysis of electromagnetic fields for engineering applications. These include the finite difference method (and the finite difference time-domain method in particular), the finite element method, and the integral equation-based moment method. These three methods are chosen because they represent the three fundamental approaches for numerical analysis of electromagnetic fields. Once the students are familiar with these three methods, they

can learn other numerical methods easily. This part also covers fast algorithms for solving integral equations and hybrid techniques that combine different numerical methods to seek for more efficient and capable solutions of complicated electromagnetic problems. The computational electromagnetics course based on this part has become increasingly popular as more areas use computational electromagnetics as an analysis and simulation tool for dealing with electromagnetic problems. At the University of Illinois, this course has been taken by many students outside the electromagnetics major and some even outside the electrical engineering major.

The following is a summary of the material covered in this book. Chapter 1 presents the basic electromagnetic theory, which includes a brief review of vector analysis, Maxwell's equations in both integral and differential forms, boundary conditions at the interface between different media and at the surface of a perfect conductor, constitutive relations that characterize the electromagnetic properties of a medium, the concepts of electromagnetic energy and power, and Maxwell's equations for time-harmonic fields. In this chapter the symbolic vector method is introduced to facilitate the vector analysis, and Maxwell's equations in integral form have been treated as fundamental postulates to derive Maxwell's equations in differential form and various boundary conditions.

In Chapter 2 we deal with electromagnetic fields radiated in free space by solving Maxwell's equations in differential form with the aid of the constitutive relations. Scalar and vector potentials are introduced as auxiliary functions to facilitate the solution. The advantage of using these auxiliary potential functions is discussed. The concept of Green's functions and dyadic Green's functions is also introduced as a means to relate the field to its source. The far-field approximation of the radiated field is considered, and the results are used to derive the Sommerfeld radiation condition.

Chapter 3 presents some important theorems and principles that can be derived from Maxwell's equations. The first is the uniqueness theorem, which is then used as a foundation to develop the image theory and the surface equivalence principle. The induction theorem, the physical equivalent, and the solution to aperture radiation are also derived as an application of the surface equivalence principle. The symmetry in Maxwell's equations is explored to develop the duality principle, and the electromagnetic Babinet's principle is presented along with its application to complementary structures.

The objective of Chapter 4 is to consider a uniform plane wave and examine its propagation in an unbounded homogeneous medium to gain a better understanding of the characteristics of wave propagation. The basic transmission-line theory is reviewed first, to introduce some basic concepts related to wave propagation such as propagation and attenuation constants and various velocities. The wave equation is then solved by separation of variables in rectangular coordinates, and the basic characteristics of a plane wave such as wave impedance and polarizations are discussed. A few simple boundary-value problems are solved, which include plane waves generated by a current sheet and reflection and transmission of a plane wave at an interface between two different half-spaces. Also discussed are plane wave propagation in uniaxial, gyrotropic, chiral, and metamaterial media and transmission into a left-handed medium.

In Chapter 5 we deal with wave propagation in either homogeneously filled or inhomogeneously filled uniform waveguides and dielectric waveguides and electromagnetic resonance in cavities. We first present a general analysis and derive the basic characteristics for waveguides and cavities, and then we use a rectangular waveguide and cavity to illustrate the analysis and the basic properties. The perturbational method is introduced to calculate the attenuation constants and quality factors for imperfect waveguides and cavities and to analyze the resonance variation due to material and geometry perturbations in a cavity. The analysis of hybrid modes in a partially filled waveguide and

in a grounded dielectric slab waveguide is described in detail. Field excitation by a current source in a waveguide and a multilayered medium is also discussed because of its importance in practical applications.

In Chapter 6 we discuss electromagnetic analysis in the cylindrical coordinate system. We first discuss the solution of the Helmholtz equation by the method of separation of variables and derive cylindrical wave functions. We then employ cylindrical wave functions to analyze circular and coaxial waveguides and cavities. This is followed by the analysis of wave propagation along a circular dielectric waveguide. After that, we derive a wave transformation that expands a plane wave in terms of cylindrical wave functions. The derived wave transformation is then used for solving various scattering problems involving a conducting or dielectric cylinder. Finally, we discuss a few radiation problems in which a line current or a cylindrical surface current radiates in the presence of a conducting cylinder or a conducting wedge. The solution is used to derive the Sommerfeld radiation condition for two-dimensional fields and to illustrate the phenomenon of the transverse field singularity at a conducting edge.

In Chapter 7 we discuss electromagnetic analysis in a spherical coordinate system. We first discuss the solution of the Helmholtz equation by the method of separation of variables and derive spherical wave functions. We then employ spherical wave functions to analyze a spherical cavity and a biconical antenna. This is followed by a wave transformation that expands a plane wave in terms of spherical wave functions. The derived wave transformation is then used for solving various scattering problems involving a conducting or a dielectric sphere. Finally, we consider the problem of radiation of a point charge to derive the addition theorem for spherical wave functions, and the radiation of a spherical surface current in the presence of a sphere or a cone to illustrate the radiation analysis in spherical coordinates and the field singularity at a sharp conducting tip.

Starting from Chapter 8, we deal with the subject of computational electromagnetics. In Chapter 8 we describe the basic principle of the finite difference method by first deriving basic finite differencing formulas and applying them to wave and diffusion equations. This is followed by the stability and dispersion analyses, which are two critical issues in the finite difference method. After that, we introduce the finite difference time-domain method for solving Maxwell's equations in both two and three dimensions. Finally, we discuss how to truncate the computational domain for the analysis of open-region electromagnetic problems using absorbing boundary conditions and perfectly matched layers, how to model dispersive media in the time domain, how to excite incident waves in a computational domain, and how to calculate far fields based on the near-field information.

Chapter 9 covers the topic of the finite element method. We first introduce the basic principle of the finite element method by considering a simple one-dimensional example. We then describe in detail the formulation of the finite element analysis of electromagnetic scalar and vector problems in the frequency domain. This is followed by the extension to the time domain, which includes a brief treatment of modeling a dispersive medium. In each case, we present several numerical examples to demonstrate the application and capability of the finite element method. Finally, we discuss the truncation of the computational domain for the analysis of unbounded electromagnetic problems using absorbing boundary conditions and perfectly matched layers, and some numerical aspects related to the implementation of the finite element method.

In Chapter 10 we first describe the basic principle of the moment method using a simple electrostatic problem. We then formulate a general integral equation for the two-dimensional Helmholtz equation and apply it to a variety of specific problems. For each specific problem, we describe its moment-method solution step by step. This is repeated

for three-dimensional electromagnetic field problems that include scattering by various conducting and dielectric objects. After that, we discuss the moment-method solution of planar and angular periodic problems and deal with the analysis of microstrip antennas and circuits on a dielectric substrate to demonstrate the unique advantage of the moment method. Finally, we use a relatively simple example to illustrate how to extend the moment-method solution from the frequency domain to the time domain.

In Chapter 11 we discuss two important topics in computational electromagnetics. The first topic is the development of various fast algorithms to solve integral equations more efficiently. These include the ones based on the fast Fourier transform, the adaptive integral method, and the fast multipole method, which all require reformulation of numerical discretization of integral equations based on their kernels, and the adaptive cross approximation algorithm, which applies directly to the moment-method matrix equation without a need for reformulation. The second topic is the development of hybrid techniques that combine different numerical methods to exploit their strengths and eliminate their weaknesses so that they can deal with complicated electromagnetic problems more efficiently. This development is illustrated through two examples. One combines the finite element method with the finite difference time-domain method, and the other combines the finite element method with the moment method. All the fast algorithms and hybrid techniques are discussed in detail along with numerical examples to demonstrate their enhanced capabilities.

In Chapter 12 we provide an overview of computational techniques developed for electromagnetic analysis, which include many of the numerical methods that are left uncovered in Chapters 8 to 11, and discuss briefly the applications and challenges of computational techniques for solving electromagnetic problems.

The writing of this book assumed that students have basic knowledge of electromagnetics (having taken at least one undergraduate electromagnetics course). As an engineering textbook, the time convention $e^{j\omega t}$ is used, and the focus is placed on solving various electromagnetic boundary-value problems. A limited number of references are listed at the end of each chapter. Each chapter contains a selected number of homework problems to test and reinforce the understanding of the course material by the students. The students are expected to complete all these homework problems, since each problem is carefully chosen and designed and there is little overlap between the homework problems. For students taking the computational electromagnetics course, they are expected to complete three projects on the finite difference time-domain, finite element, and moment methods and write a comprehensive technical report for each project.

Jian-Ming Jin

ACKNOWLEDGMENTS

Over the past 16 years since I started teaching at the University of Illinois, I have received encouragement and help from my colleagues, especially Professors Yuen-Tse Lo, Shung-Wu Lee, Weng Cho Chew, Shun Lien Chuang, Andreas C. Cangellaris, and Jose Schutt-Aine. All of them taught the graduate electromagnetics course at the University of Illinois and felt a need to have a dedicated textbook for this course. At various occasions, they encouraged me to take on this endeavor, which has been long overdue. In particular, the late Professor Y. T. Lo shared with me his teaching philosophy and provided his course notes, from which I have adopted a few homework problems, the discussion on the causality of the Fourier transform (Section 1.7.2), and the treatment of a current sheet radiation problem (Section 4.3). Professor S. L. Chuang provided me with material on wave propagation in uniaxial media (Section 4.5) and a set of optical devices that have been used to demonstrate some interesting phenomena related to the subject. Professor W. C. Chew encouraged me on the development of the graduate course on computational electromagnetics, and his dedication to the teaching of electromagnetics has been a constant inspiration. Some material in Chapter 8, Section 8.2.3 in particular, is adapted from the course notes prepared by Professor Chew and Dr. William H. Weedon. My appreciation also goes to Dr. Andrew Greenwood of the Air Force Research Laboratory, who provided me with the field contour plots of waveguide modes in rectangular and circular waveguides (Figures 5.4 and 6.3). I would also like to thank Dr. Walter Fox Smith of Haverford College for his permission to include parts of his wonderful songs on Maxwell's equations. The following figures are adapted from the course project reports of my former students: Figures 8.10 and 10.13–10.15 by Michael Tompkins, Figure 8.17 by Clara Chi, Figures 7.6 and 9.10 by Stephen Yan, and Figures 10.5–10.7 by Peng Chen, who has also assisted me in the preparation of some other figures.

I am grateful to the following people who have read parts of the manuscript and made various suggestions: Professor Binxian Lu of North China Electric Power University, Professor Dagang Fang of Nanjing University of Science and Technology, Professor Shanjie Zhang of Nanjing University, Professor Yan Shi of Xidian University, and Drs. Shu-Wei Chang and Su Yan of the University of Illinois. The earlier versions of the manuscript were tested as a textbook for the classes in 2008 and 2009 at the University of Illinois and the overall responses have been positive. Last but not the least, I would like to thank technical editors, Messrs. Jamie Hutchinson and Jerome Colburn, for editing the book and Wiley's Associate Publisher, Mr. George Telecki, for his encouragement and continued interest in publishing my books.

Finally, I dedicate this book to my family and my parents, and to the memory of late Professors Chen-To Tai of the University of Michigan and Y. T. Lo of the University of Illinois.

Jian-Ming Jin

PART I

ELECTROMAGNETIC FIELD THEORY

BASIC ELECTROMAGNETIC THEORY

The first half of this book covers the theory of electromagnetic fields and waves based on Maxwell's equations from the engineering perspective. The coverage is focused on basic concepts and principles related to electromagnetic fields and theoretical approaches to analyzing electromagnetic radiation, propagation, and scattering problems. To start, this chapter presents basic electromagnetic theory, which includes a brief review of vector analysis that is essential for the mathematical treatment of electromagnetic fields, Maxwell's equations in both integral and differential forms that govern all electromagnetic phenomena, the Lorentz force law that relates electric and magnetic fields to measurable forces, constitutive relations that characterize the electromagnetic properties of a medium, boundary conditions at interfaces between different media and at perfectly conducting surfaces, the concepts of electromagnetic energy and power, the energy conservation law as expressed by Poynting's theorem, the concept of phasors for time-harmonic fields, and finally Maxwell's equations and Poynting's theorem in the complex form for time-harmonic fields. The presentation assumes that the reader has basic knowledge of vector calculus and electromagnetics at the undergraduate level [1–7].

1.1 REVIEW OF VECTOR ANALYSIS

We all know that both electric and magnetic fields are vectors since they have both a magnitude and a direction. Hence, the study of electromagnetic fields requires basic knowledge of vector analysis. The most useful concepts in vector analysis are those of divergence, curl, and gradient. In this section we present definitions and related integral theorems for these quantities. This is followed by the introduction of a new method that can easily deal with various vector identities and the description of the Helmholtz decomposition theorem, which will be very useful for the study of Maxwell's equations.

1.1.1 Vector Operations and Integral Theorems

Assume that \mathbf{f} is a vector function,¹ a quantity whose magnitude and direction vary as functions of its position in space. The *divergence* of the vector function \mathbf{f} is defined by the limit

$$\nabla \cdot \mathbf{f} = \lim_{\Delta V \rightarrow 0} \frac{1}{\Delta V} \left[\iint_s \mathbf{f} \cdot d\mathbf{s} \right] \quad (1.1.1)$$

Theory and Computation of Electromagnetic Fields, by Jian-Ming Jin
Copyright © 2010 John Wiley & Sons, Inc.

4 THEORY AND COMPUTATION OF ELECTROMAGNETIC FIELDS

where Δv denotes an infinitesimal volume and s denotes the closed surface of this volume. The differential surface ds is normal to s and points outward. By applying Equation 1.1.1 to the differential volume constructed in rectangular, cylindrical, and spherical coordinates, we obtain the expressions of the divergence as

$$\nabla \cdot \mathbf{f} = \frac{\partial f_x}{\partial x} + \frac{\partial f_y}{\partial y} + \frac{\partial f_z}{\partial z} \quad (1.1.2)$$

$$\nabla \cdot \mathbf{f} = \frac{1}{\rho} \frac{\partial(\rho f_\rho)}{\partial \rho} + \frac{\partial f_\phi}{\rho \partial \phi} + \frac{\partial f_z}{\partial z} \quad (1.1.3)$$

$$\nabla \cdot \mathbf{f} = \frac{1}{r^2} \frac{\partial}{\partial r} (r^2 f_r) + \frac{1}{r \sin \theta} \frac{\partial}{\partial \theta} (f_\theta \sin \theta) + \frac{1}{r \sin \theta} \frac{\partial f_\phi}{\partial \phi} \quad (1.1.4)$$

in these three most important coordinate systems. It is important to remember that $\nabla \cdot \mathbf{f}$, a notation proposed by J. Willard Gibbs [8], is simply a mathematical notation for the divergence of \mathbf{f} . It should not be interpreted as the dot product between the operator ∇ and the vector \mathbf{f} ; otherwise, mistakes can easily be made in the derivation of the expressions in cylindrical and spherical coordinates. Now, consider a finite volume denoted as V , which is enclosed by surface S . By dividing this volume into an infinite number of infinitesimal volumes, applying Equation 1.1.1 to each infinitesimal volume, and summing up the results, we obtain

$$\iiint_V \nabla \cdot \mathbf{f} dV = \oint_S \mathbf{f} \cdot d\mathbf{S} \quad (1.1.5)$$

if the vector \mathbf{f} and its first derivative are continuous in volume V as well as on its surface S . Equation 1.1.5 is known as the *divergence theorem* or *Gauss' theorem*, which is very useful in electromagnetics.

In addition to the divergence, another operation that quantifies the variation of a vector function is called the *curl*. The curl of the vector function \mathbf{f} is defined by the limit

$$\nabla \times \mathbf{f} = \lim_{\Delta v \rightarrow 0} \frac{1}{\Delta v} \left[\oint_S ds \times \mathbf{f} \right] \quad (1.1.6)$$

where Δv again denotes an infinitesimal volume enclosed by surface s . Again, we should remember that $\nabla \times \mathbf{f}$ is simply a mathematical notation for the curl of \mathbf{f} , and it should not be interpreted as the cross-product between the operator ∇ and the vector \mathbf{f} . By applying Equation 1.1.6 to the differential volume constructed in rectangular, cylindrical, and spherical coordinates, we obtain the expressions of the curl as

$$\nabla \times \mathbf{f} = \hat{x} \left(\frac{\partial f_z}{\partial y} - \frac{\partial f_y}{\partial z} \right) + \hat{y} \left(\frac{\partial f_x}{\partial z} - \frac{\partial f_z}{\partial x} \right) + \hat{z} \left(\frac{\partial f_y}{\partial x} - \frac{\partial f_x}{\partial y} \right) \quad (1.1.7)$$

$$\nabla \times \mathbf{f} = \hat{\rho} \left(\frac{\partial f_z}{\rho \partial \phi} - \frac{\partial f_\phi}{\partial z} \right) + \hat{\phi} \left(\frac{\partial f_\rho}{\partial z} - \frac{\partial f_z}{\partial \rho} \right) + \hat{z} \frac{1}{\rho} \left[\frac{\partial(\rho f_\phi)}{\partial \rho} - \frac{\partial f_\rho}{\partial \phi} \right] \quad (1.1.8)$$

$$\nabla \times \mathbf{f} = \hat{r} \frac{1}{r \sin \theta} \left[\frac{\partial}{\partial \theta} (f_\phi \sin \theta) - \frac{\partial f_\theta}{\partial \phi} \right] + \hat{\theta} \frac{1}{r} \left[\frac{1}{\sin \theta} \frac{\partial f_r}{\partial \phi} - \frac{\partial}{\partial r} (rf_\phi) \right] + \hat{\phi} \frac{1}{r} \left[\frac{\partial}{\partial r} (rf_\theta) - \frac{\partial f_r}{\partial \theta} \right]. \quad (1.1.9)$$

Apparently, the curl itself is a vector that has a different magnitude and a different direction. Given a direction \hat{a} , the magnitude of the curl in this direction is given by

$$\hat{a} \cdot (\nabla \times \mathbf{f}) = \lim_{\Delta s \rightarrow 0} \frac{1}{\Delta s} \left[\oint_c \mathbf{f} \cdot d\mathbf{l} \right] \quad (1.1.10)$$

where Δs is an infinitesimal surface normal to \hat{a} and c is a closed contour bounding Δs . The differential length $d\mathbf{l}$ is tangential to the contour c , and its direction is related to that of \hat{a} by the right-hand rule. Equation 1.1.10 can be derived by applying Equation 1.1.6 to an infinitesimal disk perpendicular to \hat{a} with a vanishing thickness. Now, consider an open surface S bounded by a closed contour C . We can divide S into an infinite number of infinitesimal surfaces, then apply Equation 1.1.10 to each of the infinitesimal surfaces, and finally sum up the results to find

$$\iint_S (\nabla \times \mathbf{f}) \cdot d\mathbf{S} = \oint_C \mathbf{f} \cdot d\mathbf{l} \quad (1.1.11)$$

if the vector \mathbf{f} and its first derivative are continuous on surface S as well as along C . Equation 1.1.11 is known as *Stokes' theorem*, which is also very useful in the study of electromagnetics.

As we will see later, the divergence and curl are sufficient to characterize the variation of a vector function. The third useful operation in vector analysis is the *gradient*, which quantifies the variation of a scalar function. Let f be a scalar function of space. The gradient of this function is defined as

$$\nabla f = \lim_{\Delta v \rightarrow 0} \frac{1}{\Delta v} \left[\iint_s f d\mathbf{s} \right] \quad (1.1.12)$$

which is a vector. Its magnitude along a given direction \hat{a} is given by

$$\hat{a} \cdot \nabla f = \frac{\partial f}{\partial a} \quad (1.1.13)$$

which can be derived by applying Equation 1.1.12 to an infinitesimal circular disk perpendicular to \hat{a} with a vanishing radius and thickness. By applying Equation 1.1.12 to the differential volume constructed in rectangular, cylindrical, and spherical coordinates, we obtain the expressions of the gradient as

$$\nabla f = \hat{x} \frac{\partial f}{\partial x} + \hat{y} \frac{\partial f}{\partial y} + \hat{z} \frac{\partial f}{\partial z} \quad (1.1.14)$$

$$\nabla f = \hat{\rho} \frac{\partial f}{\partial \rho} + \hat{\phi} \frac{\partial f}{\partial \phi} + \hat{z} \frac{\partial f}{\partial z} \quad (1.1.15)$$

$$\nabla f = \hat{r} \frac{\partial f}{\partial r} + \hat{\theta} \frac{\partial f}{\partial \theta} + \hat{\phi} \frac{1}{r \sin \theta} \frac{\partial f}{\partial \phi}. \quad (1.1.16)$$

In vector analysis, another important operation is to take the divergence on the gradient of a function such as $\nabla \cdot (\nabla f)$. This operation is often referred to as the *Laplacian*, which is denoted as

$$\nabla^2 f = \nabla \cdot (\nabla f). \quad (1.1.17)$$

Its expressions in the three commonly used coordinates are given by

$$\nabla^2 f = \frac{\partial^2 f}{\partial x^2} + \frac{\partial^2 f}{\partial y^2} + \frac{\partial^2 f}{\partial z^2} \quad (1.1.18)$$

$$\nabla^2 f = \frac{1}{\rho} \frac{\partial}{\partial \rho} \left(\rho \frac{\partial f}{\partial \rho} \right) + \frac{1}{\rho^2} \frac{\partial^2 f}{\partial \phi^2} + \frac{\partial^2 f}{\partial z^2} \quad (1.1.19)$$

$$\nabla^2 f = \frac{1}{r^2} \frac{\partial}{\partial r} \left(r^2 \frac{\partial f}{\partial r} \right) + \frac{1}{r^2 \sin \theta} \frac{\partial}{\partial \theta} \left(\sin \theta \frac{\partial f}{\partial \theta} \right) + \frac{1}{r^2 \sin^2 \theta} \frac{\partial^2 f}{\partial \phi^2}. \quad (1.1.20)$$

1.1.2 Symbolic Vector Method

In vector analysis, we often have to manipulate vector expressions into different and yet equivalent forms. A difficulty in such a manipulation is that the operator ∇ cannot be treated rigorously as a vector. This difficulty can be alleviated by the introduction of the *symbolic vector method* [8]. This symbolic vector, denoted as $\tilde{\nabla}$, is defined as

$$T(\tilde{\nabla}) = \lim_{\Delta v \rightarrow 0} \frac{1}{\Delta v} \left[\iint_s T(\hat{n}) ds \right] \quad (1.1.21)$$

where Δv denotes an infinitesimal volume, s denotes the closed surface of this volume, and \hat{n} denotes the unit vector normal to the surface s and pointing outward, which is related to ds by $ds = \hat{n} ds$. The left-hand side of Equation 1.1.21, $T(\tilde{\nabla})$, represents an expression that contains the symbolic vector $\tilde{\nabla}$, such as $a\tilde{\nabla}$, $\mathbf{a} \cdot \tilde{\nabla}$, $\mathbf{a} \times \tilde{\nabla}$, and $\tilde{\nabla} \cdot (\mathbf{a} \times \mathbf{b})$. The integrand on the right-hand side, $T(\hat{n})$, represents the same expression with $\tilde{\nabla}$ being replaced by \hat{n} , so the corresponding expressions for the four examples above are $a\hat{n}$, $\mathbf{a} \cdot \hat{n}$, $\mathbf{a} \times \hat{n}$, and $\hat{n} \cdot (\mathbf{a} \times \mathbf{b})$.

Based on the definition given in Equation 1.1.21, we can show easily that

$$\tilde{\nabla} \cdot \mathbf{f} = \lim_{\Delta v \rightarrow 0} \frac{1}{\Delta v} \left[\iint_s \hat{n} \cdot \mathbf{f} ds \right] = \lim_{\Delta v \rightarrow 0} \frac{1}{\Delta v} \left[\iint_s \mathbf{f} \cdot \hat{n} ds \right] = \mathbf{f} \cdot \tilde{\nabla} \quad (1.1.22)$$

and similarly, $\tilde{\nabla} f = f \tilde{\nabla}$ and $\tilde{\nabla} \times \mathbf{f} = -\mathbf{f} \times \tilde{\nabla}$. This indicates clearly that $\tilde{\nabla}$ can be treated as a regular vector; hence, all valid vector manipulations and all algebraic identities are applicable to $\tilde{\nabla}$. However, by comparing Equation 1.1.21 with the definitions of the divergence, curl, and gradient, we also see that

$$\nabla \cdot \mathbf{f} = \tilde{\nabla} \cdot \mathbf{f} = \mathbf{f} \cdot \tilde{\nabla} \quad (1.1.23)$$

$$\nabla \times \mathbf{f} = \tilde{\nabla} \times \mathbf{f} = -\mathbf{f} \times \tilde{\nabla} \quad (1.1.24)$$

$$\nabla f = \tilde{\nabla} f = f \tilde{\nabla}. \quad (1.1.25)$$

These equations establish a relation between the symbolic vector $\tilde{\nabla}$ and the divergence, curl, and gradient operations. Given an expression that contains any of these operations, we can first convert it into an algebraic expression using Equations 1.1.23–1.1.25, then manipulate the algebraic expression using any of the valid algebraic identities, and finally convert the symbolic vector back to the divergence, curl, or gradient.

When a vector expression contains the symbolic vector $\tilde{\nabla}$ and two arbitrary functions, since $\tilde{\nabla}$ works on both functions, we can use the following chain rule to facilitate its manipulation:

$$T(\tilde{\nabla}, a, b) = T(\tilde{\nabla}_a, a, b) + T(\tilde{\nabla}_b, a, b) \quad (1.1.26)$$

where a and b represent two functions that can either be scalar or vector, $\tilde{\nabla}_a$ is the symbolic vector applying only to function a , and $\tilde{\nabla}_b$ applies only to function b . Equation 1.1.26 should not come as a surprise to anyone who is familiar with the following well-known differentiation formula:

$$\frac{\partial(ab)}{\partial x} = b \frac{\partial a}{\partial x} + a \frac{\partial b}{\partial x}. \quad (1.1.27)$$

To illustrate the application of Equation 1.1.26, we consider three examples. We first consider the expression $\nabla \cdot (ab\mathbf{b})$. Using Equation 1.1.26, we find

$$\tilde{\nabla} \cdot (ab\mathbf{b}) = \tilde{\nabla}_a \cdot (ab\mathbf{b}) + \tilde{\nabla}_b \cdot (ab\mathbf{b}) = (\tilde{\nabla}_a a) \cdot \mathbf{b} + a \tilde{\nabla}_b \cdot \mathbf{b}. \quad (1.1.28)$$

Since $\tilde{\nabla} \cdot (ab\mathbf{b}) = \nabla \cdot (ab\mathbf{b})$, $\tilde{\nabla}_a a = \nabla a$, and $\tilde{\nabla}_b \cdot \mathbf{b} = \nabla \cdot \mathbf{b}$, we obtain the vector identity

$$\nabla \cdot (ab\mathbf{b}) = \mathbf{b} \cdot (\nabla a) + a \nabla \cdot \mathbf{b}. \quad (1.1.29)$$

As the second example, we consider $\nabla \times (ab\mathbf{b})$. Using Equation 1.1.26, we find

$$\tilde{\nabla} \times (ab\mathbf{b}) = \tilde{\nabla}_a \times (ab\mathbf{b}) + \tilde{\nabla}_b \times (ab\mathbf{b}) = (\tilde{\nabla}_a a) \times \mathbf{b} + a \tilde{\nabla}_b \times \mathbf{b} \quad (1.1.30)$$

which yields the vector identity

$$\nabla \times (ab\mathbf{b}) = -\mathbf{b} \times (\nabla a) + a \nabla \times \mathbf{b}. \quad (1.1.31)$$

As the last example, we consider $\nabla \times (\mathbf{a} \times \mathbf{b})$. Using Equation 1.1.26 and the algebraic identity

$$\mathbf{c} \times (\mathbf{a} \times \mathbf{b}) = (\mathbf{c} \cdot \mathbf{b})\mathbf{a} - (\mathbf{c} \cdot \mathbf{a})\mathbf{b} \quad (1.1.32)$$

we find

$$\begin{aligned} \tilde{\nabla} \times (\mathbf{a} \times \mathbf{b}) &= \tilde{\nabla}_a \times (\mathbf{a} \times \mathbf{b}) + \tilde{\nabla}_b \times (\mathbf{a} \times \mathbf{b}) \\ &= (\tilde{\nabla}_a \cdot \mathbf{b})\mathbf{a} - (\tilde{\nabla}_a \cdot \mathbf{a})\mathbf{b} + (\tilde{\nabla}_b \cdot \mathbf{b})\mathbf{a} - (\tilde{\nabla}_b \cdot \mathbf{a})\mathbf{b} \end{aligned} \quad (1.1.33)$$

which yields the vector identity

$$\nabla \times (\mathbf{a} \times \mathbf{b}) = (\mathbf{b} \cdot \nabla)\mathbf{a} - \mathbf{b} \nabla \cdot \mathbf{a} + \mathbf{a} \nabla \cdot \mathbf{b} - (\mathbf{a} \cdot \nabla)\mathbf{b}. \quad (1.1.34)$$

These examples demonstrate the power of the symbolic vector in deriving various vector identities, which would otherwise be a rather tedious task.

Now, let us consider a finite volume V , which is enclosed by surface S . By dividing this volume into an infinite number of infinitesimal volumes, applying Equation 1.1.21 to each infinitesimal volume, and summing up the results, we obtain

$$\iiint_V T(\tilde{\nabla}) dV = \iint_S T(\hat{n}) dS \quad (1.1.35)$$

if the function involved in $T(\tilde{\nabla})$ is continuous within volume V . Equation 1.1.35 is referred to as the *generalized Gauss' theorem*, from which we can easily derive many integral theorems. For example, if we let $T(\tilde{\nabla}) = \tilde{\nabla} \cdot \mathbf{f} = \nabla \cdot \mathbf{f}$, we obtain the standard Gauss' theorem in Equation 1.1.5. If we let $T(\tilde{\nabla}) = \tilde{\nabla} \times \mathbf{f} = \nabla \times \mathbf{f}$, we obtain the so-called *curl theorem*

$$\iiint_V \nabla \times \mathbf{f} dV = \iint_S d\mathbf{S} \times \mathbf{f} \quad (1.1.36)$$

from which we can also derive Stokes' theorem given in Equation 1.1.11 by applying it to a surface with a vanishing thickness.

1.1.3 Helmholtz Decomposition Theorem

In vector analysis, there are two special vectors. One is called the *irrotational* vector, whose curl vanishes. Denoting this vector as \mathbf{F}_i , we have

$$\nabla \times \mathbf{F}_i = 0, \quad \nabla \cdot \mathbf{F}_i \neq 0. \quad (1.1.37)$$

Another special vector is called the *solenoidal* vector, whose divergence is zero. Denoting this vector as \mathbf{F}_s , we have

$$\nabla \cdot \mathbf{F}_s = 0, \quad \nabla \times \mathbf{F}_s \neq 0. \quad (1.1.38)$$

Using the symbolic vector method, we can easily prove the following two very important vector identities:

$$\nabla \times (\nabla \varphi) = 0 \quad (1.1.39)$$

$$\nabla \cdot (\nabla \times \mathbf{A}) = 0. \quad (1.1.40)$$

These identities are valid for any continuous and differentiable scalar function φ and vector function \mathbf{A} . Clearly, $\nabla \varphi$ is an irrotational vector and $\nabla \times \mathbf{A}$ is a solenoidal vector.

Although a vector function can have a complicated variation, it can be shown that any smooth vector function \mathbf{F} that vanishes at infinity can be decomposed into an irrotational and a solenoidal vector,

$$\mathbf{F} = \mathbf{F}_i + \mathbf{F}_s. \quad (1.1.41)$$

By taking the divergence and curl of Equation 1.1.41, respectively, we obtain

$$\nabla \cdot \mathbf{F} = \nabla \cdot \mathbf{F}_i, \quad \nabla \times \mathbf{F} = \nabla \times \mathbf{F}_s \quad (1.1.42)$$

which clearly indicate that the solenoidal component is related to the curl of the function and the irrotational part is related to the divergence of the function. Therefore, once both

the divergence and curl of a vector function are specified, the function is fully determined. This fact is known as the *Helmholtz decomposition theorem*.

1.1.4 Green's Theorems

From Gauss' theorem in Equation 1.1.5, we can derive some very useful integral theorems. If we substitute $\mathbf{f} = a\nabla b$ into Equation 1.1.5, where a and b are scalar functions, and apply a vector identity based on Equation 1.1.29, we obtain

$$\iiint_V (a\nabla^2 b + \nabla a \cdot \nabla b) dV = \oint_S a \frac{\partial b}{\partial n} dS \quad (1.1.43)$$

which is called the *first scalar Green's theorem*. By exchanging the positions of a and b and subtracting the resulting equation from Equation 1.1.43, we obtain

$$\iiint_V (a\nabla^2 b - b\nabla^2 a) dV = \oint_S \left(a \frac{\partial b}{\partial n} - b \frac{\partial a}{\partial n} \right) dS \quad (1.1.44)$$

which is known as the *second scalar Green's theorem*.

If we substitute $\mathbf{f} = \mathbf{a} \times \nabla \times \mathbf{b}$ into Equation 1.1.5, where both \mathbf{a} and \mathbf{b} are vector functions, and apply a vector identity, we obtain

$$\iiint_V [(\nabla \times \mathbf{a}) \cdot (\nabla \times \mathbf{b}) - \mathbf{a} \cdot (\nabla \times \nabla \times \mathbf{b})] dV = \oint_S (\mathbf{a} \times \nabla \times \mathbf{b}) \cdot d\mathbf{S} \quad (1.1.45)$$

which is called the *first vector Green's theorem*. By switching the positions of \mathbf{a} and \mathbf{b} and subtracting the resulting equation from Equation 1.1.45, we obtain

$$\iiint_V [\mathbf{b} \cdot (\nabla \times \nabla \times \mathbf{a}) - \mathbf{a} \cdot (\nabla \times \nabla \times \mathbf{b})] dV = \oint_S (\mathbf{a} \times \nabla \times \mathbf{b} - \mathbf{b} \times \nabla \times \mathbf{a}) \cdot d\mathbf{S} \quad (1.1.46)$$

which is known as the *second vector Green's theorem*. Now, if we let $\mathbf{b} = \hat{\mathbf{b}}b$, where $\hat{\mathbf{b}}$ is an arbitrary constant unit vector and b is a scalar function, and then substitute it into Equation 1.1.46, we can obtain after some vector manipulations

$$\iiint_V [b(\nabla \times \nabla \times \mathbf{a}) + \mathbf{a}\nabla^2 b + (\nabla \cdot \mathbf{a})\nabla b] dV = \oint_S \left[(\hat{\mathbf{n}} \cdot \mathbf{a})\nabla b + (\hat{\mathbf{n}} \times \mathbf{a}) \times \nabla b + (\hat{\mathbf{n}} \times \nabla \times \mathbf{a})b \right] dS \quad (1.1.47)$$

which can be called the *scalar–vector Green's theorem*.

1.2 MAXWELL'S EQUATIONS IN TERMS OF TOTAL CHARGES AND CURRENTS

Maxwell's equations are a set of four mathematical equations that relate precisely the electric and magnetic fields to their sources, which are electric charges and currents. They were established by James Clerk Maxwell (1831–1879) [9,10] based on the experimental discoveries of André-Marie Ampère (1775–1836) and Michael Faraday (1791–1867) and

a law for electricity by Carl Friedrich Gauss (1777–1855), and were reformulated into the vector form by Heinrich Hertz (1857–1894) [11] and Oliver Heaviside (1850–1925) [12]. Maxwell's equations can be expressed in both integral and differential forms. This section first presents Maxwell's equations in integral form as the fundamental postulates of electromagnetic theory, and then derives Maxwell's equations in differential form for fields in a continuous medium, which are subsequently used to derive the current continuity condition. This is followed by a brief description of the Lorentz force law that relates the electric and magnetic fields to measurable forces.



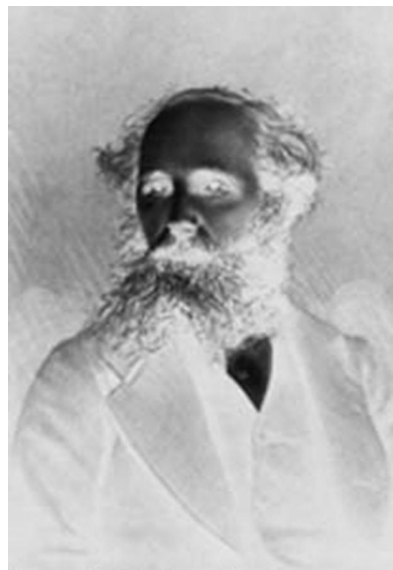
André Marie Ampère (1775–1836)



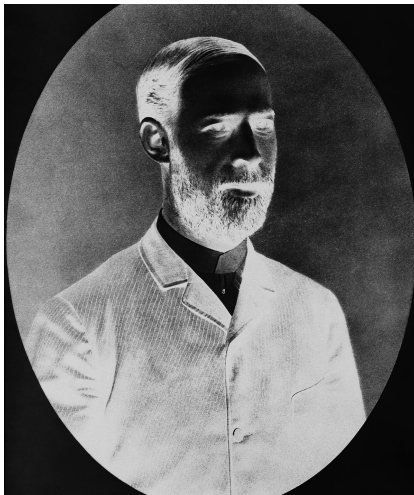
Carl Friedrich Gauss (1777–1855)



Michael Faraday (1791–1867)



James Clerk Maxwell (1831–1879)



Heinrich Hertz (1857–1894)



Oliver Heaviside (1850–1925)

Picture credits

André-Marie Ampère: Engraved by Ambroise Tardieu, 1825, courtesy AIP Emilio Segre Visual Archives
 Carl Friedrich Gauss: AIP Emilio Segre Visual Archives, Brittle Books Collection
 Michael Faraday: Photo by John Watkins, courtesy AIP Emilio Segre Visual Archives
 James Clerk Maxwell: AIP Emilio Segre Visual Archives
 Heinrich Hertz: Deutsches Museum
 Oliver Heaviside: AIP Emilio Segre Visual Archives, Brittle Books Collection

1.2.1 Maxwell's Equations in Integral Form

Consider an open surface S bounded by a closed contour C . The first two Maxwell's equations are given by

$$\oint_C \mathcal{E}(\mathbf{r}, t) \cdot d\mathbf{l} = -\frac{d}{dt} \iint_S \mathcal{B}(\mathbf{r}, t) \cdot d\mathbf{S} \quad (1.2.1)$$

$$\oint_C \mathcal{B}(\mathbf{r}, t) \cdot d\mathbf{l} = \epsilon_0 \mu_0 \frac{d}{dt} \iint_S \mathcal{E}(\mathbf{r}, t) \cdot d\mathbf{S} + \mu_0 \iint_S \mathcal{J}_{\text{total}}(\mathbf{r}, t) \cdot d\mathbf{S} \quad (1.2.2)$$

where

\mathcal{E} = electric field intensity (volts/meter)

\mathcal{B} = magnetic flux density (webers/meter²)

$\mathcal{J}_{\text{total}}$ = electric current density (amperes/meter²)

ϵ_0 = permittivity of free space (farads/meter)

μ_0 = permeability of free space (henrys/meter).

The position vector \mathbf{r} and time variable t are included explicitly to indicate that the associated quantities can be functions of position and time.² The subscript "total" in $\mathcal{J}_{\text{total}}$ is used

to denote that this is the current density of total electric currents. In the MKS unit system, the numerical values for the free-space permittivity and permeability are

$$\epsilon_0 = 8.854 \times 10^{-12} \text{ F/m} \approx \frac{1}{36\pi} \times 10^{-9} \text{ F/m} \quad (1.2.3)$$

$$\mu_0 = 4\pi \times 10^{-7} \text{ H/m}. \quad (1.2.4)$$

Equation 1.2.1 is called *Faraday's induction law*, and Equation 1.2.2 is often called *Ampère's law* or the *Maxwell–Ampère law* because Maxwell augmented the original Ampère's law with the addition of the displacement current, the first term on the right-hand side. As we will see later, this term is very important because it predicts that electromagnetic fields can propagate as waves, which was experimentally verified by Hertz in 1887. Equations 1.2.1 and 1.2.2 indicate that a time-varying magnetic flux can generate an electric field, and an electric current and a time-varying electric field can generate a magnetic field.

In a folk song about Faraday's law as expressed in Equation 1.2.1, the author, Dr. Walter Fox Smith of Haverford College, elaborated eloquently its physical meaning and practical importance in a humorous fashion. He wrote

Faraday's law of induction
The law of all sea and all land—
No lies, no deceit, no corruption
In this law so complete and so grand!

Our children will sing it in chorus—
"Circulation of vector cap E,"
Yes they'll sing as they march on before us,
"Equals negative d by dt
Of—
Magnetic flux through a surface,"
They'll conclude as we strike up the band.
We'll mark all our coins with our purpose—
"On Maxwell's equations we stand!"

It's Faraday's law of induction
That allows us to generate pow'r.
It gives voltage increase or reduction—
We could sing on and on for an hour!

By denoting the total current and total electric flux passing through the surface S as

$$\mathcal{I}(t) = \iint_S \mathcal{J}_{\text{total}}(\mathbf{r}, t) \cdot d\mathbf{S} \quad (1.2.5)$$

$$\phi_E(t) = \iint_S \mathcal{E}(\mathbf{r}, t) \cdot d\mathbf{S} \quad (1.2.6)$$

the Maxwell–Ampère law in Equation 1.2.2 can also be written as

$$\oint_C \mathcal{B} \cdot d\mathbf{l} = \mu_0 \mathcal{I} + \mu_0 \epsilon_0 \frac{d}{dt} \phi_E. \quad (1.2.7)$$

In a folk song titled "Two great guys—one great law!" Smith described the development history of this law and the contributions by Ampère and Maxwell:

*Mr. Ampère's magical, mystical, wonderful law!
Of Maxwell's equations, it is the longest and strangest of all!*

*On the left side, he wrote circulation
Of magnetic field, 'cause it was neat.
On the right hand side of his equation—
Mu-naught I—he thought it was complete.*

*Decades later, Maxwell saw disaster,
Although he thought of Ampère as a saint—
In between the plates of a capacitor
The right side's zero, but the left side ain't!*

*To fix this problem, he added to the right side
Displacement current, a brand new quantity!
It started mu-naught ϵ_0 'lon-naught and ended by
The time derivative of phi-sub-E.*

*And so to Maxwell the myst'ry was revealed—
He saw how light could move through empty space.
The changing B-field made the changing E-field,
And vice-a-versa, all at the perfect pace.*

Next, consider a volume V enclosed by a surface S . The other two Maxwell's equations are given by

$$\oint_S \mathcal{E}(\mathbf{r}, t) \cdot d\mathbf{S} = \frac{1}{\epsilon_0} \iiint_V \rho_{e,\text{total}}(\mathbf{r}, t) dV \quad (1.2.8)$$

$$\oint_S \mathcal{B}(\mathbf{r}, t) \cdot d\mathbf{S} = 0 \quad (1.2.9)$$

where $\rho_{e,\text{total}}$ denotes the electric charge density (coulombs/meter³) in volume V . Again, the subscript “total” is used to denote that $\rho_{e,\text{total}}$ represents the density of total charges. Equation 1.2.8 is called *Gauss' law*, and Equation 1.2.9 is called Gauss' law for the magnetic case. Clearly, Equation 1.2.9 indicates that the magnetic flux lines cannot be originated or terminated anywhere; they have to form closed loops. In contrast, the electric field lines, as indicated in Equation 1.2.8, can be originated from positive charges and terminated at negative charges.

By denoting the differential surface vector $d\mathbf{S} = \hat{n}dA$ and the total charge enclosed inside V as

$$\mathcal{Q}(t) = \iiint_V \rho_{e,\text{total}}(\mathbf{r}, t) dV \quad (1.2.10)$$

Gauss' law in Equation 1.2.8 can be rewritten as

$$\oint_S \mathcal{E} \cdot \hat{n} dA = \frac{\mathcal{Q}}{\epsilon_0} \quad (1.2.11)$$

This equation is the subject of another folk song by Smith, which says

*Inside, outside, count the lines to tell—
If the charge is inside, there will be net flux as well.*

*If the charge is outside, be careful and you'll see
 The goings in and goings out are equal perfectly.
 If you wish to know the field precise,
 And the charge is symmetric,
 you will find this law is nice—
 Q upon a constant—eps'lon naught they say—
 Equals closed surface integral of E dot n dA.*

Equations 1.2.1, 1.2.2, 1.2.8, and 1.2.9 are usually referred to as Maxwell's equations in integral form. They are obtained directly from experiments and are valid everywhere for any case. They have been regarded as the fundamental postulates of electromagnetic theory ever since Maxwell formulated them over 140 years ago. The entire electromagnetic theory, valid from the static to the optical regimes and from subatomic to intergalactic length scales, is based on these four equations, as we will see repeatedly in this book.

1.2.2 Maxwell's Equations in Differential Form

The integral-form Maxwell's equations are valid everywhere. Now, consider a point in a continuous medium. The fields at such a point should be continuous; therefore, we can use Stokes' and Gauss' theorems to convert Maxwell's equations in integral form into their counterparts in differential form. To be more specific, by applying Stokes' theorem to Equations 1.2.1 and 1.2.2 and using the fact that these equations are valid for any surface S , we obtain

$$\nabla \times \mathcal{E} = -\frac{\partial \mathcal{B}}{\partial t} \quad (\text{Faraday's law}) \quad (1.2.12)$$

$$\nabla \times \mathcal{B} = \epsilon_0 \mu_0 \frac{\partial \mathcal{E}}{\partial t} + \mu_0 \mathcal{J}_{\text{total}} \quad (\text{Maxwell-Ampère law}) \quad (1.2.13)$$

respectively. Here, we omit the position vector and time variable for the sake of brevity. By applying Gauss' theorem to Equations 1.2.8 and 1.2.9 and using the fact that these are valid for any volume V , we obtain

$$\nabla \cdot \mathcal{E} = \frac{\rho_{e,\text{total}}}{\epsilon_0} \quad (\text{Gauss' law}) \quad (1.2.14)$$

$$\nabla \cdot \mathcal{B} = 0 \quad (\text{Gauss' law—magnetic}) \quad (1.2.15)$$

respectively. Equations 1.2.12 and 1.2.13 can also be obtained by shrinking the closed contour in Equations 1.2.1 and 1.2.2 to a point and then invoking the alternative definition of the curl given in Equation 1.1.10. Similarly, Equations 1.2.14 and 1.2.15 can also be obtained by shrinking the closed surface in Equations 1.2.8 and 1.2.9 to a point and then invoking the definition of the divergence in Equation 1.1.1. Therefore, Maxwell's equations in differential form describe field behavior at a point in a continuous medium.

1.2.3 Current Continuity Equation

By taking the divergence of Equation 1.2.13 and applying the vector identity (Eq. 1.1.40) and Gauss' law in Equation 1.2.14, we obtain

$$\nabla \cdot \mathcal{J}_{\text{total}} = -\frac{\partial \rho_{e,\text{total}}}{\partial t}. \quad (1.2.16)$$

To understand the implication of this equation, we can simply integrate it over a finite volume and apply Gauss' theorem in Equation 1.1.5 to find

$$\oint_S \mathcal{J}_{\text{total}} \cdot d\mathbf{S} = -\frac{d}{dt} \iiint_V \rho_{e,\text{total}} dV. \quad (1.2.17)$$

It is evident that the left-hand side represents the net current leaving the volume and the right-hand side represents the reduction rate of the total charge in the volume. As a result, this equation represents the *continuity of currents* or *conservation of charges*. Because of this continuity equation, the four Maxwell's equations are not independent for time-varying fields. This can be verified easily by taking the divergence of Equations 1.2.12 and 1.2.13 and then applying Equations 1.2.16 and 1.1.40, respectively, which would yield Equations 1.2.14 and 1.2.15. This, however, does not hold for the static fields because for such a case the currents and charges are no longer related and the electric and magnetic fields are completely decoupled; hence, all four equations have to be considered.

1.2.4 The Lorentz Force Law

When a particle carrying electric charge q is placed in an electric field, it experiences a force given by $q\mathcal{E}$. When this charge is moving in a magnetic field, it experiences another force given by $q\mathbf{v} \times \mathcal{B}$, where \mathbf{v} represents the velocity vector of the charge. Combining the two forces, we obtain the total force exerted on a charged particle as

$$\mathcal{F} = q(\mathcal{E} + \mathbf{v} \times \mathcal{B}) \quad (1.2.18)$$

which is known as the *Lorentz force law*. This law is useful for understanding the interaction between electromagnetic fields and matter, as we will discuss next. It is also the principle used in the design of many electrical devices such as electric motors, magnetrons, and particle accelerators.

1.3 CONSTITUTIVE RELATIONS

Maxwell's equations, as presented above, are valid in any kind of media. Since a medium has a significant effect on electromagnetic fields, we have to consider this effect in the study of electromagnetic fields. A medium affects electromagnetic fields through three phenomena—*electric polarization*, *magnetic polarization* or simply *magnetization*, and *electric conduction*. This section discusses these three phenomena and formulates a set of equations, known as *constitutive relations*, to account for the effect of a medium on electromagnetic fields. These constitutive relations are then used to classify media into various categories.

1.3.1 Electric Polarization

We first consider the effect of electric charges in a medium on electromagnetic fields. It is well known that a matter that makes up a medium is made of molecules, which consist of atoms. In an atom, there is a nucleus consisting of neutrons and protons. The neutrons are not charged, but the protons are positively charged. Surrounding a nucleus are

negatively charged electrons, whose number equals the number of protons. These electrons are bound to the nucleus by the electric force, so they normally cannot break free; instead, they orbit around the nucleus at high speed. The center of the orbit coincides with the center of the protons so that an entire atom is electrically neutral. A molecule is made up of one or more atoms. For some molecules, the atoms are arranged such that the center of positive charges coincides with that of negative charges. This type of molecule is called a *non-polar molecule*, and in such a case, the molecules and hence the matter that is made of non-polar molecules appear electrically neutral. For some other molecules, the interaction between atoms creates a small displacement between the effective centers of positive and negative charges, thus creating a tiny electric dipole and generating a weak electric field. This type of molecule is called a *polar molecule*. However, since all polar molecules are randomly oriented, the effects of tiny electric dipoles cancel each other and the matter that is made of polar molecules is also electrically neutral.

The scenario described above changes drastically when an electric field is applied to the medium. According to the Lorentz force law, the applied electric field exerts a force on positive charges in the direction of the field, whereas it exerts a force on negative charges in the opposite direction. As a result, in both atoms and non-polar molecules, the effective center of positive charges will be displaced from the effective center of negative charges, creating a tiny electric dipole in the direction of the electric field. (Here, we assume that the applied field is not strong enough to break the bound electrons loose from the nuclei. In such a case, the matter is often called a *dielectric*.) In the case of polar molecules, because of the Lorentz force, all the randomly oriented dipoles tend to line up with the applied electric field. When a large number of electric dipoles line in the same direction, the electric fields created by the dipoles add up and these electric fields are in the opposite direction to the applied field, resulting in a weaker total electric field in the medium. To quantify the effect of tiny dipoles, a vector quantity called the *dipole moment* is defined as

$$\boldsymbol{\mu} = q\boldsymbol{\ell} \quad (1.3.1)$$

where q denotes the charge and $\boldsymbol{\ell}$ denotes the vector pointing from the effective center of the negative charge to that of the positive charge. The sum of dipole moments per unit volume is then

$$\mathcal{P} = \lim_{\Delta v \rightarrow 0} \frac{1}{\Delta v} \sum_{i=1}^{n_p} \boldsymbol{\mu}_i \quad (1.3.2)$$

where n_p denotes the number of dipoles contained in Δv . The dipole moment density \mathcal{P} is also called the *polarization intensity* or *polarization vector*.

When the dipole moment density is uniform, the positive charge of a dipole is completely canceled by the negative charge of the next dipole; hence, there is no net charge in the medium. However, when the dipole moment density is not uniform, the positive charge of a dipole cannot be completely canceled by the negative charge of the next dipole, resulting in a net charge at the point and hence a volume charge density. This volume charge density is given by

$$\rho_{e,b} = -\nabla \cdot \mathcal{P} \quad (1.3.3)$$

where the subscript b is used to denote that this is the density of the bound charges. If the medium also contains free charges, the total charge density in the medium can then be expressed as

$$\rho_{e,\text{total}} = \rho_{e,f} + \rho_{e,b} = \rho_{e,f} - \nabla \cdot \mathcal{P} \quad (1.3.4)$$

where $\rho_{e,f}$ denotes the density of free electric charges. Substituting this expression into Equation 1.2.14, we obtain

$$\nabla \cdot (\epsilon_0 \mathcal{E} + \mathcal{P}) = \rho_{e,f}. \quad (1.3.5)$$

By defining a new quantity, called the *electric flux density*, as

$$\mathcal{D} = \epsilon_0 \mathcal{E} + \mathcal{P} \quad (1.3.6)$$

which has a unit of coulombs/meter², Equation 1.3.5 can be written as

$$\nabla \cdot \mathcal{D} = \rho_{e,f}. \quad (1.3.7)$$

This expression can be regarded as Gauss' law expressed in terms of free electric charges. In addition to the volume charge density, the electric polarization also produces an electric current when it changes in time. In view of the current continuity equation (Eq. 1.2.16), the electric current density contributed by the electric polarization is

$$\mathcal{J}_p = \frac{\partial \mathcal{P}}{\partial t}. \quad (1.3.8)$$

When this current is separated from the total current, Equation 1.2.13 can also be expressed in terms of \mathcal{D} defined in Equation 1.3.6.

In most dielectric materials, the polarization intensity is usually proportional to the electric field:

$$\mathcal{P} = \epsilon_0 \chi_e \mathcal{E} \quad (1.3.9)$$

where χ_e is called the *electric susceptibility*. Consequently, the electric flux density \mathcal{D} is related to the electric field intensity \mathcal{E} by

$$\mathcal{D} = \epsilon_0 (1 + \chi_e) \mathcal{E} = \epsilon \mathcal{E} \quad (1.3.10)$$

where $\epsilon = \epsilon_0 (1 + \chi_e)$ is called the *permittivity* of the dielectric. In engineering practice, we often use the relative permittivity, defined as $\epsilon_r = \epsilon / \epsilon_0 = 1 + \chi_e$, to help us memorize the value. Since χ_e is usually a positive number, ϵ_r is usually greater than 1. Equation 1.3.10 is called the *constitutive relation for the electric field*. In free space such as vacuum and air, the polarization intensity \mathcal{P} either vanishes or is negligible; hence, the constitutive relation (Eq. 1.3.10) becomes

$$\mathcal{D} = \epsilon_0 \mathcal{E}. \quad (1.3.11)$$

1.3.2 Magnetization

Next, we consider what happens when a magnetic field is applied to a medium. As mentioned earlier, electrons orbit the nucleus continuously in an atom. Such orbiting creates a tiny current loop, which generates a very weak magnetic field. Such a current loop can be quantified by a vector called the *magnetic dipole moment*, which is defined as

$$\mathbf{m} = I\mathbf{s} \quad (1.3.12)$$

where I denotes the current and \mathbf{a} has a magnitude equal to the area of the current loop and a direction determined by the direction of the current flow via the right-hand rule. Quantum physics reveals that all electrons and protons rotate at high speed about their own axes, a motion called *spin*. Since electrons and protons are charged, such a rotation also creates current loops, which generate very weak magnetic fields and can be quantified by magnetic dipole moments as well. In the absence of any applied fields, the directions of all the magnetic dipoles are randomly oriented (except for those in a permanent magnet). As a result, the magnetic dipole moments cancel out macroscopically and the medium appears magnetically neutral. When a magnetic field is applied to the medium, the randomly oriented magnetic dipoles tend to align themselves either in the direction of the applied field or in the opposite direction. This produces an observable quantity called *magnetization intensity* or *magnetization vector* \mathcal{M} , which is defined as the sum of the magnetic dipole moments per unit volume,

$$\mathcal{M} = \lim_{\Delta v \rightarrow 0} \frac{1}{\Delta v} \sum_{i=1}^{n_m} \mathbf{m}_i \quad (1.3.13)$$

where n_m denotes the number of magnetic dipoles contained in Δv . This magnetization vector will either strengthen or weaken the total magnetic field.

When the magnetic dipole density is uniform, the electric current of a current loop is completely canceled by the current of the next current loop; hence, there is no net electric current in the medium. However, when the magnetic dipole density is not uniform, the electric current of a current loop cannot be completely canceled by the current of the next current loop, which then results in a net current at the point. The volume current density of this current is given by

$$\mathcal{J}_m = \nabla \times \mathcal{M}. \quad (1.3.14)$$

Adding this current to the current due to the electric polarization and the free current, we have the total current in the medium

$$\mathcal{J}_{\text{total}} = \mathcal{J}_p + \mathcal{J}_m + \mathcal{J}_f = \frac{\partial \mathcal{D}}{\partial t} + \nabla \times \mathcal{M} + \mathcal{J}_f \quad (1.3.15)$$

where \mathcal{J}_f denotes the density of the free electric current. Substituting this into Equation 1.2.13, we obtain

$$\nabla \times \left(\frac{\mathcal{B}}{\mu_0} - \mathcal{M} \right) = \frac{\partial \mathcal{D}}{\partial t} + \mathcal{J}_f \quad (1.3.16)$$

where we have also used Equation 1.3.6. By defining a new magnetic quantity, called the *magnetic field intensity*, as

$$\mathcal{H} = \frac{\mathcal{B}}{\mu_0} - \mathcal{M} \quad (1.3.17)$$

which has a unit of amperes/meter, Equation 1.3.16 can be written as

$$\nabla \times \mathcal{H} = \frac{\partial \mathcal{D}}{\partial t} + \mathcal{J}_f. \quad (1.3.18)$$

This equation can be regarded as the Maxwell–Ampère law in terms of free electric currents. Note that there is no electric charge associated with \mathcal{J}_m since $\nabla \cdot \mathcal{J}_m = \nabla \cdot (\nabla \times \mathcal{M}) \equiv 0$.

Equation 1.3.17 can also be written as

$$\mathcal{B} = \mu_0(\mathcal{H} + \mathcal{M}). \quad (1.3.19)$$

In most materials, the magnetization intensity is proportional to the magnetic field intensity:

$$\mathcal{M} = \chi_m \mathcal{H} \quad (1.3.20)$$

where χ_m is called the *magnetic susceptibility*. In such a case, Equation 1.3.19 becomes

$$\mathcal{B} = \mu_0(1 + \chi_m) \mathcal{H} = \mu \mathcal{H} \quad (1.3.21)$$

where $\mu = \mu_0(1 + \chi_m)$ is called the *permeability* of the material. In engineering practice, we often use the relative permeability, defined as $\mu_r = \mu/\mu_0 = 1 + \chi_m$, to help us memorize the value. For most materials in reality, the magnetization is so small that $\mu_r \approx 1$ and such materials are called *non-magnetic*. Equation 1.3.21 is called the *constitutive relation for the magnetic field*. In free space such as vacuum and air, the magnetization intensity \mathcal{M} either vanishes or is negligible; hence, the constitutive relation (Eq. 1.3.21) is reduced to

$$\mathcal{B} = \mu_0 \mathcal{H}. \quad (1.3.22)$$

1.3.3 Electric Conduction

In addition to the polarization and magnetization, a third phenomenon is called *conduction*, which happens in a medium containing free charges such as free electrons and ions. In the absence of any fields, these charges move in random directions so that they do not form electric currents macroscopically. However, when an electric field is applied to the medium, the free charges tend to flow either in the direction of the applied field or in the opposite direction depending on whether they are positively or negatively charged. As a result, they form electric currents, which are called *conduction currents*. In most materials, the current density of the conduction current is proportional to the electric field, which can be expressed as

$$\mathcal{J}_c = \sigma \mathcal{E} \quad (1.3.23)$$

where σ is called the *conductivity* having a unit of siemens/meter. When the free charges such as electrons move in a medium, they collide with atomic lattices and their energy is dissipated and converted into heat. Hence, σ is also related to the dissipation of the energy. The conduction current can be regarded as a part of the free electric current.

1.3.4 Classification of Media

The preceding discussion indicates clearly that the electromagnetic properties of a medium are reflected in the following three constitutive relations:

$$\mathcal{D} = \epsilon \mathcal{E}, \quad \mathcal{B} = \mu \mathcal{H}, \quad \mathcal{J}_c = \sigma \mathcal{E}. \quad (1.3.24)$$

Therefore, the three parameters ϵ , μ , and σ fully characterize the electromagnetic properties of a medium. Consequently, we can classify media based on the forms and values of these parameters.

Classification Based on the Spatial Dependence If any of ϵ , μ , or σ is a function of position in space, the medium is called *inhomogeneous* or *heterogeneous*. Otherwise, it is called a *homogeneous* medium, where $\nabla\epsilon = \nabla\mu = \nabla\sigma \equiv 0$. A homogeneous medium affects electromagnetic fields through the polarization current \mathcal{J}_p and the bound charges and currents on the surface of the medium.

Classification Based on the Time Dependence If any of ϵ , μ , or σ is a function of time, the medium is called *non-stationary*; otherwise, it is called *stationary*. Note that even if a medium is physically stationary, it can still be electrically non-stationary if its electromagnetic properties change with time.

Classification Based on the Directions of \mathcal{D} and \mathcal{B} If the direction of \mathcal{D} is parallel to that of \mathcal{E} and the direction of \mathcal{B} is parallel to that of \mathcal{H} , the medium is called *isotropic*. Otherwise, it is called an *anisotropic* medium. For an anisotropic medium, the constitutive relations cannot be expressed in a simple form as in Equation 1.3.24. Instead, they have to be expressed as

$$\begin{bmatrix} \mathcal{D}_x \\ \mathcal{D}_y \\ \mathcal{D}_z \end{bmatrix} = \begin{bmatrix} \epsilon_{xx} & \epsilon_{xy} & \epsilon_{xz} \\ \epsilon_{yx} & \epsilon_{yy} & \epsilon_{yz} \\ \epsilon_{zx} & \epsilon_{zy} & \epsilon_{zz} \end{bmatrix} \begin{bmatrix} \mathcal{E}_x \\ \mathcal{E}_y \\ \mathcal{E}_z \end{bmatrix}, \quad \begin{bmatrix} \mathcal{B}_x \\ \mathcal{B}_y \\ \mathcal{B}_z \end{bmatrix} = \begin{bmatrix} \mu_{xx} & \mu_{xy} & \mu_{xz} \\ \mu_{yx} & \mu_{yy} & \mu_{yz} \\ \mu_{zx} & \mu_{zy} & \mu_{zz} \end{bmatrix} \begin{bmatrix} \mathcal{H}_x \\ \mathcal{H}_y \\ \mathcal{H}_z \end{bmatrix} \quad (1.3.25)$$

which can be written compactly as

$$\mathcal{D} = \tilde{\epsilon} \cdot \mathcal{E}, \quad \mathcal{B} = \tilde{\mu} \cdot \mathcal{H} \quad (1.3.26)$$

where $\tilde{\epsilon}$ and $\tilde{\mu}$ are called permittivity and permeability tensors.³ When we discuss the reciprocity theorem, we will see that if these two tensors are symmetric, the medium is *reciprocal*; otherwise, it is *non-reciprocal*. A special case of general anisotropic media is crystals, which have a diagonal permittivity tensor,

$$\tilde{\epsilon} = \begin{bmatrix} \epsilon_{xx} & 0 & 0 \\ 0 & \epsilon_{yy} & 0 \\ 0 & 0 & \epsilon_{zz} \end{bmatrix}. \quad (1.3.27)$$

In this case, if all three diagonal elements are different, the medium is called *biaxial*. If any two of the three are the same, the medium is called *uniaxial*. Of course, if all three elements are the same, the medium is *isotropic*. A further generalization of the anisotropic medium is the so-called *bianisotropic* medium, whose constitutive relations are given by

$$\mathcal{D} = \tilde{\epsilon} \cdot \mathcal{E} + \tilde{\xi} \cdot \mathcal{H}, \quad \mathcal{B} = \tilde{\mu} \cdot \mathcal{H} + \tilde{\zeta} \cdot \mathcal{E}. \quad (1.3.28)$$

When $\tilde{\epsilon}$, $\tilde{\mu}$, $\tilde{\xi}$, and $\tilde{\zeta}$ reduce to scalars, the medium is called *bi-isotropic*. These kinds of materials are rare in nature, but they can be manufactured in laboratories.

Classification Based on the Field Dependence If any value of ϵ , μ , or σ depends on the field intensities \mathcal{E} and \mathcal{H} , then the flux densities \mathcal{D} and \mathcal{B} and the conduction current density \mathcal{J}_c are no longer linear functions of \mathcal{E} and \mathcal{H} . Such a medium is called *non-linear*; otherwise, it is called *linear*. Non-linear constitutive relations significantly complicate the study of the electromagnetic fields in the medium; nevertheless, non-linear media do exist in nature even though their applications are not widespread.

Classification Based on the Frequency Dependence If any value of ϵ or μ depends on the frequency of the field such that $\epsilon = \epsilon(f)$ or $\mu = \mu(f)$, where f denotes the frequency, the medium is called *dispersive*; otherwise, it is called *non-dispersive*. If a signal that contains multiple frequencies propagates in a dispersive medium, the shape of the signal will be distorted because different frequency components propagate at different speeds. Rigorously speaking, for a dispersive medium, the constitutive relations can no longer be written in the form of Equation 1.3.24. Because of the frequency dependence, they have to be written in terms of convolution:

$$\mathcal{D} = \epsilon_0 \mathcal{E} + \epsilon_0 \chi_e * \mathcal{E} = \epsilon_0 \mathcal{E} + \epsilon_0 \int_{-\infty}^t \chi_e(t-\tau) \mathcal{E}(\tau) d\tau \quad (1.3.29)$$

$$\mathcal{B} = \mu_0 \mathcal{H} + \mu_0 \chi_m * \mathcal{H} = \mu_0 \mathcal{H} + \mu_0 \int_{-\infty}^t \chi_m(t-\tau) \mathcal{H}(\tau) d\tau \quad (1.3.30)$$

where $*$ denotes the temporal convolution. The convolution is due to the fact that the medium cannot polarize and magnetize instantaneously in response to the applied field and, therefore, the polarization and magnetization vectors are related to the fields at previous times.

Classification Based on the Value of Conductivity If $\sigma = 0$, the medium is called a *perfect dielectric* or *insulator*. On the other hand, if $\sigma \rightarrow \infty$, the medium is called a *perfect electric conductor* (PEC). In reality, there are no such things as perfect dielectrics or perfect conductors. But, in engineering practice, these are very useful concepts because the approximation of a very good conductor as a perfect conductor and the approximation of a good dielectric as a perfect dielectric can significantly simplify the analysis of electromagnetic problems. When σ has a non-negligible finite value, the medium is called *lossy*. It should be pointed out that the conduction characterized by σ represents only one of the loss mechanisms. When a medium is exposed to a time-varying electromagnetic field, the polarization and magnetization can also cause losses, especially when the frequency of the field is very high. This is because the directions of time-varying electric and magnetic fields change rapidly and, consequently, the electric and magnetic dipoles that follow the field directions change their directions as well. When these dipoles flip back and forth, the friction between the bound charges and dipoles causes energy dissipation. This phenomenon can be described mathematically in the time domain as a damping term in the motion equation for the dipoles [13]; however (and very fortunately) its description in the frequency domain is very simple. The Fourier transforms of the permittivity and permeability simply become two complex quantities with the imaginary parts representing the polarization and magnetization losses.

Classification Based on the Value of Permeability As discussed earlier, when a magnetic field is applied to a medium, the randomly oriented magnetic dipoles tend to align themselves either in the direction of the applied field or in the opposite direction, producing a net magnetization intensity \mathcal{M} . When this net magnetization intensity is very

small and its direction is opposite to the direction of the applied field, the magnetic susceptibility χ_m is a very small negative number and the relative permeability μ_r is slightly less than 1. This type of medium is called *diamagnetic*. When the net magnetization intensity is again very small but its direction is in the direction of the applied field, the magnetic susceptibility χ_m is a very small positive number and the relative permeability μ_r is slightly greater than 1. The medium is called *paramagnetic*. For both diamagnetic and paramagnetic media, the value of μ_r differs from 1 by any amount on the order of 10^{-4} . In most engineering applications, this difference can be neglected and μ_r can be practically approximated as $\mu_r \approx 1.0$; hence, the medium can be considered as *non-magnetic*. However, there is a type of medium in which the net magnetization intensity has a very large value and its direction is the same as that of the applied field, resulting in a large relative permeability μ_r . This type of medium is called *ferromagnetic*. Ferromagnetic materials usually have a high conductivity, and hence cannot sustain an appreciable electromagnetic field. There is yet another class of materials, called *ferrites*, which have a relatively large permeability and a very small conductivity at microwave frequencies. Because of this, ferrites find many applications in the design of microwave devices.

1.4 MAXWELL'S EQUATIONS IN TERMS OF FREE CHARGES AND CURRENTS

With the constitutive relations (Eq. 1.3.24), Maxwell's equations in integral form can be written for \mathcal{E} , \mathcal{H} , \mathcal{D} , and \mathcal{B} in terms of free charges and currents as

$$\oint_c \mathcal{E} \cdot d\mathbf{l} = -\frac{d}{dt} \iint_s \mathcal{B} \cdot d\mathbf{S} \quad (\text{Faraday's law}) \quad (1.4.1)$$

$$\oint_c \mathcal{H} \cdot d\mathbf{l} = \frac{d}{dt} \iint_s \mathcal{D} \cdot d\mathbf{S} + \iint_s \mathcal{J}_f \cdot d\mathbf{S} \quad (\text{Maxwell-Ampère law}) \quad (1.4.2)$$

$$\iint_s \mathcal{D} \cdot d\mathbf{S} = \iiint_V \rho_{e,f} dV \quad (\text{Gauss' law}) \quad (1.4.3)$$

$$\iint_s \mathcal{B} \cdot d\mathbf{S} = 0 \quad (\text{Gauss' law—magnetic}). \quad (1.4.4)$$

The free current \mathcal{J}_f includes the conduction current $\mathcal{J}_c = \sigma \mathcal{E}$ and the current supplied by impressed sources.

Equations 1.4.1–1.4.4 are asymmetric because of the lack of magnetic currents and charges. Although magnetic currents and charges do not exist or have not been found so far in reality, the concepts of such currents and charges are useful because sometimes we can introduce equivalent magnetic currents and charges to simplify the analysis of some electromagnetic problems. By incorporating magnetic currents and charges, Equations 1.4.1 and 1.4.4 become

$$\oint_c \mathcal{E} \cdot d\mathbf{l} = -\frac{d}{dt} \iint_s \mathcal{B} \cdot d\mathbf{S} - \iint_s \mathcal{M}_f \cdot d\mathbf{S} \quad (\text{Faraday's law}) \quad (1.4.5)$$

$$\iint_s \mathcal{B} \cdot d\mathbf{S} = \iiint_V \rho_{m,f} dV \quad (\text{Gauss' law—magnetic}) \quad (1.4.6)$$

where \mathcal{M}_f denotes the free magnetic current density (volts/meter²) and $\rho_{m,f}$ denotes the free magnetic charge density (webers/meter³). With this modification, Maxwell's equations become more symmetric. The reader is cautioned not to confuse the magnetic current density \mathcal{M}_f with the magnetization intensity \mathcal{M} used previously.

The corresponding Maxwell's equations in differential form for fields at a point in a continuous medium can be obtained by invoking Stokes' and Gauss' theorems. They can be written as

$$\nabla \times \mathcal{E} = -\frac{\partial \mathcal{B}}{\partial t} - \mathcal{M}_f \quad (\text{Faraday's law}) \quad (1.4.7)$$

$$\nabla \times \mathcal{H} = \frac{\partial \mathcal{D}}{\partial t} + \mathcal{J}_f \quad (\text{Maxwell-Ampère law}) \quad (1.4.8)$$

$$\nabla \cdot \mathcal{D} = \rho_{e,f} \quad (\text{Gauss' law}) \quad (1.4.9)$$

$$\nabla \cdot \mathcal{B} = \rho_{m,f} \quad (\text{Gauss' law—magnetic}). \quad (1.4.10)$$

The free charges and currents also satisfy the current continuity equations, which can be derived from Equations 1.4.7–1.4.10 by taking the divergence of Equations 1.4.7 and 1.4.8 and then applying the vector identity (Eq. 1.1.40) and Gauss' laws in Equations 1.4.9 and 1.4.10. Their differential forms are given by

$$\nabla \cdot \mathcal{J}_f = -\frac{\partial \rho_{e,f}}{\partial t} \quad (1.4.11)$$

$$\nabla \cdot \mathcal{M}_f = -\frac{\partial \rho_{m,f}}{\partial t}. \quad (1.4.12)$$

The corresponding integral forms can be obtained by integrating these two equations over a finite volume and then applying Gauss' theorem in Equation 1.1.5, yielding

$$\oint_S \mathcal{J}_f \cdot d\mathbf{S} = -\frac{d}{dt} \iiint_V \rho_{e,f} dV \quad (1.4.13)$$

$$\oint_S \mathcal{M}_f \cdot d\mathbf{S} = -\frac{d}{dt} \iiint_V \rho_{m,f} dV. \quad (1.4.14)$$

Because of these continuity conditions, the four Maxwell's equations in Equations 1.4.7–1.4.10 are not independent for time-varying fields since Equations 1.4.9 and 1.4.10 can be derived from Equations 1.4.8 and 1.4.7, respectively.

Although Maxwell's equations for free charges and currents appear quite different from those for total charges and currents, both can be written uniformly in the form presented in this section with the charge and current densities defined based on the constitutive relations used. This is the subject of Problem 1.15. In engineering, we often prefer Maxwell's equations in terms of free charges and currents over the ones for total charges and currents because the total charges and currents are usually unknown before Maxwell's equations are solved, whereas the constitutive parameters ϵ , μ , and σ can usually be measured experimentally.

1.5 BOUNDARY CONDITIONS

The differential-form Maxwell's equations are valid at points in a continuous medium. They cannot be applied to discontinuous fields that may occur at interfaces between different media. Fortunately, we can employ Maxwell's equations in integral form to find the relations between the fields on the two sides of an interface. Such relations are called *boundary conditions*. The relationship between the integral-form Maxwell's equations and the differential-form Maxwell's equations and the boundary conditions is illustrated in Figure 1.1. In this section we derive these boundary conditions using Maxwell's equations for free charges and currents. Hence, all the charge and current quantities used in this section are pertinent to free charges and currents.

Before deriving the boundary conditions, let us first introduce the concept of surface currents. So far, the current density \mathcal{J}_f is actually a volume current density, which is often simply called current density. It represents the amount of current passing through a unit area normal to the direction of the current flow. Now, imagine a current flow confined in a thin layer. If the total current is kept constant while the thickness of the layer is reduced to zero, the volume current density approaches infinity, which can no longer describe the current sheet. In this case, the current distribution can be described by the surface current density, which is a vector denoted as \mathcal{J}_s . Its value represents the amount of current passing through a unit width normal to the direction of the current flow and has a unit of amperes/meter. The surface magnetic current density \mathcal{M}_s is defined similarly, which has a unit of volts/meter.

Now, let us consider an interface between two different media, and for the sake of generality a free surface current with a density of \mathcal{J}_s is assumed flowing on the interface. The normal unit vector \hat{n} on the interface is defined to point from medium 1 to medium 2. To apply Equation 1.4.2, we construct a small rectangular frame with one of its sides in medium 1 and the other in medium 2, as illustrated in Figure 1.2. The length of the frame is Δl and the width Δt is vanishingly small. Applying Equation 1.4.2 to this frame and letting $\Delta t \rightarrow 0$, we have

$$\mathcal{H}_1 \cdot \hat{t} \Delta l - \mathcal{H}_2 \cdot \hat{t} \Delta l = \mathcal{J}_s \cdot (\hat{t} \times \hat{n}) \Delta l \quad (1.5.1)$$

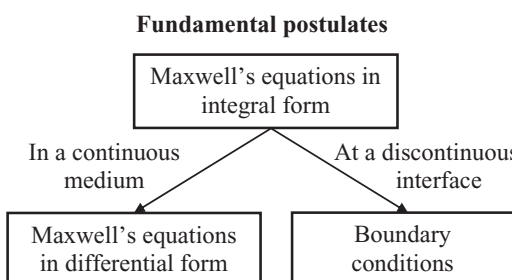


Figure 1.1 Relationship between Maxwell's equations in integral and differential forms and boundary conditions.

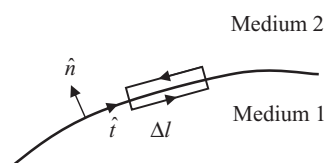


Figure 1.2 A rectangular frame across a discontinuous interface.

where \hat{t} is a tangential unit vector as shown in Figure 1.2. Since the direction of \hat{t} is not uniquely determined, it is desirable to remove it from Equation 1.5.1. For this, we rewrite \hat{t} as $\hat{t} = \hat{n} \times (\hat{t} \times \hat{n})$ and employ the vector identity

$$\mathbf{a} \cdot (\mathbf{b} \times \mathbf{c}) = \mathbf{b} \cdot (\mathbf{c} \times \mathbf{a}) = \mathbf{c} \cdot (\mathbf{a} \times \mathbf{b}) \quad (1.5.2)$$

to find

$$(\hat{n} \times \mathcal{H}_2) \cdot (\hat{t} \times \hat{n}) - (\hat{n} \times \mathcal{H}_1) \cdot (\hat{t} \times \hat{n}) = \mathcal{J}_s \cdot (\hat{t} \times \hat{n}). \quad (1.5.3)$$

Since the orientation of \hat{t} and, thus, $\hat{t} \times \hat{n}$, is arbitrary along the surface, we have

$$\hat{n} \times (\mathcal{H}_2 - \mathcal{H}_1) = \mathcal{J}_s \quad (1.5.4)$$

which indicates that the tangential component of the magnetic field intensity is discontinuous across an interface carrying a free surface electric current. By applying the same approach to Equation 1.4.5, we obtain another boundary condition

$$\hat{n} \times (\mathcal{D}_2 - \mathcal{D}_1) = -\mathcal{M}_s \quad (1.5.5)$$

showing a discontinuity in the tangential component of the electric field intensity across an interface carrying a free surface magnetic current. Since the magnetic current does not exist in reality, the tangential component of the electric field intensity is always continuous across any interfaces.

Next, we consider an interface between two different media and we assume a free surface charge distribution over the interface. The surface charge density is defined as the amount of charge over a unit area on the surface. To apply Equation 1.4.3, we construct a small pillbox with one of its faces in medium 1 and the other in medium 2, as illustrated in Figure 1.3. Each face of the pillbox has an area Δs and its thickness Δt is vanishingly small. Applying Equation 1.4.3 to this pillbox and letting $\Delta t \rightarrow 0$, we obtain

$$\mathcal{D}_{2n} \Delta s - \mathcal{D}_{1n} \Delta s = \rho_{e,s} \Delta s \quad (1.5.6)$$

or

$$\hat{n} \cdot (\mathcal{D}_2 - \mathcal{D}_1) = \rho_{e,s} \quad (1.5.7)$$

where $\rho_{e,s}$ denotes the surface electric charge density having a unit of coulombs/meter². This reveals that the normal component of the electric flux density is discontinuous across an interface carrying a free surface electric charge. By applying the same procedure to Equation 1.4.6, we obtain

$$\hat{n} \cdot (\mathcal{B}_2 - \mathcal{B}_1) = \rho_{m,s} \quad (1.5.8)$$

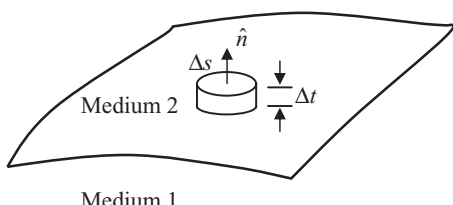


Figure 1.3 A pillbox across a discontinuous interface.

which shows that the normal component of the magnetic flux density is discontinuous across an interface carrying a free surface magnetic charge. Here, $\rho_{m,s}$ denotes the surface magnetic charge density and has a unit of webers/meter². However, since in reality the magnetic charges do not exist, the normal component of the magnetic flux density is always continuous across any interfaces.

Similar to the case for Maxwell's equations, the four boundary conditions in Equations 1.5.4, 1.5.5, 1.5.7, and 1.5.8 are not independent. When the first two are satisfied, the latter two are usually satisfied as well. Also note that unless one of the media is a perfect conductor, the electromagnetic fields usually cannot induce free surface charges or currents at the interface. Hence, the tangential component of the magnetic field intensity and the normal component of the electric flux density are continuous across an interface between two different media. However, when one of the media is a perfect conductor, the situation is different. A perfect conductor is a medium full of free charges. When an electromagnetic field is applied to this medium, the free charges, being pushed by the applied field, move themselves such that they produce an opposing field that completely cancels the applied field. This causes the formation of the surface currents and charges on the surface of a perfect conductor. If it is a PEC, its surface can support a surface electric current and charge. If it is a *perfect magnetic conductor* (PMC), the surface can support a surface magnetic current and charge. Now, assuming that medium 1 is a PEC, the boundary conditions at the surface become

$$\hat{n} \times \mathcal{B} = 0 \quad (1.5.9)$$

$$\hat{n} \times \mathcal{H} = \mathcal{J}_s \quad (1.5.10)$$

$$\hat{n} \cdot \mathcal{D} = \rho_{e,s} \quad (1.5.11)$$

$$\hat{n} \cdot \mathcal{B} = 0 \quad (1.5.12)$$

where the unit normal \hat{n} points away from the conductor. As mentioned earlier, it is unnecessary to enforce all these conditions when solving an electromagnetic problem. It is usually sufficient to enforce either Equation 1.5.9 or 1.5.12 since the other two conditions involve the induced surface current and charge densities, which are usually unknown. However, if the fields are known, Equations 1.5.10 and 1.5.11 provide a means to calculate the induced surface current and charge densities. The boundary conditions at the surface of a PMC can be deduced in a similar fashion.

We wish to point out that the boundary conditions are as important as Maxwell's equations because they describe the field behavior across a discontinuous interface, whereas the differential-form Maxwell's equations describe the field behavior in a continuous medium, as illustrated clearly in Figure 1.1. Without boundary conditions, an electromagnetic problem is usually not completely defined and cannot be solved. Furthermore, understanding these boundary conditions can allow us to have a general idea about the field distribution in a given electromagnetic problem and help us to deal with the problem more effectively.

1.6 ENERGY, POWER, AND POYNTING'S THEOREM

Energy and power are two of the most fundamental quantities in physics. They play very important roles in electromagnetics as well. In this section, we start from Maxwell's equations and establish relations between electromagnetic fields and energy and power.

To start, we consider a medium characterized by permittivity ϵ , permeability μ , and conductivity σ . Maxwell's equations (Eqs. 1.4.7 and 1.4.8) in such a medium can be written as

$$\nabla \times \mathcal{E} = -\mu \frac{\partial \mathcal{H}}{\partial t} - \mathcal{M}_i \quad (1.6.1)$$

$$\nabla \times \mathcal{H} = \epsilon \frac{\partial \mathcal{E}}{\partial t} + \sigma \mathcal{E} + \mathcal{J}_i \quad (1.6.2)$$

where \mathcal{J}_i and \mathcal{M}_i represent the actual source of the field and are often referred to as the *impressed currents*. In Equation 1.6.2, the total current is separated into the conduction current and the impressed current. By taking the dot product of Equation 1.6.1 with \mathcal{H} and the dot product of Equation 1.6.2 with \mathcal{E} and subtracting the latter from the former, we obtain

$$\mathcal{H} \cdot (\nabla \times \mathcal{E}) - \mathcal{E} \cdot (\nabla \times \mathcal{H}) = -\epsilon \mathcal{E} \cdot \frac{\partial \mathcal{E}}{\partial t} - \mu \mathcal{H} \cdot \frac{\partial \mathcal{H}}{\partial t} - \sigma \mathcal{E} \cdot \mathcal{E} - \mathcal{E} \cdot \mathcal{J}_i - \mathcal{H} \cdot \mathcal{M}_i \quad (1.6.3)$$

which can also be written as

$$\nabla \cdot (\mathcal{E} \times \mathcal{H}) + \epsilon \mathcal{E} \cdot \frac{\partial \mathcal{E}}{\partial t} + \mu \mathcal{H} \cdot \frac{\partial \mathcal{H}}{\partial t} + \sigma \mathcal{E} \cdot \mathcal{E} + \mathcal{E} \cdot \mathcal{J}_i + \mathcal{H} \cdot \mathcal{M}_i = 0 \quad (1.6.4)$$

using the vector identity $\nabla \cdot (\mathcal{E} \times \mathcal{H}) = \mathcal{H} \cdot (\nabla \times \mathcal{E}) - \mathcal{E} \cdot (\nabla \times \mathcal{H})$. To understand the physical meaning of this equation, we first integrate it over a finite volume, and by using Gauss' theorem, we obtain

$$\oint_S (\mathcal{E} \times \mathcal{H}) \cdot \hat{n} dS + \iiint_V \left(\epsilon \mathcal{E} \cdot \frac{\partial \mathcal{E}}{\partial t} + \mu \mathcal{H} \cdot \frac{\partial \mathcal{H}}{\partial t} + \sigma \mathcal{E} \cdot \mathcal{E} + \mathcal{E} \cdot \mathcal{J}_i + \mathcal{H} \cdot \mathcal{M}_i \right) dV = 0 \quad (1.6.5)$$

where S is the surface enclosing V and \hat{n} is the normal unit vector pointing outward. Next, we check the unit of each term. First, $\mathcal{E} \times \mathcal{H}$ has a unit of volts/meter · amperes/meter = watts/meter², which is the unit of power flux density. A dot product with \hat{n} and then integration over a closed surface S would yield total power passing through the surface, either entering or exiting. We denote this term as \mathcal{P}_e :

$$\mathcal{P}_e = \oint_S (\mathcal{E} \times \mathcal{H}) \cdot \hat{n} dS. \quad (1.6.6)$$

Second, we rewrite

$$\epsilon \mathcal{E} \cdot \frac{\partial \mathcal{E}}{\partial t} = \frac{1}{2} \epsilon \frac{\partial \mathcal{E}^2}{\partial t} = \frac{\partial}{\partial t} \left(\frac{1}{2} \epsilon \mathcal{E}^2 \right) = \frac{\partial \omega_e}{\partial t} \quad (1.6.7)$$

where $\omega_e = \frac{1}{2} \epsilon \mathcal{E}^2$. This quantity has a unit of farads/meter · (volts/meter)² = joules/meter³, which represents energy density. Its integral over a volume would represent the total energy in the volume:

$$\mathcal{W}_e = \iiint_V \omega_e dV = \frac{1}{2} \iiint_V \epsilon \mathcal{E}^2 dV. \quad (1.6.8)$$

Since this energy is associated with the electric field, it can be termed as the *electric energy*. Similarly, we find that

$$\mu\mathcal{H} \cdot \frac{\partial \mathcal{H}}{\partial t} = \frac{1}{2}\mu \frac{\partial \mathcal{H}^2}{\partial t} = \frac{\partial}{\partial t} \left(\frac{1}{2}\mu\mathcal{H}^2 \right) = \frac{\partial \omega_m}{\partial t} \quad (1.6.9)$$

where $\omega_m = \frac{1}{2}\mu\mathcal{H}^2$ represents the magnetic energy density. Its integration over a volume represents the total *magnetic energy* in the volume:

$$\mathcal{W}_m = \iiint_V \omega_m dV = \frac{1}{2} \iiint_V \mu\mathcal{H}^2 dV. \quad (1.6.10)$$

With these observations, we can now consider a special case, where the volume is lossless and does not contain any source. In such a case, Equation 1.6.5 can be written as

$$\mathcal{P}_e = -\frac{d(\mathcal{W}_e + \mathcal{W}_m)}{dt}. \quad (1.6.11)$$

The right-hand side represents the rate of decrease in the total energy in volume V . Based on energy conservation, the left-hand side must represent the power exiting through the surface of the volume.

With the interpretations above, we can readily find that

$$\mathcal{P}_d = \iiint_V \sigma \mathcal{E} \cdot \mathcal{E} dV = \iiint_V \sigma \mathcal{E}^2 dV \quad (1.6.12)$$

represents the power dissipated in the volume and

$$\mathcal{P}_s = -\iiint_V (\mathcal{E} \cdot \mathcal{J}_i + \mathcal{H} \cdot \mathcal{M}_i) dV \quad (1.6.13)$$

represents the power supplied by the source. By using these notations, Equation 1.6.5 can be written as

$$\mathcal{P}_s = \mathcal{P}_e + \mathcal{P}_d + \frac{d}{dt}(\mathcal{W}_e + \mathcal{W}_m) \quad (1.6.14)$$

which states that in a volume the supplied power must be equal to the sum of the exiting power, the dissipated power, and the rate of increase in the total energy in the volume. Obviously, Equation 1.6.14 is the statement of the *conservation of energy* for electromagnetic fields, which is also known as *Poynting's theorem*. Denote

$$\rho_e = \nabla \cdot (\mathcal{E} \times \mathcal{H}), \quad \rho_d = \sigma \mathcal{E} \cdot \mathcal{E}, \quad \rho_s = -(\mathcal{E} \cdot \mathcal{J}_i + \mathcal{H} \cdot \mathcal{M}_i). \quad (1.6.15)$$

Equation 1.6.4 can be written as

$$\rho_s = \rho_e + \rho_d + \frac{\partial}{\partial t}(\omega_e + \omega_m) \quad (1.6.16)$$

which is the statement of the conservation of energy in differential form. Equation 1.6.14 or 1.6.16 establishes a relation between five quantities. Knowing any four quantities, the remaining quantity can be calculated easily. This can be useful in a variety of applications where the desired quantity cannot be measured directly, but can be evaluated indirectly.

As illustrated above, $\mathcal{E} \times \mathcal{H}$ represents the power flux density in the direction determined by the cross-product. This quantity is named the *Poynting vector*, defined as

$$\mathcal{S} = \mathcal{E} \times \mathcal{H} \quad (1.6.17)$$

which indicates that once both the electric and magnetic fields are known at any point in space, the power flow density is determined and the power flow is perpendicular to the directions of the electric and magnetic fields. The directions of \mathcal{E} , \mathcal{H} , and \mathcal{S} obey the right-hand rule.

1.7 TIME-HARMONIC FIELDS

Maxwell's equations in differential form represent a set of partial differential equations in four dimensions: three spatial dimensions and one in time. Such a mathematical problem is very difficult to deal with simply because of its high dimensionality. The complexity of the problem can be greatly reduced if the number of dimensions is lowered. Very fortunately, many problems in electrical engineering deal with time-harmonic fields—fields that oscillate at a single frequency. For such a time-harmonic field, the differentiation with time can be evaluated and the time variable can be eliminated, reducing Maxwell's equations to ones containing only three spatial variables. Since a non-time-harmonic field can be decomposed into many time-harmonic fields with different frequencies, the study of time-harmonic fields also enables the solution of general time-varying problems with the aid of the Fourier transform. This section introduces the concept of the time-harmonic field, derives its Maxwell's equations, and discusses the related energy and power.

1.7.1 Time-Harmonic Fields

When the currents, charges, and fields oscillate at a single frequency, each quantity can be expressed as a sinusoidal function with an amplitude and a phase. For example, the electric field can be written as

$$\mathcal{E}(\mathbf{r}, t) = \mathbf{E}_0(\mathbf{r}) \cos[\omega t + \alpha(\mathbf{r})] \quad (1.7.1)$$

where \mathbf{E}_0 denotes the amplitude, α denotes the phase, and ω is the angular frequency. Using Euler's formula, this can be written as

$$\mathcal{E}(\mathbf{r}, t) = \mathbf{E}_0(\mathbf{r}) \operatorname{Re}[e^{j\omega t + j\alpha(\mathbf{r})}] = \operatorname{Re}[\mathbf{E}_0(\mathbf{r}) e^{j\alpha(\mathbf{r})} e^{j\omega t}] \quad (1.7.2)$$

where $j = \sqrt{-1}$ and Re stands for the real part. Now, define a complex quantity

$$\mathbf{E}(\mathbf{r}) = \mathbf{E}_0(\mathbf{r}) e^{j\alpha(\mathbf{r})} \quad (1.7.3)$$

which contains both the amplitude and phase of the field and is only a spatial function. Equation 1.7.2 can be written as

$$\mathcal{E}(\mathbf{r}, t) = \operatorname{Re}[\mathbf{E}(\mathbf{r}) e^{j\omega t}]. \quad (1.7.4)$$

The complex quantity defined in Equation 1.7.3 is called a *phasor*. By expressing each of the source and field quantities in the form of Equation 1.7.4 and substituting them into Equation 1.4.7, we obtain

$$\operatorname{Re}[\nabla \times \mathbf{E} e^{j\omega t}] = -\operatorname{Re}[j\omega \mathbf{B} e^{j\omega t}] - \operatorname{Re}[\mathbf{M}_f e^{j\omega t}]. \quad (1.7.5)$$

Since this is valid for any time variable t , we have

$$\nabla \times \mathbf{E} = -j\omega \mathbf{B} - \mathbf{M}_f \quad (\text{Faraday's law}) \quad (1.7.6)$$

which no longer contains the time variable. It represents a partial differential equation in a three-dimensional space, whereas Equation 1.4.7 is an equation in a four-dimensional space. Applying the same procedure to other Maxwell's equations, we obtain

$$\nabla \times \mathbf{H} = j\omega \mathbf{D} + \mathbf{J}_f \quad (\text{Maxwell-Ampère law}) \quad (1.7.7)$$

$$\nabla \cdot \mathbf{D} = \rho_{e,f} \quad (\text{Gauss' law}) \quad (1.7.8)$$

$$\nabla \cdot \mathbf{B} = \rho_{m,f} \quad (\text{Gauss' law—magnetic}). \quad (1.7.9)$$

Similarly, the continuity equations become

$$\nabla \cdot \mathbf{J}_f = -j\omega \rho_{e,f} \quad (1.7.10)$$

$$\nabla \cdot \mathbf{M}_f = -j\omega \rho_{m,f}. \quad (1.7.11)$$

Clearly, in this conversion, all one has to do is to replace the time derivative $\partial/\partial t$ with $j\omega$. We can do the same to Maxwell's equations in integral form and boundary conditions to obtain the corresponding equations for the phasors. In particular, the boundary conditions remain in the same form because they do not contain any time derivatives. Therefore, for time-harmonic fields, we only have to deal with Maxwell's equations in three dimensions. Once the phasors are solved for, we can use expressions such as Equations 1.7.4 to obtain the corresponding instantaneous quantities.

Dealing with an electromagnetic problem in terms of frequency not only simplifies the problem itself, but also makes the solution more interpretable. Many physical quantities of interest in electromagnetics are expressed as functions of frequency, instead of time. These quantities can be calculated directly from the phasors; hence, solution to phasors is usually sufficient in many applications.

1.7.2 Fourier Transforms

The preceding introduction of the concept of phasors gives the impression that the solution to Maxwell's equations for the phasors is restricted to time-harmonic fields. This is actually false. It is well known that an arbitrary function of time can be expressed as a Fourier integral,

$$\mathcal{F}(t) = \frac{1}{2\pi} \int_{-\infty}^{\infty} f(\omega) e^{j\omega t} d\omega \quad (1.7.12)$$

where $f(\omega)$ is called the *Fourier transform* of $\mathcal{F}(t)$ and is given by

$$f(\omega) = \int_{-\infty}^{\infty} \mathcal{F}(t) e^{-j\omega t} dt. \quad (1.7.13)$$

Accordingly, Equation 1.7.12 is called the *inverse Fourier transform*. This Fourier transform can be applied to all the source and field quantities. For example, the electric field can be written as

$$\mathcal{E}(\mathbf{r}, t) = \frac{1}{2\pi} \int_{-\infty}^{\infty} \mathbf{E}(\mathbf{r}, \omega) e^{j\omega t} d\omega \quad (1.7.14)$$

where

$$\mathbf{E}(\mathbf{r}, \omega) = \int_{-\infty}^{\infty} \mathcal{E}(\mathbf{r}, t) e^{-j\omega t} dt. \quad (1.7.15)$$

Substituting the Fourier transform for each of the source and field quantities into Equation 1.4.7, we obtain

$$\int_{-\infty}^{\infty} \nabla \times \mathbf{E}(\mathbf{r}, \omega) e^{j\omega t} d\omega = - \int_{-\infty}^{\infty} [j\omega \mathbf{B}(\mathbf{r}, \omega) + \mathbf{M}_f(\mathbf{r}, \omega)] e^{j\omega t} d\omega. \quad (1.7.16)$$

Since this is valid for any time variable t , we obtain

$$\nabla \times \mathbf{E} = -j\omega \mathbf{B} - \mathbf{M}_f \quad (1.7.17)$$

which is identical to Equation 1.7.6. Applying this procedure to other Maxwell's equations and the continuity equations, we obtain the same equations as Equations 1.7.7–1.7.11. In other words, the Fourier transform of a quantity is equivalent to its phasor. Since the Fourier-transformed Maxwell's equations contain the angular frequency ω , we say that these equations are in the *spectral domain* or the *frequency domain*, whereas the original ones are in the *time domain*. Obviously, given an arbitrary time-varying source such as the electric current $\mathcal{J}_f(\mathbf{r}, t)$, we can first find its Fourier transform $\mathbf{J}_f(\mathbf{r}, \omega)$, then solve Maxwell's equations (Eqs. 1.7.6–1.7.9) for the transforms of the field quantities for all frequencies, and finally use the inverse Fourier transform such as Equation 1.7.14 to find their true values in the time domain.

The Fourier transform is a very important technique for research in all scientific and technical fields, especially in electrical engineering. On the surface, the Fourier transforms do not seem to satisfy causality because, for example, if we want to calculate the value of $\mathcal{J}(t)$ at the instant t_0 using Equation 1.7.12, we have to know $f(\omega)$, whose calculation, according to Equation 1.7.13, requires the value of $\mathcal{J}(t)$ for all the time, including the future time with respect to t_0 . A more careful examination, however, reveals that this is not true. To show this, we can first split the Fourier transform into two parts:

$$f(\omega) = \int_{-\infty}^{t_0} \mathcal{J}(t) e^{-j\omega t} dt + \int_{t_0+0}^{\infty} \mathcal{J}(t) e^{-j\omega t} dt \quad (1.7.18)$$

where $t_0 + 0 = t_0 + \varepsilon$ with $\varepsilon \rightarrow 0$. Obviously, the second integral contains the future value, $\mathcal{J}(t)$ with $t > t_0$. Now, substituting this into the inverse Fourier transform for calculating $\mathcal{J}(t_0)$, we have

$$\mathcal{J}(t_0) = \frac{1}{2\pi} \int_{-\infty}^{\infty} \int_{-\infty}^{t_0} \mathcal{J}(t) e^{-j\omega t} dt e^{j\omega t_0} d\omega + \frac{1}{2\pi} \int_{-\infty}^{\infty} \int_{t_0+0}^{\infty} \mathcal{J}(t) e^{-j\omega t} dt e^{j\omega t_0} d\omega. \quad (1.7.19)$$

By exchanging the order of integration and using the Fourier transform of the delta function [14], we find that the second term of Equation 1.7.19 becomes

$$\frac{1}{2\pi} \int_{t_0+0}^{\infty} \mathcal{J}(t) \int_{-\infty}^{\infty} e^{j\omega(t_0-t)} d\omega dt = \int_{t_0+0}^{\infty} \delta(t_0-t) \mathcal{J}(t) dt = 0 \quad (1.7.20)$$

because t_0 is not included in the range of time integration. Hence, the future value, $\mathcal{J}(t)$ with $t > t_0$, makes no contribution to the calculation of $\mathcal{J}(t_0)$ and the Fourier transforms do not violate causality.

1.7.3 Complex Power

Although for time-harmonic fields the instantaneous value of a field quantity is related to its phasor according to Equation 1.7.4, the same is not true for other quantities such as power and energy that involve the product of two field quantities. To see this, let us consider the product between two instantaneous quantities $\mathcal{A}(t)$ and $\mathcal{B}(t)$. We can easily find that

$$\begin{aligned}\mathcal{A}(t) \circ \mathcal{B}(t) &= \operatorname{Re}[\mathbf{A}e^{j\omega t}] \circ \operatorname{Re}[\mathbf{B}e^{j\omega t}] \\ &= \frac{1}{2} \operatorname{Re}[\mathbf{A} \circ \mathbf{B}^*] + \frac{1}{2} \operatorname{Re}[\mathbf{A} \circ \mathbf{B}e^{j2\omega t}]\end{aligned}\quad (1.7.21)$$

where the circle denotes that the product can be either a dot or a cross-product and the star denotes the complex conjugate. If we take the time average over one cycle, we have

$$\overline{\mathcal{A}(t) \circ \mathcal{B}(t)} = \frac{1}{T} \int_0^T \mathcal{A}(t) \circ \mathcal{B}(t) dt = \frac{1}{2} \operatorname{Re}[\mathbf{A} \circ \mathbf{B}^*] \quad (1.7.22)$$

where $T = 2\pi/\omega$. Using this result, we can easily relate the complex field quantities to the time-average power and energy for the time-harmonic fields. For example, taking the time average of the Poynting vector, we have

$$\overline{\mathcal{S}(t)} = \overline{\mathcal{E}(t) \times \mathcal{H}(t)} = \frac{1}{2} \operatorname{Re}[\mathbf{E} \times \mathbf{H}^*]. \quad (1.7.23)$$

By defining the complex Poynting vector as

$$\mathbf{S} = \frac{1}{2} \mathbf{E} \times \mathbf{H}^* \quad (1.7.24)$$

Equation 1.7.23 becomes $\bar{\mathcal{S}} = \operatorname{Re}(\mathbf{S})$. For another example, the time-average electric energy density becomes

$$\overline{\omega_e(t)} = \frac{1}{2} \epsilon \overline{\mathcal{E}(t) \cdot \mathcal{E}(t)} = \frac{1}{4} \epsilon \operatorname{Re}[\mathbf{E} \cdot \mathbf{E}^*] = \frac{1}{4} \epsilon |\mathbf{E}|^2. \quad (1.7.25)$$

Now, let us consider the energy conservation law for the time-harmonic fields. We take the time average of Equation 1.6.16 to obtain

$$\bar{\rho_s} = \bar{\rho_e} + \bar{\rho_d} + \overline{\frac{\partial \omega_e}{\partial t}} + \overline{\frac{\partial \omega_m}{\partial t}}. \quad (1.7.26)$$

Since from Equation 1.7.21 we can see that

$$\omega_e = \frac{1}{2} \epsilon \mathcal{E}(t) \cdot \mathcal{E}(t) = \frac{1}{4} \epsilon \operatorname{Re}[\mathbf{E} \cdot \mathbf{E}^*] + \frac{1}{4} \epsilon \operatorname{Re}[\mathbf{E} \cdot \mathbf{E} e^{j2\omega t}] \quad (1.7.27)$$

and its time derivative is

$$\frac{\partial \omega_e}{\partial t} = -\frac{\omega}{2} \varepsilon \operatorname{Im} [\mathbf{E} \cdot \mathbf{E} e^{j2\omega t}] \quad (1.7.28)$$

we have $\overline{\partial \omega_e / \partial t} = 0$ and, similarly, $\overline{\partial \omega_m / \partial t} = 0$. This indicates that for time-harmonic fields, although the instantaneous energy density changes, the time average of the change vanishes. Hence, Equation 1.7.26 becomes

$$\bar{\rho}_s = \bar{\rho}_e + \bar{\rho}_d \quad (1.7.29)$$

It also follows that

$$\bar{\mathcal{P}}_s = \bar{\mathcal{P}}_e + \bar{\mathcal{P}}_d \quad (1.7.30)$$

which is applicable to a finite volume. Equations 1.7.29 and 1.7.30 represent the energy conservation law in the time-average sense for time-harmonic fields.

The energy conservation law for the time-harmonic fields can also be derived by following a procedure similar to the one described in Section 1.6. We start with the following two Maxwell's equations:

$$\nabla \times \mathbf{E} = -j\omega\mu\mathbf{H} - \mathbf{M}_i \quad (1.7.31)$$

$$\nabla \times \mathbf{H} = j\omega\varepsilon\mathbf{E} + \sigma\mathbf{E} + \mathbf{J}_i \quad (1.7.32)$$

By taking the dot product of Equation 1.7.31 with \mathbf{H}^* and the dot product of the complex conjugate of Equation 1.7.32 with \mathbf{E} , then subtracting the latter from the former, we obtain

$$\nabla \cdot (\mathbf{E} \times \mathbf{H}^*) = -j\omega\mu|\mathbf{H}|^2 + j\omega\varepsilon|\mathbf{E}|^2 - \sigma|\mathbf{E}|^2 - \mathbf{H}^* \cdot \mathbf{M}_i - \mathbf{E} \cdot \mathbf{J}_i^*. \quad (1.7.33)$$

Denoting

$$p_e = \frac{1}{2} \nabla \cdot (\mathbf{E} \times \mathbf{H}^*) \quad (1.7.34)$$

$$\bar{p}_d = \frac{1}{2} \sigma |\mathbf{E}|^2 \quad (1.7.35)$$

$$p_s = -\frac{1}{2} (\mathbf{H}^* \cdot \mathbf{M}_i + \mathbf{E} \cdot \mathbf{J}_i^*) \quad (1.7.36)$$

$$\bar{w}_e = \frac{1}{4} \varepsilon |\mathbf{E}|^2 \quad (1.7.37)$$

$$\bar{w}_m = \frac{1}{4} \mu |\mathbf{H}|^2 \quad (1.7.38)$$

we can write Equation 1.7.33 as

$$p_s = p_e + \bar{p}_d + j2\omega(\bar{w}_m - \bar{w}_e). \quad (1.7.39)$$

Integrating this over a finite volume and invoking Gauss' theorem yields its integral form

$$P_s = P_e + \bar{P}_d + j2\omega(\bar{W}_m - \bar{W}_e) \quad (1.7.40)$$

where

$$P_e = \iiint_V p_e dV = \frac{1}{2} \oint_S (\mathbf{E} \times \mathbf{H}^*) \cdot d\mathbf{S} \quad (1.7.41)$$

$$\bar{P}_d = \iiint_V \bar{p}_d dV = \frac{1}{2} \iiint_V \sigma |\mathbf{E}|^2 dV \quad (1.7.42)$$

$$P_s = \iiint_V p_s dV = -\frac{1}{2} \iiint_V (\mathbf{H}^* \cdot \mathbf{M}_i + \mathbf{E} \cdot \mathbf{J}_i^*) dV \quad (1.7.43)$$

$$\bar{W}_e = \iiint_V \bar{w}_e dV = \frac{1}{4} \iiint_V \epsilon |\mathbf{E}|^2 dV \quad (1.7.44)$$

$$\bar{W}_m = \iiint_V \bar{w}_m dV = \frac{1}{4} \iiint_V \mu |\mathbf{H}|^2 dV. \quad (1.7.45)$$

Here, P_e is called the complex exiting power, \bar{P}_d the time-average dissipated power, P_s the complex supplied power, and \bar{W}_e and \bar{W}_m the time-average electric and magnetic energies, respectively.

Equations 1.7.39 and 1.7.40 are known as *Poynting's theorem for complex phasors*. Both are complex equations whose real parts yield

$$\text{Re}(p_s) = \text{Re}(p_e) + \bar{p}_d \quad (1.7.46)$$

$$\text{Re}(P_s) = \text{Re}(P_e) + \bar{P}_d \quad (1.7.47)$$

which are identical to Equations 1.7.29 and 1.7.30. However, if we take their imaginary parts, we obtain two more equations:

$$\text{Im}(p_s) = \text{Im}(p_e) + 2\omega(\bar{W}_m - \bar{W}_e) \quad (1.7.48)$$

$$\text{Im}(P_s) = \text{Im}(P_e) + 2\omega(\bar{W}_m - \bar{W}_e). \quad (1.7.49)$$

While the meaning of Equations 1.7.46 and 1.7.47 is very clear, the meaning of Equation 1.7.48 and 1.7.49 requires some explanation, which is attempted below.

From Maxwell's equations, it can be seen that the electric and magnetic fields can have a phase difference for a general time-harmonic field. The electric energy reaches its maximum value at some moments and the magnetic energy reaches its maximum at some other moments. To be more specific, within each cycle at one moment some of the magnetic energy converts into electric energy, and at another moment some of the electric energy converts into magnetic energy. This is analogous to what happens in an *LC* circuit, where the energy stored in the inductor converts into the energy stored in the capacitor at one moment, and at another moment, the reverse happens. Now, if the maximum electric energy is not equal to, say greater than, the maximum magnetic energy in a volume, extra power is needed at the moment when the electric energy reaches its maximum value, and the same amount of power has to disappear at the other moment when the electric energy

decreases and the magnetic energy reaches its maximum value. This extra power is called *reactive power* and, because of the power conservation, it can only come either from the source or from the power outside the volume. The source contribution is reflected by $\text{Im}(P_s)$ and the external contribution is given by $\text{Im}(P_e)$. Hence, $\text{Im}(P_s)$ is related to the power generated by the source at one moment and then taken back at the other moment within a cycle. Similarly, $\text{Im}(P_e)$ represents the power leaving the volume at one moment and then reentering at the other moment within a cycle. This reactive power does not show up in the time-average supplied power or exiting power because it takes two round trips within each cycle, but it is clearly reflected in the difference between the time-average electric and magnetic energies.

To understand the concept of reactive power better, let us consider the supplied power density for a time-harmonic source whose electric field and impressed current at a specific point are assumed to be

$$\mathbf{E} = \mathbf{E}_0 e^{j\angle \mathbf{E}}, \quad \mathbf{J}_i = \mathbf{J}_{i0} e^{j\angle \mathbf{J}_i} \quad (1.7.50)$$

where \mathbf{E}_0 and \mathbf{J}_{i0} denote the amplitudes and $\angle \mathbf{E}$ and $\angle \mathbf{J}_i$ denote the phases of \mathbf{E} and \mathbf{J}_i , respectively. The complex supplied power density at the point is then

$$p_s = -\frac{1}{2} \mathbf{E} \cdot \mathbf{J}_i^* = -\frac{1}{2} \mathbf{E}_0 \cdot \mathbf{J}_{i0} e^{j(\angle \mathbf{E} - \angle \mathbf{J}_i)} \quad (1.7.51)$$

whose real and imaginary parts are

$$\text{Re}(p_s) = -\frac{1}{2} \mathbf{E}_0 \cdot \mathbf{J}_{i0} \cos(\angle \mathbf{E} - \angle \mathbf{J}_i) \quad (1.7.52)$$

$$\text{Im}(p_s) = -\frac{1}{2} \mathbf{E}_0 \cdot \mathbf{J}_{i0} \sin(\angle \mathbf{E} - \angle \mathbf{J}_i). \quad (1.7.53)$$

As discussed before, the real part represents the time-average supplied power density. To understand the imaginary part, let us examine the instantaneous power density

$$\rho_s(t) = -\mathcal{E}(t) \cdot \mathcal{J}_i(t) = -\mathbf{E}_0 \cos(\omega t + \angle \mathbf{E}) \cdot \mathbf{J}_{i0} \cos(\omega t + \angle \mathbf{J}_i). \quad (1.7.54)$$

This expression can be rewritten as

$$\begin{aligned} \rho_s(t) &= -\frac{1}{2} \mathbf{E}_0 \cdot \mathbf{J}_{i0} \cos(\angle \mathbf{E} - \angle \mathbf{J}_i) [1 + \cos(2\omega t + 2\angle \mathbf{J}_i)] \\ &\quad + \frac{1}{2} \mathbf{E}_0 \cdot \mathbf{J}_{i0} \sin(\angle \mathbf{E} - \angle \mathbf{J}_i) \sin(2\omega t + 2\angle \mathbf{J}_i). \end{aligned} \quad (1.7.55)$$

The first term contains $1 + \cos(2\omega t + 2\angle \mathbf{J}_i)$, which oscillates around one and is always positive. Its time average is the same as that in Equation 1.7.52. However, the second term contains $\sin(2\omega t + 2\angle \mathbf{J}_i)$, which oscillates around zero with either a positive or a negative value. It represents power generated at one moment and taken back at another moment and the time average is zero. This power is the reactive power mentioned earlier. Its peak value is the same as that in Equation 1.7.53. Hence, $\text{Im}(p_s)$ represents the peak value of the reactive power density. The same interpretation can be made for the exiting power involved in Equations 1.7.48 and 1.7.49.

1.7.4 Complex Permittivity and Permeability

As mentioned earlier, a medium can be lossy for a time-varying electromagnetic field because of the energy dissipation caused by the friction between bound charges and dipoles. The mathematical description of this loss is rather complicated in the time domain, but for time-harmonic fields, this loss translates into the imaginary part of a complex permittivity and/or a complex permeability. In this case, the relative permittivity and permeability can be written as

$$\epsilon_r = \epsilon'_r - j\epsilon''_r, \quad \mu_r = \mu'_r - j\mu''_r \quad (1.7.56)$$

where ϵ''_r quantifies the dielectric loss and μ''_r quantifies the magnetic loss. These two parameters are related to the electric loss tangent δ_e and the magnetic loss tangent δ_m by

$$\tan \delta_e = \frac{\epsilon''_r}{\epsilon'_r}, \quad \tan \delta_m = \frac{\mu''_r}{\mu'_r} \quad (1.7.57)$$

which are commonly used in engineering practice. Since for a linear dispersive medium, $\epsilon(\omega)$ is the Fourier transform of $\epsilon = \epsilon_0 + \epsilon_0 \chi_e(t)$, its real and imaginary parts are related by Kramers–Krönig’s relations [15,16] given by

$$\epsilon'(\omega) = \epsilon_\infty - \frac{2}{\pi} \int_0^\infty \frac{\epsilon''(z)}{z - \omega} dz, \quad \epsilon''(\omega) = \frac{2}{\pi} \int_0^\infty \frac{\epsilon'(z) - \epsilon_\infty}{z - \omega} dz \quad (1.7.58)$$

where ϵ_∞ denotes the permittivity at an infinitely high frequency, which accounts for the contribution of the polarization that adapts instantaneously to the changes of the electric field in addition to ϵ_0 . The integrals in Equation 1.7.58 are evaluated in the complex plane with the singular point $z = \omega$ excluded. Equation 1.7.58 is also called the *causality condition* since it is a direct result of $\chi_e(t)$ being a causal function. It indicates that the dielectric dispersion is always accompanied by dielectric loss and if one knows $\epsilon'(\omega)$ for the entire frequency spectrum, $\epsilon''(\omega)$ can be calculated and vice versa. A similar relation can be found between the magnetic dispersion and magnetic loss.

An additional benefit for dealing with time-harmonic fields in the frequency domain is that the conduction loss and the dielectric loss can often be combined in the analysis. This can be seen clearly by rewriting Equation 1.7.32 as

$$\begin{aligned} \nabla \times \mathbf{H} &= j\omega\epsilon\mathbf{E} + \sigma\mathbf{E} + \mathbf{J}_i \\ &= j\omega\epsilon_0 \left[\epsilon'_r - j \left(\epsilon''_r + \frac{\sigma}{\omega\epsilon_0} \right) \right] \mathbf{E} + \mathbf{J}_i \end{aligned} \quad (1.7.59)$$

In this case, the electric loss tangent can be redefined as

$$\tan \delta_e = \left(\epsilon''_r + \frac{\sigma}{\omega\epsilon_0} \right) / \epsilon'_r \quad (1.7.60)$$

to include both the dielectric and conduction losses. Consequently, an effective ϵ''_r can be defined to include the effect of σ , and conversely, an effective σ can be used to include the effect of ϵ''_r .

NOTES

1. All vectors are represented by boldfaced letters in this book. In contrast, a scalar quantity is represented by a non-boldfaced italic letter.
2. All instantaneous quantities are represented by cursive letters to distinguish them from time-invariant quantities.
3. A letter with a doubly arrowed overline denotes a tensor quantity.

REFERENCES

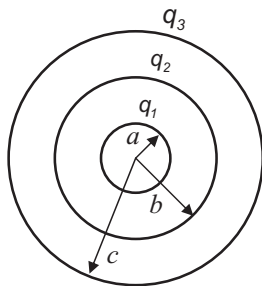
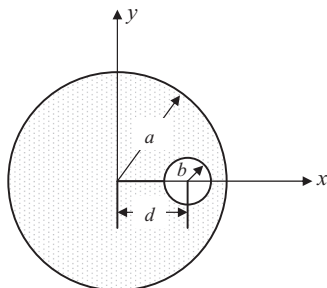
- [1] J. D. KRAUS and D. FLEISCH, *Electromagnetics with Applications* (5th edition). New York: McGraw-Hill, 1999.
- [2] D. K. CHENG, *Field and Wave Electromagnetics* (2nd edition). Reading, MA: Addison-Wesley, 1989.
- [3] C. R. PAUL, K. W. WHITES, and S. A. NASAR, *Introduction to Electromagnetic Fields* (3rd edition). New York: McGraw-Hill, 1998.
- [4] D. J. GRIFFITHS, *Introduction to Electrodynamics* (3rd edition). Upper Saddle River, NJ: Prentice Hall, 1999.
- [5] N. IDA, *Engineering Electromagnetics* (2nd edition). New York: Springer-Verlag, 2004.
- [6] N. N. RAO, *Elements of Engineering Electromagnetics* (6th edition). Upper Saddle River, NJ: Pearson Prentice Hall, 2004.
- [7] F.T. ULABY, *Fundamentals of Applied Electromagnetics* (5th edition). Upper Saddle River, NJ: Pearson Prentice Hall, 2007.
- [8] C. T. TAI, *Generalized Vector and Dyadic Analysis* (2nd edition). Piscataway, NJ: IEEE Press, 1997.
- [9] J. C. MAXWELL, A dynamic theory of the electromagnetic field, *Phil. Trans. R. Soc. Lond.*, 155: 459–512, 1865.
- [10] J. C. MAXWELL, *A Treatise on Electricity and Magnetism*. Oxford, UK: Oxford University Press, 1873. Reprinted by Dover Publications, New York, 1954.
- [11] H. HERTZ, *Electric Waves: Being Researches on the Propagation of Electric Action with Finite Velocity through Space*. London and New York: Macmillan and Company, 1893. Reprinted by Dover Publications, New York, 1954.
- [12] O. HEAVISIDE, *Electromagnetic Theory* (3 volumes published in 1893, 1899, and 1912). Reprinted by AMS Chelsea Publishing Company, 1971.
- [13] C. A. BALANIS, *Advanced Engineering Electromagnetics*. New York: Wiley, 1989.
- [14] R. BRACEWELL, *The Fourier Transform and Its Applications* (3rd edition). New York: McGraw-Hill, 2000.
- [15] J. A. KONG, *Electromagnetic Wave Theory*. Cambridge, MA: EMW Publishing, 2000.
- [16] E. J. ROTHWELL and M. J. CLOUD, *Electromagnetics* (2nd edition). Boca Raton, FL: CRC Press, 2009.

PROBLEMS

- 1.1. Starting from the definition of the divergence (Eq. 1.1.1), derive the expressions of the divergence in rectangular, cylindrical, and spherical coordinates as given in Equations 1.1.2–1.1.4. Furthermore, derive Gauss' theorem in Equation 1.1.5.
- 1.2. Derive the alternative definition of the curl in Equation 1.1.10 from the definition given in Equation 1.1.6. Furthermore, derive Stokes' theorem in Equation 1.1.11.
- 1.3. Starting from the definition of the gradient in Equation 1.1.12, derive its alternative definition in Equation 1.1.13.
- 1.4. Define R as the distance between point P located at (x, y, z) and point P' located at (x', y', z') and show that

$$\nabla \left(\frac{1}{R} \right) = -\frac{\mathbf{R}}{R^3}, \quad \nabla' \left(\frac{1}{R} \right) = \frac{\mathbf{R}}{R^3}$$

where $\mathbf{R} = \mathbf{r} - \mathbf{r}'$ and ∇' operates on the primed variables.

**Figure 1.4** Three concentric conducting spherical shells.**Figure 1.5** An infinitely long conductor with an offset hole.

- 1.5.** Use the results obtained in Problem 1.4 and show that

$$\nabla \cdot \nabla \left(\frac{1}{R} \right) = -4\pi\delta(R)$$

where $R = |\mathbf{r} - \mathbf{r}'|$.

- 1.6.** Using the symbolic vector method, prove the following vector identities:

$$\mathbf{a} \times (\nabla \times \mathbf{b}) = (\nabla \mathbf{b}) \cdot \mathbf{a} - \mathbf{a} \cdot (\nabla \mathbf{b})$$

$$\nabla \cdot (\mathbf{a} \times \mathbf{b}) = \mathbf{b} \cdot (\nabla \times \mathbf{a}) - \mathbf{a} \cdot (\nabla \times \mathbf{b}).$$

- 1.7.** Using the generalized Gauss' theorem, derive a new integral theorem

$$\iiint_V (\mathbf{b} \nabla \cdot \mathbf{a} + \mathbf{a} \cdot \nabla \mathbf{b}) dV = \iint_S (\hat{\mathbf{n}} \cdot \mathbf{a}) \mathbf{b} dS.$$

- 1.8.** Derive the scalar–vector Green's theorem in Equation 1.1.47 from the second vector Green's theorem in Equation 1.1.46.
- 1.9.** Three concentric conducting spherical shells have radii a , b , and c , and charges q_1 , q_2 , and q_3 , respectively. Assume that $a < b < c$ (Fig. 1.4). What are the potentials on these spheres? If the innermost sphere is grounded (that is, zero potential), what will be the change of the potential on the outermost sphere? (*Hint:* Find the potential inside, outside, and on a single spherical shell first.)
- 1.10.** An infinitely long cylindrical conductor of radius a has a hole of radius b whose axis is parallel to but offset by a distance d from the axis of the conductor (Fig. 1.5). Assume that a static current I uniformly distributed over the cross-section flows along the conductor in the z -direction. What is the magnetic field on the axis of the hole? (*Hint:* Use superposition.)

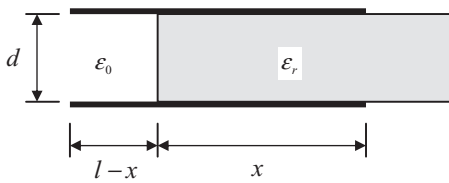


Figure 1.6 A dielectric slab inserted between two parallel plates.

- 1.11.** A parallel-plate capacitor of width w and length l at a spacing d is connected to a battery of V volts. A dielectric slab of relative permittivity ϵ_r and thickness h ($h < d$) and having the same area $w \times l$ is inserted between the plates and placed on the bottom plate. Find the force on the top plate (neglect the edge effect).
- 1.12.** A condenser consists of two parallel plates of width w and length l at a spacing d as shown in Figure 1.6. A dielectric slab of relative permittivity ϵ_r and of thickness d and the same area $w \times l$ is placed between the plates. Assume that the dielectric slab is pulled along its length from the plates so that a length x is left in between the plates. (a) Show that if Q is the total charge on the plate, there is an electric force (neglect the edge effect)

$$F = \frac{Q^2(\epsilon_r - 1)d}{2\epsilon_0 w [(l-x) + \epsilon_r x]^2}$$

pulling the slab back to its original position. (b) What is the charge over the dielectric slab portion x and also over the free-space portion $(l-x)$? (c) If the condenser is connected to a battery of V volts, what is the force? (Hint: Use the method of virtual work.)

- 1.13.** The electric charge density is distributed symmetrically in a cylinder infinitely long in the z -direction. The charge density is given by the expression

$$\rho_e(\rho) = \begin{cases} \rho_0(\rho/b)^2 & \rho \leq b \\ 0 & \rho > b \end{cases}$$

where ρ is the cylindrical coordinate, ρ_0 is a constant, and b is the radius of the cylinder. (a) Using an appropriate Maxwell's equation in the integral form and the cylindrical symmetry, find expressions for the electric field in the region $\rho < b$ and the region $\rho > b$. (b) If a grounded metallic shell is added at $\rho = a$ ($a > b$) such that the electric field $\mathbf{E} = 0$ for $\rho > a$, calculate the electric surface charge density $\rho_{e,s}$ on the shell.

- 1.14.** Consider two infinite planes parallel to the yz -plane (one at $x = 0$ and the other at $x = d$). The medium between the planes is characterized by permittivity ϵ_0 and permeability μ_0 . The electric field between the planes is given by

$$\mathcal{E} = \hat{z}A \sin \frac{\pi x}{d} \cos \frac{\pi c t}{d}$$

where A is a constant and c is the wave velocity. Outside the planes both the electric and magnetic fields are zero. (a) Calculate the electric charge density distribution (volume if any and surface). (b) Calculate the magnetic field. (c) Calculate the electric current density distribution (volume if any and surface).

- 1.15.** Even though Maxwell's equations can be expressed in terms of either total or free charges and currents, they can be more uniformly written as

$$\nabla \times \mathcal{B} = -\frac{\partial \mathcal{D}}{\partial t}, \quad \nabla \times \mathcal{H} = \frac{\partial \mathcal{D}}{\partial t} + \mathcal{J}$$

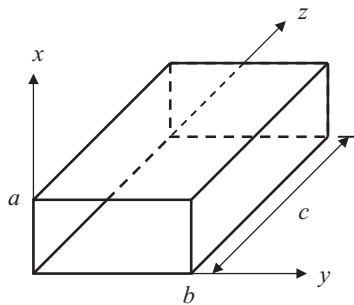


Figure 1.7 A section of a rectangular waveguide.

$$\nabla \cdot \mathcal{D} = \rho_e, \quad \nabla \cdot \mathcal{B} = 0.$$

The interpretation of the charge density ρ_e and current density \mathcal{J} depends on the constitutive relations used to relate \mathcal{D} with \mathcal{E} and \mathcal{B} with \mathcal{H} . When the free-space constitutive relations $\mathcal{D} = \epsilon_0 \mathcal{E}$ and $\mathcal{B} = \mu_0 \mathcal{H}$ are used, the charge and current densities are those of total charges and currents, which include bound charges and currents. When the material constitutive relations $\mathcal{D} = \epsilon_0 \mathcal{E} + \mathcal{P}$ and $\mathcal{B} = \mu_0 (\mathcal{H} + \mathcal{M})$ are used, the charge and current densities are those of free charges and currents since the effect of bound charges and currents have already been included in the constitutive relations. Show that these two approaches are indeed equivalent by casting Maxwell's equations in terms of \mathcal{E} and \mathcal{B} for both cases.

- 1.16. Derive corresponding boundary conditions from Maxwell's equations in terms of total charges and currents given in Equations 1.2.2 and 1.2.8. Show that the derived boundary conditions are equivalent to Equations 1.5.4 and 1.5.7, which are formulated for free charges and currents.
- 1.17. Starting from Maxwell's equations in differential form in Equations 1.4.8 and 1.4.9 and boundary conditions in Equations 1.5.4 and 1.5.7, derive the corresponding Maxwell's equations in integral form in Equations 1.4.2 and 1.4.3 that are applicable to general cases that may contain arbitrary discontinuities (including the surface currents and charges).
- 1.18. Consider a thin sheet whose conductivity is σ and thickness is t ($t \rightarrow 0$). The product σt remains a constant as $t \rightarrow 0$. The sheet is placed in free space. (a) Find the relation between the tangential components of the electric fields on both sides of the sheet. (b) Find the relation between the tangential components of the magnetic fields on both sides of the sheet (in terms of the electric current density in the sheet). (c) Furthermore, find the relation between tangential electric and magnetic fields.
- 1.19. Consider a section of a rectangular waveguide shown in Figure 1.7. There is no source of any kind in this section of the waveguide. The transverse field components at $z = 0$ are given by

$$E_x = E_0 \sin \frac{\pi y}{b}, \quad H_y = H_0 (1 + j) \sin \frac{\pi y}{b}$$

and those at $z = c$ are given by

$$E_x = \frac{E_0}{4} \sin \frac{\pi y}{b}, \quad H_y = H_0 \sin \frac{\pi y}{b}$$

where E_0 and H_0 are real numbers. Find the time-average power dissipated in the waveguide. (Express your result in terms of E_0 , H_0 , a , and b .)

- 1.20. Suppose a filament of z -directed time-harmonic electric current of 5 A is impressed along the z -axis from $z = 0$ to $z = 1$ m and is completely enclosed in a perfectly conducting circular cavity filled with a lossy material (Fig. 1.8). If $\mathbf{E} = -\hat{z}(1 + j)$ along the z -axis from $z = 0$ to

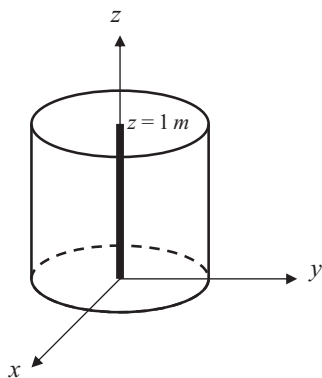


Figure 1.8 A filament of electric current placed in a perfectly conducting circular cavity.

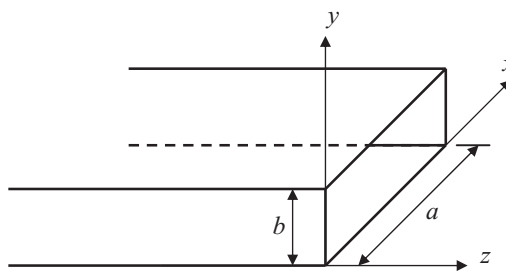


Figure 1.9 An open rectangular waveguide radiating into free space.

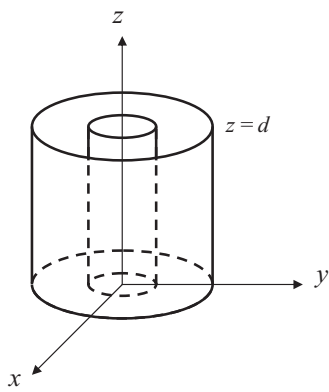


Figure 1.10 A section of a coaxial cable.

$z = 1 \text{ m}$ and the frequency is 1 kHz , determine the time-average power dissipated in the cavity and the difference between the time-average electric and magnetic energies within the cavity.

- 1.21.** Figure 1.9 shows an open rectangular waveguide radiating into free space. The field at the opening is given by

$$E_y = E_0 \sin\left(\frac{\pi x}{a}\right), \quad H_x = -(1+j)E_0 \sin\left(\frac{\pi x}{a}\right).$$

Find the time-average power radiated into the free space. (Express your result in terms of E_0 , a , and b .)

- 1.22.** Consider a section of a coaxial cable shown in Figure 1.10. The length of the section is d and the coaxial cable is formed by two cylinders of radius a and b . The transverse time-harmonic field components at $z = 0$ are given by

$$\mathbf{E}|_{z=0} = \hat{\rho} \frac{A}{\rho}, \quad \mathbf{H}|_{z=0} = \hat{\phi} \frac{B}{\rho}$$

and those at $z = d$ are given by

$$\mathbf{E}|_{z=d} = \hat{\rho} \frac{jC}{\rho}, \quad \mathbf{H}|_{z=d} = \hat{\phi} \frac{(D + jE)}{\rho}$$

where A, B, C, D , and E are real numbers. (a) Find the time-average power dissipated or gained within the volume between the planes $z = 0$ and $z = d$. (b) What are the conditions on A, B, C, D , and E (or part of them) leading to (1) dissipated time-average power and (2) gained time-average power? ■

ELECTROMAGNETIC RADIATION IN FREE SPACE

Given the constitutive relations and boundary conditions, electromagnetic fields radiated by any source can be obtained by solving Maxwell's equations in differential form. Unfortunately, Maxwell's equations are very difficult to solve for most problems of practical interest. There are only a few special cases where we can obtain an analytical solution to Maxwell's equations. In this chapter we consider the simplest case, which concerns electromagnetic radiation in an infinitely large (unbounded), homogeneous medium characterized by constant permittivity ϵ and permeability μ . Such a medium is often referred to as *free space*.¹ We first introduce the concepts of scalar and vector potentials to facilitate the solution of Maxwell's equations. We then introduce the notation of dyadic Green's function to cast the expressions for the fields radiated by currents in compact form. Finally, we study the fields radiated by an infinitesimal dipole, a finite dipole, a circular current loop, a surface current, and a phased array, and derive the Sommerfeld radiation condition that describes the field behavior at infinity.

2.1 SCALAR AND VECTOR POTENTIALS

Given a time-harmonic source defined by electric current density \mathbf{J} and magnetic current density \mathbf{M} , the electromagnetic field generated by this source satisfies Maxwell's equations

$$\nabla \times \mathbf{E} = -j\omega\mu\mathbf{H} - \mathbf{M} \quad (2.1.1)$$

$$\nabla \times \mathbf{H} = j\omega\epsilon\mathbf{E} + \mathbf{J} \quad (2.1.2)$$

$$\nabla \cdot (\epsilon\mathbf{E}) = \rho_e \quad (2.1.3)$$

$$\nabla \cdot (\mu\mathbf{H}) = \rho_m. \quad (2.1.4)$$

It is clearly observed that the electric and magnetic fields are coupled in these equations and the strength of coupling depends on the frequency. As the frequency decreases, the coupling weakens. When the frequency approaches zero ($\omega \rightarrow 0$), Equations 2.1.1–2.1.4 become

$$\nabla \times \mathbf{E} = -\mathbf{M}, \quad \nabla \cdot (\epsilon\mathbf{E}) = \rho_e \quad (2.1.5)$$

$$\nabla \times \mathbf{H} = \mathbf{J}, \quad \nabla \cdot (\mu\mathbf{H}) = \rho_m \quad (2.1.6)$$

Theory and Computation of Electromagnetic Fields, by Jian-Ming Jin
Copyright © 2010 John Wiley & Sons, Inc.

which indicate that the electric and magnetic fields are completely decoupled and therefore can be solved for independently. Such fields are called *static fields*.

2.1.1 Static Fields

In the absence of magnetic current, the static electric field is produced by electric charges and is governed by

$$\nabla \times \mathbf{E} = 0, \quad \nabla \cdot (\epsilon \mathbf{E}) = \rho_e \quad (2.1.7)$$

which represent two first-order partial differential equations for a single unknown function \mathbf{E} . To solve these two equations, we first observe that \mathbf{E} is an irrotational vector function, which can be expressed as a gradient of a scalar function. Therefore, we can let

$$\mathbf{E} = -\nabla \varphi \quad (2.1.8)$$

to satisfy the first equation in Equation 2.1.7. The scalar function φ is called the *electric scalar potential*. Substituting Equation 2.1.8 into the second equation in Equation 2.1.7, we obtain

$$-\nabla \cdot (\epsilon \nabla \varphi) = \rho_e \quad (2.1.9)$$

which represents a second-order partial differential equation. In a homogeneous medium, Equation 2.1.9 becomes

$$\nabla^2 \varphi = -\frac{\rho_e}{\epsilon} \quad (2.1.10)$$

which is called *Poisson's equation*. If the medium is infinitely large, its solution is given by

$$\varphi(\mathbf{r}) = \frac{1}{4\pi\epsilon} \iiint_V \frac{\rho_e(\mathbf{r}')}{R} dV' \quad R = |\mathbf{r} - \mathbf{r}'|. \quad (2.1.11)$$

This result can be obtained directly by applying the linear superposition principle to the potential due to a point charge. It can also be obtained mathematically by solving Poisson's equation, which will be considered for a more general case.

In the absence of magnetic charge, the static magnetic field is produced by electric currents and is governed by

$$\nabla \times \mathbf{H} = \mathbf{J}, \quad \nabla \cdot (\mu \mathbf{H}) = 0 \quad (2.1.12)$$

which represent two first-order partial differential equations for a single unknown function \mathbf{H} . To solve these two equations, we first observe that $\mathbf{B} = \mu \mathbf{H}$ is a solenoidal vector function, which can be expressed as the curl of a vector function. Therefore, we can let

$$\mathbf{B} = \nabla \times \mathbf{A} \quad (2.1.13)$$

to satisfy the second equation in Equation 2.1.12. The vector function \mathbf{A} is called the *magnetic vector potential*. Substituting Equation 2.1.13 into the first equation in Equation 2.1.12, we obtain

$$\nabla \times \left(\frac{1}{\mu} \nabla \times \mathbf{A} \right) = \mathbf{J} \quad (2.1.14)$$

which represents a second-order partial differential equation. Since \mathbf{A} is a vector function, the specification of its curl is not sufficient to uniquely determine this function. This is obvious from Equation 2.1.14 since, if \mathbf{A} is a solution, $\mathbf{A} + \nabla f$ would also be a solution in view of the vector identity $\nabla \times \nabla f \equiv 0$. Therefore, to uniquely determine \mathbf{A} , we have to specify its divergence. In a homogeneous medium, Equation 2.1.14 becomes

$$\nabla \times (\nabla \times \mathbf{A}) = \nabla (\nabla \cdot \mathbf{A}) - \nabla^2 \mathbf{A} = \mu \mathbf{J}. \quad (2.1.15)$$

With the intent to simplify Equation 2.1.15, we can set the divergence of \mathbf{A} to zero, that is,

$$\nabla \cdot \mathbf{A} = 0 \quad (2.1.16)$$

such that Equation 2.1.15 is reduced to

$$\nabla^2 \mathbf{A} = -\mu \mathbf{J} \quad (2.1.17)$$

which is a vector Poisson's equation. Equation 2.1.16 is called the *Coulomb gauge condition*. A simple comparison to Equation 2.1.10 yields the solution to \mathbf{A} in an infinite medium as

$$\mathbf{A}(\mathbf{r}) = \frac{\mu}{4\pi} \iiint_V \frac{\mathbf{J}(\mathbf{r}')}{R} dV' \quad R = |\mathbf{r} - \mathbf{r}'|. \quad (2.1.18)$$

In passing, we note that the specification of the divergence of \mathbf{A} is simply for a unique determination of \mathbf{A} . Since \mathbf{A} is an intermediate function, or an auxiliary function, introduced to facilitate solving for \mathbf{H} , its uniqueness is not important. Even if \mathbf{A} is not unique, the magnetic field obtained through Equation 2.1.13 will always be unique. Because the divergence of \mathbf{A} does not affect the solution to the magnetic field, it can be specified arbitrarily. A general rule is to set it such that the final equation becomes as simple as possible. This is illustrated clearly in the choice of the Coulomb gauge condition (Eq. 2.1.16).

This book focuses on the study of electrodynamic fields. The reader can consult one of the classical textbooks by Stratton [1], Jackson [2], and Van Bladel [3] for the treatment of many electro- and magnetostatic problems. These are also excellent references, along with others such as the ones by Harrington [4], Balanis [5], Kong [6], and Smith [7], for electrodynamic problems discussed next.

2.1.2 Time-Harmonic Fields and the Lorenz Gauge Condition

The basic approach to formulating the static electric and magnetic fields can also be employed to formulate the time-harmonic fields. However, the time-harmonic case is much more involved. To simplify the formulation, we first decompose both the electric and magnetic fields into one due to the electric source and another one due to the magnetic source [4,5]:

$$\mathbf{E} = \mathbf{E}_e + \mathbf{E}_m, \quad \mathbf{H} = \mathbf{H}_e + \mathbf{H}_m \quad (2.1.19)$$

where \mathbf{E}_e and \mathbf{H}_e satisfy

$$\nabla \times \mathbf{E}_e = -j\omega\mu\mathbf{H}_e, \quad \nabla \cdot (\epsilon\mathbf{E}_e) = \rho_e \quad (2.1.20)$$

$$\nabla \times \mathbf{H}_e = j\omega\epsilon\mathbf{E}_e + \mathbf{J}, \quad \nabla \cdot (\mu\mathbf{H}_e) = 0 \quad (2.1.21)$$

and \mathbf{E}_m and \mathbf{H}_m are governed by

$$\nabla \times \mathbf{E}_m = -j\omega\mu\mathbf{H}_m - \mathbf{M}, \quad \nabla \cdot (\epsilon\mathbf{E}_m) = 0 \quad (2.1.22)$$

$$\nabla \times \mathbf{H}_m = j\omega\epsilon\mathbf{E}_m, \quad \nabla \cdot (\mu\mathbf{H}_m) = \rho_m. \quad (2.1.23)$$

Now, we first seek solutions to \mathbf{E}_e and \mathbf{H}_e that satisfy the four equations in Equations 2.1.20 and 2.1.21. The second equation in Equation 2.1.21 reveals that $\mathbf{B}_e = \mu\mathbf{H}_e$ is a solenoidal vector function, which can be satisfied by introducing the magnetic vector potential \mathbf{A} as

$$\mathbf{B}_e = \nabla \times \mathbf{A}. \quad (2.1.24)$$

Substituting this into the first equation in Equation 2.1.20, we obtain

$$\nabla \times (\mathbf{E}_e + j\omega\mathbf{A}) = 0 \quad (2.1.25)$$

which can be satisfied by introducing the electric scalar potential φ such that

$$\mathbf{E}_e + j\omega\mathbf{A} = -\nabla\varphi. \quad (2.1.26)$$

It remains to satisfy the first equation in Equation 2.1.21 and for this, we substitute Equations 2.1.24 and 2.1.26 into it to obtain

$$\nabla \times \left(\frac{1}{\mu} \nabla \times \mathbf{A} \right) = -j\omega\epsilon\nabla\varphi + \omega^2\epsilon\mathbf{A} + \mathbf{J}. \quad (2.1.27)$$

In a homogeneous medium, this is reduced to

$$\nabla(\nabla \cdot \mathbf{A}) - \nabla^2 \mathbf{A} = -j\omega\mu\epsilon\nabla\varphi + k^2\mathbf{A} + \mu\mathbf{J} \quad (2.1.28)$$

where $k^2 = \omega^2\mu\epsilon$. Similar to the static magnetic case, the magnetic vector potential \mathbf{A} has only its curl specified by Equation 2.1.24. We can prescribe a value for its divergence to determine it uniquely without any effect on the field itself. With the intent to simplify Equation 2.1.28, we set $\nabla \cdot \mathbf{A}$ as

$$\nabla \cdot \mathbf{A} = -j\omega\mu\epsilon\varphi \quad (2.1.29)$$

so that Equation 2.1.28 is simplified as

$$\nabla^2 \mathbf{A} + k^2 \mathbf{A} = -\mu\mathbf{J}. \quad (2.1.30)$$

Once \mathbf{A} is determined, \mathbf{E}_e and \mathbf{H}_e can be evaluated as

$$\mathbf{E}_e = -j\omega\mathbf{A} + \frac{1}{j\omega\mu\epsilon} \nabla(\nabla \cdot \mathbf{A}) \quad (2.1.31)$$

$$\mathbf{H}_e = \frac{1}{\mu} \nabla \times \mathbf{A}. \quad (2.1.32)$$

Equation 2.1.29 is called the *Lorenz gauge condition*, which is introduced to define \mathbf{A} uniquely, and more importantly, to simplify the final partial differential equation for \mathbf{A} . Equation 2.1.30 is often referred to as the *vector Helmholtz equation*, whose solution is discussed in the next section. Although the electric scalar potential φ can be obtained from Equation 2.1.29 without solving an independent equation, its governing equation can be obtained by taking the divergence of Equation 2.1.26 and then substituting Equation 2.1.29 and the second equation of Equation 2.1.20 into the resulting equation, which yields

$$\nabla^2 \varphi + k^2 \varphi = -\frac{\rho_e}{\epsilon}. \quad (2.1.33)$$

This is known as the *scalar Helmholtz equation*.

The same procedure as described above can be employed to formulate \mathbf{E}_m and \mathbf{H}_m . With the introduction of the electric vector potential and magnetic scalar potential, we find

$$\mathbf{E}_m = -\frac{1}{\epsilon} \nabla \times \mathbf{F} \quad (2.1.34)$$

$$\mathbf{H}_m = -j\omega \mathbf{F} + \frac{1}{j\omega \mu \epsilon} \nabla (\nabla \cdot \mathbf{F}) \quad (2.1.35)$$

where \mathbf{F} denotes the *electric vector potential*, which is governed by the vector Helmholtz equation

$$\nabla^2 \mathbf{F} + k^2 \mathbf{F} = -\epsilon \mathbf{M}. \quad (2.1.36)$$

Substituting the expressions for $(\mathbf{E}_e, \mathbf{H}_e)$ and $(\mathbf{E}_m, \mathbf{H}_m)$ into Equation 2.1.19, we obtain the expressions of the total field as

$$\mathbf{E} = -j\omega \mathbf{A} + \frac{1}{j\omega \mu \epsilon} \nabla (\nabla \cdot \mathbf{A}) - \frac{1}{\epsilon} \nabla \times \mathbf{F} \quad (2.1.37)$$

$$\mathbf{H} = \frac{1}{\mu} \nabla \times \mathbf{A} - j\omega \mathbf{F} + \frac{1}{j\omega \mu \epsilon} \nabla (\nabla \cdot \mathbf{F}). \quad (2.1.38)$$

Note that the formulation and the result presented in this section are valid for any homogeneous media, whether they are infinite and finite. Once \mathbf{A} and \mathbf{F} are obtained by solving Equations 2.1.30 and 2.1.36 for a specific problem, the fields can be evaluated using Equations 2.1.37 and 2.1.38.

2.2 SOLUTION OF VECTOR POTENTIALS IN FREE SPACE

With the introduction of magnetic and electric vector potentials \mathbf{A} and \mathbf{F} , the solution of Maxwell's equations is reduced to the solution of the two identical second-order partial differential equations (Eqs. 2.1.30 and 2.1.36). Since these two equations are linear, their solutions can be expressed as a linear superposition of the fundamental solutions due to point sources. For example, the solution to Equation 2.1.30 can be expressed as

$$\mathbf{A}(\mathbf{r}) = \mu \iiint_V \mathbf{J}(\mathbf{r}') G(\mathbf{r}, \mathbf{r}') dV' \quad (2.2.1)$$

where $G(\mathbf{r}, \mathbf{r}')$ is the fundamental solution due to a point source. This fundamental solution is often called the *Green's function* in electromagnetics [8].

2.2.1 Delta Function and Green's Function

To find $G(\mathbf{r}, \mathbf{r}')$, we first need to describe the mathematical representation of a point source. Consider an electric charge of unit strength located at point \mathbf{r}' . When the volume of the charge approaches zero, the charge density can be described by a function

$$\delta(\mathbf{r} - \mathbf{r}') = \begin{cases} \infty & \text{for } \mathbf{r} = \mathbf{r}' \\ 0 & \text{for } \mathbf{r} \neq \mathbf{r}'. \end{cases} \quad (2.2.2)$$

Since the total charge remains as one unit, we have

$$\iiint_V \delta(\mathbf{r} - \mathbf{r}') dV = \begin{cases} 1 & \text{for } \mathbf{r}' \text{ in } V \\ 0 & \text{for } \mathbf{r}' \text{ not in } V. \end{cases} \quad (2.2.3)$$

The function defined in Equations 2.2.2 and 2.2.3 is called the *Dirac delta function* [8]. Clearly, given any function that is continuous at \mathbf{r}' , we have

$$\iiint_V f(\mathbf{r}) \delta(\mathbf{r} - \mathbf{r}') dV = \begin{cases} f(\mathbf{r}') & \text{for } \mathbf{r}' \text{ in } V \\ 0 & \text{for } \mathbf{r}' \text{ not in } V. \end{cases} \quad (2.2.4)$$

This expression represents a volume source $f(\mathbf{r}')$ as a linear superposition of an infinite number of point sources $\delta(\mathbf{r} - \mathbf{r}')$.

In one dimension, the delta function can be described as the limit of a function

$$\delta(x - x') = \lim_{\varepsilon \rightarrow 0} u_\varepsilon(x - x') \quad (2.2.5)$$

where $u_\varepsilon(x - x')$ is called a *delta family*. It can be a rectangular function of width ε and height $1/\varepsilon$, or a triangular function of width 2ε and height $1/\varepsilon$, all centered at $x = x'$. The important feature of the delta function is not its shape but the fact that its effective width approaches zero while its area remains as one unit, that is,

$$\int_a^b \delta(x - x') dx = \begin{cases} 1 & \text{for } x' \text{ in } (a, b) \\ 0 & \text{for } x' \text{ not in } (a, b) \end{cases} \quad (2.2.6)$$

such that

$$\int_a^b f(x) \delta(x - x') dx = \begin{cases} f(x') & \text{for } x' \text{ in } (a, b) \\ 0 & \text{for } x' \text{ not in } (a, b). \end{cases} \quad (2.2.7)$$

The delta function so defined is not a function in the classical sense. For this reason, it is called a *symbolic* or a *generalized function* [9]. Clearly, the delta function is a symmetric function

$$\delta(x - x') = \delta(x' - x). \quad (2.2.8)$$

The three-dimensional delta function in the rectangular, cylindrical, and spherical coordinates is related to the one-dimensional delta function by

$$\delta(\mathbf{r} - \mathbf{r}') = \delta(x - x')\delta(y - y')\delta(z - z') \quad (2.2.9)$$

$$\delta(\mathbf{r} - \mathbf{r}') = \frac{\delta(\rho - \rho')\delta(\phi - \phi')\delta(z - z')}{\rho} \quad (2.2.10)$$

$$\delta(\mathbf{r} - \mathbf{r}') = \frac{\delta(r - r')\delta(\theta - \theta')\delta(\phi - \phi')}{r^2 \sin \theta} \quad (2.2.11)$$

which all satisfy Equation 2.2.3.

With the introduction of the delta function, we can now expand the current density \mathbf{J} as a linear superposition of point sources

$$\mathbf{J}(\mathbf{r}) = \iiint_V \mathbf{J}(\mathbf{r}') \delta(\mathbf{r} - \mathbf{r}') dV'. \quad (2.2.12)$$

Substituting this expression and Equation 2.2.1 into Equation 2.1.30, we obtain

$$\iiint_V [\nabla^2 G(\mathbf{r}, \mathbf{r}') + k^2 G(\mathbf{r}, \mathbf{r}')] \mathbf{J}(\mathbf{r}') dV' = - \iiint_V \delta(\mathbf{r} - \mathbf{r}') \mathbf{J}(\mathbf{r}') dV' \quad (2.2.13)$$

which yields the equation for $G(\mathbf{r}, \mathbf{r}')$ as

$$\nabla^2 G(\mathbf{r}, \mathbf{r}') + k^2 G(\mathbf{r}, \mathbf{r}') = -\delta(\mathbf{r} - \mathbf{r}') \quad (2.2.14)$$

since Equation 2.2.13 has to be valid for any $\mathbf{J}(\mathbf{r}')$. Now, the solution to \mathbf{A} and \mathbf{F} is reduced to the solution of Equation 2.2.14, which is discussed next for the free-space case.

2.2.2 Green's Function in Free Space

The solution to Equation 2.2.14 is complicated for most problems of practical interest. However, if the medium is infinitely large and homogeneous, such as free space, it can be obtained analytically by a couple of different approaches. Here we consider the simplest approach.

To find $G(\mathbf{r}, \mathbf{r}')$ in free space, which is denoted as $G_0(\mathbf{r}, \mathbf{r}')$ to differentiate it from Green's functions for other problems, we first introduce a new coordinate system with its origin located at \mathbf{r}' . Thus, $G_0(\mathbf{r}, \mathbf{r}')$ has a spherical symmetry with respect to this point. Equation 2.2.14 then becomes

$$\frac{1}{r_1^2} \frac{d}{dr_1} \left[r_1^2 \frac{dG_0(\mathbf{r}_1, 0)}{dr_1} \right] + k^2 G_0(\mathbf{r}_1, 0) = -\delta(\mathbf{r}_1 - 0) \quad (2.2.15)$$

where $\mathbf{r}_1 = \mathbf{r} - \mathbf{r}'$ denotes the position vector in the new coordinates. For $r_1 \neq 0$, Equation 2.2.15 can be written as

$$\frac{d^2 [r_1 G_0(\mathbf{r}_1, 0)]}{dr_1^2} + k^2 [r_1 G_0(\mathbf{r}_1, 0)] = 0 \quad (2.2.16)$$

which has two independent solutions

$$r_1 G_0(\mathbf{r}_1, 0) = C e^{\pm jk r_1} \quad (2.2.17)$$

where C is a constant to be determined. One solution, $e^{-jk r_1}$, which becomes $\cos(\omega t - kr_1)$ in the time domain, represents a response, or a wave, propagating away from the point source, and the other solution, $e^{jk r_1}$, which becomes $\cos(\omega t + kr_1)$ in the time domain, represents a response, or a wave, propagating toward the point source. Since the response from a point source can only propagate away from the source, only the first solution is physically meaningful, and it can be written as

$$G_0(\mathbf{r}_1, 0) = C \frac{e^{-jk r_1}}{r_1}. \quad (2.2.18)$$

To determine the unknown constant C , we substitute Equation 2.2.18 into Equation 2.2.15 and integrate over a small sphere centered at $\mathbf{r}_1 = 0$ with its radius $\varepsilon \rightarrow 0$ to find $C = 1/4\pi$. Therefore, Equation 2.2.18 becomes

$$G_0(\mathbf{r}_1, 0) = \frac{e^{-jk r_1}}{4\pi r_1} \quad (2.2.19)$$

and when transformed back to the original coordinates, it is given by

$$G_0(\mathbf{r}, \mathbf{r}') = \frac{e^{-jk|\mathbf{r}-\mathbf{r}'|}}{4\pi |\mathbf{r}-\mathbf{r}'|}. \quad (2.2.20)$$

This function is known as the *free-space scalar Green's function*, which represents a spherical wave propagating away from the point \mathbf{r}' . As will be discussed in Chapter 4, k is known as the wavenumber, which is related to the wavelength λ by $k = 2\pi/\lambda$.

2.2.3 Field-Source Relations in Free Space

With the solution to the Green's function, the vector potentials due to electric and magnetic sources in free space are given by

$$\mathbf{A}(\mathbf{r}) = \frac{\mu}{4\pi} \iiint_V \mathbf{J}(\mathbf{r}') \frac{e^{-jkR}}{R} dV' \quad R = |\mathbf{r} - \mathbf{r}'| \quad (2.2.21)$$

$$\mathbf{F}(\mathbf{r}) = \frac{\epsilon}{4\pi} \iiint_V \mathbf{M}(\mathbf{r}') \frac{e^{-jkR}}{R} dV' \quad R = |\mathbf{r} - \mathbf{r}'|. \quad (2.2.22)$$

These vector potentials can be evaluated for any given sources, from which the fields can be calculated using Equations 2.1.37 and 2.1.38. By letting $\omega \rightarrow 0$, Equation 2.2.21 reduces to Equation 2.1.18 for the magnetostatic case.

By the inverse Fourier transform, we can obtain the vector potentials in the time domain as

$$\mathcal{A}(\mathbf{r}, t) = \frac{\mu}{4\pi} \iiint_V \frac{\mathcal{J}(\mathbf{r}', t - R/c)}{R} dV' \quad (2.2.23)$$

$$\mathcal{F}(\mathbf{r}, t) = \frac{\epsilon}{4\pi} \iiint_V \frac{\mathcal{M}(\mathbf{r}', t - R/c)}{R} dV' \quad (2.2.24)$$

where $c = 1/\sqrt{\mu\epsilon}$ denotes the propagation velocity of the field in the medium. These are called the *retarded potentials* because of the delay effect due to the finite propagation velocity. In this case, Equations 2.1.37 and 2.1.38 become

$$\mathcal{E}(\mathbf{r}, t) = -\frac{\partial \mathcal{A}(\mathbf{r}, t)}{\partial t} + \frac{1}{\mu\epsilon} \int_0^{t-R/c} \nabla[\nabla \cdot \mathcal{A}(\mathbf{r}, \tau)] d\tau - \frac{1}{\epsilon} \nabla \times \mathcal{F}(\mathbf{r}, t) \quad (2.2.25)$$

$$\mathcal{H}(\mathbf{r}, t) = \frac{1}{\mu} \nabla \times \mathcal{A}(\mathbf{r}, t) - \frac{\partial \mathcal{F}(\mathbf{r}, t)}{\partial t} + \frac{1}{\mu\epsilon} \int_0^{t-R/c} \nabla[\nabla \cdot \mathcal{F}(\mathbf{r}, \tau)] d\tau. \quad (2.2.26)$$

These equations provide a means to evaluate transient fields due to given transient sources directly in the time domain.

This book, however, focuses on the analysis of electromagnetic fields in the frequency domain. For a comprehensive treatment of electromagnetic radiation in the time domain, the reader is referred to the book by Smith [7]. The time-domain analysis, although more complicated, can exhibit the underlying physics of radiation more clearly and provide valuable insights for engineering applications.

2.2.4 Why Use Auxiliary Potential Functions

In Section 2.1.2, we formulated the fields in terms of vector potentials that in turn are related to the electric and magnetic current sources. The vector potentials are intermediate functions, which have no physical meaning. In fact, the fields can be formulated directly in terms of the current sources without using vector potentials. For example, by taking the curl of Equation 2.1.1 and then making the use of Equation 2.1.2, we obtain

$$\nabla^2 \mathbf{E} + k^2 \mathbf{E} = j\omega\mu \mathbf{J} - \frac{1}{j\omega\epsilon} \nabla(\nabla \cdot \mathbf{J}) + \nabla \times \mathbf{M}. \quad (2.2.27)$$

Similarly, we obtain for the magnetic field

$$\nabla^2 \mathbf{H} + k^2 \mathbf{H} = j\omega\epsilon \mathbf{M} - \frac{1}{j\omega\mu} \nabla(\nabla \cdot \mathbf{M}) - \nabla \times \mathbf{J}. \quad (2.2.28)$$

On the surface, Equations 2.2.27 and 2.2.28 are more complicated than Equations 2.1.30 and 2.1.36. However, their left-hand side operators are exactly the same; hence, these are the same equations that have the solutions in the same form. A simple comparison gives the solution of Equations 2.2.27 and 2.2.28 as

$$\mathbf{E}(\mathbf{r}) = -\frac{1}{4\pi} \iiint_V \left\{ j\omega\mu \mathbf{J}(\mathbf{r}') - \frac{1}{j\omega\epsilon} \nabla' [\nabla' \cdot \mathbf{J}(\mathbf{r}')] + \nabla' \times \mathbf{M}(\mathbf{r}') \right\} \frac{e^{-jkR}}{R} dV' \quad (2.2.29)$$

$$\mathbf{H}(\mathbf{r}) = -\frac{1}{4\pi} \iiint_V \left\{ j\omega\epsilon \mathbf{M}(\mathbf{r}') - \frac{1}{j\omega\mu} \nabla' [\nabla' \cdot \mathbf{M}(\mathbf{r}')] - \nabla' \times \mathbf{J}(\mathbf{r}') \right\} \frac{e^{-jkR}}{R} dV' \quad (2.2.30)$$

where ∇' denotes that the derivatives are taken with respect to \mathbf{r}' . This approach can be called the direct approach, in contrast to the one based on intermediate vector potentials (Fig. 2.1).

Mathematically, the two approaches to evaluating the fields from given sources involve the same number of calculations: a volume integral over the source region, a curl

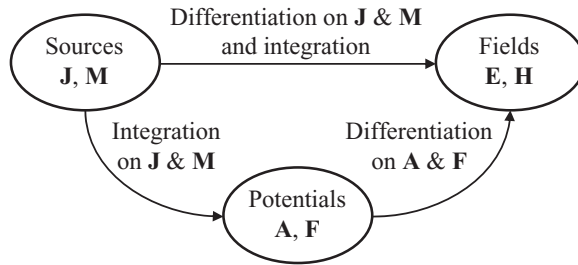


Figure 2.1 Two approaches to calculating radiated fields from sources.

operation, a divergence, and then a gradient operation. The major difference is that in Equations 2.2.29 and 2.2.30, the curl, divergence, and gradient operations are applied to the source functions (\mathbf{J} and \mathbf{M}), whereas in Equations 2.1.37 and 2.1.38 these operations are applied to the vector potential functions. For source functions that have an analytical and continuous form so that their derivatives can easily be calculated, these two approaches are indeed equivalent. Unfortunately, the source functions in many problems of practical interest do not have such a form and their derivatives do not exist in the classical sense. One example is a line current source and another example is a surface current source. In these cases, we have expressions for the current density in terms of the delta functions, but we cannot evaluate their curl, divergence, and gradient without resorting to the concept of generalized functions. Consequently, it is very difficult to use Equations 2.2.29 and 2.2.30 to calculate the fields in these cases. On the other hand, in the approach that utilizes the vector potential functions, we need only the values of the source functions to evaluate the vector potentials via Equations 2.2.21 and 2.2.22. These vector potential functions are analytical in terms of \mathbf{r} ; hence, their curl, divergence, and then gradient operations, as required by Equations 2.1.37 and 2.1.38, can always be evaluated without any difficulty. Therefore, with the introduction of vector potentials, the requirement on the form of the source functions (\mathbf{J} and \mathbf{M}) is significantly relaxed, making the approach much more useful for practical applications.

2.2.5 Free-Space Dyadic Green's Functions

Substituting Equations 2.2.21 and 2.2.22 into Equation 2.1.37, we obtain the direct field–source relation for the electric field as

$$\begin{aligned} \mathbf{E}(\mathbf{r}) = & -j\omega\mu \iiint_V \left[G_0(\mathbf{r}, \mathbf{r}') \mathbf{J}(\mathbf{r}') + \frac{1}{k^2} \nabla \nabla G_0(\mathbf{r}, \mathbf{r}') \cdot \mathbf{J}(\mathbf{r}') \right] dV' \\ & - \iiint_V \nabla G_0(\mathbf{r}, \mathbf{r}') \times \mathbf{M}(\mathbf{r}') dV'. \end{aligned} \quad (2.2.31)$$

In arriving at this expression, we have exchanged the order of integration with respect to \mathbf{r}' and differentiation with respect to \mathbf{r} and applied some common vector identities. If we introduce a new mathematical quantity defined by

$$\tilde{\mathbf{I}} = \hat{x}\hat{x} + \hat{y}\hat{y} + \hat{z}\hat{z} \quad (2.2.32)$$

it can be shown easily that

$$\mathbf{J}(\mathbf{r}') = \tilde{\mathbf{I}} \cdot \mathbf{J}(\mathbf{r}'), \quad \nabla G_0(\mathbf{r}, \mathbf{r}') \times \mathbf{M}(\mathbf{r}') = [\nabla G_0(\mathbf{r}, \mathbf{r}') \times \tilde{\mathbf{I}}] \cdot \mathbf{M}(\mathbf{r}'). \quad (2.2.33)$$

With these, Equation 2.2.31 can be written as

$$\mathbf{E}(\mathbf{r}) = -j\omega\mu \iiint_V \left[\left(\tilde{\mathbf{I}} + \frac{1}{k^2} \nabla \nabla \right) G_0(\mathbf{r}, \mathbf{r}') \right] \cdot \mathbf{J}(\mathbf{r}') dV' - \iiint_V [\nabla G_0(\mathbf{r}, \mathbf{r}') \times \tilde{\mathbf{I}}] \cdot \mathbf{M}(\mathbf{r}') dV' \quad (2.2.34)$$

which can be written more compactly as

$$\mathbf{E}(\mathbf{r}) = -j\omega\mu \iiint_V \tilde{\mathbf{G}}_{e0}(\mathbf{r}, \mathbf{r}') \cdot \mathbf{J}(\mathbf{r}') dV' - \iiint_V \tilde{\mathbf{G}}_{m0}(\mathbf{r}, \mathbf{r}') \cdot \mathbf{M}(\mathbf{r}') dV' \quad (2.2.35)$$

where

$$\tilde{\mathbf{G}}_{e0}(\mathbf{r}, \mathbf{r}') = \left(\tilde{\mathbf{I}} + \frac{1}{k^2} \nabla \nabla \right) G_0(\mathbf{r}, \mathbf{r}') \quad (2.2.36)$$

$$\tilde{\mathbf{G}}_{m0}(\mathbf{r}, \mathbf{r}') = \nabla G_0(\mathbf{r}, \mathbf{r}') \times \tilde{\mathbf{I}}. \quad (2.2.37)$$

Using these new functions, we can also write Equation 2.1.38 as

$$\mathbf{H}(\mathbf{r}) = \iiint_V \tilde{\mathbf{G}}_{m0}(\mathbf{r}, \mathbf{r}') \cdot \mathbf{J}(\mathbf{r}') dV' - j\omega\epsilon \iiint_V \tilde{\mathbf{G}}_{e0}(\mathbf{r}, \mathbf{r}') \cdot \mathbf{M}(\mathbf{r}') dV'. \quad (2.2.38)$$

The new function $\tilde{\mathbf{G}}_{e0}(\mathbf{r}, \mathbf{r}')$ defined in Equation 2.2.36 is called the *electric dyadic Green's function* of free space, and the function $\tilde{\mathbf{G}}_{m0}(\mathbf{r}, \mathbf{r}')$ defined in Equation 2.2.37 is called the *magnetic dyadic Green's function* of free space [10]. These two functions are introduced here so that the long expressions of the field-source relation can be written in compact form.

To better understand the dyadic Green's functions, a brief introduction of the new mathematical quantity *dyad* is in order. A dyad, denoted by $\tilde{\mathbf{D}}$,² is formed by two vectors side by side without any operations:

$$\tilde{\mathbf{D}} = \mathbf{AB}. \quad (2.2.39)$$

This entity by itself does not have any physical interpretation as we have for a vector. However, when it acts upon another vector, the result becomes meaningful. The major role of a dyad is that its scalar product with a vector produces another vector of different magnitude and direction. For example, its anterior scalar product with vector \mathbf{C} yields

$$\mathbf{C} \cdot \tilde{\mathbf{D}} = (\mathbf{C} \cdot \mathbf{A})\mathbf{B} \quad (2.2.40)$$

which is a vector. Its posterior scalar product with vector \mathbf{C} yields

$$\tilde{\mathbf{D}} \cdot \mathbf{C} = \mathbf{A}(\mathbf{B} \cdot \mathbf{C}) \quad (2.2.41)$$

which is also a vector. Evidently, the resulting vectors in Equations 2.2.40 and 2.2.41 are different. In addition to the two scalar products, there are two vector products. The anterior vector product is defined as

$$\mathbf{C} \times \tilde{\mathbf{D}} = (\mathbf{C} \times \mathbf{A})\mathbf{B} \quad (2.2.42)$$

and the posterior vector product is defined as

$$\tilde{\mathbf{D}} \times \mathbf{C} = \mathbf{A}(\mathbf{B} \times \mathbf{C}). \quad (2.2.43)$$

Clearly, these products are two different dyads. A dyad can have its curl and divergence and can be formed by applying a gradient to a vector. For a detailed treatment of these operations, the reader is referred to the book by Tai [11].

The dyad defined in Equation 2.2.39 is a special entity since it contains only six independent scalar components, three in each of the two vectors. A more general dyad, also called a *tensor*, is defined as

$$\tilde{\mathbf{D}} = \mathbf{D}_x \hat{x} + \mathbf{D}_y \hat{y} + \mathbf{D}_z \hat{z} \quad (2.2.44)$$

where \mathbf{D}_x , \mathbf{D}_y , and \mathbf{D}_z are vectors. Therefore, Equation 2.2.44 can be expressed as

$$\tilde{\mathbf{D}} = D_{xx} \hat{x}\hat{x} + D_{yx} \hat{y}\hat{x} + D_{zx} \hat{z}\hat{x} + D_{xy} \hat{x}\hat{y} + D_{yy} \hat{y}\hat{y} + D_{zy} \hat{z}\hat{y} + D_{xz} \hat{x}\hat{z} + D_{yz} \hat{y}\hat{z} + D_{zz} \hat{z}\hat{z} \quad (2.2.45)$$

which contains nine independent components. The special dyad defined by Equation 2.2.32 is called the *unit dyad* or *identity dyad*. It is evident that

$$\mathbf{C} \cdot \tilde{\mathbf{I}} = \tilde{\mathbf{I}} \cdot \mathbf{C} = \mathbf{C}. \quad (2.2.46)$$

With the unique capability to change both the magnitude and direction of a vector through its scalar product, a dyad becomes very useful in vector operations. It allows long field-source expressions to be cast in a very compact form.

Although it is difficult to physically interpret or describe a dyadic quantity, the meaning of the components of the dyadic Green's functions is obvious. If we express $\tilde{\mathbf{G}}_{e0}(\mathbf{r}, \mathbf{r}')$ and $\tilde{\mathbf{G}}_{m0}(\mathbf{r}, \mathbf{r}')$ in the form of Equation 2.2.44

$$\tilde{\mathbf{G}}_{e0}(\mathbf{r}, \mathbf{r}') = \mathbf{G}_{e0,x}(\mathbf{r}, \mathbf{r}')\hat{x} + \mathbf{G}_{e0,y}(\mathbf{r}, \mathbf{r}')\hat{y} + \mathbf{G}_{e0,z}(\mathbf{r}, \mathbf{r}')\hat{z} \quad (2.2.47)$$

$$\tilde{\mathbf{G}}_{m0}(\mathbf{r}, \mathbf{r}') = \mathbf{G}_{m0,x}(\mathbf{r}, \mathbf{r}')\hat{x} + \mathbf{G}_{m0,y}(\mathbf{r}, \mathbf{r}')\hat{y} + \mathbf{G}_{m0,z}(\mathbf{r}, \mathbf{r}')\hat{z} \quad (2.2.48)$$

and then substitute them into Equations 2.2.35 and 2.2.38, we can see clearly that $-j\omega\mu\mathbf{G}_{e0,u}(\mathbf{r}, \mathbf{r}')$ represents the electric field at \mathbf{r} generated by a \hat{u} -directed infinitesimal electric current element located at \mathbf{r}' , and $\mathbf{G}_{m0,u}(\mathbf{r}, \mathbf{r}')$ represents the magnetic field at \mathbf{r} generated by the same current element.

Consider the case where there is only an electric current source. By substituting Equations 2.2.35 and 2.2.38 into Equations 2.1.1 and 2.1.2 in the absence of \mathbf{M} , we obtain the relations between $\tilde{\mathbf{G}}_{e0}(\mathbf{r}, \mathbf{r}')$ and $\tilde{\mathbf{G}}_{m0}(\mathbf{r}, \mathbf{r}')$ as

$$\nabla \times \tilde{\mathbf{G}}_{e0}(\mathbf{r}, \mathbf{r}') = \tilde{\mathbf{G}}_{m0}(\mathbf{r}, \mathbf{r}') \quad (2.2.49)$$

$$\nabla \times \tilde{\mathbf{G}}_{m0}(\mathbf{r}, \mathbf{r}') = k^2 \tilde{\mathbf{G}}_{e0}(\mathbf{r}, \mathbf{r}') + \tilde{\mathbf{I}}\delta(\mathbf{r} - \mathbf{r}'). \quad (2.2.50)$$

From these, we can further use vector identities to find

$$\nabla \cdot \tilde{\mathbf{G}}_{e0}(\mathbf{r}, \mathbf{r}') = -\frac{1}{k^2} \nabla \delta(\mathbf{r} - \mathbf{r}') \quad (2.2.51)$$

$$\nabla \cdot \tilde{\mathbf{G}}_{m0}(\mathbf{r}, \mathbf{r}') = 0. \quad (2.2.52)$$

The four equations are analogous to the four Maxwell's equations. In deriving these equations, we only assumed that the fields can be expressed in the form of Equation 2.2.35 and 2.2.38. Therefore, these equations are not limited to the free-space case. The free-space

limitation is imposed in Equations 2.2.36 and 2.2.37 due to the use of the free-space scalar Green's function.

2.3 ELECTROMAGNETIC RADIATION IN FREE SPACE

With the field-source formulation developed in the preceding section, we can in principle evaluate the electromagnetic fields radiated by any kind of source in free space. Here, we consider a few examples to illustrate the procedure of evaluation. This evaluation is a basic tool for antenna analysis [12–14].

2.3.1 Infinitesimal Electric Dipole

Consider a very short current filament that has a length l and carries a time-harmonic electric current I . Such a filament is called an infinitesimal electric dipole and is characterized by the dipole moment Il with $l \rightarrow 0$. Assume that the dipole is z -directed and placed at the origin (Fig. 2.2). To find its radiated field, we first evaluate its magnetic vector potential:

$$\mathbf{A}(\mathbf{r}) = \frac{\mu}{4\pi} \iiint_V \mathbf{J}(\mathbf{r}') \frac{e^{-jkR}}{R} dV' = \frac{\mu}{4\pi} \int_{-l/2}^{l/2} \hat{z} I \frac{e^{-jkR}}{R} dz' = \hat{z} \frac{\mu Il}{4\pi r} e^{-jkr}. \quad (2.3.1)$$

To calculate the electric and magnetic fields in spherical coordinates, we can project \mathbf{A} onto the three directions to find

$$A_r = A_z \cos \theta = \frac{\mu Il}{4\pi r} e^{-jkr} \cos \theta \quad (2.3.2)$$

$$A_\theta = -A_z \sin \theta = -\frac{\mu Il}{4\pi r} e^{-jkr} \sin \theta \quad (2.3.3)$$

and $A_\phi = 0$. Hence, the magnetic field is given by

$$\mathbf{H} = \frac{1}{\mu} \nabla \times \mathbf{A} = \hat{\phi} \frac{1}{\mu r} \left[\frac{\partial}{\partial r} (r A_\theta) - \frac{\partial A_r}{\partial \theta} \right] = \hat{\phi} \frac{j k l l \sin \theta}{4\pi r} \left(1 + \frac{1}{jkr} \right) e^{-jkr} \quad (2.3.4)$$

from which the electric field can be calculated as

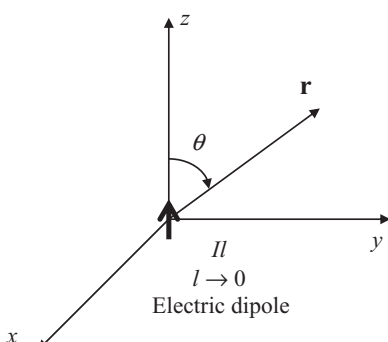


Figure 2.2 Radiation of an infinitesimal electric dipole in free space.

$$\begin{aligned}\mathbf{E} &= \frac{1}{j\omega\epsilon} \nabla \times \mathbf{H} \\ &= \hat{r} \frac{\eta Il \cos\theta}{2\pi r^2} \left(1 + \frac{1}{jkr} \right) e^{-jkr} + \hat{\theta} \frac{jk\eta Il \sin\theta}{4\pi r} \left[1 + \frac{1}{jkr} - \frac{1}{(kr)^2} \right] e^{-jkr}\end{aligned}\quad (2.3.5)$$

where $\eta = \sqrt{\mu/\epsilon}$. Figure 2.3 shows the radiated electric and magnetic fields in a plane that contains the z -axis, and the plots are rotationally symmetric about this axis.

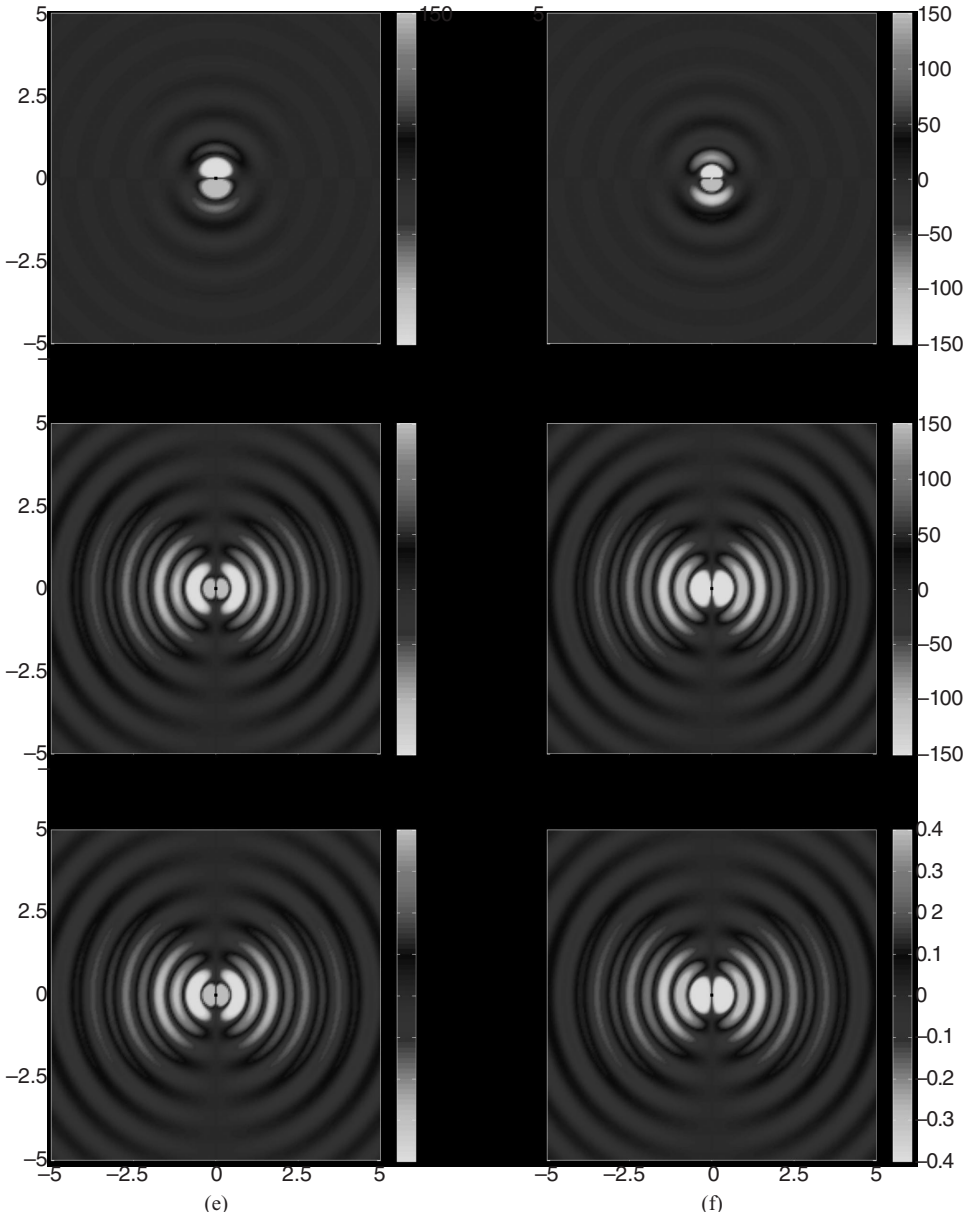


Figure 2.3 Field radiated by an infinitesimal dipole ($Il = 1 \text{ A} \cdot \text{m}$) in a $10\lambda \times 10\lambda$ region. (a) Real part of E_r (V/m). (b) Imaginary part of E_r (V/m). (c) Real part of E_θ (V/m). (d) Imaginary part of E_θ (V/m). (e) Real part of H_ϕ (A/m). (f) Imaginary part of H_ϕ (A/m). (See color insert.)

If we are interested in the field far away from the source, we have $kr \gg 1$ so that we can keep only the dominant term in the field expressions to find the non-trivial field components

$$E_\theta \approx \frac{jk\eta Il \sin \theta}{4\pi r} e^{-jkr}, \quad H_\phi \approx \frac{jkIl \sin \theta}{4\pi r} e^{-jkr}. \quad (2.3.6)$$

This is called the *far field*. Its power flow density is given by

$$\mathbf{S} = \frac{1}{2} \mathbf{E} \times \mathbf{H}^* = \hat{r} \frac{\eta}{2} \left| \frac{kIl \sin \theta}{4\pi r} \right|^2 \quad (2.3.7)$$

which has the shape of a torus. There is no radiation along either the positive or negative z -direction, and the maximum radiation occurs in the xy -plane.

Using the field obtained above, we can integrate the complex Poynting vector over a spherical surface S of radius r to find the complex exiting power as

$$P_e = \frac{1}{2} \iint_S (\mathbf{E} \times \mathbf{H}^*) \cdot d\mathbf{S} = \frac{1}{2} \int_0^{2\pi} \int_0^\pi E_\theta H_\phi^* r^2 \sin \theta d\theta d\phi = \eta \frac{\pi}{3} \left| \frac{Il}{\lambda} \right|^2 \left[1 - \frac{j}{(kr)^3} \right]. \quad (2.3.8)$$

Its real part yields the time-average radiated power as

$$\text{Re}(P_e) = \eta \frac{\pi}{3} \left| \frac{Il}{\lambda} \right|^2 \quad (2.3.9)$$

which is independent of r . Therefore, if we are interested only in the time-average radiated power, we can use the simple far-field expressions in Equation 2.3.6 to arrive at the same result. Consider the region enclosed by two spherical surfaces of radii a and b with $b > a$. The reactive power in this region is then given by

$$2\omega(\bar{W}_m - \bar{W}_e) = \eta \frac{\pi}{3} \left| \frac{Il}{\lambda} \right|^2 \left[\frac{1}{(kb)^3} - \frac{1}{(ka)^3} \right] \quad (2.3.10)$$

which indicates that the time-average electric energy surrounding the electric dipole is always greater than the time-average magnetic energy.

2.3.2 Finite Electric Dipole

The infinitesimal electric dipole does not exist in reality because of the assumption of a uniform current on the dipole. Here we consider a more realistic example, which is an electric dipole of finite length L , fed at the center (Fig. 2.4). The current induced on the dipole is usually unknown and has to be calculated by solving a boundary-value problem using a numerical method, discussed in Chapters 8–11. Here, we assume a known current distribution and then calculate its radiated field. When the dipole is shorter than a wavelength, the electric current distribution on the dipole can be approximated as

$$I(z) = I_0 \sin \left[k \left(\frac{L}{2} - |z| \right) \right] \quad (2.3.11)$$

where I_0 denotes a constant. The magnetic vector potential is then given by

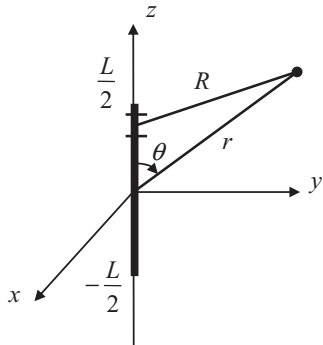


Figure 2.4 Radiation of a finite electric dipole in free space.

$$\mathbf{A} = \hat{z} \frac{\mu}{4\pi} \int_{-L/2}^{L/2} I_0 \sin \left[k \left(\frac{L}{2} - |z'| \right) \right] \frac{e^{-jkr}}{R} dz' \quad (2.3.12)$$

where $R = \sqrt{r^2 + z'^2 - 2rz' \cos \theta}$. This integral is difficult to evaluate because of its complex integrand. However, if we are interested only in the far field such that $r \gg z'$, then R can be simplified significantly as $R \approx r - z' \cos \theta$. Using this result in the exponential term and simply replacing R in the denominator by r , Equation 2.3.12 can be written as

$$\mathbf{A} = \hat{z} \frac{\mu I_0}{4\pi r} e^{-jkr} \int_{-L/2}^{L/2} \sin \left[k \left(\frac{L}{2} - |z'| \right) \right] e^{jkz' \cos \theta} dz'. \quad (2.3.13)$$

The integral can be evaluated by first breaking the integration region into two, one for $(-L/2, 0)$ and the other for $(0, L/2)$, and then repeatedly performing integration by parts. The result is given by

$$A_z = \frac{\mu I_0}{2\pi r} e^{-jkr} \frac{\cos \left(k \frac{L}{2} \cos \theta \right) - \cos \left(k \frac{L}{2} \right)}{k \sin^2 \theta} \quad (2.3.14)$$

from which the far field can be found as

$$E_\theta = \frac{j\eta I_0}{2\pi r} e^{-jkr} \frac{\cos \left(k \frac{L}{2} \cos \theta \right) - \cos \left(k \frac{L}{2} \right)}{\sin \theta} \quad (2.3.15)$$

$$H_\phi = \frac{jI_0}{2\pi r} e^{-jkr} \frac{\cos \left(k \frac{L}{2} \cos \theta \right) - \cos \left(k \frac{L}{2} \right)}{\sin \theta} \quad (2.3.16)$$

by following the same procedure used for the infinitesimal dipole case. With this field solution, the time-average power flow density and the total radiated power can readily be obtained. For a very short dipole ($kL \ll 1$), the pattern of the far field is similar to that of an infinitesimal dipole. As the length increases, the pattern becomes more directive as the radiated power is more concentrated toward $\theta = \pi/2$ (the xy -plane). However, when the length exceeds one wavelength, the single radiation beam begins to split because the current on the dipole no longer flows in the same direction according to Equation 2.3.11.

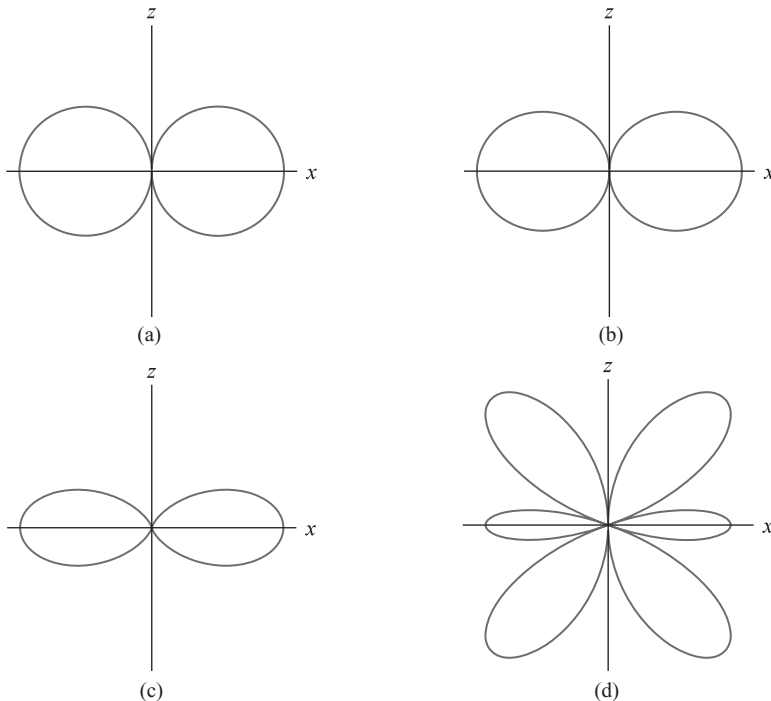


Figure 2.5 Far-field radiation patterns of finite electric dipoles of different lengths. (a) $L = \lambda/4$. (b) $L = \lambda/2$. (c) $L = \lambda$. (d) $L = 3\lambda/2$.

This reduces radiation toward $\theta = \pi/2$ and increases radiation in other directions, as illustrated in Figure 2.5. Finally, we note again that the current induced on the dipole is usually unknown and has to be numerically computed; the expression in Equation 2.3.11 is only a rough approximation.

2.3.3 Far-Field Approximation and the Sommerfeld Radiation Condition

The integrals in the vector potentials (Eqs. 2.2.21 and 2.2.22) are usually very complicated and can be evaluated only for very simple sources such as infinitesimal dipoles. Fortunately, in most practical applications, we are interested in far fields where $R \gg \lambda$ and $r \gg r'$. In such cases, the integrals can be simplified significantly. By denoting the angle between \mathbf{r} and \mathbf{r}' as ψ , we have

$$R = |\mathbf{r} - \mathbf{r}'| = \sqrt{r^2 + r'^2 - 2rr' \cos\psi} \approx r - r' \cos\psi \quad (2.3.17)$$

as illustrated in Figure 2.6. Substituting this into Equations 2.2.21 and 2.2.22, we obtain

$$\mathbf{A} = \frac{\mu}{4\pi r} e^{-jkr} \mathbf{N}, \quad \mathbf{F} = \frac{\epsilon}{4\pi r} e^{-jkr} \mathbf{L} \quad (2.3.18)$$

where

$$\mathbf{N} = \iiint_V \mathbf{J} e^{jkr' \cos\psi} dV', \quad \mathbf{L} = \iiint_V \mathbf{M} e^{jkr' \cos\psi} dV'. \quad (2.3.19)$$

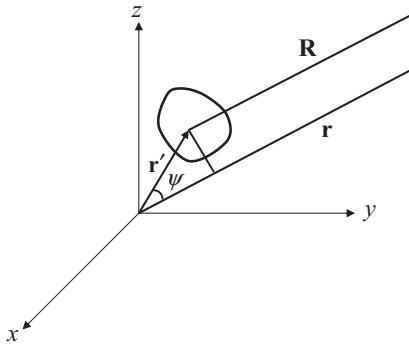


Figure 2.6 For a far-field observation point, \mathbf{R} and \mathbf{r} are practically parallel to each other.

If we further substitute Equation 2.3.18 into Equations 2.1.37 and 2.1.38 and keep only the dominant terms [5], we obtain the far fields as

$$\mathbf{E} \approx \frac{jk}{4\pi r} e^{-jkr} [\hat{r} \times \mathbf{L} - \eta(\mathbf{N} - \hat{r}N_r)] \quad (2.3.20)$$

$$\mathbf{H} \approx -\frac{jk}{4\pi r} e^{-jkr} \left[\frac{1}{\eta} (\mathbf{L} - \hat{r}L_r) + \hat{r} \times \mathbf{N} \right]. \quad (2.3.21)$$

Note that because $\hat{r} \times \mathbf{L} = \hat{\phi}L_\theta - \hat{\theta}L_\phi$ and $\mathbf{N} - \hat{r}N_r = \hat{\theta}N_\theta + \hat{\phi}N_\phi$, only the angular components of \mathbf{L} and \mathbf{N} are needed in the calculation of the far fields. The resulting far fields do not have any radial components and hence are transverse to \hat{r} :

$$\mathbf{E} \approx -\frac{jk}{4\pi r} e^{-jkr} [\hat{\theta}(L_\phi + \eta N_\theta) - \hat{\phi}(L_\theta - \eta N_\phi)] \quad (2.3.22)$$

$$\mathbf{H} \approx -\frac{jk}{4\pi r} e^{-jkr} \frac{1}{\eta} [\hat{\theta}(L_\theta - \eta N_\phi) + \hat{\phi}(L_\phi + \eta N_\theta)]. \quad (2.3.23)$$

This conclusion is valid for any kind of source located within a finite distance from the origin of the coordinates.

To evaluate \mathbf{L} and \mathbf{N} via Equation 2.3.19, we have to first find the expression for $r'\cos\psi$. For a general problem, this can be done simply by taking a dot-product between \mathbf{r}' and \hat{r} , that is,

$$\mathbf{r}' \cdot \hat{r} = \mathbf{r}' \cdot \hat{x} \sin \theta \cos \phi + \mathbf{r}' \cdot \hat{y} \sin \theta \sin \phi + \mathbf{r}' \cdot \hat{z} \cos \theta. \quad (2.3.24)$$

The expression for \mathbf{r}' to be used here depends on specific problems. From Equations 2.3.20 and 2.3.21, we find that the power flow density is given by

$$\begin{aligned} \mathbf{S} &= \frac{1}{2} \mathbf{E} \times \mathbf{H}^* \\ &= \hat{r} \left(\frac{k}{4\pi r} \right)^2 \left[\frac{1}{\eta} (|L_\theta|^2 + |L_\phi|^2) + \eta (|N_\theta|^2 + |N_\phi|^2) + 2 \operatorname{Re} (L_\phi N_\theta^* - L_\theta N_\phi^*) \right]. \end{aligned} \quad (2.3.25)$$

It is evident that while the total field due to two sources is the linear superposition of those due to each individual source, the power density is not a linear superposition as it contains cross terms.

Equations 2.3.20 and 2.3.21 indicate that the electric and magnetic far fields have a very simple relation. To see this, we take the cross-product of Equation 2.3.20 with \hat{r} to find that

$$\hat{r} \times \mathbf{E} = -\frac{jk}{4\pi r} e^{-jkr} [(\mathbf{L} - \hat{r} L_r) + \eta (\hat{r} \times \mathbf{N})] = \eta \mathbf{H}. \quad (2.3.26)$$

This result can be more explicitly written as

$$\lim_{r \rightarrow \infty} r(\nabla \times \mathbf{E} + jk\hat{r} \times \mathbf{E}) = 0. \quad (2.3.27)$$

A similar relation can also be found for the magnetic field:

$$\lim_{r \rightarrow \infty} r(\nabla \times \mathbf{H} + jk\hat{r} \times \mathbf{H}) = 0. \quad (2.3.28)$$

The two equations above are known as the *Sommerfeld radiation conditions* [15], which are applicable to any field radiated by any source located within a finite distance from the origin of the coordinates. They dictate that (1) far away from the source the fields have to propagate away from the source, (2) the electric and magnetic fields are transverse to the propagation direction and are orthogonal to each other, and (3) the magnitudes of the electric and magnetic fields have a fixed ratio equal to $\eta = \sqrt{\mu/\epsilon}$.

2.3.4 Circular Current Loop and Magnetic Dipole

With the far-field approximation developed above, we can now deal with more complicated problems. Here, we consider the radiation of a circular loop of radius a carrying a uniform time-harmonic current $\mathbf{I} = \hat{\phi}' I$ (Fig. 2.7). Since $\hat{\phi}'$ is not a constant vector, we can first decompose it into $\hat{\phi}' = -\hat{x} \sin \phi' + \hat{y} \cos \phi'$. Next, we substitute $\mathbf{r}' = a \cos \phi' \hat{x} + a \sin \phi' \hat{y}$ into Equation 2.3.24 to find $r' \cos \psi = a \sin \theta \cos(\phi - \phi')$. When these are substituted into the first equation in Equation 2.3.19, we have

$$\mathbf{N} = \int_0^{2\pi} (-\hat{x} I \sin \phi' + \hat{y} I \cos \phi') e^{jka \sin \theta \cos(\phi - \phi')} ad\phi'. \quad (2.3.29)$$

Since we are evaluating the far field, we need only N_ϕ and N_θ . The N_ϕ is given by

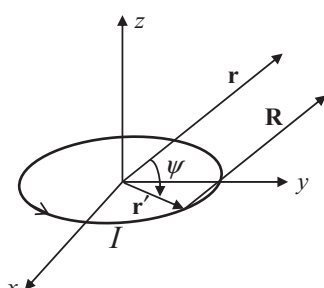


Figure 2.7 Radiation of a circular electric current loop in free space.

$$\begin{aligned}
N_\phi &= -N_x \sin \phi + N_y \cos \phi \\
&= aI \int_0^{2\pi} \cos(\phi - \phi') e^{jka \sin \theta \cos(\phi - \phi')} d\phi' \\
&= aI \int_0^\pi \cos \Phi' e^{jka \sin \theta \cos \Phi'} d\Phi' + aI \int_\pi^{2\pi} \cos \Phi' e^{jka \sin \theta \cos \Phi'} d\Phi' \\
&= aI \int_0^\pi \cos \Phi' e^{jka \sin \theta \cos \Phi'} d\Phi' - aI \left[\int_0^\pi \cos \Phi' e^{jka \sin \theta \cos \Phi'} d\Phi' \right]^*. \quad (2.3.30)
\end{aligned}$$

The integral above can be evaluated to give [16]

$$\int_0^\pi \cos \Phi' e^{jka \sin \theta \cos \Phi'} d\Phi' = j\pi J_1(ka \sin \theta) \quad (2.3.31)$$

where J_1 denotes the first-order Bessel function, which will be discussed in more detail in Chapter 6. Hence,

$$N_\phi = j2\pi aI J_1(ka \sin \theta). \quad (2.3.32)$$

It is easy to find that

$$N_\theta = N_x \cos \theta \cos \phi + N_y \cos \theta \sin \phi = 0. \quad (2.3.33)$$

Substituting Equations 2.3.32 and 2.3.33 into Equations 2.3.22 and 2.3.23, we find the far field:

$$\mathbf{E} \approx \hat{\phi} \frac{\eta ka I}{2r} e^{-jkr} J_1(ka \sin \theta) \quad (2.3.34)$$

$$\mathbf{H} \approx -\hat{\theta} \frac{ka I}{2r} e^{-jkr} J_1(ka \sin \theta). \quad (2.3.35)$$

For a small loop such that $ka \ll 1$, $J_1(ka \sin \theta) \approx (ka \sin \theta)/2$. The far field can be simplified as

$$\mathbf{E} \approx \hat{\phi} \frac{\eta (ka)^2 I}{4r} e^{-jkr} \sin \theta \quad (2.3.36)$$

$$\mathbf{H} \approx -\hat{\theta} \frac{(ka)^2 I}{4r} e^{-jkr} \sin \theta. \quad (2.3.37)$$

It is interesting to compare this result for a small electric current loop with that of the far field of a z -directed infinitesimal magnetic dipole that carries a magnetic current K and has a length l . Assuming that this dipole is located at the origin, it can be shown (see Problem 2.12) that its far field is given by

$$\mathbf{E} \approx -\hat{\phi} \frac{j k K l}{4\pi r} e^{-jkr} \sin \theta \quad (2.3.38)$$

$$\mathbf{H} \approx \hat{\theta} \frac{j k K l}{4\eta\pi r} e^{-jkr} \sin \theta. \quad (2.3.39)$$

A comparison of these with Equations 2.3.36 and 2.3.37 reveals that the two fields are identical if

$$KI = j\omega\mu IS \quad (2.3.40)$$

where $S = \pi a^2$ denotes the area of the current loop. It can be shown (see Problem 2.14) that not only their far fields, but also their near fields, are identical. Therefore, a small electric current loop is equivalent to an infinitesimal magnetic dipole with its dipole moment given by Equation 2.3.40, whose field is easier to formulate. This is a good example to show the usefulness of an equivalent magnetic source.

2.4 RADIATION BY SURFACE CURRENTS AND PHASED ARRAYS

In this section, we consider electromagnetic fields radiated by a finite planar surface current and then by an array of electric dipoles in free space. Our purpose is to study the effect of a source on its electromagnetic radiation.

2.4.1 Radiation by a Surface Current

Consider a planar electric surface current of length A and width B placed in the xy -plane (Fig. 2.8). The surface current density is given by

$$\mathbf{J}_s(x, y) = \hat{y} J_0 e^{-j(h_x x + h_y y)} \quad (2.4.1)$$

where J_0 , h_x , and h_y are constants. To evaluate the field radiated by this surface current in free space, we first evaluate the vector function \mathbf{N} using the first equation in Equation 2.3.19

$$\begin{aligned} \mathbf{N} &= \hat{y} J_0 \int_{-B/2}^{B/2} \int_{-A/2}^{A/2} e^{-j(h_x x' + h_y y')} e^{jk(x' \sin \theta \cos \phi + y' \sin \theta \sin \phi)} dx' dy' \\ &= \hat{y} J_0 AB \frac{\sin X}{X} \frac{\sin Y}{Y} \end{aligned} \quad (2.4.2)$$

where

$$X = (k \sin \theta \cos \phi - h_x) \frac{A}{2}, \quad Y = (k \sin \theta \sin \phi - h_y) \frac{B}{2}. \quad (2.4.3)$$

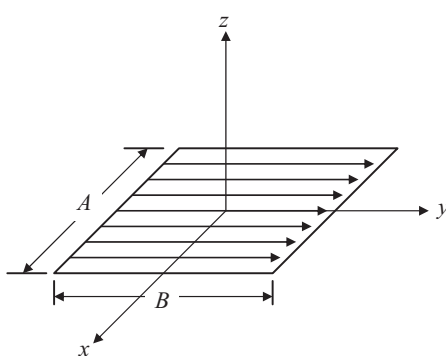


Figure 2.8 A rectangular surface current coincident with the xy -plane.

From Equation 2.3.20, we obtain the electric far field

$$E_\theta \approx -\frac{jk\eta J_0 AB}{4\pi r} e^{-jkr} \cos\theta \sin\phi \frac{\sin X}{X} \frac{\sin Y}{Y} \quad (2.4.4)$$

$$E_\phi \approx -\frac{jk\eta J_0 AB}{4\pi r} e^{-jkr} \cos\phi \frac{\sin X}{X} \frac{\sin Y}{Y}. \quad (2.4.5)$$

If the phase constants h_x and h_y can be controlled by two parameters θ_s and ϕ_s such that

$$h_x = k \sin \theta_s \cos \phi_s, \quad h_y = k \sin \theta_s \sin \phi_s \quad (2.4.6)$$

X and Y can be expressed as

$$X = (\sin \theta \cos \phi - \sin \theta_s \cos \phi_s) \frac{kA}{2}, \quad Y = (\sin \theta \sin \phi - \sin \theta_s \sin \phi_s) \frac{kB}{2}. \quad (2.4.7)$$

Clearly, the radiated field has a maximum magnitude in two directions. One direction is specified by $\theta = \theta_s$ and $\phi = \phi_s$. In this direction,

$$E_\theta \approx -\frac{jk\eta J_0 AB}{4\pi r} e^{-jkr} \cos \theta_s \sin \phi_s \quad (2.4.8)$$

$$E_\phi \approx -\frac{jk\eta J_0 AB}{4\pi r} e^{-jkr} \cos \phi_s. \quad (2.4.9)$$

The other direction is $\theta = \pi - \theta_s$ and $\phi = \phi_s$ with the same magnitude for the far field. Therefore, the directions of the maximum radiated field can be controlled effectively by the parameters θ_s and ϕ_s . Figure 2.9 shows the normalized total electric field in the decibel scale of a $5\lambda \times 5\lambda$ surface current as a function of θ and ϕ in the three-dimensional space for two cases: (1) $\theta_s = 0$ and $\phi_s = 0$; and (2) $\theta_s = 30^\circ$ and $\phi_s = 135^\circ$.

From Equations 2.4.4 and 2.4.5 in conjunction with Equation 2.4.7, it can be seen that the beamwidth of the radiated field can be controlled by A and B . Consider the case with $\theta_s = 0$ and $\phi_s = 0$ (broadside radiation) for the sake of simplicity. For the field in the E-plane ($\phi = \pi/2$), the electric field is given by

$$E_\theta \approx -\frac{j\eta J_0 A}{2\pi r} e^{-jkr} \cot \theta \sin\left(\frac{kB \sin \theta}{2}\right), \quad E_\phi \approx 0. \quad (2.4.10)$$

The first null of the field occurs at the angle $\theta_{e,\text{null}}$ given by

$$\frac{kB \sin \theta_{e,\text{null}}}{2} = \pi \quad \text{or} \quad \sin \theta_{e,\text{null}} = \frac{2\pi}{kB} = \frac{\lambda}{B} \quad (2.4.11)$$

where λ denotes the wavelength. Clearly, the larger B is, the smaller the beamwidth in the E-plane. The situation for the H-plane ($\phi = 0$) is similar. The field in this plane is given by

$$E_\theta \approx 0, \quad E_\phi \approx -\frac{j\eta J_0 B}{2\pi r} e^{-jkr} \sin\left(\frac{kA \sin \theta}{2}\right). \quad (2.4.12)$$

The first null of the field occurs at the angle $\theta_{h,\text{null}}$ given by

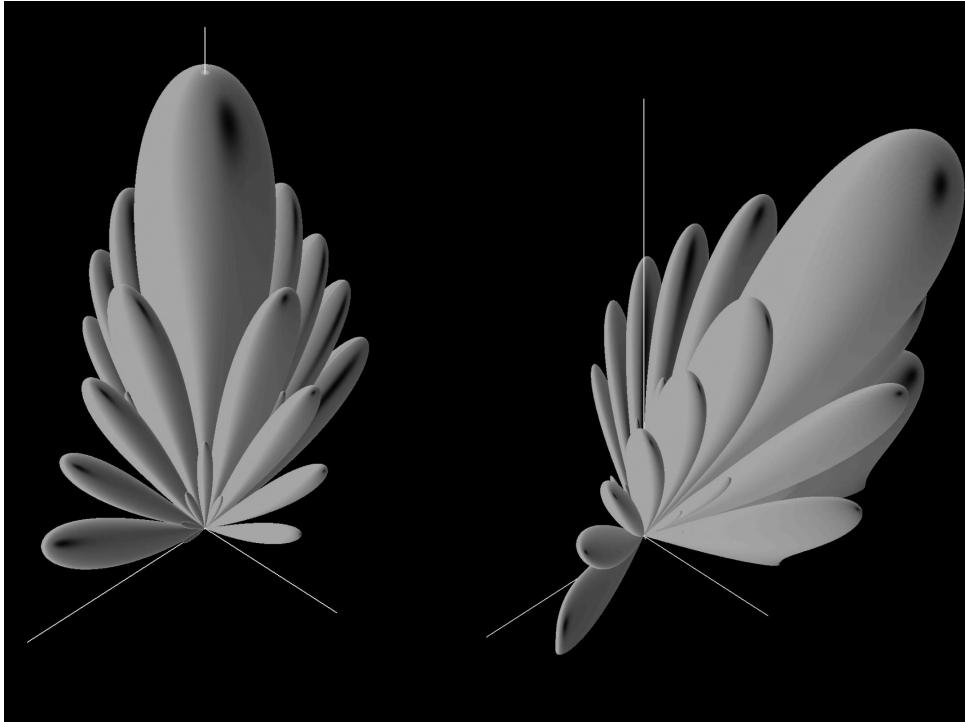


Figure 2.9 Normalized radiated field of a $5\lambda \times 5\lambda$ surface current in the upper half-space.
(a) $\theta_s = 0$ and $\phi_s = 0$. (b) $\theta_s = 30^\circ$ and $\phi_s = 135^\circ$.

$$\frac{kA \sin \theta_{h,\text{null}}}{2} = \pi \quad \text{or} \quad \sin \theta_{h,\text{null}} = \frac{2\pi}{kA} = \frac{\lambda}{A} \quad (2.4.13)$$

which shows that the beamwidth is inversely proportional to A . Therefore, the larger the area of the surface current is, the narrower the beamwidth. A narrow radiation beam is highly directive and can provide a high angular resolution for radar applications. Figure 2.10 shows the normalized total electric field as a function of θ and ϕ in the three-dimensional space for two cases: $A = B = 2\lambda$ and $A = B = 10\lambda$.

2.4.2 Radiation by a Phased Array

Although in principle one can steer the direction of a radiated field by controlling the phase distribution of a surface current and narrow its beamwidth by increasing the size of the surface current, it is difficult to realize a surface current with a desired amplitude and phase distribution in practice. To overcome this difficulty, we can replace a surface current by an array of dipoles whose amplitude and phase can be individually controlled. Such an array is called a *phased array*.

Consider an array of \hat{y} -directed dipoles placed in the xy -plane (Fig. 2.11). For simplicity, we assume that the dipoles are electrically short with dipole moment of Il . The locations of the dipoles are denoted by (x_i, y_i) , and the phases of the dipoles are denoted by ϕ_i , where $i = 1, 2, \dots, N$, with N being the total number of the dipoles. For the i th dipole,

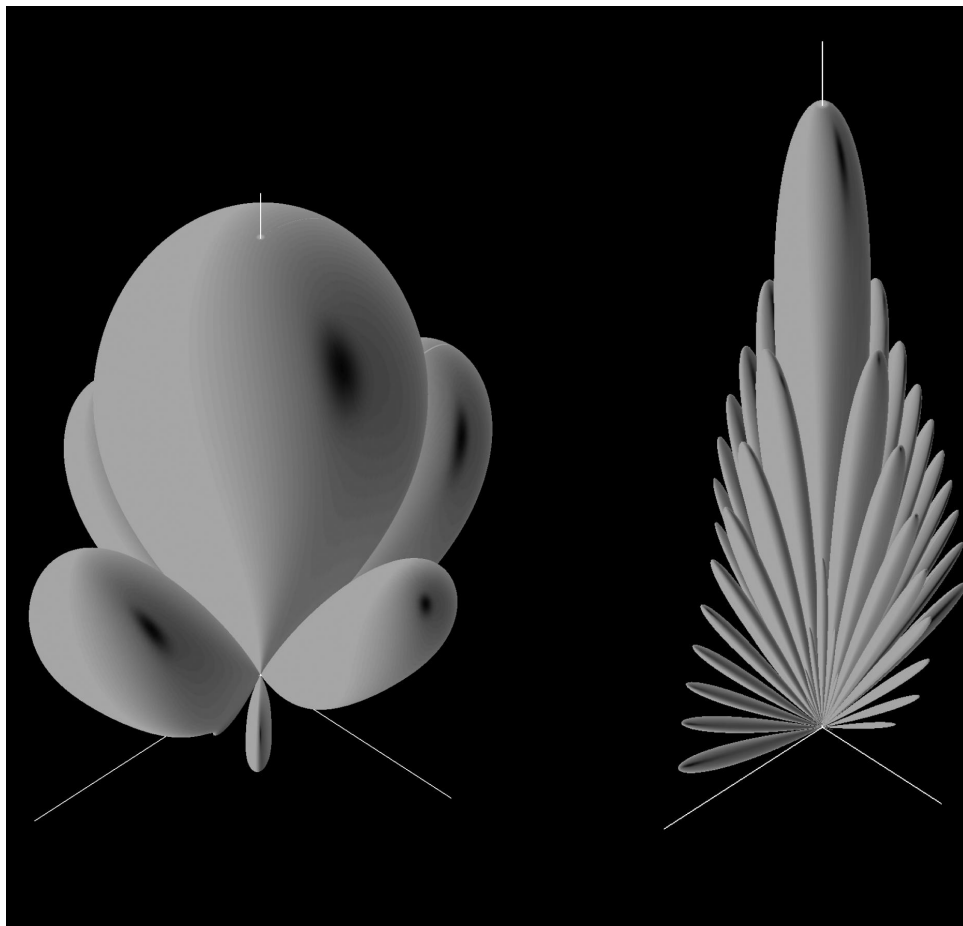


Figure 2.10 Normalized radiated field of a uniformly distributed surface current in the upper half-space for two cases. (a) $A = B = 2\lambda$. (b) $A = B = 10\lambda$.

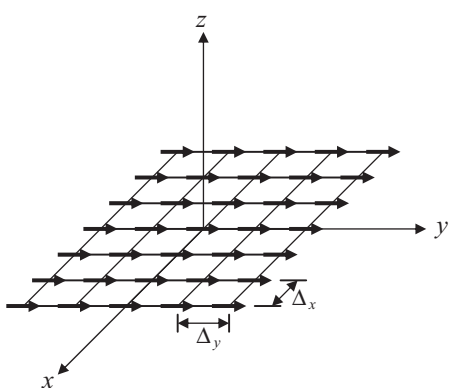


Figure 2.11 A rectangular phased array of dipoles in the xy -plane.

$$\mathbf{N}_i = \hat{y} I_i e^{j[k(x_i \sin \theta \cos \phi + y_i \sin \theta \sin \phi) + \varphi_i]} \quad (2.4.14)$$

Hence, its radiated far field is

$$E_{i\theta} \approx -\frac{jk\eta Il}{4\pi r} e^{-jkr} \cos \theta \sin \phi e^{j[k(x_i \sin \theta \cos \phi + y_i \sin \theta \sin \phi) + \varphi_i]} \quad (2.4.15)$$

$$E_{i\phi} \approx -\frac{jk\eta Il}{4\pi r} e^{-jkr} \cos \phi e^{j[k(x_i \sin \theta \cos \phi + y_i \sin \theta \sin \phi) + \varphi_i]}. \quad (2.4.16)$$

The total field radiated by the entire dipole array is obtained by summation

$$E_\theta \approx -\frac{jk\eta Il}{4\pi r} e^{-jkr} \cos \theta \sin \phi \sum_{i=1}^N e^{j[k(x_i \sin \theta \cos \phi + y_i \sin \theta \sin \phi) + \varphi_i]} \quad (2.4.17)$$

$$E_\phi \approx -\frac{jk\eta Il}{4\pi r} e^{-jkr} \cos \phi \sum_{i=1}^N e^{j[k(x_i \sin \theta \cos \phi + y_i \sin \theta \sin \phi) + \varphi_i]}. \quad (2.4.18)$$

Therefore, the total field is a product of two factors. The factor in front of the summation is the far field radiated by a \hat{y} -directed dipole located at the origin, which is often called the *element radiated field*. The summation factor is called the *array factor*, which is determined by the locations and phases of the dipoles. By denoting the pattern of the element radiated field as

$$e_\theta(\theta, \phi) = Il \cos \theta \sin \phi \quad (2.4.19)$$

$$e_\phi(\theta, \phi) = Il \cos \phi \quad (2.4.20)$$

and the array factor as

$$AF(\theta, \phi) = \sum_{i=1}^N e^{j[k(x_i \sin \theta \cos \phi + y_i \sin \theta \sin \phi) + \varphi_i]} \quad (2.4.21)$$

the total radiated far field of an array can be written as

$$\mathbf{E} \approx -\frac{jk\eta}{4\pi r} e^{-jkr} \mathbf{e}(\theta, \phi) AF(\theta, \phi). \quad (2.4.22)$$

This result is valid for any type of phased array, including those made of other types of antenna. For an array with an individually controlled amplitude for each dipole, the array factor becomes

$$AF(\theta, \phi) = \sum_{i=1}^N \frac{I_i}{I_0} e^{j[k(x_i \sin \theta \cos \phi + y_i \sin \theta \sin \phi) + \varphi_i]} \quad (2.4.23)$$

where I_i is the amplitude of the i th dipole and I_0 is the amplitude of the reference dipole that generates the element pattern $\mathbf{e}(\theta, \phi)$.

Now consider a rectangular array of dipoles having N_x dipoles along the x -direction and N_y dipoles along the y -direction (assuming that both N_x and N_y are odd numbers). The spacing between two adjacent dipoles is Δ_x along the x -direction and Δ_y along the y -direction, such that the location of the i th dipole is given by $x_i = (i_x - 1)\Delta_x$ and $y_i = (i_y - 1)\Delta_y$,

where $i_x = -N_x/2, \dots, N_x/2$ and $i_y = -N_y/2, \dots, N_y/2$. The phase of the i th dipole is $\phi_i = -h_x(i_x - 1)\Delta_x - h_y(i_y - 1)\Delta_y$. The array factor for this array becomes

$$\text{AF}(\theta, \phi) = \sum_{i_x=-N_x/2}^{N_x/2} e^{j(k \sin \theta \cos \phi - h_x(i_x - 1)\Delta_x)} \sum_{i_y=-N_y/2}^{N_y/2} e^{j(k \sin \theta \sin \phi - h_y(i_y - 1)\Delta_y)}. \quad (2.4.24)$$

The summation can be carried out to give

$$\text{AF}(\theta, \phi) = \frac{\sin\left(\frac{N_x - 1}{2}\psi_x\right)}{\sin\left(\frac{\psi_x}{2}\right)} \frac{\sin\left(\frac{N_y - 1}{2}\psi_y\right)}{\sin\left(\frac{\psi_y}{2}\right)} \quad (2.4.25)$$

where $\psi_x = (k \sin \theta \cos \phi - h_x)\Delta_x$ and $\psi_y = (k \sin \theta \sin \phi - h_y)\Delta_y$. If the phase constants h_x and h_y can be controlled by two parameters θ_s and ϕ_s according Equation 2.4.6, then

$$\psi_x = (\sin \theta \cos \phi - \sin \theta_s \cos \phi_s)k\Delta_x, \quad \psi_y = (\sin \theta \sin \phi - \sin \theta_s \sin \phi_s)k\Delta_y. \quad (2.4.26)$$

The maximum radiation occurs at $\psi_x = 2m\pi$ and $\psi_y = 2n\pi$ ($m, n = 0, 1, 2, \dots$). The directions corresponding to $m = n = 0$ are (θ_s, ϕ_s) and $(\pi - \theta_s, \phi_s)$. Therefore, the maximum radiated field can be steered into the desired direction by controlling θ_s and ϕ_s , which is similar to the case of a surface current. However, to ensure that there are only two maximum directions, the spacing between the dipoles must satisfy the conditions that $\Delta_x < \lambda$ and $\Delta_y < \lambda$. Figure 2.12 plots the array factor given in Equation 2.4.25 in the decibel scale as a function of θ and ϕ in the three-dimensional space for two arrays with uniform excitation ($\theta_s = 0$ and $\phi_s = 0$): (1) $N_x = N_y = 10$ and $\Delta_x = \Delta_y = 0.5\lambda$, and (2) $N_x = N_y = 10$ and $\Delta_x = \Delta_y = 1.0\lambda$.

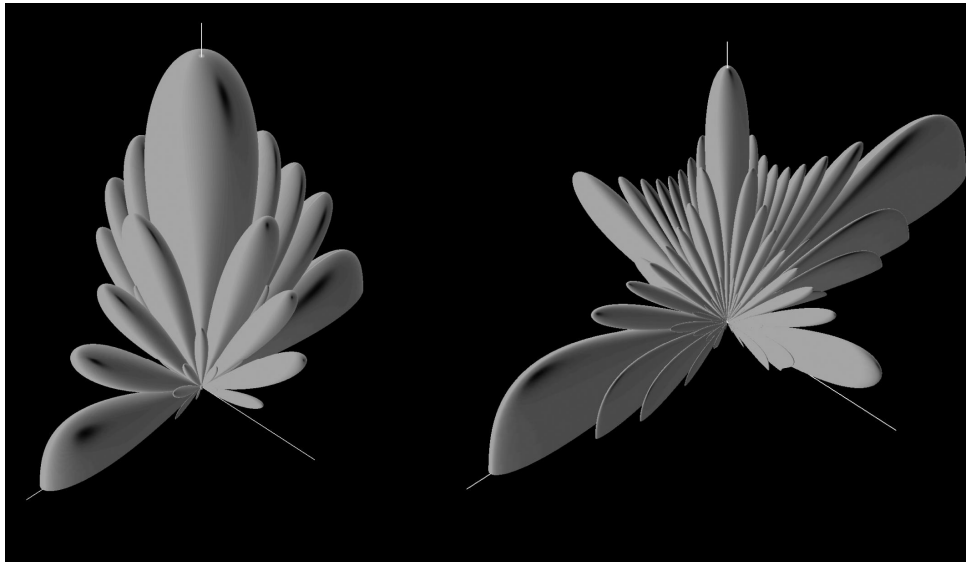


Figure 2.12 Normalized array factor in the upper half-space for two arrays with uniform excitation: (a) $N_x = N_y = 10$ and $\Delta_x = \Delta_y = 0.5\lambda$. (b) $N_x = N_y = 10$ and $\Delta_x = \Delta_y = 1.0\lambda$.

Phased arrays are of great importance in modern radar and communication systems [17–19]. By using a large number of radiating elements with an individually controlled phase and amplitude for each element, a phased array can provide an extremely high directivity and can scan across a large angular space electronically. Phased arrays have been used in radar systems for defense (e.g., ballistic missile warning systems), space probes (e.g., space track radars), weather research (e.g., tracking storms and hurricanes), and more recently for radio-frequency identification (RFID).

NOTES

1. The term *free space* is often used to describe two special media. One is a medium such as vacuum or air, which is free of any matter and whose permittivity and permeability are ϵ_0 and μ_0 . The other is an infinitely large homogeneous medium with a constant

permittivity and permeability. The specific meaning can be inferred easily from the context.

2. A dyad is also denoted by a doubly arrowed overline as for a tensor because a generalized dyad is equivalent to a tensor of rank 3.

REFERENCES

- [1] J. A. STRATTON, *Electromagnetic Theory*. New York: McGraw-Hill, 1941.
- [2] J. D. JACKSON, *Classical Electrodynamics* (3rd edition). New York: Wiley, 1999.
- [3] J. VAN BLADEL, *Electromagnetic Fields* (2nd edition). Hoboken, NJ: Wiley, 2007.
- [4] R. F. HARRINGTON, *Time-Harmonic Electromagnetic Fields*. New York: McGraw-Hill, 1961.
- [5] C. A. BALANIS, *Advanced Engineering Electromagnetics*. New York: Wiley, 1989.
- [6] J. A. KONG, *Electromagnetic Wave Theory*. Cambridge, MA: EMW Publishing, 2000.
- [7] G. S. SMITH, *An Introduction to Classical Electromagnetic Radiation*. Cambridge, UK: Cambridge University Press, 1997.
- [8] P. M. MORSE and H. FESHBACH, *Methods of Theoretical Physics*. New York: McGraw-Hill, 1953.
- [9] I. M. GEL'FAND and G. E. SHILOV, *Generalized Functions*. New York: Academic Press, 1964.
- [10] C. T. TAI, *Dyadic Green Functions in Electromagnetic Theory* (2nd edition). Piscataway, NJ: IEEE Press, 1994.
- [11] C. T. TAI, *Generalized Vector and Dyadic Analysis* (2nd edition). Piscataway, NJ: IEEE Press, 1997.
- [12] J. D. KRAUS and R. J. MARHEFKA, *Antennas: For All Applications* (3rd edition). New York: McGraw-Hill, 2002.
- [13] W. L. STUTZMAN and G. A. THIELE, *Antenna Theory and Design* (2nd edition). New York: Wiley, 1998.
- [14] C. A. BALANIS, *Antenna Theory: Analysis and Design* (3rd edition). Hoboken, NJ: Wiley, 2005.
- [15] A. SOMMERFELD, *Partial Differential Equations in Physics*. New York: Academic, 1949.
- [16] M. ABRAMOWITZ and I. A. STEGUN, Eds., *Handbook of Mathematical Functions*. New York: Dover, 1965.
- [17] R. J. MAILLOUX, *Phased Array Antenna Handbook* (2nd edition). Norwood, MA: Artech House, 2005.
- [18] Y. T. LO and S. W. LEE, Eds., *Antenna Handbook: Theory, Applications, and Design*. New York: Van Nostrand Reinhold, 1988.
- [19] C. A. BALANIS, Ed., *Modern Antenna Handbook*. Hoboken, NJ: Wiley, 2008.

PROBLEMS

- 2.1.** Consider a wire C carrying a static electric current I . Using Equations 2.1.13 and 2.1.18, derive Biot-Savart's law given by

$$\mathbf{B}(\mathbf{r}) = \frac{\mu I}{4\pi} \int_C \frac{d\mathbf{l}' \times \mathbf{R}}{R^3}$$

where $\mathbf{R} = \mathbf{r} - \mathbf{r}'$ and $d\mathbf{l}'$ points in the direction of the current flow.

- 2.2.** Show that the scalar potential of a static, infinitesimally short dipole with the electric dipole moment $\mathbf{p} = q\mathbf{l}$ located at \mathbf{r}' is given by

$$\varphi(\mathbf{r}) = \frac{\mathbf{p} \cdot (\mathbf{r} - \mathbf{r}')}{4\pi\epsilon_0 |\mathbf{r} - \mathbf{r}'|^3}$$

where \mathbf{r} denotes the observation point. Find the electric field of a \hat{z} -directed dipole located at the origin.

- 2.3.** Use the results in Problems 1.4 and 2.2 and show that the scalar potential of a polarized dielectric with a polarization intensity of \mathbf{P} is given by

$$\varphi(\mathbf{r}) = \frac{1}{4\pi\epsilon_0} \iint_S \frac{\hat{n}' \cdot \mathbf{P}(\mathbf{r}')}{|\mathbf{r} - \mathbf{r}'|} dS' - \frac{1}{4\pi\epsilon_0} \iiint_V \frac{\nabla' \cdot \mathbf{P}(\mathbf{r}')}{|\mathbf{r} - \mathbf{r}'|} dV'$$

where V denotes the volume of the dielectric and S denotes its surface. Find the surface and volume densities of the bound charges in the dielectric.

- 2.4.** Show that the vector potential of a steady, infinitesimally small circular current loop with the magnetic dipole moment $\mathbf{m} = I\mathbf{s}$ is given by

$$\mathbf{A}(\mathbf{r}) = \frac{\mu_0 \mathbf{m} \times (\mathbf{r} - \mathbf{r}')}{4\pi |\mathbf{r} - \mathbf{r}'|^3}$$

where \mathbf{r} denotes the observation point. Find the magnetic field of a small circular current loop located at the origin whose axis coincides with the z -axis.

- 2.5.** Use the results in Problems 1.4 and 2.4 and show that the vector potential of a magnetized medium with a magnetization intensity \mathbf{M} is given by

$$\mathbf{A}(\mathbf{r}) = -\frac{\mu_0}{4\pi} \iint_S \frac{\hat{n}' \times \mathbf{M}(\mathbf{r}')}{|\mathbf{r} - \mathbf{r}'|} dS' + \frac{\mu_0}{4\pi} \iiint_V \frac{\nabla' \times \mathbf{M}(\mathbf{r}')}{|\mathbf{r} - \mathbf{r}'|} dV'$$

where V denotes the volume of the magnetized medium and S denotes its surface. Find the surface and volume densities of the currents due to the magnetization.

- 2.6.** Consider a source-free medium characterized by a position-dependent permittivity $\epsilon(\mathbf{r})$ and a constant permeability μ . Starting from Maxwell's equations, derive a wave equation of the form

$$\nabla^2 \mathbf{E} + k(\mathbf{r})^2 \mathbf{E} + \nabla(\mathbf{E} \cdot \nabla \ln \epsilon(\mathbf{r})) = 0$$

where $k(\mathbf{r}) = \omega \sqrt{\mu \epsilon(\mathbf{r})}$.

- 2.7.** Consider a homogeneous medium. Show that the electric field in a source-free region satisfies the equation

$$\nabla \times \nabla \times \mathbf{E} - k^2 \mathbf{E} = 0$$

which reduces to

$$\nabla^2 \mathbf{E} + k^2 \mathbf{E} = 0$$

because of the divergence condition $\nabla \cdot \mathbf{E} = 0$. Find a solution to the second equation that does not satisfy the divergence condition.

- 2.8.** Assuming that \mathbf{J} and \mathbf{M} are continuous functions, show that Equations 2.2.29 and 2.2.30 are equivalent to Equations 2.1.37 and 2.1.38 with \mathbf{A} and \mathbf{F} given by Equations 2.2.21 and 2.2.22.
- 2.9.** Starting from Equations 2.2.49 and 2.2.50, show that $\tilde{\mathbf{G}}_e(\mathbf{r}, \mathbf{r}')$ and $\tilde{\mathbf{G}}_m(\mathbf{r}, \mathbf{r}')$ satisfy the second-order partial differential equations

$$\nabla \times \nabla \times \tilde{\mathbf{G}}_e(\mathbf{r}, \mathbf{r}') - k^2 \tilde{\mathbf{G}}_e(\mathbf{r}, \mathbf{r}') = \tilde{\mathbf{I}}\delta(\mathbf{r} - \mathbf{r}')$$

$$\nabla \times \nabla \times \tilde{\mathbf{G}}_m(\mathbf{r}, \mathbf{r}') - k^2 \tilde{\mathbf{G}}_m(\mathbf{r}, \mathbf{r}') = \nabla \times [\tilde{\mathbf{I}}\delta(\mathbf{r} - \mathbf{r}')].$$

- 2.10.** Using the result from Problem 2.9, show that $\tilde{\mathbf{G}}_e(\mathbf{r}, \mathbf{r}')$ and $\tilde{\mathbf{G}}_m(\mathbf{r}, \mathbf{r}')$ also satisfy the following equations:

$$(\nabla^2 + k^2) \tilde{\mathbf{G}}_e(\mathbf{r}, \mathbf{r}') = -\left(\tilde{\mathbf{I}} + \frac{1}{k^2} \nabla \nabla\right) \delta(\mathbf{r} - \mathbf{r}')$$

$$(\nabla^2 + k^2) \tilde{\mathbf{G}}_m(\mathbf{r}, \mathbf{r}') = -\nabla \times [\tilde{\mathbf{I}}\delta(\mathbf{r} - \mathbf{r}')]$$

which automatically lead to the solutions in Equations 2.2.36 and 2.2.37.

- 2.11.** Find the electric and magnetic fields radiated by an x -directed infinitesimal electric dipole placed at the origin.
- 2.12.** Show that the far field radiated by a z -directed infinitesimal magnetic dipole Kl is given by Equations 2.3.38 and 2.3.39.
- 2.13.** A small rectangular loop in the xy -plane carries a constant time-harmonic current I , as shown in Figure 2.13. Its length along the x -direction is a and along the y -direction is b . Find the far field radiated by this loop in the xz - and yz -planes, respectively. Show that the far field is the same as that of a magnetic dipole provided that the dipole moment is given by Equations 2.3.40 with $S = ab$.
- 2.14.** Consider a very small electric current loop shown in Figure 2.7. Find the vector potential \mathbf{A} . (*Hint:* The vector potential has only the ϕ -component, which can be obtained from $A_\phi = A_y|_{\phi=0}$.) Next, find the electric and magnetic fields from the vector potential \mathbf{A} .
- 2.15.** Two small electric current loops of the same radius a carrying the same amount of current I flowing in the same direction are placed parallel to the xy -plane. One is located at $z = -d/2$ and the other is at $z = d/2$. Find the radiated far field and the power flow density.
- 2.16.** A z -directed infinitesimal electric dipole Il is placed together with a z -directed infinitesimal magnetic dipole Kl at the origin. Find the radiated power density for two cases: (1) $Kl = \eta Il$ and (2) $Kl = j\eta Il$. Compare the results.

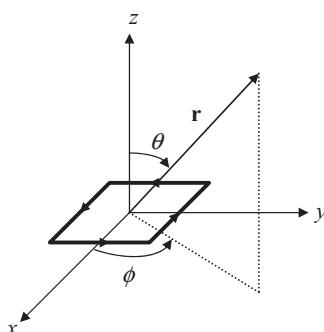


Figure 2.13 A small rectangular loop in the xy -plane carrying a constant time-harmonic current.

- 2.17.** The radiation resistance of an antenna is usually defined as $R_r = \text{Re}(P_e)/|I|^2$, where I denotes a reference current, which is I_0 in Equation 2.3.11. Calculate and plot the radiation resistance of a finite dipole (assuming it is fed at the middle) as a function of L from 0 to 2λ . Repeat for a circular loop for a from 0 to λ .
- 2.18.** Consider a uniformly distributed circular surface current with the current density $\mathbf{J}_s = \hat{\mathbf{y}}J_0$. The surface current is placed in the xy -plane and has a radius of a . Find the radiated far field and the location of the first null. Plot out the normalized radiated field as a function of θ and ϕ in the three-dimensional space for $a = 10\lambda$.
- 2.19.** Show that the direction of the first null of the array factor given in Equation 2.4.25 is

$$\begin{aligned}\phi_{\text{null}} &= \tan^{-1} \left[\frac{\sin \theta_s \sin \phi_s \pm \lambda/(N_y - 1)\Delta_y}{\sin \theta_s \cos \phi_s \pm \lambda/(N_x - 1)\Delta_x} \right] \\ \theta_{\text{null}} &= \sin^{-1} \left[\frac{\sin \theta_s \cos \phi_s \pm \lambda/(N_x - 1)\Delta_x}{\cos \phi_{\text{null}}} \right].\end{aligned}$$

- 2.20.** A circular array consists of N vertical dipoles uniformly placed on a circle in the xy -plane. Assume that the radius of the circle is a and the current on each of the dipoles is $I_i = I_0 e^{j\varphi_i}$ ($i = 1, 2, \dots, N$). First, find the array factor of the array. Then, for $N = 36$ and $a = 5\lambda$, find the phases so that the main beam radiates into the x -direction. ■

ELECTROMAGNETIC THEOREMS AND PRINCIPLES

Since electromagnetic fields are governed by Maxwell's equations, we can start from Maxwell's equations to derive some mathematical equations that reveal certain characteristics of electromagnetic fields. We have done this in the derivation of the energy conservation laws in both the time and frequency domains. In this chapter, we derive two important theorems through mathematical manipulations of Maxwell's equations. One is the uniqueness theorem, which establishes necessary conditions for a unique solution to Maxwell's equations, and the other is the reciprocity theorem, which establishes a relation between two solutions to the same Maxwell's equations due to two different sources. We then use the uniqueness theorem as a foundation to develop the image theory and the surface equivalence principle, which allow us to either solve an electromagnetic problem more easily or consider an electromagnetic problem from a different perspective. As an application of the surface equivalence principle, we derive the induction theorem and physical equivalent and formulate integral equations for scattering by conducting and dielectric objects. After that, we explore the symmetry in Maxwell's equations to develop the duality principle, which allows us to formulate a dual solution from any valid solution to an electromagnetic problem. Finally, we combine the knowledge of the uniqueness theorem, image theory, surface equivalence principle, and duality principle to deal with the problem of radiation and scattering by an aperture in an infinitely large conducting plane and discuss the related Babinet's principle and the characteristics of complementary structures.

3.1 UNIQUENESS THEOREM

Consider a volume V enclosed by a surface S and occupied by a medium characterized by permittivity ϵ , permeability μ , and conductivity σ (Fig. 3.1). The volume contains time-harmonic electric and magnetic sources specified by electric current density \mathbf{J}_i and magnetic current density \mathbf{M}_i . To check whether the electromagnetic field generated by the given sources is unique and, if yes, what conditions that make the field unique, we assume first that the sources generate two different fields denoted by $(\mathbf{E}^a, \mathbf{H}^a)$ and $(\mathbf{E}^b, \mathbf{H}^b)$, respectively. Both fields should satisfy Maxwell's equations

$$\nabla \times \mathbf{E}^a = -j\omega\mu\mathbf{H}^a - \mathbf{M}_i \quad (3.1.1)$$

$$\nabla \times \mathbf{H}^a = j\omega\epsilon\mathbf{E}^a + \sigma\mathbf{E}^a + \mathbf{J}_i \quad (3.1.2)$$

and

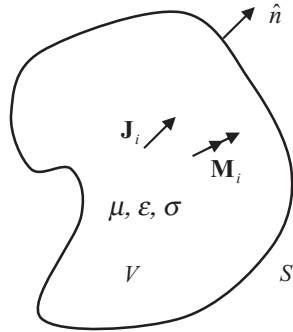


Figure 3.1 Electric and magnetic sources in a volume.

$$\nabla \times \mathbf{E}^b = -j\omega\mu\mathbf{H}^b - \mathbf{M}_i \quad (3.1.3)$$

$$\nabla \times \mathbf{H}^b = j\omega\epsilon\mathbf{E}^b + \sigma\mathbf{E}^b + \mathbf{J}_i \quad (3.1.4)$$

Subtracting the second set of equations from the first set eliminates the source terms since the sources are assumed to be the same, yielding

$$\nabla \times \delta\mathbf{E} = -j\omega\mu\delta\mathbf{H} \quad (3.1.5)$$

$$\nabla \times \delta\mathbf{H} = j\omega\epsilon\delta\mathbf{E} + \sigma\delta\mathbf{E} \quad (3.1.6)$$

where $\delta\mathbf{E} = \mathbf{E}^a - \mathbf{E}^b$ and $\delta\mathbf{H} = \mathbf{H}^a - \mathbf{H}^b$ denote the difference between the two fields. The proof of the field uniqueness is then tantamount to showing that this difference has to vanish. To examine this difference, we start from Equations 3.1.5 and 3.1.6 to find

$$\begin{aligned} \delta\mathbf{H}^* \cdot \nabla \times \delta\mathbf{E} - \delta\mathbf{E} \cdot \nabla \times \delta\mathbf{H}^* &= \nabla \cdot (\delta\mathbf{E} \times \delta\mathbf{H}^*) \\ &= -j\omega\mu|\delta\mathbf{H}|^2 + (j\omega\epsilon^* - \sigma)|\delta\mathbf{E}|^2 \end{aligned} \quad (3.1.7)$$

where the asterisk denotes complex conjugation. To check the difference everywhere, we integrate Equation 3.1.7 over volume V and then apply Gauss' theorem to obtain

$$\begin{aligned} \iiint_V \nabla \cdot (\delta\mathbf{E} \times \delta\mathbf{H}^*) dV &= \iint_S (\delta\mathbf{E} \times \delta\mathbf{H}^*) \cdot d\mathbf{S} \\ &= \iiint_V [-j\omega\mu|\delta\mathbf{H}|^2 + (j\omega\epsilon^* - \sigma)|\delta\mathbf{E}|^2] dV. \end{aligned} \quad (3.1.8)$$

It is easy to see that the surface integral would vanish under one of the following three conditions: (1) the tangential electric field ($\hat{n} \times \mathbf{E}$) is specified on the entire surface S such that $\hat{n} \times \delta\mathbf{E} = 0$ on S ; (2) the tangential magnetic field ($\hat{n} \times \mathbf{H}$) is specified on the entire surface S such that $\hat{n} \times \delta\mathbf{H} = 0$ on S ; and (3) the tangential electric field ($\hat{n} \times \mathbf{E}$) is specified over a portion of surface S and the tangential magnetic field ($\hat{n} \times \mathbf{H}$) is specified over the rest of the surface. Therefore, under one of the three conditions, Equation 3.1.8 becomes

$$\iiint_V [-j\omega\mu|\delta\mathbf{H}|^2 + (j\omega\epsilon^* - \sigma)|\delta\mathbf{E}|^2] dV = 0. \quad (3.1.9)$$

For a general lossy medium, $\mu = \mu' - j\mu''$ ($\mu'' \geq 0$) and $\epsilon = \epsilon' - j\epsilon''$ ($\epsilon'' \geq 0$). Therefore, the real part of Equation 3.1.9 becomes

$$\iiint_V [(\omega\epsilon'' + \sigma)|\delta\mathbf{E}|^2 + \omega\mu''|\delta\mathbf{H}|^2] dV = 0 \quad (3.1.10)$$

and the imaginary part becomes

$$\iiint_V [\omega\epsilon'|\delta\mathbf{E}|^2 - \omega\mu'|\delta\mathbf{H}|^2] dV = 0. \quad (3.1.11)$$

With these two equations, it can be shown easily that if the medium is lossy and $\omega > 0$, then $\delta\mathbf{E} = 0$ and $\delta\mathbf{H} = 0$ regardless of the type of loss. This conclusion is valid for any kind of medium since in the entire procedure nothing is assumed about the permittivity, permeability, and conductivity other than that the medium is lossy and the frequency is non-zero. However, if we consider the lossless and static cases as the limiting cases when the loss and frequency approach zero, but are not exactly equal to zero, then the conclusion remains valid even for the lossless and static cases.

Based on the discussions above, we can conclude that in a volume the field produced by a given source is unique when either the tangential component of the electric field is specified over the surface of the volume, or the tangential component of the magnetic field is specified over the surface of the volume, or the tangential component of the electric field is specified over one portion of the surface of the volume and the tangential component of the magnetic field is specified over the remaining portion of the surface. This statement is the *uniqueness theorem* for electromagnetic fields.

The uniqueness theorem has a number of applications. For example, it guarantees the same solution to a uniquely defined electromagnetic problem no matter what method is used to find such a solution. The uniqueness theorem establishes a one-to-one correspondence between the source and the field, which makes it possible to determine a source from its field. But the most important application for our purpose here is that the uniqueness theorem provides a solid foundation for developing the very useful image theory and the surface equivalence principle. Although the image theory and the surface equivalence principle can be derived rigorously using sophisticated mathematics, the uniqueness theorem provides a more intuitive approach to developing them without resorting to complicated mathematical manipulations.

3.2 IMAGE THEORY

In Chapter 2 we formulated the solution for the fields due to arbitrary sources in an infinitely large homogeneous space, which is referred to as free space, and derived the corresponding field–source relations. If a source radiates in an environment other than free space, the solution becomes very complicated and is usually obtained by solving a complex boundary-value problem. There are, however, a few simple non-free-space problems that can be converted into a free-space problem whose solution can then be obtained using the results derived in Chapter 2. One such problem is the radiation of a source in a homogeneous half-space above either an electrically or a magnetically conducting, infinitely large ground plane. The conversion of this problem to a free-space problem can be accomplished using the image theory presented in this section.

3.2.1 Basic Image Theory

The basic foundation of the image theory is the uniqueness theorem discussed in the preceding section. To see this, we consider a vertical electric dipole, which is an infinitesimally short electric current element, placed at $z = h$ above an infinitely large electric ground plane coinciding with the xy -plane. This problem is illustrated in Figure 3.2a. According to the basic electromagnetic theory, the field radiated by the dipole satisfies the boundary condition

$$\hat{z} \times \mathbf{E} = 0 \quad \text{at } z = 0. \quad (3.2.1)$$

One approach to solving for this field is to solve Maxwell's equations in the half-space above the ground plane together with the boundary condition (Eq. 3.2.1). An alternative is to convert this problem into an equivalent free-space problem and then obtain its solution using the free-space field-source relations. According to the uniqueness theorem, if we can construct a problem that contains the same source (the electric dipole) in the upper half-space and whose tangential component of the electric field vanishes on the xy -plane, its field in the upper half-space would be the same as that in the original problem. To construct such a problem, we can use whatever sources outside the upper half-space to cancel the tangential component of the electric field produced by the electric dipole at the xy -plane in the new problem.

To construct an equivalent problem that permits the use of the free-space solution, we first remove the electric ground plane and fill the lower half-space with the same homogeneous medium as that in the upper half-space. The electric field produced by the original electric dipole in the infinitely large homogeneous medium can then be obtained from a simple modification of Equation 2.3.5, which is given by

$$\mathbf{E}_1 = \hat{r}_1 \frac{\eta l l \cos \theta_1}{2\pi r_1^2} \left(1 + \frac{1}{jkr_1} \right) e^{-jkr_1} + \hat{\theta}_1 \frac{jk\eta l l \sin \theta_1}{4\pi r_1} \left[1 + \frac{1}{jkr_1} - \frac{1}{(kr_1)^2} \right] e^{-jkr_1} \quad (3.2.2)$$

where the variables are defined in Figure 3.3. To cancel the tangential component of the electric field at the xy -plane, we can place an electric dipole of the same magnitude and orientation at $z = -h$. The electric field produced by this dipole is

$$\mathbf{E}_2 = \hat{r}_2 \frac{\eta l l \cos \theta_2}{2\pi r_2^2} \left(1 + \frac{1}{jkr_2} \right) e^{-jkr_2} + \hat{\theta}_2 \frac{jk\eta l l \sin \theta_2}{4\pi r_2} \left[1 + \frac{1}{jkr_2} - \frac{1}{(kr_2)^2} \right] e^{-jkr_2}. \quad (3.2.3)$$

Because this dipole is placed symmetrically with respect to the original dipole, for any field point at the xy -plane,

$$r_2 = r_1 = \sqrt{\rho^2 + h^2} = a, \quad \theta_2 = \pi - \theta_1 = \tan^{-1}(\rho/h)$$

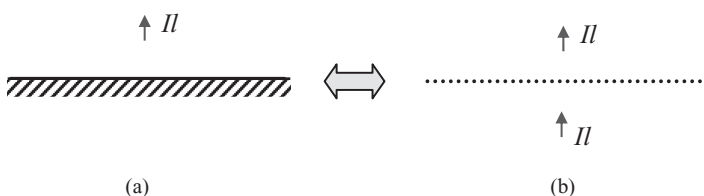


Figure 3.2 Image of a vertical electric dipole above a PEC ground plane. (a) Original problem. (b) Equivalent problem.

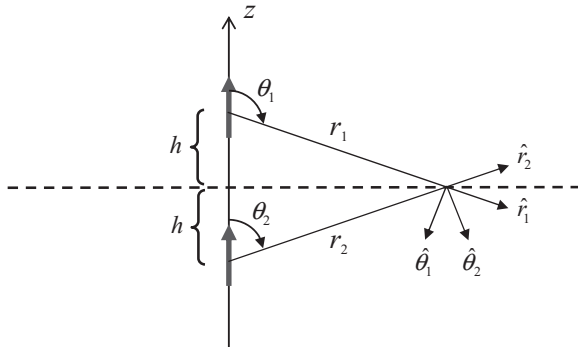


Figure 3.3 Variables and unit vectors associated with a field point at the xy -plane.

$$\hat{r}_1 = \hat{\rho}\rho/a - \hat{z}h/a, \quad \hat{\theta}_1 = -\hat{\rho}h/a - \hat{z}\rho/a$$

$$\hat{r}_2 = \hat{\rho}\rho/a + \hat{z}h/a, \quad \hat{\theta}_2 = \hat{\rho}h/a - \hat{z}\rho/a.$$

When these are substituted into Equations 3.2.2 and 3.2.3, we obtain

$$\begin{aligned} \mathbf{E} &= \mathbf{E}_1 + \mathbf{E}_2 \\ &= \hat{z} \frac{\eta Il h^2}{\pi a^4} \left(1 + \frac{1}{jka} \right) e^{-jka} - \hat{z} \frac{j k \eta I l \rho^2}{2 \pi a^3} \left[1 + \frac{1}{jka} - \frac{1}{(ka)^2} \right] e^{-jka} \quad \text{at } z = 0 \end{aligned} \quad (3.2.4)$$

which obviously has no tangential component at the xy -plane. Now, consider the upper half-space in this new problem. The source is the same as that in the original problem and the tangential component of the electric field on its bounding surface is also the same as that in the original problem; by the uniqueness theorem, we conclude that the field in the upper half-space has to be the same as that in the original problem. Therefore, this new problem is equivalent to the original problem for the field in the upper half-space. This equivalent problem is illustrated in Figure 3.2b, and the second dipole is called the *image* of the original dipole. The field produced by the image can be visualized as the field produced by the original dipole and reflected by the ground plane back into the upper half-space. Note that this equivalence is only valid for the upper half-space; the field in the lower half-space is obviously different, which is not a concern here. The solution to the original problem can be obtained by solving the equivalent problem, whose solution is the superposition of Equations 3.2.2 and 3.2.3. When the field point is far away from the source, $\theta_1 \approx \theta_2 \approx \theta$, $r_1 \approx r - h \cos \theta$, $r_2 \approx r + h \cos \theta$; hence, the electric field can be written as

$$\mathbf{E} \approx \hat{\theta} \frac{j \eta k l l}{2 \pi r} \sin \theta \cos(kh \cos \theta) e^{-jkr} \quad \theta \leq \frac{\pi}{2}. \quad (3.2.5)$$

For a horizontal electric dipole placed above an electric ground plane, as illustrated in Figure 3.4a, we can follow the same procedure to construct the equivalent problem shown in Figure 3.4b. In this equivalent problem, the ground plane is removed and its effect is replaced by an image, which is also a horizontal electric dipole of the same magnitude but having an opposite orientation. It can be shown easily that the electric field produced by the image dipole in free space cancels the tangential component of the electric

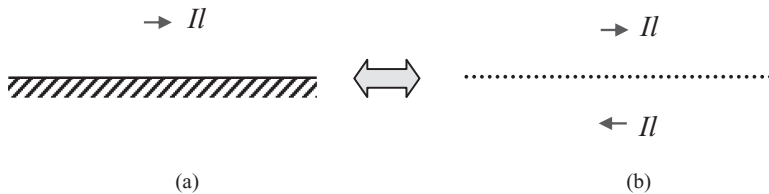


Figure 3.4 Image of a horizontal electric dipole above a PEC ground plane. (a) Original problem. (b) Equivalent problem.

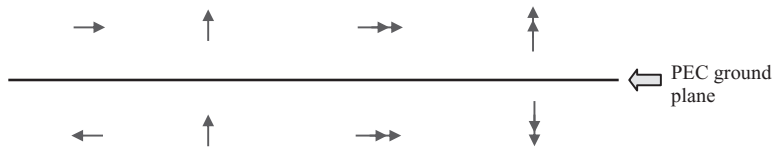


Figure 3.5 Images of electric and magnetic dipoles above a PEC ground plane.

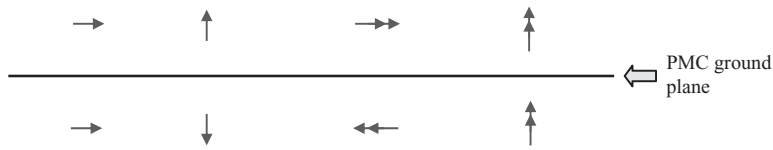


Figure 3.6 Images of electric and magnetic dipoles above a PMC ground plane.

field produced by the original dipole in free space at the xy -plane. Hence, the field produced by the dipoles in Figure 3.4b in the upper half-space is the same as the field produced by the original dipole in the presence of the ground plane.

The images for magnetic dipoles can be constructed using one of the following two approaches. The first approach is to examine the electric field produced by a magnetic dipole in free space and then find an image dipole to cancel the tangential component of the electric field at the xy -plane. The second approach is to replace a magnetic dipole by an electric current loop, then use the image theory developed above to find the image of the current loop, and, finally, convert the image loop back to a magnetic dipole. Using either approach, we find that the image of a vertical magnetic dipole above an electric ground plane is a vertical magnetic dipole of the same magnitude and opposite orientation, whereas the image of a horizontal magnetic dipole above an electric ground plane is a horizontal magnetic dipole of the same magnitude and orientation. The results are summarized in Figure 3.5. The same approach can be employed to find the images of electric and magnetic dipoles above an infinitely large magnetic ground plane. The results are shown in Figure 3.6.

Since an arbitrary current source can be decomposed into an infinite number of infinitesimally small vertical and horizontal current elements, the image theory in Figures 3.5 and 3.6 can be applied to an arbitrary current source as well. For example, given an electric current characterized by the current density $\mathbf{J}(\mathbf{r})$ above an electric ground plane coinciding with the xy -plane, it can first be decomposed into a vertical and a horizontal component as

$$\mathbf{J}(\mathbf{r}) = \mathbf{J}_v(\mathbf{r}) + \mathbf{J}_h(\mathbf{r}) = \hat{z}\hat{z} \cdot \mathbf{J}(\mathbf{r}) + [\mathbf{J}(\mathbf{r}) - \hat{z}\hat{z} \cdot \mathbf{J}(\mathbf{r})]. \quad (3.2.6)$$

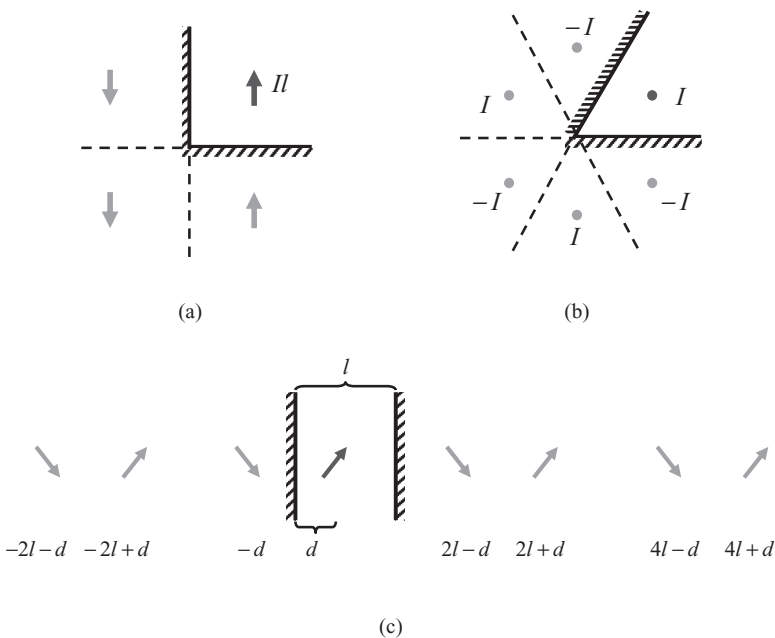


Figure 3.7 Examples of image placement. (a) A vertical electric current element in a right-angled conducting wedge. (b) A horizontal electric current line in a 60°-angled conducting wedge. (c) A tilted electric current element between two conducting planes. (There are an infinite number of images and only seven nearby images are shown.)

Based on Figure 3.5, its image is then given by

$$\begin{aligned}\mathbf{J}^{\text{im}}(\mathbf{r}) &= \mathbf{J}_v^{\text{im}}(\mathbf{r}) + \mathbf{J}_h^{\text{im}}(\mathbf{r}) = \mathbf{J}_v(\mathbf{r}_i) - \mathbf{J}_h(\mathbf{r}_i) \\ &= \hat{z}\hat{z} \cdot \mathbf{J}(\mathbf{r}_i) - \left[\mathbf{J}(\mathbf{r}_i) - \hat{z}\hat{z} \cdot \mathbf{J}(\mathbf{r}_i) \right] = 2\hat{z}\hat{z} \cdot \mathbf{J}(\mathbf{r}_i) - \mathbf{J}(\mathbf{r}_i)\end{aligned}\quad (3.2.7)$$

where $\mathbf{r}_i = x\hat{x} + y\hat{y} - z\hat{z}$ is the image position of $\mathbf{r} = x\hat{x} + y\hat{y} + z\hat{z}$.

In addition to an infinitely large electric or magnetic ground plane, the image theory can also be applied to a few special geometries such as a right-angled wedge region formed by an infinitely large vertical ground plane intersecting an infinitely large horizontal ground plane, as illustrated in Figure 3.7a, and a 60° wedge illustrated in Figure 3.7b. In both cases, multiple images are required to create a total field that satisfies the required boundary conditions on the surface of the ground planes. When a wedge has a special angle such as in these two examples, it is possible to find a finite number of images to create such a total field. For an arbitrary angle, one might have to use an infinite number of images, and since these images are located nearby the field region, the sum of their fields does not converge and a closed-form solution cannot be obtained. However, for a current element in a region between two parallel ground planes, the application of the image theory also yields an infinite number of images to create a total field to satisfy the required boundary conditions. A few nearby images are shown in Figure 3.7c. Since the images in this case are placed farther and farther away from the field region, the sum of their fields actually converges, yielding a useful solution to the problem. The image theory can also be applied to a current in a rectangular waveguide and cavity, resulting in a two- and three-dimensional array of images, respectively. Finally, we note that an image theory can also be developed for some special curved conducting surfaces and a planar dielectric

half-space or a stratified medium [1]. In these cases, the images and their formulation are much more complicated since they do not have the same shape as the original sources.

3.2.2 Half-Space Field-Source Relations

Based on the discussion above, it is obvious that for an electric current $\mathbf{J}(\mathbf{r})$ and a magnetic current $\mathbf{M}(\mathbf{r})$ residing above an electric ground plane coinciding with the xy -plane, their images are given by

$$\mathbf{J}^{\text{im}}(\mathbf{r}) = 2\hat{z}\hat{z} \cdot \mathbf{J}(\mathbf{r}_i) - \mathbf{J}(\mathbf{r}_i) \quad (3.2.8)$$

$$\mathbf{M}^{\text{im}}(\mathbf{r}) = -2\hat{z}\hat{z} \cdot \mathbf{M}(\mathbf{r}_i) + \mathbf{M}(\mathbf{r}_i) \quad (3.2.9)$$

where $\mathbf{r} = x\hat{x} + y\hat{y} + z\hat{z}$ and $\mathbf{r}_i = x\hat{x} + y\hat{y} - z\hat{z}$. According to Equation 2.2.35, the electric field produced by the original currents and their images in free space is then

$$\begin{aligned} \mathbf{E}(\mathbf{r}) = & -j\omega\mu \iiint_V \tilde{\mathbf{G}}_{e0}(\mathbf{r}, \mathbf{r}') \cdot \mathbf{J}(\mathbf{r}') dV' - \iiint_V \tilde{\mathbf{G}}_{m0}(\mathbf{r}, \mathbf{r}') \cdot \mathbf{M}(\mathbf{r}') dV' \\ & - j\omega\mu \iiint_{V_{\text{im}}} \tilde{\mathbf{G}}_{e0}(\mathbf{r}, \mathbf{r}') \cdot \mathbf{J}^{\text{im}}(\mathbf{r}') dV' - \iiint_{V_{\text{im}}} \tilde{\mathbf{G}}_{m0}(\mathbf{r}, \mathbf{r}') \cdot \mathbf{M}^{\text{im}}(\mathbf{r}') dV' \end{aligned} \quad (3.2.10)$$

where V_{im} denotes the volume occupied by the image currents. By substituting Equations 3.2.8 and 3.2.9 into Equation 3.2.10, the electric field can be expressed as

$$\begin{aligned} \mathbf{E}(\mathbf{r}) = & -j\omega\mu \iiint_V \tilde{\mathbf{G}}_{e0}(\mathbf{r}, \mathbf{r}') \cdot \mathbf{J}(\mathbf{r}') dV' - \iiint_V \tilde{\mathbf{G}}_{m0}(\mathbf{r}, \mathbf{r}') \cdot \mathbf{M}(\mathbf{r}') dV' \\ & - j\omega\mu \iiint_{V_{\text{im}}} \tilde{\mathbf{G}}_{e0}(\mathbf{r}, \mathbf{r}') \cdot [2\hat{z}\hat{z} \cdot \mathbf{J}(\mathbf{r}_i) - \mathbf{J}(\mathbf{r}_i)] dV' \\ & + \iiint_{V_{\text{im}}} \tilde{\mathbf{G}}_{m0}(\mathbf{r}, \mathbf{r}') \cdot [2\hat{z}\hat{z} \cdot \mathbf{M}(\mathbf{r}_i) - \mathbf{M}(\mathbf{r}_i)] dV'. \end{aligned} \quad (3.2.11)$$

Now, if we change the sign for z' in the integrals over the image currents, then $\mathbf{J}(\mathbf{r}'_i)$ and $\mathbf{M}(\mathbf{r}'_i)$ become $\mathbf{J}(\mathbf{r}')$ and $\mathbf{M}(\mathbf{r}')$, respectively, and V_{im} becomes V , but $\tilde{\mathbf{G}}_{e0}(\mathbf{r}, \mathbf{r}')$ and $\tilde{\mathbf{G}}_{m0}(\mathbf{r}, \mathbf{r}')$ would become $\tilde{\mathbf{G}}_{e0}(\mathbf{r}, \mathbf{r}'_i)$ and $\tilde{\mathbf{G}}_{m0}(\mathbf{r}, \mathbf{r}'_i)$. Hence,

$$\begin{aligned} \mathbf{E}(\mathbf{r}) = & -j\omega\mu \iiint_V [\tilde{\mathbf{G}}_{e0}(\mathbf{r}, \mathbf{r}') - \tilde{\mathbf{G}}_{e0}(\mathbf{r}, \mathbf{r}'_i) + 2\tilde{\mathbf{G}}_{e0}(\mathbf{r}, \mathbf{r}'_i) \cdot \hat{z}\hat{z}] \cdot \mathbf{J}(\mathbf{r}') dV' \\ & - \iiint_V [\tilde{\mathbf{G}}_{m0}(\mathbf{r}, \mathbf{r}') + \tilde{\mathbf{G}}_{m0}(\mathbf{r}, \mathbf{r}'_i) - 2\tilde{\mathbf{G}}_{m0}(\mathbf{r}, \mathbf{r}'_i) \cdot \hat{z}\hat{z}] \cdot \mathbf{M}(\mathbf{r}') dV'. \end{aligned} \quad (3.2.12)$$

This expression can be written compactly as

$$\mathbf{E}(\mathbf{r}) = -j\omega\mu \iiint_V \tilde{\mathbf{G}}_{e1}(\mathbf{r}, \mathbf{r}') \cdot \mathbf{J}(\mathbf{r}') dV' - \iiint_V \tilde{\mathbf{G}}_{m1}(\mathbf{r}, \mathbf{r}') \cdot \mathbf{M}(\mathbf{r}') dV' \quad (3.2.13)$$

where

$$\tilde{\mathbf{G}}_{e1}(\mathbf{r}, \mathbf{r}') = \tilde{\mathbf{G}}_{e0}(\mathbf{r}, \mathbf{r}') - \tilde{\mathbf{G}}_{e0}(\mathbf{r}, \mathbf{r}'_i) + 2\tilde{\mathbf{G}}_{e0}(\mathbf{r}, \mathbf{r}'_i) \cdot \hat{z}\hat{z} \quad (3.2.14)$$

$$\tilde{\mathbf{G}}_{m1}(\mathbf{r}, \mathbf{r}') = \tilde{\mathbf{G}}_{m0}(\mathbf{r}, \mathbf{r}') + \tilde{\mathbf{G}}_{m0}(\mathbf{r}, \mathbf{r}'_i) - 2\tilde{\mathbf{G}}_{m0}(\mathbf{r}, \mathbf{r}'_i) \cdot \hat{z}\hat{z} \quad (3.2.15)$$

and they are called the *half-space electric and magnetic dyadic Green's functions of the first kind* [2]. Both of them satisfy the boundary condition of the first kind on the ground plane

$$\hat{z} \times \tilde{\mathbf{G}}_{e1}(\mathbf{r}, \mathbf{r}') = 0, \quad \hat{z} \times \tilde{\mathbf{G}}_{m1}(\mathbf{r}, \mathbf{r}') = 0 \quad (3.2.16)$$

for $z = 0$. Substituting Equations 2.2.36 and 2.2.37 into Equations 3.2.14 and 3.2.15, and applying the following relations:

$$\nabla f(\mathbf{r} - \mathbf{r}') = -\nabla' f(\mathbf{r} - \mathbf{r}') \quad (3.2.17)$$

$$\nabla f(\mathbf{r} - \mathbf{r}_i') = -\nabla' f(\mathbf{r} - \mathbf{r}_i') + 2\hat{z}\hat{z} \cdot \nabla f(\mathbf{r} - \mathbf{r}_i') \quad (3.2.18)$$

where f denotes any function, we can write Equations 3.2.14 and 3.2.15 in terms of the free-space scalar Green's function as

$$\tilde{\mathbf{G}}_{e1}(\mathbf{r}, \mathbf{r}') = \left(\tilde{\mathbf{I}} - \frac{1}{k^2} \nabla' \nabla \right) [G_0(\mathbf{r}, \mathbf{r}') - G_0(\mathbf{r}, \mathbf{r}_i')] + 2\hat{z}\hat{z} G_0(\mathbf{r}, \mathbf{r}_i') \quad (3.2.19)$$

$$\tilde{\mathbf{G}}_{m1}(\mathbf{r}, \mathbf{r}') = -\nabla' [G_0(\mathbf{r}, \mathbf{r}') + G_0(\mathbf{r}, \mathbf{r}_i')] \times \tilde{\mathbf{I}}. \quad (3.2.20)$$

By following a similar procedure and employing Equation 2.2.38, the magnetic field in the half-space can be found as

$$\mathbf{H}(\mathbf{r}) = \iiint_V \tilde{\mathbf{G}}_{m2}(\mathbf{r}, \mathbf{r}') \cdot \mathbf{J}(\mathbf{r}') dV' - j\omega \epsilon \iiint_V \tilde{\mathbf{G}}_{e2}(\mathbf{r}, \mathbf{r}') \cdot \mathbf{M}(\mathbf{r}') dV' \quad (3.2.21)$$

where

$$\tilde{\mathbf{G}}_{e2}(\mathbf{r}, \mathbf{r}') = \tilde{\mathbf{G}}_{e0}(\mathbf{r}, \mathbf{r}') + \tilde{\mathbf{G}}_{e0}(\mathbf{r}, \mathbf{r}_i') - 2\tilde{\mathbf{G}}_{e0}(\mathbf{r}, \mathbf{r}_i') \cdot \hat{z}\hat{z} \quad (3.2.22)$$

$$\tilde{\mathbf{G}}_{m2}(\mathbf{r}, \mathbf{r}') = \tilde{\mathbf{G}}_{m0}(\mathbf{r}, \mathbf{r}') - \tilde{\mathbf{G}}_{m0}(\mathbf{r}, \mathbf{r}_i') + 2\tilde{\mathbf{G}}_{m0}(\mathbf{r}, \mathbf{r}_i') \cdot \hat{z}\hat{z} \quad (3.2.23)$$

and these are called the *half-space electric and magnetic dyadic Green's functions of the second kind*. Both of them satisfy the boundary condition of the second kind on the ground plane

$$\hat{z} \times \nabla \times \tilde{\mathbf{G}}_{e2}(\mathbf{r}, \mathbf{r}') = 0, \quad \hat{z} \times \nabla \times \tilde{\mathbf{G}}_{m2}(\mathbf{r}, \mathbf{r}') = 0 \quad (3.2.24)$$

for $z = 0$. They can be written in terms of the free-space scalar Green's function as

$$\tilde{\mathbf{G}}_{e2}(\mathbf{r}, \mathbf{r}') = \left(\tilde{\mathbf{I}} - \frac{1}{k^2} \nabla' \nabla \right) [G_0(\mathbf{r}, \mathbf{r}') + G_0(\mathbf{r}, \mathbf{r}_i')] - 2\hat{z}\hat{z} G_0(\mathbf{r}, \mathbf{r}_i') \quad (3.2.25)$$

$$\tilde{\mathbf{G}}_{m2}(\mathbf{r}, \mathbf{r}') = -\nabla' [G_0(\mathbf{r}, \mathbf{r}') - G_0(\mathbf{r}, \mathbf{r}_i')] \times \tilde{\mathbf{I}}. \quad (3.2.26)$$

The first- and second-kind dyadic Green's functions are related by

$$\nabla \times \tilde{\mathbf{G}}_{e2}(\mathbf{r}, \mathbf{r}') = \tilde{\mathbf{G}}_{m1}(\mathbf{r}, \mathbf{r}') \quad (3.2.27)$$

$$\nabla \times \tilde{\mathbf{G}}_{m2}(\mathbf{r}, \mathbf{r}') = k^2 \tilde{\mathbf{G}}_{e1}(\mathbf{r}, \mathbf{r}') + \tilde{\mathbf{I}} \delta(\mathbf{r} - \mathbf{r}') \quad (3.2.28)$$

and

$$\nabla \times \tilde{\mathbf{G}}_{e1}(\mathbf{r}, \mathbf{r}') = \tilde{\mathbf{G}}_{m2}(\mathbf{r}, \mathbf{r}') \quad (3.2.29)$$

$$\nabla \times \tilde{\mathbf{G}}_{m1}(\mathbf{r}, \mathbf{r}') = k^2 \tilde{\mathbf{G}}_{e2}(\mathbf{r}, \mathbf{r}') + \tilde{\mathbf{I}}\delta(\mathbf{r} - \mathbf{r}'). \quad (3.2.30)$$

All of these can be verified easily by substituting Equations 3.2.13 and 3.2.21 into Maxwell's equations.

3.3 RECIPROCITY THEOREMS

The reciprocity theorem is one of the most important theorems in electromagnetics and has a wide array of applications. This theorem relates two independent sets of electromagnetic fields. Such a relation exists because both fields are governed by the same Maxwell's equations. When the reciprocity theorem is applied to different situations, we have several different forms, two of which are discussed specifically here.

3.3.1 General Reciprocity Theorem

Consider the field $(\mathbf{E}_1, \mathbf{H}_1)$ produced by source $(\mathbf{J}_1, \mathbf{M}_1)$ in a medium characterized by (ϵ, μ, σ) . The field satisfies Maxwell's equations

$$\nabla \times \mathbf{E}_1 = -j\omega\mu\mathbf{H}_1 - \mathbf{M}_1 \quad (3.3.1)$$

$$\nabla \times \mathbf{H}_1 = j\omega\epsilon\mathbf{E}_1 + \sigma\mathbf{E}_1 + \mathbf{J}_1. \quad (3.3.2)$$

Now, consider another field $(\mathbf{E}_2, \mathbf{H}_2)$ produced by source $(\mathbf{J}_2, \mathbf{M}_2)$ in the same medium, which satisfies the same Maxwell's equations

$$\nabla \times \mathbf{E}_2 = -j\omega\mu\mathbf{H}_2 - \mathbf{M}_2 \quad (3.3.3)$$

$$\nabla \times \mathbf{H}_2 = j\omega\epsilon\mathbf{E}_2 + \sigma\mathbf{E}_2 + \mathbf{J}_2. \quad (3.3.4)$$

From these two sets of equations, we can easily obtain through pure mathematical manipulations that

$$\begin{aligned} \nabla \cdot (\mathbf{H}_2 \times \mathbf{E}_1) &= \mathbf{E}_1 \cdot \nabla \times \mathbf{H}_2 - \mathbf{H}_2 \cdot \nabla \times \mathbf{E}_1 \\ &= j\omega\epsilon\mathbf{E}_1 \cdot \mathbf{E}_2 + \sigma\mathbf{E}_1 \cdot \mathbf{E}_2 + j\omega\mu\mathbf{H}_2 \cdot \mathbf{H}_1 + \mathbf{E}_1 \cdot \mathbf{J}_2 + \mathbf{H}_2 \cdot \mathbf{M}_1 \end{aligned} \quad (3.3.5)$$

$$\begin{aligned} \nabla \cdot (\mathbf{H}_1 \times \mathbf{E}_2) &= \mathbf{E}_2 \cdot \nabla \times \mathbf{H}_1 - \mathbf{H}_1 \cdot \nabla \times \mathbf{E}_2 \\ &= j\omega\epsilon\mathbf{E}_2 \cdot \mathbf{E}_1 + \sigma\mathbf{E}_2 \cdot \mathbf{E}_1 + j\omega\mu\mathbf{H}_1 \cdot \mathbf{H}_2 + \mathbf{E}_2 \cdot \mathbf{J}_1 + \mathbf{H}_1 \cdot \mathbf{M}_2. \end{aligned} \quad (3.3.6)$$

Subtracting the second equation from the first yields

$$\nabla \cdot (\mathbf{H}_2 \times \mathbf{E}_1 - \mathbf{H}_1 \times \mathbf{E}_2) = \mathbf{E}_1 \cdot \mathbf{J}_2 + \mathbf{H}_2 \cdot \mathbf{M}_1 - \mathbf{E}_2 \cdot \mathbf{J}_1 - \mathbf{H}_1 \cdot \mathbf{M}_2 \quad (3.3.7)$$

which eliminates the constitutive parameters of the medium and relates two independent fields and their sources. This expression is called the *reciprocity theorem in differential form*. When it is applied to a finite volume V , it becomes

$$\oint\int_S (\mathbf{H}_2 \times \mathbf{E}_1 - \mathbf{H}_1 \times \mathbf{E}_2) \cdot d\mathbf{S} = \iiint_V (\mathbf{E}_1 \cdot \mathbf{J}_2 + \mathbf{H}_2 \cdot \mathbf{M}_1 - \mathbf{E}_2 \cdot \mathbf{J}_1 - \mathbf{H}_1 \cdot \mathbf{M}_2) dV \quad (3.3.8)$$

where we have applied Gauss' theorem and S denotes the surface enclosing V . This expression is called the *reciprocity theorem in integral form*. Note that the derivation of Equation 3.3.7 depends on the cancellation of the terms involving (ϵ, μ, σ) . Such a perfect cancellation occurs even if the medium is inhomogeneous and/or anisotropic as long as the permittivity, permeability, and conductivity tensors are symmetric. Furthermore, Equation 3.3.8 remains valid if the volume contains electric and/or magnetic conductors because the integrand in the surface integral vanishes on the surface of such conductors. Therefore, the reciprocity theorem as represented by Equations 3.3.7 and 3.3.8 is valid for any electromagnetic configuration as long as it does not contain any non-reciprocal media, which are anisotropic media with non-symmetric permittivity, permeability, or conductivity tensors.

3.3.2 Lorentz Reciprocity Theorem

Now we consider a few special cases for Equations 3.3.7 and 3.3.8. At a point where there is no source, Equation 3.3.7 becomes

$$\nabla \cdot (\mathbf{H}_2 \times \mathbf{E}_1 - \mathbf{H}_1 \times \mathbf{E}_2) = 0. \quad (3.3.9)$$

Similarly, in a region that does not contain any sources, Equation 3.3.8 becomes

$$\oint\int_S (\mathbf{H}_2 \times \mathbf{E}_1 - \mathbf{H}_1 \times \mathbf{E}_2) \cdot d\mathbf{S} = 0. \quad (3.3.10)$$

These two equations are called the *Lorentz reciprocity theorem* [3]. In fact, Equation 3.3.10 is also valid if S contains all the sources. This can be shown in two ways. The first way is simply to recognize that if S contains all the sources, its exterior then does not contain any sources; hence, S can also be regarded as the surface of a source-free region, for which Equation 3.3.10 applies. The second way is to recognize that if all the sources are included, the right-hand side of Equation 3.3.8 and hence the left-hand side are constant regardless of the shape of S as long as it encloses all the sources. Now, let S be a spherical surface with a radius approaching infinity. Since the fields have to satisfy the Sommerfeld radiation conditions in Equations 2.3.27 and 2.3.28, the dominant term of the integrand in the surface integral is proportional to r^{-3} ; hence, the surface integral vanishes when $r \rightarrow \infty$. Therefore, the Lorentz reciprocity theorem is valid for surfaces either containing no sources or containing all the sources. Only when the surface contains some but not all sources does the surface integral become non-zero. For example, if the volume contains only $(\mathbf{J}_1, \mathbf{M}_1)$, then Equation 3.3.8 becomes

$$\oint\int_{S_1} (\mathbf{H}_2 \times \mathbf{E}_1 - \mathbf{H}_1 \times \mathbf{E}_2) \cdot d\mathbf{S} = \iiint_{V_1} (\mathbf{H}_2 \cdot \mathbf{M}_1 - \mathbf{E}_2 \cdot \mathbf{J}_1) dV \quad (3.3.11)$$

where S_1 encloses V_1 , which contains only $(\mathbf{J}_1, \mathbf{M}_1)$.

3.3.3 Rayleigh–Carson Reciprocity Theorem

As shown above, when the volume contains all the sources, the left-hand side of Equation 3.3.8 vanishes. Hence, its right-hand side vanishes as well, yielding

$$\iiint_V (\mathbf{E}_1 \cdot \mathbf{J}_2 + \mathbf{H}_2 \cdot \mathbf{M}_1 - \mathbf{E}_2 \cdot \mathbf{J}_1 - \mathbf{H}_1 \cdot \mathbf{M}_2) dV = 0 \quad (3.3.12)$$

or

$$\iiint_V (\mathbf{E}_1 \cdot \mathbf{J}_2 - \mathbf{H}_1 \cdot \mathbf{M}_2) dV = \iiint_V (\mathbf{E}_2 \cdot \mathbf{J}_1 - \mathbf{H}_2 \cdot \mathbf{M}_1) dV. \quad (3.3.13)$$

This equation is known as the *Rayleigh–Carson reciprocity theorem* [4]. To better understand this theorem, we introduce a new concept called *reaction* [5]. Defining the reaction of the field “1” on the source “2” as

$$\langle 1, 2 \rangle = \iiint_V (\mathbf{E}_1 \cdot \mathbf{J}_2 - \mathbf{H}_1 \cdot \mathbf{M}_2) dV \quad (3.3.14)$$

and the reaction of the field “2” on the source “1” as

$$\langle 2, 1 \rangle = \iiint_V (\mathbf{E}_2 \cdot \mathbf{J}_1 - \mathbf{H}_2 \cdot \mathbf{M}_1) dV \quad (3.3.15)$$

then the Rayleigh–Carson reciprocity theorem can be expressed as

$$\langle 1, 2 \rangle = \langle 2, 1 \rangle. \quad (3.3.16)$$

The reaction $\langle 1, 2 \rangle$ can be interpreted as the “sensibility” or “detectability” of source “1” by source “2,” and the reaction $\langle 2, 1 \rangle$ can be interpreted similarly. Thus, the reciprocity theorem states that the “detectability” of source “1” by source “2” is equal to the “detectability” of source “2” by source “1” in an environment consisting of only reciprocal media.

The reciprocity theorem has a wide range of applications in theoretical, computational, and experimental electromagnetics. To illustrate a simple application, we consider the radiation of an electric current element placed tangentially on the surface of an electrically conducting object, as illustrated in Figure 3.8. Let this current element be denoted as source “1” and its radiated electric field as \mathbf{E}_1 . To find this field, we place another infinitesimally small current element $I\hat{l}$ at an arbitrary point \mathbf{r} and in an arbitrary orientation denoted as \hat{a} , and consider this as source “2.” Hence,

$$\langle 1, 2 \rangle = \iiint_V \mathbf{E}_1 \cdot \mathbf{J}_2 dV = \mathbf{E}_1(\mathbf{r}) \cdot \hat{a} I\hat{l}. \quad (3.3.17)$$

Because the field produced by source “2” has to satisfy the boundary condition $\hat{\mathbf{n}} \cdot \mathbf{E}_2 = 0$ on the surface of the conducting object, we have

$$\langle 2, 1 \rangle = \iiint_V \mathbf{E}_2 \cdot \mathbf{J}_1 dV = 0. \quad (3.3.18)$$

Based on the reciprocity theorem (Eq. 3.3.16), we have $\mathbf{E}_1(\mathbf{r}) \cdot \hat{a} = 0$. Since both \mathbf{r} and \hat{a} are arbitrary, we have $\mathbf{E}_1(\mathbf{r}) = 0$ everywhere, which indicates that when an electric current

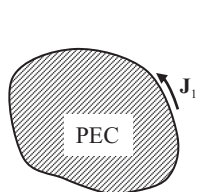


Figure 3.8 An electric current element placed tangentially on the surface of an electric conductor.

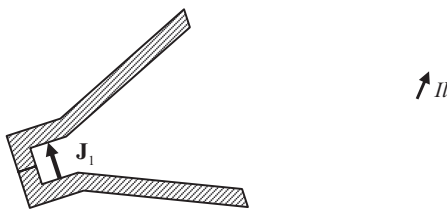


Figure 3.9 An antenna excited by an electric current element and a dipole placed at the observation point.

element is placed tangentially on the surface of an electric conductor, it does not radiate. In other words, the current element would induce a current in the conductor whose radiation cancels that of the original current. Similarly, we can show that a magnetic current placed tangentially on the surface of a perfect magnetic conductor does not radiate either.

Now, consider another example illustrated in Figure 3.9, where an antenna excited by a current element of unit magnitude radiates a field into free space. One way to determine its radiation pattern is to directly measure the radiated field in the far-field zone. Alternatively, we can use a small dipole I_ll placed at the observation point and measure the received voltage at the excitation point of the antenna. Denote the antenna excitation as source “1” and the small dipole as source “2.” The reaction $\langle 1, 2 \rangle$ is again given by Equation 3.3.17, and the reaction $\langle 2, 1 \rangle$ is given by

$$\langle 2, 1 \rangle = \iiint_V \mathbf{E}_2 \cdot \mathbf{J}_1 dV = E_2 l_1 = -V_2 \quad (3.3.19)$$

where V_2 is the received voltage, which depends on the position and orientation of source “2” and can be more explicitly denoted as $V_2(\mathbf{r}, \hat{a})$. Based on the reciprocity theorem, we have

$$\mathbf{E}_1(\mathbf{r}) \cdot \hat{a} = -\frac{V_2(\mathbf{r}, \hat{a})}{I_ll}. \quad (3.3.20)$$

Clearly, we can change the position \mathbf{r} and orientation \hat{a} of the small dipole and record the received voltage to find the radiation pattern of the antenna. If $V_2(\mathbf{r}, \hat{a})/I_ll$ is termed the receiving pattern of the antenna, the reciprocity theorem simply states that, in the absence of non-reciprocal matter, the radiation pattern of an antenna is the same as the receiving pattern.

3.4 EQUIVALENCE PRINCIPLES

In the image theory presented in Section 3.2, we have observed that if we are interested in the field in a specific region, it is possible to construct a different problem that produces the same field in that specific region. This idea can be extended to electromagnetic problems involving more complicated objects. The equivalent problem so constructed may not have a readily available solution, but it might provide a different approach to formulating the solution to the original problem. As with the image theory, the foundation for the construction of equivalent problems is the uniqueness theorem.

3.4.1 Surface Equivalence Principle

Consider the problem illustrated in Figure 3.10a, where an electromagnetic source, enclosed by a mathematical surface S , radiates a field denoted by (\mathbf{E}, \mathbf{H}) . If we are interested only in the field outside the surface S , we can replace the interior field with another

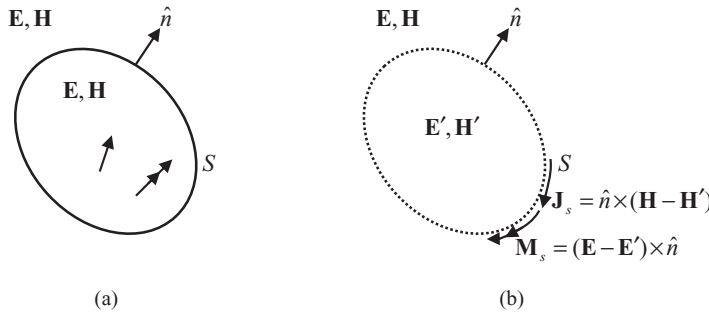


Figure 3.10 Illustration of the surface equivalence principle. (a) Original problem.
(b) Equivalent problem for the exterior field.

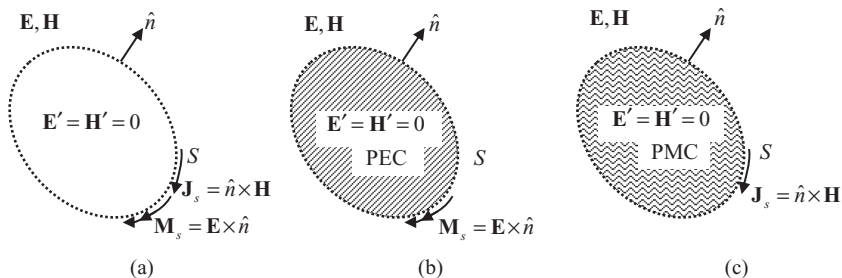


Figure 3.11 Equivalent problems. (a) With a zero interior field. (b) With the interior region filled with perfect electric conductor. (c) With the interior region filled with perfect magnetic conductor.

field denoted by $(\mathbf{E}', \mathbf{H}')$. This field, of course, has to satisfy Maxwell's equations. If we introduce a surface electric and magnetic current

$$\mathbf{J}_s = \hat{n} \times (\mathbf{H} - \mathbf{H}'), \quad \mathbf{M}_s = (\mathbf{E} - \mathbf{E}') \times \hat{n} \quad (3.4.1)$$

over the surface S , then according to the boundary conditions in Equations 1.2.18 and 1.2.19, these surface currents will produce tangential fields $\hat{n} \times \mathbf{H}$ and $\hat{n} \times \mathbf{E}$ just outside the surface S . Now, consider the exterior region in this new problem illustrated in Figure 3.10b, where it contains the same source (actually no source) as in the original problem and it has the same tangential fields on its bounding surface as in the original problem. According to the uniqueness theorem, the field produced in the exterior region has to be the same as the field in the original problem. This new problem is called the *equivalent problem*, and the introduced surface currents are called the *equivalent surface currents*. What we have described here is the basic *surface equivalence principle* [6].

Since there is no restriction imposed on the interior field other than that it has to satisfy Maxwell's equations, we can set the interior field to zero (which obviously satisfies Maxwell's equations). This results in an equivalent problem shown in Figure 3.11a. In this case, the equivalent surface currents become

$$\mathbf{J}_s = \hat{n} \times \mathbf{H}, \quad \mathbf{M}_s = \mathbf{E} \times \hat{n}. \quad (3.4.2)$$

Since the interior field is now set to zero, we can put any material inside S without affecting the field. If we fill the interior region with a perfect electric conductor, we obtain

another equivalent problem shown in Figure 3.11b. As was shown in Section 3.3, a surface electric current tangentially placed on a perfect electric conductor does not radiate; therefore, the only current that radiates in Figure 3.11b is $\mathbf{M}_s = \mathbf{E} \times \hat{n}$. If we fill the interior region with a perfect magnetic conductor, we obtain yet another equivalent problem illustrated in Figure 3.11c. It can be shown easily that a surface magnetic current tangentially placed on a perfect magnetic conductor does not radiate; hence, the only current that radiates in Figure 3.11c is $\mathbf{J}_s = \hat{n} \times \mathbf{H}$.

The surface equivalence principle presented above is valid for any medium inside and outside the surface S . If the exterior medium is unbounded and homogeneous with permittivity ϵ and permeability μ , then we can fill the interior region in Figure 3.11a with the same medium such that the entire space is now filled with an infinitely large homogeneous medium. In such a medium, the radiation of \mathbf{J}_s and \mathbf{M}_s can be formulated using the approach discussed in Chapter 2. To be more specific, the electric and magnetic fields outside S are given by

$$\mathbf{E}(\mathbf{r}) = -j\omega\mu \oint_S \tilde{\mathbf{G}}_{e0}(\mathbf{r}, \mathbf{r}') \cdot \mathbf{J}_s(\mathbf{r}') dS' - \oint_S \tilde{\mathbf{G}}_{m0}(\mathbf{r}, \mathbf{r}') \cdot \mathbf{M}_s(\mathbf{r}') dS' \quad (3.4.3)$$

$$\mathbf{H}(\mathbf{r}) = \oint_S \tilde{\mathbf{G}}_{m0}(\mathbf{r}, \mathbf{r}') \cdot \mathbf{J}_s(\mathbf{r}') dS' - j\omega\epsilon \oint_S \tilde{\mathbf{G}}_{e0}(\mathbf{r}, \mathbf{r}') \cdot \mathbf{M}_s(\mathbf{r}') dS' \quad (3.4.4)$$

and inside S , $\mathbf{E}(\mathbf{r}) = \mathbf{H}(\mathbf{r}) = 0$. Substituting Equation 3.4.2 into the above, we obtain

$$\mathbf{E}(\mathbf{r}) = -j\omega\mu \oint_S \tilde{\mathbf{G}}_{e0}(\mathbf{r}, \mathbf{r}') \cdot [\hat{n}' \times \mathbf{H}(\mathbf{r}')] dS' + \oint_S \tilde{\mathbf{G}}_{m0}(\mathbf{r}, \mathbf{r}') \cdot [\hat{n}' \times \mathbf{E}(\mathbf{r}')] dS' \quad (3.4.5)$$

$$\mathbf{H}(\mathbf{r}) = \oint_S \tilde{\mathbf{G}}_{m0}(\mathbf{r}, \mathbf{r}') \cdot [\hat{n}' \times \mathbf{H}(\mathbf{r}')] dS' + j\omega\epsilon \oint_S \tilde{\mathbf{G}}_{e0}(\mathbf{r}, \mathbf{r}') \cdot [\hat{n}' \times \mathbf{E}(\mathbf{r}')] dS' \quad (3.4.6)$$

which indicate that the fields outside a surface that encloses the source can be obtained from the tangential field components on the surface. This is, in fact, the mathematical statement of *Huygens' principle* for electromagnetic fields. In contrast, because of the presence of the perfect electric and magnetic conductors, the fields in Figures 3.11b and 3.11c cannot be formulated using the approach developed in Chapter 2. Only when S has a special shape such as a circular cylinder or a sphere is it possible to formulate the field radiated by the equivalent surface currents.

3.4.2 Application to Scattering by a Conducting Object

Now, we consider a specific application of the surface equivalence principle to the problem of scattering by a perfect electrically conducting object. The problem is illustrated in Figure 3.12a, where an electromagnetic source $(\mathbf{J}_i, \mathbf{M}_i)$ radiates in the presence of a conducting object immersed in free space. To formulate the field using the free-space field-source relations developed in Chapter 2, we construct an equivalent problem, where the conducting object is removed and replaced with the free-space medium. Furthermore, a zero field is assumed in the interior region. To produce the same exterior field as in the original problem, we place the same source $(\mathbf{J}_i, \mathbf{M}_i)$ in the exterior region and introduce the equivalent surface electric current $\mathbf{J}_s = \hat{n} \times \mathbf{H}$ over the surface S . Note that there is no need to introduce the equivalent surface magnetic current because $\hat{n} \times \mathbf{E} = 0$ in the original problem. The equivalent problem so constructed is illustrated in Figure 3.12b, which is a problem of radiation of $(\mathbf{J}_i, \mathbf{M}_i)$ and \mathbf{J}_s in free space.

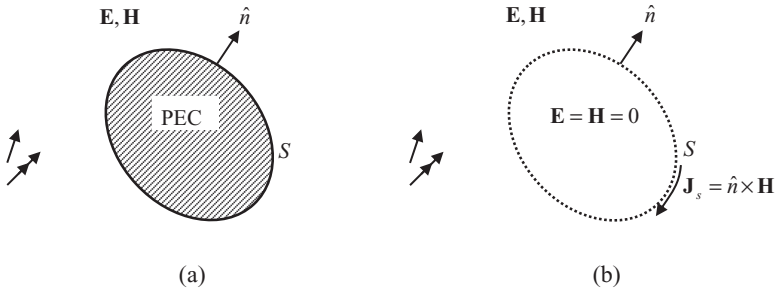


Figure 3.12 Illustration of the physical equivalent for scattering by a conducting object.
(a) Original problem. (b) Equivalent problem.

According to the field–source relation derived in Chapter 2, the radiated electric field is given by

$$\begin{aligned} \mathbf{E}(\mathbf{r}) = & -j\omega\mu \iiint_{V_s} \tilde{\mathbf{G}}_{e0}(\mathbf{r}, \mathbf{r}') \cdot \mathbf{J}_i(\mathbf{r}') dV' - \iiint_{V_s} \tilde{\mathbf{G}}_{m0}(\mathbf{r}, \mathbf{r}') \cdot \mathbf{M}_i(\mathbf{r}') dV' \\ & - j\omega\mu \oint_S \tilde{\mathbf{G}}_{e0}(\mathbf{r}, \mathbf{r}') \cdot \mathbf{J}_s(\mathbf{r}') dS' \end{aligned} \quad (3.4.7)$$

where V_s denotes the volume occupied by the source. The first two terms in Equation 3.4.7 represent the field produced by $(\mathbf{J}_i, \mathbf{M}_i)$ in free space, which is usually referred to as the *incident field* and denoted as \mathbf{E}^{inc} . Hence, Equation 3.4.7 can be written as

$$\mathbf{E}(\mathbf{r}) = \mathbf{E}^{\text{inc}}(\mathbf{r}) - j\omega\mu \oint_S \tilde{\mathbf{G}}_{e0}(\mathbf{r}, \mathbf{r}') \cdot [\hat{n}' \times \mathbf{H}(\mathbf{r}')] dS'. \quad (3.4.8)$$

The second term on the right-hand side is the difference between the total field and the incident field and is usually referred to as the *scattered field*. Similarly, we can formulate the magnetic field as

$$\mathbf{H}(\mathbf{r}) = \mathbf{H}^{\text{inc}}(\mathbf{r}) + \oint_S \tilde{\mathbf{G}}_{m0}(\mathbf{r}, \mathbf{r}') \cdot [\hat{n}' \times \mathbf{H}(\mathbf{r}')] dS' \quad (3.4.9)$$

where

$$\mathbf{H}^{\text{inc}}(\mathbf{r}) = \iiint_{V_s} \tilde{\mathbf{G}}_{m0}(\mathbf{r}, \mathbf{r}') \cdot \mathbf{J}_i(\mathbf{r}') dV' - j\omega\epsilon \iiint_{V_s} \tilde{\mathbf{G}}_{e0}(\mathbf{r}, \mathbf{r}') \cdot \mathbf{M}_i(\mathbf{r}') dV' \quad (3.4.10)$$

is the magnetic field produced by $(\mathbf{J}_i, \mathbf{M}_i)$ in free space. Although Equations 3.4.8 and 3.4.9 cannot be used directly to calculate the electric and magnetic fields because the field on the surface S required in the integrand is actually unknown, they nevertheless can be used to construct an equation in integral form that can be solved using a numerical method such as the method of moments discussed in Chapter 10.

Note that on a conducting surface, $\hat{n} \times \mathbf{H}$ represents the physically induced surface current. Hence, for this case, the equivalent surface current is also the true physical surface current. For this reason, the equivalent problem in Figure 3.12b is also called the *physical equivalent* [7]. Although Equations 3.4.8 and 3.4.9 do not provide a direct solution for a general problem, they can be used to find an approximate solution when the object is large compared with the wavelength of the incident field. As will be shown in Chapter 4, when

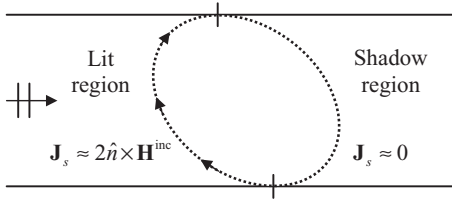


Figure 3.13 Illustration of the physical optics approximation.

a plane wave is incident upon an infinitely large planar conducting surface, the induced surface current is given by $\mathbf{J}_s = 2\hat{n} \times \mathbf{H}^{\text{inc}}$. When the source of the incident field is far away from the object, the incident field on the illuminated side of the surface can be regarded as a plane wave, and when the object is large compared with the wavelength, the surface can be regarded as an infinitely large flat surface for a field point. Therefore, the induced current on the illuminated side of the surface can be approximated as $\mathbf{J}_s \approx 2\hat{n} \times \mathbf{H}^{\text{inc}}$, whereas the induced current on the dark side of the surface can be approximated as $\mathbf{J}_s \approx 0$. This approximation is called the *physical optics approximation*. With this approximation, Equations 3.4.8 and 3.4.9 become

$$\mathbf{E}(\mathbf{r}) \approx \mathbf{E}^{\text{inc}}(\mathbf{r}) - 2j\omega\mu \iint_{S_{\text{lit}}} \tilde{\mathbf{G}}_{e0}(\mathbf{r}, \mathbf{r}') \cdot [\hat{n}' \times \mathbf{H}^{\text{inc}}(\mathbf{r}')] dS' \quad (3.4.11)$$

$$\mathbf{H}(\mathbf{r}) \approx \mathbf{H}^{\text{inc}}(\mathbf{r}) + 2 \iint_{S_{\text{lit}}} \tilde{\mathbf{G}}_{m0}(\mathbf{r}, \mathbf{r}') \cdot [\hat{n}' \times \mathbf{H}^{\text{inc}}(\mathbf{r}')] dS' \quad (3.4.12)$$

where S_{lit} denotes the portion of S that is illuminated by the incident field (Fig. 3.13).

In the physical equivalent presented above, the equivalent surface current or the actually induced surface current is unknown. However, if we retain the conducting object, we can construct an equivalent problem in such a way that the equivalent surface current is directly related to the incident field, which is known. This can be done by constructing the equivalent problem that produces the same scattered field in the exterior region as that in the original problem. As mentioned before, the scattered field is defined as the difference between the total and incident fields, that is,

$$\mathbf{E}^{\text{sc}}(\mathbf{r}) = \mathbf{E}(\mathbf{r}) - \mathbf{E}^{\text{inc}}(\mathbf{r}), \quad \mathbf{H}^{\text{sc}}(\mathbf{r}) = \mathbf{H}(\mathbf{r}) - \mathbf{H}^{\text{inc}}(\mathbf{r}). \quad (3.4.13)$$

This scattered field is the field radiated by the current induced on the conducting object. Hence, to produce such a scattered field, we need to introduce the equivalent surface currents

$$\mathbf{J}_s = \hat{n} \times \mathbf{H}^{\text{sc}}, \quad \mathbf{M}_s = \mathbf{E}^{\text{sc}} \times \hat{n}. \quad (3.4.14)$$

Because of the presence of the conducting object, \mathbf{J}_s does not radiate; hence, the only radiation comes from \mathbf{M}_s . However, since $\hat{n} \times \mathbf{E}$ vanishes on the conducting surface, \mathbf{M}_s becomes

$$\mathbf{M}_s = (\mathbf{E} - \mathbf{E}^{\text{inc}}) \times \hat{n} = \hat{n} \times \mathbf{E}^{\text{inc}} \quad (3.4.15)$$

which is related only to the incident field. Note that this equivalent current exists over the entire surface of the object. This special form of the surface equivalence principle is also known as the *induction theorem* [7], and the equivalent problem is shown in Figure 3.14b. Although in this case, the equivalent current is known, the field cannot be readily calculated

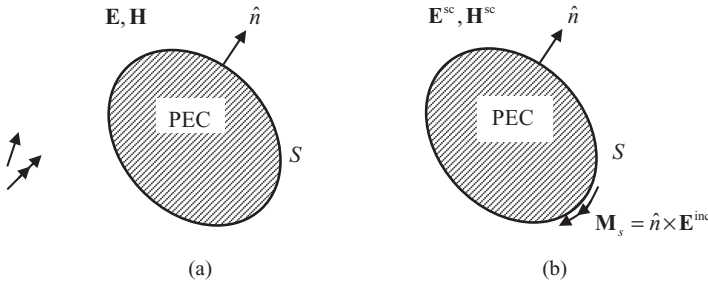


Figure 3.14 Illustration of the induction theorem for scattering by a conducting object.
(a) Original problem. (b) Equivalent problem.

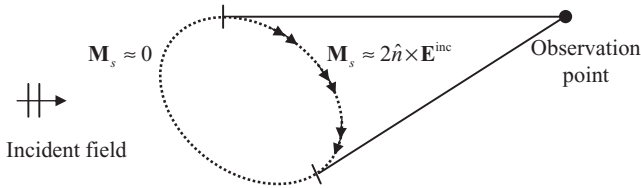


Figure 3.15 Illustration of the induction theorem with an image theory approximation.

because of the presence of the conducting object. However, if the object is very large compared with the wavelength of the incident field, we can again formulate an approximate solution, which is different from that of the physical optics approximation. When the object is very large, the surface can be approximated as an infinitely large planar surface for a current element residing on the surface. Therefore, the image theory can be applied to the current facing the observation point. With the application of the image theory, the conducting object is removed and the total surface current becomes $\mathbf{M}_s \approx 2\hat{n} \times \mathbf{E}^{inc}$ on the portion of the surface that faces toward the observation point (Fig. 3.15). The radiation of the equivalent current on the other portion of the surface that faces away from the observation point can be neglected. Hence, the field can be approximated as

$$\mathbf{E}(\mathbf{r}) \approx \mathbf{E}^{inc}(\mathbf{r}) - 2 \iint_{S_{obs}} \tilde{\mathbf{G}}_{m0}(\mathbf{r}, \mathbf{r}') \cdot [\hat{n}' \times \mathbf{E}^{inc}(\mathbf{r}')] dS' \quad (3.4.16)$$

$$\mathbf{H}(\mathbf{r}) \approx \mathbf{H}^{inc}(\mathbf{r}) - 2j\omega\epsilon \iint_{S_{obs}} \tilde{\mathbf{G}}_{e0}(\mathbf{r}, \mathbf{r}') \cdot [\hat{n}' \times \mathbf{E}^{inc}(\mathbf{r}')] dS' \quad (3.4.17)$$

where S_{obs} denotes the portion of S that can be seen from the observation point \mathbf{r} . Note that for a different observation point, S_{obs} can be different.

3.4.3 Application to Scattering by a Dielectric Object

In Section 3.4.1, the surface equivalence principle is used to construct equivalent problems for the exterior region. The equivalence principle can also be employed to construct equivalent problems for the interior region. To demonstrate this, we consider the problem of scattering by a dielectric object, illustrated in Figure 3.16a. The exterior region has permittivity ϵ_1 and permeability μ_1 . The dielectric object has permittivity ϵ_2 and permeability μ_2 . First, we can apply the surface equivalence principle to construct the equivalent problem for the exterior region shown in Figure 3.16b, where the interior field is assumed to be zero whereas the exterior field remains the same as that in the original

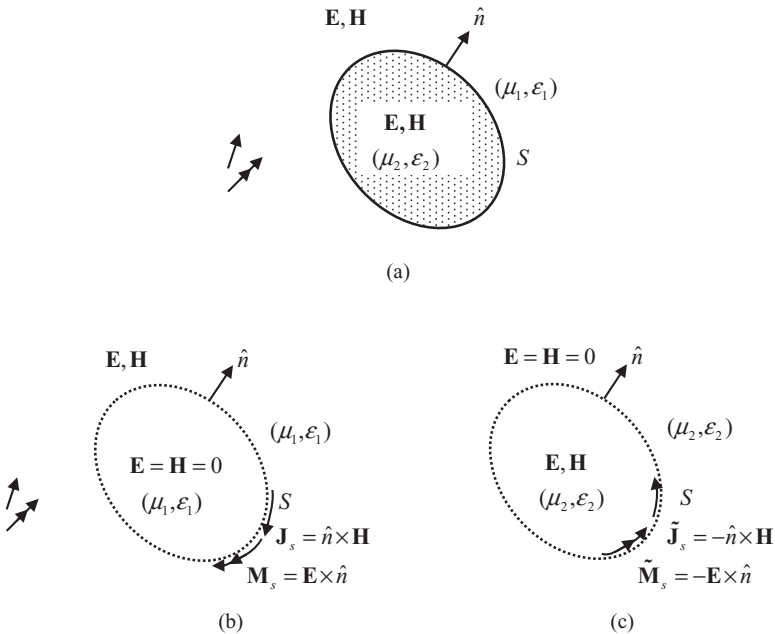


Figure 3.16 Equivalent problems for scattering by a dielectric object. (a) Original problem. (b) Equivalent problem for the exterior field. (c) Equivalent problem for the interior field.

problem. The equivalent surface currents are given by Equation 3.4.2. Since there is no interior field, the dielectric object can be replaced with a medium having permittivity ϵ_1 and permeability μ_1 . If ϵ_1 and μ_1 are constants, then the equivalent currents are radiating in an unbounded homogeneous space. The field in the exterior region can be expressed as

$$\mathbf{E}(\mathbf{r}) = \mathbf{E}^{\text{inc}}(\mathbf{r}) - j\omega\mu_1 \oint_S \tilde{\mathbf{G}}_{e0}(\mathbf{r}, \mathbf{r}'; k_1) \cdot \mathbf{J}_s(\mathbf{r}') dS' - \oint_S \tilde{\mathbf{G}}_{m0}(\mathbf{r}, \mathbf{r}'; k_1) \cdot \mathbf{M}_s(\mathbf{r}') dS' \quad (3.4.18)$$

where $\tilde{\mathbf{G}}_{e0}(\mathbf{r}, \mathbf{r}'; k_1)$ and $\tilde{\mathbf{G}}_{m0}(\mathbf{r}, \mathbf{r}'; k_1)$ are the same as $\tilde{\mathbf{G}}_{e0}(\mathbf{r}, \mathbf{r}')$ and $\tilde{\mathbf{G}}_{m0}(\mathbf{r}, \mathbf{r}')$, respectively, and k_1 is added to denote that the wavenumber involved is $k_1 = \omega\sqrt{\mu_1\epsilon_1}$. The corresponding magnetic field in the exterior region is given by

$$\mathbf{H}(\mathbf{r}) = \mathbf{H}^{\text{inc}}(\mathbf{r}) + \oint_S \tilde{\mathbf{G}}_{m0}(\mathbf{r}, \mathbf{r}'; k_1) \cdot \mathbf{J}_s(\mathbf{r}') dS' - j\omega\epsilon_1 \oint_S \tilde{\mathbf{G}}_{e0}(\mathbf{r}, \mathbf{r}'; k_1) \cdot \mathbf{M}_s(\mathbf{r}') dS'. \quad (3.4.19)$$

Next, we consider the field inside the dielectric object. To construct an equivalent problem for the interior field such that it can be formulated using free-space Green's functions, we set the exterior field to zero and replace the exterior medium with that having the permittivity and permeability of the interior medium, that is, ϵ_2 and μ_2 . To produce the same interior field as that in the original problem, we need to introduce the equivalent surface currents

$$\tilde{\mathbf{J}}_s = -\hat{n} \times \mathbf{H} = -\mathbf{J}_s, \quad \tilde{\mathbf{M}}_s = -\mathbf{E} \times \hat{n} = -\mathbf{M}_s. \quad (3.4.20)$$

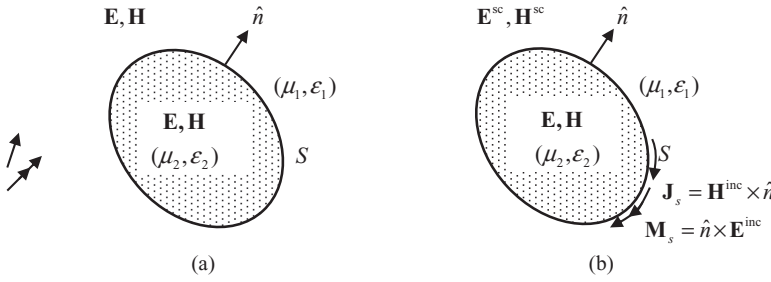


Figure 3.17 Illustration of the induction theorem for scattering by a dielectric object.
(a) Original problem. (b) Equivalent problem.

The equivalent problem so constructed involves the radiation of $(\tilde{\mathbf{J}}_s, \tilde{\mathbf{M}}_s)$ in an unbounded medium having permittivity ϵ_2 and permeability μ_2 , as shown in Figure 3.16c. If ϵ_2 and μ_2 are constants, the fields produced by $(\tilde{\mathbf{J}}_s, \tilde{\mathbf{M}}_s)$ in the interior region are given by

$$\mathbf{E}(\mathbf{r}) = -j\omega\mu_2 \iint_S \tilde{\mathbf{G}}_{e0}(\mathbf{r}, \mathbf{r}'; k_2) \cdot \tilde{\mathbf{J}}_s(\mathbf{r}') dS' - \iint_S \tilde{\mathbf{G}}_{m0}(\mathbf{r}, \mathbf{r}'; k_2) \cdot \tilde{\mathbf{M}}_s(\mathbf{r}') dS' \quad (3.4.21)$$

$$\mathbf{H}(\mathbf{r}) = \iint_S \tilde{\mathbf{G}}_{m0}(\mathbf{r}, \mathbf{r}'; k_2) \cdot \tilde{\mathbf{J}}_s(\mathbf{r}') dS' - j\omega\epsilon_2 \iint_S \tilde{\mathbf{G}}_{e0}(\mathbf{r}, \mathbf{r}'; k_2) \cdot \tilde{\mathbf{M}}_s(\mathbf{r}') dS' \quad (3.4.22)$$

where $\tilde{\mathbf{G}}_{e0}(\mathbf{r}, \mathbf{r}'; k_2)$ and $\tilde{\mathbf{G}}_{m0}(\mathbf{r}, \mathbf{r}'; k_2)$ are the free-space dyadic Green's functions with the wavenumber $k_2 = \omega\sqrt{\mu_2\epsilon_2}$. Similar to the case for a conducting scatterer, Equations 3.4.18, 3.4.19, 3.4.21, and 3.4.22 cannot be used to compute the fields directly since the surface currents \mathbf{J}_s and \mathbf{M}_s are unknown. However, they can be used to construct integral equations that can be solved for \mathbf{J}_s and \mathbf{M}_s .

Finally, we note that for scattering by a dielectric object, we can also apply the induction theorem to construct an equivalent problem that retains the scatterer and produces the total field in the interior region and the scattered field in the exterior region. The required equivalent surface currents are

$$\mathbf{J}_s = \hat{n} \times (\mathbf{H}^{sc} - \mathbf{H}) = -\hat{n} \times \mathbf{H}^{inc}, \quad \mathbf{M}_s = (\mathbf{E}^{sc} - \mathbf{E}) \times \hat{n} = -\mathbf{E}^{inc} \times \hat{n} \quad (3.4.23)$$

which are known for a given incident field or an exterior source. This equivalent problem is shown in Figure 3.17. However, this equivalent problem is not very useful because of the presence of the dielectric object, which prevents the use of the free-space field–source relations to formulate an analytical expression for the field.

3.4.4 Volume Equivalence Principle

Consider an electric and a magnetic current source $(\mathbf{J}_i, \mathbf{M}_i)$ radiating in the presence of an object characterized by permittivity $\tilde{\epsilon}$ and permeability $\tilde{\mu}$. Both the source and the object are immersed in an infinitely large free space having a constant permittivity ϵ and permeability μ . The radiated field satisfies Maxwell's equations

$$\nabla \times \mathbf{E} = -j\omega\mu(\mathbf{r})\mathbf{H} - \mathbf{M}_i \quad (3.4.24)$$

$$\nabla \times \mathbf{H} = j\omega\epsilon(\mathbf{r})\mathbf{E} + \mathbf{J}_i \quad (3.4.25)$$

where $\varepsilon(\mathbf{r})$ and $\mu(\mathbf{r})$ denote the position-dependent permittivity and permeability. Inside the object, $\varepsilon(\mathbf{r}) = \tilde{\varepsilon}$ and $\mu(\mathbf{r}) = \tilde{\mu}$; and outside the object, $\varepsilon(\mathbf{r}) = \varepsilon$ and $\mu(\mathbf{r}) = \mu$. The solution to these equations cannot be formulated easily because the permittivity and permeability are not constant throughout the entire space. However, we can rewrite these equations as

$$\nabla \times \mathbf{E} = -j\omega\mu\mathbf{H} - \mathbf{M}_{eq} - \mathbf{M}_i \quad (3.4.26)$$

$$\nabla \times \mathbf{H} = j\omega\varepsilon\mathbf{E} + \mathbf{J}_{eq} + \mathbf{J}_i \quad (3.4.27)$$

where

$$\mathbf{M}_{eq} = j\omega[\mu(\mathbf{r}) - \mu]\mathbf{H} \quad (3.4.28)$$

$$\mathbf{J}_{eq} = j\omega[\varepsilon(\mathbf{r}) - \varepsilon]\mathbf{E}. \quad (3.4.29)$$

Equations 3.4.26 and 3.4.27 represent Maxwell's equations for the field radiated by $(\mathbf{J}_i, \mathbf{M}_i, \mathbf{J}_{eq}, \mathbf{M}_{eq})$ in free space, whose solution has been formulated in Chapter 2. The effect of the object is now replaced by the two equivalent source terms $(\mathbf{J}_{eq}, \mathbf{M}_{eq})$, which are called *equivalent electric and magnetic currents* and exist only in the volume of the object. This is the statement of the *volume equivalence principle* [8,9].

From Equations 2.2.35 and 2.2.38, we obtain the expressions for the electric and magnetic fields as

$$\begin{aligned} \mathbf{E}(\mathbf{r}) = & -j\omega\mu \iiint_{V_s} \tilde{\mathbf{G}}_{e0}(\mathbf{r}, \mathbf{r}') \cdot \mathbf{J}_i(\mathbf{r}') dV' - \iiint_{V_s} \tilde{\mathbf{G}}_{m0}(\mathbf{r}, \mathbf{r}') \cdot \mathbf{M}_i(\mathbf{r}') dV' \\ & - j\omega\mu \iiint_{V_o} \tilde{\mathbf{G}}_{e0}(\mathbf{r}, \mathbf{r}') \cdot \mathbf{J}_{eq}(\mathbf{r}') dV' - \iiint_{V_o} \tilde{\mathbf{G}}_{m0}(\mathbf{r}, \mathbf{r}') \cdot \mathbf{M}_{eq}(\mathbf{r}') dV' \end{aligned} \quad (3.4.30)$$

$$\begin{aligned} \mathbf{H}(\mathbf{r}) = & \iiint_{V_s} \tilde{\mathbf{G}}_{m0}(\mathbf{r}, \mathbf{r}') \cdot \mathbf{J}_i(\mathbf{r}') dV' - j\omega\varepsilon \iiint_{V_s} \tilde{\mathbf{G}}_{e0}(\mathbf{r}, \mathbf{r}') \cdot \mathbf{M}_i(\mathbf{r}') dV' \\ & + \iiint_{V_o} \tilde{\mathbf{G}}_{m0}(\mathbf{r}, \mathbf{r}') \cdot \mathbf{J}_{eq}(\mathbf{r}') dV' - j\omega\varepsilon \iiint_{V_o} \tilde{\mathbf{G}}_{e0}(\mathbf{r}, \mathbf{r}') \cdot \mathbf{M}_{eq}(\mathbf{r}') dV' \end{aligned} \quad (3.4.31)$$

where V_s denotes the volume occupied by the source and V_o is the volume of the object. As noted earlier, the first two terms in Equations 3.4.30 and 3.4.31 represent the fields produced by $(\mathbf{J}_i, \mathbf{M}_i)$ in free space, which are usually referred to as the incident fields and denoted as \mathbf{E}^{inc} and \mathbf{H}^{inc} , respectively. With this notation, Equations 3.4.30 and 3.4.31 can be written as

$$\begin{aligned} \mathbf{E}(\mathbf{r}) = & \mathbf{E}^{inc}(\mathbf{r}) + \omega^2\mu \iiint_{V_o} \tilde{\mathbf{G}}_{e0}(\mathbf{r}, \mathbf{r}') \cdot (\tilde{\varepsilon} - \varepsilon)\mathbf{E}(\mathbf{r}') dV' \\ & - j\omega \iiint_{V_o} \tilde{\mathbf{G}}_{m0}(\mathbf{r}, \mathbf{r}') \cdot (\tilde{\mu} - \mu)\mathbf{H}(\mathbf{r}') dV' \end{aligned} \quad (3.4.32)$$

$$\begin{aligned} \mathbf{H}(\mathbf{r}) = & \mathbf{H}^{inc}(\mathbf{r}) + j\omega \iiint_{V_o} \tilde{\mathbf{G}}_{m0}(\mathbf{r}, \mathbf{r}') \cdot (\tilde{\varepsilon} - \varepsilon)\mathbf{E}(\mathbf{r}') dV' \\ & + \omega^2\varepsilon \iiint_{V_o} \tilde{\mathbf{G}}_{e0}(\mathbf{r}, \mathbf{r}') \cdot (\tilde{\mu} - \mu)\mathbf{H}(\mathbf{r}') dV' \end{aligned} \quad (3.4.33)$$

after the substitution of Equations 3.4.28 and 3.4.29. Equations 3.4.32 and 3.4.33 are called *volume integral equations*. Since \mathbf{E} and \mathbf{H} are still unknown inside V_o , Equations 3.4.32

and 3.4.33 do not constitute a solution since they cannot be used to evaluate the fields. However, they do provide two equations that can be solved using either approximate or numerical methods such as the method of moments discussed in Chapter 10. For example, if the object is a weak scatterer, which means that its permittivity and permeability are very close to those of the background or, mathematically, that $|\tilde{\epsilon} - \epsilon|/\epsilon \ll 1$ and $|\tilde{\mu} - \mu|/\mu \ll 1$, then the incident field can be used to approximate the field inside the object. With this approximation, Equations 3.4.32 and 3.4.33 can be written as

$$\begin{aligned}\mathbf{E}(\mathbf{r}) &\approx \mathbf{E}^{\text{inc}}(\mathbf{r}) + \omega^2 \mu \iiint_{V_o} \tilde{\mathbf{G}}_{e0}(\mathbf{r}, \mathbf{r}') \cdot (\tilde{\epsilon} - \epsilon) \mathbf{E}^{\text{inc}}(\mathbf{r}') dV' \\ &\quad - j\omega \iiint_{V_o} \tilde{\mathbf{G}}_{m0}(\mathbf{r}, \mathbf{r}') \cdot (\tilde{\mu} - \mu) \mathbf{H}^{\text{inc}}(\mathbf{r}') dV'\end{aligned}\quad (3.4.34)$$

$$\begin{aligned}\mathbf{H}(\mathbf{r}) &\approx \mathbf{H}^{\text{inc}}(\mathbf{r}) + j\omega \iiint_{V_o} \tilde{\mathbf{G}}_{m0}(\mathbf{r}, \mathbf{r}') \cdot (\tilde{\epsilon} - \epsilon) \mathbf{E}^{\text{inc}}(\mathbf{r}') dV' \\ &\quad + \omega^2 \epsilon \iiint_{V_o} \tilde{\mathbf{G}}_{e0}(\mathbf{r}, \mathbf{r}') \cdot (\tilde{\mu} - \mu) \mathbf{H}^{\text{inc}}(\mathbf{r}') dV'\end{aligned}\quad (3.4.35)$$

and this approximation is known as the *first-order Born approximation* [10].

Finally, we note that in the entire formulation discussed in this section, no limitation has been imposed on the form of $\tilde{\epsilon}$ and $\tilde{\mu}$. Therefore, the formulation is applicable to an inhomogeneous object whose $\tilde{\epsilon}$ and $\tilde{\mu}$ have a spatial variation, and it is also applicable to an anisotropic object whose $\tilde{\epsilon}$ and $\tilde{\mu}$ are tensors. Compared with the surface integral formulation expressed in Equations 3.4.18, 3.4.19, 3.4.21, and 3.4.22 in the preceding section, the volume integral equations are more general, but also more expensive to solve because they contain volume integrals.

3.5 DUALITY PRINCIPLE

Because of certain symmetry in Maxwell's equations, there exists a dual formulation for any formulation derived for electromagnetic fields. For example, the field produced by a magnetic source can be found through a dual formulation for the field produced by an electric source. A careful examination of Equations 2.1.20–2.1.23 reveals that Equations 2.1.22 and 2.2.23 can be obtained from Equations 2.1.20 and 2.2.21 through the transformation given in Table 3.1. Hence, the formulation for the field due to the magnetic source can be obtained directly using the transformation given in Table 3.1, where ψ denotes the magnetic scalar potential, without repeating the entire derivation.

A further examination of Maxwell's equations reveals something more interesting. Consider any set of Maxwell's equations, whether in integral or differential form and whether in the frequency or time domain. If we replace the variables in the left column of Table 3.2 with those in the right column, we recover the same Maxwell's equations. This can be verified easily using Maxwell's equations in Equations 2.1.1–2.1.4. Therefore, given any valid expression derived from Maxwell's equations, we can obtain another valid expression by replacing the variables in the left column of Table 3.2 with those in the right column. The second expression is called the *dual expression* of the first. To make Table 3.2 more compact and easy to memorize, we omitted the variables such as the flux densities, charge densities, and scalar potentials since they are directly related to the field intensities, current densities, and vector potentials.

TABLE 3.1 Duality between Fields Due to Electric and Magnetic Sources

Electric Source Case	Magnetic Source Case
\mathbf{E}_e	\mathbf{H}_m
\mathbf{H}_e	$-\mathbf{E}_m$
\mathbf{D}_e	\mathbf{B}_m
\mathbf{B}_e	$-\mathbf{D}_m$
\mathbf{J}	\mathbf{M}
ρ_e	ρ_m
ϵ	μ
μ	ϵ
\mathbf{A}	\mathbf{F}
φ	ψ

TABLE 3.2 Transformation to Obtain a Dual Formulation

Original Formulation	Dual Formulation
\mathbf{E}	\mathbf{H}
\mathbf{H}	$-\mathbf{E}$
\mathbf{J}	\mathbf{M}
\mathbf{M}	$-\mathbf{J}$
ϵ	μ
μ	ϵ
\mathbf{A}	\mathbf{F}
\mathbf{F}	$-\mathbf{A}$

The duality relations discussed above, especially the one listed in Table 3.2, are useful in practice for two purposes. The first is to verify a variety of equations formulated in electromagnetics. Many such equations are the dual forms of others and a cross-check can quickly detect potential errors and reinforce the confidence in the validity of these equations. The reader is encouraged to carry out this cross-check on some of the equations derived in Chapters 1–3. The second purpose is to obtain the dual equations directly by duality without going through the process of derivation. Of course, before doing this, one has to make certain that the original equations are correct. It is critical to understand that the dual equations so obtained are valid for the dual problems, which may not be necessarily the same as the original problems. For example, the boundary condition $\hat{\mathbf{n}} \times \mathbf{E} = 0$, which describes a perfect electrically conducting surface, has its dual counterpart as $\hat{\mathbf{n}} \times \mathbf{H} = 0$, which actually specifies a perfect magnetically conducting surface. Therefore, the dual expressions obtained by duality from the field–source relations (Eqs. 3.2.13 and 3.2.21) for the half-space above an infinitely large electrical ground plane are valid for the half-space above an infinitely large magnetic ground plane.

3.6 APERTURE RADIATION AND SCATTERING

With the uniqueness theorem, image theory, surface equivalence principle, and duality principle in hand, we can combine them and deal with the problem of radiation through and scattering by apertures in a conducting plane. Two important topics related to aperture

radiation and scattering are Babinet's principle and complementary structures, which are also covered in this section.

3.6.1 Equivalent Problems

Consider the problem illustrated in Figure 3.18a, where an electromagnetic source radiates in the presence of an infinitely large conducting sheet with an aperture. Assume that the electric field over the aperture is known and we are interested in the transmitted field in the right half-space. We can employ the surface equivalence principle illustrated in Figure 3.11b to establish an equivalent problem shown in Figure 3.18b. Here, we consider the left half-space as the interior region and the right half-space as the exterior region. When the left half-space is filled with a perfect electric conductor, the aperture is sealed and an electric ground plane is formed. The effect of the aperture field is replaced by an equivalent surface magnetic current $\mathbf{M}_s = \mathbf{E} \times \hat{\mathbf{n}}$, which exists only over the aperture region. Next, we apply the image theory to remove the electric ground plane. Since the original surface current is placed right over the ground plane, the image current coincides with the original current, yielding the sum of the surface currents as $\mathbf{M}_s = 2\mathbf{E} \times \hat{\mathbf{n}}$, which radiates in free space. This radiation can be evaluated using the approach discussed in Chapter 2.

As a simple example, consider the radiation of a rectangular waveguide opening onto a ground plane coincident with the xy -plane, as illustrated in Figure 3.19a. Assume that the electric field at the opening is given by

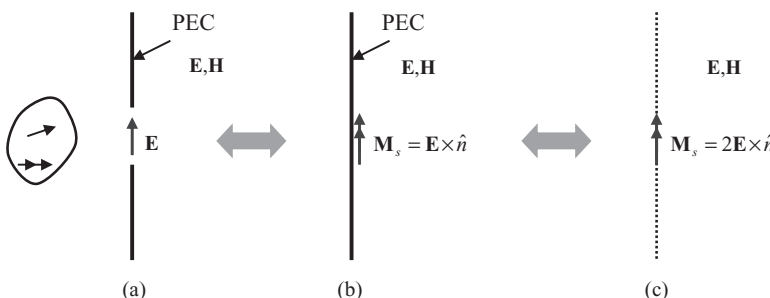


Figure 3.18 Radiation through an aperture in a conducting screen. (a) Original problem. (b) Equivalent half-space problem with an electric ground plane for the field in the right half-space. (c) Equivalent free-space problem for the field in the right half-space.

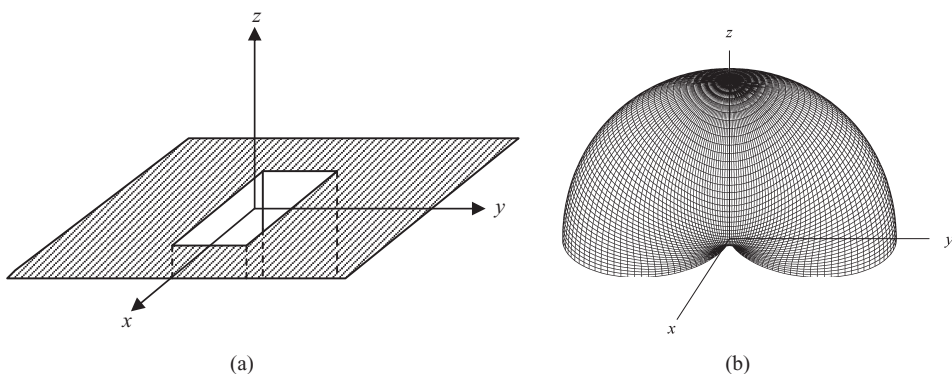


Figure 3.19 Radiation from a rectangular waveguide opening onto an infinitely large ground plane. (a) Geometry. (b) Radiation pattern.

$$\mathbf{E} = \hat{\mathbf{y}} E_0 \cos \frac{\pi x}{a}. \quad (3.6.1)$$

Based on the discussion above, the field above the ground plane can be evaluated by finding the radiation of the surface magnetic current

$$\mathbf{M}_s = 2\mathbf{E} \times \hat{\mathbf{z}} = 2\hat{\mathbf{x}} E_0 \cos \frac{\pi x}{a} \quad (3.6.2)$$

in free space. If we are interested only in the far field, it is sufficient to evaluate \mathbf{L} , which is given by

$$\mathbf{L} = \iint_{S_a} \mathbf{M}_s(\mathbf{r}') e^{jkr' \cos \psi} dS' \quad (3.6.3)$$

where S_a denotes the aperture region. For this, $r' \cos \psi = \mathbf{r}' \cdot \hat{\mathbf{r}} = x' \sin \theta \cos \phi + y' \sin \theta \sin \phi$. Hence,

$$\mathbf{L} = \hat{\mathbf{x}} 2E_0 \int_{-b/2}^{b/2} \int_{-a/2}^{a/2} \cos \frac{\pi x'}{a} e^{jk(x' \sin \theta \cos \phi + y' \sin \theta \sin \phi)} dx' dy' \quad (3.6.4)$$

which can be evaluated to yield

$$\mathbf{L} = \hat{\mathbf{x}} 8\pi a E_0 \frac{\cos\left(k \frac{a}{2} \sin \theta \cos \phi\right) \sin\left(k \frac{b}{2} \sin \theta \sin \phi\right)}{k [\pi^2 - (ka \sin \theta \cos \phi)^2] \sin \theta \sin \phi}. \quad (3.6.5)$$

The far field is then given by

$$\begin{aligned} E_\theta &= \eta H_\phi = -\frac{jke^{-jkr}}{4\pi r} L_\phi \\ &= j2aE_0 \frac{e^{-jkr}}{r} \frac{\cos\left(k \frac{a}{2} \sin \theta \cos \phi\right) \sin\left(k \frac{b}{2} \sin \theta \sin \phi\right)}{[\pi^2 - (ka \sin \theta \cos \phi)^2] \sin \theta} \end{aligned} \quad (3.6.6)$$

$$\begin{aligned} E_\phi &= -\eta H_\theta = \frac{jke^{-jkr}}{4\pi r} L_\theta \\ &= j2aE_0 \frac{e^{-jkr}}{r} \frac{\cos\left(k \frac{a}{2} \sin \theta \cos \phi\right) \sin\left(k \frac{b}{2} \sin \theta \sin \phi\right)}{[\pi^2 - (ka \sin \theta \cos \phi)^2] \tan \theta \tan \phi} \end{aligned} \quad (3.6.7)$$

for $\theta \leq \pi/2$. The field pattern is plotted in Figure 3.19b.

When there is no conducting plane to separate the right half-space from the left half-space, we can still establish an equivalent problem that permits the calculation of the field in the right half-space based on the field over an infinitely large planar surface. Consider the problem illustrated in Figure 3.20a. We can again consider it a special case of Figure 3.10a, with the left half-space as the interior region and the right half-space as the exterior region. Therefore, we can construct three different equivalent problems as

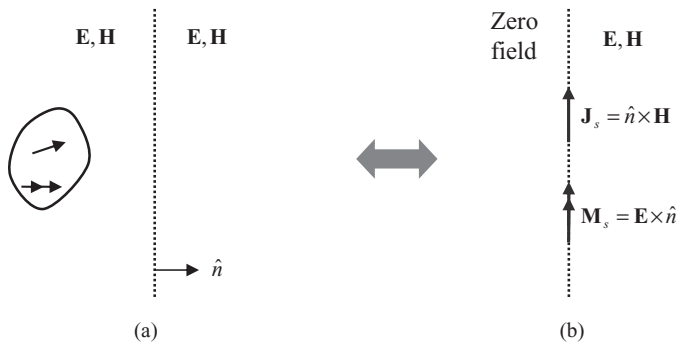


Figure 3.20 Radiation through a virtual planar surface to the right half-space. (a) Original problem. (b) Equivalent free-space problem for the field in the right half-space.

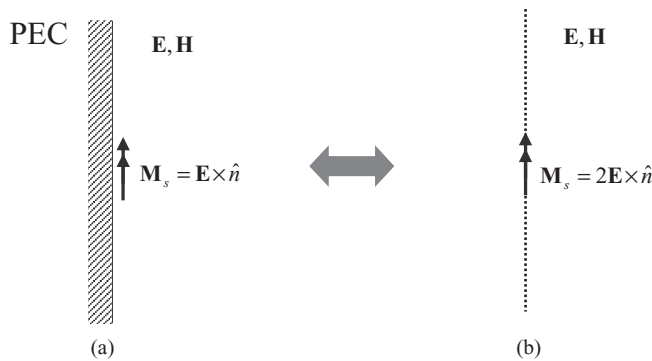


Figure 3.21 Equivalent problems for the problem in Figure 3.19a. (a) Equivalent half-space problem with an electric ground plane for the field in the right half-space. (b) Equivalent free-space problem for the field in the right half-space.

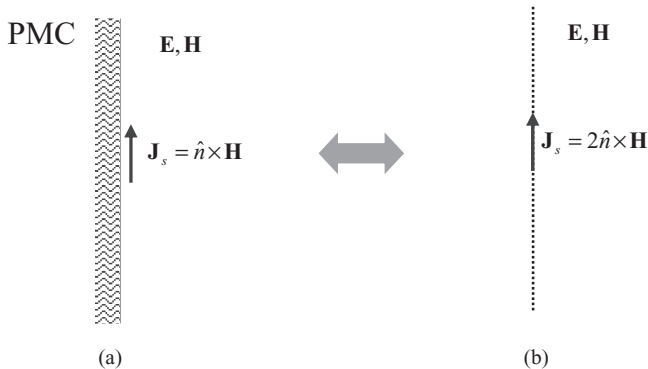


Figure 3.22 Equivalent problems for the problem in Figure 3.19a. (a) Equivalent half-space problem with a magnetic ground plane for the field in the right half-space. (b) Equivalent free-space problem for the field in the right half-space.

shown in Figures 3.11a–3.11c for the exterior fields. The equivalent problem corresponding to Figure 3.11a is illustrated in Figure 3.20b, where the equivalent surface currents radiate in free space and hence the field in the right half-space can be evaluated from $\mathbf{J}_s = \hat{n} \times \mathbf{H}$ and $\mathbf{M}_s = \mathbf{E} \times \hat{n}$ using the free-space field–source relations. The equivalent problem corresponding to Figure 3.11b is shown in Figure 3.21a, which can further be converted into a free-space problem shown in Figure 3.21b using the image theory. Therefore, the field in the right half-space can be evaluated from $\mathbf{M}_s = 2\mathbf{E} \times \hat{n}$ using again the free-space field–source relations. The equivalent problem corresponding to Figure 3.11c is given in Figure 3.22a, which can again be converted into a free-space problem shown in Figure 3.22b using the image theory. The field in the right half-space can be evaluated from $\mathbf{J}_s = 2\hat{n} \times \mathbf{H}$ using the free-space field–source relations. If the tangential fields $\hat{n} \times \mathbf{H}$ and/or $\hat{n} \times \mathbf{E}$ are known precisely over the entire planar surface, the three

equivalent problems should yield the same solution. If these tangential fields are known approximately, the three solutions will be slightly different. The choice will mainly depend on the field information available for a specific problem.

3.6.2 Babinet's Principle

A topic that is closely related to aperture radiation and scattering is Babinet's principle, which was originally developed for scalar optical fields [11]. To develop the electromagnetic version of Babinet's principle, we consider three problems. The first problem is shown in Figure 3.23a, where an electromagnetic source ($\mathbf{J}_i, \mathbf{M}_i$) radiates in a free space and the radiated field is denoted as $(\mathbf{E}^{inc}, \mathbf{H}^{inc})$. The second problem is illustrated in Figure 3.23b, where the same electromagnetic source radiates in front of an infinitely large conducting screen with an aperture. The aperture region is denoted as S_a and the area of the metallic screen is denoted as S_m . The transmitted field in the right half-space is denoted as $(\mathbf{E}_a, \mathbf{H}_a)$. The third problem is shown in Figure 3.23c, where the same electromagnetic source radiates in the presence of a perfect magnetically conducting plate having the same shape and located at the same place as the aperture. The radiated field is denoted as $(\mathbf{E}_m, \mathbf{H}_m)$.

It can be seen from the field radiated by an electric current element (Section 2.3.1) that the radiated magnetic field has no tangential component on any plane that contains the current element. Therefore, in Figure 3.23b, the electric current induced on the metallic screen generates no tangential component of the magnetic field over the aperture. The only tangential component of the magnetic field there is that of the incident field, generated by the source in free space. Hence,

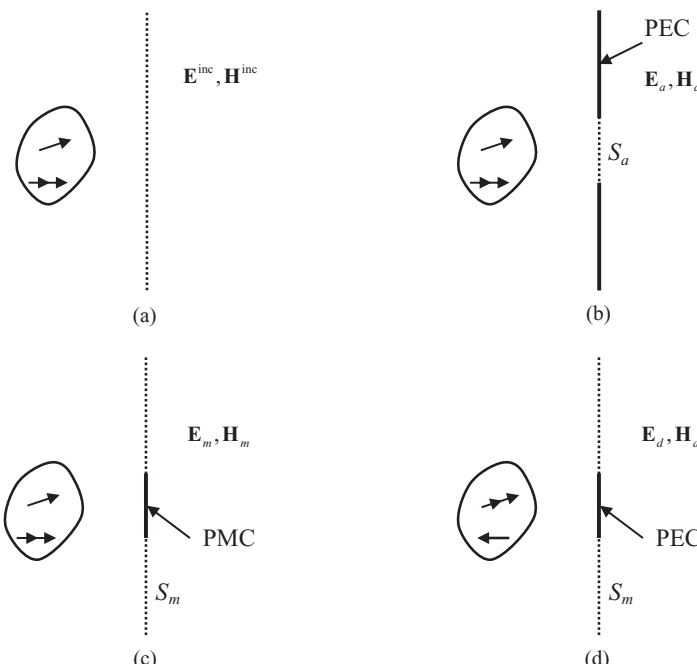


Figure 3.23 Illustration of Babinet's principle. (a) A source radiating in free space. (b) The same source radiating through an aperture in a conducting screen. (c) The same source radiating in the presence of a magnetically conducting plate. (d) The dual source radiating in the presence of an electrically conducting plate in the dual medium.

$$\hat{n} \times \mathbf{H}_a = \hat{n} \times \mathbf{H}^{\text{inc}} \quad \text{on } S_a \quad (3.6.8)$$

$$\hat{n} \times \mathbf{E}_a = 0 \quad \text{on } S_m. \quad (3.6.9)$$

Similarly, the electric field radiated by a magnetic current element has no tangential component on any plane that contains the current element. Therefore, in Figure 3.23c, the magnetic current induced on the magnetically conducting plate generates no tangential component of the electric field over S_m . Hence,

$$\hat{n} \times \mathbf{H}_m = 0 \quad \text{on } S_a \quad (3.6.10)$$

$$\hat{n} \times \mathbf{E}_m = \hat{n} \times \mathbf{E}^{\text{inc}} \quad \text{on } S_m. \quad (3.6.11)$$

Now, let us add the field in Figure 3.23b to that in Figure 3.23c. The field in the right half-space would be $(\mathbf{E}_a + \mathbf{E}_m, \mathbf{H}_a + \mathbf{H}_m)$, and the tangential fields at S_a and S_m would be

$$\hat{n} \times (\mathbf{H}_a + \mathbf{H}_m) = \hat{n} \times \mathbf{H}^{\text{inc}} \quad \text{on } S_a \quad (3.6.12)$$

$$\hat{n} \times (\mathbf{E}_a + \mathbf{E}_m) = \hat{n} \times \mathbf{E}^{\text{inc}} \quad \text{on } S_m. \quad (3.6.13)$$

Therefore, for the right half-space, the tangential component of the combined magnetic field over S_a is the same as that in Figure 3.23a, and the tangential component of the combined electric field over S_m is the same as that in Figure 3.23a. According to the uniqueness theorem, the combined field in the right half-space has to be the same as that in Figure 3.23a, or in other words,

$$\mathbf{E}_a + \mathbf{E}_m = \mathbf{E}^{\text{inc}}, \quad \mathbf{H}_a + \mathbf{H}_m = \mathbf{H}^{\text{inc}}. \quad (3.6.14)$$

This is the electromagnetic version of *Babinet's principle* and the formulation here follows that of Harrington [7]. Since the field in Figure 3.23c can also be written as

$$\mathbf{E}_m = \mathbf{E}^{\text{inc}} + \mathbf{E}_m^{\text{sc}}, \quad \mathbf{H}_m = \mathbf{H}^{\text{inc}} + \mathbf{H}_m^{\text{sc}} \quad (3.6.15)$$

where $(\mathbf{E}_m^{\text{sc}}, \mathbf{H}_m^{\text{sc}})$ denotes the scattered field produced by the induced current on the magnetic plate, Babinet's principle can also be written as

$$\mathbf{E}_a = -\mathbf{E}_m^{\text{sc}}, \quad \mathbf{H}_a = -\mathbf{H}_m^{\text{sc}}. \quad (3.6.16)$$

The electromagnetic version of Babinet's principle formulated above is based on the use of a magnetic conductor in Figure 3.23c. Since there is no magnetic conductor in reality, this principle does not have many direct applications. However, by the duality principle discussed in Section 3.5, a magnetic conductor can be converted into an electrical conductor with the transformation of electromagnetic variables according to Table 3.2. The only inconvenience in this transformation is that when $\epsilon \rightarrow \mu$ and $\mu \rightarrow \epsilon$, the characteristic impedance of free space $\eta = \sqrt{\mu/\epsilon}$ is transformed to $1/\eta = \sqrt{\epsilon/\mu}$, which is no longer the same as that of the original free space. This can be avoided by defining $\bar{\mathbf{H}} = \eta \mathbf{H}$ and $\bar{\mathbf{J}} = \eta \mathbf{J}$ so that ϵ and μ can be eliminated from Maxwell's equations and do not need any transformation. The dual problem so constructed maintains the original free space. The transformation listed in Table 3.2 then becomes

$$\mathbf{E} \rightarrow \eta \mathbf{H}, \quad \mathbf{H} \rightarrow -\frac{\mathbf{E}}{\eta}, \quad \mathbf{J} \rightarrow \frac{\mathbf{M}}{\eta}, \quad \mathbf{M} \rightarrow -\eta \mathbf{J}. \quad (3.6.17)$$

By denoting the field in this dual problem, which is shown in Figure 3.23d, as $(\mathbf{E}_d, \mathbf{H}_d)$ produced by the dual source $\mathbf{J}_d = -\mathbf{M}_i/\eta$ and $\mathbf{M}_d = \eta\mathbf{J}_i$, Equations 3.6.14 and 3.6.16 can be written as

$$\mathbf{E}_a + \eta \mathbf{H}_d = \mathbf{E}^{\text{inc}}, \quad \mathbf{H}_a - \frac{\mathbf{E}_d}{\eta} = \mathbf{H}^{\text{inc}} \quad (3.6.18)$$

and

$$\mathbf{E}_a = -\eta \mathbf{H}_d^{\text{sc}}, \quad \mathbf{H}_a = \frac{\mathbf{E}_d^{\text{sc}}}{\eta} \quad (3.6.19)$$

which are the mathematical representations of Babinet's principle for the problems in Figures 3.23b and 3.23d.

3.6.3 Complementary Antennas

As another direct application of the electromagnetic duality principle, consider two complementary structures shown in Figure 3.24. The metallic plate in Figure 3.24b is cut from an infinitely large conducting sheet and the left-over forms the structure in Figure 3.24a. When fed across cd , the structure in Figure 3.24a becomes an aperture antenna, producing a field $(\mathbf{E}_a, \mathbf{H}_a)$. We can cut a narrow slot in the plate in Figure 3.24b and feed it across ab to turn it into an antenna as well, producing another field $(\mathbf{E}_c, \mathbf{H}_c)$. The input impedance of the aperture antenna is then given by

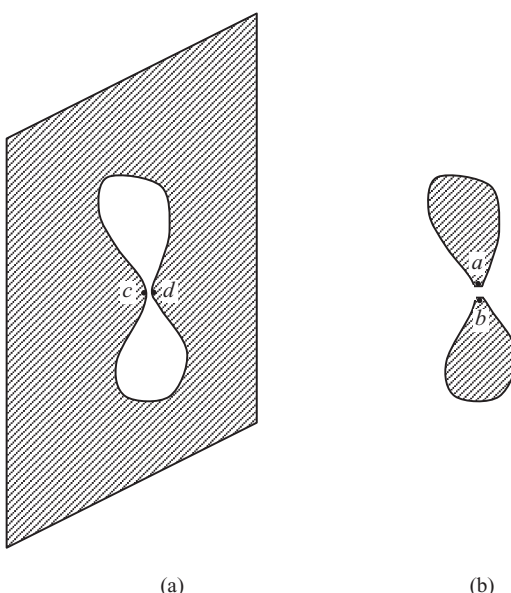


Figure 3.24 Complementary structures.
(a) An aperture antenna. (b) The complementary conducting flat plate antenna.

$$Z_a = \frac{\int_c^d \mathbf{E}_a \cdot d\mathbf{l}}{\oint_C \mathbf{H}_a \cdot d\mathbf{l}} = -\frac{\int_c^d \mathbf{E}_a \cdot d\mathbf{l}}{2 \int_a^b \mathbf{H}_a \cdot d\mathbf{l}} \quad (3.6.20)$$

where C denotes a contour enclosing the line cd and the factor of 2 comes from the fact that \mathbf{H}_a on the two sides have the same magnitude and opposite directions. The input impedance of the metallic antenna can be calculated as

$$Z_c = \frac{\int_a^b \mathbf{E}_c \cdot d\mathbf{l}}{\oint_{C'} \mathbf{H}_c \cdot d\mathbf{l}} = \frac{\int_a^b \mathbf{E}_c \cdot d\mathbf{l}}{2 \int_c^d \mathbf{H}_c \cdot d\mathbf{l}} \quad (3.6.21)$$

where C' denotes the contour enclosing ab and the factor of 2 is due to the fact that \mathbf{H}_c on the two sides have the same magnitude and opposite directions. Note that in Figure 3.24a, we have

$$\hat{n} \times \mathbf{H}_a = 0 \quad \text{on } S_a, \quad \hat{n} \times \mathbf{E}_a = 0 \quad \text{on } S_m \quad (3.6.22)$$

whereas in Figure 3.24b, we have

$$\hat{n} \times \mathbf{E}_c = 0 \quad \text{on } S_a, \quad \hat{n} \times \mathbf{H}_c = 0 \quad \text{on } S_m. \quad (3.6.23)$$

Therefore, the two problems are completely dual to each other, except for the surrounding medium, which is the same. Therefore, the two fields are related to each other by Equation 3.6.17. Substituting the transformation into Equation 3.6.21, we obtain

$$Z_c = \frac{\int_a^b \mathbf{E}_c \cdot d\mathbf{l}}{2 \int_c^d \mathbf{H}_c \cdot d\mathbf{l}} = -\frac{\eta^2 \int_a^b \mathbf{H}_a \cdot d\mathbf{l}}{2 \int_c^d \mathbf{E}_a \cdot d\mathbf{l}} = \frac{\eta^2}{4 Z_a} \quad (3.6.24)$$

or

$$Z_a Z_c = \frac{\eta^2}{4}. \quad (3.6.25)$$

Therefore, the product of the input impedances of two complementary antennas is a fixed constant. If the shapes of the two antennas are identical, their input impedances are the same, which is equal to one-half of the characteristic impedance of the surrounding medium. This fact can be exploited to design broadband antennas [12–14].

REFERENCES

-
- [1] I. V. LINDELL and E. ALANEN, Exact image theory for the Sommerfeld half-space problem, Part III: General formulation, *IEEE Trans. Antennas Propagat.*, 32(10): 1027–1032, 1984.
 - [2] C. T. TAI, *Dyadic Green Functions in Electromagnetic Theory* (2nd edition). Piscataway, NJ: IEEE Press, 1994.
 - [3] J. A. STRATTON, *Electromagnetic Theory*. New York: McGraw-Hill, 1941.
 - [4] J. R. CARSON, Reciprocal theorems in radio communication, *Proc. IRE*, 17: 952–956, 1929.
 - [5] V. H. RUMSEY, Reaction concept in electromagnetic theory, *Phys. Rev.*, 94(6): 1483–1491, 1954.

- [6] S. A. SCHELKUNOFF, Some equivalence theorems of electromagnetics and their application to radiation problems, *Bell System Tech. J.*, 15: 92–112, 1936.
- [7] R. F. HARRINGTON, *Time-Harmonic Electromagnetic Fields*. New York: McGraw-Hill, 1961.
- [8] R. F. HARRINGTON, *Field Computation by Moment Methods*. New York: Macmillan, 1968.
- [9] C. A. BALANIS, *Advanced Engineering Electromagnetics*. New York: Wiley, 1989.
- [10] W. C. CHEW, *Waves and Fields in Inhomogeneous Media*. New York: IEEE Press, 1995.
- [11] M. BORN and E. WOLF, *Principles of Optics: Electromagnetic Theory of Propagation, Interference and Diffraction of Light*. New York: Pergamon Press, 1959.
- [12] V. H. RUMSEY, *Frequency Independent Antennas*. New York: Academic Press, 1966.
- [13] Y. MUSHIAKE, *Self-Complementary Antennas: Principle of Self-Complementarity for Constant Impedance*. London: Springer-Verlag, 1996.
- [14] H. NAKANO, Frequency-independent antennas: Spirals and log-periodics. *Modern Antenna Handbook*, edited by C. A. BALANIS. Hoboken, NJ: Wiley, 2008, pp. 263–323.

PROBLEMS

- 3.1. Consider the problem illustrated in Figure 3.25, where a small circular current loop of radius a carrying a time-harmonic current I is placed in the xy -plane and centered at $(d, 0, d)$ with $d > a$, the xy -plane is covered by an infinite perfect electric conductor, and the yz -plane is covered by an infinite perfect magnetic conductor. Find the electric and magnetic fields in the far-field zone.
- 3.2. An electric current element is placed inside a metallic rectangular waveguide (Fig. 3.26). Find the images of the current element such that its field inside the waveguide can be expressed as the sum of the fields radiated by the current element itself and all the images in free space.
- 3.3. Consider an anisotropic medium characterized by permittivity tensor $\bar{\epsilon}$, permeability tensor $\bar{\mu}$, and conductivity tensor $\bar{\sigma}$. Show that the reciprocity theorem expressed in Equations 3.3.7 and 3.3.8 is still valid if all these tensors are symmetric.

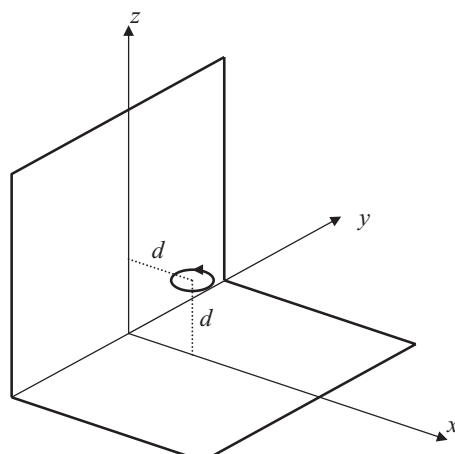


Figure 3.25 A circular current loop placed above a PEC ground plane and next to a vertical PMC ground plane.

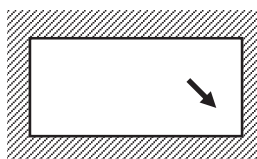


Figure 3.26 An electric current element placed inside a metallic rectangular waveguide.

- 3.4.** Consider two antennas in the presence of a conducting obstacle (Fig. 3.27). When a current source of 3A is applied at antenna B, the voltage received at antenna A is 12V. Find the voltage received at antenna B when a current source of 2A is applied at antenna A.
- 3.5.** Consider a cylindrical dipole antenna consisting of two conducting cylinders of radius a and length $L/2$ (Fig. 3.28). Assume that the gap between the two cylinders is narrow and is fed by a voltage source. Furthermore, assume that the electric field inside the gap is uniform. Show that this problem is equivalent to the problem depicted in the right figure, where a cylinder of length L is excited by a magnetic current loop at the center. Find the magnetic current K in terms of voltage V .
- 3.6.** Consider a two-port network made of all reciprocal components (Fig. 3.29). Show that when the current sources are applied at the ports, $Z_{12} = Z_{21}$. Furthermore, show that when the voltage sources are applied at the ports, $Y_{12} = Y_{21}$. (*Hint:* Use the result in Problem 3.5 to convert a voltage source into a magnetic current source.)
- 3.7.** Consider the problem of scattering by a conducting object. Use Equations 3.4.8 and 3.4.9 to derive the electric-field integral equation

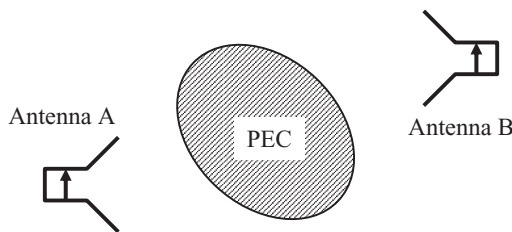


Figure 3.27 Two antennas in the presence of a conducting obstacle.

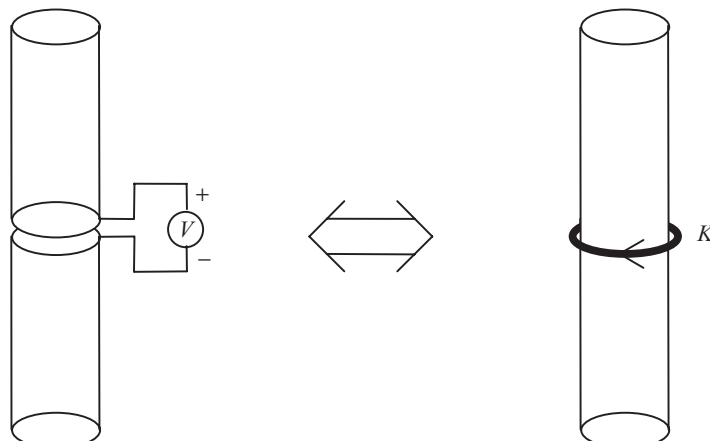


Figure 3.28 A cylindrical dipole antenna and its equivalent model.

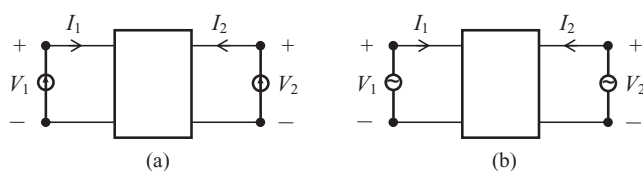


Figure 3.29 (a) Two-port network with current sources. (b) Two-port network with voltage sources.

$$j\omega\mu \oint_S \hat{n} \times \tilde{\mathbf{G}}_{e0}(\mathbf{r}, \mathbf{r}') \cdot \mathbf{J}_s(\mathbf{r}') dS' = \hat{n} \times \mathbf{E}^{\text{inc}}(\mathbf{r}) \quad \mathbf{r} \in S$$

and the magnetic-field integral equation

$$\mathbf{J}_s(\mathbf{r}) - \iint_S \hat{n} \times \tilde{\mathbf{G}}_{m0}(\mathbf{r}, \mathbf{r}') \cdot \mathbf{J}_s(\mathbf{r}') dS' = \hat{n} \times \mathbf{H}^{\text{inc}}(\mathbf{r}) \quad \mathbf{r} \in S$$

which can be solved for \mathbf{J}_s .

- 3.8.** Consider the problem of scattering by a homogeneous object having permittivity ϵ_2 and permeability μ_2 , which is immersed in an unbounded homogeneous medium characterized by ϵ_1 and μ_1 . Starting from Equations 3.4.18, 3.4.19, 3.4.21, and 3.4.22, derive the following two integral equations:

$$\begin{aligned} j\omega \oint_S \hat{n} \times [\mu_2 \tilde{\mathbf{G}}_{e0}(\mathbf{r}, \mathbf{r}'; k_2) + \mu_1 \tilde{\mathbf{G}}_{e0}(\mathbf{r}, \mathbf{r}'; k_1)] \cdot \mathbf{J}_s(\mathbf{r}') dS' \\ + \iint_S \hat{n} \times [\tilde{\mathbf{G}}_{m0}(\mathbf{r}, \mathbf{r}'; k_2) + \tilde{\mathbf{G}}_{m0}(\mathbf{r}, \mathbf{r}'; k_1)] \cdot \mathbf{M}_s(\mathbf{r}') dS' = \hat{n} \times \mathbf{E}^{\text{inc}}(\mathbf{r}) \quad \mathbf{r} \in S \\ j\omega \iint_S \hat{n} \times [\epsilon_2 \tilde{\mathbf{G}}_{e0}(\mathbf{r}, \mathbf{r}'; k_2) + \epsilon_1 \tilde{\mathbf{G}}_{e0}(\mathbf{r}, \mathbf{r}'; k_1)] \cdot \mathbf{M}_s(\mathbf{r}') dS' \\ - \iint_S \hat{n} \times [\tilde{\mathbf{G}}_{m0}(\mathbf{r}, \mathbf{r}'; k_2) + \tilde{\mathbf{G}}_{m0}(\mathbf{r}, \mathbf{r}'; k_1)] \cdot \mathbf{J}_s(\mathbf{r}') dS' = \hat{n} \times \mathbf{H}^{\text{inc}}(\mathbf{r}) \quad \mathbf{r} \in S \end{aligned}$$

which can be used to solve for \mathbf{J}_s and \mathbf{M}_s .

- 3.9.** Consider the problem of wave scattering by a perfect electrically conducting plate of size $A \times B$. Assume that the plate has zero thickness and is placed in the xy -plane. The incident field is given by

$$\mathbf{E}^{\text{inc}} = \hat{y} E_0 e^{jkz}, \quad \mathbf{H}^{\text{inc}} = \hat{x} H_0 e^{jkz}$$

with $E_0 = \eta H_0$. Apply the physical equivalent and physical optics approximation to find the scattered electric and magnetic fields.

- 3.10.** Consider the problem described in Problem 3.9. Apply the induction theorem and use the image theory approximation to find the scattered electric and magnetic fields. Compare the results with those obtained in Problem 3.9.
- 3.11.** Derive the field-source relations for a half-space above a magnetic ground plane by using the image theory and the free-space field-source relations. Verify the results against those obtained by applying the duality principle to Equations 3.2.13 and 3.2.21.
- 3.12.** An infinitely large perfectly conducting sheet in the xy -plane contains an annular slot, whose inner radius is a and outer radius is b , as shown in Figure 3.30. The slot is very narrow. Assume that the electric field across the slot is given by $\mathbf{E} = \hat{p}V/(b-a)$, where V is the voltage across the slot. Find the electric and magnetic fields in the far-field zone both above and below the conducting sheet.
- 3.13.** Consider a narrow slot in an infinitely large electrically conducting plane placed in the xz -plane (Fig. 3.31). The length of the slot is denoted by L and the width is denoted by w with ($w \ll L$). When a voltage is applied across the slot, it produces the following electric field across the slot:

$$\mathbf{E} = V \sin \left[k \left(\frac{L}{2} - |z| \right) \right] \hat{x}.$$

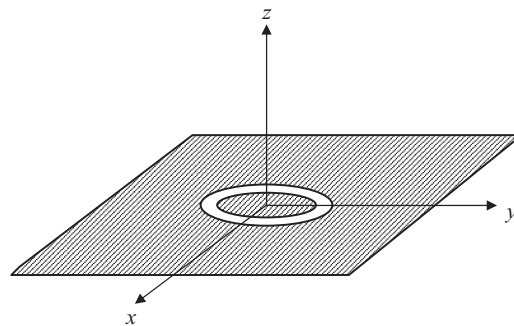


Figure 3.30 An annular slot in an infinitely large perfectly conducting sheet in the xy -plane.

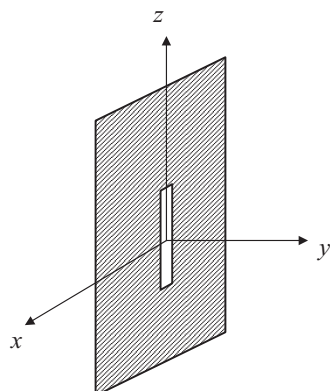


Figure 3.31 A narrow slot in an infinitely large conducting plane placed in the xz -plane.

First, use the equivalence principle to convert this problem into a free-space radiation problem for regions $y > 0$ and $y < 0$, respectively. Then, find the electric and magnetic fields in the far-field zone for regions $y > 0$ and $y < 0$, respectively.

- 3.14.** Given the electric and magnetic fields at the plane $z = h$ ($h > 0$) as

$$\mathbf{E} = \hat{\theta} \eta H_0 \frac{\sin \theta}{r} e^{-jkr}, \quad \mathbf{H} = \hat{\phi} H_0 \frac{\sin \theta}{r} e^{-jkr}$$

where $r = \sqrt{\rho^2 + h^2}$ and $\sin \theta = \rho/r$, construct three equivalent problems for the fields above the plane corresponding to those illustrated in Figures 3.20–3.22. Find the equivalent surface currents in each problem and try to evaluate the fields and compare the three results. ■

TRANSMISSION LINES AND PLANE WAVES

It has been demonstrated in Chapter 2 that an electromagnetic source can generate an electromagnetic field, which can propagate in free space. The objective of this chapter is to consider the simplest form of electromagnetic wave, a uniform plane wave, and examine its propagation in an unbounded homogeneous isotropic medium and in several special anisotropic and bi-isotropic media so that we can better understand the characteristics of wave propagation. We will also study the reflection and transmission when a uniform plane wave is incident on an interface between two different media. Since the characteristics of a uniform plane wave are similar to those of a transmission line, we will first review the basic transmission line theory to introduce some concepts related to wave propagation.

4.1 TRANSMISSION LINE THEORY

In transmission line theory, we study the distribution and propagation of electric voltage and current on a transmission line at frequencies where the line is no longer a small fraction of the wavelength, contrary to the case in low-frequency circuits. To conduct this study, we need first to establish governing differential equations and then examine the characteristics of the solution.

4.1.1 Governing Differential Equations and General Solutions

Consider a transmission line consisting of two parallel conductors whose resistance, conductance, inductance, and capacitance per unit length are denoted by R , G , L , and C , respectively. Assume that the transmission line is parallel to the z -axis. To study the behavior of the electric current and voltage on this transmission line, we take a short segment of the line and represent this short segment by the equivalent circuit shown in Figure 4.1, where Δz denotes the length of the segment.

Based on Kirchhoff's voltage and current laws, we obtain two first-order differential equations that relate the current and voltage with the parameters of the transmission line:

$$\frac{dV}{dz} + (j\omega L + R)I = 0 \quad (4.1.1)$$

$$\frac{dI}{dz} + (j\omega C + G)V = 0. \quad (4.1.2)$$

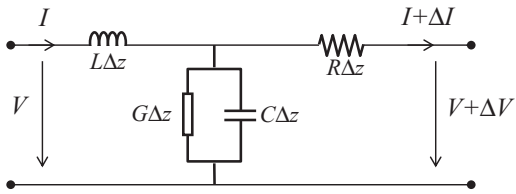


Figure 4.1 Equivalent circuit of a segment of a transmission line.

By eliminating the current I and voltage V from these two equations, respectively, we obtain the second-order differential equations for V and I as

$$\frac{d^2V}{dz^2} - \gamma^2 V = 0 \quad (4.1.3)$$

$$\frac{d^2I}{dz^2} - \gamma^2 I = 0 \quad (4.1.4)$$

where $\gamma^2 = (j\omega L + R)(j\omega C + G)$ and γ is called the *propagation constant* for a reason that will soon be obvious.

Since the current satisfies the same differential equation as does the voltage, it is sufficient to focus our study on the voltage governed by Equation 4.1.3. This equation has two independent solutions whose linear combinations yield its general solution as

$$V(z) = a_+ e^{-\gamma z} + a_- e^{\gamma z}. \quad (4.1.5)$$

To understand the physical meaning of this solution, we first consider a lossless transmission line, for which $R = G = 0$. In this case, $\gamma = j\beta = j\omega\sqrt{LC}$. The instantaneous voltage becomes

$$\begin{aligned} \mathcal{V}(z, t) &= \operatorname{Re}[V(z)e^{j\omega t}] = \operatorname{Re}[a_+ e^{j(\omega t - \beta z)} + a_- e^{j(\omega t + \beta z)}] \\ &= |a_+| \cos(\omega t - \beta z + \angle a_+) + |a_-| \cos(\omega t + \beta z + \angle a_-) \end{aligned} \quad (4.1.6)$$

where $|a_{\pm}|$ and $\angle a_{\pm}$ denote the amplitude and phase of a_{\pm} . By examining the motion of a constant phase point, it can be seen easily that the first term represents a wave propagating along the $+z$ direction, and the second term represents a wave propagating along the $-z$ direction. The speed of propagation is termed the *phase velocity*, which is given by

$$v_p = \frac{\omega}{\beta} = \frac{1}{\sqrt{LC}}. \quad (4.1.7)$$

Since β is related to the phase, it is often called the *phase constant* with a unit of rad/m. Since the wavelength is related to the phase velocity by $\lambda = v_p/f = 2\pi v_p/\omega$, the phase constant can also be expressed as

$$\beta = \frac{2\pi}{\lambda}. \quad (4.1.8)$$

Hence, the phase constant is also referred to as the *wavenumber*.

Once the voltage is found, the current on the transmission line can be obtained from Equation 4.1.1, which gives

$$I(z) = \sqrt{\frac{C}{L}}(a_+ e^{-j\beta z} - a_- e^{j\beta z}) \quad (4.1.9)$$

in the frequency domain, and

$$\mathcal{I}(z, t) = \sqrt{\frac{C}{L}}[|a_+| \cos(\omega t - \beta z + \angle a_+) - |a_-| \cos(\omega t + \beta z + \angle a_-)] \quad (4.1.10)$$

in the time domain. Consider only the wave propagating along the $+z$ direction. The power carried by this wave is

$$\mathcal{P}_+(z, t) = \mathcal{I}_+(z, t) \mathcal{V}_+(z, t) = \sqrt{\frac{C}{L}} |a_+|^2 \cos^2(\omega t - \beta z + \angle a_+). \quad (4.1.11)$$

The electric energy stored on a unit length is given by

$$\omega_{e+}(z, t) = \frac{1}{2} C \mathcal{V}_+^2(z, t) = \frac{1}{2} C |a_+|^2 \cos^2(\omega t - \beta z + \angle a_+) \quad (4.1.12)$$

and the magnetic energy stored on a unit length is given by

$$\omega_{m+}(z, t) = \frac{1}{2} L \mathcal{I}_+^2(z, t) = \frac{1}{2} L |a_+|^2 \cos^2(\omega t - \beta z + \angle a_+). \quad (4.1.13)$$

The speed of energy propagation, termed the *energy velocity*, is thus given by

$$v_e = \frac{\mathcal{P}_+(z, t)}{\omega_{e+}(z, t) + \omega_{m+}(z, t)} = \frac{1}{\sqrt{LC}} \quad (4.1.14)$$

which is the same as the phase velocity. The *characteristic impedance* of the lossless transmission line is defined as

$$Z_0 = \frac{V_+}{I_+} = \sqrt{\frac{L}{C}}. \quad (4.1.15)$$

This impedance depends only on the parameters of a transmission line and is independent of all other factors such as specific sources and terminal loads.

For a general lossy transmission line, the propagation constant is given by

$$\gamma = \pm \sqrt{(j\omega L + R)(j\omega C + G)} = \pm \alpha \pm j\beta \quad (4.1.16)$$

where

$$\alpha = \sqrt{\frac{\omega^2 LC - RG}{2}} \sqrt{1 + \frac{\omega^2 (GL + RC)^2}{(\omega^2 LC - RG)^2}} - 1 \quad (4.1.17)$$

$$\beta = \sqrt{\frac{\omega^2 LC - RG}{2}} \sqrt{1 + \frac{\omega^2 (GL + RC)^2}{(\omega^2 LC - RG)^2}} + 1. \quad (4.1.18)$$

Among the four solutions in Equation 4.1.16, the only physically meaningful solution is $\gamma = \alpha + j\beta$, and with this, the instantaneous voltage is given by

$$\begin{aligned}\mathcal{V}(z, t) &= \operatorname{Re}[V(z)e^{j\omega t}] = \operatorname{Re}[a_+ e^{j(\omega t - \beta z) - \alpha z} + a_- e^{j(\omega t + \beta z) + \alpha z}] \\ &= |a_+| e^{-\alpha z} \cos(\omega t - \beta z + \angle a_+) + |a_-| e^{\alpha z} \cos(\omega t + \beta z + \angle a_-).\end{aligned}\quad (4.1.19)$$

Clearly, the first term represents a wave propagating along the $+z$ direction, whose amplitude is attenuated according to $e^{-\alpha z}$, and the second term represents a wave propagating along the $-z$ direction, which is attenuated at the same rate. Hence, α is called the *attenuation constant* with a unit of Np/m. The corresponding current is given by

$$I(z) = \frac{\gamma}{j\omega L + R} [a_+ e^{-(\alpha+j\beta)z} - a_- e^{(\alpha+j\beta)z}] \quad (4.1.20)$$

and the characteristic impedance is

$$Z_0 = \frac{V_+}{I_+} = \frac{j\omega L + R}{\gamma} = \sqrt{\frac{j\omega L + R}{j\omega C + G}} \quad (4.1.21)$$

which has a complex value.

4.1.2 Reflection and Transmission

Now let us consider an infinitely long transmission line made of two semi-infinite transmission lines of different characteristic impedances that are joined at $z = 0$ (Fig. 4.2). The characteristic impedance is Z_{01} for $z < 0$ and Z_{02} for $z > 0$. Assume that there is a wave propagating along the $+z$ direction from the $z < 0$ side. When this wave hits the joint, a portion of its power will be reflected and the remaining portion will be transmitted and continue to propagate along the $+z$ direction. The total voltage can be written as

$$V(z) = \begin{cases} a_+ e^{-\gamma z} + \Gamma a_+ e^{\gamma z} & z < 0 \\ T a_+ e^{-\gamma z} & z > 0 \end{cases} \quad (4.1.22)$$

where a_+ denotes the amplitude of the incident wave, Γ denotes the reflection coefficient, and T denotes the transmission coefficient. The corresponding current is given by

$$I(z) = \begin{cases} (a_+ e^{-\gamma z} - \Gamma a_+ e^{\gamma z}) / Z_{01} & z < 0 \\ T a_+ e^{-\gamma z} / Z_{02} & z > 0. \end{cases} \quad (4.1.23)$$

Since the voltages and currents on both sides of the joint are the same, we obtain two equations, which can be solved for Γ and T , yielding

$$\Gamma = \frac{Z_{02} - Z_{01}}{Z_{02} + Z_{01}}, \quad T = \frac{2Z_{02}}{Z_{02} + Z_{01}}. \quad (4.1.24)$$

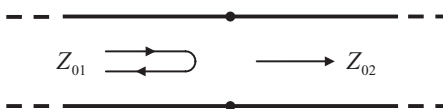


Figure 4.2 Reflection by, and transmission through, a joint between two semi-infinite transmission lines.

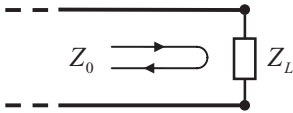


Figure 4.3 Reflection on a transmission line terminated by an impedance load.

Next we consider a uniform transmission line terminated by an impedance load Z_L at $z = z_0$ (Fig. 4.3). In this case, the voltage and current on the transmission line can be written as the superposition of the incident and reflected waves:

$$V(z) = a_+ e^{-\gamma z} + \Gamma a_+ e^{\gamma z} \quad (4.1.25)$$

$$I(z) = \frac{1}{Z_0} (a_+ e^{-\gamma z} - \Gamma a_+ e^{\gamma z}). \quad (4.1.26)$$

At $z = z_0$, the voltage and current are related by $V(z_0)/I(z_0) = Z_L$, from which we find

$$\Gamma = \frac{Z_L - Z_0}{Z_L + Z_0} e^{-2\gamma z_0}. \quad (4.1.27)$$

If we define an impedance at z as $Z(z) = V(z)/I(z)$, by substituting Equations 4.1.25 and 4.1.26 into this definition, we have

$$Z(z) = Z_0 \frac{1 + \Gamma e^{2\gamma z}}{1 - \Gamma e^{2\gamma z}} = Z_0 \frac{1 + \Gamma(z)}{1 - \Gamma(z)} \quad (4.1.28)$$

where $\Gamma(z) = \Gamma e^{2\gamma z}$ is the reflection coefficient observed at z . If we further make use of Equation 4.1.27, we find that

$$Z(z) = Z_0 \frac{Z_L \cosh \gamma l + Z_0 \sinh \gamma l}{Z_0 \cosh \gamma l + Z_L \sinh \gamma l} \quad (4.1.29)$$

where $l = z_0 - z$. For a lossless transmission line, $\gamma = j\beta$, and this is reduced to

$$Z(z) = Z_0 \frac{Z_L \cos \beta l + j Z_0 \sin \beta l}{Z_0 \cos \beta l + j Z_L \sin \beta l}. \quad (4.1.30)$$

Clearly, the value of this impedance depends on the point of observation and the load at the terminal. There are three special cases that deserve to be mentioned explicitly. (1) when $Z_L = Z_0$, $\Gamma = 0$ and $Z(z) = Z_0$; (2) when $Z_L = 0$ (short circuit), $\Gamma(z_0) = -1$ and $Z(z) = j Z_0 \tan \beta l$; and (3) when $Z_L = \infty$ (open circuit), $\Gamma(z_0) = 1$ and $Z(z) = -j Z_0 \cot \beta l$. It is interesting to note that when $\beta l = \pi/2$ or $l = \lambda/4$, a short circuit is transformed into an open circuit and an open circuit is transformed into a short circuit.

Our discussion here concerns only the basic concepts and characteristics of transmission lines, which are similar to those of plane waves. An extensive coverage of transmission line theory can be found in the book by Miner [1], which includes the analysis of a variety of transmission lines for practical applications.

4.1.3 Green's Function and Eigenfunction Expansion

Consider a transmission line with a distributed current source $i(z)$, which has a unit of amperes per unit length (Fig. 4.4). In this case, Equation 4.1.1 remains the same and Equation 4.1.2 becomes

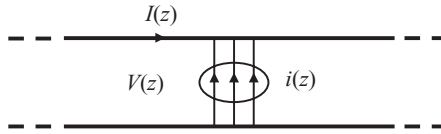


Figure 4.4 Transmission line excited by a distributed current source.

$$\frac{dI}{dz} + (j\omega C + G)V = i(z). \quad (4.1.31)$$

The second-order differential equation for V becomes

$$\frac{d^2V}{dz^2} - \gamma^2 V = -(j\omega L + R)i(z). \quad (4.1.32)$$

Because Equation 4.1.32 is a linear equation, by linear superposition its solution can be written as

$$V(z) = (j\omega L + R) \int_{z_1}^{z_2} g(z, z') i(z') dz' \quad (4.1.33)$$

where it is assumed that the source $i(z)$ is confined within the region $[z_1, z_2]$ and $g(z, z')$ is often referred to as the *Green's function*. By substituting Equation 4.1.33 into Equation 4.1.32 and noting that

$$i(z) = \int_{z_1}^{z_2} \delta(z - z') i(z') dz' \quad (4.1.34)$$

we obtain the second-order differential equation for $g(z, z')$ as

$$\frac{d^2 g(z, z')}{dz^2} - \gamma^2 g(z, z') = -\delta(z - z'). \quad (4.1.35)$$

Since $\delta(z - z') = 0$ for $z < z'$ and $z > z'$, the solution in these two regions in the case of an infinitely long transmission line is given by

$$g_0(z, z') = \begin{cases} Ae^{\gamma z} & z < z' \\ Be^{-\gamma z} & z > z' \end{cases} \quad (4.1.36)$$

where A and B are unknown constants. If the transmission line is finite, we need to add the terms representing reflected waves, whose coefficients can be determined by the impedance load at the terminals. Since $g_0(z, z')$ is related to the voltage, which must be continuous in the absence of a voltage source,

$$g_0(z, z')|_{z=z'+0} = g_0(z, z')|_{z=z'-0}. \quad (4.1.37)$$

Now by integrating Equation 4.1.35 over a small interval around z' , we obtain

$$\left. \frac{dg_0(z, z')}{dz} \right|_{z=z'+0} - \left. \frac{dg_0(z, z')}{dz} \right|_{z=z'-0} = -1. \quad (4.1.38)$$

Applying both Equations 4.1.37 and 4.1.38 to Equation 4.1.36, we can determine both A and B and thus the specific form of $g_0(z, z')$ as

$$g_0(z, z') = \frac{1}{2\gamma} \begin{cases} e^{\gamma(z-z')} & z \leq z' \\ e^{-\gamma(z-z')} & z \geq z' \end{cases} \quad (4.1.39)$$

With this Green's function, the voltage due to any distributed current source can be obtained simply by evaluating the integral in Equation 4.1.33.

The method to derive $g_0(z, z')$ described above is very similar to the approach described in Section 2.2.2. In the following, we introduce another approach, which can be extended systematically to other problems. In this approach, we expand both $g_0(z, z')$ and $\delta(z - z')$ using the Fourier transform as

$$g_0(z, z') = \frac{1}{2\pi} \int_{-\infty}^{\infty} f(h) e^{jhz} dh \quad (4.1.40)$$

$$\delta(z - z') = \frac{1}{2\pi} \int_{-\infty}^{\infty} e^{jh(z-z')} dh. \quad (4.1.41)$$

Substituting these two expressions into Equation 4.1.35, we obtain

$$f(h) = \frac{e^{-jhz'}}{h^2 + \gamma^2} \quad (4.1.42)$$

and when this is substituted into Equation 4.1.40, we have

$$g_0(z, z') = \frac{1}{2\pi} \int_{-\infty}^{\infty} \frac{e^{jh(z-z')}}{h^2 + \gamma^2} dh. \quad (4.1.43)$$

The integral can be evaluated using Cauchy's residue theorem [2]. First, we observe that the integrand has two poles, $h = \pm j\gamma$ (Fig. 4.5), and the contour integral is along the real axis and closed at infinity. To obtain a physically meaningful solution, the contour integral for the case of $z - z' < 0$ has to be closed in the lower half-plane, and for the case of $z - z' > 0$ it has to be closed in the upper half-plane. The result of integration is

$$g_0(z, z') = \frac{1}{2\gamma} \begin{cases} e^{\gamma(z-z')} & z \leq z' \\ e^{-\gamma(z-z')} & z \geq z' \end{cases} \quad (4.1.44)$$

which is identical to Equation 4.1.39.

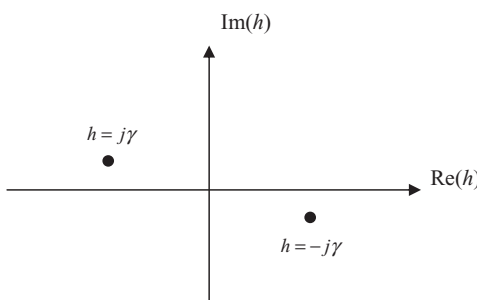


Figure 4.5 Locations of the poles of the integrand $f(h)$.

Compared with the first approach, the second approach to deriving $g_0(z, z')$ is more systematic. Although the second approach is based on the concept of Fourier transform, Equation 4.1.40 can be interpreted as expanding $g_0(z, z')$ in terms of eigenfunctions e^{jh_z} , with h as the eigenvalues. These eigenfunctions are the solution for the homogeneous equation

$$\frac{d^2 f}{dz^2} + h^2 f = 0. \quad (4.1.45)$$

Hence, this approach can be called the method of *eigenfunction expansion* [3], which can be used systematically to derive Green's functions for more complicated problems. To show this, let us rederive the three-dimensional free-space Green's function, which is the solution for Equation 2.2.14. We first expand $G_0(\mathbf{r}, \mathbf{r}')$ and $\delta(\mathbf{r} - \mathbf{r}')$ in terms of Fourier integrals as

$$\begin{aligned} G_0(\mathbf{r}, \mathbf{r}') &= \frac{1}{(2\pi)^3} \int_{-\infty}^{\infty} \int_{-\infty}^{\infty} \int_{-\infty}^{\infty} A(h_x, h_y, h_z) e^{j(h_x x + h_y y + h_z z)} dh_x dh_y dh_z \\ &= \frac{1}{(2\pi)^3} \int_{-\infty}^{\infty} \int_{-\infty}^{\infty} \int_{-\infty}^{\infty} A(\mathbf{h}) e^{j\mathbf{h} \cdot \mathbf{r}} d\mathbf{h} \end{aligned} \quad (4.1.46)$$

$$\begin{aligned} \delta(\mathbf{r} - \mathbf{r}') &= \frac{1}{(2\pi)^3} \int_{-\infty}^{\infty} \int_{-\infty}^{\infty} \int_{-\infty}^{\infty} e^{j[h_x(x-x') + h_y(y-y') + h_z(z-z')]} dh_x dh_y dh_z \\ &= \frac{1}{(2\pi)^3} \int_{-\infty}^{\infty} \int_{-\infty}^{\infty} \int_{-\infty}^{\infty} e^{j\mathbf{h} \cdot (\mathbf{r} - \mathbf{r}')} d\mathbf{h} \end{aligned} \quad (4.1.47)$$

where $A(\mathbf{h})$ is the unknown expansion coefficient to be determined. By substituting these two expressions into Equation 2.2.14, we obtain

$$A(\mathbf{h}) = \frac{e^{-j\mathbf{h} \cdot \mathbf{r}'}}{h^2 - k^2} \quad (4.1.48)$$

where $h^2 = h_x^2 + h_y^2 + h_z^2$. Hence,

$$G_0(\mathbf{r}, \mathbf{r}') = \frac{1}{(2\pi)^3} \int_{-\infty}^{\infty} \int_{-\infty}^{\infty} \int_{-\infty}^{\infty} \frac{e^{j\mathbf{h} \cdot (\mathbf{r} - \mathbf{r}')}}{h^2 - k^2} d\mathbf{h} \quad (4.1.49)$$

which is called the *spectral representation* of the three-dimensional free-space Green's function. To evaluate the spectral integrals, we convert the integrals in rectangular coordinates into those in spherical coordinates by letting

$$h_x = h \sin \theta \cos \phi, \quad h_y = h \sin \theta \sin \phi, \quad h_z = h \cos \theta \quad (4.1.50)$$

so that $d\mathbf{h}$ becomes

$$d\mathbf{h} = h^2 \sin \theta dh d\theta d\phi \quad (4.1.51)$$

Furthermore, because of the spherical symmetry of $G_0(\mathbf{r}, \mathbf{r}')$ with respect to the point \mathbf{r}' , the value of $G_0(\mathbf{r}, \mathbf{r}')$ is independent of the direction of $\mathbf{r} - \mathbf{r}'$. Therefore, we can choose

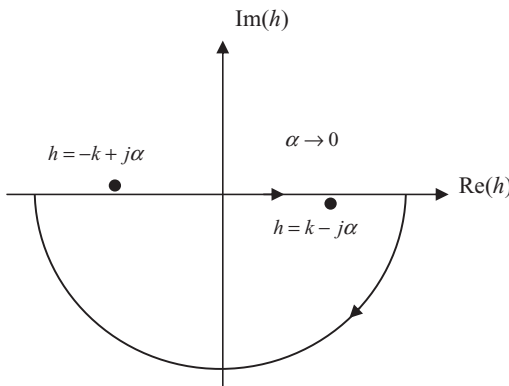


Figure 4.6 Locations of the two poles in the complex plane and the closed contour for integration.

an arbitrary $\mathbf{r} - \mathbf{r}'$ for the evaluation of $G_0(\mathbf{r}, \mathbf{r}')$. If we choose the direction of $\mathbf{r} - \mathbf{r}'$ to coincide with the z -direction, Equation 4.1.49 can be written as

$$\begin{aligned} G_0(\mathbf{r}, \mathbf{r}') &= \frac{1}{(2\pi)^3} \int_0^\infty \int_0^\pi \int_0^{2\pi} \frac{e^{jh \cos \theta |\mathbf{r}-\mathbf{r}'|}}{h^2 - k^2} h^2 \sin \theta dh d\theta d\phi \\ &= \frac{j}{(2\pi)^2 |\mathbf{r} - \mathbf{r}'|} \int_0^\infty [e^{-jh|\mathbf{r}-\mathbf{r}'|} - e^{jh|\mathbf{r}-\mathbf{r}'|}] \frac{h}{h^2 - k^2} dh \\ &= \frac{j}{(2\pi)^2 |\mathbf{r} - \mathbf{r}'|} \int_{-\infty}^\infty \frac{he^{-jh|\mathbf{r}-\mathbf{r}'|}}{h^2 - k^2} dh. \end{aligned} \quad (4.1.52)$$

This integral can now be evaluated using Cauchy's residue theorem. The integrand has two poles: $h = \pm k$. Although the problem considered here is lossless, we can treat it as a limiting case of a lossy problem. Consequently, the pole at $h = k$ is on the lower side of the real axis and the pole at $h = -k$ is on the upper side of the real axis. To have a physically meaningful solution, the contour integral must be closed in the lower half-plane, as shown in Figure 4.6. Applying Cauchy's residue theorem, we obtain

$$G_0(\mathbf{r}, \mathbf{r}') = \frac{e^{-jk|\mathbf{r}-\mathbf{r}'|}}{4\pi |\mathbf{r} - \mathbf{r}'|} \quad (4.1.53)$$

which is the same as Equation 2.2.20, even though the derivation is completely different.

4.2 WAVE EQUATIONS AND GENERAL SOLUTIONS

After the brief review of transmission line theory, we now turn our attention to the propagation of electromagnetic waves. In Chapter 2 we discovered that the electromagnetic fields produced in the far-field zone by any finite time-harmonic sources propagate along the radial direction in the form of e^{-jkr} . To understand the nature of electromagnetic wave propagation, we now consider a special wave, called a uniform plane wave, and examine its basic properties.

4.2.1 Wave Equations and Solution by Separation of Variables

Consider a homogeneous and source-free medium, where time-harmonic electromagnetic fields satisfy source-free Maxwell's equations

$$\nabla \times \mathbf{E} = -j\omega\mu\mathbf{H}, \quad \nabla \times \mathbf{H} = j\omega\epsilon\mathbf{E} + \sigma\mathbf{E} \quad (4.2.1)$$

from which we find that both \mathbf{E} and \mathbf{H} satisfy the same vector *Helmholtz equation*

$$\nabla^2 \mathbf{E} - \gamma^2 \mathbf{E} = 0, \quad \nabla^2 \mathbf{H} - \gamma^2 \mathbf{H} = 0 \quad (4.2.2)$$

where $\gamma^2 = j\omega\mu(j\omega\epsilon + \sigma)$. Each component of \mathbf{E} and \mathbf{H} satisfies the same scalar Helmholtz equation, which for E_x can be written as

$$\nabla^2 E_x - \gamma^2 E_x = 0 \quad (4.2.3)$$

or

$$\frac{\partial^2 E_x}{\partial x^2} + \frac{\partial^2 E_x}{\partial y^2} + \frac{\partial^2 E_x}{\partial z^2} - \gamma^2 E_x = 0. \quad (4.2.4)$$

The solution to this equation can be sought using the method of *separation of variables*. In this method, we first assume that E_x can be represented as the product of three functions:

$$E_x = X(x)Y(y)Z(z). \quad (4.2.5)$$

When this is substituted into Equation 4.2.4, we obtain

$$\frac{1}{X} \frac{\partial^2 X}{\partial x^2} + \frac{1}{Y} \frac{\partial^2 Y}{\partial y^2} + \frac{1}{Z} \frac{\partial^2 Z}{\partial z^2} - \gamma^2 = 0 \quad (4.2.6)$$

after being divided by XYZ . Since the first three terms are independent of each other, they have to be constant, or, in other words, Equation 4.2.6 can be separated into three equations

$$\frac{1}{X} \frac{\partial^2 X}{\partial x^2} = \gamma_x^2, \quad \frac{1}{Y} \frac{\partial^2 Y}{\partial y^2} = \gamma_y^2, \quad \frac{1}{Z} \frac{\partial^2 Z}{\partial z^2} = \gamma_z^2 \quad (4.2.7)$$

where γ_x^2 , γ_y^2 , and γ_z^2 are arbitrary constants that are constrained by $\gamma_x^2 + \gamma_y^2 + \gamma_z^2 = \gamma^2$. The solutions to these three equations are given by

$$X = A_x e^{\pm\gamma_x x}, \quad Y = A_y e^{\pm\gamma_y y}, \quad Z = A_z e^{\pm\gamma_z z} \quad (4.2.8)$$

and hence the solution to E_x is given by

$$E_x = A e^{\pm\gamma_x x \pm \gamma_y y \pm \gamma_z z} \quad (4.2.9)$$

where $A = A_x A_y A_z$ denotes an arbitrary constant. Since E_y and E_z satisfy the same scalar Helmholtz equation as does E_x , their solutions have the same form as Equation 4.2.9. Therefore, the vector field \mathbf{E} has the form

$$\mathbf{E}(x, y, z) = \mathbf{E}_0 e^{\pm \gamma_x x \pm \gamma_y y \pm \gamma_z z} \quad (4.2.10)$$

in which \mathbf{E}_0 denotes an arbitrary constant vector. By denoting $\boldsymbol{\gamma} = \gamma_x \hat{x} + \gamma_y \hat{y} + \gamma_z \hat{z}$ and $\mathbf{r} = x\hat{x} + y\hat{y} + z\hat{z}$, Equation 4.2.10 can be expressed more compactly as

$$\mathbf{E}(\mathbf{r}) = \mathbf{E}_0 e^{\pm \boldsymbol{\gamma} \cdot \mathbf{r}}. \quad (4.2.11)$$

Likewise, the magnetic field \mathbf{H} that satisfies the second vector Helmholtz equation in Equation 4.2.2 can be expressed as

$$\mathbf{H}(\mathbf{r}) = \mathbf{H}_0 e^{\pm \boldsymbol{\gamma} \cdot \mathbf{r}} \quad (4.2.12)$$

where \mathbf{H}_0 denotes another arbitrary constant vector.

Before we proceed further, let us examine the physical meaning of the solution in Equations 4.2.11 and 4.2.12. Since $\boldsymbol{\gamma}$ is a complex number, it can be written as $\boldsymbol{\gamma} = \boldsymbol{\alpha} + j\boldsymbol{\beta}$, where both $\boldsymbol{\alpha}$ and $\boldsymbol{\beta}$ are real vectors. With this, the instantaneous electric field corresponding to Equation 4.2.11 can be written as

$$\mathcal{E}(\mathbf{r}, t) = \operatorname{Re} [\mathbf{E}_0 e^{j\omega t \pm (\boldsymbol{\alpha} + j\boldsymbol{\beta}) \cdot \mathbf{r}}] = \mathbf{E}_0 e^{\pm \boldsymbol{\alpha} \cdot \mathbf{r}} \cos(\omega t \pm \boldsymbol{\beta} \cdot \mathbf{r}) \quad (4.2.13)$$

where for simplicity \mathbf{E}_0 is assumed to be a real vector here. Since $\cos(\omega t \pm \boldsymbol{\beta} \cdot \mathbf{r})$ represents a wave propagating along the $\mp \boldsymbol{\beta}$ direction whose phase is constant in the plane defined by $\boldsymbol{\beta} \cdot \mathbf{r} = \text{constant}$, $e^{\pm \boldsymbol{\gamma} \cdot \mathbf{r}}$ represents a *plane wave*. The amplitude of the wave is also uniform in the plane defined by $\boldsymbol{\alpha} \cdot \mathbf{r} = \text{constant}$. In the case that $\boldsymbol{\alpha}$ and $\boldsymbol{\beta}$ have the same direction, the equiphase and equiamplitude planes are parallel to each other, and the wave is called a *uniform plane wave*. If $\boldsymbol{\alpha}$ and $\boldsymbol{\beta}$ have different directions, the wave is called a *non-uniform plane wave* [4].

Since Equations 4.2.11 and 4.2.12 are valid for any γ_x and γ_y , the general solution to Equation 4.2.2 is the linear superposition of all possible solutions, which can be expressed as

$$\mathbf{E}(\mathbf{r}) = \int_{-\infty}^{\infty} \int_{-\infty}^{\infty} \mathbf{E}_0(\gamma_x, \gamma_y) e^{\pm \boldsymbol{\gamma} \cdot \mathbf{r}} d\gamma_x d\gamma_y \quad (4.2.14)$$

$$\mathbf{H}(\mathbf{r}) = \int_{-\infty}^{\infty} \int_{-\infty}^{\infty} \mathbf{H}_0(\gamma_x, \gamma_y) e^{\pm \boldsymbol{\gamma} \cdot \mathbf{r}} d\gamma_x d\gamma_y. \quad (4.2.15)$$

Note that γ_z is constrained by $\gamma_x^2 + \gamma_y^2 + \gamma_z^2 = \gamma^2$. Equations 4.2.14 and 4.2.15 indicate that any field at a source-free point can be expanded as a linear superposition of an infinite number of plane waves.

4.2.2 Characteristics of a Plane Wave

Let us consider the plane wave represented by Equations 4.2.11 and 4.2.12 further and study its fundamental characteristics. For this, we note that for an exponential function in the form of $e^{\boldsymbol{\gamma} \cdot \mathbf{r}}$, it can be verified easily that

$$\nabla e^{\boldsymbol{\gamma} \cdot \mathbf{r}} = \boldsymbol{\gamma} e^{\boldsymbol{\gamma} \cdot \mathbf{r}}, \quad \nabla \cdot \hat{a} e^{\boldsymbol{\gamma} \cdot \mathbf{r}} = \boldsymbol{\gamma} \cdot \hat{a} e^{\boldsymbol{\gamma} \cdot \mathbf{r}}, \quad \nabla \times \hat{a} e^{\boldsymbol{\gamma} \cdot \mathbf{r}} = \boldsymbol{\gamma} \times \hat{a} e^{\boldsymbol{\gamma} \cdot \mathbf{r}} \quad (4.2.16)$$

where \hat{a} is an arbitrary constant unit vector. By substituting Equations 4.2.11 and 4.2.12 into Maxwell's equations in Equation 4.2.1 and with the aid of Equation 4.2.16, we obtain that for a plane wave,

$$\pm \gamma \times \mathbf{E} = -j\omega\mu\mathbf{H}, \quad \pm \gamma \times \mathbf{H} = (j\omega\epsilon + \sigma)\mathbf{E}. \quad (4.2.17)$$

It is obvious that γ , \mathbf{E} , and \mathbf{H} are perpendicular to each other, that is,

$$\gamma \cdot \mathbf{E} = 0, \quad \gamma \cdot \mathbf{H} = 0, \quad \mathbf{E} \cdot \mathbf{H} = 0 \quad (4.2.18)$$

and the first two are nothing but the results of the two Maxwell's divergence equations. The wave impedance, which is the ratio of the electric field to the magnetic field, is given by

$$Z_w = \frac{|\mathbf{E}|}{|\mathbf{H}|} = \frac{j\omega\mu}{\gamma} = \frac{\gamma}{j\omega\epsilon + \sigma} = \sqrt{\frac{j\omega\mu}{j\omega\epsilon + \sigma}} \quad (4.2.19)$$

which is the same as the *intrinsic impedance* of the medium, often denoted as η . Similar to the characteristic impedance of a transmission line, the intrinsic impedance of a medium depends only on the property of the medium itself. However, the wave impedance depends on a specific electromagnetic wave. For a uniform plane wave, the wave impedance has the same value as the intrinsic impedance; for other types of wave it may not. By taking the cross-product of the first equation in Equation 4.2.17 with γ and then invoking the second equation, we obtain

$$\gamma \times (\gamma \times \mathbf{E}) = -j\omega\mu(j\omega\epsilon + \sigma)\mathbf{E} \quad (4.2.20)$$

which can further be reduced to

$$(\gamma \cdot \gamma)\mathbf{E} = j\omega\mu(j\omega\epsilon + \sigma)\mathbf{E} \quad (4.2.21)$$

since $\gamma \times (\gamma \times \mathbf{E}) = (\gamma \cdot \mathbf{E})\gamma - (\gamma \cdot \gamma)\mathbf{E} = -(\gamma \cdot \gamma)\mathbf{E}$. Because $\mathbf{E} \neq 0$, we have

$$\gamma \cdot \gamma = \gamma_x^2 + \gamma_y^2 + \gamma_z^2 = \gamma^2 = j\omega\mu(j\omega\epsilon + \sigma) \quad (4.2.22)$$

which is consistent with the constraint obtained from the method of separation of variables. This equation is called the *dispersion relation*, which relates the propagation constant to the property of the medium.

The results derived above are pertinent to a lossy medium in which γ is a complex vector. Since a complex vector is difficult to visualize, let us specialize to a lossless medium in which $\gamma = j\beta$ and β is a real vector. As shown earlier, $e^{-j\beta r}$ represents a plane wave propagating in the $\hat{\beta}$ direction. In this case, Equation 4.2.17 becomes

$$\beta \times \mathbf{E} = \omega\mu\mathbf{H}, \quad \beta \times \mathbf{H} = -\omega\epsilon\mathbf{E} \quad (4.2.23)$$

from which we have $\beta \cdot \mathbf{E} = 0$, $\beta \cdot \mathbf{H} = 0$, and $\mathbf{E} \cdot \mathbf{H} = 0$. In addition, it can be found easily that $\omega\mu\mathbf{E} \times \mathbf{H} = E^2\beta$, which indicates that the electric field vector, the magnetic field vector, and the propagation vector form a triad and obey the right-hand rule. Therefore, given any two vectors, we can easily determine the third by using our right hand. The wave impedance now becomes

$$Z_w = \frac{|\mathbf{E}|}{|\mathbf{H}|} = \frac{\omega\mu}{\beta} = \frac{\beta}{\omega\epsilon} = \sqrt{\frac{\mu}{\epsilon}} \quad (4.2.24)$$

and the dispersion relation becomes

$$\beta_x^2 + \beta_y^2 + \beta_z^2 = \beta^2 = \omega^2 \mu \epsilon. \quad (4.2.25)$$

As in transmission line theory, β is called the phase constant or wavenumber.

4.2.3 Wave Velocities and Attenuation

Consider a uniform plane wave with the instantaneous electric field given by Equation 4.2.13. Along the propagation direction $\mathbf{r} = \hat{\beta}r$, $\cos(\omega t - \boldsymbol{\beta} \cdot \mathbf{r})$ becomes $\cos(\omega t - \beta r)$; hence, the phase velocity of the wave is given by

$$v_p = \frac{\omega}{\beta}. \quad (4.2.26)$$

In a lossless medium, $\beta = \omega \sqrt{\mu \epsilon}$; therefore, $v_p = 1/\sqrt{\mu \epsilon}$. In vacuum, $\epsilon = \epsilon_0$ and $\mu = \mu_0$, and thus the phase velocity is given by

$$v_p = \frac{1}{\sqrt{\mu_0 \epsilon_0}} \approx 2.997925 \times 10^8 \text{ m/s} \quad (4.2.27)$$

which is the same as the speed of light.

The phase velocity measures the motion of a constant phase plane. Since electromagnetic waves carry energy, the motion of the energy is described by the energy velocity, which is defined as

$$v_e = \frac{\text{power flow density}}{\text{energy density}} = \frac{\mathcal{S}}{\omega_e + \omega_m}. \quad (4.2.28)$$

For a uniform plane wave in a lossless medium, the instantaneous magnetic field is given by

$$\mathcal{H}(\mathbf{r}, t) = \operatorname{Re}[\mathbf{H}_0 e^{j\omega t - \beta \cdot \mathbf{r}}] = \mathbf{H}_0 \cos(\omega t - \boldsymbol{\beta} \cdot \mathbf{r}) = \frac{\hat{\beta} \times \mathbf{E}_0}{\eta} \cos(\omega t - \boldsymbol{\beta} \cdot \mathbf{r}). \quad (4.2.29)$$

Thus, the instantaneous power flow density is

$$\mathcal{S} = \mathcal{E} \times \mathcal{H} = \hat{\beta} \frac{|\mathbf{E}_0|^2}{\eta} \cos^2(\omega t - \boldsymbol{\beta} \cdot \mathbf{r}) \quad (4.2.30)$$

which flows in the propagation direction $\hat{\beta}$. The instantaneous electric and magnetic energy densities are given by

$$\omega_e = \frac{1}{2} \epsilon \mathcal{E}^2 = \frac{1}{2} \epsilon |\mathbf{E}_0|^2 \cos^2(\omega t - \boldsymbol{\beta} \cdot \mathbf{r}) \quad (4.2.31)$$

$$\omega_m = \frac{1}{2} \mu \mathcal{H}^2 = \frac{1}{2} \mu |\mathbf{H}_0|^2 \cos^2(\omega t - \boldsymbol{\beta} \cdot \mathbf{r}) \quad (4.2.32)$$

which are equal to each other. When these are substituted into Equation 4.2.28, we obtain the energy velocity in a lossless medium as

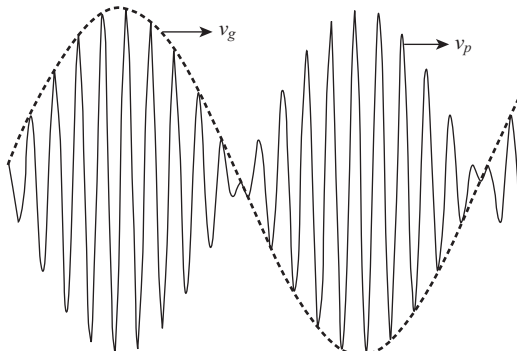


Figure 4.7 Group velocity v_g and phase velocity v_p .

$$v_e = \frac{1}{\eta\epsilon} = \frac{1}{\sqrt{\mu\epsilon}} \quad (4.2.33)$$

which is the same as the phase velocity v_p . Note that this is true only for a uniform plane wave and may not hold for other types of wave.

When we deal with propagation of electromagnetic waves used for communication, we often use *group velocity* to characterize the propagation of signals. To understand the concept of group velocity, we consider two waves propagating at two slightly different frequencies, whose combined electric field is given by

$$\begin{aligned} \mathcal{E}(\mathbf{r}, t) &= \mathbf{E}_0 \cos[(\omega + \Delta\omega)t - (\beta + \Delta\beta) \cdot \mathbf{r}] + \mathbf{E}_0 \cos[(\omega - \Delta\omega)t - (\beta - \Delta\beta) \cdot \mathbf{r}] \\ &= 2\mathbf{E}_0 \cos(\Delta\omega t - \Delta\beta \cdot \mathbf{r}) \cos(\omega t - \beta \cdot \mathbf{r}). \end{aligned} \quad (4.2.34)$$

The waveform along the propagation direction is plotted in Figure 4.7 for one instant of time. It is a product of two sinusoids: $\cos(\Delta\omega t - \Delta\beta \cdot \mathbf{r})$ and $\cos(\omega t - \beta \cdot \mathbf{r})$. The second sinusoid propagates at the phase velocity given by Equation 4.2.26. The first sinusoid, which appears as the envelope of the wave and is often called a wave packet, moves at a different velocity, which is defined as the *group velocity*. Along the propagation direction β , this velocity is given by

$$v_g = \frac{\Delta\omega}{\Delta\beta} \quad \text{for } \Delta\omega \rightarrow 0. \quad (4.2.35)$$

Usually, β can be expressed as the function of ω ; hence, the group velocity can be written as

$$v_g = \frac{\Delta\omega}{\Delta\beta} = \left(\frac{\Delta\beta}{\Delta\omega} \right)^{-1} = \left(\frac{d\beta}{d\omega} \right)^{-1}. \quad (4.2.36)$$

In a lossless dispersion-free medium, $\beta = \omega\sqrt{\mu\epsilon}$ and both ϵ and μ are independent of frequency. The group velocity is then given by

$$v_g = \frac{1}{\sqrt{\mu\epsilon}} \quad (4.2.37)$$

which is the same as the phase velocity and also the energy velocity. However, if β changes with frequency, the phase velocity changes accordingly, and hence,

$$\frac{d\beta}{d\omega} = \frac{d}{d\omega} \left(\frac{\omega}{v_p} \right) = \frac{1}{v_p} - \frac{\omega}{v_p^2} \frac{dv_p}{d\omega}. \quad (4.2.38)$$

The group velocity is then given by

$$v_g = \frac{v_p}{1 - \frac{\omega}{v_p} \frac{dv_p}{d\omega}} \quad (4.2.39)$$

which shows clearly the relationship between the group and phase velocities. In a medium with no dispersion, $dv_p/d\omega = 0$, then $v_g = v_p$. In a medium with normal dispersion, $dv_p/d\omega < 0$, then $v_g < v_p$. On the other hand, in a medium with anomalous dispersion, $dv_p/d\omega > 0$, then $v_g > v_p$. Therefore, we can control the group velocity by utilizing a dispersive medium, making it possible to design slow- and fast-wave devices. In many situations with normal dispersion, the group velocity is the same as the energy velocity [5].

In a medium with conduction loss (for simplicity, we ignore dielectric and magnetic losses here), the propagation constant is given by $\gamma = \alpha + j\beta = \sqrt{j\omega\mu(j\omega\epsilon + \sigma)}$, where

$$\alpha = \omega \sqrt{\frac{\mu\epsilon}{2}} \sqrt{1 + \left(\frac{\sigma}{\omega\epsilon}\right)^2} - 1, \quad \beta = \omega \sqrt{\frac{\mu\epsilon}{2}} \sqrt{1 + \left(\frac{\sigma}{\omega\epsilon}\right)^2} + 1. \quad (4.2.40)$$

For a good dielectric, $(\sigma/\omega\epsilon)^2 \ll 1$; hence, Equation 4.2.40 and the intrinsic impedance can be approximated as

$$\alpha \approx \frac{\sigma}{2} \sqrt{\frac{\mu}{\epsilon}}, \quad \beta \approx \omega \sqrt{\mu\epsilon}, \quad \eta \approx \sqrt{\frac{\mu}{\epsilon}} \quad (4.2.41)$$

whereas for a good conductor, $(\sigma/\omega\epsilon)^2 \gg 1$; thus, Equation 4.2.40 and the intrinsic impedance can be approximated as

$$\alpha \approx \sqrt{\frac{\omega\mu\sigma}{2}}, \quad \beta \approx \sqrt{\frac{\omega\mu\sigma}{2}}, \quad \eta \approx (1+j)\sqrt{\frac{\omega\mu}{2\sigma}}. \quad (4.2.42)$$

These approximations are useful for engineering applications.

4.2.4 Linear, Circular, and Elliptical Polarizations

A distinct feature of electromagnetic waves is *polarization*. Simply put, polarization is related to the direction of the electric field and its variation in time. To facilitate our discussion, we assume, without loss of generality, that the propagation is along the z -direction. Hence, the electric field of a uniform plane wave can be written as

$$\mathbf{E} = \mathbf{E}_0 e^{-j\beta z} = (\hat{x}E_{0x} + \hat{y}E_{0y})e^{-j\beta z} \quad (4.2.43)$$

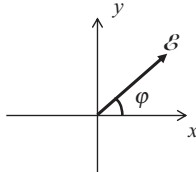


Figure 4.8 Direction of electric field.

where E_{0x} and E_{0y} are complex magnitudes in general. This field cannot have a z -component because otherwise it would violate the divergence condition $\nabla \cdot \mathbf{E} = 0$. The instantaneous field becomes

$$\begin{aligned}\mathcal{E}(t) &= \operatorname{Re} \left[(\hat{x}E_{0x} + \hat{y}E_{0y})e^{j(\omega t - \beta z)} \right] \\ &= \hat{x}|E_{0x}| \cos(\omega t - \beta z + \angle E_{0x}) + \hat{y}|E_{0y}| \cos(\omega t - \beta z + \angle E_{0y}).\end{aligned}\quad (4.2.44)$$

The direction of the electric field vector can be described by the angle between this vector and the $+x$ axis (Fig. 4.8), which is given by

$$\varphi(t) = \tan^{-1} \frac{|E_{0y}| \cos(\omega t - \beta z + \angle E_{0y})}{|E_{0x}| \cos(\omega t - \beta z + \angle E_{0x})}. \quad (4.2.45)$$

It is clear that when $\angle E_{0x} = \angle E_{0y}$, $\varphi = C$ or $\pi + C$, where C is a constant. Therefore, the electric field vector at a point is always directed along a line. Such a field is called *linearly polarized*, or said to have *linear polarization*. The corresponding magnetic field is

$$\mathcal{H}(t) = \hat{y} \frac{|E_{0x}|}{\eta} \cos(\omega t - \beta z + \angle E_{0x}) - \hat{x} \frac{|E_{0y}|}{\eta} \cos(\omega t - \beta z + \angle E_{0y}) \quad (4.2.46)$$

and the instantaneous power flow density is

$$\begin{aligned}\mathcal{S}(t) &= \mathcal{E}(t) \times \mathcal{H}(t) = \hat{z} \frac{|E_{0x}|^2 + |E_{0y}|^2}{\eta} \cos^2(\omega t - \beta z + \angle E_{0x}) \\ &= \hat{z} \frac{|E_0|^2}{\eta} \cos^2(\omega t - \beta z + \angle E_{0x}).\end{aligned}\quad (4.2.47)$$

Obviously, the power flow density changes with time and position, and its average over a period is given by $|E_0|^2 / 2\eta$.

When $\angle E_{0x} \neq \angle E_{0y}$, it can be seen from Equation 4.2.45 that φ would change with time. In particular, if $\angle E_{0x} - \angle E_{0y} = \pi/2$, then

$$\mathcal{E}(t) = \hat{x}|E_{0x}| \cos(\omega t - \beta z + \angle E_{0x}) + \hat{y}|E_{0y}| \sin(\omega t - \beta z + \angle E_{0x}) \quad (4.2.48)$$

and

$$\varphi(t) = \tan^{-1} \frac{|E_{0y}| \sin(\omega t - \beta z + \angle E_{0x})}{|E_{0x}| \cos(\omega t - \beta z + \angle E_{0x})}. \quad (4.2.49)$$

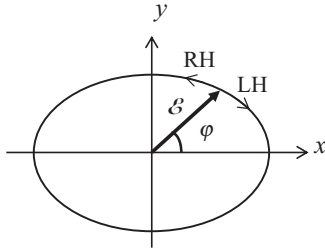


Figure 4.9 Right- and left-hand elliptical polarizations.

First, we find from Equation 4.2.48 that

$$\left(\frac{\mathcal{E}_x}{|E_{0x}|}\right)^2 + \left(\frac{\mathcal{E}_y}{|E_{0y}|}\right)^2 = 1 \quad (4.2.50)$$

which is an equation that describes an ellipse in the xy -plane. Therefore, the tip of the electric field vector draws an ellipse and thus the field is called *elliptically polarized*. Second, we find from Equation 4.2.49 that if we fix z and increase t , φ increases and the electric field rotates clockwise if we look along the propagation direction, which is along the z -axis (Fig. 4.9). Hence, the polarization is called *clockwise elliptical polarization* or *right-hand elliptical polarization*. The second name comes from the observation that if we point the thumb of our right hand in the propagation direction, our four fingers point in the direction of rotation of the electric field vector. In the special case that $|E_{0x}| = |E_{0y}|$, the ellipse becomes a circle, and the field is called *clockwise circularly polarized* or *right-hand circularly polarized* (RHCP). By following the same approach, we can show that when $\angle E_{0x} - \angle E_{0y} = -\pi/2$ and $|E_{0x}| \neq |E_{0y}|$, the electric field is *counterclockwise elliptically polarized* or *left-hand elliptically polarized*. If $|E_{0x}| = |E_{0y}|$, the field then is *counterclockwise circularly polarized* or *left-hand circularly polarized* (LHCP). For a circularly polarized wave, the corresponding magnetic field is

$$\mathcal{H}(t) = \hat{y} \frac{|E_{0x}|}{\eta} \cos(\omega t - \beta z + \angle E_{0x}) \pm \hat{x} \frac{|E_{0x}|}{\eta} \sin(\omega t - \beta z + \angle E_{0x}) \quad (4.2.51)$$

and the instantaneous power flow density can be found as

$$\mathcal{S}(t) = \mathcal{E}(t) \times \mathcal{H}(t) = \hat{z} \frac{|E_{0x}|^2}{\eta} \quad (4.2.52)$$

which is a constant. Therefore, for a circularly polarized wave having the same maximum amplitude as that of a linearly polarized wave, its power flow density is twice the time-average power flow density of the linearly polarized wave.

In a general case where E_{0x} and E_{0y} are two complex numbers with a difference in their phases denoted by $\angle E_{0x} - \angle E_{0y} = \vartheta$ ($-\pi < \vartheta \leq \pi$), Equation 4.2.44 becomes

$$\mathcal{E}(t) = \hat{x} |E_{0x}| \cos(\omega t - \beta z + \angle E_{0x}) + \hat{y} |E_{0y}| \cos(\omega t - \beta z + \angle E_{0x} - \vartheta). \quad (4.2.53)$$

It can be shown that in this case

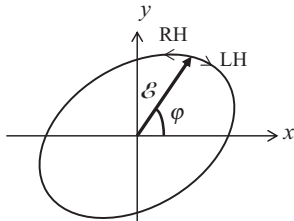


Figure 4.10 General right- and left-hand elliptical polarizations.

$$\left(\frac{\mathcal{E}_x}{|E_{0x}|}\right)^2 - \frac{2\mathcal{E}_x\mathcal{E}_y \cos \vartheta}{|E_{0x}||E_{0y}|} + \left(\frac{\mathcal{E}_y}{|E_{0y}|}\right)^2 = \sin^2 \vartheta \quad (4.2.54)$$

which describes a general ellipse (Fig. 4.10) whose rotation is determined by the value of ϑ . If $\vartheta < 0$, it is a left-hand elliptical polarization, and if $\vartheta > 0$ it is a right-hand elliptical polarization. When $\vartheta = 0$, the field becomes linearly polarized.

From the field expressions, it can be recognized immediately that an elliptically or circularly polarized wave can be considered a superposition of two linearly polarized waves. It is less obvious to recognize that a linearly polarized wave can also be decomposed into two elliptically or circularly polarized waves rotating in opposite directions. Consider the following linearly polarized wave as an example:

$$\mathbf{E} = \mathbf{E}_0 e^{-j\beta z} = \hat{x} |A| e^{-j\beta z}. \quad (4.2.55)$$

This expression is equivalent to

$$\mathbf{E} = \left(\hat{x} \frac{|A|}{2} + j\hat{y} \frac{|B|}{2} \right) e^{-j\beta z} + \left(\hat{x} \frac{|A|}{2} - j\hat{y} \frac{|B|}{2} \right) e^{-j\beta z}. \quad (4.2.56)$$

The first term on the right-hand side is recognized as a left-hand elliptically polarized wave, and the second term represents a right-hand elliptically polarized wave. If we set $|B|=|A|$, these two waves are circularly polarized.

4.2.5 Wave Propagation in Metamaterials

Metamaterials are artificially made materials that exhibit certain unusual properties, such as negative permittivity and permeability, which cannot be found in natural materials [6]. By judiciously placing short wires and small rings in a normal medium, one can elicit macroscopically negative permittivity and permeability within a narrow frequency band [7–9]. Because of the frequency dispersion, such a medium contains both dielectric and magnetic losses, as dictated by Equation 1.7.58. However, let us ignore these losses and examine how a plane wave propagates in this type of medium.

First, we consider a medium with a negative permittivity $\epsilon = -\epsilon'$ and a positive permeability $\mu = \mu'$, where both ϵ' and μ' have positive values. In such a medium, the dispersion relation (Eq. 4.2.22) becomes $\gamma^2 = \omega^2 \mu' \epsilon'$ so that $\gamma = \alpha = \omega \sqrt{\mu' \epsilon'}$. Therefore, a plane wave is attenuated and cannot propagate in this medium even though no losses are assumed. The same phenomenon is observed for a medium with a positive permittivity $\epsilon = \epsilon'$ and a negative permeability $\mu = -\mu'$. Frequency selective surfaces and photonic crystals can be considered examples of this kind of medium, where their periodic structures

produce a negative effective permittivity or permeability within a certain frequency band that blocks propagation of electromagnetic waves. Such a band is often referred to as a *stopband* or *bandgap*.

Next, we consider a medium with both a negative permittivity $\epsilon = -\epsilon'$ and a negative permeability $\mu = -\mu'$. For a uniform plane wave represented by $e^{-j\beta r}$, Maxwell's curl equations become

$$\beta \times \mathbf{E} = -\omega \mu' \mathbf{H}, \quad \beta \times \mathbf{H} = \omega \epsilon' \mathbf{E} \quad (4.2.57)$$

from which we have $\beta \cdot \mathbf{E} = 0$, $\beta \cdot \mathbf{H} = 0$, and $\mathbf{E} \cdot \mathbf{H} = 0$, which are the same as the characteristics observed for a plane wave in a regular medium. In addition, we also find that $\beta = \omega \sqrt{\mu' \epsilon'}$, which indicates that the wave can propagate without attenuation. However, from either of the two equations in Equation 4.2.57, we further find that

$$\mathbf{E} \times \mathbf{H} = -\sqrt{\frac{\epsilon'}{\mu'}} E^2 \hat{\beta}. \quad (4.2.58)$$

Since $\mathbf{E} \times \mathbf{H}$ points in the direction of power flow and $\hat{\beta}$ represents the direction of the phase velocity, Equation 4.2.58 reveals that the power flows in the opposite direction of the phase velocity. Since the electric field vector, the magnetic field vector, and the propagation vector are now related by the left-hand rule, such a medium is often referred to as a *left-handed medium*, whose unique property can be exploited for designing novel microwave and optical devices [10,11]. It is important to remember that when we choose a physically meaningful solution to a wave equation in a left-handed medium, the choice now should be based on the direction of power flow, instead of the phase velocity. For example, the propagation constant γ in a left-handed medium should be chosen as $\gamma = \alpha - j\beta$ rather than $\gamma = \alpha + j\beta$. Consequently, the scalar Green's function in an unbounded homogeneous left-handed medium should be

$$G_0(\mathbf{r}, \mathbf{r}') = \frac{e^{jk|\mathbf{r}-\mathbf{r}'|}}{4\pi |\mathbf{r}-\mathbf{r}'|} \quad (4.2.59)$$

to ensure that the power propagates away from the source, where $k = \omega \sqrt{\mu' \epsilon'}$.

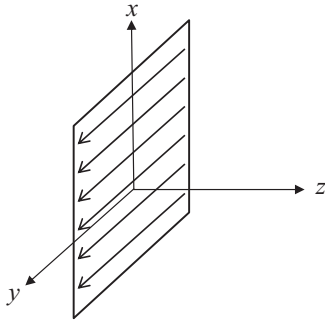
4.3 PLANE WAVES GENERATED BY A CURRENT SHEET

In this section, we consider the problem of solving for the fields generated by an infinitely large electric current sheet placed in the xy -plane and immersed in an unbounded homogeneous medium having permittivity ϵ and permeability μ . The surface current density is given by

$$\mathbf{J}_s = \hat{y} J_0 e^{-jbx} \quad (4.3.1)$$

where J_0 is a constant. The problem is illustrated in Figure 4.11. For special problems like this that involve a uniform surface current, the solution can be found by expanding the fields in a proper form and then applying boundary conditions across the surface current to determine the unknown expansion coefficients.

Since the source is confined in the xy -plane, the field in the region other than the xy -plane satisfies the source-free vector Helmholtz equations in Equation 4.2.2, whose

**Figure 4.11** Infinitely large current sheet in the xy -plane.

general solutions are given by Equations 4.2.14 and 4.2.15. Since the field is related to the surface current by $\hat{z} \times [\mathbf{H}(z=0+) - \mathbf{H}(z=0-)] = \mathbf{J}_s$, we immediately recognize that the field can be expressed as

$$\mathbf{H} = \begin{cases} \mathbf{A} e^{-jhx + j\beta_z z} & z < 0 \\ \mathbf{B} e^{-jhx - j\beta_z z} & z > 0 \end{cases} \quad (4.3.2)$$

where \mathbf{A} and \mathbf{B} are the unknown vectors to be determined and $\beta_z = \sqrt{\omega^2 \mu \epsilon - h^2}$. In addition, we obtain

$$B_x - A_x = J_0, \quad B_y - A_y = 0. \quad (4.3.3)$$

In writing Equation 4.3.2, we considered the fact that the field produced by the current sheet should propagate away from the sheet. Since in the source-free region $\nabla \cdot \mathbf{H} = 0$, we further obtain

$$hB_x + \beta_z B_z = 0, \quad hA_x - \beta_z A_z = 0. \quad (4.3.4)$$

From $\nabla \times \mathbf{H} = j\omega \epsilon \mathbf{E}$, we find the electric field as

$$\mathbf{E} = -\frac{1}{\omega \epsilon} \begin{cases} (\hat{x}h - \hat{z}\beta_z) \times \mathbf{A} e^{-jhx + j\beta_z z} & z < 0 \\ (\hat{x}h + \hat{z}\beta_z) \times \mathbf{B} e^{-jhx - j\beta_z z} & z > 0 \end{cases} \quad (4.3.5)$$

and since the tangential component of the electric field is continuous across the xy -plane, that is, $\hat{z} \times \mathbf{E}(z=0+) = \hat{z} \times \mathbf{E}(z=0-)$, we obtain two more equations:

$$hB_z - \beta_z B_x = hA_z + \beta_z A_x, \quad B_y = -A_y. \quad (4.3.6)$$

Solving Equations 4.3.3, 4.3.4, and 4.3.6 simultaneously, we obtain

$$B_x = -A_x = \frac{J_0}{2}, \quad B_y = A_y = 0, \quad B_z = A_z = -\frac{h}{\beta_z} \frac{J_0}{2}. \quad (4.3.7)$$

Hence, the electric and magnetic fields generated by the current sheet are obtained as

$$\mathbf{E} = -\hat{y} \frac{\omega \mu J_0}{2\beta_z} \begin{cases} e^{-jhx + j\beta_z z} & z < 0 \\ e^{-jhx - j\beta_z z} & z > 0 \end{cases} \quad (4.3.8)$$

$$\mathbf{H} = \frac{J_0}{2\beta_z} \begin{cases} (-\hat{x}\beta_z - \hat{z}h)e^{-jhx+j\beta_z z} & z < 0 \\ (\hat{x}\beta_z - \hat{z}h)e^{-jhx-j\beta_z z} & z > 0 \end{cases} \quad (4.3.9)$$

which represent a plane wave propagating in the direction of $\beta = \hat{x}h - \hat{z}\beta_z$ in the region $z < 0$ and a plane wave propagating in the direction of $\beta = \hat{x}h + \hat{z}\beta_z$ in the region $z > 0$. The propagation direction is completely controlled by h , as in the case of a finite surface current discussed in Section 2.4.1.

From the solution procedure described above, we can see that for certain special problems, we can find the solution by

1. formulating the expression of either the electric or the magnetic field with an unknown coefficient based on the general solution in the source-free region,
2. finding the other field using Maxwell's equations, and
3. applying the boundary conditions to determine the unknown coefficient.

This simple approach turns out to be very useful since it can be applied to many simplified electromagnetic problems, as will be illustrated through many examples in the next three chapters.

4.4 REFLECTION AND TRANSMISSION

In this section, we will follow the approach outlined in Section 4.3 to deal with the problem of reflection and transmission when a uniform plane wave is incident on an infinitely large planar interface between two homogeneous half-spaces filled with different media. Without any loss of generality, we assume that the interface coincides with the xy -plane; the medium in the half-space $z < 0$ is characterized by permittivity ϵ_1 and permeability μ_1 ; and the medium in the half-space $z > 0$ is characterized by permittivity ϵ_2 and permeability μ_2 . We will first consider the case of normal incidence and then deal with the case of oblique incidence.

4.4.1 Reflection and Transmission at Normal Incidence

Consider a uniform plane wave propagating along the z -direction and incident on the interface from the $z < 0$ side (Fig. 4.12). The electric field of this incident wave can be written as

$$\mathbf{E}^i = \hat{x}E_0 e^{-j\beta_1 z} \quad (4.4.1)$$

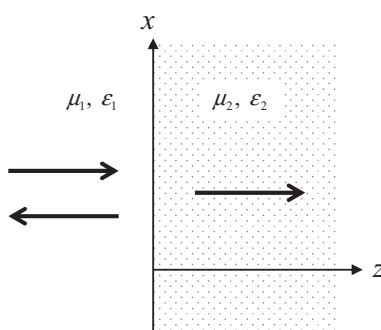


Figure 4.12 Plane wave incident normally on an interface.

where $\beta_1 = \omega\sqrt{\mu_1\epsilon_1}$ and E_0 denotes the amplitude of the field. Because of the discontinuous interface, the incident wave will be partially reflected back into the region $z < 0$ and partially transmitted into the region $z > 0$. The electric fields of the reflected and transmitted waves can be written as

$$\mathbf{E}^r = \hat{x}RE_0 e^{j\beta_1 z} \quad (4.4.2)$$

and

$$\mathbf{E}^t = \hat{x}TE_0 e^{-j\beta_2 z} \quad (4.4.3)$$

respectively, where $\beta_2 = \omega\sqrt{\mu_2\epsilon_2}$, and R and T denote the unknown reflection and transmission coefficients to be determined. From Maxwell's equation $\nabla \times \mathbf{E} = -j\omega\mu\mathbf{H}$, the corresponding magnetic fields are found as

$$\mathbf{H}^i = \hat{y} \frac{E_0}{\eta_1} e^{-j\beta_1 z}, \quad \mathbf{H}^r = -\hat{y} \frac{RE_0}{\eta_1} e^{j\beta_1 z}, \quad \mathbf{H}^t = \hat{y} \frac{TE_0}{\eta_2} e^{-j\beta_2 z} \quad (4.4.4)$$

where $\eta_1 = \sqrt{\mu_1/\epsilon_1}$ and $\eta_2 = \sqrt{\mu_2/\epsilon_2}$. Since there is neither electric nor magnetic surface current at the interface, the tangential components of the electric and magnetic fields have to be continuous; hence, $\hat{z} \times \mathbf{E}(z=0+) = \hat{z} \times \mathbf{E}(z=0-)$ and $\hat{z} \times \mathbf{H}(z=0+) = \hat{z} \times \mathbf{H}(z=0-)$. Application of these two boundary conditions yields

$$1 + R = T, \quad \frac{1}{\eta_1}(1 - R) = \frac{1}{\eta_2}T \quad (4.4.5)$$

from which we find that

$$R = \frac{\eta_2 - \eta_1}{\eta_2 + \eta_1}, \quad T = \frac{2\eta_2}{\eta_2 + \eta_1}. \quad (4.4.6)$$

Clearly, if $\eta_2 = \eta_1$, which means that the intrinsic impedances are the same on both sides of the interface, then $R = 0$ and $T = 1$, indicating that there is no reflection and all of the incident wave is transmitted through the interface. On the other hand, if medium 2 is a perfect conductor, then $\eta_2 = 0$; consequently, $R = -1$ and $T = 0$, indicating that the entire incident wave is reflected back by the interface. In this case, the electric and magnetic fields in the region $z < 0$ become

$$\mathbf{E} = \mathbf{E}^i + \mathbf{E}^r = \hat{x}E_0(e^{-j\beta_1 z} - e^{j\beta_1 z}) = -\hat{x}2jE_0 \sin \beta_1 z \quad (4.4.7)$$

$$\mathbf{H} = \mathbf{H}^i + \mathbf{H}^r = \hat{y} \frac{E_0}{\eta_1}(e^{-j\beta_1 z} + e^{j\beta_1 z}) = \hat{y} \frac{2E_0}{\eta_1} \cos \beta_1 z. \quad (4.4.8)$$

The complex Poynting vector is

$$\mathbf{S} = \frac{1}{2} \mathbf{E} \times \mathbf{H}^* = \hat{z} \frac{2|E_0|^2}{j\eta_1} \sin \beta_1 z \cos \beta_1 z = \hat{z} \frac{|E_0|^2}{j\eta_1} \sin(2\beta_1 z) \quad (4.4.9)$$

whose real part is zero, which indicates that there is no average power flow associated with the total field. Such a wave is called a purely *standing wave*.

For a general case that $\eta_2 \neq \eta_1$ and $\eta_2 \neq 0$, the electric field in the region $z < 0$ is given by

$$\mathbf{E} = \mathbf{E}^i + \mathbf{E}^r = \hat{x}E_0(e^{-j\beta_1 z} + Re^{j\beta_1 z}) \quad (4.4.10)$$

and the magnitude of the field is given by

$$|E| = |E_0| \sqrt{1 + |R|^2 + 2|R|\cos(2\beta_1 z + \angle R)}. \quad (4.4.11)$$

This field represents a partially standing wave with a *standing wave ratio* (SWR) given by

$$\text{SWR} = \frac{|E|_{\max}}{|E|_{\min}} = \frac{1+|R|}{1-|R|}. \quad (4.4.12)$$

If we rewrite Equation 4.4.10 as

$$\mathbf{E} = \hat{x}RE_0(e^{-j\beta_1 z} + e^{j\beta_1 z}) + \hat{x}(1-R)E_0e^{-j\beta_1 z} \quad (4.4.13)$$

it is then clear that this field is a superposition of a purely standing wave and a traveling wave. The time-average power flow density is contributed only by the traveling wave, which is

$$\text{Re}(\mathbf{S}) = \hat{z} \frac{|E_0|^2}{2\eta_1} (1 - |R|^2). \quad (4.4.14)$$

The same result can be obtained by subtracting the power flow density of the reflected wave from that of the incident wave.

4.4.2 Reflection and Transmission at Oblique Incidence

The same basic solution approach for the normal incidence case can be employed to deal with the case when the incident wave impinges on the interface at an angle from its normal direction, although the solution process is more complicated. For such an oblique incidence, we have to consider two different situations. To describe them, we first define the *plane of incidence* as the plane formed by a vector normal to the interface (such as \hat{z}) and a vector along the propagation direction of the incident wave. If the interface coincides with the xy -plane and the propagation direction is parallel to the xz -plane, the plane of incidence is then the xz -plane. As described in Section 4.2.4, any uniform plane wave can be decomposed into two orthogonal linearly polarized waves. Hence, we need to consider two linearly polarized incident waves so that their combination can yield the solution to any kind of incident plane wave. One linearly polarized wave has its electric field perpendicular to the plane of incidence—we refer to this case as *perpendicular polarization*—and the other linearly polarized wave has its electric field parallel to the plane of incidence, which is referred to as *parallel polarization*.

We consider the perpendicular polarization case first, which is illustrated in Figure 4.13. When a plane wave is incident on an infinitely large planar interface, since the field at every point on the interface is reflected and transmitted in exactly the same manner, the reflected and transmitted waves are also plane waves, although their amplitudes and

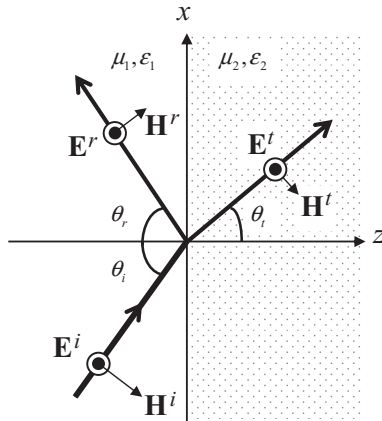


Figure 4.13 Perpendicular polarized plane wave incident obliquely on an interface.

propagation directions are different from those of the incident wave and are unknown at this moment. Based on the expression for a plane wave, we can write down the expressions of the incident, reflected, and transmitted electric fields as

$$\mathbf{E}^i = \hat{y}E_0 e^{-j\beta^i \cdot \mathbf{r}} = \hat{y}E_0 e^{-j\beta_1(x \sin \theta_i + z \cos \theta_i)} \quad (4.4.15)$$

$$\mathbf{E}^r = \hat{y}R_{\perp}E_0 e^{-j\beta^r \cdot \mathbf{r}} = \hat{y}R_{\perp}E_0 e^{-j\beta_1(x \sin \theta_r - z \cos \theta_r)} \quad (4.4.16)$$

$$\mathbf{E}' = \hat{y}T_{\perp}E_0 e^{-j\beta'^r \cdot \mathbf{r}} = \hat{y}T_{\perp}E_0 e^{-j\beta_2(x \sin \theta_t + z \cos \theta_t)} \quad (4.4.17)$$

where E_0 and θ_i denote the amplitude and the angle of the incident field, which are known; R_{\perp} and T_{\perp} denote the unknown reflection and transmission coefficients; and θ_r and θ_t denote the unknown angles of the reflected and transmitted waves measured from the normal of the interface. The goal of analysis is to determine R_{\perp} , T_{\perp} , θ_r , and θ_t . For this, we first use $\nabla \times \mathbf{E} = -j\omega\mu\mathbf{H}$ to find the corresponding magnetic fields as

$$\mathbf{H}^i = (-\hat{x} \cos \theta_i + \hat{z} \sin \theta_i) \frac{E_0}{\eta_1} e^{-j\beta_1(x \sin \theta_i + z \cos \theta_i)} \quad (4.4.18)$$

$$\mathbf{H}^r = (\hat{x} \cos \theta_r + \hat{z} \sin \theta_r) \frac{R_{\perp}E_0}{\eta_1} e^{-j\beta_1(x \sin \theta_r - z \cos \theta_r)} \quad (4.4.19)$$

$$\mathbf{H}' = (-\hat{x} \cos \theta_t + \hat{z} \sin \theta_t) \frac{T_{\perp}E_0}{\eta_2} e^{-j\beta_2(x \sin \theta_t + z \cos \theta_t)}. \quad (4.4.20)$$

Next, we apply the boundary conditions that require the continuity of the tangential field components, $\hat{z} \times \mathbf{E}(z=0+) = \hat{z} \times \mathbf{E}(z=0-)$ and $\hat{z} \times \mathbf{H}(z=0+) = \hat{z} \times \mathbf{H}(z=0-)$, which yield

$$e^{-j\beta_1 \sin \theta_i x} + R_{\perp} e^{-j\beta_1 \sin \theta_r x} = T_{\perp} e^{-j\beta_2 \sin \theta_t x} \quad (4.4.21)$$

$$\cos \theta_i \frac{1}{\eta_1} e^{-j\beta_1 \sin \theta_i x} - \cos \theta_r \frac{R_{\perp}}{\eta_1} e^{-j\beta_1 \sin \theta_r x} = \cos \theta_t \frac{T_{\perp}}{\eta_2} e^{-j\beta_2 \sin \theta_t x}. \quad (4.4.22)$$

These two equations have to be satisfied for any values of x ($-\infty < x < \infty$). It can be shown mathematically that this is only possible when the associated phases match in each term. Consequently,

$$\beta_1 \sin \theta_i = \beta_1 \sin \theta_r = \beta_2 \sin \theta_t \quad (4.4.23)$$

which is known as *phase matching*. Since $\beta_1 = \omega\sqrt{\mu_1\epsilon_1}$ and $\beta_2 = \omega\sqrt{\mu_2\epsilon_2}$, we obtain

$$\theta_r = \theta_i, \quad \frac{\sin \theta_t}{\sin \theta_i} = \sqrt{\frac{\mu_1 \epsilon_1}{\mu_2 \epsilon_2}} \quad (4.4.24)$$

which are called *Snell's laws* of reflection and refraction. Because of Equation 4.4.23, Equations 4.4.21 and 4.4.22 are reduced to

$$1 + R_{\perp} = T_{\perp}, \quad \cos \theta_i \frac{1}{\eta_1} - \cos \theta_r \frac{R_{\perp}}{\eta_1} = \cos \theta_t \frac{T_{\perp}}{\eta_2} \quad (4.4.25)$$

whose solution yields the reflection and transmission coefficients

$$R_{\perp} = \frac{\eta_2 \cos \theta_i - \eta_1 \cos \theta_t}{\eta_2 \cos \theta_i + \eta_1 \cos \theta_t}, \quad T_{\perp} = \frac{2\eta_2 \cos \theta_i}{\eta_2 \cos \theta_i + \eta_1 \cos \theta_t}. \quad (4.4.26)$$

If we define the wave impedance looking into the z -direction as $Z_z = -E_y/H_x$, then the wave impedances for perpendicular polarized waves in the two regions are

$$Z_{z1} = \frac{\eta_1}{\cos \theta_i}, \quad Z_{z2} = \frac{\eta_2}{\cos \theta_t}. \quad (4.4.27)$$

As a result, Equation 4.4.26 can be written as

$$R_{\perp} = \frac{Z_{z2} - Z_{z1}}{Z_{z2} + Z_{z1}}, \quad T_{\perp} = \frac{2Z_{z2}}{Z_{z2} + Z_{z1}} \quad (4.4.28)$$

which has the same form as the solution in a transmission line expressed in Equation 4.1.24.

For the parallel polarization case illustrated in Figure 4.14, the incident, reflected, and transmitted electric fields can be written as

$$\mathbf{E}^i = (\hat{x} \cos \theta_i - \hat{z} \sin \theta_i) E_0 e^{-j\beta_1(x \sin \theta_i + z \cos \theta_i)} \quad (4.4.29)$$

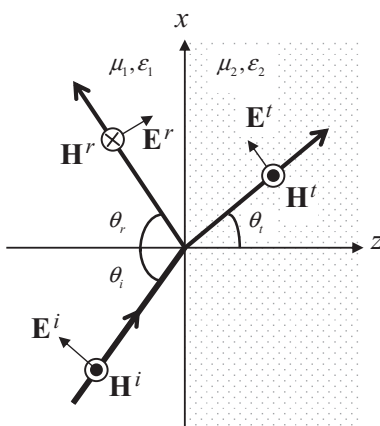


Figure 4.14 Parallel polarized plane wave incident obliquely on an interface.

$$\mathbf{E}^r = (\hat{x} \cos \theta_r + \hat{z} \sin \theta_r) R_{\parallel} E_0 e^{-j\beta_1(x \sin \theta_r - z \cos \theta_r)} \quad (4.4.30)$$

$$\mathbf{E}^t = (\hat{x} \cos \theta_t - \hat{z} \sin \theta_t) T_{\parallel} E_0 e^{-j\beta_2(x \sin \theta_t + z \cos \theta_t)}. \quad (4.4.31)$$

By following the same procedure as for the perpendicular polarization case, we obtain the same Snell's laws of reflection and refraction as expressed in Equation 4.4.24 because of phase matching, and the reflection and transmission coefficients as

$$R_{\parallel} = \frac{\eta_2 \cos \theta_t - \eta_1 \cos \theta_i}{\eta_2 \cos \theta_t + \eta_1 \cos \theta_i}, \quad T_{\parallel} = \frac{2\eta_2 \cos \theta_i}{\eta_2 \cos \theta_t + \eta_1 \cos \theta_i}. \quad (4.4.32)$$

Again, if we define the wave impedance looking into the z -direction as $Z_z = E_x/H_y$, then the wave impedances for parallel polarized waves in the two regions are given by

$$Z_{z1} = \eta_1 \cos \theta_i, \quad Z_{z2} = \eta_2 \cos \theta_t, \quad (4.4.33)$$

and Equation 4.4.32 can be written in the forms similar to Equation 4.4.28. (Note that the transmission coefficient in the form similar to the second equation in Equation 4.4.28 is defined for E_x , which can be related to T_{\parallel} using Equations 4.4.29 and 4.4.31.) Therefore, the results in transmission line theory can be used to obtain solutions for plane wave problems as long as we define wave impedances correctly.

Before we discuss the results derived in this section further, we note that when the right half-space is occupied by a perfect electric conductor such that $\eta_2 = 0$, we find that for both polarizations, the total tangential component of the magnetic field on the surface of the conductor (the xy -plane) is

$$\hat{n} \times \mathbf{H} = \hat{n} \times (\mathbf{H}^i + \mathbf{H}^r) = 2\hat{n} \times \mathbf{H}^i. \quad (4.4.34)$$

This result is valid for any plane wave since any plane wave can be decomposed into a perpendicular and a parallel polarized wave. Therefore, for a large and smooth conducting surface, the induced surface current for any incident wave is $\mathbf{J}_s \approx 2\hat{n} \times \mathbf{H}^i$, which is called *physical optics approximation*, as discussed in Section 3.4.2.

4.4.3 Total Transmission and Total Reflection

Now let us examine the results in Equations 4.4.26 and 4.4.32 more carefully. First, we find that the reflection could vanish in both perpendicular and parallel polarization cases. The corresponding incident angle is called the *Brewster angle* and is denoted as θ_B . In this case, the total incident wave is transmitted across the interface into the right half-space. Hence, the phenomenon is called *zero reflection* or *total transmission*. For perpendicular polarization, this occurs when

$$\eta_2 \cos \theta_B = \eta_1 \cos \theta_i. \quad (4.4.35)$$

This equation can be solved together with Snell's law of refraction to yield

$$\sin \theta_B = \sqrt{\frac{\epsilon_2/\epsilon_1 - \mu_2/\mu_1}{\mu_1/\mu_2 - \mu_2/\mu_1}}. \quad (4.4.36)$$

Obviously, this phenomenon can happen only when $\mu_1 \neq \mu_2$ and cannot occur at an interface between two different non-magnetic media. For parallel polarization, reflection vanishes when

$$\eta_2 \cos \theta_t = \eta_1 \cos \theta_B \quad (4.4.37)$$

which can be solved together with Snell's law of refraction to yield

$$\sin \theta_B = \sqrt{\frac{\epsilon_2/\epsilon_1 - \mu_2/\mu_1}{\epsilon_2/\epsilon_1 - \epsilon_1/\epsilon_2}}. \quad (4.4.38)$$

If the media on both sides of an interface are non-magnetic or have the same permeability, this is reduced to

$$\sin \theta_B = \sqrt{\frac{\epsilon_2}{\epsilon_1 + \epsilon_2}} \quad \text{or} \quad \tan \theta_B = \sqrt{\frac{\epsilon_2}{\epsilon_1}}. \quad (4.4.39)$$

Provided that $\epsilon_1 \neq \epsilon_2$, there is always a real solution for θ_B in this case. Hence, total transmission can usually occur for parallel polarization. Figure 4.15 plots the reflection and transmission coefficients for an interface between two non-magnetic dielectric media with $\epsilon_1 = \epsilon_0$ and $\epsilon_2 = 2.5\epsilon_0$, which shows clearly that zero reflection occurs for parallel polarization at $\theta_B = 57.7^\circ$.

Next, we explore another very interesting phenomenon related to reflection. We first rewrite Snell's law of refraction as

$$\sin \theta_i = \sqrt{\frac{\mu_1 \epsilon_1}{\mu_2 \epsilon_2}} \sin \theta_t. \quad (4.4.40)$$

Clearly, when $\sin \theta_i = \sqrt{\mu_2 \epsilon_2 / \mu_1 \epsilon_1}$, $\sin \theta_t = 1$ or $\theta_t = \pi/2$. Consequently, $R_\perp = 1$ and $R_\parallel = -1$, which indicate that the entire incident wave is reflected. This phenomenon is called *total reflection*. The corresponding incident angle is called the *critical angle*, which is given by

$$\theta_c = \sin^{-1} \sqrt{\frac{\mu_2 \epsilon_2}{\mu_1 \epsilon_1}}. \quad (4.4.41)$$

Evidently, this critical angle exists only when $\mu_1 \epsilon_1 > \mu_2 \epsilon_2$. When $\theta_i = \theta_c$, the transmitted field becomes

$$\mathbf{E}' = \hat{y} 2E_0 e^{-j\beta_2 x}, \quad \mathbf{E}' = -\hat{z} 2E_0 e^{-j\beta_2 x} \quad (4.4.42)$$

for perpendicular and parallel polarizations, respectively. Both represent a uniform plane wave propagating in the x -direction. The time-average power flow densities for the incident, reflected, and transmitted waves are found as

$$\mathbf{S}^i \Big|_{\theta_i=\theta_c} = \hat{\beta}^i \frac{|E_0|^2}{2\eta_1}, \quad \mathbf{S}^r \Big|_{\theta_i=\theta_c} = \hat{\beta}^r \frac{|E_0|^2}{2\eta_1}, \quad \mathbf{S}' \Big|_{\theta_i=\theta_c} = \hat{x} \frac{2|E_0|^2}{\eta_2}. \quad (4.4.43)$$

Although this result looks odd at a glance, it does not violate the power conservation law, because for any closed surface, the total power entering into the surface is always equal

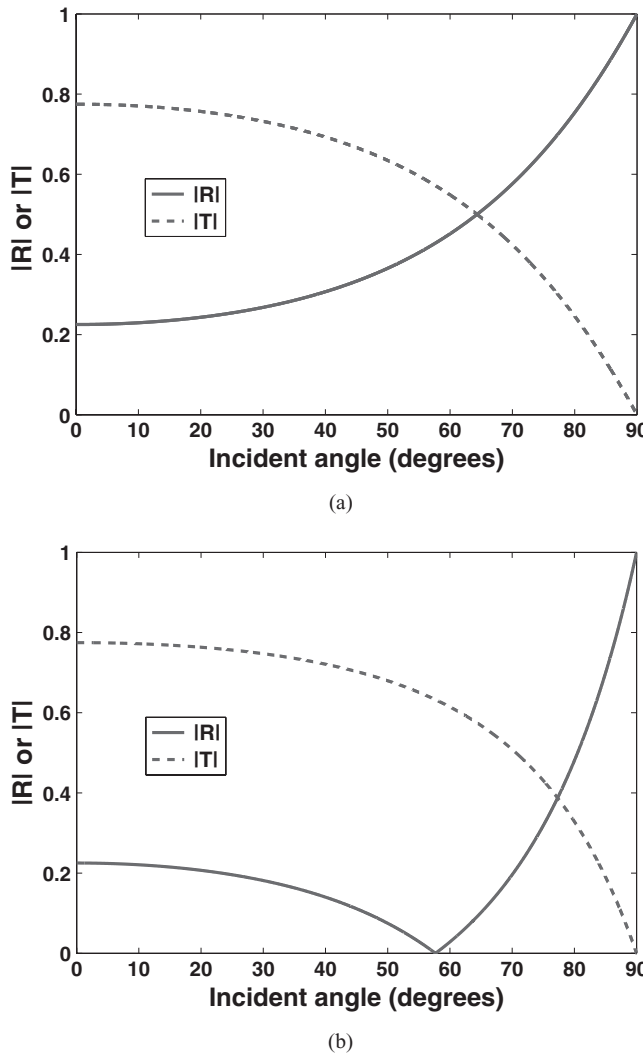


Figure 4.15 Reflection and transmission coefficients for an interface between two dielectric media with $\epsilon_1 = \epsilon_0$ and $\epsilon_2 = 2.5\epsilon_0$, respectively. (a) Perpendicular polarization. (b) Parallel polarization.

to the total power leaving the surface. The reader might find it interesting to ponder this question: If the total incident power is reflected back to the left half-space, where does the transmitted power in the right half-space come from?

When the incident angle exceeds the critical angle ($\theta_i > \theta_c$), both R_{\perp} and R_{\parallel} become complex; however, $|R_{\perp}| = 1$ and $|R_{\parallel}| = 1$, which still results in total reflection. In this case, $\sin \theta_i > 1$ and $\cos \theta_i = \sqrt{1 - \sin^2 \theta_i} = \pm j\sqrt{\sin^2 \theta_i - 1}$. To make the results physically meaningful, the minus sign should be chosen for $\cos \theta_i$. The transmitted field becomes

$$\mathbf{E}^t = \hat{\mathbf{y}} T_{\perp} E_0 e^{-\alpha_e z} e^{-j\beta_2 x \sin \theta_i} \quad (4.4.44)$$

for perpendicular polarization and

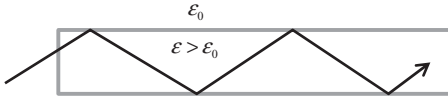


Figure 4.16 Propagation of optical wave in an optical waveguide.

$$\mathbf{E}^t = (\hat{x} \cos \theta_t - \hat{z} \sin \theta_t) T_{\parallel 0} E_0 e^{-\alpha_e z} e^{-j\beta_2 x \sin \theta_t} \quad (4.4.45)$$

for parallel polarization, where $\alpha_e = \beta_2 \sqrt{\sin^2 \theta_t - 1}$. These two expressions still represent waves propagating along the x -direction. However, the amplitude of the wave is attenuated along the z -direction with an attenuation constant α_e . This is a non-uniform plane wave since its equiamplitude planes are not parallel to its equiphasic planes. The phase velocity along the x -direction is

$$v_p = \frac{\omega}{\beta_2 \sin \theta_t} \quad (4.4.46)$$

which is smaller than the phase velocity of a uniform plane wave in the same medium, resulting in a so-called *slow wave*. The time-average power flow is still in the x -direction, but there is instantaneous power flow along the $\pm z$ directions, whose time average vanishes.

The phenomenon of total reflection has many applications in electromagnetics and optics. The most prominent one is the design of optical waveguides or optical fibers, where an optical wave is coupled into an optical fiber and propagates along the fiber under the condition that the wave bounces inside the fiber at an angle greater than the critical angle, as illustrated in Figure 4.16.

4.4.4 Transmission into a Left-Handed Medium

Now let us consider an interesting problem in which a uniform plane wave is incident on a left-handed medium. This problem is identical to the one treated in Sections 4.4.1 and 4.4.2, except that the permittivity and permeability of the right half-space are now both negative, $\epsilon_2 = -\epsilon'_2$ and $\mu_2 = -\mu'_2$ with $\epsilon'_2 > 0$ and $\mu'_2 > 0$. As we are now familiar with the approach to solving this kind of problem, we consider only the perpendicular polarization case, as illustrated in Figure 4.17. In this case, the incident and reflected fields are the same as those given in Equations 4.4.15 and 4.4.16 for the electric fields, and Equations 4.4.18 and 4.4.19 for the magnetic fields. The only difference is in the expressions for the transmitted field. Since in a left-handed medium the power propagates in the opposite direction of the phase velocity, the phase of the transmitted field must propagate toward the interface to ensure that its power propagates away from the interface. Hence, the transmitted electric field should be expressed as

$$\mathbf{E}^t = \hat{y} T_{\perp} E_0 e^{-j\beta' r} = \hat{y} T_{\perp} E_0 e^{-j\beta'_2 (x \sin \theta_t - z \cos \theta_t)} \quad (4.4.47)$$

where $\beta'_2 = \omega \sqrt{\mu'_2 \epsilon'_2}$. The corresponding magnetic field is given by

$$\mathbf{H}^t = -(\hat{x} \cos \theta_t + \hat{z} \sin \theta_t) \frac{T_{\perp} E_0}{\eta'_2} e^{-j\beta'_2 (x \sin \theta_t - z \cos \theta_t)} \quad (4.4.48)$$

where $\eta'_2 = \sqrt{\mu'_2/\epsilon'_2}$. The phase matching yields the value of θ_t as

$$\sin\theta_t = \sqrt{\frac{\mu_1\epsilon_1}{\mu'_2\epsilon'_2}} \sin\theta_i \quad (4.4.49)$$

which has the same expression as the one in Equation 4.4.24. However, the definition of θ_t is now different from the previous one. Application of the boundary conditions yields the same reflection and transmission coefficients as those in Equation 4.4.26, except that $\eta_2 = \eta'_2$. In fact, all the results, including those for the parallel polarization case, can be obtained readily from those derived in Sections 4.4.1 and 4.4.2 by letting $\beta_2 = -\beta'_2$ and $\eta_2 = \eta'_2$. The Poynting vector for the transmitted wave is

$$\mathbf{S}' = \frac{1}{2} \mathbf{E}' \times \mathbf{H}'^* = (-\hat{x} \sin\theta_t + \hat{z} \cos\theta_t) \frac{|T_\perp E_0|^2}{2\eta'_2} \quad (4.4.50)$$

which indicates that indeed the power flows away from the interface. The phenomenon illustrated in Figure 4.17 can be used theoretically to design a perfect lens [7], as illustrated in Figure 4.18. This illustration is, however, simplified because in reality a source produces not only traveling waves but also evanescent waves, whose reflection and transmission should also be considered in the analysis. Moreover, the inevitable loss in a left-handed medium will also have an impact on the image of the original object.

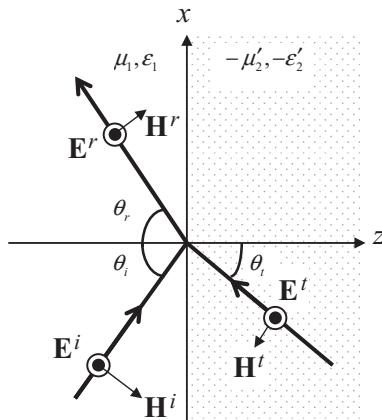


Figure 4.17 Plane wave transmitted into a left-handed medium.

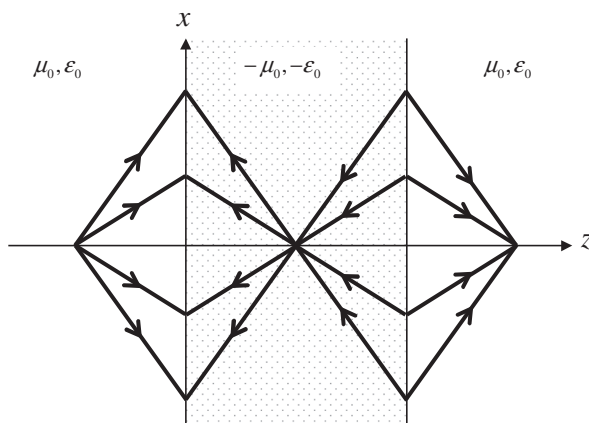


Figure 4.18 Field produced by a point source refocused by a left-handed medium slab.

4.4.5 Plane Waves versus Transmission Lines

In Sections 4.4.1 and 4.4.2, we observed that the reflection and transmission coefficients of a plane wave perpendicularly incident on a discontinuous interface have the same form as the results for a transmission line with a discontinuous jump in its characteristic impedance. Even for oblique incidence, the results can be cast into the same form with a properly defined wave impedance. The similarity in the results is not accidental. It is due to the similarity in their governing differential equations. For a plane wave propagating in the xz -plane, the electric field satisfies the differential equation

$$\frac{d^2 E}{dz^2} + \beta_z^2 E = 0 \quad (4.4.51)$$

and so does the magnetic field, where $\beta_z = \sqrt{\omega^2 \mu \epsilon - \beta_x^2} = \sqrt{\omega^2 \mu \epsilon - \beta^2 \sin^2 \theta_i}$. This is the same differential equation as Equation 4.1.3 if we let its γ be $\gamma = j\beta_z$. Hence, all the results obtained for transmission lines can be employed directly for plane waves propagating in media with discontinuous interfaces perpendicular to the z -axis as long as we use β_z to replace the β in the transmission line and use the wave impedance defined in Equations 4.4.27 and 4.4.33, depending on the polarization of the wave, to replace the characteristic impedance in the transmission line. This analogy can be very useful in dealing with the problem of reflection by a multilayered medium because the impedance transformation formula given in Equation 4.1.30 can be used to find an equivalent wave impedance at the first interface, from which the reflection coefficient can be obtained immediately.

4.5 PLANE WAVES IN ANISOTROPIC AND BI-ISOTROPIC MEDIA

In this section, we study the propagation of plane waves in some special anisotropic and bi-isotropic media [12–14] using the same approach as that used for the plane wave propagation in free space. The purpose is to reinforce our mastery of the analysis approach and deepen our understanding of the effect of the material property of the medium on wave propagation. The problem of wave propagation in a general anisotropic or bianisotropic medium is very complicated; here, we consider three special media to simplify the analysis.

4.5.1 Plane Waves in Uniaxial Media

Consider a plane wave, whose electric field can be expressed as $\mathbf{E} = \mathbf{E}_0 e^{-j\beta r}$, propagating in a uniaxial medium, whose permittivity is given by

$$\tilde{\epsilon} = \begin{bmatrix} \epsilon & 0 & 0 \\ 0 & \epsilon & 0 \\ 0 & 0 & \epsilon_z \end{bmatrix}. \quad (4.5.1)$$

For such a plane wave, the first two source-free Maxwell's equations become

$$\nabla \times \mathbf{E} = -j\omega \mu \mathbf{H} \rightarrow \boldsymbol{\beta} \times \mathbf{E} = \omega \mu \mathbf{H} \quad (4.5.2)$$

$$\nabla \times \mathbf{H} = j\omega \tilde{\epsilon} \cdot \mathbf{E} \rightarrow \boldsymbol{\beta} \times \mathbf{H} = -\omega \tilde{\epsilon} \cdot \mathbf{E} \quad (4.5.3)$$

from which we obtain

$$\beta \times (\beta \times \mathbf{E}) = -\omega^2 \mu \epsilon \cdot \mathbf{E}. \quad (4.5.4)$$

To simplify the analysis, we first assume that the wave propagates in the x -direction such that $\beta = \hat{x}\beta_x$. Under this assumption, Equation 4.5.4 becomes

$$\begin{bmatrix} -\omega^2 \mu \epsilon & 0 & 0 \\ 0 & \beta_x^2 - \omega^2 \mu \epsilon & 0 \\ 0 & 0 & \beta_x^2 - \omega^2 \mu \epsilon_z \end{bmatrix} \begin{bmatrix} E_x \\ E_y \\ E_z \end{bmatrix} = 0. \quad (4.5.5)$$

It is immediately observed that $E_x = 0$ and Equation 4.5.5 can be reduced to

$$\begin{bmatrix} \beta_x^2 - \omega^2 \mu \epsilon & 0 \\ 0 & \beta_x^2 - \omega^2 \mu \epsilon_z \end{bmatrix} \begin{bmatrix} E_y \\ E_z \end{bmatrix} = 0. \quad (4.5.6)$$

For this equation to have a non-trivial solution, the determinant of its coefficient matrix must vanish, which yields

$$(\beta_x^2 - \omega^2 \mu \epsilon)(\beta_x^2 - \omega^2 \mu \epsilon_z) = 0. \quad (4.5.7)$$

Equation 4.5.7 has two solutions. The first solution is given by

$$\beta_x^2 - \omega^2 \mu \epsilon = 0 \quad \text{or} \quad \beta_x = \omega \sqrt{\mu \epsilon} = k_o. \quad (4.5.8)$$

With this, $E_y \neq 0$ and $E_z = 0$; hence, the electric field intensity and flux density can be written as

$$\mathbf{E} = \hat{y} E_0 e^{-jk_o x}, \quad \mathbf{D} = \hat{y} \epsilon E_0 e^{-jk_o x} \quad (4.5.9)$$

from which the magnetic field intensity and flux density can be found as

$$\mathbf{H} = \hat{z} \sqrt{\frac{\epsilon}{\mu}} E_0 e^{-jk_o x}, \quad \mathbf{B} = \mu \mathbf{H}. \quad (4.5.10)$$

It is clear that in this solution, ϵ_z does not have any effect. The dispersion relation given in Equation 4.5.8 and the fields given in Equations 4.5.9 and 4.5.10 are the same as those in an isotropic medium with a permittivity of ϵ . For this reason, the wave corresponding to this solution is called an *ordinary wave*.

The second solution to Equation 4.5.7 is given by

$$\beta_x^2 - \omega^2 \mu \epsilon_z = 0 \quad \text{or} \quad \beta_x = \omega \sqrt{\mu \epsilon_z} = k_e. \quad (4.5.11)$$

Under this solution, $E_y = 0$ and $E_z \neq 0$; hence, the electric field intensity and flux density are given by

$$\mathbf{E} = \hat{z} E_0 e^{-jk_e x}, \quad \mathbf{D} = \hat{z} \epsilon E_0 e^{-jk_e x} \quad (4.5.12)$$

and the magnetic field intensity and flux density are given by

$$\mathbf{H} = \hat{y} \sqrt{\frac{\epsilon_z}{\mu}} E_0 e^{-jk_e x}, \quad \mathbf{B} = \mu \mathbf{H}. \quad (4.5.13)$$

The effect of ϵ_z is clearly seen in both the phase constant and wave impedance. In fact, the dispersion relation given in Equation 4.5.11 and the fields given in Equations 4.5.12 and 4.5.13 are the same as those in an isotropic medium with a permittivity of ϵ_z . For this reason, the wave corresponding to this solution is called an *extraordinary wave*.

Clearly, the ordinary wave is affected only by ϵ because its electric field has only a y -component and the permittivity in the y -direction is ϵ . Similarly, the extraordinary wave is affected only by ϵ_z because its electric field has only a z -component and the permittivity in the z -direction is ϵ_z . The permittivity affects a plane wave through the electric field, which can actually be seen very easily from the constitutive relation $\mathbf{D} = \tilde{\epsilon} \cdot \mathbf{E}$. Now, if we introduce a conductivity in the z -direction, the permittivity tensor becomes

$$\tilde{\epsilon} = \begin{bmatrix} \epsilon & 0 & 0 \\ 0 & \epsilon & 0 \\ 0 & 0 & \epsilon_z - j\sigma_z/\omega \end{bmatrix}. \quad (4.5.14)$$

Based on the analysis above, the ordinary wave will not be affected by this conductivity and its wavenumber remains as $k_o = \omega\sqrt{\mu\epsilon}$. However, the wavenumber for the extraordinary wave becomes

$$k_e = \omega \sqrt{\mu \left(\epsilon_z - j \frac{\sigma_z}{\omega} \right)} \approx \sqrt{\frac{\omega \mu \sigma_z}{2}} - j \sqrt{\frac{\omega \mu \sigma_z}{2}} \quad (4.5.15)$$

for a large value of σ_z . Apparently, the extraordinary wave will be attenuated. If this attenuation, which depends on the value of σ_z and the thickness of the material in the x -direction, is sufficiently large that the extraordinary wave eventually becomes negligible after transmission, the material is called a *Polaroid*. When a plane wave with any polarization enters a Polaroid, the transmitted wave is linearly polarized with only a y -component for the electric field (Fig. 4.19).

To illustrate another application of the uniaxial medium, consider the plane wave

$$\mathbf{E} = \left(\hat{y} \frac{1}{\sqrt{2}} + \hat{z} \frac{1}{\sqrt{2}} \right) E_0 e^{-j\beta_x x} \quad (4.5.16)$$

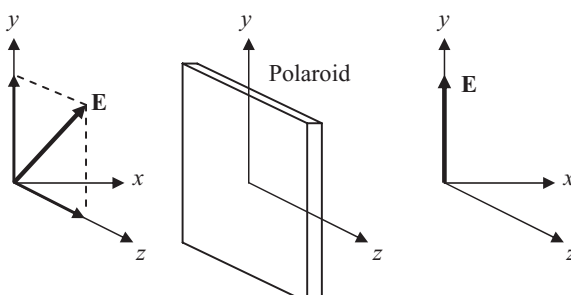


Figure 4.19 Transmission through a Polaroid.

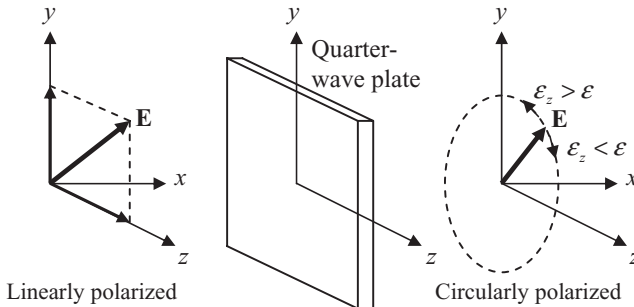


Figure 4.20 Transmission through a quarter-wave plate.

passing through a dielectric slab made of the uniaxial medium characterized by Equation 4.5.1. Once it enters the uniaxial medium, the y - and z -components propagate at two different phase velocities, which are determined by their wavenumbers. Right after passing through the slab, the electric field becomes

$$\mathbf{E} = \hat{y} \frac{E_0}{\sqrt{2}} e^{-jk_o d} + \hat{z} \frac{E_0}{\sqrt{2}} e^{-jk_e d} = \left[\hat{y} + \hat{z} e^{-j(k_e - k_o)d} \right] \frac{E_0}{\sqrt{2}} e^{-jk_o d} \quad (4.5.17)$$

where d denotes the thickness of the dielectric slab. In writing Equation 4.5.17, we ignored the wave reflection at the surfaces of the dielectric slab. Equation 4.5.17 represents an elliptically polarized plane wave. In particular, if the thickness is chosen such that $(k_e - k_o)d = \pm(n + 1/2)\pi$ with n being an integer, Equation 4.5.17 becomes

$$\mathbf{E} = (\hat{y} \pm j\hat{z}) \frac{E_0}{\sqrt{2}} e^{-jk_o d} \quad (4.5.18)$$

which represents a circularly polarized plane wave. Such a dielectric slab is called a *quarter-wave plate*, which can convert a linearly polarized plane wave into a circularly polarized wave (Fig. 4.20). The direction of rotation of the electric field depends on the values of ϵ and ϵ_z .

The results obtained above are also applicable to the case when the propagation vector lies in the xy -plane such that $\beta = \hat{x}\beta_x + \hat{y}\beta_y$, because the permittivity in the y -direction is the same as that in the x -direction. In this case, the ordinary wave has the electric field parallel to the xy -plane and wavenumber $k_o = \omega\sqrt{\mu\epsilon}$. The extraordinary wave has the electric field in the z -direction and wavenumber $k_e = \omega\sqrt{\mu\epsilon_z}$. The two waves propagate at different phase velocities. When a plane wave with both polarizations is incident obliquely on the interface between air and this uniaxial medium from the air side, the transmitted field is split into two plane waves that propagate in two different directions based on their polarizations, resulting in a phenomenon known as *birefringence* (Fig. 4.21).

Now that we have considered a simple special case, we turn our attention to a more general case, in which the propagation vector lies in the xz -plane such that $\beta = \hat{x}\beta_x + \hat{z}\beta_z$. Under this assumption, Equation 4.5.4 becomes

$$\begin{bmatrix} \beta_z^2 - \omega^2 \mu \epsilon & 0 & -\beta_x \beta_z \\ 0 & \beta_x^2 + \beta_z^2 - \omega^2 \mu \epsilon & 0 \\ -\beta_x \beta_z & 0 & \beta_x^2 - \omega^2 \mu \epsilon_z \end{bmatrix} \begin{bmatrix} E_x \\ E_y \\ E_z \end{bmatrix} = 0. \quad (4.5.19)$$

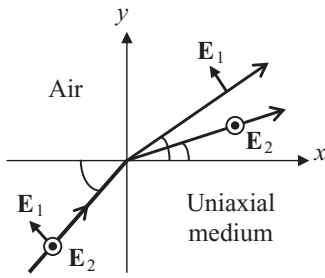


Figure 4.21 Plane wave transmitted from air into a uniaxial medium.

For this equation to have a nontrivial solution, the determinant of its coefficient matrix must vanish, which yields

$$(\beta_x^2 + \beta_z^2 - \omega^2 \mu \epsilon) [(\beta_x^2 - \omega^2 \mu \epsilon_z)(\beta_z^2 - \omega^2 \mu \epsilon) - \beta_x^2 \beta_z^2] = 0. \quad (4.5.20)$$

Again, this equation has two solutions. The first solution is given by

$$\beta_x^2 + \beta_z^2 - \omega^2 \mu \epsilon = 0. \quad (4.5.21)$$

With this solution, $E_y \neq 0$ and $E_x = E_z = 0$; hence, the electric field intensity and flux density can be written as

$$\mathbf{E} = \hat{y} E_0 e^{-j\beta r}, \quad \mathbf{D} = \hat{y} \epsilon E_0 e^{-j\beta r} \quad (4.5.22)$$

from which the magnetic field intensity and flux density can be found as

$$\mathbf{H} = \frac{1}{\omega \mu} (-\hat{x} \beta_z + \hat{z} \beta_x) E_0 e^{-j\beta r}, \quad \mathbf{B} = \mu \mathbf{H}. \quad (4.5.23)$$

This solution is not affected by ϵ_z and is the same as the ordinary-wave solution discussed earlier, as illustrated in Figure 4.22a.

The second solution to Equation 4.5.20 is given by

$$(\beta_z^2 - \omega^2 \mu \epsilon)(\beta_x^2 - \omega^2 \mu \epsilon_z) - \beta_x^2 \beta_z^2 = 0 \quad (4.5.24)$$

which can also be written as

$$\frac{\beta_x^2}{\omega^2 \mu \epsilon_z} + \frac{\beta_z^2}{\omega^2 \mu \epsilon} = 1. \quad (4.5.25)$$

Under this solution, $E_y = 0$ and $(\beta_z^2 - \omega^2 \mu \epsilon) E_x - \beta_x \beta_z E_z = 0$, which can also be written as

$$\epsilon \beta_x E_x + \epsilon_z \beta_z E_z = 0. \quad (4.5.26)$$

This equation is nothing but $\beta \cdot \mathbf{D} = 0$, which can also be obtained from Equation 4.5.3. With these, the electric field intensity and flux density are given by

$$\mathbf{E} = \left(\hat{x} - \hat{z} \frac{\beta_x \epsilon}{\beta_z \epsilon_z} \right) E_{x0} e^{-j\beta r}, \quad \mathbf{D} = \left(\hat{x} - \hat{z} \frac{\beta_x}{\beta_z} \right) \epsilon E_{x0} e^{-j\beta r} \quad (4.5.27)$$

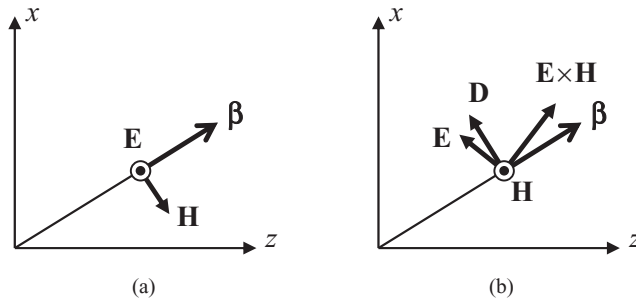


Figure 4.22 Plane wave propagation in a uniaxial medium. (a) Ordinary wave. (b) Extraordinary wave.

and the magnetic field intensity and flux density are given by

$$\mathbf{H} = \hat{y} \frac{\omega \epsilon}{\beta_z} E_{x0} e^{-j\beta \cdot r}, \quad \mathbf{B} = \mu \mathbf{H}. \quad (4.5.28)$$

In this case, both ϵ and ϵ_z affect the wave propagation and the degree of the effect depends on the propagation direction. If the wave propagates in the x -direction, the effect of ϵ disappears and the wave reduces to the extraordinary wave discussed earlier. If the wave propagates in the z -direction, the effect of ϵ_z disappears and the wave becomes an ordinary wave. Other than these two special directions, the phase constants β_x and β_z depend on the propagation direction. More interesting, since \mathbf{E} is not parallel to \mathbf{D} , the Poynting vector $\frac{1}{2} \mathbf{E} \times \mathbf{H}^*$ is not in the direction of β ; hence, the power flows in a direction different from the propagation direction. This wave is called a *general extraordinary wave*, as illustrated in Figure 4.22b. Therefore, even if the ordinary and extraordinary waves propagate in the same direction, their energy propagates in different directions, exhibiting again the phenomenon of birefringence.

4.5.2 Plane Waves in Gyrotropic Media

Now we consider a more complicated problem, which concerns a plane wave propagating in a gyrotropic medium whose permittivity is given by

$$\tilde{\epsilon} = \begin{bmatrix} \epsilon & -j\epsilon_g & 0 \\ j\epsilon_g & \epsilon & 0 \\ 0 & 0 & \epsilon_z \end{bmatrix}. \quad (4.5.29)$$

Following the same approach, we find the general dispersion relation as

$$\beta \times (\beta \times \mathbf{E}) = -\omega^2 \mu \tilde{\epsilon} \cdot \mathbf{E} \quad (4.5.30)$$

which can be analyzed to find possible wave solutions in such a gyrotropic medium. To simplify the analysis, we assume, without the loss of generality, that the propagation vector lies in the xz -plane such that $\beta = \hat{x}\beta_x + \hat{z}\beta_z$. Under this assumption, Equation 4.5.30 becomes

$$\begin{bmatrix} \beta_z^2 - \omega^2 \mu \epsilon & j\omega^2 \mu \epsilon_g & -\beta_x \beta_z \\ -j\omega^2 \mu \epsilon_g & \beta_x^2 + \beta_z^2 - \omega^2 \mu \epsilon & 0 \\ -\beta_x \beta_z & 0 & \beta_x^2 - \omega^2 \mu \epsilon_z \end{bmatrix} \begin{bmatrix} E_x \\ E_y \\ E_z \end{bmatrix} = 0. \quad (4.5.31)$$

Let $\beta = \hat{x}\beta \sin \theta + \hat{z}\beta \cos \theta$, $k = \omega\sqrt{\mu\epsilon}$, $k_z = \omega\sqrt{\mu\epsilon_z}$, and $k_g = \omega\sqrt{\mu\epsilon_g}$. Equation 4.5.31 can be rewritten as

$$\begin{bmatrix} \beta^2 \cos^2 \theta - k^2 & jk_g^2 & -\beta^2 \sin \theta \cos \theta \\ -jk_g^2 & \beta^2 - k^2 & 0 \\ -\beta^2 \sin \theta \cos \theta & 0 & \beta^2 \sin^2 \theta - k_z^2 \end{bmatrix} \begin{bmatrix} E_x \\ E_y \\ E_z \end{bmatrix} = 0. \quad (4.5.32)$$

For this equation to have a non-trivial solution, the determinant of its coefficient matrix must vanish, which yields

$$(\beta^2 - k^2)(k^2 k_z^2 - k^2 \beta^2 \sin^2 \theta - k_z^2 \beta^2 \cos^2 \theta) - k_g^4 (\beta^2 \sin^2 \theta - k_z^2) = 0. \quad (4.5.33)$$

This equation can be written compactly as

$$A\beta^4 - B\beta^2 + C = 0 \quad (4.5.34)$$

where $A = k^2 \sin^2 \theta + k_z^2 \cos^2 \theta$, $B = (k^4 - k_g^4) \sin^2 \theta + k^2 k_z^2 (1 + \cos^2 \theta)$, and $C = (k^4 - k_g^4) k_z^2$. The solution for Equation 4.5.34 is given by

$$\beta^2 = \frac{B \pm \sqrt{B^2 - 4AC}}{2A} \quad (4.5.35)$$

which gives the phase constant as a function of the propagation direction. From Equation 4.5.32, we also find that

$$\frac{E_x}{E_y} = \frac{\beta^2 - k^2}{jk_g^2}, \quad \frac{E_x}{E_z} = \frac{\beta^2 \sin^2 \theta - k_z^2}{\beta^2 \sin \theta \cos \theta}. \quad (4.5.36)$$

Therefore, the electric field can be written as

$$\mathbf{E} = \left(\hat{x} + \hat{y} \frac{jk_g^2}{\beta^2 - k^2} + \hat{z} \frac{\beta^2 \sin \theta \cos \theta}{\beta^2 \sin^2 \theta - k_z^2} \right) \mathbf{E}_{x0} e^{-j\beta(x \sin \theta + z \cos \theta)} \quad (4.5.37)$$

and the magnetic field can be obtained from this using the first Maxwell's equation.

To study further the wave characteristics in the gyroscopic medium, we consider two special cases. In the first case, the wave propagates in the z -direction, that is, $\theta = 0$ and $\beta = \hat{z}\beta$. Clearly, for this case, Equation 4.5.35 becomes

$$\beta^2 = \beta_{\pm}^2 = k^2 \pm k_g^2 = \omega^2 \mu (\epsilon \pm \epsilon_g) \quad (4.5.38)$$

and Equation 4.5.36 becomes

$$\frac{E_x}{E_y} = \frac{\beta^2 - k^2}{jk_g^2} = \frac{\pm k_g^2}{jk_g^2} = \mp j, \quad E_z = 0. \quad (4.5.39)$$

Hence, the electric field in Equation 4.5.37 becomes

$$\mathbf{E} = (\hat{x} \pm j\hat{y})E_{x0}e^{-j\beta_{\pm}z} \quad (4.5.40)$$

which indicates that when a plane wave propagates in the z -direction, its left-hand circularly polarized component will propagate with a wavenumber $\beta_+ = \omega\sqrt{\mu(\epsilon + \epsilon_g)}$ or a phase velocity $v_{p+} = \omega/\beta_+$, and its right-hand circularly polarized component will propagate with a different wavenumber $\beta_- = \omega\sqrt{\mu(\epsilon - \epsilon_g)}$ or a different phase velocity $v_{p-} = \omega/\beta_-$. Now, consider a linearly polarized plane wave, say, $\mathbf{E} = \hat{x}E_0e^{-j\beta z}$, entering the gyroscopic medium. Once it has entered the medium, the electric field becomes

$$\mathbf{E} = \frac{1}{2}(\hat{x} - j\hat{y})E_0e^{-j\beta_-z} + \frac{1}{2}(\hat{x} + j\hat{y})E_0e^{-j\beta_+z}. \quad (4.5.41)$$

At any point in the medium, say, $z = d$, the electric field is

$$\begin{aligned} \mathbf{E} &= \frac{1}{2}(\hat{x} - j\hat{y})E_0e^{-j\beta_-d} + \frac{1}{2}(\hat{x} + j\hat{y})E_0e^{-j\beta_+d} \\ &= \frac{1}{2}\hat{x}E_0(e^{-j\beta_-d} + e^{-j\beta_+d}) - \frac{1}{2}j\hat{y}E_0(e^{-j\beta_-d} - e^{-j\beta_+d}). \end{aligned} \quad (4.5.42)$$

To see the polarization of this field, we examine the ratio of the x - and y -components to find

$$\begin{aligned} \frac{E_x}{E_y} &= \frac{\frac{1}{2}E_0(e^{-j\beta_-d} + e^{-j\beta_+d})}{\frac{1}{2}jE_0(e^{-j\beta_-d} - e^{-j\beta_+d})} = j \frac{e^{j(\beta_+-\beta_-)d/2} + e^{-j(\beta_+-\beta_-)d/2}}{e^{j(\beta_+-\beta_-)d/2} - e^{-j(\beta_+-\beta_-)d/2}} \\ &= \cot\left[\frac{(\beta_+ - \beta_-)d}{2}\right] \end{aligned} \quad (4.5.43)$$

which indicates a linear polarization. However, the polarization is rotated by an angle from its original direction and this angle is given by

$$\theta_F = \frac{(\beta_+ - \beta_-)d}{2}. \quad (4.5.44)$$

This phenomenon is known as the *Faraday rotation* (Fig. 4.23).

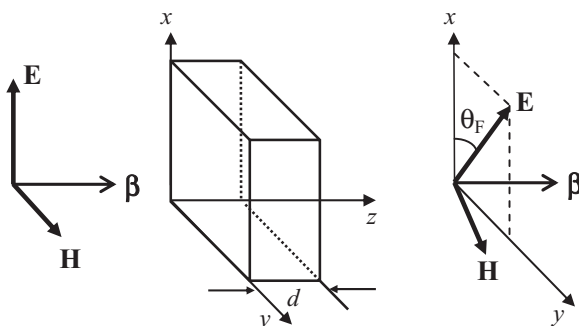


Figure 4.23 Transmission through a gyroscopic medium—Faraday rotation.

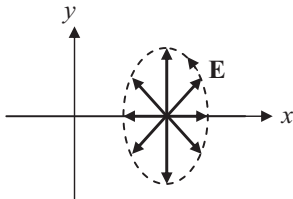


Figure 4.24 Elliptically polarized wave rotating in the xy -plane and propagating in the x -direction.

The second special case assumes that the wave propagates in the x -direction, that is, $\theta = \pi/2$ and $\beta = \hat{x}\beta$. For this case, one of the solutions in Equation 4.5.35 becomes

$$\beta^2 = k_z^2 = \omega^2 \mu \epsilon_z \quad (4.5.45)$$

and the electric field in Equation 4.5.37 is reduced to

$$\mathbf{E} = \hat{z} E_0 e^{-j\beta x}. \quad (4.5.46)$$

This wave is the same as the extraordinary wave discussed in the preceding section since it is affected solely by ϵ_z . The other solution in Equation 4.5.35 is given by

$$\beta^2 = k^2 - \frac{k_g^4}{k^2} = \omega^2 \mu \epsilon - \frac{\omega^2 \mu \epsilon_g^2}{\epsilon} \quad (4.5.47)$$

and the electric field in Equation 4.5.37 becomes

$$\mathbf{E} = \left(\hat{x} - \hat{y} \frac{j\epsilon}{\epsilon_g} \right) E_{x0} e^{-j\beta x}. \quad (4.5.48)$$

We can easily transform this expression into the time domain and then find that the electric field rotates in the xy -plane and the tip of the electric field vector draws an ellipse. This is usually called elliptical polarization; however, this wave is different from the elliptically polarized plane wave discussed earlier in that the rotation of the electric field is not perpendicular to the propagation direction. Instead, it rotates in the plane that contains the propagation wave vector, as illustrated in Figure 4.24.

4.5.3 Plane Waves in Chiral Media

A chiral medium is a bi-isotropic medium, in which the field intensities and flux densities are related by the constitutive relations [15–17]

$$\mathbf{D} = \epsilon \mathbf{E} - j\chi \mathbf{H}, \quad \mathbf{B} = \mu \mathbf{H} + j\chi \mathbf{E} \quad (4.5.49)$$

where χ is called the *chirality parameter*. For a plane wave in this medium, Maxwell's equations become

$$\boldsymbol{\beta} \times \mathbf{E} = \omega \mathbf{B}, \quad \boldsymbol{\beta} \times \mathbf{H} = -\omega \mathbf{D} \quad (4.5.50)$$

$$\boldsymbol{\beta} \cdot \mathbf{D} = 0, \quad \boldsymbol{\beta} \cdot \mathbf{B} = 0. \quad (4.5.51)$$

Substituting Equation 4.5.49 into Equation 4.5.50, we obtain

$$\begin{bmatrix} \beta \times \bar{\mathbf{I}} - j\omega\chi\bar{\mathbf{I}} & -\omega\mu\bar{\mathbf{I}} \\ \omega\epsilon\bar{\mathbf{I}} & \beta \times \bar{\mathbf{I}} - j\omega\chi\bar{\mathbf{I}} \end{bmatrix} \cdot \begin{bmatrix} \mathbf{E} \\ \mathbf{H} \end{bmatrix} = 0 \quad (4.5.52)$$

where $\bar{\mathbf{I}}$ denotes the unit tensor. Since the medium is isotropic, we can study wave propagation by assuming without loss of generality that the wave propagates in the z -direction. Under this assumption, $D_z = B_z = 0$, which yields $E_z = H_z = 0$. Equation 4.5.52 then becomes

$$\begin{bmatrix} -\beta & j\omega\chi \\ j\omega\chi & \beta \end{bmatrix} \begin{bmatrix} E_x \\ E_y \end{bmatrix} = - \begin{bmatrix} 0 & \omega\mu \\ \omega\mu & 0 \end{bmatrix} \begin{bmatrix} H_x \\ H_y \end{bmatrix} \quad (4.5.53)$$

$$\begin{bmatrix} -\beta & j\omega\chi \\ j\omega\chi & \beta \end{bmatrix} \begin{bmatrix} H_x \\ H_y \end{bmatrix} = \begin{bmatrix} 0 & \omega\epsilon \\ \omega\epsilon & 0 \end{bmatrix} \begin{bmatrix} E_x \\ E_y \end{bmatrix}. \quad (4.5.54)$$

By eliminating the magnetic field, we have

$$\begin{bmatrix} 2j\omega\chi\beta & \beta^2 + \omega^2\chi^2 - \omega^2\mu\epsilon \\ \beta^2 + \omega^2\chi^2 - \omega^2\mu\epsilon & -2j\omega\chi\beta \end{bmatrix} \begin{bmatrix} E_x \\ E_y \end{bmatrix} = 0. \quad (4.5.55)$$

For this equation to have a non-trivial solution, the determinant of its coefficient matrix must vanish, which yields

$$\beta_{\pm} = \omega\sqrt{\mu\epsilon} \pm \omega\chi. \quad (4.5.56)$$

The solution to Equation 4.5.55 is then given by

$$\frac{E_x}{E_y} = \pm j. \quad (4.5.57)$$

Therefore, there are two types of wave that can propagate in a chiral medium. One is a left-hand circularly polarized wave, which propagates at the phase velocity

$$v_{p+} = \frac{\omega}{\beta_+} = \frac{1}{\sqrt{\mu\epsilon + \chi}}. \quad (4.5.58)$$

The other is a right-hand circularly polarized wave, which propagates at the phase velocity

$$v_{p-} = \frac{\omega}{\beta_-} = \frac{1}{\sqrt{\mu\epsilon - \chi}}. \quad (4.5.59)$$

Any plane wave, upon entering a chiral medium, will be decomposed into two circularly polarized waves that propagate at different phase velocities. Because of the difference in the phase velocity, a chiral medium can exhibit interesting phenomena such as Faraday rotation and birefringence as in a gyrotrropic medium. However, a gyrotrropic medium is non-reciprocal, whereas a chiral medium is reciprocal.

REFERENCES

- [1] G. F. MINER, *Lines and Electromagnetic Fields for Engineers*. Oxford, UK: Oxford University Press, 1996.
- [2] P. M. MORSE and H. FESHBACH, *Methods of Theoretical Physics*. New York: McGraw-Hill, 1953.
- [3] C. T. TAI, *Dyadic Green Functions in Electromagnetic Theory* (2nd edition). Piscataway, NJ: IEEE Press, 1994.
- [4] R. F. HARRINGTON, *Time-Harmonic Electromagnetic Fields*. New York: McGraw-Hill, 1961.
- [5] S. RAMO, J. R. WHINNERY, and T. VAN DUZER, *Fields and Waves in Communication Electronics* (3rd edition). New York: Wiley, 1994.
- [6] V. G. VESELAGO, The electrodynamics of substances with simultaneously negative values of ϵ and μ , *Sov. Phys. Usp.*, 10(4): 509–514, 1968.
- [7] J. B. PENDRY, Negative refraction makes a perfect lens, *Phys. Rev. Lett.*, 85(18): 3966–3969, 2000.
- [8] R. A. SHELBY, D. R. SMITH, and S. SCHULTZ, Experimental verification of a negative refractive index of refraction, *Sci.*, 292: 77–79, 2001.
- [9] C. CALOZ, C.-C. CHANG, and T. ITOH, Full-wave verification of the fundamental properties of left-handed materials in waveguide configurations, *J. Appl. Phys.*, 90(11): 5483–5486, 2001.
- [10] G. V. ELEFTHERIADES and K. G. BALMAIN, *Negative Refraction Metamaterials: Fundamental Principles and Applications*. Hoboken, NJ: Wiley, 2005.
- [11] N. ENGHETA and R. W. ZIOLKOWSKI, Eds., *Electromagnetic Metamaterials: Physics and Engineering Explorations*. Hoboken, NJ: Wiley, 2006.
- [12] J. A. KONG, *Electromagnetic Wave Theory*. Cambridge, MA: EMW Publishing, 2000.
- [13] S. L. CHUANG, *Physics of Photonic Devices* (2nd edition). Hoboken, NJ: Wiley, 2009.
- [14] C. G. SOMEDA, *Electromagnetic Waves* (2nd edition). Boca Raton, FL: CRC Press, 2006.
- [15] D. L. JAGGARD, A. R. MICELSON, and C. H. PAPAS, On electromagnetic waves in chiral media, *Appl. Phys.*, 18: 211–216, 1978.
- [16] N. ENGHETA and D. L. JAGGARD, Electromagnetic chirality and its applications, *IEEE Antennas Propagat. Soc. Newslett.*, 30: 6–12, 1988.
- [17] I. V. LINDELL, A. H. SIHVOLA, S. A. TRETYAKOV, and A. J. VIITANEN, *Electromagnetic Waves in Chiral and Bi-Isotropic Media*. Norwood, MA: Artech, 1994.

PROBLEMS

- 4.1.** Consider a lossless transmission line with negative inductance and capacitance per unit length. Starting from Kirchhoff's laws, derive the governing equation for the voltage and current. Find the phase velocity and energy velocity.
- 4.2.** Find the voltage and current on a semi-infinite transmission line with a point voltage source shown in Figure 4.25.
- 4.3.** Find the voltage and current on a finite transmission line with a point current source shown in Figure 4.26.
- 4.4.** Consider a lossless transmission line illustrated in Figure 4.27 with a distributed voltage source $v(x)$, which has a unit of volts per unit length. Formulate the solution to this problem using Green's function.
- 4.5.** Consider a semi-infinite transmission line connected to a finite transmission line of different characteristic impedance, which is then terminated by an impedance load (Fig. 4.28). Find the reflected voltage and current on the semi-infinite transmission line.
- 4.6.** Consider two transmission lines of length L , which are terminated by Z_1 at $z = 0$ and Z_2 at $z = L$. The first transmission line has distributed voltage source $v_a(z)$ and current source $i_a(z)$, and the voltage and current on the line are denoted by $V_a(z)$ and $I_a(z)$. The second transmission line has distributed voltage source $v_b(z)$ and current source $i_b(z)$, and the voltage and current on the line are denoted by $Z_b(z)$ and $I_b(z)$. Show the following general reciprocity theorem:

$$\int_0^L [v_a(z)I_b(z) - i_a(z)V_b(z)] dz = \int_0^L [v_b(z)I_a(z) - i_b(z)V_a(z)] dz.$$

- 4.7.** The electric field of a plane wave is given by $\mathbf{E} = \hat{x}(e^{-j\beta z} + \Gamma e^{j\beta z})$, where $\beta = \omega\sqrt{\epsilon_0\mu_0}$ and Γ is an unknown. The ratio between electric and magnetic fields at $z = d$ is given by

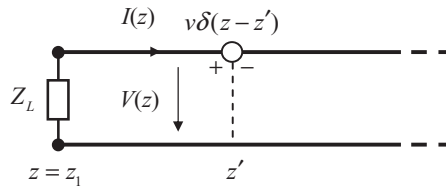


Figure 4.25 Semi-infinite transmission line with a voltage source.

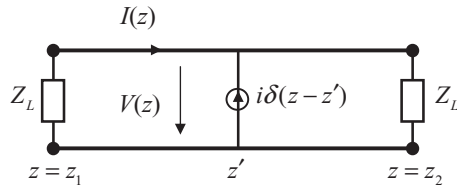


Figure 4.26 Finite transmission line with a current source.

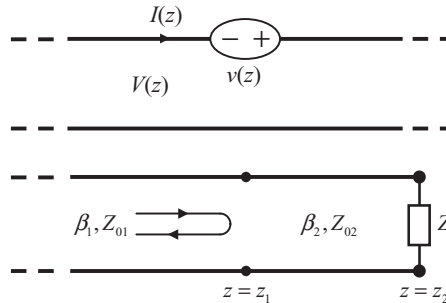


Figure 4.27 Transmission line excited by a distributed voltage source.

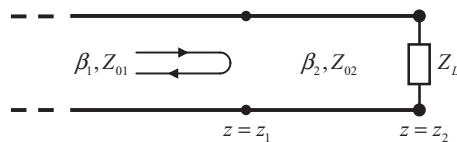


Figure 4.28 Transmission line terminated by an impedance load.

$E_x/H_y|_{z=d} = Z_d$, where Z_d is a given (possibly complex) constant. (a) Find the unknown Γ . (b) Find the standing wave ratio (SWR) for $z < d$. Under what conditions on Z_d does the SWR become unity, and under what condition does it approach infinity? (c) Find the time-average power flow density.

- 4.8. A left-hand elliptically polarized plane wave with a frequency of 10 MHz is propagating in the positive z -direction in free space. The time-average Poynting vector (average power density) of the wave is 10^{-6} W/m². If at any plane $z = \text{constant}$, the ratio of the maximum to minimum value of the electric field intensity is 2, find the maximum value of the electric field intensity.
- 4.9. A right-hand elliptically polarized plane wave with a frequency of 1 GHz is propagating in the positive z -direction in free space. (a) If at any plane $z = \text{constant}$, the ratio of the maximum to the minimum value of the electric field intensity is 3, and the maximum value of the electric field intensity is 1 V/m, find the time-average Poynting vector (average power flow density) of the wave. (b) If this plane wave is reflected by the surface of a half-space occupied by a homogeneous, isotropic, and non-magnetic ($\mu = \mu_0$) medium whose permittivity is denoted by ϵ , find the angle of incidence, in terms of ϵ , at which the reflected plane wave becomes linearly polarized.
- 4.10. First, start from Equation 4.2.53 and derive Equation 4.2.54. Next, show that the semimajor axis A and the semiminor axis B of the ellipse defined by Equation 4.2.54 are related by

$$A^2 + B^2 = |E_{0x}|^2 + |E_{0y}|^2$$

and the angle of inclination ψ (the angle between the semimajor axis and the x -axis) is given by

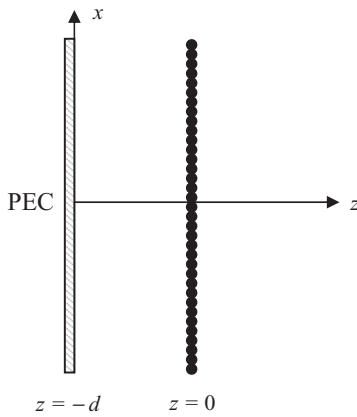


Figure 4.29 Infinitely large current sheet placed in front of an infinitely large perfect electric conductor (PEC) plane.

$$\tan 2\psi = \frac{2|E_{0x}||E_{0y}|}{|E_{0x}|^2 - |E_{0y}|^2} \cos \vartheta.$$

- 4.11.** Consider an infinitely large current sheet in the xy -plane, as shown in Figure 4.11, with the surface current density given in Equation 4.3.1. An infinitely large perfect electrically conducting plane is placed at $z = -d$ (Fig. 4.29). (a) Find the electric and magnetic fields produced by the current sheet in the regions $-d < z < 0$ and $z > 0$. (b) Find the time-average power radiated by the current sheet of a unit area. (c) Find all possible values for d under which the time-average radiated power vanishes.
- 4.12.** This problem has two parts. (a) Show that if the displacement current is neglected, the differential equation of the conduction current density ($\mathbf{J}_c = \sigma \mathbf{E}$, σ is a constant) in a conductor is given by
- $$\nabla^2 \mathbf{J}_c = \mu \sigma \frac{\partial \mathbf{J}_c}{\partial t}.$$
- (b) An infinite half-space (below the $z = 0$ plane) having permeability μ and conductivity σ carries a sinusoidal (time-harmonic) current of angular frequency ω in the x -direction. Assume that $|\mathbf{J}_c| = 1 \text{ A/m}^2$ when $z = 0$ and there is no variation along the y -direction. Using the differential equation from part (a), find the solution for the current density in the half-space. Express your result in terms of skin depth.
- 4.13.** A planar conductor is coated with a layer of magnetic material of thickness t , permittivity ϵ_0 , and permeability $\mu = \mu' - j\mu''$. A uniform plane wave is incident normally on the coated conductor. (a) Find the expression for the time-average power absorbed by the coated material per square meter. (b) Find the explicit result if the material is very thin.
- 4.14.** A plane wave is incident (from free space) obliquely upon an infinitely large dielectric slab with thickness d and permittivity and permeability ϵ_d and μ_d . Find the reflected and transmitted fields and the field inside the dielectric slab for both perpendicular and parallel polarizations.
- 4.15.** A plane wave is incident (from free space) upon a semi-infinite medium made of $N = 100$ different lossless dielectric slabs with permittivity and permeability ϵ_n and μ_n ($n = 1, 2, \dots, N$). The layered region is ended with a half-space with permittivity and permeability ϵ_{N+1} and μ_{N+1} . The incident angle is θ_i from the normal direction of the surface. (a) Find the propagation direction $\theta_{t,n}$ in the 10th and 99th slabs and also in the exit half-space. (b) What is the condition leading to the total reflection in free space?

- 4.16.** To reduce the reflection of a normally incident plane wave from a conducting wall, a very thin sheet ($\beta d \ll 1$) of conductive material with parameters σ , ϵ_0 , and μ_0 is placed at the distance $\lambda/4$ from the wall.
- What should the thickness of the conducting sheet be to have no reflected wave to the left of the conducting sheet?
 - Suppose the frequency is increased by 10%. What will be the SWR to the left of the conducting sheet?
 - If you can cover your car with such a sheet, can you beat a police radar gun? Why?
- 4.17.** A plane wave is incident from medium 1 and reflected at the planar interface between media 1 and 2 (see Figs. 4.13 and 4.14). Both media are isotropic and non-magnetic ($\mu = \mu_0$). The permittivities of the media are denoted by ϵ_1 and ϵ_2 , respectively.
- For a circularly polarized incident plane wave, find the angle of incidence, in terms of ϵ_1 and ϵ_2 , at which the reflected wave becomes linearly polarized. State the polarization (i.e., the direction of the electric field) of the reflected wave.
 - When a right-hand circularly polarized plane wave is incident at the critical angle (for total reflection), determine the polarization of the reflected wave. Write down the expression of the critical angle.
 - If medium 2 is replaced by a uniaxial medium with a permittivity given by

$$\tilde{\epsilon} = \begin{bmatrix} \epsilon_2 & 0 & 0 \\ 0 & \epsilon_y & 0 \\ 0 & 0 & \epsilon_2 \end{bmatrix}$$

and the incident wave is a circularly polarized plane wave, find the angle of incidence at which the reflected wave becomes linearly polarized. Write down the expressions of the critical angles for both parallel and perpendicular polarizations.

- 4.18.** A uniform plane wave is incident at an angle θ_i from air (μ_0 , ϵ_0) to an isotropic plasma with μ_0 and $\epsilon_p = \epsilon_0 [1 - (\omega_p^2/\omega^2)]$, as shown in Figure 4.13. Determine the reflected and transmitted waves for the perpendicular polarization at $\omega = \omega_p$ for the incident electric field given by $\mathbf{E}^i = \hat{y} E_0 e^{-jk_0(x \sin \theta_i + z \cos \theta_i)}$, where $k_0 = \omega \sqrt{\mu_0 \epsilon_0}$.
- 4.19.** Consider the experimental setup shown in Figure 4.30. On the left is a Polaroid with the passing axis in the vertical direction. In the middle is a quarter-wave plate whose fast axis is rotated α degrees away from the vertical direction. On the right is a Polaroid with the passing axis in the horizontal direction. A vertically polarized plane wave having an ampli-

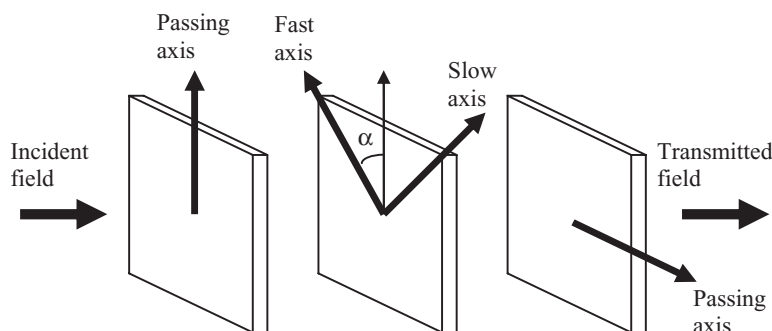


Figure 4.30 Experimental setup of a Polaroid, a quarter-wave plate, and another Polaroid.

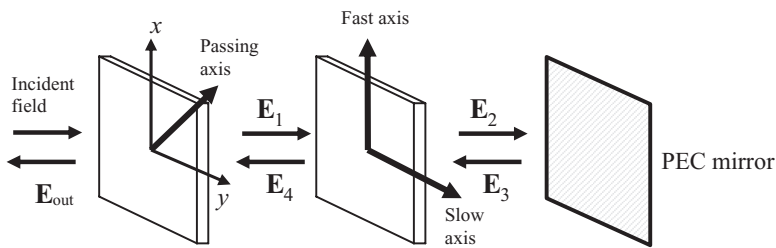


Figure 4.31 Experimental setup of a Polaroid, a quarter-wave plate, and a PEC reflector.

tude of E_0 is incident from the left side. Ignore the reflections from all interfaces. Find the amplitude of the transmitted field on the right side in terms of E_0 and α .

- 4.20.** Consider the experimental setup shown in Figure 4.31, where the passing axis of the Polaroid makes 45° with the x and y axes. Assume that both the Polaroid and quarter-wave plate are non-reflective and the mirror is a perfect electric conductor. Given a randomly polarized plane wave \mathbf{E}^i propagating along the z -direction, find the expression for the electric fields \mathbf{E}_1 , \mathbf{E}_2 , \mathbf{E}_3 , \mathbf{E}_4 , and \mathbf{E}_{out} .
- 4.21.** For a LiNbO₃ crystal with the permittivity given by
- $$\tilde{\epsilon} = \begin{pmatrix} 2.297 & 0 & 0 \\ 0 & 2.297 & 0 \\ 0 & 0 & 2.209 \end{pmatrix}.$$
- a. Write down the dispersion relations for the ordinary waves and the extraordinary waves propagating in the yz -plane.
 - b. Find the explicit expressions of the field quantities \mathbf{E} , \mathbf{H} , \mathbf{D} , and \mathbf{B} for ordinary and extraordinary waves.
- 4.22.** Consider a ferrite with the permeability given by
- $$\tilde{\mu} = \begin{pmatrix} \mu_1 & ja & 0 \\ -ja & \mu_1 & 0 \\ 0 & 0 & \mu_0 \end{pmatrix}.$$
- a. Find the characteristic polarizations with corresponding propagation constants for a wave propagating in the z -direction.
 - b. Find the characteristic polarizations with corresponding propagation constants for a wave propagating in the x -direction. ■

FIELDS AND WAVES IN RECTANGULAR COORDINATES

Starting with this chapter, we will discuss how to solve a variety of electromagnetic boundary-value problems in the three most commonly used coordinate systems: rectangular, cylindrical, and spherical. In this chapter we deal with problems best described with rectangular coordinates. These include wave propagation in rectangular waveguides and dielectric slab waveguides, resonances in rectangular cavities, and fields due to sources in a planar multilayered medium. However, since this is the first time we consider waveguides and cavities, we also discuss the general properties of waveguides and cavities of an arbitrary cross-section. These properties are also applicable to other types of waveguides and cavities, such as those treated in the next two chapters.

5.1 UNIFORM WAVEGUIDES

In general, any structure that can guide electromagnetic waves from one end to the other end can be called a *waveguide*. Under this general definition, parallel-wire transmission lines, coaxial cables, microstrip lines, coplanar slot lines, hollow metallic pipes of various cross-sections, and dielectric slabs or cylinders can all be called waveguides. In a certain sense, even free space can be considered a waveguide because it allows a wave to propagate from one place to another. In microwave engineering, the term *waveguide* usually refers to either a hollow or a partially filled metallic pipe of a rectangular, circular, or elliptical cross-section. It was found over a century ago [1] that a hollow metallic pipe could transmit electromagnetic waves from one end to the other because it supports a non-trivial solution of Maxwell's equations. In this section, we discuss electromagnetic analysis of this type of waveguide under an assumption that there is no variation of any kind (in geometry or material composition) along its longitudinal direction. Such a waveguide is often called a *uniform waveguide*.

5.1.1 General Analysis

Consider an infinitely long metallic waveguide of an arbitrary cross-section, filled with a homogeneous medium having a permittivity of ϵ and a permeability of μ , and having its infinite axis along the z -axis (Fig. 5.1). For an electromagnetic wave propagating in the z -direction, its electric and magnetic fields can be expressed as

$$\mathbf{E} = \mathbf{E}_t + \hat{z}E_z = [\mathbf{e}_t(x, y) + \hat{z}e_z(x, y)]e^{-jk_z z} \quad (5.1.1)$$

$$\mathbf{H} = \mathbf{H}_t + \hat{z}H_z = [\mathbf{h}_t(x, y) + \hat{z}h_z(x, y)]e^{-jk_z z} \quad (5.1.2)$$

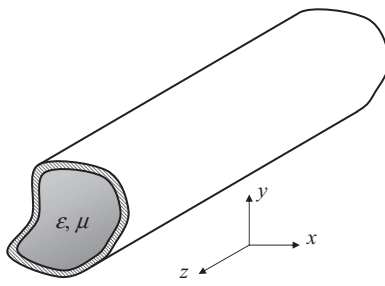


Figure 5.1 Uniform waveguide of an arbitrary cross-section.

where k_z denotes the propagation constant along the z -direction. An electromagnetic analysis of the waveguide is to determine possible solutions of the source-free Maxwell's equations in the form of Equations 5.1.1 and 5.1.2 that can be supported by the waveguide. The solution contains the field distribution and the propagation constant.

To seek possible solutions to Maxwell's equations, we substitute Equations 5.1.1 and 5.1.2 into the first Maxwell's equation, $\nabla \times \mathbf{E} = -j\omega\mu\mathbf{H}$, to find

$$\left(\nabla_t + \hat{z} \frac{\partial}{\partial z} \right) \times (\mathbf{E}_t + \hat{z} E_z) = -j\omega\mu(\mathbf{H}_t + \hat{z} H_z). \quad (5.1.3)$$

This equation can be written as

$$\nabla_t \times \mathbf{E}_t - \hat{z} \times \nabla_t E_z - jk_z \hat{z} \times \mathbf{E}_t = -j\omega\mu(\mathbf{H}_t + \hat{z} H_z) \quad (5.1.4)$$

whose transverse and longitudinal components are

$$\hat{z} \times \nabla_t E_z + jk_z \hat{z} \times \mathbf{E}_t = j\omega\mu\mathbf{H}_t \quad (5.1.5)$$

$$\nabla_t \times \mathbf{E}_t = -j\omega\mu H_z \hat{z}. \quad (5.1.6)$$

Similarly, from the second source-free Maxwell's equation we obtain

$$\hat{z} \times \nabla_t H_z + jk_z \hat{z} \times \mathbf{H}_t = -j\omega\epsilon\mathbf{E}_t \quad (5.1.7)$$

$$\nabla_t \times \mathbf{H}_t = j\omega\epsilon E_z \hat{z}. \quad (5.1.8)$$

By taking the cross-product of Equation 5.1.5 with \hat{z} ,

$$\hat{z} \times (\hat{z} \times \nabla_t E_z) + jk_z \hat{z} \times (\hat{z} \times \mathbf{E}_t) = j\omega\mu\hat{z} \times \mathbf{H}_t \quad (5.1.9)$$

and then using Equation 5.1.7 to eliminate $\hat{z} \times \mathbf{H}_t$, we obtain

$$(k^2 - k_z^2)\mathbf{E}_t = j\omega\mu\hat{z} \times \nabla_t H_z - jk_z \nabla_t E_z \quad (5.1.10)$$

or

$$\mathbf{E}_t = \frac{1}{k_z^2} (j\omega\mu\hat{z} \times \nabla_t H_z - jk_z \nabla_t E_z) \quad (5.1.11)$$

where $k_t^2 = k^2 - k_z^2$ and $k^2 = \omega^2\mu\epsilon$. Similarly, by eliminating \mathbf{E}_t from Equations 5.1.5 and 5.1.7, we obtain

$$\mathbf{H}_t = \frac{1}{k_t^2} (-j\omega\epsilon\hat{z}\times\nabla_t E_z - jk_z\nabla_t H_z). \quad (5.1.12)$$

Equations 5.1.11 and 5.1.12 indicate that once E_z and H_z are solved for, all other field components can be obtained. Therefore, to analyze wave propagation in a waveguide, we need only solve for E_z and H_z . Note that Equations 5.1.11 and 5.1.12 are derived without imposing the homogeneity requirement on the permittivity and permeability. Therefore, they are also valid for inhomogeneously or partially filled waveguides.

To find the equations satisfied by E_z and H_z , we substitute Equation 5.1.12 into Equation 5.1.8 and Equation 5.1.11 into Equation 5.1.6 to find

$$\nabla_t \times \left[\frac{1}{k_t^2} (\omega\epsilon\hat{z}\times\nabla_t E_z + k_z\nabla_t H_z) \right] = -\omega\epsilon E_z \hat{z} \quad (5.1.13)$$

$$\nabla_t \times \left[\frac{1}{k_t^2} (\omega\mu\hat{z}\times\nabla_t H_z - k_z\nabla_t E_z) \right] = -\omega\mu H_z \hat{z}. \quad (5.1.14)$$

For a homogeneously filled waveguide, where both ϵ and μ are constants, these two equations reduce to

$$\nabla_t^2 E_z + k_t^2 E_z = 0 \quad \text{in } \Omega \quad (5.1.15)$$

$$\nabla_t^2 H_z + k_t^2 H_z = 0 \quad \text{in } \Omega \quad (5.1.16)$$

where $\nabla_t^2 = \nabla_t \cdot \nabla_t$ denotes the transverse Laplacian operator and Ω denotes the cross-section of the waveguide. Since the waveguide has no geometrical variation in the z -direction, E_z satisfies the boundary condition

$$E_z = 0 \quad \text{on } \Gamma \quad (5.1.17)$$

where Γ denotes the waveguide's inner conducting surface. Since $\hat{n} \cdot \mathbf{H} = 0$ on the conducting surface, where \hat{n} denotes the unit normal vector, by using Equation 5.1.12 we have

$$\hat{n} \cdot \mathbf{H} = \hat{n} \cdot \mathbf{H}_t = \frac{1}{k_t^2} [-j\omega\epsilon\hat{n} \cdot (\hat{z} \times \nabla_t E_z) - jk_z\hat{n} \cdot \nabla_t H_z] = 0. \quad (5.1.18)$$

Since $\hat{n} \cdot (\hat{z} \times \nabla_t E_z) = (\hat{n} \times \hat{z}) \cdot \nabla_t E_z$ represents a tangential derivative of E_z and $E_z = 0$ on Γ , the first term in the brackets vanishes. Therefore, we obtain $\hat{n} \cdot \nabla_t H_z = 0$ or

$$\frac{\partial H_z}{\partial n} = 0 \quad \text{on } \Gamma. \quad (5.1.19)$$

This boundary condition can also be obtained by applying $\hat{n} \times \mathbf{E} = 0$ to (5.1.11).

The Helmholtz equations (Eqs. 5.1.15 and 5.1.16) and the boundary conditions (Eqs. 5.1.17 and 5.1.19) indicate that in a homogeneously filled uniform waveguide, E_z and H_z are neither coupled by the medium in the waveguide nor coupled by the boundary of the waveguide. Therefore, E_z and H_z can exist independently. As a result, we can have two independent sets of solutions. One set has $E_z \neq 0$ and $H_z = 0$, and the other set has $E_z = 0$ and $H_z \neq 0$. The fields corresponding to the first set of solutions are called *transverse magnetic* (TM) waveguide modes since the magnetic field is transverse to the z -direction. The fields corresponding to the second set of solutions are called *transverse electric* (TE)

waveguide modes since the electric field is transverse to the z -direction. To analyze TM waveguide modes, we first solve the boundary-value problem defined by the partial differential equation in Equation 5.1.15 and the boundary condition in Equation 5.1.17 for E_z and k_t . Once E_z and k_t are solved for, the other field components can be obtained from Equations 5.1.11 and 5.1.12, or, more explicitly,

$$\mathbf{E}_t = -\frac{jk_z}{k_t^2} \nabla_t E_z, \quad \mathbf{H}_t = -\frac{j\omega\epsilon}{k_t^2} \hat{z} \times \nabla_t E_z. \quad (5.1.20)$$

Similarly, to analyze TE waveguide modes, we first solve the boundary-value problem defined by the partial differential equation in Equation 5.1.16 and the boundary condition in Equation 5.1.19 for H_z and k_t . Once H_z and k_t are solved for, the other field components can be obtained from Equations 5.1.11 and 5.1.12, or, more explicitly,

$$\mathbf{E}_t = \frac{j\omega\mu}{k_t^2} \hat{z} \times \nabla_t H_z, \quad \mathbf{H}_t = -\frac{jk_z}{k_t^2} \nabla_t H_z. \quad (5.1.21)$$

The fact that either E_z or H_z has to exist in this type of waveguide can be understood easily from the first two Maxwell's equations in integral form:

$$\oint_c \mathbf{E} \cdot d\mathbf{l} = -j\omega\mu \iint_S \mathbf{H} \cdot d\mathbf{S} \quad (5.1.22)$$

$$\oint_c \mathbf{H} \cdot d\mathbf{l} = j\omega\epsilon \iint_S \mathbf{E} \cdot d\mathbf{S} + \mathbf{J}. \quad (5.1.23)$$

Consider a waveguide mode with a TM field. Since there exists no magnetic charge, the magnetic field lines close upon themselves. The closed-contour integration along a magnetic field line results in a non-zero left-hand side in Equation 5.1.23. Since there is no inner conductor in the type of waveguide considered here, $\mathbf{J} = 0$; hence, the electric field \mathbf{E} must have a z -component in order to satisfy Equation 5.1.23. The corresponding field is a TM waveguide mode. Similarly, for a waveguide mode with a TE field, the electric field lines either close upon themselves or originate from and terminate at the waveguide's conducting surface. The closed-contour integration along an electric field line generally results in a non-zero left-hand side in Equation 5.1.22. To satisfy Equation 5.1.22, the magnetic field must have a z -component, which corresponds to a TE waveguide mode.

Because of the existence of the z -component in either the electric or magnetic field, the power flow density in the waveguide, as represented by the Poynting vector $\mathbf{S} = \frac{1}{2} \mathbf{E} \times \mathbf{H}^*$, does not point exactly into the z -direction, although the net power flow does. Therefore, electromagnetic waves in a waveguide propagate in a zigzag manner. This phenomenon will be illustrated more clearly later. However, if a waveguide is made of two or more separate conductors and filled with a homogeneous material, such as a coaxial waveguide or a parallel-wire transmission line, it is possible to have a TE field whose closed-contour integration vanishes because of the different potentials on the two conductors. Hence, a TE field does not have to be supported by a magnetic field with a z -component. Although the closed-contour integration of a magnetic field is still non-zero because of the absence of magnetic charges, a TM field can now be supported by the electric current on a conductor enclosed by the magnetic field lines. Hence, a TM field does not have to be supported by an electric field with a z -component. In this case, the waveguide mode is called *transverse electromagnetic* (TEM) mode, since both the electric and magnetic fields are transverse to the propagation direction. The propagation constant of this

mode is k . Because both the electric and magnetic fields are transverse to the z -direction, the Poynting vector $\mathbf{S} = \frac{1}{2} \mathbf{E} \times \mathbf{H}^*$ points directly into the z -direction, meaning that the electromagnetic wave propagates straight in the z -direction. From Equations 5.1.5–5.1.8, we find that for a TEM mode, the fields are governed by the following equations:

$$\nabla_t \times \mathbf{E}_t = 0, \quad \hat{z} \times \mathbf{E}_t = \eta \mathbf{H}_t \quad (5.1.24)$$

$$\nabla_t \times \mathbf{H}_t = 0, \quad \hat{z} \times \mathbf{H}_t = -\frac{1}{\eta} \mathbf{E}_t \quad (5.1.25)$$

where $\eta = \sqrt{\mu/\epsilon}$.

The discussions above illustrated clearly why the waveguide modes in a homogeneously filled uniform waveguide as shown in Figure 5.1 can be classified into either TE or TM modes. Mathematically, the field expressions for these two sets of modes can also be derived based on vector potentials. From Equation 2.1.38, it is obvious that by letting $\mathbf{A} = \hat{z} A_z$ and $\mathbf{F} = 0$, where A_z satisfies the Helmholtz equation $\nabla^2 A_z + k^2 A_z = 0$, we obtain a magnetic field with no z -component,

$$\mathbf{E} = -j\omega \hat{z} A_z + \frac{1}{j\omega \mu \epsilon} \frac{\partial}{\partial z} \nabla A_z \quad (5.1.26)$$

$$\mathbf{H} = \frac{1}{\mu} \nabla \times (\hat{z} A_z) = -\frac{1}{\mu} \hat{z} \times \nabla A_z \quad (5.1.27)$$

which represents a TM field. Similarly, we can see from Equation 2.1.37 that by letting $\mathbf{A} = 0$ and $\mathbf{F} = \hat{z} F_z$, where F_z satisfies the Helmholtz equation $\nabla^2 F_z + k^2 F_z = 0$, we obtain an electric field with no z -component,

$$\mathbf{E} = -\frac{1}{\epsilon} \nabla \times (\hat{z} F_z) = \frac{1}{\epsilon} \hat{z} \times \nabla F_z \quad (5.1.28)$$

$$\mathbf{H} = -j\omega \hat{z} F_z + \frac{1}{j\omega \mu \epsilon} \frac{\partial}{\partial z} \nabla F_z \quad (5.1.29)$$

which represents a TE field. These expressions provide an alternative approach to analyzing waveguide modes. In this approach, we first find the general solution to A_z and F_z by solving the Helmholtz equation, then obtain the field expressions from Equations 5.1.26–5.1.29, and finally apply the boundary conditions to the fields to determine k_i and k_z .

5.1.2 General Characteristics

Before we analyze a specific rectangular waveguide, let us first discuss some general characteristics that are applicable to all homogeneously filled uniform waveguides based on the equations obtained above.

When we solve the Helmholtz equation (Eq. 5.1.15) and apply the boundary condition (Eq. 5.1.17), we obtain an infinite number of solutions, which can be denoted as k_{ti} and E_{zi} ($i = 1, 2, \dots$) and correspond to TM modes. Similarly, when we solve the Helmholtz equation (Eq. 5.1.16) and apply the boundary condition (Eq. 5.1.19), we obtain another infinite number of solutions, which can be denoted as k_{ti} and H_{zi} ($i = 1, 2, \dots$) and correspond to TE modes. The second set of k_{ti} is not necessarily the same as the first set, although the same notation is used for convenience. For each mode, the propagation constant is given by

$$k_z = \sqrt{k^2 - k_t^2} = \sqrt{\omega^2 \mu \epsilon - k_t^2} \quad (5.1.30)$$

where the mode index is omitted here as well as in the formulas below for simplicity (but it is understood that these formulas are applicable to each mode). It is obvious that this propagation constant can have either a real or an imaginary value, depending on the frequency:

$$k_z = \begin{cases} \sqrt{\omega^2 \mu \epsilon - k_t^2} & \omega \sqrt{\mu \epsilon} > k_t \\ 0 & \omega \sqrt{\mu \epsilon} = k_t \\ -j\sqrt{k_t^2 - \omega^2 \mu \epsilon} & \omega \sqrt{\mu \epsilon} < k_t \end{cases} \quad (5.1.31)$$

When $\omega \sqrt{\mu \epsilon} > k_t$, the mode can propagate in the waveguide. On the other hand, when $\omega \sqrt{\mu \epsilon} < k_t$, the mode will be attenuated. The point when the mode changes from propagation to attenuation is called *cutoff*. The corresponding *cutoff wavenumber*, *cutoff wavelength*, and *cutoff frequency* are given by

$$k_c = k_t, \quad \lambda_c = \frac{2\pi}{k_c}, \quad \omega_c = \frac{k_c}{\sqrt{\mu \epsilon}} \quad \text{or} \quad f_c = \frac{k_c}{2\pi \sqrt{\mu \epsilon}}. \quad (5.1.32)$$

This cutoff phenomenon is distinctly different from the electrical behavior in traditional two-wire transmission lines and coaxial cables, where electromagnetic waves of any frequency can propagate. This characteristic is due to the zigzag propagation of waves in a waveguide. As will be seen, waves at cutoff bounce around exactly in the transverse directions; consequently, they do not transmit power in the longitudinal direction.

From the propagation constant k_z given in Equation 5.1.31, we can define a guided wavelength λ_g :

$$k_z = \frac{2\pi}{\lambda_g}, \quad \lambda_g = \frac{2\pi}{k_z} = \frac{\lambda}{\sqrt{1 - (k_c/k)^2}} \quad (5.1.33)$$

which represents the wave variation along the z -direction within one cycle. The associated phase velocity is then given by

$$v_p = \frac{\omega}{k_z} = \frac{c}{\sqrt{1 - (k_c/k)^2}} \quad (5.1.34)$$

where $c = 1/\sqrt{\mu \epsilon}$. It is obvious that the phase velocity in a waveguide is greater than the speed of light. However, the group velocity is not [2]. Based on its definition in Equation 4.2.36, we obtain the group velocity as

$$v_g = \left(\frac{dk_z}{d\omega} \right)^{-1} = c \sqrt{1 - \left(\frac{k_c}{k} \right)^2} \quad (5.1.35)$$

which is smaller than the speed of light. As mentioned earlier, the energy propagates in a waveguide in a zigzag manner; hence, its velocity in the z -direction is also smaller than the speed of light. Consider a TM mode as an example. Based on Equation 5.1.20, the time-average total power flow in the waveguide is

$$\bar{P}_z = \frac{1}{2} \iint_{\Omega} \operatorname{Re}(\mathbf{E} \times \mathbf{H}^*) \cdot \hat{z} d\Omega = \frac{\omega \epsilon k_z}{2k_t^4} \iint_{\Omega} (\nabla_t E_z) \cdot (\nabla_t E_z^*) d\Omega. \quad (5.1.36)$$

The time-average electric energy per unit length is

$$\bar{W}_e = \frac{1}{4} \iint_{\Omega} \epsilon \mathbf{E} \cdot \mathbf{E}^* d\Omega = \frac{\epsilon}{4} \iint_{\Omega} \left[\frac{k_z^2}{k_t^4} (\nabla_t E_z) \cdot (\nabla_t E_z^*) + E_z \cdot E_z^* \right] d\Omega \quad (5.1.37)$$

and the time-average magnetic energy per unit length is

$$\bar{W}_m = \frac{1}{4} \iint_{\Omega} \mu \mathbf{H} \cdot \mathbf{H}^* d\Omega = \frac{\mu}{4} \frac{k^2}{k_t^4} \iint_{\Omega} (\nabla_t E_z) \cdot (\nabla_t E_z^*) d\Omega. \quad (5.1.38)$$

Using the vector identity

$$\nabla_t \cdot (E_z \nabla_t E_z^*) = (\nabla_t E_z) \cdot (\nabla_t E_z^*) + E_z \nabla_t \cdot \nabla_t E_z^* = (\nabla_t E_z) \cdot (\nabla_t E_z^*) + E_z \nabla_t^2 E_z^* \quad (5.1.39)$$

and the two-dimensional divergence theorem, we have

$$\begin{aligned} \iint_{\Omega} (\nabla_t E_z) \cdot (\nabla_t E_z^*) d\Omega &= \oint_{\Gamma} E_z (\nabla_t E_z^*) \cdot \hat{n} d\Gamma - \iint_{\Omega} E_z \nabla_t^2 E_z^* d\Omega \\ &= k_t^2 \iint_{\Omega} E_z E_z^* d\Omega. \end{aligned} \quad (5.1.40)$$

To arrive at this, we have applied the boundary condition (Eq. 5.1.17) and the Helmholtz equation (Eq. 5.1.15). Substituting Equation 5.1.40 into Equations 5.1.36–5.1.38, we obtain the energy velocity in the waveguide as

$$v_e = \frac{\bar{P}_z}{\bar{W}_e + \bar{W}_m} = \frac{\omega k_z}{k^2} = c \sqrt{1 - \left(\frac{k_c}{k} \right)^2} \quad (5.1.41)$$

which is the same as the group velocity. It can be shown similarly that the energy velocity of the TE mode is the same as that given in Equation 5.1.41.

Another important parameter that characterizes wave propagation is the wave impedance in the direction of propagation. From Equations 5.1.20 and 5.1.21, we find that for a TM mode, the wave impedance is given by

$$Z_w^{\text{TM}} = \frac{k_z}{\omega \epsilon} = \eta \sqrt{1 - \left(\frac{k_c}{k} \right)^2} = \begin{cases} \text{Resistive} & f > f_c \\ 0 & f = f_c \\ \text{Capacitive} & f < f_c \end{cases} \quad (5.1.42)$$

whereas for a TE mode, the wave impedance is given by

$$Z_w^{\text{TE}} = \frac{\omega \mu}{k_z} = \frac{\eta}{\sqrt{1 - (k_c/k)^2}} = \begin{cases} \text{Resistive} & f > f_c \\ \infty & f = f_c \\ \text{Inductive} & f < f_c \end{cases} \quad (5.1.43)$$

where $\eta = \sqrt{\mu/\epsilon}$. At cutoff, a waveguide appears as a short circuit to TM modes and an open circuit for TE modes.

A very important property of waveguide modes is their orthogonality [3,4]. It can be shown that the fields of different modes are orthogonal to each other. We first consider the case for the TM modes. First, by applying the second scalar Green's theorem (Eq.

1.1.44) to a very short section of a waveguide, we can easily derive its two-dimensional version,

$$\iint_{\Omega} (a \nabla^2 b - b \nabla^2 a) d\Omega = \oint_{\Gamma} \left(a \frac{\partial b}{\partial n} - b \frac{\partial a}{\partial n} \right) d\Gamma. \quad (5.1.44)$$

Now we let $a = e_{zi}^{\text{TM}}$ and $b = e_{zj}^{\text{TM}}$, where e_z is related to E_z according to Equation 5.1.1 and i and j denote the mode indices. The right-hand side of Equation 5.1.44 vanishes because of the boundary condition in Equation 5.1.17. With the substitution of Equation 5.1.15, the left-hand side becomes

$$(k_{ti}^2 - k_{tj}^2) \iint_{\Omega} e_{zi}^{\text{TM}} \cdot e_{zj}^{\text{TM}} d\Omega = 0. \quad (5.1.45)$$

If $k_{ti} \neq k_{tj}$, we have

$$\iint_{\Omega} e_{zi}^{\text{TM}} \cdot e_{zj}^{\text{TM}} d\Omega = 0 \quad i \neq j. \quad (5.1.46)$$

For degenerate modes, which have physically different field distributions but with the same value of k_t (that is, $k_{ti} = k_{tj}$), we can take e_{zi}^{TM} as the first independent mode and subtract its projection from e_{zj}^{TM} to construct the second orthogonal mode as $\tilde{e}_{zj}^{\text{TM}} = e_{zj}^{\text{TM}} - \alpha e_{zi}^{\text{TM}}$, with α given by

$$\alpha = \frac{\iint_{\Omega} e_{zi}^{\text{TM}} \cdot e_{zj}^{\text{TM}} d\Omega}{\iint_{\Omega} e_{zi}^{\text{TM}} \cdot e_{zi}^{\text{TM}} d\Omega}. \quad (5.1.47)$$

This process can be extended to the case with multiple degenerate modes [3].

Next, by applying the first scalar Green's theorem (Eq. 1.1.43) to a thin slice of a waveguide, we can easily derive its two-dimensional version,

$$\iint_{\Omega} (a \nabla^2 b + \nabla a \cdot \nabla b) d\Omega = \oint_{\Gamma} a \frac{\partial b}{\partial n} d\Gamma. \quad (5.1.48)$$

Again, we let $a = e_{zi}^{\text{TM}}$ and $b = e_{zj}^{\text{TM}}$ and make use of Equations 5.1.15 and 5.1.17 to find

$$\iint_{\Omega} (\nabla e_{zi}^{\text{TM}} \cdot \nabla e_{zj}^{\text{TM}} - k_{tj}^2 e_{zi}^{\text{TM}} \cdot e_{zj}^{\text{TM}}) d\Omega = 0. \quad (5.1.49)$$

Application of Equation 5.1.46 to this equation yields

$$\iint_{\Omega} \nabla e_{zi}^{\text{TM}} \cdot \nabla e_{zj}^{\text{TM}} d\Omega = 0 \quad i \neq j. \quad (5.1.50)$$

With this result, we can immediately see from Equation 5.1.20 that

$$\iint_{\Omega} \mathbf{e}_{ti}^{\text{TM}} \cdot \mathbf{e}_{tj}^{\text{TM}} d\Omega = 0 \quad i \neq j \quad (5.1.51)$$

$$\iint_{\Omega} \mathbf{h}_{ti}^{\text{TM}} \cdot \mathbf{h}_{tj}^{\text{TM}} d\Omega = 0 \quad i \neq j \quad (5.1.52)$$

$$\iint_{\Omega} (\mathbf{e}_{ti}^{\text{TM}} \times \mathbf{h}_{tj}^{\text{TM}}) \cdot \hat{z} d\Omega = 0 \quad i \neq j. \quad (5.1.53)$$

By following a similar procedure, we can show that for the TE modes, the following orthogonal relations hold:

$$\iint_{\Omega} h_{zi}^{\text{TE}} \cdot h_{zj}^{\text{TE}} d\Omega = 0 \quad i \neq j \quad (5.1.54)$$

$$\iint_{\Omega} \mathbf{e}_{ti}^{\text{TE}} \cdot \mathbf{e}_{tj}^{\text{TE}} d\Omega = 0 \quad i \neq j \quad (5.1.55)$$

$$\iint_{\Omega} \mathbf{h}_{ti}^{\text{TE}} \cdot \mathbf{h}_{tj}^{\text{TE}} d\Omega = 0 \quad i \neq j \quad (5.1.56)$$

$$\iint_{\Omega} (\mathbf{e}_{ti}^{\text{TE}} \times \mathbf{h}_{tj}^{\text{TE}}) \cdot \hat{z} d\Omega = 0 \quad i \neq j. \quad (5.1.57)$$

We can further show that both TE and TM modes are mutually orthogonal:

$$\iint_{\Omega} e_{zi}^{\text{TM}} \cdot h_{zj}^{\text{TE}} d\Omega = 0 \quad (5.1.58)$$

$$\iint_{\Omega} \mathbf{e}_{ti}^{\text{TM}} \cdot \mathbf{e}_{tj}^{\text{TE}} d\Omega = 0 \quad (5.1.59)$$

$$\iint_{\Omega} \mathbf{h}_{ti}^{\text{TM}} \cdot \mathbf{h}_{tj}^{\text{TE}} d\Omega = 0 \quad (5.1.60)$$

$$\iint_{\Omega} (\mathbf{e}_{ti}^{\text{TM}} \times \mathbf{h}_{tj}^{\text{TE}}) \cdot \hat{z} d\Omega = 0 \quad (5.1.61)$$

$$\iint_{\Omega} (\mathbf{h}_{ti}^{\text{TM}} \times \mathbf{e}_{tj}^{\text{TE}}) \cdot \hat{z} d\Omega = 0. \quad (5.1.62)$$

To show Equations 5.1.59–5.1.62, we have to prove that

$$\iint_{\Omega} (\hat{z} \times \nabla e_{zi}^{\text{TM}}) \cdot \nabla h_{zj}^{\text{TE}} d\Omega = 0. \quad (5.1.63)$$

This can be accomplished by first rewriting the integrand as

$$(\hat{z} \times \nabla e_{zi}^{\text{TM}}) \cdot \nabla h_{zj}^{\text{TE}} = -\nabla h_{zj}^{\text{TE}} \cdot [\nabla \times (\hat{z} e_{zi}^{\text{TM}})] = -\nabla \cdot (\hat{z} e_{zi}^{\text{TM}} \times \nabla h_{zj}^{\text{TE}}) \quad (5.1.64)$$

because $\nabla \times \nabla h_{zj}^{\text{TE}} \equiv 0$ and then substituting it into the two-dimensional Gauss' divergence theorem to find

$$\iint_{\Omega} (\hat{z} \times \nabla e_{zi}^{\text{TM}}) \cdot \nabla h_{zj}^{\text{TE}} d\Omega = -\oint_{\Gamma} (\hat{z} e_{zi}^{\text{TM}} \times \nabla h_{zj}^{\text{TE}}) \cdot \hat{n} d\Gamma. \quad (5.1.65)$$

The right-hand side vanishes because of the boundary conditions on Γ .

The orthogonal relations derived above are useful for the analysis of fields excited by currents in waveguides. They also reveal the fact that the energies and powers of different modes are not coupled. Therefore, the total energy of an electromagnetic wave is the sum of the energies of its individual modes, and the total power flow is the sum of the power flows of its individual modes.

5.1.3 Uniform Rectangular Waveguide

As discussed above, a uniform waveguide can support both TE and TM modes. Assuming that the modes propagate in the z -direction with a propagation constant of k_z , the field

components for the TM modes are given by Equation 5.1.20, which can be written more explicitly as

$$E_x = -\frac{jk_z}{k_t^2} \frac{\partial E_z}{\partial x}, \quad H_x = \frac{j\omega\epsilon}{k_t^2} \frac{\partial E_z}{\partial y} \quad (5.1.66)$$

$$E_y = -\frac{jk_z}{k_t^2} \frac{\partial E_z}{\partial y}, \quad H_y = -\frac{j\omega\epsilon}{k_t^2} \frac{\partial E_z}{\partial x} \quad (5.1.67)$$

whereas the field components for the TE modes are given by Equation 5.1.21, which can be written as

$$E_x = -\frac{j\omega\mu}{k_t^2} \frac{\partial H_z}{\partial y}, \quad H_x = -\frac{jk_z}{k_t^2} \frac{\partial H_z}{\partial x} \quad (5.1.68)$$

$$E_y = \frac{j\omega\mu}{k_t^2} \frac{\partial H_z}{\partial x}, \quad H_y = -\frac{jk_z}{k_t^2} \frac{\partial H_z}{\partial y}. \quad (5.1.69)$$

Alternatively, the analysis of the TE and TM modes can be performed directly in terms of A_z and F_z , both of which satisfy the Helmholtz equation [5,6]. The field expressions for the TM modes can be derived from Equations 5.1.26 and 5.1.27, which, in rectangular coordinates, become

$$E_x = -\frac{j}{\omega\mu\epsilon} \frac{\partial^2 A_z}{\partial x \partial z}, \quad H_x = \frac{1}{\mu} \frac{\partial A_z}{\partial y} \quad (5.1.70)$$

$$E_y = -\frac{j}{\omega\mu\epsilon} \frac{\partial^2 A_z}{\partial y \partial z}, \quad H_y = -\frac{1}{\mu} \frac{\partial A_z}{\partial x} \quad (5.1.71)$$

$$E_z = -\frac{j}{\omega\mu\epsilon} \left(\frac{\partial^2 A_z}{\partial z^2} + k^2 A_z \right), \quad H_z = 0. \quad (5.1.72)$$

The field expressions for the TE modes can be derived from Equation 5.1.28 and 5.1.29, which become

$$E_x = -\frac{1}{\epsilon} \frac{\partial F_z}{\partial y}, \quad H_x = -\frac{j}{\omega\mu\epsilon} \frac{\partial^2 F_z}{\partial x \partial z} \quad (5.1.73)$$

$$E_y = \frac{1}{\epsilon} \frac{\partial F_z}{\partial x}, \quad H_y = -\frac{j}{\omega\mu\epsilon} \frac{\partial^2 F_z}{\partial y \partial z} \quad (5.1.74)$$

$$E_z = 0, \quad H_z = -\frac{j}{\omega\mu\epsilon} \left(\frac{\partial^2 F_z}{\partial z^2} + k^2 F_z \right). \quad (5.1.75)$$

Both approaches involve a similar amount of work. The analysis in terms of E_z and H_z is usually more convenient for those who are familiar with boundary conditions on a conducting surface as it avoids the use of auxiliary variables A_z and F_z .

Consider a rectangular waveguide that is infinitely long along the z -axis, is uniformly filled with a homogeneous material having a permittivity of ϵ and a permeability of μ , and has a cross-section of $a \times b$ (Fig. 5.2). Since E_z satisfies the Helmholtz

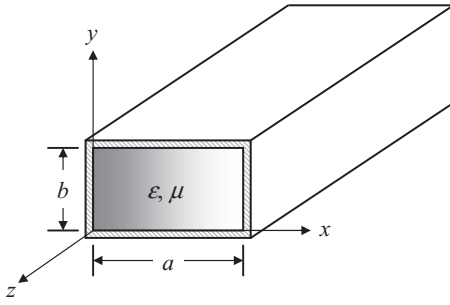


Figure 5.2 Uniformly filled rectangular waveguide.

equation $\nabla^2 E_z + k^2 E_z = 0$, based on the solution by separation of variables, it has the general form

$$E_z(x, y, z) = (A \cos k_x x + B \sin k_x x)(C \cos k_y y + D \sin k_y y) e^{-jk_z z} \quad (5.1.76)$$

where $k_x^2 + k_y^2 + k_z^2 = k^2 = \omega^2 \mu \epsilon$. By applying the boundary conditions at the conducting wall of the waveguide, $E_z|_{x=0} = E_z|_{x=a} = 0$ and $E_z|_{y=0} = E_z|_{y=b} = 0$, we find that $A = 0$, $C = 0$, $\sin k_x a = 0$, and $\sin k_y b = 0$. The last two equations are called *characteristic equations* that determine *characteristic values* k_x and k_y . The solutions to these two equations are

$$k_x = \frac{m\pi}{a} \quad m = 1, 2, \dots; \quad k_y = \frac{n\pi}{b} \quad n = 1, 2, \dots \quad (5.1.77)$$

Hence, the propagation constant is given by

$$k_{zmn} = \sqrt{k^2 - k_x^2 - k_y^2} = \sqrt{\omega^2 \mu \epsilon - \left(\frac{m\pi}{a}\right)^2 - \left(\frac{n\pi}{b}\right)^2}. \quad (5.1.78)$$

With this, Equation 5.1.76 can be written as

$$E_z = E_{mn} \sin \frac{m\pi x}{a} \sin \frac{n\pi y}{b} e^{-jk_{zmn} z} \quad (5.1.79)$$

where E_{mn} is a constant. Substituting this into Equations 5.1.66 and 5.1.67, we obtain the other field components

$$E_x = -E_{mn} \frac{jk_{zmn}}{k_{zmn}^2} \frac{m\pi}{a} \cos \frac{m\pi x}{a} \sin \frac{n\pi y}{b} e^{-jk_{zmn} z} \quad (5.1.80)$$

$$E_y = -E_{mn} \frac{jk_{zmn}}{k_{zmn}^2} \frac{n\pi}{b} \sin \frac{m\pi x}{a} \cos \frac{n\pi y}{b} e^{-jk_{zmn} z} \quad (5.1.81)$$

$$H_x = E_{mn} \frac{j\omega \epsilon}{k_{zmn}^2} \frac{n\pi}{b} \sin \frac{m\pi x}{a} \cos \frac{n\pi y}{b} e^{-jk_{zmn} z} \quad (5.1.82)$$

$$H_y = -E_{mn} \frac{j\omega \epsilon}{k_{zmn}^2} \frac{m\pi}{a} \cos \frac{m\pi x}{a} \sin \frac{n\pi y}{b} e^{-jk_{zmn} z} \quad (5.1.83)$$

$$H_z = 0 \quad (5.1.84)$$

where $k_{mn}^2 = (m\pi/a)^2 + (n\pi/b)^2$. These represent the modal field of the TM_{mn} mode. The cutoff wavenumbers, wavelengths, and frequencies are given by

$$k_{cmn} = k_{tmn} = \sqrt{\left(\frac{m\pi}{a}\right)^2 + \left(\frac{n\pi}{b}\right)^2} \quad (5.1.85)$$

$$\lambda_{cmn} = \frac{2\pi}{k_{cmn}} = 2\sqrt{\sqrt{\left(\frac{m}{a}\right)^2 + \left(\frac{n}{b}\right)^2}} \quad (5.1.86)$$

$$f_{cmn} = \frac{1}{2\sqrt{\mu\epsilon}} \sqrt{\left(\frac{m}{a}\right)^2 + \left(\frac{n}{b}\right)^2}. \quad (5.1.87)$$

The first TM mode is the TM_{11} mode, whose cutoff wavelength and frequency are given by

$$\lambda_{c11} = \frac{2ab}{\sqrt{a^2 + b^2}}, \quad f_{c11} = \frac{\sqrt{a^2 + b^2}}{2ab\sqrt{\mu\epsilon}}. \quad (5.1.88)$$

Substituting Equation 5.1.85 into Equations 5.1.33–5.1.35, 5.1.41, and 5.1.42, we obtain the expressions for the guided wavelength, phase, group, and energy velocities, and wave impedance.

For the TE modes, since H_z satisfies the Helmholtz equation $\nabla^2 H_z + k^2 H_z = 0$, it also has the general form

$$H_z(x, y, z) = (A' \cos k_x x + B' \sin k_x x)(C' \cos k_y y + D' \sin k_y y)e^{-jk_z z} \quad (5.1.89)$$

where $k_x^2 + k_y^2 + k_z^2 = k^2 = \omega^2 \mu\epsilon$. The boundary conditions in this case are $E_y|_{x=0} = E_y|_{x=a} = 0$ and $E_x|_{y=0} = E_x|_{y=b} = 0$, which are equivalent to

$$\left. \frac{\partial H_z}{\partial x} \right|_{x=0,a} = 0, \quad \left. \frac{\partial H_z}{\partial y} \right|_{y=0,b} = 0 \quad (5.1.90)$$

respectively. By applying these boundary conditions, we find that $B' = 0$, $D' = 0$, $\sin k_x a = 0$, and $\sin k_y b = 0$. The last two equations are called characteristic equations that determine characteristic values k_x and k_y . The solutions to these two equations are

$$k_x = \frac{m\pi}{a} \quad m = 0, 1, 2, \dots; \quad k_y = \frac{n\pi}{b} \quad n = 0, 1, 2, \dots \quad (5.1.91)$$

except for $m = n = 0$, because this would yield a trivial solution. Hence, the propagation constant has the same form as Equation 5.1.78. Equation 5.1.89 can be written as

$$H_z = H_{mn} \cos \frac{m\pi x}{a} \cos \frac{n\pi y}{b} e^{-jk_{zmn} z} \quad (5.1.92)$$

where H_{mn} denotes a constant. The other field components are given by

$$E_x = H_{mn} \frac{j\omega\mu}{k_{tmn}^2} \frac{n\pi}{b} \cos \frac{m\pi x}{a} \sin \frac{n\pi y}{b} e^{-jk_{zmn} z} \quad (5.1.93)$$

$$E_y = -H_{mn} \frac{j\omega\mu}{k_{tmm}^2} \frac{m\pi}{a} \sin \frac{m\pi x}{a} \cos \frac{n\pi y}{b} e^{-jk_{zmn}z} \quad (5.1.94)$$

$$E_z = 0 \quad (5.1.95)$$

$$H_x = H_{mn} \frac{jk_{zmn}}{k_{tmm}^2} \frac{m\pi}{a} \sin \frac{m\pi x}{a} \cos \frac{n\pi y}{b} e^{-jk_{zmn}z} \quad (5.1.96)$$

$$H_y = H_{mn} \frac{jk_{zmn}}{k_{tmm}^2} \frac{n\pi}{b} \cos \frac{m\pi x}{a} \sin \frac{n\pi y}{b} e^{-jk_{zmn}z}. \quad (5.1.97)$$

These represent the modal field of the TE_{mn} mode. The cutoff wavenumbers, wavelengths, and frequencies are the same as those for the TM_{mn} mode except that now both m and n start from zero, excluding the case with $m = n = 0$. Assuming that $a > b$, the first TE mode is the TE_{10} mode, whose cutoff wavelength and frequency are given by

$$\lambda_{c10} = 2a, \quad f_{c10} = \frac{1}{2a\sqrt{\mu\epsilon}}. \quad (5.1.98)$$

The next ones are the TE_{20} and TE_{01} modes, whose cutoff wavelengths and frequencies are given by

$$\lambda_{c20} = a, \quad f_{c20} = \frac{1}{a\sqrt{\mu\epsilon}} \quad (5.1.99)$$

$$\lambda_{c01} = 2b, \quad f_{c01} = \frac{1}{2b\sqrt{\mu\epsilon}}. \quad (5.1.100)$$

The guided wavelength and phase, group, and energy velocities are also the same as those for the TM_{mn} modes except for the wave impedance, which can be obtained from Equation 5.1.43.

Comparing Equations 5.1.98–5.1.100 with Equation 5.1.88, it is obvious that the dominant mode among all the modes in a rectangular waveguide with $a > b$ is the TE_{10} mode. The next mode would be either the TE_{20} or the TE_{01} mode, depending on the relative value of a with respect to b . These are followed by the TE_{11} and TM_{11} modes. The distribution of the cutoff frequencies for a rectangular waveguide with $a/b = 2$ is shown in Figure 5.3. In most applications, a waveguide is used in the single-mode frequency range, where only the TE_{10} mode propagates.

Equations 5.1.79–5.1.84 and Equation 5.1.92–5.1.97 provide complete information about the distribution of the modal fields. The transverse field distribution of the first 30 modes in a rectangular waveguide with $a/b = 2$ is plotted in Figure 5.4. The solid lines represent electric field lines, and the dashed lines represent the magnetic field lines. For the TE modes, the electric field lines are confined in the transverse plane (either forming

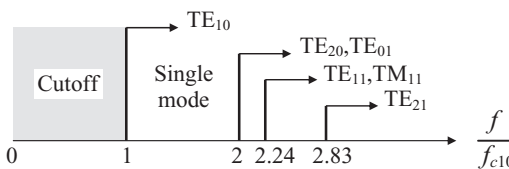


Figure 5.3 Cutoff frequency distribution for a 2:1 rectangular waveguide.

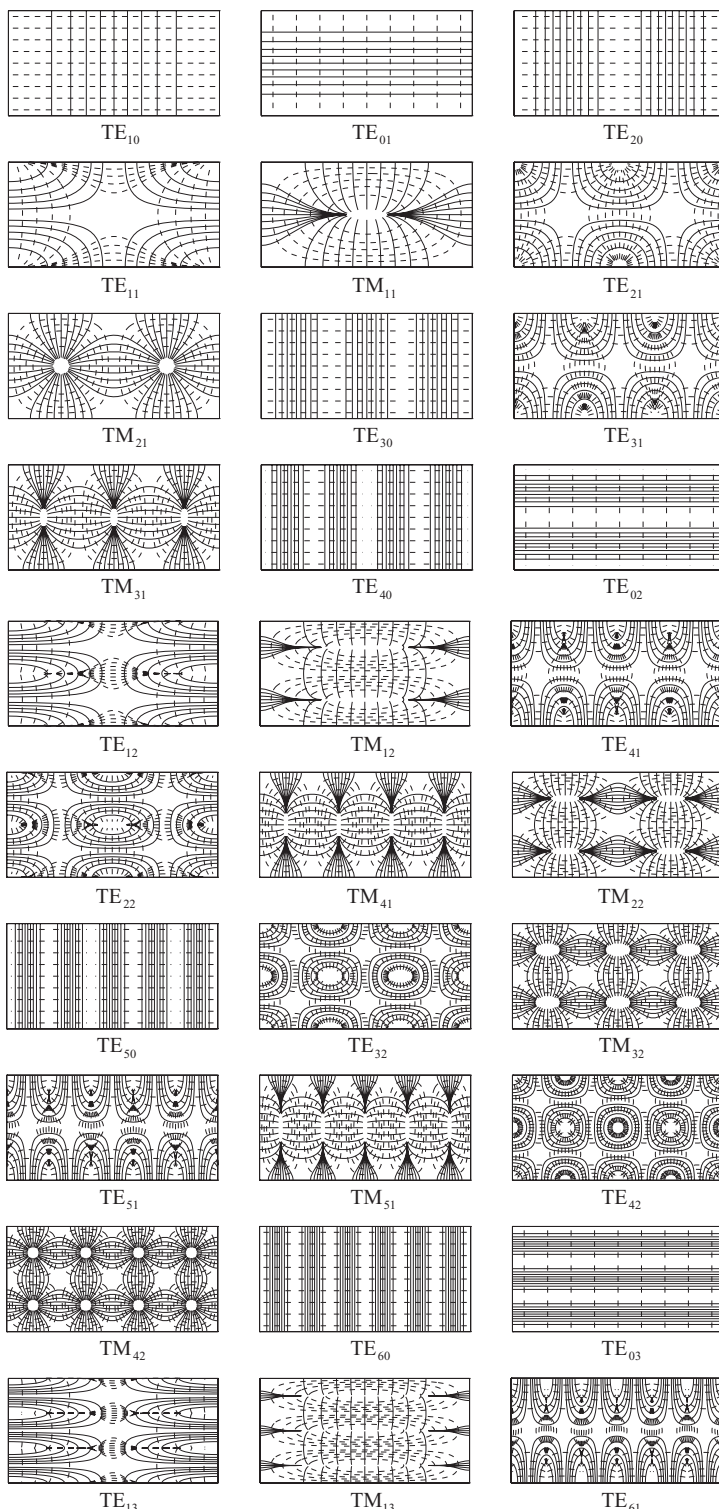


Figure 5.4 Transverse field distribution of the first 30 modes in a 2:1 rectangular waveguide.

self-closed contours or originating and terminating at the waveguide wall because of the surface electric charges there), whereas the magnetic field lines will turn into the longitudinal direction at the places where the dashed lines end. Conversely, for the TM modes, the magnetic field lines are confined in the transverse plane (always forming self-closed contours since there are no magnetic charges), whereas the electric field lines can turn into the longitudinal direction at the places where the solid lines end. The field distribution in the longitudinal direction can also be visualized using the derived field expressions. From the field distribution, we can also easily find the surface current distribution on the waveguide wall ($\mathbf{J}_s = \hat{n} \times \mathbf{H}$). Having a good understanding of the surface current distributions for each mode is very helpful to designing waveguide devices. For example, if one intends to cut a thin slot on the waveguide wall without disturbing the field inside the waveguide, the slot should be cut along the electric current lines. On the other hand, if the goal is to couple the field from inside the waveguide to the outside, as in the case of a waveguide slotted antenna, then the slot should be cut across the electric current lines so that a significant field can be built across the slot.

Since most rectangular waveguides operate with the dominant TE_{10} mode, it is worthwhile to examine its field distribution in more detail. The non-zero components of the electric and magnetic fields of the TE_{10} mode are given by

$$E_y = -H_{10} \frac{j\omega\mu a}{\pi} \sin \frac{\pi x}{a} e^{-jk_{z10}z} \quad (5.1.101)$$

$$H_x = H_{10} \frac{jk_{z10}a}{\pi} \sin \frac{\pi x}{a} e^{-jk_{z10}z} \quad (5.1.102)$$

$$H_z = H_{10} \cos \frac{\pi x}{a} e^{-jk_{z10}z}. \quad (5.1.103)$$

The surface current density on the top and bottom walls of the waveguide is

$$\mathbf{J}_s = \left(\mp \hat{x} \cos \frac{\pi x}{a} \pm \hat{z} \frac{jk_{z10}a}{\pi} \sin \frac{\pi x}{a} \right) H_{10} e^{-jk_{z10}z} \quad (5.1.104)$$

and that on the side walls of the waveguide is

$$\mathbf{J}_s = -\hat{y} H_{10} e^{-jk_{z10}z}. \quad (5.1.105)$$

Therefore, the current lines on the side walls are vertically directed, whereas the current lines on the top and bottom walls contain both transverse and longitudinal components (Fig. 5.5). The longitudinal component is dominant at the center ($x = a/2$) and the transverse component is dominant near the sides ($x = 0$ and $x = a$).

The field expressions (Eqs. 5.1.101–5.1.103) can also be rewritten as

$$\mathbf{E} = -\hat{y} \frac{k\eta}{k_{x10}} \frac{H_{10}}{2} \left[e^{j(k_{x10}x - k_{z10}z)} - e^{-j(k_{x10}x + k_{z10}z)} \right] \quad (5.1.106)$$

$$\mathbf{H} = \left(\hat{x} \frac{k_{z10}}{k_{x10}} + \hat{z} \right) \frac{H_{10}}{2} e^{j(k_{x10}x - k_{z10}z)} - \left(\hat{x} \frac{k_{z10}}{k_{x10}} - \hat{z} \right) \frac{H_{10}}{2} e^{-j(k_{x10}x + k_{z10}z)} \quad (5.1.107)$$

where $k_{x10} = \pi/a$. These two equations indicate that the field of the TE_{10} mode can be decomposed into two plane waves of equal amplitude propagating in two different direc-

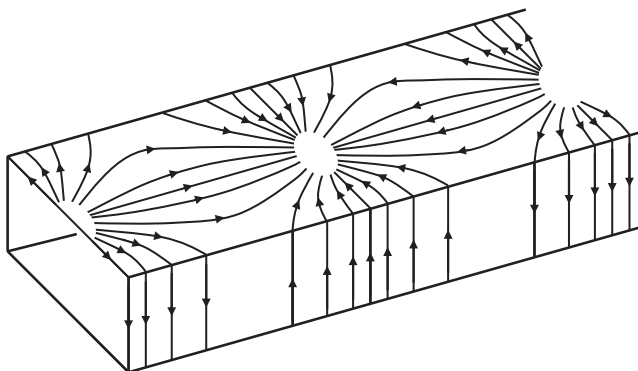


Figure 5.5 Surface current on the wall of a rectangular waveguide for the TE_{10} mode.

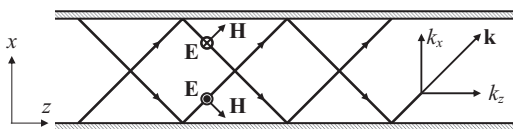


Figure 5.6 Ray picture of the TE_{10} mode propagation in a rectangular waveguide.

tions in the xz -plane, as illustrated in Figure 5.6. The angle between the propagation direction and the z -axis is given by $\vartheta_{10} = \tan^{-1}(k_{x10}/k_{z10})$. As the frequency approaches cutoff, $k_{z10} \rightarrow 0$; hence, $\vartheta_{10} \rightarrow 90^\circ$. At cutoff, the two plane waves simply bounce back and forth in the transverse direction; as a result, no power propagates in the z -direction. A similar wave propagation picture can be obtained for every waveguide mode, except that the wave propagation is no longer confined in the xz -plane, and the angle between the propagation direction and the z -axis is given by $\vartheta_{mn} = \tan^{-1}(k_{tmn}/k_{zmn})$.

5.1.4 Losses in Waveguides and Attenuation Constant

The analysis so far assumes that the waveguide is made of a perfect electric conductor and that the medium in the waveguide is completely lossless. When the conductor is imperfect and/or the medium is lossy, there will be some attenuation to propagating waves. The attenuation due to an imperfect conductor is called *conductor loss*, and the attenuation due to a lossy medium is called *dielectric loss* [6,7]. Before we analyze these two types of loss, we first derive a general formula to relate the attenuation constant to the dissipated power in a general waveguide.

For a lossy waveguide, the propagation constant becomes complex, $k_z = \beta - j\alpha$, where α denotes the attenuation constant and β denotes the phase constant. The propagating electric and magnetic fields can be expressed as

$$\mathbf{E} = \mathbf{E}_t + \hat{z}E_z = [\mathbf{e}_t(x, y) + \hat{z}e_z(x, y)]e^{-(\alpha+j\beta)z} \quad (5.1.108)$$

$$\mathbf{H} = \mathbf{H}_t + \hat{z}H_z = [\mathbf{h}_t(x, y) + \hat{z}h_z(x, y)]e^{-(\alpha+j\beta)z}. \quad (5.1.109)$$

The complex Poynting vector becomes

$$\mathbf{S} = \frac{1}{2}\mathbf{E} \times \mathbf{H}^* = \frac{1}{2}\mathbf{e} \times \mathbf{h}^* e^{-2\alpha z} \quad (5.1.110)$$

whose real part yields the time-average power flow density

$$\bar{\mathcal{J}} = \frac{1}{2} \operatorname{Re}(\mathbf{e} \times \mathbf{h}^*) e^{-2\alpha z} = \bar{\mathcal{J}}|_{z=0} e^{-2\alpha z}. \quad (5.1.111)$$

The time-average power flow in a waveguide can be obtained by integrating over the cross-section of the waveguide,

$$\bar{P}_z(z) = \iint_{\Omega} \bar{\mathcal{J}} \cdot \hat{z} d\Omega = \iint_{\Omega} \bar{\mathcal{J}}|_{z=0} \cdot \hat{z} d\Omega e^{-2\alpha z} = \bar{P}_{z0} e^{-2\alpha z}. \quad (5.1.112)$$

Its derivative with respect to z gives

$$\frac{d\bar{P}_z(z)}{dz} = -2\alpha \bar{P}_{z0} e^{-2\alpha z} \quad (5.1.113)$$

hence

$$\alpha = -\frac{1}{2\bar{P}_{z0}} \left. \frac{d\bar{P}_z(z)}{dz} \right|_{z=0}. \quad (5.1.114)$$

Therefore, the evaluation of α amounts to finding $d\bar{P}_z/dz$. This can be accomplished by applying the power conservation law in Equation 1.7.47 to a short section of the waveguide from $z = 0$ to $z = \Delta z$. This power conservation law can be rewritten as

$$\bar{P}_s = \bar{P}_e + \bar{P}_d \quad (5.1.115)$$

where \bar{P}_s denotes the time-average power supplied by a source, \bar{P}_e denotes the time-average power leaving the surface enclosing the short section, and \bar{P}_d denotes the time-average dissipated power in the section.

Now let us consider the attenuation due to the finite conductivity of the waveguide wall. In this case, both \bar{P}_s and \bar{P}_d vanish; hence, Equation 5.1.115 becomes $\bar{P}_e = 0$, which means that the power entering through the front surface at $z = 0$ equals the power exiting at the back surface at $z = \Delta z$ plus the power exiting through the inner surface of the waveguide wall, which is eventually dissipated in the imperfect conductor. This fact can be expressed mathematically as

$$\bar{P}_e = -\bar{P}_z|_{z=0} + \bar{P}_z|_{z=\Delta z} + \oint_{\Gamma} \bar{\mathcal{J}} \cdot \hat{n} d\Gamma \Delta z = 0 \quad (5.1.116)$$

from which we obtain

$$\left. \frac{d\bar{P}_z(z)}{dz} \right|_{z=0} = -\oint_{\Gamma} \bar{\mathcal{J}}|_{z=0} \cdot \hat{n} d\Gamma \quad (5.1.117)$$

where Γ is the contour enclosing Ω . Therefore, the attenuation constant due to the conductor loss can be obtained as

$$\alpha_c = \frac{\oint_{\Gamma} \bar{\mathcal{J}}|_{z=0} \cdot \hat{n} d\Gamma}{2 \iint_{\Omega} \bar{\mathcal{J}}|_{z=0} \cdot \hat{z} d\Omega} = \frac{\operatorname{Re} \oint_{\Gamma} (\mathbf{e} \times \mathbf{h}^*) \cdot \hat{n} d\Gamma}{2 \operatorname{Re} \iint_{\Omega} (\mathbf{e} \times \mathbf{h}^*) \cdot \hat{z} d\Omega}. \quad (5.1.118)$$

This expression can further be written as

$$\alpha_c = \frac{\operatorname{Re} \oint_{\Gamma} (\mathbf{e}_{tw} \times \mathbf{h}_{tw}^*) \cdot \hat{n} d\Gamma}{2 \operatorname{Re} \iint_{\Omega} (\mathbf{e}_t \times \mathbf{h}_t^*) \cdot \hat{z} d\Omega} \quad (5.1.119)$$

where \mathbf{e}_{tw} and \mathbf{h}_{tw} denote the electric and magnetic field components tangential to the waveguide wall. On the surface of an imperfect conductor with a surface impedance of $Z_s = R_s + jX_s$, the tangential electric and magnetic fields are related by $\hat{n} \times \mathbf{E}_{tw} = Z_s \mathbf{H}_{tw}$. Since $(\mathbf{e}_{tw} \times \mathbf{h}_{tw}^*) \cdot \hat{n} = (\hat{n} \times \mathbf{e}_{tw}) \cdot \mathbf{h}_{tw}^* = Z_s \mathbf{h}_{tw} \cdot \mathbf{h}_{tw}^*$, Equation 5.1.119 can be written as

$$\alpha_c = \frac{R_s \oint_{\Gamma} |\mathbf{h}_{tw}|^2 d\Gamma}{2 \operatorname{Re} \iint_{\Omega} (\mathbf{e}_t \times \mathbf{h}_t^*) \cdot \hat{z} d\Omega}. \quad (5.1.120)$$

For a good conductor, $R_s = \sqrt{\omega \mu / 2\sigma}$.

It is obvious from Equation 5.1.120 that we need to know the field distribution in a waveguide in order to evaluate the attenuation constant. For a waveguide made of an imperfect conductor, it is difficult to find the field distribution exactly. However, if the imperfect conductor is close to a perfect conductor, we can use the field distribution obtained from the corresponding perfect waveguide to approximate the field distribution in the imperfect waveguide. This method is called the *perturbational method*. For example, we can use the field distribution of the TE₁₀ mode of a perfect rectangular waveguide to evaluate the attenuation constant of the TE₁₀ mode in an imperfect rectangular waveguide. The result is

$$\alpha_c = \frac{R_s}{\eta b} \left[1 + \frac{2b}{a} \left(\frac{f_{c10}}{f} \right)^2 \right] \sqrt{1 - \left(\frac{f_{c10}}{f} \right)^2}. \quad (5.1.121)$$

As can be observed, when the frequency approaches the cutoff frequency, the attenuation increases drastically. This phenomenon can be explained easily from the picture of ray propagation in Figure 5.6. When approaching cutoff, the wave bounces more times within a unit length, causing more reflection loss because of the imperfect conducting surface.

Next we consider the attenuation due to the dielectric loss of the medium in the waveguide. Assuming that the waveguide is made of a perfect conductor, Equation 5.1.115 becomes

$$\bar{P}_e + \bar{P}_d = -\bar{P}_z|_{z=0} + \bar{P}_z|_{z=\Delta z} + \omega \epsilon'' \iint_{\Omega} |\mathbf{E}|^2 d\Omega \Delta z = 0 \quad (5.1.122)$$

which yields

$$\left. \frac{d\bar{P}_z(z)}{dz} \right|_{z=0} = -\omega \epsilon'' \iint_{\Omega} |\mathbf{E}|^2 d\Omega. \quad (5.1.123)$$

Hence, the attenuation constant due to the dielectric loss is given by

$$\alpha_d = \frac{\omega \epsilon'' \iint_{\Omega} |\mathbf{E}|^2 d\Omega}{2 \operatorname{Re} \iint_{\Omega} (\mathbf{e}_t \times \mathbf{h}_t^*) \cdot \hat{z} d\Omega}. \quad (5.1.124)$$

Again, when the dielectric loss is very small, we can use the perturbational method by assuming that the field distribution is similar to that in a waveguide with a lossless dielectric. Using this approach, we can find the attenuation constant of the TE_{10} mode in a rectangular waveguide due to the dielectric loss as

$$\alpha_d = \frac{\eta\omega\epsilon''}{2} \sqrt{1 - \left(\frac{f_{c10}}{f}\right)^2}. \quad (5.1.125)$$

Alternatively, the attenuation constant can be calculated more directly from the propagation constant

$$k_z = \sqrt{k^2 - k_c^2} = \sqrt{\omega^2 \mu \epsilon - k_c^2} = \sqrt{\omega^2 \mu (\epsilon' - j\epsilon'') - k_c^2}. \quad (5.1.126)$$

Letting $k_z = \beta - j\alpha_d$ and solving for α_d and β , we have

$$\alpha_d = \sqrt{\frac{\omega^2 \mu \epsilon' - k_c^2}{2}} \sqrt{1 + \left(\frac{\omega^2 \mu \epsilon''}{\omega^2 \mu \epsilon' - k_c^2}\right)^2 - 1} \quad (5.1.127)$$

$$\beta = \sqrt{\frac{\omega^2 \mu \epsilon' - k_c^2}{2}} \sqrt{1 + \left(\frac{\omega^2 \mu \epsilon''}{\omega^2 \mu \epsilon' - k_c^2}\right)^2 + 1}. \quad (5.1.128)$$

When $\epsilon''/\epsilon' \ll 1 - (f_c/f)^2$, these two expressions can be approximated as

$$\alpha_d \approx \frac{\eta\omega\epsilon''}{2} \sqrt{1 - \left(\frac{f_c}{f}\right)^2} \quad (5.1.129)$$

$$\beta \approx \omega \sqrt{\mu \epsilon'} \sqrt{1 - \left(\frac{f_c}{f}\right)^2}. \quad (5.1.130)$$

Equation 5.1.129 is consistent with Equation 5.1.125. Again, when the frequency approaches the cutoff frequency, the attenuation due to dielectric loss increases drastically. This phenomenon can also be explained easily from the picture of ray propagation in Figure 5.6. When approaching cutoff, the wave travels a longer distance within a unit length and thus experiences more dielectric dissipation.

5.2 UNIFORM CAVITIES

It is well known that in a perfect LC circuit, the electric current is given by $I = V/(j\omega L + 1/j\omega C) = j\omega CV/(1 - \omega^2 LC)$. Therefore, when $\omega = 1/\sqrt{LC}$, the circuit can maintain a constant current even when the excitation voltage disappears. This phenomenon is called *resonance* in a circuit. In electromagnetics, there is a similar resonance phenomenon, which happens when an electromagnetic field is excited in a container made of a perfect conductor. When the field is excited at a certain frequency, the container can sustain the electromagnetic field even after the excitation disappears. Such a container is called a *resonant cavity*. In this section, we consider a special class of cavity

that is formed by placing a perfect conductor on both ends of a section of a uniform waveguide [2–6].

5.2.1 General Theory

To determine whether a cavity can sustain an electromagnetic field, all we have to do is to find whether it can support a non-trivial solution to the source-free Maxwell's equations. For a cavity made of a section of a uniform waveguide with both ends sealed by a perfect conductor, the answer is obvious. Since the waveguide can support waves propagating in both the positive and negative z -directions, it can also support a linear combination of the waves, caused by reflections at the two ends.

Since a uniform waveguide filled with a homogeneous medium supports TE and TM waveguide modes, there are corresponding TE and TM cavity modes in a uniform cavity filled with a homogeneous medium. Assume that the cavity starts at $z = 0$ and ends at $z = c$. To satisfy the boundary conditions at the both ends, the longitudinal component of the electric field for the TM modes is given by

$$E_z = e_z(x, y) \cos k_z z \quad (5.2.1)$$

where $k_z = p\pi/c$ ($p = 0, 1, 2, \dots$). The transverse field components are given by

$$\mathbf{E}_t = -\frac{k_z}{k_t^2} \nabla_t e_z \sin k_z z, \quad \mathbf{H}_t = -\frac{j\omega\epsilon}{k_t^2} \hat{z} \times \nabla_t e_z \cos k_z z. \quad (5.2.2)$$

The k_z (determined by the length) and k_t (determined by the cross-section) satisfy the dispersion relation

$$k_t^2 + k_z^2 = k^2 = \omega^2 \mu \epsilon \quad (5.2.3)$$

which indicates that the non-trivial solution exists only at the frequency

$$\omega_r = \frac{\sqrt{k_t^2 + k_z^2}}{\sqrt{\mu \epsilon}}, \quad f_r = \frac{\sqrt{k_t^2 + k_z^2}}{2\pi\sqrt{\mu \epsilon}} \quad (5.2.4)$$

which is called the *resonant frequency* of the cavity. Since there are an infinite number of discrete k_t and k_z , a cavity has an infinite number of resonant frequencies. The field distribution for each resonant frequency is called a *resonant mode*.

The case for the TE modes is similar. The longitudinal component of the magnetic field for the TE modes is given by

$$H_z = h_z(x, y) \sin k_z z \quad (5.2.5)$$

where $k_z = p\pi/c$ ($p = 1, 2, \dots$). The transverse field components are given by

$$\mathbf{E}_t = \frac{j\omega\mu}{k_t^2} \hat{z} \times \nabla_t h_z \sin k_z z, \quad \mathbf{H}_t = \frac{k_z}{k_t^2} \nabla_t h_z \cos k_z z \quad (5.2.6)$$

where k_z and k_t also satisfy the dispersion relation in Equation 5.2.3; hence, the resonant frequencies are also given by Equation 5.2.4.

By applying the energy conservation law (Eq. 1.7.40) to a perfect cavity, it is easy to see that in a cavity, $\bar{W}_e = \bar{W}_m$. However, it can also be seen from the field expressions in Equations 5.2.1, 5.2.2, 5.2.5, and 5.2.6 that the electric and magnetic fields are completely

out of phase. When the electric energy reaches the maximum, the magnetic energy vanishes completely, and vice versa. Therefore, the electric energy converts to the magnetic energy at one moment and the magnetic energy converts back to the electric energy at another moment, and this process continues on forever, which is similar to what happens in a perfect LC circuit. Using the second vector Green's theorem (Eq. 1.1.46), it can be shown that all the cavity modes are orthogonal to each other, that is,

$$\iiint_V \mathbf{E}_i \cdot \mathbf{E}_j dV = 0, \quad \iiint_V \mathbf{H}_i \cdot \mathbf{H}_j dV = 0 \quad i \neq j \quad (5.2.7)$$

where i and j denote mode indices. This orthogonality holds even for degenerate modes that have the same resonant frequencies.

If a cavity is imperfect because of either the conductor loss of the cavity wall or the dielectric loss of the medium in the cavity or both, the cavity is characterized by the *quality factor*, defined by

$$Q = \omega \frac{\text{stored energy}}{\text{dissipated power}} = \omega \frac{\bar{W}}{\bar{P}_d} = \omega \frac{\bar{W}_e + \bar{W}_m}{\bar{P}_d}. \quad (5.2.8)$$

Since in a cavity $\bar{W}_e = \bar{W}_m$, the quality factor can also be written as

$$Q = \omega \frac{2\bar{W}_e}{\bar{P}_d} = \omega \frac{2\bar{W}_m}{\bar{P}_d} \quad (5.2.9)$$

where the stored energy is

$$\bar{W}_e = \frac{\epsilon'}{4} \iiint_V |\mathbf{E}|^2 dV, \quad \bar{W}_m = \frac{\mu}{4} \iiint_V |\mathbf{H}|^2 dV. \quad (5.2.10)$$

The dissipated power can be decomposed into two parts due to the conductor and dielectric losses:

$$\bar{P}_d = \bar{P}_{dc} + \bar{P}_{dd}. \quad (5.2.11)$$

Hence, Equation 5.2.8 can be written as

$$\frac{1}{Q} = \frac{\bar{P}_{dc}}{\omega \bar{W}} + \frac{\bar{P}_{dd}}{\omega \bar{W}} = \frac{1}{Q_c} + \frac{1}{Q_d} \quad (5.2.12)$$

where Q_c denotes the quality factor due to the conductor loss and Q_d is the quality factor due to the dielectric loss. Based on our discussions in Section 5.1.4, the dissipated power due to the conductor loss is

$$\bar{P}_{dc} = \frac{R_s}{2} \iint_S |\mathbf{H}_t|^2 dS \quad (5.2.13)$$

where R_s denotes the surface resistance of the cavity wall and \mathbf{H}_t denotes the tangential magnetic field on the wall, and the dissipated power due to the dielectric loss is

$$\bar{P}_{dd} = \frac{\omega \epsilon''}{2} \iiint_V |\mathbf{E}|^2 dV. \quad (5.2.14)$$

Therefore,

$$Q_c = \frac{\omega \epsilon' \iiint_V |\mathbf{E}|^2 dV}{R_s \iint_S |\mathbf{H}_t|^2 dS}, \quad Q_d = \frac{\epsilon'}{\epsilon''}. \quad (5.2.15)$$

For imperfect cavities, it is often difficult to obtain the field expressions to be used in the calculation of the quality factor. However, if a cavity has a small loss, we can use the field expressions for a perfect cavity in the calculation, as in the perturbational method.

5.2.2 Rectangular Cavity

Now we consider a rectangular cavity in Figure 5.7 as a specific example to illustrate the cavity analysis. Based on the results for the rectangular waveguide and the discussions in Section 5.2.1, we have the field expressions for the TM_{mnp} modes as

$$E_x = -E_{mnp} \frac{1}{k_{tmn}^2} \frac{m\pi}{a} \frac{p\pi}{c} \cos \frac{m\pi x}{a} \sin \frac{n\pi y}{b} \sin \frac{p\pi z}{c} \quad (5.2.16)$$

$$E_y = -E_{mnp} \frac{1}{k_{tmn}^2} \frac{n\pi}{b} \frac{p\pi}{c} \sin \frac{m\pi x}{a} \cos \frac{n\pi y}{b} \sin \frac{p\pi z}{c} \quad (5.2.17)$$

$$E_z = E_{mnp} \sin \frac{m\pi x}{a} \sin \frac{n\pi y}{b} \cos \frac{p\pi z}{c} \quad (5.2.18)$$

$$H_x = E_{mnp} \frac{j\omega\epsilon}{k_{tmn}^2} \frac{n\pi}{b} \sin \frac{m\pi x}{a} \cos \frac{n\pi y}{b} \cos \frac{p\pi z}{c} \quad (5.2.19)$$

$$H_y = -E_{mnp} \frac{j\omega\epsilon}{k_{tmn}^2} \frac{m\pi}{a} \cos \frac{m\pi x}{a} \sin \frac{n\pi y}{b} \cos \frac{p\pi z}{c} \quad (5.2.20)$$

$$H_z = 0 \quad (5.2.21)$$

where E_{mnp} is a constant and $k_{tmn}^2 = (m\pi/a)^2 + (n\pi/b)^2$. The resonant frequencies are given by

$$\omega_r = \frac{1}{\sqrt{\mu\epsilon}} \sqrt{\left(\frac{m\pi}{a}\right)^2 + \left(\frac{n\pi}{b}\right)^2 + \left(\frac{p\pi}{c}\right)^2} \quad m = 1, 2, \dots; n = 1, 2, \dots; p = 0, 1, \dots \quad (5.2.22)$$

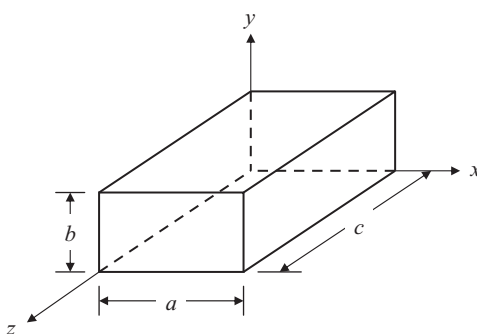


Figure 5.7 Uniformly filled rectangular cavity.

For the TE_{mnp} modes, the field expressions are given by

$$E_x = H_{mnp} \frac{j\omega\mu}{k_{tmm}^2} \frac{n\pi}{b} \cos \frac{m\pi x}{a} \sin \frac{n\pi y}{b} \sin \frac{p\pi z}{c} \quad (5.2.23)$$

$$E_y = -H_{mnp} \frac{j\omega\mu}{k_{tmm}^2} \frac{m\pi}{a} \sin \frac{m\pi x}{a} \cos \frac{n\pi y}{b} \sin \frac{p\pi z}{c} \quad (5.2.24)$$

$$E_z = 0 \quad (5.2.25)$$

$$H_x = -H_{mnp} \frac{1}{k_{tmm}^2} \frac{m\pi}{a} \frac{p\pi}{c} \sin \frac{m\pi x}{a} \cos \frac{n\pi y}{b} \cos \frac{p\pi z}{c} \quad (5.2.26)$$

$$H_y = -H_{mnp} \frac{1}{k_{tmm}^2} \frac{n\pi}{b} \frac{p\pi}{c} \cos \frac{m\pi x}{a} \sin \frac{n\pi y}{b} \cos \frac{p\pi z}{c} \quad (5.2.27)$$

$$H_z = H_{mnp} \cos \frac{m\pi x}{a} \cos \frac{n\pi y}{b} \sin \frac{p\pi z}{c} \quad (5.2.28)$$

where H_{mnp} denotes a constant. The resonant frequencies are also given by Equation 5.2.22 except now that both m and n start from 0 (excluding $m = n = 0$) and p starts from 1.

For a rectangular cavity with $c > a > b$, the dominant cavity mode is the TE₁₀₁ mode, whose resonant frequency is

$$\omega_{r101}^{\text{TE}} = \frac{\pi}{\sqrt{\mu\epsilon}} \sqrt{\frac{1}{a^2} + \frac{1}{c^2}}. \quad (5.2.29)$$

Its modal field is given by

$$\mathbf{E} = -\hat{y}H_{101} \frac{j\omega\mu a}{\pi} \sin \frac{\pi x}{a} \sin \frac{\pi z}{c} \quad (5.2.30)$$

$$\mathbf{H} = -\hat{x}H_{101} \frac{a}{c} \sin \frac{\pi x}{a} \cos \frac{\pi z}{c} + \hat{z}H_{101} \cos \frac{\pi x}{a} \sin \frac{\pi z}{c} \quad (5.2.31)$$

where H_{101} is an arbitrary constant. These two expressions can be rewritten as

$$\mathbf{E} = H_{101} \frac{\omega\mu a}{4\pi j} \left[-\hat{y}e^{j(\pi x/a+\pi z/c)} + \hat{y}e^{j(\pi x/a-\pi z/c)} + \hat{y}e^{-j(\pi x/a-\pi z/c)} - \hat{y}e^{-j(\pi x/a+\pi z/c)} \right] \quad (5.2.32)$$

$$\begin{aligned} \mathbf{H} = H_{101} \frac{1}{4j} & \left[\left(-\hat{x}\frac{a}{c} + \hat{z} \right) e^{j(\pi x/a+\pi z/c)} - \left(\hat{x}\frac{a}{c} + \hat{z} \right) e^{j(\pi x/a-\pi z/c)} \right. \\ & \left. + \left(\hat{x}\frac{a}{c} + \hat{z} \right) e^{-j(\pi x/a-\pi z/c)} + \left(\hat{x}\frac{a}{c} - \hat{z} \right) e^{-j(\pi x/a+\pi z/c)} \right]. \end{aligned} \quad (5.2.33)$$

This field is seen as the superposition of four plane waves bouncing around in the xz -plane, reflected by the cavity walls, as illustrated in Figure 5.8. Substituting Equations 5.2.30 and 5.2.31 into Equation 5.2.15, we find that the quality factor for the TE₁₀₁ mode of an imperfect rectangular cavity due to the conductor loss is

$$Q_c = \frac{\pi\eta}{2R_s} \frac{b(a^2+c^2)^{3/2}}{ac(a^2+c^2)+2b(a^3+c^3)}. \quad (5.2.34)$$

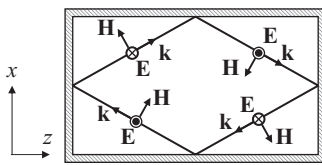


Figure 5.8 Ray picture of the TE_{101} mode resonating in a rectangular cavity.

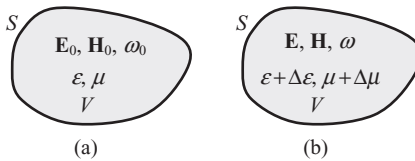


Figure 5.9 Material perturbation in a cavity.
(a) Original cavity. (b) Perturbed cavity.

5.2.3 Material and Geometry Perturbations

In practical applications, a cavity may be perturbed intentionally from its perfect form by either a small material loading or a small geometry deformation. For example, the resonant frequency of a cavity can be tuned slightly to a desired value by deforming its shape. The permittivity of a piece of material can be measured by loading it into a cavity and measuring the shift of the resonant frequency. However, when a cavity is perturbed, it is often difficult to find a rigorous solution to its resonant frequencies. It is, therefore, practically useful to develop a simple, approximate approach to evaluating the resonant frequency shift [5].

We first consider the problem where a perturbation is introduced to the permittivity and permeability of the medium in a cavity. The original cavity is illustrated in Figure 5.9a, where the field satisfies Maxwell's equations

$$\nabla \times \mathbf{E}_0 = -j\omega_0 \mu \mathbf{H}_0, \quad \nabla \times \mathbf{H}_0 = j\omega_0 \epsilon \mathbf{E}_0. \quad (5.2.35)$$

The cavity with a perturbed medium is shown in Figure 5.9b, where the field satisfies Maxwell's equations

$$\nabla \times \mathbf{E} = -j\omega(\mu + \Delta\mu) \mathbf{H}, \quad \nabla \times \mathbf{H} = j\omega(\epsilon + \Delta\epsilon) \mathbf{E}. \quad (5.2.36)$$

From these two equations, we obtain

$$\nabla \cdot (\mathbf{E} \times \mathbf{H}_0^*) = \mathbf{H}_0^* \cdot \nabla \times \mathbf{E} - \mathbf{E} \cdot \nabla \times \mathbf{H}_0^* = j\omega_0 \epsilon \mathbf{E} \cdot \mathbf{E}_0^* - j\omega(\mu + \Delta\mu) \mathbf{H} \cdot \mathbf{H}_0^* \quad (5.2.37)$$

$$\nabla \cdot (\mathbf{H} \times \mathbf{E}_0^*) = \mathbf{E}_0^* \cdot \nabla \times \mathbf{H} - \mathbf{H} \cdot \nabla \times \mathbf{E}_0^* = j\omega(\epsilon + \Delta\epsilon) \mathbf{E} \cdot \mathbf{E}_0^* - j\omega_0 \mu \mathbf{H} \cdot \mathbf{H}_0^* \quad (5.2.38)$$

and their difference is

$$\nabla \cdot (\mathbf{H} \times \mathbf{E}_0^* - \mathbf{E} \times \mathbf{H}_0^*) = j[(\omega - \omega_0)\epsilon + \omega\Delta\epsilon] \mathbf{E} \cdot \mathbf{E}_0^* + j[(\omega - \omega_0)\mu + \omega\Delta\mu] \mathbf{H} \cdot \mathbf{H}_0^*. \quad (5.2.39)$$

Integrating this equation over the volume of the cavity and applying Gauss' divergence theorem yields

$$\begin{aligned} & \oint_S (\mathbf{H} \times \mathbf{E}_0^* - \mathbf{E} \times \mathbf{H}_0^*) \cdot d\mathbf{S} \\ &= \iiint_V \{ j[(\omega - \omega_0)\epsilon + \omega\Delta\epsilon] \mathbf{E} \cdot \mathbf{E}_0^* + j[(\omega - \omega_0)\mu + \omega\Delta\mu] \mathbf{H} \cdot \mathbf{H}_0^* \} dV. \end{aligned} \quad (5.2.40)$$

The surface integral vanishes because of the boundary conditions on the cavity wall. The remaining equation can be rearranged to give

$$\frac{\omega - \omega_0}{\omega} = - \frac{\iiint_V (\Delta\epsilon \mathbf{E} \cdot \mathbf{E}_0^* + \Delta\mu \mathbf{H} \cdot \mathbf{H}_0^*) dV}{\iiint_V (\epsilon \mathbf{E} \cdot \mathbf{E}_0^* + \mu \mathbf{H} \cdot \mathbf{H}_0^*) dV}. \quad (5.2.41)$$

When the perturbation is small, the field in the perturbed cavity can be approximated by the field in the original cavity, which yields

$$\frac{\omega - \omega_0}{\omega} \approx - \frac{\iiint_V [\Delta\epsilon |\mathbf{E}_0|^2 + \Delta\mu |\mathbf{H}_0|^2] dV}{\iiint_V [\epsilon |\mathbf{E}_0|^2 + \mu |\mathbf{H}_0|^2] dV}. \quad (5.2.42)$$

This result tells that, first, an increase in the permittivity and permeability would lower the resonant frequency of a cavity and, second, one can shift the resonant frequency most effectively by perturbing the permittivity at places having a strong electric field and perturbing the permeability at places having a strong magnetic field. For example, placing a thin dielectric slab at the bottom of a rectangular cavity can effectively shift the resonant frequency of the TE₁₀₁ mode. However, there would be little effect if it were placed on any of the side walls.

As a simple example to show the application of the perturbational method discussed above, consider an empty rectangular cavity loaded with a thin dielectric slab having a thickness of t and a permittivity of ϵ . For the TE₁₀₁ mode, its electric field has only a vertical component; hence, the electric field inside the dielectric field is $E = E_0/\epsilon_r$. Using this result in Equation 5.2.42, we obtain the resonant frequency shift for the TE₁₀₁ mode as

$$\frac{\omega - \omega_0}{\omega} \approx - \frac{\epsilon - \epsilon_0}{2\epsilon} \frac{t}{b}. \quad (5.2.43)$$

Next we consider the problem where a perturbation is introduced to the geometry of a cavity, as illustrated in Figure 5.10b. The surface and volume of the original cavity are denoted as S and V , and those of the perturbed cavity are denoted as S' and V' . The field in the original cavity is governed by Equation 5.2.35, and the field in the perturbed cavity satisfies Maxwell's equations

$$\nabla \times \mathbf{E} = -j\omega\mu\mathbf{H}, \quad \nabla \times \mathbf{H} = j\omega\epsilon\mathbf{E}. \quad (5.2.44)$$

By following a similar procedure used for material perturbation, we obtain

$$\nabla \cdot (\mathbf{H} \times \mathbf{E}_0^* - \mathbf{E} \times \mathbf{H}_0^*) = j(\omega - \omega_0) \epsilon \mathbf{E} \cdot \mathbf{E}_0^* + j(\omega - \omega_0) \mu \mathbf{H} \cdot \mathbf{H}_0^*. \quad (5.2.45)$$

Integrating this over the volume of the original cavity and applying Gauss' divergence theorem, we obtain

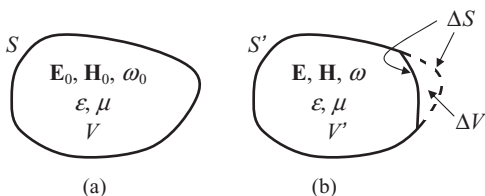


Figure 5.10 Geometry perturbation in a cavity. (a) Original cavity. (b) Perturbed cavity.

$$\oint\int_S (\mathbf{H} \times \mathbf{E}_0^* - \mathbf{E} \times \mathbf{H}_0^*) \cdot d\mathbf{S} = j(\omega - \omega_0) \iiint_V (\epsilon \mathbf{E} \cdot \mathbf{E}_0^* + \mu \mathbf{H} \cdot \mathbf{H}_0^*) dV. \quad (5.2.46)$$

Because of the boundary condition $\hat{n} \times \mathbf{E}_0 = 0$, the surface integral over the first integrand vanishes. Since $\hat{n} \times \mathbf{E} = 0$ on S' , we have

$$\oint\int_S (\mathbf{E} \times \mathbf{H}_0^*) \cdot d\mathbf{S} = \oint\int_S (\mathbf{E} \times \mathbf{H}_0^*) \cdot d\mathbf{S} - \oint\int_{S'} (\mathbf{E} \times \mathbf{H}_0^*) \cdot d\mathbf{S} = \oint\int_{\Delta S} (\mathbf{E} \times \mathbf{H}_0^*) \cdot \hat{n} dS \quad (5.2.47)$$

where $\Delta S = S - S'$ denotes the surface that consists of the parts of S and S' that are not shared with each other and \hat{n} points away from ΔS . Therefore, Equation 5.2.46 can be written as

$$\omega - \omega_0 = \frac{j \oint\int_{\Delta S} (\mathbf{E} \times \mathbf{H}_0^*) \cdot \hat{n} dS}{\iiint_V (\epsilon \mathbf{E} \cdot \mathbf{E}_0^* + \mu \mathbf{H} \cdot \mathbf{H}_0^*) dV}. \quad (5.2.48)$$

Since $\nabla \cdot (\mathbf{E} \times \mathbf{H}_0^*) = \mathbf{H}_0^* \cdot \nabla \times \mathbf{E} - \mathbf{E} \cdot \nabla \times \mathbf{H}_0^* = j\omega_0 \epsilon \mathbf{E} \cdot \mathbf{E}_0^* - j\omega \mu \mathbf{H} \cdot \mathbf{H}_0^*$, by using Gauss' divergence theorem, Equation 5.2.48 can also be written as

$$\omega - \omega_0 = \frac{\iiint_{\Delta V} (\omega \mu \mathbf{H} \cdot \mathbf{H}_0^* - \omega_0 \epsilon \mathbf{E} \cdot \mathbf{E}_0^*) dV}{\iiint_V (\epsilon \mathbf{E} \cdot \mathbf{E}_0^* + \mu \mathbf{H} \cdot \mathbf{H}_0^*) dV} \quad (5.2.49)$$

where $\Delta V = V - V'$, which is the volume enclosed by ΔS . If the perturbation is small so that the field in the perturbed cavity can be approximated by the field in the original cavity, Equation 5.2.49 can be approximated as

$$\frac{\omega - \omega_0}{\omega_0} \approx \frac{\iiint_{\Delta V} [\mu |\mathbf{H}_0|^2 - \epsilon |\mathbf{E}_0|^2] dV}{\iiint_V [\epsilon |\mathbf{E}_0|^2 + \mu |\mathbf{H}_0|^2] dV}. \quad (5.2.50)$$

This result reveals that the shift of the resonant frequency depends on the place where the geometry is perturbed. If a dent is made at the place where the magnetic field is strong and the electric field is weak, the resonant frequency is increased. On the other hand, if a dent is made at the place where the electric field is strong and the magnetic field is weak, the resonant frequency is decreased.

To give a simple example, consider an empty rectangular cavity with a dent of volume ΔV at the center of the bottom wall ($x = a/2, y = 0$, and $z = c/2$). Based on Equation 5.2.50, the shift of the resonant frequency of the TE_{101} mode would be

$$\frac{\omega - \omega_0}{\omega_0} \approx -\frac{2\Delta V}{abc} \quad (5.2.51)$$

which indicates a decrease in the resonant frequency. On the other hand, if a dent of volume ΔV is made at the center of either the left or right side wall ($x = 0$ or $x = a$) or at the center of either the front or back side wall ($z = 0$ or $z = c$), the shift of the resonant frequency is

$$\frac{\omega - \omega_0}{\omega_0} \approx \frac{2c\Delta V}{(a^2 + c^2)ab}, \quad \frac{\omega - \omega_0}{\omega_0} \approx \frac{2a\Delta V}{(a^2 + c^2)bc} \quad (5.2.52)$$

respectively, which indicates an increase in the resonant frequency.

5.3 PARTIALLY FILLED WAVEGUIDES AND DIELECTRIC SLAB WAVEGUIDES

Different from a homogeneously filled uniform waveguide, an inhomogeneously filled or partially filled waveguide or a dielectric waveguide cannot support either TE or TM modes. In this section, we first show rigorously that E_z and H_z are coupled in a general inhomogeneously filled or a dielectric waveguide. We then use a partially filled rectangular waveguide and a grounded dielectric slab waveguide to demonstrate the analysis of hybrid modes that contain both E_z and H_z .

5.3.1 General Theory

As mentioned in Section 5.1.1, the transverse field components of a propagating wave in a uniform waveguide, whether it is homogeneously filled or inhomogeneously filled, can be expressed in terms of E_z and H_z . The expressions are given by Equations 5.1.11 and 5.1.12. To find the governing equation for E_z , we substitute Equation 5.1.12 into Equation 5.1.8 to obtain

$$\nabla_t \times \left[\frac{\omega\epsilon}{k_t^2} (\hat{z} \times \nabla_t E_z) \right] + \nabla_t \times \left(\frac{k_z}{k_t^2} \nabla_t H_z \right) + \omega\epsilon E_z \hat{z} = 0. \quad (5.3.1)$$

By taking the scalar-product with \hat{z} and using the fact that both ϵ and k_t are position-dependent in an inhomogeneously filled waveguide whereas k_z is independent of position, Equation 5.3.1 can be written as

$$\nabla_t \cdot \left(\frac{\epsilon}{k_t^2} \nabla_t E_z \right) + \frac{k_z}{\omega} \hat{z} \cdot \left[\nabla_t \times \left(\frac{1}{k_t^2} \nabla_t H_z \right) \right] + \epsilon E_z = 0. \quad (5.3.2)$$

Following a similar procedure by substituting Equation 5.1.11 into Equation 5.1.6, we obtain the governing equation for H_z as

$$\nabla_t \cdot \left(\frac{\mu}{k_t^2} \nabla_t H_z \right) - \frac{k_z}{\omega} \hat{z} \cdot \left[\nabla_t \times \left(\frac{1}{k_t^2} \nabla_t E_z \right) \right] + \mu H_z = 0. \quad (5.3.3)$$

Equations 5.3.2 and 5.3.3 indicate that in an inhomogeneously filled waveguide, both E_z and H_z in general are closely coupled—one cannot exist without the other, except for a few special cases. Consequently, there cannot exist either TE or TM modes, and the modes supported by the waveguide have to contain both E_z and H_z . Such waveguide modes are called *hybrid modes*. A careful examination of Equations 5.3.2 and 5.3.3 can reveal a few more interesting points. First, the coupling between E_z and H_z is clearly caused by the position-dependent k_t due to the inhomogeneity of the medium in the waveguide. For a homogeneously filled waveguide, k_t is independent of position and the second term in Equations 5.3.2 and 5.3.3 vanishes because $\nabla_t \times \nabla_t f \equiv 0$. Equations 5.3.2 and 5.3.3 then reduce to Equations 5.1.15 and 5.1.16, and E_z and H_z become decoupled. When a waveguide is filled with piecewise homogeneous media, E_z and H_z are coupled by the discontinuous interface. Second, when $k_z = 0$, the second term in Equations 5.3.2 and 5.3.3 vanishes and E_z and H_z are decoupled. In other words, all hybrid modes are reduced to either TE or TM modes at cutoff. Those that are reduced to TM modes at cutoff are called *EH modes* because the electric field E_z dominates over H_z . The other modes that are reduced to TE modes at cutoff are referred to as *HE modes* because the magnetic field H_z dominates over E_z . Note that these definitions are applicable only to inhomogeneously filled metallic wave-

guides because for open dielectric waveguides the cutoff is defined differently, as we will see in Section 5.3.3. Third, unlike Equations 5.1.15 and 5.1.16, which involve only k_t , Equations 5.3.2 and 5.3.3 contain both ω and k_z besides k_t . As a result, k_t is a function of frequency. Therefore, the propagation constant k_z of a hybrid mode in an inhomogeneously filled waveguide does not have a simple relation with ω , as in the case for the modes in a homogeneously filled waveguide. Since all other parameters such as the phase, group, and energy velocities and wave impedances are all related to k_z , these parameters do not have a simple relation with ω either. They have to be calculated for each frequency.

Despite all the differences and complications, the hybrid modes in an inhomogeneously filled waveguide are still orthogonal to each other in the following manner [3]:

$$\iint_{\Omega} (\mathbf{e}_i \times \mathbf{h}_j) \cdot \hat{z} d\Omega = 0, \quad \iint_{\Omega} (\mathbf{h}_i \times \mathbf{e}_j) \cdot \hat{z} d\Omega = 0 \quad i \neq j. \quad (5.3.4)$$

To show this, we first consider

$$\nabla \cdot (\mathbf{E}_i \times \mathbf{H}_j - \mathbf{E}_j \times \mathbf{H}_i) = \nabla_t \cdot (\mathbf{E}_i \times \mathbf{H}_j - \mathbf{E}_j \times \mathbf{H}_i) - j(k_{zi} + k_{zj}) \hat{z} \cdot (\mathbf{E}_i \times \mathbf{H}_j - \mathbf{E}_j \times \mathbf{H}_i). \quad (5.3.5)$$

Integrating this result over the cross-section of the waveguide and then applying the two-dimensional Gauss' divergence theorem and the boundary condition at the waveguide wall, we obtain

$$(k_{zi} + k_{zj}) \iint_{\Omega} (\mathbf{E}_i \times \mathbf{H}_j - \mathbf{E}_j \times \mathbf{H}_i) \cdot \hat{z} d\Omega = 0 \quad (5.3.6)$$

or

$$(k_{zi} + k_{zj}) \iint_{\Omega} (\mathbf{e}_{ti} \times \mathbf{h}_{tj} - \mathbf{e}_{tj} \times \mathbf{h}_{ti}) \cdot \hat{z} d\Omega = 0. \quad (5.3.7)$$

Now if we let $(\mathbf{E}_j, \mathbf{H}_j)$ represent the mode propagating in the negative z -direction, which can be expressed as

$$\mathbf{E} = \mathbf{E}_t + \hat{z} E_z = [\mathbf{e}_t(x, y) - \hat{z} e_z(x, y)] e^{jk_z z} \quad (5.3.8)$$

$$\mathbf{H} = \mathbf{H}_t + \hat{z} H_z = [-\mathbf{h}_t(x, y) + \hat{z} h_z(x, y)] e^{jk_z z} \quad (5.3.9)$$

where \mathbf{e}_t , e_z , \mathbf{h}_t , and h_z are the same as those in Equations 5.1.1 and 5.1.2, by repeating the same steps as outlined above, we obtain

$$(k_{zi} - k_{zj}) \iint_{\Omega} (\mathbf{E}_i \times \mathbf{H}_j - \mathbf{E}_j \times \mathbf{H}_i) \cdot \hat{z} d\Omega = 0 \quad (5.3.10)$$

or

$$(k_{zi} - k_{zj}) \iint_{\Omega} (-\mathbf{e}_{ti} \times \mathbf{h}_{tj} - \mathbf{e}_{tj} \times \mathbf{h}_{ti}) \cdot \hat{z} d\Omega = 0. \quad (5.3.11)$$

Adding Equation 5.3.11 to and subtracting it from Equation 5.3.7 yields, respectively,

$$\iint_{\Omega} (\mathbf{e}_{ti} \times \mathbf{h}_{tj}) \cdot \hat{z} d\Omega = 0, \quad \iint_{\Omega} (\mathbf{e}_{tj} \times \mathbf{h}_{ti}) \cdot \hat{z} d\Omega = 0 \quad (5.3.12)$$

which can be written as Equation 5.3.4. Although the derivation above assumed that $k_{zi} \neq k_{zj}$, it can be shown that the results are also valid for degenerate modes [3].

5.3.2 Partially Filled Rectangular Waveguide

Consider a rectangular metallic waveguide filled with two homogeneous materials (Fig. 5.11). The material occupying the region $0 < y < h$ has a permittivity of ϵ_1 and a permeability of μ_1 , and the material occupying the region $h < y < b$ has a permittivity of ϵ_2 and a permeability of μ_2 . As discussed above, such a dielectric waveguide cannot support general TE and TM modes because E_z and H_z are coupled at the discontinuous material interface. Instead, it can support only hybrid waveguide modes that contain both E_z and H_z .

In each region, both E_z and H_z satisfy the Helmholtz equation. The solutions that satisfy boundary conditions at the waveguide walls can be expressed as

$$E_{1z} = A_1 \sin k_x x \sin k_{1y} y e^{-jk_z z} \quad (5.3.13)$$

$$H_{1z} = B_1 \cos k_x x \cos k_{1y} y e^{-jk_z z} \quad (5.3.14)$$

in the region $0 < y < h$ and

$$E_{2z} = A_2 \sin k_x x \sin k_{2y} (b - y) e^{-jk_z z} \quad (5.3.15)$$

$$H_{2z} = B_2 \cos k_x x \cos k_{2y} (b - y) e^{-jk_z z} \quad (5.3.16)$$

in the region $h < y < b$, where $k_x = m\pi/a$ and

$$k_x^2 + k_{1y}^2 + k_z^2 = k_1^2 = \omega^2 \mu_1 \epsilon_1 \quad (5.3.17)$$

$$k_x^2 + k_{2y}^2 + k_z^2 = k_2^2 = \omega^2 \mu_2 \epsilon_2 \quad (5.3.18)$$

From Equations 5.3.13–5.3.16, we obtain the other field components in the region $0 < y < h$ as

$$E_{1x} = (-A_1 k_x k_z + B_1 \omega \mu_1 k_{1y}) \frac{j}{k_{1t}^2} \cos k_x x \sin k_{1y} y e^{-jk_z z} \quad (5.3.19)$$

$$E_{1y} = (-A_1 k_{1y} k_z - B_1 \omega \mu_1 k_x) \frac{j}{k_{1t}^2} \sin k_x x \cos k_{1y} y e^{-jk_z z} \quad (5.3.20)$$

$$H_{1x} = (A_1 \omega \epsilon_1 k_{1y} + B_1 k_x k_z) \frac{j}{k_{1t}^2} \sin k_x x \cos k_{1y} y e^{-jk_z z} \quad (5.3.21)$$

$$H_{1y} = (-A_1 \omega \epsilon_1 k_x + B_1 k_{1y} k_z) \frac{j}{k_{1t}^2} \cos k_x x \sin k_{1y} y e^{-jk_z z} \quad (5.3.22)$$

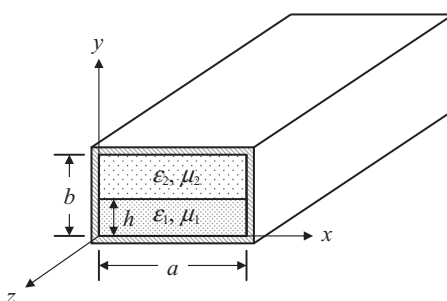


Figure 5.11 Rectangular waveguide filled with two homogeneous media.

and the other field components in the region $h < y < b$ as

$$E_{2x} = (-A_2 k_x k_z - B_2 \omega \mu_2 k_{2y}) \frac{j}{k_{2t}^2} \cos k_x x \sin k_{2y} (b-y) e^{-jk_z z} \quad (5.3.23)$$

$$E_{2y} = (A_2 k_{2y} k_z - B_2 \omega \mu_2 k_x) \frac{j}{k_{2t}^2} \sin k_x x \cos k_{2y} (b-y) e^{-jk_z z} \quad (5.3.24)$$

$$H_{2x} = (-A_2 \omega \epsilon_2 k_{2y} + B_2 k_x k_z) \frac{j}{k_{2t}^2} \sin k_x x \cos k_{2y} (b-y) e^{-jk_z z} \quad (5.3.25)$$

$$H_{2y} = (-A_2 \omega \epsilon_2 k_x - B_2 k_{2y} k_z) \frac{j}{k_{2t}^2} \cos k_x x \sin k_{2y} (b-y) e^{-jk_z z} \quad (5.3.26)$$

where $k_{1t}^2 = k_1^2 - k_z^2$ and $k_{2t}^2 = k_2^2 - k_z^2$.

At the discontinuous interface $y = h$, we have the following field continuity conditions:

$$E_{1z}|_{y=h} = E_{2z}|_{y=h}, \quad H_{1z}|_{y=h} = H_{2z}|_{y=h} \quad (5.3.27)$$

$$E_{1x}|_{y=h} = E_{2x}|_{y=h}, \quad H_{1x}|_{y=h} = H_{2x}|_{y=h}. \quad (5.3.28)$$

Substituting the field expressions into these equations, we obtain

$$A_1 \sin k_{1y} h = A_2 \sin k_{2y} (b-h) \quad (5.3.29)$$

$$B_1 \cos k_{1y} h = B_2 \cos k_{2y} (b-h) \quad (5.3.30)$$

$$(A_1 k_x k_z - B_1 \omega \mu_1 k_{1y}) \frac{\sin k_{1y} h}{k_{1t}^2} = (A_2 k_x k_z + B_2 \omega \mu_2 k_{2y}) \frac{\sin k_{2y} (b-h)}{k_{2t}^2} \quad (5.3.31)$$

$$(A_1 \omega \epsilon_1 k_{1y} + B_1 k_x k_z) \frac{\cos k_{1y} h}{k_{1t}^2} = (-A_2 \omega \epsilon_2 k_{2y} + B_2 k_x k_z) \frac{\cos k_{2y} (b-h)}{k_{2t}^2}. \quad (5.3.32)$$

Eliminating A_2 and B_2 , we have

$$A_1 k_x k_z \left(\frac{1}{k_{1t}^2} - \frac{1}{k_{2t}^2} \right) \tan k_{1y} h - B_1 \left[\frac{\omega \mu_1 k_{1y}}{k_{1t}^2} \tan k_{1y} h + \frac{\omega \mu_2 k_{2y}}{k_{2t}^2} \tan k_{2y} (b-h) \right] = 0 \quad (5.3.33)$$

$$A_1 \left[\frac{\omega \epsilon_1 k_{1y}}{k_{1t}^2} \cot k_{1y} h + \frac{\omega \epsilon_2 k_{2y}}{k_{2t}^2} \cot k_{2y} (b-h) \right] + B_1 k_x k_z \left(\frac{1}{k_{1t}^2} - \frac{1}{k_{2t}^2} \right) \cot k_{1y} h = 0. \quad (5.3.34)$$

Equations 5.3.33 and 5.3.34 can be written as a matrix equation for unknown A_1 and B_1 . To have a non-trivial solution for A_1 and B_1 , the determinant of the coefficient matrix must vanish, which yields

$$\begin{aligned} & \left[\frac{\omega \mu_1 k_{1y}}{k_{1t}^2} \tan k_{1y} h + \frac{\omega \mu_2 k_{2y}}{k_{2t}^2} \tan k_{2y} (b-h) \right] \left[\frac{\omega \epsilon_1 k_{1y}}{k_{1t}^2} \cot k_{1y} h + \frac{\omega \epsilon_2 k_{2y}}{k_{2t}^2} \cot k_{2y} (b-h) \right] \\ & + \left[k_x k_z \left(\frac{1}{k_{1t}^2} - \frac{1}{k_{2t}^2} \right) \right]^2 = 0. \end{aligned} \quad (5.3.35)$$

This transcendental equation can be solved together with Equations 5.3.17 and 5.3.18 for an infinite set of values of k_{1y} , k_{2y} , and k_z , each corresponding to a waveguide mode.

To solve Equation 5.3.35, we first expand it, simplify it, and rewrite it in a compact format as

$$AX^2 + BX + C = 0 \quad (5.3.36)$$

where

$$X = \tan k_{1y} h \cot k_{2y} (b - h) \quad (5.3.37)$$

$$A = \omega^2 \mu_1 \epsilon_2 k_{1y} k_{2y}, \quad B = k_{1y}^2 k_2^2 + k_{2y}^2 k_1^2, \quad C = \omega^2 \mu_2 \epsilon_1 k_{1y} k_{2y}. \quad (5.3.38)$$

The two solutions to Equation 5.3.36 are then given by

$$X = \frac{-B \pm \sqrt{B^2 - 4AC}}{2A} = \begin{cases} -\mu_2 k_{1y} / \mu_1 k_{2y} \\ -\epsilon_1 k_{2y} / \epsilon_2 k_{1y} \end{cases} \quad (5.3.39)$$

or more specifically,

$$\frac{\mu_1}{k_{1y}} \tan k_{1y} h = -\frac{\mu_2}{k_{2y}} \tan k_{2y} (b - h) \quad (5.3.40)$$

$$\frac{k_{1y}}{\epsilon_1} \tan k_{1y} h = -\frac{k_{2y}}{\epsilon_2} \tan k_{2y} (b - h). \quad (5.3.41)$$

Substituting the first solution (Eq. 5.3.40) into Equations 5.3.29–5.3.32, we obtain

$$A_1 k_{1y} k_z + B_1 \omega \mu_1 k_x = 0, \quad A_2 k_{2y} k_z - B_2 \omega \mu_2 k_x = 0 \quad (5.3.42)$$

which indicate that when k_z is reduced to zero, $B_1 = B_2 = 0$ provided that $k_x \neq 0$ (i.e., $m \neq 0$). Hence, the hybrid modes corresponding to the roots of Equation 5.3.40 are reduced to TM modes at cutoff. These modes are called *hybrid EH_{mn} modes* since E_z dominates over H_z near cutoff, where n denotes the index of the root of Equation 5.3.40. The cutoff wavenumber can be obtained by solving Equation 5.3.40 by setting $k_z = 0$. When the second solution is substituted into Equations 5.3.29–5.3.32, we obtain

$$A_1 \omega \epsilon_1 k_x - B_1 k_{1y} k_z = 0, \quad A_2 \omega \epsilon_2 k_x + B_2 k_{2y} k_z = 0 \quad (5.3.43)$$

which indicate that when k_z is reduced to zero, $A_1 = A_2 = 0$ provided that $k_x \neq 0$ or $m \neq 0$. Hence, the hybrid modes corresponding to the roots of Equation 5.3.41 are reduced to TE modes at cutoff. These modes are called *hybrid HE_{mn} modes* since H_z dominates over E_z near cutoff. The cutoff wavenumber can be obtained by solving Equation 5.3.41 by setting $k_z = 0$.

Now let us consider the special case with $m = 0$. In this case, A_1 and B_1 , hence E_z and H_z , are completely decoupled. For the first solution given by Equation 5.3.40, it can be seen from Equation 5.3.42 that $A_1 = A_2 = 0$ and $(B_1, B_2) \neq 0$, which corresponds to TE_{0n} modes.¹ For the second solution given by Equation 5.3.41, it can be seen from Equation 5.3.43 that $(A_1, A_2) \neq 0$ and $B_1 = B_2 = 0$, which corresponds to TM_{0n} modes. However, from the field expressions Equation 5.3.13–5.3.16, it is evident that when $m = 0$ and $B_1 = B_2 = 0$, all the field components vanish. Hence, TM_{0n} modes do not really exist since they represent trivial solutions. The decoupling of E_z and H_z when $m = 0$ can actually be

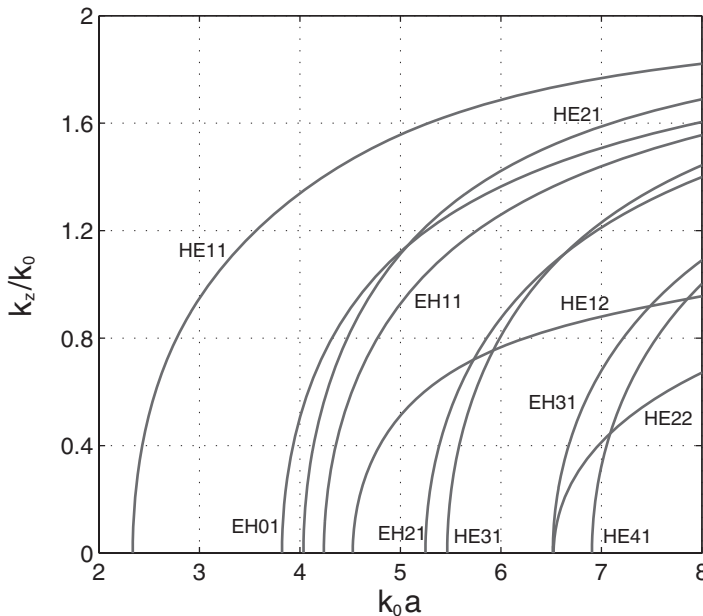


Figure 5.12 Dispersion curves of the hybrid modes in a half-filled rectangular waveguide with $a/b = 2$, $h/b = 0.5$, and $\epsilon_r = 4$.

predicted directly from their governing equations (Eqs. 5.3.2 and 5.3.3), which can be written in the rectangular coordinates as

$$\frac{\partial}{\partial x} \left(\frac{\epsilon}{k_t^2} \frac{\partial E_z}{\partial x} \right) + \frac{\partial}{\partial y} \left(\frac{\epsilon}{k_t^2} \frac{\partial E_z}{\partial y} \right) + \frac{k_z}{\omega} \left[\frac{\partial}{\partial x} \left(\frac{1}{k_t^2} \frac{\partial H_z}{\partial y} \right) - \frac{\partial}{\partial y} \left(\frac{1}{k_t^2} \frac{\partial H_z}{\partial x} \right) \right] + \epsilon E_z = 0 \quad (5.3.44)$$

$$\frac{\partial}{\partial x} \left(\frac{\mu}{k_t^2} \frac{\partial H_z}{\partial x} \right) + \frac{\partial}{\partial y} \left(\frac{\mu}{k_t^2} \frac{\partial H_z}{\partial y} \right) - \frac{k_z}{\omega} \left[\frac{\partial}{\partial x} \left(\frac{1}{k_t^2} \frac{\partial E_z}{\partial y} \right) - \frac{\partial}{\partial y} \left(\frac{1}{k_t^2} \frac{\partial E_z}{\partial x} \right) \right] + \mu H_z = 0. \quad (5.3.45)$$

Clearly, if E_z , H_z , and k_t have no variation along the x -direction, the coupling terms vanish; hence, E_z and H_z become decoupled.

Figure 5.12 shows the dispersion curves of the hybrid modes in a half-filled rectangular waveguide with $a/b = 2$, $h/b = 0.5$, and $\epsilon_r = 4$. The results are obtained by solving Equations 5.3.40 and 5.3.41 together with Equations 5.3.17 and 5.3.18 using the bisection algorithm in conjunction with the Newton-Raphson method [8].

5.3.3 Dielectric Slab Waveguide on a Ground Plane

Consider an infinitely large dielectric slab of thickness h residing on a ground plane (Fig. 5.13). For this configuration, we can have separate TE and TM modes if the modal fields have no variation in the x -direction for the reason just discussed above. For the TM modes, the longitudinal electric field component in the dielectric slab is given by

$$E_{1z} = A_l \sin k_{yd} y e^{-jk_z z} \quad 0 \leq y \leq h \quad (5.3.46)$$

where $k_{yd}^2 + k_z^2 = k_d^2 = \omega^2 \mu_d \epsilon_d$. The other nonzero field components can be obtained as

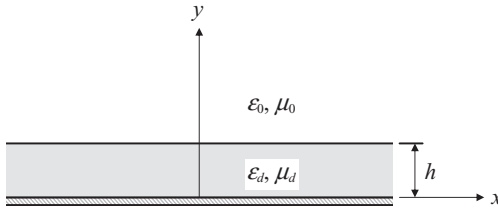


Figure 5.13 Ground-backed dielectric slab waveguide.

$$E_{1y} = -A_1 \frac{jk_z}{k_{yd}} \cos k_{yd} y e^{-jk_z z} \quad (5.3.47)$$

$$H_{1x} = A_1 \frac{j\omega\epsilon_d}{k_{yd}} \cos k_{yd} y e^{-jk_z z}. \quad (5.3.48)$$

For modes to propagate in the z -direction without any leakage loss, the longitudinal electric field component above the dielectric slab should have the form

$$E_{2z} = A_2 e^{-\alpha y} e^{-jk_z z} \quad y \geq h \quad (5.3.49)$$

where $k_z^2 - \alpha^2 = k_0^2 = \omega^2 \mu_0 \epsilon_0$. The other non-zero field components are given by

$$E_{2y} = -A_2 \frac{jk_z}{\alpha} e^{-\alpha y} e^{-jk_z z} \quad (5.3.50)$$

$$H_{2x} = A_2 \frac{j\omega\epsilon_0}{\alpha} e^{-\alpha y} e^{-jk_z z}. \quad (5.3.51)$$

Applying the field continuity conditions at the interface $y = h$ yields the following characteristic equation to determine the propagation constant:

$$\frac{k_{yd}}{\epsilon_d} \tan k_{yd} h = \frac{\alpha}{\epsilon_0}. \quad (5.3.52)$$

A similar analysis of the TE modes yield the characteristic equation

$$\frac{k_{yd}}{\mu_d} \cot k_{yd} h = -\frac{\alpha}{\mu_0} \quad (5.3.53)$$

which can be solved for α , k_{yd} , and k_z .

The main difference between an open dielectric waveguide as the one considered here and a waveguide bounded by a conducting wall is that the mode cutoff is defined differently. In all previous bounded waveguides, the cutoff is defined when $k_z = 0$. In an open waveguide, since $\alpha^2 = k_z^2 - k_0^2 = k_z^2 - \omega^2 \mu_0 \epsilon_0$, it is obvious that when $k_z < k_0$, α becomes imaginary and the wave would propagate in the y -direction as well, losing power as it propagates along the z -direction. Therefore, the cutoff for an open waveguide is defined when $\alpha = 0$ or $k_z = k_0$. With this definition, at cutoff the characteristic equations (Eqs. 5.3.52 and 5.3.53) become

$$\tan k_{yd} h = 0 \quad \text{for TM modes} \quad (5.3.54)$$

$$\cot k_{yd} h = 0 \quad \text{for TE modes.} \quad (5.3.55)$$

The solutions are

$$k_{yd}h = n\pi \quad n = 0, 1, 2, \dots \quad \text{for TM modes} \quad (5.3.56)$$

$$k_{yd}h = \frac{(2n-1)\pi}{2} \quad n = 1, 2, \dots \quad \text{for TE modes.} \quad (5.3.57)$$

Since at cutoff, $k_{yd} = \omega_c \sqrt{\mu_d \epsilon_d - \mu_0 \epsilon_0}$, the cutoff frequencies are found as

$$\omega_c = \frac{n\pi}{h\sqrt{\mu_d \epsilon_d - \mu_0 \epsilon_0}} \quad n = 0, 1, 2, \dots \quad \text{for TM modes} \quad (5.3.58)$$

$$\omega_c = \frac{(2n-1)\pi}{2h\sqrt{\mu_d \epsilon_d - \mu_0 \epsilon_0}} \quad n = 1, 2, \dots \quad \text{for TE modes.} \quad (5.3.59)$$

Clearly, the dominant TM mode has no cutoff frequency. Note that for $\alpha > 0$, Equations 5.3.52 and 5.3.53 have solutions only when k_{yd} is real. Therefore, k_z is upper bounded by k_d ; hence, the lossless propagation can occur only when $k_0 < k_z < k_d$. Consequently, there are only a finite number of propagating modes at a frequency. Figure 5.14 gives the dispersion curves of the first several TE and TM modes.

To gain a better understanding of wave propagation in a dielectric slab waveguide, we rewrite Equations 5.3.46–5.3.48 as

$$\mathbf{E}_1 = \frac{A_1}{2j} \left[\left(\hat{y} \frac{k_z}{k_{yd}} + \hat{z} \right) e^{j(k_{yd}y - k_z z)} + \left(\hat{y} \frac{k_z}{k_{yd}} - \hat{z} \right) e^{-j(k_{yd}y + k_z z)} \right] \quad (5.3.60)$$

$$\mathbf{H}_1 = \frac{A_1}{2j} \frac{\omega \epsilon_d}{k_{yd}} \left[-\hat{x} e^{j(k_{yd}y - k_z z)} - \hat{x} e^{-j(k_{yd}y + k_z z)} \right] \quad (5.3.61)$$

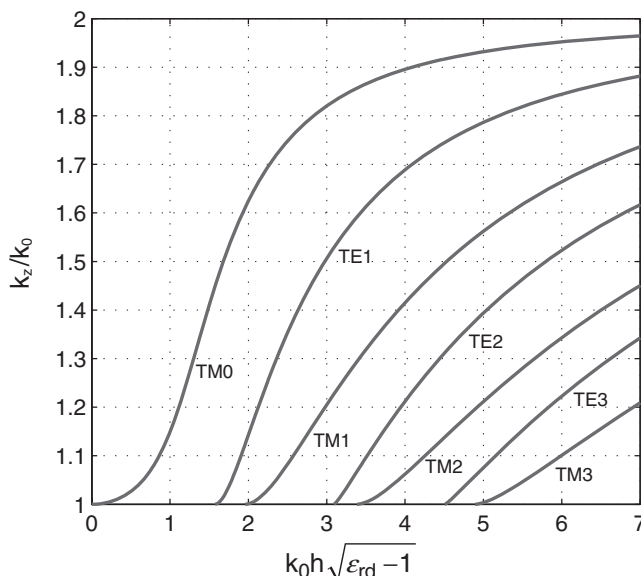


Figure 5.14 Dispersion curves of the first few modes in a ground-backed dielectric slab waveguide.

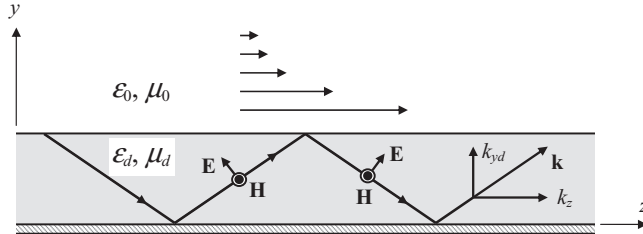


Figure 5.15 Ray picture of wave propagation in a dielectric slab waveguide backed by a ground plane.

which are recognized as the superposition of two plane waves propagating in the dielectric slab (Fig. 5.15). The angle between the propagation direction and the z -axis is given by $\vartheta = \tan^{-1}(k_{yd}/k_z)$. At cutoff, $k_z = \omega_c \sqrt{\mu_0 \epsilon_0}$ and $k_{yd} = \omega_c \sqrt{\mu_d \epsilon_d - \mu_0 \epsilon_0}$; hence, this angle becomes

$$\vartheta_c = \tan^{-1} \sqrt{\frac{\mu_d \epsilon_d}{\mu_0 \epsilon_0} - 1} \quad (5.3.62)$$

corresponding to plane waves incident on the dielectric-air interface at the critical angle. Above cutoff, the incident angle would be greater than the critical angle. The dielectric-air interface would provide total reflection; therefore, the waves would be able to propagate along the z -direction without any attenuation. The field above the dielectric slab forms a non-uniform plane wave that propagates in the z -direction with a decayed amplitude in the y -direction.

If the field has a variation along the x -direction due to either excitation or any other field confinement mechanisms, the TE and TM modes can no longer exist. The modes have to be hybrid that contain both E_z and H_z , which for a given k_x can be assumed as

$$E_{1z} = A_1 \begin{cases} \cos k_x x \\ \sin k_x x \end{cases} \sin k_{yd} y e^{-jk_z z} \quad 0 \leq y \leq h \quad (5.3.63)$$

$$H_{1z} = B_1 \begin{cases} \sin k_x x \\ \cos k_x x \end{cases} \cos k_{yd} y e^{-jk_z z} \quad 0 \leq y \leq h \quad (5.3.64)$$

in the dielectric slab and

$$E_{2z} = A_2 \begin{cases} \cos k_x x \\ \sin k_x x \end{cases} e^{-\alpha_y} e^{-jk_z z} \quad y \geq h \quad (5.3.65)$$

$$H_{2z} = B_2 \begin{cases} \sin k_x x \\ \cos k_x x \end{cases} e^{-\alpha_y} e^{-jk_z z} \quad y \geq h \quad (5.3.66)$$

in the air above the dielectric slab. The dispersion relations are

$$k_x^2 + k_{yd}^2 + k_z^2 = k_d^2 = \omega^2 \mu_d \epsilon_d, \quad k_x^2 - \alpha_y^2 + k_z^2 = k_0^2 = \omega^2 \mu_0 \epsilon_0. \quad (5.3.67)$$

By following a similar procedure described in Section 5.3.2, we find two sets of solutions. One set of solutions can be obtained by solving

$$\frac{k_{yd}}{\epsilon_d} \tan k_{yd} h = \frac{\alpha}{\epsilon_0} \quad (5.3.68)$$

and the corresponding coefficients are related by

$$A_1 \omega \epsilon_d k_x \mp B_1 k_{yd} k_z = 0, \quad A_2 \omega \epsilon_0 k_x \mp B_2 \alpha k_z = 0. \quad (5.3.69)$$

The second set of solutions can be obtained by solving

$$\frac{k_{yd}}{\mu_d} \cot k_{yd} h = -\frac{\alpha}{\mu_0} \quad (5.3.70)$$

and the corresponding coefficients are related by

$$A_1 k_{yd} k_z \mp B_1 \omega \mu_d k_x = 0, \quad A_2 \alpha k_z \pm B_2 \omega \mu_0 k_x = 0. \quad (5.3.71)$$

To determine the nature of these two sets of modes, we can no longer examine the case when $k_z = 0$. Instead, we need to investigate what happens at cutoff or above cutoff defined by $\alpha = 0$. From Equation 5.3.69, it is evident that for a given value of k_x when $\alpha \rightarrow 0$, $A_2 \rightarrow 0$; hence, the modes corresponding to the roots of Equation 5.3.68 become TE-like modes (they are not exactly TE modes since $A_1 \neq 0$). These modes are designated as HE modes because H_z is dominant at cutoff. However, the H_z dominance is true only near cutoff. As can be seen from Equation 5.3.69, when the value of α increases, the ratio $|E_z/H_z|$ increases. In particular, when $\alpha > k_x$, E_z is relatively strong and the HE modes become TM-like. On the other hand, for the modes corresponding to the roots of Equation 5.3.70, it can be seen from Equations 5.3.71 that $B_2 \rightarrow 0$ when $\alpha \rightarrow 0$ and the modes become TM-like. These can be designated as EH modes since E_z is dominant at cutoff. Again, this E_z dominance is true only near cutoff. It is obvious from Equation 5.3.71 that as the value of α increases, the ratio $|E_z/H_z|$ decreases. When $\alpha > k_x$, H_z is relatively strong and the EH modes become TE-like. For the special case with $k_x = 0$, the HE modes become TM modes and the EH modes become TE modes, which is consistent with the results obtained earlier in this section.

5.4 FIELD EXCITATION IN WAVEGUIDES

In Sections 5.1 and 5.3, we discussed wave propagation in various waveguides by solving source-free Maxwell's equations. The solution yields all possible modes that can be supported by the waveguides. In this section, we make use of these results to formulate the solution of fields excited by a current source in a waveguide. We first consider a simple case, which involves the excitation of fields in a general uniform waveguide by a planar surface current. We then treat a general problem, which concerns the fields excited by a volumetric current source.

5.4.1 Excitation by Planar Surface Currents

Consider a uniform waveguide along the z -direction excited by a surface current \mathbf{J}_s placed at $z = 0$, as illustrated in Figure 5.16. This surface current will excite a wave on the right-hand side propagating in the positive z -direction and another wave on the left-hand side propagating in the negative z -direction. Since any field in the source-free region of a

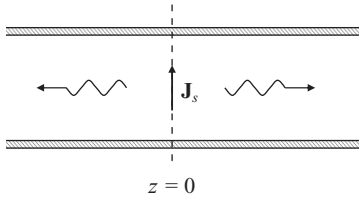


Figure 5.16 Field excitation by a surface current source in a waveguide.

waveguide can be expanded in terms of waveguide modes, the wave on the right-hand side can be expressed as

$$\mathbf{E}^+ = \sum_{i=1}^{\infty} a_i \mathbf{E}_i^+, \quad \mathbf{H}^+ = \sum_{i=1}^{\infty} a_i \mathbf{H}_i^+ \quad z > 0 \quad (5.4.1)$$

and the wave on the left-hand side can be expressed as

$$\mathbf{E}^- = \sum_{i=1}^{\infty} b_i \mathbf{E}_i^-, \quad \mathbf{H}^- = \sum_{i=1}^{\infty} b_i \mathbf{H}_i^- \quad z < 0 \quad (5.4.2)$$

where $(\mathbf{E}_i^+, \mathbf{H}_i^+)$ represent waveguide modes propagating in the positive z -direction

$$\mathbf{E}_i^+ = (\mathbf{e}_{ii} + \hat{z} e_{zi}) e^{-jk_{zi}z}, \quad \mathbf{H}_i^+ = (\mathbf{h}_{ii} + \hat{z} h_{zi}) e^{-jk_{zi}z} \quad (5.4.3)$$

and $(\mathbf{E}_i^-, \mathbf{H}_i^-)$ represent waveguide modes propagating in the negative z -direction

$$\mathbf{E}_i^- = (\mathbf{e}_{ii} - \hat{z} e_{zi}) e^{jk_{zi}z}, \quad \mathbf{H}_i^- = (-\mathbf{h}_{ii} + \hat{z} h_{zi}) e^{jk_{zi}z}. \quad (5.4.4)$$

To determine the unknown expansion coefficients a_i and b_i , we apply the boundary conditions across the surface current:

$$\hat{z} \times (\mathbf{E}^+ - \mathbf{E}^-) = 0, \quad \hat{z} \times (\mathbf{H}^+ - \mathbf{H}^-) = \mathbf{J}_s \quad \text{at } z = 0. \quad (5.4.5)$$

Doing so, we obtain

$$\sum_{i=1}^{\infty} a_i \mathbf{e}_{ii} = \sum_{i=1}^{\infty} b_i \mathbf{e}_{ii}, \quad \sum_{i=1}^{\infty} (a_i + b_i) \hat{z} \times \mathbf{h}_{ii} = \mathbf{J}_s. \quad (5.4.6)$$

Application of the orthogonality of waveguide modes yields

$$a_i = b_i = -\frac{1}{2\kappa_i} \iint_{\Omega} (\mathbf{e}_{ii} \times \mathbf{h}_{ii}) \cdot \hat{z} d\Omega \quad (5.4.7)$$

where κ_i is a normalization constant given by

$$\kappa_i = \iint_{\Omega} (\mathbf{e}_{ii} \times \mathbf{h}_{ii}) \cdot \hat{z} d\Omega. \quad (5.4.8)$$

To demonstrate the application of the approach described above, we consider a rectangular waveguide excited by a time-harmonic line current I placed at $x = a/2$ and $z = 0$ and extended from the bottom to the top of the waveguide (Fig. 5.17). This line current can be treated as a surface current with a surface current density given by

$$\mathbf{J}_s = \hat{y} I \delta(x - a/2). \quad (5.4.9)$$

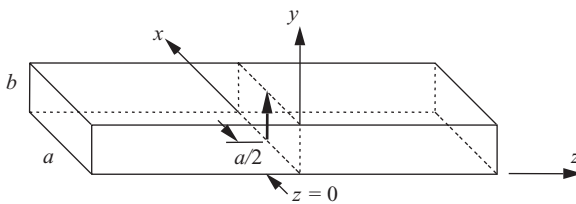


Figure 5.17 Rectangular waveguide excited by a current probe placed at $x = a/2$ and $z = 0$.

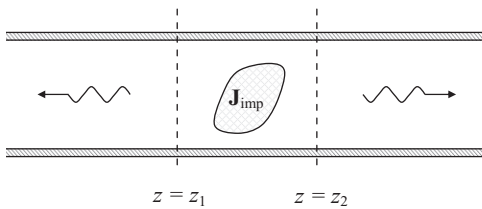


Figure 5.18 Field excitation by a volumetric current source in a waveguide.

The modal fields of a rectangular waveguide are given by Equations 5.1.79–5.1.84 for the TM modes and by Equations 5.1.92–5.1.97 for the TE modes, where E_{mn} and H_{mn} can be considered as the unknown expansion coefficients. From Equation 5.4.7, we find that $E_{mn} = 0$ and

$$H_{m0} = \frac{m\pi I}{ja^2} \sin \frac{m\pi}{2} \sqrt{k^2 - \left(\frac{m\pi}{a}\right)^2}, \quad H_{mn} = 0 \quad n > 0. \quad (5.4.10)$$

This result indicates the line current in Equations 5.4.9 cannot excite any TM modes and it can excite only those TE modes with $m = 1, 3, 5, \dots$ and $n = 0$.

5.4.2 Excitation by General Volumetric Currents

We now consider a much more general problem, which deals with the fields excited by a general volumetric current in a general uniform waveguide. The problem is shown in Figure 5.18, where the current source \mathbf{J}_{imp} is confined within $[z_1, z_2]$. Since the field excited by the source in the waveguide can be expressed as the sum of all waveguide modes, we can expand the electric and magnetic fields as

$$\mathbf{E} = \sum_{i=1}^{\infty} a_i(z) \mathbf{E}_i^+ + \sum_{i=1}^{\infty} b_i(z) \mathbf{E}_i^- \quad (5.4.11)$$

$$\mathbf{H} = \sum_{i=1}^{\infty} a_i(z) \mathbf{H}_i^+ + \sum_{i=1}^{\infty} b_i(z) \mathbf{H}_i^- \quad (5.4.12)$$

where \mathbf{E}_i^\pm and \mathbf{H}_i^\pm are defined by Equations 5.4.3 and 5.4.4. Furthermore, the expansion coefficients $a_i(z)$ and $b_i(z)$ satisfy the following conditions

$$a_i(z)|_{z < z_1} = a_i(z_1) = 0, \quad a_i(z)|_{z > z_2} = a_i(z_2) = \text{constant} \quad (5.4.13)$$

$$b_i(z)|_{z > z_2} = b_i(z_2) = 0, \quad b_i(z)|_{z < z_1} = b_i(z_1) = \text{constant}. \quad (5.4.14)$$

To determine the expansion coefficients $a_i(z)$ and $b_i(z)$, we apply the reciprocity theorem represented by Equations 3.3.8 to the volume confined within $[z_1, z_2]$ by letting $\mathbf{E}_1 = \mathbf{E}_j^-$, $\mathbf{H}_1 = \mathbf{H}_j^-$, $\mathbf{E}_2 = \mathbf{E}$, and $\mathbf{H}_2 = \mathbf{H}$ to find

$$\oint\int_S (\mathbf{H} \times \mathbf{E}_j^- - \mathbf{H}_j^- \times \mathbf{E}) \cdot d\mathbf{S} = \iiint_V \mathbf{J}_{\text{imp}} \cdot \mathbf{E}_j^- dV. \quad (5.4.15)$$

The surface S consists of the waveguide wall, over which the surface integral vanishes because of the boundary condition $\hat{n} \times \mathbf{E}_j^- = \hat{n} \times \mathbf{E} = 0$, the cross-section at $z = z_1$, which is denoted as Ω_1 , and the cross-section at $z = z_2$, which is denoted as Ω_2 . Substituting Equations 5.4.11 and 5.4.12 into Equation 5.4.15 and applying the orthogonal relation (Eq. 5.3.12), we find

$$\begin{aligned} \oint\int_S (\mathbf{H} \times \mathbf{E}_j^- - \mathbf{H}_j^- \times \mathbf{E}) \cdot d\mathbf{S} &= a_j(z_2) \iint_{\Omega_2} (\mathbf{H}_j^+ \times \mathbf{E}_j^- - \mathbf{H}_j^- \times \mathbf{E}_j^+) \cdot \hat{z} d\Omega \\ &= 2a_j(z_2) \iint_{\Omega} (\mathbf{h}_{ij} \times \mathbf{e}_{ij}) \cdot \hat{z} d\Omega. \end{aligned} \quad (5.4.16)$$

Hence,

$$a_i(z) = -\frac{1}{2\kappa_i} \iiint_V \mathbf{J}_{\text{imp}} \cdot \mathbf{E}_i^- dV \quad z > z_2 \quad (5.4.17)$$

where κ_i is given by Equation 5.4.8. Similarly, we can apply the reciprocity theorem (Eq. 3.3.8) to the volume confined within $[z_1, z_2]$ by letting $\mathbf{E}_1 = \mathbf{E}_j^+$, $\mathbf{H}_1 = \mathbf{H}_j^+$, $\mathbf{E}_2 = \mathbf{E}$, and $\mathbf{H}_2 = \mathbf{H}$. Following the same procedure, we find

$$b_i(z) = -\frac{1}{2\kappa_i} \iiint_V \mathbf{J}_{\text{imp}} \cdot \mathbf{E}_i^+ dV \quad z < z_1. \quad (5.4.18)$$

Therefore, given any current source, we can evaluate Equation 5.4.17 to obtain the amplitudes of the waveguide modes propagating in the positive z -direction and evaluate Equation 5.4.18 to find the amplitudes of the modes propagating in the negative z -direction. Note that the field expansion in Equation 5.4.11 is complete only for the source-free region, where the electric field is purely solenoidal [3]. In the source region, the electric field contains an irrotational component, which is missing in the expansion in Equation 5.4.11. By including this irrotational component in the field expansion, one can derive rigorous but complicated expressions for the fields everywhere in a waveguide. The results can be expressed compactly in terms of dyadic Green's functions [3,9].

When \mathbf{J}_{imp} is a surface current in the plane $z = 0$, which can be expressed as $\mathbf{J}_{\text{imp}} = \mathbf{J}_s \delta(z)$, Equations 5.4.17 and 5.4.18 become

$$a_i = b_i = -\frac{1}{2\kappa_i} \iint_{\Omega} \mathbf{e}_{ii} \cdot \mathbf{J}_s d\Omega \quad (5.4.19)$$

which is the same as Equation 5.4.7. This is expected because a surface current can always be considered as a special volumetric current. Nevertheless, this exercise provides a quick cross-check between two different formulations.

All the results derived in this section indicate clearly that when an electric current is used to excite a specific mode in a waveguide, the current should be placed at the place where the desired mode has a strong modal electric field, and the direction of the current should be parallel to the direction of the modal electric field. Based on

this observation, we can design various feeds to effectively excite desired modes in a waveguide [5,7].

5.5 FIELDS IN PLANAR LAYERED MEDIA

Many electrical engineering applications involve various layered media. Examples of such applications include design of microstrip circuits and antennas and high-frequency integrated circuits. In this section, we consider the problem of electromagnetic radiation by an electric current source in a planar layered medium. To simplify the analysis, we assume that the source is placed above the layered medium.

Since an arbitrary electric current can be decomposed into an infinite number of electric dipoles, its radiation can be obtained from the solution of the dipole radiation. For the problem considered here, there are two distinct dipoles: *vertical electric dipole* (VED) and *horizontal electric dipole* (HED). Therefore, we will treat these two dipoles first by assuming that they are placed at the origin of the chosen coordinate system.

The basic approach to dealing with a dipole radiation above a layered medium is to find its radiation in free space first, then use this radiated field as the incident field on the layered medium to find the reflected field, and finally obtain the total field as the superposition of the incident and reflected fields [10,11]. However, since the field radiated by a dipole has a complicated waveform, its reflection from a layered medium is difficult to find directly. For this, we will employ the two-dimensional Fourier transform to decompose the dipole radiated field into an infinite number of plane waves, whose reflection by a layered medium can be found rather easily.

5.5.1 Spectral Green's Function and Sommerfeld Identity

In Section 4.1.3, we derived the free-space Green's function $G_0(\mathbf{r}, \mathbf{r}')$ by solving the partial differential equation

$$\nabla^2 G_0(\mathbf{r}, \mathbf{r}') + k^2 G_0(\mathbf{r}, \mathbf{r}') = -\delta(\mathbf{r} - \mathbf{r}') \quad (5.5.1)$$

using the three-dimensional Fourier transform. An alternative solution can be obtained by expanding $G_0(\mathbf{r}, \mathbf{r}')$ and $\delta(\mathbf{r} - \mathbf{r}')$ in terms of two-dimensional Fourier integrals as

$$G_0(\mathbf{r}, \mathbf{r}') = \frac{1}{(2\pi)^2} \int_{-\infty}^{\infty} \int_{-\infty}^{\infty} \tilde{G}_0(k_x, k_y; z, z') e^{j[k_x(x-x')+k_y(y-y')]} dk_x dk_y \quad (5.5.2)$$

$$\delta(\mathbf{r} - \mathbf{r}') = \frac{1}{(2\pi)^2} \int_{-\infty}^{\infty} \int_{-\infty}^{\infty} e^{j[k_x(x-x')+k_y(y-y')]} dk_x dk_y \delta(z - z') \quad (5.5.3)$$

where $\tilde{G}_0(k_x, k_y; z, z')$ is the unknown function to be determined, which is often referred to as the *free-space spectral Green's function*. By substituting these two expressions into Equation 5.5.1, we obtain

$$\left(\frac{d^2}{dz^2} + k_z^2 \right) \tilde{G}_0(k_x, k_y; z, z') = -\delta(z - z') \quad (5.5.4)$$

where $k_z^2 = k^2 - k_x^2 - k_y^2$. This is the same equation as Equation 4.1.35, whose solution is given by Equation 4.1.39. Hence, the solution to Equation 5.5.4 is

$$\tilde{G}_0(k_x, k_y; z, z') = \frac{1}{2jk_z} \begin{cases} e^{-jk_z(z-z')} & z \geq z' \\ e^{jk_z(z-z')} & z \leq z' \end{cases} \quad (5.5.5)$$

With this, Equation 5.5.2 can be written as

$$G_0(\mathbf{r}, \mathbf{r}') = \frac{1}{(2\pi)^2} \int_{-\infty}^{\infty} \int_{-\infty}^{\infty} \frac{e^{j[k_x(x-x')+k_y(y-y')]}}{2jk_z} e^{-jk_z|z-z'|} dk_x dk_y. \quad (5.5.6)$$

The integrals can be converted into the ones based on cylindrical coordinates by letting $x = \rho \cos \phi$, $y = \rho \sin \phi$, $k_x = k_\rho \cos \alpha$, and $k_y = k_\rho \sin \alpha$. Furthermore, since $G_0(\mathbf{r}, \mathbf{r}')$ is symmetric about ρ' , we can choose $\rho - \rho'$ to point in the x -direction to simplify the resulting integrals without compromising the generality of the solution. By doing so, Equation 5.5.6 can be written as

$$G_0(\mathbf{r}, \mathbf{r}') = \frac{1}{(2\pi)^2} \int_0^{2\pi} \int_0^{\infty} \frac{e^{jk_\rho|\rho-\rho'|\cos\alpha}}{2jk_z} e^{-jk_z|z-z'|} k_\rho dk_\rho d\alpha. \quad (5.5.7)$$

By using the integral representation of the Bessel function [12]

$$J_0(u) = \frac{1}{2\pi} \int_0^{2\pi} e^{ju\cos v} dv \quad (5.5.8)$$

where $J_0(u)$ is called the *zeroth-order Bessel function of the first kind*, Equation 5.5.7 can further be written as

$$G_0(\mathbf{r}, \mathbf{r}') = \frac{1}{4\pi j} \int_0^{\infty} \frac{k_\rho}{k_z} J_0(k_\rho |\rho - \rho'|) e^{-jk_z|z-z'|} dk_\rho. \quad (5.5.9)$$

Since $G_0(\mathbf{r}, \mathbf{r}')$ is also given by Equation 2.2.20 or 4.1.53, we have

$$\frac{e^{-jk|\mathbf{r}-\mathbf{r}'|}}{|\mathbf{r}-\mathbf{r}'|} = \int_0^{\infty} \frac{k_\rho}{jk_z} J_0(k_\rho |\rho - \rho'|) e^{-jk_z|z-z'|} dk_\rho \quad (5.5.10)$$

what is known as the *Sommerfeld identity*. This equation decomposes a spherical wave into an infinite number of plane waves propagating along the z -axis.

5.5.2 Vertical Electric Dipole above a Layered Medium

For a z -directed infinitesimal electric dipole placed at the origin, the current density can be expressed as $\mathbf{J}(\mathbf{r}') = \hat{z}\delta(\mathbf{r}')$, and its field in free space with permittivity ϵ_0 and permeability μ_0 can be obtained from Equations 2.2.34 and 2.2.38, which yields

$$\mathbf{E}(\mathbf{r}) = -j\omega\mu_0 \left(\hat{z} + \frac{1}{k_0^2} \nabla \frac{\partial}{\partial z} \right) \frac{e^{-jk_0 r}}{4\pi r} \quad (5.5.11)$$

$$\mathbf{H}(\mathbf{r}) = -\hat{z} \times \nabla \frac{e^{-jk_0 r}}{4\pi r}. \quad (5.5.12)$$

Their z -components are

$$E_z(\mathbf{r}) = -j\omega\mu_0 \left(1 + \frac{1}{k_0^2} \frac{\partial^2}{\partial z^2}\right) \frac{e^{-jk_0 r}}{4\pi r}, \quad H_z(\mathbf{r}) = 0. \quad (5.5.13)$$

Obviously, this field can be regarded as the TM field. Substituting Equation 5.5.10 into the expression above, we have

$$E_z(\mathbf{r}) = -\frac{1}{4\pi\omega\epsilon_0} \int_0^\infty \frac{k_\rho^3}{k_{z,0}} J_0(k_\rho\rho) e^{-jk_{z,0}|z|} dk_\rho \quad (5.5.14)$$

where $k_{z,0} = \sqrt{k_0^2 - k_\rho^2}$. By using Equation 5.1.20, we can find the transverse components as

$$E_\rho(\mathbf{r}) = \pm \frac{j}{4\pi\omega\epsilon_0} \int_0^\infty k_\rho^2 J'_0(k_\rho\rho) e^{-jk_{z,0}|z|} dk_\rho \quad (5.5.15)$$

$$H_\phi(\mathbf{r}) = \frac{j}{4\pi} \int_0^\infty \frac{k_\rho^2}{k_{z,0}} J'_0(k_\rho\rho) e^{-jk_{z,0}|z|} dk_\rho \quad (5.5.16)$$

where the “+” sign in Equation 5.5.15 is for $z > 0$ and the “−” sign is for $z < 0$, and $J'_0(u) = dJ_0(u)/du$.

Now consider the problem illustrated in Figure 5.19, where the vertical electric dipole is placed above a layered medium. The effect of the layered medium is to reflect the field produced by the dipole in free space. Therefore, the field derived above can be considered as an incident field on the layered medium,

$$E_z^{\text{inc}}(\mathbf{r}) = -\frac{1}{4\pi\omega\epsilon_0} \int_0^\infty \frac{k_\rho^3}{k_{z,0}} J_0(k_\rho\rho) e^{jk_{z,0}z} dk_\rho. \quad (5.5.17)$$

Because of the phase-matching condition, the transverse variation of the reflected and transmitted fields is the same as that of the incident field. Hence, the reflected field can be written as

$$E_z^{\text{ref}}(\mathbf{r}) = -\frac{1}{4\pi\omega\epsilon_0} \int_0^\infty \frac{k_\rho^3}{k_{z,0}} J_0(k_\rho\rho) R^{\text{TM}} e^{-jk_{z,0}z} dk_\rho. \quad (5.5.18)$$

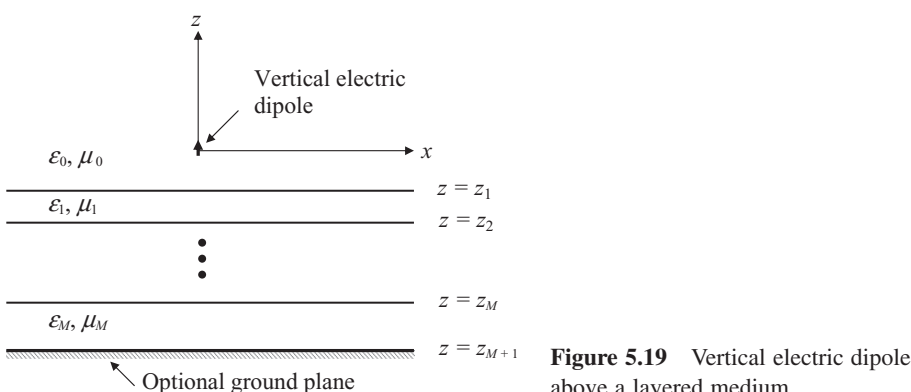


Figure 5.19 Vertical electric dipole above a layered medium.

The field in each layer consists of waves propagating in the positive and negative z -directions, which can be expressed as

$$E_z^{(i)}(\mathbf{r}) = -\frac{1}{4\pi\omega\epsilon_i} \int_0^\infty \frac{k_\rho^3}{k_{z,i}} J_0(k_\rho\rho) \left[A^{(i)} e^{jk_{z,i}z} + B^{(i)} e^{-jk_{z,i}z} \right] dk_\rho \quad (5.5.19)$$

$$\text{where } k_{z,i} = \sqrt{k_i^2 - k_\rho^2} = \sqrt{\omega^2 \mu_i \epsilon_i - k_\rho^2}.$$

To determine the unknown coefficients in Equation 5.5.19 and the reflection coefficient in Equation 5.5.18, we apply the field continuity conditions across each interface. For example, across the interface between layers $i-1$ and i , which is located at $z = z_i$, we have

$$\frac{1}{k_{z,i-1}} \left[A^{(i-1)} e^{jk_{z,i-1}z_i} + B^{(i-1)} e^{-jk_{z,i-1}z_i} \right] = \frac{1}{k_{z,i}} \left[A^{(i)} e^{jk_{z,i}z_i} + B^{(i)} e^{-jk_{z,i}z_i} \right] \quad (5.5.20)$$

$$\frac{1}{\epsilon_{i-1}} \left[A^{(i-1)} e^{jk_{z,i-1}z_i} - B^{(i-1)} e^{-jk_{z,i-1}z_i} \right] = \frac{1}{\epsilon_i} \left[A^{(i)} e^{jk_{z,i}z_i} - B^{(i)} e^{-jk_{z,i}z_i} \right]. \quad (5.5.21)$$

From these, we find

$$\frac{B^{(i-1)}}{A^{(i-1)}} = \frac{R_E^{(i)} - 1}{R_E^{(i)} + 1} e^{j2k_{z,i-1}z_i} \quad i = 1, 2, \dots, M \quad (5.5.22)$$

where

$$R_E^{(i)} = \frac{\epsilon_i k_{z,i-1}}{\epsilon_{i-1} k_{z,i}} \frac{e^{jk_{z,i}z_i} + \frac{B^{(i)}}{A^{(i)}} e^{-jk_{z,i}z_i}}{e^{jk_{z,i}z_i} - \frac{B^{(i)}}{A^{(i)}} e^{-jk_{z,i}z_i}} \quad i = 1, 2, \dots, M. \quad (5.5.23)$$

These two equations provide a recursive scheme to calculate $B^{(i-1)}/A^{(i-1)}$ from $i = M$ to $i = 1$. The starting value $B^{(M)}/A^{(M)}$ depends on the M th layer. If this layer is unbounded (i.e., it extends to $z = -\infty$), $B^{(M)}/A^{(M)} = 0$. If this layer is backed by a ground plane (i.e., a perfectly conducting plane) placed at $z = z_{M+1}$, $B^{(M)}/A^{(M)} = e^{j2k_{z,M}z_{M+1}}$. At the last step of the recursive process, the value of $B^{(0)}/A^{(0)}$ is simply the desired reflection coefficient R^{TM} in Equation 5.5.18. Once R^{TM} is obtained, the total field above the layered medium is

$$E_z(\mathbf{r}) = -\frac{1}{4\pi\omega\epsilon_0} \int_0^\infty \frac{k_\rho^3}{k_{z,0}} J_0(k_\rho\rho) \left[e^{-jk_{z,0}|z|} + R^{\text{TM}} e^{-jk_{z,0}z} \right] dk_\rho \quad z \geq z_1 \quad (5.5.24)$$

from which other field components can be obtained. The field in each layer can also be found by evaluating $A^{(i)}$ and $B^{(i)}$ for $i = 1$ to $i = M$ using Equation 5.5.21 and the values of $B^{(i)}/A^{(i)}$ calculated previously.

5.5.3 Horizontal Electric Dipole above a Layered Medium

When the electric dipole is placed horizontally at the origin and points in the x -direction, the current density can be expressed as $\mathbf{J}(\mathbf{r}') = \hat{x}\delta(\mathbf{r}')$. From Equations 2.2.34 and 2.2.38, we find its radiated field in free space as

$$\mathbf{E}(\mathbf{r}) = -j\omega\mu_0 \left(\hat{x} + \frac{1}{k_0^2} \nabla \frac{\partial}{\partial x} \right) \frac{e^{-jk_0 r}}{4\pi r} \quad (5.5.25)$$

$$\mathbf{H}(\mathbf{r}) = -\hat{x} \times \nabla \frac{e^{-jk_0 r}}{4\pi r}. \quad (5.5.26)$$

Their z -components are

$$E_z(\mathbf{r}) = \frac{1}{j\omega\epsilon_0} \frac{\partial^2}{\partial x \partial z} \frac{e^{-jk_0 r}}{4\pi r} \quad (5.5.27)$$

$$H_z(\mathbf{r}) = -\frac{\partial}{\partial y} \frac{e^{-jk_0 r}}{4\pi r}. \quad (5.5.28)$$

Therefore, this field is a superposition of a TM and a TE field. Substituting Equation 5.5.10 into these two equations, we have

$$E_z(\mathbf{r}) = \pm \frac{j}{4\pi\omega\epsilon_0} \cos\phi \int_0^\infty k_\rho^2 J'_0(k_\rho\rho) e^{-jk_{z,0}|z|} dk_\rho \quad (5.5.29)$$

$$H_z(\mathbf{r}) = \frac{j}{4\pi} \sin\phi \int_0^\infty \frac{k_\rho^2}{k_{z,0}} J'_0(k_\rho\rho) e^{-jk_{z,0}|z|} dk_\rho. \quad (5.5.30)$$

When this dipole is placed above a layered medium (Fig. 5.20), its total field consists of the field derived above and the reflected field due to the layered medium:

$$E_z(\mathbf{r}) = \frac{j}{4\pi\omega\epsilon_0} \cos\phi \int_0^\infty k_\rho^2 J'_0(k_\rho\rho) [\pm e^{-jk_{z,0}|z|} - R^{\text{TM}} e^{-jk_{z,0}z}] dk_\rho \quad z \geq z_1 \quad (5.5.31)$$

$$H_z(\mathbf{r}) = \frac{j}{4\pi} \sin\phi \int_0^\infty \frac{k_\rho^2}{k_{z,0}} J'_0(k_\rho\rho) [e^{-jk_{z,0}|z|} + R^{\text{TE}} e^{-jk_{z,0}z}] dk_\rho \quad z \geq z_1. \quad (5.5.32)$$

It can be shown that the reflection coefficient R^{TM} is the same as the one in Equation 5.5.24. To find the reflection coefficient R^{TE} , we first write down the field H_z in the i th layer as

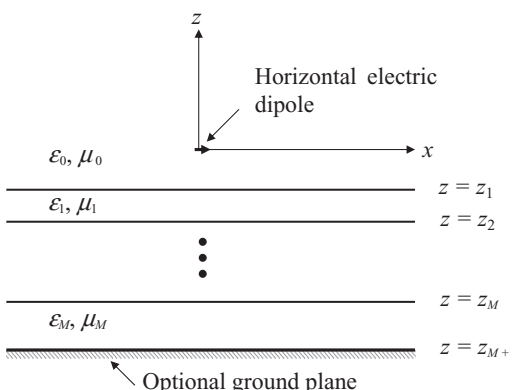


Figure 5.20 Horizontal electric dipole above a layered medium.

$$H_z^{(i)}(\mathbf{r}) = \frac{j}{4\pi} \sin \phi \int_0^\infty \frac{k_\rho^2}{k_{z,i}} J'_0(k_\rho \rho) [C^{(i)} e^{jk_{z,i} z} + D^{(i)} e^{-jk_{z,i} z}] dk_\rho. \quad (5.5.33)$$

The corresponding transverse field components can be found from Equation 5.1.21. By applying the field continuity conditions across each interface, we obtain

$$\frac{\mu_{i-1}}{k_{z,i-1}} [C^{(i-1)} e^{jk_{z,i-1} z_i} + D^{(i-1)} e^{-jk_{z,i-1} z_i}] = \frac{\mu_i}{k_{z,i}} [C^{(i)} e^{jk_{z,i} z_i} + D^{(i)} e^{-jk_{z,i} z_i}] \quad (5.5.34)$$

$$C^{(i-1)} e^{jk_{z,i-1} z_i} - D^{(i-1)} e^{-jk_{z,i-1} z_i} = C^{(i)} e^{jk_{z,i} z_i} - D^{(i)} e^{-jk_{z,i} z_i}. \quad (5.5.35)$$

From these, we find

$$\frac{D^{(i-1)}}{C^{(i-1)}} = \frac{R_H^{(i)} - 1}{R_H^{(i)} + 1} e^{j2k_{z,i-1} z_i} \quad i = 1, 2, \dots, M \quad (5.5.36)$$

where

$$R_H^{(i)} = \frac{\mu_i k_{z,i-1}}{\mu_{i-1} k_{z,i}} \frac{e^{jk_{z,i} z_i} + \frac{D^{(i)}}{C^{(i)}} e^{-jk_{z,i} z_i}}{e^{jk_{z,i} z_i} - \frac{D^{(i)}}{C^{(i)}} e^{-jk_{z,i} z_i}} \quad i = 1, 2, \dots, M. \quad (5.5.37)$$

These two equations provide a recursive algorithm to calculate $D^{(i-1)}/C^{(i-1)}$ from $i = M$ to $i = 1$. The starting value $D^{(M)}/C^{(M)}$ depends on the M th layer. If this layer is unbounded (i.e., it extends to $z = -\infty$), then $D^{(M)}/C^{(M)} = 0$. If this layer is backed by a ground plane placed at $z = z_{M+1}$, then $D^{(M)}/C^{(M)} = -e^{j2k_{z,M} z_{M+1}}$. At the last step of the recursive process, the value of $D^{(0)}/C^{(0)}$ is simply the desired reflection coefficient R^{TE} in Equation 5.5.32. Once R^{TE} is obtained, the unknown constants in each layer $C^{(i)}$ and $D^{(i)}$ can be calculated for $i = 1$ to $i = M$ using Equation 5.5.35 and the values of $D^{(i)}/C^{(i)}$ calculated previously. These, in turn, can be used to find the field in each layer.

5.5.4 Dipoles on a Grounded Dielectric Slab

A ground-backed dielectric slab is the most widely used configuration for microwave and millimeter-wave antennas and circuits. The results derived in Sections 5.5.2 and 5.5.3 can be simplified greatly for this configuration. Assume that the dielectric slab has a relative permittivity of ϵ_r and a thickness of h , and the top surface coincides with the xy -plane (Fig. 5.21). In this case, $B^{(1)}/A^{(1)} = e^{-j2k_{zd} h}$, where $k_{zd} = \sqrt{\epsilon_r k_0^2 - k_\rho^2}$; hence,

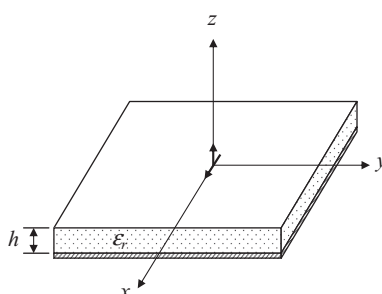


Figure 5.21 Dipoles on the top of a dielectric slab backed by a ground plane.

$$R_E^{(1)} = \frac{\epsilon_r k_{z0}}{jk_{zd}} \cot k_{zd} h. \quad (5.5.38)$$

From Equation 5.5.22, we have

$$R^{\text{TM}} = \frac{B^{(0)}}{A^{(0)}} = \frac{\epsilon_r k_{z0} - jk_{zd} \tan k_{zd} h}{\epsilon_r k_{z0} + jk_{zd} \tan k_{zd} h}. \quad (5.5.39)$$

Therefore, the field radiated by the vertical electric dipole above the dielectric slab is

$$E_z^{\text{VED}}(\mathbf{r}) = -\frac{1}{2\pi\omega\epsilon_0} \int_0^\infty J_0(k_\rho\rho) \frac{\epsilon_r k_\rho^3}{\epsilon_r k_{z0} + jk_{zd} \tan k_{zd} h} e^{-jk_{z0}z} dk_\rho \quad z \geq 0. \quad (5.5.40)$$

The TM part of the field radiated by the horizontal electric dipole above the dielectric slab is given by

$$E_z^{\text{HED}}(\mathbf{r}) = -\frac{1}{2\pi\omega\epsilon_0} \cos\phi \int_0^\infty J'_0(k_\rho\rho) \frac{k_\rho^2 k_{zd} \tan k_{zd} h}{\epsilon_r k_{z0} + jk_{zd} \tan k_{zd} h} e^{-jk_{z0}z} dk_\rho \quad z \geq 0. \quad (5.5.41)$$

To evaluate the TE part, we first find that $D^{(1)}/C^{(1)} = -e^{-j2k_{zd}h}$, from which we have

$$R_H^{(1)} = \frac{jk_{z0}}{k_{zd}} \tan k_{zd} h. \quad (5.5.42)$$

From Equation 5.5.36, we then obtain

$$R^{\text{TE}} = \frac{D^{(0)}}{C^{(0)}} = \frac{jk_{z0} \tan k_{zd} h - k_{zd}}{jk_{z0} \tan k_{zd} h + k_{zd}}. \quad (5.5.43)$$

Therefore, the TE part of the field radiated by the horizontal electric dipole above the dielectric slab is given by

$$H_z^{\text{HED}}(\mathbf{r}) = -\frac{1}{2\pi} \sin\phi \int_0^\infty J'_0(k_\rho\rho) \frac{k_\rho^2 \tan k_{zd} h}{jk_{z0} \tan k_{zd} h + k_{zd}} e^{-jk_{z0}z} dk_\rho \quad z \geq 0. \quad (5.5.44)$$

Once the z -components of the field are found, all other components can be obtained using Equations 5.1.11 and 5.1.12.

Although we have derived the expressions for the fields excited by an electric dipole in a layered medium, the evaluation of the integrals involved in these expressions is quite challenging. These integrals are called the *Sommerfeld integrals*, which are similar to the one in the Sommerfeld identity, except for more complicated integrands. The reader can consult the books by Chew [10] and Kong [11] for a detailed discussion on the properties and evaluation of these integrals.

NOTE

-
1. Since the modes obtained from Equation 5.3.40 were defined as EH_{mn} modes previously, it follows that the TE_{0n} modes are actually the EH_{0n} modes.

REFERENCES

- [1] Lord Rayleigh, On the passage of electric waves through tubes, or the vibrations of dielectric cylinders, *Phil. Mag.*, 43: 125–132, 1897.
- [2] S. RAMO, J. R. WHINNERY, and T. Van DUZER, *Fields and Waves in Communication Electronics* (3rd edition). New York: Wiley, 1994.
- [3] R. E. COLLIN, *Field Theory of Guided Waves* (2nd Edition). New York: IEEE Press, 1991.
- [4] C. G. SOMEDA, *Electromagnetic Waves* (2nd edition). Boca Raton, FL: CRC Press, 2006.
- [5] R. F. HARRINGTON, *Time-Harmonic Electromagnetic Fields*. New York: McGraw-Hill, 1961.
- [6] C. A. BALANIS, *Advanced Engineering Electromagnetics*. New York: Wiley, 1989.
- [7] U. S. INAN and A. S. INAN, *Electromagnetic Waves*. Upper Saddle River, NJ: Prentice Hall, 2000.
- [8] W. H. PRESS, S. A. TEUKOLSKY, W. T. VETTERLING, and B. P. FLANNERY, *Numerical Recipes* (2nd Edition). Cambridge, UK: Cambridge University Press, 1992.
- [9] C. T. TAI, *Dyadic Green Functions in Electromagnetic Theory* (2nd edition). Piscataway, NJ: IEEE Press, 1994.
- [10] W. C. CHEW, *Waves and Fields in Inhomogeneous Media*. Piscataway, NJ: IEEE Press, 1995.
- [11] J. A. KONG, *Electromagnetic Wave Theory*. Cambridge, MA: EMW Publishing, 2000.
- [12] M. ABRAMOWITZ and I. A. STEGUN, Eds., *Handbook of Mathematical Functions*. New York: Dover, 1965.

PROBLEMS

- 5.1.** Consider a parallel-plate waveguide that consists of an infinitely large conducting plate placed at $y = 0$ and another one at $y = b$. Assuming that the field has no variation in the x -direction, formulate the TM ($\mathbf{H} = \hat{x}H_x$) and TE ($\mathbf{E} = \hat{x}E_x$) modes propagating in the z -direction and find their cutoff wavenumbers; propagation constants; phase, group, and energy velocities; and wave impedances.
- 5.2.** Sketch the top view of the electric and magnetic field distributions of the TE_{10} and TM_{11} modes in the rectangular waveguide shown in Figure 5.2.
- 5.3.** Although the waveguide modes form a complete set so that their combination can represent any field in the waveguide, their formulation is not unique. For example, for the rectangular waveguide shown in Figure 5.2, we can also formulate a complete set of waveguide modes that consist of transverse electric to x (TE_x) and transverse magnetic to x (TM_x) modes. Formulate the modal fields of these modes and find their cutoff wavenumbers, propagation constants, and wave impedances.
- 5.4.** Find the attenuation constant of the TM_{11} mode of an empty rectangular waveguide made of a conductor with a conductivity of σ .
- 5.5.** Find the quality factor of the TM_{110} mode in an empty rectangular cavity made of a conductor with a conductivity of σ .
- 5.6.** Consider a cavity with a protruded surface. The volume of protrusion over the original cavity is ΔV . Find the formula to calculate the shift of the resonant frequency and compare it with Equation 5.2.49.
- 5.7.** A small thin circular dielectric disk of radius r and thickness t is placed at the center of the bottom wall of a rectangular cavity. Find the shift of the resonant frequency of the TE_{101} mode.
- 5.8.** Consider the waveguide shown in Figure 5.11. Show that in general a waveguide mode without both E_z and H_z cannot satisfy all the boundary conditions at the discontinuous interface $y = h$.
- 5.9.** Although the waveguide in Figure 5.11 cannot support either TE_z or TM_z modes, it can support both TE_y and TM_y modes. Formulate these waveguide modes and find the transcendental equations to determine the propagation constants. Compare the results with those in Section 5.3.2.

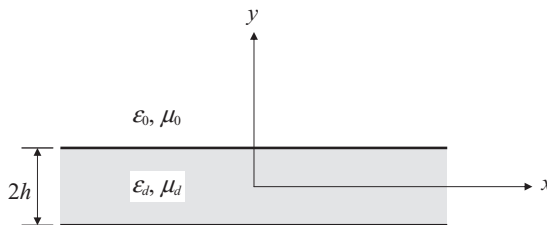


Figure 5.22 Dielectric slab waveguide.

- 5.10. Consider a dielectric slab waveguide illustrated in Figure 5.22. Formulate the TE and TM modes that have no variation in the x -direction. Discuss the relation between this problem and the one shown in Figure 5.13.
- 5.11. Consider a dielectric slab waveguide on a ground plane (Fig. 5.13). Starting from Equations 5.3.63–5.3.67, complete the analysis of hybrid modes and derive Equations 5.3.68–5.3.71.
- 5.12. Consider the problem illustrated in Figure 5.17. Assume that the waveguide on the left-hand side is terminated by a conductor at $z = -d$. Find the field excited by the current probe.
- 5.13. Based on Equations 5.4.17 and 5.4.18, design the configuration of an electric current to excite the TE_{01} , TE_{20} , TE_{11} , and TM_{11} modes in a rectangular waveguide, respectively.
- 5.14. Consider the problems illustrated in Figures 4.13 and 4.14. If the medium in the right half-space is replaced by a planar layered medium, formulate a recursive process with all the necessary formulas to calculate the reflected fields and fields in each layer.
- 5.15. Evaluate the integrals in Equations 5.5.40, 5.5.41, and 5.5.44 to find the far fields radiated by a vertical and a horizontal electric dipole placed on the top of a grounded dielectric slab (Fig. 5.21). (*Hint:* Use the method of stationary phase.)
- 5.16. Find the far fields radiated by a vertical and horizontal electric dipole placed on the top of a grounded dielectric slab (Fig. 5.21) using the reciprocity theorem. Compare the results with those obtained in Problem 5.15. ■

CHAPTER 6

FIELDS AND WAVES IN CYLINDRICAL COORDINATES

In this chapter we discuss electromagnetic analysis in the cylindrical coordinate system. We first discuss the solution of the Helmholtz equation by the method of separation of variables and derive cylindrical wave functions. We then employ cylindrical wave functions to analyze circular and coaxial waveguides and cavities. This is followed by the analysis of wave propagation along circular dielectric waveguides. After that, we derive a wave transformation that expands a plane wave in terms of cylindrical wave functions. The derived wave transformation is then used for solving various scattering problems involving a conducting or a dielectric cylinder. Finally, we discuss a few radiation problems where a line current or a cylindrical surface current radiates in the presence of a conducting cylinder or a conducting wedge. The solutions will be used to derive the Sommerfeld radiation condition for two-dimensional fields and to illustrate the phenomenon of the transverse field singularity at a conducting edge.

6.1 SOLUTION OF WAVE EQUATION

In cylindrical coordinates, the Helmholtz equation $\nabla^2\psi + k^2\psi = 0$ can be written as

$$\frac{\partial^2\psi}{\partial\rho^2} + \frac{1}{\rho}\frac{\partial\psi}{\partial\rho} + \frac{1}{\rho^2}\frac{\partial^2\psi}{\partial\phi^2} + \frac{\partial^2\psi}{\partial z^2} + k^2\psi = 0. \quad (6.1.1)$$

The particular solutions to this equation are called *cylindrical wave functions* and can be obtained using the method of separation of variables.

6.1.1 Solution by Separation of Variables

We first assume that the solution to Equation 6.1.1 can be written in the following product form

$$\psi(\rho, \phi, z) = P(\rho)\Phi(\phi)Z(z). \quad (6.1.2)$$

By substituting this into Equation 6.1.1 and then dividing the entire equation by $P(\rho)\Phi(\phi)Z(z)$, we obtain

$$\frac{1}{P}\frac{d^2P}{d\rho^2} + \frac{1}{\rho P}\frac{dP}{d\rho} + \frac{1}{\rho^2\Phi}\frac{d^2\Phi}{d\phi^2} + \frac{1}{Z}\frac{d^2Z}{dz^2} + k^2 = 0. \quad (6.1.3)$$

Since only the fourth term contains z and all other terms are independent of z , the fourth term must be a constant, which yields

$$\frac{d^2Z}{dz^2} + h^2 Z = 0 \quad (6.1.4)$$

where h^2 denotes an arbitrary constant that can only be determined in specific problems. Equation 6.1.4 has a well-known solution given by

$$Z(z) = A(h)e^{-jhz} + B(h)e^{jhz} \quad (6.1.5)$$

where A and B are arbitrary constants. With this separation, Equation 6.1.3 is reduced to

$$\frac{\rho^2}{P} \frac{d^2P}{d\rho^2} + \frac{\rho}{P} \frac{dP}{d\rho} + \frac{1}{\Phi} \frac{d^2\Phi}{d\phi^2} + (k^2 - h^2)\rho^2 = 0 \quad (6.1.6)$$

after a multiplication by ρ^2 . Since only the third term depends on ϕ and the rest of the terms depend only on ρ , Equation 6.1.6 can be separated into two equations

$$\frac{1}{\Phi} \frac{d^2\Phi}{d\phi^2} = -m^2 \quad (6.1.7)$$

$$\frac{\rho^2}{P} \frac{d^2P}{d\rho^2} + \frac{\rho}{P} \frac{dP}{d\rho} + (k^2 - h^2)\rho^2 = m^2 \quad (6.1.8)$$

which can also be written as

$$\frac{d^2\Phi}{d\phi^2} + m^2\Phi = 0 \quad (6.1.9)$$

$$\rho^2 \frac{d^2P}{d\rho^2} + \rho \frac{dP}{d\rho} + [(k_\rho \rho)^2 - m^2]P = 0 \quad (6.1.10)$$

where m^2 denotes another arbitrary constant that can only be determined in specific problems and $k_\rho^2 = k^2 - h^2$. Equation 6.1.9 has a well-known solution given by

$$\Phi(\phi) = c_m \cos m\phi + d_m \sin m\phi \quad (6.1.11)$$

where c_m and d_m are arbitrary combination constants.

Equation 6.1.10 is known as the *cylindrical Bessel equation*, whose two linearly independent solutions are denoted as $J_m(k_\rho \rho)$ and $Y_m(k_\rho \rho)$, which are known as the *cylindrical Bessel functions*, or simply the *Bessel functions*, of the first and second kind, respectively. A general solution is a linear combination of these two solutions

$$P(\rho) = a_m J_m(k_\rho \rho) + b_m Y_m(k_\rho \rho) \quad (6.1.12)$$

where a_m and b_m are constants. Although both $J_m(k_\rho \rho)$ and $Y_m(k_\rho \rho)$ have complicated expressions and possess many special properties [1], it is sufficient for our purpose to remember the following properties

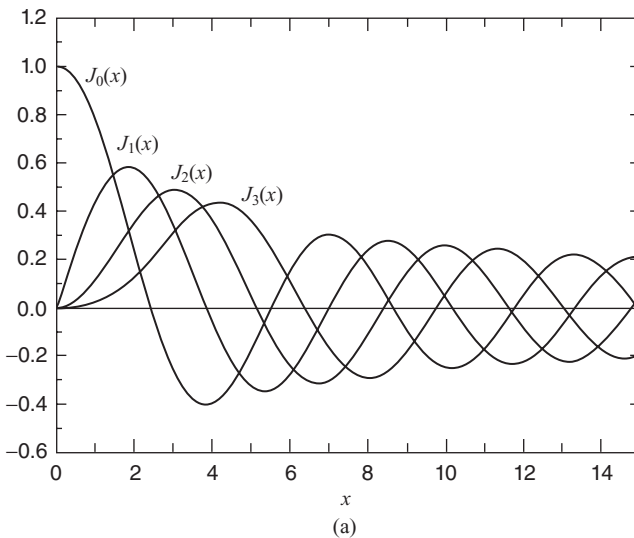
$$J_m(k_\rho \rho) \rightarrow \text{finite} \quad \text{when } k_\rho \rho \rightarrow 0 \quad (6.1.13)$$

$$Y_m(k_\rho \rho) \rightarrow \infty \quad \text{when } k_\rho \rho \rightarrow 0. \quad (6.1.14)$$

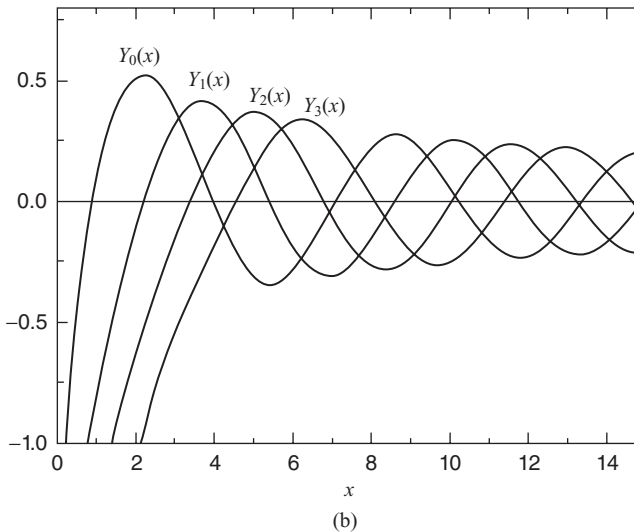
Other special properties will be discussed later when necessary. Figure 6.1 plots the first few Bessel functions of an integer order to show the distinct behavior of these functions [2].

Based on the individual solutions discussed above, a particular solution of Equation 6.1.1 is given by

$$\psi_{mh}(\rho, \phi, z) = [a_m J_m(k_\rho \rho) + b_m Y_m(k_\rho \rho)] [c_m \cos m\phi + d_m \sin m\phi] [A(h)e^{-jhz} + B(h)e^{jhz}]. \quad (6.1.15)$$



(a)



(b)

Figure 6.1 Cylindrical Bessel functions with an integer order. (a) Bessel functions of the first kind $J_m(x)$. (b) Bessel functions of the second kind $Y_m(x)$.

Since this solution is valid for any m and h , the general solution to Equation 6.1.1 is a linear combination of all possible solutions, which can be expressed as a summation over all possible m and an integration over all possible h :

$$\begin{aligned}\psi(\rho, \phi, z) = & \sum_m \int [a_m J_m(k_\rho \rho) + b_m Y_m(k_\rho \rho)] [c_m \cos m\phi + d_m \sin m\phi] \\ & \times [A(h)e^{-jhz} + B(h)e^{jhz}] dh.\end{aligned}\quad (6.1.16)$$

Here we assume that m is a discrete number and h is continuous. As mentioned before, m and h depend on specific problems. If m is continuous, the summation then becomes an integral, and if h is a discrete number, the integral then becomes a summation.

6.1.2 Cylindrical Wave Functions

A cylindrical wave function is defined as a particular solution to the Helmholtz equation in the cylindrical coordinate system [3]. This solution is given by Equation 6.1.15 derived in the preceding subsection and can be denoted as ψ_{mh} . Obviously, there are an infinite number of cylindrical wave functions, and these functions form a complete set such that any solution of the Helmholtz equation can be represented by a linear superposition of these functions as expressed in Equation 6.1.16. However, the form of a cylindrical wave function is not unique. For example, instead of using e^{-jhz} and e^{jhz} as the two linearly independent solutions of Equation 6.1.4, we can also choose to use $\sin hz$ and $\cos hz$ as the two linearly independent solutions of Equation 6.1.4. Other combinations are also possible as long as the two solutions are linearly independent so that one cannot be fully represented by the other. In principle, it does not matter what two specific solutions are used. The final solution, if solved correctly, is always the same. However, choosing appropriate forms can usually simplify the solution process. In general, we should choose the solutions that resemble the final solution closely. For example, for a problem unbounded in the z -direction, e^{-jhz} and e^{jhz} are appropriate choices since they represent waves propagating along the positive and negative z -directions. If a problem is finite in the z -direction, $\sin hz$ and $\cos hz$ would be better choices since they can be used more conveniently to satisfy boundary conditions at the two ends.

Similarly, in the angular direction, in addition to $\sin m\phi$ and $\cos m\phi$, we can also choose $e^{-jm\phi}$ and $e^{jm\phi}$ as the two independent solutions of Equation 6.1.9. The second choice is particularly convenient in the expansion of a general solution because $e^{-jm\phi}$ can be represented by $e^{jm\phi}$ when m is extended to include negative values, which would result in a more compact expression. In the radial direction, in addition to $J_m(k_\rho \rho)$ and $Y_m(k_\rho \rho)$, the two other commonly used linearly independent solutions of Equation 6.1.10 are the *Hankel functions* of the first and second kind, denoted as $H_m^{(1)}(k_\rho \rho)$ and $H_m^{(2)}(k_\rho \rho)$ and defined as

$$H_m^{(1)}(k_\rho \rho) = J_m(k_\rho \rho) + jY_m(k_\rho \rho) \quad (6.1.17)$$

$$H_m^{(2)}(k_\rho \rho) = J_m(k_\rho \rho) - jY_m(k_\rho \rho). \quad (6.1.18)$$

By substituting the large-argument expressions of $J_m(k_\rho \rho)$ and $Y_m(k_\rho \rho)$ [1]

$$J_m(k_\rho \rho) \approx \sqrt{\frac{2}{\pi k_\rho \rho}} \cos\left(k_\rho \rho - \frac{m\pi}{2} - \frac{\pi}{4}\right) \quad \text{when } k_\rho \rho \gg 1 \quad (6.1.19)$$

$$Y_m(k_\rho \rho) \approx \sqrt{\frac{2}{\pi k_\rho \rho}} \sin\left(k_\rho \rho - \frac{m\pi}{2} - \frac{\pi}{4}\right) \quad \text{when } k_\rho \rho \gg 1 \quad (6.1.20)$$

into the definitions above, we find the asymptotic forms of $H_m^{(1)}(k_\rho \rho)$ and $H_m^{(2)}(k_\rho \rho)$ as

$$H_m^{(1)}(k_\rho \rho) \approx \sqrt{\frac{2}{\pi k_\rho \rho}} e^{j(k_\rho \rho - m\pi/2 - \pi/4)} \quad \text{when } k_\rho \rho \gg 1 \quad (6.1.21)$$

$$H_m^{(2)}(k_\rho \rho) \approx \sqrt{\frac{2}{\pi k_\rho \rho}} e^{-j(k_\rho \rho - m\pi/2 - \pi/4)} \quad \text{when } k_\rho \rho \gg 1 \quad (6.1.22)$$

which indicate clearly that $H_m^{(1)}(k_\rho \rho)$ represents a cylindrical wave propagating along the negative ρ -direction, whereas $H_m^{(2)}(k_\rho \rho)$ represents a cylindrical wave propagating along the positive ρ -direction. Therefore, if a problem is unbounded in the ρ -direction, $H_m^{(1)}(k_\rho \rho)$ and $H_m^{(2)}(k_\rho \rho)$ would be better choices to expand the general solution. However, if a problem is finite in the ρ -direction, $J_m(k_\rho \rho)$ and $Y_m(k_\rho \rho)$ might be used more conveniently.

For a specific problem, its cylindrical wave functions ψ_{mh} should contain at most only one constant at the front since Equation 6.1.1 is a homogeneous equation. In other words, both m and h should be determined and, in addition, the ratio of the two combination constants in each of $P(\rho)$, $\Phi(\phi)$, and $Z(z)$ should also be determined. The determination of these constants can be accomplished by application of boundary conditions in the specific problem. In general, there are two boundary conditions in each direction: one at each end. If there are no specific boundary conditions given, we then need to determine the constants based on the characteristics of the solution and the wave functions. For example, if we intend to study wave propagation in an infinitely long waveguide along the z -direction, we can set $B(h) = 0$ in Equation 6.1.15 to study the wave propagating along the positive z -direction or set $A(h) = 0$ to study the wave propagating along the negative z -direction. For another example, if the solution domain includes the z -axis and the solution is finite at the z -axis, we have to set $b_m = 0$ in Equation 6.1.15 to exclude $Y_m(k_\rho \rho)$. On the other hand, if the solution domain is unbounded in the ρ -direction and the solution represents a wave propagating in the positive ρ -direction, we should set $b_m = -ja_m$ or equivalently choose $H_m^{(2)}(k_\rho \rho)$ as the function in the ρ -direction. Finally, if ϕ is unbounded and the solution is single-valued, then $\Phi(\phi)$ should satisfy the periodic condition $\Phi(\phi + 2\pi) = \Phi(\phi)$, which in turn requires m to be integers. In that case, both $\sin m\phi$ and $\cos m\phi$ are correct solutions—they represent two identical solutions except for a rotation of $\pi/2$.

6.2 CIRCULAR AND COAXIAL WAVEGUIDES AND CAVITIES

As discussed in the preceding chapter, a uniform waveguide and cavity can support both transverse electric (TE) and transverse magnetic (TM) modes. The field expressions for the TE modes can be derived from Equations 2.1.37 and 2.1.38 by letting $\mathbf{A} = 0$ and $\mathbf{F} = \hat{z}F_z$, where F_z satisfies the Helmholtz equation. In cylindrical coordinates, this yields

$$E_\rho = -\frac{1}{\epsilon\rho} \frac{\partial F_z}{\partial\phi}, \quad H_\rho = \frac{1}{j\omega\mu\epsilon} \frac{\partial^2 F_z}{\partial\rho\partial z} \quad (6.2.1)$$

$$E_\phi = \frac{1}{\epsilon} \frac{\partial F_z}{\partial\rho}, \quad H_\phi = \frac{1}{j\omega\mu\epsilon} \frac{1}{\rho} \frac{\partial^2 F_z}{\partial\phi\partial z} \quad (6.2.2)$$

$$E_z = 0, \quad H_z = \frac{1}{j\omega\mu\epsilon} \left(\frac{\partial^2}{\partial z^2} + k^2 \right) F_z. \quad (6.2.3)$$

Similarly, the field expressions for the TM modes can be derived from Equations 2.1.37 and 2.1.38 by letting $\mathbf{A} = \hat{z}A_z$ and $\mathbf{F} = 0$, where A_z satisfies the Helmholtz equation. In cylindrical coordinates, this yields

$$E_\rho = \frac{1}{j\omega\mu\epsilon} \frac{\partial^2 A_z}{\partial\rho\partial z}, \quad H_\rho = \frac{1}{\mu\rho} \frac{\partial A_z}{\partial\phi} \quad (6.2.4)$$

$$E_\phi = \frac{1}{j\omega\mu\epsilon} \frac{1}{\rho} \frac{\partial^2 A_z}{\partial\phi\partial z}, \quad H_\phi = -\frac{1}{\mu} \frac{\partial A_z}{\partial\rho} \quad (6.2.5)$$

$$E_z = \frac{1}{j\omega\mu\epsilon} \left(\frac{\partial^2}{\partial z^2} + k^2 \right) A_z, \quad H_z = 0. \quad (6.2.6)$$

Alternatively, the analysis of the TE and TM modes can be performed directly in terms of H_z and E_z , both of which satisfy the Helmholtz equation. Assuming that the modes propagate in the z -direction with a propagation constant of k_z , the field components for the TE modes are given by

$$E_\rho = -\frac{j\omega\mu}{k_\rho^2} \frac{1}{\rho} \frac{\partial H_z}{\partial\phi}, \quad H_\rho = -\frac{jk_z}{k_\rho^2} \frac{\partial H_z}{\partial\rho} \quad (6.2.7)$$

$$E_\phi = \frac{j\omega\mu}{k_\rho^2} \frac{\partial H_z}{\partial\rho}, \quad H_\phi = -\frac{jk_z}{k_\rho^2} \frac{1}{\rho} \frac{\partial H_z}{\partial\phi} \quad (6.2.8)$$

whereas the field components for the TM modes are given by

$$E_\rho = -\frac{jk_z}{k_\rho^2} \frac{\partial E_z}{\partial\rho}, \quad H_\rho = \frac{j\omega\epsilon}{k_\rho^2} \frac{1}{\rho} \frac{\partial E_z}{\partial\phi} \quad (6.2.9)$$

$$E_\phi = -\frac{jk_z}{k_\rho^2} \frac{1}{\rho} \frac{\partial E_z}{\partial\phi}, \quad H_\phi = -\frac{j\omega\epsilon}{k_\rho^2} \frac{\partial E_z}{\partial\rho}. \quad (6.2.10)$$

where $k_\rho^2 = k^2 - k_z^2$. The analysis in terms of H_z and E_z is sometimes more convenient as it avoids the use of auxiliary variables F_z and A_z .

6.2.1 Circular Waveguide

We first consider wave propagation in an empty circular conducting waveguide [4–9]. For a circular waveguide whose axis coincides with the z -axis (Fig. 6.2), since ϕ is not

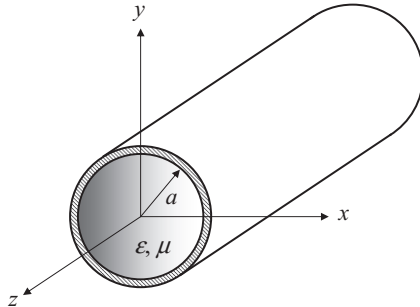


Figure 6.2 Uniformly filled circular waveguide.

TABLE 6.1 The First Few Roots of $J_m(z) = 0$

$m \backslash n$	1	2	3	4
0	2.404826	5.520078	8.653728	11.79153
1	3.831706	7.015587	10.17347	13.32369
2	5.135622	8.417244	11.61984	14.79595
3	6.380162	9.761023	13.01520	16.22347
4	7.588342	11.06471	14.37254	17.61597

bounded, m in the cylindrical wave function must be an integer to have a single-valued solution. Furthermore, since the field is finite along the z -axis, the Bessel functions of the second kind must be excluded. Hence, for the TM modes, E_z takes the form

$$E_z = E_0 J_m(k_\rho \rho) \begin{Bmatrix} \sin m\phi \\ \cos m\phi \end{Bmatrix} e^{-jk_z z} \quad m = 0, 1, 2, \dots \quad (6.2.11)$$

where E_0 is a constant. To determine k_ρ , we apply the boundary condition at the conducting wall of the waveguide, $E_z|_{\rho=a} = 0$, to find that $J_m(k_\rho a) = 0$. Denoting the roots of $J_m(z) = 0$ as χ_{mn} ($n = 1, 2, \dots$), we have $k_\rho a = \chi_{mn}$; hence, $k_\rho = \chi_{mn}/a$ and the propagation constant of the TM_{mn} mode is then given by

$$k_{zmn}^{\text{TM}} = \sqrt{k^2 - k_\rho^2} = \sqrt{\omega^2 \mu \epsilon - \left(\frac{\chi_{mn}}{a}\right)^2}. \quad (6.2.12)$$

The cutoff wavenumbers and frequencies are given by

$$k_{cmn}^{\text{TM}} = \frac{\chi_{mn}}{a} \quad \text{and} \quad f_{cmn}^{\text{TM}} = \frac{\chi_{mn}}{2\pi a \sqrt{\mu \epsilon}}. \quad (6.2.13)$$

The first few values of χ_{mn} are given in Table 6.1 [2].

The other field components of the TM_{mn} modes can be obtained by substituting Equation 6.2.11 into Equations 6.2.9 and 6.2.10, which yields

$$E_\rho = -E_0 \frac{j k_z}{k_\rho} J'_m(k_\rho \rho) \begin{Bmatrix} \sin m\phi \\ \cos m\phi \end{Bmatrix} e^{-jk_z z} \quad (6.2.14)$$

$$E_\phi = \mp E_0 \frac{jk_z}{\rho k_\rho^2} J_m(k_\rho \rho) \begin{Bmatrix} \cos m\phi \\ \sin m\phi \end{Bmatrix} e^{-jk_z z} \quad (6.2.15)$$

$$H_\rho = \pm E_0 \frac{jm\omega\epsilon}{\rho k_\rho^2} J_m(k_\rho \rho) \begin{Bmatrix} \cos m\phi \\ \sin m\phi \end{Bmatrix} e^{-jk_z z} \quad (6.2.16)$$

$$H_\phi = -E_0 \frac{j\omega\epsilon}{k_\rho} J'_m(k_\rho \rho) \begin{Bmatrix} \sin m\phi \\ \cos m\phi \end{Bmatrix} e^{-jk_z z}. \quad (6.2.17)$$

The analysis of the TE modes follows a similar procedure. For the same reasons discussed earlier, H_z takes the form

$$H_z = H_0 J_m(k_\rho \rho) \begin{Bmatrix} \sin m\phi \\ \cos m\phi \end{Bmatrix} e^{-jk_z z} \quad m = 0, 1, 2, \dots \quad (6.2.18)$$

where H_0 is a constant. To determine k_ρ , we apply the boundary condition at the conducting wall of the waveguide, $E_\phi|_{\rho=a}=0$, to find that $J'_m(k_\rho a)=0$. Denoting the roots of $J'_m(z)=0$ as χ'_{mn} ($n=1, 2, \dots$), we have $k_\rho a = \chi'_{mn}$; hence, $k_\rho = \chi'_{mn}/a$ and the propagation constant of the TE_{mn} mode is then given by

$$k_{zmn}^{\text{TE}} = \sqrt{k^2 - k_\rho^2} = \sqrt{\omega^2 \mu \epsilon - \left(\frac{\chi'_{mn}}{a}\right)^2}. \quad (6.2.19)$$

The cutoff wavenumbers and frequencies are given by

$$k_{cmn}^{\text{TE}} = \frac{\chi'_{mn}}{a} \quad \text{and} \quad f_{cmn}^{\text{TE}} = \frac{\chi'_{mn}}{2\pi a \sqrt{\mu \epsilon}}. \quad (6.2.20)$$

The first few values of χ'_{mn} are given in Table 6.2 [2].

The other field components of the TE_{mn} modes can be obtained by substituting Equation 6.2.18 into Equations 6.2.7 and 6.2.8, which yields

$$E_\rho = \mp H_0 \frac{jm\omega\mu}{\rho k_\rho^2} J_m(k_\rho \rho) \begin{Bmatrix} \cos m\phi \\ \sin m\phi \end{Bmatrix} e^{-jk_z z} \quad (6.2.21)$$

$$E_\phi = H_0 \frac{j\omega\mu}{k_\rho} J'_m(k_\rho \rho) \begin{Bmatrix} \sin m\phi \\ \cos m\phi \end{Bmatrix} e^{-jk_z z} \quad (6.2.22)$$

TABLE 6.2 The First Few Roots of $J'_m(z)=0$

$m \backslash n$	1	2	3	4
0	3.831706	7.015587	10.17347	13.32369
1	1.841184	5.331443	9.536316	11.70600
2	3.054237	6.706133	9.969468	13.17037
3	4.201189	8.015237	11.34592	14.58585
4	5.317553	9.282396	12.68191	15.96411

$$H_\rho = -H_0 \frac{jk_z}{k_\rho} J'_m(k_\rho \rho) \begin{cases} \sin m\phi \\ \cos m\phi \end{cases} e^{-jk_z z} \quad (6.2.23)$$

$$H_\phi = \mp H_0 \frac{jmk_z}{pk_\rho^2} J_m(k_\rho \rho) \begin{cases} \cos m\phi \\ \sin m\phi \end{cases} e^{-jk_z z}. \quad (6.2.24)$$

Once all the field components are available, other physical quantities such as wave impedance, power flow density, and phase and energy velocities can be derived based on their definitions. The attenuation constant due to small conductor and material losses can also be analyzed using the perturbational method discussed in Chapter 5.

By comparing the data in Tables 6.1 and 6.2, we find that among all the waveguide modes in a circular waveguide, the dominant mode is the TE₁₁ mode, since this mode has the lowest cutoff frequency. Its cutoff wavelength is $\lambda_{c11}^{TE} = 3.4126a$. The first higher-order mode is the TM₀₁ mode, whose cutoff wavelength is $\lambda_{c01}^{TM} = 2.6127a$. The transverse field distribution of the first 30 modes is plotted in Figure 6.3. The solid lines represent electric field lines and the dashed lines represent the magnetic field lines. For the TE modes, the electric field lines are confined in the transverse plane (either forming self-closed contours or terminating at the waveguide wall because of the surface electric charges there), whereas the magnetic field lines will turn into the longitudinal direction at the places where the dashed lines end. Conversely, for the TM modes, the magnetic field lines are confined in the transverse plane (forming self-closed contours since there are no magnetic charges), whereas the electric field lines can turn into the longitudinal direction at the places where the solid lines end. From the field distribution, we can also easily find the surface current distribution on the waveguide wall ($\mathbf{J}_s = \hat{n} \times \mathbf{H}$). As mentioned in Chapter 5, having a good understanding of the surface current distribution for each mode is very helpful to designing waveguide devices.

6.2.2 Coaxial Waveguide

The analysis of a coaxial waveguide (Fig. 6.4) is similar to that for a circular waveguide. The only difference is that because of the existence of the inner conductor, the field region does not include the z -axis. Therefore, both the Bessel functions of the first and second kind should be included. For the TM modes, E_z takes the form

$$E_z = [a_m J_m(k_\rho \rho) + b_m Y_m(k_\rho \rho)] \begin{cases} \sin m\phi \\ \cos m\phi \end{cases} e^{-jk_z z} \quad m = 0, 1, 2, \dots \quad (6.2.25)$$

To determine one of the combination constants and k_ρ , we apply the boundary condition at the surfaces of the inner and outer conductors, $E_z|_{\rho=a} = E_z|_{\rho=b} = 0$, to find that

$$a_m J_m(k_\rho a) + b_m Y_m(k_\rho a) = 0 \quad (6.2.26)$$

$$a_m J_m(k_\rho b) + b_m Y_m(k_\rho b) = 0. \quad (6.2.27)$$

To have a non-trivial solution for a_m and b_m , the determinant of the coefficient matrix must vanish, which yields

$$J_m(k_\rho a)Y_m(k_\rho b) - Y_m(k_\rho a)J_m(k_\rho b) = 0. \quad (6.2.28)$$

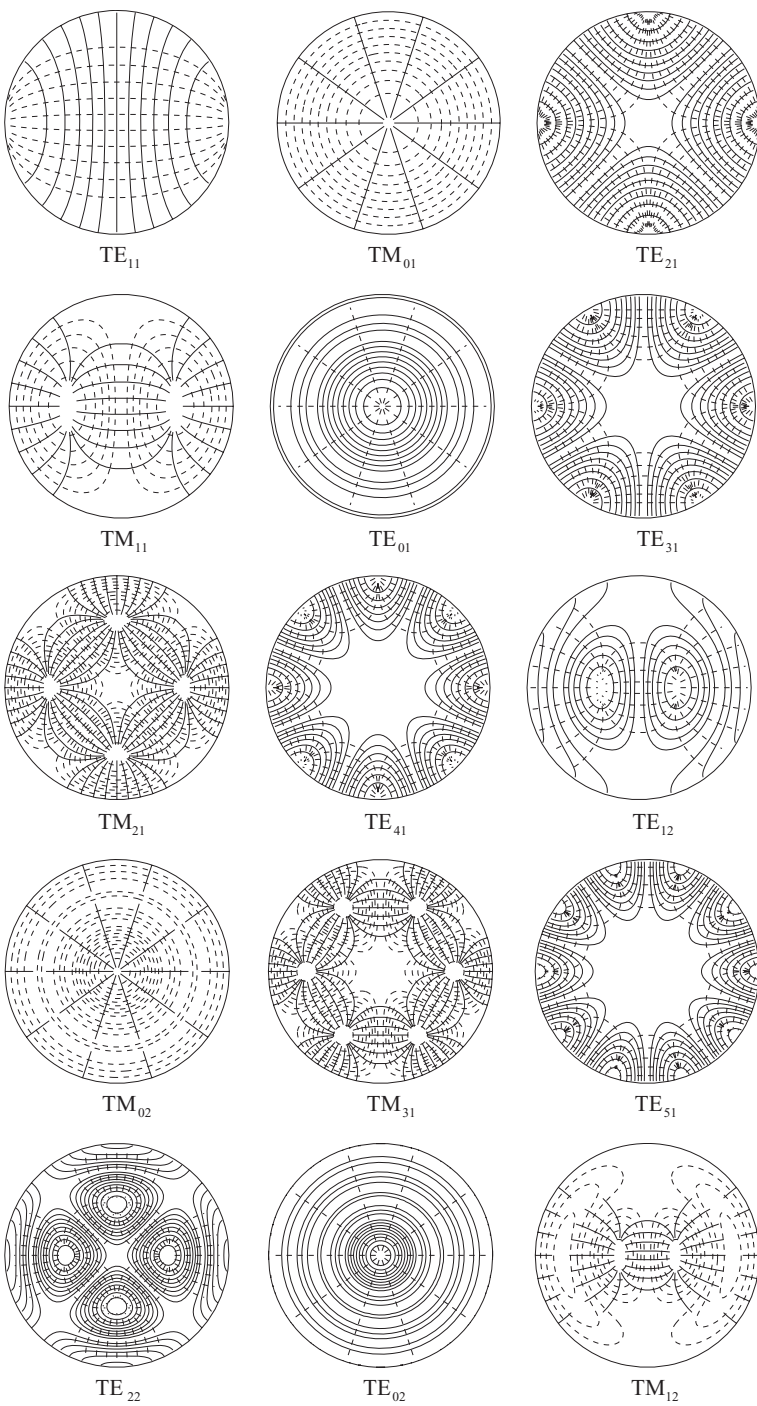


Figure 6.3 Transverse field distribution of the first 30 modes in a circular waveguide.

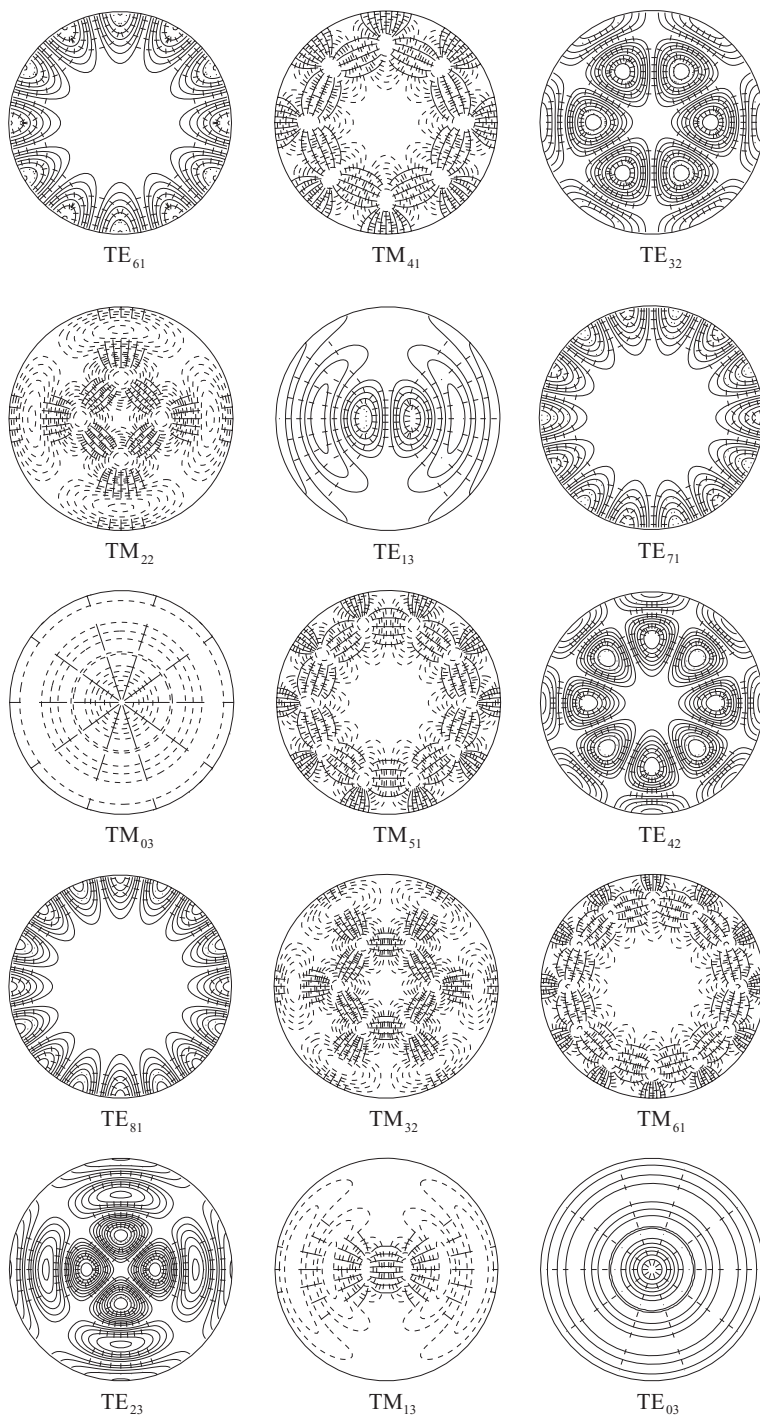
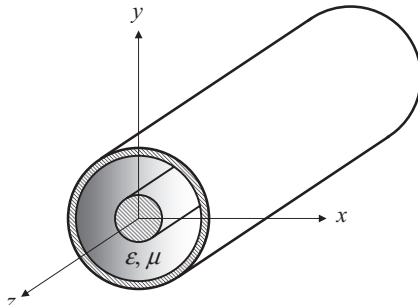


Figure 6.3 Transverse field distribution of the first 30 modes in a circular waveguide (*continued*).

**Figure 6.4** Uniformly filled coaxial waveguide.

The roots of this equation determine the values of k_ρ , which can be denoted as $k_{\rho mn}$, from which the propagation constant can be determined. Other field components can be derived by substituting Equation 6.2.25 into Equations 6.2.9 and 6.2.10.

For the TE modes, H_z takes the form

$$H_z = [a'_m J_m(k_\rho \rho) + b'_m Y_m(k_\rho \rho)] \begin{cases} \sin m\phi \\ \cos m\phi \end{cases} e^{-jk_z z} \quad m = 0, 1, 2, \dots \quad (6.2.29)$$

To determine one of the combination constants and k_ρ , we apply the boundary condition at the surfaces of the inner and outer conductors, $E_\phi|_{\rho=a} = E_\phi|_{\rho=b} = 0$, to find that

$$a'_m J'_m(k_\rho a) + b'_m Y'_m(k_\rho a) = 0 \quad (6.2.30)$$

$$a'_m J'_m(k_\rho b) + b'_m Y'_m(k_\rho b) = 0. \quad (6.2.31)$$

To have a non-trivial solution for a'_m and b'_m , the determinant of the coefficient matrix must vanish, which yields

$$J'_m(k_\rho a)Y'_m(k_\rho b) - Y'_m(k_\rho a)J'_m(k_\rho b) = 0. \quad (6.2.32)$$

The roots of this equation determine the values of k_ρ , which can be denoted as $k'_{\rho mn}$, from which the propagation constant can be determined. Other field components can be derived by substituting Equation 6.2.29 into Equations 6.2.7 and 6.2.8.

The analysis of the TE and TM modes described above is based on the assumption that $k_\rho \neq 0$ or $k_z \neq k$. When $k_\rho = 0$, it is possible to have a solution for the transverse field components provided that $E_z = H_z = 0$, which is evident in Equations 6.2.7–6.2.10. In this case, the Helmholtz equation is reduced to

$$\frac{\partial^2 \psi}{\partial \rho^2} + \frac{1}{\rho} \frac{\partial \psi}{\partial \rho} + \frac{1}{\rho^2} \frac{\partial^2 \psi}{\partial \phi^2} = 0 \quad (6.2.33)$$

or

$$\frac{\partial^2 \psi}{\partial \rho^2} + \frac{1}{\rho} \frac{\partial \psi}{\partial \rho} - \frac{m^2}{\rho^2} \psi = 0. \quad (6.2.34)$$

When $m = 0$, this equation has a non-trivial solution given by

$$\psi = C \ln \rho e^{-jkz}. \quad (6.2.35)$$

When this is used as the solution for A_z , its substitution into Equations 6.2.4–6.2.6 yields

$$E_\rho = -\frac{C}{\sqrt{\mu\epsilon}} \frac{1}{\rho} e^{-jkz}, \quad E_\phi = E_z = 0 \quad (6.2.36)$$

$$H_\phi = -\frac{C}{\mu} \frac{1}{\rho} e^{-jkz}, \quad H_\rho = H_z = 0. \quad (6.2.37)$$

This special solution is called the transverse electromagnetic (TEM) mode, whose propagation constant is given by $k_z = k = \omega\sqrt{\mu\epsilon}$, which does not have a cutoff frequency. Clearly, this mode cannot exist in a circular waveguide because the field would be singular at the z -axis. Note that the TEM mode can exist in a coaxial waveguide because this waveguide consists of two separate conductors. As long as a waveguide is made of two or more than two separate conductors and is filled with a homogeneous medium, it can generally support a TEM mode. The fact that the TEM mode does not have a cutoff frequency makes coaxial waveguides very useful for signal transmission.

From the field expressions, it is easy to find that the phase, energy, and group velocities of the TEM mode are all equal to $1/\sqrt{\mu\epsilon}$ and the wave impedance is $\sqrt{\mu/\epsilon}$. We can also find that the total current on the inner conductor is

$$I(z) = \int_0^{2\pi} H_\phi \Big|_{\rho=a} a d\phi = -C \frac{2\pi}{\mu} e^{-jkz} \quad (6.2.38)$$

and the voltage between the inner and outer conductors is

$$V(z) = \int_a^b E_\rho d\rho = -\frac{C}{\sqrt{\mu\epsilon}} \ln \frac{b}{a} e^{-jkz}. \quad (6.2.39)$$

Therefore, the characteristic impedance of the coaxial waveguide is

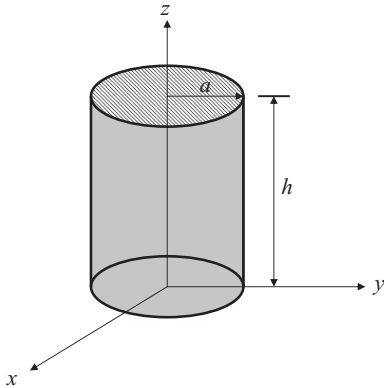
$$Z_c = \frac{V(z)}{I(z)} = \frac{1}{2\pi} \sqrt{\frac{\mu}{\epsilon}} \ln \frac{b}{a}. \quad (6.2.40)$$

For an air-filled coaxial waveguide, $Z_c \approx 50\Omega$ when $b/a = 2.3$ and $Z_c \approx 75\Omega$ when $b/a = 3.5$.

6.2.3 Cylindrical Cavity

When a finite section of a circular waveguide or a coaxial waveguide is terminated with a perfect conductor at both ends (Fig. 6.5), we have a circular cylindrical cavity or a coaxial cavity. The analysis of these cavities is very simple. Because of the terminations, the field inside a cavity is a standing wave along the z -direction, instead of a traveling wave as in an infinitely long waveguide. For example, for the TM modes in a circular cylindrical cavity having a length of h , E_z takes the form

$$E_z = E_0 J_m(k_\rho \rho) \begin{cases} \sin m\phi \\ \cos m\phi \end{cases} \cos \frac{p\pi z}{h} \quad (6.2.41)$$

**Figure 6.5** Uniformly filled circular cavity.

where $k_\rho = \chi_{mn}/a$, $m = 0, 1, 2, \dots$; $n = 1, 2, \dots$; and $p = 0, 1, 2, \dots$. The specific form of the function along the z -direction is determined by the boundary conditions $E_{\rho,\phi}|_{z=0} = E_{\rho,\phi}|_{z=h} = 0$. Since $k_\rho^2 + k_z^2 = k^2 = \omega^2 \mu \epsilon$, we obtain the resonant frequency for the TM_{mnp} mode of the cavity as

$$\omega_{r mnp}^{\text{TM}} = \frac{1}{\sqrt{\mu \epsilon}} \sqrt{\left(\frac{\chi_{mn}}{a}\right)^2 + \left(\frac{p\pi}{h}\right)^2}. \quad (6.2.42)$$

For the TE modes, H_z takes the form

$$H_z = H_0 J_m(k_\rho \rho) \begin{cases} \sin m\phi \\ \cos m\phi \end{cases} \sin \frac{p\pi z}{h} \quad (6.2.43)$$

where $k_\rho = \chi'_{mn}/a$, $m = 0, 1, 2, \dots$; $n = 1, 2, \dots$; and $p = 1, 2, \dots$. The specific z -dependence form is determined by the boundary conditions $H_z|_{z=0} = H_z|_{z=h} = 0$. The resonant frequency for the TE_{mnp} mode of the cavity is

$$\omega_{r mnp}^{\text{TE}} = \frac{1}{\sqrt{\mu \epsilon}} \sqrt{\left(\frac{\chi'_{mn}}{a}\right)^2 + \left(\frac{p\pi}{h}\right)^2}. \quad (6.2.44)$$

Among all the TM_{mnp} and TE_{mnp} modes, the dominant mode is either the TM_{010} mode or TE_{111} mode, whose resonant frequencies are given by

$$\omega_{r 010}^{\text{TM}} = \frac{2.4048}{a \sqrt{\mu \epsilon}}, \quad \omega_{r 111}^{\text{TE}} = \frac{1}{\sqrt{\mu \epsilon}} \sqrt{\left(\frac{1.8412}{a}\right)^2 + \left(\frac{\pi}{h}\right)^2} \quad (6.2.45)$$

respectively. For an imperfect cavity, the quality factor due to small conductor and material losses can be evaluated using the perturbational method discussed in Chapter 5.

6.3 CIRCULAR DIELECTRIC WAVEGUIDE

Because of their high conductor loss, empty metallic waveguides such as the circular and coaxial waveguides discussed in Section 6.2 are impractical for transmitting signals at

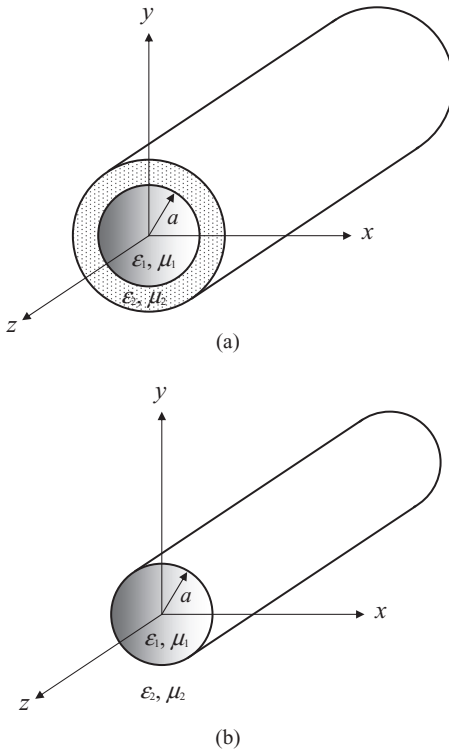


Figure 6.6 Circular dielectric waveguide.
 (a) Two-layered dielectric waveguide.
 (b) Simplified model.

optical frequencies. A better choice is to use dielectric waveguides with a very low dielectric loss. Among various dielectric waveguides, circular dielectric waveguides, commonly known as *optical fibers*, are the most popular choice [7–12]. A typical circular dielectric waveguide consists of two layers: an inner layer (core) with a higher permittivity and an outer layer (cladding) with a slightly lower permittivity, as illustrated in Figure 6.6a. Above the cutoff frequency, electromagnetic waves propagate in the inner layer and decay exponentially in the outer layer as a result of total reflection at the interface between the two layers. Because of this, the outer layer can be approximated as having an infinitely large radius to simplify the otherwise very complicated analysis of a two-layer dielectric waveguide.

6.3.1 Analysis of Hybrid Modes

Consider the simplified model of a two-layer circular dielectric waveguide shown in Figure 6.6b. The inner layer is assumed to have a permittivity of ϵ_1 and a radius of a , the outer layer is assumed to have a permittivity of ϵ_2 , and both layers are assumed to be non-magnetic ($\mu_1 = \mu_2 = \mu_0$). As discussed in Section 5.3, such a dielectric waveguide cannot support general TE and TM modes because E_z and H_z are coupled at the discontinuous dielectric interface. Instead, it can support only hybrid waveguide modes that contain both E_z and H_z . The E_z and H_z can be expressed as

$$E_{1z} = A_1 J_m(k_1 \rho) \begin{cases} \sin m\phi \\ \cos m\phi \end{cases} e^{-jk_z z} \quad (6.3.1)$$

$$H_{1z} = B_1 J_m(k_{1\rho}\rho) \begin{Bmatrix} \cos m\phi \\ \sin m\phi \end{Bmatrix} e^{-jk_z z} \quad (6.3.2)$$

in the inner layer ($\rho < a$) and

$$E_{2z} = A_2 H_m^{(2)}(k_{2\rho}\rho) \begin{Bmatrix} \sin m\phi \\ \cos m\phi \end{Bmatrix} e^{-jk_z z} \quad (6.3.3)$$

$$H_{2z} = B_2 H_m^{(2)}(k_{2\rho}\rho) \begin{Bmatrix} \cos m\phi \\ \sin m\phi \end{Bmatrix} e^{-jk_z z} \quad (6.3.4)$$

in the outer layer ($\rho > a$), where $k_{1\rho} = \sqrt{\omega^2 \mu_0 \epsilon_1 - k_z^2}$ and $k_{2\rho} = \sqrt{\omega^2 \mu_0 \epsilon_2 - k_z^2}$. For a propagating mode, all the power is assumed to propagate along the waveguide, and there should be no power radiating in the radial direction. This can happen only when $k_z^2 > \omega^2 \mu_0 \epsilon_2$ so that $k_{2\rho}$ becomes a purely imaginary number, denoted as $k_{2\rho} = -j\alpha_{2\rho}$, resulting in an exponentially decayed field in the radial direction. Since the Hankel function of the second kind for a purely imaginary argument can be written as

$$H_m^{(2)}(-j\alpha_{2\rho}\rho) = \frac{2}{\pi} j^{m+1} K_m(\alpha_{2\rho}\rho) \quad (6.3.5)$$

where K_m is called the *modified Bessel function of the second kind* [1], Equations 6.3.3 and 6.3.4 can also be written as

$$E_{2z} = A'_2 K_m(\alpha_{2\rho}\rho) \begin{Bmatrix} \sin m\phi \\ \cos m\phi \end{Bmatrix} e^{-jk_z z} \quad (6.3.6)$$

$$H_{2z} = B'_2 K_m(\alpha_{2\rho}\rho) \begin{Bmatrix} \cos m\phi \\ \sin m\phi \end{Bmatrix} e^{-jk_z z}. \quad (6.3.7)$$

Figure 6.7 plots the first few $K_m(x)$, which clearly shows the exponential decay behavior.

From Equations 6.3.1 and 6.3.2, we obtain the other field components in the inner dielectric layer as

$$E_{1\rho} = -\frac{j}{k_{1\rho}^2} \left[A_1 k_z k_{1\rho} J'_m(k_{1\rho}\rho) \mp B_1 \frac{m\omega\mu_0}{\rho} J_m(k_{1\rho}\rho) \right] \begin{Bmatrix} \sin m\phi \\ \cos m\phi \end{Bmatrix} e^{-jk_z z} \quad (6.3.8)$$

$$E_{1\phi} = -\frac{j}{k_{1\rho}^2} \left[\pm A_1 \frac{mk_z}{\rho} J_m(k_{1\rho}\rho) - B_1 \omega \mu_0 k_{1\rho} J'_m(k_{1\rho}\rho) \right] \begin{Bmatrix} \cos m\phi \\ \sin m\phi \end{Bmatrix} e^{-jk_z z} \quad (6.3.9)$$

$$H_{1\rho} = -\frac{j}{k_{1\rho}^2} \left[\mp A_1 \frac{m\omega\epsilon_1}{\rho} J_m(k_{1\rho}\rho) + B_1 k_z k_{1\rho} J'_m(k_{1\rho}\rho) \right] \begin{Bmatrix} \cos m\phi \\ \sin m\phi \end{Bmatrix} e^{-jk_z z} \quad (6.3.10)$$

$$H_{1\phi} = -\frac{j}{k_{1\rho}^2} \left[A_1 \omega \epsilon_1 k_{1\rho} J'_m(k_{1\rho}\rho) \mp B_1 \frac{mk_z}{\rho} J_m(k_{1\rho}\rho) \right] \begin{Bmatrix} \sin m\phi \\ \cos m\phi \end{Bmatrix} e^{-jk_z z}. \quad (6.3.11)$$

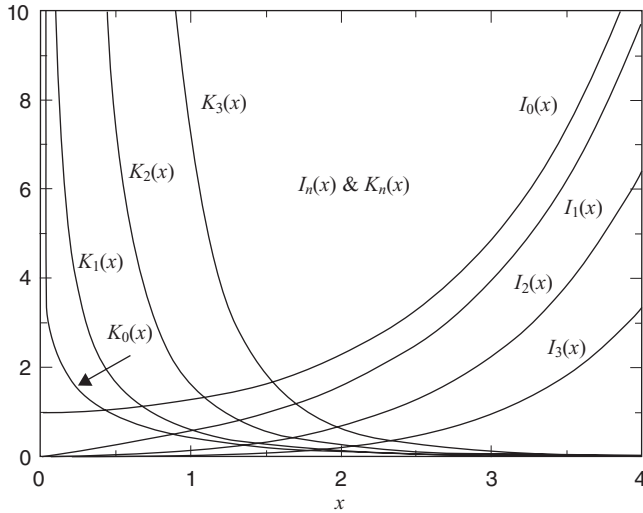


Figure 6.7 Modified Bessel functions of the first and second kind.

Similarly, from Equations 6.3.6 and 6.3.7, we obtain the other field components in the outer dielectric layer as

$$E_{2\rho} = \frac{j}{\alpha_{2\rho}^2} \left[A'_2 k_z \alpha_{2\rho} K'_m(\alpha_{2\rho}\rho) \mp B'_2 \frac{m\omega\mu_0}{\rho} K_m(\alpha_{2\rho}\rho) \right] \begin{Bmatrix} \sin m\phi \\ \cos m\phi \end{Bmatrix} e^{-jk_z z} \quad (6.3.12)$$

$$E_{2\phi} = \frac{j}{\alpha_{2\rho}^2} \left[\pm A'_2 \frac{mk_z}{\rho} K_m(\alpha_{2\rho}\rho) - B'_2 \omega\mu_0 \alpha_{2\rho} K'_m(\alpha_{2\rho}\rho) \right] \begin{Bmatrix} \cos m\phi \\ \sin m\phi \end{Bmatrix} e^{-jk_z z} \quad (6.3.13)$$

$$H_{2\rho} = \frac{j}{\alpha_{2\rho}^2} \left[\mp A'_2 \frac{m\omega\epsilon_2}{\rho} K_m(\alpha_{2\rho}\rho) + B'_2 k_z \alpha_{2\rho} K'_m(\alpha_{2\rho}\rho) \right] \begin{Bmatrix} \cos m\phi \\ \sin m\phi \end{Bmatrix} e^{-jk_z z} \quad (6.3.14)$$

$$H_{2\phi} = \frac{j}{\alpha_{2\rho}^2} \left[A'_2 \omega\epsilon_2 \alpha_{2\rho} K'_m(\alpha_{2\rho}\rho) \mp B'_2 \frac{mk_z}{\rho} K_m(\alpha_{2\rho}\rho) \right] \begin{Bmatrix} \sin m\phi \\ \cos m\phi \end{Bmatrix} e^{-jk_z z}. \quad (6.3.15)$$

At the interface between the inner and outer layers, we have the following field continuity conditions

$$E_{1z}|_{\rho=a} = E_{2z}|_{\rho=a}, \quad H_{1z}|_{\rho=a} = H_{2z}|_{\rho=a} \quad (6.3.16)$$

$$E_{1\phi}|_{\rho=a} = E_{2\phi}|_{\rho=a}, \quad H_{1\phi}|_{\rho=a} = H_{2\phi}|_{\rho=a}. \quad (6.3.17)$$

Substituting the field expressions into these equations, we obtain

$$A_1 J_m(k_{1\rho} a) = A'_2 K_m(\alpha_{2\rho} a) \quad (6.3.18)$$

$$B_1 J_m(k_{1\rho} a) = B'_2 K_m(\alpha_{2\rho} a) \quad (6.3.19)$$

$$\begin{aligned} & \frac{1}{k_{1\rho}^2} \left[\pm A_1 \frac{mk_z}{a} J_m(k_{1\rho}a) - B_1 \omega \mu_0 k_{1\rho} J'_m(k_{1\rho}a) \right] \\ &= -\frac{1}{\alpha_{2\rho}^2} \left[\pm A'_2 \frac{mk_z}{a} K_m(\alpha_{2\rho}a) - B'_2 \omega \mu_0 \alpha_{2\rho} K'_m(\alpha_{2\rho}a) \right] \end{aligned} \quad (6.3.20)$$

$$\begin{aligned} & \frac{1}{k_{1\rho}^2} \left[A_1 \omega \epsilon_1 k_{1\rho} J'_m(k_{1\rho}a) \mp B_1 \frac{mk_z}{a} J_m(k_{1\rho}a) \right] \\ &= -\frac{1}{\alpha_{2\rho}^2} \left[A'_2 \omega \epsilon_2 \alpha_{2\rho} K'_m(\alpha_{2\rho}a) \mp B'_2 \frac{mk_z}{a} K_m(\alpha_{2\rho}a) \right]. \end{aligned} \quad (6.3.21)$$

Eliminating A'_2 and B'_2 , we have

$$A_1 \frac{mk_z}{\omega a} \left(\frac{1}{k_{1\rho}^2} + \frac{1}{\alpha_{2\rho}^2} \right) \mp B_1 \left[\frac{\mu_0}{k_{1\rho}} \frac{J'_m(k_{1\rho}a)}{J_m(k_{1\rho}a)} + \frac{\mu_0}{\alpha_{2\rho}} \frac{K'_m(\alpha_{2\rho}a)}{K_m(\alpha_{2\rho}a)} \right] = 0 \quad (6.3.22)$$

$$A_1 \left[\frac{\epsilon_1}{k_{1\rho}} \frac{J'_m(k_{1\rho}a)}{J_m(k_{1\rho}a)} + \frac{\epsilon_2}{\alpha_{2\rho}} \frac{K'_m(\alpha_{2\rho}a)}{K_m(\alpha_{2\rho}a)} \right] \mp B_1 \frac{mk_z}{\omega a} \left(\frac{1}{k_{1\rho}^2} + \frac{1}{\alpha_{2\rho}^2} \right) = 0. \quad (6.3.23)$$

Equations 6.3.22 and 6.3.23 can be written as a matrix equation for unknown A_1 and B_1 . To have a non-trivial solution for A_1 and B_1 , the determinant of the coefficient matrix must vanish,

$$\det \begin{bmatrix} \mp \frac{mk_z}{\omega a} \left(\frac{1}{k_{1\rho}^2} + \frac{1}{\alpha_{2\rho}^2} \right) & \frac{\mu_0}{k_{1\rho}} \frac{J'_m(k_{1\rho}a)}{J_m(k_{1\rho}a)} + \frac{\mu_0}{\alpha_{2\rho}} \frac{K'_m(\alpha_{2\rho}a)}{K_m(\alpha_{2\rho}a)} \\ \frac{\epsilon_1}{k_{1\rho}} \frac{J'_m(k_{1\rho}a)}{J_m(k_{1\rho}a)} + \frac{\epsilon_2}{\alpha_{2\rho}} \frac{K'_m(\alpha_{2\rho}a)}{K_m(\alpha_{2\rho}a)} & \mp \frac{mk_z}{\omega a} \left(\frac{1}{k_{1\rho}^2} + \frac{1}{\alpha_{2\rho}^2} \right) \end{bmatrix} = 0 \quad (6.3.24)$$

which yields

$$\begin{aligned} & \left(\frac{mk_z}{\omega a} \right)^2 \left(\frac{1}{k_{1\rho}^2} + \frac{1}{\alpha_{2\rho}^2} \right)^2 - \left[\frac{\mu_0}{k_{1\rho}} \frac{J'_m(k_{1\rho}a)}{J_m(k_{1\rho}a)} + \frac{\mu_0}{\alpha_{2\rho}} \frac{K'_m(\alpha_{2\rho}a)}{K_m(\alpha_{2\rho}a)} \right] \\ & \times \left[\frac{\epsilon_1}{k_{1\rho}} \frac{J'_m(k_{1\rho}a)}{J_m(k_{1\rho}a)} + \frac{\epsilon_2}{\alpha_{2\rho}} \frac{K'_m(\alpha_{2\rho}a)}{K_m(\alpha_{2\rho}a)} \right] = 0. \end{aligned} \quad (6.3.25)$$

Given a frequency, this transcendental equation can be solved together with

$$k_{1\rho} = \sqrt{\omega^2 \mu_0 \epsilon_1 - k_z^2}, \quad \alpha_{2\rho} = \sqrt{k_z^2 - \omega^2 \mu_0 \epsilon_2} \quad (6.3.26)$$

for a finite number of real-valued k_z , each corresponding to a propagating waveguide mode.

6.3.2 Characteristics of Hybrid Modes

To facilitate further discussion, we first rewrite Equations 6.3.25 and 6.3.26 as

$$(m\delta)^2 \left(\frac{1}{u^2} + \frac{1}{v^2} \right)^2 - \left[\frac{1}{u} \frac{J'_m(u)}{J_m(u)} + \frac{1}{v} \frac{K'_m(v)}{K_m(v)} \right] \left[\frac{\epsilon_{r1}}{u} \frac{J'_m(u)}{J_m(u)} + \frac{\epsilon_{r2}}{v} \frac{K'_m(v)}{K_m(v)} \right] = 0 \quad (6.3.27)$$

$$u = k_{1\rho} a = k_0 a \sqrt{\epsilon_{r1} - \delta^2}, \quad v = \alpha_{2\rho} a = k_0 a \sqrt{\delta^2 - \epsilon_{r2}} \quad (6.3.28)$$

where $\delta = k_z/k_0$. Now we consider the solution of Equations 6.3.27 and 6.3.28, first for a special case of $m = 0$ and then for general cases with $m \neq 0$.

TM_{0n} and TE_{0n} Modes When $m = 0$ (axisymmetric), we observe from Equations 6.3.22 and 6.3.23 that A_1 and B_1 , hence E_z and H_z , are completely decoupled. Equation 6.3.27 is reduced to

$$\left[\frac{1}{u} \frac{J'_0(u)}{J_0(u)} + \frac{1}{v} \frac{K'_0(v)}{K_0(v)} \right] \left[\frac{\epsilon_{r1}}{u} \frac{J'_0(u)}{J_0(u)} + \frac{\epsilon_{r2}}{v} \frac{K'_0(v)}{K_0(v)} \right] = 0 \quad (6.3.29)$$

which has two obvious solutions. One solution is given by

$$\frac{\epsilon_{r1}}{u} \frac{J'_0(u)}{J_0(u)} + \frac{\epsilon_{r2}}{v} \frac{K'_0(v)}{K_0(v)} = 0. \quad (6.3.30)$$

With this, $A_1 \neq 0$ and $B_1 = 0$; hence, $E_z \neq 0$ and $H_z = 0$. This solution yields TM_{0n} modes, whose propagation constants k_z can be obtained by solving Equation 6.3.30 together with Equation 6.3.28. The cutoff wavenumbers can be determined by setting $v = 0$ in Equation 6.3.30, which yields $J_0(u) = 0$. The first several roots of this equation are given in the first row of Table 6.1. By denoting these roots as χ_{0n} , the cutoff wavenumbers are given by

$$k_{c0n}^{\text{TM}} = \frac{\chi_{0n}}{a \sqrt{\epsilon_{r1} - \epsilon_{r2}}}. \quad (6.3.31)$$

The second solution is given by

$$\frac{1}{u} \frac{J'_0(u)}{J_0(u)} + \frac{1}{v} \frac{K'_0(v)}{K_0(v)} = 0 \quad (6.3.32)$$

and with this, $A_1 = 0$ and $B_1 \neq 0$; hence, $E_z = 0$ and $H_z \neq 0$. This solution yields TE_{0n} modes, whose propagation constants k_z can be obtained by solving Equation 6.3.32 together with Equation 6.3.28. The cutoff wavenumbers can be determined by setting $v = 0$ in Equation 6.3.32, which again yields $J_0(u) = 0$. Hence, the cutoff wavenumbers of the TE_{0n} modes are the same as those of the TM_{0n} modes, which are given by Equation 6.3.31. In fact, for most optical waveguides, the values of ϵ_{r1} and ϵ_{r2} are close to each other with a relative difference on the order of 0.01 [10], resulting in similar values for the propagation constants k_{z0n}^{TM} and k_{z0n}^{TE} . From Table 6.1, it can be seen that the cutoff wavenumbers of the first TE_{0n} and TM_{0n} modes are given by $k_{c01}^{\text{TE}} = k_{c01}^{\text{TM}} = 2.4048/a\sqrt{\epsilon_{r1} - \epsilon_{r2}}$.

Hybrid EH_{mn} and HE_{mn} Modes When $m \neq 0$, we observe from Equations 6.3.22 and 6.3.23 that A_1 and B_1 , hence E_z and H_z , are closely coupled. Therefore, the waveguide modes are hybrid ones that contain both E_z and H_z . To solve Equation 6.3.27, we further simplify it by letting

$$p_m(u) = \frac{1}{u} \frac{J'_m(u)}{J_m(u)}, \quad q_m(v) = \frac{1}{v} \frac{K'_m(v)}{K_m(v)}. \quad (6.3.33)$$

Hence, Equation 6.3.27 becomes

$$(m\delta)^2 \left(\frac{1}{u^2} + \frac{1}{v^2} \right)^2 - [p_m(u) + q_m(v)][\epsilon_{r1} p_m(u) + \epsilon_{r2} q_m(v)] = 0. \quad (6.3.34)$$

The two solutions of this equation are given by

$$p_m(u) = -\frac{\epsilon_{r1} + \epsilon_{r2}}{2\epsilon_{r1}} q_m(v) \pm \sqrt{\frac{(m\delta)^2}{\epsilon_{r1}} \left(\frac{1}{u^2} + \frac{1}{v^2} \right)^2 + \frac{(\epsilon_{r1} - \epsilon_{r2})^2}{4\epsilon_{r1}^2} q_m^2(v)}. \quad (6.3.35)$$

From Equation 6.3.28, we find that

$$\delta^2 = \frac{\epsilon_{r2} u^2 + \epsilon_{r1} v^2}{u^2 + v^2}, \quad u^2 + v^2 = (\epsilon_{r1} - \epsilon_{r2})(k_0 a)^2. \quad (6.3.36)$$

When these are substituted into Equation 6.3.35, the resulting equation is a function of u only for given values of m , ϵ_{r1} , ϵ_{r2} , and $k_0 a$. Therefore, it can be solved for a set of roots, which can be denoted as $u_{mn}^{(\pm)}$ ($n = 1, 2, \dots$), where the superscript corresponds to the sign chosen in Equation 6.3.35. Once $u_{mn}^{(\pm)}$ are obtained, we can calculate $v_{mn}^{(\pm)}$ from the second equation in Equation 6.3.36 and then find $\delta_{mn}^{(\pm)}$ from the first equation in Equation 6.3.36, which finally yields the propagation constants $k_{zmn}^{(\pm)}$ based on the definition of δ . Each propagation constant corresponds to a propagating waveguide mode. Alternatively, for a given δ , we can use Equation 6.3.35 and the first equation in Equation 6.3.36 to solve for $u_{mn}^{(\pm)}$ and $v_{mn}^{(\pm)}$, from which we can then find the corresponding values for $k_0 a$. Repeating this calculation for $\sqrt{\epsilon_{r2}} \leq \delta < \sqrt{\epsilon_{r1}}$ can generate dispersion curves that relate k_z/k_0 to $k_0 a$.

To classify hybrid modes and investigate the characteristics of the hybrid modes further, we consider the ratio between E_z and H_z . From Equations 6.3.22 and 6.3.23, we find

$$\left| \frac{E_z}{H_z} \right| = \left| \frac{A_1}{B_1} \right| = \frac{\eta_0}{m\delta} |p_m(u) + q_m(v)| \left(\frac{1}{u^2} + \frac{1}{v^2} \right)^{-1} \quad (6.3.37)$$

and

$$\left| \frac{E_z}{H_z} \right| = \left| \frac{A_1}{B_1} \right| = \eta_0 \left(\frac{1}{u^2} + \frac{1}{v^2} \right) \frac{m\delta}{|\epsilon_{r1} p_m(u) + \epsilon_{r2} q_m(v)|} \quad (6.3.38)$$

where $\eta_0 = \sqrt{\mu_0/\epsilon_0}$. These two equations are actually equivalent and it is sufficient to consider only one of them. When approaching cutoff, $\alpha_{2\rho} \rightarrow 0$, $\delta \rightarrow \sqrt{\epsilon_{r2}}$, and $v \rightarrow 0$. By using the small-argument approximation for the modified Bessel functions [1],

$$\lim_{z \rightarrow 0} K_m(z) \rightarrow \frac{(m-1)!}{2} \left(\frac{z}{2} \right)^{-m} \quad m > 0 \quad (6.3.39)$$

we can find easily that

$$\lim_{v \rightarrow 0} q_m(v) \rightarrow -\frac{m}{v^2}. \quad (6.3.40)$$

Therefore, from either Equation 6.3.37 or 6.3.38 we find

$$\left| \frac{E_z}{H_z} \right|_{\text{At cutoff}} = \frac{\eta_0}{\sqrt{\epsilon_{r2}}} = \eta_2 \quad (6.3.41)$$

which indicates that there is no dominance of E_z or H_z at cutoff and the ratio between E_z and H_z is the same for all hybrid modes.

Next consider what happens above cutoff, when $\alpha_{2\rho} > 0$, $\delta > \sqrt{\epsilon_{r2}}$, and $v > 0$. Equation 6.3.35 can be rewritten as

$$p_m(u) + q_m(v) = \frac{\epsilon_{r1} - \epsilon_{r2}}{2\epsilon_{r1}} q_m(v) \pm \sqrt{\frac{(m\delta)^2}{\epsilon_{r1}} \left(\frac{1}{u^2} + \frac{1}{v^2} \right)^2 + \frac{(\epsilon_{r1} - \epsilon_{r2})^2}{4\epsilon_{r1}^2} q_m^2(v)} \quad (6.3.42)$$

or equivalently as

$$\epsilon_{r1} p_m(u) + \epsilon_{r2} q_m(v) = \frac{\epsilon_{r2} - \epsilon_{r1}}{2} q_m(v) \pm \sqrt{\epsilon_{r1} (m\delta)^2 \left(\frac{1}{u^2} + \frac{1}{v^2} \right)^2 + \frac{(\epsilon_{r1} - \epsilon_{r2})^2}{4} q_m^2(v)}. \quad (6.3.43)$$

Since $q_m(v) < 0$, we find from these two equations that

$$|p_m(u) + q_m(v)|^{(+)} < |p_m(u) + q_m(v)|^{(-)} \quad (6.3.44)$$

and

$$|\epsilon_{r1} p_m(u) + \epsilon_{r2} q_m(v)|^{(+)} > |\epsilon_{r1} p_m(u) + \epsilon_{r2} q_m(v)|^{(-)} \quad (6.3.45)$$

where the superscript (+) indicates that the positive sign is chosen in Equations 6.3.42 and 6.3.43 and, similarly the superscript (-) indicates that the negative sign is chosen. When these are substituted into Equations 6.3.37 and 6.3.38, we find

$$\left| \frac{E_z}{H_z} \right|^{(+)} < \left| \frac{E_z}{H_z} \right|^{(-)}. \quad (6.3.46)$$

Therefore, for the solution obtained with the “+” sign in Equation 6.3.35, the electric (magnetic) field is relatively weaker (stronger) than the electric (magnetic) field corresponding to the solution obtained with the “-” sign. Based on the analysis in Section 5.3.3, the hybrid modes obtained with the “+” sign in Equation 6.3.35 are called EH_{mn} modes since they are TE-like. In contrast, the modes obtained with the “-” sign are termed HE_{mn} modes since they are TM-like. When $m = 0$, the EH_{mn} modes become the TE_{0n} modes and the HE_{mn} modes become the TM_{0n} modes. This can be verified by setting $m = 0$ in Equation 6.3.35. With the choice of the “+” sign, Equation 6.3.35 is reduced to Equation 6.3.32, which is the characteristic equation for the TE_{0n} modes. However, when the “-” sign is chosen, Equation 6.3.35 is reduced to Equation 6.3.30, which is the characteristic equation for the TM_{0n} modes.

Now we attempt to find the cutoff frequencies of the hybrid modes. As mentioned earlier, for practical optical waveguides, the difference between ϵ_{r1} and ϵ_{r2} is very small to minimize the modal distortion, and typically $(\epsilon_{r1} - \epsilon_{r2})/\epsilon_{r1}$ is on the order of 0.01. Therefore, Equation 6.3.35 can be approximated as

$$p_m(u) \approx -q_m(v) \pm \frac{m\delta}{\sqrt{\epsilon_{r1}}} \left(\frac{1}{u^2} + \frac{1}{v^2} \right). \quad (6.3.47)$$

At cutoff, $k_z = \omega \sqrt{\mu_0 \epsilon_2}$ and $\alpha_{2p} \rightarrow 0$ so that $\delta = \sqrt{\epsilon_{r2}}$ and $v \rightarrow 0$. Furthermore, from the recursive relations of the Bessel functions [1],

$$J'_m(z) = -\frac{m}{z} J_m(z) + J_{m-1}(z) = \frac{m}{z} J_m(z) - J_{m+1}(z) \quad (6.3.48)$$

$$K'_m(z) = -\frac{m}{z} K_m(z) - K_{m-1}(z) = \frac{m}{z} K_m(z) - K_{m+1}(z) \quad (6.3.49)$$

we find

$$p_m(u) = \frac{1}{u} \frac{J'_m(u)}{J_m(u)} = -\frac{m}{u^2} + \frac{1}{u} \frac{J_{m-1}(u)}{J_m(u)} = \frac{m}{u^2} - \frac{1}{u} \frac{J_{m+1}(u)}{J_m(u)} \quad (6.3.50)$$

$$q_m(v) = \frac{1}{v} \frac{K'_m(v)}{K_m(v)} = -\frac{m}{v^2} - \frac{1}{v} \frac{K_{m-1}(v)}{K_m(v)} = \frac{m}{v^2} - \frac{1}{v} \frac{K_{m+1}(v)}{K_m(v)}. \quad (6.3.51)$$

By substituting these into Equation 6.3.47, we obtain

$$\frac{1}{u} \frac{J_{m-1}(u)}{J_m(u)} = \frac{1}{v} \frac{K_{m-1}(v)}{K_m(v)} \quad (6.3.52)$$

for the HE_{mn} modes and

$$\frac{1}{u} \frac{J_{m+1}(u)}{J_m(u)} = -\frac{1}{v} \frac{K_{m+1}(v)}{K_m(v)} \quad (6.3.53)$$

for the EH_{mn} modes. By using the small-argument approximation given in Equation 6.3.39, it can be shown easily that

$$\lim_{v \rightarrow 0} \frac{1}{v} \frac{K_{m-1}(v)}{K_m(v)} \sim \frac{1}{2(m-1)}, \quad \lim_{v \rightarrow 0} \frac{1}{v} \frac{K_{m+1}(v)}{K_m(v)} \rightarrow \infty. \quad (6.3.54)$$

Therefore, the characteristic equation for the cutoff of the HE_{mn} modes becomes

$$\frac{u_c J_m(u_c)}{J_{m-1}(u_c)} \approx 2(m-1) \quad (6.3.55)$$

and the equation for the cutoff of the EH_{mn} modes becomes

$$\frac{u_c J_m(u_c)}{J_{m+1}(u_c)} \approx 0. \quad (6.3.56)$$

In particular, for $m = 1$, we have

$$\frac{u_c J_1(u_c)}{J_0(u_c)} \approx 0 \quad \text{or} \quad u_c J_1(u_c) \approx 0 \quad (6.3.57)$$

for the HE_{1n} modes. The first root is $u_{c11}^{\text{HE}} = 0$, and the other roots are given by $u_{c1n}^{\text{HE}} = \chi_{1n-1}$ where χ_{1n-1} satisfies $J_1(\chi_{1n-1}) = 0$. The cutoff wavenumbers are then given by

$$k_{c1n}^{\text{HE}} = \frac{u_{c1n}^{\text{HE}}}{a\sqrt{\epsilon_{r1} - \epsilon_{r2}}} = \frac{\chi_{1n-1}}{a\sqrt{\epsilon_{r1} - \epsilon_{r2}}}. \quad (6.3.58)$$

Clearly, the HE_{11} mode is the dominant mode, which has a cutoff wavenumber of $k_{c11}^{\text{HE}} = 0$; hence, no cutoff frequency. The next mode is the HE_{12} mode, whose cutoff wavenumber is given by $k_{c12}^{\text{HE}} = 3.8317/a\sqrt{\epsilon_{r1} - \epsilon_{r2}}$. For the EH_{1n} modes, Equation 6.3.56 becomes

$$\frac{u_c J_1(u_c)}{J_2(u_c)} \approx 0 \quad \text{or} \quad J_1(u_c) \approx 0 \quad \text{except for } u_c = 0. \quad (6.3.59)$$

The $u_c = 0$ is excluded because it does not satisfy the first equation, as it can be shown easily that $\lim_{u \rightarrow 0} u J_1(u)/J_2(u) \neq 0$. The roots of Equation 6.3.59 are given by $u_{c1n}^{\text{EH}} = \chi_{1n}$, where χ_{1n} satisfies $J_1(\chi_{1n}) = 0$. The cutoff wavenumbers are given by

$$k_{c1n}^{\text{EH}} = \frac{u_{c1n}^{\text{EH}}}{a\sqrt{\epsilon_{r1} - \epsilon_{r2}}} = \frac{\chi_{1n}}{a\sqrt{\epsilon_{r1} - \epsilon_{r2}}}. \quad (6.3.60)$$

Clearly, the cutoff wavenumbers of the EH_{1n} modes are the same as those of the HE_{1n+1} modes.

Based on the cutoff wavenumbers obtained for all the modes in the circular dielectric waveguide, it is seen that the dominant mode is the HE_{11} mode, which has a cutoff wavenumber of $k_{c11}^{\text{HE}} = 0$. Among the modes with $m = 0$ and 1, the first higher-order modes are the TE_{01} and TM_{01} modes, which have a cutoff wavenumber of $k_{c01}^{\text{TE}} = k_{c01}^{\text{TM}} = 2.4048/a\sqrt{\epsilon_{r1} - \epsilon_{r2}}$, and the second higher-order modes are the EH_{11} and HE_{12} modes, which have a cutoff wavenumber of $k_{c11}^{\text{EH}} = k_{c12}^{\text{HE}} = 3.8317/a\sqrt{\epsilon_{r1} - \epsilon_{r2}}$. Figure 6.8 shows the dispersion curves of the first several waveguide modes in a circular dielectric waveguide with $\epsilon_{r1} = 2.19$ and $\epsilon_{r2} = 2.13$.

6.4 WAVE TRANSFORMATION AND SCATTERING ANALYSIS

In this section, we consider scattering of a plane wave by circular conducting, dielectric, and layered dielectric cylinders to illustrate the basic steps to carry out scattering analysis [4,7,13,14]. For this we have to expand a plane wave in terms of cylindrical wave functions. This expansion is called *wave transformation*.

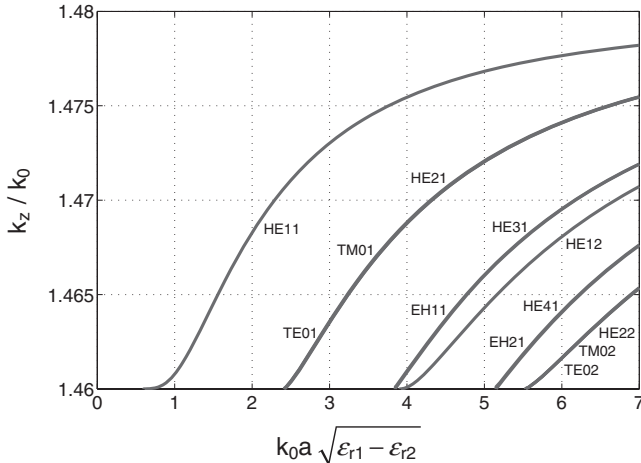


Figure 6.8 Dispersion curves of the first several waveguide modes in a circular dielectric waveguide with $\epsilon_{r1} = 2.19$ and $\epsilon_{r2} = 2.13$.

6.4.1 Wave Transformation

Consider a plane wave propagating in the x -direction in a medium with wavenumber k . The wave function can be written as

$$\psi = e^{-j k x} = e^{-j k \rho \cos \phi}. \quad (6.4.1)$$

Since this function satisfies the scalar Helmholtz equation, it can be expanded in terms of cylindrical wave functions,

$$e^{-j k \rho \cos \phi} = \sum_{n=-\infty}^{\infty} a_n J_n(k\rho) e^{jn\phi}. \quad (6.4.2)$$

This can also be considered as the Fourier series expansion of a periodic function. To determine a_n , we multiply Equation 6.4.2 by $e^{-jm\phi}$ and then integrate it over ϕ to obtain

$$\int_0^{2\pi} e^{-j k \rho \cos \phi} e^{-jm\phi} d\phi = \sum_{n=-\infty}^{\infty} a_n J_n(k\rho) \int_0^{2\pi} e^{j(n-m)\phi} d\phi = 2\pi a_m J_m(k\rho). \quad (6.4.3)$$

From the integral representation of the Bessel functions [1], we have

$$\int_0^{2\pi} e^{j(k\rho \cos \phi + m\phi)} d\phi = 2\pi j^m J_m(k\rho) \quad (6.4.4)$$

which yields

$$a_m = (-j)^m = j^{-m}. \quad (6.4.5)$$

Therefore, Equation 6.4.2 becomes

$$e^{-j k x} = \sum_{n=-\infty}^{\infty} j^{-n} J_n(k\rho) e^{jn\phi} \quad (6.4.6)$$

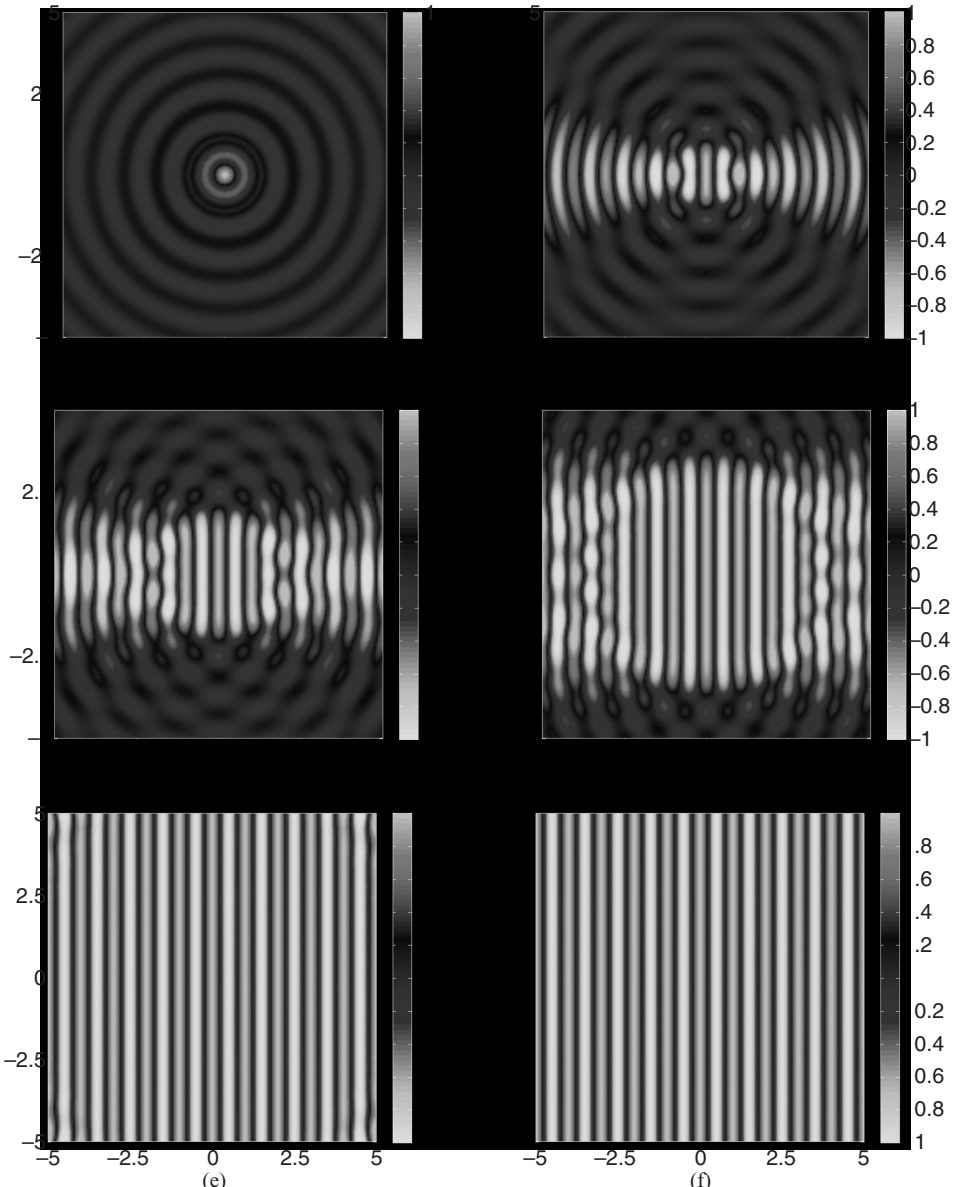


Figure 6.9 Illustration of the cylindrical wave transformation. The plots show the real part of the right-hand side of Equation 6.4.6 when the summation is evaluated from $n=-M$ to M . Clearly, a plane wave is formed in a $10\lambda \times 10\lambda$ region by increasing the number of terms in the summation. (a) $M=1$. (b) $M=5$. (c) $M=10$. (d) $M=20$. (e) $M=40$. (f) $M=80$. (See color insert.)

which expresses a plane wave in terms of a linear superposition of cylindrical waves. Figure 6.9 shows how a plane wave is formed by increasing the number of terms in the summation in Equation 6.4.6.

6.4.2 Scattering by a Circular Conducting Cylinder

With the plane-to-cylindrical wave transformation derived above, we can easily solve the problem of plane wave scattering by a conducting cylinder. Assume that the cylinder has

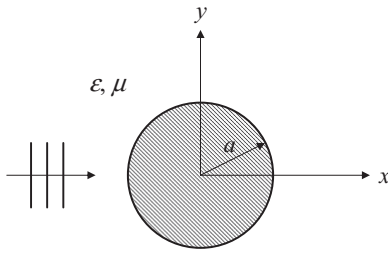


Figure 6.10 Plane wave scattering by a conducting cylinder.

a radius of a , its axis coincides with the z -axis, and the surrounding homogeneous medium has a permittivity of ϵ and a permeability of μ (Fig. 6.10). First of all, any plane wave perpendicular to the cylinder can be decomposed into the superposition of a TM-polarized wave, which has only a z -component for its electric field, and a TE-polarized wave, which has only a z -component for its magnetic field. Therefore, it is sufficient to consider these two incident plane waves.

For a TM-polarized incident plane wave, its electric field can be expressed as

$$\mathbf{E}^{\text{inc}} = \hat{z} E_z^{\text{inc}} = \hat{z} E_0 e^{-jkx} \quad (6.4.7)$$

where E_0 is a constant. Applying Equation 6.4.6 to this expression yields the incident wave expressed in terms of cylindrical waves,

$$E_z^{\text{inc}} = E_0 \sum_{n=-\infty}^{\infty} j^{-n} J_n(k\rho) e^{jn\phi}. \quad (6.4.8)$$

When this wave is incident upon the conducting cylinder, it induces an electric current on the surface of the cylinder, which radiates a secondary field. This field is called the *scattered field*. Since the scattered field propagates away from the cylinder, it can be expressed as

$$E_z^{\text{sc}} = E_0 \sum_{n=-\infty}^{\infty} a_n H_n^{(2)}(k\rho) e^{jn\phi}. \quad (6.4.9)$$

The superposition of the incident and scattered fields gives the total field, which satisfies the boundary condition

$$E_z|_{\rho=a} = [E_z^{\text{inc}} + E_z^{\text{sc}}]|_{\rho=a} = 0. \quad (6.4.10)$$

Substituting Equations 6.4.8 and 6.4.9 into this boundary condition yields

$$a_n = -j^{-n} \frac{J_n(ka)}{H_n^{(2)}(ka)}. \quad (6.4.11)$$

Hence, the scattered field is given by

$$E_z^{\text{sc}} = -E_0 \sum_{n=-\infty}^{\infty} j^{-n} \frac{J_n(ka)}{H_n^{(2)}(ka)} H_n^{(2)}(k\rho) e^{jn\phi}. \quad (6.4.12)$$

For a TE-polarized incident plane wave, its magnetic field can be expressed as

$$\mathbf{H}^{\text{inc}} = \hat{z}H_z^{\text{inc}} = \hat{z}H_0 e^{-jkx} \quad (6.4.13)$$

where H_0 is a constant. Applying Equation 6.4.6 to this expression yields the incident wave expressed in terms of cylindrical waves,

$$H_z^{\text{inc}} = H_0 \sum_{n=-\infty}^{\infty} j^{-n} J_n(k\rho) e^{jn\phi}. \quad (6.4.14)$$

Since the incident electric field is perpendicular to the z -axis, the induced electric current on the cylinder flows perpendicularly to the z -axis as well. Therefore, the scattered electric field is also perpendicular to the z -axis, and the scattered magnetic field has only the z -component. This field can be expressed as

$$H_z^{\text{sc}} = H_0 \sum_{n=-\infty}^{\infty} b_n H_n^{(2)}(k\rho) e^{jn\phi}. \quad (6.4.15)$$

The total magnetic field is then given by

$$H_z = H_z^{\text{inc}} + H_z^{\text{sc}} = H_0 \sum_{n=-\infty}^{\infty} [j^{-n} J_n(k\rho) + b_n H_n^{(2)}(k\rho)] e^{jn\phi} \quad (6.4.16)$$

which can then be substituted in Maxwell's equation $\nabla \times \mathbf{H} = j\omega\epsilon\mathbf{E}$ to find

$$E_\phi = -\frac{1}{j\omega\epsilon} \frac{\partial H_z}{\partial \rho} = j\eta H_0 \sum_{n=-\infty}^{\infty} [j^{-n} J'_n(k\rho) + b_n H_n^{(2)'}(k\rho)] e^{jn\phi}. \quad (6.4.17)$$

Next, we apply the boundary condition

$$E_\phi \Big|_{\rho=a} = [E_\phi^{\text{inc}} + E_\phi^{\text{sc}}] \Big|_{\rho=a} = 0 \quad (6.4.18)$$

to determine b_n as

$$b_n = -j^{-n} \frac{J'_n(ka)}{H_n^{(2)'}(ka)}. \quad (6.4.19)$$

Hence, the scattered magnetic field is given by

$$H_z^{\text{sc}} = -H_0 \sum_{n=-\infty}^{\infty} j^{-n} \frac{J'_n(ka)}{H_n^{(2)'}(ka)} H_n^{(2)}(k\rho) e^{jn\phi}. \quad (6.4.20)$$

For scattering analysis, an important parameter to characterize the scattering property of an infinitely long cylinder is called *scattering width*, which is defined as

$$\sigma_{2D}(\phi) = \lim_{\rho \rightarrow \infty} \left[2\pi\rho \frac{|E^{\text{sc}}|^2}{|E^{\text{inc}}|^2} \right] = \lim_{\rho \rightarrow \infty} \left[2\pi\rho \frac{|H^{\text{sc}}|^2}{|H^{\text{inc}}|^2} \right]. \quad (6.4.21)$$

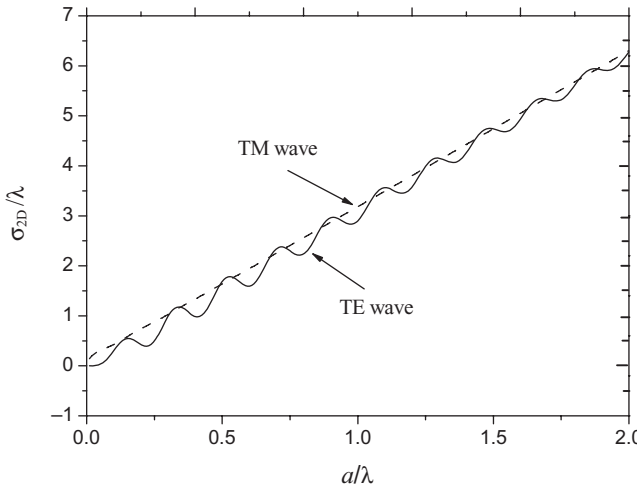


Figure 6.11 Echo width of a conducting cylinder as a function of its normalized radius.

Since the large-argument approximation of the Hankel function is given by

$$H_n^{(2)}(k\rho) \approx \sqrt{\frac{2}{\pi k\rho}} e^{-j(k\rho - n\pi/2 - \pi/4)} \quad \text{when } k\rho \rightarrow \infty \quad (6.4.22)$$

it is obvious that the scattering width is independent of the distance ρ and the magnitude of the incident field. Instead, it is a function of only the observation angle and the wave-number. It has a unit of width, such as m or λ . When plotted in the logarithmic scale, we usually first normalize it with m or λ such that the plotted quantity is $10\log(\sigma_{2D}/m)$ or $10\log(\sigma_{2D}/\lambda)$, whose unit is often labeled as dBm or dBw. Figure 6.11 shows the scattering width in the backscatter direction, which is also known as *echo width*, of a circular conducting cylinder as a function of its normalized radius. It is interesting to note that the echo width approaches a constant value of πa for the TM polarization case and oscillates around πa for the TE polarization case. The oscillation in the TE case is due to creeping waves that travel around the cylinder, which are absent in the TM case. This phenomenon can be seen clearly by examining the field distribution on the surface of the cylinder. Figure 6.12 displays the scattered and total fields as well as the bistatic scattering width for a conducting cylinder with a radius of 1λ for both TM and TE polarization cases. The word “bistatic” is used to indicate that the observation angle ϕ is different from the angle of incidence.

6.4.3 Scattering by a Circular Dielectric Cylinder

The solution to plane wave scattering by a dielectric cylinder follows the same approach discussed above for the conducting cylinder. The scattered field can again be expanded as Equation 6.4.9 for the TM polarization case and Equation 6.4.15 for the TE polarization case. The only difference is that the field can now penetrate into the dielectric cylinder; hence, there is an internal field inside the cylinder. Assume that the dielectric cylinder has a radius of a , a permittivity of ϵ_d , and a permeability of μ_d and the background has a permittivity of ϵ and a permeability of μ (Fig. 6.13). For the TM polarization case, the electric field inside the cylinder can be expanded as

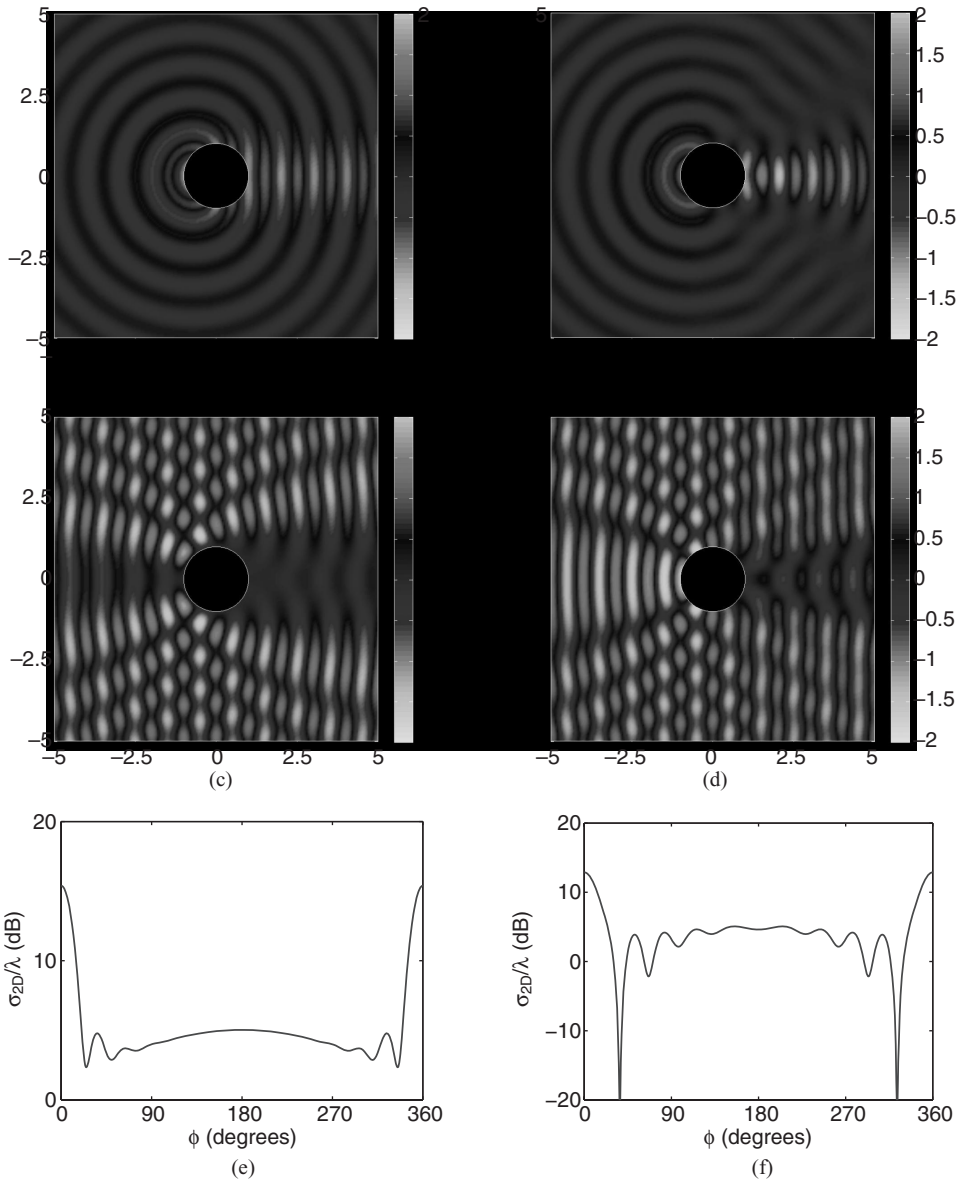


Figure 6.12 Scattering by a circular conducting cylinder with a radius of 1λ . (a) Snapshot of the scattered field E_z^{sc} . (b) Snapshot of the scattered field H_z^{sc} . (c) Snapshot of the total field E_z . (d) Snapshot of the total field H_z . (e) Scattering width for the TM case. (f) Scattering width for the TE case. The values of the fields are normalized by the magnitude of their respective incident fields. (See color insert.)

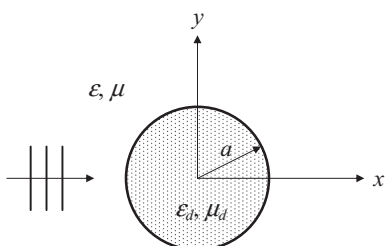


Figure 6.13 Plane wave scattering by a dielectric cylinder.

$$E_z^{\text{int}} = E_0 \sum_{n=-\infty}^{\infty} c_n J_n(k_d \rho) e^{jn\phi} \quad (6.4.23)$$

where $k_d = \omega \sqrt{\mu_d \epsilon_d}$. The Bessel functions of the first kind are used here because the field is finite along the z -axis. From the electric field continuity condition, we have

$$[E_z^{\text{inc}} + E_z^{\text{sc}}]_{\rho=a} = [E_z^{\text{int}}]_{\rho=a} \quad (6.4.24)$$

which yields

$$j^{-n} J_n(ka) + a_n H_n^{(2)}(ka) = c_n J_n(k_d a). \quad (6.4.25)$$

Next, we use Maxwell's equation $\nabla \times \mathbf{E} = j\omega \mu \mathbf{H}$ to find

$$H_\phi = \frac{1}{j\omega \mu} \frac{\partial E_z}{\partial \rho}. \quad (6.4.26)$$

Hence,

$$H_\phi^{\text{inc}} + H_\phi^{\text{sc}} = \frac{E_0}{j\eta} \sum_{n=-\infty}^{\infty} [j^{-n} J'_n(k\rho) + a_n H_n^{(2)\prime}(k\rho)] e^{jn\phi} \quad (6.4.27)$$

$$H_\phi^{\text{int}} = \frac{E_0}{j\eta_d} \sum_{n=-\infty}^{\infty} c_n J'_n(k_d \rho) e^{jn\phi} \quad (6.4.28)$$

where $\eta_d = \sqrt{\mu_d / \epsilon_d}$. From the magnetic field continuity condition, we have

$$[H_\phi^{\text{inc}} + H_\phi^{\text{sc}}]_{\rho=a} = [H_\phi^{\text{int}}]_{\rho=a} \quad (6.4.29)$$

which yields

$$j^{-n} J'_n(ka) + a_n H_n^{(2)\prime}(ka) = \frac{\eta}{\eta_d} c_n J'_n(k_d a). \quad (6.4.30)$$

Solving Equations 6.4.25 and 6.4.30 together, we obtain

$$a_n = -j^{-n} \frac{\sqrt{\mu_r} J'_n(ka) J_n(k_d a) - \sqrt{\epsilon_r} J_n(ka) J'_n(k_d a)}{\sqrt{\mu_r} H_n^{(2)\prime}(ka) J_n(k_d a) - \sqrt{\epsilon_r} H_n^{(2)}(ka) J'_n(k_d a)} \quad (6.4.31)$$

$$c_n = \frac{j^{-(n+1)}}{\pi k a} \frac{2\sqrt{\mu_r}}{\sqrt{\mu_r} H_n^{(2)\prime}(ka) J_n(k_d a) - \sqrt{\epsilon_r} H_n^{(2)}(ka) J'_n(k_d a)} \quad (6.4.32)$$

where $\epsilon_r = \epsilon_d / \epsilon$ and $\mu_r = \mu_d / \mu$ denote the relative permittivity and permeability of the cylinder with respect to the background medium. In obtaining Equation 6.4.32, we have employed the well-known Wronskian relation for the Bessel functions $J_n(z)H_n^{(2)\prime}(z) - J'_n(z)H_n^{(2)}(z) = 2/j\pi z$ [1].

For the TE polarization case, the magnetic field inside the cylinder can be expanded as

$$H_z^{\text{int}} = H_0 \sum_{n=-\infty}^{\infty} d_n J_n(k_d \rho) e^{jn\phi}. \quad (6.4.33)$$

Following the same procedure described above, we obtain

$$b_n = -j^{-n} \frac{\sqrt{\epsilon_r} J'_n(ka) J_n(k_d a) - \sqrt{\mu_r} J_n(ka) J'_n(k_d a)}{\sqrt{\epsilon_r} H_n^{(2)\prime}(ka) J_n(k_d a) - \sqrt{\mu_r} H_n^{(2)}(ka) J'_n(k_d a)} \quad (6.4.34)$$

$$d_n = \frac{j^{-(n+1)}}{\pi k a} \frac{2\sqrt{\epsilon_r}}{\sqrt{\epsilon_r} H_n^{(2)\prime}(ka) J_n(k_d a) - \sqrt{\mu_r} H_n^{(2)}(ka) J'_n(k_d a)}. \quad (6.4.35)$$

This solution can also be obtained from that of the TM polarization case by using the duality principle.

For a cylinder having a conductivity σ , ϵ_d has a complex value with an imaginary part of $\sigma/j\omega$. When $\sigma \rightarrow \infty$, Equations 6.4.31, 6.4.32, 6.4.34, and 6.4.35 are reduced to

$$a_n = -j^{-n} \frac{J_n(ka)}{H_n^{(2)}(ka)}, \quad c_n = 0 \quad (6.4.36)$$

$$b_n = -j^{-n} \frac{J'_n(ka)}{H_n^{(2)\prime}(ka)}, \quad d_n = 0 \quad (6.4.37)$$

which are the same as the solution for scattering by a perfectly conducting cylinder given by Equations 6.4.11 and 6.4.19.

Figure 6.14 displays the scattered and total fields as well as the bistatic scattering width for a dielectric cylinder with a radius of 1λ and a relative permittivity of 4.0 for both TM and TE polarization cases. The fields inside the cylinder vary drastically because of multiple bounces by the surface of the cylinder and resonances inside the cylinder.

6.4.4 Scattering by a Circular Multilayer Dielectric Cylinder

Consider a dielectric cylinder consisting of m layers with the radius, permittivity, and permeability of each layer denoted by a_i , ϵ_i , and μ_i ($i = 1, 2, \dots, m$), respectively (Fig. 6.15). For a TM-polarized incident plane wave given by Equation 6.4.7, the scattered field can again be expanded as Equation 6.4.9, which is repeated here as

$$E_z^{\text{sc}} = E_0 \sum_{n=-\infty}^{\infty} a_n H_n^{(2)}(k\rho) e^{jn\phi}. \quad (6.4.38)$$

The total field in the m th layer (the outermost) can be written as

$$E_z^{(m)} = E_0 \sum_{n=-\infty}^{\infty} [c_n^{(m)} H_n^{(1)}(k_m \rho) + d_n^{(m)} H_n^{(2)}(k_m \rho)] e^{jn\phi}. \quad (6.4.39)$$

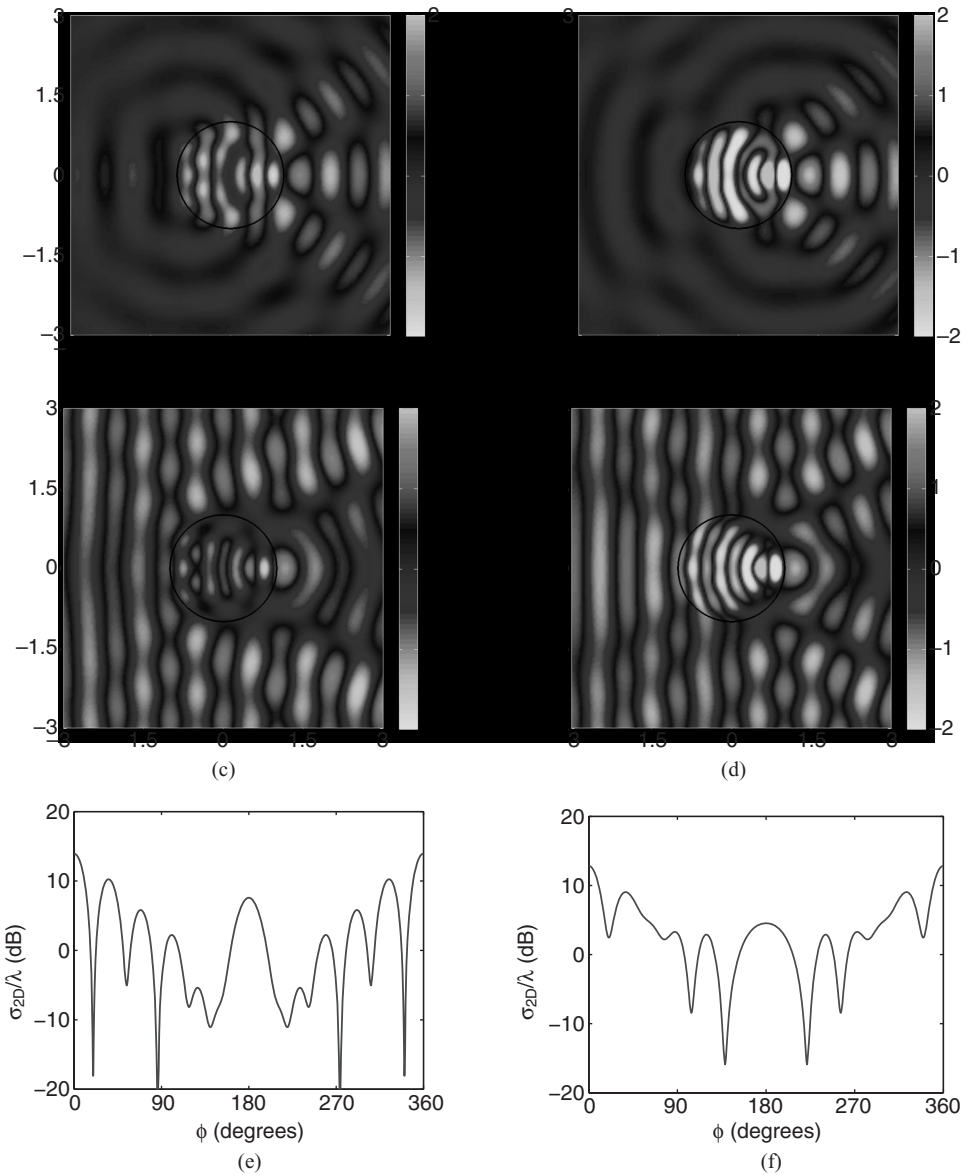


Figure 6.14 Scattering by a circular dielectric cylinder with a radius of 1λ and a relative permittivity of 4.0. (a) Snapshot of the scattered field E_z^{sc} . (b) Snapshot of the scattered field H_z^{sc} . (c) Snapshot of the total field E_z . (d) Snapshot of the total field H_z . (e) Scattering width for the TM case. (f) Scattering width for the TE case. The values of the fields are normalized by the magnitude of their respective incident fields. (See color insert.)

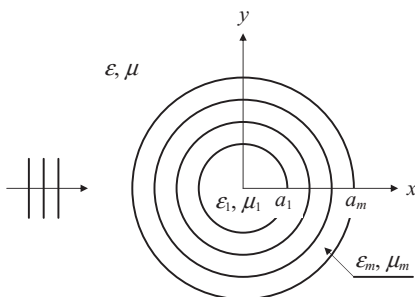


Figure 6.15 Plane wave scattering by a multilayer dielectric cylinder.

Application of the field continuity conditions at $\rho = a_m$ yields

$$j^{-n} J_n(ka_m) + a_n H_n^{(2)}(ka_m) = c_n^{(m)} H_n^{(1)}(k_m a_m) + d_n^{(m)} H_n^{(2)}(k_m a_m) \quad (6.4.40)$$

$$\sqrt{\frac{\epsilon}{\mu}} \left[j^{-n} J'_n(ka_m) + a_n H_n^{(2)\prime}(ka_m) \right] = \sqrt{\frac{\epsilon_m}{\mu_m}} \left[c_n^{(m)} H_n^{(1)\prime}(k_m a_m) + d_n^{(m)} H_n^{(2)\prime}(k_m a_m) \right] \quad (6.4.41)$$

where ϵ and μ denote the permittivity and permeability of the background medium. Solving these two equations for a_n , we have

$$a_n = -j^{-n} \frac{J_n(ka_m) - R_E^{(m)} J'_n(ka_m)}{H_n^{(2)}(ka_m) - R_E^{(m)} H_n^{(2)\prime}(ka_m)} \quad (6.4.42)$$

where

$$R_E^{(m)} = \sqrt{\frac{\epsilon \mu_m}{\mu \epsilon_m}} \frac{H_n^{(1)}(k_m a_m) + \frac{d_n^{(m)}}{c_n^{(m)}} H_n^{(2)}(k_m a_m)}{H_n^{(1)\prime}(k_m a_m) + \frac{d_n^{(m)}}{c_n^{(m)}} H_n^{(2)\prime}(k_m a_m)}. \quad (6.4.43)$$

Therefore, it amounts to finding $d_n^{(m)} / c_n^{(m)}$ to compute the scattered field. For this, let us consider the field in the i th layer, which can be written as

$$E_z^{(i)} = E_0 \sum_{n=-\infty}^{\infty} \left[c_n^{(i)} H_n^{(1)}(k_i \rho) + d_n^{(i)} H_n^{(2)}(k_i \rho) \right] e^{jn\phi}. \quad (6.4.44)$$

Application of the field continuity conditions at $\rho = a_i$ ($i = 1, 2, \dots, m-1$) yields

$$c_n^{(i+1)} H_n^{(1)}(k_{i+1} a_i) + d_n^{(i+1)} H_n^{(2)}(k_{i+1} a_i) = c_n^{(i)} H_n^{(1)}(k_i a_i) + d_n^{(i)} H_n^{(2)}(k_i a_i) \quad (6.4.45)$$

$$\sqrt{\frac{\epsilon_{i+1}}{\mu_{i+1}}} \left[c_n^{(i+1)} H_n^{(1)\prime}(k_{i+1} a_i) + d_n^{(i+1)} H_n^{(2)\prime}(k_{i+1} a_i) \right] = \sqrt{\frac{\epsilon_i}{\mu_i}} \left[c_n^{(i)} H_n^{(1)\prime}(k_i a_i) + d_n^{(i)} H_n^{(2)\prime}(k_i a_i) \right]. \quad (6.4.46)$$

From these two equations, we can find that

$$\frac{d_n^{(i+1)}}{c_n^{(i+1)}} = -\frac{H_n^{(1)}(k_{i+1} a_i) - R_E^{(i)} H_n^{(1)\prime}(k_{i+1} a_i)}{H_n^{(2)}(k_{i+1} a_i) - R_E^{(i)} H_n^{(2)\prime}(k_{i+1} a_i)} \quad (6.4.47)$$

where

$$R_E^{(i)} = \sqrt{\frac{\epsilon_{i+1} \mu_i}{\mu_{i+1} \epsilon_i}} \frac{H_n^{(1)}(k_i a_i) + \frac{d_n^{(i)}}{c_n^{(i)}} H_n^{(2)}(k_i a_i)}{H_n^{(1)\prime}(k_i a_i) + \frac{d_n^{(i)}}{c_n^{(i)}} H_n^{(2)\prime}(k_i a_i)}. \quad (6.4.48)$$

Note that Equation 6.4.43 can be written as Equation 6.4.48 by letting $\epsilon_{m+1} = \epsilon$ and $\mu_{m+1} = \mu$.

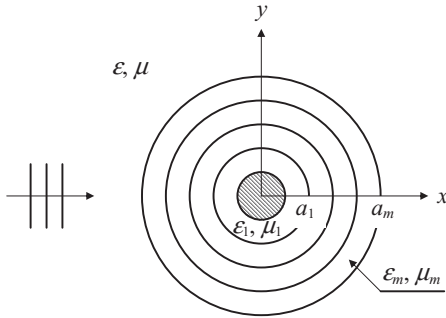


Figure 6.16 Plane wave scattering by a multilayer dielectric cylinder containing a conducting cylinder inside the innermost layer.

Equations 6.4.47 and 6.4.48 provide a recursive procedure to calculate $d_n^{(i)} / c_n^{(i)}$ for $i = 2, 3, \dots, m$ and $R_E^{(i)}$ for $i = 1, 2, \dots, m$ once the value of $d_n^{(1)} / c_n^{(1)}$ is known: $d_n^{(1)} / c_n^{(1)} \rightarrow R_E^{(1)} \rightarrow d_n^{(2)} / c_n^{(2)} \rightarrow R_E^{(2)} \rightarrow \dots \rightarrow d_n^{(m)} / c_n^{(m)} \rightarrow R_E^{(m)}$. Once $R_E^{(m)}$ is obtained, the coefficient a_n for the scattered field is calculated using Equation 6.4.42. If the first layer (the innermost layer) is homogeneous (Fig. 6.15), the field has to be finite at $\rho = 0$, which requires that $c_n^{(1)} = d_n^{(1)}$ or $d_n^{(1)} / c_n^{(1)} = 1$. If the first layer contains a perfectly conducting cylinder having a radius of a_0 ($a_0 < a_1$), as illustrated in Figure 6.16, application of the boundary condition $E_z^{(1)}|_{\rho=a_0} = 0$ yields

$$\frac{d_n^{(1)}}{c_n^{(1)}} = -\frac{H_n^{(1)}(k_1 a_0)}{H_n^{(2)}(k_1 a_0)}. \quad (6.4.49)$$

The solution for scattering of a TE-polarized incident plane wave can be obtained conveniently by employing the duality principle. The scattered field can be expanded as

$$H_z^{\text{sc}} = H_0 \sum_{n=-\infty}^{\infty} b_n H_n^{(2)}(k\rho) e^{jn\phi} \quad (6.4.50)$$

where the expansion coefficients are given by

$$b_n = -j^{-n} \frac{J_n(ka_m) - R_H^{(m)} J'_n(ka_m)}{H_n^{(2)}(ka_m) - R_H^{(m)} H_n^{(2)\prime}(ka_m)}. \quad (6.4.51)$$

The $R_H^{(m)}$ can be calculated using the recursive formulas

$$R_H^{(i)} = \sqrt{\frac{\mu_{i+1} \epsilon_i}{\epsilon_{i+1} \mu_i}} \frac{H_n^{(1)}(k_i a_i) + \frac{d_n^{(i)}}{c_n^{(i)}} H_n^{(2)}(k_i a_i)}{H_n^{(1)\prime}(k_i a_i) + \frac{d_n^{(i)}}{c_n^{(i)}} H_n^{(2)\prime}(k_i a_i)} \quad i = 2, 3, \dots, m \quad (6.4.52)$$

$$\frac{d_n^{(i)}}{c_n^{(i)}} = -\frac{H_n^{(1)}(k_i a_{i-1}) - R_H^{(i-1)} H_n^{(1)\prime}(k_i a_{i-1})}{H_n^{(2)}(k_i a_{i-1}) - R_H^{(i-1)} H_n^{(2)\prime}(k_i a_{i-1})} \quad i = 2, 3, \dots, m. \quad (6.4.53)$$

For a homogeneous first layer, we have $d_n^{(1)} / c_n^{(1)} = 1$ to make the field finite at $\rho = 0$. If the first layer contains a perfectly conducting cylinder having a radius of a_0 ($a_0 < a_1$), application of the boundary condition $E_\phi^{(1)}|_{\rho=a_0} = 0$ yields

$$\frac{d_n^{(1)}}{c_n^{(1)}} = -\frac{H_n^{(1)\prime}(k_1 a_0)}{H_n^{(2)\prime}(k_1 a_0)}. \quad (6.4.54)$$

Note that in both TM and TE polarization cases, if we are also interested in the fields inside the cylinder, we can calculate the expansion coefficients $c_n^{(i)}$ and $d_n^{(i)}$ for each layer, starting from the m th layer, then the $(m-1)$ th layer, and all the way back to the first layer, using the values of a_n or b_n and the ratio $d_n^{(i)}/c_n^{(i)}$ calculated during the recursive process.

6.5 RADIATION BY INFINITELY LONG CURRENTS

In this section we deal with radiation problems where the source is placed nearby the object of interest. We first consider the radiation by an infinitely long line current and by a circular cylindrical surface current and derive the addition theorem for the Hankel functions. We then consider the radiation in the presence of a conducting cylinder and a conducting wedge and use the second solution to discuss the field singularity at its edge.

6.5.1 Line Current Radiation in Free Space

We first consider the radiation by a time-harmonic, uniform, infinitely long line current placed along the z -axis (Fig. 6.17). The magnetic vector potential can be calculated using Equation 2.2.21, which yields

$$\mathbf{A} = \hat{z} A_z = \hat{z} \frac{\mu}{4\pi} \int_{-\infty}^{\infty} I \frac{e^{-jkR}}{R} dz' \quad R = \sqrt{\rho^2 + (z-z')^2} \quad (6.5.1)$$

whose evaluation appears quite complicated. To circumvent this difficulty, let us solve for A_z directly from the Helmholtz equation

$$\nabla^2 A_z + k^2 A_z = -\mu I \delta(\mathbf{p}) \quad (6.5.2)$$

which is reduced to

$$\nabla^2 A_z + k^2 A_z = 0 \quad \text{for } \rho \neq 0. \quad (6.5.3)$$

Since the line current is placed on the z -axis and is uniform along the z -direction, A_z is independent of ϕ and z . Hence, its solution takes the form

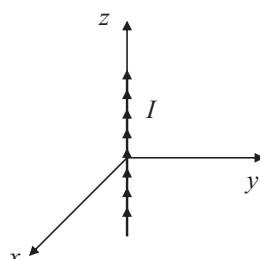


Figure 6.17 Radiation by an infinitely long line current along the z -axis.

$$A_z = CH_0^{(2)}(k\rho) \quad (6.5.4)$$

where C is a constant to be determined. For this, we first integrate Equation 6.5.2 over a small circular area σ_ϵ with a vanishing radius ϵ to find

$$\iint_{\sigma_\epsilon} \nabla^2 A_z \, ds = -\mu I. \quad (6.5.5)$$

The left-hand side can be written as

$$\begin{aligned} \iint_{\sigma_\epsilon} \nabla^2 A_z \, ds &= \iint_{\sigma_\epsilon} \nabla \cdot \nabla A_z \, ds = \oint_{c_\epsilon} \nabla A_z \cdot \hat{n} \, dl = \oint_{c_\epsilon} \frac{\partial A_z}{\partial \rho} \, dl \\ &= \int_0^{2\pi} \frac{\partial A_z}{\partial \rho} \, \epsilon d\phi = 2\pi \epsilon \left. \frac{\partial A_z}{\partial \rho} \right|_{\rho=\epsilon} \end{aligned} \quad (6.5.6)$$

where c_ϵ is the closed contour of σ_ϵ . We then substitute Equation 6.5.4 into Equation 6.5.6 and employ the small-argument approximation for $H_0^{(2)}$ given by

$$H_0^{(2)}(x) \approx -j \frac{2}{\pi} \ln x \quad \text{when } x \rightarrow 0 \quad (6.5.7)$$

to evaluate Equation 6.5.6. The result is then substituted into Equation 6.5.6 to find that $C = \mu I / 4j$. Hence,

$$A_z = \frac{\mu I}{4j} H_0^{(2)}(k\rho) \quad (6.5.8)$$

and the corresponding electric and magnetic fields are given by

$$E_z = -\frac{k^2 I}{4\omega \epsilon} H_0^{(2)}(k\rho), \quad H_\phi = \frac{kI}{4j} H_1^{(2)}(k\rho). \quad (6.5.9)$$

If the line current is located at $\rho = \rho'$ instead of $\rho = 0$, A_z is then given by

$$A_z = \frac{\mu I}{4j} H_0^{(2)}(k|\rho - \rho'|) \quad (6.5.10)$$

and the corresponding electric and magnetic fields are given by

$$E_z = -\frac{\eta kI}{4} H_0^{(2)}(k|\rho - \rho'|), \quad H_\phi = -\frac{I}{4j} \frac{\partial}{\partial \rho} H_0^{(2)}(k|\rho - \rho'|). \quad (6.5.11)$$

In the far-field zone ($\rho \gg \rho'$ and $k\rho \gg 1$), $|\rho - \rho'| \approx \rho - \rho' \cos(\phi - \phi')$. By using the large-argument approximation for $H_0^{(2)}(x)$ given by

$$H_0^{(2)}(x) \approx \sqrt{\frac{2}{j\pi x}} e^{-jx} \quad \text{when } x \rightarrow \infty \quad (6.5.12)$$

Equation 6.5.11 becomes

$$E_z \approx -\eta I \sqrt{\frac{k}{j8\pi\rho}} e^{-jk[\rho-\rho'\cos(\phi-\phi')]} \quad (6.5.13)$$

$$H_\phi \approx I \sqrt{\frac{k}{j8\pi\rho}} e^{-jk[\rho-\rho'\cos(\phi-\phi')]} \quad (6.5.14)$$

For an infinitely long current with a finite cross-section and a current density of $J_z(\rho)$, the magnetic vector can be obtained by linear superposition,

$$A_z(\rho) = \frac{\mu}{4j} \iint_S H_0^{(2)}(k|\rho - \rho'|) J_z(\rho') dS' \quad (6.5.15)$$

and the far field is given by

$$E_z \approx -\eta \sqrt{\frac{k}{j8\pi\rho}} e^{-jk\rho} \iint_S e^{jk\rho'\cos(\phi-\phi')} J_z(\rho') dS' \quad (6.5.16)$$

$$H_\phi \approx \sqrt{\frac{k}{j8\pi\rho}} e^{-jk\rho} \iint_S e^{jk\rho'\cos(\phi-\phi')} J_z(\rho') dS'. \quad (6.5.17)$$

By taking the derivative of the far field with respect to ρ , we find that

$$\lim_{\rho \rightarrow \infty} \sqrt{\rho} \left(\frac{\partial E_z}{\partial \rho} + jk E_z \right) = 0. \quad (6.5.18)$$

This is the *Sommerfeld radiation condition* for two-dimensional fields. It is also valid for other field components such as E_ϕ , H_z , and H_ϕ .

6.5.2 Radiation by a Cylindrical Surface Current

Now we consider the radiation of a time-harmonic cylindrical surface current having a radius of ρ' and a surface current density of $\mathbf{J}_s = \hat{z} J_s(\phi)$, as illustrated in Figure 6.18. For simplicity, the medium inside the cylindrical surface is assumed to be the same as that outside the surface. Although the magnetic vector potential A_z can be obtained by using

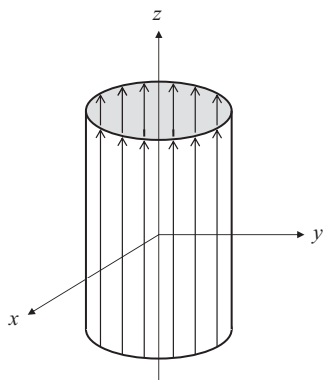


Figure 6.18 Radiation by a cylindrical surface current.

Equation 6.5.15, a better approach is again to seek the solution based on cylindrical wave expansion. Since A_z satisfies the homogeneous Helmholtz equation both inside and outside the cylindrical surface current, it can be expanded as

$$A_z^{\text{int}}(\rho, \phi) = \sum_{n=-\infty}^{\infty} a_n J_n(k\rho) e^{jn\phi} \quad \rho < \rho' \quad (6.5.19)$$

$$A_z^{\text{ext}}(\rho, \phi) = \sum_{n=-\infty}^{\infty} b_n H_n^{(2)}(k\rho) e^{jn\phi} \quad \rho > \rho'. \quad (6.5.20)$$

The corresponding electric and magnetic field components E_z and H_ϕ are given by

$$E_z^{\text{int}}(\rho, \phi) = -\frac{jk^2}{\omega \mu \epsilon} \sum_{n=-\infty}^{\infty} a_n J_n(k\rho) e^{jn\phi} \quad \rho < \rho' \quad (6.5.21)$$

$$H_\phi^{\text{int}}(\rho, \phi) = -\frac{k}{\mu} \sum_{n=-\infty}^{\infty} a_n J'_n(k\rho) e^{jn\phi} \quad \rho < \rho' \quad (6.5.22)$$

$$E_z^{\text{ext}}(\rho, \phi) = -\frac{jk^2}{\omega \mu \epsilon} \sum_{n=-\infty}^{\infty} b_n H_n^{(2)}(k\rho) e^{jn\phi} \quad \rho > \rho' \quad (6.5.23)$$

$$H_\phi^{\text{ext}}(\rho, \phi) = -\frac{k}{\mu} \sum_{n=-\infty}^{\infty} b_n H_n^{(2)\prime}(k\rho) e^{jn\phi} \quad \rho > \rho'. \quad (6.5.24)$$

Applying the electric and magnetic field continuity conditions $E_z^{\text{ext}}(\rho', \phi) = E_z^{\text{int}}(\rho', \phi)$ and $H_\phi^{\text{ext}}(\rho', \phi) - H_\phi^{\text{int}}(\rho', \phi) = J_s(\phi)$, we find

$$a_n J_n(k\rho') = b_n H_n^{(2)}(k\rho') \quad (6.5.25)$$

$$a_n J'_n(k\rho') - b_n H_n^{(2)\prime}(k\rho') = \frac{\mu}{2\pi k} \int_0^{2\pi} J_s(\phi) e^{-jn\phi} d\phi. \quad (6.5.26)$$

These equations can be solved to give

$$a_n = \frac{\pi k \rho'}{2j} c_n H_n^{(2)}(k\rho') \quad (6.5.27)$$

$$b_n = \frac{\pi k \rho'}{2j} c_n J_n(k\rho') \quad (6.5.28)$$

where

$$c_n = \frac{\mu}{2\pi k} \int_0^{2\pi} J_s(\phi) e^{-jn\phi} d\phi. \quad (6.5.29)$$

The solution obtained above is valid for J_s as an arbitrary function of ϕ . For a line current placed at $\rho = \rho'$, J_s can be expressed as $J_s(\phi) = I\delta(\phi - \phi')/\rho'$. Consequently,

$$c_n = \frac{\mu I}{2\pi k \rho'} e^{-jn\phi'} \quad (6.5.30)$$

and

$$A_z(\rho, \phi) = \frac{\mu I}{4j} \sum_{n=-\infty}^{\infty} \begin{cases} J_n(k\rho)H_n^{(2)}(k\rho') \\ J_n(k\rho')H_n^{(2)}(k\rho) \end{cases} e^{jn(\phi-\phi')} \quad \begin{cases} \rho < \rho' \\ \rho > \rho'. \end{cases} \quad (6.5.31)$$

Comparing Equation 6.5.31 with Equation 6.5.10, we obtain

$$H_0^{(2)}(k|\rho - \rho'|) = \sum_{n=-\infty}^{\infty} \begin{cases} J_n(k\rho)H_n^{(2)}(k\rho') \\ J_n(k\rho')H_n^{(2)}(k\rho) \end{cases} e^{jn(\phi-\phi')} \quad \begin{cases} \rho < \rho' \\ \rho > \rho'. \end{cases} \quad (6.5.32)$$

which is called the *addition theorem for the Hankel function*. This equation expands an off-centered cylindrical wave in terms of a superposition of centered cylindrical wave functions. By taking its real and imaginary parts, we can obtain the *addition theorem for the Bessel functions*. Figure 6.19 shows how an off-centered cylindrical wave is formed by increasing the number of terms in the summation in Equation 6.5.32.

6.5.3 Radiation in the Presence of a Circular Conducting Cylinder

Next we consider the problem where a perfectly conducting cylinder of radius a is inserted inside the cylindrical surface current shown in Figure 6.18. The new problem is illustrated in Figure 6.20. There are two approaches to dealing with this problem. One is to follow the basic steps in the preceding subsection. The only difference is that the expression of A_z inside the cylindrical surface current should include $Y_n(k\rho)$ because the field region no longer includes the z -axis in this case. To satisfy the boundary condition $E_z|_{\rho=a} = 0$, we can expand A_z as

$$A_z^{\text{int}}(\rho, \phi) = \sum_{n=-\infty}^{\infty} \tilde{a}_n [Y_n(ka)J_n(k\rho) - J_n(ka)Y_n(k\rho)] e^{jn\phi} \quad a \leq \rho < \rho'. \quad (6.5.33)$$

The A_z outside the cylindrical surface current can still be expanded as in Equation 6.5.20. The expansion coefficients \tilde{a}_n and b_n can then be determined by using the field continuity conditions across the surface current.

The other approach is to utilize the result derived in the preceding subsection. More specifically, we can treat the field radiated by the cylindrical surface current in the absence of the conducting cylinder as the incident field. Based on Equations 6.5.21 and 6.5.23, this incident field is given by

$$E_z^{\text{inc}}(\rho, \phi) = -\frac{\pi k^3 \rho'}{2\omega \mu \epsilon} \sum_{n=-\infty}^{\infty} c_n \begin{cases} J_n(k\rho)H_n^{(2)}(k\rho') \\ J_n(k\rho')H_n^{(2)}(k\rho) \end{cases} e^{jn\phi} \quad \begin{cases} \rho < \rho' \\ \rho > \rho'. \end{cases} \quad (6.5.34)$$

This incident field will induce a surface current on the conducting cylinder; that surface current, in turn, will radiate a scattered field. The scattered field can be expanded as

$$E_z^{\text{sc}}(\rho, \phi) = \sum_{n=-\infty}^{\infty} d_n H_n^{(2)}(k\rho) e^{jn\phi} \quad \rho \geq a. \quad (6.5.35)$$

Since the total field satisfies the boundary condition $E_z|_{\rho=a} = 0$, we immediately find

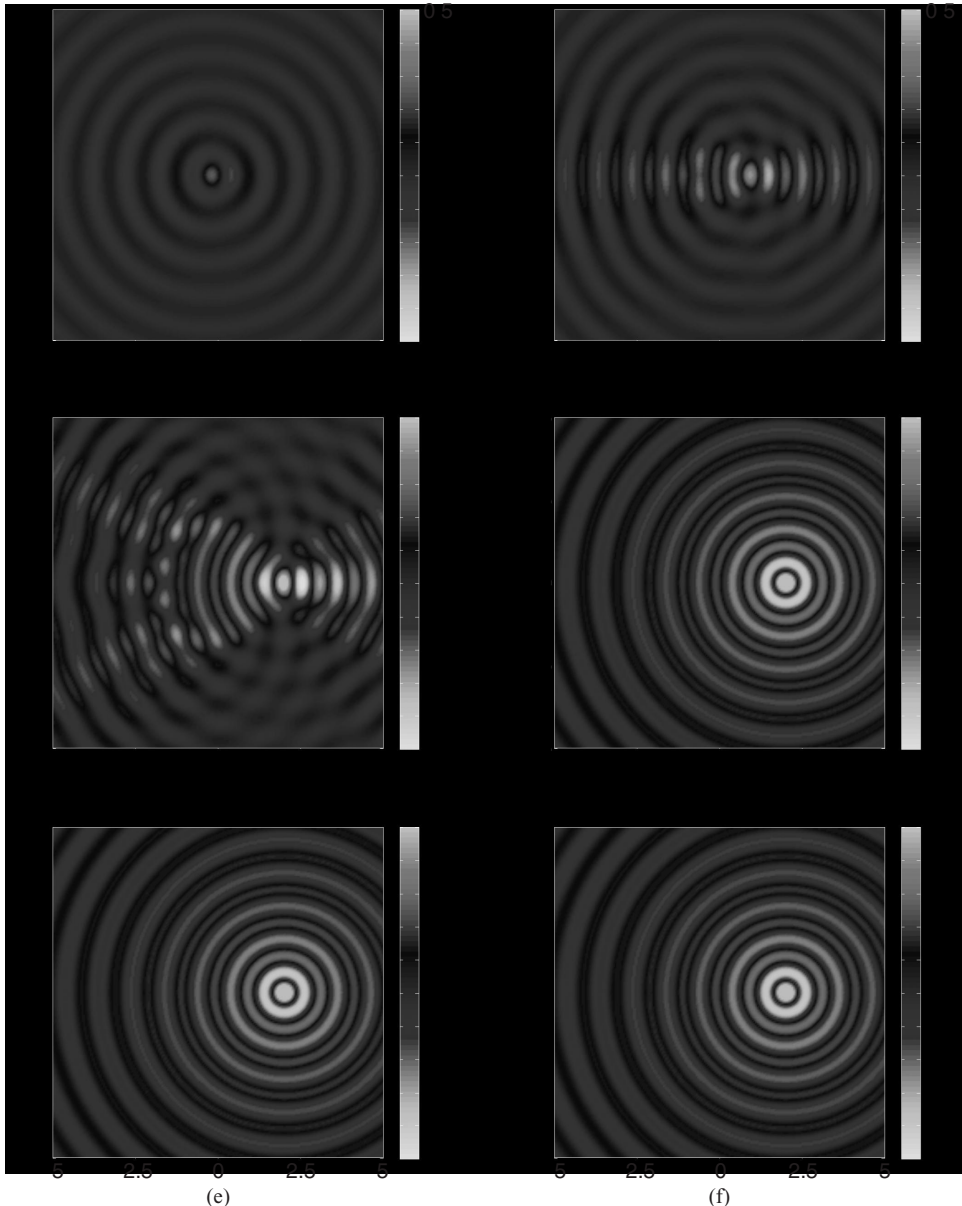


Figure 6.19 Illustration of the addition theorem for the Hankel function. The plots show the real part of the right-hand side of Equation 6.5.32 in a $10\lambda \times 10\lambda$ region when the summation is evaluated from $n=-M$ to M . Clearly, an off-centered cylindrical wave is formed by increasing the number of terms in the summation. (a) $M=1$. (b) $M=5$. (c) $M=10$. (d) $M=15$. (e) $M=20$. (f) $M=40$. (See color insert.)

$$d_n = \frac{\pi k^3 \rho'}{2\omega \mu \epsilon} \frac{c_n J_n(ka) H_n^{(2)}(k\rho')}{H_n^{(2)}(ka)}. \quad (6.5.36)$$

Therefore, the scattered field is given by

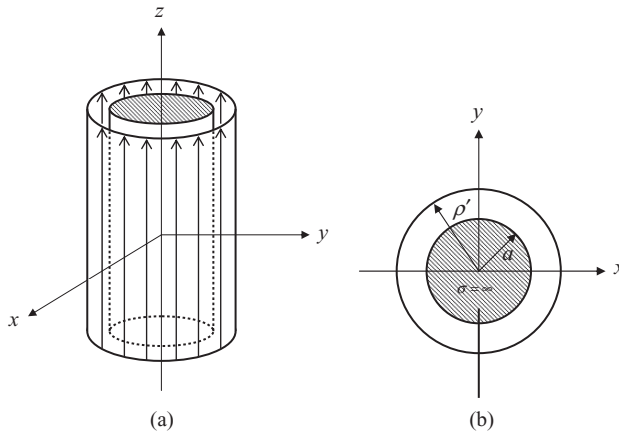


Figure 6.20 Radiation by a cylindrical surface current in the presence of a conducting cylinder.
(a) Three-dimensional view. (b) Cross-sectional view.

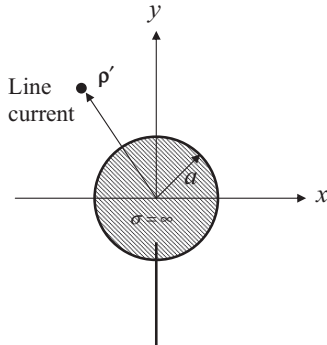


Figure 6.21 Radiation by an infinitely long line current in the presence of a conducting cylinder.

$$E_z^{\text{sc}}(\rho, \phi) = \frac{\pi k^3 \rho'}{2\omega \mu \epsilon} \sum_{n=-\infty}^{\infty} c_n \frac{J_n(ka) H_n^{(2)}(k\rho')}{H_n^{(2)}(ka)} H_n^{(2)}(k\rho) e^{jn\phi} \quad \rho \geq a. \quad (6.5.37)$$

Superimposing this to the incident field in Equation 6.5.34 yields the total field radiated by the cylindrical surface current in the presence of a conducting cylinder.

If the cylindrical surface current is reduced to a line current located at \$\rho = \rho'\$, as illustrated in Figure 6.21, \$c_n\$ is then given by Equation 6.5.30. The scattered field becomes

$$E_z^{\text{sc}}(\rho, \phi) = \frac{\eta k I}{4} \sum_{n=-\infty}^{\infty} \frac{J_n(ka) H_n^{(2)}(k\rho')}{H_n^{(2)}(ka)} H_n^{(2)}(k\rho) e^{jn(\phi-\phi')} \quad \rho \geq a \quad (6.5.38)$$

and the total field is given by

$$E_z(\rho, \phi) = \frac{\eta k I}{4} \left[\sum_{n=-\infty}^{\infty} \frac{J_n(ka) H_n^{(2)}(k\rho')}{H_n^{(2)}(ka)} H_n^{(2)}(k\rho) e^{jn(\phi-\phi')} - H_0^{(2)}(k|\rho - \rho'|) \right] \quad \rho \geq a. \quad (6.5.39)$$

Figure 6.22 shows the scattered and total fields radiated by an electric line current placed \$1\lambda\$ in front of a conducting cylinder with a radius of \$1\lambda\$.

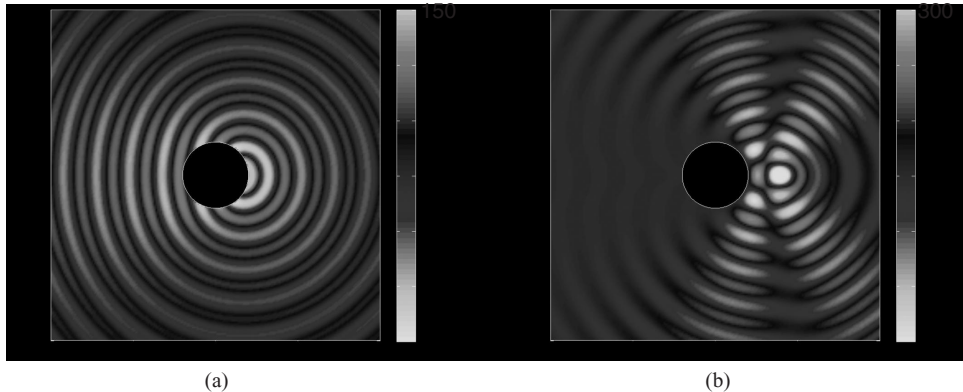


Figure 6.22 Radiation of an electric line current ($I=1\text{ A}$) placed 1λ away from a conducting cylinder with a radius of 1λ . (a) Snapshot of the scattered field E_z^{sc} (V/m). (b) Snapshot of the total field E_z (V/m). (See color insert.)

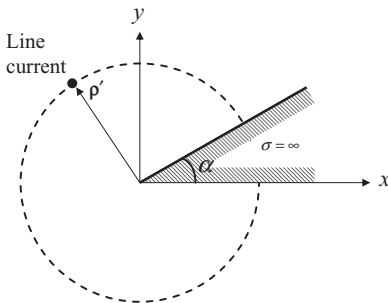


Figure 6.23 Radiation by an infinitely long line current in the presence of a conducting wedge.

6.5.4 Radiation in the Presence of a Conducting Wedge

The analysis approaches discussed so far in this section can be extended to deal with a variety of other two-dimensional problems. Here we consider one more example to illustrate the analysis procedure and discuss the field singularity problem at a conducting edge. The problem is that of the radiation of a line current in the presence of a conducting wedge (Fig. 6.23). The lower surface of the wedge is placed at $\phi = 0$, and the upper surface is located at $\phi = \alpha$. The line current is placed at $\rho = \rho'$ with $\alpha < \phi < 2\pi$. We can consider this line current as a special cylindrical surface current with the surface current density given by $J_s(\phi) = I\delta(\phi - \phi')/\rho'$. Therefore, A_z can be expanded as

$$A_z(\rho, \phi) = \sum_v \begin{cases} J_v(k\rho)H_v^{(2)}(k\rho') \\ J_v(k\rho')H_v^{(2)}(k\rho) \end{cases} [a_v \cos v\phi + b_v \sin v\phi] \quad \begin{cases} \rho < \rho' \\ \rho > \rho' \end{cases} \quad (6.5.40)$$

where v is undetermined at this moment. This expansion has built in the field continuity condition $E_z|_{\rho=\rho'+0} = E_z|_{\rho=\rho'-0}$. By applying the boundary conditions $E_z|_{\phi=\alpha} = E_z|_{\phi=2\pi} = 0$, A_z is found to have the form

$$A_z(\rho, \phi) = \sum_{m=1}^{\infty} \begin{cases} J_m(k\rho)H_m^{(2)}(k\rho') \\ J_m(k\rho')H_m^{(2)}(k\rho) \end{cases} \frac{a_m}{\sin m\alpha} \sin m(\phi - \alpha) \quad \begin{cases} \rho < \rho' \\ \rho > \rho' \end{cases} \quad (6.5.41)$$

where $v = m\pi/(2\pi - \alpha)$. Next, we apply the magnetic field continuity condition $H_\phi|_{\rho=\rho'+0} - H_\phi|_{\rho=\rho'-0} = J_s$ to find a_v and the result is

$$a_v = -\frac{j\pi\mu I}{2\pi - \alpha} \sin v\alpha \sin v(\phi' - \alpha). \quad (6.5.42)$$

Therefore, A_z is given by

$$A_z(\rho, \phi) = -\frac{j\pi\mu I}{2\pi - \alpha} \sum_{m=1}^{\infty} \begin{cases} J_v(k\rho)H_v^{(2)}(k\rho') \\ J_v(k\rho')H_v^{(2)}(k\rho) \end{cases} \begin{cases} \sin v(\phi' - \alpha) \sin v(\phi - \alpha) & \rho < \rho' \\ \rho > \rho' & \end{cases} \quad (6.5.43)$$

and the field components are given by

$$E_z(\rho, \phi) = -\frac{\pi\eta kI}{2\pi - \alpha} \sum_{m=1}^{\infty} \begin{cases} J_v(k\rho)H_v^{(2)}(k\rho') \\ J_v(k\rho')H_v^{(2)}(k\rho) \end{cases} \begin{cases} \sin v(\phi' - \alpha) \sin v(\phi - \alpha) & \rho < \rho' \\ \rho > \rho' & \end{cases} \quad (6.5.44)$$

$$H_\rho(\rho, \phi) = -\frac{j\pi I}{(2\pi - \alpha)\rho} \sum_{m=1}^{\infty} v \begin{cases} J_v(k\rho)H_v^{(2)}(k\rho') \\ J_v(k\rho')H_v^{(2)}(k\rho) \end{cases} \begin{cases} \sin v(\phi' - \alpha) \cos v(\phi - \alpha) & \rho < \rho' \\ \rho > \rho' & \end{cases} \quad (6.5.45)$$

$$H_\phi(\rho, \phi) = \frac{j\pi kI}{2\pi - \alpha} \sum_{m=1}^{\infty} \begin{cases} J'_v(k\rho)H_v^{(2)}(k\rho') \\ J_v(k\rho')H_v^{(2)\prime}(k\rho) \end{cases} \begin{cases} \sin v(\phi' - \alpha) \sin v(\phi - \alpha) & \rho < \rho' \\ \rho > \rho' & \end{cases} \quad (6.5.46)$$

When the line current is placed far away from the edge of the wedge, we obtain the solution of plane wave scattering by the conducting wedge [7,13,14]. Figure 6.24 shows the field radiated by a line current in the presence of a 30°-angled conducting wedge for two cases. In the first case, the line current is placed 3λ above the tip of the wedge, and in the second case, the line current is placed 100λ above the tip of the wedge. In the second case, the incident wave can be considered as a plane wave for the region displayed in the figure. The phenomenon of edge diffraction is shown clearly in the plots.

It is of interest to examine the field behavior very close to the edge of the conducting wedge, where $k\rho \ll 1$. Since $J_v(z) \sim z^v$ and $J'_v(z) \sim z^{v-1}$ when $z \rightarrow 0$, it is found that

$$H_\rho, H_\phi \sim \rho^{v-1} \quad \text{when } k\rho \ll 1. \quad (6.5.47)$$

For $m = 1$, $v = \pi/(2\pi - \alpha)$, which is less than 1 when $\alpha < \pi$. Therefore,

$$H_\rho, H_\phi \rightarrow \infty \quad \text{as } \rho \rightarrow 0 \quad (6.5.48)$$

or in other words, both H_ρ and H_ϕ become singular at the edge of a wedge with an internal angle smaller than π ! Since the induced surface current density on the wedge is related to H_ρ , the induced surface current density also becomes singular at the edge of the wedge! This phenomenon is called the *edge singularity* of electromagnetic fields [14,15]. In particular, when $\alpha = 0$ (the wedge becomes a half-plane), $v = \frac{1}{2}$; both H_ρ and H_ϕ behave as $\rho^{-1/2}$ close to the edge. When $\alpha = \pi/2$ (the right-angled wedge), $v = \frac{2}{3}$; both H_ρ and H_ϕ behave as $\rho^{-1/3}$ close to the edge. Therefore, the smaller the internal angle, the stronger the field singularity. The singularity is strongest at the edge of a half-plane and vanishes when $\alpha \geq \pi$.

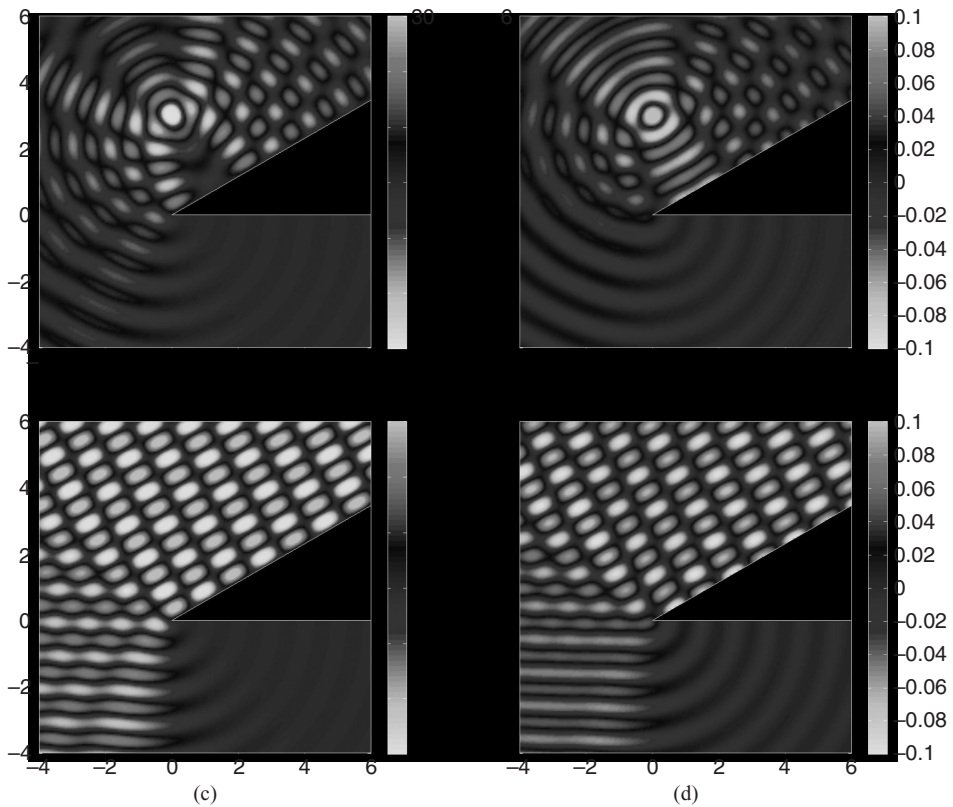


Figure 6.24 Snapshots of the field radiated by a line current in the presence of a 30° -angled conducting wedge. (a) E_z (V/m) produced by an electric current ($I=0.1\text{ A}$) placed 3λ above the wedge. (b) H_z (A/m) produced by a magnetic current ($K=37.7\text{ V}$) placed 3λ above the wedge. (c) E_z (V/m) produced by an electric current ($I=1\text{ A}$) placed 100λ above the wedge. (d) H_z (A/m) produced by a magnetic current ($K=377\text{ V}$) placed 100λ above the wedge. (See color insert.)

By analyzing the radiation of a magnetic current line in the presence of a conducting wedge, it can be found that the transverse electric field components possess the same edge singularity,

$$E_\rho, E_\phi \sim \rho^{\nu-1} \quad \text{when } k\rho \ll 1. \quad (6.5.49)$$

Since the induced surface charge density on the wedge is related to E_ϕ , the induced surface charge density also becomes singular at the edge of the wedge with an internal angle smaller than π . Note that for both the electric and magnetic fields, only the transverse components are singular whereas the component parallel to the edge remains finite. Furthermore, since real-world wedges do not have perfectly sharp edges, even the transverse field components are finite although their values can be very large depending on the sharpness of the edges. Figure 6.25 plots the field singularity around the edge of a conducting wedge for three different internal angles.

6.5.5 Radiation by a Finite Current

In all of the examples treated so far in this section, the current sources are assumed to be infinitely long in the z -direction and have no variation in this direction. For problems with

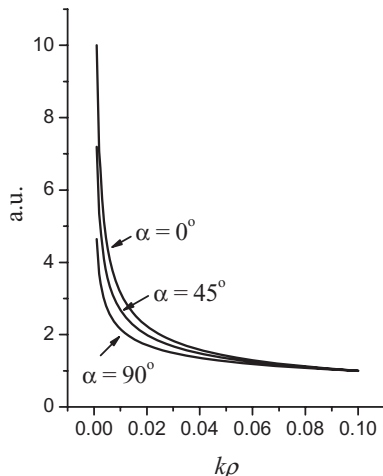


Figure 6.25 Field singularity (arbitrary unit) around the edge of a conducting wedge.

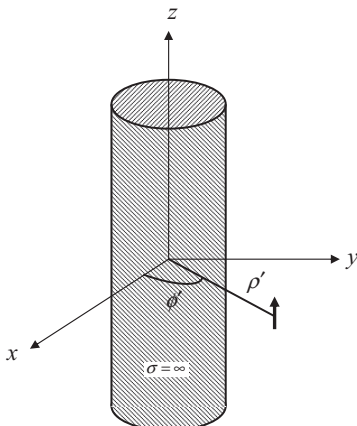


Figure 6.26 Radiation by an infinitesimally short dipole in the presence of a conducting cylinder.

a finite current source, we can first expand the current using the Fourier transform, then find the solution for each Fourier component, and obtain the final solution through the Fourier integral [4]. To show this, let us consider the radiation of a z -directed infinitesimal dipole in the presence of a circular conducting cylinder (Fig. 6.26).

Without loss of generality, the dipole is assumed to reside at $(\rho', \phi', 0)$. The current density of this dipole can then be written as

$$\mathbf{J}(\rho, \phi, z) = \hat{z} \frac{Il}{\rho} \delta(\rho - \rho') \delta(\phi - \phi') \delta(z). \quad (6.5.50)$$

By expanding $\delta(z)$ in terms of a Fourier integral, we have

$$\mathbf{J}(\rho, \phi, z) = \hat{z} \int_{-\infty}^{\infty} \frac{Il}{2\pi\rho} \delta(\rho - \rho') \delta(\phi - \phi') e^{jhz} dh. \quad (6.5.51)$$

Therefore, the dipole can be expressed as a linear superposition of an infinite number of z -directed line currents with the magnitude of $Il e^{jhz} / 2\pi$. By following the discussion in Section 6.5.3, we can find the z -component of the electric field produced by the line current as

$$\tilde{E}_z(\rho, \phi, h) = \frac{\eta k_\rho I}{8\pi} \left[\sum_{n=-\infty}^{\infty} \frac{J_n(k_\rho a) H_n^{(2)}(k_\rho \rho')}{H_n^{(2)}(k_\rho a)} H_n^{(2)}(k_\rho \rho) e^{jn(\phi-\phi')} - H_0^{(2)}(k_\rho |\rho - \rho'|) \right] e^{jhz} \quad (6.5.52)$$

where $k_\rho = \sqrt{k^2 - h^2}$. The electric field produced by the dipole is then given by

$$E_z(\rho, \phi, z) = \int_{-\infty}^{\infty} \tilde{E}_z(\rho, \phi, h) dh. \quad (6.5.53)$$

Other field components, such as E_ρ , E_ϕ , H_ρ , and H_ϕ , can be found in a similar manner. Note that in this case, E_ρ and E_ϕ no longer vanish as in the case of an infinitely long uniform current.

REFERENCES

- [1] M. ABRAMOWITZ and I. A. STEGUN, Eds., *Handbook of Mathematical Functions*. New York: Dover, 1965.
- [2] S. J. ZHANG and J. M. JIN, *Computation of Special Functions*. New York: Wiley, 1996.
- [3] P. M. MORSE and H. FESHBACH, *Methods of Theoretical Physics*. New York: McGraw-Hill, 1953.
- [4] R. F. HARRINGTON, *Time-Harmonic Electromagnetic Fields*. New York: McGraw-Hill, 1961.
- [5] R. E. COLLIN, *Field Theory of Guided Waves* (2nd Edition). New York: IEEE Press, 1991.
- [6] S. RAMO, J. R. WHINNERY, and T. VAN DUZER, *Fields and Waves in Communication Electronics* (3rd edition). New York: Wiley, 1994.
- [7] C. A. BALANIS, *Advanced Engineering Electromagnetics*. New York: Wiley, 1989.
- [8] U. S. INAN and A. S. INAN, *Electromagnetic Waves*. Upper Saddle River, NJ: Prentice Hall, 2000.
- [9] C. G. SOMEDA, *Electromagnetic Waves* (2nd edition). Boca Raton, FL: CRC Press, 2006.
- [10] N. S. KAPANY and J. J. BURKE, *Optical Waveguides*. New York: Academic, 1972.
- [11] A. W. SNYDER and J. D. LOVE, *Optical Waveguide Theory*. London, U.K.: Chapman and Hall, 1983.
- [12] K. OKAMOTO, *Fundamentals of Optical Waveguides* (2nd edition). Burlington, MA: Academic, 2005.
- [13] J. J. BOWMAN, T. B. A. SENIOR, and P. L. E. USLENGHI, Eds., *Electromagnetic and Acoustic Scattering by Simple Shapes* (revised printing). New York: Hemisphere Publishing Corporation, 1987.
- [14] J. VAN BLADEL, *Electromagnetic Fields* (2nd edition). Hoboken, NJ: Wiley, 2007.
- [15] J. VAN BLADEL, *Singular Electromagnetic Fields and Sources*. New York: IEEE Press, 1996.

PROBLEMS

- 6.1.** Analyze the TE and TM modes in a half-circular waveguide shown in Figure 6.27 and determine the propagation constants and modal fields for all possible modes.
- 6.2.** Analyze the TE and TM modes in a circular waveguide with a conducting strip placed at $\phi = 0$, as shown in Figure 6.28. Examine all the field components at $\rho = 0$ and discuss your discoveries.
- 6.3.** Consider a radial waveguide formed by four conducting surfaces placed at $z = 0$, $z = h$, $\phi = 0$, and $\phi = \phi_0$, respectively. Analyze the TE and TM (with respect to z) modes that propagate along the radial direction. Find the wave impedances for inward- and outward-traveling modes and discuss their differences from the modes in a uniform waveguide.
- 6.4.** By using the perturbational method, find the attenuation constant of the TEM mode in a coaxial waveguide due to its imperfect inner and outer conductors and imperfect dielectric filling.
- 6.5.** An infinitely long conducting cylinder of radius a is coated with a layer of dielectric whose outer radius is b (Fig. 6.29). Analyze the hybrid modes in this waveguide structure.

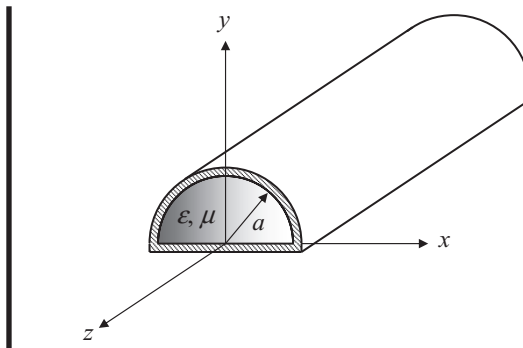


Figure 6.27 Uniformly filled half-circular waveguide.

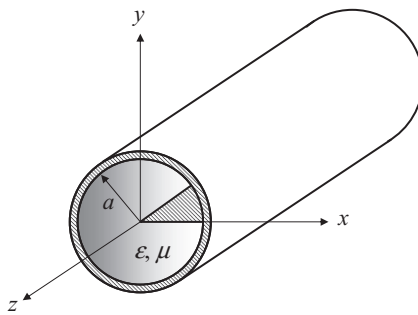


Figure 6.28 Uniformly filled circular waveguide with a conducting strip.

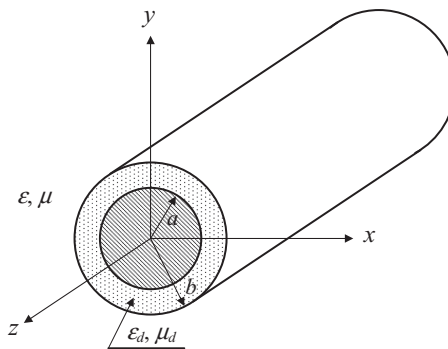


Figure 6.29 Infinitely long dielectric coated circular conducting cylinder.

6.6. Derive the wave transformations

$$\cos(\rho \sin \phi) = \sum_{n=0}^{\infty} \epsilon_n J_{2n}(\rho) \cos 2n\phi$$

$$\sin(\rho \sin \phi) = \sum_{n=0}^{\infty} \epsilon_n J_{2n+1}(\rho) \sin(2n+1)\phi$$

where $\epsilon_n = 1$ for $n = 0$ and $\epsilon_n = 2$ for $n \neq 0$.

- 6.7.** Consider the problem of scattering of a TM-polarized plane wave by a conducting cylinder of radius a coated with a layer of dielectric having a thickness of d , a permittivity of ϵ_d , and a permeability of μ_d . Find the scattered field and the scattering width. Repeat the solution for a TE-polarized incident plane wave.

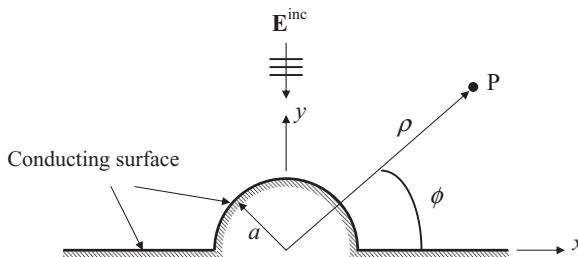


Figure 6.30 Plane wave scattering by a conducting half-cylinder placed on an infinitely large conducting ground.

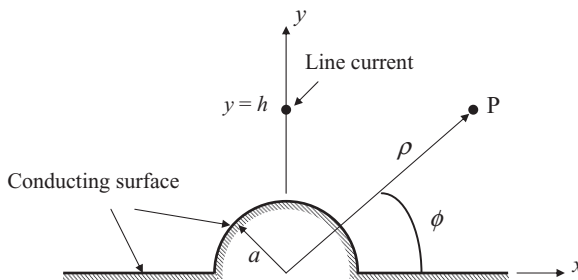


Figure 6.31 Line current radiating in the presence of a conducting half-cylinder placed on an infinitely large conducting ground.

- 6.8. A z -directed cylindrical surface current of radius a has a current distribution of $J_s(\phi) = A \sin \phi$, where A is a constant. Find the specific expressions for the field produced by this cylindrical surface current. Examine the magnetic field inside the cylinder at low frequency where $ka \ll 1$. Repeat the solution for $J_s(\phi) = Ae^{j\phi}$ and examine the polarization of the interior magnetic field.
- 6.9. Consider a cylindrical sheet of radius a having a surface impedance of Z_s . A time-harmonic line current I is placed along the z -axis. Find the fields for both $\rho < a$ and $\rho > a$. (Note that the boundary condition across the impedance surface is given by $H_\phi|_{\rho=a+0} - H_\phi|_{\rho=a-0} = E_z|_{\rho=a}/Z_s$.)
- 6.10. An infinitely long line magnetic current K at $\rho = \rho'$ is placed parallel to an infinitely long circular conducting cylinder. Find the electric and magnetic fields radiated by the magnetic current.
- 6.11. A z -directed infinitesimal magnetic dipole Kl is placed $\rho = \rho'$ and $z = 0$ in the presence of a conducting wedge. Find the electric and magnetic fields radiated by this dipole.
- 6.12. An infinitely long circular conducting cylinder has an aperture of length l and width w centered at $\phi = 0$ and $z = 0$ with $w \ll l$ and $l \ll \lambda$. Assume that the length of the aperture is along the z -direction and the aperture contains a field $\mathbf{E}^{ap} = \hat{z}E_0$. Find the field radiated by the aperture outside the conducting cylinder.
- 6.13. A time-harmonic plane wave, whose electric field is given by $\mathbf{E}^{inc} = \hat{z}E_0 e^{jky}$ with E_0 being a constant, is incident on a conducting half-cylinder placed on an infinitely large conducting ground (Fig. 6.30). Find the field scattered by the half-cylinder.
- 6.14. Repeat Problem 6.13 when the incident plane wave is given by $\mathbf{H}^{inc} = \hat{z}H_0 e^{jky}$ where H_0 is a constant.
- 6.15. A time-harmonic electric line current I is placed horizontally above a conducting half-cylinder on an infinite ground plane (Fig. 6.31). Find the field radiated by this current. ■

FIELDS AND WAVES IN SPHERICAL COORDINATES

In this chapter we discuss electromagnetic analysis in a spherical coordinate system. We first discuss the solution of the Helmholtz equation by the method of separation of variables and derive spherical wave functions. We then employ spherical wave functions to analyze a spherical cavity and a biconical antenna. This is followed by a wave transformation that expands a plane wave in terms of spherical wave functions. The derived wave transformation is then used for solving various scattering problems involving a conducting or a dielectric sphere. Finally, we consider the problem of radiation of a point charge to derive the addition theorem for spherical wave functions and then the radiation of a spherical surface current in the presence of a sphere or a cone to illustrate the radiation analysis in spherical coordinates and the field singularity at a sharp conducting tip.

7.1 SOLUTION OF WAVE EQUATION

In spherical coordinates, the Helmholtz equation $\nabla^2\psi + k^2\psi = 0$ can be written as

$$\frac{1}{r^2} \frac{\partial}{\partial r} \left(r^2 \frac{\partial \psi}{\partial r} \right) + \frac{1}{r^2 \sin \theta} \frac{\partial}{\partial \theta} \left(\sin \theta \frac{\partial \psi}{\partial \theta} \right) + \frac{1}{r^2 \sin^2 \theta} \frac{\partial^2 \psi}{\partial \phi^2} + k^2 \psi = 0. \quad (7.1.1)$$

The particular solutions to this equation are called *spherical wave functions* and can be obtained using the method of separation of variables.

7.1.1 Solution by Separation of Variables

We first assume that the solution to Equation 7.1.1 can be written in the following product form

$$\psi(r, \theta, \phi) = R(r)\Theta(\theta)\Phi(\phi). \quad (7.1.2)$$

By substituting this into Equation 7.1.1, then dividing the entire equation by $R(r)\Theta(\theta)\Phi(\phi)$, and multiplying it by $r^2 \sin^2 \theta$, we obtain

$$\frac{\sin^2 \theta}{R} \frac{d}{dr} \left(r^2 \frac{dR}{dr} \right) + \frac{\sin \theta}{\Theta} \frac{d}{d\theta} \left(\sin \theta \frac{d\Theta}{d\theta} \right) + \frac{1}{\Phi} \frac{d^2 \Phi}{d\phi^2} + k^2 r^2 \sin^2 \theta = 0. \quad (7.1.3)$$

Since only the third term contains ϕ and all other terms are independent of ϕ , the third term must be a constant, which yields

$$\frac{d^2\Phi}{d\phi^2} + m^2\Phi = 0 \quad (7.1.4)$$

where m^2 denotes an arbitrary constant that can only be determined in specific problems. Equation 7.1.4 has a well-known solution given by Equation 6.1.11. With this separation, Equation 7.1.3 is reduced to

$$\frac{1}{R} \frac{d}{dr} \left(r^2 \frac{dR}{dr} \right) + \frac{1}{\Theta \sin \theta} \frac{d}{d\theta} \left(\sin \theta \frac{d\Theta}{d\theta} \right) + k^2 r^2 - \frac{m^2}{\sin^2 \theta} = 0 \quad (7.1.5)$$

after a division by $\sin^2 \theta$. Since the first and the third terms depend only on r and the other two terms depend only on θ , Equation 7.1.5 can be separated into two equations

$$\frac{1}{R} \frac{d}{dr} \left(r^2 \frac{dR}{dr} \right) + k^2 r^2 = n(n+1) \quad (7.1.6)$$

$$\frac{1}{\Theta \sin \theta} \frac{d}{d\theta} \left(\sin \theta \frac{d\Theta}{d\theta} \right) - \frac{m^2}{\sin^2 \theta} = -n(n+1) \quad (7.1.7)$$

which can also be written as

$$\frac{d}{dr} \left(r^2 \frac{dR}{dr} \right) + [k^2 r^2 - n(n+1)] R = 0 \quad (7.1.8)$$

$$\frac{1}{\sin \theta} \frac{d}{d\theta} \left(\sin \theta \frac{d\Theta}{d\theta} \right) + \left[n(n+1) - \frac{m^2}{\sin^2 \theta} \right] \Theta = 0 \quad (7.1.9)$$

where $n(n+1)$ denotes another arbitrary constant that can only be determined in specific problems.

Equation 7.1.8 is known as the *spherical Bessel equation*, whose two linearly independent solutions are denoted as $j_n(kr)$ and $y_n(kr)$, which are known as the *n*th-order *spherical Bessel functions* of the first and second kind, respectively. A general solution is a linear combination of these two solutions,

$$R(r) = a_n j_n(kr) + b_n y_n(kr) \quad (7.1.10)$$

where a_n and b_n are arbitrary constants. Although both $j_n(kr)$ and $y_n(kr)$ have complicated expressions and possess many special properties [1], it is sufficient for our purpose to remember the following properties:

$$j_n(kr) \rightarrow \text{finite} \quad \text{when } kr \rightarrow 0 \quad (7.1.11)$$

$$y_n(kr) \rightarrow \infty \quad \text{when } kr \rightarrow 0. \quad (7.1.12)$$

Other special properties will be discussed later when necessary. Figure 7.1 plots the first few spherical Bessel functions of an integer order to show their distinct behavior [2].

Equation 7.1.9 is known as *Legendre's equation*, whose two linearly independent solutions are denoted as $P_n^m(\cos \theta)$ and $Q_n^m(\cos \theta)$, which are known as the *associated Legendre functions* of the first and second kind, respectively, of degree n and order m . A general solution is a linear combination of these two solutions,

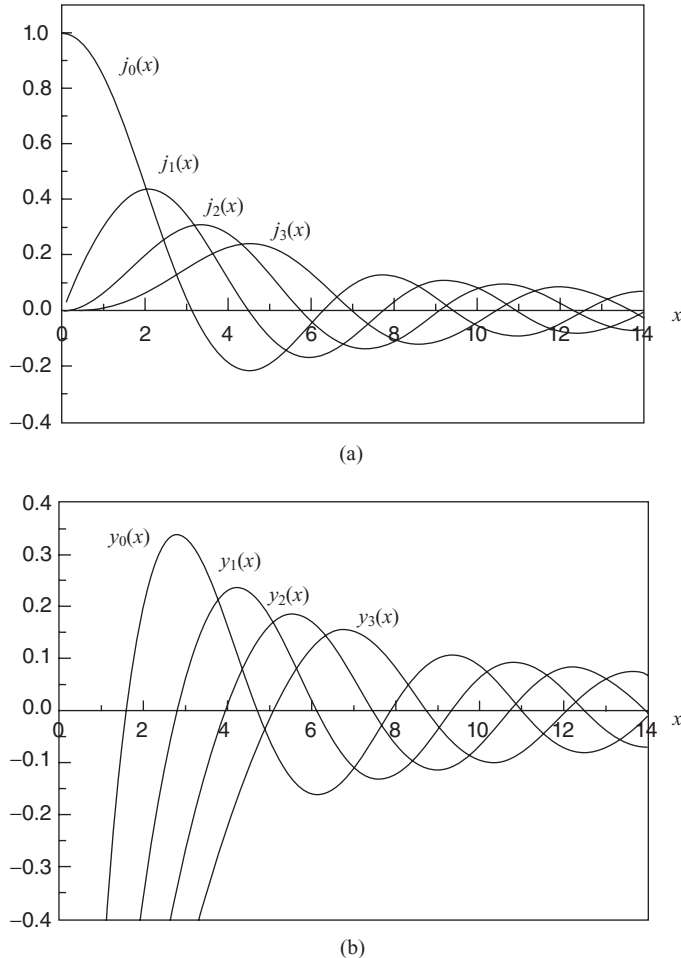


Figure 7.1 Spherical Bessel functions of an integer order. (a) Spherical Bessel functions of the first kind $j_n(x)$. (b) Spherical Bessel functions of the second kind $y_n(x)$.

$$\Theta(\theta) = c_{mn} P_n^m(\cos \theta) + d_{mn} Q_n^m(\cos \theta) \quad (7.1.13)$$

where c_{mn} and d_{mn} are arbitrary constants. Although both $P_n^m(\cos \theta)$ and $Q_n^m(\cos \theta)$ have complicated expressions and possess many special properties [1], it is sufficient for our purpose to remember the following properties:

$$P_n^m(\cos \theta) \Big|_{\theta=0,\pi} \rightarrow \text{finite} \quad (7.1.14)$$

$$Q_n^m(\cos \theta) \Big|_{\theta=0,\pi} \rightarrow \infty. \quad (7.1.15)$$

Again, other special properties will be discussed later only when necessary.

Based on the individual solutions discussed above, a particular solution for Equation 7.1.1 is given by

$$\begin{aligned}\psi_{mn}(r, \theta, \phi) = & [a_n j_n(kr) + b_n y_n(kr)] [c_{mn} P_n^m(\cos \theta) + d_{mn} Q_n^m(\cos \theta)] \\ & \times [e_m \cos m\phi + f_m \sin m\phi].\end{aligned}\quad (7.1.16)$$

Since this solution is valid for any m and n , the general solution to Equation 7.1.1 is a linear combination of all possible solutions, which can be expressed as a summation over all possible m and n :

$$\begin{aligned}\psi(r, \theta, \phi) = & \sum_{m,n} [a_n j_n(kr) + b_n y_n(kr)] [c_{mn} P_n^m(\cos \theta) + d_{mn} Q_n^m(\cos \theta)] \\ & \times [e_m \cos m\phi + f_m \sin m\phi].\end{aligned}\quad (7.1.17)$$

7.1.2 Spherical Wave Functions

Any combination in the particular solution given by Equation 7.1.16 is called a spherical wave function [3]. This function can be denoted as ψ_{mn} . Obviously, there are an infinite number of spherical wave functions, and these functions form a complete set such that any solution of the Helmholtz equation can be represented by a linear superposition of these functions as expressed in Equation 7.1.17. However, the form of a spherical wave function is not unique. As with cylindrical wave functions, the solution in the ϕ -direction can be expressed as the linear combination of $e^{-im\phi}$ and $e^{im\phi}$, in addition to $\sin m\phi$ and $\cos m\phi$.

In the θ -direction, if $n = v$ is not an integer, in addition to $P_v^m(\cos \theta)$ and $Q_v^m(\cos \theta)$, $P_v^m(\cos \theta)$ and $P_v^m(-\cos \theta)$ are also linearly independent and their linear combination can be used in a spherical wave function. An important property regarding $P_v^m(\cos \theta)$ is that [1]

$$P_v^m(\cos \theta) \Big|_{\theta=\pi} \rightarrow \infty, \quad P_v^m(-\cos \theta) \Big|_{\theta=0} \rightarrow \infty \quad (7.1.18)$$

for $v \neq$ integer. When n is an integer, $P_n^m(-\cos \theta)$ is no longer linearly independent of $P_n^m(\cos \theta)$, and we need to use $Q_n^m(\cos \theta)$ as the other linearly independent solution. For an integer n , $P_n^m(\cos \theta)$ is also called the *associated Legendre polynomial*, which can be expressed as

$$P_n^m(x) = (-1)^m (1-x^2)^{m/2} \frac{d^m}{dx^m} P_n(x) \quad (7.1.19)$$

where $P_n(x)$ is called the *Legendre polynomial* given by

$$P_n(x) = \frac{1}{2^n n!} \frac{d^n}{dx^n} (x^2 - 1)^n \quad (7.1.20)$$

which is a polynomial of order n . Obviously, $P_n^m(x) = 0$ when $m > n$. Figure 7.2 plots the first several Legendre polynomials as a function of x and θ [2].

In the radial direction, in addition to $j_n(kr)$ and $y_n(kr)$, the two other commonly used linearly independent solutions of Equation 7.1.8 are the *spherical Hankel functions* of the first and second kind, denoted as $h_n^{(1)}(kr)$ and $h_n^{(2)}(kr)$ and defined as

$$h_n^{(1)}(kr) = j_n(kr) + jy_n(kr) \quad (7.1.21)$$

$$h_n^{(2)}(kr) = j_n(kr) - jy_n(kr). \quad (7.1.22)$$

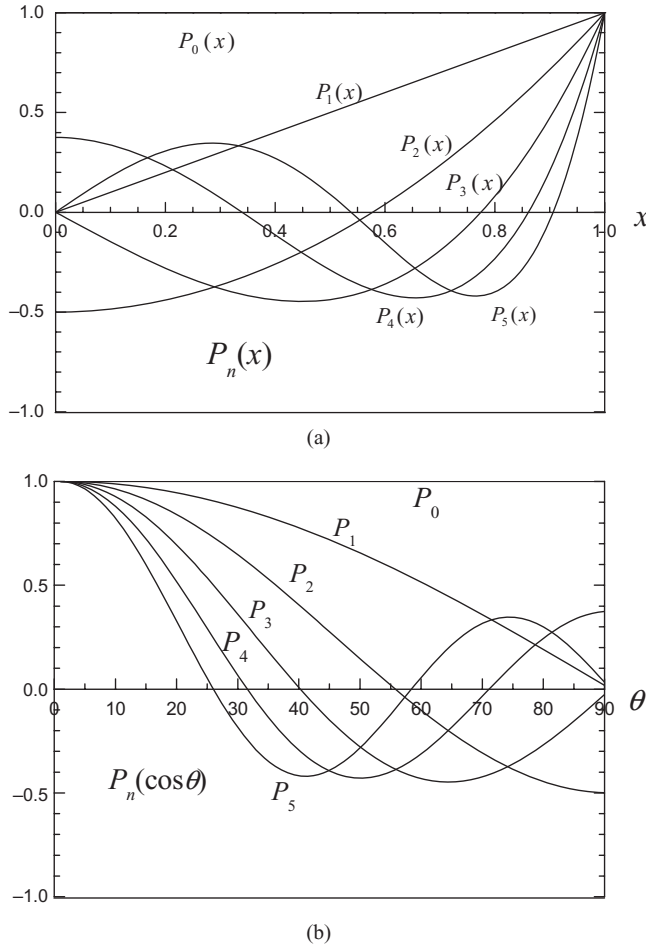


Figure 7.2 The first few Legendre polynomials $P_n(x)$ and $P_n(\cos \theta)$. (a) $P_n(x)$ as a function of x . (b) $P_n(\cos \theta)$ as a function of θ .

By substituting the large-argument expressions of $j_n(kr)$ and $y_n(kr)$ [1]

$$j_n(kr) \approx \frac{1}{kr} \cos\left(kr - \frac{n\pi}{2} - \frac{\pi}{2}\right) \quad \text{when } kr \gg 1 \quad (7.1.23)$$

$$y_n(kr) \approx \frac{1}{kr} \sin\left(kr - \frac{n\pi}{2} - \frac{\pi}{2}\right) \quad \text{when } kr \gg 1 \quad (7.1.24)$$

into the definitions above, we find the asymptotic forms of $h_n^{(1)}(kr)$ and $h_n^{(2)}(kr)$ as

$$h_n^{(1)}(kr) \approx \frac{1}{kr} e^{j(kr - n\pi/2 - \pi/2)} \quad \text{when } kr \gg 1 \quad (7.1.25)$$

$$h_n^{(2)}(kr) \approx \frac{1}{kr} e^{-j(kr - n\pi/2 - \pi/2)} \quad \text{when } kr \gg 1 \quad (7.1.26)$$

which indicate clearly that $h_n^{(1)}(kr)$ represents a spherical wave propagating along the negative r -direction, whereas $h_n^{(2)}(kr)$ represents a spherical wave propagating along the positive r -direction. Therefore, if a problem is unbounded in the r -direction, $h_n^{(1)}(kr)$ and $h_n^{(2)}(kr)$ would be better choices to expand the general solution. However, if a problem is finite in the r -direction, $j_n(kr)$ and $y_n(kr)$ might be used more conveniently.

For a specific problem, its spherical wave functions ψ_{mn} should contain at most one arbitrary coefficient since Equation 7.1.1 is a homogeneous equation. In other words, both m and n should be determined, and, in addition, the ratio of the two combination constants in each of $R(r)$, $\Phi(\phi)$, and $\Theta(\theta)$ should also be determined. The determination of these constants can be accomplished by application of boundary conditions in a specific problem. In general, there are two boundary conditions in each direction: one at each end. If there are no specific boundary conditions given, we then need to determine the constants based on the characteristics of the solution. For example, if ϕ is unbounded and the solution is single-valued, then $\Phi(\phi)$ should satisfy the periodic condition $\Phi(\phi + 2\pi) = \Phi(\phi)$, which in turn requires m to be integers. In that case, both $\sin m\phi$ and $\cos m\phi$ are correct solutions—they represent two identical solutions except for a rotation of $\pi/2$. If the solution domain includes both the positive and negative z -axes (i.e., $0 \leq \theta \leq \pi$) and the solution is finite there, we have to set $d_{mn} = 0$ in Equation 7.1.16 to exclude $Q_n^m(\cos \theta)$. On the other hand, if the solution domain includes the positive z -axis but excludes the negative z -axis (i.e., $0 \leq \theta < \pi$), we can use $P_v^m(\cos \theta)$ as the solution in the θ -direction. If the solution domain excludes the positive z -axis but includes the negative z -axis (i.e., $0 < \theta \leq \pi$), we can use $P_v^m(-\cos \theta)$ as the solution in the θ -direction. If the solution domain excludes both the positive and negative z -axes (i.e., $0 < \theta < \pi$), the solution in the θ -direction is then formed by a linear combination of $P_v^m(\cos \theta)$ and $P_v^m(-\cos \theta)$ or a linear combination of $P_v^m(\cos \theta)$ and $Q_v^m(\cos \theta)$. Finally, if the solution domain is unbounded in the r -direction and the solution represents a wave propagating in the positive r -direction, we should set $b_n = -ja_n$ in Equation 7.1.16, or equivalently, choose $h_n^{(2)}(kr)$ as the function in the r -direction.

7.1.3 TE_r and TM_r Modes

To study fields and waves in spherical coordinates, it is often convenient and sometimes necessary to express fields and waves as linear superpositions of TE_r and TM_r modes [4,5]. The TE_r modes have the electric field transverse to the radial direction, whereas the TM_r modes have the magnetic field transverse to the radial direction. The field expressions of the TE_r modes can be obtained by letting $\mathbf{A} = 0$ and $\mathbf{F} = \hat{r}F_r$, then calculating $\mathbf{E} = -\nabla \times \mathbf{F}/\epsilon$ and $\mathbf{H} = -\nabla \times \mathbf{E}/j\omega\mu$, which yields

$$E_r = 0, \quad H_r = \frac{1}{j\omega\mu\epsilon} \left(\frac{\partial^2}{\partial r^2} + k^2 \right) F_r \quad (7.1.27)$$

$$E_\theta = -\frac{1}{\epsilon} \frac{1}{r \sin \theta} \frac{\partial F_r}{\partial \phi}, \quad H_\theta = \frac{1}{j\omega\mu\epsilon} \frac{1}{r} \frac{\partial^2 F_r}{\partial r \partial \theta} \quad (7.1.28)$$

$$E_\phi = \frac{1}{\epsilon} \frac{1}{r} \frac{\partial F_r}{\partial \theta}, \quad H_\phi = \frac{1}{j\omega\mu\epsilon} \frac{1}{r \sin \theta} \frac{\partial^2 F_r}{\partial r \partial \phi}. \quad (7.1.29)$$

Similarly, the field expressions of the TM_r modes can be derived by letting $\mathbf{A} = \hat{r}A_r$ and $\mathbf{F} = 0$, then calculating $\mathbf{H} = \nabla \times \mathbf{A}/\mu$ and $\mathbf{E} = \nabla \times \mathbf{H}/j\omega\epsilon$:

$$E_r = \frac{1}{j\omega\mu\epsilon} \left(\frac{\partial^2}{\partial r^2} + k^2 \right) A_r, \quad H_r = 0 \quad (7.1.30)$$

$$E_\theta = \frac{1}{j\omega\mu\epsilon} \frac{1}{r} \frac{\partial^2 A_r}{\partial r \partial \theta}, \quad H_\theta = \frac{1}{\mu} \frac{1}{r \sin \theta} \frac{\partial A_r}{\partial \phi} \quad (7.1.31)$$

$$E_\phi = \frac{1}{j\omega\mu\epsilon} \frac{1}{r \sin \theta} \frac{\partial^2 A_r}{\partial r \partial \phi}, \quad H_\phi = -\frac{1}{\mu} \frac{1}{r} \frac{\partial A_r}{\partial \theta}. \quad (7.1.32)$$

Note that we did not use Equations 2.1.37 and 2.1.38 to derive these field expressions because Equations 2.1.37 and 2.1.38 assumed the Lorenz gauge condition for \mathbf{A} and \mathbf{F} . As we will see next, the Lorenz gauge condition is not a suitable gauge condition for $\mathbf{A} = \hat{r}A_r$ and $\mathbf{F} = \hat{r}F_r$ and we have to choose a different gauge condition.

To use Equations 7.1.27–7.1.32 to find the specific field expressions, we have to obtain the expressions of A_r and F_r by solving their governing partial differential equations. Unfortunately, since \hat{r} is not a constant vector, when $\mathbf{A} = \hat{r}A_r$ and $\mathbf{F} = \hat{r}F_r$ are substituted into the vector Helmholtz equations $\nabla^2 \mathbf{A} + k^2 \mathbf{A} = 0$ and $\nabla^2 \mathbf{F} + k^2 \mathbf{F} = 0$, respectively, A_r and F_r do not satisfy the scalar Helmholtz equation. Therefore, although the equations for the vector potentials \mathbf{A} and \mathbf{F} have a simple form because of the use of the Lorenz gauge condition, the equations for their radial components do not have a simple form. Recall that the Lorenz gauge condition is not the only gauge condition that we have to use, and we are actually free to choose whatever gauge condition to simplify the final equation for A_r and F_r . To see this, let us consider the case of $\mathbf{A} = \hat{r}A_r$. To find a simpler equation for A_r , we first substitute $\mathbf{A} = \hat{r}A_r$ into Equation 2.1.28 before applying any gauge condition. In a source-free region, this equation can be written as

$$\nabla(\nabla \cdot \mathbf{A}) - \nabla^2 \mathbf{A} = -j\omega\mu\epsilon\nabla\varphi + k^2 \mathbf{A} \quad (7.1.33)$$

which becomes three scalar equations given by

$$\frac{1}{r \sin \theta} \left[-\frac{\partial}{\partial \theta} \left(\frac{\sin \theta}{r} \frac{\partial A_r}{\partial \theta} \right) - \frac{\partial}{\partial \phi} \left(\frac{1}{r \sin \theta} \frac{\partial A_r}{\partial \phi} \right) \right] - k^2 A_r = -j\omega\epsilon\mu \frac{\partial \varphi}{\partial r} \quad (7.1.34)$$

$$\frac{1}{r} \frac{\partial^2 A_r}{\partial r \partial \theta} = -j \frac{\omega\mu\epsilon}{r} \frac{\partial \varphi}{\partial \theta} \quad (7.1.35)$$

$$\frac{1}{r \sin \theta} \frac{\partial^2 A_r}{\partial r \partial \phi} = -j \frac{\omega\mu\epsilon}{r \sin \theta} \frac{\partial \varphi}{\partial \phi}. \quad (7.1.36)$$

A careful examination of these three equations reveals that the last two equations can be satisfied by simply letting

$$\frac{\partial A_r}{\partial r} = -j\omega\mu\epsilon\varphi. \quad (7.1.37)$$

With this, the remaining first equation becomes

$$\frac{\partial^2 A_r}{\partial r^2} + \frac{1}{r^2 \sin \theta} \frac{\partial}{\partial \theta} \left(\sin \theta \frac{\partial A_r}{\partial \theta} \right) + \frac{1}{r^2 \sin^2 \theta} \frac{\partial^2 A_r}{\partial \phi^2} + k^2 A_r = 0 \quad (7.1.38)$$

which can further be written as

$$(\nabla^2 + k^2) \frac{A_r}{r} = 0. \quad (7.1.39)$$

Therefore, with the gauge condition given by Equation 7.1.37, A_r/r satisfies the scalar Helmholtz equation. Hence, its solution is given by

$$\frac{A_r(r, \theta, \phi)}{r} = [a_n j_n(kr) + b_n y_n(kr)] [c_{mn} P_n^m(\cos \theta) + d_{mn} Q_n^m(\cos \theta)] [e_m \cos m\phi + f_m \sin m\phi] \quad (7.1.40)$$

or

$$A_r(r, \theta, \phi) = [a_n \hat{J}_n(kr) + b_n \hat{Y}_n(kr)] [c_{mn} P_n^m(\cos \theta) + d_{mn} Q_n^m(\cos \theta)] [e_m \cos m\phi + f_m \sin m\phi] \quad (7.1.41)$$

where $\hat{J}_n(kr) = kr j_n(kr)$ and $\hat{Y}_n(kr) = kr y_n(kr)$ are called the *Riccati–Bessel functions* of the first and second kind, respectively, which are plotted in Figure 7.3. When their argument vanishes, they become

$$\hat{J}_n(kr) \rightarrow 0 \quad \text{when } kr \rightarrow 0 \quad (7.1.42)$$

$$\hat{Y}_n(kr) \rightarrow \begin{cases} -1 & n=0 \\ \infty & n \neq 0 \end{cases} \quad \text{when } kr \rightarrow 0. \quad (7.1.43)$$

The same discussion applies to the case of $\mathbf{F} = \hat{r}F_r$; consequently, the solution of F_r has the same form as Equation 7.1.41.

7.2 SPHERICAL CAVITY

Consider a spherical cavity of radius a made of a perfect electric conductor and filled with a homogeneous, lossless material (Fig. 7.4). To find the TE_r and TM_r modes, we first consider the solution to A_r and F_r . First of all, since the field region is unbounded in the ϕ -direction, m must be integers and both $\cos m\phi$ and $\sin m\phi$ should remain in A_r and F_r . Second, since the field region contains the z -axis, where $\theta = 0$ or π , the solution to A_r and F_r should not include $Q_n^m(\cos \theta)$. Instead, it should contain only $P_n^m(\cos \theta)$ and n should be integers so that $P_n^m(\cos \theta)$ is finite at $\theta = 0$ and π . Furthermore, for a specific n , the value of m is restricted to $m = 0, 1, \dots, n$ since $P_n^m(\cos \theta) = 0$ for $m > n$. Third, since the field region includes the origin where the field should be finite, the solution to A_r and F_r should not include $\hat{Y}_n(kr)$ (even though $\hat{Y}_0(kr)$ is finite at $r = 0$, its inclusion would yield a singular field at $r = 0$, which is evident from Equations 7.1.27 to 7.1.32). Therefore, the solution to A_r and F_r can be written as

$$A_r(r, \theta, \phi), F_r(r, \theta, \phi) = C \hat{J}_n(kr) P_n^m(\cos \theta) \begin{Bmatrix} \cos m\phi \\ \sin m\phi \end{Bmatrix} \quad n = 0, 1, 2, \dots; m = 0, 1, \dots, n \quad (7.2.1)$$

where C denotes an arbitrary constant.

For the TE_r modes, the non-zero electric field components are given by

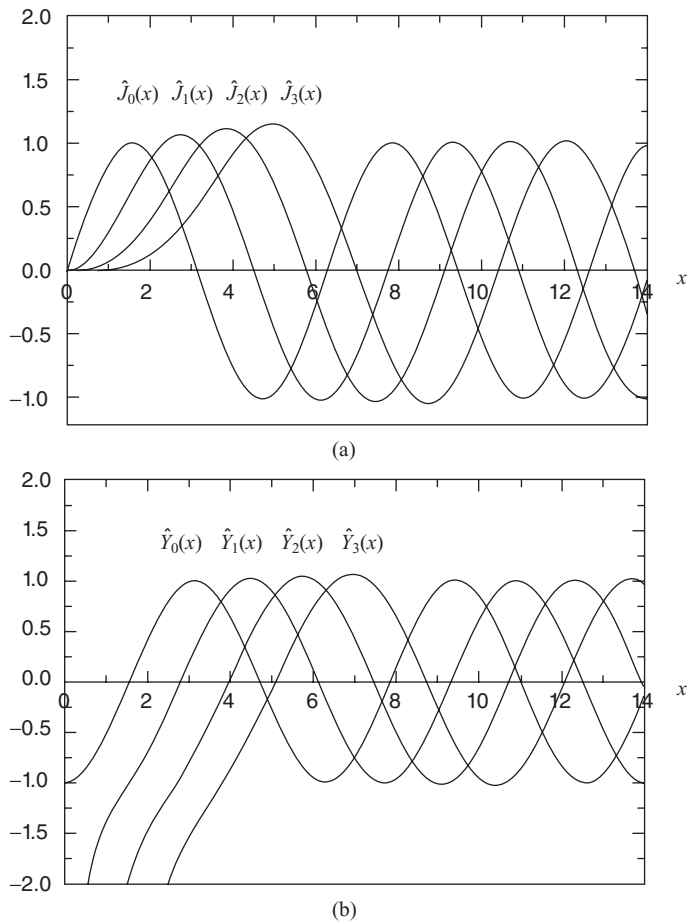


Figure 7.3 Riccati–Bessel functions of an integer order. (a) Riccati–Bessel functions of the first kind $\hat{J}_n(x)$. (b) Riccati–Bessel functions of the second kind $\hat{Y}_n(x)$.

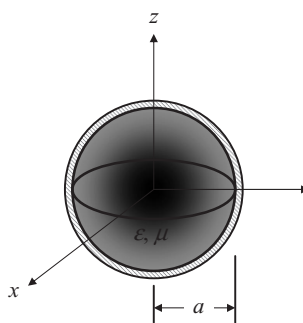


Figure 7.4 Uniformly filled spherical cavity.

$$E_\theta = -\frac{1}{\epsilon r \sin \theta} \frac{\partial F_r}{\partial \phi} = \pm C \frac{m}{\epsilon r \sin \theta} \hat{J}_n(kr) P_n^m(\cos \theta) \begin{cases} \sin m\phi \\ \cos m\phi \end{cases} \quad (7.2.2)$$

$$E_\phi = \frac{1}{\epsilon r} \frac{\partial F_r}{\partial \theta} = C \frac{1}{\epsilon r} \hat{J}_n(kr) \frac{\partial P_n^m(\cos \theta)}{\partial \theta} \begin{cases} \cos m\phi \\ \sin m\phi \end{cases}. \quad (7.2.3)$$

Applying the boundary condition $E_\theta|_{r=a} = E_\phi|_{r=a} = 0$, we obtain the characteristic equation for determining the resonant wavenumbers as

$$\hat{J}_n(ka) = 0. \quad (7.2.4)$$

If we denote the roots (characteristic values) of this equation as ζ_{np} such that $\hat{J}_n(\zeta_{np}) = 0$, the resonant wavenumbers and hence the resonant frequencies are given by

$$k_{r mnp}^{\text{TE}} = \frac{\zeta_{np}}{a}, \quad f_{r mnp}^{\text{TE}} = \frac{\zeta_{np}}{2\pi a \sqrt{\mu\epsilon}} \quad n = 1, 2, \dots; m = 0, 1, \dots, n; p = 1, 2, \dots. \quad (7.2.5)$$

The cases with $n = 0$ are excluded because they represent trivial solutions, since for such cases $m = 0$ because $P_n^m(\cos \theta) = 0$ for $m > n$ and, furthermore, $\partial P_0^0(\cos \theta)/\partial \theta = 0$ as $P_0^0(\cos \theta) = 1$. The first several values of ζ_{np} are given in Table 7.1.

For the TM_r modes, the electric field transverse components are given by

$$E_\theta = \frac{1}{j\omega\mu\epsilon r} \frac{\partial^2 A_r}{\partial r \partial \theta} = C \frac{k}{j\omega\mu\epsilon r} \hat{J}'_n(kr) \frac{\partial P_n^m(\cos \theta)}{\partial \theta} \begin{cases} \cos m\phi \\ \sin m\phi \end{cases} \quad (7.2.6)$$

$$E_\phi = \frac{1}{j\omega\mu\epsilon r \sin \theta} \frac{\partial^2 A_r}{\partial r \partial \phi} = \mp C \frac{k}{j\omega\mu\epsilon r \sin \theta} \hat{J}'_n(kr) P_n^m(\cos \theta) \begin{cases} \sin m\phi \\ \cos m\phi \end{cases}. \quad (7.2.7)$$

Applying the boundary condition $E_\theta|_{r=a} = E_\phi|_{r=a} = 0$, we obtain the characteristic equation for determining the resonant wavenumbers as

$$\hat{J}'_n(ka) = 0. \quad (7.2.8)$$

If we denote the roots (characteristic values) of this equation as ζ'_{np} such that $\hat{J}'_n(\zeta'_{np}) = 0$, the resonant wavenumbers and hence the resonant frequencies are given by

$$k_{r mnp}^{\text{TM}} = \frac{\zeta'_{np}}{a}, \quad f_{r mnp}^{\text{TM}} = \frac{\zeta'_{np}}{2\pi a \sqrt{\mu\epsilon}} \quad n = 1, 2, \dots; m = 0, 1, \dots, n; p = 1, 2, \dots. \quad (7.2.9)$$

TABLE 7.1 The First Few Roots of $\hat{J}_n(z) = 0$

$n \backslash p$	1	2	3	4
1	4.493409	7.725252	10.90412	14.06619
2	5.763459	9.095011	12.32294	15.51460
3	6.987932	10.41712	13.69802	16.92362
4	8.182561	11.70491	15.03966	18.30126

TABLE 7.2 The First Few Roots of $\hat{J}'_n(z) = 0$

$n \backslash p$	1	2	3	4
1	2.743707	6.116764	9.316616	12.48594
2	3.870239	7.443087	10.71301	13.92052
3	4.973420	8.721751	12.06359	15.31356
4	6.061949	9.967547	13.38012	16.67415

Again, the cases with $n = 0$ are excluded because they represent trivial solutions. The first several values of ζ'_{np} are given in Table 7.2.

A comparison of the data in Tables 7.1 and 7.2 indicates that the dominant mode in a spherical cavity is the $\text{TM}_{r,m11}$ mode, whose resonant wavenumber and frequency are

$$k_{r,m11}^{\text{TM}} = \frac{2.7437}{a}, \quad f_{r,m11}^{\text{TM}} = \frac{0.4367}{a\sqrt{\mu\epsilon}}. \quad (7.2.10)$$

When $m = 0$, its non-zero electric and magnetic field components are

$$E_r = \frac{2}{r^2} \cos \theta \hat{J}_1(\zeta'_{11} r/a) \quad (7.2.11)$$

$$E_\theta = -\frac{\zeta'_{11}}{ar} \sin \theta \hat{J}'_1(\zeta'_{11} r/a) \quad (7.2.12)$$

$$H_\phi = -\frac{j\omega\epsilon}{r} \sin \theta \hat{J}_1(\zeta'_{11} r/a) \quad (7.2.13)$$

where $\zeta'_{11} = 2.7437$, and we set $C = j\omega\mu\epsilon$ to simplify the field expressions. The first TE_r mode in a spherical cavity is the $\text{TE}_{r,m11}$ mode, whose resonant wavenumber and frequency are

$$k_{r,m11}^{\text{TE}} = \frac{4.4934}{a}, \quad f_{r,m11}^{\text{TE}} = \frac{0.7151}{a\sqrt{\mu\epsilon}}. \quad (7.2.14)$$

When $m = 0$, its non-zero electric and magnetic field components are

$$E_\phi = -\frac{j\omega\mu}{r} \sin \theta \hat{J}_1(\zeta_{11} r/a) \quad (7.2.15)$$

$$H_r = \frac{2}{r^2} \cos \theta \hat{J}_1(\zeta_{11} r/a) \quad (7.2.16)$$

$$H_\theta = -\frac{\zeta_{11}}{ar} \sin \theta \hat{J}'_1(\zeta_{11} r/a) \quad (7.2.17)$$

where $\zeta_{11} = 4.4934$, and again we set $C = j\omega\mu\epsilon$ to simplify the field expressions. Note that none of these field components is singular at $r = 0$ even though their expressions contain $1/r$ or $1/r^2$. These singular terms are canceled by the Riccati–Bessel functions.

7.3 BICONICAL ANTENNA

Having considered a spherical cavity, which is finite in the radial direction, we now consider a biconical antenna, where the field can propagate into infinity. Since the analysis of a finite biconical antenna is rather involved, we first consider an infinitely long model, where the cones extend to infinity [5].

7.3.1 Infinitely Long Model

Consider an electromagnetic system made of two semi-infinitely long perfect electrically conducting cones whose axes coincide with the z -axis, as illustrated in Figure 7.5a. The tips of the two cones join at $z = 0$. Both the upper and lower cones are assumed to have an internal half-angle of θ_0 . Therefore, the region that can support electromagnetic fields is $0 < r < \infty$, $-\infty < \phi < \infty$, and $\theta_0 \leq \theta \leq \pi - \theta_0$.

To find the TE_r and TM_r modes that can propagate in this system, we first consider the solution to A_r and F_r . First of all, since the field region is unbounded in the ϕ -direction, m must be integers and both $\cos m\phi$ and $\sin m\phi$ should remain in A_r and F_r . Second, since the field region does not contain the z -axis, the solution to A_r and F_r should include both $P_v^m(\cos \theta)$ and $Q_v^m(\cos \theta)$ or $P_v^m(\cos \theta)$ and $P_v^m(-\cos \theta)$, where v has to be determined by the boundary conditions (we use v , instead of n , to emphasize that the order here may not be an integer anymore). Third, since the field region extends to infinity in the radial direction, the solution to A_r and F_r should include the Riccati–Hankel functions $\hat{H}_v^{(2)}(kr)$, defined as $\hat{H}_v^{(2)}(kr) = kr h_v^{(2)}(kr)$, if we intend to investigate modes propagating in the r -direction. Therefore, the solution to A_r and F_r can be written as

$$A_r(r, \theta, \phi), F_r(r, \theta, \phi) = \hat{H}_v^{(2)}(kr) [C_1 P_v^m(\cos \theta) + C_2 P_v^m(-\cos \theta)] \begin{Bmatrix} \cos m\phi \\ \sin m\phi \end{Bmatrix} \quad m = 0, 1, 2, \dots \quad (7.3.1)$$

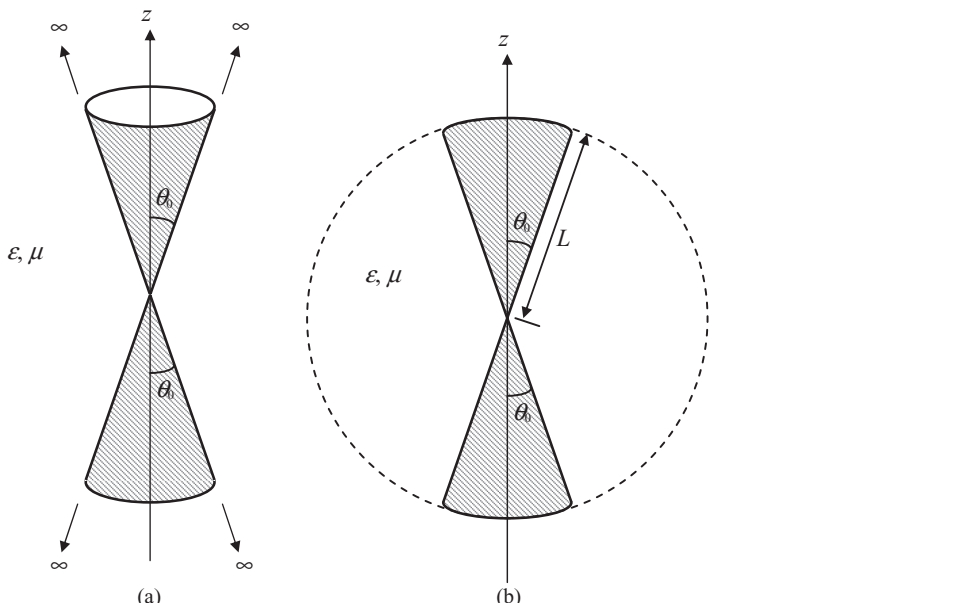


Figure 7.5 Biconical antenna. (a) Infinitely long model. (b) Finite model. The dashed line shows a fictitious spherical surface coinciding with the top and bottom surfaces of the biconical antenna.

where C_1 and C_2 denote arbitrary constants, whose ratio can be determined by the boundary conditions of the problem.

To determine the values for v , we need to apply the boundary conditions at the surfaces of the conducting cones, which require that $E_\phi|_{\theta=\theta_0} = E_\phi|_{\theta=\pi-\theta_0} = 0$. For the TE_r modes, E_ϕ is given by

$$E_\phi = \frac{1}{\epsilon r} \frac{\partial F_r}{\partial \theta} = \frac{1}{\epsilon r} \hat{H}_v^{(2)}(kr) \left[C_1 \frac{dP_v^m(\cos \theta)}{d\theta} + C_2 \frac{dP_v^m(-\cos \theta)}{d\theta} \right] \begin{Bmatrix} \cos m\phi \\ \sin m\phi \end{Bmatrix}. \quad (7.3.2)$$

Applying the boundary conditions described above, we obtain

$$C_1 \frac{dP_v^m(\cos \theta)}{d\theta} \Big|_{\theta=\theta_0} + C_2 \frac{dP_v^m(-\cos \theta)}{d\theta} \Big|_{\theta=\theta_0} = 0 \quad (7.3.3)$$

$$C_1 \frac{dP_v^m(\cos \theta)}{d\theta} \Big|_{\theta=\pi-\theta_0} + C_2 \frac{dP_v^m(-\cos \theta)}{d\theta} \Big|_{\theta=\pi-\theta_0} = 0. \quad (7.3.4)$$

To have a non-trivial solution for C_1 and C_2 , the determinant of the coefficient matrix must vanish, which yields the characteristic equation for determining the values of v as

$$\frac{dP_v^m(\cos \theta)}{d\theta} \Big|_{\theta=\theta_0} \frac{dP_v^m(-\cos \theta)}{d\theta} \Big|_{\theta=\pi-\theta_0} - \frac{dP_v^m(-\cos \theta)}{d\theta} \Big|_{\theta=\theta_0} \frac{dP_v^m(\cos \theta)}{d\theta} \Big|_{\theta=\pi-\theta_0} = 0. \quad (7.3.5)$$

Unlike the modes in a uniform waveguide whose cross-section is constant, all the TE_r modes here have no cutoff frequencies, and their propagation constants are k when $kr \gg 1$.

For the TM_r modes, E_ϕ is given by

$$E_\phi = \frac{1}{j\omega\mu\epsilon} \frac{1}{r \sin \theta} \frac{\partial^2 A_r}{\partial r \partial \phi} = \mp \frac{k}{j\omega\mu\epsilon} \frac{m}{r \sin \theta} \hat{H}_v^{(2)\prime}(kr) \left[C_1 P_v^m(\cos \theta) + C_2 P_v^m(-\cos \theta) \right] \begin{Bmatrix} \sin m\phi \\ \cos m\phi \end{Bmatrix}. \quad (7.3.6)$$

Applying the boundary conditions $E_\phi|_{\theta=\theta_0} = E_\phi|_{\theta=\pi-\theta_0} = 0$, we obtain

$$C_1 P_v^m(\cos \theta_0) + C_2 P_v^m(-\cos \theta_0) = 0 \quad (7.3.7)$$

$$C_1 P_v^m(-\cos \theta_0) + C_2 P_v^m(\cos \theta_0) = 0. \quad (7.3.8)$$

To have a non-trivial solution for C_1 and C_2 , the determinant of the coefficient matrix must vanish, which yields the characteristic equation for determining the values of v as

$$[P_v^m(\cos \theta_0)]^2 - [P_v^m(-\cos \theta_0)]^2 = 0. \quad (7.3.9)$$

Like the TE_r modes, the TM_r modes here do not have cutoff frequencies either, and their propagation constants are k when $kr \gg 1$.

A special case of particular interest is the TM_r mode with $v = 0$ and $m = 0$. The A_r for this case can be written as

$$\begin{aligned} A_r(r, \theta, \phi) &= \hat{H}_0^{(2)}(kr) [C_1 P_0^0(\cos \theta) + C_2 Q_0^0(\cos \theta)] \\ &= \hat{H}_0^{(2)}(kr) [C_1 P_0(\cos \theta) + C_2 Q_0(\cos \theta)]. \end{aligned} \quad (7.3.10)$$

Since $\hat{H}_0^{(2)}(kr) = je^{-jkr}$, $P_0(\cos \theta) = 1$, and $Q_0(\cos \theta) = \ln[\cot(\theta/2)]$, Equation 7.3.10 can also be written as

$$A_r(r, \theta, \phi) = \left[C_1 + C_2 \ln\left(\cot \frac{\theta}{2}\right) \right] je^{-jkr}. \quad (7.3.11)$$

The corresponding field components can be found as

$$E_\theta = \frac{1}{j\omega\mu\epsilon} \frac{1}{r} \frac{\partial^2 A_r}{\partial r \partial \theta} = jC_2 \frac{k}{\omega\mu\epsilon} \frac{1}{r \sin \theta} e^{-jkr} \quad (7.3.12)$$

$$H_\phi = -\frac{1}{\mu} \frac{1}{r} \frac{\partial A_r}{\partial \theta} = jC_2 \frac{1}{\mu r \sin \theta} e^{-jkr} \quad (7.3.13)$$

and all other field components are zero. This is actually a TEM mode since both E_r and H_r vanish. The wave impedance is

$$Z_w = \frac{E_\theta}{H_\phi} = \frac{k}{\omega\epsilon} = \sqrt{\frac{\mu}{\epsilon}} = \eta \quad (7.3.14)$$

as can be expected for a TEM wave.

The biconical structure can be considered as a transmission line that transmits waves from the origin to infinity. In that case, the quantity of interest is the characteristic impedance. The voltage along this transmission line can be calculated as

$$V(r) = \int_{\theta_0}^{\pi-\theta_0} \mathbf{E} \cdot d\mathbf{l} = \int_{\theta_0}^{\pi-\theta_0} E_\theta r d\theta = jC_2 \frac{2ke^{-jkr}}{\omega\mu\epsilon} \ln\left(\cot \frac{\theta_0}{2}\right) \quad (7.3.15)$$

and the current can be found as

$$I(r) = \oint_C \mathbf{H} \cdot d\mathbf{l} = \int_0^{2\pi} H_\phi r \sin \theta d\phi = jC_2 \frac{2\pi e^{-jkr}}{\mu}. \quad (7.3.16)$$

Hence, the characteristic impedance is

$$Z_c = \frac{V}{I} = \frac{\eta}{\pi} \ln\left(\cot \frac{\theta_0}{2}\right). \quad (7.3.17)$$

If the biconical structure is regarded as an antenna with the excitation at the origin, the quantity of interest is the input impedance, which can be calculated as the ratio between the voltage and current at the feed point. Based on Equations 7.3.15 and 7.3.16, this input impedance is given by

$$Z_{in} = \frac{V(0)}{I(0)} = \frac{\eta}{\pi} \ln\left(\cot \frac{\theta_0}{2}\right) \quad (7.3.18)$$

which is the same as the characteristic impedance.

7.3.2 Finite Biconical Antenna

Since its input impedance is independent of frequency, an infinitely long biconical antenna is a frequency-independent antenna. However, for practical applications, a biconical antenna must be truncated. The antenna so obtained would be a broadband antenna, the lower limit of whose bandwidth is determined by the overall length of the antenna and the upper limit is determined by the feeding structure at the center. Because of truncation, there will be reflection at the end of the antenna [6]. To include the effect of this reflection, in addition to the dominant mode in Equation 7.3.11 and its reflection, we have to consider the higher-order reflected field, which can be expressed as

$$A_r^{\text{ref}}(r, \theta, \phi) = \sum_v \hat{J}_v(kr)[a_v P_v(\cos \theta) + b_v P_v(-\cos \theta)] \quad 0 \leq r < L \quad (7.3.19)$$

where L denotes the half-length of the truncated biconical antenna, as illustrated in Figure 7.5b. Here $\hat{J}_v(kr)$ is used in Equation 7.3.19 because the reflected field should remain finite everywhere. The constants a_v and b_v are related by

$$a_v P_v(\cos \theta_0) + b_v P_v(-\cos \theta_0) = 0 \quad (7.3.20)$$

$$a_v P_v(-\cos \theta_0) + b_v P_v(\cos \theta_0) = 0 \quad (7.3.21)$$

because of the boundary conditions at $\theta = \theta_0$ and $\theta = \pi - \theta_0$. This yields the characteristic equation for v as

$$[P_v(\cos \theta_0)]^2 - [P_v(-\cos \theta_0)]^2 = 0 \quad (7.3.22)$$

which has two solutions as

$$P_v(\cos \theta_0) + P_v(-\cos \theta_0) = 0 \quad (7.3.23)$$

$$P_v(\cos \theta_0) - P_v(-\cos \theta_0) = 0. \quad (7.3.24)$$

For v determined by Equation 7.3.23, we have $a_v = b_v$ from either Equation 7.3.20 or Equation 7.3.21, and the resulting fields E_θ^{ref} and H_ϕ^{ref} are antisymmetric with respect to θ . Such fields cannot be excited by a symmetric incident field in Equations 7.3.12 and 7.3.13. For v determined by Equation 7.3.24, we have $a_v = -b_v$ from either Equation 7.3.20 or Equation 7.3.21, and the resulting fields E_θ^{ref} and H_ϕ^{ref} are symmetric with respect to θ . Denoting the solution of Equation 7.3.24 as v_i ($i = 1, 2, \dots$), Equation 7.3.19 can be written as

$$A_r^{\text{ref}}(r, \theta, \phi) = \sum_{i=1,2}^{\infty} a_{v_i} \hat{J}_{v_i}(kr) L_{v_i}(\cos \theta) \quad 0 \leq r < L \quad (7.3.25)$$

where $L_{v_i}(\cos \theta) = P_{v_i}(\cos \theta) - P_{v_i}(-\cos \theta)$.

Outside the spherical surface that encloses the biconical antenna, as illustrated by the dashed line in Figure 7.5b, we have the total radiated field that can be expressed as

$$A_r^{\text{ext}}(r, \theta, \phi) = \sum_{n=0}^{\infty} c_n \hat{H}_n^{(2)}(kr) P_n(\cos \theta) \quad r > L \quad (7.3.26)$$

where $P_n(\cos \theta)$ ($n = 0, 1, 2, \dots$) is used here because the field region includes the z -axis. Since the field is symmetric with respect to θ because of the symmetric excitation, $c_n = 0$ for even n . Hence, Equation 7.3.26 is reduced to

$$A_r^{\text{ext}}(r, \theta, \phi) = \sum_{n=1,3}^{\infty} c_n \hat{H}_n^{(2)}(kr) P_n(\cos \theta) \quad r > L. \quad (7.3.27)$$

Based on the discussions above, the electric and magnetic fields inside the spherical surface ($0 \leq r < L$) are the superposition of the dominant radiation and reflection modes and the higher-order reflected field, with the transverse components given by

$$E_{\theta}^{\text{int}} = \frac{jk}{\omega \mu \epsilon} \frac{1}{r \sin \theta} \left[(e^{-jkr} + Re^{jkr}) + \sin^2 \theta \sum_{i=1,2}^{\infty} a_{v_i} \hat{J}'_{v_i}(kr) L'_{v_i}(\cos \theta) \right] \quad (7.3.28)$$

$$H_{\phi}^{\text{int}} = \frac{1}{\mu r \sin \theta} \left[j(e^{-jkr} - Re^{jkr}) + \sin^2 \theta \sum_{i=1,2}^{\infty} a_{v_i} \hat{J}_{v_i}(kr) L'_{v_i}(\cos \theta) \right] \quad (7.3.29)$$

where we have set $C_2 = 1$ and R denotes the reflection coefficient of the dominant mode. The transverse field components outside the spherical surface ($r > L$) are

$$E_{\theta}^{\text{ext}} = \frac{jk}{\omega \mu \epsilon} \frac{\sin \theta}{r} \sum_{n=1,3}^{\infty} c_n \hat{H}_n^{(2)\prime}(kr) P'_n(\cos \theta) \quad (7.3.30)$$

$$H_{\phi}^{\text{ext}} = \frac{1}{\mu} \frac{\sin \theta}{r} \sum_{n=1,3}^{\infty} c_n \hat{H}_n^{(2)}(kr) P'_n(\cos \theta). \quad (7.3.31)$$

To determine R , a_{v_i} , and c_n , we apply the field continuity conditions at the spherical surface ($r = L$) to find

$$\begin{aligned} & \frac{1}{\sin \theta} (e^{-jkl} + Re^{jkl}) + \sin \theta \sum_{i=1,2}^{\infty} a_{v_i} \hat{J}'_{v_i}(kl) L'_{v_i}(\cos \theta) \\ &= \sin \theta \sum_{n=1,3}^{\infty} c_n \hat{H}_n^{(2)\prime}(kl) P'_n(\cos \theta) \quad \theta_0 \leq \theta \leq \pi - \theta_0 \end{aligned} \quad (7.3.32)$$

$$\begin{aligned} & \frac{j}{\sin \theta} (e^{-jkl} - Re^{jkl}) + \sin \theta \sum_{i=1,2}^{\infty} a_{v_i} \hat{J}_{v_i}(kl) L'_{v_i}(\cos \theta) \\ &= \sin \theta \sum_{n=1,3}^{\infty} c_n \hat{H}_n^{(2)}(kl) P'_n(\cos \theta) \quad \theta_0 \leq \theta \leq \pi - \theta_0. \end{aligned} \quad (7.3.33)$$

By (1) integrating either Equation 7.3.32 or Equation 7.3.33 directly from θ_0 and $\pi - \theta_0$, (2) multiplying Equation 7.3.32 by $P'_n(\cos \theta)$ and integrating from 0 to π , and (3) multiplying Equation 7.3.33 by $L'_{v_i}(\cos \theta)$ and integrating from θ_0 and $\pi - \theta_0$, and applying the orthogonality of the Legendre functions, we obtain a set of linear equations that can be solved for R , a_{v_i} , and c_n . Although the basic idea is straightforward, the entire process is quite tedious. The interested reader can consult the book by Schelkunoff [6]. Once these expansion coefficients are obtained, we can obtain the field distributions, from which all other quantities of interest can be calculated. For example, the voltage between the cones is given by

$$V(r) = \int_{\theta_0}^{\pi - \theta_0} \mathbf{E} \cdot d\mathbf{l} = \int_{\theta_0}^{\pi - \theta_0} E_{\theta}^{\text{int}} r d\theta = \frac{2jk}{\omega \mu \epsilon} (e^{-jkr} + Re^{jkr}) \ln \left(\cot \frac{\theta_0}{2} \right) \quad (7.3.34)$$

since the contribution from the higher-order reflected field in Equation 7.3.28 vanishes after the integration. The current on the cone flowing in the radial direction can be found as

$$\begin{aligned} I(r) &= \oint_C \mathbf{H} \cdot d\mathbf{l} = \int_0^{2\pi} H_\phi^{\text{int}} r \sin \theta d\phi \\ &= \frac{2\pi}{\mu} \left[j(e^{-jkr} - Re^{jkr}) + \sin^2 \theta_0 \sum_{i=1,2}^{\infty} a_{v_i} \hat{J}_{v_i}(kr) L'_{v_i}(\cos \theta_0) \right]. \end{aligned} \quad (7.3.35)$$

At $r = 0$, the input impedance is given by

$$Z_{\text{in}} = \frac{V(0)}{I(0)} = \frac{\eta}{\pi} \frac{1+R}{1-R} \ln \left(\cot \frac{\theta_0}{2} \right) \quad (7.3.36)$$

where R can be obtained by integrating Equation 7.3.32 directly from θ_0 and $\pi - \theta_0$, yielding

$$(e^{-jkl} + Re^{jkl}) \ln \left(\cot \frac{\theta_0}{2} \right) = \sum_{n=1,3}^{\infty} c_n \hat{H}_n^{(2)\prime}(kl) P_n(\cos \theta_0) \quad (7.3.37)$$

which can be solved for R . Apparently, because of the presence of L in Equation 7.3.37, R is a function of frequency; hence, the input impedance would exhibit certain frequency variation over its bandwidth.

As an example, Figure 7.6a shows the snapshot of the magnetic field H_ϕ of the TEM mode radiated by an infinitely long biconical antenna with $\theta_0 = 20^\circ$ in a region with a radius of 5λ . Figure 7.6b shows the same snapshot for a finite biconical antenna with $L = 3\lambda$. The effect of the antenna truncation is shown clearly on the radiated field.

7.4 WAVE TRANSFORMATION AND SCATTERING ANALYSIS

In this section, we deal with a few scattering problems as examples to illustrate how to solve electromagnetic boundary-value problems in spherical coordinates. For this, we first discuss the expansion of a plane wave in terms of spherical wave functions. Then we consider scattering of a plane wave by a conducting sphere and a dielectric sphere [4,5,7–9].

7.4.1 Wave Transformation

Consider a plane wave propagating along the z -direction. The wave function can be written as

$$\psi = e^{-j kz} = e^{-j k r \cos \theta}. \quad (7.4.1)$$

Since ψ satisfies the scalar Helmholtz equation and is independent of ϕ , it can be expanded in terms of spherical wave functions with $m = 0$. Hence,

$$e^{-j k r \cos \theta} = \sum_{n=0}^{\infty} a_n j_n(kr) P_n(\cos \theta) \quad (7.4.2)$$

where $P_n(\cos \theta) = P_n^0(\cos \theta)$ are the Legendre polynomials. To determine a_n , we multiply Equation 7.4.2 by $P_m(\cos \theta) \sin \theta$ and then integrate it over θ to obtain

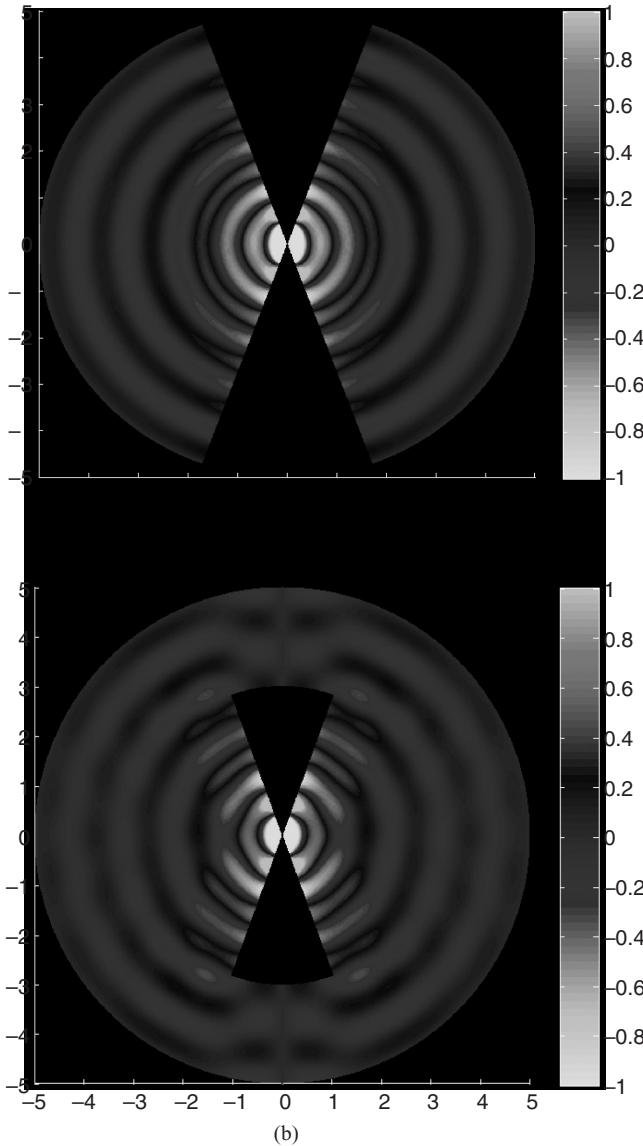


Figure 7.6 Radiation by a biconical antenna with an internal half-angle of $\theta_0 = 20^\circ$ in a region with a radius of 5λ . (a) Snapshot of the magnetic field H_ϕ of the TEM mode radiated by an infinitely long biconical antenna. (b) Snapshot of the magnetic field H_ϕ radiated by a truncated finite biconical antenna with $L = 3\lambda$. (See color insert.)

$$\int_0^\pi e^{-jkr\cos\theta} P_m(\cos\theta) \sin\theta d\theta = \sum_{n=0}^{\infty} a_n j_n(kr) \int_0^\pi P_n(\cos\theta) P_m(\cos\theta) \sin\theta d\theta. \quad (7.4.3)$$

Since the Legendre polynomials satisfy the following orthogonal relation [1]

$$\int_0^\pi P_n(\cos\theta) P_m(\cos\theta) \sin\theta d\theta = \begin{cases} 0 & n \neq m \\ \frac{2}{2n+1} & n = m \end{cases} \quad (7.4.4)$$

Equation 7.4.3 becomes

$$\int_0^\pi e^{-jkr\cos\theta} P_m(\cos\theta) \sin\theta d\theta = \frac{2a_m}{2m+1} j_m(kr). \quad (7.4.5)$$

Next we take the derivative of Equation 7.4.5 m times with respect to kr and then let $kr \rightarrow 0$. The left-hand side becomes

$$\begin{aligned} \left[\frac{d^m}{d(kr)^m} \int_0^\pi e^{-jkr\cos\theta} P_m(\cos\theta) \sin\theta d\theta \right]_{kr=0} &= (-j)^m \int_0^\pi \cos^m \theta P_m(\cos\theta) \sin\theta d\theta \\ &= (-j)^m \int_{-1}^1 x^m P_m(x) dx. \end{aligned} \quad (7.4.6)$$

Substituting the following expression for the Legendre polynomials

$$P_m(x) = \frac{1}{2^m m!} \frac{d^m}{dx^m} (x^2 - 1)^m \quad (7.4.7)$$

and then performing integration by parts m times, we can eventually find that

$$\left[\frac{d^m}{d(kr)^m} \int_0^\pi e^{-jkr\cos\theta} P_m(\cos\theta) \sin\theta d\theta \right]_{kr=0} = (-j)^m \frac{2m!}{1 \cdot 3 \cdot 5 \cdots (2m+1)}. \quad (7.4.8)$$

By using the small-argument expression of the spherical Bessel functions,

$$j_m(kr) \sim \frac{(kr)^m}{1 \cdot 3 \cdot 5 \cdots (2m+1)} \quad kr \rightarrow 0 \quad (7.4.9)$$

we find that

$$\left[\frac{d^m}{d(kr)^m} \frac{2a_m}{2m+1} j_m(kr) \right]_{kr=0} = \frac{2a_m}{2m+1} \frac{m!}{1 \cdot 3 \cdot 5 \cdots (2m+1)}. \quad (7.4.10)$$

From Equations 7.4.8 and 7.4.10, we obtain $a_m = (-j)^m (2m+1)$. Hence, Equation 7.4.2 becomes

$$e^{-jkr\cos\theta} = \sum_{n=0}^{\infty} j^{-n} (2n+1) j_n(kr) P_n(\cos\theta). \quad (7.4.11)$$

This relation is called a *wave transformation*, which expresses a plane wave in terms of a linear superposition of spherical waves. A similar transformation can be derived that expresses a cylindrical wave in terms of a linear superposition of spherical waves. Conversely, a spherical wave can also be expanded in terms of plane waves or cylindrical waves. Figure 7.7 shows how a plane wave propagating along the z -direction is formed by increasing the number of terms in the summation in Equation 7.4.11.

7.4.2 Expansion of a Plane Wave

Now we attempt to expand the spherical components of a plane wave in terms of spherical wave functions. Consider the electric field of an x -polarized incident plane wave

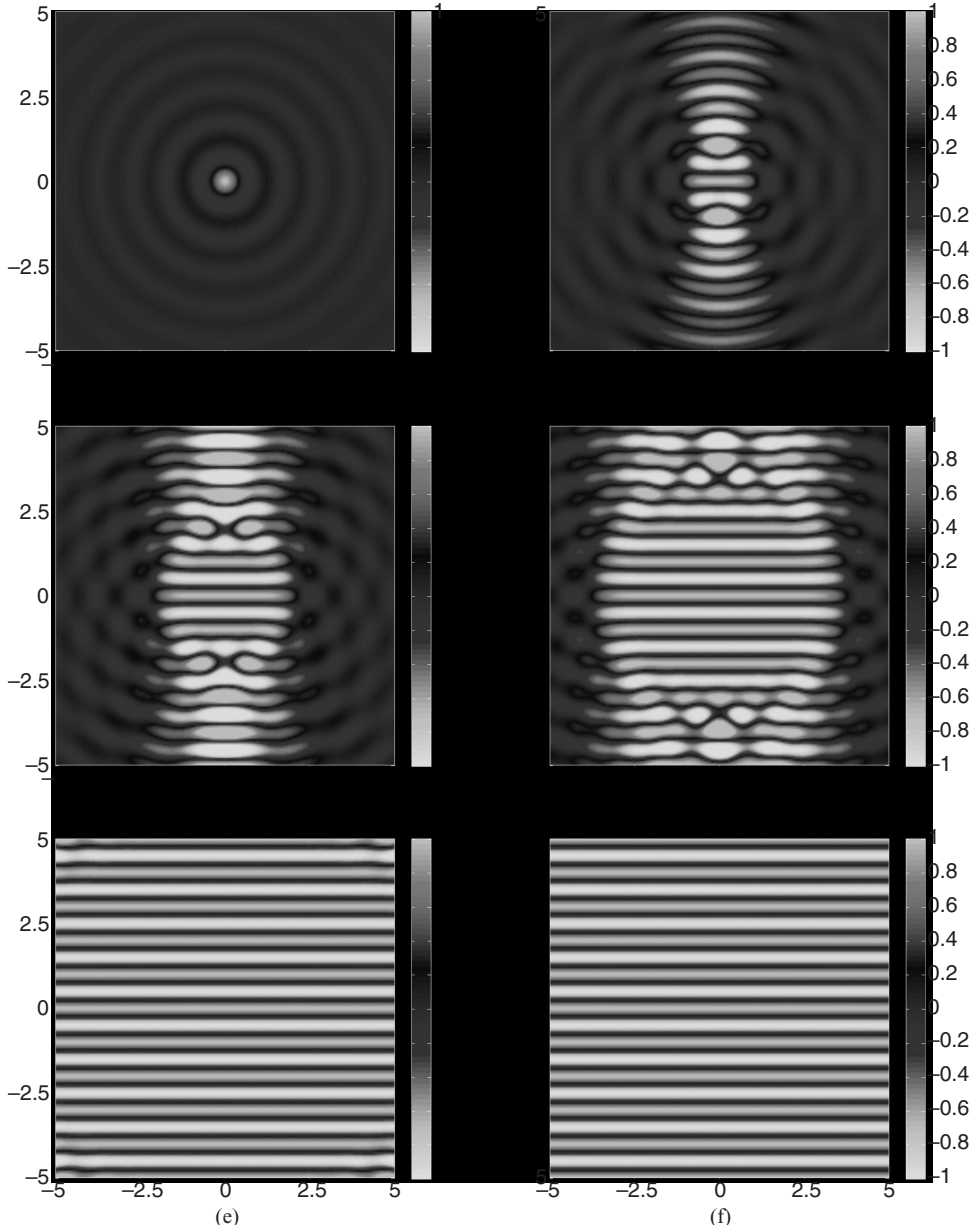


Figure 7.7 Illustration of the spherical wave transformation. The plots show the real part of the right-hand side of Equation 7.4.11 when the summation is evaluated from $n = 0$ to M . Clearly, a plane wave in a $10\lambda \times 10\lambda$ region is formed by increasing the number of terms in the summation. (a) $M = 1$. (b) $M = 5$. (c) $M = 10$. (d) $M = 20$. (e) $M = 40$. (f) $M = 80$. (See color insert.)

$$\mathbf{E}^{\text{inc}} = \hat{x}E_0 e^{-j kz} = \hat{x}E_0 e^{-j kr \cos\theta}. \quad (7.4.12)$$

Its spherical components can be written as

$$E_r^{\text{inc}} = E_0 \sin\theta \cos\phi e^{-j kr \cos\theta} = \frac{E_0 \cos\phi}{jkr} \frac{\partial}{\partial\theta} e^{-j kr \cos\theta} \quad (7.4.13)$$

$$E_r^{\text{inc}} = E_0 \cos \theta \cos \phi e^{-jkr \cos \theta} \quad (7.4.14)$$

$$E_\theta^{\text{inc}} = -E_0 \sin \phi e^{-jkr \cos \theta}. \quad (7.4.15)$$

Substituting Equation 7.4.11 into the expressions above, we have

$$E_r^{\text{inc}} = E_0 \frac{\cos \phi}{jkr} \sum_{n=0}^{\infty} j^{-n} (2n+1) j_n(kr) \frac{dP_n(\cos \theta)}{d\theta} \quad (7.4.16)$$

$$E_\theta^{\text{inc}} = E_0 \cos \theta \cos \phi \sum_{n=0}^{\infty} j^{-n} (2n+1) j_n(kr) P_n(\cos \theta) \quad (7.4.17)$$

$$E_\phi^{\text{inc}} = -E_0 \sin \phi \sum_{n=0}^{\infty} j^{-n} (2n+1) j_n(kr) P_n(\cos \theta). \quad (7.4.18)$$

These expressions can also be written in terms of the Riccati–Bessel functions as

$$E_r^{\text{inc}} = E_0 \frac{\cos \phi}{j(kr)^2} \sum_{n=0}^{\infty} j^{-n} (2n+1) \hat{J}_n(kr) P_n^1(\cos \theta) \quad (7.4.19)$$

$$E_\theta^{\text{inc}} = E_0 \frac{\cos \theta \cos \phi}{kr} \sum_{n=0}^{\infty} j^{-n} (2n+1) \hat{J}_n(kr) P_n(\cos \theta) \quad (7.4.20)$$

$$E_\phi^{\text{inc}} = -E_0 \frac{\sin \phi}{kr} \sum_{n=0}^{\infty} j^{-n} (2n+1) \hat{J}_n(kr) P_n(\cos \theta) \quad (7.4.21)$$

where we have applied the relation $dP_n(\cos \theta)/d\theta = P_n^1(\cos \theta)$. From these expressions, we can easily obtain the corresponding magnetic field components as

$$H_r^{\text{inc}} = H_0 \frac{\sin \phi}{j(kr)^2} \sum_{n=0}^{\infty} j^{-n} (2n+1) \hat{J}_n(kr) P_n^1(\cos \theta) \quad (7.4.22)$$

$$H_\theta^{\text{inc}} = H_0 \frac{\cos \theta \sin \phi}{kr} \sum_{n=0}^{\infty} j^{-n} (2n+1) \hat{J}_n(kr) P_n(\cos \theta) \quad (7.4.23)$$

$$H_\phi^{\text{inc}} = H_0 \frac{\cos \phi}{kr} \sum_{n=0}^{\infty} j^{-n} (2n+1) \hat{J}_n(kr) P_n(\cos \theta) \quad (7.4.24)$$

where $H_0 = E_0 / \eta$.

By comparing Equation 7.4.19 with Equations 7.1.30 and 7.4.22 with Equation 7.1.27 and noting that the Riccati–Bessel functions satisfy the governing partial differential equation

$$\frac{d^2 \hat{J}_n(z)}{dz^2} + \hat{J}_n(z) - \frac{n(n+1)}{z^2} \hat{J}_n(z) = 0 \quad (7.4.25)$$

we find A_r and F_r for the incident field as

$$A_r^{\text{inc}} = E_0 \frac{\cos \phi}{\omega} \sum_{n=0}^{\infty} j^{-n} \frac{2n+1}{n(n+1)} \hat{J}_n(kr) P_n^1(\cos \theta) \quad (7.4.26)$$

$$F_r^{\text{inc}} = H_0 \frac{\sin \phi}{\omega} \sum_{n=0}^{\infty} j^{-n} \frac{2n+1}{n(n+1)} \hat{J}_n(kr) P_n^1(\cos \theta). \quad (7.4.27)$$

Substituting these into Equations 7.1.28, 7.1.29, 7.1.31, and 7.1.32, we obtain the θ - and ϕ -components of the electric and magnetic fields as

$$E_{\theta}^{\text{inc}} = -\frac{E_0 \cos \phi}{kr} \sum_{n=1}^{\infty} j^{-n} \frac{2n+1}{n(n+1)} \left[j\hat{J}'_n(kr) \frac{dP_n^1(\cos \theta)}{d\theta} + \hat{J}_n(kr) \frac{P_n^1(\cos \theta)}{\sin \theta} \right] \quad (7.4.28)$$

$$E_{\phi}^{\text{inc}} = \frac{E_0 \sin \phi}{kr} \sum_{n=1}^{\infty} j^{-n} \frac{2n+1}{n(n+1)} \left[j\hat{J}'_n(kr) \frac{P_n^1(\cos \theta)}{\sin \theta} + \hat{J}_n(kr) \frac{dP_n^1(\cos \theta)}{d\theta} \right] \quad (7.4.29)$$

$$H_{\theta}^{\text{inc}} = -\frac{H_0 \sin \phi}{kr} \sum_{n=1}^{\infty} j^{-n} \frac{2n+1}{n(n+1)} \left[\hat{J}_n(kr) \frac{P_n^1(\cos \theta)}{\sin \theta} + j\hat{J}'_n(kr) \frac{dP_n^1(\cos \theta)}{d\theta} \right] \quad (7.4.30)$$

$$H_{\phi}^{\text{inc}} = -\frac{H_0 \cos \phi}{kr} \sum_{n=1}^{\infty} j^{-n} \frac{2n+1}{n(n+1)} \left[\hat{J}_n(kr) \frac{dP_n^1(\cos \theta)}{d\theta} + j\hat{J}'_n(kr) \frac{P_n^1(\cos \theta)}{\sin \theta} \right]. \quad (7.4.31)$$

These expressions can be shown to be equivalent to Equations 7.4.20, 7.4.21, 7.4.23, and 7.4.24 by using the properties of the associated Legendre polynomials and Riccati–Bessel functions.

7.4.3 Scattering by a Conducting Sphere

With the expansion of the incident plane wave, we are now ready to deal with the scattering of the plane wave by a conducting sphere of radius a , which is centered at the origin of the spherical coordinate system (Fig. 7.8). Since any wave can be expanded in terms of the TE_r and TM_r waves, in view of Equations 7.4.26 and 7.4.27, we can expand A_r and F_r for the scattered field as

$$A_r^{\text{sc}} = E_0 \frac{\cos \phi}{\omega} \sum_{n=0}^{\infty} a_n \hat{H}_n^{(2)}(kr) P_n^1(\cos \theta) \quad (7.4.32)$$

$$F_r^{\text{sc}} = H_0 \frac{\sin \phi}{\omega} \sum_{n=0}^{\infty} b_n \hat{H}_n^{(2)}(kr) P_n^1(\cos \theta). \quad (7.4.33)$$

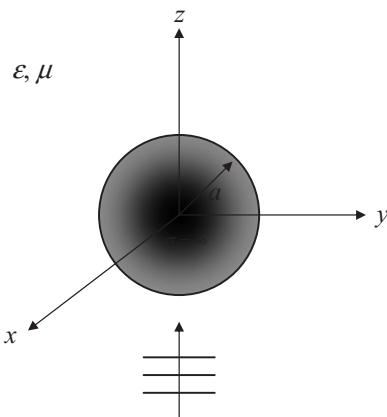


Figure 7.8 Plane wave scattering by a conducting sphere.

The corresponding spherical components of the scattered electric and magnetic fields are

$$E_r^{\text{sc}} = E_0 \frac{\cos \phi}{j(kr)^2} \sum_{n=0}^{\infty} a_n n(n+1) \hat{H}_n^{(2)}(kr) P_n^1(\cos \theta) \quad (7.4.34)$$

$$E_{\theta}^{\text{sc}} = -\frac{E_0 \cos \phi}{kr} \sum_{n=1}^{\infty} \left[a_n j \hat{H}_n^{(2)\prime}(kr) \frac{dP_n^1(\cos \theta)}{d\theta} + b_n \hat{H}_n^{(2)}(kr) \frac{P_n^1(\cos \theta)}{\sin \theta} \right] \quad (7.4.35)$$

$$E_{\phi}^{\text{sc}} = \frac{E_0 \sin \phi}{kr} \sum_{n=1}^{\infty} \left[a_n j \hat{H}_n^{(2)\prime}(kr) \frac{P_n^1(\cos \theta)}{\sin \theta} + b_n \hat{H}_n^{(2)}(kr) \frac{dP_n^1(\cos \theta)}{d\theta} \right] \quad (7.4.36)$$

$$H_r^{\text{sc}} = H_0 \frac{\sin \phi}{j(kr)^2} \sum_{n=0}^{\infty} b_n n(n+1) \hat{H}_n^{(2)}(kr) P_n^1(\cos \theta) \quad (7.4.37)$$

$$H_{\theta}^{\text{sc}} = -\frac{H_0 \sin \phi}{kr} \sum_{n=1}^{\infty} \left[a_n \hat{H}_n^{(2)}(kr) \frac{P_n^1(\cos \theta)}{\sin \theta} + b_n j \hat{H}_n^{(2)\prime}(kr) \frac{dP_n^1(\cos \theta)}{d\theta} \right] \quad (7.4.38)$$

$$H_{\phi}^{\text{sc}} = -\frac{H_0 \cos \phi}{kr} \sum_{n=1}^{\infty} \left[a_n \hat{H}_n^{(2)}(kr) \frac{dP_n^1(\cos \theta)}{d\theta} + b_n j \hat{H}_n^{(2)\prime}(kr) \frac{P_n^1(\cos \theta)}{\sin \theta} \right]. \quad (7.4.39)$$

Since the tangential components of the total electric field should vanish on the surface of the conducting sphere, we have

$$\left[E_{\theta}^{\text{inc}} + E_{\theta}^{\text{sc}} \right]_{r=a} = 0 \quad \text{and} \quad \left[E_{\phi}^{\text{inc}} + E_{\phi}^{\text{sc}} \right]_{r=a} = 0. \quad (7.4.40)$$

Application of these boundary conditions yields

$$a_n = -j^{-n} \frac{2n+1}{n(n+1)} \frac{\hat{J}'_n(ka)}{\hat{H}_n^{(2)\prime}(ka)} \quad (7.4.41)$$

$$b_n = -j^{-n} \frac{2n+1}{n(n+1)} \frac{\hat{J}_n(ka)}{\hat{H}_n^{(2)}(ka)} \quad (7.4.42)$$

from which the scattered field everywhere can be evaluated. This solution is called the *Mie series solution*. Figure 7.9 displays the scattered and total fields for a conducting sphere with a radius of 1λ in two planes. One is called the E-plane, which contains the vector **E**, and the other is called the H-plane, which contains the vector **H**. In this case, the E-plane is the xz -plane and the H-plane is the yz -plane.

In the far-field region, where $kr \gg 1$, we can use the large-argument approximation of the Riccati–Hankel functions

$$\hat{H}_n^{(2)}(kr) \approx j^{n+1} e^{-jkr} \quad \text{for } kr \rightarrow \infty \quad (7.4.43)$$

to find the dominant components of the scattered electric field as

$$E_{\theta}^{\text{sc}} \approx -jE_0 \cos \phi \frac{e^{-jkr}}{kr} \sum_{n=1}^{\infty} j^n \left[a_n \frac{dP_n^1(\cos \theta)}{d\theta} + b_n \frac{P_n^1(\cos \theta)}{\sin \theta} \right] \quad (7.4.44)$$

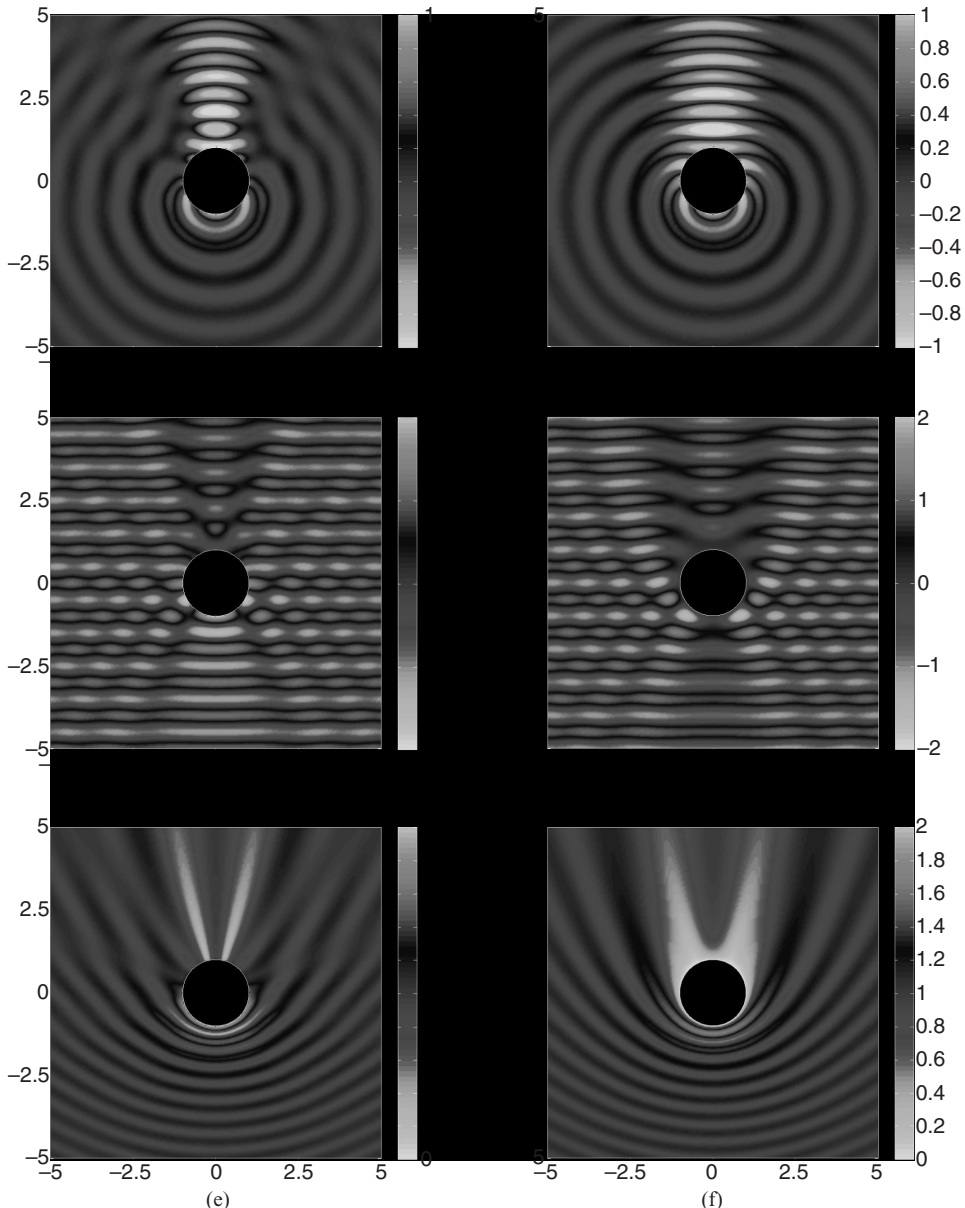


Figure 7.9 Scattering by a conducting sphere with a radius of 1λ . (a) Snapshot of the scattered magnetic field ηH_ϕ^{sc} in the E-plane. (b) Snapshot of the scattered electric field E_ϕ^{sc} in the H-plane. (c) Snapshot of the total magnetic field ηH_ϕ in the E-plane. (d) Snapshot of the total electric field E_ϕ in the H-plane. (e) Magnitude of the total magnetic field ηH_ϕ in the E-plane. (f) Magnitude of the total electric field E_ϕ in the H-plane. The values of the fields are normalized by the magnitude of the incident electric field. (See color insert.)

$$E_\phi^{\text{sc}} \approx jE_0 \sin \phi \frac{e^{-jkr}}{kr} \sum_{n=1}^{\infty} j^n \left[a_n \frac{P_n^1(\cos \theta)}{\sin \theta} + b_n \frac{dP_n^1(\cos \theta)}{d\theta} \right]. \quad (7.4.45)$$

From these far-field expressions, the *bistatic radar cross-section* (RCS) can be evaluated based on its definition

$$\sigma_{3D}(\theta, \phi) = \lim_{r \rightarrow \infty} \left[4\pi r^2 \frac{|E^{sc}|^2}{|E^{inc}|^2} \right]. \quad (7.4.46)$$

From the expression of the far field, it is obvious that the RCS is independent of the distance r and the magnitude of the incident field. Instead, it is only a function of angles and the wavenumber. It has a unit of area such as m^2 or λ^2 . When it is plotted in the logarithmic scale, we usually first normalize it with m^2 or λ^2 such that the plotted quantity is $10\log(\sigma_{3D}/\text{m}^2)$ or $10\log(\sigma_{3D}/\lambda^2)$, whose unit is often labeled as dBsm or dBsw. Figure 7.10 shows the bistatic RCS of a conducting sphere with three different radii in both E- and H-planes.

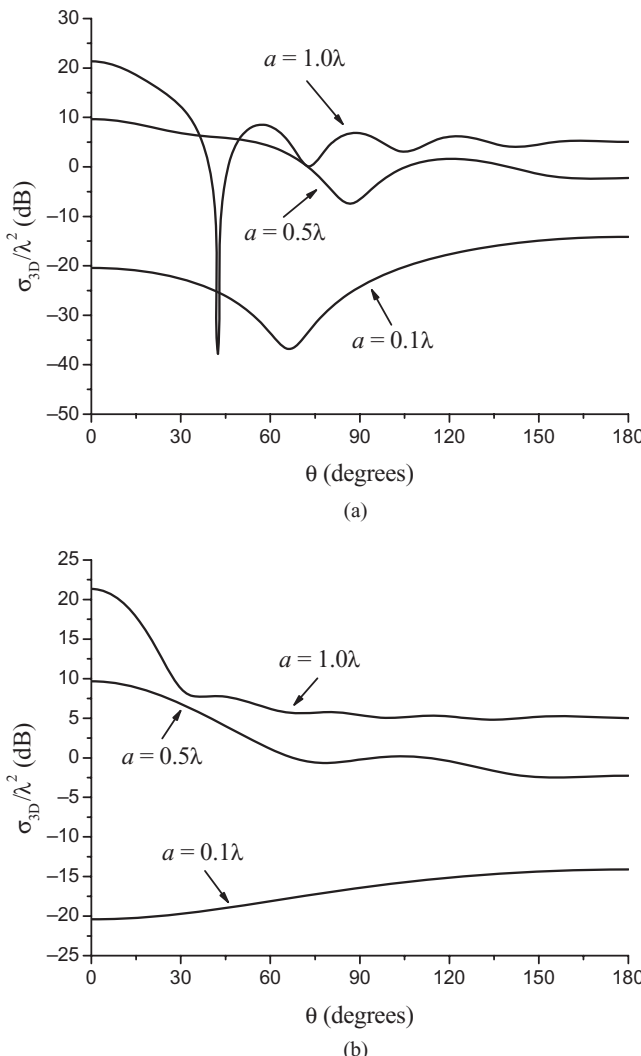


Figure 7.10 Bistatic RCS of a conducting sphere for the angle of incidence $\theta^{inc} = 180^\circ$. (a) In the E-plane. (b) In the H-plane.

The value of the RCS characterizes the scattering property of an object. Its value equals the size of an isotropic scatterer that would scatter the same amount of the power density into the observation direction as does the object of interest. An isotropic scatterer intercepts a certain amount of incident power, equal to its cross-sectional area times the power density of the incident wave, and then scatters uniformly into all directions. When the observation direction is the same as the incident direction, the RCS is often referred to as the *monostatic RCS* or simply as the *backscatter RCS*. In this case, the incident direction is $\theta = \pi$, and from the property of the associated Legendre polynomials, we have

$$\left[\frac{P_n^1(\cos \theta)}{\sin \theta} \right]_{\theta=\pi} = - \left[\frac{dP_n^1(\cos \theta)}{d\theta} \right]_{\theta=\pi} = (-1)^n \frac{n(n+1)}{2}. \quad (7.4.47)$$

Hence, the monostatic RCS of a conducting sphere is given by

$$\sigma_{3D} = \frac{\lambda^2}{4\pi} \left| \sum_{n=1}^{\infty} (-1)^n \frac{2n+1}{\hat{H}_n^{(2)'}(ka)\hat{H}_n^{(2)}(ka)} \right|^2. \quad (7.4.48)$$

Its value normalized with respect to πa^2 —the cross-section of the sphere—is plotted in Figure 7.11 as a function of a/λ . It can be seen that there are three distinct regions. In the first region, where $a/\lambda < 0.1$, by using the small-argument approximation for the Riccati–Bessel functions, the RCS can be found approximately as

$$\lim_{a/\lambda \rightarrow 0} \sigma_{3D} \approx \frac{9\lambda^2}{4\pi} (ka)^6 \propto \frac{1}{\lambda^4}. \quad (7.4.49)$$

The value of the RCS increases drastically as the wavelength decreases or as the frequency increases. This region is referred to as the *Rayleigh scattering region*. In the second region, where $0.1 < a/\lambda < 2$, the value of the RCS oscillates around πa^2 . This region is called the *resonance region*, and Equation 7.4.48 has to be evaluated through a summation of series until it reaches convergence. In the third region, where $a/\lambda > 2$, Equation 7.4.48 can be evaluated approximately by using the large-argument approximation for the Riccati–Bessel functions, yielding

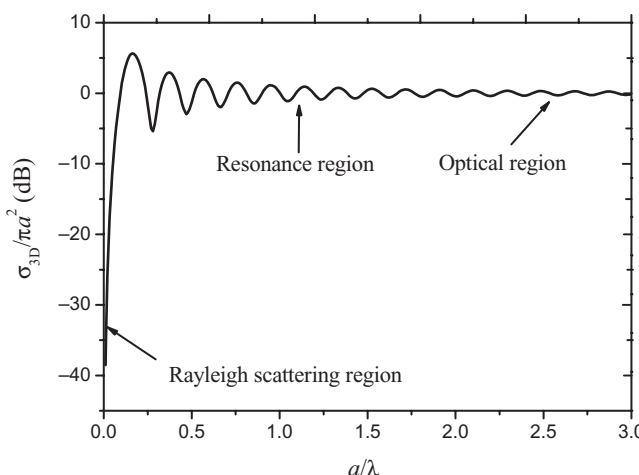


Figure 7.11 Monostatic RCS of a conducting sphere as a function of its normalized radius.

$$\lim_{a/\lambda \rightarrow \infty} \sigma_{3D} \approx \pi a^2. \quad (7.4.50)$$

This region is called the *optical region*, where the sphere is large as compared with the wavelength.

7.4.4 Scattering by a Dielectric Sphere

The solution to plane wave scattering by a dielectric sphere follows the same approach as discussed above for the conducting sphere. The scattered field can again be expanded as Equations 7.4.32–7.3.39. Assume that the dielectric sphere has a radius of a , a permittivity of ϵ_d , and a permeability of μ_d (Fig. 7.12). The field inside the sphere can be expanded in terms of the TE _{r} and TM _{r} waves, and in view of Equations 7.4.26 and 7.4.27, we can expand A_r and F_r for the internal field as

$$A_r^{\text{int}} = E_0 \frac{\cos \phi}{\omega} \sum_{n=0}^{\infty} c_n \hat{J}_n(k_d r) P_n^1(\cos \theta) \quad (7.4.51)$$

$$F_r^{\text{int}} = E_0 \frac{\sin \phi}{\omega \eta_d} \sum_{n=0}^{\infty} d_n \hat{J}_n(k_d r) P_n^1(\cos \theta) \quad (7.4.52)$$

where $k_d = \omega \sqrt{\mu_d \epsilon_d}$ and $\eta_d = \sqrt{\mu_d / \epsilon_d}$. The corresponding spherical components of the internal electric and magnetic fields are

$$E_r^{\text{int}} = E_0 \frac{\cos \phi}{j(k_d r)^2} \sum_{n=0}^{\infty} c_n n(n+1) \hat{J}_n(k_d r) P_n^1(\cos \theta) \quad (7.4.53)$$

$$E_\theta^{\text{int}} = -\frac{E_0 \cos \phi}{k_d r} \sum_{n=1}^{\infty} \left[c_n j \hat{J}'_n(k_d r) \frac{d P_n^1(\cos \theta)}{d \theta} + d_n \hat{J}_n(k_d r) \frac{P_n^1(\cos \theta)}{\sin \theta} \right] \quad (7.4.54)$$

$$E_\phi^{\text{int}} = \frac{E_0 \sin \phi}{k_d r} \sum_{n=1}^{\infty} \left[c_n j \hat{J}'_n(k_d r) \frac{P_n^1(\cos \theta)}{\sin \theta} + d_n \hat{J}_n(k_d r) \frac{d P_n^1(\cos \theta)}{d \theta} \right] \quad (7.4.55)$$

$$H_r^{\text{int}} = E_0 \frac{\sin \phi}{j \eta_d (k_d r)^2} \sum_{n=0}^{\infty} d_n n(n+1) \hat{J}_n(k_d r) P_n^1(\cos \theta) \quad (7.4.56)$$

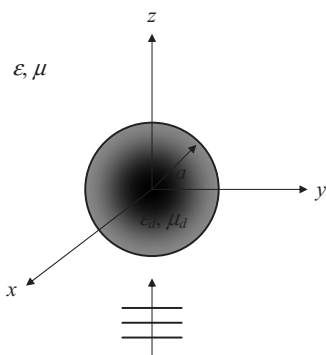


Figure 7.12 Plane wave scattering by a dielectric sphere.

$$H_{\theta}^{\text{int}} = -\frac{E_0 \sin \phi}{\eta_d k_d r} \sum_{n=1}^{\infty} \left[c_n \hat{J}_n(k_d r) \frac{P_n^1(\cos \theta)}{\sin \theta} + d_n j \hat{J}'_n(k_d r) \frac{dP_n^1(\cos \theta)}{d\theta} \right] \quad (7.4.57)$$

$$H_{\phi}^{\text{int}} = -\frac{E_0 \cos \phi}{\eta_d k_d r} \sum_{n=1}^{\infty} \left[c_n \hat{J}_n(k_d r) \frac{dP_n^1(\cos \theta)}{d\theta} + d_n j \hat{J}'_n(k_d r) \frac{P_n^1(\cos \theta)}{\sin \theta} \right]. \quad (7.4.58)$$

Since the tangential components of the electric and magnetic fields should be continuous across the surface of the dielectric sphere, we have

$$[E_{\theta}^{\text{inc}} + E_{\theta}^{\text{sc}}]_{r=a} = [E_{\theta}^{\text{int}}]_{r=a}, \quad [E_{\phi}^{\text{inc}} + E_{\phi}^{\text{sc}}]_{r=a} = [E_{\phi}^{\text{int}}]_{r=a} \quad (7.4.59)$$

$$[H_{\theta}^{\text{inc}} + H_{\theta}^{\text{sc}}]_{r=a} = [H_{\theta}^{\text{int}}]_{r=a}, \quad [H_{\phi}^{\text{inc}} + H_{\phi}^{\text{sc}}]_{r=a} = [H_{\phi}^{\text{int}}]_{r=a}. \quad (7.4.60)$$

Application of these boundary conditions yields

$$j^{-n} \frac{2n+1}{n(n+1)} \hat{J}_n(ka) + a_n \hat{H}_n^{(2)}(ka) = \frac{\mu}{\mu_d} c_n \hat{J}_n(k_d a) \quad (7.4.61)$$

$$j^{-n} \frac{2n+1}{n(n+1)} \hat{J}'_n(ka) + a_n \hat{H}_n^{(2)\prime}(ka) = \frac{k}{k_d} c_n \hat{J}'_n(k_d a) \quad (7.4.62)$$

$$j^{-n} \frac{2n+1}{n(n+1)} \hat{J}_n(ka) + b_n \hat{H}_n^{(2)}(ka) = \frac{k}{k_d} d_n \hat{J}_n(k_d a) \quad (7.4.63)$$

$$j^{-n} \frac{2n+1}{n(n+1)} \hat{J}'_n(ka) + b_n \hat{H}_n^{(2)\prime}(ka) = \frac{\mu}{\mu_d} d_n \hat{J}'_n(k_d a) \quad (7.4.64)$$

which can be solved to yield

$$a_n = j^{-n} \frac{2n+1}{n(n+1)} \frac{\sqrt{\epsilon_r} \hat{J}'_n(ka) \hat{J}_n(k_d a) - \sqrt{\mu_r} \hat{J}_n(ka) \hat{J}'_n(k_d a)}{\sqrt{\mu_r} \hat{H}_n^{(2)}(ka) \hat{J}'_n(k_d a) - \sqrt{\epsilon_r} \hat{H}_n^{(2)\prime}(ka) \hat{J}_n(k_d a)} \quad (7.4.65)$$

$$b_n = j^{-n} \frac{2n+1}{n(n+1)} \frac{\sqrt{\mu_r} \hat{J}'_n(ka) \hat{J}_n(k_d a) - \sqrt{\epsilon_r} \hat{J}_n(ka) \hat{J}'_n(k_d a)}{\sqrt{\epsilon_r} \hat{H}_n^{(2)}(ka) \hat{J}'_n(k_d a) - \sqrt{\mu_r} \hat{H}_n^{(2)\prime}(ka) \hat{J}_n(k_d a)} \quad (7.4.66)$$

$$c_n = j^{-n} \frac{2n+1}{n(n+1)} \frac{j \sqrt{\epsilon_r} \mu_r}{\sqrt{\mu_r} \hat{H}_n^{(2)}(ka) \hat{J}'_n(k_d a) - \sqrt{\epsilon_r} \hat{H}_n^{(2)\prime}(ka) \hat{J}_n(k_d a)} \quad (7.4.67)$$

$$d_n = j^{-n} \frac{2n+1}{n(n+1)} \frac{j \sqrt{\epsilon_r} \mu_r}{\sqrt{\epsilon_r} \hat{H}_n^{(2)}(ka) \hat{J}'_n(k_d a) - \sqrt{\mu_r} \hat{H}_n^{(2)\prime}(ka) \hat{J}_n(k_d a)} \quad (7.4.68)$$

where $\epsilon_r = \epsilon_d / \epsilon$ and $\mu_r = \mu_d / \mu$ denote the relative permittivity and permeability of the sphere with respect to the background. In obtaining these results, we have employed the Wronskian relation for the Riccati–Bessel functions $\hat{J}_n(z) \hat{H}_n^{(2)\prime}(z) - \hat{J}'_n(z) \hat{H}_n^{(2)}(z) = -j$.

For a sphere having a conductivity σ , ϵ_d has a complex value with an imaginary part of $\sigma/j\omega$. When $\sigma \rightarrow \infty$, Equations 7.4.65–7.4.68 are reduced to

$$a_n = -j^{-n} \frac{2n+1}{n(n+1)} \frac{\hat{J}'_n(ka)}{\hat{H}_n^{(2)'}(ka)}, \quad c_n = 0 \quad (7.4.69)$$

$$b_n = -j^{-n} \frac{2n+1}{n(n+1)} \frac{\hat{J}_n(ka)}{\hat{H}_n^{(2)}(ka)}, \quad d_n = 0 \quad (7.4.70)$$

which are the same as the solution for scattering by a perfectly conducting sphere.

For a very small dielectric sphere with $ka \ll 1$ and $k_d a \ll 1$, the series in the solution decays very quickly as n increases. This is evident from the small-argument approximation of the Riccati–Bessel functions

$$\hat{J}_n(z) \sim \frac{z^{n+1}}{1 \cdot 3 \cdot 5 \cdots (2n+1)} \quad \text{when } z \rightarrow 0. \quad (7.4.71)$$

Therefore, an approximate solution can be obtained by keeping only the first term. By using the small-argument approximation

$$\hat{J}_1(z) \approx \frac{z^2}{3}, \quad \hat{H}_1^{(2)}(z) \approx \frac{j}{z} \quad \text{when } z \rightarrow 0 \quad (7.4.72)$$

the coefficients for the first terms are found as

$$a_1 \approx -(ka)^3 \frac{\epsilon_r - 1}{\epsilon_r + 2}, \quad b_1 \approx -(ka)^3 \frac{\mu_r - 1}{\mu_r + 2} \quad (7.4.73)$$

$$c_1 \approx \frac{9}{2j(\epsilon_r + 2)}, \quad d_1 \approx \frac{9}{2j(\mu_r + 2)} \sqrt{\frac{\mu_r}{\epsilon_r}}. \quad (7.4.74)$$

The RCS is again found to be proportional to $1/\lambda^4$, which is characteristic of Rayleigh scattering. This type of scattering by dust in the atmosphere explains why the sky is blue during a sunny day and why the sky is red in the west at sunset.

To show the scattering characteristics, Figure 7.13 displays the scattered and total fields in both E- and H-planes for a dielectric sphere with a radius of 1λ and a relative permittivity of 2.56. Figure 7.14 plots the bistatic RCS of the sphere with three different radii, and Figure 7.15 shows the monostatic RCS as a function of its radius. The Rayleigh scattering characteristic is clearly observed in Figure 7.15.

7.4.5 Scattering by a Multilayer Dielectric Sphere

The solution of scattering by a dielectric sphere can further be extended to the case of a multilayer dielectric sphere. Assume that the sphere consists of m layers with the radius, permittivity, and permeability of each layer denoted by a_i , ϵ_i , and μ_i ($i = 1, 2, \dots, m$), respectively (Fig. 7.16). The scattered field can be represented by

$$A_r^{\text{sc}} = E_0 \frac{\cos \phi}{\omega} \sum_{n=0}^{\infty} a_n \hat{H}_n^{(2)}(kr) P_n^1(\cos \theta) \quad (7.4.75)$$

$$F_r^{\text{sc}} = H_0 \frac{\sin \phi}{\omega} \sum_{n=0}^{\infty} b_n \hat{H}_n^{(2)}(kr) P_n^1(\cos \theta). \quad (7.4.76)$$

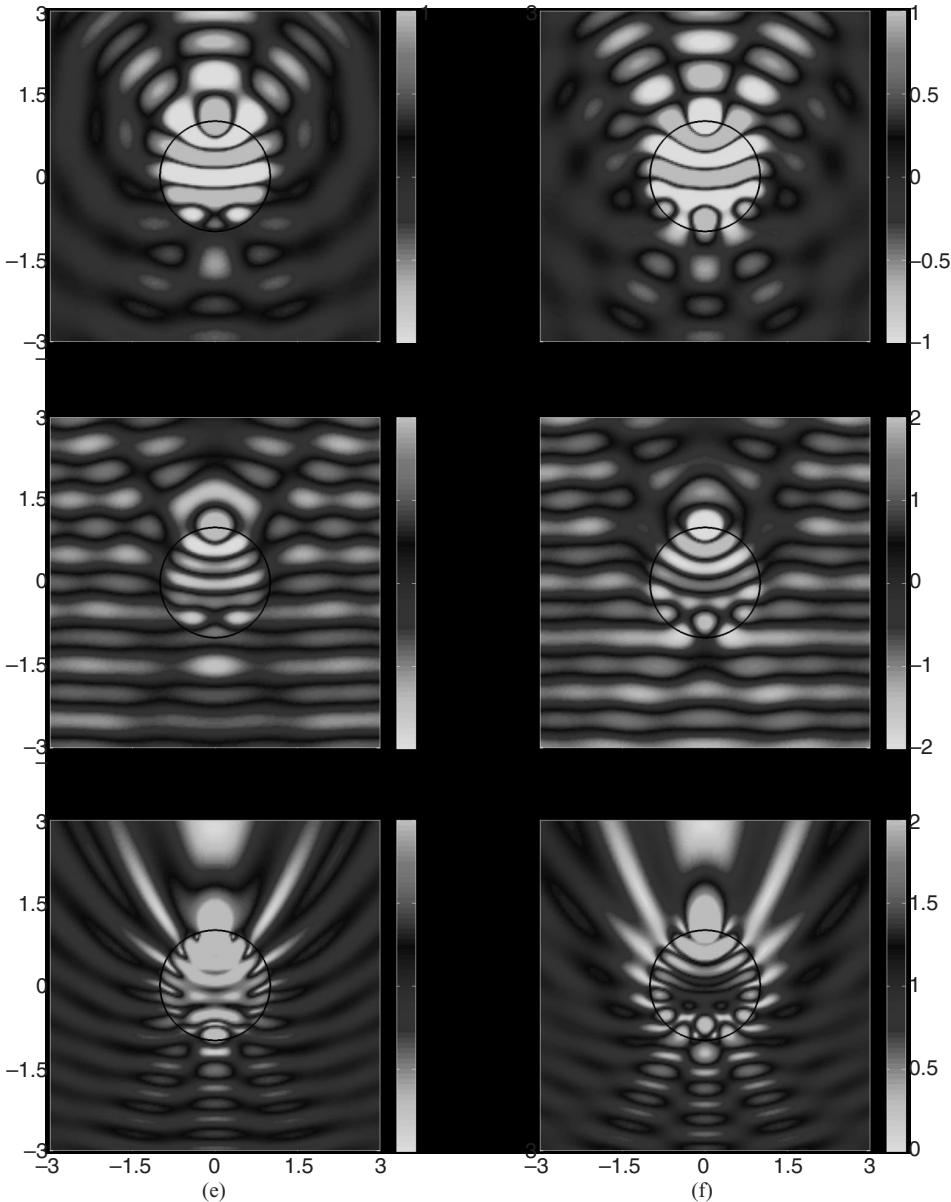


Figure 7.13 Scattering by a dielectric sphere with a radius of 1λ and a relative permittivity of 2.56. (a) Snapshot of the scattered magnetic field ηH_ϕ^{sc} in the E-plane. (b) Snapshot of the scattered electric field E_ϕ^{sc} in the H-plane. (c) Snapshot of the total magnetic field ηH_ϕ in the E-plane. (d) Snapshot of the total electric field E_ϕ in the H-plane. (e) Magnitude of the total magnetic field ηH_ϕ in the E-plane. (f) Magnitude of the total electric field E_ϕ in the H-plane. The values of the fields are normalized by the magnitude of the incident electric field. (See color insert.)

The field in the i th layer ($i = 1, 2, \dots, m$) can be represented by

$$A_r^{(i)} = E_0 \frac{\cos \phi}{\omega} \sum_{n=0}^{\infty} [c_n^{(i)} \hat{H}_n^{(1)}(k_i r) + d_n^{(i)} \hat{H}_n^{(2)}(k_i r)] P_n^1(\cos \theta) \quad (7.4.77)$$

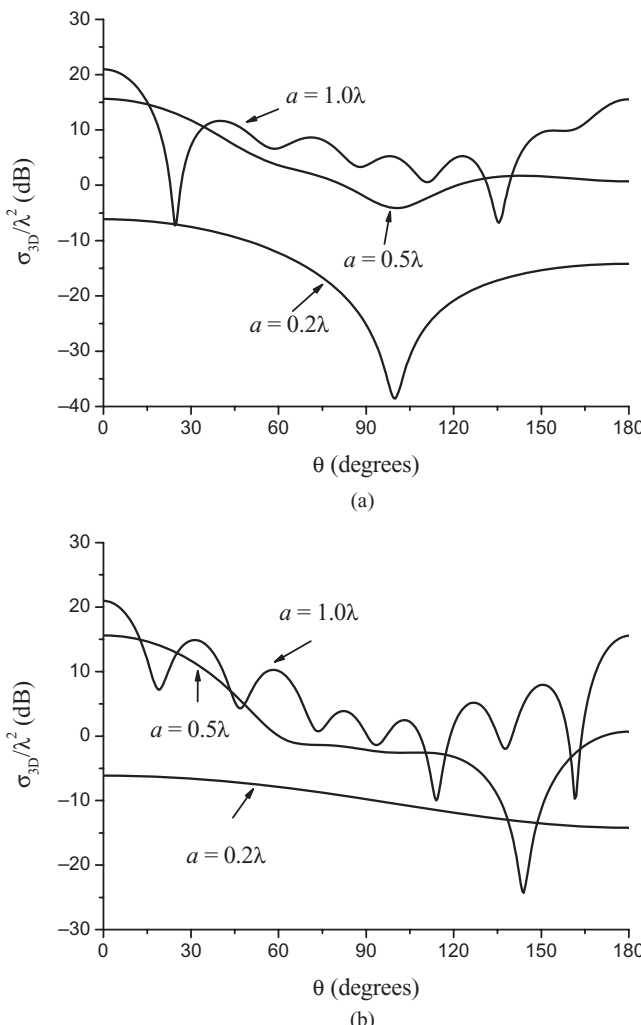


Figure 7.14 Bistatic RCS of a dielectric sphere with a relative permittivity of 2.56 and the angle of incidence $\theta^{inc} = 180^\circ$. (a) In the E-plane. (b) In the H-plane.

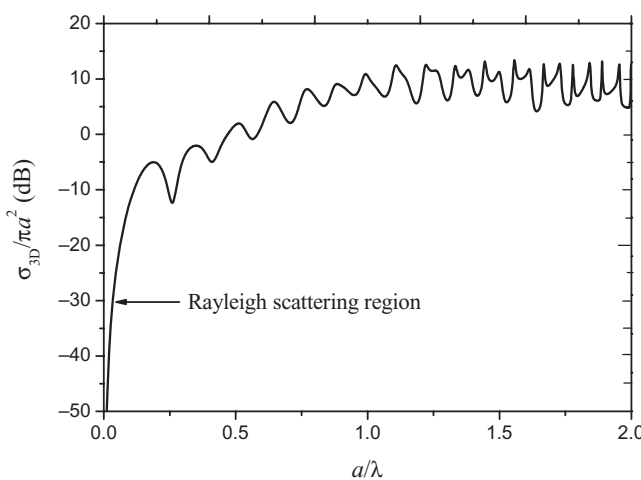


Figure 7.15 Monostatic RCS of a dielectric sphere with a relative permittivity of 2.56.

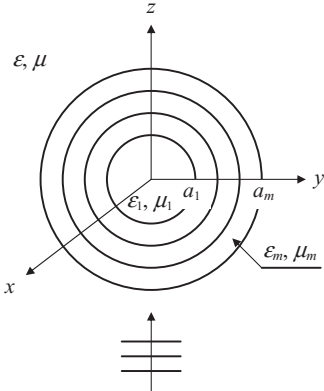


Figure 7.16 Plane wave scattering by a multilayer dielectric sphere.

$$F_r^{(i)} = E_0 \frac{\sin \phi}{\omega n_i} \sum_{n=0}^{\infty} [\tilde{c}_n^{(i)} \hat{H}_n^{(1)}(k_i r) + \tilde{d}_n^{(i)} \hat{H}_n^{(2)}(k_i r)] P_n^l(\cos \theta) \quad (7.4.78)$$

where $k_i = \omega \sqrt{\mu_i \epsilon_i}$ and $\eta_i = \sqrt{\mu_i / \epsilon_i}$.

Application of the field continuity conditions at $r = a_i$ ($i = 1, 2, \dots, m - 1$) yields

$$\frac{1}{\mu_{i+1}} [c_n^{(i+1)} \hat{H}_n^{(1)}(k_{i+1} a_i) + d_n^{(i+1)} \hat{H}_n^{(2)}(k_{i+1} a_i)] = \frac{1}{\mu_i} [c_n^{(i)} \hat{H}_n^{(1)}(k_i a_i) + d_n^{(i)} \hat{H}_n^{(2)}(k_i a_i)] \quad (7.4.79)$$

$$\frac{1}{k_{i+1}} [c_n^{(i+1)} \hat{H}_n^{(1)\prime}(k_{i+1} a_i) + d_n^{(i+1)} \hat{H}_n^{(2)\prime}(k_{i+1} a_i)] = \frac{1}{k_i} [c_n^{(i)} \hat{H}_n^{(1)\prime}(k_i a_i) + d_n^{(i)} \hat{H}_n^{(2)\prime}(k_i a_i)] \quad (7.4.80)$$

$$\frac{1}{k_{i+1}} [\tilde{c}_n^{(i+1)} \hat{H}_n^{(1)}(k_{i+1} a_i) + \tilde{d}_n^{(i+1)} \hat{H}_n^{(2)}(k_{i+1} a_i)] = \frac{1}{k_i} [\tilde{c}_n^{(i)} \hat{H}_n^{(1)}(k_i a_i) + \tilde{d}_n^{(i)} \hat{H}_n^{(2)}(k_i a_i)] \quad (7.4.81)$$

$$\frac{1}{\mu_{i+1}} [\tilde{c}_n^{(i+1)} \hat{H}_n^{(1)\prime}(k_{i+1} a_i) + \tilde{d}_n^{(i+1)} \hat{H}_n^{(2)\prime}(k_{i+1} a_i)] = \frac{1}{\mu_i} [\tilde{c}_n^{(i)} \hat{H}_n^{(1)\prime}(k_i a_i) + \tilde{d}_n^{(i)} \hat{H}_n^{(2)\prime}(k_i a_i)]. \quad (7.4.82)$$

From these equations, we can calculate recursively

$$\hat{R}_H^{(i)} = \sqrt{\frac{\mu_{i+1} \epsilon_i}{\epsilon_{i+1} \mu_i}} \frac{\hat{H}_n^{(1)}(k_i a_i) + \frac{d_n^{(i)}}{c_n^{(i)}} \hat{H}_n^{(2)}(k_i a_i)}{\hat{H}_n^{(1)\prime}(k_i a_i) + \frac{d_n^{(i)}}{c_n^{(i)}} \hat{H}_n^{(2)\prime}(k_i a_i)} \quad i = 2, 3, \dots, m \quad (7.4.83)$$

$$\hat{R}_E^{(i)} = \sqrt{\frac{\epsilon_{i+1} \mu_i}{\mu_{i+1} \epsilon_i}} \frac{\hat{H}_n^{(1)}(k_i a_i) + \frac{\tilde{d}_n^{(i)}}{\tilde{c}_n^{(i)}} \hat{H}_n^{(2)}(k_i a_i)}{\hat{H}_n^{(1)\prime}(k_i a_i) + \frac{\tilde{d}_n^{(i)}}{\tilde{c}_n^{(i)}} \hat{H}_n^{(2)\prime}(k_i a_i)} \quad i = 2, 3, \dots, m \quad (7.4.84)$$

where $\epsilon_{m+1} = \epsilon$, $\mu_{m+1} = \mu$, and

$$\frac{d_n^{(i)}}{c_n^{(i)}} = - \frac{\hat{H}_n^{(1)}(k_i a_{i-1}) - \hat{R}_H^{(i-1)} \hat{H}_n^{(1)\prime}(k_i a_{i-1})}{\hat{H}_n^{(2)}(k_i a_{i-1}) - \hat{R}_H^{(i-1)} \hat{H}_n^{(2)\prime}(k_i a_{i-1})} \quad i = 2, 3, \dots, m \quad (7.4.85)$$

$$\frac{\tilde{d}_n^{(i)}}{\tilde{c}_n^{(i)}} = -\frac{\hat{H}_n^{(1)}(k_i a_{i-1}) - \hat{R}_E^{(i-1)} \hat{H}_n^{(1)\prime}(k_i a_{i-1})}{\hat{H}_n^{(2)}(k_i a_{i-1}) - \hat{R}_E^{(i-1)} \hat{H}_n^{(2)\prime}(k_i a_{i-1})} \quad i = 2, 3, \dots, m. \quad (7.4.86)$$

The starting values for this recursive calculation are $d_n^{(1)}/c_n^{(1)}$ and $\tilde{d}_n^{(1)}/\tilde{c}_n^{(1)}$, which depend on the innermost sphere (the first layer). If this layer is uniform (Fig. 7.16), $d_n^{(1)}/c_n^{(1)} = 1$ and $\tilde{d}_n^{(1)}/\tilde{c}_n^{(1)} = 1$, so that the field remains finite and continuous at the center. If this layer contains a perfectly conducting sphere having a radius of a_0 ($a_0 < a_1$), as illustrated in Figure 7.17, application of the boundary conditions $E_\theta^{(1)}|_{\rho=a_0} = 0$ and $E_\phi^{(1)}|_{\rho=a_0} = 0$ yields

$$\frac{d_n^{(1)}}{c_n^{(1)}} = -\frac{\hat{H}_n^{(1)\prime}(k_1 a_0)}{\hat{H}_n^{(2)\prime}(k_1 a_0)}, \quad \frac{\tilde{d}_n^{(1)}}{\tilde{c}_n^{(1)}} = -\frac{\hat{H}_n^{(1)}(k_1 a_0)}{\hat{H}_n^{(2)}(k_1 a_0)}. \quad (7.4.87)$$

Once $\hat{R}_H^{(m)}$ and $\hat{R}_E^{(m)}$ are calculated at the end of the recursive process, we apply the field continuity conditions at $r = a_m$ to find

$$j^{-n} \frac{2n+1}{n(n+1)} \hat{J}_n(ka) + a_n \hat{H}_n^{(2)}(ka) = \frac{\mu}{\mu_m} [c_n^{(m)} \hat{H}_n^{(1)}(k_m a_m) + d_n^{(m)} \hat{H}_n^{(2)}(k_m a_m)] \quad (7.4.88)$$

$$j^{-n} \frac{2n+1}{n(n+1)} \hat{J}'_n(ka) + a_n \hat{H}_n^{(2)\prime}(ka) = \frac{k}{k_m} [c_n^{(m)} \hat{H}_n^{(1)\prime}(k_m a_m) + d_n^{(m)} \hat{H}_n^{(2)\prime}(k_m a_m)] \quad (7.4.89)$$

$$j^{-n} \frac{2n+1}{n(n+1)} \hat{J}_n(ka) + b_n \hat{H}_n^{(2)}(ka) = \frac{k}{k_m} [\tilde{c}_n^{(m)} \hat{H}_n^{(1)}(k_m a_m) + \tilde{d}_n^{(m)} \hat{H}_n^{(2)}(k_m a_m)] \quad (7.4.90)$$

$$j^{-n} \frac{2n+1}{n(n+1)} \hat{J}'_n(ka) + b_n \hat{H}_n^{(2)\prime}(ka) = \frac{\mu}{\mu_m} [\tilde{c}_n^{(m)} \hat{H}_n^{(1)\prime}(k_m a_m) + \tilde{d}_n^{(m)} \hat{H}_n^{(2)\prime}(k_m a_m)]. \quad (7.4.91)$$

From these equations, we can solve for a_n and b_n , and the results are

$$a_n = -j^{-n} \frac{2n+1}{n(n+1)} \frac{\hat{J}_n(ka_m) - \hat{R}_H^{(m)} \hat{J}'_n(ka_m)}{\hat{H}_n^{(2)}(ka_m) - \hat{R}_H^{(m)} \hat{H}_n^{(2)\prime}(ka_m)} \quad (7.4.92)$$

$$b_n = -j^{-n} \frac{2n+1}{n(n+1)} \frac{\hat{J}_n(ka_m) - \hat{R}_E^{(m)} \hat{J}'_n(ka_m)}{\hat{H}_n^{(2)}(ka_m) - \hat{R}_E^{(m)} \hat{H}_n^{(2)\prime}(ka_m)}. \quad (7.4.93)$$

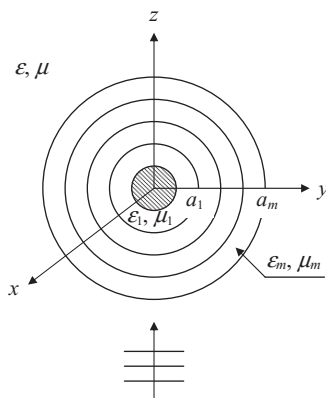


Figure 7.17 Plane wave scattering by a multilayer dielectric sphere containing a conducting core.

Once a_n and b_n are obtained, the scattered field can be calculated using Equations 7.4.32–7.4.39. If we are also interested in the fields inside the sphere, we can calculate the expansion coefficients $c_n^{(i)}$, $d_n^{(i)}$, $\tilde{c}_n^{(i)}$, and $\tilde{d}_n^{(i)}$ for each layer, starting from the m th layer, then the $(m - 1)$ th layer, and all the way back to the first layer, using the values of a_n and b_n and the ratios $d_n^{(i)}/c_n^{(i)}$ and $\tilde{d}_n^{(i)}/\tilde{c}_n^{(i)}$ calculated during the recursive process.

7.5 ADDITION THEOREM AND RADIATION ANALYSIS

In this section, we first derive the addition theorem for expanding an off-centered spherical wave in terms of spherical wave functions. We then deal with a few radiation problems in spherical coordinates, which include radiation by a spherical surface current in free space, in the presence of a conducting or dielectric sphere, and in the presence of a conducting cone.

7.5.1 Addition Theorem for Spherical Wave Functions

Consider a time-harmonic point charge q placed at \mathbf{r}' . The potential due to this charge satisfies Equation 2.1.33, which can be written as

$$\nabla^2 \varphi + k^2 \varphi = -\frac{q}{\epsilon} \delta(\mathbf{r} - \mathbf{r}'). \quad (7.5.1)$$

Based on the method discussed in Chapter 2, the solution to this equation is

$$\varphi(\mathbf{r}) = \frac{q}{4\pi\epsilon} \frac{e^{-jk|\mathbf{r}-\mathbf{r}'|}}{|\mathbf{r}-\mathbf{r}'|} \quad (7.5.2)$$

which reduces to a well-known result in electrostatics.

Now let us solve Equation 7.5.1 from a different perspective. We can regard this point charge as a spherical surface charge with a radius of r' and a surface charge density of

$$\rho_{e,s}(\mathbf{r}) = q \frac{\delta(\theta - \theta')\delta(\phi - \phi')}{r'^2 \sin \theta}. \quad (7.5.3)$$

The potential inside and outside the spherical surface charge satisfies the homogeneous Helmholtz equation

$$\nabla^2 \varphi + k^2 \varphi = 0 \quad r < r' \text{ or } r > r'. \quad (7.5.4)$$

The solution to this equation is derived in Section 7.1, which takes the form of Equation 7.1.17. To simplify the solution, let us further assume that the point charge is placed on the z -axis (Fig. 7.18) so that the potential is independent of ϕ ; hence, $m = 0$ and $\theta' = 0$. The solution to Equation 7.5.4 can be simplified as

$$\varphi(r, \theta, \phi) = \sum_{n=0}^{\infty} a_n \begin{cases} j_n(kr) h_n^{(2)}(kr') \\ j_n(kr') h_n^{(2)}(kr) \end{cases} P_n(\cos \theta) \quad \begin{cases} r < r' \\ r > r' \end{cases} \quad (7.5.5)$$

where we have enforced the continuity of the potential across the spherical surface charge. To determine a_n , we apply the boundary condition in Equation 1.5.7, which can be written as

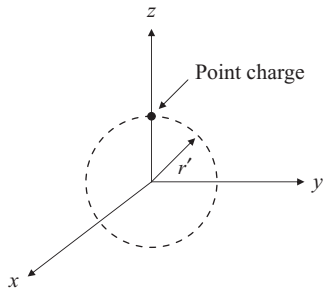


Figure 7.18 Point charge placed on the z -axis. The dashed line shows a fictitious spherical surface intersecting the point charge.

$$\varepsilon \frac{\partial \varphi}{\partial r} \Big|_{r=r'+0} - \varepsilon \frac{\partial \varphi}{\partial r} \Big|_{r=r'-0} = -\rho_{e,s} \Big|_{\theta'=0, \phi'=0}. \quad (7.5.6)$$

Substituting Equations 7.5.3 and 7.5.5 into Equation 7.5.6 and integrating over ϕ , we obtain

$$\sum_{n=0}^{\infty} a_n k \varepsilon [j_n(kr') h_n^{(2)\prime}(kr') - j'_n(kr') h_n^{(2)\prime}(kr')] P_n(\cos \theta) = -q \frac{\delta(\theta)}{2\pi r'^2 \sin \theta}. \quad (7.5.7)$$

This equation can be simplified by using the Wronskian relation for the spherical Bessel functions

$$j_n(z) h_n^{(2)\prime}(z) - j'_n(z) h_n^{(2)}(z) = -j [j_n(z) y'_n(z) - j'_n(z) y_n(z)] = -\frac{j}{z^2} \quad (7.5.8)$$

and the result is

$$\sum_{n=0}^{\infty} a_n P_n(\cos \theta) \sin \theta = -jkq \frac{\delta(\theta)}{2\pi \varepsilon}. \quad (7.5.9)$$

Now we multiply it by $P_m(\cos \theta)$, integrate over θ , and apply the orthogonal relation for the Legendre polynomials given in Equation 7.4.4 to find

$$a_n = -jkq \frac{2n+1}{4\pi \varepsilon} \int_0^\pi \delta(\theta) P_n(\cos \theta) d\theta = -jkq \frac{2n+1}{4\pi \varepsilon} \quad (7.5.10)$$

since $P_n(1) = 1$. Therefore, Equation 7.5.5 becomes

$$\varphi(r, \theta, \phi) = -\frac{jkq}{4\pi \varepsilon} \sum_{n=0}^{\infty} (2n+1) \begin{Bmatrix} j_n(kr) h_n^{(2)}(kr') \\ j_n(kr') h_n^{(2)}(kr) \end{Bmatrix} P_n(\cos \theta) \quad \begin{cases} r < r' \\ r > r' \end{cases} \quad (7.5.11)$$

which is valid for the point charge on the z -axis. If the point charge is located at an arbitrary point \mathbf{r}' , all we have to do is to replace θ by the angle between \mathbf{r} and \mathbf{r}' , or equivalently, to replace $\cos \theta$ by $\hat{\mathbf{r}} \cdot \hat{\mathbf{r}'}$. Hence, the solution is given by

$$\varphi(\mathbf{r}) = -\frac{jkq}{4\pi \varepsilon} \sum_{n=0}^{\infty} (2n+1) \begin{Bmatrix} j_n(kr) h_n^{(2)}(kr') \\ j_n(kr') h_n^{(2)}(kr) \end{Bmatrix} P_n(\hat{\mathbf{r}} \cdot \hat{\mathbf{r}'}) \quad \begin{cases} r < r' \\ r > r' \end{cases} \quad (7.5.12)$$

where $\hat{\mathbf{r}} \cdot \hat{\mathbf{r}'} = \cos \theta \cos \theta' + \sin \theta \sin \theta' \cos(\phi - \phi')$. Equation 7.5.12 is the solution to Equation 7.5.1 in terms of spherical wave functions.

Since the solution to a well-defined boundary-value problem is unique, Equation 7.5.12 should be the same as Equation 7.5.2. By equating the two solutions, we obtain

$$\frac{e^{-jk|\mathbf{r}-\mathbf{r}'|}}{|\mathbf{r}-\mathbf{r}'|} = -jk \sum_{n=0}^{\infty} (2n+1) \begin{cases} j_n(kr) h_n^{(2)}(kr') \\ j_n(kr') h_n^{(2)}(kr) \end{cases} P_n(\hat{r} \cdot \hat{r}') \quad \begin{cases} r < r' \\ r > r' \end{cases} \quad (7.5.13)$$

which is known as the *addition theorem* for spherical wave functions [7]. It expands a spherical wave originated at \mathbf{r}' as a superposition of an infinite number of spherical waves originated at the origin of the spherical coordinate system. Since $h_0^{(2)}(z) = je^{-jz}/z$, Equation 7.5.13 can also be written as

$$h_0^{(2)}(k|\mathbf{r}-\mathbf{r}'|) = \sum_{n=0}^{\infty} (2n+1) \begin{cases} j_n(kr) h_n^{(2)}(kr') \\ j_n(kr') h_n^{(2)}(kr) \end{cases} P_n(\hat{r} \cdot \hat{r}') \quad \begin{cases} r < r' \\ r > r' \end{cases} \quad (7.5.14)$$

Note that $P_n(\hat{r} \cdot \hat{r}')$ can be further expanded in terms of $P_n^m(\cos \theta)$ and $e^{jm\phi}$, resulting in an addition theorem in a more complicated form. Figure 7.19 shows how an off-centered spherical wave is formed by increasing the number of terms in Equation 7.5.14.

7.5.2 Radiation of a Spherical Surface Current

Now we consider the radiation by a spherical surface current whose radius is r' and whose surface current density is given by $\mathbf{J}_s = \hat{\phi} J_s(\theta)$, as illustrated in Figure 7.20. For simplicity, we assumed that the current has no variation in the azimuth direction. However, the treatment described below can be extended easily to deal with any azimuth variations. Because of this specific form of the current density, the radiated electric field has no radial component; hence, the radiated field is a TE _{r} wave. This field can be derived from Equations 7.1.27–7.1.29 with F_r given by

$$F_r = \sum_{n=0}^{\infty} \begin{cases} a_n \hat{J}_n(kr) \\ b_n \hat{H}_n^{(2)}(kr) \end{cases} P_n(\cos \theta) \quad \begin{cases} r < r' \\ r > r' \end{cases} \quad (7.5.15)$$

The non-zero transverse electric and magnetic field components are

$$E_\phi = \frac{1}{\epsilon r} \frac{\partial F_r}{\partial \theta} = \frac{1}{\epsilon r} \sum_{n=1}^{\infty} \begin{cases} a_n \hat{J}_n(kr) \\ b_n \hat{H}_n^{(2)}(kr) \end{cases} \frac{dP_n(\cos \theta)}{d\theta} \quad \begin{cases} r < r' \\ r > r' \end{cases} \quad (7.5.16)$$

$$H_\theta = \frac{1}{j\omega\mu\epsilon} \frac{1}{r} \frac{\partial^2 F_r}{\partial r \partial \theta} = \frac{k}{j\omega\mu\epsilon r} \sum_{n=1}^{\infty} \begin{cases} a_n \hat{J}'_n(kr) \\ b_n \hat{H}'_n^{(2)}(kr) \end{cases} \frac{dP_n(\cos \theta)}{d\theta} \quad \begin{cases} r < r' \\ r > r' \end{cases} \quad (7.5.17)$$

where the $n = 0$ term vanishes since $dP_0(\cos \theta)/d\theta = 0$. Applying the boundary conditions across the surface electric current, $E_\phi|_{r=r'+0} = E_\phi|_{r=r'-0}$ and $H_\theta|_{r=r'+0} - H_\theta|_{r=r'-0} = J_s(\theta)$, we find that

$$a_n \hat{J}_n(kr') = b_n \hat{H}_n^{(2)}(kr') \quad (7.5.18)$$

$$b_n \hat{H}'_n^{(2)}(kr') - a_n \hat{J}'_n(kr') = f_n \quad (7.5.19)$$

where

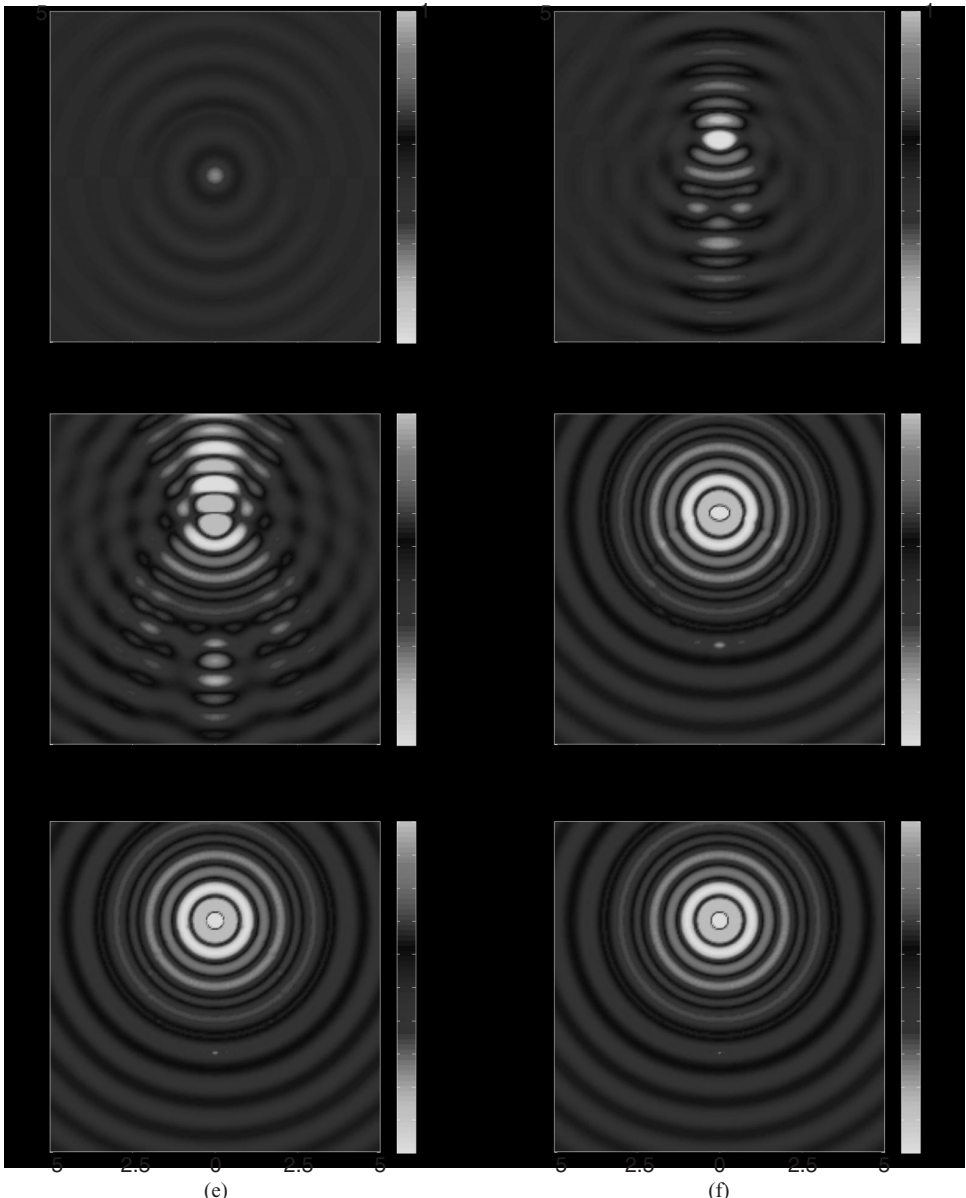


Figure 7.19 Illustration of the addition theorem for the spherical Hankel function. The plots show the real part of the right-hand side of Equation 7.5.14 in a $10\lambda \times 10\lambda$ region when the summation is evaluated from $n = 0$ to M . Clearly, an off-centered spherical wave is formed by increasing the number of terms in the summation. (a) $M = 1$. (b) $M = 5$. (c) $M = 10$. (d) $M = 20$. (e) $M = 40$. (f) $M = 80$. (See color insert.)

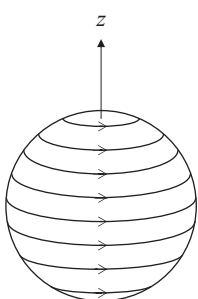


Figure 7.20 Axisymmetric spherical surface current in free space.

$$f_n = \frac{j\omega\mu\epsilon r'}{k} \frac{2n+1}{2n(n+1)} \int_0^\pi J_s(\theta) \frac{dP_n(\cos\theta)}{d\theta} \sin\theta d\theta. \quad (7.5.20)$$

In arriving at Equation 7.5.19, we applied the orthogonal relation [1]

$$\int_0^\pi \frac{dP_n(\cos\theta)}{d\theta} \frac{dP_m(\cos\theta)}{d\theta} \sin\theta d\theta = \begin{cases} 0 & n \neq m \\ \frac{2n(n+1)}{2n+1} & n = m. \end{cases} \quad (7.5.21)$$

From Equations 7.5.18 and 7.5.19, we can solve for a_n and b_n , and the results are

$$a_n = j\hat{H}_n^{(2)}(kr')f_n, \quad b_n = j\hat{J}_n(kr')f_n \quad (7.5.22)$$

where we have invoked the Wronskian relation (Eq. 7.5.8). Therefore, the non-zero field components generated by the spherical surface current are

$$E_\phi = \frac{j}{\epsilon r} \sum_{n=1}^{\infty} f_n \begin{Bmatrix} \hat{H}_n^{(2)}(kr') \hat{J}_n(kr) \\ \hat{J}_n(kr') \hat{H}_n^{(2)}(kr) \end{Bmatrix} \frac{dP_n(\cos\theta)}{d\theta} \quad \begin{array}{ll} r < r' \\ r > r' \end{array} \quad (7.5.23)$$

$$H_r = \frac{1}{\omega\mu\epsilon r^2} \sum_{n=1}^{\infty} n(n+1) f_n \begin{Bmatrix} \hat{H}_n^{(2)}(kr') \hat{J}_n(kr) \\ \hat{J}_n(kr') \hat{H}_n^{(2)}(kr) \end{Bmatrix} P_n(\cos\theta) \quad \begin{array}{ll} r < r' \\ r > r' \end{array} \quad (7.5.24)$$

$$H_\theta = \frac{k}{\omega\mu\epsilon r} \sum_{n=1}^{\infty} f_n \begin{Bmatrix} \hat{H}_n^{(2)}(kr') \hat{J}'_n(kr) \\ \hat{J}_n(kr') \hat{H}_n^{(2)\prime}(kr) \end{Bmatrix} \frac{dP_n(\cos\theta)}{d\theta} \quad \begin{array}{ll} r < r' \\ r > r' \end{array} \quad (7.5.25)$$

This field can also be regarded as a TE_{*z*} wave, which can be solved by using F_z instead of F_r . Since F_z satisfies the Helmholtz equation, its solution involves the regular spherical Bessel and Hankel functions instead of the Riccati–Bessel and Hankel functions. The final solution, however, should be the same. This solution is left for the reader as an exercise.

Now let us consider two interesting special cases. First, when $J_s(\theta) = J_0 \sin\theta$ with J_0 being a constant, Equation 7.5.20 can be evaluated to give

$$f_1 = -\frac{j\omega\mu\epsilon r'}{k} J_0, \quad f_n = 0 \quad n \neq 1. \quad (7.5.26)$$

The magnetic field inside the spherical surface current becomes

$$H_r = -\frac{j2r'}{kr^2} J_0 \hat{H}_1^{(2)}(kr') \hat{J}_1(kr) \cos\theta \quad (7.5.27)$$

$$H_\theta = \frac{jr'}{r} J_0 \hat{H}_1^{(2)}(kr') \hat{J}'_1(kr) \sin\theta. \quad (7.5.28)$$

At a very low frequency, we can employ the small-argument approximations in Equation 7.4.72 to find

$$H_r \approx \frac{2}{3} J_0 \cos\theta, \quad H_\theta \approx -\frac{2}{3} J_0 \sin\theta. \quad (7.5.29)$$

The resulting total magnetic field can be written as

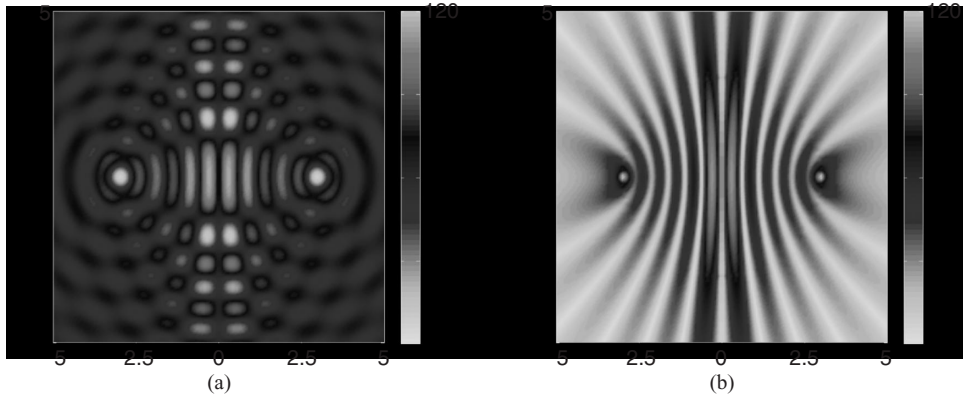


Figure 7.21 Field radiated by a circular current loop having a uniform current of 1 A and a radius of 3λ . (a) Snapshot of E_ϕ . (b) Magnitude of E_ϕ (See color insert.)

$$\mathbf{H} = \hat{r} H_r + \hat{\theta} H_\theta \approx \frac{2}{3} J_0 (\hat{r} \cos \theta - \hat{\theta} \sin \theta) = \hat{z} \frac{2}{3} J_0 \quad (7.5.30)$$

which is perfectly uniform when $kr' \rightarrow 0$. This result is very useful in applications that require a uniform magnetic field such as in the design of magnets for magnetic resonance imaging.

The second special case is when the spherical surface current is reduced to a horizontal current loop of radius a centered on the z -axis at $z = z_0$ and carrying current I_0 . In this case, the surface current density can be written as

$$J_s(\theta) = I_0 \frac{\delta(\theta - \theta')}{r'} \quad (7.5.31)$$

where $r' = \sqrt{z_0^2 + a^2}$ and $\theta' = \tan^{-1}(a/z_0)$. Substituting this into Equation 7.5.20, we have

$$f_n = \frac{j\omega\mu\epsilon I_0}{kr'} \left. \frac{2n+1}{2n(n+1)} \frac{dP_n(\cos \theta)}{d\theta} \right|_{\theta=\theta'} \quad (7.5.32)$$

In particular, if the current loop is placed in the xy -plane such that $z_0 = 0$ and $r' = a$, Equation 7.5.32 is reduced to

$$f_n = \begin{cases} \frac{j\omega\mu\epsilon I_0}{k} (-1)^{(n+1)/2} \frac{2n+1}{2} \frac{1 \cdot 3 \cdot 5 \cdots (n-2)}{2 \cdot 4 \cdot 6 \cdots (n+1)} & n = \text{odd} \\ 0 & n = \text{even} \end{cases} \quad (7.5.33)$$

where we have used the special values for $P'_n(0)$ [1]. Substituting Equation 7.5.32 or Equation 7.5.33 into Equations 7.5.23–7.5.25, we obtain accurate expressions for the field generated by a circular current loop placed at $z = z_0$ or $z = 0$. Figure 7.21 shows the field radiated by such a current loop with a radius of 3λ in the xz -plane.

7.5.3 Radiation in the Presence of a Sphere

If a conducting sphere of radius a is placed inside the spherical surface current, as illustrated in Figure 7.22a, we can treat the field produced by the spherical surface current in

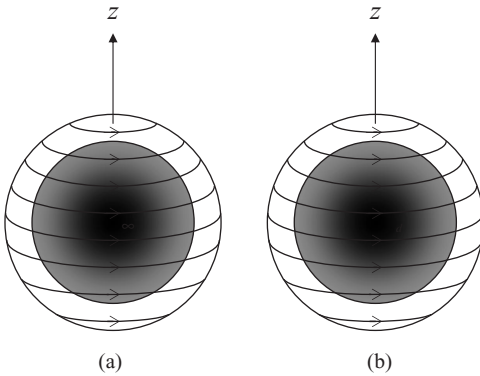


Figure 7.22 Spherical surface current loaded with a sphere. (a) A conducting core. (b) A dielectric core.

the absence of the conducting sphere as the incident field. This incident field induces a surface current on the conducting sphere, which radiates a field called the scattered field. To satisfy the boundary condition on the surface of the conducting sphere, based on the form of the incident field in Equation 7.5.23, the scattered electric field takes the form

$$E_{\phi}^{\text{sc}} = \frac{j}{\epsilon r} \sum_{n=1}^{\infty} c_n \hat{H}_n^{(2)}(kr) \frac{dP_n(\cos \theta)}{d\theta} \quad r > a. \quad (7.5.34)$$

Substituting this into the boundary condition $[E_{\phi}^{\text{inc}} + E_{\phi}^{\text{sc}}]_{r=a} = 0$, we obtain

$$c_n = -f_n \frac{\hat{J}_n(ka)}{\hat{H}_n^{(2)}(ka)} \hat{H}_n^{(2)}(kr'). \quad (7.5.35)$$

Hence, the total field is given by

$$E_{\phi} = \frac{j}{\epsilon r} \sum_{n=1}^{\infty} f_n \left[\left\{ \frac{\hat{H}_n^{(2)}(kr') \hat{J}_n(kr)}{\hat{J}_n(kr') \hat{H}_n^{(2)}(kr)} \right\} - \frac{\hat{J}_n(ka)}{\hat{H}_n^{(2)}(ka)} \hat{H}_n^{(2)}(kr') \hat{H}_n^{(2)}(kr) \right] \frac{dP_n(\cos \theta)}{d\theta} \quad \begin{cases} a < r < r' \\ r > r'. \end{cases} \quad (7.5.36)$$

If a dielectric sphere having a radius of a , a permittivity of ϵ_d , and a permeability of μ_d is placed inside the spherical surface current, as illustrated in Figure 7.22b, in addition to the scattered field, which can still be expressed by Equation 7.5.34, there is a field that penetrates into the interior of the dielectric sphere. This field has the form

$$E_{\phi}^{\text{int}} = \frac{j}{\epsilon_d r} \sum_{n=1}^{\infty} d_n \hat{J}_n(k_d r) \frac{dP_n(\cos \theta)}{d\theta} \quad r < a \quad (7.5.37)$$

where $k_d = \omega \sqrt{\mu_d \epsilon_d}$. The corresponding θ -components of the scattered and interior magnetic fields are given by

$$H_{\theta}^{\text{sc}} = \frac{k}{\omega \mu \epsilon r} \sum_{n=1}^{\infty} c_n \hat{H}_n^{(2)\prime}(kr) \frac{dP_n(\cos \theta)}{d\theta} \quad r > a \quad (7.5.38)$$

$$H_{\theta}^{\text{int}} = \frac{k_d}{\omega \mu_d \epsilon_d r} \sum_{n=1}^{\infty} d_n \hat{J}_n'(k_d r) \frac{dP_n(\cos \theta)}{d\theta} \quad r < a. \quad (7.5.39)$$

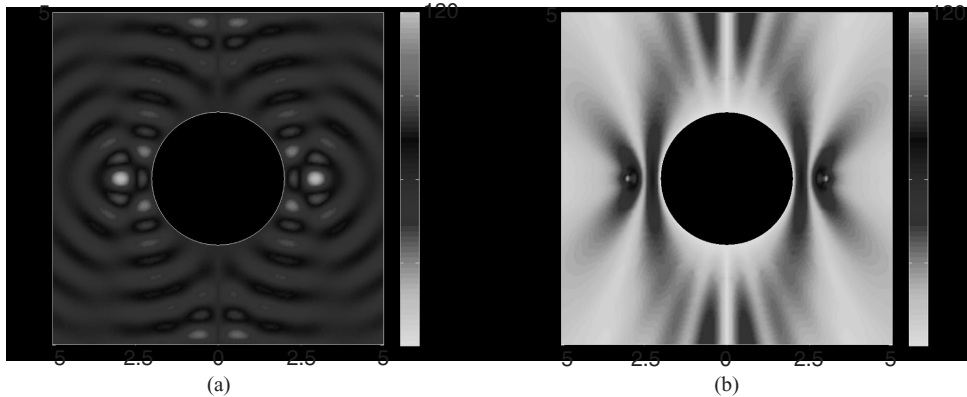


Figure 7.23 Field radiated by a circular current loop having a uniform current of 1 A and a radius of 3λ in the presence of a conducting sphere with a radius of 2λ . (a) Snapshot of E_ϕ . (b) Magnitude of E_ϕ . (See color insert.)

Applying the field continuity conditions

$$\left[E_\phi^{\text{inc}} + E_\phi^{\text{sc}} \right]_{r=a} = \left[E_\phi^{\text{int}} \right]_{r=a}, \quad \left[H_\theta^{\text{inc}} + H_\theta^{\text{sc}} \right]_{r=a} = \left[H_\theta^{\text{int}} \right]_{r=a} \quad (7.5.40)$$

and solving for c_n and d_n , we obtain

$$c_n = f_n \hat{H}_n^{(2)}(kr') \frac{\sqrt{\mu_r} \hat{J}'_n(ka) \hat{J}_n(k_d a) - \sqrt{\epsilon_r} \hat{J}_n(ka) \hat{J}'_n(k_d a)}{\sqrt{\epsilon_r} \hat{H}_n^{(2)}(ka) \hat{J}'_n(k_d a) - \sqrt{\mu_r} \hat{H}_n^{(2)\prime}(ka) \hat{J}_n(k_d a)} \quad (7.5.41)$$

$$d_n = f_n \hat{H}_n^{(2)}(kr') \frac{j \epsilon_r \sqrt{\mu_r}}{\sqrt{\epsilon_r} \hat{H}_n^{(2)}(ka) \hat{J}'_n(k_d a) - \sqrt{\mu_r} \hat{H}_n^{(2)\prime}(ka) \hat{J}_n(k_d a)} \quad (7.5.42)$$

where $\epsilon_r = \epsilon_d / \epsilon$ and $\mu_r = \mu_d / \mu$ denote the relative permittivity and permeability of the sphere with respect to the background.

As noted before, a current loop can be considered as a special spherical surface current. Hence, the solution above also provides the expressions for the field radiated by a current loop in the presence of a conducting or dielectric sphere. Furthermore, since a small electric current loop is equivalent to a magnetic dipole, the solution to radiation by a vertical magnetic dipole on the z -axis in the presence of a sphere can also be obtained. Figure 7.23 shows the field radiated by a circular current loop with a radius of 3λ in the presence of a conducting sphere having a radius of 2λ . The radiation is reduced significantly by the presence of the conducting sphere and its particular distance (1λ) from the current.

7.5.4 Radiation in the Presence of a Conducting Cone

As the last example to illustrate the solution of radiation in spherical coordinates, we consider an infinitely long conducting cone partially enclosed by an incomplete spherical magnetic surface current of radius r' , as illustrated in Figure 7.24. The internal half-angle of the cone is assumed to be θ_0 , and the magnetic surface current density is assumed to be $\mathbf{M}_s = \hat{\phi} M_s(\theta)$, which is axisymmetric to simplify the analysis. This current will radiate a TM_r wave, which can be constructed from A_r given by

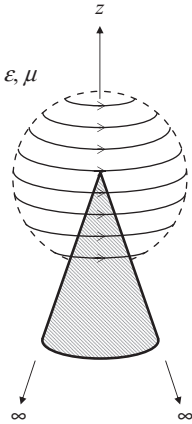


Figure 7.24 Spherical surface current radiating in the presence of an infinitely long conducting cone.

$$A_r = \sum_v \begin{cases} a_v \hat{J}_v(kr) \\ b_v \hat{H}_v^{(2)}(kr) \end{cases} P_v(\cos \theta) \quad \begin{cases} r < r' \\ r > r'. \end{cases} \quad (7.5.43)$$

The $P_v(\cos \theta)$ is used here because it is the only solution that is finite at $\theta = 0$. The corresponding non-zero field components can be obtained from Equations 7.1.30–7.1.32, and the results are

$$E_r = \frac{1}{j\omega\mu\epsilon r^2} \sum_v v(v+1) \begin{cases} a_v \hat{J}_v(kr) \\ b_v \hat{H}_v^{(2)}(kr) \end{cases} P_v(\cos \theta) \quad \begin{cases} r < r' \\ r > r'. \end{cases} \quad (7.5.44)$$

$$E_\theta = \frac{k}{j\omega\mu\epsilon r} \sum_v \begin{cases} a_v \hat{J}'_v(kr) \\ b_v \hat{H}'_v(kr) \end{cases} \frac{dP_v(\cos \theta)}{d\theta} \quad \begin{cases} r < r' \\ r > r'. \end{cases} \quad (7.5.45)$$

$$H_\phi = -\frac{1}{\mu r} \sum_v \begin{cases} a_v \hat{J}_v(kr) \\ b_v \hat{H}_v^{(2)}(kr) \end{cases} \frac{dP_v(\cos \theta)}{d\theta} \quad \begin{cases} r < r' \\ r > r'. \end{cases} \quad (7.5.46)$$

Application of the boundary condition $E_r|_{\theta=\pi-\theta_0} = 0$ yields the characteristic equation

$$P_v(-\cos \theta_0) = 0 \quad (7.5.47)$$

which can be used to determine the values of v . These characteristic values can be denoted as v_i ($i = 1, 2, \dots$). Applying the boundary conditions across the surface magnetic current, $H_\phi|_{r=r'+0} = H_\phi|_{r=r'-0}$ and $E_\theta|_{r=r'+0} - E_\theta|_{r=r'-0} = -M_s(\theta)$, we find that

$$a_{v_i} \hat{J}_{v_i}(kr') = b_{v_i} \hat{H}_{v_i}^{(2)}(kr') \quad (7.5.48)$$

$$b_{v_i} \hat{H}_{v_i}^{(2)\prime}(kr') - a_{v_i} \hat{J}'_{v_i}(kr') = g_{v_i} \quad (7.5.49)$$

where

$$g_{v_i} = -\frac{j\omega\mu\epsilon r'}{kN_{v_i}} \int_0^{\pi-\theta_0} M_s(\theta) \frac{dP_{v_i}(\cos \theta)}{d\theta} \sin \theta d\theta \quad (7.5.50)$$

$$N_{v_i} = -\frac{v_i(v_i+1)}{2v_i+1} \left[P'_{v_i}(\cos \theta) \frac{\partial P_{v_i}(\cos \theta)}{\partial v_i} \right]_{\theta=\pi-\theta_0}. \quad (7.5.51)$$

In arriving at Equation 7.5.49, we applied the orthogonal relation [4]

$$\int_0^{\pi-\theta_0} \frac{dP_{v_i}(\cos \theta)}{d\theta} \frac{dP_{v_j}(\cos \theta)}{d\theta} \sin \theta d\theta = \begin{cases} 0 & i \neq j \\ N_{v_i} & i = j. \end{cases} \quad (7.5.52)$$

From Equations 7.5.48 and 7.5.49, we can solve for a_{v_i} and b_{v_i} , and the results are

$$a_{v_i} = j\hat{H}_{v_i}^{(2)}(kr')g_{v_i}, \quad b_{v_i} = j\hat{J}_{v_i}(kr')g_{v_i} \quad (7.5.53)$$

where we have invoked the Wronskian relation for $\hat{J}_{v_i}(kr')$ and $\hat{H}_{v_i}^{(2)}(kr')$. Therefore, the non-zero field components become

$$E_r = \frac{1}{\omega\mu\epsilon r^2} \sum_{i=1}^{\infty} v_i(v_i+1) g_{v_i} \begin{cases} \hat{H}_{v_i}^{(2)}(kr')\hat{J}'_{v_i}(kr) \\ \hat{J}_{v_i}(kr')\hat{H}_{v_i}^{(2)}(kr) \end{cases} P_{v_i}(\cos \theta) \quad \begin{cases} r < r' \\ r > r' \end{cases} \quad (7.5.54)$$

$$E_\theta = \frac{k}{\omega\mu\epsilon r} \sum_{i=1}^{\infty} g_{v_i} \begin{cases} \hat{H}_{v_i}^{(2)}(kr')\hat{J}'_{v_i}(kr) \\ \hat{J}_{v_i}(kr')\hat{H}_{v_i}^{(2)}(kr) \end{cases} \frac{dP_{v_i}(\cos \theta)}{d\theta} \quad \begin{cases} r < r' \\ r > r' \end{cases} \quad (7.5.55)$$

$$H_\phi = -\frac{j}{\mu r} \sum_{i=1}^{\infty} g_{v_i} \begin{cases} \hat{H}_{v_i}^{(2)}(kr')\hat{J}_{v_i}(kr) \\ \hat{J}_{v_i}(kr')\hat{H}_{v_i}^{(2)}(kr) \end{cases} \frac{dP_{v_i}(\cos \theta)}{d\theta} \quad \begin{cases} r < r' \\ r > r' \end{cases} \quad (7.5.56)$$

As in the case discussed earlier, a magnetic current loop of radius a carrying current M_0 and residing on the z -axis at $z = z_0$ can be considered as a special surface current with the surface current density

$$M_s(\theta) = M_0 \frac{\delta(\theta - \theta')}{r'} \quad (7.5.57)$$

where $r' = \sqrt{z_0^2 + a^2}$ and $\theta' = \tan^{-1}(a/z_0)$. Substituting this into Equation 7.5.50, we have

$$g_{v_i} = -\frac{j\omega\mu\epsilon}{kN_{v_i}} \left[\sin \theta \frac{dP_{v_i}(\cos \theta)}{d\theta} \right]_{\theta=\theta'} \quad (7.5.58)$$

which can be used to evaluate the field produced by a magnetic current loop in the presence of a conducting cone. Since a small magnetic current loop is equivalent to an electric dipole, the solution to radiation by a vertical dipole along the z -axis in the presence of a conducting cone can also be obtained.

It is also interesting to examine the field at the tip of the conducting cone. From the basic property of $P_v(\cos \theta)$, we know that when $\theta_0 < \pi/2$, the first solution to Equation 7.5.47 has a value less than 1, that is, $v_i < 1$. Very close to the tip, $kr \ll 1$; hence,

$$\hat{J}_v(kr) \sim (kr)^{v+1}, \quad \hat{J}'_v(kr) \sim (kr)^v \quad kr \rightarrow 0. \quad (7.5.59)$$

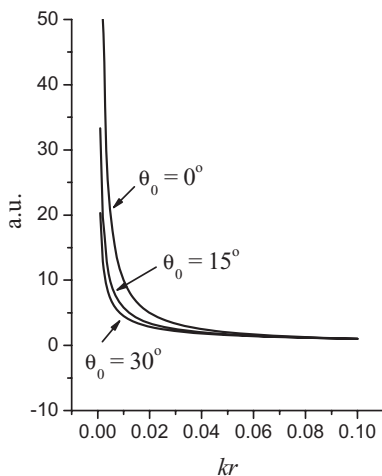


Figure 7.25 Field singularity (arbitrary unit) around the tip of a conducting cone.

Substituting this into Equations 7.5.54 and 7.5.55, we have

$$E_r, E_\theta \sim (kr)^{v_1-1} \quad kr \rightarrow 0 \quad (7.5.60)$$

which shows clearly that these two components are singular at the tip since $v_1 < 1$. A dual analysis shows that the magnetic field components H_r and H_θ have a similar singularity at the tip. Hence, the associated surface charge density and current density also exhibit such singularity. The degree of singularity depends on the internal angle of the cone. Specific values for various θ_0 are given by Van Bladel [9,10]. In particular, for $\theta_0 = 0$ (the case of a needle), the field has the highest degree of singularity and is proportional to $(kr)^{-1}$. When $\theta_0 \geq \pi/2$, the singularity disappears. Figure 7.25 plots the field singularity around the tip of a conducting cone for three different internal half-angles. Therefore, in most engineering applications it is critical to remove sharp conducting tips to avoid undesirable high field intensity.

REFERENCES

- [1] M. ABRAMOWITZ and I. A. STEGUN, Eds., *Handbook of Mathematical Functions*. New York: Dover, 1965.
- [2] S. J. ZHANG and J. M. JIN, *Computation of Special Functions*. New York: Wiley, 1996.
- [3] P. M. MORSE and H. FESHBACH, *Methods of Theoretical Physics*. New York: McGraw-Hill, 1953.
- [4] R. F. HARRINGTON, *Time-Harmonic Electromagnetic Fields*. New York: McGraw-Hill, 1961.
- [5] C. A. BALANIS, *Advanced Engineering Electromagnetics*. New York: Wiley, 1989.
- [6] S. A. SCHELKUNOFF, *Advanced Antenna Theory*. New York: Wiley, 1952.
- [7] J. A. STRATTON, *Electromagnetic Theory*. New York: McGraw-Hill, 1941.
- [8] J. J. BOWMAN, T. B. A. SENIOR, and P. L. E. USLENGHI, Eds., *Electromagnetic and Acoustic Scattering by Simple Shapes* (revised printing). New York: Hemisphere Publishing Corporation, 1987.
- [9] J. VAN BLADEL, *Electromagnetic Fields* (2nd edition). Hoboken, NJ: Wiley, 2007.
- [10] J. VAN BLADEL, *Singular Electromagnetic Fields and Sources*. New York: IEEE Press, 1996.

PROBLEMS

- 7.1. Consider an empty metallic spherical cavity of radius b loaded with a concentric solid metallic sphere of radius a . Find characteristic equations that determine the resonant frequencies of the TE_r and TM_r modes.
- 7.2. Consider an empty metallic hemispherical cavity of radius a , whose base coincides with the xy -plane (Fig. 7.26a). Find characteristic equations that determine the resonant frequencies of the TE_r and TM_r modes. Repeat the solution when the hemispherical cavity is placed vertically such that its base coincides with the xz -plane (Fig. 7.26b).
- 7.3. Calculate the quality factor for the dominant mode in a spherical cavity made of a good but imperfect conductor and filled with a good but imperfect dielectric.
- 7.4. Consider an empty, perfectly conducting circular cone whose internal half-angle is θ_0 , as illustrated in Figure 7.27a. This cone can be regarded as a non-uniform circular waveguide with a gradually increasing cross-section. Determine the waveguide modes supported by this structure. Repeat the analysis when the cone is flipped vertically, as shown in Figure 7.27b.
- 7.5. Consider an infinitely long metallic horn, shown in Figure 7.28, whose four conducting walls are placed at $\phi = 0$, $\phi = \phi_0$, $\theta = \theta_0$, and $\theta = 90^\circ$, respectively. Find the modal fields for the TE_r and the TM_r modes that propagate along the positive radial direction.
- 7.6. An infinite free space can be considered a spherical waveguide, where waveguide modes travel either inward or outward along the radial direction, even though there is no structure guiding the waves. Formulate both the TE_r and the TM_r modes and derive the wave impedances of the inward- and outward-traveling modes.

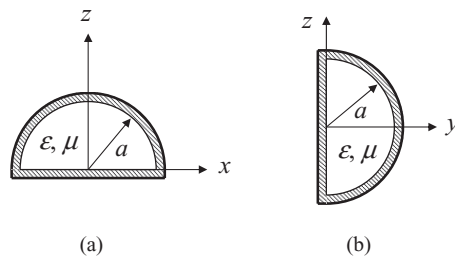


Figure 7.26 Hemispherical cavity. (a) Horizontally placed. (b) Vertically placed.

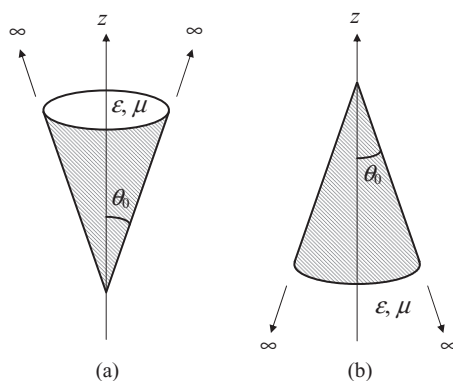


Figure 7.27 Infinitely long conducting cone as a non-uniform circular waveguide. (a) For waves propagating along the positive z -axis. (b) For waves propagating along the negative z -axis.

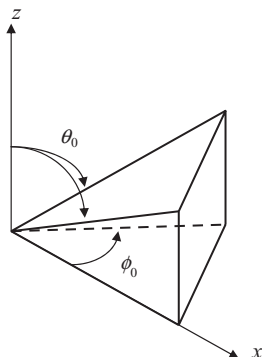


Figure 7.28 Infinitely long horn as a non-uniform waveguide.

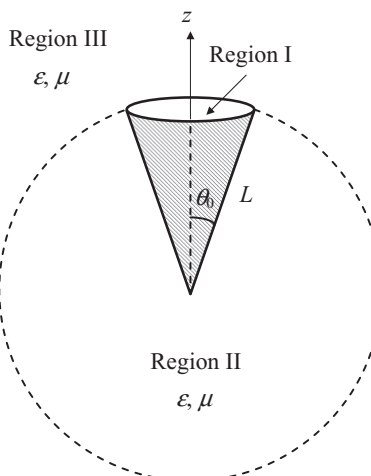


Figure 7.29 Finite circular horn antenna. The dashed line shows a fictitious spherical surface coinciding with the opening of the horn.

- 7.7. Consider a circular horn antenna that has a finite length of L and an internal half-angle of θ_0 (Fig. 7.29). A source placed inside the cone excites the dominant mode in the circular cone that propagates toward the opening. Formulate the solution for the fields in regions I, II, and III.
- 7.8. Derive the orthogonal relation given in Equation 7.4.4. (*Hint:* Apply the second scalar Green's theorem [Eq. 1.1.44] to a spherical surface and let a and b be spherical wave functions.)
- 7.9. Consider the problem of scattering of a plane wave by a conducting sphere of radius a coated with a layer of dielectric having a thickness of d , a permittivity of ϵ_d , and a permeability of μ_d . Find the scattered field and the radar cross-section.
- 7.10. Consider the problem of scattering of a plane wave by a conducting hemisphere placed on a ground plane that coincides with the xy -plane. Formulate the solution to the scattered field for a plane wave incident from above. Discuss how to solve this problem if a plane wave is incident from an arbitrary direction.
- 7.11. Consider the problem shown in Figure 7.20 and treated in Section 7.5.2. Since the field produced by the spherical surface current is also a TE_z wave, solve the problem using F_z and compare the solution with that given in Equations 7.5.23–7.5.25.

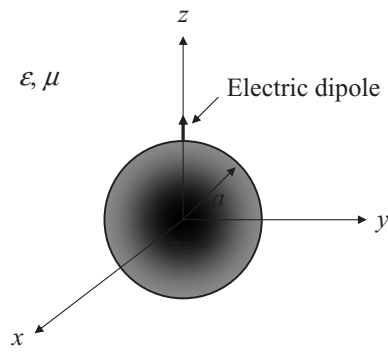


Figure 7.30 Electric dipole on the top of a conducting sphere.

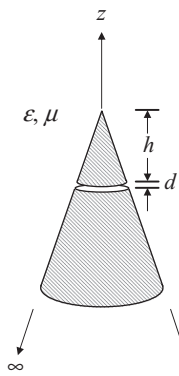


Figure 7.31 Slotted infinitely long conducting cone.

- 7.12. Derive the orthogonal relation given in Equation 7.5.52. (*Hint:* Apply the second scalar Green's theorem [Eq. 1.1.44] to the volume enclosed by the spherical surface shown by the dashed line in Figure 7.24 and use spherical wave functions for a and b .)
- 7.13. Consider an electric dipole placed vertically on the top of a conducting sphere of radius a (Fig. 7.30). Find the radiated field and calculate the radiation patterns for $a = 0.5\lambda$ and $a = 5\lambda$.
- 7.14. Consider an infinitely long, solid conducting cone that has a slot of width d and an internal half-angle of θ_0 , as illustrated in Figure 7.31. A time-harmonic voltage V of frequency ω is applied across the slot. Find the radiated field and calculate the radiation patterns for $d = 0.1\lambda$, $h = 2\lambda$, and $\theta_0 = 15^\circ$. ■

PART ***II***

*ELECTROMAGNETIC
FIELD COMPUTATION*

THE FINITE DIFFERENCE METHOD

Computational electromagnetics deals with the art and science of solving Maxwell's equations numerically using modern electronic computers. Thanks to the rapidly increasing capability of computers, computational electromagnetics has become a very important analytical tool in electromagnetics and radio-frequency (RF) and microwave engineering. The main reason is the predictive power of Maxwell's theory as proven over the years—Maxwell's theory can predict the design performances or experimental outcomes if Maxwell's equations are solved correctly. Moreover, Maxwell's theory, which governs the basic principles behind the manipulation of electricity, is also extremely pertinent in many electrical engineering and scientific technologies. Examples of these technologies are radar, remote sensing, geoelectromagnetics, bioelectromagnetics, antennas, wireless communication, optics, and high-frequency circuits. Furthermore, Maxwell's theory is valid over a broad range of frequencies, from static to optical, and over a large dynamic range of length-scales, from subatomic to intergalactic. Because of these, there is always a quest to solve Maxwell's equations accurately from first principles using numerical methods, so that increasingly complex problems can be analyzed.

After the establishment of Maxwell's theory in the 19th century, the early electromagnetic analyses were carried out for simple shapes such as spheres, cylinders, and planes. As the scientific and engineering demand for sophistication rose, solutions to more complex geometries were needed. As a result, approximate techniques were developed to solve Maxwell's equations. One can view circuit theory as a reduced form of Maxwell's theory in the low-frequency limit, where approximate analyses of many complex geometries have been obtained with astounding success. At the other end of the spectrum, high-frequency ray theory, diffraction theory, and perturbation theory were developed to provide approximate solutions to Maxwell's equations. With the advent of computer technology, numerical methods were developed in the 1960s to allow more versatility and accuracy in the solution methods. Among many numerical methods, the finite difference method, the finite element method, and the method of moments are the most predominant ones and together they form the core of computational electromagnetics.

The *finite difference method* (FDM) is a numerical procedure for converting partial differential equations (PDEs) of a boundary-value problem into a set of algebraic equations that can be used to compute an approximate solution to the boundary-value problem. Among all the numerical methods, the finite difference method is the oldest and also the simplest. Its simplicity, however, makes it very robust and efficient. The method has been widely used in a variety of engineering fields. Its application to the analysis of electromagnetic problems was empowered by the development of a unique scheme for the discretization of the time-domain Maxwell's equations [1], which is known today as the *finite*

difference time-domain (FDTD) method. With the further development, the FDTD became probably the most popular numerical technique for solving complex electromagnetic problems [2,3]. Indeed, one can quickly code the FDTD method for a specific problem and gain basic understanding of the underlying electromagnetic physics through numerical simulations.

In this chapter, we describe the basic principle of the finite difference method by first deriving basic finite differencing formulas and applying them to wave and diffusion equations. This is followed by the stability and dispersion analyses, which are two very critical issues in the finite difference method. After that, we introduce the FDTD method for solving Maxwell's equations in both two and three dimensions. Finally, we discuss how to truncate the computational domain for the analysis of open-region electromagnetic problems using absorbing boundary conditions (ABCs) and perfectly matched layers (PMLs).

8.1 FINITE DIFFERENCING FORMULAS

The basic idea of the finite difference method is to approximate the differentiation operators in the partial differential equations. This approximation can be obtained directly from the well-known definition of the derivatives. Consider a function $f(x)$ shown in Figure 8.1. If we wish to calculate its first derivative at x , we have three choices. The first is to increase x by a small value Δx and calculate the difference between the values of $f(x)$ at the two points. This yields

$$f'(x) = \frac{df}{dx} \approx \frac{f(x + \Delta x) - f(x)}{\Delta x} \quad (8.1.1)$$

which is called the *forward differencing formula*. Similarly, we can decrease x by a small value Δx to obtain

$$f'(x) = \frac{df}{dx} \approx \frac{f(x) - f(x - \Delta x)}{\Delta x} \quad (8.1.2)$$

which is called the *backward differencing formula*. The third choice is to take the average of Equations 8.1.1 and 8.1.2 to obtain

$$f'(x) = \frac{df}{dx} \approx \frac{f(x + \Delta x) - f(x - \Delta x)}{2\Delta x} \quad (8.1.3)$$

which is called the *central differencing formula*. The differencing formulas for the second derivative can be obtained by applying the differencing formulas above to the first derivative. This would lead to many differencing formulas for the second derivative because of

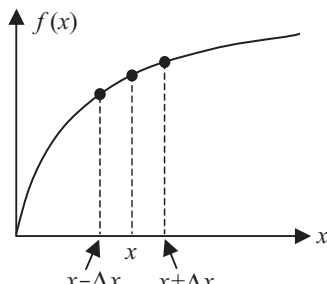


Figure 8.1 Finite difference approximation.

a variety of combinations. The most widely used formula is to apply the central differencing formula to the central-difference approximation of the first derivative

$$f''(x) = \frac{d^2 f}{dx^2} \approx \frac{f'(x + \Delta x/2) - f'(x - \Delta x/2)}{\Delta x} \quad (8.1.4)$$

which results in

$$f''(x) = \frac{d^2 f}{dx^2} \approx \frac{f(x + \Delta x) - 2f(x) + f(x - \Delta x)}{(\Delta x)^2}. \quad (8.1.5)$$

Clearly, all the differencing formulas are approximate representations of the derivatives. The accuracy of the approximation improves as the value of Δx decreases. However, these formulas do not provide a specific relation between the accuracy or the error and Δx . Because of this, we now derive these formulas using a different approach. We start with the Taylor series

$$f(x + \Delta x) = f(x) + f'(x)\Delta x + \frac{1}{2}f''(x)(\Delta x)^2 + \frac{1}{6}f'''(x)(\Delta x)^3 + \dots \quad (8.1.6)$$

from which we obtain

$$f'(x) = \frac{f(x + \Delta x) - f(x)}{\Delta x} + O(\Delta x) \quad (8.1.7)$$

where $O(\Delta x)$ denotes the sum of all the remaining terms containing $(\Delta x)^p$ with $p \geq 1$. It is now evident that the dominant error of the forward differencing formula is proportional to Δx ; hence, forward differencing is first-order accurate. Similarly, from the Taylor series

$$f(x - \Delta x) = f(x) - f'(x)\Delta x + \frac{1}{2}f''(x)(\Delta x)^2 - \frac{1}{6}f'''(x)(\Delta x)^3 + \dots \quad (8.1.8)$$

we obtain

$$f'(x) = \frac{f(x) - f(x - \Delta x)}{\Delta x} + O(\Delta x) \quad (8.1.9)$$

which indicates that the backward differencing formula is also first-order accurate. However, by subtracting Equation 8.1.8 from Equation 8.1.6, we obtain

$$f'(x) = \frac{f(x + \Delta x) - f(x - \Delta x)}{2\Delta x} + O[(\Delta x)^2] \quad (8.1.10)$$

which reveals that the central differencing formula is second-order accurate, a clear distinction between the central and other differencing formulas. If we sum Equations 8.1.6 and 8.1.8, we find

$$f''(x) = \frac{f(x + \Delta x) - 2f(x) + f(x - \Delta x)}{(\Delta x)^2} + O[(\Delta x)^2] \quad (8.1.11)$$

which indicates that central differencing for the second derivative is also second-order accurate. That is why Equation 8.1.5 is the most widely used differencing formula for the second derivative.

8.2 ONE-DIMENSIONAL ANALYSIS

To illustrate the application of finite differencing in the discretization of partial differential equations, we consider two one-dimensional examples. The first one is related to a diffusion equation, and the second is related to a wave equation.

8.2.1 Solution of the Diffusion Equation

When a medium is very lossy, such that the conduction current dominates the displacement current, we can neglect the displacement current to find that the electric field satisfies the following second-order partial differential equation:

$$\nabla \times \nabla \times \mathcal{E} + \mu\sigma \frac{\partial \mathcal{E}}{\partial t} = -\mu \frac{\partial \mathcal{J}_i}{\partial t}. \quad (8.2.1)$$

Assuming that both \mathcal{J}_i and \mathcal{E} have only the z -component and vary only in the x -direction, Equation 8.2.1 is reduced to

$$\frac{\partial^2 \mathcal{E}_z}{\partial x^2} - \mu\sigma \frac{\partial \mathcal{E}_z}{\partial t} = \mu \frac{\partial \mathcal{J}_z}{\partial t} \quad (8.2.2)$$

where the subscript i on \mathcal{J}_z is omitted for convenience. This kind of equation is called a *diffusion equation* or a *parabolic partial differential equation*.

To discretize Equation 8.2.2, we can first divide the solution domain along the x -axis into many small segments of equal length. Hence, x is discretized into a number of points and can be expressed as $x = i\Delta x$ with $i = 0, 1, 2, \dots, M$ (Fig. 8.2). Similarly, the time axis can be discretized into a number of uniformly distributed instants and can be represented as $t = n\Delta t$ with $n = 0, 1, 2, \dots, N$, where Δt denotes the time interval between two adjacent instants. With this uniform discretization in both space and time, $\mathcal{E}_z(x, t)$ can be written as

$$\mathcal{E}_z(x, t) = \mathcal{E}_z(i\Delta x, n\Delta t) = \mathcal{E}_z^n(i) \quad (8.2.3)$$

and other quantities can be expressed similarly. By applying central differencing to the second derivative about x and forward differencing to the first derivative in time, Equation 8.2.2 can be written as

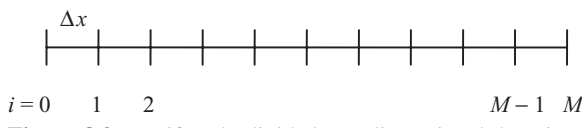


Figure 8.2 Uniformly divided one-dimensional domain.

$$\begin{aligned} & \frac{\mathcal{E}_z(x+\Delta x, t) - 2\mathcal{E}_z(x, t) + \mathcal{E}_z(x-\Delta x, t)}{(\Delta x)^2} - \mu\sigma \frac{\mathcal{E}_z(x, t+\Delta t) - \mathcal{E}_z(x, t)}{\Delta t} \\ &= \mu \frac{\mathcal{J}_z(x, t+\Delta t) - \mathcal{J}_z(x, t)}{\Delta t}. \end{aligned} \quad (8.2.4)$$

By using the compact notation introduced in Equation 8.2.3, this equation becomes

$$\frac{\mathcal{E}_z^n(i+1) - 2\mathcal{E}_z^n(i) + \mathcal{E}_z^n(i-1)}{(\Delta x)^2} - \mu\sigma \frac{\mathcal{E}_z^{n+1}(i) - \mathcal{E}_z^n(i)}{\Delta t} = \mu \frac{\mathcal{J}_z^{n+1}(i) - \mathcal{J}_z^n(i)}{\Delta t}. \quad (8.2.5)$$

Moving the most advanced field quantity to the left-hand side and keeping everything else on the right-hand side, we obtain

$$\mathcal{E}_z^{n+1}(i) = \mathcal{E}_z^n(i) + \frac{\Delta t}{\mu\sigma(\Delta x)^2} [\mathcal{E}_z^n(i+1) - 2\mathcal{E}_z^n(i) + \mathcal{E}_z^n(i-1)] - \frac{1}{\sigma} [\mathcal{J}_z^{n+1}(i) - \mathcal{J}_z^n(i)]. \quad (8.2.6)$$

A careful examination of this equation reveals that if we know the source information and the initial values of the field, say, at $n = 0$, we can use this equation to compute the field values at $n = 1$, then at $n = 2$, and so on until $n = N$. This process is called *time stepping* or *time marching*; hence, Equation 8.2.6 is called the *time-stepping formula*. Equation 8.2.6 is only first-order accurate because of the use of the forward differencing formula in time.

If we attempt to implement the time-stepping algorithm based on Equation 8.2.6, we encounter a difficulty in calculating the fields at the boundary of the solution domain, that is, at $x = 0$ and $x = M\Delta x$, because the calculation of $\mathcal{E}_z^{n+1}(0)$ and $\mathcal{E}_z^{n+1}(M)$ requires the values of $\mathcal{E}_z^n(-1)$ and $\mathcal{E}_z^n(M+1)$, respectively, both of which are outside the solution domain and are unknown. This difficulty arises because the description of the boundary-value problem considered here is incomplete; it lacks the necessary boundary conditions. The commonly encountered boundary conditions are the Dirichlet and Neumann conditions. The *Dirichlet condition* specifies the value of the field at the boundary. For the present example at $x = 0$, it can be expressed as

$$\mathcal{E}_z(x=0, t) = \phi(t). \quad (8.2.7)$$

With this condition, the field at the boundary is already known and needs no calculation. The *Neumann condition* prescribes the value of the normal derivative of the field at the boundary, and it can be expressed as

$$\left. \frac{\partial \mathcal{E}_z(x, t)}{\partial x} \right|_{x=0} = \psi(t). \quad (8.2.8)$$

This can be discretized using central differencing, and the result is

$$\mathcal{E}_z^n(-1) = \mathcal{E}_z^n(1) - 2\Delta x \psi^n \quad (8.2.9)$$

which can be used in the calculation of $\mathcal{E}_z^{n+1}(0)$. Other more complicated boundary conditions will be discussed later when we deal with ABCs.

8.2.2 Solution of the Wave Equation

When a medium is lossless, the electric field satisfies the following second-order partial differential equation:

$$\nabla \times \nabla \times \mathcal{E} + \mu\epsilon \frac{\partial^2 \mathcal{E}}{\partial t^2} = -\mu \frac{\partial \mathcal{J}_i}{\partial t}. \quad (8.2.10)$$

Assuming that both \mathcal{J}_i and \mathcal{E} have only the z -component and vary only in the x -direction, Equation 8.2.10 is reduced to

$$\frac{\partial^2 \mathcal{E}_z}{\partial x^2} - \mu\epsilon \frac{\partial^2 \mathcal{E}_z}{\partial t^2} = \mu \frac{\partial \mathcal{J}_z}{\partial t} \quad (8.2.11)$$

where the subscript i on \mathcal{J}_z is again omitted for convenience. This kind of equation is called a *wave equation* or a *hyperbolic partial differential equation*. The velocity of the wave propagation is given by $c = 1/\sqrt{\mu\epsilon}$.

By discretizing the spatial and time domains uniformly as described earlier and employing central differencing for both the spatial and the time derivatives, we can convert Equation 8.2.11 into

$$\begin{aligned} & \frac{\mathcal{E}_z^n(i+1) - 2\mathcal{E}_z^n(i) + \mathcal{E}_z^n(i-1)}{(\Delta x)^2} - \mu\epsilon \frac{\mathcal{E}_z^{n+1}(i) - 2\mathcal{E}_z^n(i) + \mathcal{E}_z^{n-1}(i)}{(\Delta t)^2} \\ &= \mu \frac{\mathcal{J}_z^{n+1}(i) - \mathcal{J}_z^{n-1}(i)}{2\Delta t} \end{aligned} \quad (8.2.12)$$

from which we obtain the second-order accurate time-stepping formula as

$$\begin{aligned} \mathcal{E}_z^{n+1}(i) &= 2\mathcal{E}_z^n(i) - \mathcal{E}_z^{n-1}(i) + \frac{(\Delta t)^2}{\mu\epsilon(\Delta x)^2} [\mathcal{E}_z^n(i+1) - 2\mathcal{E}_z^n(i) + \mathcal{E}_z^n(i-1)] \\ &\quad - \frac{\Delta t}{2\epsilon} [\mathcal{J}_z^{n+1}(i) - \mathcal{J}_z^{n-1}(i)]. \end{aligned} \quad (8.2.13)$$

With the knowledge of the source current, the initial values of the field, and the boundary conditions, we can use this equation to compute the field values step by step. Note that in this case, we need the initial values of the field at two time instants, say, at $n = 0$ and $n = 1$, because the partial differential equation contains the second derivative in time.

8.2.3 Stability Analysis

Based on the finite difference formulation for the solution of the diffusion and wave equations described above, it is clear that one has to choose proper values for Δx and Δt to carry out the computation. In general, Δx has to be small enough to resolve the spatial variation of the field, and Δt has to be small enough to resolve the temporal variation of the field. Typically, if the highest frequency of interest is f such that the corresponding wavelength is $\lambda = c/f$ and the period is $T = 1/f$, Δx and Δt should be chosen to satisfy $\Delta x < \lambda/20$ and $\Delta t < T/20$. Of course, the specific choice will be based on the specific problem and the desired accuracy. However, since the spatial and temporal variations of

a field are related, Δx and Δt may not be chosen independently. In fact, an improper choice can make the time-stepping process unstable, in which case the computed field grows exponentially and is completely non-physical. To find a proper choice for Δx and Δt , it is necessary to carry out a stability analysis on the time-stepping equation.

To illustrate the process of the stability analysis, we first consider Equation 8.2.6. If we discard the source term, the energy contained in the field over the solution domain should not increase with time, based on the law of energy conservation. In fact, the energy should decrease due to the loss in the medium. This observation provides the basis for the stability analysis. To examine the energy of the field, we first expand the field in terms of a Fourier series

$$\mathcal{O}_z^n(i) = \sum_{m=-\infty}^{\infty} A_m^n e^{jk_m i \Delta x}, \quad k_m = \frac{m\pi}{L} \quad (8.2.14)$$

where $L = M\Delta x$ denotes the length of the solution domain. It is well known that the energy of the field is proportional to the sum of the squares of the amplitudes of the Fourier modes. Hence, to ensure that the energy does not increase as n increases, we can simply check the amplitudes of the Fourier modes. To do this, we substitute Equation 8.2.14 into the source-free version of Equation 8.2.6 to find

$$A_m^{n+1} = (1 - 2r)A_m^n + r(e^{jk_m \Delta x} + e^{-jk_m \Delta x})A_m^n = \left[1 - 4r \sin^2\left(\frac{k_m \Delta x}{2}\right) \right] A_m^n \quad (8.2.15)$$

where $r = \Delta t / \mu\sigma(\Delta x)^2$. Next, we define an amplification factor g_m as

$$g_m = \frac{A_m^{n+1}}{A_m^n} = 1 - 4r \sin^2\left(\frac{k_m \Delta x}{2}\right) \quad (8.2.16)$$

and to satisfy the law of energy conservation, $|g_m| \leq 1$ for all k_m . From Equation 8.2.16, it is evident that the maximum value of g_m is 1 and the minimum value is $(1 - 4r)$. Hence, to ensure $|g_m| \leq 1$, we have

$$1 - 4r \geq -1 \quad \text{or} \quad r \leq \frac{1}{2} \quad (8.2.17)$$

which gives

$$\Delta t \leq \frac{1}{2} \mu\sigma(\Delta x)^2. \quad (8.2.18)$$

Under this condition, the energy of the field will not increase as n increases, and the time-stepping process will be stable. This condition is called the *stability condition* and because of its existence, the time-stepping process based on Equation 8.2.6 is called *conditionally stable*.

We can apply the same approach to the time-stepping formula in Equation 8.2.13 to find its stability condition. By substituting Equation 8.2.14 into the source-free version of Equation 8.2.13, we obtain

$$A_m^{n+1} = 2 \left[1 - 2r \sin^2\left(\frac{k_m \Delta x}{2}\right) \right] A_m^n - A_m^{n-1} \quad (8.2.19)$$

where $r = (\Delta t)^2 / \mu\epsilon(\Delta x)^2$. From Equation 8.2.19, we find

$$g_m^2 - 2\alpha_m g_m + 1 = 0, \quad \alpha_m = 1 - 2r \sin^2\left(\frac{k_m \Delta x}{2}\right). \quad (8.2.20)$$

Here, we assume that

$$g_m = \frac{A_m^{n+1}}{A_m^n} = \frac{A_m^n}{A_m^{n-1}}. \quad (8.2.21)$$

This is a valid assumption because the time-stepping formula is the same for each time step. The solution to Equation 8.2.20 is

$$g_m = \alpha_m \pm \sqrt{\alpha_m^2 - 1}. \quad (8.2.22)$$

It is obvious that $|g_m| \leq 1$ can be satisfied only if $\alpha_m^2 \leq 1$. In fact, when $\alpha_m^2 \leq 1$, $|g_m| = 1$; hence, the energy will remain as a constant. This is expected because the medium considered in Equation 8.2.13 is lossless. Since the maximum value of α_m is 1 and the minimum value is $(1 - 2r)$, the condition $\alpha_m^2 \leq 1$ can be satisfied only if

$$1 - 2r \geq -1 \quad \text{or} \quad r \leq 1 \quad (8.2.23)$$

which gives

$$\Delta t \leq \Delta x \sqrt{\mu\epsilon} = \frac{\Delta x}{c}. \quad (8.2.24)$$

Therefore, the time-stepping based on Equation 8.2.13 is also conditionally stable, and to ensure its stability, the chosen time-step size has to satisfy Equation 8.2.24.

An observant reader might have wondered earlier why central differencing was not used for the time derivative in Equation 8.2.2 to derive a second-order accurate time-stepping formula, which would become

$$\mathcal{C}_z^{n+1}(i) = \mathcal{C}_z^{n-1}(i) + \frac{2\Delta t}{\mu\sigma(\Delta x)^2} [\mathcal{C}_z^n(i+1) - 2\mathcal{C}_z^n(i) + \mathcal{C}_z^n(i-1)] - \frac{1}{\sigma} [\mathcal{J}_z^{n+1}(i) - \mathcal{J}_z^{n-1}(i)]. \quad (8.2.25)$$

However, if we carry out the stability analysis on this equation, we find

$$g_m^2 + 2\alpha_m g_m - 1 = 0, \quad \alpha_m = \frac{4\Delta t}{\mu\sigma(\Delta x)^2} \sin^2\left(\frac{k_m \Delta x}{2}\right) \quad (8.2.26)$$

whose solution is

$$g_m = -\alpha_m \pm \sqrt{\alpha_m^2 + 1}. \quad (8.2.27)$$

It is clear that no matter what value one chooses for α_m , there is at least one solution for which $|g_m| > 1$, making the time-stepping process of Equation 8.2.25 unstable. This example clearly demonstrates the importance of the stability analysis.

8.2.4 Numerical Dispersion Analysis

When the finite difference method is used to simulate wave propagation, the simulated wave propagates at a velocity slightly different from the exact velocity because of the numerical discretization. This results in an error in the phase of the wave solution. Such a phenomenon is called *numerical dispersion*, and the resultant error is called the *numerical phase error*. To quantify this error, we can assume a plane wave propagation on the finite difference grid and examine the numerical wavenumber based on the time-stepping formula. To show this, let us assume that a plane wave propagates in the x -direction, which can be analytically written as

$$\mathcal{E}_z(x, t) = \operatorname{Re} [E_0 e^{j(\omega t - kx)}] \quad (8.2.28)$$

where $k = \omega\sqrt{\mu\varepsilon}$. On the finite difference grid, the simulated wave can be expressed as

$$\mathcal{E}_z^n(i) = \operatorname{Re} [E_0 e^{j(\omega n\Delta t - \tilde{k}\Delta x)}] \quad (8.2.29)$$

where \tilde{k} denotes the numerical wavenumber. Substituting this into the source-free version of Equation 8.2.13, we obtain

$$\cos(\omega\Delta t) = (1 - r) + r \cos(\tilde{k}\Delta x) \quad (8.2.30)$$

where $r = (\Delta t)^2 / \mu\varepsilon(\Delta x)^2$. From this equation, we can calculate the numerical wavenumber as

$$\tilde{k} = \frac{1}{\Delta x} \cos^{-1} \left(1 - \frac{2}{r} \sin^2 \frac{\omega\Delta t}{2} \right) \quad (8.2.31)$$

and then examine its difference from the exact wavenumber. To obtain a more obvious expression, we can approximate the cosine functions in Equation 8.2.30 by the first three terms in their series expansion to find

$$k^2 - \frac{1}{12} k^2 (\omega\Delta t)^2 \approx \tilde{k}^2 - \frac{1}{12} \tilde{k}^2 (\tilde{k}\Delta x)^2 \quad (8.2.32)$$

or

$$\frac{\tilde{k} - k}{k} \approx \frac{1}{24} [(k\Delta x)^2 - (\omega\Delta t)^2]. \quad (8.2.33)$$

Apparently, if we choose $\Delta t = \Delta x\sqrt{\mu\varepsilon} = \Delta x/c$, the numerical wavenumber \tilde{k} will be the same as the exact wavenumber k . However, if we choose a different Δt , there will be a small difference between the two wavenumbers. For example, if we choose $\Delta t = 0.5\Delta x\sqrt{\mu\varepsilon}$, Equation 8.2.33 would become

$$\frac{\tilde{k} - k}{k} \approx \frac{1}{32} (k\Delta x)^2 = \frac{\pi^2}{8} \left(\frac{\Delta x}{\lambda} \right)^2 \quad (8.2.34)$$

where λ denotes the wavelength. In this case, as the wave propagates on the finite difference grid, it will have an error in its phase. This error can accumulate if the wave

propagates for a long time, and eventually it can corrupt the numerical solution. Equation 8.2.34 shows that this error decreases quadratically with $\Delta x/\lambda$, indicating that the solution converges in the second order. Therefore, this error can be controlled by reducing Δx .

In passing, we note that the one-dimensional wave propagation is a special problem because the propagation direction is fixed. In this case, we can always choose Δt properly to eliminate the phase error. The situation for the two- and three-dimensional cases is, however, drastically different in that the propagation direction is usually unknown and spatially dependent. It would no longer be possible to adjust Δt to eliminate the phase error. A numerical dispersion analysis is highly desirable, as it can shed light on how the phase error behaves given a certain finite difference discretization.

8.3 TWO-DIMENSIONAL ANALYSIS

Having practiced on one-dimensional examples, we now can proceed to slightly more complicated two-dimensional problems. We consider first the wave equation in the time domain and then discuss the finite difference method for the analysis of time-harmonic fields.

8.3.1 Analysis in the Time Domain

Consider a problem in which both the source and medium are uniform along the z -axis; hence, the field generated has no variation along the z -direction either. If the source is electric current flowing in the z -direction, it will generate an electric field with only a z -component. The second-order differential equation for the electric field in a general case is

$$\nabla \times \nabla \times \mathcal{E} + \mu\epsilon \frac{\partial^2 \mathcal{E}}{\partial t^2} + \mu\sigma \frac{\partial \mathcal{E}}{\partial t} = -\mu \frac{\partial \mathcal{J}_i}{\partial t}. \quad (8.3.1)$$

For the two-dimensional case described above, it reduces to

$$\frac{\partial^2 \mathcal{E}_z}{\partial x^2} + \frac{\partial^2 \mathcal{E}_z}{\partial y^2} - \mu\epsilon \frac{\partial^2 \mathcal{E}_z}{\partial t^2} - \mu\sigma \frac{\partial \mathcal{E}_z}{\partial t} = \mu \frac{\partial \mathcal{J}_z}{\partial t}. \quad (8.3.2)$$

In this case, we can first enclose the solution domain in a rectangular box and divide the box into many small rectangles with a size of $\Delta x \times \Delta y$ (Fig. 8.3). A grid point can be specified by two integers (i, j) . Then, by applying central differencing to Equation 8.3.2, we obtain

$$\begin{aligned} & \frac{\mathcal{E}_z^n(i+1, j) - 2\mathcal{E}_z^n(i, j) + \mathcal{E}_z^n(i-1, j)}{(\Delta x)^2} + \frac{\mathcal{E}_z^n(i, j+1) - 2\mathcal{E}_z^n(i, j) + \mathcal{E}_z^n(i, j-1)}{(\Delta y)^2} \\ & - \mu\epsilon_{ij} \frac{\mathcal{E}_z^{n+1}(i, j) - 2\mathcal{E}_z^n(i, j) + \mathcal{E}_z^{n-1}(i, j)}{(\Delta t)^2} - \mu\sigma_{ij} \frac{\mathcal{E}_z^{n+1}(i, j) - \mathcal{E}_z^{n-1}(i, j)}{2\Delta t} \\ & = \mu \frac{\mathcal{J}_z^{n+1}(i, j) - \mathcal{J}_z^{n-1}(i, j)}{2\Delta t} \end{aligned} \quad (8.3.3)$$

where ϵ_{ij} and σ_{ij} denote the values of ϵ and σ at the grid point (i, j) and μ is assumed to be constant. This yields the time-stepping formula given by

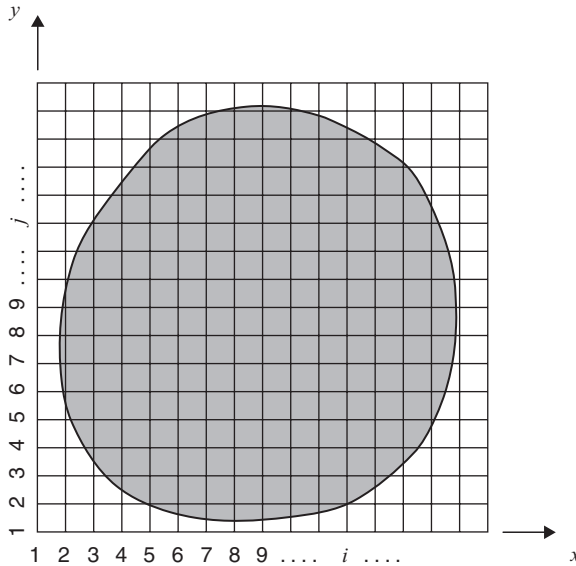


Figure 8.3 Finite difference mesh of a two-dimensional domain.

$$\begin{aligned} \mathcal{C}_z^{n+1}(i, j) = & \left[\frac{\mu\sigma_{ij}}{2\Delta t} + \frac{\mu\varepsilon_{ij}}{(\Delta t)^2} \right]^{-1} \left\{ 2\mathcal{C}_z^n(i, j) \left[\frac{\mu\varepsilon_{ij}}{(\Delta t)^2} - \frac{1}{(\Delta x)^2} - \frac{1}{(\Delta y)^2} \right] \right. \\ & + \mathcal{C}_z^{n-1}(i, j) \left[\frac{\mu\sigma_{ij}}{2\Delta t} - \frac{\mu\varepsilon_{ij}}{(\Delta t)^2} \right] + \frac{1}{(\Delta x)^2} [\mathcal{C}_z^n(i+1, j) + \mathcal{C}_z^n(i-1, j)] \\ & \left. + \frac{1}{(\Delta y)^2} [\mathcal{C}_z^n(i, j+1) + \mathcal{C}_z^n(i, j-1)] - \frac{\mu}{2\Delta t} [\mathcal{J}_z^{n+1}(i, j) - \mathcal{J}_z^{n-1}(i, j)] \right\}. \quad (8.3.4) \end{aligned}$$

With the information about the source, initial conditions, and boundary conditions, this formula can be used to compute the field at each grid point for a new time step by step.

The stability analysis of Equation 8.3.4 is straightforward, although much more tedious. Ignoring the loss, it would yield the following stability condition:

$$\Delta t \leq \frac{\sqrt{\mu\varepsilon}}{\sqrt{\frac{1}{(\Delta x)^2} + \frac{1}{(\Delta y)^2}}} = \frac{1}{c\sqrt{\frac{1}{(\Delta x)^2} + \frac{1}{(\Delta y)^2}}}. \quad (8.3.5)$$

If the medium is inhomogeneous, one should use the smallest value for ε in the choice of Δt . One can also perform the numerical dispersion analysis to find

$$\left[\frac{1}{c\Delta t} \sin \frac{\omega\Delta t}{2} \right]^2 = \left[\frac{1}{\Delta x} \sin \frac{\tilde{k}_x \Delta x}{2} \right]^2 + \left[\frac{1}{\Delta y} \sin \frac{\tilde{k}_y \Delta y}{2} \right]^2 \quad (8.3.6)$$

which can be approximated to yield

$$\frac{\tilde{k} - k}{k} \approx \frac{1}{24} [(k\Delta x)^2 \cos^4 \phi^i + (k\Delta y)^2 \sin^4 \phi^i - (\omega\Delta t)^2] \quad (8.3.7)$$

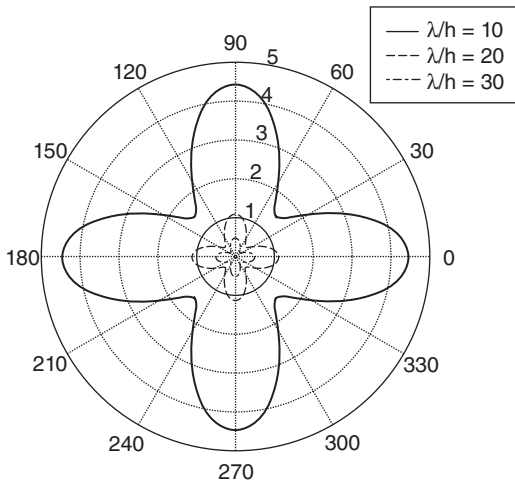


Figure 8.4 Numerical phase error in degrees per wavelength as a function of the wave propagation direction.

where ϕ^i denotes the propagation angle with the x -axis. In contrast to the one-dimensional case, there is no magical choice for Δt that can eliminate this error in all directions. If we choose $\Delta x = \Delta y = h$ and $\Delta t = 0.5h/c$, Equation 8.3.7 becomes

$$\frac{\tilde{k} - k}{k} \approx \frac{(kh)^2}{24} \left[\cos^4 \phi^i + \sin^4 \phi^i - \frac{1}{4} \right] = \frac{\pi^2}{24} \left(\frac{h}{\lambda} \right)^2 [2 + \cos(4\phi^i)]. \quad (8.3.8)$$

Clearly, this phase error is a function of the propagation angle, and it is smallest when the angle is in the diagonal direction. This error is plotted in Figure 8.4 for $\lambda/h=10$, $\lambda/h=20$, and $\lambda/h=30$.

8.3.2 Analysis in the Frequency Domain

The finite difference method can also be applied to solving Maxwell's equations in the frequency domain. The frequency-domain counterpart of Equation 8.3.2 can be written as

$$\frac{\partial^2 E_z}{\partial x^2} + \frac{\partial^2 E_z}{\partial y^2} + k^2 \epsilon_c E_z = g \quad (8.3.9)$$

where $g = j\omega\mu J_z$ and $\epsilon_c = 1 - j\sigma/\omega\epsilon$, which may be a function of position. By using the central differencing, this equation can be converted into

$$\begin{aligned} & \frac{E_z(i+1, j) - 2E_z(i, j) + E_z(i-1, j)}{(\Delta x)^2} + \frac{E_z(i, j+1) - 2E_z(i, j) + E_z(i, j-1)}{(\Delta y)^2} \\ & + k^2 \epsilon_{c,ij} E_z(i, j) = g(i, j). \end{aligned} \quad (8.3.10)$$

An equation like this can be written for every grid point whose field value is to be computed. As a result, we obtain a set of linear equations that must be solved simultaneously for the field values at the grid points with the aid of the boundary conditions. There are two ways to solve this linear system of equations. One is to use the Gaussian elimination method. Since the coefficient matrix in this system is very sparse—there are at most five

non-zero entries in each row, no matter how large the system dimension is—solvers that can exploit this sparsity should be used. The second way is to use an iterative method such as the Gauss–Seidel method to seek an approximate solution. In this method, we first set all $E_z(i, j)$ to zero, that is, $E_z^{(0)}(i, j) = 0$. Then, we calculate a new set of values for $E_z(i, j)$ using Equation 8.3.10, or more specifically,

$$\begin{aligned} E_z^{(l+1)}(i, j) = & \left[\frac{2}{(\Delta x)^2} + \frac{2}{(\Delta y)^2} - k^2 \epsilon_{c,ij} \right]^{-1} \left\{ \frac{1}{(\Delta x)^2} [E_z^{(l)}(i+1, j) + E_z^{(l)}(i-1, j)] \right. \\ & \left. + \frac{1}{(\Delta y)^2} [E_z^{(l)}(i, j+1) + E_z^{(l)}(i, j-1)] - g(i, j) \right\} \end{aligned} \quad (8.3.11)$$

for $l = 0$. Here, we use the superscript l to denote the iteration number. This process can be repeated until convergence is achieved, that is, the values of $E_z(i, j)$ do not change any more as l increases. The convergence of this iterative solution can be improved by using the successive over-relaxation scheme, which iterates based on

$$E_z^{(l+1)}(i, j) = E_z^{(l)}(i, j) + \frac{\omega}{4} R^{(l)}(i, j) \quad (8.3.12)$$

where $R^{(l)}(i, j)$ denotes the residue of Equation 8.3.11 at the l th iteration and ω is the relaxation factor chosen according to $1 < \omega < 2$. More advanced iterative solvers, such as those based on the Krylov subspace method, can also be employed to solve the linear system of equations formed by Equation 8.3.10.

8.4 YEE'S FDTD SCHEME

Although the finite difference approach described in Section 8.3 can be readily adopted for three-dimensional analyses, one would encounter several serious difficulties in doing so, all because in that approach the field is sampled at grid points. When a grid point resides on an interface between two different media, one must enforce the tangential continuity of the field, which is found to be rather tedious. More seriously, when a grid point resides on an edge or corner of a conductor or dielectric, the field is undefined because of the field singularity. A unique discretization scheme, developed by Yee in 1966 [1], successfully overcame all these difficulties.

8.4.1 Two-Dimensional Analysis

Let us reconsider the two-dimensional electromagnetic problem with a source $\mathcal{J}_i = \hat{z}\mathcal{J}_z$. Maxwell's equations for this problem can be reduced to

$$\frac{\partial \mathcal{E}_z}{\partial y} = -\mu \frac{\partial \mathcal{H}_x}{\partial t} \quad (8.4.1)$$

$$\frac{\partial \mathcal{E}_z}{\partial x} = \mu \frac{\partial \mathcal{H}_y}{\partial t} \quad (8.4.2)$$

$$\frac{\partial \mathcal{H}_y}{\partial x} - \frac{\partial \mathcal{H}_x}{\partial y} = \epsilon \frac{\partial \mathcal{E}_z}{\partial t} + \sigma \mathcal{E}_z + \mathcal{J}_z \quad (8.4.3)$$

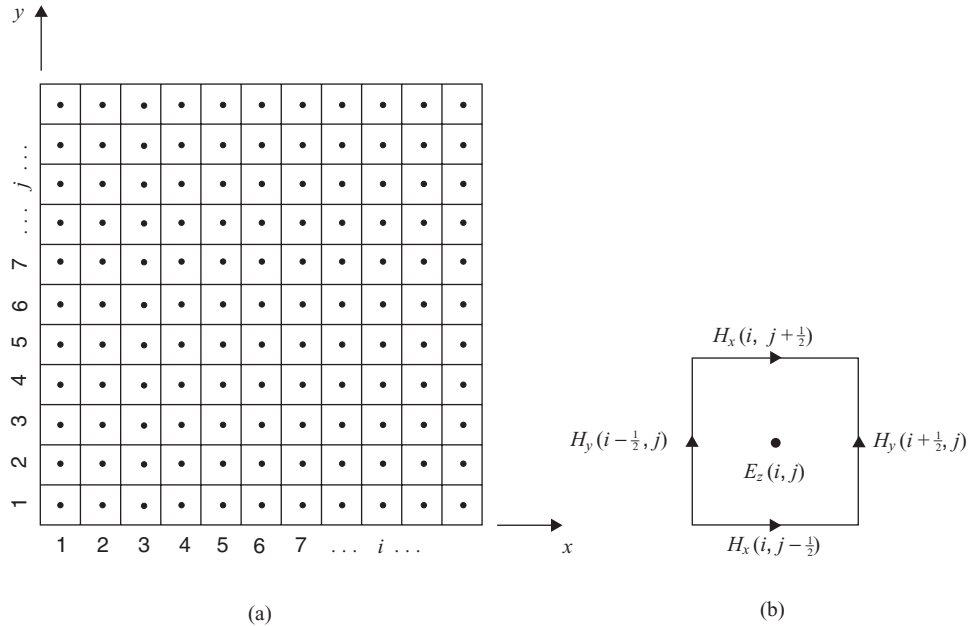


Figure 8.5 (a) Finite difference mesh for Yee's FDTD algorithm. (b) Assignment of field components on an FDTD cell.

To solve for $(\mathcal{E}_z, \mathcal{H}_x, \mathcal{H}_y)$, we again enclose the solution region in a rectangular area and then divide the rectangular area uniformly into many small rectangular cells, as illustrated in Figure 8.5a. The center of each cell is denoted by two integers (i, j) , where \mathcal{E}_z is sampled. The magnetic field components are sampled along the edges of the cells, as shown in Figure 8.5b. By sampling the electric field at $t = n\Delta t$ and the magnetic field at $t = (n + \frac{1}{2})\Delta t$ and using central differencing, Equation 8.4.1 can be discretized as

$$\frac{\mathcal{E}_z^n(i, j+1) - \mathcal{E}_z^n(i, j)}{\Delta y} = -\mu \frac{\mathcal{H}_x^{n+1/2}(i, j + \frac{1}{2}) - \mathcal{H}_x^{n-1/2}(i, j + \frac{1}{2})}{\Delta t} \quad (8.4.4)$$

from which we obtain

$$\mathcal{H}_x^{n+1/2}(i, j + \frac{1}{2}) = \mathcal{H}_x^{n-1/2}(i, j + \frac{1}{2}) - \frac{\Delta t}{\mu \Delta y} [\mathcal{E}_z^n(i, j+1) - \mathcal{E}_z^n(i, j)]. \quad (8.4.5)$$

Similarly, from Equations 8.4.2 and 8.4.3, we obtain

$$\mathcal{H}_y^{n+1/2}(i + \frac{1}{2}, j) = \mathcal{H}_y^{n-1/2}(i + \frac{1}{2}, j) + \frac{\Delta t}{\mu \Delta x} [\mathcal{E}_z^n(i+1, j) - \mathcal{E}_z^n(i, j)] \quad (8.4.6)$$

$$\begin{aligned} \mathcal{E}_z^{n+1}(i, j) = & \frac{1}{\beta(i, j)} \left\{ \alpha(i, j) \mathcal{E}_z^n(i, j) + \frac{1}{\Delta x} [\mathcal{H}_y^{n+1/2}(i + \frac{1}{2}, j) - \mathcal{H}_y^{n+1/2}(i - \frac{1}{2}, j)] \right. \\ & \left. - \frac{1}{\Delta y} [\mathcal{H}_x^{n+1/2}(i, j + \frac{1}{2}) - \mathcal{H}_x^{n+1/2}(i, j - \frac{1}{2})] - \mathcal{J}_z^{n+1/2}(i, j) \right\} \end{aligned} \quad (8.4.7)$$

where

$$\alpha = \frac{\epsilon}{\Delta t} - \frac{\sigma}{2} \quad \text{and} \quad \beta = \frac{\epsilon}{\Delta t} + \frac{\sigma}{2}. \quad (8.4.8)$$

Hence, given the initial values for \mathcal{E}_z , \mathcal{H}_x , and \mathcal{H}_y and proper boundary conditions, we can use Equations 8.4.5 and 8.4.6 to calculate \mathcal{H}_x and \mathcal{H}_y and then use Equation 8.4.7 to calculate \mathcal{E}_z . It is interesting to observe that in this scheme, the spatial grids for the electric and the magnetic fields are offset by a half grid point and the temporal sampling points are also offset by a half time step. More importantly, the magnetic field components are assigned along the edges of the rectangular cells according to the edge direction: \mathcal{H}_x is assigned to the edges parallel to x and \mathcal{H}_y is assigned to the edges parallel to y . Such an assignment makes the field uniquely defined and automatically ensures the tangential continuity of the fields. It can be shown that the stability condition for this scheme is the same as given in Equation 8.3.5 and the numerical dispersion error is the same as given in Equation 8.3.8. The time-stepping process based on Equations 8.4.5–8.4.7 is also called *leapfrog time integration*.

Note that Equations 8.4.5–8.4.7 can also be derived directly from Maxwell's equations in integral form without using the finite differencing formulas. This is left to the reader as an exercise.

8.4.2 Three-Dimensional Analysis

The extension from two to three dimensions is rather straightforward with Yee's algorithm. Consider Maxwell's equations in the time domain:

$$\nabla \times \mathcal{E} = -\mu \frac{\partial \mathcal{H}}{\partial t} \quad (8.4.9)$$

$$\nabla \times \mathcal{H} = \epsilon \frac{\partial \mathcal{E}}{\partial t} + \sigma \mathcal{E} + \mathcal{J}_r \quad (8.4.10)$$

These two vector equations can be written as six scalar equations given by

$$\frac{\partial \mathcal{E}_z}{\partial y} - \frac{\partial \mathcal{E}_y}{\partial z} = -\mu \frac{\partial \mathcal{H}_x}{\partial t} \quad (8.4.11)$$

$$\frac{\partial \mathcal{E}_x}{\partial z} - \frac{\partial \mathcal{E}_z}{\partial x} = -\mu \frac{\partial \mathcal{H}_y}{\partial t} \quad (8.4.12)$$

$$\frac{\partial \mathcal{E}_y}{\partial x} - \frac{\partial \mathcal{E}_x}{\partial y} = -\mu \frac{\partial \mathcal{H}_z}{\partial t} \quad (8.4.13)$$

$$\frac{\partial \mathcal{H}_z}{\partial y} - \frac{\partial \mathcal{H}_y}{\partial z} = \epsilon \frac{\partial \mathcal{E}_x}{\partial t} + \sigma \mathcal{E}_x + \mathcal{J}_x \quad (8.4.14)$$

$$\frac{\partial \mathcal{H}_x}{\partial z} - \frac{\partial \mathcal{H}_z}{\partial x} = \epsilon \frac{\partial \mathcal{E}_y}{\partial t} + \sigma \mathcal{E}_y + \mathcal{J}_y \quad (8.4.15)$$

$$\frac{\partial \mathcal{H}_y}{\partial x} - \frac{\partial \mathcal{H}_x}{\partial y} = \epsilon \frac{\partial \mathcal{E}_z}{\partial t} + \sigma \mathcal{E}_z + \mathcal{J}_z \quad (8.4.16)$$

To solve these equations for the electric and magnetic fields in a volume V , we enclose the volume V in a rectangular box and then divide the box into many small rectangular cells, as shown in Figure 8.6a. We then assign the electric field components at the center of each edge of the cells and the magnetic field components at the center of each face of the cells, as illustrated in Figure 8.6b. If the entire grid is offset by one-half of a cell in each direction, then on this dual grid the magnetic field components would reside at the center of each edge of the cells and the electric field components would reside at the center of each face of the cells. By using the central differencing scheme, Equations 8.4.11–8.4.13 can be converted into

$$\begin{aligned}\mathcal{H}_x^{n+1/2}(i, j + \frac{1}{2}, k + \frac{1}{2}) &= \mathcal{H}_x^{n-1/2}(i, j + \frac{1}{2}, k + \frac{1}{2}) - \frac{\Delta t}{\mu \Delta y} [\mathcal{E}_z^n(i, j + 1, k + \frac{1}{2}) - \mathcal{E}_z^n(i, j, k + \frac{1}{2})] \\ &\quad + \frac{\Delta t}{\mu \Delta z} [\mathcal{E}_y^n(i, j + \frac{1}{2}, k + 1) - \mathcal{E}_y^n(i, j + \frac{1}{2}, k)]\end{aligned}\quad (8.4.17)$$

$$\begin{aligned}\mathcal{H}_y^{n+1/2}(i + \frac{1}{2}, j, k + \frac{1}{2}) &= \mathcal{H}_y^{n-1/2}(i + \frac{1}{2}, j, k + \frac{1}{2}) - \frac{\Delta t}{\mu \Delta z} [\mathcal{E}_x^n(i + \frac{1}{2}, j, k + 1) - \mathcal{E}_x^n(i + \frac{1}{2}, j, k)] \\ &\quad + \frac{\Delta t}{\mu \Delta x} [\mathcal{E}_z^n(i + 1, j, k + \frac{1}{2}) - \mathcal{E}_z^n(i, j, k + \frac{1}{2})]\end{aligned}\quad (8.4.18)$$

$$\begin{aligned}\mathcal{H}_z^{n+1/2}(i + \frac{1}{2}, j + \frac{1}{2}, k) &= \mathcal{H}_z^{n-1/2}(i + \frac{1}{2}, j + \frac{1}{2}, k) \\ &\quad - \frac{\Delta t}{\mu \Delta x} [\mathcal{E}_y^n(i + 1, j + \frac{1}{2}, k) - \mathcal{E}_y^n(i, j + \frac{1}{2}, k)] \\ &\quad + \frac{\Delta t}{\mu \Delta y} [\mathcal{E}_x^n(i + \frac{1}{2}, j + 1, k) - \mathcal{E}_x^n(i + \frac{1}{2}, j, k)]\end{aligned}\quad (8.4.19)$$

where i , j , and k stand for the x , y , and z coordinates of a specific cell ($x = i\Delta x$, $y = j\Delta y$, $z = k\Delta z$). Similarly, Equations 8.4.14–8.4.16 can be discretized to yield

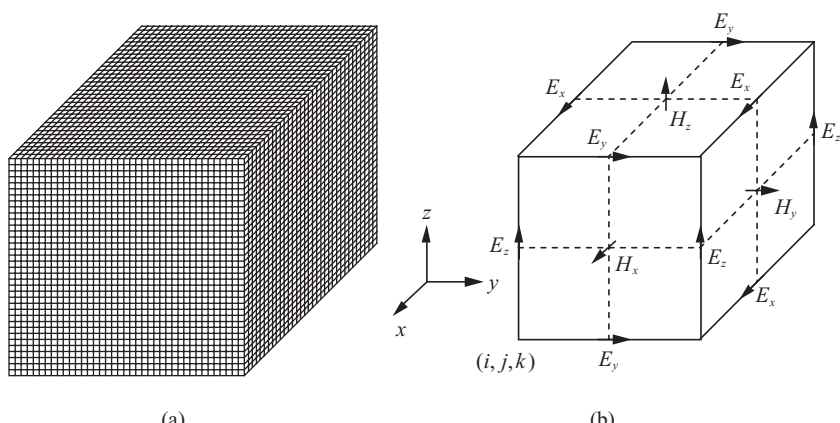


Figure 8.6 FDTD discretization. (a) A computational domain discretized into many small rectangular cells. (b) Assignment of the field components on an FDTD cell for Yee's algorithm.

$$\begin{aligned} \mathcal{E}_x^{n+1}(i+\frac{1}{2}, j, k) = & \frac{1}{\beta(i+\frac{1}{2}, j, k)} \left\{ \alpha(i+\frac{1}{2}, j, k) \mathcal{E}_x^n(i+\frac{1}{2}, j, k) \right. \\ & + \frac{1}{\Delta y} \left[\mathcal{H}_z^{n+1/2}(i+\frac{1}{2}, j+\frac{1}{2}, k) - \mathcal{H}_z^{n+1/2}(i+\frac{1}{2}, j-\frac{1}{2}, k) \right] \\ & - \frac{1}{\Delta z} \left[\mathcal{H}_y^{n+1/2}(i+\frac{1}{2}, j, k+\frac{1}{2}) - \mathcal{H}_y^{n+1/2}(i+\frac{1}{2}, j, k-\frac{1}{2}) \right] \\ & \left. - \mathcal{J}_x^{n+1/2}(i+\frac{1}{2}, j, k) \right\} \end{aligned} \quad (8.4.20)$$

$$\begin{aligned} \mathcal{E}_y^{n+1}(i, j+\frac{1}{2}, k) = & \frac{1}{\beta(i, j+\frac{1}{2}, k)} \left\{ \alpha(i, j+\frac{1}{2}, k) \mathcal{E}_y^n(i, j+\frac{1}{2}, k) \right. \\ & + \frac{1}{\Delta z} \left[\mathcal{H}_x^{n+1/2}(i, j+\frac{1}{2}, k+\frac{1}{2}) - \mathcal{H}_x^{n+1/2}(i, j+\frac{1}{2}, k-\frac{1}{2}) \right] \\ & - \frac{1}{\Delta x} \left[\mathcal{H}_z^{n+1/2}(i+\frac{1}{2}, j+\frac{1}{2}, k) - \mathcal{H}_z^{n+1/2}(i-\frac{1}{2}, j+\frac{1}{2}, k) \right] \\ & \left. - \mathcal{J}_y^{n+1/2}(i, j+\frac{1}{2}, k) \right\} \end{aligned} \quad (8.4.21)$$

$$\begin{aligned} \mathcal{E}_z^{n+1}(i, j, k+\frac{1}{2}) = & \frac{1}{\beta(i, j, k+\frac{1}{2})} \left\{ \alpha(i, j, k+\frac{1}{2}) \mathcal{E}_z^n(i, j, k+\frac{1}{2}) \right. \\ & + \frac{1}{\Delta x} \left[\mathcal{H}_y^{n+1/2}(i+\frac{1}{2}, j, k+\frac{1}{2}) - \mathcal{H}_y^{n+1/2}(i-\frac{1}{2}, j, k+\frac{1}{2}) \right] \\ & - \frac{1}{\Delta y} \left[\mathcal{H}_x^{n+1/2}(i, j+\frac{1}{2}, k+\frac{1}{2}) - \mathcal{H}_x^{n+1/2}(i, j-\frac{1}{2}, k+\frac{1}{2}) \right] \\ & \left. - \mathcal{J}_z^{n+1/2}(i, j, k+\frac{1}{2}) \right\} \end{aligned} \quad (8.4.22)$$

where α and β are the same as defined in Equation 8.4.8. Equations 8.4.17–8.4.22 can also be derived directly from Maxwell's equations in integral form without using the finite differencing formulas.

Clearly, given the source current, the initial values for the electric and magnetic fields, and the boundary conditions, we can use Equations 8.4.17–8.4.19 to calculate the magnetic field, and Equations 8.4.20–8.4.22 to calculate the electric field at a new time step. The discretization above is of second-order in accuracy in terms of the cell size, and for a stable time marching, the time step has to satisfy the stability criterion

$$\Delta t \leq \frac{1}{c \sqrt{\frac{1}{(\Delta x)^2} + \frac{1}{(\Delta y)^2} + \frac{1}{(\Delta z)^2}}}. \quad (8.4.23)$$

The numerical dispersion error can be readily extended from Equation 8.3.6 for the two-dimensional case and is given by

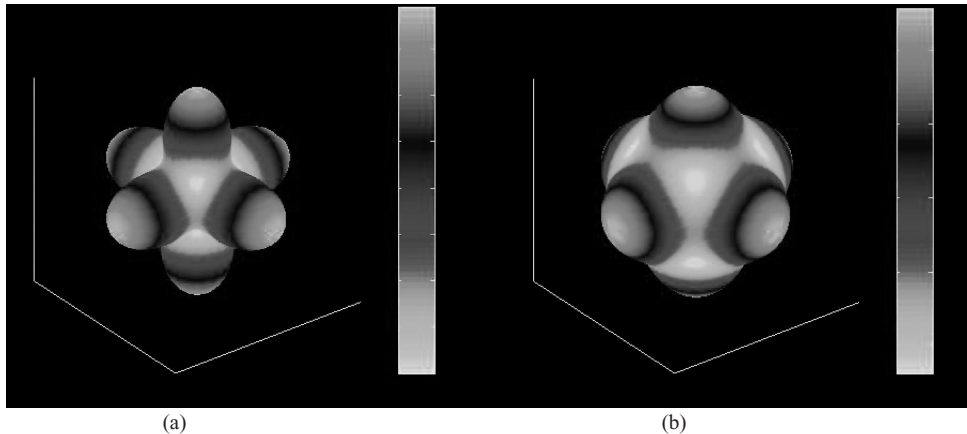


Figure 8.7 Variation of the numerical phase error in degrees per wavelength for (a) $\lambda/h = 10$ and (b) $\lambda/h = 20$. (See color insert.)

$$\frac{\tilde{k} - k}{k} \approx \frac{1}{24} \left\{ [(k\Delta x)^2 \cos^4 \phi^i + (k\Delta y)^2 \sin^4 \phi^i] \sin^4 \theta^i + (k\Delta z)^2 \cos^4 \theta^i - (\omega\Delta t)^2 \right\} \quad (8.4.24)$$

where (ϕ^i, θ^i) denotes the wave's propagation direction. If we choose $\Delta x = \Delta y = \Delta z = h$ and $\Delta t = 0.5h/c$, Equation 8.4.24 becomes

$$\begin{aligned} \frac{\tilde{k} - k}{k} &\approx \frac{(kh)^2}{24} \left\{ [\cos^4 \phi^i + \sin^4 \phi^i] \sin^4 \theta^i + \cos^4 \theta^i - \frac{1}{4} \right\} \\ &= \frac{\pi^2}{6} \left(\frac{h}{\lambda} \right)^2 \left\{ [\cos^4 \phi^i + \sin^4 \phi^i] \sin^4 \theta^i + \cos^4 \theta^i - \frac{1}{4} \right\} \end{aligned} \quad (8.4.25)$$

which is plotted in Figure 8.7 for $\lambda/h = 10$ and 20 to show the angular variation.

8.5 ABSORBING BOUNDARY CONDITIONS

One of the major challenges in the use of the finite difference method for solving unbounded (open-region) electromagnetic problems is the truncation of the infinite space into a finite computational domain. This truncation can be accomplished by introducing an artificial surface to enclose the region of interest. However, to emulate the original open-region environment, the artificial truncation surface should absorb as much of the field incident on the truncation surface as possible in order to reduce any artificially reflected fields. Typical approaches to achieving this in the finite difference method include the use of a mathematical boundary condition and the use of fictitious absorbing material layers.

8.5.1 One-Dimensional ABC

To introduce the basic idea of absorbing boundary conditions, we consider the one-dimensional problem treated in Section 8.2.2. We assume that the solution domain is now unbounded ($-\infty < x < \infty$), but the source is confined within a finite region ($a \leq x \leq b$). This source will generate waves propagating toward the $+\hat{x}$ direction in the region $x > b$ and toward the $-\hat{x}$ direction in the region $x < a$. To solve this problem using the finite differ-

ence method, we truncate the infinite solution domain into a finite one $[A, B]$, where $A < a$ and $B > b$. Next, we need to formulate a boundary condition that allows a wave to propagate through $x = A$ and $x = B$ without any reflection. Let us take the point at $x = B$ as an example. At this point, the wave propagates in the $+\hat{x}$ direction and can be expressed as

$$E_z(x) = E_0 e^{-jkx} \quad (8.5.1)$$

where E_0 denotes the unknown constant and $k = \omega\sqrt{\mu\varepsilon} = \omega/c$. Taking a derivative with respect to x yields

$$\frac{\partial E_z}{\partial x} = -jkE_0 e^{-jkx} = -jkE_z(x) = -\frac{j\omega}{c} E_z(x) \quad (8.5.2)$$

which relates the normal derivative of the field to the value of the field. This relation can be considered a *boundary condition of the third kind*. When transformed into the time domain, it becomes

$$\frac{\partial \mathcal{E}_z(x, t)}{\partial x} = -\frac{1}{c} \frac{\partial \mathcal{E}_z(x, t)}{\partial t}. \quad (8.5.3)$$

When this boundary condition is applied to the boundary at $x = B$, the wave can pass through it without any reflection, hence the name *absorbing boundary condition* (ABC). A similar ABC can be derived for the other boundary at $x = A$.

To discretize Equation 8.5.3 at $x = B$, we can employ backward differencing for the derivative about x and forward differencing for the derivative about t to obtain

$$\frac{\mathcal{E}_z^n(M) - \mathcal{E}_z^n(M-1)}{\Delta x} = -\frac{1}{c} \frac{\mathcal{E}_z^{n+1}(M) - \mathcal{E}_z^n(M)}{\Delta t} \quad (8.5.4)$$

which yields the time-stepping formula

$$\mathcal{E}_z^{n+1}(M) = \mathcal{E}_z^n(M) - \frac{c\Delta t}{\Delta x} [\mathcal{E}_z^n(M) - \mathcal{E}_z^n(M-1)]. \quad (8.5.5)$$

Its stability condition is $\Delta t \leq \Delta x/c$, which is the same as Equation 8.2.24. When $\Delta t = \Delta x/c$, Equation 8.5.5 becomes $\mathcal{E}_z^{n+1}(M) = \mathcal{E}_z^n(M-1)$. Equation 8.5.5 is only first-order accurate. A better discretization of Equation 8.5.3 is to apply it at $x = (M - \frac{1}{2})\Delta x$ and $t = (n + \frac{1}{2})\Delta t$ with the second-order accurate central differencing, yielding

$$\frac{\mathcal{E}_z^{n+1/2}(M) - \mathcal{E}_z^{n+1/2}(M-1)}{\Delta x} = -\frac{1}{c} \frac{\mathcal{E}_z^{n+1}(M - \frac{1}{2}) - \mathcal{E}_z^n(M - \frac{1}{2})}{\Delta t}. \quad (8.5.6)$$

By using the average for the fields at the half grid point and half time step, which is also second-order accurate, we obtain the time-stepping formula

$$\mathcal{E}_z^{n+1}(M) = \mathcal{E}_z^n(M-1) - \frac{\Delta x - c\Delta t}{\Delta x + c\Delta t} [\mathcal{E}_z^n(M) - \mathcal{E}_z^{n+1}(M-1)]. \quad (8.5.7)$$

This formula is unconditionally stable, and, as can be expected, when $\Delta t = \Delta x/c$, it also reduces to $\mathcal{E}_z^{n+1}(M) = \mathcal{E}_z^n(M-1)$.

8.5.2 Two-Dimensional ABCs

The approach for the one-dimensional case can be extended into two and three dimensions. Here, we discuss the two-dimensional case to illustrate the process and the basic difference from the one-dimensional case. Consider a boundary along the y -axis and a plane wave incident on this boundary (Fig. 8.8). If this boundary is completely transparent, the wave will propagate without any reflection. Thus, the wave can be expressed as

$$\varphi(x, y) = Ae^{-j(k_x x + k_y y)} \quad (8.5.8)$$

where A is a constant, $k_x = k \cos \theta$, and $k_y = k \sin \theta$. Taking the derivative with respect to x , we obtain

$$\frac{\partial \varphi}{\partial x} = -jk_x A e^{-j(k_x x + k_y y)} = -jk_x \varphi(x, y) = -jk \cos \theta \varphi(x, y) \quad (8.5.9)$$

which has the form of a boundary condition of the third kind. This boundary condition can completely absorb a plane wave incident at an angle θ from the x -axis. Unfortunately, in a general problem the wave incident at the absorbing boundary is usually not a plane wave, and, furthermore, one does not know the angle of incidence. Since an arbitrary wave can be decomposed into many plane waves incident at different angles, a point on the absorbing boundary actually sees many plane waves from many different directions. Therefore, a useful boundary condition must be independent of the angle of incidence. If we set $\theta = 0$ in Equation 8.5.9, we obtain an approximate boundary condition as

$$\frac{\partial \varphi}{\partial x} \approx -jk\varphi \quad (8.5.10)$$

which is called the *first-order absorbing boundary condition*. The reflection coefficient associated with this condition is

$$R = \frac{\cos \theta - 1}{\cos \theta + 1} \quad (8.5.11)$$

which reduces to zero at $\theta = 0$, as expected.

Clearly, for a general two-dimensional problem, no exact ABC exists. The only thing one can do is to improve its accuracy. To derive a better ABC, we rewrite Equation 8.5.9 as

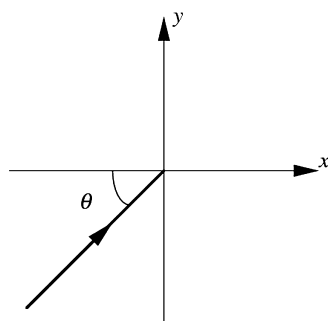


Figure 8.8 Plane wave incident on the yz -plane.

$$\frac{\partial \varphi}{\partial x} = -jk_x \varphi = -j\sqrt{k^2 - k_y^2} \varphi = -jk \sqrt{1 - \left(\frac{k_y}{k}\right)^2} \varphi \quad (8.5.12)$$

and expand the square root into a Taylor series since $(k_y/k)^2 \leq 1$. By keeping the first two terms of the Taylor series, we obtain

$$\frac{\partial \varphi}{\partial x} \approx -jk \left[1 - \frac{1}{2} \left(\frac{k_y}{k} \right)^2 \right] \varphi = -jk \varphi + \frac{j}{2k} k_y^2 \varphi. \quad (8.5.13)$$

Since $\partial^2 \varphi / \partial y^2 = -k_y^2 \varphi$, Equation 8.5.13 can be written as

$$\frac{\partial \varphi}{\partial x} \approx -jk \varphi - \frac{j}{2k} \frac{\partial^2 \varphi}{\partial y^2} \quad (8.5.14)$$

which is called the *second-order absorbing boundary condition*. The reflection coefficient associated with this condition is

$$R = \frac{\cos \theta + \frac{1}{2} \sin^2 \theta - 1}{\cos \theta - \frac{1}{2} \sin^2 \theta + 1} \quad (8.5.15)$$

which also reduces to zero at $\theta = 0$ but is much smaller than Equation 8.5.11 at other angles. However, both Equations 8.5.11 and 8.5.15 have a significant reflection at near-grazing angles.

To convert Equation 8.5.14 into the time domain, we can first use $k = \omega/c$ to rewrite it as

$$\frac{\partial \varphi}{\partial x} \approx -j \frac{\omega}{c} \varphi - \frac{jc}{2\omega} \frac{\partial^2 \varphi}{\partial y^2} \quad (8.5.16)$$

or

$$j\omega \frac{\partial \varphi}{\partial x} \approx \frac{\omega^2}{c} \varphi + \frac{c}{2} \frac{\partial^2 \varphi}{\partial y^2}. \quad (8.5.17)$$

Then, by replacing $j\omega$ with $\partial/\partial t$, we obtain

$$\frac{\partial^2 \varphi}{\partial t \partial x} \approx -\frac{1}{c} \frac{\partial^2 \varphi}{\partial t^2} + \frac{c}{2} \frac{\partial^2 \varphi}{\partial y^2} \quad (8.5.18)$$

which is often referred to as the *Engquist–Majda absorbing boundary condition*.

The finite difference representation of Equation 8.5.18 can be obtained by discretizing the left-hand side as

$$\begin{aligned} \frac{\partial^2 \varphi}{\partial t \partial x} &\approx \frac{\partial}{\partial t} \frac{\varphi(M, j) - \varphi(M-1, j)}{\Delta x} \\ &\approx \frac{[\varphi^{n+1}(M, j) - \varphi^{n+1}(M-1, j)] - [\varphi^n(M, j) - \varphi^n(M-1, j)]}{\Delta x \Delta t} \end{aligned} \quad (8.5.19)$$

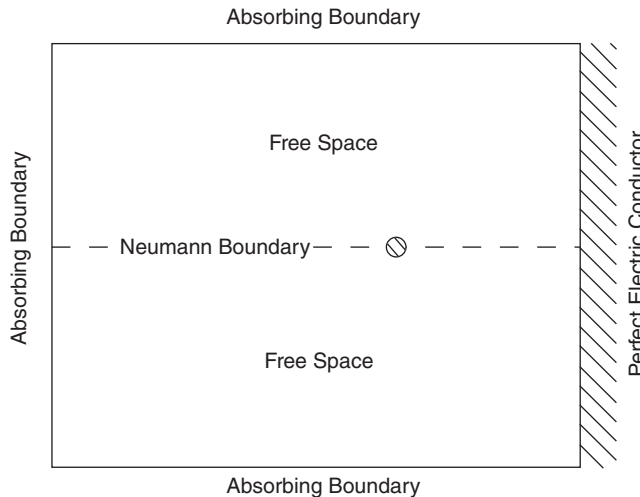


Figure 8.9 Illustration of the computation domain truncated by absorbing and Neumann boundaries for the problem of a line source radiating in front of an infinitely large conducting plane.

and employing central differencing for the right-hand side. The resulting time-stepping formula is given by

$$\begin{aligned} \varphi^{n+1}(M, j) = & \left[\frac{1}{\Delta x \Delta t} + \frac{1}{c(\Delta t)^2} \right]^{-1} \left\{ \frac{1}{\Delta x \Delta t} [\varphi^{n+1}(M-1, j) - \varphi^n(M-1, j)] \right. \\ & + \left[\frac{1}{\Delta x \Delta t} + \frac{2}{c(\Delta t)^2} - \frac{c}{(\Delta y)^2} \right] \varphi^n(M, j) - \frac{1}{c(\Delta t)^2} \varphi^{n-1}(M, j) \\ & \left. + \frac{c}{2(\Delta y)^2} [\varphi^n(M, j-1) + \varphi^n(M, j+1)] \right\} \end{aligned} \quad (8.5.20)$$

which can be used to compute the field at the absorbing boundary.

To demonstrate the application of the ABC, we consider a line current source radiating in front of an infinitely large conducting surface. The computational domain can be truncated as illustrated in Figure 8.9. Because of symmetry, the computational domain can be further reduced by one-half by placing a Neumann boundary in the middle. To simulate this problem, Equation 8.3.4 is used to compute the fields inside the computational domain, and equations similar to Equation 8.5.20 are used to compute the fields on the absorbing boundary. Figure 8.10 shows several snapshots before and after the wave hits the absorbing boundary. It can be seen that the ABC works well, as it has little disturbance to the incident waves.

8.5.3 Perfectly Matched Layers

Instead of using a mathematical boundary condition, the computational domain can also be truncated by using absorptive materials. Whereas it is extremely costly to model the absorbers used in anechoic chambers because of their electrically large thickness and their wedged and pyramidal shapes, one can instead design thin layers of artificial absorbers solely for simulation purposes. A popular absorber model was proposed by Berenger for

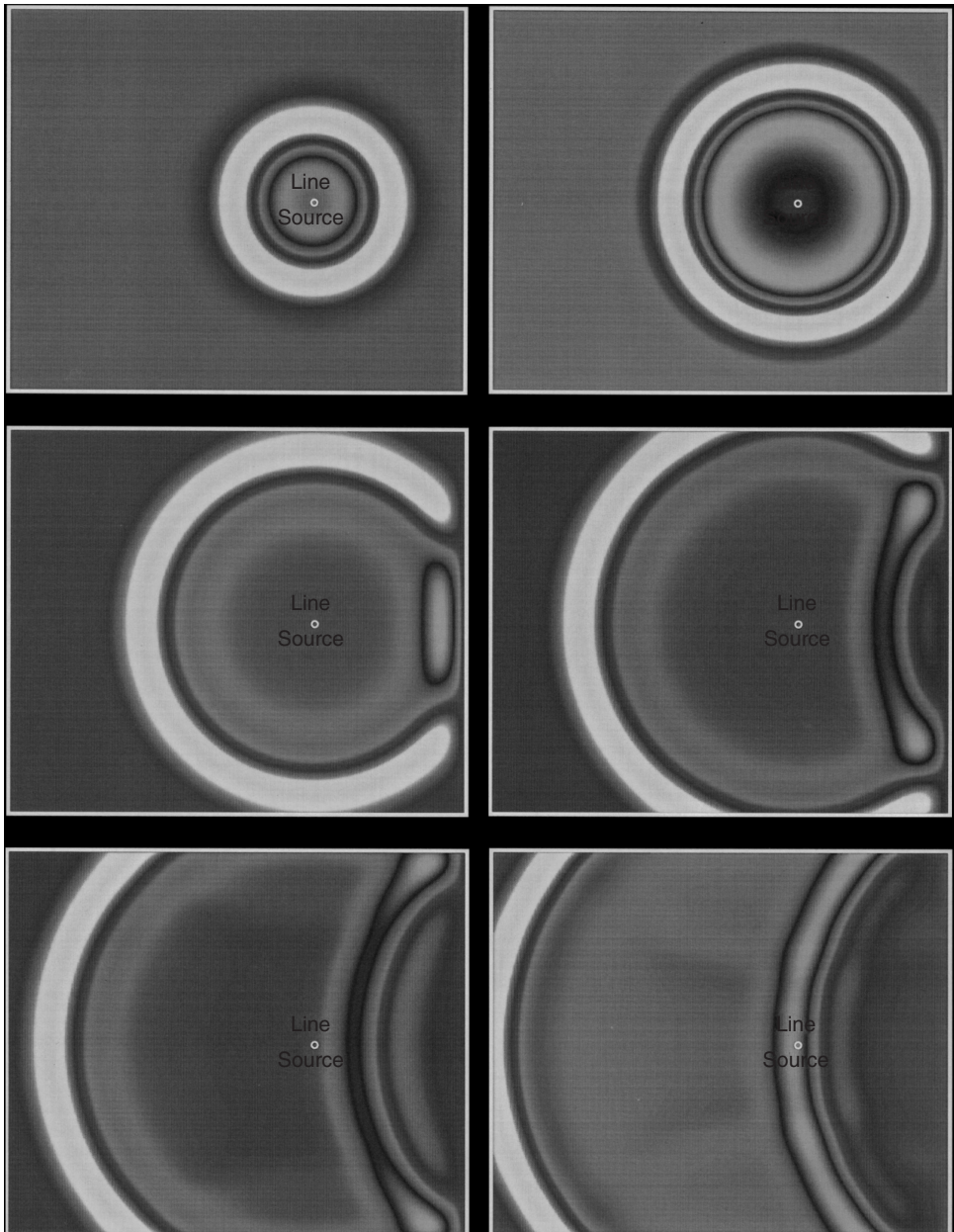


Figure 8.10 Snapshots of the electric field radiated by the line current in front of an infinitely large conducting plane. (See color insert.)

the FDTD simulation and is known as the *perfectly matched layer* (PML) [4]. A PML is an artificial material that is theoretically designed to create no reflections regardless of the frequency, polarization, and angle of incidence of a plane wave incident upon its interface. The frequency independence is especially important because it enables broadband simulation with a time-domain method. In its original form, the PML was formulated with the aid of non-physical “split” fields [4,5]. Later, it was found that the PML could be derived alternatively from a modified form of Maxwell’s equations based on stretched coordinates [6].

To introduce the basic idea of the PML, we consider the modified source-free Maxwell's equations [6],

$$\nabla_s \times \mathbf{E} = -j\omega\mu\mathbf{H} \quad (8.5.21)$$

$$\nabla_s \times \mathbf{H} = j\omega\epsilon\mathbf{E} \quad (8.5.22)$$

$$\nabla_s \cdot (\epsilon\mathbf{E}) = 0 \quad (8.5.23)$$

$$\nabla_s \cdot (\mu\mathbf{H}) = 0 \quad (8.5.24)$$

where ∇_s is defined by

$$\nabla_s = \hat{x}\frac{1}{s_x}\frac{\partial}{\partial x} + \hat{y}\frac{1}{s_y}\frac{\partial}{\partial y} + \hat{z}\frac{1}{s_z}\frac{\partial}{\partial z}. \quad (8.5.25)$$

Clearly, ∇_s can be considered as the standard ∇ operator in Cartesian coordinates whose x , y , and z axes are stretched by factors of s_x , s_y , and s_z , respectively. Here, we assume that s_x , s_y , and s_z are either constants or functions of x , y , and z , respectively, that is, $s_x = s_x(x)$, $s_y = s_y(y)$, and $s_z = s_z(z)$.

Now let us examine the wave characteristics governed by the modified Maxwell's equations. For this, consider a plane wave whose electric and magnetic fields are given by

$$\mathbf{E} = \mathbf{E}_0 e^{-jk\mathbf{r}} = \mathbf{E}_0 e^{-j(k_x x + k_y y + k_z z)} \quad (8.5.26)$$

$$\mathbf{H} = \mathbf{H}_0 e^{-jk\mathbf{r}} = \mathbf{H}_0 e^{-j(k_x x + k_y y + k_z z)}. \quad (8.5.27)$$

Substituting these into Equations 8.5.21–8.5.24 yields

$$\mathbf{k}_s \times \mathbf{E} = \omega\mu\mathbf{H} \quad (8.5.28)$$

$$\mathbf{k}_s \times \mathbf{H} = -\omega\epsilon\mathbf{E} \quad (8.5.29)$$

$$\mathbf{k}_s \cdot \mathbf{E} = 0 \quad (8.5.30)$$

$$\mathbf{k}_s \cdot \mathbf{H} = 0 \quad (8.5.31)$$

where

$$\mathbf{k}_s = \hat{x}\frac{k_x}{s_x} + \hat{y}\frac{k_y}{s_y} + \hat{z}\frac{k_z}{s_z}. \quad (8.5.32)$$

Taking the cross-product of Equation 8.5.28 with \mathbf{k}_s , we have

$$\mathbf{k}_s \times (\mathbf{k}_s \times \mathbf{E}) = \omega\mu\mathbf{k}_s \times \mathbf{H} = -\omega^2\mu\epsilon\mathbf{E} \quad (8.5.33)$$

which becomes

$$(\mathbf{k}_s \cdot \mathbf{k}_s)\mathbf{E} = \omega^2\mu\epsilon\mathbf{E} \quad (8.5.34)$$

since $\mathbf{k}_s \times (\mathbf{k}_s \times \mathbf{E}) = \mathbf{k}_s(\mathbf{k}_s \cdot \mathbf{E}) - (\mathbf{k}_s \cdot \mathbf{k}_s)\mathbf{E}$ and $\mathbf{k}_s \cdot \mathbf{E} = 0$. This gives the dispersion relation

$$\mathbf{k}_s \cdot \mathbf{k}_s = \omega^2 \mu \epsilon = k^2 \quad (8.5.35)$$

or

$$\left(\frac{k_x}{s_x} \right)^2 + \left(\frac{k_y}{s_y} \right)^2 + \left(\frac{k_z}{s_z} \right)^2 = k^2. \quad (8.5.36)$$

The solution to this equation is

$$k_x = ks_x \sin \theta \cos \phi, \quad k_y = ks_y \sin \theta \sin \phi, \quad k_z = ks_z \cos \theta. \quad (8.5.37)$$

This indicates that if s_x is a complex number with a negative imaginary part, the wave will be attenuated in the x -direction, and the same is true in the other two directions. The wave impedance is given by

$$\eta = \frac{|\mathbf{E}|}{|\mathbf{H}|} = \frac{|k_s|}{\omega \epsilon} = \frac{\omega \mu}{|k_s|} = \sqrt{\frac{\mu}{\epsilon}} \quad (8.5.38)$$

which is independent of the coordinate stretching.

Next we consider the reflection of a plane wave by an interface between two half-spaces in the stretched coordinate system (Fig. 8.11). The interface coincides with the xy -plane. For the TE_z case, the incident, reflected, and transmitted fields can be written as

$$\mathbf{E}^i = \mathbf{E}_0 e^{-j\mathbf{k}^i \cdot \mathbf{r}} \quad (8.5.39)$$

$$\mathbf{E}^r = R_{\text{TE}} \mathbf{E}_0 e^{-j\mathbf{k}^r \cdot \mathbf{r}} \quad (8.5.40)$$

$$\mathbf{E}^t = T_{\text{TE}} \mathbf{E}_0 e^{-j\mathbf{k}^t \cdot \mathbf{r}} \quad (8.5.41)$$

where \mathbf{E}_0 is a constant vector perpendicular to \hat{z} , and R_{TE} and T_{TE} denote the reflection and transmission coefficients, respectively. Using the phase-matching and tangential continuity conditions for \mathbf{E} and \mathbf{H} , we obtain

$$R_{\text{TE}} = \frac{k_{1z} s_{2z} \mu_2 - k_{2z} s_{1z} \mu_1}{k_{1z} s_{2z} \mu_2 + k_{2z} s_{1z} \mu_1} \quad (8.5.42)$$

where the subscript 1 is used to denote the parameters in the upper half-space and the subscript 2 to denote those in the lower half-space. Similarly, we can find the reflection coefficient for the TM_z case as

$$R_{\text{TM}} = \frac{k_{1z} s_{2z} \epsilon_2 - k_{2z} s_{1z} \epsilon_1}{k_{1z} s_{2z} \epsilon_2 + k_{2z} s_{1z} \epsilon_1}. \quad (8.5.43)$$

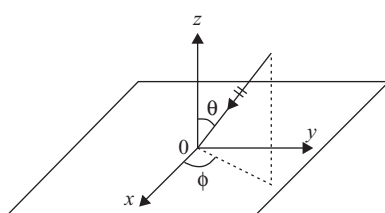


Figure 8.11 Plane wave incident on the interface between the upper and lower half-spaces.

From the phase-matching conditions $k_{1x} = k_{2x}$ and $k_{1y} = k_{2y}$, we obtain

$$k_1 s_{1x} \sin \theta_1 \cos \phi_1 = k_2 s_{2x} \sin \theta_2 \cos \phi_2 \quad (8.5.44)$$

$$k_1 s_{1x} \sin \theta_1 \sin \phi_1 = k_2 s_{2x} \sin \theta_2 \sin \phi_2. \quad (8.5.45)$$

Clearly, if we choose $\epsilon_1 = \epsilon_2$, $\mu_1 = \mu_2$, $s_{1x} = s_{2x}$, and $s_{1y} = s_{2y}$, we have $\theta_1 = \theta_2$ and $\phi_1 = \phi_2$, and consequently,

$$R_{\text{TE}} = 0, \quad R_{\text{TM}} = 0 \quad (8.5.46)$$

which remains true regardless of (1) the choice of s_{1z} and s_{2z} , (2) the angle of incidence, and (3) the frequency. Because of this, the interface is called a *perfectly matched interface*.

Since the perfectly matched interface in the xy -plane is independent of s_{1z} and s_{2z} , we can choose whatever values for s_{1z} and s_{2z} without causing any reflection. If we choose $s_{2z} = s' - js''$, where s' and s'' are real numbers with $s' \geq 1$ and $s'' \geq 0$, then $k_{2z} = k_2(s' - js'')\cos\theta$. The transmitted wave will be attenuated exponentially by the factor $\exp(k_2 s'' z \cos\theta)$ in the $-\hat{z}$ direction. If we truncate medium 2 into a layer with a finite thickness L and place a conducting surface at its back, the magnitude of the reflection coefficient becomes

$$|R(\theta)| = e^{-2k_2 \int_0^L s''(z) dz \cos\theta}. \quad (8.5.47)$$

Clearly, this reflection has a minimum value for the normal incidence and the maximum value at the grazing incidence. This characteristic is very similar to that of the mathematical ABCs. However, for a PML, we can systematically reduce its reflection simply by increasing the value of $\int_0^L s''(z) dz$.

The conductor-backed PML can be used to truncate the computational domain for the FDTD simulations. The basic scheme is sketched in Figure 8.12, where the problem of interest is boxed by a conductor-backed PML. The choice of the PML parameters depends on its position. For the PML perpendicular to the x -axis, we choose

$$s_x = s' - js'', \quad s_y = s_z = 1 \quad (8.5.48)$$

and for the PML perpendicular to the y -axis, we choose

$$s_y = s' - js'', \quad s_x = s_z = 1. \quad (8.5.49)$$

For the four corner regions, we choose

$$s_x = s_y = s' - js'', \quad s_z = 1 \quad (8.5.50)$$

to satisfy the conditions for a perfectly matched interface. The extension to the three-dimensional case is straightforward. Note that because of the truncation of the PML with a conducting surface, it is necessary to make sure that the truncated PML provides sufficient attenuation so that after the field is reflected by the truncation boundary, it becomes negligible when it reenters the physical solution domain. This can be done relatively easily since the PML attenuation can be estimated with a simple formula given in Equation 8.5.47. However, since the PML primarily attenuates waves propagating normal to the

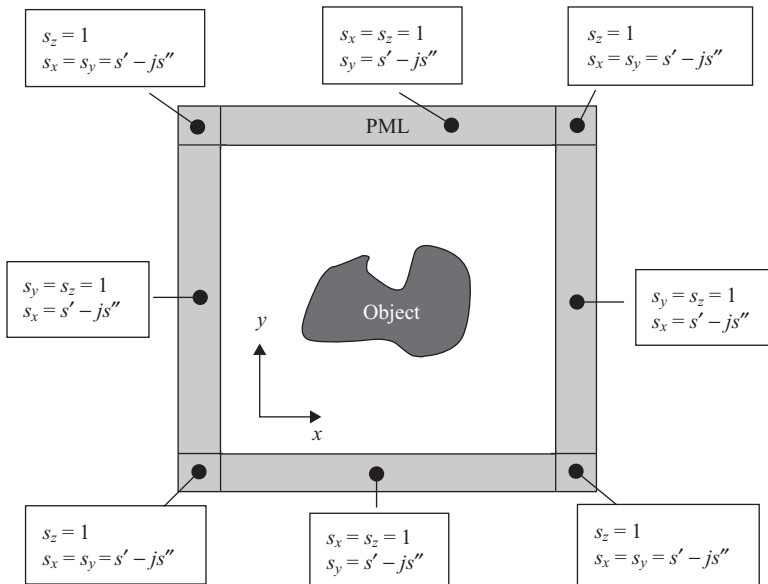


Figure 8.12 Computational domain truncated using the conductor-backed PMLs.

PML, the truncated PML will provide less attenuation for obliquely incident waves; consequently, a significant non-physical reflection can occur for a wave incident at a near grazing angle. For this reason, the PML has to be placed some distance away from all the sources of the field.

Now, let us address the implementation of the PML in the FDTD solution. For this, we first have to transform the modified Maxwell's equations (Eqs. 8.5.21–8.5.24) into the time domain. Consider Equation 8.5.21 first. Based on Equation 8.5.25, we have

$$\nabla_s \times \mathbf{E} = \frac{1}{s_x} \frac{\partial}{\partial x} (\hat{x} \times \mathbf{E}) + \frac{1}{s_y} \frac{\partial}{\partial y} (\hat{y} \times \mathbf{E}) + \frac{1}{s_z} \frac{\partial}{\partial z} (\hat{z} \times \mathbf{E}). \quad (8.5.51)$$

Since s_x , s_y , and s_z are different complex numbers, to move them away from the denominator we split the magnetic field vector to write Equation 8.5.21 as

$$\frac{1}{s_x} \frac{\partial}{\partial x} (\hat{x} \times \mathbf{E}) = -j\omega\mu \mathbf{H}_{sx} \quad (8.5.52)$$

$$\frac{1}{s_y} \frac{\partial}{\partial y} (\hat{y} \times \mathbf{E}) = -j\omega\mu \mathbf{H}_{sy} \quad (8.5.53)$$

$$\frac{1}{s_z} \frac{\partial}{\partial z} (\hat{z} \times \mathbf{E}) = -j\omega\mu \mathbf{H}_{sz} \quad (8.5.54)$$

where $\mathbf{H}_{sx} + \mathbf{H}_{sy} + \mathbf{H}_{sz} = \mathbf{H}$. By choosing s_x , s_y , and s_z to have the following forms

$$s_x = 1 - j \frac{\sigma_x}{\omega\epsilon}, \quad s_y = 1 - j \frac{\sigma_y}{\omega\epsilon}, \quad s_z = 1 - j \frac{\sigma_z}{\omega\epsilon} \quad (8.5.55)$$

we can readily transform Equations 8.5.52–8.5.54 into the time domain as

$$\frac{\partial}{\partial x}(\hat{x} \times \mathcal{E}) = -\mu \frac{\partial \mathcal{H}_{sx}}{\partial t} - \frac{\sigma_x \mu}{\epsilon} \mathcal{H}_{sx} \quad (8.5.56)$$

$$\frac{\partial}{\partial y}(\hat{y} \times \mathcal{E}) = -\mu \frac{\partial \mathcal{H}_{sy}}{\partial t} - \frac{\sigma_y \mu}{\epsilon} \mathcal{H}_{sy} \quad (8.5.57)$$

$$\frac{\partial}{\partial z}(\hat{z} \times \mathcal{E}) = -\mu \frac{\partial \mathcal{H}_{sz}}{\partial t} - \frac{\sigma_z \mu}{\epsilon} \mathcal{H}_{sz}. \quad (8.5.58)$$

Following a similar procedure, we can split the electric field and transform Equation 8.5.22 into the following three equations

$$\frac{\partial}{\partial x}(\hat{x} \times \mathcal{H}) = \epsilon \frac{\partial \mathcal{E}_{sx}}{\partial t} + \sigma_x \mathcal{E}_{sx} \quad (8.5.59)$$

$$\frac{\partial}{\partial y}(\hat{y} \times \mathcal{H}) = \epsilon \frac{\partial \mathcal{E}_{sy}}{\partial t} + \sigma_y \mathcal{E}_{sy} \quad (8.5.60)$$

$$\frac{\partial}{\partial z}(\hat{z} \times \mathcal{H}) = \epsilon \frac{\partial \mathcal{E}_{sz}}{\partial t} + \sigma_z \mathcal{E}_{sz} \quad (8.5.61)$$

where $\mathcal{E}_{sx} + \mathcal{E}_{sy} + \mathcal{E}_{sz} = \mathcal{E}$.

These modified time-domain Maxwell's equations can be discretized using Yee's FDTD scheme. Specifically, Equations 8.5.56–8.5.58 can be discretized to yield the time-stepping formulas for the magnetic field, and Equations 8.5.59–8.5.61 can be discretized to produce the time-stepping formulas for the electric field. Consider a two-dimensional TM_z problem, where $\mathcal{E} = \hat{z} \mathcal{E}_z$ and $\mathcal{H} = \hat{x} \mathcal{H}_x + \hat{y} \mathcal{H}_y$. For this problem, it can be seen from Equations 8.5.56–8.5.58 that $\mathcal{H}_{sx} = \hat{y} \mathcal{H}_y$, $\mathcal{H}_{sy} = \hat{x} \mathcal{H}_x$, and $\mathcal{H}_{sz} = 0$; hence, Equations 8.5.56 and 5.5.57 become

$$\frac{\partial \mathcal{E}_z}{\partial x} = \mu \frac{\partial \mathcal{H}_y}{\partial t} + \frac{\sigma_x \mu}{\epsilon} \mathcal{H}_y \quad (8.5.62)$$

$$\frac{\partial \mathcal{E}_z}{\partial y} = -\mu \frac{\partial \mathcal{H}_x}{\partial t} - \frac{\sigma_y \mu}{\epsilon} \mathcal{H}_x. \quad (8.5.63)$$

It can also be seen from Equations 8.5.59–8.5.61 that $\mathcal{E}_{sx} = \hat{z} \mathcal{E}_{sx,z}$, $\mathcal{E}_{sy} = \hat{z} \mathcal{E}_{sy,z}$, and $\mathcal{E}_{sz} = 0$; hence, Equations 8.5.59 and 5.5.60 become

$$\frac{\partial \mathcal{H}_y}{\partial x} = \epsilon \frac{\partial \mathcal{E}_{sx,z}}{\partial t} + \sigma_x \mathcal{E}_{sx,z} \quad (8.5.64)$$

$$\frac{\partial \mathcal{H}_x}{\partial y} = -\epsilon \frac{\partial \mathcal{E}_{sy,z}}{\partial t} - \sigma_y \mathcal{E}_{sy,z} \quad (8.5.65)$$

where $\mathcal{E}_{sx,z} + \mathcal{E}_{sy,z} = \mathcal{E}_z$. The finite difference discretization of Equations 8.5.62–8.5.65 yields the time-stepping formulas

$$\mathcal{H}_x^{n+1/2}(i, j + \frac{1}{2}) = \frac{1}{\beta_y(i, j + \frac{1}{2})} \left\{ \alpha_y(i, j + \frac{1}{2}) \mathcal{H}_x^{n-1/2}(i, j + \frac{1}{2}) - \frac{\epsilon}{\mu \Delta y} [\mathcal{E}_z^n(i, j + 1) - \mathcal{E}_z^n(i, j)] \right\} \quad (8.5.66)$$

$$\mathcal{H}_y^{n+1/2}(i + \frac{1}{2}, j) = \frac{1}{\beta_x(i + \frac{1}{2}, j)} \left\{ \mathcal{H}_y^{n-1/2}(i + \frac{1}{2}, j) \alpha_x(i + \frac{1}{2}, j) + \frac{\epsilon}{\mu \Delta x} [\mathcal{E}_z^n(i + 1, j) - \mathcal{E}_z^n(i, j)] \right\} \quad (8.5.67)$$

$$\mathcal{E}_{sx,z}^{n+1}(i, j) = \frac{1}{\beta_x(i, j)} \left\{ \mathcal{E}_{sy,z}^n(i, j) \alpha_x(i, j) + \frac{1}{\Delta x} [\mathcal{H}_y^{n+1/2}(i + \frac{1}{2}, j) - \mathcal{H}_y^{n+1/2}(i - \frac{1}{2}, j)] \right\} \quad (8.5.68)$$

$$\mathcal{E}_{sy,z}^{n+1}(i, j) = \frac{1}{\beta_y(i, j)} \left\{ \mathcal{E}_{sy,z}^n(i, j) \alpha_y(i, j) - \frac{1}{\Delta y} [\mathcal{H}_x^{n+1/2}(i, j + \frac{1}{2}) - \mathcal{H}_x^{n+1/2}(i, j - \frac{1}{2})] \right\} \quad (8.5.69)$$

where

$$\alpha_{x,y} = \frac{\epsilon}{\Delta t} - \frac{\sigma_{x,y}}{2}, \quad \beta_{x,y} = \frac{\epsilon}{\Delta t} + \frac{\sigma_{x,y}}{2}. \quad (8.5.70)$$

Besides splitting the field vectors, the PML can also be implemented in the FDTD algorithm by using auxiliary vectors and solving the related auxiliary differential equations [7]. As will be shown in Section 9.5.3, the PML is equivalent to an anisotropic dispersive absorber whose permittivity and permeability are given by

$$\tilde{\epsilon} = \epsilon \begin{bmatrix} \frac{s_y s_z}{s_x} & 0 & 0 \\ 0 & \frac{s_z s_x}{s_y} & 0 \\ 0 & 0 & \frac{s_x s_y}{s_z} \end{bmatrix}, \quad \tilde{\mu} = \mu \begin{bmatrix} \frac{s_y s_z}{s_x} & 0 & 0 \\ 0 & \frac{s_z s_x}{s_y} & 0 \\ 0 & 0 & \frac{s_x s_y}{s_z} \end{bmatrix} \quad (8.5.71)$$

where ϵ and μ denote the permittivity and permeability of the medium terminated by the PML and s_x , s_y , and s_z are given by Equation 8.5.55. The first two Maxwell's equations in such a medium can be written as

$$\nabla \times \mathbf{E} = -j\omega \begin{bmatrix} s_y & 0 & 0 \\ 0 & s_z & 0 \\ 0 & 0 & s_x \end{bmatrix} \cdot \mathbf{B} \quad (8.5.72)$$

$$\nabla \times \mathbf{H} = j\omega \begin{bmatrix} s_y & 0 & 0 \\ 0 & s_z & 0 \\ 0 & 0 & s_x \end{bmatrix} \cdot \mathbf{D} \quad (8.5.73)$$

where \mathbf{D} and \mathbf{B} are auxiliary vectors, which are related to \mathbf{E} and \mathbf{H} by

$$\mathbf{D} = \epsilon \begin{bmatrix} s_z/s_x & 0 & 0 \\ 0 & s_x/s_y & 0 \\ 0 & 0 & s_y/s_z \end{bmatrix} \cdot \mathbf{E} \quad (8.5.74)$$

$$\mathbf{B} = \mu \begin{bmatrix} s_z/s_x & 0 & 0 \\ 0 & s_x/s_y & 0 \\ 0 & 0 & s_y/s_z \end{bmatrix} \cdot \mathbf{H} \quad (8.5.75)$$

The x -components of Equations 8.5.72 and 8.5.73 can be transformed into the time domain as

$$[\nabla \times \mathcal{E}]_x = -\frac{\partial \mathcal{B}_x}{\partial t} - \frac{\sigma_y}{\epsilon} \mathcal{B}_x \quad (8.5.76)$$

$$[\nabla \times \mathcal{H}]_x = \frac{\partial \mathcal{D}_x}{\partial t} + \frac{\sigma_y}{\epsilon} \mathcal{D}_x. \quad (8.5.77)$$

Their FDTD discretization based on Yee's scheme yields

$$\begin{aligned} \mathcal{B}_x^{n+1/2}(i, j + \frac{1}{2}, k + \frac{1}{2}) = & \frac{1}{\beta_y(i, j + \frac{1}{2}, k + \frac{1}{2})} \left\{ \alpha_y(i, j + \frac{1}{2}, k + \frac{1}{2}) \mathcal{B}_x^{n-1/2}(i, j + \frac{1}{2}, k + \frac{1}{2}) \right. \\ & - \frac{\epsilon}{\Delta y} \left[\mathcal{E}_z^n(i, j + 1, k + \frac{1}{2}) - \mathcal{E}_z^n(i, j, k + \frac{1}{2}) \right] \\ & \left. + \frac{\epsilon}{\Delta z} \left[\mathcal{E}_y^n(i, j + \frac{1}{2}, k + 1) - \mathcal{E}_y^n(i, j + \frac{1}{2}, k) \right] \right\} \end{aligned} \quad (8.5.78)$$

$$\begin{aligned} \mathcal{D}_x^{n+1}(i + \frac{1}{2}, j, k) = & \frac{1}{\beta_y(i + \frac{1}{2}, j, k)} \left\{ \alpha_y(i + \frac{1}{2}, j, k) \mathcal{D}_x^n(i + \frac{1}{2}, j, k) \right. \\ & + \frac{\epsilon}{\Delta y} \left[\mathcal{H}_z^{n+1/2}(i + \frac{1}{2}, j + \frac{1}{2}, k) - \mathcal{H}_z^{n+1/2}(i + \frac{1}{2}, j - \frac{1}{2}, k) \right] \\ & \left. - \frac{\epsilon}{\Delta z} \left[\mathcal{H}_y^{n+1/2}(i + \frac{1}{2}, j, k + \frac{1}{2}) - \mathcal{H}_y^{n+1/2}(i + \frac{1}{2}, j, k - \frac{1}{2}) \right] \right\} \end{aligned} \quad (8.5.79)$$

where α_y and β_y are the same as defined in Equation 8.5.70. The x -components of Equations 8.5.74 and 8.5.75 can also be transformed into the time domain as

$$\frac{\partial \mathcal{D}_x}{\partial t} + \frac{\sigma_x}{\epsilon} \mathcal{D}_x = \epsilon \frac{\partial \mathcal{E}_x}{\partial t} + \sigma_z \mathcal{E}_x \quad (8.5.80)$$

$$\frac{\partial \mathcal{B}_x}{\partial t} + \frac{\sigma_x}{\epsilon} \mathcal{B}_x = \mu \frac{\partial \mathcal{H}_x}{\partial t} + \mu \frac{\sigma_z}{\epsilon} \mathcal{H}_x. \quad (8.5.81)$$

They can be discretized to yield

$$\mathcal{E}_x^{n+1}(i + \frac{1}{2}, j, k) = \frac{1}{\beta_z} \left[\alpha_z \mathcal{E}_x^n + \frac{1}{\varepsilon} \beta_x \mathcal{D}_x^{n+1} - \frac{1}{\varepsilon} \alpha_x \mathcal{D}_x^n \right] \quad (8.5.82)$$

$$\mathcal{H}_x^{n+1/2}(i, j + \frac{1}{2}, k + \frac{1}{2}) = \frac{1}{\beta_z} \left[\alpha_z \mathcal{H}_x^{n-1/2} + \frac{1}{\mu} \beta_x \mathcal{B}_x^{n+1/2} - \frac{1}{\mu} \alpha_x \mathcal{B}_x^{n-1/2} \right] \quad (8.5.83)$$

where α_x and β_x are defined in Equation 8.5.70 and α_z and β_z are defined similarly. In these two equations, the location indexes on the right-hand side are omitted because they are the same as for the quantity on the left-hand side in each equation. Note that outside the PML, Equations 8.5.82 and 8.5.83 simply reduce to $\mathcal{E}_x^{n+1} = \mathcal{D}_x^{n+1}/\varepsilon$ and $\mathcal{H}_x^{n+1/2} = \mathcal{B}_x^{n+1/2}/\mu$, as expected.

Equations 8.5.78, 8.5.79, 8.5.82, and 8.5.83 are obtained from the x -components of Equations 8.5.72–8.5.75. Another eight equations can be obtained from their y - and z -components. The resulting 12 equations can be used to calculate all the fields step by step. Given the field values at time steps n and $n - \frac{1}{2}$, we first use the equations like Equation 8.5.78 to calculate $\mathcal{B}^{n+1/2}$, which can then be used in the equations like Equation 8.5.83 to calculate $\mathcal{H}^{n+1/2}$. The values of $\mathcal{H}^{n+1/2}$ are then used in the equations similar to Equation 8.5.79 to calculate \mathcal{D}^{n+1} , which are then used in the equations similar to Equation 8.5.82 to calculate \mathcal{E}^{n+1} . This completes one time stepping, and the process then continues. This PML implementation has been found to be very robust and accurate for terminating the FDTD computational grids.

Although theoretically the PML interface is reflectionless, this may not hold true in numerical simulations. When a material property changes abruptly (in this case the value of $\sigma_{x,y,z}$ jumps from 0 outside the PML to a constant inside the PML) and the spatial discretization is not sufficiently dense to resolve the change, undesirable numerical reflections may occur [8]. One approach to avoiding this problem is to vary the material parameters $\sigma_{x,y,z}$ smoothly within the PML. For example, we can set $\sigma_{x,y,z}$ as an m th-order polynomial:

$$\sigma_{x,y,z} = \sigma_{\max} \left(\frac{l}{L} \right)^m \quad m = 1, 2, \dots \quad (8.5.84)$$

where l denotes the distance from the PML surface, L is the thickness of the PML, and σ_{\max} is the maximum conductivity inside the PML. Doing so, we actually replace the big jump in the value of $\sigma_{x,y,z}$ at the PML surface with a series of increments inside the PML, which can effectively reduce the undesired reflection caused by the finite spatial discretization. It is found that $m = 2$ or 3 is generally a good choice. With Equation 8.5.84, the reflection coefficient is given by

$$|R(\theta)| = e^{-2\eta\sigma_{\max}L\cos\theta/(m+1)}. \quad (8.5.85)$$

Hence, the absorbing performance of the PML can be improved by increasing the value of the product of the maximum conductivity and the PML thickness. For a specified reflection coefficient $R(0)$, the value of σ_{\max} can be determined via

$$\sigma_{\max} = -\frac{m+1}{2\eta L} \ln |R(0)|. \quad (8.5.86)$$

Apart from the numerical constraints discussed above, the PML is also known to have a poor absorption for evanescent waves. Hence, in problems in which evanescent waves are

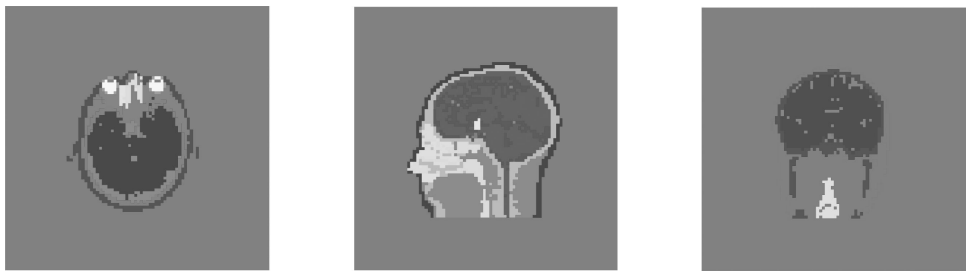


Figure 8.13 Axial, sagittal, and coronal slices of the head model used in the FDTD calculation. (After Chen et al. [12], Copyright © 1998 IEEE.) (See color insert.)

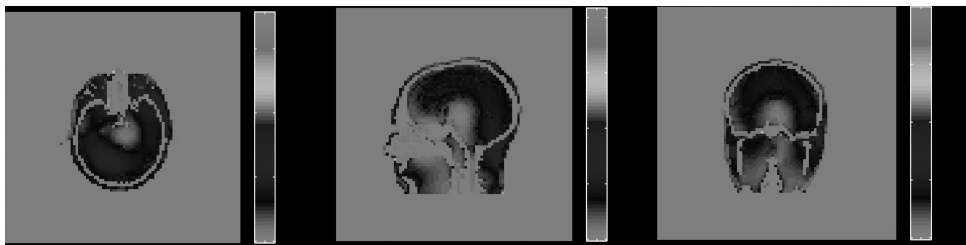


Figure 8.14 SAR (W/kg) distribution in the axial, sagittal, and coronal slices at 256 MHz. (After Chen et al. [12], © 1998 IEEE.) (See color insert.)

significant, the PML must be placed sufficiently far away from the source of evanescent waves to allow them to die out before reaching the PML. A modified version of the PML, referred to as the *complex-frequency-shifted* (CFS) PML, has been proposed in the FDTD method to provide better absorption of evanescent waves [9,10]. However, the CFS PML cannot absorb low-frequency propagating waves. This problem has recently been alleviated by using the second-order PML, which absorbs both the evanescent and propagating waves for all frequencies [11].

To demonstrate the application of the three-dimensional FDTD method in conjunction with PML, we consider the computation of the electric and magnetic fields inside the human head placed in a shielded RF birdcage coil [12]. The electromagnetic model of the human head is highly inhomogeneous and consists of 14 different tissues. Three slices of this model are shown in Figure 8.13. The birdcage coil has a diameter of 26 cm and a length of 26 cm, and it consists of 16 elements. The maximum electric current in the elements is assumed to be 1 A. The coil is placed inside a cylindrical shield that has a diameter of 32 cm and a length of 32 cm. The entire structure is enclosed by a rectangular PML box, which truncates the computational domain. The computed electric field is displayed in terms of *specific absorption rate* (SAR) defined as

$$\text{SAR} = \frac{\sigma |\mathbf{E}|^2}{\rho} \quad (8.5.87)$$

where σ denotes the electric conductivity and ρ denotes the density of the tissue. Figure 8.14 displays the distribution of SAR in the three slices at 256 MHz, and Figure 8.15 shows the corresponding magnetic field distribution.

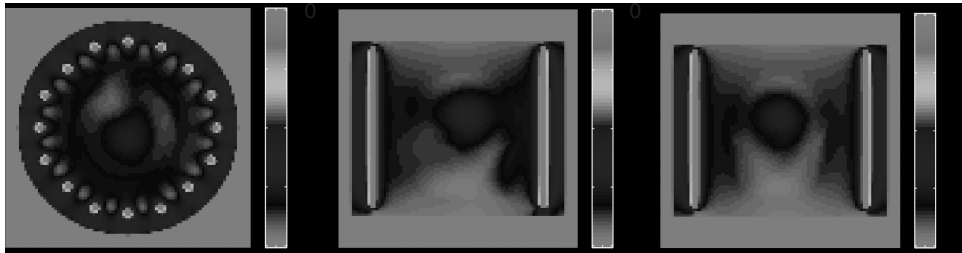


Figure 8.15 Magnetic field (A/m) distribution in the axial, sagittal, and coronal slices at 256 MHz. (After Chen et al. [12], © 1998 IEEE.) (See color insert.)

8.6 MODELING OF DISPERSIVE MEDIA

One of the important advantages of a time-domain-based analysis is the ability to obtain a broadband solution through the use of a broadband source and the Fourier transform with only one time-domain simulation. However, many media used in practical applications are dispersive since their electromagnetic properties, such as permittivity and permeability, vary with the frequency of electromagnetic fields. To obtain an accurate broadband solution, we have to account for the effect of such medium dispersion. There are two approaches commonly used to model dispersive media in the FDTD simulation of electromagnetic problems. One is based on a recursive convolution technique [13,14], and the other resorts to the solution of an auxiliary differential equation [15–17]. In this section we describe these two approaches for the modeling of electrically dispersive media. The modeling of magnetically dispersive media and both electrically and magnetically dispersive media can be carried out with a similar treatment.

8.6.1 Recursive Convolution Approach

Consider an electrically dispersive medium in which the electric flux density $\mathcal{D}(t)$ is related to the electric field intensity $\mathcal{E}(t)$ by the constitutive relation

$$\begin{aligned}\mathcal{D}(t) &= \varepsilon_{\infty} \mathcal{E}(t) + \varepsilon_0 \tilde{\chi}_e(t) * \mathcal{E}(t) \\ &= \varepsilon_{\infty} \mathcal{E}(t) + \varepsilon_0 \int_0^t \tilde{\chi}_e(t-\tau) \mathcal{E}(\tau) d\tau\end{aligned}\quad (8.6.1)$$

where ε_{∞} denotes the permittivity at the optical frequency, $\tilde{\chi}_e(t) = (1 - \varepsilon_{\infty}/\varepsilon_0)\delta(t) + \chi_e(t)$, with $\chi_e(t)$ representing the electrical susceptibility, and $*$ denotes the time convolution. In Equation 8.6.1, it is assumed that $\mathcal{E}(t) \equiv 0$ for $t \leq 0$. By taking the time derivative of Equation 8.6.1, we obtain

$$\frac{\partial \mathcal{D}(t)}{\partial t} = \varepsilon_{\infty} \frac{\partial \mathcal{E}(t)}{\partial t} + \varepsilon_0 \tilde{\chi}_e(t) * \frac{\partial \mathcal{E}(t)}{\partial t}. \quad (8.6.2)$$

The time discretization of the second term on the right-hand side at $t = (n + \frac{1}{2})\Delta t$ is given by

$$\left. \tilde{\chi}_e(t) * \frac{\partial \mathcal{E}(t)}{\partial t} \right|_{t=(n+1/2)\Delta t} \cong \int_0^{\Delta t/2} \tilde{\chi}_e(\tau) \dot{\mathcal{E}}(n\Delta t - \tau) d\tau + \sum_{k=0}^{n-1} \int_{(k+1/2)\Delta t}^{(k+3/2)\Delta t} \tilde{\chi}_e(\tau) \dot{\mathcal{E}}(n\Delta t - \tau) d\tau \quad (8.6.3)$$

where $\dot{\mathcal{E}}$ denotes the first derivative of \mathcal{E} . Assuming that $\dot{\mathcal{E}}$ is constant over the time integration intervals and adopting central differencing to approximate $\dot{\mathcal{E}}$, we obtain

$$\tilde{\chi}_e(t) * \frac{\partial \mathcal{E}(t)}{\partial t} \Big|_{t=(n+1/2)\Delta t} \equiv \tilde{\chi}_e^0 \frac{\mathcal{E}^{n+1} - \mathcal{E}^n}{\Delta t} + \sum_{k=0}^{n-1} \tilde{\chi}_e^{k+1} \frac{\mathcal{E}^{n-k} - \mathcal{E}^{n-k-1}}{\Delta t} \quad (8.6.4)$$

where

$$\tilde{\chi}_e^0 = \int_0^{\Delta t/2} \tilde{\chi}_e(\tau) d\tau \quad (8.6.5)$$

$$\tilde{\chi}_e^{k+1} = \int_{(k+1/2)\Delta t}^{(k+3/2)\Delta t} \tilde{\chi}_e(\tau) d\tau \quad k = 0, 1, 2, \dots \quad (8.6.6)$$

Equation 8.6.4 can then be used in the discretization of the Maxwell–Ampère law:

$$\nabla \times \mathcal{H} = \frac{\partial \mathcal{D}}{\partial t} + \sigma \mathcal{E} \quad (8.6.7)$$

which results in

$$(\nabla \times \mathcal{H})^{n+1/2} = \frac{\epsilon_\infty + \tilde{\chi}_e^0}{\Delta t} (\mathcal{E}^{n+1} - \mathcal{E}^n) + \frac{\sigma}{2} (\mathcal{E}^{n+1} + \mathcal{E}^n) + \epsilon_0 \sum_{k=0}^{n-1} \frac{\tilde{\chi}_e^{k+1}}{\Delta t} (\mathcal{E}^{n-k} - \mathcal{E}^{n-k-1}). \quad (8.6.8)$$

This yields the time-stepping equation

$$\mathcal{E}^{n+1} = \frac{1}{\beta} [\alpha \mathcal{E}^n + (\nabla \times \mathcal{H})^{n+1/2} - \epsilon_0 \psi^n] \quad (8.6.9)$$

where

$$\psi^n = \sum_{k=0}^{n-1} \frac{\tilde{\chi}_e^{k+1}}{\Delta t} (\mathcal{E}^{n-k} - \mathcal{E}^{n-k-1}) \quad (8.6.10)$$

$$\alpha = \frac{\epsilon_\infty + \tilde{\chi}_e^0}{\Delta t} - \frac{\sigma}{2} \quad \text{and} \quad \beta = \frac{\epsilon_\infty + \tilde{\chi}_e^0}{\Delta t} + \frac{\sigma}{2}. \quad (8.6.11)$$

From Equation 8.6.9, we can derive equations similar to Equations 8.4.20–8.4.22 to time-advance the electric field components.

In the formulation described above, the evaluation of the summation in Equation 8.6.10 is very time-consuming. However, the susceptibility for many practical media, such as Debye, Lorentz, and Drude media [3], can be represented by a pole expansion

$$\tilde{\chi}_e(t) = \sum_{p=1}^{N_p} a_p e^{-b_p t} u(t). \quad (8.6.12)$$

In such a case,

$$\tilde{\chi}_e^0 = \sum_{p=1}^{N_p} \frac{a_p}{b_p} \left(1 - e^{-b_p \Delta t / 2}\right) \quad (8.6.13)$$

$$\tilde{\chi}_e^{k+1} = \sum_{p=1}^{N_p} \frac{a_p}{b_p} e^{-b_p(k+1/2)\Delta t} \left(1 - e^{-b_p \Delta t}\right) \quad k = 0, 1, 2, \dots \quad (8.6.14)$$

With this, the summation in Equation 8.6.9 can be written as

$$\psi^n = \sum_{p=1}^{N_p} \psi_p^n \quad (8.6.15)$$

where ψ_p^n is given by

$$\psi_p^n = \sum_{k=0}^{n-1} \frac{a_p}{b_p \Delta t} e^{-b_p(k+1/2)\Delta t} \left(1 - e^{-b_p \Delta t}\right) (\mathcal{E}^{n-k} - \mathcal{E}^{n-k-1}). \quad (8.6.16)$$

It is not difficult to see that ψ_p^n can be evaluated recursively as

$$\psi_p^n = \frac{a_p}{b_p \Delta t} e^{-b_p \Delta t / 2} \left(1 - e^{-b_p \Delta t}\right) (\mathcal{E}^n - \mathcal{E}^{n-1}) + e^{-b_p \Delta t} \psi_p^{n-1}. \quad (8.6.17)$$

As a result, ψ^n can be evaluated very efficiently, and the evaluation requires only \mathcal{E}^{n-1} and \mathcal{E}^n , in contrast to all the past fields in a general case. Note that complex poles always appear in a pair, which are complex conjugates of each other. Hence, when b_p is a complex number, there is another complex conjugate pole b_p^* . Consequently, even though ψ_p^n can have a complex value, ψ^n always has a real value.

8.6.2 Auxiliary Differential Equation Approach

An alternative approach to modeling the medium dispersion is to calculate the convolution in Equation 8.6.2 by solving an auxiliary differential equation. First, we notice that the Laplace transform of Equation 8.6.12 for the single-pole case is given by

$$\tilde{\chi}_e(\omega) = \frac{a_p}{j\omega + b_p} \quad (8.6.18)$$

where both a_p and b_p have real values. Next, we denote the second term on the right-hand side of Equation 8.6.2 as the polarization current,

$$\mathcal{J}_p(t) = \epsilon_0 \tilde{\chi}_e(t) * \frac{\partial \mathcal{E}(t)}{\partial t} \quad (8.6.19)$$

whose Laplace transform is given by

$$\mathcal{J}_p(\omega) = j\omega \epsilon_0 \tilde{\chi}_e(\omega) \mathcal{E}(\omega). \quad (8.6.20)$$

Substituting Equation 8.6.18 into this equation, we obtain

$$(j\omega + b_p) \mathcal{J}_p(\omega) = j\omega \epsilon_0 a_p \mathcal{E}(\omega) \quad (8.6.21)$$

which can be transformed back into the time domain as

$$\frac{\partial \mathcal{J}_p(t)}{\partial t} + b_p \mathcal{J}_p(t) = \epsilon_0 a_p \frac{\partial \mathcal{E}(t)}{\partial t}. \quad (8.6.22)$$

The central-difference approximation of this equation at $t = (n + \frac{1}{2})\Delta t$ yields

$$\frac{\mathcal{J}_p^{n+1} - \mathcal{J}_p^n}{\Delta t} + b_p \mathcal{J}_p^{n+1/2} = \epsilon_0 a_p \frac{\mathcal{E}^{n+1} - \mathcal{E}^n}{\Delta t} \quad (8.6.23)$$

from which we obtain

$$\mathcal{J}_p^{n+1} = \frac{2\epsilon_0 a_p (\mathcal{E}^{n+1} - \mathcal{E}^n) + (2 - b_p \Delta t) \mathcal{J}_p^n}{2 + b_p \Delta t} \quad (8.6.24)$$

$$\mathcal{J}_p^{n+1/2} = \frac{\mathcal{J}_p^{n+1} + \mathcal{J}_p^n}{2} = \frac{\epsilon_0 a_p (\mathcal{E}^{n+1} - \mathcal{E}^n) + 2 \mathcal{J}_p^n}{2 + b_p \Delta t}. \quad (8.6.25)$$

When Equation 8.6.25 is employed in the discretization of the Maxwell–Ampère law given in Equation 8.6.7, we obtain the time-stepping equation

$$\mathcal{E}^{n+1} = \frac{1}{\beta'} \left[\alpha' \mathcal{E}^n + (\nabla \times \mathcal{H})^{n+1/2} - \frac{2 \mathcal{J}_p^n}{2 + b_p \Delta t} \right] \quad (8.6.26)$$

where

$$\alpha' = \frac{\epsilon_\infty - \sigma}{\Delta t} - \frac{\sigma}{2} + \frac{\epsilon_0 a_p}{2 + b_p \Delta t} \quad \text{and} \quad \beta' = \frac{\epsilon_\infty}{\Delta t} + \frac{\sigma}{2} + \frac{\epsilon_0 a_p}{2 + b_p \Delta t}. \quad (8.6.27)$$

Clearly, in this approach, once we calculate \mathcal{E}^n and $\mathcal{H}^{n+1/2}$, we can first use Equation 8.6.24 to compute \mathcal{J}_p^n and then employ Equation 8.6.26 to compute \mathcal{E}^{n+1} .

The approach described above can be extended to multipole cases. Consider, for example, the double-pole case whose poles are complex. In this case, the two poles must be complex conjugates of each other. Hence, the susceptibility can be represented by

$$\tilde{\chi}_e(\omega) = \frac{a_p}{j\omega + b_p} + \frac{a_p^*}{j\omega + b_p^*} \quad (8.6.28)$$

which can be further written as

$$\tilde{\chi}_e(\omega) = \frac{2j\omega \operatorname{Re}(a_p) + 2 \operatorname{Re}(a_p b_p)}{(j\omega)^2 + 2j\omega \operatorname{Re}(b_p) + |b_p|^2}. \quad (8.6.29)$$

The corresponding auxiliary differential equation for the polarization current becomes

$$\frac{\partial^2 \mathcal{J}_p(t)}{\partial t^2} + 2b'_p \frac{\partial \mathcal{J}_p(t)}{\partial t} + |b_p|^2 \mathcal{J}_p(t) = 2\epsilon_0 a'_p \frac{\partial^2 \mathcal{E}(t)}{\partial t^2} + 2\epsilon_0 \operatorname{Re}(a_p b_p) \frac{\partial \mathcal{E}(t)}{\partial t} \quad (8.6.30)$$

where $a'_p = \operatorname{Re}(a_p)$ and $b'_p = \operatorname{Re}(b_p)$. The central-difference discretization of this equation yields the time-stepping equation for \mathcal{J}_p as

$$\begin{aligned} \mathcal{J}_p^{n+1} = & \frac{1}{1+b'_p \Delta t} \left[2\epsilon_0 a'_p (\mathcal{E}^{n+1} - 2\mathcal{E}^n + \mathcal{E}^{n-1}) + \epsilon_0 \Delta t \operatorname{Re}(a_p b_p) (\mathcal{E}^{n+1} - \mathcal{E}^{n-1}) \right. \\ & \left. + \left(2 - |b_p \Delta t|^2 \right) \mathcal{J}_p^n - (1 - b'_p \Delta t) \mathcal{J}_p^{n-1} \right] \end{aligned} \quad (8.6.31)$$

and \mathcal{J}_p at $t = (n + \frac{1}{2})\Delta t$ as

$$\begin{aligned} \mathcal{J}_p^{n+1/2} = & \frac{1}{2(1+b'_p \Delta t)} \left[2\epsilon_0 a'_p (\mathcal{E}^{n+1} - 2\mathcal{E}^n + \mathcal{E}^{n-1}) + \epsilon_0 \Delta t \operatorname{Re}(a_p b_p) (\mathcal{E}^{n+1} - \mathcal{E}^{n-1}) \right. \\ & \left. + \left(3 + b'_p \Delta t - |b_p \Delta t|^2 \right) \mathcal{J}_p^n - (1 - b'_p \Delta t) \mathcal{J}_p^{n-1} \right]. \end{aligned} \quad (8.6.32)$$

When Equation 8.6.32 is adopted in the discretization of Equation 8.6.7, we obtain the time-stepping equation for \mathcal{E} as

$$\mathcal{E}^{n+1} = \frac{1}{\beta''} \left[\alpha'' \mathcal{E}^n + \gamma'' \mathcal{E}^{n-1} + (\nabla \times \mathcal{H})^{n+1/2} - \left(3 + b'_p \Delta t - |b_p \Delta t|^2 \right) \mathcal{J}_p^n + (1 - b'_p \Delta t) \mathcal{J}_p^{n-1} \right] \quad (8.6.33)$$

where

$$\alpha'' = \frac{\epsilon_\infty}{\Delta t} - \frac{\sigma}{2} + \frac{2\epsilon_0 a'_p}{1+b'_p \Delta t} \quad (8.6.34)$$

$$\beta'' = \frac{\epsilon_\infty}{\Delta t} + \frac{\sigma}{2} + \epsilon_0 \frac{2a'_p + \Delta t \operatorname{Re}(a_p b_p)}{2(1+b'_p \Delta t)} \quad (8.6.35)$$

$$\gamma'' = \epsilon_0 \frac{\Delta t \operatorname{Re}(a_p b_p) - 2a'_p}{2(1+b'_p \Delta t)}. \quad (8.6.36)$$

Therefore, once we calculate \mathcal{E}^n and $\mathcal{H}^{n+1/2}$, we can first use Equation 8.6.31 to compute \mathcal{J}_p^n and then employ Equation 8.6.33 to compute \mathcal{E}^{n+1} .

8.7 WAVE EXCITATION AND FAR-FIELD CALCULATION

In this section we discuss two practical issues in the FDTD simulation of electromagnetic scattering and radiation problems. The first one is how to model wave excitation due to a source outside the computational domain, such as the case in a scattering analysis. The second issue is how to calculate far fields from the FDTD solution of near fields. The

far-field calculation is often encountered when we want to calculate radar cross-sections in a scattering analysis and radiation patterns in an antenna radiation analysis.

8.7.1 Modeling of Wave Excitation

When the source of an electromagnetic field is inside the computational domain and is specified by the electric current density, the incorporation of the source into the FDTD simulation is straightforward. The FDTD formulation can also be extended easily to incorporate sources specified by the equivalent magnetic current density. When the source of a field is outside the computational domain, the modeling of the source is more involved. In this case, we first recognize that the ABC or the PML used to truncate the computational domain should absorb only the scattered field instead of the total field. The scattered field is defined as the difference between the total field and the field produced by the source in the absence of the object to be considered. The latter is also known as the incident field. With this recognition, we can design two numerical schemes to model the excitation due to an external source.

The first approach is to employ the scattered field in the FDTD simulation. In other words, we first write Maxwell's equations for the scattered field and then apply the FDTD method to discretize these equations to obtain the time-stepping formulas. If the background medium is free space, Maxwell's equations for the scattered field (\mathcal{E}^{sc} , \mathcal{H}^{sc}) are given by

$$\nabla \times \mathcal{E}^{\text{sc}} = -\mu \frac{\partial \mathcal{H}^{\text{sc}}}{\partial t} + \mathcal{M}_{\text{eq}} \quad (8.7.1)$$

$$\nabla \times \mathcal{H}^{\text{sc}} = \epsilon \frac{\partial \mathcal{E}^{\text{sc}}}{\partial t} + \sigma \mathcal{E}^{\text{sc}} + \mathcal{J}_{\text{eq}} \quad (8.7.2)$$

where

$$\mathcal{J}_{\text{eq}} = (\epsilon - \epsilon_0) \frac{\partial \mathcal{E}^{\text{inc}}}{\partial t} + \sigma \mathcal{E}^{\text{inc}}, \quad \mathcal{M}_{\text{eq}} = (\mu - \mu_0) \frac{\partial \mathcal{H}^{\text{inc}}}{\partial t}. \quad (8.7.3)$$

These equations are obtained by substituting $\mathcal{E} = \mathcal{E}^{\text{inc}} + \mathcal{E}^{\text{sc}}$ and $\mathcal{H} = \mathcal{H}^{\text{inc}} + \mathcal{H}^{\text{sc}}$ into Equations 8.4.9 and 8.4.10 and then by invoking the fact that the incident field (\mathcal{E}^{inc} , \mathcal{H}^{inc}) satisfies the free-space Maxwell's equations. Since the incident field is known for any place and any time, the equivalent electric and magnetic current densities in Equation 8.7.3, which exist only inside the object to be considered, can be evaluated and used as the excitation of the scattered field. The FDTD discretization of Equations 8.7.1 and 8.7.2 is similar to the formulation described in Section 8.4.2. When the object contains perfect electrically conducting (PEC) surfaces, we need to apply boundary conditions on these surfaces. For the scattered field, these boundary conditions become

$$\hat{n} \times \mathcal{E}^{\text{sc}} = -\hat{n} \times \mathcal{E}^{\text{inc}}, \quad \hat{n} \cdot \mathcal{H}^{\text{sc}} = -\hat{n} \cdot \mathcal{H}^{\text{inc}} \quad (8.7.4)$$

to ensure that the tangential component of the total electric field and the normal component of the total magnetic field vanish on the PEC surface. These two boundary conditions can be implemented easily whether the PEC coincides with the electric-field grid or with the magnetic-field grid.

The approach described above requires calculation of the equivalent currents (Eq. 8.7.3) over the entire penetrable volume of the object and application of the boundary

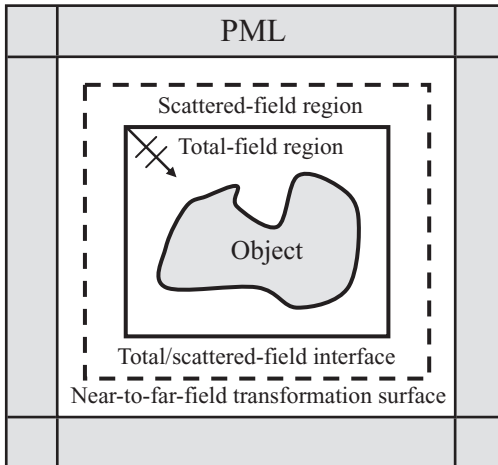


Figure 8.16 Typical setup for FDTD simulation of scattering problems. A total/scattered-field interface is introduced as a Huygens' surface to excite the incident field in the total-field region. A near-to-far-field transformation is employed to calculate far fields based on the near fields on the surface. (See color insert.)

conditions (Eq. 8.7.4) to the PEC surface of the object. This may result in a much longer computation time when the object is large and complex. An alternative approach is to introduce a surface, usually a rectangular box, placed between the object and the ABC or PML (Fig. 8.16). Inside this surface, the FDTD is applied to the total field, and outside the surface, the FDTD is applied to the scattered field. By doing this, there is no need to introduce the volumetric equivalent sources inside the object and modify the boundary conditions on the PEC surfaces because the total field is used around the object. Meanwhile, the ABC or PML absorbs only the scattered field. The excitation will enter the computational domain at the surface that separates the total and scattered fields. This surface is often referred to as a *Huygens' surface*, and the approach is called the *total- and scattered-field decomposition method* [18].

To illustrate the implementation of the total- and scattered-field decomposition algorithm, we consider one side of a rectangular Huygens' surface that is specified by $i = i_{\min}$, which is a surface perpendicular to the x -axis. We assume that the scattered field is employed for the region to the left of the surface ($i < i_{\min}$) and the total field is employed for the region to the right of the surface ($i > i_{\min}$). Furthermore, we assume that this surface coincides with the electric-field grid (or, in other words, it contains the discrete \mathcal{E}_y and \mathcal{E}_z) and that the total field is used for the field components (\mathcal{E}_y , \mathcal{E}_z , and \mathcal{H}_x) on this surface ($i = i_{\min}$). Then, whenever the scattered field $\mathcal{E}_y^{sc,n}(i_{\min}, j + \frac{1}{2}, k)$ and $\mathcal{E}_z^{sc,n}(i_{\min}, j, k + \frac{1}{2})$ are required in a time-stepping calculation using Equations 8.4.18 and 8.4.19, they are replaced with

$$\mathcal{E}_y^{sc,n}(i_{\min}, j + \frac{1}{2}, k) \rightarrow \mathcal{E}_y^n(i_{\min}, j + \frac{1}{2}, k) - \mathcal{E}_y^{inc,n}(i_{\min}, j + \frac{1}{2}, k) \quad (8.7.5)$$

$$\mathcal{E}_z^{sc,n}(i_{\min}, j, k + \frac{1}{2}) \rightarrow \mathcal{E}_z^n(i_{\min}, j, k + \frac{1}{2}) - \mathcal{E}_z^{inc,n}(i_{\min}, j, k + \frac{1}{2}). \quad (8.7.6)$$

Similarly, whenever the total field $\mathcal{H}_y^{n+1/2}(i_{\min} - \frac{1}{2}, j, k + \frac{1}{2})$ and $\mathcal{H}_z^{n+1/2}(i_{\min} - \frac{1}{2}, j + \frac{1}{2}, k)$ are required in a time-stepping calculation using Equations 8.4.21 and 8.4.22, they are replaced with

$$\mathcal{H}_y^{n+1/2}(i_{\min} - \frac{1}{2}, j, k + \frac{1}{2}) \rightarrow \mathcal{H}_y^{\text{sc}, n+1/2}(i_{\min} - \frac{1}{2}, j, k + \frac{1}{2}) + \mathcal{H}_y^{\text{inc}, n+1/2}(i_{\min} - \frac{1}{2}, j, k + \frac{1}{2}) \quad (8.7.7)$$

$$\mathcal{H}_z^{n+1/2}(i_{\min} - \frac{1}{2}, j + \frac{1}{2}, k) \rightarrow \mathcal{H}_z^{\text{sc}, n+1/2}(i_{\min} - \frac{1}{2}, j + \frac{1}{2}, k) + \mathcal{H}_z^{\text{inc}, n+1/2}(i_{\min} - \frac{1}{2}, j + \frac{1}{2}, k). \quad (8.7.8)$$

It is clear that this implementation requires only the incident electric fields on the Huygens' surface and the incident magnetic fields one-half grid away from the surface. In principle, this should excite the desired incident field inside the total-field region and no incident field in the scattered-field region. However, because of the numerical dispersion error discussed in Section 8.2.4, the incident field excited inside the total-field region will have a small phase error, and there will be a small amount of leakage of the incident field into the scattered-field region. Special treatment can be carried out to reduce the phase error and undesired leakage [19,20].

For a plane wave incident from the direction $(\theta^{\text{inc}}, \phi^{\text{inc}})$, the incident electric field is given by

$$\mathcal{E}^{\text{inc}}(\mathbf{r}, t) = (\cos \alpha \hat{\theta} + \sin \alpha \hat{\phi}) E_0 \mathcal{J} \left[t - \hat{k}^{\text{inc}} \cdot (\mathbf{r} - \mathbf{r}_0) / c_0 \right] \quad (8.7.9)$$

where α denotes the polarization angle, E_0 denotes the peak field strength, \mathbf{r}_0 denotes a reference position vector, c_0 denotes the speed of light, \hat{k}^{inc} denotes the unit vector along the incident direction, which is given by

$$\hat{k}^{\text{inc}} = -(\sin \theta^{\text{inc}} \cos \phi^{\text{inc}} \hat{x} + \sin \theta^{\text{inc}} \sin \phi^{\text{inc}} \hat{y} + \cos \theta^{\text{inc}} \hat{z}) \quad (8.7.10)$$

and finally, $\mathcal{J} \left[t - \hat{k}^{\text{inc}} \cdot (\mathbf{r} - \mathbf{r}_0) / c_0 \right]$ denotes the temporal profile of the incident field. For a Gaussian pulse, the temporal profile and its frequency spectrum are given by

$$\mathcal{J}(t) = \exp \left[-\frac{1}{2} (t/\tau_p)^2 \right] \quad (8.7.11)$$

$$f(\omega) = \sqrt{2\pi} \tau_p \exp \left[-\frac{1}{2} (\omega \tau_p)^2 \right] \quad (8.7.12)$$

where τ_p denotes the characteristic time. A Gaussian pulse contains a dc component, which is usually undesirable in a numerical simulation, but we can eliminate the dc component by taking a time derivative, which yields a differentiated Gaussian pulse, or a Neumann pulse, as

$$\mathcal{J}(t) = -\frac{t}{\tau_p} \exp \left[-\frac{1}{2} (t/\tau_p)^2 \right] \quad (8.7.13)$$

$$f(\omega) = j\omega \sqrt{2\pi} (\tau_p)^2 \exp \left[-\frac{1}{2} (\omega \tau_p)^2 \right]. \quad (8.7.14)$$

Another alternative is a modulated Gaussian pulse, defined as

$$\mathcal{J}(t) = \exp \left[-\frac{1}{2} (t/\tau_p)^2 \right] \sin \omega_0 t \quad (8.7.15)$$

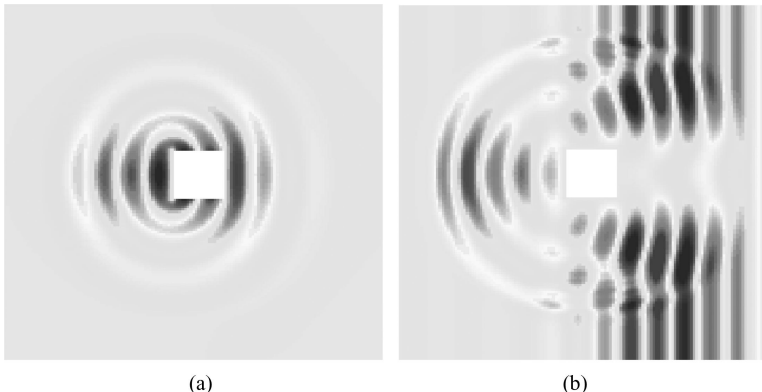


Figure 8.17 Scattering of a TM-polarized, modulated Gaussian pulse by a square conducting cylinder. (a) Snapshot of the scattered electric field. (b) Snapshot of the total electric field. (See color insert.)

$$f(\omega) = -j\sqrt{\pi/2}\tau_p \left\{ \exp\left\{-\frac{1}{2}[(\omega - \omega_0)\tau_p]^2\right\} - \exp\left\{-\frac{1}{2}[(\omega + \omega_0)\tau_p]^2\right\} \right\} \quad (8.7.16)$$

where ω_0 denotes the modulation frequency. In certain applications where one is interested in a steady-state solution at a single frequency, a tapered sinusoidal temporal profile can be used,

$$\mathcal{J}(t) = [1 - \exp(-t/\tau_p)] \sin \omega_0 t \quad (8.7.17)$$

where $\tau_p = 3T \sim 5T$ and $T = 2\pi/\omega_0$. The taper function gradually increases the amplitude of the sinusoid signal to reduce noises caused by the time discretization of the signal.

To give an example, we consider a TM-polarized plane wave incident normally on an infinitely long, square conducting cylinder. The incident wave has a temporal profile of a modulated Gaussian pulse. A snapshot of the scattered electric field is shown in Figure 8.17a, and a snapshot of the corresponding total electric field is displayed in Figure 8.17b. For the scattered-field calculation, the excitation is introduced through the boundary condition at the conducting surface, whereas for the total-field calculation, the incident field is excited by using a Huygens' surface.

8.7.2 Near-to-Far Field Transformation

A FDTD calculation typically yields numerical results for the electric and magnetic fields inside and nearby the object to be considered. When we need to find far fields, we have to calculate them from the near fields. This procedure is referred to as the *near-to-far-field* (NTF) transformation. To accomplish this, we can introduce a closed surface to enclose the entire object, which can be placed in the scattered-field region in a scattering analysis (Fig. 8.16). By denoting this surface as S_{NTF} , we can calculate the equivalent surface electric and magnetic current densities as $\mathcal{J}_s^{\text{eq}} = \hat{n} \times \mathcal{H}$ and $\mathcal{M}_s^{\text{eq}} = \mathcal{E} \times \hat{n}$. For scattering analysis, the scattered fields can be used to define these equivalent surface currents since the incident fields have no contribution to the scattered far fields. Based on the surface equivalence principle discussed in Section 3.4, we can let these equivalent currents radiate in free space, from which we obtain the field anywhere outside S_{NTF} . To this end, we can use one of the following two approaches.

The first approach is to calculate the far field in the frequency domain. We first calculate $\mathcal{J}_s^{\text{eq}}$ and $\mathcal{M}_s^{\text{eq}}$ over the entire period and then transform them into the frequency domain using the Fourier transform. Then we employ the technique discussed in Section 2.3.3 to find the far field as

$$E_\theta(\mathbf{r}) = -\frac{jk_0 e^{-jk_0 r}}{4\pi r} (L_\phi + Z_0 N_\theta) \quad (8.7.18)$$

$$E_\phi(\mathbf{r}) = \frac{jk_0 e^{-jk_0 r}}{4\pi r} (L_\theta - Z_0 N_\phi) \quad (8.7.19)$$

where Z_0 is the free-space impedance and

$$\mathbf{N}(\hat{\mathbf{r}}) = \iint_{S_{\text{NTF}}} \mathbf{J}_s^{\text{eq}}(\hat{\mathbf{r}}') e^{jk_0 \mathbf{r}' \cdot \hat{\mathbf{r}}} dS' \quad (8.7.20)$$

$$\mathbf{L}(\hat{\mathbf{r}}) = \iint_{S_{\text{NTF}}} \mathbf{M}_s^{\text{eq}}(\hat{\mathbf{r}}') e^{jk_0 \mathbf{r}' \cdot \hat{\mathbf{r}}} dS'. \quad (8.7.21)$$

The second approach is to calculate the far field directly in the time domain. The required formulas can be obtained from Equations 8.7.18 to 8.7.21 through the Laplace transform:

$$\mathcal{E}_\theta(\mathbf{r}, t) = -\frac{1}{4\pi r c_0} \left[\frac{\partial}{\partial t} \mathcal{L}_\phi \left(\hat{\mathbf{r}}, t - \frac{\mathbf{r} \cdot \hat{\mathbf{k}}}{c_0} \right) + Z_0 \frac{\partial}{\partial t} \mathcal{N}_\theta \left(\hat{\mathbf{r}}, t - \frac{\mathbf{r} \cdot \hat{\mathbf{k}}}{c_0} \right) \right] \quad (8.7.22)$$

$$\mathcal{E}_\phi(\mathbf{r}, t) = \frac{1}{4\pi r c_0} \left[\frac{\partial}{\partial t} \mathcal{L}_\theta \left(\hat{\mathbf{r}}, t - \frac{\mathbf{r} \cdot \hat{\mathbf{k}}}{c_0} \right) - Z_0 \frac{\partial}{\partial t} \mathcal{N}_\phi \left(\hat{\mathbf{r}}, t - \frac{\mathbf{r} \cdot \hat{\mathbf{k}}}{c_0} \right) \right] \quad (8.7.23)$$

where

$$\mathcal{N}(\hat{\mathbf{r}}, \tau) = \iint_{S_{\text{NTF}}} \mathcal{J}_s^{\text{eq}} \left(\mathbf{r}', \tau + \frac{\mathbf{r}' \cdot \hat{\mathbf{r}}}{c_0} \right) dS' \quad (8.7.24)$$

$$\mathcal{L}(\hat{\mathbf{r}}, \tau) = \iint_{S_{\text{NTF}}} \mathcal{M}_s^{\text{eq}} \left(\mathbf{r}', \tau + \frac{\mathbf{r}' \cdot \hat{\mathbf{r}}}{c_0} \right) dS'. \quad (8.7.25)$$

Comparing the two approaches, the frequency-domain NTF transformation is most suitable for computing far-field patterns with dense angular sampling at only a few frequencies, while the time-domain NTF transformation is most suitable for computing far-field patterns over a wide frequency range at only a few observation angles.

8.8 SUMMARY

In this chapter we described the basic principle and formulation of the finite difference method for analysis of electromagnetic problems. We started with the construction of the finite differencing formulas and demonstrated their applications in solving one-dimensional diffusion and wave equations. Taking the advantage of the simplicity of one-dimensional problems, we discussed the stability analysis, which tells whether and under which condi-

tion a time-stepping formula is stable, and the numerical dispersion analysis, which quantifies the numerical phase error in the finite difference simulation of wave propagation. We then extended the finite difference method to the analysis of two-dimensional problems both in the time and frequency domains, which showed the major difference between the two analyses: The field in the time domain can be computed by time stepping, whereas the problem in the frequency domain can be solved only through a linear system of equations. After that, we introduced Yee's unique, yet highly powerful, FDTD scheme for solving Maxwell's equations, which has been considered a major breakthrough in the finite difference method. This was followed by the discussion of one of the most important issues for the finite difference simulation of open-region electromagnetic problems: the truncation of the infinite solution domain into a finite computational domain. We derived analytical ABCs and described a popular material-based ABC: the PML. Next, we described two methods to model dispersive media in the FDTD simulation; one was based on the evaluation of a convolution, and the other was based on the solution of an auxiliary differential equation. Finally, we discuss two practical issues in the FDTD simulation of electromagnetic scattering and radiation problems: modeling of wave excitation due to an external source and calculation of far fields from the near-field solution.

As mentioned at the beginning, the major advantages of the finite difference method are its simplicity, robustness, and power. The major disadvantage lies in its geometrical modeling of complex objects since an object is usually modeled by a collection of rectangular cells. This would result in a staircase approximation of curved surfaces or any surfaces that do not conform to the regular grids. Although it is possible to modify the finite difference scheme to model complex geometries more accurately, the simplicity and efficiency of the method would be compromised, and such a task would be best left for the finite element method, to be discussed in the next chapter. We also note that in this chapter we covered only the conditionally stable algorithms. Although it is possible to develop unconditionally stable algorithms, which place no restriction on the time-step size, these algorithms usually require solving a linear system of equations in each time step, thus significantly increasing the cost of the solution. It is hoped that this chapter provides the reader with a basic understanding of the finite difference method for the simulation of electromagnetic fields. The reader who wishes to study the finite difference method further can consult Taflove and Hagness [3] for a more detailed treatment of the method, including discussions on a variety of advanced topics and application examples.

REFERENCES

- [1] K. S. YEE, Numerical solution of initial boundary value problems involving Maxwell's equations in isotropic media, *IEEE Trans. Antennas Propagat.*, 14(3): 302–307, 1966.
- [2] K. S. KUNZ and R. J. LUEBBERS, *The Finite Difference Time Domain Method for Electromagnetics*. Boca Raton, FL: CRC Press, 1994.
- [3] A. TAFLOVE and S. C. HAGNESS, *Computational Electrodynamics: The Finite Difference Time Domain Method* (3rd edition). Norwood, MA: Artech House, 2005.
- [4] J.-P. BERENGER, A perfectly matched layer for the absorption of electromagnetic waves, *J. Comput. Phys.*, 114(2): 185–200, 1994.
- [5] D. S. KATZ, E. T. THIELE, and A. TAFLOVE, Validation and extension to three dimensions of the Berenger PML absorbing boundary condition for FD-TD meshes, *IEEE Microwave Guided Wave Lett.*, 4(8): 268–270, 1994.
- [6] W. C. CHEW and W. H. WEEDON, A 3D perfectly matched medium from modified Maxwell's equations with stretched coordinates, *Microw. Opt. Tech. Lett.*, 7(13): 599–604, 1994.
- [7] S. D. GEDNEY, Perfectly matched layer absorbing boundary conditions. *Computational Electrodynamics: The Finite Difference Time Domain Method* (3rd edition), edited by A. TAFLOVE and S. C. HAGNESS. Norwood, MA: Artech House, 2005, pp. 273–328.
- [8] W. C. CHEW and J. M. JIN, Perfectly matched layers in the discretized space: An analysis and optimization, *Electromagn.*, 16(4): 325–340, 1996.
- [9] M. KUZUOGLU and R. MITTRA, Frequency dependence of the constitutive parameters of causal perfectly

- anisotropic absorbers, *IEEE Microwave Guided Lett.*, 6(12): 447–449, 1996.
- [10] J. A. RODEN and S. D. GEDNEY, Convolution PML (CPML): An efficient FDTD implementation of the CFS-PML for arbitrary media, *Microw. Opt. Tech. Lett.*, 27(5): 334–339, 2000.
- [11] D. CORREIA and J. M. JIN, On the development of a higher-order PML, *IEEE Trans. Antennas Propagat.*, 53(12): 4157–4163, 2005.
- [12] J. CHEN, Z. FENG and J. M. JIN, Numerical simulation of SAR and B1-field inhomogeneity of shielded RF coils loaded with the human head, *IEEE Trans. Biomed. Eng.*, 45(5): 650–659, 1998.
- [13] R. J. LUEBBERS and F. HUNSSBERGER, FDTD for N th-order dispersive media, *IEEE Trans. Antennas Propagat.*, 40(11): 1297–1301, 1992.
- [14] D. F. KELLEY and R. J. LUBBERS, Piecewise linear recursive convolution for dispersive media using FDTD, *IEEE Trans. Antennas Propagat.*, 44(6): 792–797, 1996.
- [15] T. KASHIWA and I. FUKAI, A treatment by FDTD method of the dispersive characteristics associated with electronic polarization, *Microw. Opt. Technol. Lett.*, 3(6): 203–205, 1990.
- [16] R. JOSEPH, S. HAGNESS, and A. TAFLOVE, Direct time integration of Maxwell's equations in linear dispersive media with absorption for scattering and propagation of femtosecond electromagnetic pulses, *Optics Lett.*, 16(18): 1412–1414, 1991.
- [17] M. OKONIEWSKI, M. MROZOWSKI, and M. A. STUCHLY, Simple treatment of multi-term dispersion in FDTD, *IEEE Microwave Guided Wave Lett.*, 7(5): 121–123, 1997.
- [18] D. MEREWETHER, R. FISHER, and F. W. SMITH, On implementing a numerical Huygens' source scheme in a finite-difference program to illuminate scattering bodies, *IEEE Trans. Nucl. Sci.*, 27(6): 1829–1833, 1980.
- [19] T. MARTIN and L. PETTERSSON, Dispersion compensation for Huygens' sources and far-zone transformations in FDTD, *IEEE Trans. Antennas Propagat.*, 48(4): 494–501, 2000.
- [20] M. E. WATTS and R. E. DIAZ, Perfect plane-wave injection into a finite FDTD domain through teleportation of fields, *Electromagn.*, 23(2): 187–201, 2003.

PROBLEMS

8.1. Derive the forward and backward differencing formulas for the second derivative and show that they are both first-order accurate.

8.2. Apply the forward differencing formula derived in Problem 8.1 to the second derivative in time of the wave equation (Eq. 8.2.11) while keeping the central differencing for the spatial derivative. Derive the time-stepping formula and analyze its stability. Repeat the problem by using backward differencing for the second derivative in time.

8.3. Apply central differencing to the following equation,

$$\frac{\partial^2 \mathcal{E}_z}{\partial x^2} - \mu \epsilon \frac{\partial^2 \mathcal{E}_z}{\partial t^2} - \mu \sigma \frac{\partial \mathcal{E}_z}{\partial t} = \mu \frac{\partial \mathcal{J}_z}{\partial t}$$

to derive the time-stepping formula. Carry out the stability analysis and find the stability condition. Discuss the effect of the loss term on the stability analysis.

8.4. Perform the stability analysis on the time-stepping formula in Equation 8.3.4 and derive the stability condition shown in Equation 8.3.5.

8.5. Perform the numerical dispersion analysis on the time-stepping formula in Equation 8.3.4 and derive Equation 8.3.6 and then Equation 8.3.7.

8.6. Consider the shielded microstrip transmission line sketched in Figure 8.18a. Assume that the strip line has a voltage of 1V and the ground has a voltage of 0V. Formulate the finite difference solution for the electric potential. Furthermore, formulate an approach to calculating the capacitance and inductance per unit length and then the characteristic impedance of the transmission line.

8.7. Consider a dielectric-loaded rectangular waveguide sketched in Figure 8.18b. Formulate the finite difference solution to calculate the cutoff wavenumbers for both EH and HE modes as defined in Section 5.3.2.

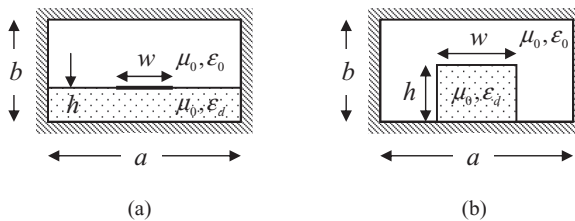


Figure 8.18 (a) Shielded microstrip line. (b) Dielectric loaded waveguide.

- 8.8. Augment Equations 8.4.1 and 8.4.2 with the magnetic conduction loss term and derive their time-stepping formulas using Yee's FDTD scheme.
- 8.9. Augment Equations 8.4.11–8.4.13 with the magnetic conduction loss term and derive their time-stepping formulas using Yee's FDTD scheme.
- 8.10. Derive the time-stepping formulas in Equations 8.4.5–8.4.7 using Maxwell's equations in integral form in conjunction with the mid-point integration.
- 8.11. Apply the following rational function approximation

$$\sqrt{1 - \left(\frac{k_y}{k}\right)^2} = \frac{1 - \frac{3}{4}S^2}{1 - \frac{1}{4}S^2}, \quad S = \frac{k_y}{k}$$

to Equation 8.5.12 to derive a third-order absorbing boundary condition. Furthermore, derive the reflection coefficient of this boundary condition.

- 8.12. Show that if ∇_s in Equations 8.5.21 and 8.5.22 is defined as

$$\nabla_s = \hat{x} \frac{1}{s_x^{1-\alpha}} \frac{\partial}{\partial x} \frac{1}{s_x^\alpha} + \hat{y} \frac{1}{s_y^{1-\alpha}} \frac{\partial}{\partial y} \frac{1}{s_y^\alpha} + \hat{z} \frac{1}{s_z^{1-\alpha}} \frac{\partial}{\partial z} \frac{1}{s_z^\alpha},$$

a perfectly matched interface still exists regardless of the value of α . Note that when $\alpha = \frac{1}{2}$, ∇_s becomes a symmetric operator.

- 8.13. Derive the time-stepping formulas from the modified Maxwell's equations (Eqs. 8.5.56–8.5.61). Describe the use of the resulting time-stepping formulas to complete one time stepping.
- 8.14. Derive the time-stepping formulas from the y - and z -components of Equations 8.5.72–8.5.75.
- 8.15. Develop an FDTD program to calculate the radiation of an infinitely long current by solving the time-domain Maxwell's equations with a PML absorbing boundary condition. After the code is validated, consider the case in which the infinitely long current radiates in the presence of an infinitely large conducting sheet with one or two slots. Present your work in the form of a formal paper (including Abstract, Introduction, Formulation, Results, Conclusion, and References).
- 8.16. Using Yee's FDTD scheme, formulate a numerical solution to calculate the scattered field by a rectangular conducting cylinder for both TM- and TE-polarized incident waves. Discuss approaches to implementing the incident field in the FDTD solution and calculating the far field from the near-field solution. ■

THE FINITE ELEMENT METHOD

Like the finite difference method, the *finite element method* (FEM) is a numerical procedure to convert partial differential equations into a set of linear algebraic equations to obtain approximate solutions to boundary-value problems of mathematical physics. Instead of approximating the differential operators, the finite element method approximates the solution of a partial differential equation. Since the method was first proposed by Courant in 1943 to solve variational problems in potential theory [1], it has been developed and applied extensively to problems of structural analysis and increasingly to problems in other fields. Today, the finite element method is recognized as a general preeminent method applicable to a wide variety of engineering and mathematical problems, including those in microwave engineering and electromagnetics.

The first application of the finite element method to microwave engineering and electromagnetics appeared in 1969 when Silvester employed it to analyze wave propagation in a hollow waveguide [2]. The importance of the method was quickly recognized and successful applications were achieved for the analysis of a variety of electrostatic, magnetostatic, and dielectric-loaded waveguide problems. In 1974, Mei developed a technique that combined the finite element method with eigenfunction expansion to deal with open-region electromagnetic problems such as antenna and scattering analysis [3]. In 1982, Marin developed an alternative method that combined the finite element method and a boundary integral equation to deal with open-region scattering problems [4].

An important breakthrough in the finite element analysis of vector electromagnetic field problems occurred in the 1980s with the development of edge-based vector elements [5–7]. These new elements accurately model the nature of the electric and magnetic fields and eliminate many of the problems associated with traditional node-based scalar elements. Since the development of the vector elements, the finite element method has become a very powerful numerical technique in computational electromagnetics. Today, the method is used as a major design tool for antennas and microwave devices. Its basic principle and a variety of applications have been described in many books, such as those of Silvester and Ferrari [8] and Jin [9].

In this chapter we introduce the basic principle of the finite element method by first considering a simple one-dimensional example. We then describe in detail the formulation of the finite element analysis of scalar and vector problems in the frequency domain. This is followed by the extension to the time domain. In each case, we present several numerical examples to demonstrate the application and capability of the finite element method. Finally, we discuss the truncation of the computational domain for the analysis of unbounded electromagnetic problems using absorbing boundary conditions (ABCs) and perfectly matched layers (PMLs) and some other numerical aspects in the implementation of the finite element method.

9.1 INTRODUCTION TO THE FINITE ELEMENT METHOD

To illustrate the basic principle of the finite element method, we start with a brief description of the weighted residual method and a simple example that solves the one-dimensional Helmholtz equation.

9.1.1 The General Principle

The finite element method can be formulated using either the weighted residual method or the variational method. The weighted residual method starts directly from the partial differential equation of the boundary-value problem, whereas the variational method starts from the variational representation of the boundary-value problem. In this chapter we choose to use the weighted residual method for its simplicity.

To introduce the basic principle of the weighted residual method, we consider a partial differential equation, which can be written symbolically as

$$\mathcal{L}\varphi = f \quad (9.1.1)$$

where \mathcal{L} denotes the differential operator, φ denotes the unknown solution to be found, and f denotes the source function. To seek the solution for φ , we first expand it using a set of *basis functions*

$$\varphi = \sum_{j=1}^N c_j v_j \quad (9.1.2)$$

where v_j ($j = 1, 2, \dots, N$) denote the basis functions whose linear combination is able to represent the unknown solution and c_j are the corresponding unknown expansion coefficients. The weighted residual method attempts to determine c_j by substituting Equation 9.1.2 into Equation 9.1.1 and then integrating the resulting equation with a *weighting function* w_i over the entire solution domain Ω , which yields

$$\int_{\Omega} w_i \mathcal{L} \left(\sum_{j=1}^N c_j v_j \right) d\Omega = \int_{\Omega} w_i f d\Omega. \quad (9.1.3)$$

Given a set of weighting functions, this equation defines a set of linear algebraic equations that can be solved for c_j after the boundary conditions of the problem are applied. It then remains to choose the weighting functions w_i . Among various choices for w_i , the most popular one is to choose $w_i = v_i$, and the resulting formulation is called *Galerkin's method*. With this choice, Equation 9.1.3 becomes

$$\sum_{j=1}^N c_j \int_{\Omega} v_i \mathcal{L}(v_j) d\Omega = \int_{\Omega} v_i f d\Omega \quad i = 1, 2, \dots, N \quad (9.1.4)$$

or

$$\sum_{j=1}^N S_{ij} c_j = b_i \quad i = 1, 2, \dots, N \quad (9.1.5)$$

where

$$S_{ij} = \int_{\Omega} v_i \mathcal{L}(v_j) d\Omega \quad (9.1.6)$$

$$b_i = \int_{\Omega} v_i f d\Omega. \quad (9.1.7)$$

For a self-adjoint problem,

$$\int_{\Omega} v_i \mathcal{L}(v_j) d\Omega = \int_{\Omega} v_j \mathcal{L}(v_i) d\Omega \quad (9.1.8)$$

hence, $S_{ij} = S_{ji}$. In this case, the coefficient matrix of the linear system defined by Equation 9.1.5 is symmetric.

In the formulation described above, the most critical part is to find a set of basis functions that can be used to expand the unknown solution. For complicated two- and three-dimensional problems having irregularly shaped solution domains, this is very difficult, if not impossible. The basic idea of the finite element method is to divide the solution domain into small subdomains, which are called *finite elements*, and then use simple functions, such as linear and quadratic functions, to approximate the unknown solution over each element. It is this idea of using subdomain basis functions that gave birth to a highly powerful numerical technique capable of modeling very complicated boundary-value problems in engineering and physical sciences.

9.1.2 One-Dimensional Example

To illustrate the specific formulation of the finite element method, we consider a one-dimensional boundary-value problem defined by the Helmholtz equation

$$\frac{d^2\varphi(x)}{dx^2} + k^2 \varphi(x) = f(x) \quad 0 < x < L \quad (9.1.9)$$

together with the boundary conditions

$$\varphi|_{x=0} = p \quad (9.1.10)$$

$$\left[\frac{d\varphi}{dx} + \gamma \varphi \right]_{x=L} = q. \quad (9.1.11)$$

Two different boundary conditions are used here to demonstrate their different treatment. The Neumann boundary condition can be considered as a special case of Equation 9.1.11 with $\gamma = 0$.

The first step of the finite element method is to divide the solution domain $(0, L)$ into small subdomains, which in this case are short segments. These segments are the finite elements, and the joints between the segments are called *nodes* (Fig. 9.1). We can always

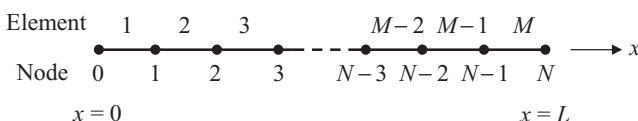


Figure 9.1 One-dimensional domain subdivided into linear elements.

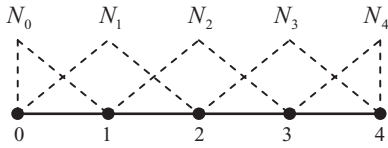


Figure 9.2 One-dimensional linear basis functions.

make the elements small enough such that the unknown solution over each element can be obtained by linear interpolation between the values of φ at the two ends of the element. Doing so, we can express the unknown solution as

$$\varphi(x) = \sum_{j=0}^N \varphi_j N_j(x) \quad (9.1.12)$$

where φ_j denotes the unknown value of φ at the node between the j th and $(j+1)$ th elements, and $N_j(x)$ is the associated basis function. Except for the first and last nodes, $N_j(x)$ is a *triangle function* that has a non-vanishing value only over the j th and $(j+1)$ th elements. More specifically, $N_j(x)$ has a value of 1 at the j th node and decreases linearly to zero at the two neighboring nodes. At the first and last nodes, $N_j(x)$ spans only one element (Fig. 9.2). Because of the boundary condition in Equation 9.1.10, Equation 9.1.12 can also be written as

$$\varphi(x) = \sum_{j=1}^N \varphi_j N_j(x) + \varphi_0 N_0(x) = \sum_{j=1}^N \varphi_j N_j(x) + p N_0(x). \quad (9.1.13)$$

Hence, only φ_j ($j = 1, 2, \dots, N$) are to be determined.

Next, we apply Galerkin's method by multiplying Equation 9.1.9 by $N_i(x)$ ($i = 1, 2, \dots, N$) and integrating over $(0, L)$ to find

$$\int_0^L N_i(x) \left[\frac{d^2 \varphi(x)}{dx^2} + k^2 \varphi(x) \right] dx = \int_0^L N_i(x) f(x) dx. \quad (9.1.14)$$

Using integration by parts, we obtain

$$\int_0^L \left[\frac{dN_i(x)}{dx} \frac{d\varphi(x)}{dx} - k^2 N_i(x) \varphi(x) \right] dx - \left[N_i(x) \frac{d\varphi(x)}{dx} \right]_{x=L} = - \int_0^L N_i(x) f(x) dx \quad (9.1.15)$$

where we used the fact that $N_i(x)$ ($i = 1, 2, \dots, N$) vanishes at $x = 0$. The application of the boundary condition in Equation 9.1.11 yields

$$\int_0^L \left[\frac{dN_i(x)}{dx} \frac{d\varphi(x)}{dx} - k^2 N_i(x) \varphi(x) \right] dx - [N_i(x)(q - \gamma\varphi)]_{x=L} = - \int_0^L N_i(x) f(x) dx. \quad (9.1.16)$$

Now, we can substitute Equation 9.1.13 into Equation 9.1.16 to obtain a set of linear equations

$$\sum_{j=1}^N K_{ij} \varphi_j = b_i \quad i = 1, 2, \dots, N \quad (9.1.17)$$

where

$$K_{ij} = \int_0^L \left[\frac{dN_i(x)}{dx} \frac{dN_j(x)}{dx} - k^2 N_i(x) N_j(x) \right] dx + \gamma \delta_{iN} \delta_{jN} \quad (9.1.18)$$

$$b_i = q \delta_{iN} - p \int_0^L \left[\frac{dN_i(x)}{dx} \frac{dN_0(x)}{dx} - k^2 N_i(x) N_0(x) \right] dx - \int_0^L N_i(x) f(x) dx \quad (9.1.19)$$

where $\delta_{iN} = 1$ for $i = N$ and $\delta_{iN} = 0$ for $i \neq N$, and δ_{jN} is defined similarly. Since $N_i(x)$ and $N_j(x)$ overlap only when $j = i \pm 1$, K_{ij} is non-zero only for K_{ii} , $K_{i+1,i}$, and $K_{i,i+1}$, and for all other i and j , $K_{ij} = 0$. Therefore, $[K]$ is a very sparse, symmetric matrix; for each row, there are at most three non-zero entries. In fact, for this one-dimensional problem, $[K]$ is a tridiagonal matrix. This is a very important property of the finite element method, because with a very sparse matrix the linear system can be generated and solved very efficiently.

The integrals in Equation 9.1.18 can be evaluated analytically, resulting in

$$K_{ii} = \left[\frac{1}{l^{(i)}} + \frac{1}{l^{(i+1)}} \right] - k^2 \left[\frac{l^{(i)}}{3} + \frac{l^{(i+1)}}{3} \right] \quad i = 1, 2, \dots, N-1 \quad (9.1.20)$$

$$K_{i+1,i} = K_{i,i+1} = -\frac{1}{l^{(i)}} - k^2 \frac{l^{(i)}}{6} \quad i = 1, 2, \dots, N-1 \quad (9.1.21)$$

$$K_{NN} = \frac{1}{l^{(M)}} - k^2 \frac{l^{(M)}}{3} + \gamma \quad (9.1.22)$$

where $l^{(i)} = x_{i+1} - x_i$ denotes the length of the i th element. The integrals in Equation 9.1.19 can also be evaluated analytically if the source function $f(x)$ can be approximated as a constant within each element, and the results are

$$b_1 = -f^{(1)} \frac{l^{(1)}}{2} - f^{(2)} \frac{l^{(2)}}{2} + \left(\frac{1}{l^{(1)}} + k^2 \frac{l^{(1)}}{6} \right) p \quad (9.1.23)$$

$$b_i = -f^{(i)} \frac{l^{(i)}}{2} - f^{(i+1)} \frac{l^{(i+1)}}{2} \quad i = 2, 3, \dots, N-1 \quad (9.1.24)$$

$$b_N = q - f^{(M)} \frac{l^{(M)}}{2} \quad (9.1.25)$$

where $f^{(i)}$ denotes the average value of $f(x)$ over the i th element. Solving the linear system of equations defined in Equation 9.1.17, we obtain the solution to φ_j ($j = 1, 2, \dots, N$), from which the solution everywhere can be evaluated using Equation 9.1.13.

As in the finite difference analysis, when the finite element method is used to simulate wave propagation, the simulated wave will propagate with a slightly different wave-number from its exact value because of the numerical discretization. This will cause an error to the phase of the solution and this error will accumulate as the wave propagates. For the one-dimensional case, the numerical dispersion analysis to quantify the phase error is straightforward. For simplicity, we assume a uniform discretization such that $l^{(i)} = h$ and then consider a plane wave propagating along the x -direction,

$$\varphi(x) = \varphi_0 e^{-jkx}. \quad (9.1.26)$$

The finite element solution of this plane wave will have the form

$$\varphi_i = \varphi_0 e^{-\tilde{k}ih} \quad (9.1.27)$$

where \tilde{k} denotes the numerical wavenumber. Substituting this into the finite element equation for φ_i , which is given by

$$K_{i,i-1}\varphi_{i-1} + K_{ii}\varphi_i + K_{i,i+1}\varphi_{i+1} = 0 \quad (9.1.28)$$

or more specifically,

$$-\left(\frac{1}{h} + k^2 \frac{h}{6}\right)\varphi_{i-1} + 2\left(\frac{1}{h} - k^2 \frac{h}{3}\right)\varphi_i - \left(\frac{1}{h} + k^2 \frac{h}{6}\right)\varphi_{i+1} = 0 \quad (9.1.29)$$

we obtain

$$\left(\frac{1}{h} + k^2 \frac{h}{6}\right)\cos(\tilde{k}h) = \frac{1}{h} - k^2 \frac{h}{3} \quad (9.1.30)$$

from which the numerical wavenumber can be calculated as

$$\tilde{k} = \frac{1}{h} \cos^{-1} \left[\frac{6 - 2(kh)^2}{6 + (kh)^2} \right]. \quad (9.1.31)$$

A more insightful result can be obtained by approximating the cosine function in Equation 9.1.30 with the first two terms of its Taylor expansion. The result is

$$\frac{\tilde{k} - k}{k} \approx \frac{1}{12}(kh)^2 = \frac{\pi^2}{3} \left(\frac{h}{\lambda} \right)^2 \quad (9.1.32)$$

which shows that the numerical dispersion decreases with the element size quadratically, which is the same as what is observed in the finite difference solution. However, if we employ the second-order basis functions in Equation 9.1.12 to expand the solution, which can be done rather easily, we would obtain a solution whose phase error is proportional to $(h/\lambda)^4$! Therefore, it is much more effective to reduce the phase error by increasing the order of the basis functions than by reducing the size of the finite elements. If the p th-order basis functions are used, the phase error is proportional to $(h/\lambda)^{2p}$. This is one of the major advantages of the finite element method over the conventional finite difference method.

9.2 FINITE ELEMENT ANALYSIS OF SCALAR FIELDS

With the understanding of the basic principle of the finite element method, we now proceed to the finite element analysis of scalar problems, which can be either two- or three-dimensional. We formulate the finite element solution and then demonstrate the application of the method to some two-dimensional field problems.

9.2.1 The Boundary-Value Problem

Consider the problem of calculating the static electric potential φ due to electric charge density ρ_e distributed in domain Ω . The domain can be two- or three-dimensional and is

filled with a medium having a permittivity ϵ . Based on Maxwell's equations, the electric field generated by the charge satisfies the following two equations:

$$\nabla \times \mathbf{E} = 0, \quad \nabla \cdot (\epsilon \mathbf{E}) = \rho_e. \quad (9.2.1)$$

The first equation can be satisfied by representing the electric field as

$$\mathbf{E} = -\nabla \varphi \quad (9.2.2)$$

because of the vector identity $\nabla \times \nabla \varphi \equiv 0$, where φ is known as the electric scalar potential. The equation governing φ can then be obtained by substituting Equation 9.2.2 into the second equation in Equation 9.2.1, which yields Poisson's equation

$$-\nabla \cdot (\epsilon \nabla \varphi) = \rho_e \quad \text{on } \Omega. \quad (9.2.3)$$

In addition to Poisson's equation in Equation 9.2.3, φ must satisfy certain boundary conditions to have a unique solution. Typical boundary conditions include the Dirichlet condition, which specifies the value of the potential on the boundary, and the Neumann condition, which prescribes the normal derivative of the potential. To illustrate the treatment of both boundary conditions, the following boundary conditions are assumed for this example:

$$\varphi = \varphi_D \quad \text{on } \Gamma_D \quad (9.2.4)$$

$$\hat{n} \cdot (\epsilon \nabla \varphi) = \kappa_N \quad \text{on } \Gamma_N \quad (9.2.5)$$

where φ_D denotes the specified value of the potential on the Dirichlet boundary Γ_D and κ_N denotes the prescribed value for the normal derivative of the potential on the Neumann boundary Γ_N . The entire boundary of domain Ω comprises Γ_D and Γ_N and is denoted by Γ .

9.2.2 Finite Element Formulation

The boundary-value problem described by Equations 9.2.3–9.2.5 is usually too complex to have a closed-form solution. This is particularly true when Ω has an irregular shape and the medium, characterized by ϵ , is inhomogeneous. In this case, a numerical solution is the only alternative. Among numerical methods, the finite element method is very powerful because of its ability to deal with arbitrary shapes and inhomogeneous media. As mentioned before, the basic principle of the finite element method is to divide the entire domain into many small subdomains, called finite elements, and then seek an approximate solution in each of the subdomains. The commonly used subdomains are triangular elements in two dimensions and tetrahedral elements in three dimensions (Fig. 9.3) because of their flexibility to model complex shapes, although other elements can also be used for special problems.

Once the domain Ω is divided into small elements, the potential in each element can be approximated by simple functions, such as linear, quadratic, and cubic functions. This approximation can be obtained by interpolating the potential values at a set of discrete points on the element. For example, the potential in a triangular element (Fig. 9.4) can be approximated as

$$\varphi^{(e)}(x, y) = a + bx + cy \quad (9.2.6)$$

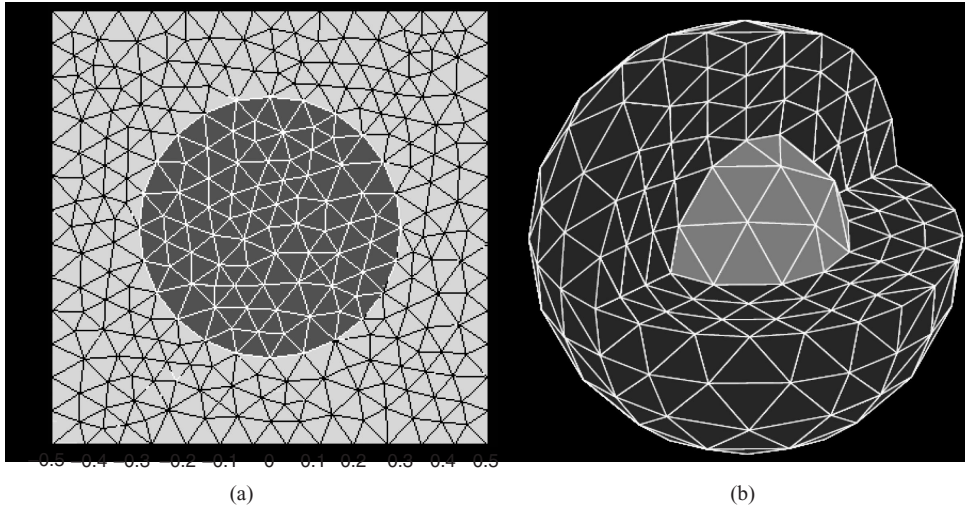


Figure 9.3 Finite element mesh with (a) triangular elements and (b) tetrahedral elements (only the surface mesh is shown here for clarity).

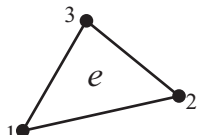


Figure 9.4 Linear triangular element.

where the superscript e denotes that this expression is confined to this specific element. Now, applying Equation 9.2.6 to each of the three vertices (nodes) of the triangular element yields

$$\varphi_1^{(e)} = a + bx_1^{(e)} + cy_1^{(e)} \quad (9.2.7)$$

$$\varphi_2^{(e)} = a + bx_2^{(e)} + cy_2^{(e)} \quad (9.2.8)$$

$$\varphi_3^{(e)} = a + bx_3^{(e)} + cy_3^{(e)} \quad (9.2.9)$$

where $(x_l^{(e)}, y_l^{(e)})$ ($l = 1, 2, 3$) denotes the coordinates of node l of element e and $\varphi_l^{(e)}$ denotes the value of the potential at this node. Solving Equations 9.2.7–9.2.9 for a , b , and c and substituting them into Equation 9.2.6, we obtain

$$\varphi^{(e)}(x, y) = N_1^{(e)}(x, y)\varphi_1^{(e)} + N_2^{(e)}(x, y)\varphi_2^{(e)} + N_3^{(e)}(x, y)\varphi_3^{(e)} \quad (9.2.10)$$

where $N_l^{(e)}(x, y)$ ($l = 1, 2, 3$) are called *interpolating functions*. They are given by

$$N_l^{(e)}(x, y) = \frac{1}{2\Delta^{(e)}}(a_l^{(e)} + b_l^{(e)}x + c_l^{(e)}y) \quad (9.2.11)$$

in which

$$\begin{aligned} a_1^{(e)} &= x_2^{(e)}y_3^{(e)} - x_3^{(e)}y_2^{(e)}, & b_1^{(e)} &= y_2^{(e)} - y_3^{(e)}, & c_1^{(e)} &= x_3^{(e)} - x_2^{(e)} \\ a_2^{(e)} &= x_3^{(e)}y_1^{(e)} - x_1^{(e)}y_3^{(e)}, & b_2^{(e)} &= y_3^{(e)} - y_1^{(e)}, & c_2^{(e)} &= x_1^{(e)} - x_3^{(e)} \\ a_3^{(e)} &= x_1^{(e)}y_2^{(e)} - x_2^{(e)}y_1^{(e)}, & b_3^{(e)} &= y_1^{(e)} - y_2^{(e)}, & c_3^{(e)} &= x_2^{(e)} - x_1^{(e)} \end{aligned} \quad (9.2.12)$$

and

$$\Delta^{(e)} = \frac{1}{2}(b_1^{(e)}c_2^{(e)} - b_2^{(e)}c_1^{(e)}) = \text{area of element } e. \quad (9.2.13)$$

It is evident that the interpolation functions, also known as *basis functions* and *expansion functions*, are completely determined by the coordinates of the three nodes. It can be shown that the interpolation functions so derived have the following property

$$N_l^{(e)}(x_k^{(e)}, y_k^{(e)}) = \begin{cases} 1 & l = k \\ 0 & l \neq k \end{cases} \quad (9.2.14)$$

which guarantees the continuity of the interpolated potential across edges between two elements. The same approach can be employed to derive the interpolation functions for a tetrahedral element, which is left to the reader as an exercise.

When the potential in each element is interpolated using its values at the nodes, the potential in the entire domain can be expressed as

$$\varphi = \sum_{j=1}^N N_j \varphi_j + \sum_{j=1}^{N_D} N_j^D \varphi_j^D \quad (9.2.15)$$

where N denotes the total number of nodes at which the potential is unknown, and N_D denotes the number of nodes on Γ_D where the potential is given by Equation 9.2.4. Furthermore, φ_j denotes the value of the potential at node j and N_j is the corresponding interpolation or basis function; φ_j^D and N_j^D denote the corresponding quantities associated with Γ_D . This interpolation function (N_j or N_j^D) comprises the interpolation functions in all the elements that are directly connected to the associated node. Figure 9.5 shows a linear interpolation function in a two-dimensional triangular mesh.

The expansion in Equation 9.2.15 can now be substituted into Equation 9.2.3 to determine the unknown potentials, φ_j , using the weighted residual method. Based on this method, a suitable testing or weighting function w_i is applied to Equation 9.2.3, and the resulting equation is integrated over the problem domain, yielding

$$-\int_{\Omega} w_i [\nabla \cdot (\epsilon \nabla \varphi)] d\Omega = \int_{\Omega} w_i \rho_e d\Omega. \quad (9.2.16)$$

By using the vector identity

$$w_i [\nabla \cdot (\epsilon \nabla \varphi)] = \nabla \cdot (w_i \epsilon \nabla \varphi) - \epsilon \nabla \varphi \cdot \nabla w_i \quad (9.2.17)$$

and Gauss' theorem

$$\int_{\Omega} \nabla \cdot (w_i \epsilon \nabla \varphi) d\Omega = \oint_{\Gamma} \hat{n} \cdot (w_i \epsilon \nabla \varphi) d\Gamma \quad (9.2.18)$$

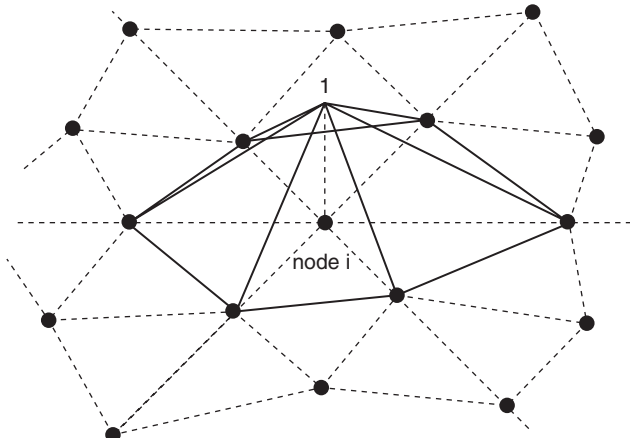


Figure 9.5 Basis function N_i for linear triangular elements.

Equation 9.2.16 can be written as

$$\int_{\Omega} \varepsilon \nabla w_i \cdot \nabla \varphi d\Omega = \int_{\Omega} w_i \rho_e d\Omega + \oint_{\Gamma} \hat{n} \cdot (\varepsilon \nabla \varphi) w_i d\Gamma \quad (9.2.19)$$

where one of the del operators is now transferred from φ to w_i . Substituting Equation 9.2.5 into Equation 9.2.19, we obtain

$$\int_{\Omega} \varepsilon \nabla w_i \cdot \nabla \varphi d\Omega = \int_{\Omega} w_i \rho_e d\Omega + \int_{\Gamma_D} \hat{n} \cdot (\varepsilon \nabla \varphi) w_i d\Gamma + \int_{\Gamma_N} \kappa_N w_i d\Gamma. \quad (9.2.20)$$

This equation is called the *weak-form representation* of the boundary-value problem defined by Equations 9.2.3–9.2.5. The corresponding solution is called the *weak-form solution*, which satisfies Equation 9.2.3 in the weighted average sense.

Next, a suitable weighting function needs to be chosen for w_i . Using Galerkin's method, we choose

$$w_i = N_i \quad i = 1, 2, \dots, N \quad (9.2.21)$$

where N_i is the interpolation function associated with unknown φ_i . Substituting Equations 9.2.15 and 9.2.21 into Equation 9.2.20, we obtain

$$\sum_{j=1}^N \varphi_j \int_{\Omega} \varepsilon \nabla N_i \cdot \nabla N_j d\Omega = \int_{\Omega} \rho_e N_i d\Omega + \int_{\Gamma_N} \kappa_N N_i d\Gamma - \sum_{j=1}^{N_D} \varphi_j^D \int_{\Omega} \varepsilon \nabla N_i \cdot \nabla N_j^D d\Omega. \quad (9.2.22)$$

Note that the integral over Γ_D in Equation 9.2.22 disappears here since N_i vanishes on Γ_D . Equation 9.2.22 can be written more compactly as

$$\sum_{j=1}^N K_{ij} \varphi_j = b_i \quad i = 1, 2, \dots, N \quad (9.2.23)$$

where

$$K_{ij} = \int_{\Omega} \varepsilon \nabla N_i \cdot \nabla N_j d\Omega \quad (9.2.24)$$

$$b_i = \int_{\Omega} \rho_e N_i d\Omega + \int_{\Gamma_N} \kappa_N N_i d\Gamma - \sum_{j=1}^{N_D} \varphi_j^D \int_{\Omega} \epsilon \nabla N_i \cdot \nabla N_j^D d\Omega. \quad (9.2.25)$$

Equation 9.2.23 represents a set of linear equations, which can also be written in matrix form as

$$[K]\{\varphi\} = \{b\} \quad (9.2.26)$$

where $[K]$ is an $N \times N$ square and symmetric matrix, $\{\varphi\}$ is an $N \times 1$ column vector containing the unknown potential values at all the nodes except those on Γ_D , and $\{b\}$ is the $N \times 1$ known vector contributed by the known charge density and the Dirichlet and Neumann boundary conditions. The matrix equation (Eq. 9.2.26) can be solved using one of the many standard matrix solvers, and its solution yields the potential values at all the nodes. The potential elsewhere can then be obtained by interpolation in Equation 9.2.15.

A very important property of the finite element method is that its matrix $[K]$ is extremely sparse. This becomes obvious from Equation 9.2.24, which is non-zero only when N_i and N_j overlap with each other. Since N_i is non-zero only within the elements directly connected to node i , it overlaps with N_j only when nodes i and j belong to the same element. Hence, in each row of matrix $[K]$, there are only a few non-zero entries no matter how large the dimension of the matrix is. Therefore, the memory required to store $[K]$ is proportional to $O(N)$, and the solution can be made very efficient by using special solvers that can exploit the property of sparsity. Such solvers are often referred to as *sparse solvers*. As a result, the finite element method is very suitable for large-scale applications, where one has to deal with a very large number of unknowns.

In the actual implementation of the finite element method described above, it might prove difficult to find the explicit expressions of N_i and N_j to evaluate K_{ij} since nodes may be connected to different numbers of elements, each having a different shape. To alleviate this difficulty, Equation 9.2.24 can be rewritten as

$$K_{ij} = \sum_{e=1}^M \int_{\Omega^{(e)}} \epsilon \nabla N_i \cdot \nabla N_j d\Omega \quad (9.2.27)$$

where $\Omega^{(e)}$ denotes the domain of element e and M denotes the total number of elements in Ω . Using Equation 9.2.27, we can process elements one by one and calculate the contribution of each element to $[K]$. This process is called *assembly*. To facilitate this process, we define a connectivity array for each finite element mesh, which describes the relation between the element numbers and the node numbers. This connectivity array can be defined as $n(3, e)$ for a triangular mesh and $n(4, e)$ for a tetrahedral mesh, where $e = 1, 2, \dots, M$. The value of $n(1, e)$ is assigned as the node number of the first node in element e , $n(2, e)$ the node number of the second node in element e , and so on. For the triangular mesh shown in Figure 9.6, the connectivity array is given in Table 9.1. Obviously, the numbering in this connectivity array is not unique. For instance, the nodes in the first element can be numbered as 4, 3, 1 or 3, 1, 4. This is not a problem since different numbering does not affect the result as long as the nodes are numbered counterclockwise (simply to ensure that the area as calculated in Equation 9.2.13 is always positive). Now, assuming that $i = n(l, e)$ and $j = n(k, e)$, Equation 9.2.27 can be written as

$$K_{ij} = \sum_{e=1}^M \int_{\Omega^{(e)}} \epsilon \nabla N_l^{(e)} \cdot \nabla N_k^{(e)} d\Omega \quad (9.2.28)$$

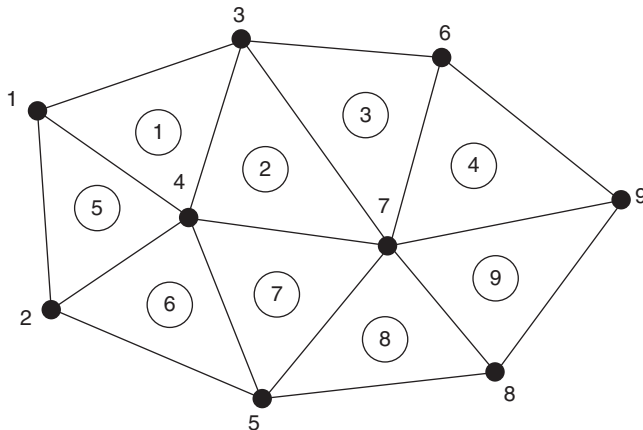


Figure 9.6 Finite element mesh with elements and nodes numbered.

TABLE 9.1 Element-to-Node Connectivity Array for a Triangular Mesh

e	$n(1, e)$	$n(2, e)$	$n(3, e)$
1	1	4	3
2	4	7	3
3	3	7	6
4	7	9	6
5	2	4	1
6	2	5	4
7	5	7	4
8	5	8	7
9	7	8	9

where $N_l^{(e)}$ and $N_k^{(e)}$ are the interpolation functions defined for element e , which are given by Equation 9.2.11 for a triangular element.

Although the summation in Equation 9.2.28 should be carried out over all the elements, only the elements that are connected to nodes i and j have non-trivial contributions to the value of K_{ij} . Therefore, a direct implementation based on Equation 9.2.28 is inefficient. A more efficient assembly process is to go through each element and calculate

$$K_{lk}^{(e)} = \int_{\Omega^{(e)}} \epsilon \nabla N_l^{(e)} \cdot \nabla N_k^{(e)} d\Omega \quad (9.2.29)$$

where $l, k = 1, 2, 3$ for a triangular element and $l, k = 1, 2, 3, 4$ for a tetrahedral element. Once each $K_{lk}^{(e)}$ is calculated, it is added to K_{ij} , where the values of i and j are given by $i = n(l, e)$ and $j = n(k, e)$, except when node i , or node j , or both reside on Γ_D . When this is done for all the elements, the matrix $[K]$ is fully assembled. For the triangular mesh in Figure 9.6 with the connectivity array defined in Table 9.1, the first few non-zero K_{ij} so assembled are

$$\begin{aligned} K_{11} &= K_{11}^{(1)} + K_{33}^{(5)}, & K_{12} &= K_{31}^{(5)}, & K_{13} &= K_{13}^{(1)}, & K_{14} &= K_{12}^{(1)} + K_{32}^{(5)} \\ K_{22} &= K_{11}^{(5)} + K_{11}^{(6)}, & K_{24} &= K_{12}^{(5)} + K_{13}^{(6)}, & K_{25} &= K_{12}^{(6)}. \end{aligned} \quad (9.2.30)$$

The assembly process to calculate $\{b\}$ based on Equation 9.2.25 is similar and is left to the reader as an exercise.

The integral in Equation 9.2.29 can be evaluated either numerically or analytically. For an analytical evaluation, the following integration formulas are found very useful:

$$\iint_{\Delta^{(e)}} (N_1^{(e)})^l (N_2^{(e)})^m (N_3^{(e)})^n d\Omega = \frac{l! m! n!}{(l+m+n+2)!} 2\Delta^{(e)} \quad (9.2.31)$$

for integration over a triangular element and

$$\iiint_{V^{(e)}} (N_1^{(e)})^l (N_2^{(e)})^m (N_3^{(e)})^n (N_4^{(e)})^p d\Omega = \frac{l! m! n! p!}{(l+m+n+p+3)!} 6V^{(e)} \quad (9.2.32)$$

for integration over a tetrahedral element, where $V^{(e)}$ denotes the volume of the tetrahedral element. For example, if the value of the permittivity is a constant or can be approximated as a constant in a triangular element e and is denoted as $\epsilon^{(e)}$, by using Equation 9.2.31 we can evaluate the integral in Equation 9.2.29 to find

$$K_{lk}^{(e)} = \frac{\epsilon^{(e)}}{4\Delta^{(e)}} (b_l^{(e)} b_k^{(e)} + c_l^{(e)} c_k^{(e)}) \quad (9.2.33)$$

where $b_l^{(e)}$, $b_k^{(e)}$, $c_l^{(e)}$, and $c_k^{(e)}$ are defined in Equation 9.2.12.

9.2.3 Application Examples

We present four examples here to demonstrate the finite element analysis based on the formulation described in this section. The first example is related to the analysis of a homogeneous waveguide. Typical waveguide analysis involves finding the propagation constants and field distributions of the propagation modes in an infinitely long waveguide. Since the waveguide is assumed to be uniform in its longitudinal direction, say the z -direction, it is sufficient to consider the cross-section of the waveguide, reducing the analysis to a two-dimensional problem.

It is well known that in a homogeneous waveguide, there exist two sets of modes: transverse magnetic (TM) and transverse electric (TE) modes. For the TM modes, analysis can be done by considering only the z -component of the electric field, E_z , since all other field components can be derived from E_z . Starting from Maxwell's equations and assuming that the fields propagate in the z -direction with a propagation constant β , we can derive the second-order partial differential equation for E_z as

$$\nabla_t^2 E_z + k_c^2 E_z = 0 \quad \text{on } \Omega \quad (9.2.34)$$

where Ω denotes the cross-section of the waveguide, ∇_t^2 denotes the two-dimensional Laplacian given by

$$\nabla_t^2 = \nabla_t \cdot \nabla_t = \frac{\partial^2}{\partial x^2} + \frac{\partial^2}{\partial y^2} \quad (9.2.35)$$

and $k_c^2 = k^2 - \beta^2$ with $k = \omega\sqrt{\mu\epsilon}$. Obviously, once k_c^2 is found, β can be calculated for any frequency. The boundary condition is

$$E_z = 0 \quad \text{on } \Gamma \quad (9.2.36)$$

where Γ denotes the conducting waveguide wall.

Applying the finite element formulation described earlier to the boundary-value problem defined by Equations 9.2.34 and 9.2.36, we obtain the matrix equation

$$[A]\{E_z\} = k_c^2[B]\{E_z\} \quad (9.2.37)$$

where the elements of matrices $[A]$ and $[B]$ are given by

$$A_{ij} = \iint_{\Omega} \nabla_t N_i \cdot \nabla_t N_j d\Omega \quad i, j = 1, 2, \dots, N \quad (9.2.38)$$

$$B_{ij} = \iint_{\Omega} N_i \cdot N_j d\Omega \quad i, j = 1, 2, \dots, N. \quad (9.2.39)$$

In the above, N denotes the total number of nodes *excluding* those on Γ because of the boundary condition in Equation 9.2.36. Equation 9.2.37 has a non-trivial solution only when the determinant of the matrix $[A] - k_c^2[B]$ vanishes. The corresponding values of k_c^2 are called the eigenvalues. For each eigenvalue, there is a non-trivial solution for $\{E_z\}$, which is called the eigenvector. Mathematically, Equation 9.2.37 represents a generalized eigenvalue problem, which can be solved using one of the many standard algorithms. Its solution gives the value of the cutoff wavenumber k_c and the corresponding field distribution $\{E_z\}$ for each waveguide mode.

The analysis of the TE modes is similar. The second-order partial differential equation for H_z is given by

$$\nabla_t^2 H_z + k_c^2 H_z = 0 \quad \text{on } \Omega \quad (9.2.40)$$

and the boundary condition becomes

$$\frac{\partial H_z}{\partial n} = 0 \quad \text{on } \Gamma. \quad (9.2.41)$$

The finite element analysis of this boundary-value problem results in the generalized eigenvalue problem

$$[A]\{H_z\} = k_c^2[B]\{H_z\} \quad (9.2.42)$$

where the elements of matrices $[A]$ and $[B]$ are the same as those given by Equations 9.2.38 and 9.2.39, except that now N denotes the total number of nodes *including* those on the waveguide wall Γ .

The second example concerns the electric field produced by infinitely long electric currents in a bounded inhomogeneous medium. Assuming that the currents follow in the z -direction and that both the currents and the medium have no variation of any kind along the z -direction, the electric field so generated would have only the z -component. Starting from Maxwell's equations, we can find the partial differential equation for E_z as

$$\nabla_t \cdot \left(\frac{1}{\mu_r} \nabla_t E_z \right) + k_0^2 \epsilon_r E_z = j\omega \mu_0 J_z \quad (9.2.43)$$

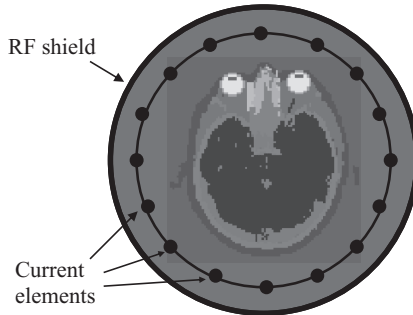


Figure 9.7 Two-dimensional model of a shielded 16-element birdcage coil loaded with the human head. (See color insert.)

which is a generalized version of the Helmholtz equation. This equation, together with the boundary condition applicable to the bounding surface of the problem domain, uniquely defines a boundary-value problem. The finite element analysis of this boundary-value problem would yield the matrix equation

$$[K]\{E_z\} = \{b\} \quad (9.2.44)$$

where

$$K_{ij} = \iint_{\Omega} \left[\frac{1}{\mu_r} \nabla_i N_i \cdot \nabla_j N_j - k_0^2 \epsilon_r N_i \cdot N_j \right] d\Omega \quad i, j = 1, 2, \dots, N \quad (9.2.45)$$

$$b_i = -j\omega\mu_0 \iint_{\Omega} J_z N_i d\Omega \quad i = 1, 2, \dots, N. \quad (9.2.46)$$

In the above, N denotes the total number of nodes excluding those on perfectly conducting surfaces.

As an example, Figure 9.7 shows the two-dimensional model of a shielded birdcage coil loaded with the human head [10]. This model consists of a cylindrical conducting shell having a diameter of 30 cm with 16 conducting wires equally spaced on a cylindrical surface having a diameter of 26 cm. Each of the wires carries a time-harmonic electric current given by

$$I_l = I_0 \cos\left(\omega t + \frac{l-1}{8}\pi\right) \quad (9.2.47)$$

where I_l denotes the current in the l th wire and I_0 denotes the maximum current. The purpose of this coil is to generate a uniform, circularly polarized, TM field to excite nuclei for magnetic resonance imaging. The human head is placed inside the coil and its surface is about 3.6 cm away from the wires. The electromagnetic model of the head consists of nine different tissues with different material properties. This problem can be analyzed by solving Equation 9.2.44 for the electric field E_z , from which the magnetic field can be calculated using Maxwell's equation

$$\mathbf{H} = \frac{j}{\omega\mu} \nabla \times \mathbf{E} = \frac{j}{\omega\mu} \left(\hat{x} \frac{\partial E_z}{\partial y} - \hat{y} \frac{\partial E_z}{\partial x} \right). \quad (9.2.48)$$

Figure 9.8 displays the magnitude of the magnetic field at 64, 128, 171, and 256 MHz for $I_0 = 1$ A. The field inhomogeneity is mainly due to the presence of the human head and is much more pronounced at higher frequencies.

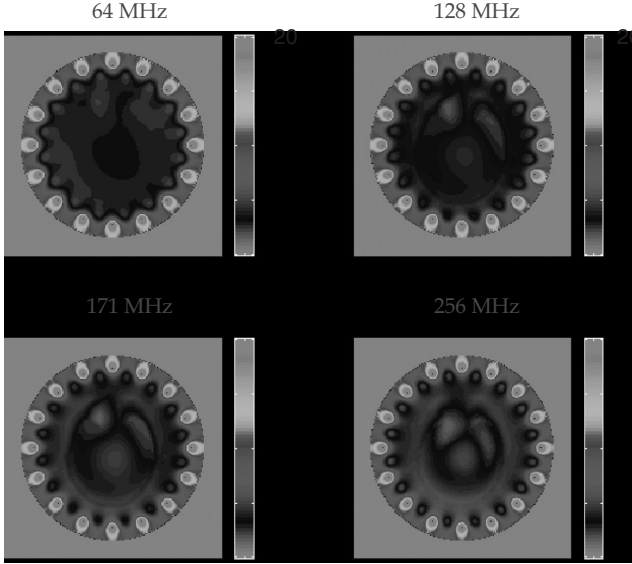


Figure 9.8 Magnitude of the magnetic field inside the loaded birdcage coil at four different frequencies. (After Jin and Chen [10], Copyright © 1997 ISMRM.) (See color insert.)

As the third example, we consider the analysis of plane wave scattering by an infinitely long conducting object in free space along the z -direction. In this case, the problem domain is unbounded, and to carry out the finite element analysis, one can introduce an artificial cylindrical surface to enclose the scatterer to truncate the computational domain. If this artificial surface is placed far away from the scatterer, the scattered field there would approximately satisfy the Sommerfeld radiation condition. For the E_z -polarized incident field, this condition is given by

$$\hat{n} \cdot \nabla_t E_z^{\text{sc}} + jk_0 E_z^{\text{sc}} \approx 0 \quad \text{on } \Gamma_a \quad (9.2.49)$$

where Γ_a denotes the artificial surface. The Helmholtz equation for the scattered field is given by

$$\nabla_t^2 E_z^{\text{sc}} + k_0^2 E_z^{\text{sc}} = 0 \quad (9.2.50)$$

and at the conducting surface of the scatterer, the boundary condition for the scattered field is

$$E_z^{\text{sc}} = -E_z^{\text{inc}} \quad \text{on } \Gamma_D \quad (9.2.51)$$

where E_z^{inc} denotes the incident field. The finite element analysis of this problem yields the matrix equation

$$[K] \{E_z^{\text{sc}}\} = \{b\} \quad (9.2.52)$$

where

$$K_{ij} = \iint_{\Omega} [\nabla_t N_i \cdot \nabla_t N_j - k_0^2 N_i \cdot N_j] d\Omega + jk_0 \oint_{\Gamma_a} N_i \cdot N_j d\Gamma \quad i, j = 1, 2, \dots, N \quad (9.2.53)$$



Figure 9.9 Magnitude of the magnetic field for a plane wave incident from the left to right and scattered by a conducting airfoil. (See color insert.)

$$b_i = \sum_{j=1}^{N_D} E_{zj}^{\text{inc}} \iint_{\Omega} [\nabla_t N_i \cdot \nabla_t N_j^D - k_0^2 N_i \cdot N_j^D] d\Omega \quad i = 1, 2, \dots, N \quad (9.2.54)$$

in which N denotes the total number of nodes including those on Γ_a , but excluding all those on the perfectly conducting surface Γ_D .

It should be obvious that this scattering analysis can be extended in a straightforward manner to the H_z -polarization as well as to more complicated scatterers such as those consisting of dielectrics and impedance surfaces. This is left to the reader as an exercise. Figure 9.9 shows the magnetic field distribution for an H_z -polarized plane wave scattered by a conducting airfoil.

The last example deals with the finite element analysis of antenna radiation. Similar to the scattering analysis, a large artificial boundary is first introduced to enclose the entire antenna or the aperture of the antenna. The Sommerfeld radiation condition similar to Equation 9.2.49 is then applied directly to the radiated field at the artificial boundary. The radiated field in the computational domain satisfies the same partial differential equation as Equation 9.2.43. If the antenna is fed by a waveguide instead of a current source inside the computational domain, the waveguide can be truncated and over the truncation port, the field can be approximated as the superposition of the incident field and the field reflected by the antenna:

$$E_z(x, y) = E_z^{\text{inc}}(x, y) + E_z^{\text{ref}}(x, y) \approx E_0 e_z(y) e^{-jk_x x} + R E_0 e_z(y) e^{jk_x x} \quad (9.2.55)$$

where E_0 denotes the magnitude of the incident field, $e_z(y)$ is the model field distribution, k_x is the propagation constant along the waveguide, and R denotes the unknown reflection coefficient. By taking the derivative with respect to x , we have

$$\begin{aligned} \frac{\partial E_z}{\partial x} &= -jk_x E_0 e_z(y) e^{-jk_x x} + jk_x R E_0 e_z(y) e^{jk_x x} \\ &= jk_x E_z - 2jk_x E_z^{\text{inc}} \end{aligned} \quad (9.2.56)$$

which can be used as the boundary condition at the waveguide port. In this case, the incident field from the waveguide provides the excitation to the antenna. Once the field is calculated using the finite element method, the reflection coefficient can be obtained from Equation 9.2.55, from which the input impedance can be evaluated as well. The antenna radiation pattern can also be computed based on the calculated near field using the surface

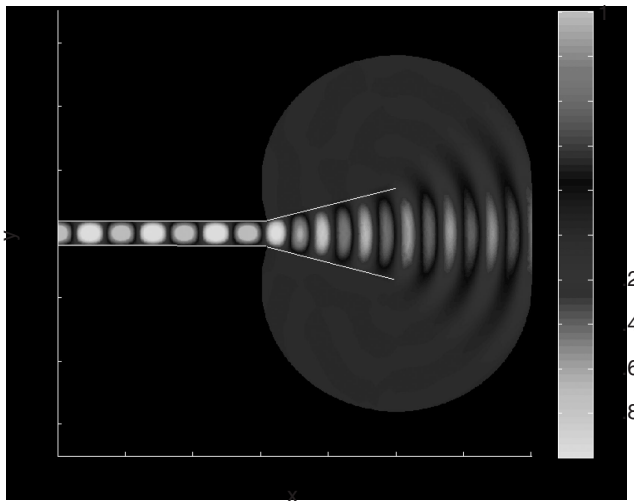


Figure 9.10 Snapshot of the radiated field E_z by a two-dimensional waveguide-fed horn antenna excited by the first TM_z mode. (See color insert.)

equivalence principle. Figure 9.10 shows the radiated field of a two-dimensional horn antenna fed by a parallel-plate waveguide. The incident field in the waveguide is the first TM_z mode.

9.3 FINITE ELEMENT ANALYSIS OF VECTOR FIELDS

The finite element method described in Section 9.2 can be extended to deal with problems involving vector fields. This extension is very important since all electrodynamic problems in three dimensions deal with vector electromagnetic fields. In this section, we focus on the finite element method in the frequency domain by first defining the boundary-value problem, then formulating its finite element solution, and finally demonstrating the application through a few examples.

9.3.1 The Boundary-Value Problem

Consider the problem of calculating the electric field intensity \mathbf{E} due to electric current density \mathbf{J}_{imp} in a domain Ω characterized by permittivity ϵ and permeability μ . Again, the domain can be either two- or three-dimensional. To calculate \mathbf{E} , we have to solve Maxwell's equations

$$\nabla \times \mathbf{E} = -j\omega\mu\mathbf{H} \quad (9.3.1)$$

$$\nabla \times \mathbf{H} = j\omega\epsilon\mathbf{E} + \mathbf{J}_{\text{imp}} \quad (9.3.2)$$

$$\nabla \cdot (\epsilon\mathbf{E}) = -\frac{1}{j\omega} \nabla \cdot \mathbf{J}_{\text{imp}} \quad (9.3.3)$$

$$\nabla \cdot (\mu\mathbf{H}) = 0 \quad (9.3.4)$$

subject to certain boundary conditions. By eliminating \mathbf{H} in Equations 9.3.1 and 9.3.2, we can derive the vector wave equation for \mathbf{E} as

$$\nabla \times \left(\frac{1}{\mu_r} \nabla \times \mathbf{E} \right) - k_0^2 \epsilon_r \mathbf{E} = -jk_0 Z_0 \mathbf{J}_{\text{imp}} \quad \text{on } \Omega \quad (9.3.5)$$

where $\mu_r = \mu/\mu_0$ and $\epsilon_r = \epsilon/\epsilon_0$ are the relative permeability and permittivity, respectively, $k_0 = \omega\sqrt{\mu_0\epsilon_0}$ and $Z_0 = \sqrt{\mu_0/\epsilon_0}$ are the free-space wavenumber and intrinsic impedance, respectively.

Typical boundary conditions for the electric field include the homogeneous Dirichlet condition on a perfectly conducting surface and the mixed boundary condition on an impedance surface. To illustrate the treatment of these two conditions, the following are assumed for this example:

$$\hat{n} \times \mathbf{E} = \mathbf{P} \quad \text{on } \Gamma_D \quad (9.3.6)$$

$$\hat{n} \times \left(\frac{1}{\mu_r} \nabla \times \mathbf{E} \right) + \frac{jk_0}{\eta_r} \hat{n} \times (\hat{n} \times \mathbf{E}) = \mathbf{K}_N \quad \text{on } \Gamma_N \quad (9.3.7)$$

where \mathbf{P} is the prescribed value for the tangential electric field on Γ_D , η_r denotes the normalized surface impedance on Γ_N , and \mathbf{K}_N is a known function representing a boundary source on Γ_N .

9.3.2 Finite Element Formulation

As was done for the scalar problem discussed in Section 9.2, instead of solving the boundary-value problem defined by Equations 9.3.5–9.3.7 directly, we can seek its weak-form solution by multiplying Equation 9.3.5 by an appropriate weighting function \mathbf{W}_i and integrating over the problem domain, which yields

$$\int_{\Omega} \mathbf{W}_i \cdot \left[\nabla \times \left(\frac{1}{\mu_r} \nabla \times \mathbf{E} \right) - k_0^2 \epsilon_r \mathbf{E} \right] d\Omega = -jk_0 Z_0 \int_{\Omega} \mathbf{W}_i \cdot \mathbf{J}_{\text{imp}} d\Omega. \quad (9.3.8)$$

By invoking the vector identity

$$\nabla \cdot \left[\mathbf{W}_i \times \left(\frac{1}{\mu_r} \nabla \times \mathbf{E} \right) \right] = \frac{1}{\mu_r} (\nabla \times \mathbf{W}_i) \cdot (\nabla \times \mathbf{E}) - \mathbf{W}_i \cdot \left[\nabla \times \left(\frac{1}{\mu_r} \nabla \times \mathbf{E} \right) \right] \quad (9.3.9)$$

and Gauss' theorem

$$\int_{\Omega} \nabla \cdot \left[\mathbf{W}_i \times \left(\frac{1}{\mu_r} \nabla \times \mathbf{E} \right) \right] d\Omega = \oint_{\Gamma} \hat{n} \cdot \left[\mathbf{W}_i \times \left(\frac{1}{\mu_r} \nabla \times \mathbf{E} \right) \right] d\Gamma \quad (9.3.10)$$

we obtain the weak-form representation of Equation 9.3.5 as

$$\begin{aligned} \int_{\Omega} \left[\frac{1}{\mu_r} (\nabla \times \mathbf{W}_i) \cdot (\nabla \times \mathbf{E}) - k_0^2 \epsilon_r \mathbf{W}_i \cdot \mathbf{E} \right] d\Omega &= \int_{\Gamma_D} \frac{1}{\mu_r} (\hat{n} \times \mathbf{W}_i) \cdot (\nabla \times \mathbf{E}) d\Gamma \\ &\quad - \int_{\Gamma_N} \left[\frac{jk_0}{\eta_r} (\hat{n} \times \mathbf{W}_i) \cdot (\hat{n} \times \mathbf{E}) + \mathbf{W}_i \cdot \mathbf{K}_N \right] d\Gamma - jk_0 Z_0 \int_{\Omega} \mathbf{W}_i \cdot \mathbf{J}_{\text{imp}} d\Omega \end{aligned} \quad (9.3.11)$$

after the boundary condition in Equation 9.3.7 is applied.

To find a numerical solution of Equation 9.3.11 using the finite element method, the entire domain Ω is first divided into small finite elements, such as triangular elements for a two-dimensional domain and tetrahedral elements for a three-dimensional domain. Within each small element, \mathbf{E} can be interpolated using a set of discrete values. One approach is to assign \mathbf{E} at a few points on the element and then interpolate \mathbf{E} elsewhere using a set of scalar interpolation functions, as was done in a scalar problem in Section 9.2. This approach turns out to be very problematic because of a series of difficulties associated with applying correct boundary conditions to the interpolated \mathbf{E} -field. A better approach is to assign the tangential component of \mathbf{E} at each edge of the element and then interpolate \mathbf{E} elsewhere using a set of vector basis functions. For example, the field in a triangular element can be interpolated as

$$\mathbf{E}^{(e)}(x, y) = \mathbf{N}_{12}^{(e)}(x, y)E_{12}^{(e)} + \mathbf{N}_{13}^{(e)}(x, y)E_{13}^{(e)} + \mathbf{N}_{23}^{(e)}(x, y)E_{23}^{(e)} \quad (9.3.12)$$

and the field in a tetrahedral element can be interpolated as

$$\begin{aligned} \mathbf{E}^{(e)}(x, y, z) = & \mathbf{N}_{12}^{(e)}(x, y, z)E_{12}^{(e)} + \mathbf{N}_{13}^{(e)}(x, y, z)E_{13}^{(e)} + \mathbf{N}_{14}^{(e)}(x, y, z)E_{14}^{(e)} \\ & + \mathbf{N}_{23}^{(e)}(x, y, z)E_{23}^{(e)} + \mathbf{N}_{24}^{(e)}(x, y, z)E_{24}^{(e)} + \mathbf{N}_{34}^{(e)}(x, y, z)E_{34}^{(e)} \end{aligned} \quad (9.3.13)$$

where $E_{lk}^{(e)}$ denotes the tangential component of \mathbf{E} at the edge that connects nodes l and k of element e , and $\mathbf{N}_{lk}^{(e)}$ is the corresponding interpolation or basis function. Denoting the linear scalar interpolation functions associated with nodes l and k of a triangular or tetrahedral element as $N_l^{(e)}$ and $N_k^{(e)}$, respectively, the vector basis functions in Equations 9.3.12 and 9.3.13 can be written as

$$\mathbf{N}_{lk}^{(e)}(\mathbf{r}) = \left[N_l^{(e)} \nabla N_k^{(e)} - N_k^{(e)} \nabla N_l^{(e)} \right] \ell_{lk}^{(e)} \quad l < k \quad (9.3.14)$$

where $\ell_{lk}^{(e)}$ denotes the signed length of the edge that connects nodes l and k . The $\ell_{lk}^{(e)}$ take a positive sign when $n(l, e) < n(k, e)$; otherwise, it takes a negative sign, which ensures that the vector basis functions defined over the elements that share the common edge point to the same direction along the edge. In contrast to those in Equation 9.2.11, the basis functions defined in Equation 9.3.14 are vector functions and the corresponding element is called a *vector element* or *edge element*, in contrast to the previous scalar element or nodal element. Figure 9.11 shows the vector basis function $\mathbf{N}_{lk}^{(e)}$ for a triangular element. Clearly, such basis functions have a tangential component only along the associated edge, and as such they ensure the tangential continuity of the interpolated field while allowing the normal component to be discontinuous. Hence, they can be used to expand the vector field \mathbf{E} accurately.

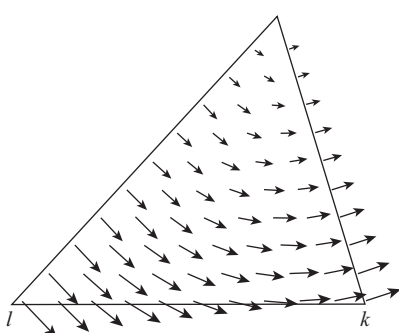


Figure 9.11 Vector basis function $\mathbf{N}_{lk}^{(e)}$ for a linear triangular element.

When the electric field \mathbf{E} is interpolated in each element using its tangential values at the edges of the element, the interpolated field \mathbf{E} in the entire domain Ω can be expressed as

$$\mathbf{E} = \sum_{j=1}^{N_{\text{edge}}} \mathbf{N}_j E_j + \sum_{j=1}^{N_D} \mathbf{N}_j^D E_j^D \quad (9.3.15)$$

where N_{edge} denotes the total number of edges excluding those on Γ_D , E_j denotes the tangential component of \mathbf{E} at the j th edge, and \mathbf{N}_j is the corresponding vector basis function. Furthermore, N_D denotes the total number of edges on Γ_D , and E_j^D and \mathbf{N}_j^D denote the tangential electric fields and the corresponding basis functions on these edges. Obviously, for an edge inside Ω , \mathbf{N}_j spans over several neighboring elements that share the common edge (edge j). Figure 9.12 shows a vector basis function for an interior edge in a triangular mesh. Also note that with the second term in Equation 9.3.15, the interpolated field satisfies the required boundary condition in Equation 9.3.6.

By substituting Equation 9.3.15 into Equation 9.3.11 and using the vector basis function \mathbf{N}_i as the weighting function \mathbf{W}_i , we obtain

$$\sum_{j=1}^{N_{\text{edge}}} K_{ij} E_j = b_i \quad i = 1, 2, \dots, N_{\text{edge}} \quad (9.3.16)$$

where

$$K_{ij} = \int_{\Omega} \left[\frac{1}{\mu_r} (\nabla \times \mathbf{N}_i) \cdot (\nabla \times \mathbf{N}_j) - k_0^2 \epsilon_r \mathbf{N}_i \cdot \mathbf{N}_j \right] d\Omega + jk_0 \int_{\Gamma_N} \left[\frac{1}{\eta_r} (\hat{n} \times \mathbf{N}_i) \cdot (\hat{n} \times \mathbf{N}_j) \right] d\Gamma \quad (9.3.17)$$

$$\begin{aligned} b_i = & -jk_0 Z_0 \int_{\Omega} \mathbf{N}_i \cdot \mathbf{J}_{\text{imp}} d\Omega - \int_{\Gamma_N} \mathbf{N}_i \cdot \mathbf{K}_N d\Gamma \\ & - \sum_{j=1}^{N_D} E_j^D \int_{\Omega} \left[\frac{1}{\mu_r} (\nabla \times \mathbf{N}_i) \cdot (\nabla \times \mathbf{N}_j^D) - k_0^2 \epsilon_r \mathbf{N}_i \cdot \mathbf{N}_j^D \right] d\Omega. \end{aligned} \quad (9.3.18)$$

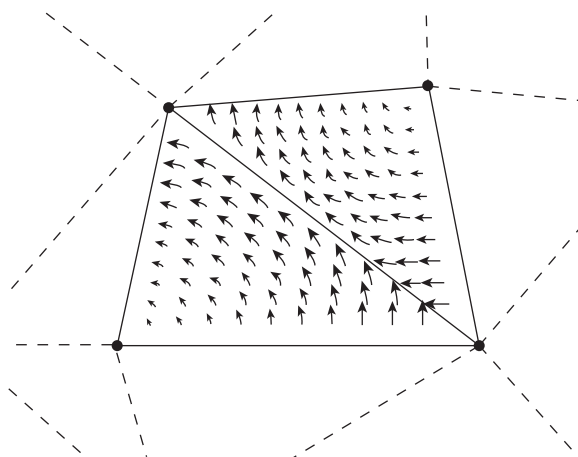


Figure 9.12 Vector basis function \mathbf{N}_i for linear triangular elements.

Note that the integral over Γ_D in Equation 9.3.11 vanishes here since $\hat{n} \times \mathbf{N}_i = 0$ on Γ_D . Equation 9.3.16 can be written compactly as

$$[K]\{E\} = \{b\} \quad (9.3.19)$$

which can be solved for $\{E\}$. Because the elemental interactions in Equation 9.3.17 are local in nature, $[K]$ is a sparse and symmetric matrix that can be solved efficiently using a sparse matrix solver. Once $\{E\}$ is obtained, the field everywhere in Ω can be calculated using Equation 9.3.15.

The assembly process to calculate $[K]$ is similar to that for nodal elements described in Section 9.2.2. To illustrate this process more specifically, we consider the calculation of $[K]$ as contributed by the first integral in Equation 9.3.17 using the finite element mesh shown in Figure 9.13. To facilitate the calculation, we define another connectivity array, an element-to-edge connectivity array, to describe the relation between the element numbers and edge numbers. This array can be defined as $ne(l, k; e)$, which is assigned the edge number of the edge that connects nodes l and k of element e . For the triangular mesh in Figure 9.13, this connectivity array is given in Table 9.2.

To calculate $[K]$ as contributed by the first integral in Equation 9.3.17, we go through each element and calculate

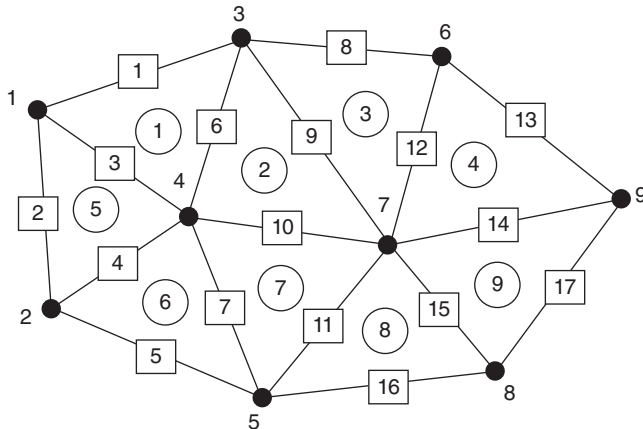


Figure 9.13 Finite element mesh with elements, nodes, and edges numbered.

TABLE 9.2 Element-to-Edge Connectivity Array for a Triangular Mesh

e	$ne(1, 2; e)$	$ne(1, 3; e)$	$ne(2, 3; e)$
1	3	1	6
2	10	6	9
3	9	8	12
4	14	12	13
5	4	2	3
6	5	4	7
7	11	7	10
8	16	11	15
9	15	14	17

$$K_{lk;l'k'}^{(e)} = \int_{\Omega^{(e)}} \left[\frac{1}{\mu_r} (\nabla \times \mathbf{N}_{lk}^{(e)}) \cdot (\nabla \times \mathbf{N}_{l'k'}^{(e)}) - k_0^2 \epsilon_r \mathbf{N}_{lk}^{(e)} \cdot \mathbf{N}_{l'k'}^{(e)} \right] d\Omega \quad (9.3.20)$$

where $l < k$ and $l' < k'$. Once each $K_{lk;l'k'}^{(e)}$ is calculated, it is added to K_{ij} , where the values of i and j are given by $i = ne(l, k; e)$ and $j = ne(l', k'; e)$, except when edge i , or edge j , or both reside on Γ_D . When this is done for all the elements, the matrix $[K]$ as contributed by the first integral in Equation 9.3.17 is fully assembled. For the triangular mesh in Figure 9.13, the first few non-zero K_{ij} so assembled are

$$\begin{aligned} K_{11} &= K_{13;13}^{(1)}, & K_{13} &= K_{13;12}^{(1)}, & K_{16} &= K_{13;23}^{(1)} \\ K_{22} &= K_{13;13}^{(5)}, & K_{23} &= K_{13;23}^{(5)}, & K_{24} &= K_{13;12}^{(5)} \\ K_{33} &= K_{12;12}^{(1)} + K_{23;23}^{(5)}, & K_{34} &= K_{23;12}^{(5)}, & K_{36} &= K_{12;23}^{(1)}. \end{aligned} \quad (9.3.21)$$

The contribution of the second integral in Equation 9.3.17 can be calculated in a similar fashion. The assembly of $\{b\}$ based on Equation 9.3.18 follows a similar process.

The integral in Equation 9.3.20 can be evaluated either numerically or analytically with the aid of Equation 9.2.31 or 9.2.32. For example, if the values of the relative permittivity and permeability are constants or can be approximated as constants $\epsilon_r^{(e)}$ and $\mu_r^{(e)}$, Equation 9.3.20 for a triangular element can be evaluated analytically, and the result is given by

$$\begin{aligned} K_{12;12}^{(e)} &= \frac{\ell_{12}^{(e)} \ell_{12}^{(e)}}{\Delta^{(e)}} \left[\frac{1}{24\mu_r^{(e)}} (f_{11}^{(e)} + f_{22}^{(e)} - f_{12}^{(e)}) - k_0^2 \epsilon_r^{(e)} \right] \\ K_{13;13}^{(e)} &= \frac{\ell_{13}^{(e)} \ell_{13}^{(e)}}{\Delta^{(e)}} \left[\frac{1}{24\mu_r^{(e)}} (f_{11}^{(e)} + f_{33}^{(e)} - f_{13}^{(e)}) - k_0^2 \epsilon_r^{(e)} \right] \\ K_{23;23}^{(e)} &= \frac{\ell_{23}^{(e)} \ell_{23}^{(e)}}{\Delta^{(e)}} \left[\frac{1}{24\mu_r^{(e)}} (f_{22}^{(e)} + f_{33}^{(e)} - f_{23}^{(e)}) - k_0^2 \epsilon_r^{(e)} \right] \\ K_{12;13}^{(e)} &= \frac{\ell_{12}^{(e)} \ell_{13}^{(e)}}{\Delta^{(e)}} \left[\frac{1}{48\mu_r^{(e)}} (f_{11}^{(e)} + 2f_{23}^{(e)} - f_{12}^{(e)} - f_{13}^{(e)}) + k_0^2 \epsilon_r^{(e)} \right] \\ K_{12;23}^{(e)} &= \frac{\ell_{12}^{(e)} \ell_{23}^{(e)}}{\Delta^{(e)}} \left[\frac{1}{48\mu_r^{(e)}} (f_{12}^{(e)} + f_{23}^{(e)} - 2f_{13}^{(e)} - f_{22}^{(e)}) - k_0^2 \epsilon_r^{(e)} \right] \\ K_{13;23}^{(e)} &= \frac{\ell_{13}^{(e)} \ell_{23}^{(e)}}{\Delta^{(e)}} \left[\frac{1}{48\mu_r^{(e)}} (f_{33}^{(e)} + 2f_{12}^{(e)} - f_{13}^{(e)} - f_{23}^{(e)}) + k_0^2 \epsilon_r^{(e)} \right] \end{aligned} \quad (9.3.22)$$

where $f_{lk}^{(e)} = b_l^{(e)} b_k^{(e)} + c_l^{(e)} c_k^{(e)}$ with $b_l^{(e)}$, $b_k^{(e)}$, $c_l^{(e)}$, and $c_k^{(e)}$ being defined in Equation 9.2.12.

9.3.3 Application Examples

In this section we consider three examples to demonstrate the accuracy and capability of the finite element method for analysis of complicated electromagnetic problems. These examples are related to the analysis of inhomogeneous waveguides, microwave devices, and scattering by three-dimensional objects.

Unlike homogeneous waveguides, a general inhomogeneous waveguide cannot support either TM or TE modes. The actual waveguide modes contain both E_z and H_z simultaneously, and they are called *hybrid modes*. The analysis of these hybrid modes is far more complicated than that of a homogeneous waveguide. The finite element formulation presented in the following is the most accurate and versatile approach for such an analysis.

For all the propagating modes, the expression for the electric field can be written as a product between a vector function of x and y and an exponential function of z ,

$$\mathbf{E}(x, y, z) = \left[\frac{1}{\beta} \mathbf{e}_t(x, y) + j\hat{z} e_z(x, y) \right] e^{-j\beta z} \quad (9.3.23)$$

where β represents the propagation constant, $\mathbf{e}_t(x, y)$ represents the transverse component and $e_z(x, y)$ represents the longitudinal component. By introducing the weighting function

$$\mathbf{W}(x, y, z) = \left[\frac{1}{\beta} \mathbf{w}_t(x, y) - j\hat{z} w_z(x, y) \right] e^{j\beta z} \quad (9.3.24)$$

the weak form of the vector wave equation for the electrical field can be found as

$$\begin{aligned} & \iint_{\Omega} \left\{ \frac{1}{\mu_r} (\nabla_t \times \mathbf{w}_t) \cdot (\nabla_t \times \mathbf{e}_t) - k_0^2 \epsilon_r \mathbf{w}_t \cdot \mathbf{e}_t \right. \\ & \left. + \beta^2 \left[\frac{1}{\mu_r} (\mathbf{w}_t + \nabla_t w_z) \cdot (\mathbf{e}_t + \nabla_t e_z) - k_0^2 \epsilon_r w_z \cdot e_z \right] \right\} d\Omega = 0 \end{aligned} \quad (9.3.25)$$

where Ω represents the cross-section of the waveguide and ∇_t denotes the transverse del operator.

When Ω is subdivided into small finite elements, $\mathbf{e}_t(x, y)$ and $e_z(x, y)$ can be expanded as

$$\mathbf{e}_t(x, y) = \sum_{j=1}^{N_{\text{edge}}} \mathbf{N}_j(x, y) e_{t,j} \quad (9.3.26)$$

$$e_z(x, y) = \sum_{j=1}^N N_j(x, y) e_{z,j} \quad (9.3.27)$$

where N_{edge} denotes the total number of edges, excluding those on the waveguide conducting surface, and N denotes the total number of nodes, also excluding those on the waveguide conducting surface. Substituting these into Equation 9.3.25 and letting $\mathbf{w}_t = \mathbf{N}_i$ and $w_z = N_i$, we obtain a generalized eigenvalue problem

$$\begin{bmatrix} A_{tt} & 0 \\ 0 & 0 \end{bmatrix} \begin{Bmatrix} e_t \\ e_z \end{Bmatrix} = -\beta^2 \begin{bmatrix} B_{nn} & B_{nz} \\ B_{zt} & B_{zz} \end{bmatrix} \begin{Bmatrix} e_t \\ e_z \end{Bmatrix} \quad (9.3.28)$$

in which

$$A_{tt,ij} = \iint_{\Omega} \left[\frac{1}{\mu_r} (\nabla_t \times \mathbf{N}_i) \cdot (\nabla_t \times \mathbf{N}_j) - k_0^2 \epsilon_r \mathbf{N}_i \cdot \mathbf{N}_j \right] d\Omega \quad (9.3.29)$$

$$B_{tt,ij} = \iint_{\Omega} \frac{1}{\mu_r} \mathbf{N}_i \cdot \mathbf{N}_j d\Omega \quad (9.3.30)$$

$$B_{tz,ij} = \iint_{\Omega} \frac{1}{\mu_r} \mathbf{N}_i \cdot \nabla_t N_j d\Omega \quad (9.3.31)$$

$$B_{zt,ij} = \iint_{\Omega} \frac{1}{\mu_r} \nabla_t N_i \cdot \mathbf{N}_j d\Omega \quad (9.3.32)$$

$$B_{zz,ij} = \iint_{\Omega} \left[\frac{1}{\mu_r} \nabla_t N_i \cdot \nabla_t N_j - k_0^2 \epsilon_r N_i N_j \right] d\Omega. \quad (9.3.33)$$

From Equation 9.3.28, we can solve for a set of eigenvalues β^2 and the corresponding eigenvectors $\{e_x, e_z\}^T$ for a given value of k_0 . These eigenvalues and eigenvectors give the propagation constant and field distribution of each waveguide mode. Figure 9.14 shows the dispersion curves for an insulated image guide, calculated using the method described here.

Now we turn to the analysis of microwave devices. A microwave device has typically one or a few ports, and it is usually characterized by S-parameters. To perform the finite element analysis of a microwave device, it is necessary to terminate each port to

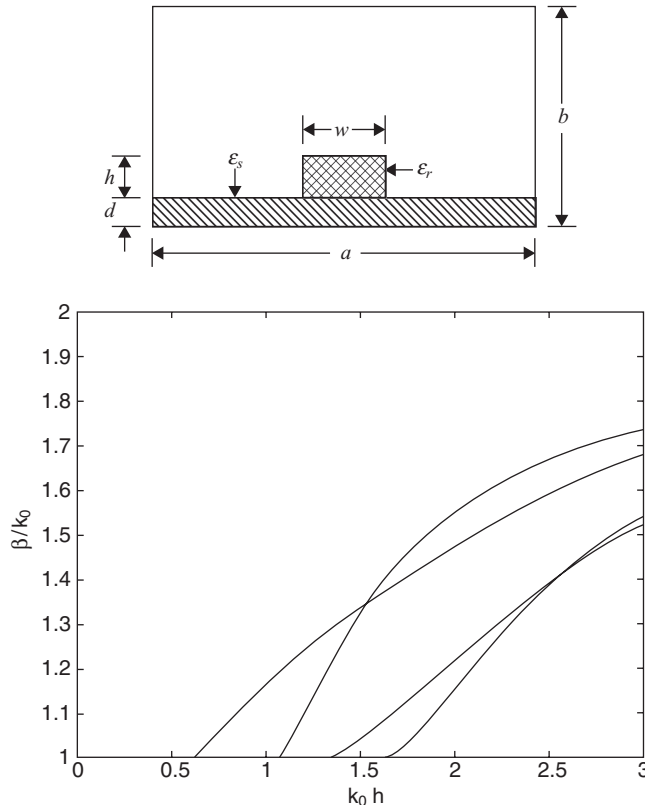


Figure 9.14 Dispersion characteristics of an insulated image guide ($w/h = 2.25$, $d/h = 0.5$, $a/h = 13.5$, $b/h = 8.0$, $\epsilon_r = 3.8$, and $\epsilon_s = 1.5$).

limit the size of the computational domain. A boundary condition is then required at each port to define the boundary-value problem uniquely. To derive such a boundary condition, we need to know the propagation constants and field distributions of the waveguide modes. For most waveguides, such as rectangular, circular, and coaxial waveguides, the propagation constants and modal fields can be obtained analytically. For other waveguides, such as partially filled waveguides, they can be calculated using the finite element method just described. Once the waveguide modes are known, the total electric field at a port can be written as the sum of the incident field and all the modes excited by the device, from which a boundary condition can be derived.

For simplicity, let us first consider a rectangular waveguide input port and furthermore assume that the port is chosen sufficiently far away from the device that only the dominant mode reflected by the device reaches the port and all higher-order modes are attenuated before reaching the port. Under this assumption, the total electric field at the input port can be written as

$$\begin{aligned}\mathbf{E}(u, v, w) &= \mathbf{E}^{\text{inc}}(u, v, w) + \mathbf{E}^{\text{ref}}(u, v, w) \\ &= E_0 \mathbf{e}_{10}(u, v) e^{-j\beta w} + R E_0 \mathbf{e}_{10}(u, v) e^{j\beta w}\end{aligned}\quad (9.3.34)$$

where E_0 denotes the amplitude of the incident field, R denotes the reflection coefficient, and $\mathbf{e}_{10}(u, v)$ and β are given by

$$\mathbf{e}_{10}(u, v) = \hat{v} \sin \frac{\pi u}{a}, \quad \beta = \sqrt{k^2 - \left(\frac{\pi}{a}\right)^2} \quad (9.3.35)$$

which represent the mode distribution and propagation constant of the dominant TE_{10} mode with a denoting the width of the waveguide. Here, (u, v, w) represent local coordinates established at the port such that (u, v) coincide with the port and w points toward the device. From Equation 9.3.34, we can find

$$\hat{n} \times (\nabla \times \mathbf{E}) = -j\beta \mathbf{E}^{\text{inc}} + j\beta \mathbf{E}^{\text{ref}} = j\beta \mathbf{E} - 2j\beta \mathbf{E}^{\text{inc}} \quad (9.3.36)$$

which can also be written as

$$\hat{n} \times (\nabla \times \mathbf{E}) + j\beta \hat{n} \times (\hat{n} \times \mathbf{E}) = -2j\beta \mathbf{E}^{\text{inc}}. \quad (9.3.37)$$

This equation is similar to Equation 9.3.7, whose treatment has been described in detail. By following the same approach, we can derive a similar boundary condition for an output port as

$$\hat{n} \times (\nabla \times \mathbf{E}) + j\beta \hat{n} \times (\hat{n} \times \mathbf{E}) = 0. \quad (9.3.38)$$

Inside the device, the field satisfies the vector wave equation

$$\nabla \times \left(\frac{1}{\mu_r} \nabla \times \mathbf{E} \right) - k_0^2 \epsilon_r \mathbf{E} = 0 \quad (9.3.39)$$

which, together with Equations 9.3.37 and 9.3.38 and other applicable boundary conditions, defines a boundary-value problem uniquely. This problem can readily be solved using the finite element method described in this section.

The approach described above can be extended to include higher-order reflected modes such that the truncation ports can be placed very close to the device. It can also be generalized to deal with inhomogeneously filled waveguide ports, for which the modes can no longer be expressed as TEM, TE, and TM modes. If we denote the electric and magnetic modal functions as \mathbf{e}_m and \mathbf{h}_m for mode m , which satisfy the modal orthogonal relation

$$\iint_{S_p} (\mathbf{h}_m \times \mathbf{e}_n) \cdot \hat{w} dS = \begin{cases} K_m & m = n \\ 0 & m \neq n \end{cases} \quad (9.3.40)$$

then the total field at the waveguide port can be expanded as

$$\mathbf{E} = \mathbf{E}^{\text{inc}} + \mathbf{E}^{\text{ref}} = \mathbf{E}^{\text{inc}} + \sum_{m=1}^{\infty} a_m \mathbf{e}_m e^{\gamma_m w}. \quad (9.3.41)$$

The expansion coefficient can be determined using Equation 9.3.40 as

$$a_m = \frac{1}{K_m} \iint_{S_p} [\mathbf{h}_m \times (\mathbf{E} - \mathbf{E}^{\text{inc}})] \cdot \hat{w} dS. \quad (9.3.42)$$

Applying a curl operator to both sides of Equation 9.3.41 and using Maxwell's equations for the modal fields, we obtain

$$\hat{n} \times (\nabla \times \mathbf{E}) = \hat{n} \times (\nabla \times \mathbf{E}^{\text{inc}}) - j\omega\mu \sum_{m=1}^{\infty} a_m (\hat{n} \times \mathbf{h}_m) e^{\gamma_m w}. \quad (9.3.43)$$

Since

$$\mathbf{h}_m e^{\gamma_m w} = \frac{j}{\omega\mu} \nabla \times (\mathbf{e}_m e^{\gamma_m w}) = \frac{j}{\omega\mu} (\nabla_t + \gamma_m \hat{w}) \times \mathbf{e}_m e^{\gamma_m w} \quad (9.3.44)$$

we have

$$\hat{w} \times \mathbf{h}_m = \frac{1}{j\omega\mu} (\gamma_m \mathbf{e}_{t,m} - \nabla_t e_{w,m}) \quad (9.3.45)$$

where $\mathbf{e}_{t,m}$ denotes the transverse component of \mathbf{e}_m , $e_{w,m}$ denotes its longitudinal component, and ∇_t denotes the transverse del operator, that is, $\nabla_t = \nabla - \hat{w} \partial/\partial w$. Substituting this into Equations 9.3.42 and 9.3.43, we obtain the waveguide port boundary condition as

$$\hat{n} \times (\nabla \times \mathbf{E}) + \mathcal{P}(\mathbf{E}) = \mathbf{U}^{\text{inc}} \quad (9.3.46)$$

with

$$\mathcal{P}(\mathbf{E}) = \sum_{m=1}^{\infty} \frac{1}{j\omega\mu K_m} (\gamma_m \mathbf{e}_{t,m} - \nabla_t e_{w,m}) \iint_{S_p} (\gamma_m \mathbf{e}_{t,m} - \nabla_t e_{w,m}) \cdot \mathbf{E} dS \quad (9.3.47)$$

$$\mathbf{U}^{\text{inc}} = \hat{n} \times (\nabla \times \mathbf{E}^{\text{inc}}) + \sum_{m=1}^{\infty} \frac{1}{j\omega\mu K_m} (\gamma_m \mathbf{e}_{t,m} - \nabla_t e_{w,m}) \iint_{S_p} (\gamma_m \mathbf{e}_{t,m} - \nabla_t e_{w,m}) \cdot \mathbf{E}^{\text{inc}} dS. \quad (9.3.48)$$

The boundary condition in Equation 9.3.46 can be incorporated into the finite element formulation in a rather straightforward manner.

Once the fields inside the device and at its ports have been obtained, the S-parameters can be calculated based on their definitions. Figure 9.15 shows the transmission coefficient S_{12} for a cylindrical cavity resonator [11]. The input and output ports are WR75 waveguides, coupled to the internal resonator through two rectangular slots. Figure 9.16 shows the S-parameters for an overlap-gap-coupled microstrip filter [12], which is a two-layer structure sitting on a ground plane. Detailed dimension parameters are given in Figure 9.16a and both the reflection and transmission coefficients are compared with measured data. The agreement is generally good, and the discrepancy is likely caused by the measurement uncertainty.

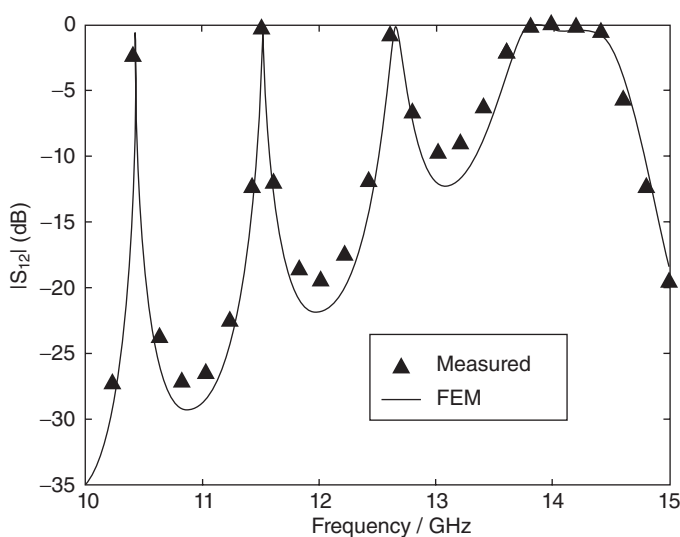
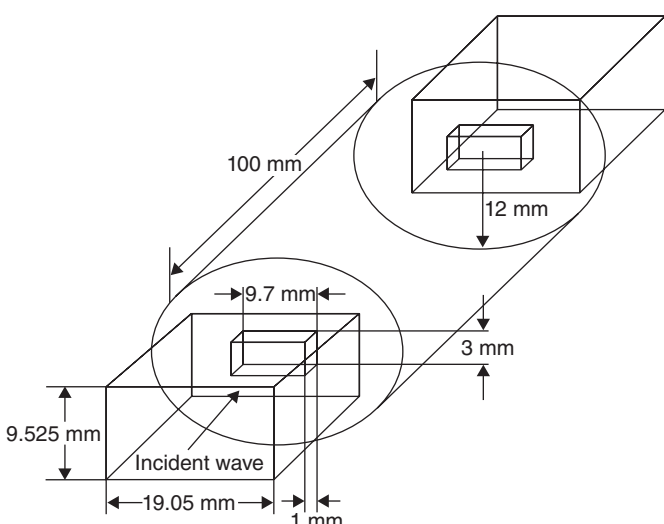


Figure 9.15 Transmission coefficient S_{12} of a cylindrical cavity resonator. (After Liu et al. [11], Copyright © 2002 Wiley.)

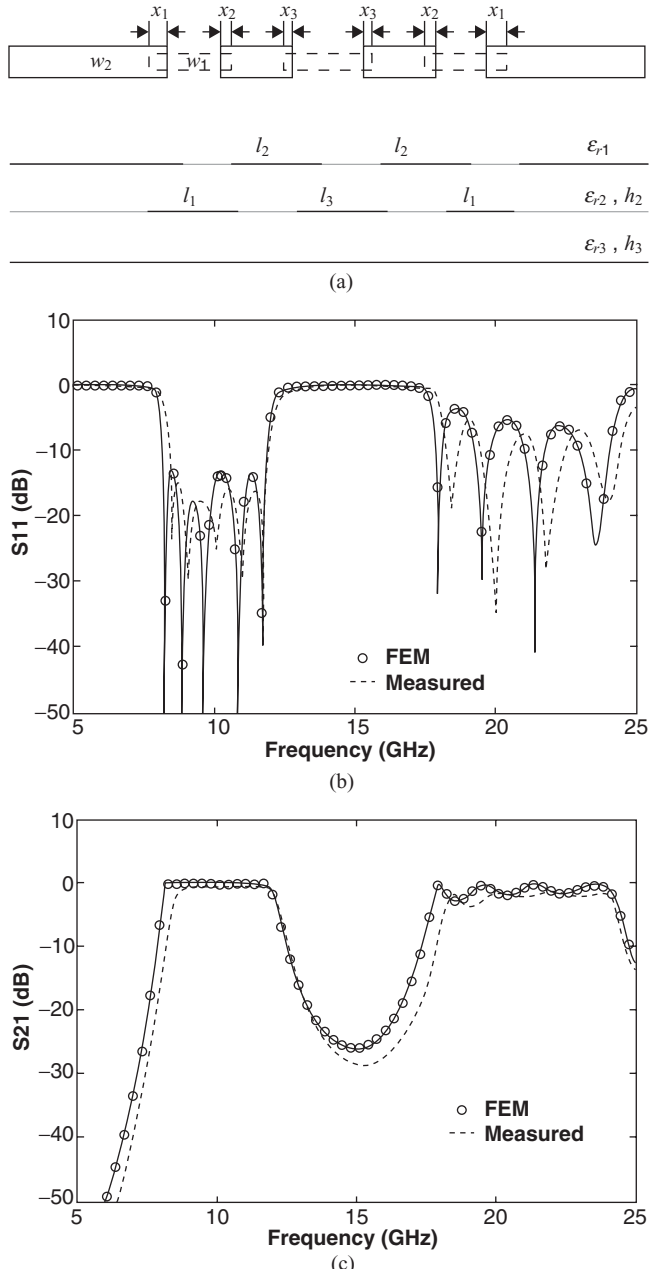


Figure 9.16 S-parameters for an overlap-gap-coupled microstrip filter. (a) Top and side view of the geometry ($\epsilon_{r1} = 1.0$, $\epsilon_{r2} = 9.8$, $\epsilon_{r3} = 2.2$, $h_2 = h_3 = 0.254\text{ mm}$, $w_1 = 0.812\text{ mm}$, $w_2 = 0.458\text{ mm}$, $l_1 = 6.990\text{ mm}$, $l_2 = 6.457\text{ mm}$, $l_3 = 7.242\text{ mm}$, $x_1 = 1.311\text{ mm}$, $x_2 = 0.386\text{ mm}$, $x_3 = 0.269\text{ mm}$). (b) S_{11} . (c) S_{21} . (After Lee and Jin [12], Copyright © IEEE 2007.)

The third example concerns the problem of electromagnetic wave scattering by a three-dimensional object. The main difficulty in the finite element analysis of this type of scattering problem is how to deal with the surrounding infinitely large open space. A common approach is to introduce an artificial surface to truncate the infinite solution domain into a finite one, as was done for the two-dimensional case in the preceding section.

Inside this artificial surface, the electric field satisfies the same vector wave equation as Equation 9.3.39, assuming that the source of the incident field resides outside the truncation surface. In addition to this, a boundary condition is required at this surface for a unique solution of the electromagnetic fields. This boundary condition should be transparent to the scattered field, that is, it should let the scattered field pass through without any reflection. Unfortunately, there is no simple boundary condition that meets this requirement. Over the years, a variety of approximate boundary conditions, also called ABCs, have been developed to satisfy this requirement approximately. The simplest ABC is the well-known Sommerfeld radiation condition, which states that if the truncation surface is sufficiently far away from the scatterer, the scattered field satisfies the relation

$$\hat{n} \times \left(\frac{1}{\mu_r} \nabla \times \mathbf{E}^{\text{sc}} \right) + \frac{jk_0}{\eta_r} \hat{n} \times (\hat{n} \times \mathbf{E}^{\text{sc}}) \approx 0 \quad (9.3.49)$$

where \hat{n} denotes the unit vector normal to the truncation surface, and $\mu_r = 1$ and $\eta_r = 1$ if the truncation surface is placed in free space. Furthermore, \mathbf{E}^{sc} denotes the scattered field, which is the difference between the total and the incident fields,

$$\mathbf{E}^{\text{sc}} = \mathbf{E} - \mathbf{E}^{\text{inc}}. \quad (9.3.50)$$

By using Equation 9.3.50, the ABC can be written for the total field as

$$\hat{n} \times \left(\frac{1}{\mu_r} \nabla \times \mathbf{E} \right) + \frac{jk_0}{\eta_r} \hat{n} \times (\hat{n} \times \mathbf{E}) \approx \mathbf{U}^{\text{inc}} \quad (9.3.51)$$

where

$$\mathbf{U}^{\text{inc}} = \hat{n} \times \left(\frac{1}{\mu_r} \nabla \times \mathbf{E}^{\text{inc}} \right) + \frac{jk_0}{\eta_r} \hat{n} \times (\hat{n} \times \mathbf{E}^{\text{inc}}). \quad (9.3.52)$$

The boundary condition in Equation 9.3.51 is nothing more than the mixed boundary condition in Equation 9.3.7.

The scattering problem can also be simulated by calculating the scattered field directly. The ABC remains the same as Equation 9.3.49, and the vector wave equation can be obtained by substituting Equation 9.3.50 into Equation 9.3.39 to find

$$\nabla \times \left(\frac{1}{\mu_r} \nabla \times \mathbf{E}^{\text{sc}} \right) - k_0^2 \epsilon_r \mathbf{E}^{\text{sc}} = \mathbf{F}^{\text{inc}} \quad (9.3.53)$$

where

$$\mathbf{F}^{\text{inc}} = -\nabla \times \left(\frac{1}{\mu_r} \nabla \times \mathbf{E}^{\text{inc}} \right) + k_0^2 \epsilon_r \mathbf{E}^{\text{inc}}. \quad (9.3.54)$$

If the scatterer contains perfectly conducting surfaces, the following boundary condition should be enforced on such surfaces:

$$\hat{n} \times \mathbf{E}^{\text{sc}} = -\hat{n} \times \mathbf{E}^{\text{inc}} \quad (9.3.55)$$

to satisfy the boundary condition $\hat{n} \times \mathbf{E} = 0$.

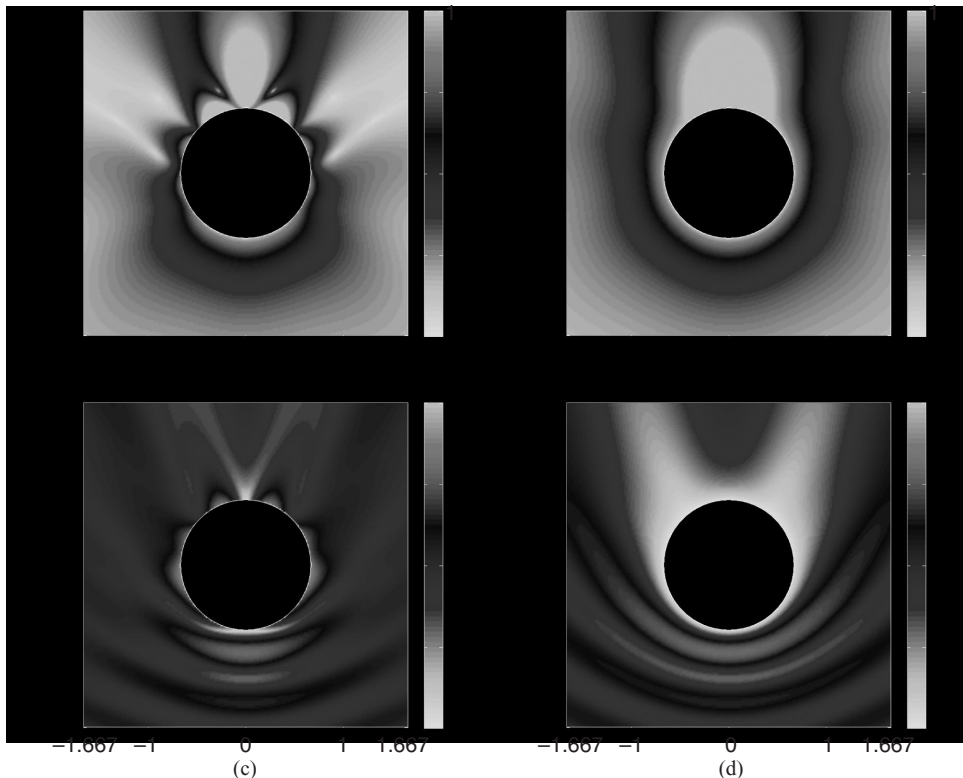


Figure 9.17 Scattering by a metallic sphere having a radius of 0.667λ . (a) Magnitude of the scattered electric field in the E-plane. (b) Magnitude of the scattered electric field in the H-plane. (c) Magnitude of the total electric field in the E-plane. (d) Magnitude of the total electric field in the H-plane. The values of the fields are normalized by the magnitude of the incident electric field. (See color insert.)

As an example, we consider the problem of plane wave scattering by a perfectly conducting sphere having a radius of 0.667λ . The scattered and total fields to be computed by the finite element method are shown in Figure 9.17. For the finite element analysis, the mesh is truncated by an artificial spherical surface placed 1λ away from the surface of the sphere. Once the field is computed in the computational domain, the scattered far-field and then the bistatic radar cross-section (RCS) can be calculated based on the surface equivalence principle. The result is given in Figure 9.18 and is compared with the Mie series solution.

9.4 FINITE ELEMENT ANALYSIS IN THE TIME DOMAIN

The finite element formulation described in Section 9.3 is carried out in the frequency domain. It takes the frequency as an input parameter and solves for the electric field at that specific frequency. However, for some applications, we are interested in the fields over a broad frequency band. In such a case, we have to repeat a frequency-dependent analysis at many frequencies, which can be quite time-consuming. Furthermore, when a problem is non-linear (where the material properties depend on the field strengths) or non-stationary (where the material properties change over time), it is difficult

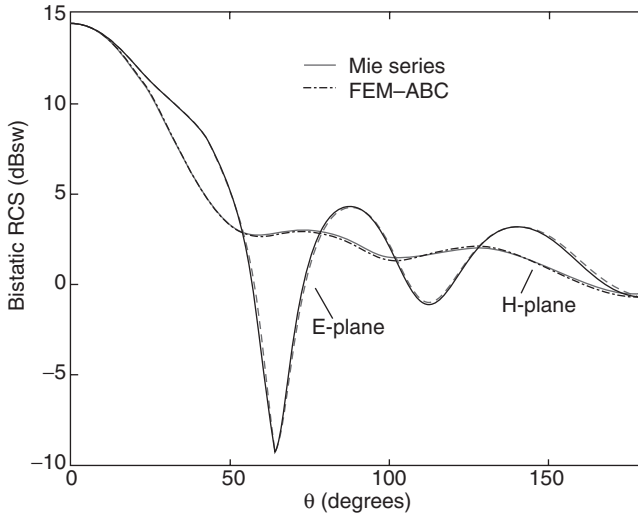


Figure 9.18 Bistatic RCS of a metallic sphere having a radius of 0.667λ .

to use a frequency domain-based method to model such a problem accurately. These two challenges can be alleviated by using the finite element method formulated in the time domain.

9.4.1 The Boundary-Value Problem

In the time domain, the first two of Maxwell's equations (Eqs. 9.3.1 and 9.3.2) become

$$\nabla \times \mathcal{E}(t) = -\mu \frac{\partial \mathcal{H}(t)}{\partial t} \quad (9.4.1)$$

$$\nabla \times \mathcal{H}(t) = \epsilon \frac{\partial \mathcal{E}(t)}{\partial t} + \sigma \mathcal{E}(t) + \mathcal{J}_{\text{imp}}(t) \quad (9.4.2)$$

where σ denotes the conductivity. The boundary condition corresponding to Equation 9.3.6 remains the same, repeated here as

$$\hat{n} \times \mathcal{E}(t) = \mathcal{P}(t) \quad \text{on } \Gamma_D \quad (9.4.3)$$

and the boundary condition corresponding to Equation 9.3.7 becomes

$$\hat{n} \times \left[\frac{1}{\mu} \nabla \times \mathcal{E}(t) \right] + Y \hat{n} \times \left[\hat{n} \times \frac{\partial}{\partial t} \mathcal{E}(t) \right] = \mathcal{K}_N(t) \quad \text{on } \Gamma_N \quad (9.4.4)$$

where Y denotes the surface admittance on boundary Γ_N . By eliminating the magnetic field from Equations 9.4.1 and 9.4.2, we obtain the vector wave equation for the electric field as

$$\nabla \times \left[\frac{1}{\mu} \nabla \times \mathcal{E}(t) \right] + \epsilon \frac{\partial^2 \mathcal{E}(t)}{\partial t^2} + \sigma \frac{\partial \mathcal{E}(t)}{\partial t} = -\frac{\partial \mathcal{J}_{\text{imp}}(t)}{\partial t}. \quad (9.4.5)$$

9.4.2 Finite Element Formulation

Following the same approach employed in the frequency domain, we obtain the weak-form representation of the boundary-value problem defined by Equations 9.4.3–9.4.5 as

$$\begin{aligned} & \int_{\Omega} \left[\frac{1}{\mu} (\nabla \times \mathbf{W}_i) \cdot (\nabla \times \mathcal{E}) + \epsilon \mathbf{W}_i \cdot \frac{\partial^2 \mathcal{E}}{\partial t^2} + \sigma \mathbf{W}_i \cdot \frac{\partial \mathcal{E}}{\partial t} \right] d\Omega \\ &= - \int_{\Gamma_N} \left[Y(\hat{n} \times \mathbf{W}_i) \cdot \left(\hat{n} \times \frac{\partial \mathcal{E}}{\partial t} \right) + \mathbf{W}_i \cdot \mathcal{H}_N \right] d\Gamma - \int_{\Omega} \mathbf{W}_i \cdot \frac{\partial \mathcal{J}_{\text{imp}}}{\partial t} d\Omega. \end{aligned} \quad (9.4.6)$$

Note that the vector weighting function is assumed to satisfy the boundary condition $\hat{n} \times \mathbf{W}_i = 0$ on Γ_D since Equation 9.4.3 will be enforced explicitly in the solution of Equation 9.4.6.

To seek the finite element solution of Equation 9.4.6, we first perform the spatial discretization in the exactly same manner as in the frequency domain. To be more specific, by subdividing the solution volume into small finite elements and expanding the electric field within each element using vector basis functions, we can express the electric field as

$$\mathcal{E}(r, t) = \sum_{j=1}^{N_{\text{edge}}} \mathbf{N}_j(\mathbf{r}) \mathcal{E}_j(t) + \sum_{j=1}^{N_D} \mathbf{N}_j^D(\mathbf{r}) \mathcal{E}_j^D(t). \quad (9.4.7)$$

Substituting Equation 9.4.7 into Equation 9.4.6 and letting $\mathbf{W}_i = \mathbf{N}_i$ yields a second-order ordinary differential equation

$$[T] \frac{d^2 \{\mathcal{E}\}}{dt^2} + [R] \frac{d\{\mathcal{E}\}}{dt} + [S]\{\mathcal{E}\} = \{\mathcal{J}\} \quad (9.4.8)$$

where $[T]$, $[R]$, and $[S]$ represent sparse, symmetric matrices whose elements are given by

$$T_{ij} = \int_{\Omega} \epsilon \mathbf{N}_i \cdot \mathbf{N}_j d\Omega \quad (9.4.9)$$

$$R_{ij} = \int_{\Omega} \sigma \mathbf{N}_i \cdot \mathbf{N}_j d\Omega + \int_{\Gamma_N} Y(\hat{n} \times \mathbf{N}_i) \cdot (\hat{n} \times \mathbf{N}_j) d\Gamma \quad (9.4.10)$$

$$S_{ij} = \int_{\Omega} \frac{1}{\mu} (\nabla \times \mathbf{N}_i) \cdot (\nabla \times \mathbf{N}_j) d\Omega. \quad (9.4.11)$$

Furthermore, $\{\mathcal{E}\} = [\mathcal{E}_1, \mathcal{E}_2, \dots, \mathcal{E}_{N_{\text{edge}}}]^T$, and the elements of the excitation vector $\{\mathcal{J}\}$ are given by

$$\begin{aligned} \mathcal{J}_i &= - \int_{\Omega} \mathbf{N}_i \cdot \frac{\partial \mathcal{J}_{\text{imp}}}{\partial t} d\Omega - \int_{\Gamma_N} \mathbf{N}_i \cdot \mathcal{H}_N d\Gamma \\ &\quad - \sum_{j=1}^{N_D} \int_{\Omega} \left[\frac{1}{\mu} (\nabla \times \mathbf{N}_i) \cdot (\nabla \times \mathbf{N}_j^D) \mathcal{E}_j^D + \mathbf{N}_i \cdot \mathbf{N}_j^D \left(\epsilon \frac{d^2 \mathcal{E}_j^D}{dt^2} + \sigma \frac{d \mathcal{E}_j^D}{dt} \right) \right] d\Omega. \end{aligned} \quad (9.4.12)$$

Equation 9.4.8 can be solved by using direct integration or the finite difference method discussed in Chapter 8. In the finite difference method, the time variable t is

uniformly discretized such that it is represented by $t = n\Delta t$ ($n = 0, 1, \dots$), where Δt is denoted as the time step. The continuous differentiation is then approximated by a finite difference, which yields an equation that allows the calculation of the unknown vector $\{\mathcal{E}\}$ at any instant based on its previous values. This process is called *time marching* or *time stepping*. To show this, consider the use of central differencing for both the first and second derivatives

$$\frac{d\{\mathcal{E}\}}{dt} \approx \frac{\{\mathcal{E}\}^{n+1} - \{\mathcal{E}\}^{n-1}}{2\Delta t} \quad (9.4.13)$$

$$\frac{d^2\{\mathcal{E}\}}{dt^2} \approx \frac{\{\mathcal{E}\}^{n+1} - 2\{\mathcal{E}\}^n + \{\mathcal{E}\}^{n-1}}{(\Delta t)^2}. \quad (9.4.14)$$

Substituting these into Equation 9.4.8, we obtain the time-stepping formula as

$$\begin{aligned} \left\{ \frac{1}{(\Delta t)^2} [T] + \frac{1}{2\Delta t} [R] \right\} \{\mathcal{E}\}^{n+1} &= \left\{ \frac{2}{(\Delta t)^2} [T] - [S] \right\} \{\mathcal{E}\}^n \\ &\quad - \left\{ \frac{1}{(\Delta t)^2} [T] - \frac{1}{2\Delta t} [R] \right\} \{\mathcal{E}\}^{n-1} + \{\mathcal{J}\}^n \end{aligned} \quad (9.4.15)$$

which can be used to find $\{\mathcal{E}\}^{n+1}$ based on the previous field values $\{\mathcal{E}\}^n$ and $\{\mathcal{E}\}^{n-1}$ and the excitation $\{\mathcal{J}\}^n$. Given the initial values of $\{\mathcal{E}\}$, that is, $\{\mathcal{E}\}^0$ and $\{\mathcal{E}\}^1$, and the values of the excitation vector $\{\mathcal{J}\}$, Equation 9.4.15 can be employed to compute all the subsequent values for $\{\mathcal{E}\}$. Note that to compute each new $\{\mathcal{E}\}$, one has to solve a matrix equation at each time step. Similar time-marching equations can be derived using the forward and backward differencing formulas.

It can be shown that the use of forward differencing will result in an unstable time-marching equation (the value of $\{\mathcal{E}\}^n$ increases exponentially as n increases, yielding a non-physical solution). The use of backward differencing will result in an unconditionally stable (the time step size Δt is not constrained by the spatial discretization) time-marching equation, which unfortunately is only first-order accurate—the accuracy of the solution is proportional to $O(\Delta t)$. The time-marching equation (Eq. 9.4.15) obtained using central differencing is second-order accurate and is conditionally stable—the time marching is stable only when Δt is smaller than a certain value dictated by the spatial discretization. For Equation 9.4.8, the best choice is to use a differencing formula derived from the Newmark-beta integration method [13], which is equivalent to using central differencing for the first and second derivatives and using a weighted average for the undifferentiated quantities

$$\{\mathcal{E}\} \approx \beta \{\mathcal{E}\}^{n+1} + (1-2\beta) \{\mathcal{E}\}^n + \beta \{\mathcal{E}\}^{n-1} \quad (9.4.16)$$

$$\{\mathcal{J}\} \approx \beta \{\mathcal{J}\}^{n+1} + (1-2\beta) \{\mathcal{J}\}^n + \beta \{\mathcal{J}\}^{n-1} \quad (9.4.17)$$

where β is a parameter that takes a value between 0 and 1. Substituting these into Equation 9.4.8, we obtain

$$\begin{aligned} \left\{ \frac{1}{(\Delta t)^2} [T] + \frac{1}{2\Delta t} [R] + \beta [S] \right\} \{\mathcal{E}\}^{n+1} &= \left\{ \frac{2}{(\Delta t)^2} [T] - (1-2\beta) [S] \right\} \{\mathcal{E}\}^n \\ &- \left\{ \frac{1}{(\Delta t)^2} [T] - \frac{1}{2\Delta t} [R] + \beta [S] \right\} \{\mathcal{E}\}^{n-1} + \beta \{\mathcal{S}\}^{n+1} + (1-2\beta) \{\mathcal{S}\}^n + \beta \{\mathcal{S}\}^{n-1}. \end{aligned} \quad (9.4.18)$$

Obviously, when $\beta = 0$, this equation reduces to the one obtained using central differencing. When $\beta \geq \frac{1}{4}$, this equation is unconditionally stable while maintaining its second-order accuracy.

The formulation described above assumes that the media involved are dispersion-free. In other words, both the permeability μ and the permittivity ϵ are invariant with respect to frequency. This formulation can be modified to deal with dispersive media, and to demonstrate this we consider the case where only the permittivity ϵ is a function of frequency while the permeability μ remains frequency-independent (electrically dispersive material). In this case, the electric flux density $\mathcal{D}(t)$ is related to the electric field intensity $\mathcal{E}(t)$ by the constitutive relation in Equation 8.6.1, which is repeated here for convenience as

$$\begin{aligned} \mathcal{D}(t) &= \epsilon_{\infty} \mathcal{E}(t) + \epsilon_0 \tilde{\chi}_e(t) * \mathcal{E}(t) \\ &= \epsilon_{\infty} \mathcal{E}(t) + \epsilon_0 \int_0^t \tilde{\chi}_e(t-\tau) \mathcal{E}(\tau) d\tau \end{aligned} \quad (9.4.19)$$

where it has been assumed that $\mathcal{E}(t) \equiv 0$ for $t \leq 0$. From Maxwell's equations and the constitutive relation above, we obtain

$$\nabla \times \left[\frac{1}{\mu} \nabla \times \mathcal{E}(t) \right] + \epsilon_{\infty} \frac{\partial^2 \mathcal{E}(t)}{\partial t^2} + \epsilon_0 \frac{\partial^2}{\partial t^2} [\tilde{\chi}_e(t) * \mathcal{E}(t)] = -\frac{\partial \mathcal{J}_{\text{imp}}(t)}{\partial t}. \quad (9.4.20)$$

If we further assume that $[\partial \mathcal{E}(t)/\partial t]_{t=0} = 0$, it can be shown that

$$\frac{\partial^2}{\partial t^2} [\tilde{\chi}_e(t) * \mathcal{E}(t)] = \tilde{\chi}_e(t) * \frac{\partial^2 \mathcal{E}(t)}{\partial t^2} \quad (9.4.21)$$

and consequently, Equation 9.4.20 can be written as

$$\nabla \times \left[\frac{1}{\mu} \nabla \times \mathcal{E}(t) \right] + \epsilon_{\infty} \frac{\partial^2 \mathcal{E}(t)}{\partial t^2} + \epsilon_0 \tilde{\chi}_e(t) * \frac{\partial^2 \mathcal{E}(t)}{\partial t^2} = -\frac{\partial \mathcal{J}_{\text{imp}}(t)}{\partial t}. \quad (9.4.22)$$

The weak-form representation of Equation 9.4.22 becomes

$$\begin{aligned} \int_{\Omega} \left[\frac{1}{\mu} (\nabla \times \mathbf{W}_i) \cdot (\nabla \times \mathcal{E}) + \epsilon_{\infty} \mathbf{W}_i \cdot \frac{\partial^2 \mathcal{E}}{\partial t^2} + \epsilon_0 \mathbf{W}_i \cdot \tilde{\chi}_e(t) * \frac{\partial^2 \mathcal{E}}{\partial t^2} \right] d\Omega \\ = - \int_{\Gamma_N} \left[Y(\hat{n} \times \mathbf{W}_i) \cdot \left(\hat{n} \times \frac{\partial \mathcal{E}}{\partial t} \right) + \mathbf{W}_i \cdot \mathcal{K}_N \right] d\Gamma - \int_{\Omega} \mathbf{W}_i \cdot \frac{\partial \mathcal{J}_{\text{imp}}}{\partial t} d\Omega. \end{aligned} \quad (9.4.23)$$

The convolution term can be written in semidiscrete form as

$$\tilde{\chi}_e(t) * \frac{\partial^2 \mathcal{E}(t)}{\partial t^2} \Big|_{t=n\Delta t} \equiv \int_0^{\Delta t/2} \tilde{\chi}_e(\tau) \ddot{\mathcal{E}}(n\Delta t - \tau) d\tau + \sum_{k=0}^{n-1} \int_{(k+1/2)\Delta t}^{(k+3/2)\Delta t} \tilde{\chi}_e(\tau) \ddot{\mathcal{E}}(n\Delta t - \tau) d\tau \quad (9.4.24)$$

where $\ddot{\mathcal{E}}$ denotes the second derivative of \mathcal{E} . For the plasma-, Debye-, and Lorentz-type materials, the electrical susceptibility $\tilde{\chi}_e(t)$ can be written as

$$\tilde{\chi}_e(t) = \operatorname{Re} [ae^{-bt} u(t)] \quad (9.4.25)$$

where $u(t)$ represents the unit step function and a and b are parameters related to specific materials. Consequently, by assuming that $\ddot{\mathcal{E}}$ is constant over the time integration intervals, Equation 9.4.24 can be written as

$$\begin{aligned} \tilde{\chi}_e(t) * \frac{\partial^2 \mathcal{E}(t)}{\partial t^2} \Big|_{t=n\Delta t} &\equiv \left[\int_0^{\Delta t/2} \tilde{\chi}_e(\tau) d\tau \right] \ddot{\mathcal{E}}^n + \sum_{k=0}^{n-1} \left[\int_{(k+1/2)\Delta t}^{(k+3/2)\Delta t} \tilde{\chi}_e(\tau) d\tau \right] \ddot{\mathcal{E}}^{n-k-1} \\ &= \operatorname{Re} \left[\frac{a}{b} (1 - e^{-b\Delta t/2}) \right] \ddot{\mathcal{E}}^n + \sum_{k=0}^{n-1} \operatorname{Re} \left[\frac{a}{b} (1 - e^{-b\Delta t}) e^{-b(k+1/2)\Delta t} \right] \ddot{\mathcal{E}}^{n-k-1}. \end{aligned} \quad (9.4.26)$$

The application of spatial discretization by the finite element method in conjunction with the Newmark-beta method with $\beta = \frac{1}{4}$ for the time integration to Equation 9.4.23 yields the time-stepping equation

$$\begin{aligned} \left\{ \frac{1}{(\Delta t)^2} [T] + \frac{1}{2\Delta t} [R] + \frac{1}{4} [S] \right\} \{\mathcal{E}\}^{n+1} &= \left\{ \frac{2}{(\Delta t)^2} [T] - \frac{1}{2} [S] \right\} \{\mathcal{E}\}^n \\ &\quad - \left\{ \frac{1}{(\Delta t)^2} [T] - \frac{1}{2\Delta t} [R] + \frac{1}{4} [S] \right\} \{\mathcal{E}\}^{n-1} - \{\Psi\}^n \\ &\quad + \frac{1}{4} [\{\mathcal{S}\}^{n+1} + 2\{\mathcal{S}\}^n + \{\mathcal{S}\}^{n-1}] \end{aligned} \quad (9.4.27)$$

where all the matrices and vectors are the same as those in Equation 9.4.18 except that

$$T_{ij} = \operatorname{Re} \left[\varepsilon_\infty + \varepsilon_0 \frac{a}{b} (1 - e^{-b\Delta t/2}) \right] \int_\Omega \mathbf{N}_i \cdot \mathbf{N}_j d\Omega \quad (9.4.28)$$

$$\{\Psi\}^n = \sum_{k=0}^{n-1} \operatorname{Re} [\Phi]^k \left(\{\mathcal{E}\}^{n-k} - 2\{\mathcal{E}\}^{n-k-1} + \{\mathcal{E}\}^{n-k-2} \right) \quad (9.4.29)$$

in which

$$\Phi_{ij}^k = \varepsilon_0 \left[\frac{a}{b} (1 - e^{-b\Delta t}) e^{-b(k+1/2)\Delta t} \right] \int_\Omega \mathbf{N}_i \cdot \mathbf{N}_j d\Omega. \quad (9.4.30)$$

The recursive relationship $[\Phi]^k = e^{-b\Delta t} [\Phi]^{k-1}$ allows Equation 9.4.29 to be evaluated recursively as

$$\{\Psi\}^n = \operatorname{Re} [\{\tilde{\Psi}\}^n] \quad (9.4.31)$$

$$\{\tilde{\Psi}\}^n = [\Phi]^0 \left(\{\mathcal{E}\}^n - 2\{\mathcal{E}\}^{n-1} + \{\mathcal{E}\}^{n-2} \right) + e^{-b\Delta t} \{\tilde{\Psi}\}^{n-1}. \quad (9.4.32)$$

The use of this recursive convolution significantly saves computation time and memory.

The approach described above can be extended further to deal with magnetically dispersive and doubly (both electrically and magnetically) dispersive materials. The reader is referred to Reference [14] for the detailed treatment.

9.4.3 Application Examples

We consider two examples to demonstrate the finite element analysis in the time domain. The first example calculates the input impedance of a microstrip patch antenna geometry consisting of a $5.0\text{cm} \times 3.4\text{cm}$ rectangular conducting patch residing on a dielectric substrate having a thickness of $d = 0.0877\text{ cm}$, relative permittivity $\epsilon_r = 2.17$, and conductivity $\sigma = 0.362\text{ ms/m}$. The substrate is housed in a $7.5\text{ cm} \times 5.1\text{ cm}$ rectangular cavity recessed in a ground plane (Fig. 9.19). The patch, centered at $x = 0$ and $y = 0$, is excited by a current probe applied at $x_f = 1.22\text{ cm}$ and $y_f = 0.85\text{ cm}$. A $50\text{-}\Omega$ -impedance load is placed at $x_L = -2.2\text{ cm}$ and $y_L = -1.5\text{ cm}$. Figure 9.20 shows the input impedance of the antenna as a function of frequency from 1 to 4GHz [15]. The results are calculated using the time-domain finite element method (TD-FEM) and are compared with those obtained using its frequency-domain counterpart (FD-FEM). Both solutions agree with each other quite well.

In the second example, a logarithmic spiral antenna consisting of two free-standing conducting arms is simulated [16]. The front view of the antenna is shown in Figure 9.21a. The centerline of the arms is prescribed by $r = r_0 \tau^{\phi/2\pi}$ in the polar coordinate system where r_0 is a constant and τ is the scaling factor chosen to be 1.588. The inner and outer radii of the spiral are 0.22 and 3.5 cm, respectively. In the simulation, the antenna is fed by the probe feed model [9]. A detailed view of the feed region is shown in Figure 9.21b. A 0.56-mm-long current probe is placed at the center to excite the antenna, and the voltage across the feed is measured along the two observation probes placed 0.28 mm away from the current probe. The calculated input resistance (solid line) and reactance (dashed line) versus frequency are shown in Figure 9.21c. The curves exhibit a transition from the resonance region to the broadband region as the frequency increases and a nice broadband

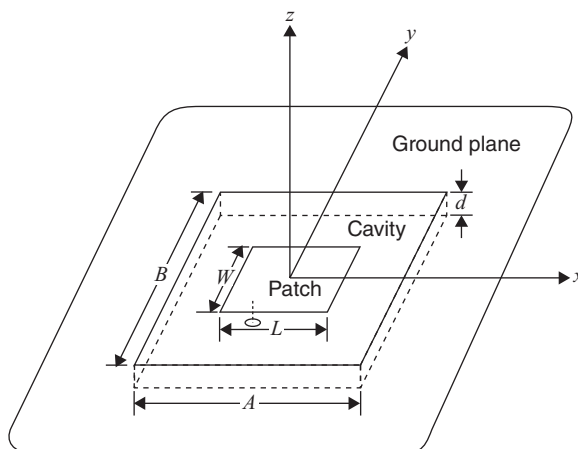


Figure 9.19 Microstrip patch antenna recessed in a ground plane. The antenna is fed by a coaxial line, which is modeled as an electric current probe.

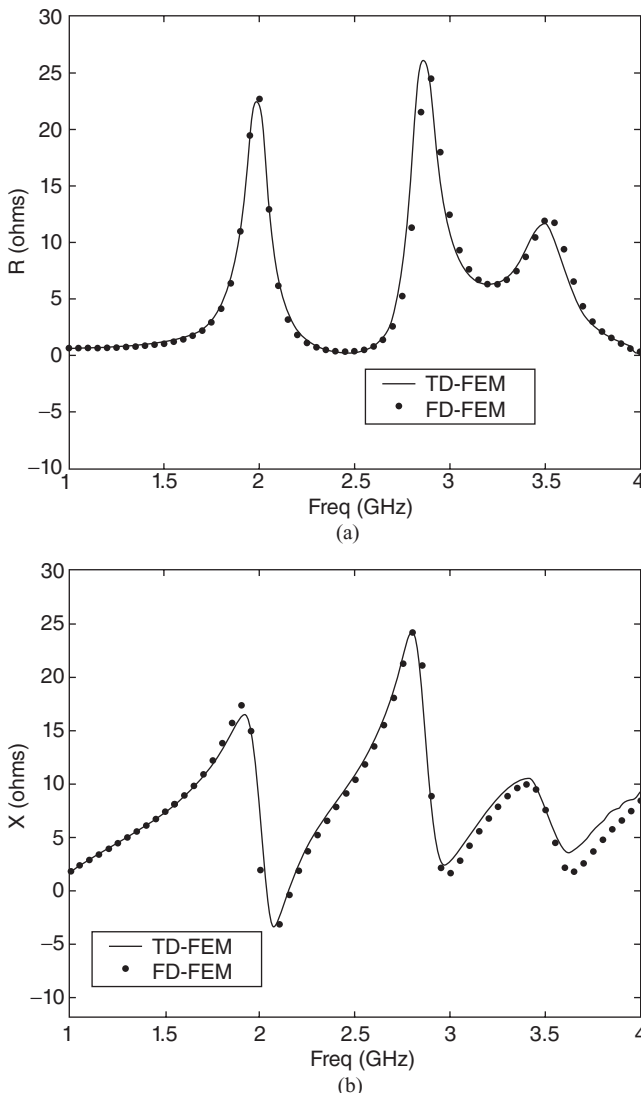


Figure 9.20 Input impedance of a loaded microstrip patch antenna. (a) Resistance.
(b) Reactance. (After Jiao and Jin [15], Copyright © Wiley 2002.)

behavior for frequencies beyond 8 GHz. We also observe that the calculated input impedance converges to the theoretical value (188.5Ω for the two-arm self-complementary antenna) at the higher-frequency end.

9.5 ABSORBING BOUNDARY CONDITIONS

As in the finite difference method, truncating an infinitely large solution domain into a finite computational domain is one of the major challenges in the use of the finite element method for solving open-region electromagnetic problems. Both ABCs and PMLs have been widely used for the mesh truncation in the finite element method.

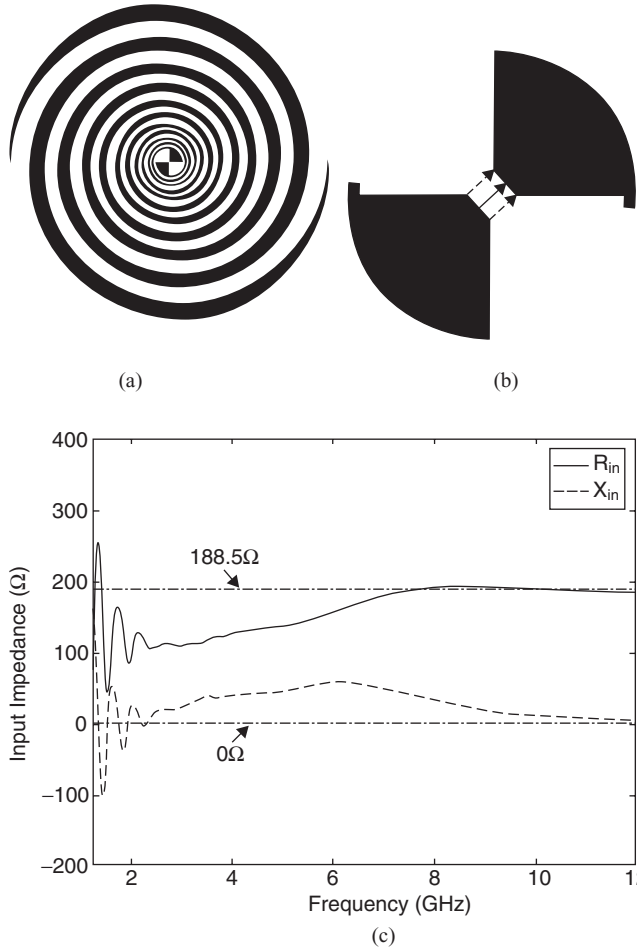


Figure 9.21 Two-arm logarithmic spiral antenna. (a) Geometry of the arms. (b) Enlarged feed region. (c) Input impedance. (After Lou and Jin [16], Copyright © IEEE 2005.)

9.5.1 Two-Dimensional ABCs

The ABCs developed in Chapter 8 can readily be used for the finite element analysis. These include the first-order condition given in Equation 8.5.10, which can be written as

$$\frac{\partial \varphi}{\partial n} \approx -jk\varphi \quad (9.5.1)$$

and the second-order condition given in Equation 8.5.14, which can be written as

$$\frac{\partial \varphi}{\partial n} \approx -jk\varphi - \frac{j}{2k} \frac{\partial^2 \varphi}{\partial s^2} \quad (9.5.2)$$

where $\partial/\partial n$ denotes the normal derivative and $\partial^2/\partial s^2$ denotes the second tangential derivative. These conditions are derived for planar boundaries. With the finite element method, we can now employ curved boundaries for mesh truncation, which often yields a significant improvement on the absorbing performance. Although Equations 9.5.1 and 9.5.2 can

be used for curved surfaces, it is more desirable to use the ones that take into account the curvature effect of the absorbing boundary.

ABCs for curved boundaries can be derived by considering the asymptotic form of the wave solution valid at a large distance from the source. For the two-dimensional case, the field far away from the source can be expressed as

$$\varphi(\rho, \phi) \approx A(\phi) \frac{e^{-jk\rho}}{\sqrt{\rho}}. \quad (9.5.3)$$

Taking the partial derivative with respect to ρ yields

$$\frac{\partial \varphi}{\partial \rho} \approx \left(-jk - \frac{1}{2\rho} \right) A(\phi) \frac{e^{-jk\rho}}{\sqrt{\rho}} = \left(-jk - \frac{1}{2\rho} \right) \varphi \quad (9.5.4)$$

which is referred to as the *first-order ABC*. Clearly, for a very large ρ , this reduces to Equation 9.5.1. This approach can be extended to derive more accurate higher-order ABCs by considering a more accurate asymptotic form of the wave solution given by

$$\varphi(\rho, \phi) = \frac{e^{-jk\rho}}{\sqrt{\rho}} \sum_{n=0}^{\infty} \frac{a_n(\phi)}{\rho^n}. \quad (9.5.5)$$

Substituting this expression into the Helmholtz equation

$$\frac{1}{\rho} \frac{\partial}{\partial \rho} \left(\rho \frac{\partial \varphi}{\partial \rho} \right) + \frac{1}{\rho^2} \frac{\partial^2 \varphi}{\partial \phi^2} + k^2 \varphi = 0 \quad (9.5.6)$$

we obtain the recurrence relation for $a_n(\phi)$ as

$$-2jk(n+1)a_{n+1} = \left(n + \frac{1}{2} \right)^2 a_n + \frac{\partial^2 a_n}{\partial \phi^2}. \quad (9.5.7)$$

Now, with the intention to derive a boundary condition, we take the partial derivative of Equation 9.5.5 with respect to ρ to find

$$\frac{\partial \varphi}{\partial \rho} = \left(-jk - \frac{1}{2\rho} \right) \varphi - \frac{e^{-jk\rho}}{\sqrt{\rho}} \sum_{n=1}^{\infty} \frac{n a_n(\phi)}{\rho^{n+1}}. \quad (9.5.8)$$

If we neglect the terms of order $O(\rho^{-5/2})$, we obtain the first-order ABC (Eq. 9.5.4). However, we can use Equation 9.5.7 and try to keep a few more leading terms. After some manipulations, we obtain

$$\frac{\partial \varphi}{\partial \rho} = \left(-jk - \frac{1}{2\rho} + \frac{1}{8jk\rho^2} + \frac{1}{8k^2\rho^3} \right) \varphi + \left(\frac{1}{2jk\rho^2} + \frac{1}{2k^2\rho^3} \right) \frac{\partial^2 \varphi}{\partial \phi^2} + O\left(\frac{1}{\rho^{9/2}}\right). \quad (9.5.9)$$

If we neglect the terms of order $O(\rho^{-9/2})$, we obtain the *second-order ABC* [17]

$$\frac{\partial \varphi}{\partial \rho} \approx \left(-jk - \frac{1}{2\rho} + \frac{1}{8jk\rho^2} + \frac{1}{8k^2\rho^3} \right) \varphi + \left(\frac{1}{2jk\rho^2} + \frac{1}{2k^2\rho^3} \right) \frac{\partial^2 \varphi}{\partial \phi^2}. \quad (9.5.10)$$

The heuristic approach described above can be used to derive higher-order ABCs by keeping more leading terms. A more systematic approach is to define a sequence of operators as

$$\mathcal{B}_m = \left(\frac{\partial}{\partial \rho} + jk + \frac{4m-3}{2\rho} \right) \mathcal{B}_{m-1} \quad (9.5.11)$$

with $\mathcal{B}_0 = 1$ [18]. It can be shown that the operator \mathcal{B}_m annihilates the first m terms in Equation 9.5.5, which yields

$$\mathcal{B}_m \varphi = O(\rho^{-2m-1/2}). \quad (9.5.12)$$

To see this, first consider $\mathcal{B}_1 \varphi$, which can be written as

$$\mathcal{B}_1 \varphi = \left(\frac{\partial}{\partial \rho} + jk + \frac{1}{2\rho} \right) \varphi = -\frac{e^{-jk\rho}}{\sqrt{\rho}} \sum_{n=1}^{\infty} \frac{na_n(\phi)}{\rho^{n+1}} = O(\rho^{-5/2}). \quad (9.5.13)$$

Next, we assume that

$$\mathcal{B}_{m-1} \varphi = \frac{e^{-jk\rho}}{\sqrt{\rho}} \sum_{n=2(m-1)}^{\infty} \frac{b_n(\phi)}{\rho^n} = O(\rho^{-2(m-1)-1/2}) \quad (9.5.14)$$

and consider $\mathcal{B}_m \varphi$. From Equations 9.5.11 and 9.5.14, we have

$$\mathcal{B}_m \varphi = \left(\frac{\partial}{\partial \rho} + jk + \frac{4m-3}{2\rho} \right) \mathcal{B}_{m-1} \varphi = \frac{2(m-1)}{\rho} \mathcal{B}_{m-1} \varphi - \frac{e^{-jk\rho}}{\sqrt{\rho}} \sum_{n=2(m-1)}^{\infty} \frac{nb_n(\phi)}{\rho^{n+1}}. \quad (9.5.15)$$

Substituting Equation 9.5.14 into this yields

$$\begin{aligned} \mathcal{B}_m \varphi &= \frac{e^{-jk\rho}}{\sqrt{\rho}} \left[\frac{2(m-1)}{\rho} \sum_{n=2(m-1)}^{\infty} \frac{b_n(\phi)}{\rho^n} - \sum_{n=2(m-1)}^{\infty} \frac{nb_n(\phi)}{\rho^{n+1}} \right] \\ &= \frac{e^{-jk\rho}}{\sqrt{\rho}} \left[\sum_{n=2m-1}^{\infty} \frac{2(m-1)b_n(\phi)}{\rho^{n+1}} - \sum_{n=2m-1}^{\infty} \frac{nb_n(\phi)}{\rho^{n+1}} \right] \\ &= \frac{e^{-jk\rho}}{\sqrt{\rho}} \sum_{n=2m-1}^{\infty} \frac{c_n(\phi)}{\rho^{n+1}} = O(\rho^{-2m-1/2}) \end{aligned} \quad (9.5.16)$$

which proves Equation 9.5.12. Hence, Equation 9.5.12 can be used to derive higher-order ABCs systematically. Nevertheless, the second-order condition is the most widely used one, because it can be implemented easily and its use maintains the symmetry and the sparsity pattern of the original finite element matrix.

For a non-circular boundary, the ABCs can be obtained by the substitutions

$$\frac{\partial}{\partial \rho} \rightarrow \frac{\partial}{\partial n}, \quad \frac{1}{\rho} \rightarrow \kappa(s), \quad \frac{1}{\rho^2} \frac{\partial^2}{\partial \phi^2} \rightarrow \frac{\partial^2}{\partial s^2} \quad (9.5.17)$$

where s is measured along the boundary and $\kappa(s)$ denotes the curvature of the boundary. With these substitutions, the first- and second-order ABCs (Eqs. 9.5.4 and 9.5.10) become

$$\frac{\partial \varphi}{\partial n} \approx \left(-jk - \frac{\kappa}{2} \right) \varphi \quad (9.5.18)$$

$$\frac{\partial \varphi}{\partial n} \approx \left(-jk - \frac{\kappa}{2} + \frac{\kappa^2}{8jk} + \frac{\kappa^3}{8k^2} \right) \varphi + \left(\frac{1}{2jk} + \frac{\kappa}{2k^2} \right) \frac{\partial^2 \varphi}{\partial s^2}. \quad (9.5.19)$$

Whereas Equation 9.5.18 can be used on a non-smooth boundary, it is preferable to use Equation 9.5.19 on a smooth boundary so that it does not destroy the symmetry and sparsity pattern of the original finite element matrix.

9.5.2 Three-Dimensional ABCs

As stated in Section 9.3.3, for three-dimensional electromagnetic problems, the simplest ABC is the Sommerfeld radiation condition, given by

$$\hat{n} \times (\nabla \times \mathbf{E}) \approx -jk \hat{n} \times (\hat{n} \times \mathbf{E}) \quad (9.5.20)$$

where \hat{n} is the normal vector of the absorbing surface. This condition provides a perfect absorption for normally incident fields. For fields incident at a large angle from the normal, it gives rise to a significant reflection. However, when the surface is placed sufficiently far away from the source of the fields, most fields would be incident on the absorbing surface at small angles from the normal and hence would be absorbed more efficiently. The implementation of Equation 9.5.20 in the finite element analysis is straightforward since it can be considered as a special case of Equation 9.3.7.

The ABC in Equation 9.5.20 is only of the first order. Higher-order conditions [19,20] can be obtained based on the asymptotic expansion of the vector wave solution given by

$$\mathbf{E}(r, \theta, \phi) = \frac{e^{-jkr}}{r} \sum_{n=0}^{\infty} \frac{\mathbf{A}_n(\theta, \phi)}{r^n}. \quad (9.5.21)$$

As in the two-dimensional case, we can construct an m th-order differential operator that annihilates the first m terms in Equation 9.5.21. Consider the differential operator \mathcal{L}_m , defined as

$$\mathcal{L}_m \mathbf{u} = \hat{r} \times \nabla \times \mathbf{u} - \left(jk + \frac{m}{r} \right) \mathbf{u} \quad m = 0, 1, 2, \dots \quad (9.5.22)$$

It can be shown easily that

$$\begin{aligned} \mathcal{L}_m \left[\frac{e^{-jkr}}{r} \frac{\mathbf{A}_{n,t}(\theta, \phi)}{r^n} \right] &= \left[-\frac{1}{r} \left(1 + \frac{\partial}{\partial r} \right) - \left(jk + \frac{m}{r} \right) \right] \frac{e^{-jkr}}{r} \frac{\mathbf{A}_{n,t}(\theta, \phi)}{r^n} \\ &= (n-m) \frac{e^{-jkr}}{r} \frac{\mathbf{A}_{n,t}(\theta, \phi)}{r^{n+1}} \end{aligned} \quad (9.5.23)$$

where the subscript t denotes the part of the vector transverse to the radial direction. We can further show that

$$\begin{aligned} \mathcal{L}_m \left[\nabla_t \left(\frac{e^{-jkr}}{r} \frac{A_{n,r}(\theta, \phi)}{r^n} \right) \right] &= \frac{(n+1-m)}{r} \left(\hat{\theta} \frac{1}{r} \frac{\partial}{\partial \theta} + \hat{\phi} \frac{1}{r \sin \theta} \frac{\partial}{\partial \phi} \right) \frac{e^{-jkr}}{r} \frac{A_{n,r}(\theta, \phi)}{r^n} \\ &= (n+1-m) \nabla_t \left(\frac{e^{-jkr}}{r} \frac{A_{n,r}(\theta, \phi)}{r^{n+1}} \right) \end{aligned} \quad (9.5.24)$$

where the subscript r denotes the radial component of the associated vector. Note that in both cases, the effect of \mathcal{L}_m is to produce an integer and increase the power of r by 1 without affecting the angular dependence. Based on this observation, we can define an operator \mathcal{B}_m as

$$\mathcal{B}_m \mathbf{u} = (\mathcal{L}_{m-1})^m \mathbf{u}_t + s(\mathcal{L}_m)^{m-1} \nabla_t u_r \quad m = 1, 2, 3, \dots \quad (9.5.25)$$

where s is an arbitrary number [20]. The superscript m on \mathcal{L}_{m-1} denotes that the operator \mathcal{L}_{m-1} is to be applied m times, and the superscript $m-1$ on \mathcal{L}_m denotes that the operator \mathcal{L}_m is to be applied $m-1$ times. Using the results of Equations 9.5.23 and 9.5.24 repeatedly, we can show that

$$\begin{aligned} \mathcal{B}_m \left[\frac{e^{-jkr}}{r} \frac{\mathbf{A}_n(\theta, \phi)}{r^n} \right] &= (n+1-m)(n+2-m)\cdots(n-1)n \frac{e^{-jkr}}{r} \frac{\mathbf{A}_{n,t}(\theta, \phi)}{r^{n+m}} \\ &\quad + s(n+1-m)(n+2-m)\cdots(n-2)(n-1) \nabla_t \left(\frac{e^{-jkr}}{r} \frac{\mathbf{A}_{n,r}(\theta, \phi)}{r^{n+m-1}} \right). \end{aligned} \quad (9.5.26)$$

Since $A_{0,r} = 0$, which is a well-known fact for the field expansion, it can be seen that the right-hand side of Equation 9.5.26 vanishes for $n = 0, 1, 2, \dots, m-1$. In other words, when \mathcal{B}_m is applied to Equation 9.5.21, it annihilates the first m terms. Only the terms with $n > m-1$ remain, but, after being operated on by \mathcal{B}_m , these terms are proportional to $1/r^{n+m+1}$ (note that in spherical coordinates, ∇_t contains a factor of $1/r$). Hence, when \mathcal{B}_m is applied to Equation 9.5.21, we have

$$\mathcal{B}_m \mathbf{E} = O(r^{-(2m+1)}). \quad (9.5.27)$$

Therefore,

$$\mathcal{B}_m \mathbf{E} \approx 0 \quad (9.5.28)$$

can be considered as an approximate boundary condition applicable to a spherical surface that encloses all sources of the field.

Equation 9.5.28 provides a systematic approach to deriving ABCs. For example, consider $m = 1$. We find

$$\mathcal{B}_1 \mathbf{E} = \hat{r} \times \nabla \times \mathbf{E}_t - jk \mathbf{E}_t + s \nabla_t E_r \approx 0. \quad (9.5.29)$$

Since $\hat{r} \times \nabla \times (\hat{r} E_r) = \nabla_t E_r$, Equation 9.5.29 can be written as

$$\hat{r} \times \nabla \times \mathbf{E} \approx -jk \hat{r} \times \hat{r} \times \mathbf{E} - (s-1) \nabla_t E_r. \quad (9.5.30)$$

The direct implementation of this condition in the finite element analysis would result in an asymmetric matrix because of the term containing $\nabla_t E_r$. This term can, however, be

removed by choosing $s = 1$. With this choice, Equation 9.5.30 reduces to the Sommerfeld radiation condition in Equation 9.5.20. When this condition is applied to a planar surface, the reflection coefficient is given by

$$R_{\text{TE}} = R_{\text{TM}} = \frac{\cos \theta - 1}{\cos \theta + 1} \quad (9.5.31)$$

for both TE and TM plane waves. Now, consider $m = 2$. We first find that

$$\begin{aligned} \mathcal{B}_2 \mathbf{E} &= \mathcal{L}_1 \left[\mathcal{L}_1(\mathbf{E}_t) \right] + s \mathcal{L}_2(\nabla_t E_r) \\ &= -2 \left(jk + \frac{1}{r} \right) \hat{r} \times \nabla \times \mathbf{E} + 2jk \left(jk + \frac{1}{r} \right) \mathbf{E}_t + \nabla \times \left[\hat{r} \hat{r} \cdot (\nabla \times \mathbf{E}) \right] \\ &\quad + (s-1) \nabla_t (\nabla_t \cdot \mathbf{E}) + (2-s) jk \nabla_t E_r \end{aligned} \quad (9.5.32)$$

which yields an approximate second-order ABC

$$\hat{r} \times \nabla \times \mathbf{E} \approx -jk \hat{r} \times \hat{r} \times \mathbf{E} + \frac{r}{2(jkr+1)} \left\{ \nabla \times \left[\hat{r} \hat{r} \cdot (\nabla \times \mathbf{E}) \right] + \nabla_t (\nabla_t \cdot \mathbf{E}) \right\} \quad (9.5.33)$$

where we set $s = 2$ to remove the term containing $\nabla_t E_r$, which would otherwise compromise the symmetry of the finite element matrix. When applied to a planar surface, Equation 9.5.33 gives the reflection coefficient

$$R_{\text{TE}} = \frac{\cos \theta + \frac{1}{2} \sin^2 \theta - 1}{\cos \theta - \frac{1}{2} \sin^2 \theta + 1} \quad (9.5.34)$$

for a TE incident plane wave and

$$R_{\text{TM}} = \frac{\cos \theta + \frac{1}{2} \sin^2 \theta \cos \theta - 1}{\cos \theta - \frac{1}{2} \sin^2 \theta \cos \theta + 1} \quad (9.5.35)$$

for a TM incident plane wave. Equation 9.5.34 is the same as that of the true second-order ABC, whereas Equation 9.5.35 is slightly worse, which is the consequence of setting $s = 2$. If we set $s = 1$, then R_{TM} would have the same expression as Equation 9.5.34.

The implementation of Equation 9.5.33 in the finite element analysis is described in detail in Reference [9]. When Equation 9.5.33 is used on a smooth absorbing boundary, the weak-form solution to Equation 9.3.5 is given by

$$\begin{aligned} \int_{\Omega} \left[\frac{1}{\mu_r} (\nabla \times \mathbf{W}_i) \cdot (\nabla \times \mathbf{E}) - k_0^2 \epsilon_r \mathbf{W}_i \cdot \mathbf{E} \right] d\Omega + \int_{\Gamma_{\text{ABC}}} \left[jk_0 (\hat{n} \times \mathbf{W}_i) \cdot (\hat{n} \times \mathbf{E}) \right. \\ \left. + \beta (\nabla \times \mathbf{W}_i)_n \cdot (\nabla \times \mathbf{E})_n + \beta (\nabla_t \cdot \mathbf{W}_i) (\nabla_t \cdot \mathbf{E}) \right] d\Gamma = -jk_0 Z_0 \int_{\Omega} \mathbf{W}_i \cdot \mathbf{J}_{\text{imp}} d\Omega \end{aligned} \quad (9.5.36)$$

where Γ_{ABC} denotes the absorbing boundary, and $\beta = 1/(2jk_0 + 2\kappa)$, with κ being the curvature of the boundary. For a spherical surface, $\hat{n} = \hat{r}$ and $\kappa = 1/r$. Figure 9.22 compares the measured monostatic RCS at normal incidence for a metallic cube with the corresponding pattern computed by the finite element method using the second-order ABC [21]. The absorbing boundary was placed 0.15λ from the edge of the cube. In this calculation, the

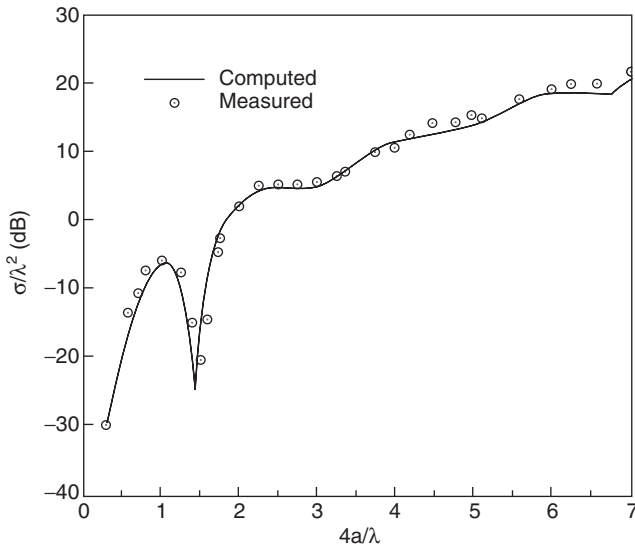


Figure 9.22 Monostatic RCS of a metallic cube of side length a . (After Chatterjee et al. [21], Copyright © 1993 IEEE.)

term $\beta(\nabla_t \cdot \mathbf{W}_i)(\nabla_t \cdot \mathbf{E})$ was neglected for simplicity. A more accurate treatment of this term has been described in Reference [22].

9.5.3 Perfectly Matched Layers

As in the case for the finite difference method, the PML is an effective approach to truncating the computational domain for the finite element method. However, the implementation of the PML based on either the split-field or the stretched-coordinate formulation in the finite element method is rather inconvenient. A better approach is to consider the PML as an anisotropic absorbing medium [23,24] so that it can be implemented in the finite element method without much modification. This can be accomplished by converting the modified Maxwell's equations (Eqs. 8.5.21–8.5.24) based on stretched coordinates into regular-looking Maxwell's equations. Let \mathbf{E}^c and \mathbf{H}^c denote the field quantities used in the modified Maxwell's equations (Eqs. 8.5.21–8.5.24). We can define the new field quantities \mathbf{E}^a and \mathbf{H}^a such that

$$\mathbf{E}^a = \begin{bmatrix} s_x & 0 & 0 \\ 0 & s_y & 0 \\ 0 & 0 & s_z \end{bmatrix} \cdot \mathbf{E}^c, \quad \mathbf{H}^a = \begin{bmatrix} s_x & 0 & 0 \\ 0 & s_y & 0 \\ 0 & 0 & s_z \end{bmatrix} \cdot \mathbf{H}^c. \quad (9.5.37)$$

With this, we can easily find

$$\nabla_s \times \mathbf{E}^c = \begin{bmatrix} \frac{1}{s_y s_z} & 0 & 0 \\ 0 & \frac{1}{s_z s_x} & 0 \\ 0 & 0 & \frac{1}{s_x s_y} \end{bmatrix} \cdot \nabla \times \mathbf{E}^a, \quad \mathbf{H}^c = \begin{bmatrix} \frac{1}{s_x} & 0 & 0 \\ 0 & \frac{1}{s_y} & 0 \\ 0 & 0 & \frac{1}{s_z} \end{bmatrix} \cdot \mathbf{H}^a. \quad (9.5.38)$$

Substituting these into Equation 8.5.21, we obtain

$$\nabla \times \mathbf{E}^a = -j\omega\mu\tilde{\Lambda} \cdot \mathbf{H}^a \quad (9.5.39)$$

where

$$\tilde{\Lambda} = \begin{bmatrix} \frac{s_y s_z}{s_x} & 0 & 0 \\ 0 & \frac{s_z s_x}{s_y} & 0 \\ 0 & 0 & \frac{s_x s_y}{s_z} \end{bmatrix}. \quad (9.5.40)$$

Similarly, Equations 8.5.22–8.5.24 can be converted into

$$\nabla \times \mathbf{H}^a = j\omega\epsilon\tilde{\Lambda} \cdot \mathbf{E}^a \quad (9.5.41)$$

$$\nabla \cdot (\epsilon\tilde{\Lambda} \cdot \mathbf{E}^a) = 0 \quad (9.5.42)$$

$$\nabla \cdot (\mu\tilde{\Lambda} \cdot \mathbf{H}^a) = 0. \quad (9.5.43)$$

These equations are recognized as the ordinary Maxwell's equations for an anisotropic medium with a permittivity tensor $\epsilon\tilde{\Lambda}$ and a permeability tensor $\mu\tilde{\Lambda}$. Just like the modified Maxwell's equations (Eqs. 8.5.21–8.5.24), they reduce to the regular Maxwell's equations outside the PML, where $s_x = s_y = s_z = 1$. However, inside the PML, the field quantities are different from those in Equations 8.5.21–8.5.24, which nevertheless is not important because the fields inside the PML are of no interest. Since Equations 9.5.39 and 9.5.41–9.5.43 are derived directly from Equations 8.5.21–8.5.24, they define an anisotropic medium that has no reflection for an incident plane wave on its interface regardless of frequency, polarization, and angle of incidence.

The perfectly matched anisotropic absorbing medium described above is derived based on the property of the modified Maxwell's equations. It can also be derived independently without such a priori knowledge [23]. We can start with Maxwell's equations in an anisotropic medium

$$\nabla \times \mathbf{E} = -j\omega\mu\tilde{\Lambda} \cdot \mathbf{H} \quad (9.5.44)$$

$$\nabla \times \mathbf{H} = j\omega\epsilon\tilde{\Lambda} \cdot \mathbf{E} \quad (9.5.45)$$

$$\nabla \cdot (\epsilon\tilde{\Lambda} \cdot \mathbf{E}) = 0 \quad (9.5.46)$$

$$\nabla \cdot (\mu\tilde{\Lambda} \cdot \mathbf{H}) = 0 \quad (9.5.47)$$

where $\tilde{\Lambda}$ is the unknown diagonal tensor to be determined and is denoted here as

$$\tilde{\Lambda} = \begin{bmatrix} a & 0 & 0 \\ 0 & b & 0 \\ 0 & 0 & c \end{bmatrix}. \quad (9.5.48)$$

For a plane wave propagating in this medium, Equations 9.5.44 and 9.5.45 become

$$\mathbf{k} \times \mathbf{E} = \omega \mu \tilde{\Lambda} \cdot \mathbf{H} \quad (9.5.49)$$

$$\mathbf{k} \times \mathbf{H} = -\omega \varepsilon \tilde{\Lambda} \cdot \mathbf{E} \quad (9.5.50)$$

where \mathbf{k} denotes the propagation vector. We can eliminate \mathbf{H} to find

$$\mathbf{k} \times (\tilde{\Lambda}^{-1} \cdot \mathbf{k} \times \mathbf{E}) = \omega \mu \mathbf{k} \times \mathbf{H} = -\omega^2 \mu \varepsilon \mathbf{E} \quad (9.5.51)$$

which can be written more specifically as

$$\begin{bmatrix} k^2 a - \frac{k_y^2}{c} - \frac{k_z^2}{b} & \frac{k_x k_y}{c} & \frac{k_z k_x}{b} \\ \frac{k_x k_y}{c} & k^2 b - \frac{k_z^2}{a} - \frac{k_x^2}{c} & \frac{k_y k_z}{a} \\ \frac{k_z k_x}{b} & \frac{k_y k_z}{a} & k^2 c - \frac{k_x^2}{b} - \frac{k_y^2}{a} \end{bmatrix} \cdot \mathbf{E} = 0 \quad (9.5.52)$$

where $k^2 = \omega^2 \mu \varepsilon$. For this equation to have a non-trivial solution, the determinant of its coefficient matrix must vanish, which yields the dispersion relation

$$\frac{k_x^2}{bc} + \frac{k_y^2}{ac} + \frac{k_z^2}{ab} = k^2. \quad (9.5.53)$$

The solution to this equation is

$$k_x = k \sqrt{bc} \sin \theta \cos \phi, \quad k_y = k \sqrt{ac} \sin \theta \sin \phi, \quad k_z = k \sqrt{ab} \cos \theta \quad (9.5.54)$$

which indicates that each individual component of the propagation vector can be manipulated through the choice of a , b , and c .

Next, we consider an interface coincident with the xy -plane, with the upper half-space filled with a uniform medium characterized by μ and ε and the lower half-space filled with the anisotropic medium discussed above (Fig. 9.23). For a TE_z -polarized plane wave incident upon the interface from the upper half-space, the incident, reflected, and transmitted fields can be written as

$$\mathbf{E}^i = \hat{y} E_0 e^{jk(x \sin \theta^i + z \cos \theta^i)} \quad (9.5.55)$$

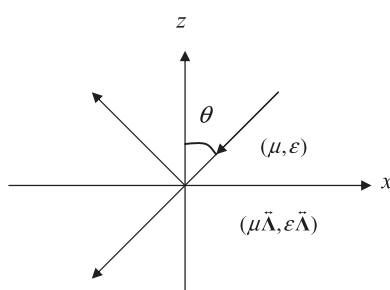


Figure 9.23 Plane wave incident on the surface of an anisotropic medium.

$$\mathbf{E}^r = \hat{y}R_{\text{TE}}E_0 e^{jk(x \sin \theta^r - z \cos \theta^r)} \quad (9.5.56)$$

$$\mathbf{E}' = \hat{y}T_{\text{TE}}E_0 e^{jk(x \sqrt{bc} \sin \theta' + z \sqrt{ab} \cos \theta')} \quad (9.5.57)$$

For convenience, the incidence is restricted in the xz -plane; however, this does not compromise the generality of the result in any way. From Maxwell's equations, we find the corresponding magnetic fields as

$$\mathbf{H}^i = (\hat{x} \cos \theta^i - \hat{z} \sin \theta^i) \frac{E_0}{\eta} e^{jk(x \sin \theta^i + z \cos \theta^i)} \quad (9.5.58)$$

$$\mathbf{H}^r = -(\hat{x} \cos \theta^r + \hat{z} \sin \theta^r) R_{\text{TE}} \frac{E_0}{\eta} e^{jk(x \sin \theta^r - z \cos \theta^r)} \quad (9.5.59)$$

$$\mathbf{H}' = \left(\hat{x} \sqrt{\frac{b}{a}} \cos \theta' - \hat{z} \sqrt{\frac{b}{c}} \sin \theta' \right) T_{\text{TE}} \frac{E_0}{\eta} e^{jk(x \sqrt{bc} \sin \theta' + z \sqrt{ab} \cos \theta')} \quad (9.5.60)$$

The enforcement of tangential continuity for both \mathbf{E} and \mathbf{H} at the interface ($z = 0$) yields

$$\sin \theta^r = \sqrt{bc} \sin \theta' = \sin \theta^i \quad (9.5.61)$$

and

$$1 + R_{\text{TE}} = T_{\text{TE}} \quad (9.5.62)$$

$$\cos \theta^i - R_{\text{TE}} \cos \theta^r = T_{\text{TE}} \sqrt{\frac{b}{a}} \cos \theta' \quad (9.5.63)$$

from which we obtain

$$R_{\text{TE}} = \frac{\cos \theta^i - \sqrt{\frac{b}{a}} \cos \theta'}{\cos \theta^i + \sqrt{\frac{b}{a}} \cos \theta'} \quad (9.5.64)$$

Following the same procedure, we find the reflection coefficient for the TM_z case as

$$R_{\text{TM}} = -\frac{\cos \theta^i - \sqrt{\frac{b}{a}} \cos \theta'}{\cos \theta^i + \sqrt{\frac{b}{a}} \cos \theta'} \quad (9.5.65)$$

which has the same magnitude as that of R_{TE} .

Examining the results above carefully, we can find that if $\sqrt{bc} = 1$, then $\theta' = \theta^i$, and if we further let $a = b$, then $R_{\text{TE}} = R_{\text{TM}} = 0$. In other words, if $\tilde{\Lambda}$ in Equation 9.5.48 is defined such as

$$a = b = \frac{1}{c} \quad (9.5.66)$$

the anisotropic medium's interface is reflectionless for a plane wave of any frequency, polarization, and angle of incidence. In this case, Equation 9.5.54 becomes

$$k_x = k \sin \theta \cos \phi, \quad k_y = k \sin \theta \sin \phi, \quad k_z = ka \cos \theta \quad (9.5.67)$$

indicating that we can attenuate the wave in the z -direction through the choice of a . If we choose $a = s_z$, $\tilde{\Lambda}$ becomes

$$\tilde{\Lambda} = \begin{bmatrix} s_z & 0 & 0 \\ 0 & s_z & 0 \\ 0 & 0 & 1/s_z \end{bmatrix} \quad (9.5.68)$$

which is identical to Equation 9.5.40 for the PML interface perpendicular to the z -axis, for which $s_x = s_y = 1$.

With the PML, we can set up a computational domain such as the one shown in Figure 8.12 for the simulation of an open-region electromagnetic problem. However, the flexibility of the finite element method also permits the use of non-rectangular PMLs. In fact, both cylindrical and spherical PMLs have already been formulated and employed successfully in finite element analysis [25,26]. As discussed in Chapter 8, for numerical simulation, the PML must still be truncated with an outer boundary, and this is typically done with a conducting surface. Therefore, it is necessary to make sure that the PML provides sufficient attenuation such that after the field is reflected by the truncation boundary, it becomes negligible when it reenters the physical solution domain.

By adopting the anisotropic absorbing medium model, the implementation of the PML in the frequency-domain finite element method is straightforward. The weak-form wave equation for the PML is the same as Equation 9.3.11, except that $(\nabla \times \mathbf{W}_i) \cdot (\nabla \times \mathbf{E})$ and $\mathbf{W}_i \cdot \mathbf{E}$ are replaced by $(\nabla \times \mathbf{W}_i) \cdot \tilde{\Lambda}^{-1} \cdot (\nabla \times \mathbf{E})$ and $\mathbf{W}_i \cdot \tilde{\Lambda} \cdot \mathbf{E}$, respectively. The implementation of the PML in the time-domain finite element method is, however, much more involved since the permittivity and permeability tensors are frequency-dependent. Therefore, the PML has to be modeled as an anisotropic, dispersive medium [27]. Toward this end, the general procedure for the time-domain finite element modeling of dispersive media described in Section 9.4 can be applied. A major advantage of the PML over ABCs is that the absorbing performance of the PML can be improved systematically by simply increasing the number of layers or, equivalently, by increasing the conductivity and discretization inside the PML.

As a validation example, Figure 9.24 shows the VV-polarized monostatic RCS of a metallic double ogive at 9 GHz, which is formed by joining two different half-ogives [26]. The top piece has a half-length of 12.7 cm, a maximum radius of 2.54 cm, and a half-angle of 22.62° at the tip, and the bottom has a half-length of 6.35 cm, a maximum radius of 2.54 cm, and a half-angle of 46.4° at the tip. For the finite element analysis, the computational domain was truncated using a cylindrical PML. The calculated results compare very well with measured data.

9.6 SOME NUMERICAL ASPECTS

When solving a problem using the finite element method, one first sets up the mesh, then fills the matrix equation based on the mesh together with the boundary conditions, and finally solves the resulting system of linear equations. The computational issues of mesh generation and matrix solvers are discussed in this section.

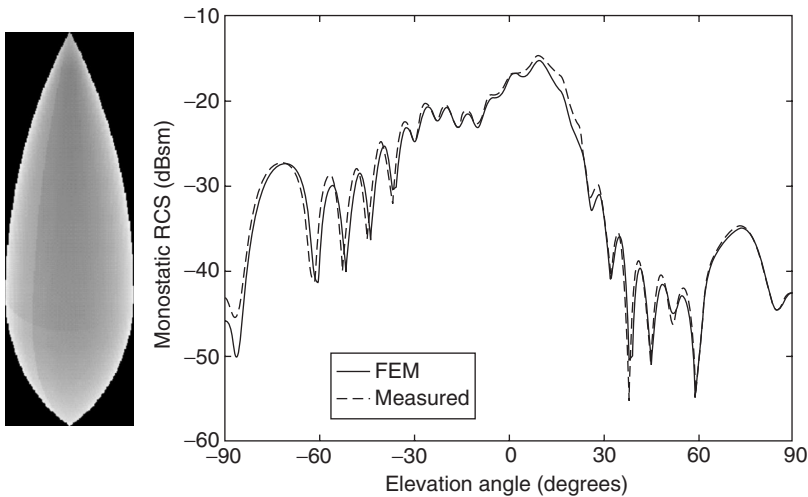


Figure 9.24 VV-polarized monostatic RCS of a metallic double ogive at 9GHz. (After Greenwood and Jin [26], Copyright © 1999 IEEE.)

9.6.1 Mesh Generation

The finite element method assumes the availability of a mesh on the structure under consideration. However, obtaining this mesh is not trivial. Finite element meshes can be split into two main categories: structured and unstructured meshes. Structured meshes have the property that all elements have the same number of neighbors, while unstructured meshes have no such constraint. While structured meshes can be constructed using quadrilateral or hexahedral elements, unstructured meshes most often consist of triangular or tetrahedral elements since any polygonal (polyhedral) domain may be meshed into triangular (tetrahedral) elements.

The quality of an unstructured mesh is determined by the shape regularity of its elements, which is defined on an elemental basis as the ratio between the radius of the largest inscribed circle (sphere) and the maximum dimension of the element. The most widely used approaches to constructing unstructured meshes are octree, Delaunay, and advancing front. The first approach breaks the structure into blocks and continues to subdivide the blocks until a desired geometrical resolution is obtained, and then meshes the blocks into tetrahedral elements. The second approach utilizes the Delaunay criterion (which states that any node must not be contained within the circumsphere of any tetrahedra within the mesh) to create a tetrahedral mesh from a given set of nodes and then refine the mesh by inserting new nodes. The third approach starts from an already meshed boundary, to which elements are progressively added toward the interior to generate a mesh for the entire domain.

9.6.2 Matrix Solvers

An efficient solution of the finite element matrix equation is very important, since in the course of solving a problem with finite elements most computer resources (memory and time) are usually expended on this step. The important issues are matrix storage schemes, matrix solvers (direct or iterative), and matrix preconditioners (in the iterative case).

The matrices produced by the finite element method are sparse with only a very small percentage of non-zero elements. By storing only the non-zero entries, the matrix

storage requirement is reduced from $O(N^2)$ to $O(N)$. Popular approaches to sparse storage are compressed row and compressed column storage.

The choice of matrix solver can have a significant impact on computational efficiency, so it is important to choose a solver that best suits the properties of the matrix. There are two types of matrix solvers. The first type comprises *direct solvers* based on Gaussian elimination or *LU* decomposition. These solvers are commonly used for full matrices but are also applicable to sparse matrices stored in a band format, or even a fully sparse format in the case of the frontal and multifrontal methods [28,29]. The alternative to direct solvers are *iterative solvers*, where very little extra memory is required, since these solvers are based on calculating successive matrix–vector products according to an iterative algorithm to converge to the solution [30]. The main drawback of such algorithms is that they might require an exceedingly large number of iterations to converge, depending mainly on the locations of the eigenvalues of the matrix in the complex plane; if the eigenvalues are all located close to (1,0), convergence is usually rapid. This problem is addressed by using a preconditioner to move the eigenvalues closer to (1,0) and thereby reduce the iteration count. A preconditioner can be constructed based on physical insight into the problem or the structure of the original matrix.

9.6.3 Higher-Order Elements

Most finite element formulations use basis functions that vary linearly within every element. However, it is also possible, and often very advantageous, to consider basis functions of higher polynomial orders. Such basis functions have been developed for scalar nodal elements [8,9] and for vector elements [31,32].

Higher-order basis functions can be categorized into two classes: *interpolatory* and *hierarchical*. Interpolatory basis functions relate to a set of elemental points, such that every basis function is of the same order and is equal to unity at one point and zero at all others. Hierarchical basis functions, on the other hand, are formed by adding new higher-order basis functions to the lower-order ones; thus, the elemental solution is expanded in terms of basis functions of differing polynomial orders. Both approaches have the same accuracy, but one may be favored over the other, depending on the application. Interpolatory basis functions generally lead to better conditioned matrices, while hierarchical basis functions permit the use of different elemental orders in a single finite element solution.

Since higher-order basis functions interpolate the solution field much more accurately, the finite element method may be expected to yield much more accurate results as the elemental order is increased. Specifically, for smooth functions it can be shown that if p is the order of the basis functions, h denotes the elemental size divided by the order of the element, and λ denotes the excitation wavelength, the interpolation error is of the order $O[(h/\lambda)^{p+1}]$. Therefore, in the case of smooth solutions, the finite element solution error may be reduced accordingly by using higher-order basis functions. If the true solution to the finite element analysis contains a singularity, this interpolation error estimate does not hold any more, and it becomes more advantageous to use smaller elements of low polynomial order around the singularity.

When the finite element method is applied to the Helmholtz equations (scalar as well as vector cases), the simulated wave propagates at a speed slightly different from the exact value. Consequently, there is a numerical error in the phase of the numerical solution, which is called *numerical phase error*. Analysis based on the finite element discretization of plane wave propagation in a uniform medium shows that the phase error per wavelength is proportional to $O[(h/\lambda)^{2p}]$. From this result follows the very important conclusion that phase errors may be decreased exponentially by increasing the order of

the elements. Therefore, higher-order elements are especially suitable for simulating large-scale wave propagation problems.

9.6.4 Curvilinear Elements

In the same way that elemental basis functions can be defined to arbitrary polynomial order, the geometric representation of the elements can also be defined to arbitrary polynomial order. The elements shown in Figure 9.3 are of linear geometric order since all edges and faces are straight and flat and thus can be described by linear functions of position. Such elements are termed rectilinear. Elements of higher geometric polynomial order may be defined by modeling elemental edges and faces with higher-order polynomial functions of position. For example, one may require the edge of a triangular element to pass through two of its vertex nodes together with an additional node that may not lie on the straight line connecting the vertices. In this case, a second-order geometric representation would suffice. Such elemental representations are very useful when modeling curved boundaries and are termed curvilinear. When the order of geometrical representation is the same as the order of the basis functions, the element is called *isoparametric*. Otherwise, it is either called *subparametric* (when the order of geometrical modeling is lower) or *superparametric* (when the order of geometrical modeling is higher).

9.6.5 Adaptive Finite Element Analysis

Associated with any finite element solution is an error due to the approximate representation of the solution on the mesh. Quantifying this error is an important extension to the finite element method, since it opens up the possibility of adaptive finite element analysis, which can enhance the efficiency of the finite element method significantly.

The goal of an adaptive finite element analysis is to optimize the mesh size (designated by h) and element orders (designated by p) with which a given accuracy can be obtained with a minimum number of unknowns. This is accomplished in the following way: Choose an initial coarse discretization and solve the problem. Based on the solution, estimate the error distribution and the global solution error, as measured in a relevant quantity such as energy. Based on the error distribution, refine the solution representation selectively with respect to h and/or p . Re-solve the problem using the new discretization and repeat the process. Iterate in this way until the global error measure drops below a required level.

The core component of this process is the error estimation, which is termed *a posteriori* error estimation since an existing solution is required. Many different approaches to a posteriori error estimation exist [33,34]. Usually the error estimator is derived mathematically, based on the finite element formulation at hand and the output quantity of interest, but sometimes one can construct it based on physical insight alone. For example, for vector field problems one can use the residues of the governing partial differential equation and the Neumann boundary condition to estimate the error over each element. The field continuity condition across each element edge (face) can also be incorporated into the error estimation.

9.7 SUMMARY

In this chapter we described the basic principle and formulation of the finite element method for analysis of electromagnetic problems. We started with a simple example to illustrate the basic principle and steps of the finite element method. We then formulated

the finite element analysis of scalar fields and proceeded to the finite element analysis of vector fields by solving a vector wave equation using vector basis functions, which are also known as edge elements. After that, we extended the finite element analysis of vector fields into the time domain. In each case, examples are presented to demonstrate the accuracy and capabilities of the finite element method. We also discussed one of the most important issues in the finite element analysis of open-region problems—the use of ABCs and PMLs for truncating the computational domain. It is hoped that this chapter will provide the reader basic understanding of the finite element method for the simulation of electromagnetic fields. The reader is encouraged to consult more advanced books, such as References [8] and [9], for a more comprehensive treatment, and Reference [14], for many application examples.

REFERENCES

- [1] R. L. COURANT, Variational methods for the solution of problems of equilibrium and vibration, *Bull. Amer. Math. Soc.*, 49(1): 1–23, 1943.
- [2] P. P. SILVESTER, Finite element solution of homogeneous waveguide problems, *Alta Freq.*, 38: 313–317, 1969.
- [3] K. K. MEI, Unimoment method of solving antenna and scattering problems, *IEEE Trans. Antennas Propagat.*, 22(6): 760–766, 1974.
- [4] S. P. MARIN, Computing scattering amplitudes for arbitrary cylinders under incident plane waves, *IEEE Trans. Antennas Propagat.*, 30(6): 1045–1049, 1982.
- [5] J. C. NEDELEC, Mixed finite elements in \mathbb{R}^3 , *Numer. Math.*, 35: 315–341, 1980.
- [6] A. BOSSAVIT and J. C. VERITE, A mixed FEM-BIEM method to solve 3-D eddy current problems, *IEEE Trans. Magn.*, 18(2): 431–435, 1982.
- [7] M. L. BARTON and Z. J. CENDES, New vector finite elements for three-dimensional magnetic field computation, *J. Appl. Phys.*, 61: 3919–3921, 1987.
- [8] P. P. SILVESTER and R. L. FERRARI, *Finite Elements for Electrical Engineers* (3rd edition). Cambridge, UK: Cambridge University Press, 1996.
- [9] J.-M. JIN, *The Finite Element Method in Electromagnetics* (2nd edition). New York: Wiley, 2002.
- [10] J. M. JIN and J. CHEN, On the SAR and field inhomogeneity of birdcage coils loaded with the human head, *Magn. Reson. Med.*, 38(6): 953–963, 1997.
- [11] J. LIU, J.-M. JIN, E. K. N. YUNG, and R. S. CHEN, A fast three-dimensional higher-order finite element analysis of microwave waveguide devices, *Microw. Opt. Tech. Lett.*, 32(5): 344–352, 2002.
- [12] S. H. LEE and J. M. JIN, Adaptive solution space projection for fast and robust wideband finite-element simulation of microwave components, *IEEE Microw. Wireless Compon. Lett.*, 17(7): 474–476, 2007.
- [13] N. M. NEWMARK, A method of computation for structural dynamics, *J. Eng. Mech. Div., Proc. Am. Soc. Civil Eng.*, 85: 67–94, 1959.
- [14] J.-M. JIN and D. J. RILEY, *Finite Element Analysis of Antennas and Arrays*. Hoboken, NJ: Wiley, 2008.
- [15] D. JIAO and J. M. JIN, Time-domain finite element simulation of cavity-backed microstrip patch antennas, *Microw. Opt. Tech. Lett.*, 32(4): 251–254, 2002.
- [16] Z. LOU and J. M. JIN, Modeling and simulation of broadband antennas using the time-domain finite element method, *IEEE Trans. Antennas Propagat.*, 53(12): 4099–4110, 2005.
- [17] R. MITTRA and O. M. RAMAHI, Absorbing boundary conditions for the direct solution of partial differential equations arising in electromagnetic scattering problems. *PIER 2: Finite Element and Finite Difference Methods in Electromagnetic Scattering*, edited by M. A. MORGAN. New York: Elsevier, 1990, pp. 133–173.
- [18] A. BAYLISS, M. GUNZBURGER, and E. TURKEL, Boundary conditions for the numerical solution of elliptic equations in exterior regions, *SIAM J. Appl. Math.*, 42: 430–451, 1982.
- [19] A. F. PETERSON, Absorbing boundary conditions for the vector wave equation, *Microw. Opt. Tech. Lett.*, 1(2): 62–64, 1988.
- [20] J. P. WEBB and V. N. KANELLOPOULOS, Absorbing boundary conditions for the finite element solution of the vector wave equation, *Microw. Opt. Tech. Lett.*, 2(10): 370–372, 1989.
- [21] A. CHATTERJEE, J. M. JIN, and J. L. VOLAKIS, Edge-based finite elements and vector ABCs applied to 3D scattering, *IEEE Trans. Antennas Propagat.*, 41(2): 221–226, 1993.
- [22] M. M. BOTHA and D. B. DAVIDSON, Rigorous, auxiliary variable-based implementation of a second-order ABC for the vector FEM, *IEEE Trans. Antennas Propagat.*, 54(11): 3499–3504, 2006.
- [23] Z. S. SACKS, D. M. KINGSLAND, R. LEE, and J.-F. LEE, A perfectly matched anisotropic absorber for use as an absorbing boundary condition, *IEEE Trans. Antennas Propagat.*, 43(12): 1460–1463, 1995.
- [24] S. D. GEDNEY, An anisotropic perfectly matched layer absorbing medium for the truncation of FDTD lattices, *IEEE Trans. Antennas Propagat.*, 44(12): 1630–1639, 1996.
- [25] W. C. CHEW, J. M. JIN, and E. MICHELSSEN, Complex coordinate stretching as a generalized absorbing

- boundary condition, *Microw. Opt. Tech. Lett.*, 15(6): 363–369, 1997.
- [26] A. D. GREENWOOD and J. M. JIN, A novel efficient algorithm for scattering from a complex BOR using vector FEM and cylindrical PML, *IEEE Trans. Antennas Propagat.*, 47(4): 620–629, 1999.
- [27] D. JIAO, J. M. JIN, E. MICHELSSEN, and D. RILEY, Time-domain finite-element simulation of three-dimensional scattering and radiation problems using perfectly matched layers, *IEEE Trans. Antennas Propagat.*, 51(2): 296–305, 2003.
- [28] B. M. IRONS, A frontal method solution program for finite element analysis, *Int. J. Numer. Meth. Eng.*, 2: 5–32, 1970.
- [29] J. W. H. LIU, The multifrontal method for sparse matrix solution: theory and practice, *SIAM Rev.*, 34: 82–109, 1992.
- [30] R. BARRETT, M. BERRY, T. F. CHAN, J. DEMMEL, J. DONATO, J. DONGARRA, V. EIJKHOUT, R. POZO, C. ROMINE, and H. V. der VORST, *Templates for the Solution of Linear Systems: Building Blocks for Iterative Methods* (2nd edition). Philadelphia, PA: SIAM, 1994.
- [31] R. D. GRAGLIA, D. R. WILTON, and A. F. PETERSON, Higher order interpolatory vector bases for computational electromagnetics, *IEEE Trans. Antennas Propagat.*, 45(3): 329–342, 1997.
- [32] J. P. WEBB, Hierarchical vector basis functions of arbitrary order for triangular and tetrahedral finite elements, *IEEE Trans. Antennas Propagat.*, 47(8): 1244–1253, 1999.
- [33] M. AINSWORTH and J. T. ODEN, A posteriori error estimation in finite element analysis, *Comput. Meth. Appl. Mech. Eng.*, 142: 1–88, 1997.
- [34] J. T. ODEN, L. DEMKOWICZ, W. RACHOWICZ, and T. A. WESTERMANN, Toward a universal $h-p$ adaptive finite element strategy, part 2: A posteriori error estimation, *Comput. Meth. Appl. Mech. Eng.*, 77: 113–180, 1989.

PROBLEMS

- 9.1.** Consider a one-dimensional boundary-value problem defined by the partial differential equation

$$\frac{d^2\varphi(x)}{dx^2} + \varphi(x) = 1 \quad 0 < x < 1$$

and the boundary conditions

$$\varphi|_{x=0} = 1, \quad \varphi|_{x=1} = 0.$$

By following the procedure described in Section 9.1.2, dividing the solution domain into three segments, and using linear basis functions, find the finite element solution of the problem and compare the solution with the exact solution.

- 9.2.** A one-dimensional quadratic interpolation requires three nodes on an element: one at each end and one at the middle. First derive one-dimensional quadratic interpolation or basis functions. Then, repeat Problem 9.1 using only one element with the quadratic basis functions and compare the solution with the exact solution.

- 9.3.** Assume that in Problem 9.1, the boundary condition at $x = 1$ is changed to

$$\left[\frac{d\varphi}{dx} + j\varphi \right]_{x=1} = 0.$$

By dividing the solution domain into three segments and using linear basis functions, find the finite element solution of the problem and compare the solution with the exact solution.

- 9.4.** Following the procedure similar to the derivation of Equation 9.2.11 for a triangular element, derive the linear interpolation functions on a tetrahedral element.

- 9.5.** The objective of this exercise is to derive Equation 9.2.31. As the first step, show that transformations $\xi = N_1^{(e)}(x, y)$ and $\eta = N_2^{(e)}(x, y)$ map the triangle in Figure 9.4 into a right triangle in the $\xi\eta$ -plane. Second, show that $N_3^{(e)}(x, y) = 1 - \xi - \eta$ and $dxdy = 2\Delta^{(e)}d\xi d\eta$ so that

$$\iint_{\Delta^{(e)}} (N_1^{(e)})^l (N_2^{(e)})^m (N_3^{(e)})^n d\Omega = 2\Delta^{(e)} \int_0^1 \xi^l \int_0^{1-\xi} \eta^m (1-\xi-\eta)^n d\eta d\xi.$$

Finally, evaluate the integrals to derive Equation 9.2.31.

- 9.6.** Write a computer program to calculate the cutoff wavenumber and field distribution of the TE and TM modes of an empty rectangular waveguide. Compare the results with the analytical solution.
- 9.7.** Equations 9.2.49–9.2.54 describe the formulation of two-dimensional scattering by a conducting cylinder in terms of the scattered field. First, extend the formulation for scattering by a dielectric cylinder. Then, reformulate the problem in terms of the total field.
- 9.8.** Show that the weak-form solution to the three-dimensional scattering problem defined by Equations 9.3.41 and 9.3.37 is given by

$$\begin{aligned} & \iiint_V \left[\frac{1}{\mu_r} (\nabla \times \mathbf{W}_i) \cdot (\nabla \times \mathbf{E}^{sc}) - k_0^2 \epsilon_r \mathbf{W}_i \cdot \mathbf{E}^{sc} \right] dV + jk_0 \iint_{S_{ABC}} (\hat{n} \times \mathbf{W}_i) \cdot (\hat{n} \times \mathbf{E}^{sc}) dS \\ &= - \iiint_{V_{sc}} \left[\frac{1}{\mu_r} (\nabla \times \mathbf{W}_i) \cdot (\nabla \times \mathbf{E}^{inc}) - k_0^2 \epsilon_r \mathbf{W}_i \cdot \mathbf{E}^{inc} \right] dV + jk_0 Z_0 \iint_{S_{sc}} \mathbf{W}_i \cdot (\hat{n} \times \mathbf{H}^{inc}) dS \end{aligned}$$

where V_{sc} denotes the volume of the dielectric scatterer and S_{sc} denotes its surface.

- 9.9.** Consider the one-dimensional problem defined by the partial differential equation

$$\frac{\partial^2 \varphi(x, t)}{\partial x^2} - \frac{1}{c^2} \frac{\partial^2 \varphi(x, t)}{\partial t^2} - \mu\sigma \frac{\partial \varphi(x, t)}{\partial t} = \mathcal{J}(x, t) \quad 0 < x < L$$

and the boundary conditions

$$\varphi(x, t)|_{x=0} = \rho(t)$$

$$\left[\frac{\partial \varphi(x, t)}{\partial x} + \frac{1}{c} \frac{\partial \varphi(x, t)}{\partial t} \right]_{x=L} = \gamma(t).$$

Discretize this problem using the finite element method and derive the discrete system given by

$$[T] \frac{d^2 \{\varphi\}}{dt^2} + [R] \frac{d\{\varphi\}}{dt} + [S]\{\varphi\} = \{\beta\}.$$

Derive the specific expressions for the elements of matrices $[T]$, $[R]$, and $[S]$ and vector $\{\beta\}$.

- 9.10.** Derive the second-order absorbing boundary condition using Equations 9.5.11 and 9.5.12 and show that it is equivalent to the one in Equation 9.5.10.
- 9.11.** Consider the boundary-value problem defined by the Helmholtz equation

$$\nabla^2 \varphi(x, y) + k^2 \varphi(x, y) = f(x, y)$$

and the absorbing boundary condition in Equation 9.5.19. Derive its weak-form representation, which would yield a symmetric finite element matrix.

- 9.12.** Show that when Equation 9.5.33 is applied to a flat surface, the reflection coefficient is given by Equation 9.5.34 for the TE incident wave and by Equation 9.5.35 for the TM incident wave.

- 9.13.** Show that the vector wave equation for Maxwell's equations (Eqs. 9.5.44–9.5.47) with $\tilde{\Lambda}$ given by Equation 9.5.40 and $s_{x,y,z} = 1 - j\sigma_{x,y,z}/\omega\epsilon$ is given by

$$\nabla \times [\tilde{\mathbf{L}}_2(j\omega) \cdot \nabla \times \mathbf{E}] - \tilde{\mathbf{L}}_1(j\omega) \cdot \mathbf{E} = 0$$

where

$$\begin{aligned} \tilde{\mathbf{L}}_1(s) &= s^2 \epsilon \tilde{\Lambda}(s) \\ &= \epsilon s^2 + s \begin{bmatrix} \sigma_y + \sigma_z - \sigma_x & 0 & 0 \\ 0 & \sigma_z + \sigma_x - \sigma_y & 0 \\ 0 & 0 & \sigma_x + \sigma_y - \sigma_z \end{bmatrix} \\ &\quad + \frac{1}{\epsilon} \begin{bmatrix} (\sigma_x - \sigma_y)(\sigma_x - \sigma_z) & 0 & 0 \\ 0 & (\sigma_y - \sigma_z)(\sigma_y - \sigma_x) & 0 \\ 0 & 0 & (\sigma_z - \sigma_x)(\sigma_z - \sigma_y) \end{bmatrix} \\ &\quad - \frac{1}{\epsilon^2} \begin{bmatrix} \sigma_x(\sigma_x - \sigma_y)(\sigma_x - \sigma_z) & 0 & 0 \\ 0 & \sigma_y(\sigma_y - \sigma_z)(\sigma_y - \sigma_x) & 0 \\ 0 & 0 & \sigma_z(\sigma_z - \sigma_x)(\sigma_z - \sigma_y) \end{bmatrix} \\ &\quad \cdot \begin{bmatrix} \frac{\epsilon}{s\epsilon + \sigma_x} & 0 & 0 \\ 0 & \frac{\epsilon}{s\epsilon + \sigma_y} & 0 \\ 0 & 0 & \frac{\epsilon}{s\epsilon + \sigma_z} \end{bmatrix} \\ \tilde{\mathbf{L}}_2(s) &= \frac{1}{\mu} \tilde{\Lambda}^{-1}(s) = \frac{1}{\mu} \\ &\quad \left[\begin{bmatrix} \frac{\sigma_x - \sigma_y}{\sigma_y - \sigma_z} \sigma_y & 0 & 0 \\ 0 & \frac{\sigma_y - \sigma_z}{\sigma_z - \sigma_x} \sigma_z & 0 \\ 0 & 0 & \frac{\sigma_z - \sigma_x}{\sigma_x - \sigma_y} \sigma_x \end{bmatrix} \begin{bmatrix} \frac{\epsilon}{s\epsilon + \sigma_y} & 0 & 0 \\ 0 & \frac{\epsilon}{s\epsilon + \sigma_z} & 0 \\ 0 & 0 & \frac{\epsilon}{s\epsilon + \sigma_x} \end{bmatrix} \right. \\ &\quad \left. + \frac{1}{\mu\epsilon} \begin{bmatrix} 0 & \frac{\sigma_y - \sigma_z}{\sigma_z - \sigma_x} \sigma_z & 0 \\ 0 & 0 & \frac{\sigma_z - \sigma_x}{\sigma_x - \sigma_y} \sigma_x \end{bmatrix} \begin{bmatrix} \frac{\epsilon}{s\epsilon + \sigma_z} & 0 & 0 \\ 0 & \frac{\epsilon}{s\epsilon + \sigma_x} & 0 \\ 0 & 0 & \frac{\epsilon}{s\epsilon + \sigma_y} \end{bmatrix} \right. \\ &\quad \left. + \frac{1}{\mu\epsilon} \begin{bmatrix} \frac{\sigma_z - \sigma_x}{\sigma_y - \sigma_z} \sigma_z & 0 & 0 \\ 0 & \frac{\sigma_x - \sigma_y}{\sigma_z - \sigma_x} \sigma_x & 0 \\ 0 & 0 & \frac{\sigma_y - \sigma_z}{\sigma_x - \sigma_y} \sigma_y \end{bmatrix} \begin{bmatrix} \frac{\epsilon}{s\epsilon + \sigma_z} & 0 & 0 \\ 0 & \frac{\epsilon}{s\epsilon + \sigma_x} & 0 \\ 0 & 0 & \frac{\epsilon}{s\epsilon + \sigma_y} \end{bmatrix} \right]. \end{aligned}$$

- 9.14.** Show that the Laplace transform of the vector wave equation in Problem 9.13 is given by

$$\nabla \times [\tilde{\mathcal{L}}_2(t) \cdot \nabla \times \mathcal{E}(t)] - \tilde{\mathcal{L}}_1(t) \cdot \mathcal{E}(t) = 0$$

where

$$\begin{aligned} \tilde{\mathcal{L}}_1(t) &= \epsilon \frac{\partial^2}{\partial t^2} + \begin{bmatrix} \sigma_y + \sigma_z - \sigma_x & 0 & 0 \\ 0 & \sigma_z + \sigma_x - \sigma_y & 0 \\ 0 & 0 & \sigma_x + \sigma_y - \sigma_z \end{bmatrix} \frac{\partial}{\partial t} \\ &\quad + \frac{1}{\epsilon} \begin{bmatrix} (\sigma_x - \sigma_y)(\sigma_x - \sigma_z) & 0 & 0 \\ 0 & (\sigma_y - \sigma_z)(\sigma_y - \sigma_x) & 0 \\ 0 & 0 & (\sigma_z - \sigma_x)(\sigma_z - \sigma_y) \end{bmatrix} \\ &\quad - \frac{1}{\epsilon^2} \begin{bmatrix} \sigma_x(\sigma_x - \sigma_y)(\sigma_x - \sigma_z) & 0 & 0 \\ 0 & \sigma_y(\sigma_y - \sigma_z)(\sigma_y - \sigma_x) & 0 \\ 0 & 0 & \sigma_z(\sigma_z - \sigma_x)(\sigma_z - \sigma_y) \end{bmatrix} \\ &\quad \cdot \begin{bmatrix} e^{-\frac{\sigma_x}{\epsilon}t} & 0 & 0 \\ 0 & e^{-\frac{\sigma_y}{\epsilon}t} & 0 \\ 0 & 0 & e^{-\frac{\sigma_z}{\epsilon}t} \end{bmatrix} u(t)^* \\ \tilde{\mathcal{L}}_2(t) &= \frac{1}{\mu} + \frac{1}{\mu\epsilon} \begin{bmatrix} \frac{\sigma_x - \sigma_y}{\sigma_y - \sigma_z} \sigma_y & 0 & 0 \\ 0 & \frac{\sigma_y - \sigma_z}{\sigma_z - \sigma_x} \sigma_z & 0 \\ 0 & 0 & \frac{\sigma_z - \sigma_x}{\sigma_x - \sigma_y} \sigma_x \end{bmatrix} \begin{bmatrix} e^{-\frac{\sigma_y}{\epsilon}t} & 0 & 0 \\ 0 & e^{-\frac{\sigma_z}{\epsilon}t} & 0 \\ 0 & 0 & e^{-\frac{\sigma_x}{\epsilon}t} \end{bmatrix} u(t)^* \\ &\quad + \frac{1}{\mu\epsilon} \begin{bmatrix} \frac{\sigma_z - \sigma_x}{\sigma_y - \sigma_z} \sigma_z & 0 & 0 \\ 0 & \frac{\sigma_x - \sigma_y}{\sigma_z - \sigma_x} \sigma_x & 0 \\ 0 & 0 & \frac{\sigma_y - \sigma_z}{\sigma_x - \sigma_y} \sigma_y \end{bmatrix} \begin{bmatrix} e^{-\frac{\sigma_z}{\epsilon}t} & 0 & 0 \\ 0 & e^{-\frac{\sigma_x}{\epsilon}t} & 0 \\ 0 & 0 & e^{-\frac{\sigma_y}{\epsilon}t} \end{bmatrix} u(t)^*. \end{aligned}$$

- 9.15.** Select a problem of interest to you (problems related to your research are preferred). Develop a finite element formulation and computer program to solve the problem. Present your work in the form of a formal paper (including Abstract, Introduction, Formulation, Results, Conclusion, and References). ■

CHAPTER 10

THE METHOD OF MOMENTS

The *method of moments* (MoM), also known as the *moment method*, is another powerful numerical technique developed to rise up to the challenge of solving increasingly complex problems in electromagnetics. Like the finite element method, the moment method transforms the governing equation of a boundary-value problem into a matrix equation to enable its solution on digital computers. Although the basic mathematical concepts of the moment method were in existence during the early twentieth century, true interest in it did not arise until the mid-1960s, with the publication of pioneering work by Mei and Van Bladel [1], Andreasen [2], Oshiro [3], Richmond [4], and others. The unified formulation of the method was presented by Harrington in his seminal book [5] in 1968. Since then, the method has been developed further and applied to a variety of important electromagnetic problems [6–10]. Today, it has become one of the predominant methods in computational electromagnetics. The moment method is particularly well suited to open-region electromagnetic problems such as wave scattering and antenna radiation. It is very efficient for problems involving either impenetrable or homogeneous objects. Its capability has been further enhanced by the development of a variety of fast algorithms that can deal with very large moment-method matrix equations.

In this chapter we first describe the basic principle of the moment method using a simple electrostatic problem. We then formulate a general integral equation for the two-dimensional Helmholtz equation and apply it to a variety of specific problems. For each specific problem, we describe its moment-method solution. This process is repeated for three-dimensional electromagnetic field problems, which include scattering by various conducting and dielectric objects. After that, we discuss the moment-method solution of planar and angular periodic problems and deal with the analysis of microstrip antennas and circuits on a dielectric substrate to demonstrate the unique advantage of the moment method. Finally, we use a relatively simple example to illustrate how to extend the moment-method solution from the frequency domain to the time domain.

10.1 INTRODUCTION TO THE METHOD OF MOMENTS

The solutions to Maxwell's equations can be sought directly by solving the partial differential equations related directly to Maxwell's equations, as was done in the finite difference and finite element methods. Alternatively, they can be obtained by solving an integral equation derived from Maxwell's equations. For example, in the electrostatic case, an integral equation can be derived using the *Green's function* approach. A Green's function is a point source response, and in this case it is the potential produced by a point charge. In the capacitance problem, where we are interested in finding the total capacitance

of a piece of metallic conductor, we can formulate an integral equation to solve for the charges on the conductor. Using the Green's function approach, we can write, by the principle of linear superposition, that the total potential due to the charges on the surface of a metallic conductor is

$$\varphi(\mathbf{r}) = \iint_S G(\mathbf{r}, \mathbf{r}') \rho_s(\mathbf{r}') dS' \quad (10.1.1)$$

where S is the surface of the metallic object, $\rho_s(\mathbf{r}')$ is the surface charge density on the metallic surface, $\varphi(\mathbf{r})$ is the potential generated by the surface charge, and $G(\mathbf{r}, \mathbf{r}')$ is the Green's function or point source response, given by

$$G(\mathbf{r}, \mathbf{r}') = \frac{1}{4\pi\epsilon_0 |\mathbf{r} - \mathbf{r}'|}. \quad (10.1.2)$$

On the metallic surface S , $\varphi(\mathbf{r})$ must be a constant. As a consequence, we have

$$\Phi = \iint_S G(\mathbf{r}, \mathbf{r}') \rho_s(\mathbf{r}') dS' \quad \mathbf{r} \in S. \quad (10.1.3)$$

Equation 10.1.3 is an integral equation where Φ is a known constant, $G(\mathbf{r}, \mathbf{r}')$ is a known function, and $\rho_s(\mathbf{r}')$ is the unknown surface charge density on the metallic surface. This integral equation can be solved for the unknown $\rho_s(\mathbf{r}')$.

The example above typifies an integral equation in electromagnetics. It turns out that integral equations can also be derived for dielectric and metallic bodies for electrostatic and electrodynamic problems. These integral equations are generally solved using the moment method. Notice that the function $\rho_s(\mathbf{r}')$ in Equation 10.1.3 has infinite degrees of freedom. Such infinite degrees of freedom cannot be handled by a computer. We say that $\rho_s(\mathbf{r}')$ is a function representing a vector in an infinite-dimensional space. To make Equation 10.1.3 solvable by a computer, we approximate its solution in a finite-dimensional subspace using the moment method. To illustrate this procedure, we choose a set of functions called *basis functions* that can be used to approximate $\rho_s(\mathbf{r}')$. For example, we let

$$\rho_s(\mathbf{r}') = \sum_{n=1}^N c_n v_n(\mathbf{r}') \quad (10.1.4)$$

where $v_n(\mathbf{r}')$ are the basis functions that can be used to approximate $\rho_s(\mathbf{r}')$, and c_n are the unknown coefficients yet to be determined. In this manner, we have given $\rho_s(\mathbf{r}')$ only N degrees of freedom. The basis functions $v_n(\mathbf{r}')$ can usually be categorized into two types. One type of basis function is defined over the entire surface and is often referred to as an *entire-domain* basis function. Such basis functions can be formulated rather easily if the shape of the entire surface is regular. However, for irregular shapes, such basis functions are very difficult, if not impossible, to formulate. In this case, we can adopt the basic idea of the finite element method by first subdividing the entire surface into many small surfaces, as illustrated in Figure 10.1, and then employ simple functions as basis functions for each small surface. This type of basis function is called a *subdomain* or *subsectional* basis function; such basis functions are much more versatile than the entire-domain basis functions.

Once the basis functions are chosen, substituting Equation 10.1.4 into Equation 10.1.3, we obtain an equation that contains a finite number of degrees of freedom

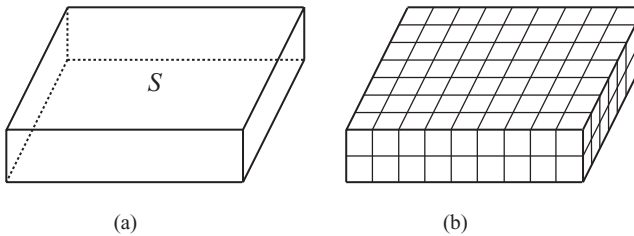


Figure 10.1 (a) A piece of metallic conductor charged to potential Φ . (b) Discretization of the surface into small surface patches.

$$\sum_{n=1}^N c_n \iint_S G(\mathbf{r}, \mathbf{r}') v_n(\mathbf{r}') dS' = \Phi \quad \mathbf{r} \in S. \quad (10.1.5)$$

However, this equation still does not enable us to solve for c_n —we have to convert it into a matrix equation. To this end, we choose a set of functions $w_1(\mathbf{r}), w_2(\mathbf{r}), \dots, w_N(\mathbf{r})$, and multiply Equation 10.1.5 by these functions individually, and integrate over the surface S to obtain

$$\sum_{n=1}^N c_n \iint_S w_m(\mathbf{r}) \iint_S G(\mathbf{r}, \mathbf{r}') v_n(\mathbf{r}') dS' dS = \iint_S w_m(\mathbf{r}) \Phi dS \quad m = 1, 2, \dots, N. \quad (10.1.6)$$

This equation can be written in a more compact form as

$$\sum_{n=1}^N A_{mn} c_n = b_m \quad m = 1, 2, \dots, N \quad (10.1.7)$$

where A_{mn} is evaluated from the double integrals that depend only on m and n , and b_m is evaluated from the integral on the right-hand side, which depends only on the index m . Equation 10.1.7 defines a matrix equation that can be solved for c_n , which in turn can be used in Equation 10.1.4 to provide an approximate solution $\rho_s(\mathbf{r}')$.

In a more abstract level, the solution procedure above can be presented as follows. An integral equation can be expressed as

$$\mathcal{L}\varphi = f \quad (10.1.8)$$

where \mathcal{L} denotes the integral operator, φ denotes the unknown solution to be sought, and f is a known driving term for the integral equation. To seek the solution for φ , we pick a finite basis set to approximate the solution

$$\varphi = \sum_{n=1}^N c_n v_n \quad (10.1.9)$$

and its substitution into Equation 10.1.8 yields

$$\sum_{n=1}^N c_n \mathcal{L}(v_n) = f. \quad (10.1.10)$$

We next convert this equation into a matrix equation by testing it with w_m ($m = 1, 2, \dots, N$) and integrating over the solution domain. This yields

$$\sum_{n=1}^N c_n \int_{\Omega} w_m \mathcal{L}(v_n) d\Omega = \int_{\Omega} w_m f d\Omega \quad m = 1, 2, \dots, N \quad (10.1.11)$$

which can be abstractly written as

$$\sum_{n=1}^N c_n \langle w_m, \mathcal{L}(v_n) \rangle = \langle w_m, f \rangle \quad m = 1, 2, \dots, N \quad (10.1.12)$$

where $\langle \bullet \rangle$ is an abbreviation for an integration. The functions w_m are usually referred to as *testing* or *weighting* functions.

Equation 10.1.12 defines a set of linear algebraic equations that can be solved for c_n . It can be written as a matrix equation

$$[A]\{c\} = \{b\} \quad (10.1.13)$$

where $[A]$ is called the *system matrix*, whose elements are given by

$$A_{mn} = \langle w_m, \mathcal{L}(v_n) \rangle \quad m, n = 1, 2, \dots, N \quad (10.1.14)$$

and $\{b\}$ and $\{c\}$ are called the *source* and *unknown vectors*, respectively, with the elements of $\{b\}$ given by

$$b_m = \langle w_m, f \rangle \quad m = 1, 2, \dots, N. \quad (10.1.15)$$

The solution procedure described above is called the *method of moments* because Equation 10.1.12 is equivalent to taking the moments of Equation 10.1.10. It is also known as the *weighted residual method* because Equation 10.1.12 can be interpreted as setting the weighted residual of Equation 10.1.10 to zero. The solution procedure works for both differential and integral operators. In fact, it is identical to that of the finite element method described in Section 9.1.1. The only difference here is that the equation considered here is an integral equation for which \mathcal{L} is an integral operator involving a Green's function. This difference, however, has a quite significant consequence on the choices of the basis and testing functions. In the finite element method, because of the necessity of taking differentiation, the basis functions have to be at least first-order (i.e., linear) and the testing functions are often chosen to be the same as the basis functions. In the moment method, the choice of basis functions is more forgiving because of the integral operator; the simplest choice can be the zeroth order, which is simply a constant. The choice of testing functions is also more versatile, and the simplest can be the delta functions or the zeroth-order functions, which can greatly simplify the integration.

Now, let us return to the electrostatic problem considered earlier and divide the surface of the metallic conductor into N small triangular or quadrilateral patches or cells. If these cells are small enough, the charge density $\rho_s(\mathbf{r}')$ can be considered constant over each cell. This is equivalent to the use of zeroth-order basis functions, defined as

$$v_n(\mathbf{r}') = \begin{cases} 1 & \mathbf{r}' \in s_n \\ 0 & \text{elsewhere} \end{cases} \quad (10.1.16)$$

where s_n denotes the n th cell. This type of basis function is sometimes referred to as a *pulse basis function*. Next, we need to choose a set of testing functions w_m . The simplest choice is the delta function

$$w_m(\mathbf{r}) = \delta(\mathbf{r} - \mathbf{r}_m) \quad (10.1.17)$$

where \mathbf{r}_m denotes the center of the m th cell. This choice is called *point collocation*. It is equivalent to enforcing Equation 10.1.5 at the center of each cell; therefore, this technique is sometimes referred to as *point matching*. With the choices in Equations 10.1.16 and 10.1.17, A_{mn} in Equation 10.1.7 is given by

$$A_{mn} = \iint_{S_n} G(\mathbf{r}_m, \mathbf{r}') dS' \quad (10.1.18)$$

and $b_m = \Phi$. The integral in Equation 10.1.18 can be evaluated approximately using the midpoint integration when $m \neq n$. When $m = n$, we can approximate S_n as a circular disc of the same area and then evaluate the potential at its center. These approximations yield

$$A_{mn} = \begin{cases} \frac{1}{4\pi\epsilon} \frac{s_n}{|\mathbf{r}_m - \mathbf{r}_n|} & m \neq n \\ \frac{1}{2\epsilon} \sqrt{\frac{s_n}{\pi}} & m = n \end{cases} \quad (10.1.19)$$

where $|\mathbf{r}_m - \mathbf{r}_n| = \sqrt{(x_m - x_n)^2 + (y_m - y_n)^2 + (z_m - z_n)^2}$. With this, the matrix equation in Equation 10.1.7 can be readily computed and solved for the expansion coefficients c_n .

Besides the delta functions, we can also choose to use the zeroth-order functions as the testing functions

$$w_m(\mathbf{r}) = \begin{cases} 1 & \mathbf{r} \in S_m \\ 0 & \text{elsewhere} \end{cases} \quad (10.1.20)$$

and this choice is called *subdomain collocation*. This is equivalent to enforcing Equation 10.1.5 over the entire cell, but in the average sense. With this, A_{mn} in Equation 10.1.7 becomes

$$A_{mn} = \iint_{S_m} \iint_{S_n} G(\mathbf{r}, \mathbf{r}') dS' dS. \quad (10.1.21)$$

and $b_m = \Phi s_m$. Again, the matrix equation in Equation 10.1.7 can now be computed and solved for the expansion coefficients c_n . In this case, the system matrix $[A]$ is symmetric. Once the expansion coefficients c_n are computed, the total charge on the metallic object can be evaluated as

$$Q = \iint_S \rho_s(\mathbf{r}') dS' = \sum_{n=1}^N c_n s_n \quad (10.1.22)$$

from which we obtain the capacitance of the object as $C = Q/\Phi$. The result for the capacitance is independent of the value of Φ and depends only on the geometry of the object.

From this electrostatic example, we can also see three major differences between the moment method and the finite element method besides the choices for basis and testing functions. One major difference is that for a three-dimensional analysis, the finite element method requires discretization of a volumetric domain, whereas the moment-method

solution can be obtained via discretization of a surface domain. In other words, the problem dimension is one less in the moment method than in the finite element method. This reduction in the problem dimension greatly reduces the number of unknowns in the moment-method solution. The second major difference is that for solving an open-region problem, the finite element method requires truncating an infinite domain into a finite one and then formulating an approximate boundary condition at the truncation boundary. This, however, is completely avoided in the moment method because of the use of an appropriate Green's function, which automatically accounts for the field behavior at infinity. Hence, there is no need to use any approximate absorbing boundary conditions or perfectly matched layers. The third major difference is that the system matrix in the moment method is a full matrix because of the use of a Green's function, whereas the finite element matrix is extremely sparse, which is much more efficient to calculate and solve and takes much less memory to store. This is the price for the moment method to pay for the two advantages elucidated earlier.

The example above also demonstrates clearly the basic steps to perform a moment-method analysis. The first step is to formulate an integral equation for the problem under consideration. The second step is to expand the unknown solution using a set of basis functions. The third step is to choose a set of testing functions to convert the integral equation into a matrix equation. The last step is to solve the matrix equation for the expansion coefficients and then calculate the desired quantities. In the next two sections, we formulate the moment-method solution of the Helmholtz equations in free space in both two and three dimensions.

10.2 TWO-DIMENSIONAL ANALYSIS

As we know, two-dimensional electromagnetic problems can always be formulated as scalar problems with a scalar Helmholtz equation as the governing equation. In this section we first formulate the general integral equation for the open-region two-dimensional scalar problem and then use it for the moment-method solution for scattering by conducting and dielectric cylinders.

10.2.1 Formulation of Integral Equations

Consider the problem of a scalar wave produced by a source $f(\rho)$ in the presence of an arbitrarily shaped object immersed in free space, as illustrated in Figure 10.2. Assume that both the source and the object have no variation along the z -axis; thus, we only have to consider a plane perpendicular to the z -axis. Exterior to the object, the wave function $\phi(\rho)$ satisfies the inhomogeneous Helmholtz equation

$$\nabla^2 \phi(\rho) + k_0^2 \phi(\rho) = f(\rho) \quad \rho \in \Omega_{\infty} \quad (10.2.1)$$

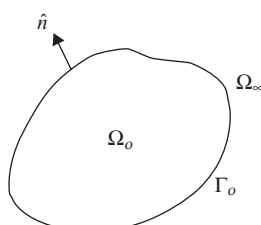


Figure 10.2 Two-dimensional object in free space.

where k_0 is the wavenumber and Ω_∞ denotes the exterior region. The wave function should also satisfy the radiation condition

$$\sqrt{\rho} \left[\frac{\partial \varphi(\rho)}{\partial \rho} + jk_0 \varphi(\rho) \right] = 0 \quad \rho \rightarrow \infty \quad (10.2.2)$$

which simply indicates that the wave propagates outward into infinity without reflection. To establish an integral equation for this problem, we introduce the free-space Green's function G_0 , which satisfies the inhomogeneous Helmholtz equation

$$\nabla^2 G_0(\rho, \rho') + k_0^2 G_0(\rho, \rho') = -\delta(\rho - \rho') \quad (10.2.3)$$

and the same radiation condition as Equation 10.2.2, where δ denotes the Dirac delta function. This free-space Green's function is given by

$$G_0(\rho, \rho') = \frac{1}{4j} H_0^{(2)}(k_0 |\rho - \rho'|) \quad (10.2.4)$$

where $H_0^{(2)}$ denotes the zeroth-order Hankel function of the second kind.

We first multiply Equation 10.2.1 by G_0 and Equation 10.2.3 by φ , and then integrate the difference of the resulting equations over the entire exterior region to obtain

$$\begin{aligned} & \iint_{\Omega_\infty} [G_0(\rho, \rho') \nabla^2 \varphi(\rho) - \varphi(\rho) \nabla^2 G_0(\rho, \rho')] d\Omega \\ &= \iint_{\Omega_s} G_0(\rho, \rho') f(\rho) d\Omega + \iint_{\Omega_\infty} \varphi(\rho) \delta(\rho - \rho') d\Omega \end{aligned} \quad (10.2.5)$$

where Ω_s denotes the source region where $f(\rho) \neq 0$. Applying the second scalar Green's theorem

$$\iint_{\Omega} (a \nabla^2 b - b \nabla^2 a) d\Omega = \oint_{\Gamma} \left(a \frac{\partial b}{\partial n} - b \frac{\partial a}{\partial n} \right) d\Gamma \quad (10.2.6)$$

where Γ denotes the boundary enclosing Ω , we have

$$\begin{aligned} & \oint_{\Gamma_o} \left[\varphi(\rho) \frac{\partial G_0(\rho, \rho')}{\partial n} - G_0(\rho, \rho') \frac{\partial \varphi(\rho)}{\partial n} \right] d\Gamma + \oint_{\Gamma_\infty} \left[G_0(\rho, \rho') \frac{\partial \varphi(\rho)}{\partial \rho} - \varphi(\rho) \frac{\partial G_0(\rho, \rho')}{\partial \rho} \right] d\Gamma \\ & - \iint_{\Omega_s} G_0(\rho, \rho') f(\rho) d\Omega = \iint_{\Omega_\infty} \varphi(\rho) \delta(\rho - \rho') d\Omega \end{aligned} \quad (10.2.7)$$

where Γ_o denotes the boundary of the object and Γ_∞ denotes a circle with a radius approaching infinity. Note that the unit normal in Equation 10.2.6 is defined to point away from Ω , whereas the unit normal in Figure 10.1 points toward Ω_∞ . Since both G_0 and φ satisfy the radiation condition, the boundary integral over Γ_∞ vanishes. Using the definition of the Dirac delta function, we obtain

$$\begin{aligned} & \oint_{\Gamma_o} \left[\varphi(\rho) \frac{\partial G_0(\rho, \rho')}{\partial n} - G_0(\rho, \rho') \frac{\partial \varphi(\rho)}{\partial n} \right] d\Gamma - \iint_{\Omega_s} G_0(\rho, \rho') f(\rho) d\Omega \\ &= \begin{cases} \varphi(\rho') & \rho' \in \Omega_\infty \\ 0 & \rho' \in \Omega_o \end{cases} \end{aligned} \quad (10.2.8)$$

where Ω_o denotes the interior region of the object. Exchanging ρ and ρ' and using the symmetry of G_0 , we have

$$\oint_{\Gamma_o} \left[\varphi(\rho) \frac{\partial G_0(\rho, \rho')}{\partial n'} - G_0(\rho, \rho') \frac{\partial \varphi(\rho')}{\partial n'} \right] d\Gamma' - \iint_{\Omega_s} G_0(\rho, \rho') f(\rho') d\Omega' \\ = \begin{cases} \varphi(\rho) & \rho \in \Omega_\infty \\ 0 & \rho \in \Omega_o. \end{cases} \quad (10.2.9)$$

Equation 10.2.9 provides the foundation to establish an integral equation for φ and $\partial \varphi / \partial n$ on the boundary of the object. However, before we proceed further, we notice that when the object is absent, the boundary integral vanishes. Hence,

$$\varphi(\rho) = - \iint_{\Omega_s} G_0(\rho, \rho') f(\rho') d\Omega'. \quad (10.2.10)$$

We call this the incident wave and denote it as $\varphi^{\text{inc}}(\rho)$. With this notation, Equation 10.2.9 can be written as

$$\varphi^{\text{inc}}(\rho) + \oint_{\Gamma_o} \left[\varphi(\rho') \frac{\partial G_0(\rho, \rho')}{\partial n'} - G_0(\rho, \rho') \frac{\partial \varphi(\rho')}{\partial n'} \right] d\Gamma' = \begin{cases} \varphi(\rho) & \rho \in \Omega_\infty \\ 0 & \rho \in \Omega_o \end{cases} \quad (10.2.11)$$

where the boundary integral term corresponds to the scattered wave.

Equation 10.2.11 is the mathematical representation of Huygens' principle for scalar fields. It states that, once the field and its normal derivative are known on the boundary of a domain, the field everywhere in that domain can be evaluated. To establish an integral equation from Equation 10.2.11, we have to apply it to Γ_o . However, when we set ρ on Γ_o , the boundary integral in Equation 10.2.11 becomes singular at $\rho = \rho'$ because both $H_0^{(2)}(k_0 |\rho - \rho'|)$ and its derivative are singular when their argument vanishes. To deal with this singularity, we can first deform Γ_o into the shape shown in Figure 10.3a, which contains two parts, one being $\Gamma_o - 2\varepsilon$ and the other being a semicircle centered at ρ and having a radius of ε , and then let $\varepsilon \rightarrow 0$. Doing so, we have

$$\oint_{\Gamma_o} [\cdot] d\Gamma' = \lim_{\varepsilon \rightarrow 0} \left\{ \int_{\Gamma_o - 2\varepsilon} [\cdot] d\Gamma' + \int_0^\pi [\cdot] \varepsilon d\phi \right\}. \quad (10.2.12)$$

We denote the first integral on the right-hand side as

$$\oint_{\Gamma_o} [\cdot] d\Gamma' = \lim_{\varepsilon \rightarrow 0} \int_{\Gamma_o - 2\varepsilon} [\cdot] d\Gamma' \quad (10.2.13)$$

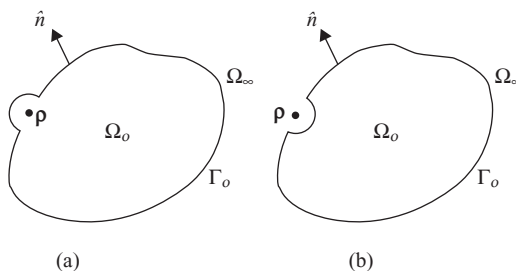


Figure 10.3 (a) Deformed Γ_o such that ρ resides inside Ω_o . (b) Deformed Γ_o such that ρ resides outside Ω_o .

which is an integral along Γ_o , but with the singular point excluded. For the second integral, we have

$$\lim_{\varepsilon \rightarrow 0} \int_0^\pi [\bullet] \varepsilon d\phi = \frac{1}{4j} \lim_{\varepsilon \rightarrow 0} \int_0^\pi \left[\varphi(\mathbf{p}') \frac{\partial H_0^{(2)}(k\varepsilon)}{\partial \varepsilon} - H_0^{(2)}(k\varepsilon) \frac{\partial \varphi(\mathbf{p}')}{\partial n'} \right] \varepsilon d\phi. \quad (10.2.14)$$

Since $\varepsilon \rightarrow 0$, we can use the small-argument approximation

$$H_0^{(2)}(z) \approx 1 - j \frac{2}{\pi} \ln \left(\frac{\gamma z}{2} \right) \quad \text{when } z \rightarrow 0 \quad (10.2.15)$$

where $\gamma \approx 1.781$. This yields

$$\lim_{\varepsilon \rightarrow 0} \int_0^\pi [\bullet] \varepsilon d\phi = -\frac{1}{2} \varphi(\mathbf{p}). \quad (10.2.16)$$

Note that with the deformed boundary in Figure 10.3a, $\mathbf{p} \in \Omega_o$. With this observation, substituting Equation 10.2.16 into Equation 10.2.12 and then into Equation 10.2.11, we obtain

$$\varphi^{\text{inc}}(\mathbf{p}) + \oint_{\Gamma_o} \left[\varphi(\mathbf{p}') \frac{\partial G_0(\mathbf{p}, \mathbf{p}')}{\partial n'} - G_0(\mathbf{p}, \mathbf{p}') \frac{\partial \varphi(\mathbf{p}')}{\partial n'} \right] d\Gamma' = \frac{1}{2} \varphi(\mathbf{p}) \quad \mathbf{p} \in \Gamma_o. \quad (10.2.17)$$

The same result can be obtained by deforming the boundary into the one shown in Figure 10.3b (see Problem 10.16).

Equation 10.2.17 provides the necessary integral equation for the solution of the Helmholtz equation. Since both φ and $\partial \varphi / \partial n$ on the boundary are unknown, we need another relation between the two quantities to make the problem solvable. This second relation comes from the boundary condition if the object is impenetrable or from the formulation of the interior field if the object is penetrable. We consider a few cases in the following to illustrate this process.

10.2.2 Scattering by a Conducting Cylinder

Consider wave scattering by an infinitely long conducting cylinder. For transverse magnetic (TM) polarization, the electric field satisfies the Helmholtz equation

$$\nabla^2 E_z(\mathbf{p}) + k_0^2 E_z(\mathbf{p}) = jk_0 Z_0 J_{i,z}(\mathbf{p}) \quad \mathbf{p} \in \Omega_\infty \quad (10.2.18)$$

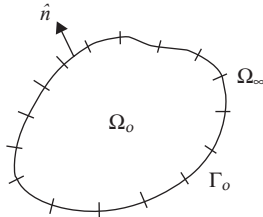
where $J_{i,z}(\mathbf{p})$ denotes the source of the incident field. On the surface of the cylinder,

$$E_z(\mathbf{p}') = 0 \quad \mathbf{p}' \in \Gamma_o \quad (10.2.19)$$

$$\frac{\partial E_z(\mathbf{p}')}{\partial n'} = jk_0 Z_0 H_t(\mathbf{p}') = jk_0 Z_0 J_{s,z}(\mathbf{p}') \quad \mathbf{p}' \in \Gamma_o \quad (10.2.20)$$

where $J_{s,z}(\mathbf{p}')$ denotes the surface current density induced by the incident field. Substituting these into Equation 10.2.17, we obtain the integral equation

$$E_z^{\text{inc}}(\mathbf{p}) - jk_0 Z_0 \int_{\Gamma_o} G_0(\mathbf{p}, \mathbf{p}') J_{s,z}(\mathbf{p}') d\Gamma' = 0 \quad \mathbf{p} \in \Gamma_o. \quad (10.2.21)$$

Figure 10.4 Contour Γ_o divided into short segments.

This equation is referred to as the *electric-field integral equation* (EFIE) because it is formulated in terms of the electric field.

To solve Equation 10.2.21, we can divide Γ_o into small segments (Fig. 10.4) and approximate the surface current density over each segment as a constant. A point matching procedure would yield

$$\sum_{n=1}^N Z_{mn} J_{z,n} = V_m \quad m = 1, 2, \dots, N \quad (10.2.22)$$

where

$$Z_{mn} = jk_0 Z_0 \int_{s_n} G_0(\rho_m, \rho') d\Gamma' \quad (10.2.23)$$

$$V_m = E_z^{\text{inc}}(\rho_m) \quad (10.2.24)$$

where s_n denotes the n th segment and ρ_m denotes the center of the m th segment. For $m \neq n$, the integral in Equation 10.2.23 can be evaluated using the midpoint integration, and for $m = n$, we can use the small-argument approximation for the Hankel function to find

$$Z_{mn} = \begin{cases} \frac{k_0 Z_0 s_n}{4} H_0^{(2)}(k_0 |\rho_m - \rho_n|) & m \neq n \\ \frac{k_0 Z_0 s_n}{4} \left[1 - j \frac{2}{\pi} \ln \left(\frac{k_0 \gamma s_n}{4e} \right) \right] & m = n \end{cases} \quad (10.2.25)$$

where $e \approx 2.7183$. Clearly, the system matrix in Equation 10.2.22 can be made symmetric by multiplying each equation in Equation 10.2.22 by s_m . The solution of this system of equations yields the surface current density, from which the field everywhere can be computed from Equation 10.2.11, which in this case becomes

$$E_z(\rho) = E_z^{\text{inc}}(\rho) - jk_0 Z_0 \oint_{\Gamma_o} G_0(\rho, \rho') J_{s,z}(\rho') d\Gamma' \quad \rho \in \Omega_{\infty}. \quad (10.2.26)$$

The analysis for transverse electric (TE) polarization follows the same approach. In this case, the magnetic field satisfies the Helmholtz equation

$$\nabla^2 H_z(\rho) + k_0^2 H_z(\rho) = -[\nabla \times \mathbf{J}_i(\rho)]_z \quad \rho \in \Omega_{\infty} \quad (10.2.27)$$

where $\nabla \times \mathbf{J}_i(\rho)$ denotes the source of the incident field. On the surface of the cylinder,

$$H_z(\rho') = -J_{s,t}(\rho') \quad \rho' \in \Gamma_o \quad (10.2.28)$$

$$\frac{\partial H_z(\mathbf{p}')}{\partial n'} = 0 \quad \mathbf{p}' \in \Gamma_o \quad (10.2.29)$$

where $J_{s,t}(\mathbf{p}')$ denotes the surface current density induced by the incident field. Substituting these into Equation 10.2.17, we obtain the integral equation

$$H_z^{\text{inc}}(\mathbf{p}) - \oint_{\Gamma_o} \frac{\partial G_0(\mathbf{p}, \mathbf{p}')}{\partial n'} J_{s,t}(\mathbf{p}') d\Gamma' = -\frac{1}{2} J_{s,t}(\mathbf{p}) \quad \mathbf{p} \in \Gamma_o \quad (10.2.30)$$

This equation is called the *magnetic-field integral equation* (MFIE) because it is formulated in terms of the magnetic field.

To solve Equation 10.2.30, we can divide Γ_o into small segments and approximate the surface current density over each segment as a constant. A point matching procedure would yield

$$\sum_{n=1}^N Z_{mn} J_{t,n} = V_m \quad m = 1, 2, \dots, N \quad (10.2.31)$$

where

$$Z_{mn} = \oint_{s_n} \frac{\partial G_0(\mathbf{p}_m, \mathbf{p}')}{\partial n'} d\Gamma' - \frac{1}{2} \delta_{mn} \quad (10.2.32)$$

$$V_m = H_z^{\text{inc}}(\mathbf{p}_m) \quad (10.2.33)$$

where $\delta_{mn} = 1$ for $m = n$ and $\delta_{mn} = 0$ for $m \neq n$. To evaluate the integral in Equation 10.2.32, we note that

$$\begin{aligned} \frac{\partial G_0(\mathbf{p}_m, \mathbf{p}')}{\partial n'} &= \frac{1}{4j} \hat{n}' \cdot \nabla' H_0^{(2)}(k_0 |\mathbf{p}_m - \mathbf{p}'|) \\ &= -\frac{k_0}{4j} H_1^{(2)}(k_0 |\mathbf{p}_m - \mathbf{p}'|) \hat{n}' \cdot \nabla' |\mathbf{p}_m - \mathbf{p}'| \\ &= \frac{k_0}{4j} H_1^{(2)}(k_0 |\mathbf{p}_m - \mathbf{p}'|) \frac{\hat{n}' \cdot (\mathbf{p}_m - \mathbf{p}')}{|\mathbf{p}_m - \mathbf{p}'|}. \end{aligned} \quad (10.2.34)$$

Using the midpoint integration, we obtain

$$Z_{mn} = \begin{cases} \frac{k_0 S_n}{4j} H_1^{(2)}(k_0 |\mathbf{p}_m - \mathbf{p}_n|) \frac{\hat{n}' \cdot (\mathbf{p}_m - \mathbf{p}_n)}{|\mathbf{p}_m - \mathbf{p}_n|} & m \neq n \\ -\frac{1}{2} & m = n. \end{cases} \quad (10.2.35)$$

The solution of Equation 10.2.31 yields the surface current density, from which the field everywhere can be computed from Equation 10.2.11, which in this case becomes

$$H_z(\mathbf{p}) = H_z^{\text{inc}}(\mathbf{p}) - \oint_{\Gamma_o} \frac{\partial G_0(\mathbf{p}, \mathbf{p}')}{\partial n'} J_{s,t}(\mathbf{p}') d\Gamma' \quad \mathbf{p} \in \Omega_\infty. \quad (10.2.36)$$

We consider two examples to illustrate the application of the moment method discussed in this section. Figure 10.5 shows the moment-method solution of plane wave scattering by a circular conducting cylinder with a radius of 1.0λ . In particular, Figures 10.5a and 10.5b plot the induced surface current density and the computed results are compared with the analytical solution. The computed surface current density is then

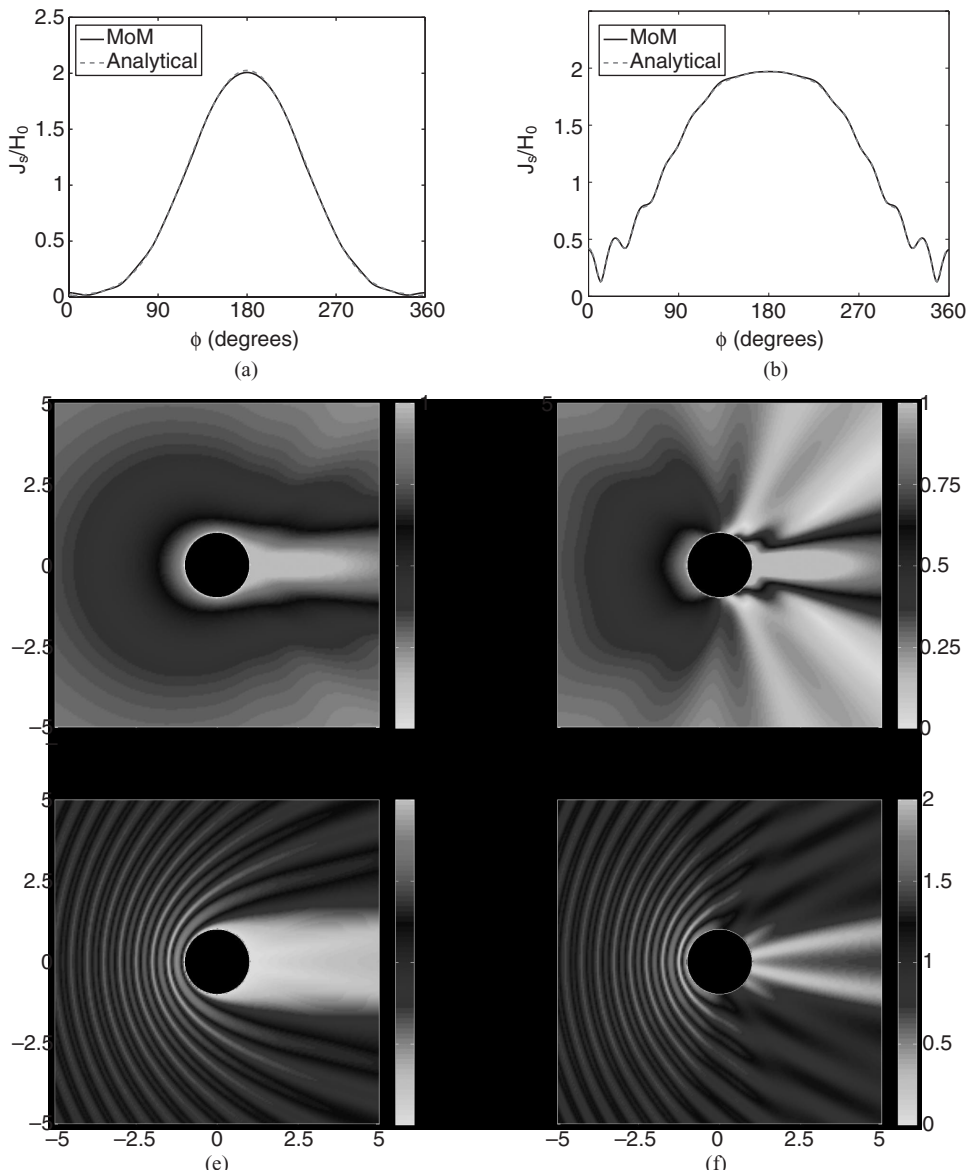


Figure 10.5 Scattering by a circular conducting cylinder with a radius of 1λ . The incident wave propagates from the left to right. The left and right columns show the results for the TM and TE polarizations, respectively. (a) Magnitude of the induced surface current density $J_{s,z}$. (b) Magnitude of the induced surface current density $J_{s,r}$. (c) Magnitude of the scattered field E_z^{sc} . (d) Magnitude of the scattered field H_z^{sc} . (e) Magnitude of the total field E_z . (f) Magnitude of the total field H_z . The values of the fields are normalized by the magnitude of their respective incident fields. (See color insert.)

used to calculate the scattered and total fields using Equations 10.2.26 and 10.2.36, and the results are plotted in Figures 10.5c–10.5f. The fields plotted here are basically the same as those in Figures 6.12a–6.12d except that they are now plotted in terms of their magnitudes instead of the time-domain snapshots. Equations 10.2.26 and 10.2.36 can also be used to compute the scattered far field, from which the bistatic scattering width can be calculated. The results are basically identical to the ones shown in Figures 6.12e and 6.12f.

The second example deals with plane wave scattering by a $3\lambda \times 3\lambda$ square conducting cylinder. Figures 10.6a and 10.6b plot the induced surface current density, where s is measured from the mid-point of the back side of the cylinder. For comparison, the approximate solution based on physical optics is also plotted in the figures. The edge singularity is clearly observed in the moment-method solution for the TM case, and the interference of the surface waves excited by edge diffraction is also shown clearly in the TE case, both of which are not predicted by the physical optics approximation. The calculated scattered and total fields based on the computed surface current density are plotted in Figures 10.6c–10.6f. The bistatic scattering width for this square cylinder is shown in Figure 10.7 together with that for a $1\lambda \times 1\lambda$ square conducting cylinder. It is interesting to note the perfect symmetry in the scattered-field pattern of a square cylinder for the TE case, which can be explained using the induction theorem discussed in Section 3.4.2. The results for this square cylinder case have been verified by the finite element analysis described in Section 9.2.3. The moment method is more efficient than the finite element method for calculating the induced surface current density and the scattering width, but is less efficient than the finite element method for the calculation of the near-field distribution.

10.2.3 Scattering by a Conducting Strip

The formulation above is developed for an arbitrary conducting cylinder with a finite cross-section. It has to be modified to deal with very thin conducting strips (approximated by zero thickness). The modification for the TM polarization is straightforward. Take a horizontal strip for an example. In this case, Γ_o consists of the upper and lower surfaces; hence,

$$\begin{aligned} \int_{\Gamma_o} G_0(\rho, \rho') J_{s,z}(\rho') d\Gamma' &= \int_{\Gamma^+} G_0(\rho, \rho') J_{s,z}^+(\rho') d\Gamma' + \int_{\Gamma^-} G_0(\rho, \rho') J_{s,z}^-(\rho) d\Gamma' \\ &= \int_{\Gamma^+} G_0(\rho, \rho') [J_{s,z}^+(\rho') + J_{s,z}^-(\rho')] d\Gamma' \end{aligned} \quad (10.2.37)$$

where Γ^+ denotes the upper surface of the strip and Γ^- denotes its lower surface. Substituting this into Equation 10.2.21, we obtain

$$E_z^{\text{inc}}(\rho) - jk_0 Z_0 \int_{\Gamma} G_0(\rho, \rho') J_{s,z}^t(\rho') d\Gamma' = 0 \quad \rho \in \Gamma \quad (10.2.38)$$

where $\Gamma = \Gamma^+ = \Gamma^-$ denotes one surface of the strip and $J_{s,z}^t = J_{s,z}^+ + J_{s,z}^-$ denotes the sum of the upper and lower surface current densities. The moment-method solution procedure is identical to the one described in Section 10.2.2.

Unfortunately, the same approach cannot be applied to Equation 10.2.30 for the TE polarization. We have to derive the EFIE for the TE polarization first and then apply it to a conducting strip. To illustrate this procedure, consider a horizontal flat strip residing on the x -axis with its surface perpendicular to the y -axis. In this case, Equation 10.2.36 can

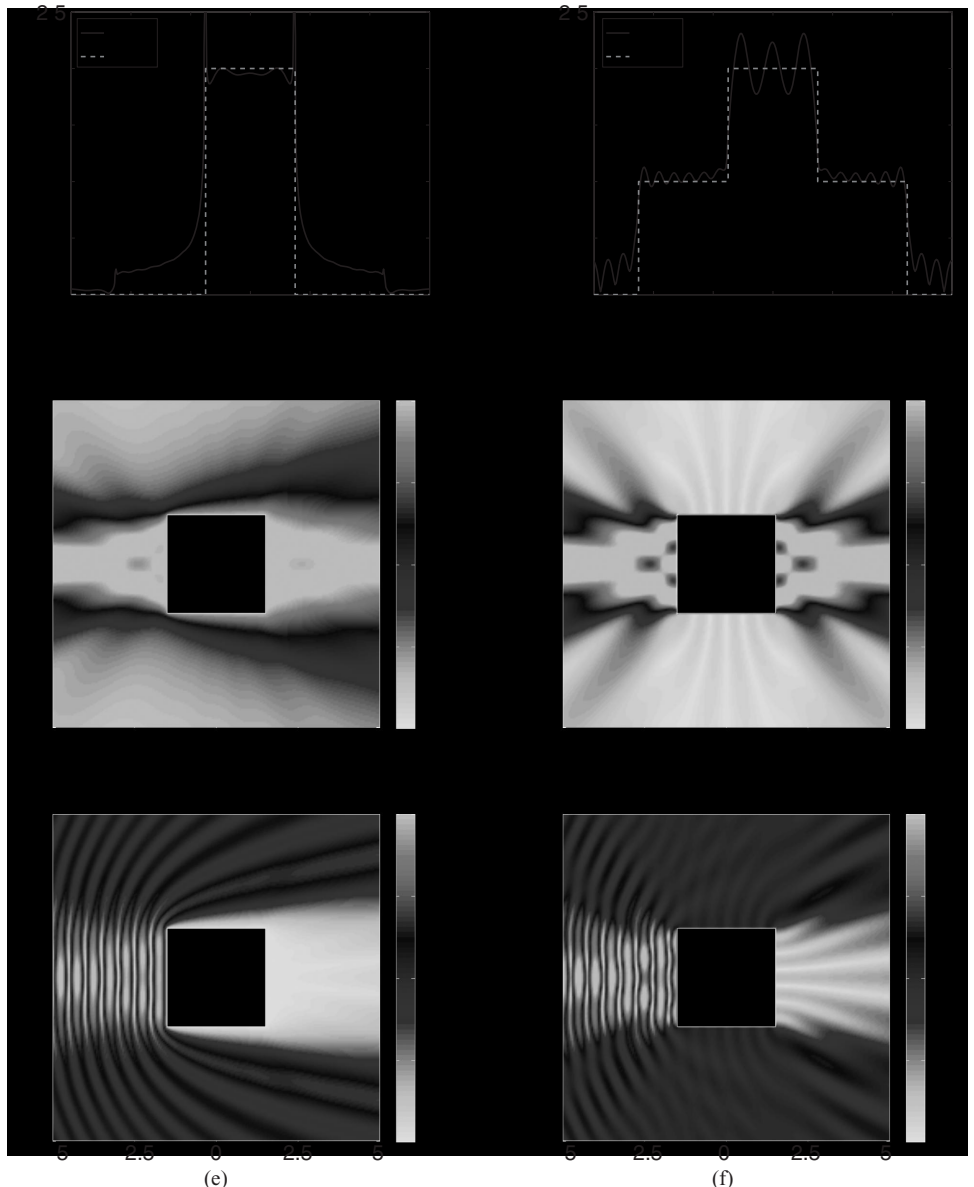


Figure 10.6 Scattering by a square conducting cylinder with a cross-section of $3\lambda \times 3\lambda$. The incident wave propagates from the left to right. The left and right columns show the results for the TM and TE polarizations, respectively. (a) Magnitude of the induced surface current density $J_{s,z}$. (b) Magnitude of the induced surface current density $J_{s,r}$. (c) Magnitude of the scattered field E_z^{sc} . (d) Magnitude of the scattered field H_z^{sc} . (e) Magnitude of the total field E_z . (f) Magnitude of the total field H_z . The values of the fields are normalized by the magnitude of their respective incident fields. (See color insert.)

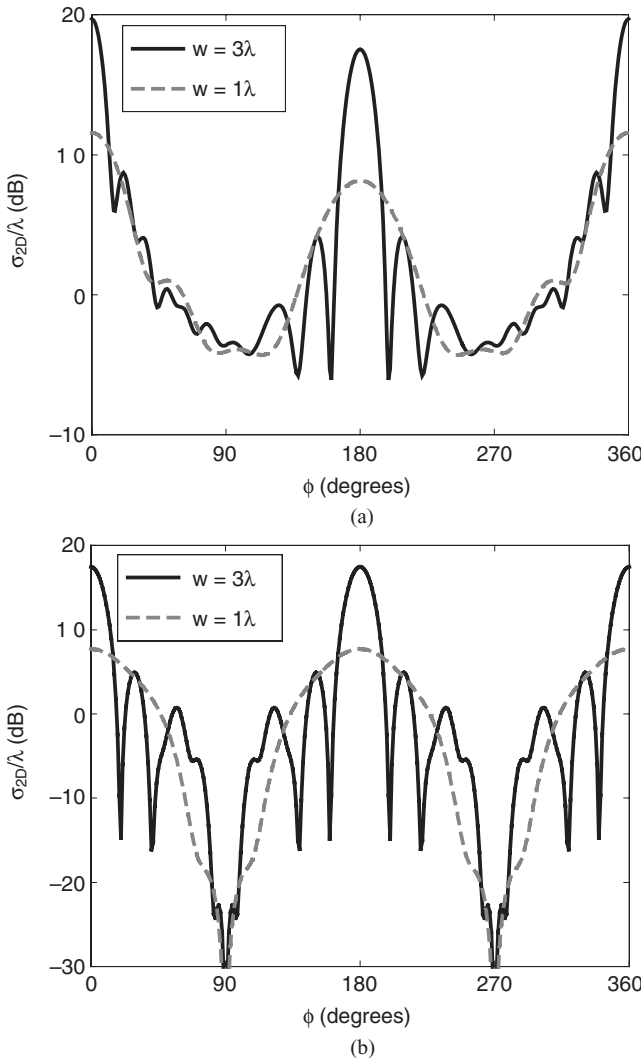


Figure 10.7 Bistatic scattering width for square conducting cylinders having a cross-section of $1\lambda \times 1\lambda$ and $3\lambda \times 3\lambda$, respectively, with the angle of incidence $\phi^{\text{inc}} = 180^\circ$. (a) TM polarization. (b) TE polarization.

be written as

$$H_z(\rho) = H_z^{\text{inc}}(\rho) + \int_{\Gamma^+} \frac{\partial G_0(\rho, x')}{\partial y} J_{s,t}^+(x') dx' - \int_{\Gamma^-} \frac{\partial G_0(\rho, x')}{\partial y} J_{s,t}^-(x') dx' \quad (10.2.39)$$

where we used the fact that $\partial G_0 / \partial y' = -\partial G_0 / \partial y$. By taking the derivative with respect to y , we obtain

$$E_x(\rho) = E_x^{\text{inc}}(\rho) - \frac{jZ_0}{k_0} \left[\int_{\Gamma^+} \frac{\partial^2 G_0(\rho, x')}{\partial y^2} J_{s,t}^+(x') dx' - \int_{\Gamma^-} \frac{\partial^2 G_0(\rho, x')}{\partial y^2} J_{s,t}^-(x') dx' \right] \quad (10.2.40)$$

which can also be written as

$$E_x(\mathbf{p}) = E_x^{\text{inc}}(\mathbf{p}) + \frac{jZ_0}{k_0} \int_{\Gamma^+} \left(k_0^2 + \frac{\partial^2}{\partial x^2} \right) G_0(\mathbf{p}, x') [J_{s,t}^+(x') - J_{s,t}^-(x')] dx'. \quad (10.2.41)$$

Setting \mathbf{p} on the strip, we obtain the integral equation

$$\frac{Z_0}{4k_0} \int_{-w/2}^{w/2} \left(k_0^2 + \frac{\partial^2}{\partial x^2} \right) H_0^{(2)}(k_0 |x - x'|) J_{s,t}^t(x') dx' = E_x^{\text{inc}}(x) \quad x \in (-w/2, w/2) \quad (10.2.42)$$

where w denotes the width of the strip and $J_{s,t}^t = J_{s,t}^+ - J_{s,t}^-$. Note that the tangential direction on the lower surface of the strip is opposite to that on the upper surface; therefore, $J_{s,t}^t$ actually represents the sum of the upper and lower surface currents.

The moment-method solution of Equation 10.2.42 using the pulse basis functions and point matching is straightforward, resulting in a system of equations similar to Equation 10.2.31 with

$$Z_{mn} = \frac{Z_0}{4k_0} \int_{x_n - \Delta x/2}^{x_n + \Delta x/2} \left(k_0^2 + \frac{\partial^2}{\partial x'^2} \right) H_0^{(2)}(k_0 |x_m - x'|) dx' \quad (10.2.43)$$

$$V_m = E_x^{\text{inc}}(x_m) \quad (10.2.44)$$

where Δx denotes the width of the segments. Although the integral in Equation 10.2.43 can be evaluated approximately, much better accuracy can be obtained by using the first-order basis and testing functions. With the first-order basis functions, the current can be expanded as

$$J_{s,t}^t(x') = \sum_{n=1}^{N-1} \Lambda_n(x') J_{t,n} \quad (10.2.45)$$

where Λ_n is a triangular function (Fig. 10.8) defined as

$$\Lambda_n(x') = \begin{cases} \frac{x' - x_{n-1}}{x_n - x_{n-1}} & x_{n-1} \leq x' \leq x_n \\ \frac{x_{n+1} - x'}{x_{n+1} - x_n} & x_n \leq x' \leq x_{n+1}. \end{cases} \quad (10.2.46)$$

This expansion ensures that the current $J_{s,t}^t$ vanishes at the edges of the strip. When the same triangular functions are used as testing functions, we obtain

$$\sum_{n=1}^{N-1} Z_{mn} J_{t,n} = V_m \quad m = 1, 2, \dots, N-1 \quad (10.2.47)$$

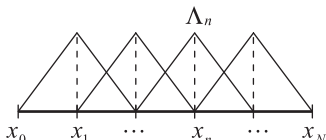


Figure 10.8 Illustration of triangular basis functions Λ_n .

where

$$Z_{mn} = \frac{Z_0}{4k_0} \int_{x_{m-1}}^{x_{m+1}} \Lambda_m(x) \int_{x_{n-1}}^{x_{n+1}} \Lambda_n(x') \left(k_0^2 + \frac{\partial^2}{\partial x'^2} \right) H_0^{(2)}(k_0 |x - x'|) dx' dx \quad (10.2.48)$$

$$V_m = \int_{x_{m-1}}^{x_{m+1}} \Lambda_m(x) E_x^{\text{inc}}(x) dx. \quad (10.2.49)$$

Using integration by parts, we can transfer the derivatives on $H_0^{(2)}$ to one on Λ_n and another on Λ_m , resulting in

$$Z_{mn} = \frac{Z_0}{4k_0} \int_{x_{m-1}}^{x_{m+1}} \int_{x_{n-1}}^{x_{n+1}} \left(k_0^2 \Lambda_m \Lambda_n - \frac{d\Lambda_m}{dx} \frac{d\Lambda_n}{dx'} \right) H_0^{(2)}(k_0 |x - x'|) dx' dx \quad (10.2.50)$$

which has a less singular integrand and can be evaluated more accurately.

10.2.4 Scattering by a Homogeneous Dielectric Cylinder

If the object is a penetrable, homogeneous dielectric cylinder, the field inside the object satisfies the Helmholtz equation

$$\nabla^2 \phi(\rho) + k_i^2 \phi(\rho) = 0 \quad \rho \in \Omega_o \quad (10.2.51)$$

where $k_i = k_0 \sqrt{\mu_r \epsilon_r}$ and μ_r and ϵ_r are the relative permeability and permittivity of the dielectric cylinder. Multiplying this equation by the Green's function

$$G_i(\rho, \rho') = \frac{1}{4j} H_0^{(2)}(k_i |\rho - \rho'|) \quad (10.2.52)$$

which satisfies the Helmholtz equation

$$\nabla^2 G_i(\rho, \rho') + k_i^2 G_i(\rho, \rho') = -\delta(\rho - \rho') \quad (10.2.53)$$

and integrating over Ω_o , after some manipulations we obtain

$$\oint_{\Gamma_o} \left[G_i(\rho, \rho') \frac{\partial \phi(\rho')}{\partial n'} - \phi(\rho') \frac{\partial G_i(\rho, \rho')}{\partial n'} \right] d\Gamma' = \begin{cases} 0 & \rho \in \Omega_\infty \\ \phi(\rho) & \rho \in \Omega_o \end{cases} \quad (10.2.54)$$

which relates the interior field to the field and its normal derivative on the boundary. Applying this to Γ_o , we obtain

$$\oint_{\Gamma_o} \left[G_i(\rho, \rho') \frac{\partial \phi(\rho')}{\partial n'} - \phi(\rho') \frac{\partial G_i(\rho, \rho')}{\partial n'} \right] d\Gamma' = \frac{1}{2} \phi(\rho) \quad \rho \in \Gamma_o. \quad (10.2.55)$$

This equation, together with Equation 10.2.17, provides a complete system for solving for ϕ and $\partial \phi / \partial n$ on the boundary.

Now let us specialize to the TM and TE polarizations. For TM polarization, $\phi = E_z$. Equation 10.2.17 becomes

$$\frac{1}{2} E_z(\rho) - \oint_{\Gamma_o} \left[E_z(\rho') \frac{\partial G_0(\rho, \rho')}{\partial n'} - jk_0 Z_0 G_0(\rho, \rho') H_t(\rho') \right] d\Gamma' = E_z^{\text{inc}}(\rho) \quad \rho \in \Gamma_o \quad (10.2.56)$$

and Equation 10.2.55 becomes

$$\frac{1}{2} E_z(\rho) + \oint_{\Gamma_o} \left[E_z(\rho') \frac{\partial G_i(\rho, \rho')}{\partial n'} - jk_0 Z_0 \mu_r G_i(\rho, \rho') H_t(\rho') \right] d\Gamma' = 0 \quad \rho \in \Gamma_o. \quad (10.2.57)$$

Because of the continuity of the tangential components of the electric and magnetic fields, E_z and H_t in Equation 10.2.56 are the same as their counterparts in Equation 10.2.57; hence, Equations 10.2.56 and 10.2.57 can be solved together for E_z and H_t on Γ_o . For TE polarization, $\varphi = H_z$, Equation 10.2.17 becomes

$$\frac{1}{2} H_z(\rho) - \oint_{\Gamma_o} \left[H_z(\rho') \frac{\partial G_0(\rho, \rho')}{\partial n'} + jk_0 Y_0 G_0(\rho, \rho') E_t(\rho') \right] d\Gamma' = H_z^{\text{inc}}(\rho) \quad \rho \in \Gamma_o \quad (10.2.58)$$

and Equation 10.2.55 becomes

$$\frac{1}{2} H_z(\rho) + \oint_{\Gamma_o} \left[H_z(\rho') \frac{\partial G_i(\rho, \rho')}{\partial n'} + jk_0 Y_0 \epsilon_r G_i(\rho, \rho') E_t(\rho') \right] d\Gamma' = 0 \quad \rho \in \Gamma_o \quad (10.2.59)$$

where $Y_0 = 1/Z_0$. Because of the continuity of the tangential components of the electric and magnetic fields, H_z and E_t in Equation 10.2.58 are the same as their counterparts in Equation 10.2.59; hence, Equations 10.2.58 and 10.2.59 can be solved together for H_z and E_t on Γ_o . The moment-method solution using the pulse basis functions and point matching is straightforward and is left for the reader as an exercise.

10.3 THREE-DIMENSIONAL ANALYSIS

The basic methodology for the two-dimensional analysis can be extended for the analysis of three-dimensional vector fields. In this section we first derive general integral equations and then consider a variety of specific applications. Note that besides the approach presented below, which is based on Green's theorems, another approach to formulating integral equations is to employ the equivalence principle discussed in Chapter 3. As it will be seen, the two approaches result in identical integral equations.

10.3.1 Formulation of Integral Equations

Consider the problem of electromagnetic fields (\mathbf{E} , \mathbf{H}) produced by an electric current source of density \mathbf{J}_i in the presence of an arbitrarily shaped object in free space, as illustrated in Figure 10.9. The \mathbf{E} and \mathbf{H} satisfy the vector wave equation

$$\nabla \times \nabla \times \mathbf{E}(\mathbf{r}) - k_0^2 \mathbf{E}(\mathbf{r}) = -jk_0 Z_0 \mathbf{J}_i(\mathbf{r}) \quad \mathbf{r} \in V_\infty \quad (10.3.1)$$

$$\nabla \times \nabla \times \mathbf{H}(\mathbf{r}) - k_0^2 \mathbf{H}(\mathbf{r}) = \nabla \times \mathbf{J}_i(\mathbf{r}) \quad \mathbf{r} \in V_\infty \quad (10.3.2)$$

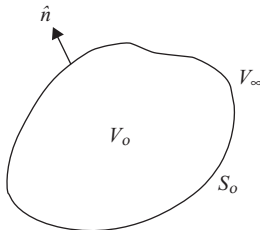


Figure 10.9 Three-dimensional object in free space.

where V_∞ denotes the exterior region, and the Sommerfeld radiation condition

$$r \left[\nabla \times \begin{pmatrix} \mathbf{E} \\ \mathbf{H} \end{pmatrix} + jk_0 \hat{r} \times \begin{pmatrix} \mathbf{E} \\ \mathbf{H} \end{pmatrix} \right] = 0 \quad r \rightarrow \infty. \quad (10.3.3)$$

To derive the integral equations for both \mathbf{E} and \mathbf{H} , we introduce the three-dimensional Green's function G_0 that satisfies the scalar Helmholtz equation

$$\nabla^2 G_0(\mathbf{r}, \mathbf{r}') + k_0^2 G_0(\mathbf{r}, \mathbf{r}') = -\delta(\mathbf{r} - \mathbf{r}') \quad (10.3.4)$$

and the radiation condition

$$r \left[\frac{\partial G_0(\mathbf{r}, \mathbf{r}')}{\partial r} + jk_0 G_0(\mathbf{r}, \mathbf{r}') \right] = 0 \quad r \rightarrow \infty. \quad (10.3.5)$$

The solution to Equations 10.3.4 and 10.3.5 has a well-known form as

$$G_0(\mathbf{r}, \mathbf{r}') = \frac{e^{-jk_0|\mathbf{r}-\mathbf{r}'|}}{4\pi |\mathbf{r}-\mathbf{r}'|}. \quad (10.3.6)$$

Next we make use of the scalar–vector Green's theorem

$$\begin{aligned} & \iiint_V [b(\nabla \times \nabla \times \mathbf{a}) + \mathbf{a} \nabla^2 b + (\nabla \cdot \mathbf{a}) \nabla b] dV \\ &= \oint_{S_\infty} [(\hat{n} \cdot \mathbf{a}) \nabla b + (\hat{n} \times \mathbf{a}) \times \nabla b + (\hat{n} \times \nabla \times \mathbf{a}) b] dS \end{aligned} \quad (10.3.7)$$

by letting $V = V_\infty$, $\mathbf{a} = \mathbf{E}$, and $b = G_0$ to find

$$\begin{aligned} & \iiint_{V_\infty} [G_0(\nabla \times \nabla \times \mathbf{E}) + \mathbf{E} \nabla^2 G_0 + (\nabla \cdot \mathbf{E}) \nabla G_0] dV \\ &= \oint_{S_\infty} [(\hat{r} \cdot \mathbf{E}) \nabla G_0 + (\hat{r} \times \mathbf{E}) \times \nabla G_0 + (\hat{r} \times \nabla \times \mathbf{E}) G_0] dS \\ &\quad - \oint_{S_o} [(\hat{n} \cdot \mathbf{E}) \nabla G_0 + (\hat{n} \times \mathbf{E}) \times \nabla G_0 + (\hat{n} \times \nabla \times \mathbf{E}) G_0] dS. \end{aligned} \quad (10.3.8)$$

By making use of Equations 10.3.1 and 10.3.4, the left-hand side of Equation 10.3.8 becomes

$$\begin{aligned} & \iiint_{V_\infty} \left[-jk_0 Z_0 \mathbf{J}_i G_0 - \mathbf{E} \delta(\mathbf{r} - \mathbf{r}') + \frac{jZ_0}{k_0} (\nabla \cdot \mathbf{J}_i) \nabla G_0 \right] dV \\ &= -jk_0 Z_0 \iiint_{V_s} \left[\mathbf{J}_i G_0 - \frac{1}{k_0^2} (\nabla \cdot \mathbf{J}_i) \nabla G_0 \right] dV - \begin{cases} \mathbf{E}(\mathbf{r}') & \mathbf{r}' \in V_\infty \\ 0 & \mathbf{r}' \in V_o \end{cases} \quad (10.3.9) \end{aligned}$$

where V_s denotes the volume of the source where $\mathbf{J}_i \neq 0$. Using the radiation conditions in Equations 10.3.3 and 10.3.5, we can show that the integrand in the first integral on the right-hand side of Equation 10.3.8 vanishes. As a result, Equation 10.3.8 becomes

$$\begin{aligned} & \oint\oint_{S_o} \left[(\hat{n} \cdot \mathbf{E}) \nabla G + (\hat{n} \times \mathbf{E}) \times \nabla G_0 + (\hat{n} \times \nabla \times \mathbf{E}) G_0 \right] dS \\ & - jk_0 Z_0 \iiint_{V_s} \left[\mathbf{J}_i G_0 - \frac{1}{k_0^2} (\nabla \cdot \mathbf{J}_i) \nabla G_0 \right] dV = \begin{cases} \mathbf{E}(\mathbf{r}') & \mathbf{r}' \in V_\infty \\ 0 & \mathbf{r}' \in V_o \end{cases} \quad (10.3.10) \end{aligned}$$

which, after switching the primed and unprimed coordinates, can also be written as

$$\begin{aligned} & \oint\oint_{S_o} \left[(\hat{n}' \cdot \mathbf{E}) \nabla' G_0 + (\hat{n}' \times \mathbf{E}) \times \nabla' G_0 - jk_0 Z_0 (\hat{n}' \times \mathbf{H}) G_0 \right] dS' \\ & - jk_0 Z_0 \iiint_{V_s} \left[\mathbf{J}_i G_0 - \frac{1}{k_0^2} (\nabla' \cdot \mathbf{J}_i) \nabla' G_0 \right] dV' = \begin{cases} \mathbf{E}(\mathbf{r}) & \mathbf{r} \in V_\infty \\ 0 & \mathbf{r} \in V_o \end{cases} \quad (10.3.11) \end{aligned}$$

Note that in the absence of the object, Equation 10.3.11 becomes

$$\mathbf{E}(\mathbf{r}) = -jk_0 Z_0 \iiint_{V_s} \left[\mathbf{J}_i G_0 - \frac{1}{k_0^2} (\nabla' \cdot \mathbf{J}_i) \nabla' G_0 \right] dV' \quad (10.3.12)$$

which is defined as the incident field and denoted as \mathbf{E}^{inc} . Hence, Equation 10.3.11 can also be written as

$$\mathbf{E}^{inc}(\mathbf{r}) - \oint\oint_{S_o} \left[(\hat{n}' \cdot \mathbf{E}) \nabla G_0 + (\hat{n}' \times \mathbf{E}) \times \nabla G_0 + jk_0 Z_0 (\hat{n}' \times \mathbf{H}) G_0 \right] dS' = \begin{cases} \mathbf{E}(\mathbf{r}) & \mathbf{r} \in V_\infty \\ 0 & \mathbf{r} \in V_o \end{cases} \quad (10.3.13)$$

where we used the fact that $\nabla' G_0 = -\nabla G_0$. Similarly, if we let $\mathbf{a} = \mathbf{H}$, we obtain

$$\mathbf{H}^{inc}(\mathbf{r}) - \oint\oint_{S_o} \left[(\hat{n}' \cdot \mathbf{H}) \nabla G_0 + (\hat{n}' \times \mathbf{H}) \times \nabla G_0 - jk_0 Y_0 (\hat{n}' \times \mathbf{E}) G_0 \right] dS' = \begin{cases} \mathbf{H}(\mathbf{r}) & \mathbf{r} \in V_\infty \\ 0 & \mathbf{r} \in V_o \end{cases} \quad (10.3.14)$$

where

$$\mathbf{H}^{inc}(\mathbf{r}) = \iiint_{V_s} \mathbf{J}_i \times \nabla' G_0 dV'. \quad (10.3.15)$$

Both Equations 10.3.13 and 10.3.14 contain the undesired normal component of the field on surface S_o . However, by using the surface vector analysis, it can be shown that

$$\hat{n}' \cdot \mathbf{E} = \frac{jZ_0}{k_0} \nabla' \cdot (\hat{n}' \times \mathbf{H}) \quad (10.3.16)$$

$$\hat{n}' \cdot \mathbf{H} = \frac{Y_0}{jk_0} \nabla' \cdot (\hat{n}' \times \mathbf{E}). \quad (10.3.17)$$

Substituting these into Equations 10.3.13 and 10.3.14 finally yields

$$\begin{aligned} \mathbf{E}^{\text{inc}}(\mathbf{r}) - \iint_{S_o} & \left[\frac{jZ_0}{k_0} \nabla' \cdot (\hat{n}' \times \mathbf{H}) \nabla G_0 + (\hat{n}' \times \mathbf{E}) \times \nabla G_0 + jk_0 Z_0 (\hat{n}' \times \mathbf{H}) G_0 \right] dS' \\ &= \begin{cases} \mathbf{E}(\mathbf{r}) & \mathbf{r} \in V_\infty \\ 0 & \mathbf{r} \in V_o \end{cases} \end{aligned} \quad (10.3.18)$$

$$\begin{aligned} \mathbf{H}^{\text{inc}}(\mathbf{r}) - \iint_{S_o} & \left[\frac{Y_0}{jk_0} \nabla' \cdot (\hat{n}' \times \mathbf{E}) \nabla G_0 + (\hat{n}' \times \mathbf{H}) \times \nabla G_0 - jk_0 Y_0 (\hat{n}' \times \mathbf{E}) G_0 \right] dS' \\ &= \begin{cases} \mathbf{H}(\mathbf{r}) & \mathbf{r} \in V_\infty \\ 0 & \mathbf{r} \in V_o. \end{cases} \end{aligned} \quad (10.3.19)$$

To write these in a compact form, we define the operators

$$\mathcal{L}(\mathbf{X}) = jk_0 \iint_{S_o} \left[\mathbf{X}(\mathbf{r}') G_0(\mathbf{r}, \mathbf{r}') + \frac{1}{k_0^2} \nabla' \cdot \mathbf{X}(\mathbf{r}') \nabla G_0(\mathbf{r}, \mathbf{r}') \right] dS' \quad (10.3.20)$$

$$\mathcal{K}(\mathbf{X}) = \iint_{S_o} \mathbf{X}(\mathbf{r}') \times \nabla G_0(\mathbf{r}, \mathbf{r}') dS' \quad (10.3.21)$$

and introduce the equivalent surface currents

$$\bar{\mathbf{J}}_s(\mathbf{r}') = \hat{n}' \times \bar{\mathbf{H}}(\mathbf{r}') = Z_0 \hat{n}' \times \mathbf{H}(\mathbf{r}'), \quad \mathbf{M}_s(\mathbf{r}') = \mathbf{E}(\mathbf{r}') \times \hat{n}'. \quad (10.3.22)$$

As a result, Equations 10.3.18 and 10.3.19 can be written as

$$\mathbf{E}^{\text{inc}}(\mathbf{r}) - \mathcal{L}(\bar{\mathbf{J}}_s) + \mathcal{K}(\mathbf{M}_s) = \begin{cases} \mathbf{E}(\mathbf{r}) & \mathbf{r} \in V_\infty \\ 0 & \mathbf{r} \in V_o \end{cases} \quad (10.3.23)$$

$$\bar{\mathbf{H}}^{\text{inc}}(\mathbf{r}) - \mathcal{L}(\mathbf{M}_s) - \mathcal{K}(\bar{\mathbf{J}}_s) = \begin{cases} \bar{\mathbf{H}}(\mathbf{r}) & \mathbf{r} \in V_\infty \\ 0 & \mathbf{r} \in V_o. \end{cases} \quad (10.3.24)$$

Note that we scaled the electric current density ($\bar{\mathbf{J}}_s = Z_0 \mathbf{J}_s$) and the magnetic field intensity ($\bar{\mathbf{H}} = Z_0 \mathbf{H}$) simply to make the equations more compact. In the absence of the exterior source (i.e., the incident field), these two equations are identical to Equations 3.4.5 and 3.4.6, which were derived using the surface equivalence principle.

The two equations above provide the foundation to derive integral equations for $\bar{\mathbf{J}}_s$ and \mathbf{M}_s , which can be obtained by taking the cross-product with \hat{n} and letting \mathbf{r} approach S_o . However, when \mathbf{r} approaches S_o , the integrals in Equations 10.3.20 and 10.3.21 contain a singular point at $\mathbf{r} = \mathbf{r}'$. To evaluate the singular integrals, we can deform S_o as shown in Figure 10.10a or 10.10b so that S_o consists of two parts: One is S_o minus a vanishingly

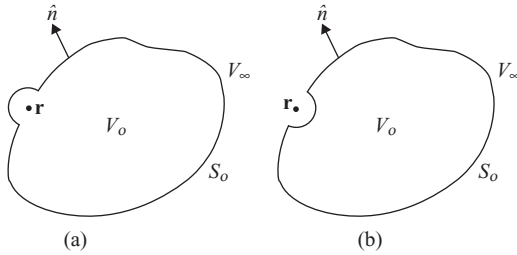


Figure 10.10 (a) Deformed S_o such that \mathbf{r} resides inside V_o . (b) Deformed S_o such that \mathbf{r} resides outside V_o .

small disc centered at \mathbf{r} , and the other is a small hemispherical surface with a vanishingly small radius ε . Hence,

$$\mathcal{L}(\mathbf{X}) = \lim_{\varepsilon \rightarrow 0} \left\{ \iint_{S_o - \sigma_\varepsilon} [\bullet] dS' + \int_0^{2\pi} \int_0^{\pi/2} [\bullet] \varepsilon^2 \sin \theta d\theta d\phi \right\} \quad (10.3.25)$$

$$\mathcal{K}(\mathbf{X}) = \lim_{\varepsilon \rightarrow 0} \left\{ \iint_{S_o - \sigma_\varepsilon} [\bullet] dS' + \int_0^{2\pi} \int_0^{\pi/2} [\bullet] \varepsilon^2 \sin \theta d\theta d\phi \right\}. \quad (10.3.26)$$

It can be shown easily that the singular term has no contribution to the evaluation of $\hat{n} \times \mathcal{L}(\mathbf{X})$. However, the singular term in $\hat{n} \times \mathcal{K}(\mathbf{X})$ does not vanish, and to evaluate it, we let $\mathbf{X} = \hat{n} \times \mathbf{Y}$ and consider

$$\begin{aligned} \hat{n} \times \int_0^{2\pi} \int_0^{\pi/2} \mathbf{X} \times \nabla G_0 \varepsilon^2 \sin \theta d\theta d\phi &= \pm \hat{n} \times \int_0^{2\pi} \int_0^{\pi/2} (\hat{n}' \times \mathbf{Y}) \times \hat{r}' \frac{e^{-jk_0\varepsilon}}{4\pi} \sin \theta d\theta d\phi \\ &= \pm \hat{n} \times \int_0^{2\pi} \int_0^{\pi/2} (\hat{n}' \cdot \hat{r}') \mathbf{Y} \frac{e^{-jk_0\varepsilon}}{4\pi} \sin \theta d\theta d\phi \\ &= \pm \hat{n} \times \int_0^{2\pi} \int_0^{\pi/2} \mathbf{Y} \frac{e^{-jk_0\varepsilon}}{4\pi} \sin \theta d\theta d\phi \\ &= \pm \frac{1}{2} \mathbf{X} \quad \varepsilon \rightarrow 0 \end{aligned} \quad (10.3.27)$$

where \hat{r}' is the unit vector normal to the hemispherical surface. The “+” sign corresponds to the deformation in Figure 10.10a, whereas the “−” sign corresponds to the deformation in Figure 10.10b. Hence, $\hat{n} \times \mathcal{K}(\mathbf{X})$ can be written as

$$\hat{n} \times \mathcal{K}(\mathbf{X}) = \hat{n} \times \lim_{\varepsilon \rightarrow 0} \iint_{S_o - \sigma_\varepsilon} \mathbf{X} \times \nabla G_0 dS' \pm \frac{1}{2} \mathbf{X} = \hat{n} \times \tilde{\mathcal{K}}(\mathbf{X}) \pm \frac{1}{2} \mathbf{X} \quad (10.3.28)$$

where $\tilde{\mathcal{K}}(\mathbf{X})$ is the same integral as in Equation 10.3.21, except that the singular point $\mathbf{r} = \mathbf{r}'$ is now removed.

Now, by taking the cross-product of Equations 10.3.23 and 10.3.24 with \hat{n} , letting \mathbf{r} approach S_o , and using Equation 10.3.28, we obtain

$$\frac{1}{2} \mathbf{M}_s - \hat{n} \times \mathcal{L}(\bar{\mathbf{J}}_s) + \hat{n} \times \tilde{\mathcal{K}}(\mathbf{M}_s) = -\hat{n} \times \mathbf{E}^{\text{inc}}(\mathbf{r}) \quad \mathbf{r} \in S_o \quad (10.3.29)$$

$$\frac{1}{2} \bar{\mathbf{J}}_s + \hat{n} \times \mathcal{L}(\mathbf{M}_s) + \hat{n} \times \tilde{\mathcal{K}}(\bar{\mathbf{J}}_s) = \hat{n} \times \bar{\mathbf{H}}^{\text{inc}}(\mathbf{r}) \quad \mathbf{r} \in S_o. \quad (10.3.30)$$

Equation 10.3.29 is the EFIE and Equation 10.3.30 is the MFIE in vector form for three-dimensional fields [11]. When applied to specific objects, they can be solved for $\bar{\mathbf{J}}_s$ and \mathbf{M}_s , from which the electric and magnetic fields everywhere in V_∞ can be evaluated using Equations 10.3.23 and 10.3.24 (see Problem 10.17).

10.3.2 Scattering and Radiation by a Conducting Wire

If the object is a conducting wire, because of the boundary condition, $\mathbf{M}_s = \mathbf{E} \times \hat{n} = 0$. Furthermore, if the wire is thin, we can neglect the transverse component of the current on the wire and assume that the longitudinal component is uniformly distributed over the periphery of the wire. Under these assumptions, Equation 10.3.29 becomes

$$jk_0 Z_0 \int_C \left[\hat{l} \cdot \hat{l}' I(\mathbf{r}') G_0(\mathbf{r}, \mathbf{r}') + \frac{1}{k_0^2} \frac{dI(\mathbf{r}')}{dl'} \frac{dG_0(\mathbf{r}, \mathbf{r}')}{dl} \right] dl' = \hat{l} \cdot \mathbf{E}^{\text{inc}}(\mathbf{r}) \quad \mathbf{r} \in C \quad (10.3.31)$$

where C denotes the path of the wire, \hat{l} denotes the tangential unit vector along the wire, and I is the electric current on the wire. To seek its moment-method solution, we first divide the wire into short segments no longer than one-fifth of a wavelength. Since Equation 10.3.31 involves the differentiation of the current, for an accurate solution we can choose basis functions that can be differentiated at least once to expand the current. The most convenient choice is triangular basis functions, shown in Figure 10.11. The expansion of the current can then be written as

$$I(\mathbf{r}') = \sum_{n=1}^{N-1} \Lambda_n(\mathbf{r}') I_n \quad (10.3.32)$$

where Λ_n denotes the triangular basis functions spanning the $(n - 1)$ th and n th segments, similar to that defined in Equation 10.2.46. Note that the expansion in Equation 10.3.32 ensures that at the ends of the wire, the current vanishes. Substituting this expansion into Equation 10.3.31, we obtain

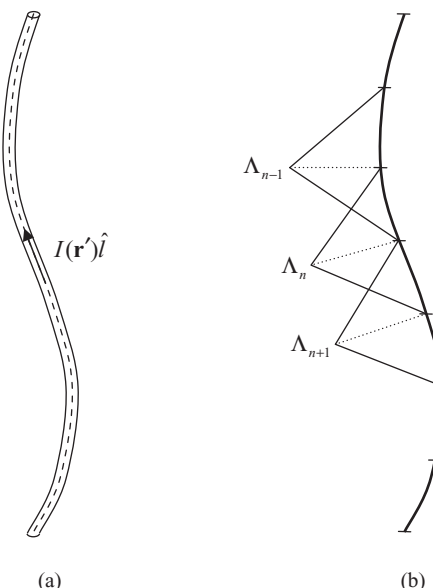


Figure 10.11 (a) A conducting wire carrying current I . (b) Discretization of a wire and the triangular basis functions Λ_n .

$$jk_0 Z_0 \sum_{n=1}^{N-1} I_n \int_C \left[\hat{l} \cdot \hat{l}'_n \Lambda_n(\mathbf{r}') G_0(\mathbf{r}, \mathbf{r}') + \frac{1}{k_0^2} \frac{d\Lambda_n(\mathbf{r}')}{dl'} \frac{dG_0(\mathbf{r}, \mathbf{r}')}{dl} \right] dl' = \hat{l} \cdot \mathbf{E}^{\text{inc}}(\mathbf{r}) \quad \mathbf{r} \in C. \quad (10.3.33)$$

Next we choose a set of testing functions to convert this equation into a matrix equation. Since the integrand contains the derivative of G_0 , we can choose testing functions that can also be differentiated at least once so that we can transfer the derivative away from G_0 to the testing function. A good choice is Λ_m , which results in Galerkin's formulation. With this choice, we obtain

$$\sum_{n=1}^{N-1} Z_{mn} I_n = V_m \quad m = 1, 2, \dots, N-1 \quad (10.3.34)$$

where

$$Z_{mn} = jk_0 Z_0 \int_C \Lambda_m(\mathbf{r}) \hat{l}_m \cdot \int_C \hat{l}'_n \Lambda_n(\mathbf{r}') G_0(\mathbf{r}, \mathbf{r}') dl' dl + \frac{jZ_0}{k_0} \int_C \Lambda_m(\mathbf{r}) \int_C \frac{d\Lambda_n(\mathbf{r}')}{dl'} \frac{dG_0(\mathbf{r}, \mathbf{r}')}{dl} dl' dl \quad (10.3.35)$$

$$V_m = \int_C \Lambda_m(\mathbf{r}) \hat{l}_m \cdot \mathbf{E}^{\text{inc}}(\mathbf{r}) dl. \quad (10.3.36)$$

By using integration by parts, Equation 10.3.35 can also be written as

$$Z_{mn} = jk_0 Z_0 \int_C \Lambda_m(\mathbf{r}) \hat{l}_m \cdot \int_C \hat{l}'_n \Lambda_n(\mathbf{r}') G_0(\mathbf{r}, \mathbf{r}') dl' dl - \frac{jZ_0}{k_0} \int_C \frac{d\Lambda_m(\mathbf{r})}{dl} \int_C \frac{d\Lambda_n(\mathbf{r}')}{dl'} G_0(\mathbf{r}, \mathbf{r}') dl' dl \quad (10.3.37)$$

which has a less singular integrand and thus can be evaluated more accurately. The integrals in Equation 10.3.37 can be evaluated effectively using numerical integration when Λ_m and Λ_n do not overlap. When they overlap, we can divide each segment into several smaller subsegments and approximate Λ_m and Λ_n within each subsegment as a constant in the first term. When the two subsegments do not overlap, the integrals can again be evaluated by numerical integration. When they overlap, we have to evaluate the integral

$$\psi = \int_{\Delta l} \int_{\Delta l} G_0(\mathbf{r}, \mathbf{r}') dl' dl = \frac{1}{4\pi} \int_{\Delta l} \int_{\Delta l} \frac{e^{-jk_0 R}}{R} dl' dl \quad (10.3.38)$$

where Δl denotes a short segment and $R = |\mathbf{r} - \mathbf{r}'| = \sqrt{a^2 + (l - l')^2}$, with a being the radius of the wire. Here we used the so-called *thin-wire approximation*, which places the testing function on the axis of the wire and the basis function on the surface of the wire to avoid the singularity in G_0 . Expanding the exponential in Equation 10.3.38 into a Maclaurin series, we obtain

$$\psi = \frac{1}{4\pi} \int_{\Delta l} \int_{\Delta l} \left(\frac{1}{R} - jk_0 - \frac{k_0^2}{2} R + \dots \right) dl' dl. \quad (10.3.39)$$

By keeping only the first two terms, Equation 10.3.39 can be evaluated to give

$$\psi = \frac{\Delta l}{2\pi} \left[\ln \left(\frac{\Delta l}{a} + \sqrt{1 + \frac{(\Delta l)^2}{a^2}} \right) - \sqrt{1 + \frac{a^2}{(\Delta l)^2}} + \frac{a}{\Delta l} \right] - \frac{jk_0}{4\pi} (\Delta l)^2 \quad (10.3.40)$$

which can be simplified to

$$\psi = \frac{\Delta l}{2\pi} \left(\ln \frac{2\Delta l}{a} - 1 \right) - \frac{jk_0}{4\pi} (\Delta l)^2 \quad (10.3.41)$$

when $\Delta l \gg a$.

The formulation here can also be used to analyze wire antennas. In this case, we can simply set $V_m = V_0$ at the feed point and $V_m = 0$ elsewhere, where V_0 denotes the voltage at the feed point. This simple model is called the delta-gap source, illustrated in Figure 10.12a, and the input impedance of the antenna can be calculated as

$$Z_{\text{in}} = \frac{V_0}{I_m} \quad (10.3.42)$$

where I_m denotes the current at the feed point. Alternatively, we can model the voltage source as a magnetic frill current, shown in Figure 10.12b. In the absence of the wire antenna, the field produced by this magnetic frill current can be evaluated, which can then be used as the incident field for the calculation of the excitation vector in Equation 10.3.36. The input admittance can be calculated using a more accurate variational formula [12],

$$Y_{\text{in}} = -\frac{\langle \mathbf{M}_a, \mathbf{H}_a \rangle}{V_0^2} - \frac{\langle \mathbf{M}_a, \mathbf{H}_s \rangle}{V_0^2} \quad (10.3.43)$$

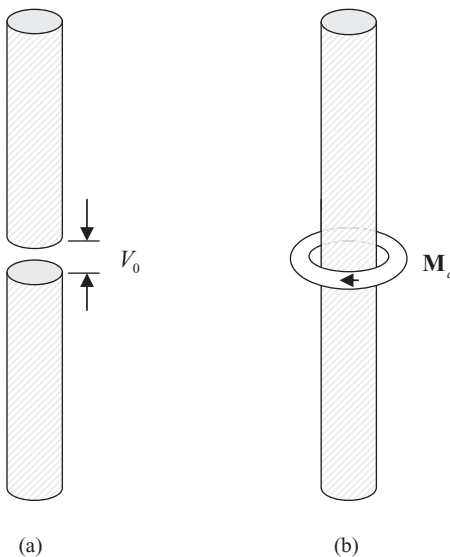


Figure 10.12 (a) Delta-gap voltage source.
(b) Magnetic frill current source.

where \mathbf{M}_a denotes the surface current density of the magnetic frill, \mathbf{H}_a denotes the magnetic field generated by the magnetic frill in the absence of the antenna, and \mathbf{H}_s denotes the magnetic field generated by the induced current on the antenna.

The moment method described above has been applied to the analysis of a 2.0-m-long and 1.0-cm-thick wire antenna with a 90° bend at the feed point, whose geometry is shown in Figure 10.13. For the numerical simulation, the wire antenna was divided into 99 segments and the input impedance was calculated using Equation 10.3.42. The admittance is plotted in Figure 10.14 as a function of frequency, showing resonances when the length of the wire is an odd multiple of one-half of a wavelength. The first resonance is expected to occur near $f_o = 75$ MHz (the theoretical value for an infinitely thin dipole antenna), and the simulation at this frequency yielded an input impedance of

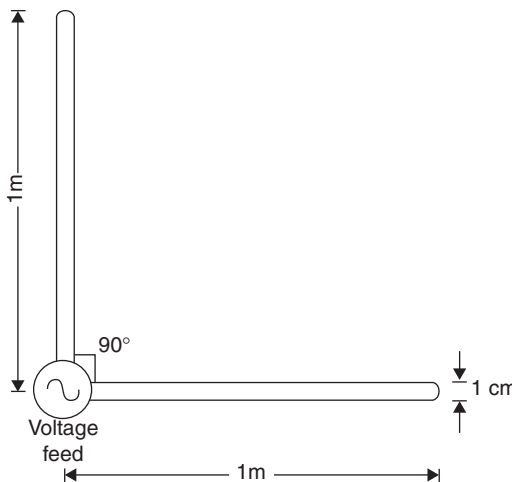


Figure 10.13 Geometry of a 2.0-m wire antenna with a 90° bend at the feed point.

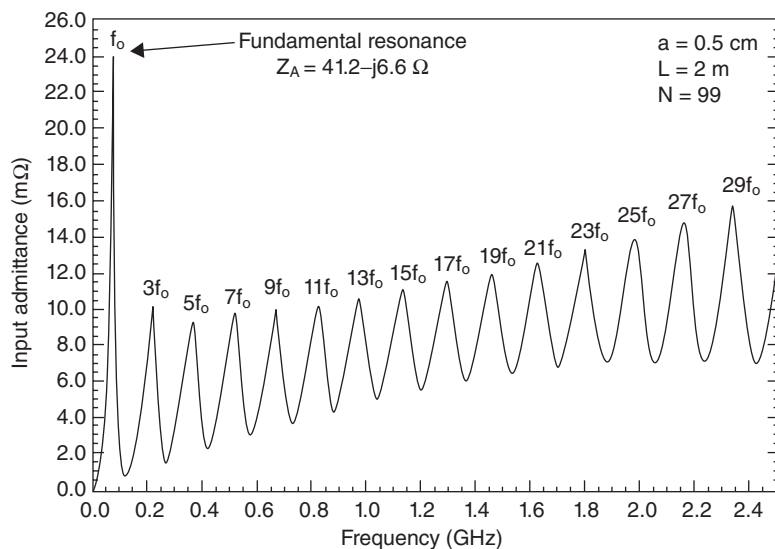


Figure 10.14 Input admittance versus frequency for a 2.0-m wire antenna with a 90° bend at the feed point.

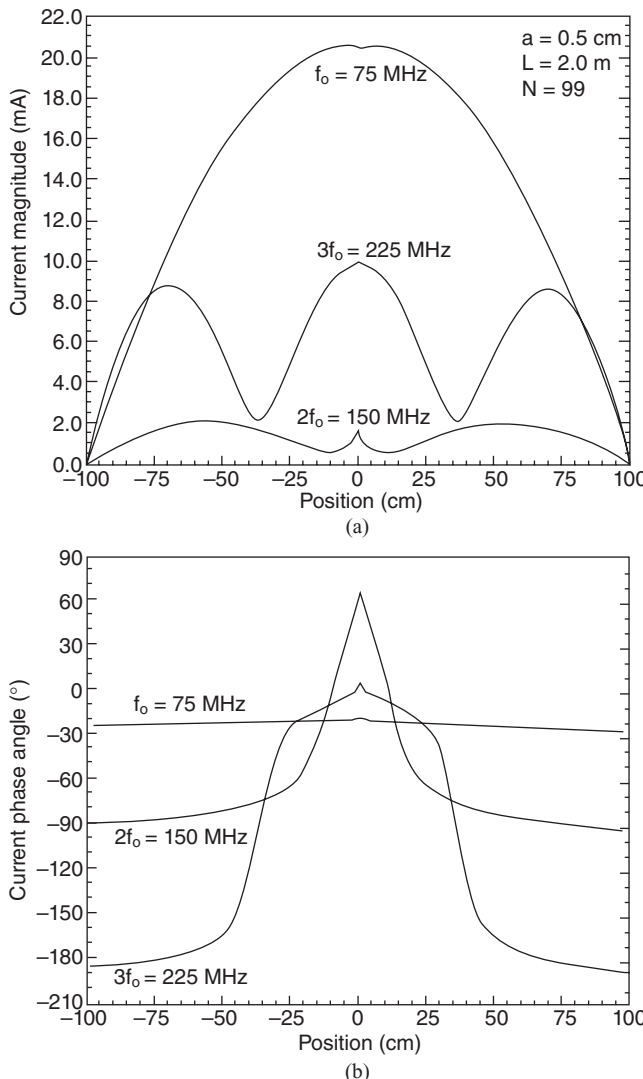


Figure 10.15 Current distributions on the bent wire antenna at 75, 150, and 225 MHz.
 (a) Magnitude. (b) Phase.

$Z_{in} = 41.2 - j6.6 \Omega$. The current distributions at f_o , as well as at $2f_o$ and $3f_o$, are given in Figure 10.15, showing a significantly larger magnitude when the frequency is close to resonance. A more refined frequency sweep found that the first resonant frequency is actually 73 MHz, which is slightly lower than 75 MHz because of the finite thickness of the wire antenna.

10.3.3 Scattering by a Conducting Body

If the object is an arbitrary, volumetric perfect electric conductor, \mathbf{E} satisfies the boundary condition

$$\hat{n} \times \mathbf{E}(\mathbf{r}) = 0 \quad \mathbf{r} \in S_o. \quad (10.3.44)$$

Hence, $\mathbf{M}_s = 0$, and Equations 10.3.29 and 10.3.30 reduce to

$$\hat{n} \times \mathcal{L}(\bar{\mathbf{J}}_s) = \hat{n} \times \mathbf{E}^{\text{inc}}(\mathbf{r}) \quad \mathbf{r} \in S_o \quad (10.3.45)$$

$$\frac{1}{2} \bar{\mathbf{J}}_s + \hat{n} \times \tilde{\mathcal{K}}(\bar{\mathbf{J}}_s) = \hat{n} \times \bar{\mathbf{H}}^{\text{inc}}(\mathbf{r}) \quad \mathbf{r} \in S_o. \quad (10.3.46)$$

Either of these two equations can be used to solve for $\bar{\mathbf{J}}_s$. However, for a given S_o , \mathcal{L} can be singular at certain frequencies when the exterior medium is lossless. Consequently, Equation 10.3.45 may give erroneous solutions at these frequencies. This is known as the *problem of interior resonance*, and the singular frequencies correspond to the resonant frequencies of a cavity formed by covering S_o with a perfect conductor and then filling its interior with the exterior medium. A similar problem occurs in Equation 10.3.46 as well. To eliminate this problem, we can combine Equations 10.3.45 and 10.3.46 to find

$$\frac{1}{2} \bar{\mathbf{J}}_s + \hat{n} \times \tilde{\mathcal{K}}(\bar{\mathbf{J}}_s) - \hat{n} \times [\hat{n} \times \mathcal{L}(\bar{\mathbf{J}}_s)] = \hat{n} \times \bar{\mathbf{H}}^{\text{inc}}(\mathbf{r}) - \hat{n} \times [\hat{n} \times \mathbf{E}^{\text{inc}}(\mathbf{r})] \quad \mathbf{r} \in S_o \quad (10.3.47)$$

which is known as the *combined-field integral equation* (CFIE) [13]. This combination results in an integral operator corresponding to that for a cavity with a resistive wall whose resonant frequencies are complex. As a result, it cannot be singular for a real frequency. Note that, in contrast to the traditional CFIE, which assigns a weighting factor to the EFIE and another weighting factor to the MFIE before their combination, the weighting factors are fixed here as $\frac{1}{2}$, or, in other words, both the EFIE and the MFIE are combined with an equal weight.

To solve Equation 10.3.47 for the surface current density, we can first divide the surface S_o into small triangular patches. We then have to formulate a set of basis functions to expand the surface current density. A popular choice is the *triangular rooftop function* [14], which is also known as the *Rao–Wilton–Glisson (RWG) function*. This function is defined over two triangular elements joined at a common edge l_n :

$$\Lambda_n(\mathbf{r}) = \begin{cases} \frac{l_n}{2A_n^+} \rho_n^+ & \mathbf{r} \in T_n^+ \\ \frac{l_n}{2A_n^-} \rho_n^- & \mathbf{r} \in T_n^- \end{cases} \quad (10.3.48)$$

where T_n^\pm denote the two triangles associated with the n th edge, A_n^\pm are the areas of triangles T_n^\pm , l_n is the length of the n th edge, and ρ_n^\pm are the vectors defined in Figure 10.16a. The vector plot of $\Lambda_n(\mathbf{r})$ is illustrated in Figure 10.16b. The most important feature of this

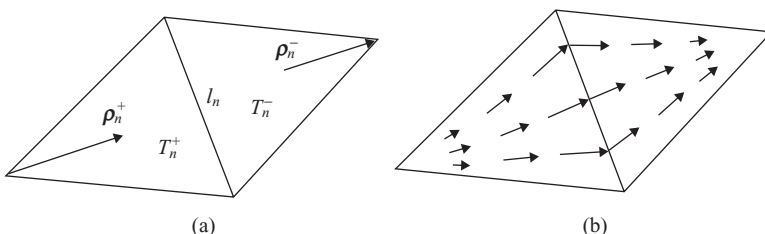


Figure 10.16 (a) Two triangles joined at a common edge. (b) Vector plot of the RWG function.

basis function is that its normal component to edge l_n is a constant (normalized to 1), whereas the normal components to other edges are zero. This feature guarantees the continuity of current flow over all edges.

Using the RWG basis functions defined in Equation 10.3.48, we can expand the surface current density as

$$\bar{\mathbf{J}}_s(\mathbf{r}) = \sum_{n=1}^N I_n \boldsymbol{\Lambda}_n(\mathbf{r}) \quad (10.3.49)$$

where N is the number of unknowns, which is the number of edges shared by two triangular patches. Using the same basis functions as the testing functions, we can convert Equation 10.3.47 into the matrix equation

$$\sum_{n=1}^N Z_{mn} I_n = V_m \quad m = 1, 2, \dots, N \quad (10.3.50)$$

in which

$$Z_{mn} = \iint_{S_o} \boldsymbol{\Lambda}_m \cdot \left[\frac{1}{2} \boldsymbol{\Lambda}_n + \hat{n} \times \tilde{\mathcal{K}}(\boldsymbol{\Lambda}_n) + \mathcal{L}(\boldsymbol{\Lambda}_n) \right] dS \quad (10.3.51)$$

$$V_m = \iint_{S_o} \boldsymbol{\Lambda}_m \cdot [\hat{n} \times \bar{\mathbf{H}}^{\text{inc}} + \mathbf{E}^{\text{inc}}] dS. \quad (10.3.52)$$

The evaluation of V_m is quite simple and can be accomplished numerically using a Gaussian quadrature, since the integrand is well behaved or non-singular. The evaluation of the double surface integrals in Z_{mn} requires more effort. When $\boldsymbol{\Lambda}_m$ and $\boldsymbol{\Lambda}_n$ do not overlap, the evaluation can be accomplished numerically using a Gaussian quadrature without any difficulty. However, when $\boldsymbol{\Lambda}_m$ and $\boldsymbol{\Lambda}_n$ overlap, the integrand can become singular. Whereas it can be shown that the integrand involving $\tilde{\mathcal{K}}$ has a singularity of $1/R$, the integrand involving \mathcal{L} has a singularity of $1/R^2$ because of the del operator on G_0 . Using the explicit expression for \mathcal{L} , we have

$$\iint_{S_o} \boldsymbol{\Lambda}_m \cdot \mathcal{L}(\boldsymbol{\Lambda}_n) dS = jk_0 \iint_{S_o} \boldsymbol{\Lambda}_m \cdot \left[\iint_{S_o} \left(\boldsymbol{\Lambda}_n G_0 + \frac{1}{k_0^2} \nabla' \cdot \boldsymbol{\Lambda}_n \nabla G_0 \right) dS' \right] dS. \quad (10.3.53)$$

However, by using the surface divergence theorem, the del operator on G_0 can be transferred away from G_0 to $\boldsymbol{\Lambda}_m$. The integral then becomes

$$\begin{aligned} \iint_{S_o} \boldsymbol{\Lambda}_m \cdot \mathcal{L}(\boldsymbol{\Lambda}_n) dS &= jk_0 \iint_{S_o} \boldsymbol{\Lambda}_m \cdot \iint_{S_o} \boldsymbol{\Lambda}_n G_0 dS' dS \\ &\quad - \frac{j}{k_0} \iint_{S_o} (\nabla \cdot \boldsymbol{\Lambda}_m) \iint_{S_o} (\nabla' \cdot \boldsymbol{\Lambda}_n) G_0 dS' dS \end{aligned} \quad (10.3.54)$$

whose integrand has a singularity of $1/R$.

To evaluate the double surface integrals with a singularity of $1/R$, the following method [15] has been found very effective. The first surface integral, say the one with respect to dS , can be evaluated using numerical integration such as a Gaussian quadrature. The remaining surface integral can then be written as

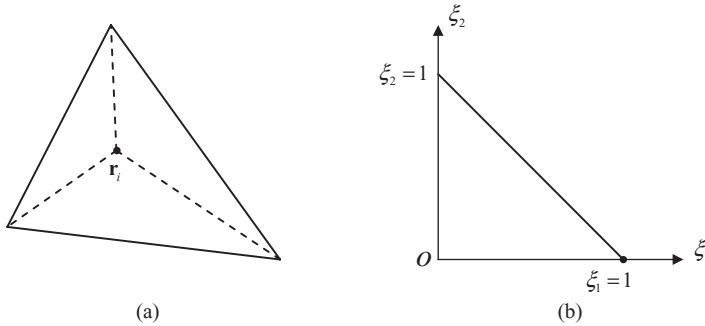


Figure 10.17 A quadrature point divides a triangle into three subtriangles. (b) Each subtriangle is mapped into the $\xi_1\xi_2$ plane as a right-angled triangle.

$$I = \iint_{\Delta} \frac{f(\mathbf{r}_i, \mathbf{r}')}{|\mathbf{r}_i - \mathbf{r}'|} dS' \quad \mathbf{r}_i \in \Delta \quad (10.3.55)$$

where \mathbf{r}_i denotes the quadrature point for the first surface integral and Δ denotes a triangular patch. To evaluate Equation 10.3.55, we first divide Δ into three subtriangles by connecting \mathbf{r}_i to the three vertices, as shown in Figure 10.17a. Hence, Equation 10.3.55 becomes

$$I = \sum_{e=1}^3 \iint_{\Delta^e} \frac{f(\mathbf{r}_i, \mathbf{r}')}{|\mathbf{r}_i - \mathbf{r}'|} dS'. \quad (10.3.56)$$

We then map each subtriangle Δ^e into a right-angled triangle in the $\xi_1\xi_2$ -plane with the singular point located at $\xi_1^e = 1$, which is illustrated in Figure 10.17b. This mapping is very straightforward even if the original subtriangle is in a curvilinear form. The integral in Equation 10.3.56 then becomes

$$I = \sum_{e=1}^3 \int_0^1 \int_0^{1-\xi_1^e} \frac{f(\xi_1^e, \xi_2^e)}{\rho} J(\xi_1^e, \xi_2^e) d\xi_2^e d\xi_1^e \quad (10.3.57)$$

where $J(\xi_1^e, \xi_2^e)$ is the Jacobian of the transformation, $f(\xi_1^e, \xi_2^e)$ is the original $f(\mathbf{r}_i, \mathbf{r}')$ expressed in the new variables, and $\rho = |\mathbf{r}_i - \mathbf{r}'|$. Now, we introduce the transformation $\xi_2^e = (1 - \xi_1^e)u$ so that Equation 10.3.57 becomes

$$I = \sum_{e=1}^3 \int_0^1 \int_0^1 \frac{f[\xi_1^e, (1 - \xi_1^e)u]}{\rho} J[\xi_1^e, (1 - \xi_1^e)u] (1 - \xi_1^e) du d\xi_1^e. \quad (10.3.58)$$

It can be shown that ρ can be written as $\rho = (1 - \xi_1^e)\sqrt{q(\xi_1^e, u, \mathbf{r}_i)}$, where q is analytic in the entire integration domain. Using this expression, Equation 10.3.58 becomes

$$I = \sum_{e=1}^3 \int_0^1 \int_0^1 \frac{f[\xi_1^e, (1 - \xi_1^e)u]}{\sqrt{q(\xi_1^e, u, \mathbf{r}_i)}} J[\xi_1^e, (1 - \xi_1^e)u] du d\xi_1^e \quad (10.3.59)$$

which is now non-singular and can be evaluated by applying the one-dimensional Gauss-Legendre quadrature to each integral. It should be pointed out that, in the actual numerical implementation, it is not necessary to find the expression for q . The Gauss-Legendre quadrature can be applied directly to Equation 10.3.58.

To give an example, consider a benchmark geometry, which is a 9.936-inch-long conducting object having the shape of an almond [16], whose triangular surface mesh is shown in Figure 10.18. The almond is placed horizontally with its longer axis aligned with the x -axis and its sharp tip pointing toward the \hat{x} -direction. Figure 10.19 shows the surface current density induced by a plane wave incident horizontally at an azimuth angle of 30°

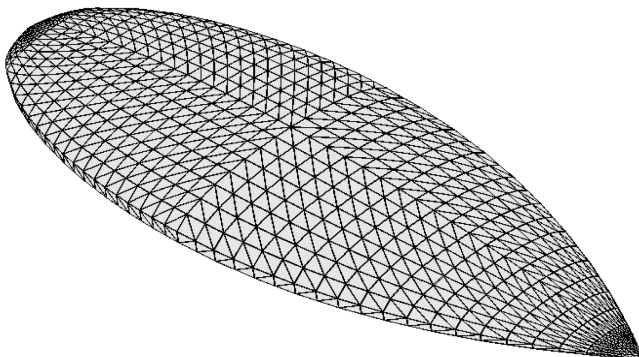
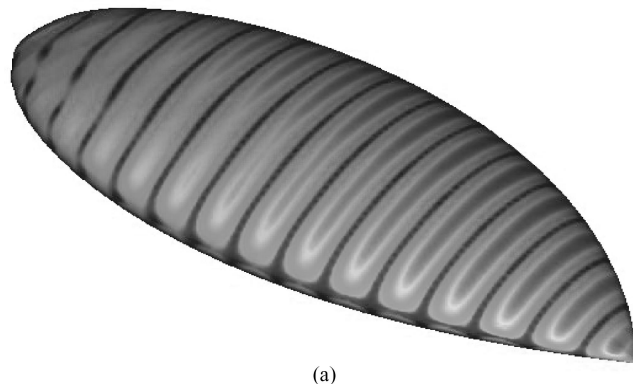
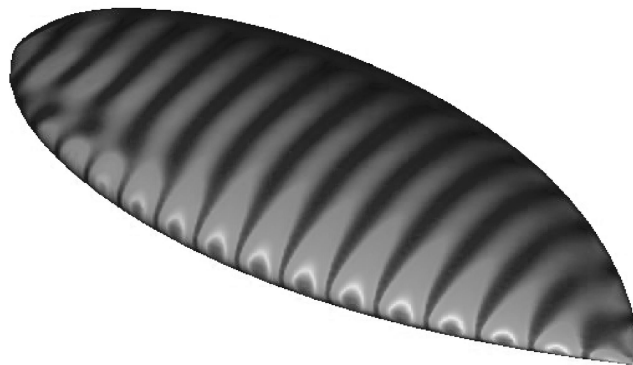


Figure 10.18 Triangular mesh for an almond.



(a)



(b)

Figure 10.19 Snapshot of the induced surface electric current density on a 9.936-inch-long conducting almond with a 10-GHz plane wave incident horizontally from an azimuth angle of 30° away from the tip. (a) Vertical polarization. (b) Horizontal polarization. (See color insert.)

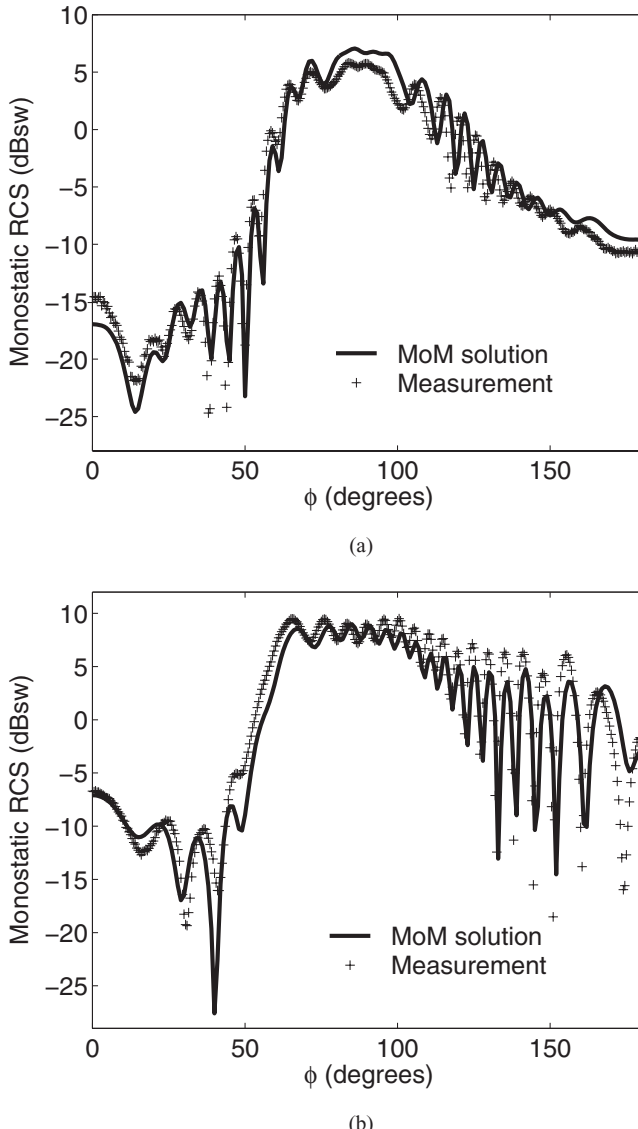


Figure 10.20 Monostatic RCS of a 9.936-inch-long conducting almond at 10GHz. (a) VV polarization. (b) HH polarization.

away from the tip at 10GHz. The monostatic radar cross-section (RCS) at 10GHz is also computed in the xy -plane for both VV and HH polarizations. The results are shown in Figure 10.20 and are compared with measured data [16]. The difference is largely due to measurement error. Note that a much denser mesh than the one shown in Figure 10.18 was used for the moment-method computation.

10.3.4 Scattering by a Homogeneous Dielectric Body

If the object is a homogeneous body, we can apply the scalar–vector Green’s theorem to the interior of the object to formulate two more integral equations:

$$\eta_i \mathcal{L}_i(\bar{\mathbf{J}}_s) - \mathcal{K}_i(\mathbf{M}_s) = \begin{cases} 0 & \mathbf{r} \in V_\infty \\ \mathbf{E}(\mathbf{r}) & \mathbf{r} \in V_o \end{cases} \quad (10.3.60)$$

$$\mathcal{L}_i(\mathbf{M}_s) + \eta_i \mathcal{K}_i(\bar{\mathbf{J}}_s) = \begin{cases} 0 & \mathbf{r} \in V_\infty \\ \eta_i \bar{\mathbf{H}}(\mathbf{r}) & \mathbf{r} \in V_o \end{cases} \quad (10.3.61)$$

where $\eta_i = \sqrt{\mu_r / \epsilon_r}$ and

$$\mathcal{L}_i(\mathbf{X}) = jk_i \oint_{S_o} \left[\mathbf{X}(\mathbf{r}') G_i(\mathbf{r}, \mathbf{r}') + \frac{1}{k_i^2} \nabla' \cdot \mathbf{X}(\mathbf{r}') \nabla G_i(\mathbf{r}, \mathbf{r}') \right] dS' \quad (10.3.62)$$

$$\mathcal{K}_i(\mathbf{X}) = \oint_{S_o} \mathbf{X}(\mathbf{r}') \times \nabla G_i(\mathbf{r}, \mathbf{r}') dS' \quad (10.3.63)$$

with $k_i = k_0 \sqrt{\mu_r \epsilon_r}$ being the wavenumber inside the object and

$$G_i(\mathbf{r}, \mathbf{r}') = \frac{e^{-jk_i |\mathbf{r} - \mathbf{r}'|}}{4\pi |\mathbf{r} - \mathbf{r}'|}. \quad (10.3.64)$$

Taking the cross-product of these with \hat{n} and letting \mathbf{r} approach S_o , we have

$$\frac{1}{2} \mathbf{M}_s + \eta_i \hat{n} \times \mathcal{L}_i(\bar{\mathbf{J}}_s) - \hat{n} \times \tilde{\mathcal{K}}_i(\mathbf{M}_s) = 0 \quad \mathbf{r} \in S_o \quad (10.3.65)$$

$$\frac{1}{2} \eta_i \bar{\mathbf{J}}_s - \hat{n} \times \mathcal{L}_i(\mathbf{M}_s) - \eta_i \hat{n} \times \tilde{\mathcal{K}}_i(\bar{\mathbf{J}}_s) = 0 \quad \mathbf{r} \in S_o. \quad (10.3.66)$$

One of these two equations can be used with one of Equations 10.3.29 and 10.3.30 to form a complete system for the solution of $\bar{\mathbf{J}}_s$ and \mathbf{M}_s . Again, to overcome the problem of interior resonance, one can combine the EFIE and MFIE to form the CFIE for the interior field:

$$\begin{aligned} & \left[\frac{1}{2} \eta_i \bar{\mathbf{J}}_s - \hat{n} \times \mathcal{L}_i(\mathbf{M}_s) - \eta_i \hat{n} \times \tilde{\mathcal{K}}_i(\bar{\mathbf{J}}_s) \right] \\ & + \hat{n} \times \left[\frac{1}{2} \mathbf{M}_s + \eta_i \hat{n} \times \mathcal{L}_i(\bar{\mathbf{J}}_s) - \hat{n} \times \tilde{\mathcal{K}}_i(\mathbf{M}_s) \right] = 0 \quad \mathbf{r} \in S_o \end{aligned} \quad (10.3.67)$$

which is necessary only if the interior medium is lossless. This CFIE can then be used together with the CFIE for the exterior field

$$\begin{aligned} & \left[\frac{1}{2} \bar{\mathbf{J}}_s + \hat{n} \times \mathcal{L}(\mathbf{M}_s) + \hat{n} \times \tilde{\mathcal{K}}(\bar{\mathbf{J}}_s) \right] + \hat{n} \times \left[\frac{1}{2} \mathbf{M}_s - \hat{n} \times \mathcal{L}(\bar{\mathbf{J}}_s) + \hat{n} \times \tilde{\mathcal{K}}(\mathbf{M}_s) \right] \\ & = \hat{n} \times \bar{\mathbf{H}}^{\text{inc}}(\mathbf{r}) - \hat{n} \times [\hat{n} \times \mathbf{E}^{\text{inc}}(\mathbf{r})] \quad \mathbf{r} \in S_o \end{aligned} \quad (10.3.68)$$

to form a complete system [17].

A better alternative to the CFIE formulation is, however, to combine the EFIEs (Eqs. 10.3.65 and 10.3.29) for the interior and exterior fields to form a new integral equation

$$\hat{n} \times [\mathcal{L}(\bar{\mathbf{J}}_s) + \eta_i \mathcal{L}_i(\bar{\mathbf{J}}_s)] - \hat{n} \times [\tilde{\mathcal{K}}(\mathbf{M}_s) + \tilde{\mathcal{K}}_i(\mathbf{M}_s)] = \hat{n} \times \mathbf{E}^{\text{inc}}(\mathbf{r}) \quad \mathbf{r} \in S_o. \quad (10.3.69)$$

This is then solved in conjunction with the integral equation obtained by combining the MFIEs (Eqs. 10.3.66 and 10.3.30) for the interior and exterior fields

$$\hat{n} \times \left[\mathcal{L}(\mathbf{M}_s) + \frac{1}{\eta_i} \mathcal{L}_i(\mathbf{M}_s) \right] + \hat{n} \times \left[\tilde{\mathcal{K}}(\bar{\mathbf{J}}_s) + \tilde{\mathcal{K}}_i(\bar{\mathbf{J}}_s) \right] = \hat{n} \times \bar{\mathbf{H}}^{\text{inc}}(\mathbf{r}) \quad \mathbf{r} \in S_o. \quad (10.3.70)$$

This formulation is due to Poggio and Miller [11], Chang and Harrington [18], and Wu and Tsai [19], and is found to be free of interior resonance and yields accurate and stable solutions [20]. It is often referred to as the *PMCHWT formulation* after the initials of these authors. Another combination, called the Müller formulation, is discussed in Problem 10.12.

The numerical discretization of either the CFIEs or the PMCHWT equations using the moment method is straightforward. We can first divide S_o into small triangular patches and then employ the RWG functions to expand $\bar{\mathbf{J}}_s$ and \mathbf{M}_s as

$$\bar{\mathbf{J}}_s(\mathbf{r}) = \sum_{n=1}^N I_n \boldsymbol{\Lambda}_n(\mathbf{r}) \quad (10.3.71)$$

$$\mathbf{M}_s(\mathbf{r}) = \sum_{n=1}^N K_n \boldsymbol{\Lambda}_n(\mathbf{r}). \quad (10.3.72)$$

Then, we substitute these expressions into either the CFIEs or the PMCHWT equations and employ the RWG functions as the testing functions to arrive at the matrix equations

$$\sum_{n=1}^N A_{mn} I_n + \sum_{n=1}^N B_{mn} K_n = f_m \quad m = 1, 2, \dots, N \quad (10.3.73)$$

$$\sum_{n=1}^N C_{mn} I_n + \sum_{n=1}^N D_{mn} K_n = g_m \quad m = 1, 2, \dots, N \quad (10.3.74)$$

which can be solved together to obtain the expansion coefficients I_n and K_n . The matrices and excitation vectors depend on the integral equations used. If the CFIEs are adopted, then

$$A_{mn} = \iint_{S_o} \boldsymbol{\Lambda}_m \cdot \left[\frac{1}{2} \boldsymbol{\Lambda}_n + \mathcal{L}(\boldsymbol{\Lambda}_n) + \hat{n} \times \tilde{\mathcal{K}}(\boldsymbol{\Lambda}_n) \right] dS \quad (10.3.75)$$

$$B_{mn} = \iint_{S_o} \boldsymbol{\Lambda}_m \cdot \left[\frac{1}{2} \hat{n} \times \boldsymbol{\Lambda}_n + \hat{n} \times \mathcal{L}(\boldsymbol{\Lambda}_n) - \tilde{\mathcal{K}}(\boldsymbol{\Lambda}_n) \right] dS \quad (10.3.76)$$

$$C_{mn} = \iint_{S_o} \boldsymbol{\Lambda}_m \cdot \left[\frac{1}{2} \eta_i \boldsymbol{\Lambda}_n - \eta_i \mathcal{L}_i(\boldsymbol{\Lambda}_n) - \eta_i \hat{n} \times \tilde{\mathcal{K}}_i(\boldsymbol{\Lambda}_n) \right] dS \quad (10.3.77)$$

$$D_{mn} = \iint_{S_o} \boldsymbol{\Lambda}_m \cdot \left[\frac{1}{2} \hat{n} \times \boldsymbol{\Lambda}_n - \eta_i \hat{n} \times \mathcal{L}_i(\boldsymbol{\Lambda}_n) + \tilde{\mathcal{K}}_i(\boldsymbol{\Lambda}_n) \right] dS \quad (10.3.78)$$

$$f_m = \iint_{S_o} \boldsymbol{\Lambda}_m \cdot \left[\hat{n} \times \bar{\mathbf{H}}^{\text{inc}} + \mathbf{E}^{\text{inc}} \right] dS \quad (10.3.79)$$

$$g_m = 0. \quad (10.3.80)$$

If the PMCHWT equations are employed, then

$$A_{mn} = \iint_{S_o} \boldsymbol{\Lambda}_m \cdot [\mathcal{L}(\boldsymbol{\Lambda}_n) + \eta_i \mathcal{L}_i(\boldsymbol{\Lambda}_n)] dS \quad (10.3.81)$$

$$B_{mn} = -\iint_{S_o} \boldsymbol{\Lambda}_m \cdot [\tilde{\mathcal{K}}(\boldsymbol{\Lambda}_n) + \tilde{\mathcal{K}}_i(\boldsymbol{\Lambda}_n)] dS \quad (10.3.82)$$

$$C_{mn} = \iint_{S_o} \boldsymbol{\Lambda}_m \cdot [\tilde{\mathcal{H}}(\boldsymbol{\Lambda}_n) + \tilde{\mathcal{H}}_i(\boldsymbol{\Lambda}_n)] dS \quad (10.3.83)$$

$$D_{mn} = \iint_{S_o} \boldsymbol{\Lambda}_m \cdot \left[\mathcal{L}(\boldsymbol{\Lambda}_n) + \frac{1}{\eta_i} \mathcal{L}_i(\boldsymbol{\Lambda}_n) \right] dS \quad (10.3.84)$$

$$f_m = \iint_{S_o} \boldsymbol{\Lambda}_m \cdot \mathbf{E}^{\text{inc}} dS \quad (10.3.85)$$

$$g_m = \iint_{S_o} \boldsymbol{\Lambda}_m \cdot \bar{\mathbf{H}}^{\text{inc}} dS. \quad (10.3.86)$$

The numerical integration techniques discussed in the preceding section can be adapted here to evaluate the surface integrals.

Numerical experiments have shown that while the PMCHWT formulation always yields accurate solutions, the CFIE formulation as implemented based on Equations 10.3.75–10.3.80 has a quite low accuracy. A careful examination [21] reveals that the lower accuracy is due to the poor choice of the testing function. For example, given a vector equation $a\hat{x} = 5\hat{x}$, a good testing vector to convert it into a scalar equation by taking the dot product is \hat{x} or anything that contains an appreciable amount of \hat{x} , which yields the solution $a = 5$. If the testing vector is orthogonal or nearly orthogonal to the vector equation, it will not be able to convert the vector equation accurately. In our case here, it can be seen that while $\boldsymbol{\Lambda}_m$ is a good testing function for $\mathcal{L}(\boldsymbol{\Lambda}_n)$ and $\mathcal{L}_i(\boldsymbol{\Lambda}_n)$, it is a poor testing function for $\tilde{\mathcal{K}}(\boldsymbol{\Lambda}_n)$ and $\tilde{\mathcal{K}}_i(\boldsymbol{\Lambda}_n)$. In the PMCHWT formulation, both $\bar{\mathbf{J}}_s$ and \mathbf{M}_s are well tested. However, in the CFIE formulation, only $\bar{\mathbf{J}}_s$ is well tested, while \mathbf{M}_s is poorly tested. If we replace $\boldsymbol{\Lambda}_m$ with $\hat{n} \times \boldsymbol{\Lambda}_m$ in Equations 10.3.75–10.3.80, the situation becomes opposite: Only \mathbf{M}_s is well tested and $\bar{\mathbf{J}}_s$ would be poorly tested. Therefore, to test both $\bar{\mathbf{J}}_s$ and \mathbf{M}_s well, we have to use the combination of $\boldsymbol{\Lambda}_m$ and $\hat{n} \times \boldsymbol{\Lambda}_m$:

$$\mathbf{t}_m = \boldsymbol{\Lambda}_m + \hat{n} \times \boldsymbol{\Lambda}_m \quad (10.3.87)$$

as the testing function. The final equation has the same form as before except that $\boldsymbol{\Lambda}_m$ is replaced by \mathbf{t}_m in Equations 10.3.75–10.3.80.

As a numerical example, Figure 10.21 plots the numerical results obtained by solving the PMCHWT equations using the moment method for plane wave scattering by a two-layer dielectric sphere at 1.2 GHz [22]. The inner sphere has a radius of 0.9 m and a relative permittivity of $\epsilon_r = 1.44 - j0.2$, and the outer layer has a radius of 1.0 m and a relative permittivity of $\epsilon_r = 1.75 - j0.8$. The numerical results are compared with the exact solution based on the Mie series, showing excellent agreement. The root-mean-square (RMS) error is only 0.11 and 0.07 dB, respectively, for the $\theta\theta$ and $\phi\phi$ polarizations.

10.3.5 Scattering by an Inhomogeneous Dielectric Body

If the object is inhomogeneous and characterized by the position-dependent permittivity $\epsilon(\mathbf{r})$ and permeability $\mu(\mathbf{r})$, the fields everywhere satisfy Maxwell's equations

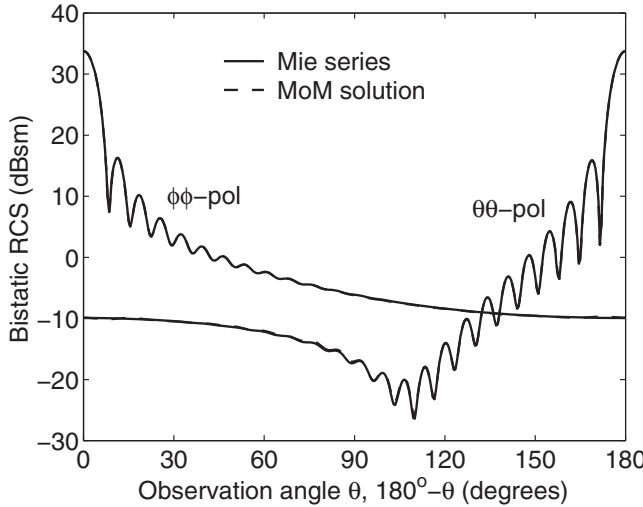


Figure 10.21 Bistatic RCS of a two-layer dielectric sphere at 1.2 GHz. The inner sphere has a radius of 0.9 m and a relative permittivity of $\epsilon_r = 1.44 - j0.2$, and the outer layer has a radius of 1.0 m and a relative permittivity of $\epsilon_r = 1.75 - j0.8$. (After Donepudi et al. [22], Copyright © IEEE 2003.)

$$\nabla \times \mathbf{E} = -j\omega\mu(\mathbf{r})\mathbf{H} \quad (10.3.88)$$

$$\nabla \times \mathbf{H} = j\omega\epsilon(\mathbf{r})\mathbf{E} + \mathbf{J}_i. \quad (10.3.89)$$

Rewriting these two equations as

$$\nabla \times \mathbf{E} = -j\omega\mu_0\mathbf{H} - j\omega[\mu(\mathbf{r}) - \mu_0]\mathbf{H} \quad (10.3.90)$$

$$\nabla \times \mathbf{H} = j\omega\epsilon_0\mathbf{E} + j\omega[\epsilon(\mathbf{r}) - \epsilon_0]\mathbf{E} + \mathbf{J}_i \quad (10.3.91)$$

or equivalently,

$$\nabla \times \mathbf{E} = -j\omega\mu_0\mathbf{H} - \mathbf{M}_{eq} \quad (10.3.92)$$

$$\nabla \times \mathbf{H} = j\omega\epsilon_0\mathbf{E} + \mathbf{J}_{eq} + \mathbf{J}_i \quad (10.3.93)$$

where

$$\mathbf{M}_{eq} = j\omega[\mu(\mathbf{r}) - \mu_0]\mathbf{H}, \quad \mathbf{J}_{eq} = j\omega[\epsilon(\mathbf{r}) - \epsilon_0]\mathbf{E} \quad (10.3.94)$$

we immediately recognize that the problem can be considered as the radiation of the currents \mathbf{J}_i , \mathbf{J}_{eq} , and \mathbf{M}_{eq} in free space with permittivity ϵ_0 and permeability μ_0 . This is in fact the volume equivalence principle discussed in Chapter 3.

By eliminating the magnetic field in Equations 10.3.92 and 10.3.93, we obtain

$$\nabla \times \nabla \times \mathbf{E}(\mathbf{r}) - k_0^2 \mathbf{E}(\mathbf{r}) = -jk_0 Z_0 [\mathbf{J}_{eq}(\mathbf{r}) + \mathbf{J}_i(\mathbf{r})] - \nabla \times \mathbf{M}_{eq}(\mathbf{r}) \quad (10.3.95)$$

and a similar procedure yields

$$\nabla \times \nabla \times \mathbf{H}(\mathbf{r}) - k_0^2 \mathbf{H}(\mathbf{r}) = \nabla \times [\mathbf{J}_{eq}(\mathbf{r}) + \mathbf{J}_i(\mathbf{r})] - jk_0 Y_0 \mathbf{M}_{eq}(\mathbf{r}). \quad (10.3.96)$$

Multiplying these two equations by G_0 defined in Equation 10.3.6, integrating them over the entire space including the object, and making use of Green's theorem, we obtain the electric field everywhere as

$$\begin{aligned}\mathbf{E}(\mathbf{r}) = & \mathbf{E}^{\text{inc}}(\mathbf{r}) - jk_0 Z_0 \iiint_{V_o} \left[\mathbf{J}_{\text{eq}}(\mathbf{r}') G_0(\mathbf{r}, \mathbf{r}') + \frac{1}{k_0^2} \mathbf{J}_{\text{eq}}(\mathbf{r}') \cdot \nabla \nabla G_0(\mathbf{r}, \mathbf{r}') \right] dV' \\ & - \iiint_{V_o} \mathbf{M}_{\text{eq}}(\mathbf{r}') \times \nabla' G_0(\mathbf{r}, \mathbf{r}') dV'\end{aligned}\quad (10.3.97)$$

and the magnetic field everywhere as

$$\begin{aligned}\mathbf{H}(\mathbf{r}) = & \mathbf{H}^{\text{inc}}(\mathbf{r}) + \iiint_{V_o} \mathbf{J}_{\text{eq}}(\mathbf{r}') \times \nabla' G_0(\mathbf{r}, \mathbf{r}') dV' \\ & - jk_0 Y_0 \iiint_{V_o} \left[\mathbf{M}_{\text{eq}}(\mathbf{r}') G_0(\mathbf{r}, \mathbf{r}') + \frac{1}{k_0^2} \mathbf{M}_{\text{eq}}(\mathbf{r}') \cdot \nabla \nabla G_0(\mathbf{r}, \mathbf{r}') \right] dV'\end{aligned}\quad (10.3.98)$$

where \mathbf{E}^{inc} and \mathbf{H}^{inc} denote the incident fields defined by Equations 10.3.12 and 10.3.15. It can be shown that these two equations are equivalent to Equations 3.4.32 and 3.4.33 obtained using the volume equivalence principle with the aid of the free-space field-source relations. Here, they are derived using the scalar–vector Green's theorem.

Substituting Equation 10.3.94 into Equations 10.3.97 and 10.3.98 and applying them to the volume of the object, we obtain

$$\begin{aligned}\mathbf{E}(\mathbf{r}) - \iiint_{V_o} \{ k_0^2 [\epsilon_r(\mathbf{r}') - 1] \mathbf{E}(\mathbf{r}') G_0(\mathbf{r}, \mathbf{r}') + [\epsilon_r(\mathbf{r}') - 1] \mathbf{E}(\mathbf{r}') \cdot \nabla \nabla G_0(\mathbf{r}, \mathbf{r}') \} dV' \\ + jk_0 Z_0 \iiint_{V_o} [\mu_r(\mathbf{r}') - 1] \mathbf{H}(\mathbf{r}') \times \nabla' G_0(\mathbf{r}, \mathbf{r}') dV' = \mathbf{E}^{\text{inc}}(\mathbf{r}) \quad \mathbf{r} \in V_o\end{aligned}\quad (10.3.99)$$

$$\begin{aligned}\mathbf{H}(\mathbf{r}) - \iiint_{V_o} \{ k_0^2 [\mu_r(\mathbf{r}') - 1] \mathbf{H}(\mathbf{r}') G_0(\mathbf{r}, \mathbf{r}') + [\mu_r(\mathbf{r}') - 1] \mathbf{H}(\mathbf{r}') \cdot \nabla \nabla G_0(\mathbf{r}, \mathbf{r}') \} dV' \\ - jk_0 Y_0 \iiint_{V_o} [\epsilon_r(\mathbf{r}') - 1] \mathbf{E}(\mathbf{r}') \times \nabla' G_0(\mathbf{r}, \mathbf{r}') dV' = \mathbf{H}^{\text{inc}}(\mathbf{r}) \quad \mathbf{r} \in V_o\end{aligned}\quad (10.3.100)$$

which are usually referred to as the *volume integral equations* (VIE).

Equations 10.3.99 and 10.3.100 can be used to solve for the unknown fields inside the object. The solution procedure involves (1) subdividing the volume of the object into small volumetric elements such as cubic and tetrahedral cells, (2) expanding the unknown fields in terms of properly formulated basis functions, (3) converting Equations 10.3.99 and 10.3.100 into matrix equations using a set of properly selected testing functions, and finally (4) solving the matrix equations to obtain the expansion coefficients. Some successful examples have been reported [23,24]. However, because the domain of discretization is a volume and the resulting matrices are dense, this solution is very expensive. Consequently, this method can be applied only to small inhomogeneous objects or objects with a small inhomogeneous volume, unless the matrix equation is solved using one of fast algorithms discussed Chapter 11.

10.4 ANALYSIS OF PERIODIC STRUCTURES

Periodic structures are commonly found in electromagnetic and optical applications. The electromagnetic properties of a periodic structure can be analyzed using a numerical method. The unique periodic feature of the structure can be exploited to make the numerical analysis highly efficient. In this section, we consider two periodic structures to illustrate the analysis using the moment method.

10.4.1 Scattering by a Planar Periodic Conducting Patch Array

Consider a periodic array of perfectly conducting patches in the xy -plane, whose periodic length is T_x in the x -direction and T_y in the y -direction. A uniform plane wave is incident from the direction specified by θ^{inc} and ϕ^{inc} ; hence, the incident electric field can be written as

$$\mathbf{E}^{\text{inc}}(\mathbf{r}) = \mathbf{E}_0 e^{-j\mathbf{k}^{\text{inc}} \cdot \mathbf{r}} \quad (10.4.1)$$

where the incident wave vector is given by

$$\begin{aligned} \mathbf{k}^{\text{inc}} &= -\hat{x}k_x^{\text{inc}} - \hat{y}k_y^{\text{inc}} - \hat{z}k_z^{\text{inc}} \\ &= -\hat{x}k_0 \sin \theta^{\text{inc}} \cos \phi^{\text{inc}} - \hat{y}k_0 \sin \theta^{\text{inc}} \sin \phi^{\text{inc}} - \hat{z}k_0 \cos \theta^{\text{inc}}. \end{aligned} \quad (10.4.2)$$

This incident field induces a surface electric current on the conducting patches, and the surface current density has the form

$$\mathbf{J}_s(x, y) = \mathbf{j}(x, y) e^{j(k_x^{\text{inc}} x + k_y^{\text{inc}} y)} \quad (10.4.3)$$

where $\mathbf{j}(x, y)$ is a periodic function having the same periodic lengths as the periodic array. This is known as *Floquet's theorem*. Therefore, $\mathbf{j}(x, y)$ can be expanded in a Fourier series

$$\mathbf{j}(x, y) = \sum_{p=-\infty}^{\infty} \sum_{q=-\infty}^{\infty} \tilde{\mathbf{j}}_{pq} e^{j(k_{xp} x + k_{yq} y)} \quad (10.4.4)$$

where

$$\tilde{\mathbf{j}}_{pq} = \frac{1}{T_x T_y} \iint_{S_p} \mathbf{j}(x, y) e^{-j(k_{xp} x + k_{yq} y)} dx dy \quad (10.4.5)$$

in which S_p denotes the area of a single patch and

$$k_{xp} = \frac{2\pi p}{T_x}, \quad k_{yq} = \frac{2\pi q}{T_y}. \quad (10.4.6)$$

As a result, Equation 10.4.3 can be written as

$$\mathbf{J}_s(x, y) = \sum_{p=-\infty}^{\infty} \sum_{q=-\infty}^{\infty} \tilde{\mathbf{j}}_{pq} e^{j(k'_{xp} x + k'_{yq} y)} \quad (10.4.7)$$

where

$$k'_{xp} = k_x^{\text{inc}} + \frac{2\pi p}{T_x}, \quad k'_{yq} = k_y^{\text{inc}} + \frac{2\pi q}{T_y}. \quad (10.4.8)$$

Given a surface current $\tilde{\mathbf{j}}_{pq} e^{j(k'_{xp}x+k'_{yq}y)}$ in the xy -plane, it is rather straightforward, by applying the boundary conditions across the plane together with phase matching, to find that it produces an electric field whose transverse component is given by

$$\mathbf{E}_{T,pq}(\mathbf{r}) = -jk_0 Z_0 \tilde{\tilde{\mathbf{G}}}(k'_{xp}, k'_{yq}) \cdot \tilde{\mathbf{j}}_{pq} e^{j(k'_{xp}x+k'_{yq}y \mp k_{zpq}z)} \quad z \geq 0 \quad (10.4.9)$$

where

$$\begin{aligned} \tilde{\tilde{\mathbf{G}}}(k'_{xp}, k'_{yq}) &= \hat{x}\hat{x}\tilde{G}_{xx} + \hat{x}\hat{y}\tilde{G}_{xy} + \hat{y}\hat{x}\tilde{G}_{yx} + \hat{y}\hat{y}\tilde{G}_{yy} \\ &= \frac{j}{2k_{zpq}k_0^2} \left[\hat{x}\hat{x}(k_0^2 - k_{xp}^2) - \hat{x}\hat{y}k_{xp}k_{yq} - \hat{y}\hat{x}k_{xp}k_{yq} + \hat{y}\hat{y}(k_0^2 - k_{yq}^2) \right] \end{aligned} \quad (10.4.10)$$

in which $k_{zpq} = \sqrt{k_0^2 - k_{xp}^2 - k_{yq}^2}$. Hence, the transverse component of the total scattered field is given by

$$\mathbf{E}_T^{\text{sc}}(\mathbf{r}) = -jk_0 Z_0 \sum_{p=-\infty}^{\infty} \sum_{q=-\infty}^{\infty} \tilde{\tilde{\mathbf{G}}}(k'_{xp}, k'_{yq}) \cdot \tilde{\mathbf{j}}_{pq} e^{j(k'_{xp}x+k'_{yq}y \mp k_{zpq}z)} \quad z \geq 0 \quad (10.4.11)$$

and the application of the boundary condition on the perfectly conducting patches yields

$$jk_0 Z_0 \sum_{p=-\infty}^{\infty} \sum_{q=-\infty}^{\infty} \tilde{\tilde{\mathbf{G}}}(k'_{xp}, k'_{yq}) \cdot \tilde{\mathbf{j}}_{pq} e^{j(k'_{xp}x+k'_{yq}y)} = \mathbf{E}_T^{\text{inc}}(\mathbf{r}) \quad \mathbf{r} \in S_p \quad (10.4.12)$$

or

$$\sum_{p=-\infty}^{\infty} \sum_{q=-\infty}^{\infty} \tilde{\tilde{\mathbf{G}}}(k'_{xp}, k'_{yq}) \cdot \tilde{\mathbf{j}}_{pq} e^{j(k'_{xp}x+k'_{yq}y)} = \frac{1}{jk_0 Z_0} \mathbf{E}_{0,T} \quad \mathbf{r} \in S_p \quad (10.4.13)$$

where $\mathbf{E}_{0,T}$ denotes the transverse component of \mathbf{E}_0 , which is defined in Equation 10.4.1. Equation 10.4.13 provides the necessary integral equation for the solution of \mathbf{J}_s with the integral embedded in the definition of $\tilde{\mathbf{j}}_{pq}$.

Equation 10.4.13 can be solved for \mathbf{J}_s using the moment method via a discretization of S_p into either triangular or rectangular cells. Here we describe a highly efficient moment-method solution based on a uniform discretization of S_p into rectangular cells [25,26]. To start, we first subdivide the region of one period into $M \times N$ rectangular cells of dimension $\Delta x \times \Delta y$. The conducting patch S_p can then be modeled approximately by a collection of these rectangular cells. For simplicity, we first use piecewise constant basis functions to expand $\mathbf{j}(x, y)$:

$$\mathbf{j}(x, y) = \sum_{m=-M/2}^{M/2-1} \sum_{n=-N/2}^{N/2-1} \mathbf{j}_{mn} \Pi_m(x) \Pi_n(y) \quad (10.4.14)$$

where

$$\Pi_m(x) = \begin{cases} 1 & |x - m\Delta x| < \Delta x/2 \\ 0 & |x - m\Delta x| > \Delta x/2 \end{cases} \quad (10.4.15)$$

and $\Pi_n(y)$ is defined similarly. From Equation 10.4.5, we find

$$\tilde{\mathbf{j}}_{pq} = \frac{1}{MN} \operatorname{sinc}\left(\frac{p\pi}{M}\right) \operatorname{sinc}\left(\frac{q\pi}{N}\right) \sum_{m=-M/2}^{M/2-1} \sum_{n=-N/2}^{N/2-1} \mathbf{j}_{mn} e^{-j(2\pi pm/M + 2\pi qn/N)}. \quad (10.4.16)$$

Substituting this into Equation 10.4.13 and integrating over $\Pi_m(x)\Pi_n(y)$, we obtain

$$\begin{aligned} \frac{1}{MN} \sum_{p=-\infty}^{\infty} \sum_{q=-\infty}^{\infty} \tilde{\mathbf{G}}(k'_{xp}, k'_{yq}) \operatorname{sinc}^2\left(\frac{p\pi}{M}\right) \operatorname{sinc}^2\left(\frac{q\pi}{N}\right) \\ \cdot \left[\sum_{m=-M/2}^{M/2-1} \sum_{n=-N/2}^{N/2-1} \mathbf{j}_{mn} e^{-j(2\pi pm/M + 2\pi qn/N)} \right] e^{j(2\pi pm'/M + 2\pi qn'/N)} = \frac{1}{jk_0 Z_0} \mathbf{E}_{0,T} \end{aligned} \quad (10.4.17)$$

for $m' = -M/2, -M/2+1, \dots, M/2-1$ and $n' = -N/2, -N/2+1, \dots, N/2-1$. Equation 10.4.17 provides a set of linear equations to solve for \mathbf{j}_{mn} , which can be written as

$$\sum_{m=-M/2}^{M/2-1} \sum_{n=-N/2}^{N/2-1} \tilde{\mathbf{Z}}_{m'n'mn} \cdot \mathbf{j}_{mn} = \frac{1}{jk_0 Z_0} \mathbf{E}_{0,T} \quad (10.4.18)$$

where the coefficient matrix is given by

$$\tilde{\mathbf{Z}}_{m'n'mn} = \frac{1}{MN} \sum_{p=-\infty}^{\infty} \sum_{q=-\infty}^{\infty} \tilde{\mathbf{G}}(k'_{xp}, k'_{yq}) \operatorname{sinc}^2\left(\frac{p\pi}{M}\right) \operatorname{sinc}^2\left(\frac{q\pi}{N}\right) e^{-j(2\pi p(m-m')/M + 2\pi q(n-n')/N)}. \quad (10.4.19)$$

The evaluation of this matrix is time-consuming because the summation converges slowly. Moreover, since k'_{xp} and k'_{yq} depend on the angle of incidence, this matrix is different for different angles of incidence, which makes the calculation even slower if one desires to analyze the angular characteristics of a periodic array.

However, because of uniform discretization, Equation 10.4.17 can be cast into a special form to enable a more efficient solution. This can be done by splitting an infinite summation into two summations

$$\sum_{p=-\infty}^{\infty} [\cdot] = \sum_{u=-\infty}^{\infty} \sum_{p'=-M/2}^{M/2-1} [\cdot], \quad \sum_{q=-\infty}^{\infty} [\cdot] = \sum_{v=-\infty}^{\infty} \sum_{q'=-N/2}^{N/2-1} [\cdot] \quad (10.4.20)$$

where $p = p' + uM$ and $q = q' + vN$. With this, Equation 10.4.17 can be written as

$$\begin{aligned} \frac{1}{MN} \sum_{p'=-M/2}^{M/2} \sum_{q'=-N/2}^{N/2} \tilde{\mathbf{A}}(k'_{xp'}, k'_{yq'}) \cdot \left[\sum_{m=-M/2}^{M/2-1} \sum_{n=-N/2}^{N/2-1} \mathbf{j}_{mn} e^{-j(2\pi p'm/M + 2\pi q'n/N)} \right] \\ \times e^{j(2\pi p'm'/M + 2\pi q'n'/N)} = \frac{1}{jk_0 Z_0} \mathbf{E}_{0,T} \end{aligned} \quad (10.4.21)$$

where

$$\tilde{\tilde{\mathbf{A}}}(k'_{xp}, k'_{yq}) = \sum_{u=-\infty}^{\infty} \sum_{v=-\infty}^{\infty} \tilde{\tilde{\mathbf{G}}}(k'_{xp}, k'_{yq}) \operatorname{sinc}^2\left(\frac{p\pi}{M}\right) \operatorname{sinc}^2\left(\frac{q\pi}{N}\right). \quad (10.4.22)$$

Based on the definition of the discrete Fourier transform (DFT) and its inverse, Equation 10.4.21 can be symbolically written as

$$\mathcal{F}_D^{-1}\left\{\tilde{\tilde{\mathbf{A}}}(k'_{xp}, k'_{yq}) \cdot [\mathcal{F}_D\{\mathbf{j}_{mn}\}]\right\} = \frac{1}{jk_0 Z_0} \mathbf{E}_{0,T} \quad (10.4.23)$$

where \mathcal{F}_D denotes the DFT and \mathcal{F}_D^{-1} denotes the corresponding inverse DFT. Therefore, if we solve Equation 10.4.21, which is equivalent to Equation 10.4.17, using an iterative algorithm, the matrix–vector product can be efficiently evaluated using the fast Fourier transform (FFT).

Although the summation in Equation 10.4.21 can be computed efficiently by using the FFT, the evaluation of the summation in Equation 10.4.22 still suffers from slow convergence because for large (u, v) its terms are of the order

$$\tilde{\tilde{\mathbf{A}}}(k'_{xp}, k'_{yq}) \sim \frac{1}{\sqrt{u^2 + v^2}} \left[\hat{x}\hat{x}\frac{1}{v^2} + \hat{x}\hat{y}\frac{1}{uv} + \hat{y}\hat{x}\frac{1}{uv} + \hat{y}\hat{y}\frac{1}{u^2} \right] \quad (10.4.24)$$

which decays slowly. To speed up the convergence and also to obtain a more accurate solution, we can employ rooftop basis functions to expand $\mathbf{j}(x, y)$ as well as to serve as testing functions. These rooftop functions are shown in Figure 10.22, and when they are used as basis functions, $\mathbf{j}(x, y)$ can be expanded as

$$j_x(x, y) = \sum_{m=-M/2}^{M/2-1} \sum_{n=-N/2}^{N/2-1} j_{xmn} \Lambda_{m+1/2}(x) \Pi_n(y) \quad (10.4.25)$$

$$j_y(x, y) = \sum_{m=-M/2}^{M/2-1} \sum_{n=-N/2}^{N/2-1} j_{ymn} \Pi_m(x) \Lambda_{n+1/2}(y) \quad (10.4.26)$$

where

$$\Lambda_m(x) = \begin{cases} 1 - \frac{|x - m\Delta x|}{\Delta x} & |x - m\Delta x| < \Delta x \\ 0 & |x - m\Delta x| > \Delta x \end{cases} \quad (10.4.27)$$

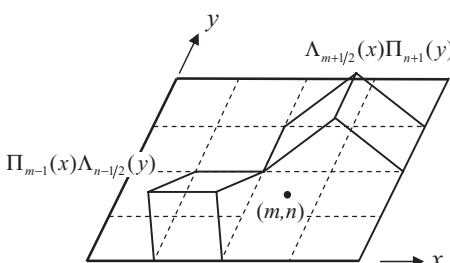


Figure 10.22 Illustration of rooftop functions.

and $\Lambda_n(y)$ is defined similarly. From Equation 10.4.5, we find

$$\tilde{j}_{xpq} = \frac{1}{MN} \operatorname{sinc}^2\left(\frac{p\pi}{M}\right) \operatorname{sinc}\left(\frac{q\pi}{N}\right) e^{-j\pi p/M} \sum_{m=-M/2}^{M/2-1} \sum_{n=-N/2}^{N/2-1} j_{xmn} e^{-j(2\pi pm/M + 2\pi qn/N)} \quad (10.4.28)$$

$$\tilde{j}_{ypq} = \frac{1}{MN} \operatorname{sinc}\left(\frac{p\pi}{M}\right) \operatorname{sinc}^2\left(\frac{q\pi}{N}\right) e^{-j\pi q/N} \sum_{m=-M/2}^{M/2-1} \sum_{n=-N/2}^{N/2-1} j_{ymn} e^{-j(2\pi pm/M + 2\pi qn/N)}. \quad (10.4.29)$$

Substituting these into Equation 10.4.13 and integrating its *x*-component with $\Lambda_{m'+1/2}(x)\Pi_{n'}(y)$ and the *y*-component with $\Pi_{m'}(x)\Lambda_{n'+1/2}(y)$, we eventually obtain

$$\begin{aligned} & \frac{1}{MN} \sum_{p'=-M/2}^{M/2} \sum_{q'=-N/2}^{N/2} \tilde{A}(k'_{xp'}, k'_{yq'}) \cdot \left[\sum_{m=-M/2}^{M/2-1} \sum_{n=-N/2}^{N/2-1} \mathbf{j}_{mn} e^{-j(2\pi p'm/M + 2\pi q'n/N)} \right] \\ & \times e^{j(2\pi p'm'/M + 2\pi q'n'/N)} = \frac{1}{jk_0 Z_0} \mathbf{E}_{0,T} \end{aligned} \quad (10.4.30)$$

where

$$\tilde{A}_{xx}(k'_{xp'}, k'_{yq'}) = \sum_{u=-\infty}^{\infty} \sum_{v=-\infty}^{\infty} \tilde{G}_{xx}(k'_{xp}, k'_{yq}) \operatorname{sinc}^4\left(\frac{p\pi}{M}\right) \operatorname{sinc}^2\left(\frac{q\pi}{N}\right) \quad (10.4.31)$$

$$\tilde{A}_{xy}(k'_{xp'}, k'_{yq'}) = \sum_{u=-\infty}^{\infty} \sum_{v=-\infty}^{\infty} \tilde{G}_{xy}(k'_{xp}, k'_{yq}) \operatorname{sinc}^3\left(\frac{p\pi}{M}\right) \operatorname{sinc}^3\left(\frac{q\pi}{N}\right) e^{j(\pi p/M - \pi q/N)} \quad (10.4.32)$$

$$\tilde{A}_{yx}(k'_{xp'}, k'_{yq'}) = \sum_{u=-\infty}^{\infty} \sum_{v=-\infty}^{\infty} \tilde{G}_{yx}(k'_{xp}, k'_{yq}) \operatorname{sinc}^3\left(\frac{p\pi}{M}\right) \operatorname{sinc}^3\left(\frac{q\pi}{N}\right) e^{-j(\pi p/M - \pi q/N)} \quad (10.4.33)$$

$$\tilde{A}_{yy}(k'_{xp'}, k'_{yq'}) = \sum_{u=-\infty}^{\infty} \sum_{v=-\infty}^{\infty} \tilde{G}_{yy}(k'_{xp}, k'_{yq}) \operatorname{sinc}^2\left(\frac{p\pi}{M}\right) \operatorname{sinc}^4\left(\frac{q\pi}{N}\right). \quad (10.4.34)$$

Again, Equation 10.4.30 can be written in the form of Equation 10.4.23, which can be evaluated efficiently using the FFT. However, the summations in Equations 10.4.31–10.4.34 converge much more quickly because for large (*u*, *v*) the terms in these summations are of the order

$$\tilde{A}_{xx}, \tilde{A}_{xy}, \tilde{A}_{yx}, \tilde{A}_{yy} \sim \frac{1}{(uv)^2 \sqrt{u^2 + v^2}} \quad (10.4.35)$$

which decay much faster than Equation 10.4.24. Moreover, the solution has a better accuracy since the expansion of the surface current is more accurate.

It is obvious that the moment-method solution described above can be extended to deal with a planar periodic array in a multilayer medium [27]. Figure 10.23 shows the specular reflection and forward transmission coefficients of a circular patch array as a function of the angle of incidence at 10.4 GHz. The patches have a radius of 0.625 cm, and the unit cells have a dimension of 2.0 cm × 2.0 cm. The patches reside on a dielectric slab having a thickness of 0.2 cm and a relative permittivity of $\epsilon_r = 3.5$. The circular patch in a unit cell is approximately modeled as a collection of square cells. In this case, higher-order Bragg diffractions occur when $\theta^{\text{inc}} > 26^\circ$.

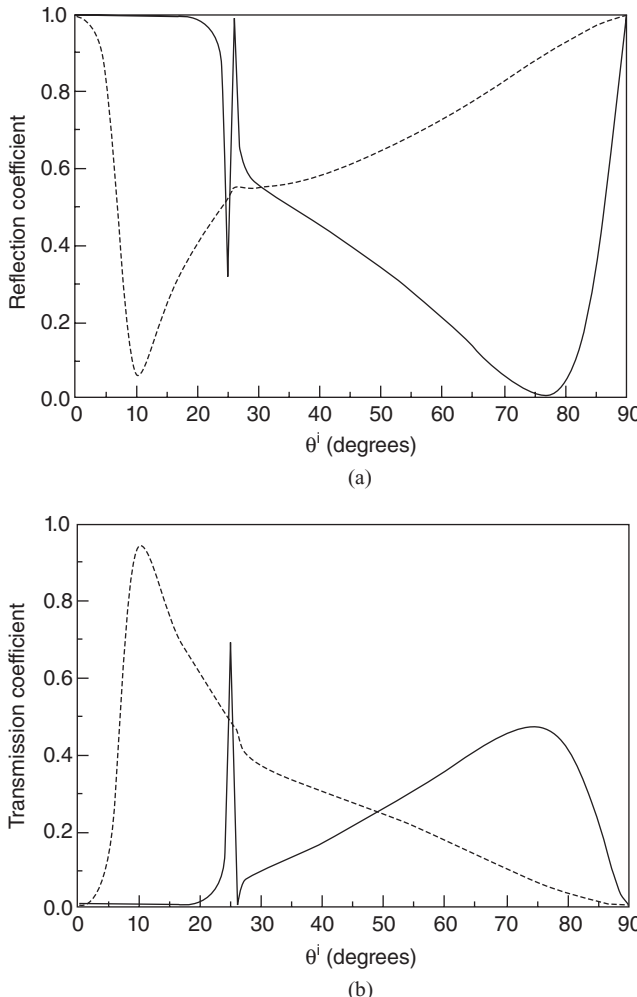


Figure 10.23 Specular reflection and transmission coefficients of a circular patch infinite array on a top of an infinitely large dielectric slab. (a) Reflection coefficient. (b) Transmission coefficient. Solid lines: TM incidence. Dashed lines: TE incidence. (After Jin and Volakis [27], Copyright © IEEE 1990.)

10.4.2 Scattering by a Discrete Body-of-Revolution Object

For the planar periodic structure considered in the preceding subsection, the excitation is a uniform plane wave and, as such, the induced current and the scattered field are periodic functions with a constant phase shift. Because of those properties, the analysis can be confined into a single periodic region, which is often referred to as a unit cell. In this section, we consider a different example in which certain geometrical symmetry, such as geometrical repetition, is exploited to speed up the numerical analysis even though the excitation and, hence, the induced currents and scattered fields do not have any special form.

Consider a conducting object that is generated by rotating successively $K - 1$ times a portion or a slice of the object about an axis through an angle of $\phi_s = 2\pi/K$ radians. Such an object is rotationally periodic since its shape remains invariant when it is rotated by a multiple of ϕ_s . This object is also called a *discrete body-of-revolution* (DBOR) as it

possesses discrete rotational symmetry. To utilize the geometrical repetition of this object in the moment-method solution described in Section 10.3.3, we can first mesh the surface of the first slice into small triangular patches and then rotate this mesh successively $K - 1$ times to obtain a triangular surface mesh for the entire object. If we further number the unknowns in the first slice first, then in the second slice, and so on in a consistent manner, the moment-method matrix equation given in Equation 10.3.50 can be written in the form

$$\begin{bmatrix} [Z]^{(1)} & [Z]^{(2)} & \cdots & [Z]^{(K)} \\ [Z]^{(K)} & [Z]^{(1)} & \cdots & [Z]^{(K-1)} \\ \vdots & \vdots & \ddots & \vdots \\ [Z]^{(2)} & [Z]^{(3)} & \cdots & [Z]^{(1)} \end{bmatrix} \begin{Bmatrix} \{I\}^{(1)} \\ \{I\}^{(2)} \\ \vdots \\ \{I\}^{(K)} \end{Bmatrix} = \begin{Bmatrix} \{V\}^{(1)} \\ \{V\}^{(2)} \\ \vdots \\ \{V\}^{(K)} \end{Bmatrix}. \quad (10.4.36)$$

This kind of matrix is called a *block-circulant matrix*. Next, we multiply the k th row by $e^{-jm(k-1)\phi_s}$ and then sum all the rows to obtain

$$[Z]_m \{I\}_m = \{V\}_m \quad (10.4.37)$$

where

$$[Z]_m = \sum_{k=1}^K [Z]^{(k)} e^{jm(k-1)\phi_s} \quad (10.4.38)$$

$$\{I\}_m = \sum_{k=1}^K \{I\}^{(k)} e^{-jm(k-1)\phi_s} \quad (10.4.39)$$

$$\{V\}_m = \sum_{k=1}^K \{V\}^{(k)} e^{-jm(k-1)\phi_s}. \quad (10.4.40)$$

Equations 10.4.39 and 10.4.40 define a discrete Fourier transform, and their inverse transforms are given by

$$\{I\}^{(k)} = \frac{1}{K} \sum_{m=1}^K \{I\}_m e^{jm(k-1)\phi_s} \quad (10.4.41)$$

$$\{V\}^{(k)} = \frac{1}{K} \sum_{m=1}^K \{V\}_m e^{jm(k-1)\phi_s}. \quad (10.4.42)$$

The formulation above provides an efficient solution to Equation 10.4.36 [28]. Given an excitation vector $\{V\}^{(k)}$ ($k = 1, 2, \dots, K$), we first use Equation 10.4.40 to calculate its Fourier modes $\{V\}_m$ ($m = 1, 2, \dots, K$). We then solve Equation 10.4.37 for $\{I\}_m$ ($m = 1, 2, \dots, K$), from which we use Equation 10.4.41 to find the solution vector $\{I\}^{(k)}$ ($k = 1, 2, \dots, K$). Since the dimension of the matrix equation in Equation 10.4.37 is K times smaller than that of Equation 10.4.36, the computation time and memory requirements are reduced by a factor of K^2 when a direct solver is used. When K is large, the saving can be quite significant. Note that the DFT and the inverse DFT required in Equations 10.4.38, 10.4.40, and 10.4.41 can also be computed efficiently using the FFT. Obviously, this technique can be extended easily to the moment-method analysis of other types of objects.

10.5 ANALYSIS OF MICROSTRIP ANTENNAS AND CIRCUITS

As mentioned earlier, the major advantage of the moment method is the use of an appropriate Green's function in the formulation of the required integral equation. This Green's function can be used to include certain effects, such as the Sommerfeld radiation condition, into the integral equation so that there is no need to model such effects explicitly in the moment-method solution. In all the problems considered so far, we employed free-space Green's functions. Here we consider a problem where a special Green's function is employed to include the effect of a non-free-space environment. For the sake of clarity, we consider the simplest case in the analysis of microstrip antennas and circuits by assuming that microstrip antennas and circuits are printed on the top surface of a single-layer electrically grounded dielectric substrate.

10.5.1 Formulation of Integral Equations

Consider a microstrip conductor printed on the top surface of an infinitely large, single-layer dielectric substrate backed by a conducting ground plane. An excitation, whether it is an incident plane wave or an impressed voltage or current source, will induce a surface electric current on the microstrip, which will radiate an electromagnetic field everywhere (Fig. 10.24). Denote this surface current as \mathbf{J}_s . To formulate an integral equation, we have to find the electric field radiated by \mathbf{J}_s . Since \mathbf{J}_s is a function of x and y , we can first expand it into a Fourier integral

$$\mathbf{J}_s(x, y) = \frac{1}{4\pi^2} \int_{-\infty}^{\infty} \int_{-\infty}^{\infty} \tilde{\mathbf{J}}_s(k_x, k_y) e^{j(k_x x + k_y y)} dk_x dk_y \quad (10.5.1)$$

where

$$\tilde{\mathbf{J}}_s(k_x, k_y) = \int_{-\infty}^{\infty} \int_{-\infty}^{\infty} \mathbf{J}_s(x, y) e^{-j(k_x x + k_y y)} dx dy. \quad (10.5.2)$$

Now, consider a surface current $\tilde{\mathbf{J}}_s(k_x, k_y) e^{j(k_x x + k_y y)}$ sitting on the surface of an electrically grounded substrate having a thickness of h and a relative permittivity of ϵ_r . Assuming that the surface of the substrate coincides with the xy -plane, we can derive the expression for the electric field by applying the boundary conditions across the xy -plane and at the ground plane and then invoking phase matching (a tedious but bearable procedure). Then by integrating the result over k_x and k_y , we find the transverse component of the electric field due to \mathbf{J}_s as [29,30]

$$\mathbf{E}_T(\mathbf{r}) = -jk_0 Z_0 \int_{-\infty}^{\infty} \int_{-\infty}^{\infty} \tilde{\mathbf{G}}_T(\mathbf{r}; x', y') \cdot \mathbf{J}_s(x', y') dx' dy' \quad (10.5.3)$$

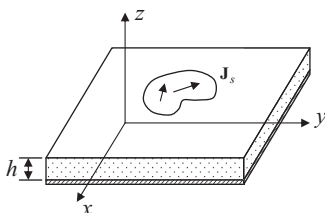


Figure 10.24 Surface electric current \mathbf{J}_s radiating in the presence of a grounded substrate.

in which

$$\tilde{\mathbf{G}}_T(\mathbf{r}; x', y') = \frac{1}{4\pi^2} \int_{-\infty}^{\infty} \int_{-\infty}^{\infty} \tilde{\mathbf{G}}_T(k_x, k_y) e^{j[k_x(x-x')+k_y(y-y')-k_{z0}z]} dk_x dk_y \quad (10.5.4)$$

for $z \geq 0$ and

$$\tilde{\mathbf{G}}_T(\mathbf{r}; x', y') = \frac{1}{4\pi^2} \int_{-\infty}^{\infty} \int_{-\infty}^{\infty} \tilde{\mathbf{G}}_T(k_x, k_y) e^{j[k_x(x-x')+k_y(y-y')]} \frac{\sin k_{zd}(z+h)}{\sin k_{zd}h} dk_x dk_y \quad (10.5.5)$$

for $-h \leq z \leq 0$, where

$$\tilde{\mathbf{G}}_T(k_x, k_y) = (\hat{x}\hat{x} + \hat{y}\hat{y})\tilde{G}_A(k_x, k_y) - \frac{1}{k_0^2}(k_x\hat{x} + k_y\hat{y})(k_x\hat{x} + k_y\hat{y})\tilde{G}_\phi(k_x, k_y). \quad (10.5.6)$$

In the above, $k_{z0} = \sqrt{k_0^2 - k_x^2 - k_y^2}$, $k_{zd} = \sqrt{\epsilon_r k_0^2 - k_x^2 - k_y^2}$, and

$$\tilde{G}_A(k_x, k_y) = \frac{1}{D_{TE}} \quad (10.5.7)$$

$$\tilde{G}_\phi(k_x, k_y) = \frac{jk_{z0} - k_{zd} \tan k_{zd}h}{D_{TE} D_{TM}} \quad (10.5.8)$$

where

$$D_{TE} = jk_{z0} + k_{zd} \cot k_{zd}h, \quad D_{TM} = j\epsilon_r k_{z0} - k_{zd} \tan k_{zd}h. \quad (10.5.9)$$

Substituting Equation 10.5.6 into Equation 10.5.4 or 10.5.5 and then into Equation 10.5.3, we obtain

$$\begin{aligned} \mathbf{E}_T(\mathbf{r}) &= -jk_0 Z_0 \int_{-\infty}^{\infty} \int_{-\infty}^{\infty} \left[G_A(\mathbf{r}; x', y') \mathbf{J}_s(x', y') + \frac{1}{k_0^2} \nabla_t \nabla_t G_\phi(\mathbf{r}; x', y') \cdot \mathbf{J}_s(x', y') \right] dx' dy' \\ &= -jk_0 Z_0 \int_{-\infty}^{\infty} \int_{-\infty}^{\infty} \left[G_A(\mathbf{r}; x', y') \mathbf{J}_s(x', y') + \frac{1}{k_0^2} \nabla_t G_\phi(\mathbf{r}; x', y') \nabla' \cdot \mathbf{J}_s(x', y') \right] dx' dy' \end{aligned} \quad (10.5.10)$$

where $\nabla_t = \hat{x}\partial/\partial x + \hat{y}\partial/\partial y$ and we have employed a vector identity and the surface divergence theorem to transfer one del operator to the surface current density. The expressions of G_A and G_ϕ are given by

$$G_A(\mathbf{r}; x', y') = \frac{1}{4\pi^2} \int_{-\infty}^{\infty} \int_{-\infty}^{\infty} \tilde{G}_A(k_x, k_y) e^{j[k_x(x-x')+k_y(y-y')-k_{z0}z]} dk_x dk_y \quad (10.5.11)$$

$$G_\phi(\mathbf{r}; x', y') = \frac{1}{4\pi^2} \int_{-\infty}^{\infty} \int_{-\infty}^{\infty} \tilde{G}_\phi(k_x, k_y) e^{j[k_x(x-x')+k_y(y-y')-k_{z0}z]} dk_x dk_y \quad (10.5.12)$$

for $z \geq 0$. The expressions for $-h \leq z \leq 0$ can be obtained by replacing the exponential function $e^{-jk_{z0}z}$ with $\sin k_{zd}(z+h)/\sin k_{zd}h$, as it was done from Equations 10.5.4 and 10.5.5.

The double integrals in Equations 10.5.11 and 10.5.12 over k_x and k_y can be converted into a single integral by letting $k_x = k_\rho \cos \alpha$ and $k_y = k_\rho \sin \alpha$ and evaluating the integrals over k_ρ and α , that is,

$$\int_{-\infty}^{\infty} \int_{-\infty}^{\infty} [\bullet] dk_x dk_y = \int_0^{\infty} \int_0^{2\pi} [\bullet] k_\rho d\alpha dk_\rho. \quad (10.5.13)$$

By using the integral representation of the Bessel function

$$\int_0^{2\pi} e^{ik_\rho |\mathbf{p} - \mathbf{p}'| \cos(\phi - \alpha)} d\alpha = 2\pi J_0(k_\rho |\mathbf{p} - \mathbf{p}'|) \quad (10.5.14)$$

we have

$$G_A(\mathbf{r}; \mathbf{p}') = \frac{1}{2\pi} \int_0^{\infty} \tilde{G}_A(k_\rho) J_0(k_\rho |\mathbf{p} - \mathbf{p}'|) e^{-jk_{z0}z} k_\rho dk_\rho \quad (10.5.15)$$

$$G_\varphi(\mathbf{r}; \mathbf{p}') = \frac{1}{2\pi} \int_0^{\infty} \tilde{G}_\varphi(k_\rho) J_0(k_\rho |\mathbf{p} - \mathbf{p}'|) e^{-jk_{z0}z} k_\rho dk_\rho \quad (10.5.16)$$

for $z \geq 0$, where $k_{z0} = \sqrt{k_0^2 - k_\rho^2}$ and $k_{zd} = \sqrt{\epsilon_r k_0^2 - k_\rho^2}$. The integrals in these two equations are known as the Sommerfeld integrals. By expressing the Bessel function in terms of the Hankel functions, these results can be alternatively expressed as

$$G_A(\mathbf{r}; \mathbf{p}') = \frac{1}{4\pi} \int_{-\infty}^{\infty} \tilde{G}_A(k_\rho) H_0^{(2)}(k_\rho |\mathbf{p} - \mathbf{p}'|) e^{-jk_{z0}z} k_\rho dk_\rho \quad (10.5.17)$$

$$G_\varphi(\mathbf{r}; \mathbf{p}') = \frac{1}{4\pi} \int_{-\infty}^{\infty} \tilde{G}_\varphi(k_\rho) H_0^{(2)}(k_\rho |\mathbf{p} - \mathbf{p}'|) e^{-jk_{z0}z} k_\rho dk_\rho. \quad (10.5.18)$$

The integration can be performed along the real axis C_0 in the complex k_ρ plane or along any other deformed path C_1 passing through the origin and lying in the first and third quadrants, as shown in Figure 10.25. The integration path C_0 can be deformed to C_1 because no singularity is encountered in the deformation.

To establish an integral equation to solve for \mathbf{J}_s , we apply Equation 10.5.10 to the surface of the microstrip conductor denoted by S_p and enforce the boundary condition $\mathbf{E}_T^{\text{exc}}(\mathbf{r}) + \mathbf{E}_T(\mathbf{r}) = 0$ for $\mathbf{r} \in S_p$, to find

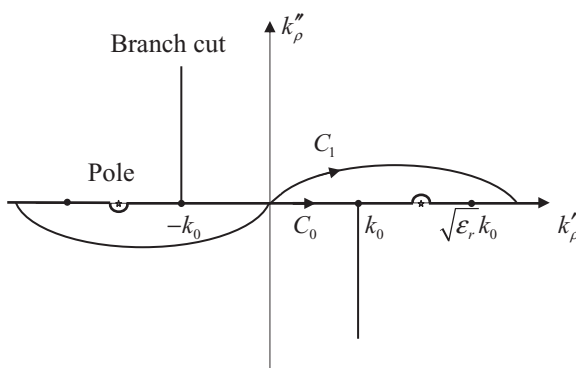


Figure 10.25 Integration contours C_0 and C_1 in the complex k_ρ plane.

$$\iint_{S_p} \left[G_A(\rho, \rho') \mathbf{J}_s(\rho') + \frac{1}{k_0^2} \nabla G_\phi(\rho, \rho') \nabla' \cdot \mathbf{J}_s(\rho') \right] dS' = \frac{1}{jk_0 Z_0} \mathbf{E}_T^{\text{exc}}(\rho) \quad \rho \in S_p \quad (10.5.19)$$

where $G_A(\rho, \rho')$ and $G_\phi(\rho, \rho')$ are obtained by setting $z=0$ in Equations 10.5.15 and 10.5.16 and $\mathbf{E}_T^{\text{exc}}$ denotes the transverse component of the excitation field—the field excited by a source in the presence of the grounded dielectric substrate without the microstrip. For example, for the scattering case it would be the sum of the incident field and the field reflected by the grounded substrate. Equation 10.5.19 is often called the *mixed-potential integral equation* (MPIE), which is actually equivalent to the EFIE.

As mentioned earlier, we considered a single-layer dielectric substrate here simply for the sake of clarity. In fact, the MPIE can be formulated for more general multilayer media with sources either residing on the top surface or embedded in the media [31–33]. The derivation can be facilitated by using a transmission-line analog for a multilayer medium. The final equation is similar to Equation 10.5.19, although the Green's functions are different. The formulation can further be extended to the cases with vertical electric currents in the media, which would allow the analysis of complex three-dimensional circuits in a multilayer medium.

10.5.2 The Moment-Method Solution

The solution of the integral equation (Eq. 10.5.19) using the moment method is straightforward. The first step is to subdivide the surface of the microstrip conductor into small triangular patches. The second step is to expand the surface current in terms of certain basis functions. If RWG basis functions are chosen, the surface current can be expanded as

$$\mathbf{J}_s(\rho') = \sum_{n=1}^N I_n \boldsymbol{\Lambda}_n(\rho') \quad (10.5.20)$$

where N is the number of unknowns, which is the number of edges shared by two triangular patches. Using the same basis functions as the testing functions, we can convert Equation 10.5.19 into the matrix equation

$$\sum_{n=1}^N Z_{mn} I_n = V_m \quad m = 1, 2, \dots, N \quad (10.5.21)$$

in which

$$Z_{mn} = \iint_{S_p} \iint_{S_p} \left[\boldsymbol{\Lambda}_m(\rho) \cdot G_A(\rho, \rho') \boldsymbol{\Lambda}_n(\rho') - \frac{1}{k_0^2} \nabla \cdot \boldsymbol{\Lambda}_m(\rho) G_\phi(\rho, \rho') \nabla' \cdot \boldsymbol{\Lambda}_n(\rho') \right] dS' dS \quad (10.5.22)$$

$$V_m = \frac{1}{jk_0 Z_0} \iint_{S_p} \boldsymbol{\Lambda}_m(\rho) \cdot \mathbf{E}_T^{\text{exc}}(\rho) dS. \quad (10.5.23)$$

10.5.3 Evaluation of Green's Functions

Although the moment-method formulation is straightforward, the main difficulty occurs in the evaluation of $G_A(\rho, \rho')$ and $G_\phi(\rho, \rho')$. Note that since both $G_A(\rho, \rho')$ and $G_\phi(\rho, \rho')$

depend only on $\rho = |\mathbf{p} - \mathbf{p}'|$, it would be sufficient to consider the evaluation of the Sommerfeld integrals

$$G_A(\rho) = \frac{1}{2\pi} \int_0^\infty \tilde{G}_A(k_\rho) J_0(k_\rho \rho) k_\rho dk_\rho \quad (10.5.24)$$

$$G_\phi(\rho) = \frac{1}{2\pi} \int_0^\infty \tilde{G}_\phi(k_\rho) J_0(k_\rho \rho) k_\rho dk_\rho. \quad (10.5.25)$$

Unfortunately, these integrals cannot be evaluated analytically for a general integrand, and the numerical integration is time-consuming because the integrand involved is highly oscillatory and decays slowly. Over the past several decades, much research has been conducted for an efficient evaluation of these integrals [34]. One of the efficient techniques is called the *discrete complex image method* (DCIM) [35,36], which is based on the Sommerfeld identity [37] given by

$$\frac{e^{-jkr}}{r} = \int_0^\infty \frac{1}{jk_z} J_0(k_\rho \rho) e^{-jk_z |z|} k_\rho dk_\rho \quad (10.5.26)$$

or equivalently,

$$\frac{e^{-jkr}}{r} = \int_{-\infty}^{\infty} \frac{1}{j2k_z} H_0^{(2)}(k_\rho \rho) e^{-jk_z |z|} k_\rho dk_\rho \quad (10.5.27)$$

where $k = \sqrt{k_\rho^2 + k_z^2}$ and $r = \sqrt{\rho^2 + z^2}$.

The basic idea of the DCIM is to represent $G_A(\rho)$ and $G_\phi(\rho)$ as a summation of contributions from their free-space component, quasi-dynamic images, surface waves, and complex images. To illustrate this clearly, we first consider $G_A(\rho)$ by following the treatment presented in Reference [36]. If the grounded substrate is removed, then

$$\tilde{G}_A(k_\rho) \rightarrow \frac{1}{j2k_{z0}} \quad (10.5.28)$$

which would yield the free-space Green's function. Hence, we can first extract this dominant term from $G_A(\rho)$ by

$$G_A(\rho) = \frac{e^{-jk_0 r_0}}{4\pi r_0} + \frac{1}{2\pi} \int_0^\infty \left[\tilde{G}_A(k_\rho) - \frac{1}{j2k_{z0}} \right] J_0(k_\rho \rho) k_\rho dk_\rho \quad (10.5.29)$$

where $r_0 = \rho$. Next, we observe that when the frequency approaches zero, $k_0 \rightarrow 0$ and $k_{z0} \approx k_{zd}$. Under this situation,

$$\tilde{G}_A(k_\rho) - \frac{1}{j2k_{z0}} = \frac{1}{D_{TE}} - \frac{1}{j2k_{z0}} \rightarrow -\frac{1}{j2k_{z0}} e^{-j2k_{z0} h} \quad (10.5.30)$$

which represents a dominant term at low frequencies. Extracting this term out, we have

$$G_A(\rho) = \frac{e^{-jk_0 r_0}}{4\pi r_0} - \frac{e^{-jk_0 r_1}}{4\pi r_1} + \frac{1}{2\pi} \int_0^\infty \left[\tilde{G}_A(k_\rho) - \frac{1}{j2k_{z0}} (1 - e^{-j2k_{z0} h}) \right] J_0(k_\rho \rho) k_\rho dk_\rho \quad (10.5.31)$$

where $r_1 = \sqrt{\rho^2 + (2h)^2}$. Clearly, the second term here represents the quasi-dynamic image [38]. Since a grounded substrate can support surface waves, which would dominate when ρ becomes large, and since the surface waves cannot be represented by spherical waves, it is necessary to extract out the contribution from surface waves explicitly. For $G_A(\rho)$, the associated TE surface waves correspond to the poles of $\tilde{G}_A(k_\rho)$, which occur at $D_{\text{TE}} = 0$ or

$$jk_{z0} + k_{zd} \cot k_{zd} h = 0 \quad (10.5.32)$$

whose solutions can be denoted as $k_{\rho p}$. The contributions of these poles to the integral can be evaluated explicitly, and the result is

$$G_A^{(\text{sw})}(\rho) = \frac{1}{2j} \sum_{p(\text{TE})} R_{A,p} H_0^{(2)}(k_{\rho p} \rho) k_{\rho p} \quad (10.5.33)$$

where $R_{A,p}$ represents the residue at the pole $k_\rho = k_{\rho p}$, which is given by

$$R_{A,p} = \lim_{k_\rho \rightarrow k_{\rho p}} (k_\rho - k_{\rho p}) \tilde{G}_A(k_\rho). \quad (10.5.34)$$

With this extraction, Equation 10.5.31 can be written as

$$G_A(\rho) = G_{A,0}(\rho) + G_A^{(\text{sw})}(\rho) + \frac{1}{2\pi} \int_0^\infty \frac{F_1(k_\rho)}{j2k_{z0}} J_0(k_\rho \rho) k_\rho dk_\rho \quad (10.5.35)$$

where

$$G_{A,0}(\rho) = \frac{e^{-jk_0 r_0}}{4\pi r_0} - \frac{e^{-jk_0 r_1}}{4\pi r_1} \quad (10.5.36)$$

$$\frac{F_1(k_\rho)}{j2k_{z0}} = \tilde{G}_A(k_\rho) - \frac{1 - e^{-j2k_{z0} h}}{j2k_{z0}} - \sum_{p(\text{TE})} \frac{2k_{\rho p} R_{A,p}}{k_\rho^2 - k_{\rho p}^2}. \quad (10.5.37)$$

The remaining integral in Equation 10.5.35 can be evaluated by first approximating $F_1(k_\rho)$ by a sum of complex exponentials, since $F_1(k_\rho)$ is now non-oscillatory and decays very quickly. This approximation can be written as

$$F_1(k_\rho) \approx \sum_{i=1}^M a_i e^{-b_i k_{z0}} \quad (10.5.38)$$

where a_i and b_i can be calculated using either the Prony method [39] or the generalized pencil-of-function (GPOF) method [40]. With this approximation, Equation 10.5.35 can finally be written as

$$G_A(\rho) \approx G_{A,0}(\rho) + G_A^{(\text{sw})}(\rho) + G_A^{(\text{ci})}(\rho) \quad (10.5.39)$$

where

$$G_A^{(\text{ci})}(\rho) = \sum_{i=1}^M a_i \frac{e^{-jk_0 r_i}}{4\pi r_i} \quad r_i = \sqrt{\rho^2 - b_i^2}. \quad (10.5.40)$$

It is obvious that each term in Equation 10.5.40 represents a spherical wave of amplitude a_i originated at $\rho = 0$ and $z = jb_i$. Since a_i and b_i are complex numbers in general, the source for each term can be interpreted as a complex image and, hence, Equation 10.5.40 is the contribution from a series of complex images.

The procedure described above can be applied to the calculation of $G_\varphi(\rho)$ given in Equation 10.5.25. We first extract the free-space term to have

$$G_\varphi(\rho) = \frac{e^{-jk_0r_0}}{4\pi r_0} + \frac{1}{2\pi} \int_0^\infty \left[\tilde{G}_\varphi(k_\rho) - \frac{1}{j2k_{z0}} \right] J_0(k_\rho\rho) k_\rho dk_\rho. \quad (10.5.41)$$

Next, we observe that when the frequency approaches zero, $k_0 \rightarrow 0$ and $k_{z0} \approx k_{zd}$ and

$$\tilde{G}_\varphi(k_\rho) - \frac{1}{j2k_{z0}} \rightarrow \frac{1}{j2k_{z0}} \left[K \frac{1 - e^{-j4k_{z0}h}}{1 - Ke^{-j2k_{z0}h}} - e^{-j2k_{z0}h} \right] \quad (10.5.42)$$

where $K = (1 - \varepsilon_r)/(1 + \varepsilon_r)$. Expanding the first term in the brackets in Taylor series and keeping the two leading terms, we have

$$\begin{aligned} \tilde{G}_\varphi(k_\rho) - \frac{1}{j2k_{z0}} &\rightarrow \frac{1}{j2k_{z0}} \left[K(1 - e^{-j4k_{z0}h})(1 + Ke^{-j2k_{z0}h}) - e^{-j2k_{z0}h} \right] \\ &\rightarrow \frac{1}{j2k_{z0}} \left[K + (K^2 - 1)e^{-j2k_{z0}h} - Ke^{-j4k_{z0}h} - K^2 e^{-j6k_{z0}h} \right]. \end{aligned} \quad (10.5.43)$$

With this extraction of the quasi-dynamic terms, Equation 10.5.41 becomes

$$G_\varphi(\rho) = G_{\varphi,0}(\rho) + \frac{1}{2\pi} \int_0^\infty \left[\tilde{G}_\varphi(k_\rho) - \tilde{G}_{\varphi,0}(k_\rho) \right] J_0(k_\rho\rho) k_\rho dk_\rho \quad (10.5.44)$$

where

$$\tilde{G}_{\varphi,0}(k_\rho) = \frac{1}{j2k_{z0}} \left[(1 + K) + (K^2 - 1)e^{-j2k_{z0}h} - Ke^{-j4k_{z0}h} - K^2 e^{-j6k_{z0}h} \right] \quad (10.5.45)$$

$$G_{\varphi,0}(\rho) = (1 + K) \frac{e^{-jk_0r_0}}{4\pi r_0} + (K^2 - 1) \frac{e^{-jk_0r_1}}{4\pi r_1} - K \frac{e^{-jk_0r_2}}{4\pi r_2} - K^2 \frac{e^{-jk_0r_3}}{4\pi r_3} \quad (10.5.46)$$

in which $r_n = \sqrt{\rho^2 + (2nh)^2}$. Next, we extract the surface-wave component from the Sommerfeld integral in Equation 10.5.44. It is clear from the expression of $\tilde{G}_\varphi(k_\rho)$ given in Equation 10.5.8 that there are two sets of surface waves—one corresponds to $D_{TE} = 0$ and the other corresponds to $D_{TM} = 0$. The first set consists of TE surface waves, whose propagation constants k_ρ can be calculated by solving Equation 10.5.32. The second set consists of TM surface waves, whose propagation constants k_ρ can be calculated by solving the following transcendental equation

$$j\varepsilon_r k_{z0} - k_{zd} \tan k_{zd} h = 0. \quad (10.5.47)$$

The contributions of these poles to the integral can be evaluated explicitly as

$$G_{\varphi}^{(\text{sw})}(\rho) = \frac{1}{2j} \sum_{p(\text{TE,TM})} R_{\varphi,p} H_0^{(2)}(k_{\rho p} \rho) k_{\rho p} \quad (10.5.48)$$

where $R_{\varphi p}$ represents the residue at the pole $k_p = k_{\rho p}$, which is given by

$$R_{\varphi,p} = \lim_{k_p \rightarrow k_{\rho p}} (k_p - k_{\rho p}) \tilde{G}_{\varphi}(k_p). \quad (10.5.49)$$

With this extraction, Equation 10.5.44 can be written as

$$G_{\varphi}(\rho) = G_{\varphi,0}(\rho) + G_{\varphi}^{(\text{sw})}(\rho) + \frac{1}{2\pi} \int_0^{\infty} \frac{F_2(k_p)}{j2k_{z0}} J_0(k_p \rho) k_p dk_p \quad (10.5.50)$$

where

$$\begin{aligned} \frac{F_2(k_p)}{j2k_{z0}} &= \tilde{G}_{\varphi}(k_p) - \frac{1}{j2k_{z0}} \left[1 + K(1 - e^{-j4k_{z0}h})(1 + Ke^{-j2k_{z0}h}) - e^{-j2k_{z0}h} \right] \\ &\quad - \sum_{p(\text{TE,TM})} \frac{2k_{\rho p} R_{\varphi,p}}{k_p^2 - k_{\rho p}^2}. \end{aligned} \quad (10.5.51)$$

The remaining integral in Equation 10.5.50 can be evaluated by first approximating $F_2(k_p)$ by a sum of complex exponentials, since after the free-space, quasi-dynamic, and surface-wave terms are extracted, $F_2(k_p)$ is now non-oscillatory and decays very quickly. This approximation can be written as

$$F_2(k_p) \approx \sum_{i=1}^M a'_i e^{-b'_i k_{z0}} \quad (10.5.52)$$

where a'_i and b'_i can be calculated using either the Prony or the GPOF method. With this approximation, Equation 10.5.50 can finally be written as

$$G_{\varphi}(\rho) \approx G_{\varphi,0}(\rho) + G_{\varphi}^{(\text{sw})}(\rho) + G_{\varphi}^{(\text{ci})}(\rho) \quad (10.5.53)$$

where

$$G_{\varphi}^{(\text{ci})}(\rho) = \sum_{i=1}^M a'_i \frac{e^{-jk_0 r'_i}}{4\pi r'_i} \quad r_i = \sqrt{\rho^2 - b'^2_i}. \quad (10.5.54)$$

Again, each term in Equation 10.5.54 represents a complex image with a complex amplitude and a complex location. With the DCIM, we have now obtained the closed-form expressions for $G_A(\rho)$ and $G_{\varphi}(\rho)$, which can be used in the calculation of Z_{mn} in Equation 10.5.22 for the moment-method solution.

The DCIM can be applied to the evaluation of Green's functions for a multilayer medium [41–44]. The major challenge for the multilayer medium application is the calculation of the surface-wave poles $k_{\rho p}$ and the associated residues $R_{A,p}$ and $R_{\varphi,p}$ for both TE and TM cases. To this end, the technique proposed in Reference [45] has been found to be very effective [44]. In this technique, the surface-wave poles $k_{\rho p}$ and the associated residues $R_{A,p}$ and $R_{\varphi,p}$ are determined through a recursive process by a numerical evaluation

of a contour integral in the complex k_p plane. The integration begins with a rectangular box enclosing all possible surface-wave poles. If the calculated value of the contour integral is non-zero, which indicates that the contour contains a pole or poles, then we subdivide the box into four subboxes and calculate the contour integral along each of them. This process is repeated until the locations of k_{pp} and residues $R_{A,p}$ and $R_{q,p}$ for all the poles inside the initial box are determined to a desired accuracy.

10.5.4 Far-Field Calculation and Application Examples

Once the surface current \mathbf{J}_s is calculated using the moment method, the radiated field in the far zone can be evaluated by the stationary phase method, which is a commonly used approach. A much simpler approach is to employ the reciprocity theorem [46]. In this approach, an infinitesimally small current element is placed at the observation point. Because this current element is located far from \mathbf{J}_s , the wave it produces can be regarded as a plane wave when incident upon the substrate where \mathbf{J}_s resides. More specifically, let the field radiated by \mathbf{J}_s be denoted as \mathbf{E}^{rad} , the field produced by the current element in the presence of the grounded substrate (with the microstrip removed) be denoted as \mathbf{E}_D , and the current density of the current element be denoted as \mathbf{J}_D . Note that \mathbf{E}_D can be found easily and it consists of the incident and reflected fields. According to the reciprocity theorem, we have

$$\iiint \mathbf{E}^{\text{rad}} \cdot \mathbf{J}_D dV = \iint_{S_p} \mathbf{E}_D \cdot \mathbf{J}_s dS. \quad (10.5.55)$$

Assuming that the current element has a dipole moment of Il and is located at (r, θ, ϕ) and oriented in the \hat{a} -direction, then Equation 10.5.55 becomes

$$\hat{a} \cdot \mathbf{E}^{\text{rad}}(r, \theta, \phi) = \frac{1}{Il} \iint_{S_p} \mathbf{E}_D \cdot \mathbf{J}_s dS. \quad (10.5.56)$$

To find the θ - and ϕ -components of the radiated field, we let $\hat{a} = \hat{\theta}$ and $\hat{\phi}$, respectively, and then use the expression of the field produced by a current element to find

$$E_\theta^{\text{rad}}(r, \theta, \phi) = -\frac{jk_0 Z_0 e^{-jk_0 r}}{4\pi r} \iint_{S_p} \mathbf{E}_D^{(\theta)} \cdot \mathbf{J}_s dS \quad (10.5.57)$$

$$E_\phi^{\text{rad}}(r, \theta, \phi) = -\frac{jk_0 Z_0 e^{-jk_0 r}}{4\pi r} \iint_{S_p} \mathbf{E}_D^{(\phi)} \cdot \mathbf{J}_s dS \quad (10.5.58)$$

where $\mathbf{E}_D^{(\theta)}$ and $\mathbf{E}_D^{(\phi)}$ denote the total electric field excited by the incident plane wave with a unit magnitude and with the electric field polarized in the $\hat{\theta}$ - and $\hat{\phi}$ -directions, respectively.

As a simple example, the moment method is applied to the analysis of a microstrip double stub on a single-layer dielectric substrate having a thickness of $h = 0.127$ mm and a relative permittivity of $\epsilon_r = 9.9$ [47]. The calculated S-parameters are compared with the measured data in Figure 10.26, showing very good agreement. As another example, the radiation from a series-fed microstrip antenna array is analyzed [46], and the E-plane radiation pattern is shown in Figure 10.27. The calculated result compares well with the experimental result. More examples can be found in References [46–48].

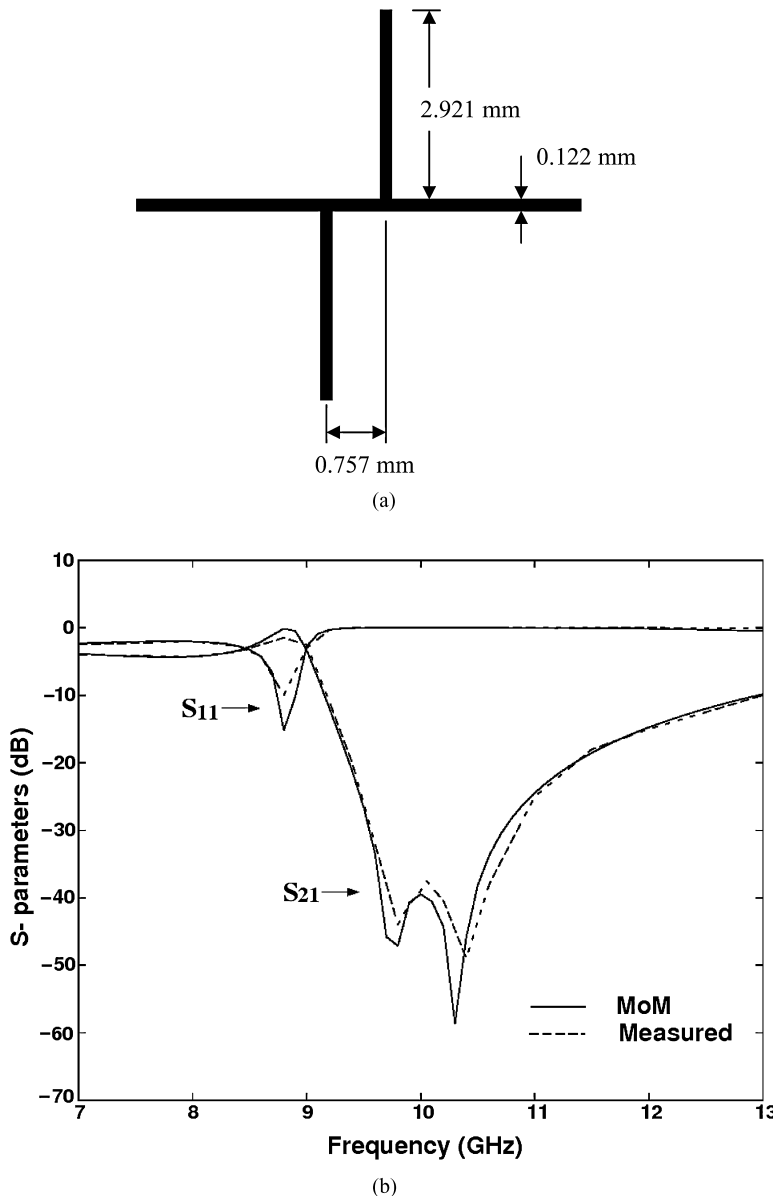


Figure 10.26 S-parameters for a microstrip double stub. (a) Geometry ($\epsilon_r = 9.9$, $h = 0.127$ mm, the line width is 0.122 mm, the stub length is 2.921 mm, and the spacing between the two stubs is 0.757 mm). (b) S-parameters. (After Ling et al. [47], Copyright © IEEE 1999.)

10.6 THE MOMENT METHOD IN THE TIME DOMAIN

Although the moment method is often employed for the frequency-domain analysis of electromagnetic problems, it can also be implemented in the time domain to obtain all the advantages associated with a time-domain analysis [49–56]. However, the time-domain moment-method analysis is more complicated in formulation and more expensive in simulation. Much research effort has been devoted recently to make this analysis more robust

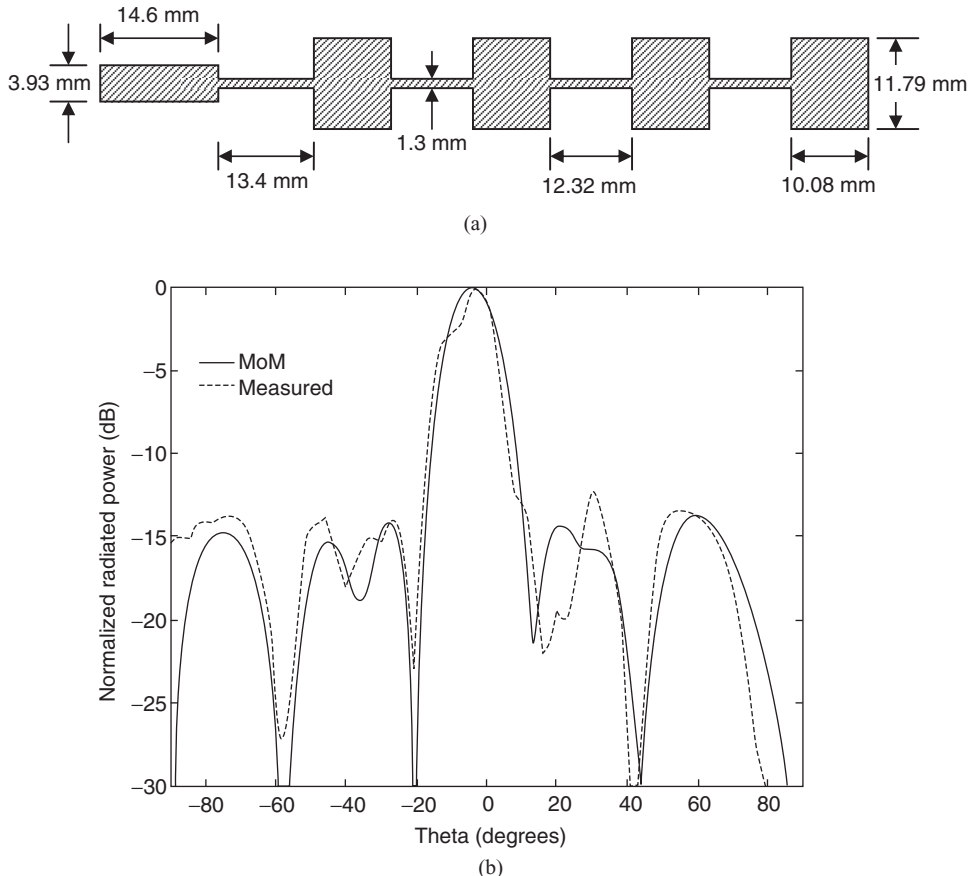


Figure 10.27 E-plane radiation pattern of a series-fed microstrip antenna array at 9.42 GHz. (a) Geometry (the antenna array is printed on a substrate of relative permittivity $\epsilon_r = 2.1$ and thickness $h = 1.575$ mm). (b) Normalized radiated power. (After Ling and Jin [46], Copyright © Wiley 1997.)

and efficient. In this section, we use a relatively simple example to illustrate the formulation of the time-domain moment method and its solution process.

10.6.1 Time-Domain Integral Equations

As in the frequency-domain formulation, the first step of the time-domain moment-method analysis is to formulate the required integral equation in the time domain. This can be accomplished by applying the Laplace transform to the integral equations in the frequency domain. To illustrate this, we consider the problem of scattering by a conducting object. The EFIE for this problem is given by Equation 10.3.45, which can be more explicitly written as

$$\hat{n} \times \iint_{S_o} [(jk_0)^2 \bar{\mathbf{J}}_s(\mathbf{r}') G_0(\mathbf{r}, \mathbf{r}') - \nabla' \cdot \bar{\mathbf{J}}_s(\mathbf{r}') \nabla G_0(\mathbf{r}, \mathbf{r}')] dS' = jk_0 \hat{n} \times \mathbf{E}^{\text{inc}}(\mathbf{r}) \quad (10.6.1)$$

whose Laplace transform is given by

$$\hat{n} \times \iint_{S_o} \left[\frac{\partial^2 \bar{\mathcal{J}}_s(\mathbf{r}', t - R/c_0)}{\partial t^2} - c_0 \nabla' \cdot \frac{\nabla' \cdot \bar{\mathcal{J}}_s(\mathbf{r}', t - R/c_0)}{4\pi R} \right] dS' = \hat{n} \times \frac{\partial \mathcal{E}^{\text{inc}}(\mathbf{r}, t)}{\partial t} \quad (10.6.2)$$

where $c_0 = \omega/k_0$ and $R = |\mathbf{r} - \mathbf{r}'|$. Equation 10.6.2 is called a *time-domain integral equation* (TDIE), and in this case, it is specifically the time-domain EFIE. Similarly, the MFIE in Equation 10.3.46 can be transformed into the time domain as

$$\frac{1}{2} \frac{\partial \bar{\mathcal{J}}_s(\mathbf{r}, t)}{\partial t} - \hat{n} \times \iint_{S_o} \nabla \times \frac{\partial \bar{\mathcal{J}}_s(\mathbf{r}', t - R/c_0)}{\partial t} dS' = \hat{n} \times \frac{\partial \bar{\mathcal{H}}^{\text{inc}}(\mathbf{r}, t)}{\partial t} \quad (10.6.3)$$

which can be combined with Equation 10.6.2 to form the time-domain CFIE.

10.6.2 Marching-On-in-Time Solution

To solve a TDIE, we first have to expand the unknown function in both the spatial and temporal spaces. The spatial expansion can have the same form as adopted in the frequency domain. If we use the RWG basis functions for the spatial expansion, $\bar{\mathcal{J}}_s(\mathbf{r}', t)$ can be expressed as

$$\bar{\mathcal{J}}_s(\mathbf{r}', t) \equiv \sum_{n=1}^{N_s} \mathcal{I}_n(t) \Lambda_n(\mathbf{r}') \quad (10.6.4)$$

where N_s denotes the number of edges shared by two triangular patches. To solve for the unknown expansion coefficients, which are functions of time, we also have to expand them using temporal basis functions such that

$$\mathcal{I}_n(t) \equiv \sum_{l=1}^{N_t} \mathcal{I}_n^{(l)} T_l(t) \quad (10.6.5)$$

where N_t denotes the total number of temporal samples or time steps and $T_l(t) = T(t - l\Delta t)$ denotes the temporal basis functions. The common choices for $T(t)$ are a piecewise quadratic function [53]

$$T(t) = \begin{cases} \frac{1}{2} \left(\frac{t}{\Delta t} \right)^2 + \frac{3t}{2\Delta t} + 1 & -\Delta t \leq t \leq 0 \\ -\left(\frac{t}{\Delta t} \right)^2 + 1 & 0 \leq t \leq \Delta t \\ \frac{1}{2} \left(\frac{t}{\Delta t} \right)^2 - \frac{3t}{2\Delta t} + 1 & \Delta t \leq t \leq 2\Delta t \\ 0 & \text{elsewhere} \end{cases} \quad (10.6.6)$$

and the shifted quadratic B-spline function [57]

$$T(t) = \begin{cases} \frac{1}{2} \left(\frac{t}{\Delta t} + 1 \right)^2 & -\Delta t \leq t \leq 0 \\ -\left(\frac{t}{\Delta t} \right)^2 + \frac{t}{\Delta t} + \frac{1}{2} & 0 \leq t \leq \Delta t \\ \frac{1}{2} \left(\frac{t}{\Delta t} - 1 \right)^2 - \left(\frac{t}{\Delta t} - 1 \right) + \frac{1}{2} & \Delta t \leq t \leq 2\Delta t \\ 0 & \text{elsewhere} \end{cases} \quad (10.6.7)$$

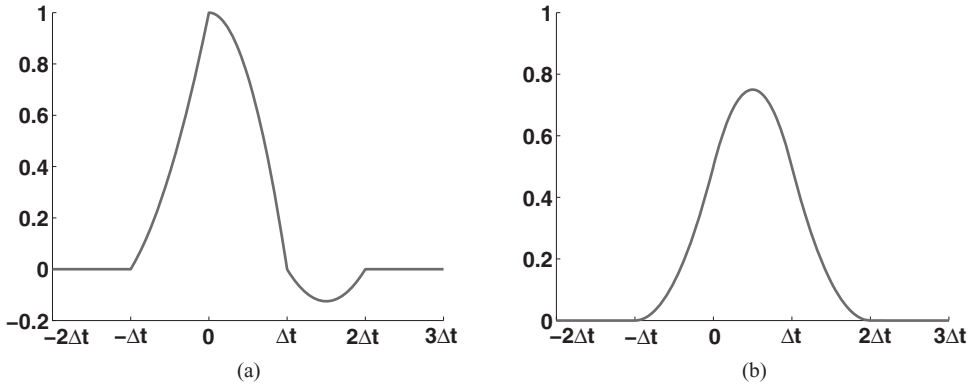


Figure 10.28 (a) Piecewise quadratic function. (b) Shifted quadratic B-spline function.

which are plotted in Figure 10.28.

By combining Equations 10.6.4 and 10.6.5, we have the complete discretization of the unknown function as

$$\bar{\mathcal{J}}_s(\mathbf{r}', t) \equiv \sum_{n=1}^{N_s} \sum_{l=1}^{N_t} \mathcal{I}_n^{(l)} \Lambda_n(\mathbf{r}') T(t - l\Delta t). \quad (10.6.8)$$

Apparently, the total number of unknown expansion coefficients is $N_s N_t$, which can be a very large number. To convert an integral equation into a matrix equation, we also have to select a set of testing functions. A popular choice for spatial testing is $\Lambda_m(\mathbf{r})$, which is same as the one typically used in the frequency domain. With the intent to obtain a time-stepping solution, the temporal testing is often carried out with the delta function $\delta(t - k\Delta t)$.

Now, let us use the EFIE to illustrate the discretization process. Substituting Equation 10.6.8 into Equation 10.6.2, testing it with $\Lambda_m(\mathbf{r})\delta(t - k\Delta t)$, and integrating the resulting equation, we obtain

$$[Z^{(0)}] \{ \mathcal{I} \}^{(1)} = \{ \mathcal{V} \}^{(1)} \quad (10.6.9)$$

$$[Z^{(1)}] \{ \mathcal{I} \}^{(1)} + [Z^{(0)}] \{ \mathcal{I} \}^{(2)} = \{ \mathcal{V} \}^{(2)} \quad (10.6.10)$$

$$[Z^{(2)}] \{ \mathcal{I} \}^{(1)} + [Z^{(1)}] \{ \mathcal{I} \}^{(2)} + [Z^{(0)}] \{ \mathcal{I} \}^{(3)} = \{ \mathcal{V} \}^{(3)} \quad (10.6.11)$$

and so on, which can be written uniformly as

$$[Z^{(0)}] \{ \mathcal{I} \}^{(k)} = \{ \mathcal{V} \}^{(k)} - \sum_{l=1}^{k-1} [Z^{(k-l)}] \{ \mathcal{I} \}^{(l)} \quad k = 1, 2, 3, \dots \quad (10.6.12)$$

In the above, $\{ \mathcal{I} \}^{(k)} = [\mathcal{I}_1^{(k)}, \mathcal{I}_2^{(k)}, \mathcal{I}_3^{(k)}, \dots, \mathcal{I}_{N_s}^{(k)}]^T$, and it is assumed that $\{ \mathcal{I} \}^{(k)} = 0$ for $k \leq 0$. Furthermore,

$$Z_{mn}^{(k-l)} = \iint_{S_o} \Lambda_m(\mathbf{r}) \cdot \iint_{S_o} \left[\frac{\Lambda_n(\mathbf{r}')}{4\pi c_0 R} \ddot{T}^{(k-l)} - c_0 \nabla \frac{\nabla' \cdot \Lambda_n(\mathbf{r}')}{4\pi R} T^{(k-l)} \right] dS' dS \quad (10.6.13)$$

$$\mathcal{V}_m^{(k)} = \iint_{S_o} \Lambda_m(\mathbf{r}) \cdot \dot{\mathcal{E}}^{\text{inc}}(\mathbf{r}, k\Delta t) dS \quad (10.6.14)$$

where $T^{(k-l)} = T((k-l)\Delta t - R/c_0)$, $\ddot{T} = \partial^2 T(t)/\partial t^2$, and $\dot{\mathcal{E}}^{\text{inc}} = \partial \mathcal{E}^{\text{inc}}(\mathbf{r}, t)/\partial t$. Two observations can be made based on the property of $T(t)$. First, since $T(t) = 0$ for $t < -\Delta t$, we can show that $Z_{mn}^{(0)} = 0$ for $R > c_0\Delta t$; hence, $[Z^{(0)}]$ is an extremely sparse matrix and represents the immediate interactions between the basis and testing functions within Δt . Second, since $T(t) = 0$ for $t > 2\Delta t$, we can also easily show that $Z_{mn}^{(k-l)} = 0$ for $k-l > R_{\max}/(c_0\Delta t) + 2$, where R_{\max} denotes the maximum linear dimension of the object (the maximum distance between any two points on S_o). Consequently, the number of terms in the summation of Equation 10.6.12 is limited.

Equation 10.6.12 can be used to compute the unknown current expansion coefficients step by step. Given the excitation vector $\{\mathcal{V}\}^{(k)}$, we can first use Equation 10.6.9 to compute $\{\mathcal{T}\}^{(1)}$, then use Equation 10.6.10 to compute $\{\mathcal{T}\}^{(2)}$, then use Equation 10.6.11 to compute $\{\mathcal{T}\}^{(3)}$, and so on. This process is called *marching-on-in-time* (MOT). In each step, we have to solve a matrix equation involving $[Z^{(0)}]$. Since this matrix is very sparse, it can be solved very efficiently. The most time-consuming part is actually to calculate the right-hand sides, which involves a summation of a series of matrix–vector products. As the time marching continues, the number of matrix–vector product terms increases and eventually reaches the maximum number of $R_{\max}/(c_0\Delta t) + 2$.

As an example, we consider the problem of plane wave scattering by a two-layer dielectric sphere, whose inner layer (core) has a radius of 0.8 m and a relative permittivity of 1.5 and whose outer layer has a radius of 1.0 m and a relative permittivity of 2.0. The monostatic RCS from 0 to 200 MHz is plotted in Figure 10.29, and the numerical results computed by the MOT are compared with the Mie series solution. With the MOT, we obtain the solution over the entire frequency band with one time-domain computation.

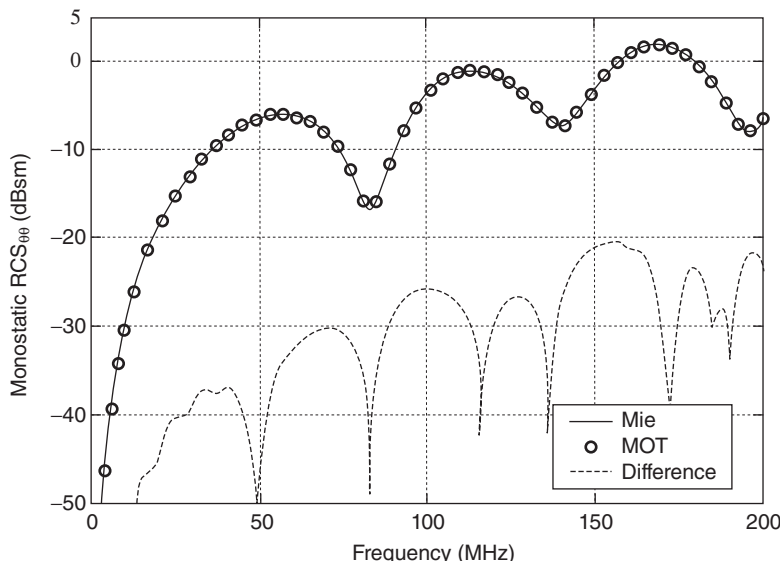


Figure 10.29 Monostatic RCS of a two-layer dielectric sphere whose inner layer (core) has a radius of 0.8 m and a relative permittivity of 1.5 and whose outer layer has a radius of 1.0 m and a relative permittivity of 2.0.

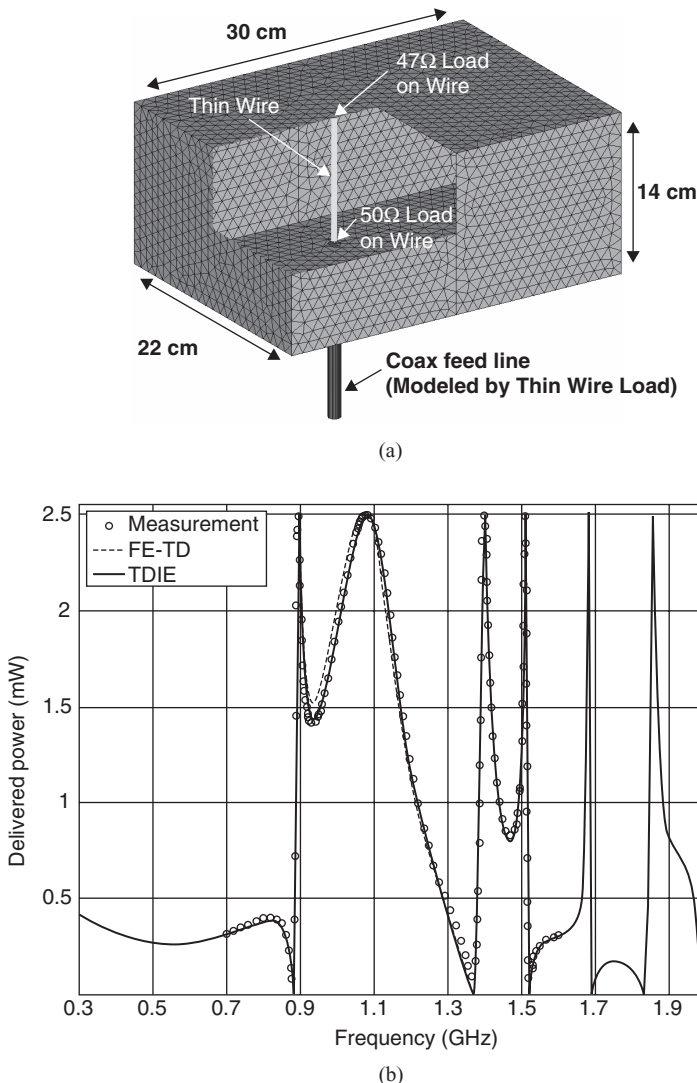


Figure 10.30 Rectangular cavity fed by a coaxial waveguide whose inner conductor is extended into the cavity and terminated by a 47Ω resistor. (a) Geometry. (b) Power delivered into the cavity. (After Bagci et al. [58], Copyright © IEEE 2007.)

As a more complex example, we consider a rectangular cavity fed by a coaxial waveguide, as shown Figure 10.30a. The inner conductor of the waveguide with a radius $a = 0.8\text{ mm}$ is extended from the lower surface to the upper surface of the cavity and terminated with a 47Ω lumped resistor on the upper surface. A delta-gap voltage source with a 50Ω impedance is used to represent the excitation from the coaxial waveguide. The temporal profile of the voltage source is specified by the amplitude $V_0 = 1\text{ V}$, center frequency $f_0 = 1.15\text{ GHz}$, and bandwidth $f_{bw} = 0.85\text{ GHz}$. To resolve all resonances of the cavity, the simulation is carried out for 15,000 time steps with a step size $\Delta t = 2\text{ ps}$. Figure 10.30b shows the power delivered to the cavity as computed by the TDIE solver [58] and compared with measured values [59] and results computed by a finite element-time domain (FE-TD) solver [60].

10.7 SUMMARY

In this chapter, we described the numerical procedure of the method of moments and its application to a variety of electromagnetic problems. We first used a static example—the calculation of the capacitance of a piece of conductor—to introduce the basic concept and the general principle of the moment method. This was followed by the formulation of a general integral equation for the Helmholtz equation in two dimensions, which was then specialized to the cases of electromagnetic scattering by a conducting cylinder, a conducting strip, and a homogeneous dielectric cylinder for both TE and TM polarizations. We then proceeded to three-dimensional problems, where a general integral equation was first formulated for the vector wave equation and its moment-method solution was then discussed for electromagnetic scattering and radiation by a conducting wire, a conducting body, a homogeneous dielectric body, and an inhomogeneous dielectric body. To demonstrate the application of the moment method to some important special problems, we considered the formulation of scattering by planar and angular periodic structures, where the unique features of the problem were exploited to reduce the computational domain and increase the efficiency of the moment-method solution. Furthermore, we illustrated the basic procedure of the moment method for the analysis of microstrip structures, which have a wide range of application in high-frequency circuits and antennas, and demonstrated the use of an appropriate Green's function to account for the effect of non-free-space background. Finally, we briefly discussed the application of the moment method in the time domain, which involved the transformation of integral equations from the frequency domain into the time domain and then the numerical solution via the MOT technique.

REFERENCES

- [1] K. K. MEI and J. Van BLADEL, Scattering by perfectly conducting rectangular cylinders, *IEEE Trans. Antennas Propagat.*, 11(2): 185–192, 1963.
- [2] M. G. ANDREASEN, Scattering from parallel metallic cylinders with arbitrary cross section, *IEEE Trans. Antennas Propagat.*, 12(6): 746–754, 1964.
- [3] F. K. OSHIRO, Source distribution techniques for the solution of general electromagnetic scattering problems, *Proc. First GISAT Symp. Mitre Corp.*, 1: 83–107, 1965.
- [4] J. H. RICHMOND, Scattering by a dielectric cylinder of arbitrary cross section shape, *IEEE Trans. Antennas Propagat.*, 13(3): 334–341, 1965.
- [5] R. F. HARRINGTON, *Field Computation by Moment Methods*. New York: Macmillan, 1968.
- [6] E. K. MILLER, L. MEDGYESI-MITSCHANG, and E. H. NEWMAN, Eds., *Computational Electromagnetics: Frequency-Domain Method of Moments*. New York: IEEE Press, 1992.
- [7] R. MITTRA, Ed., *Computer Techniques for Electromagnetics*. Elmsford, NY: Pergamon, 1973.
- [8] R. C. HANSEN, Ed., *Moment Methods in Antennas and Scattering*. Norwood, MA: Artech House, 1990.
- [9] J. J. H. WANG, *Generalized Moment Methods in Electromagnetics*. New York: Wiley, 1991.
- [10] A. F. PETERSON, S. L. RAY, and R. MITTRA, *Computational Methods for Electromagnetics*. New York: IEEE Press, 1997.
- [11] A. J. POGGIO and E. K. MILLER, Integral equation solutions of three-dimensional scattering problems. *Computer Techniques for Electromagnetics*, edited by R. MITTRA. Elmsford, NY: Permagon, 1973, pp. 159–264.
- [12] W. C. CHEW, Z. NIE, and Y. T. LO, The effect of feed on the input impedance of a microstrip antenna, *Microw. Opt. Tech. Lett.*, 3(3): 79–83, 1990.
- [13] J. R. MAUTZ and R. F. HARRINGTON, H-field, E-field, and combined-field solutions for conducting body of revolution, *AEU*, 32(4): 157–164, 1978.
- [14] S. M. RAO, D. R. WILTON, and A. W. GLISSON, Electromagnetic scattering by surfaces of arbitrary shape, *IEEE Trans. Antennas Propagat.*, 30(3): 409–418, 1982.
- [15] M. G. DUFFY, Quadrature over a pyramid or cube of integrands with a singularity at a vertex, *SIAM J. Numer. Anal.*, 19(6): 1260–1262, 1982.
- [16] A. C. WOO, H. T. G. WANG, M. J. SCHUH, and M. L. SANDERS, Benchmark radar targets for the validation of computational electromagnetics programs, *IEEE Antennas Propagat. Mag.*, 35(1): 84–89, 1993.

- [17] S. M. RAO and D. R. WILTON, E-field, H-field, and combined field solution for arbitrarily shaped three-dimensional dielectric bodies, *Electromagn.*, 10(4): 407–421, 1990.
- [18] Y. CHANG and R. F. HARRINGTON, A surface formulation for characteristic modes of material bodies, *IEEE Trans. Antennas Propagat.*, 25(6): 789–795, 1977.
- [19] T. K. WU and L. L. TSAI, Scattering from arbitrarily-shaped lossy dielectric bodies of revolution, *Radio Sci.*, 12(5): 709–718, 1977.
- [20] J. R. MAUTZ and R. F. HARRINGTON, Electromagnetic scattering from a homogeneous material body of revolution, *AEU*, 33: 71–80, 1979.
- [21] X. Q. SHENG, J. M. JIN, J. M. SONG, W. C. CHEW, and C. C. LU, Solution of combined-field integral equation using multi-level fast multipole method for scattering by homogeneous bodies, *IEEE Trans. Antennas Propagat.*, 46(11): 1718–1726, 1998.
- [22] K. DONEPUDI, J. M. JIN, and W. C. CHEW, A higher-order multilevel fast multipole algorithm for scattering from mixed conducting/dielectric bodies, *IEEE Trans. Antennas Propagat.*, 51(10): 2814–2821, 2003.
- [23] D. E. LIVESAY and K. M. CHEN, Electromagnetic fields induced inside arbitrarily shaped biological bodies, *IEEE Trans. Microwave Theory Tech.*, 22(12): 1273–1280, 1974.
- [24] D. H. SCHUBERT, D. R. WILTON, and A. W. GLISSON, A tetrahedral modeling method for electromagnetic scattering by arbitrarily shaped inhomogeneous dielectric bodies, *IEEE Trans. Antennas Propagat.*, 32(1): 77–85, 1984.
- [25] T. A. CWIK and R. MITTRA, Scattering from a periodic array of free-standing arbitrarily shaped perfectly conducting or resistive patches, *IEEE Trans. Antennas Propagat.*, 35(11): 1226–1234, 1987.
- [26] C. H. CHAN and R. MITTRA, On the analysis of frequency-selective surfaces using subdomain basis functions, *IEEE Trans. Antennas Propagat.*, 38(1): 40–50, 1990.
- [27] J. M. JIN and J. L. VOLAKIS, Electromagnetic scattering by a perfectly conducting patch array on a dielectric slab, *IEEE Trans. Antennas Propagat.*, 38(4): 556–563, 1990.
- [28] R. M. SHARPE, Electromagnetic scattering and radiation by discrete body of revolution, M.S. thesis, University of Houston, TX, 1987.
- [29] N. K. UZUNOGLU, N. G. ALEXOPOULOS, and J. G. FIKIOROS, Radiation properties of microstrip dipoles, *IEEE Trans. Antennas Propagat.*, 27(6): 853–858, 1979.
- [30] J. R. MOSIG and F. E. GARDIOL, A dynamical radiation model for microstrip structures. *Advances in Electronics and Electron Physics*, edited by P. HAWKES. New York: Academic Press, 1982, pp. 139–238.
- [31] K. A. MICHALSKI and D. ZHENG, Electromagnetic scattering and radiation by surfaces of arbitrary shape in layered media—Part I: Theory, *IEEE Trans. Antennas Propagat.*, 38(3): 335–344, 1990.
- [32] K. A. MICHALSKI and J. R. MOSIG, Multilayered media Green's functions in integral equation formulations, *IEEE Trans. Antennas Propagat.*, 45(3): 508–519, 1997.
- [33] W. C. CHEW, *Waves and Fields in Inhomogeneous Media*. Piscataway, NJ: IEEE Press, 1995.
- [34] J. R. MOSIG, Integral equation techniques. *Numerical Techniques for Microwave and Millimeter-Wave Passive Structures*, edited by T. ITOH. New York: Wiley, 1988, pp. 133–213.
- [35] D. G. FANG, J. J. YANG, and G. Y. DELISLE, Discrete image theory for horizontal electric dipole in a multi-layer medium, *Proc. Inst. Elect. Eng. H*, 135(5): 297–303, 1988.
- [36] Y. L. CHOW, J. J. YANG, D. G. FANG, and G. E. HOWARD, A closed-form spatial Green's function for the thick microstrip substrate, *IEEE Trans. Microwave Theory Tech.*, 39(3): 588–592, 1991.
- [37] J. A. STRATTON, *Electromagnetic Theory*. New York: McGraw-Hill, 1941.
- [38] Y. L. CHOW, An approximate dynamic spatial Green's function in three dimensions for finite length microstrip lines, *IEEE Trans. Microwave Theory Tech.*, 28(4): 393–397, 1980.
- [39] R. W. HAMMING, *Numerical Methods for Scientists and Engineers*. New York: Dover, 1973.
- [40] Y. HUA and T. K. SARKAR, Generalized pencil-of-function method for extracting poles of an EM system from its transient response, *IEEE Trans. Antennas Propagat.*, 37(2): 229–234, 1989.
- [41] J. J. YANG, Y. L. CHOW, G. E. HOWARD, and D. G. FANG, Complex images of an electric dipole in homogeneous and layered dielectrics between two ground planes, *IEEE Trans. Microwave Theory Tech.*, 40(3): 595–600, 1992.
- [42] R. A. KIPP and C. H. CHAN, Complex image method for sources in bounded regions of multilayer structures, *IEEE Trans. Microwave Theory Tech.*, 42(5): 860–865, 1994.
- [43] M. I. AKSUN, A robust approach for the derivation of closed-form Green's functions, *IEEE Trans. Microwave Theory Tech.*, 44(5): 651–658, 1996.
- [44] F. LING and J. M. JIN, Discrete complex image method for Green's functions of general multilayer media, *IEEE Microwave Guided Wave Lett.*, 10(10): 400–402, 2000.
- [45] B. HU and W. C. CHEW, Fast inhomogeneous plane wave algorithm for electromagnetic solutions in layered medium structures—2D case, *Radio Sci.*, 35(1): 31–43, 2000.
- [46] F. LING and J. M. JIN, Scattering and radiation analysis of microstrip antennas using discrete complex image method and reciprocity theorem, *Microw. Opt. Tech. Lett.*, 16(4): 212–216, 1997.
- [47] F. LING, D. JIAO, and J. M. JIN, Efficient electromagnetic modeling of microstrip structures in multilayer media, *IEEE Trans. Microwave Theory Tech.*, 47(9): 1810–1818, 1999.
- [48] F. LING, J. LIU, and J. M. JIN, Efficient electromagnetic modeling of three-dimensional multilayer microstrip antennas and circuits, *IEEE Trans. Microwave Theory Tech.*, 50(6): 1628–1635, 2002.

- [49] B. P. RYNNE and P. D. SMITH, Stability of time marching algorithms for the electric field integral equations, *J. Electromagn. Waves Applicat.*, 4(12): 1181–1205, 1990.
- [50] S. M. RAO and D. R. WILTON, Transient scattering by conducting surfaces of arbitrary shape, *IEEE Trans. Antennas Propagat.*, 39(1): 56–61, 1991.
- [51] D. A. VECHINSKI and S. M. RAO, A stable procedure to calculate the transient scattering by conducting surfaces of arbitrary shape, *IEEE Trans. Antennas Propagat.*, 40(6): 661–665, 1992.
- [52] P. J. DAVIES, A stability analysis of a time marching scheme for the general surface electric field integral equation, *Appl. Numer. Math.*, 27: 35–57, 1998.
- [53] G. MANARA, A. MONORCHIO, and R. REGGIANNINI, A space-time discretization criterion for a stable time-marching solution of the electric field integral equation, *IEEE Trans. Antennas Propagat.*, 45(4): 527–532, 1997.
- [54] M. J. BLUCK and S. P. WALKER, Time-domain BIE analysis of large three-dimensional electromagnetic scattering problems, *IEEE Trans. Antennas Propagat.*, 45(5): 894–901, 1997.
- [55] B. SHANKER, A. A. ERGIN, K. AYGÜN, and E. MICHIELSEN, Analysis of transient electromagnetic scattering from closed surfaces using the combined field integral equation, *IEEE Trans. Antennas Propagat.*, 48(7): 1064–1074, 2000.
- [56] D. S. WEILE, G. PISHARODY, N.-W. CHEN, B. SHANKER, and E. MICHIELSEN, A novel scheme for the solution of the time-domain integral equations of electromagnetics, *IEEE Trans. Antennas Propagat.*, 52(1): 283–295, 2004.
- [57] P. WANG, M. Y. XIA, J. M. JIN, and L. Z. ZHOU, Time-domain integral equation solvers using quadratic B-spline temporal basis functions, *Microw. Opt. Tech. Lett.*, 49(5): 1154–1159, 2007.
- [58] H. BAGCI, A. E. YILMAZ, J. M. JIN, and E. MICHIELSEN, Fast and rigorous analysis of EMC/EMI phenomena of electrically large and complex cable-loaded structures, *IEEE Trans. Electromagn. Compat.*, 49(2): 361–381, 2007.
- [59] M. LI, K.-P. MA, D. M. HOCKANSON, J. L. DREWNIAK, T. H. HUBING, and T. P. V. DOREN, Numerical and experimental corroboration of an FDTD thin-slot model for slots near corners of shielding enclosures, *IEEE Trans. Electromagn. Compat.*, 39(3): 225–232, 1997.
- [60] F. EDELVIK, G. LEDFELT, P. LOTSEDT, and D. J. RILEY, An unconditionally stable subcell model for arbitrarily oriented thin wires in the FETD method, *IEEE Trans. Antennas Propagat.*, 51(8): 1797–1805, 2003.
- [61] C. MÜLLER, *Foundations of the Mathematical Theory of Electromagnetic Waves*. Berlin, Germany: Springer, 1969.

PROBLEMS

- 10.1.** Consider a square conducting plate having a size of $1\text{ cm} \times 1\text{ cm}$ and immersed in a homogeneous medium having a permittivity of ϵ_0 . Apply the procedure described in Section 10.1 with point collocation to calculate its charge distribution and capacitance. Perform the calculation by subdividing the plate into 10×10 , 20×20 , and 30×30 cells, respectively, and examine the convergence of the numerical solution.
- 10.2.** Compare the accuracy of the approximate result in Equation 10.1.19 with the following exact result for rectangular cells:

$$\begin{aligned} A_{mn} &= \frac{1}{4\pi\epsilon} \iint_{S_n} \frac{1}{|\mathbf{r}_m - \mathbf{r}'|} dS' \\ &= \frac{1}{4\pi\epsilon} \int_{y_n - \Delta y/2}^{y_n + \Delta y/2} \int_{x_n - \Delta x/2}^{x_n + \Delta x/2} \frac{1}{\sqrt{(x_m - x')^2 + (y_m - y')^2}} dx' dy' \\ &= \frac{1}{4\pi\epsilon} \left\{ (x_m - x') \ln[(y_m - y') + R] + (y_m - y') \ln[(x_m - x') + R] \right\} \Big|_{x' = x_n - \Delta x/2, y' = y_n - \Delta y/2}^{x' = x_n + \Delta x/2, y' = y_n + \Delta y/2} \end{aligned}$$

where $R = \sqrt{(x_m - x')^2 + (y_m - y')^2}$. Repeat the calculations in Problem 10.1 using this formula and examine the difference in the calculated capacitance values.

10.3. Repeat Problem 10.1 using subdomain collocation and the following integration formula:

$$\begin{aligned}
 A_{mn} &= \iint_{S_m} \iint_{S_n} G(\mathbf{r}, \mathbf{r}') dS' ds \\
 &= \frac{1}{4\pi\epsilon} \int_{y_m - \Delta y/2}^{y_m + \Delta y/2} \int_{x_m - \Delta x/2}^{x_m + \Delta x/2} \int_{y_n - \Delta y/2}^{y_n + \Delta y/2} \int_{x_n - \Delta x/2}^{x_n + \Delta x/2} \frac{1}{\sqrt{(x - x')^2 + (y - y')^2}} dx' dy' dx dy \\
 &= \frac{1}{4\pi\epsilon} \left\{ \frac{(x - x')^2 (y - y')}{2} \ln[(y - y') + R] + \frac{(x - x')(y - y')^2}{2} \ln[(x - x') + R] \right. \\
 &\quad \left. - \frac{(x - x')(y - y')}{4} [(x - x') + (y - y')] - \frac{R^3}{6} \right\} \Big|_{\substack{x' = x_n + \Delta x/2, y' = y_n + \Delta y/2, x = x_m + \Delta x/2, y = y_m + \Delta y/2 \\ x' = x_n - \Delta x/2, y' = y_n - \Delta y/2, x = x_m - \Delta x/2, y = y_m - \Delta y/2}}
 \end{aligned}$$

where $R = \sqrt{(x - x')^2 + (y - y')^2}$. Compare the results with those obtained in Problems 10.1 and 10.2.

10.4. Write a computer program to implement the formulation developed in Section 10.2.2. Calculate the induced surface current distribution on a square conducting cylinder of $1\lambda \times 1\lambda$ due to an incident plane wave and then evaluate the scattered far field for both TM and TE polarizations. Repeat the calculation for a $3\lambda \times 3\lambda$ cylinder.

10.5. Consider a cylinder whose surface is characterized by the impedance boundary condition

$$\frac{\partial \varphi(\rho)}{\partial n} + \gamma \varphi(\rho) = 0 \quad \rho \in \Gamma_o.$$

Formulate the integral equations for both TM and TE polarizations by using Equation 10.2.11. Calculate the induced surface current distribution on a square cylinder of $3\lambda \times 3\lambda$ with a surface impedance of 100Ω and then evaluate its bistatic and monostatic scattering widths.

10.6. Show that the integral in Equation 10.2.43 can be evaluated to give

$$Z_{mn} \equiv \begin{cases} \frac{k_0 Z_0 \Delta x}{4} H_0^{(2)}(k_0 |m - n| \Delta x) + \frac{Z_0}{4} [\pm H_1^{(2)}(k_0 |m - n - \frac{1}{2}| \Delta x) \\ \mp H_1^{(2)}(k_0 |m - n + \frac{1}{2}| \Delta x)] & m \neq n \\ \frac{k_0 Z_0 \Delta x}{4} \left[1 - j \frac{2}{\pi} \ln \left(\frac{k_0 \gamma \Delta x}{4e^{3/2}} \right) - j \frac{1}{\pi} \frac{16}{(k_0 \Delta x)^2} \right] & m = n. \end{cases}$$

10.7. Consider an infinitely long dielectric cylinder having a position-dependent relative permittivity $\epsilon_r(\rho)$ and permeability $\mu_r(\rho)$. Formulate integral equations of wave scattering for TE and TM polarizations and discuss the numerical solution by the moment method.

10.8. Based on the formulation described in Section 10.3.2, write a computer program to calculate the current distribution and input impedance of a linear antenna having a length of 0.5λ and a radius of 0.001λ . Examine the effects of the discretization density Δl and the delta-gap width on the numerical solution of the current distribution and input impedance.

10.9. Consider a straight wire excited by a magnetic frill current at the center, as illustrated in Figure 10.12b. Show that the excitation field in the absence of the wire is given by

$$E_z^{\text{inc}}(\rho = 0, z) = -\frac{V_0}{2 \ln(b/a)} \left[\frac{e^{-jk_0 R_1}}{R_1} - \frac{e^{-jk_0 R_2}}{R_2} \right]$$

where $R_1 = \sqrt{z^2 + a^2}$ and $R_2 = \sqrt{z^2 + b^2}$ with a and b being the inner and outer radii of the frill, which are chosen to match the characteristic impedance of the transmission line

delivering the feeding voltage V_0 . Use this excitation to replace the delta-gap source in Problem 10.8 and calculate the current distribution and input impedance.

- 10.10. Apply the EFIE (Eq. 10.3.45) to a rectangular conducting plate of a vanishing thickness and formulate its moment-method solution using rectangular rooftop basis functions to expand J_x in terms of f_n^x and J_y in terms of f_n^y and the same functions as testing functions, where f_n^x and f_n^y are shown in Figure 10.22. Discuss the evaluation of the matrix elements.
- 10.11. Show that the integral operator of the EFIE (Eq. 10.3.45) is singular at frequencies corresponding to the resonant frequencies of a cavity formed by filling the interior of S_o with the exterior medium. (*Hint:* Try to formulate the integral equation for a cavity and use the argument that a cavity can sustain resonant modes without a source.)
- 10.12. Derive the following integral equations for scattering by a homogeneous dielectric object by combining the EFIEs (Eqs. 10.3.29 and 10.3.65) and the MFIEs (Eqs. 10.3.30 and 10.3.66), respectively:

$$-\frac{1+\varepsilon_r}{2} \mathbf{M}_s + \hat{n} \times [\mathcal{L}(\bar{\mathbf{J}}_s) - \sqrt{\mu_r \varepsilon_r} \mathcal{L}_i(\bar{\mathbf{J}}_s)] - \hat{n} \times [\tilde{\mathcal{K}}(\mathbf{M}_s) - \varepsilon_r \tilde{\mathcal{K}}_i(\mathbf{M}_s)] = \hat{n} \times \mathbf{E}^{\text{inc}}(\mathbf{r})$$

$$\frac{1+\mu_r}{2} \bar{\mathbf{J}}_s + \hat{n} \times [\mathcal{L}(\mathbf{M}_s) - \sqrt{\mu_r \varepsilon_r} \mathcal{L}_i(\mathbf{M}_s)] + \hat{n} \times [\tilde{\mathcal{K}}(\bar{\mathbf{J}}_s) - \mu_r \tilde{\mathcal{K}}_i(\bar{\mathbf{J}}_s)] = \hat{n} \times \bar{\mathbf{H}}^{\text{inc}}(\mathbf{r}).$$

This is the well-known Müller formulation [61]. Discuss the major differences between the Müller formulation and the PMCHWT formulation and their implications in numerical implementation.

- 10.13. Given a surface current $\tilde{\mathbf{j}}_{pq} e^{j(k'_{xp}x+k'_{yp}y)}$ in the xy -plane, derive the expression of the transverse component of the electric field as given in Equation 10.4.9 and then the expression for the z -component. Next, examine the expression given in Equation 10.4.11. Find the condition for a Floquet mode (p, q) to become a propagating mode and find the equations to determine the propagation direction. Finally, given a moment-method solution of \mathbf{j}_{mn} , find the expressions to calculate the specular reflection and transmission coefficients, which correspond to the zeroth-order Floquet mode ($p = q = 0$).
- 10.14. Consider a microstrip substrate with a relative permittivity $\varepsilon_r = 12.6$ and a thickness $h = 1$ mm. Apply the DCIM to calculate $G_A(\rho)$ and $G_\phi(\rho)$ at frequency $f = 30$ GHz. In the calculation of $G_A(\rho)$, plot $j2k_{z0}\tilde{G}_A(k_\rho)$, $j2k_{z0}\tilde{G}_A(k_\rho)-1$, $j2k_{z0}\tilde{G}_A(k_\rho)-1+e^{-j2k_{z0}h}$, and $F_1(k_\rho)$, and examine their behaviors. In the calculation of $G_\phi(\rho)$, plot $j2k_{z0}\tilde{G}_\phi(k_\rho)$, $j2k_{z0}\tilde{G}_\phi(k_\rho)-1$, $j2k_{z0}[\tilde{G}_\phi(k_\rho)-\tilde{G}_{\phi,0}(k_\rho)]$, and $F_2(k_\rho)$, and examine their behaviors.
- 10.15. Formulate the time-domain integral equations and their MOT solution for scattering by a homogeneous dielectric object.
- 10.16. Equation 10.2.11 was derived through a liberal application of the second scalar Green's theorem, which is usually not permissible in the classical sense because $G_0(\mathbf{p}, \mathbf{p}')$ is singular at $\mathbf{p} = \mathbf{p}'$ when $\mathbf{p} \in \Omega_\infty$. A more rigorous derivation can be carried out by excluding a vanishingly small circular area σ_ϵ centered at \mathbf{p} from Ω_∞ so that $G_0(\mathbf{p}, \mathbf{p}')$ is continuous everywhere in $\Omega_\infty - \sigma_\epsilon$. In fact, this approach can also be applied to the case when $\mathbf{p} \in \Gamma_o$ to derive Equation 10.2.17 naturally. Derive Equations 10.2.11 and 10.2.17 using this approach.
- 10.17. Equations 10.3.13 and 10.3.14 were derived through a liberal application of the scalar–vector Green's theorem, which is usually not permissible in the classical sense because $G_0(\mathbf{r}, \mathbf{r}')$ is singular at $\mathbf{r} = \mathbf{r}'$ when $\mathbf{r} \in V_\infty$. A more rigorous derivation can be carried out by excluding a vanishingly small spherical volume v_ϵ centered at \mathbf{r} from V_∞ so that $G_0(\mathbf{r}, \mathbf{r}')$ is continuous everywhere in $V_\infty - v_\epsilon$. This approach can also be applied to the case when $\mathbf{r} \in S_o$ to derive Equations 10.3.29 and 10.3.30 naturally. Derive Equations 10.3.13 and 10.3.29 using this approach. ■

FAST ALGORITHMS AND HYBRID TECHNIQUES

This chapter covers two important subjects in computational electromagnetics. One is the development of fast algorithms, and the other is the development of hybrid techniques. *Fast algorithms* are defined as algorithms that can solve a matrix equation, or an integral equation that can be discretized into a matrix equation via the moment method, with a reduced computational complexity¹—that is, with reduced computation time and memory requirements. As we have seen in Chapter 10, the discretization of an integral equation via the moment method yields a fully populated matrix equation, which is very expensive to generate, store, and solve, especially when the dimension of the matrix is large. A fast solution of such a matrix equation can not only reduce the computation time and memory requirements but can also greatly expand the capabilities of the moment method for solving large and complex problems. In this chapter, we describe four fast algorithms: the *conjugate gradient–fast Fourier transform* (CG–FFT) method, the *adaptive integral method* (AIM), the *fast multipole method* (FMM), and the *adaptive cross-approximation* (ACA) method.

Hybrid techniques are defined as techniques that combine two or more different methods for a more efficient or accurate numerical solution of complicated electromagnetic problems. As we have seen in the preceding three chapters, different numerical methods have different strengths and weaknesses. A better solution can be obtained if these methods can be combined such that their strengths are retained and their weaknesses are removed. In this chapter, we describe two hybrid techniques to demonstrate the basic principles and increased capabilities of hybrid techniques. One combines the time-domain finite element method with the finite difference time-domain (FDTD) method. The other combines the finite element method with the moment method based on boundary integral equations.

11.1 INTRODUCTION TO FAST ALGORITHMS

In contrast to the finite difference and finite element methods, which are based on partial differential equations and yield extremely sparse system matrices, the integral equation–based moment method yields a fully populated system matrix because of the use of a Green’s function. The high computational complexity associated with the solution of full matrices becomes a major limitation on the capability of the moment method. When a direct method such as Gaussian elimination or *LU* decomposition is employed to solve the matrix equation, the operation count is proportional to $O(N^3)$ and the memory requirement is proportional to $O(N^2)$, where N denotes the dimension of the matrix. Such a high

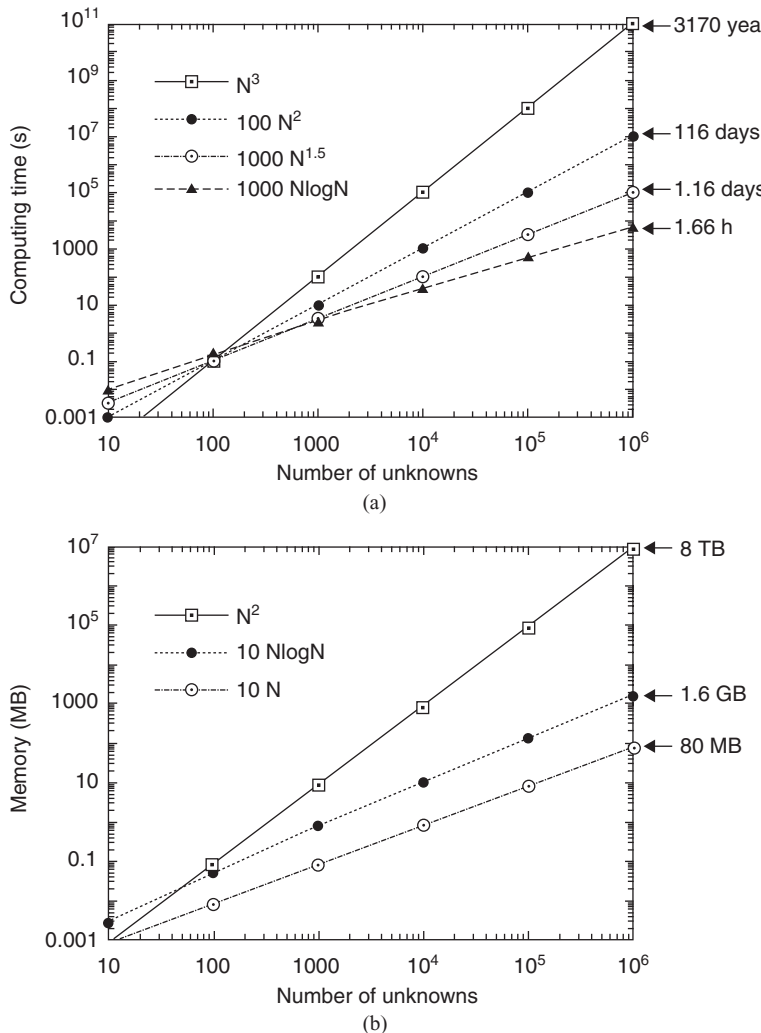


Figure 11.1 Computational complexity of a few hypothetical numerical schemes.
(a) Computation time versus the number of unknowns. (b) Memory requirement versus the number of unknowns.

computational complexity severely limits the application of the moment method. When an iterative method is employed to solve the matrix equation, the operation count for each iteration is proportional to $O(N^2)$ because an iterative solver usually calculates one or two matrix–vector products for each iteration. The memory requirement remains the same as that for a direct method. Hence, the total computation time is proportional to $O(N_{\text{iter}} N^2)$, where N_{iter} denotes the number of iterations required to reach certain convergence. If N_{iter} is small, an iterative method can be faster than the *LU* decomposition method for one right-hand side. However, the iterative solution must be repeated for every right-hand side. Because of this, for a long time, the moment method was limited to one-, two-, and small three-dimensional problems. To fully understand the implications of the high computational complexity of traditional direct and iterative methods, we plot four curves in Figure 11.1a for the projected computation times of four hypothetical numerical algorithms as a function of the matrix dimension, that is, the number of unknowns, and three curves in

Figure 11.1b for the projected memory requirements as a function of the matrix dimension. As can be seen clearly, with a computational complexity of $O(N^3)$ or $O(N^2)$, the required computation time and memory increase exponentially with the number of unknowns and can quickly exceed what can be afforded by most powerful computers available today.

Whereas there is not much one can do with the computational complexity of a direct method, it is found that, by using some special techniques, both the computation time per iteration and the memory requirements for an iterative solver can be reduced significantly. Such special techniques are called *fast solvers* or *fast algorithms*, which are characterized by a reduced computational complexity and are especially important for dealing with large-scale problems. Historically, the CG–FFT method was the first fast solver developed for computational electromagnetics [1–17]. It still remains as the most efficient fast solver because of its relative simplicity. Unfortunately, the necessity of using staircase approximation for geometrical modeling severely restricted its applications. This approximation was later eliminated by the development of the AIM [18–22], the precorrected–FFT method [23,24], and their variations [25,26]. These methods use arbitrary basis functions, which are projected on a uniform grid to enable the use of FFT. The key concept in these methods is the decomposition of the moment-method matrix into near- and far-interaction components. The methods are very effective for planar and inhomogeneous structures because they reduce the computational complexity to $O(N\log N)$, as does the traditional FFT-based method. However, they are less efficient for impenetrable and homogeneous objects, since the surface basis functions in the moment method have to be projected onto a three-dimensional grid, resulting in a computational complexity of $O(N^{1.5} \log N)$. For such problems, the FMM has been developed [27–53] and has been shown to be more efficient, as it eventually reduces the computational complexity to $O(N\log N)$. In a certain sense, the FMM can be considered as FFT on an arbitrary grid. The FMM also employs the important concept of decomposing the moment-method matrix into near- and far-interaction components. This enables the major part of the matrix–vector product to be computed rapidly using multipole or plane wave expansions. In addition to the CG–FFT, AIM, and FMM, whose formulations are based on the specific form of the integral equation to be solved, a reduced computational complexity for a solution of the moment-method matrix equation can also be achieved by compressing the moment-method matrix. One such compressing method is the ACA method [54–59], which has been applied to solving integral equations of scattering. This method has a unique advantage in that it works directly on the matrix regardless of the form of the integral equation that is used to generate the matrix.

The plots in Figure 11.1 demonstrate clearly the benefit of fast solvers with a reduced computational complexity. When the computational complexity is reduced to $O(N\log N)$, the computation time and memory requirements are reduced significantly, especially for large-scale problems. With the fast solvers, problems modeled with millions of unknowns can now be solved regularly with computation times in terms of minutes or hours instead of days.

11.2 CONJUGATE GRADIENT–FFT METHOD

The FFT is the best-known fast algorithm ever developed for science and engineering applications. Through an ingenious design, the FFT calculates a discrete convolution in $O(N\log N)$ steps instead of $O(N^2)$ steps as required by a direct computation. A careful examination of the integral equations formulated in Chapter 10 reveals that all the integrals involved are actually convolutions. Therefore, if these integrals are discretized on a

uniform grid, the resultant matrix–vector product can be evaluated using the FFT with only $O(N \log N)$ operations instead of $O(N^2)$ operations for a direct calculation of the matrix–vector product. This idea was first developed by Bojarski [1] and has been improved and applied to many electromagnetic problems [2–17]. When it is used in conjunction with the CG method [60,61] for solving the moment-method matrix equation, the method is often referred to as the CG–FFT method.² In this section, we introduce this method using a one-, two-, and three-dimensional example.

11.2.1 Scattering by a Conducting Strip or Wire

The moment-method solution of electromagnetic wave scattering by a conducting strip was formulated in Section 10.2.3, and the solution to scattering and radiation by a conducting wire was described in Section 10.3.2. If the conducting strip is flat or the wire is straight and the discretization is uniform, the elements of the moment-method matrix Z_{mn} depend only on the values of $m - n$; hence, the matrix is translationally invariant. Such a matrix is called a *Toeplitz matrix*, whose matrix–vector multiplication can be evaluated efficiently using the FFT. To be more specific, if the moment-method matrix equation is written as

$$\sum_{n=1}^N Z_{mn} I_n = V_m \quad (11.2.1)$$

the left-hand side can be written in the form of a cyclic convolution

$$\sum_{n=1}^N Z_{mn} I_n = Z_m \otimes I_m \quad (11.2.2)$$

where $Z_m = Z_{m1}$ and \otimes denotes the cyclic convolution. This convolution can be evaluated using the discrete Fourier transform (DFT)

$$[Z]\{I\} = \mathcal{F}_D^{-1}\{\mathcal{F}_D\{Z^P\} \circ \mathcal{F}_D\{I^P\}\} \quad (11.2.3)$$

where \mathcal{F}_D denotes the DFT, \mathcal{F}_D^{-1} denotes the corresponding inverse DFT, \circ denotes the Hadamard product, and $\{Z^P\}$ and $\{I^P\}$ are vectors with their elements given by

$$Z_m^P = \begin{cases} Z_m & m = 1, 2, \dots, N_p/2+1 \\ Z_{N_p-m+2} & m = N_p/2+2, N_p/2+3, \dots, N_p \end{cases} \quad (11.2.4)$$

$$I_m^P = \begin{cases} I_m & m = 1, 2, \dots, N \\ 0 & m = N+1, N+2, \dots, N_p \end{cases} \quad (11.2.5)$$

where $N_p \geq 2N - 1$. The superscript P in $\{Z^P\}$ and $\{I^P\}$ is used to emphasize that these two vectors are expanded to the length of N_p . The left-hand side of Equation 11.2.3 takes the first N elements of the right-hand side. The DFTs can be evaluated efficiently using the FFT. The memory required for the calculation is proportional to $O(N)$, and the computation time is proportional to $O(N \log N)$.

11.2.2 Scattering by a Conducting Plate

Consider the problem of wave scattering by a conducting planar plate in the xy -plane. The electric-field integral equation (EFIE) for the induced current \mathbf{J}_s is given by Equation 10.3.45, which can be written explicitly as

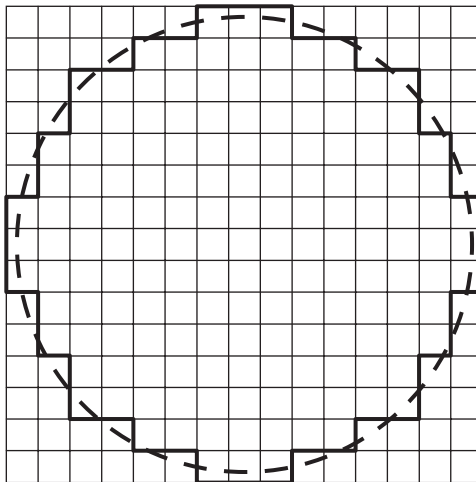


Figure 11.2 Arbitrarily shaped plate (a circular plate is shown in the figure) placed in a uniform rectangular mesh and modeled as a collection of small rectangular cells. The original plate is shown by the dashed line, and the staircase approximation is shown by the thick solid line.

$$jk_0 Z_0 \hat{z} \times \iint_S \left[\mathbf{J}_s(\mathbf{r}') G_0(\mathbf{r}, \mathbf{r}') + \frac{1}{k_0^2} \nabla' \cdot \mathbf{J}_s(\mathbf{r}') \nabla G_0(\mathbf{r}, \mathbf{r}') \right] dS' = \hat{z} \times \mathbf{E}^{\text{inc}}(\mathbf{r}) \quad \mathbf{r} \in S \quad (11.2.6)$$

where S denotes the surface area of the plate. For this problem, there is no need to use the combined-field integral equation (CFIE) since the surface S is an open surface, which does not support any interior resonance.

With the intent of computing the left-hand side of Equation 11.2.6 via the FFT, we place the conducting plate in a rectangular area whose left lower corner is located at the origin. This rectangular area is then divided into $(M + 1) \times (N + 1)$ small rectangular cells whose side lengths are Δx and Δy along the x - and y -directions, respectively. Therefore, the plate is modeled as a collection of small rectangular cells (Fig. 11.2). The next step is to discretize Equation 11.2.6 based on the uniform grid. To this end, many discretization schemes have been proposed in the past, which differ primarily in the manner in which the two del operators appearing in Equation 11.2.6 are treated. The simplest approach is first to rewrite Equation 11.2.6 as

$$jk_0 Z_0 \hat{z} \times \iint_S \left[\tilde{\mathbf{I}} + \frac{1}{k_0^2} \nabla \nabla \right] \cdot G_0(\mathbf{r}, \mathbf{r}') \mathbf{J}_s(\mathbf{r}') dS' = \hat{z} \times \mathbf{E}^{\text{inc}}(\mathbf{r}) \quad \mathbf{r} \in S \quad (11.2.7)$$

and then employ the analytical Fourier transform of G_0 . With this, the spatial derivatives contained in the del operators become simple algebraic multiplicative factors in the spectral domain [2,3]. This approach allows the use of simple pulse functions as the basis and testing functions; however, it requires a large FFT pad to reduce aliasing errors since the analytical Fourier transform of G_0 extends over the entire space. To reduce the size of the FFT pad and to eliminate aliasing errors, another approach was considered where the integral equation is first cast in a discrete form before invoking the convolution theorem to evaluate the integrals [1,4,5]. In this approach, the derivatives contained in the del operators can be approximated via finite differences and calculated via the DFT [4,5].

The approaches above share a common feature that the del operators act directly upon G_0 . However, by using the divergence theorem, one of the del operators in Equation 11.2.7 can be transferred onto the current density, as in Equation 11.2.6, provided that the basis functions are differentiable. This concept was adopted in Reference [6], where the

rooftop basis functions were employed for the expansion of \mathbf{J}_s and point matching was then used to cast the integral equation in a discrete form before invoking the convolution theorem. This approach yielded a much more accurate and efficient solution. Later, another approach [8] was proposed that further transferred the other del operator from G_0 to the testing functions, which were chosen to be the rooftop functions as well. The resulting algorithm was compared with all other existing algorithms and exhibited the best performance. Here, we first describe this approach.

To discretize Equation 11.2.6 we expand the x - and y -components of the current density as

$$J_x(x', y') = \sum_{m'=1}^M \sum_{n'=1}^{N+1} J_x(m', n') T_{m'n'}^x(x', y') \quad (11.2.8)$$

$$J_y(x', y') = \sum_{m'=1}^{M+1} \sum_{n'=1}^N J_y(m', n') T_{m'n'}^y(x', y') \quad (11.2.9)$$

where $J_{xy}(m', n')$ denote the expansion coefficients, which are non-zero only if the associated cell is within S . The functions $T_{m'n'}^{x,y}(x', y')$ represent the rooftop functions given by

$$T_{m'n'}^x(x', y') = \Lambda_{m'}(x') \Pi_{n'-1/2}(y') \quad (11.2.10)$$

$$T_{m'n'}^y(x', y') = \Pi_{m'-1/2}(x') \Lambda_{n'}(y') \quad (11.2.11)$$

where $\Lambda_m(x)$ and $\Pi_m(x)$ are defined by Equations 10.4.27 and 10.4.15, respectively, and $\Lambda_n(y)$ and $\Pi_n(y)$ are defined similarly.

Substituting Equations 11.2.8 and 11.2.9 into Equation 11.2.6 and using $T_{mn}^x(x, y)\hat{x}$ and $T_{mn}^y(x, y)\hat{y}$ as the testing functions, we obtain

$$\begin{aligned} & \sum_{m'=1}^M \sum_{n'=1}^{N+1} G_T^x(m, n; m', n') J_x(m', n') \\ & + \frac{1}{\Delta x} \sum_{m'=1}^{M+1} \sum_{n'=1}^{N+1} [G_p(m, n; m', n') - G_p(m+1, n; m', n')] \\ & \times \left\{ \frac{1}{\Delta x} [J_x(m', n') - J_x(m'-1, n')] + \frac{1}{\Delta y} [J_y(m', n') - J_y(m', n'-1)] \right\} = b_x(m, n) \end{aligned} \quad (11.2.12)$$

$$\begin{aligned} & \sum_{m'=1}^{M+1} \sum_{n'=1}^N G_T^y(m, n; m', n') J_y(m', n') \\ & + \frac{1}{\Delta y} \sum_{m'=1}^{M+1} \sum_{n'=1}^{N+1} [G_p(m, n; m', n') - G_p(m, n+1; m', n')] \\ & \times \left\{ \frac{1}{\Delta x} [J_x(m', n') - J_x(m'-1, n')] + \frac{1}{\Delta y} [J_y(m', n') - J_y(m', n'-1)] \right\} = b_y(m, n) \end{aligned} \quad (11.2.13)$$

where

$$G_T^{x,y}(m, n; m', n') = jk_0 Z_0 \iint_S T_{mn}^{x,y}(x, y) \left[\iint_S T_{m'n'}^{x,y}(x', y') G_0(\mathbf{r}, \mathbf{r}') dS' \right] dS \quad (11.2.14)$$

$$G_p(m, n; m', n') = \frac{Z_0}{jk_0} \iint_S P_{mn}(x, y) \left[\iint_S P_{m'n'}(x', y') G_0(\mathbf{r}, \mathbf{r}') dS' \right] dS \quad (11.2.15)$$

$$b_{x,y}(m, n) = \iint_S T_{mn}^{x,y}(x, y) E_{x,y}^{\text{inc}}(x, y) dS \quad (11.2.16)$$

in which $P_{mn}(x, y) = \Pi_{m-1/2}(x)\Pi_{n-1/2}(y)$.

It can be shown that $G_T^{x,y}(m, n; m', n')$ and $G_p(m, n; m', n')$ are functions of the differences $m - m'$ and $n - n'$. Making use of this translational invariance property, the linear system can be written more explicitly as

$$\begin{aligned} & G_T^x(m, n) \otimes J_x(m, n) + \frac{1}{\Delta x} [G_p(m, n) - G_p(m+1, n)] \\ & \otimes \left\{ \frac{1}{\Delta x} [J_x(m, n) - J_x(m-1, n)] + \frac{1}{\Delta y} [J_y(m, n) - J_y(m, n-1)] \right\} = b_x(m, n) \end{aligned} \quad (11.2.17)$$

$$\begin{aligned} & G_T^y(m, n) \otimes J_y(m, n) + \frac{1}{\Delta y} [G_p(m, n) - G_p(m, n+1)] \\ & \otimes \left\{ \frac{1}{\Delta x} [J_x(m, n) - J_x(m-1, n)] + \frac{1}{\Delta y} [J_y(m, n) - J_y(m, n-1)] \right\} = b_y(m, n) \end{aligned} \quad (11.2.18)$$

where $G_T^{x,y}(m, n) = G_T^{x,y}(m, n; 1, 1)$ and $G_p(m, n) = G_p(m, n; 1, 1)$. These linear equations can be written in matrix form as

$$\begin{bmatrix} G_{xx} & G_{xy} \\ G_{yx} & G_{yy} \end{bmatrix} \begin{Bmatrix} J_x \\ J_y \end{Bmatrix} = \begin{Bmatrix} b_x \\ b_y \end{Bmatrix} \quad (11.2.19)$$

where $[G_{pq}]$ ($p, q = x, y$) are square matrices. The matrix–vector products can be written as

$$\begin{aligned} [G_{xx}] \{J_x\} &= \mathcal{F}_D^{-1} \left\{ \tilde{G}_T^{xp}(u, v) \circ \tilde{J}_x^P(u, v) \right\} \\ &+ \mathcal{F}_D^{-1} \left\{ \frac{1}{(\Delta x)^2} [1 - F_x(u)] \tilde{G}_P^P(u, v) \circ [1 - F_x^*(u)] \tilde{J}_x^P(u, v) \right\} \end{aligned} \quad (11.2.20)$$

$$[G_{xy}] \{J_y\} = \mathcal{F}_D^{-1} \left\{ \frac{1}{\Delta x \Delta y} [1 - F_x(u)] \tilde{G}_P^P(u, v) \circ [1 - F_y^*(v)] \tilde{J}_y^P(u, v) \right\} \quad (11.2.21)$$

$$[G_{yx}] \{J_x\} = \mathcal{F}_D^{-1} \left\{ \frac{1}{\Delta x \Delta y} [1 - F_y(v)] \tilde{G}_P^P(u, v) \circ [1 - F_x^*(u)] \tilde{J}_x^P(u, v) \right\} \quad (11.2.22)$$

$$\begin{aligned} [G_{yy}] \{J_y\} &= \mathcal{F}_D^{-1} \left\{ \tilde{G}_T^{yp}(u, v) \circ \tilde{J}_y^P(u, v) \right\} \\ &+ \mathcal{F}_D^{-1} \left\{ \frac{1}{(\Delta y)^2} [1 - F_y(v)] \tilde{G}_P^P(u, v) \circ [1 - F_y^*(v)] \tilde{J}_y^P(u, v) \right\} \end{aligned} \quad (11.2.23)$$

where $\tilde{J}_x^P(u, v)$ denotes the DFT of the expanded vector $J_x^P(m, n)$, which is given by

$$J_x^P(m, n) = \begin{cases} J_x(m, n) & 1 \leq m \leq M, 1 \leq n \leq N+1 \\ 0 & M+1 \leq m \leq 2M+2, N+2 \leq n \leq 2N+2 \end{cases} \quad (11.2.24)$$

and $\tilde{G}_T^{xp}(u, v)$ denotes the DFT of $G_T^{xp}(m, n)$ given by

$$G_T^{xp}(m, n) = \begin{cases} G_T^x(m, n) & 1 \leq m \leq M+1, 1 \leq n \leq N+1 \\ G_T^x(2M+4-m, n) & M+2 \leq m \leq 2M+2, 1 \leq n \leq N+1 \\ G_T^x(m, 2N+4-n) & 1 \leq m \leq M+1, N+2 \leq n \leq 2N+2 \\ G_T^x(2M+4-m, 2N+4-n) & M+2 \leq m \leq 2M+2, N+2 \leq n \leq 2N+2. \end{cases} \quad (11.2.25)$$

The $\tilde{J}_y^p(u, v)$, $\tilde{G}_T^{yp}(u, v)$, and $\tilde{G}_p^p(u, v)$ are defined similarly. Also,

$$F_x(u) = \exp\left(\frac{j\pi u}{M+1}\right), \quad F_y(v) = \exp\left(\frac{j\pi v}{N+1}\right). \quad (11.2.26)$$

By properly combining terms, only four FFTs (two forward and two inverse FFTs) are needed to compute a matrix–vector product, excluding the computation of $\tilde{G}_T^{xp}(u, v)$ and $\tilde{G}_p^p(u, v)$, which need be done only once. Thus, the memory requirement is reduced to $O(MN)$ and the computation time is reduced to $O(MN \log MN)$ as opposed to $O(M^2N^2)$ for a direct calculation.

The formulation above has been demonstrated to be very accurate and efficient. It has also been extended to deal with microstrip antennas and circuits using the layered-medium Green's function [10]. However, the formulation itself is quite complicated, and the implementation is by no means straightforward. In the following, we describe a much simpler, but equally effective, algorithm to solve this problem. This algorithm is a modified version of the one proposed by Zwamborn and van den Berg [7], which splits the computation of the matrix–vector product into two stages. To describe this algorithm, we first rewrite Equation 11.2.6 or Equation 11.2.7 as

$$-\hat{z} \times (k_0^2 + \nabla \nabla \cdot) \mathbf{A}(\mathbf{r}) = \hat{z} \times \mathbf{E}^{\text{inc}}(\mathbf{r}) \quad \mathbf{r} \in S \quad (11.2.27)$$

where

$$\mathbf{A}(\mathbf{r}) = \frac{Z_0}{jk_0} \iint_S G_0(\mathbf{r}, \mathbf{r}') \mathbf{J}_s(\mathbf{r}') dS'. \quad (11.2.28)$$

Next we expand \mathbf{A} as

$$A_x(x, y) = \sum_{m'=1}^M \sum_{n'=1}^{N+1} A_x(m', n') T_{m'n'}^x(x, y) \quad (11.2.29)$$

$$A_y(x, y) = \sum_{m'=1}^{M+1} \sum_{n'=1}^N A_y(m', n') T_{m'n'}^y(x, y) \quad (11.2.30)$$

and test Equation 11.2.27 with $T_{mn}^x(x, y)\hat{x}$ and $T_{mn}^y(x, y)\hat{y}$, respectively. This yields

$$\begin{aligned} & \sum_{m'=1}^M \sum_{n'=1}^{N+1} K_{xx}(m, n; m', n') A_x(m', n') \\ & + \sum_{m'=1}^{M+1} \sum_{n'=1}^N K_{xy}(m, n; m', n') A_y(m', n') = b_x(m, n) \end{aligned} \quad (11.2.31)$$

$$\begin{aligned} & \sum_{m=1}^M \sum_{n=1}^{N+1} K_{yx}(m, n; m', n') A_x(m', n') \\ & + \sum_{m'=1}^{M+1} \sum_{n'=1}^N K_{yy}(m, n; m', n') A_y(m', n') = b_y(m, n) \end{aligned} \quad (11.2.32)$$

where

$$K_{xx}(m, n; m', n') = \iint_S \left(\frac{\partial T_{mn}^x}{\partial x} \frac{\partial T_{m'n'}^x}{\partial x} - k_0^2 T_{mn}^x T_{m'n'}^x \right) dx dy \quad (11.2.33)$$

$$K_{xy}(m, n; m', n') = \iint_S \frac{\partial T_{mn}^x}{\partial x} \frac{\partial T_{m'n'}^y}{\partial y} dx dy \quad (11.2.34)$$

$$K_{yx}(m, n; m', n') = \iint_S \frac{\partial T_{mn}^y}{\partial y} \frac{\partial T_{m'n'}^x}{\partial x} dx dy \quad (11.2.35)$$

$$K_{yy}(m, n; m', n') = \iint_S \left(\frac{\partial T_{mn}^y}{\partial y} \frac{\partial T_{m'n'}^y}{\partial y} - k_0^2 T_{mn}^y T_{m'n'}^y \right) dx dy \quad (11.2.36)$$

and $b_{xy}(m, n)$ is the same as that in Equation 11.2.16. The integrals above can be evaluated easily. Equations 11.2.31 and 11.2.32 can be written in matrix form as

$$\begin{bmatrix} K_{xx} & K_{xy} \\ K_{yx} & K_{yy} \end{bmatrix} \begin{Bmatrix} A_x \\ A_y \end{Bmatrix} = \begin{Bmatrix} b_x \\ b_y \end{Bmatrix} \quad (11.2.37)$$

where the coefficient matrix is sparse and symmetric.

Next we express $A_{x,y}(m, n)$ in terms of $J_{x,y}(m, n)$, which can be accomplished easily by substituting Equations 11.2.8 and 11.2.9 into Equation 11.2.28, yielding

$$A_x(m, n) = \frac{Z_0}{jk_0} \sum_{m'=1}^M \sum_{n'=1}^{N+1} J_x(m', n') \iint_S T_{m'n'}^x(x', y') G_0(\mathbf{r}_{mn}^x, \mathbf{r}') dS' \quad (11.2.38)$$

$$A_y(m, n) = \frac{Z_0}{jk_0} \sum_{m'=1}^{M+1} \sum_{n'=1}^N J_y(m', n') \iint_S T_{m'n'}^y(x', y') G_0(\mathbf{r}_{mn}^y, \mathbf{r}') dS' \quad (11.2.39)$$

where $\mathbf{r}_{mn}^x = (m-1)\Delta x \hat{x} + (n-\frac{1}{2})\Delta y \hat{y}$ and $\mathbf{r}_{mn}^y = (m-\frac{1}{2})\Delta x \hat{x} + (n-1)\Delta y \hat{y}$. These can be written in convolution form as

$$A_x(m, n) = G_x(m, n) \otimes J_x(m, n) \quad (11.2.40)$$

$$A_y(m, n) = G_y(m, n) \otimes J_y(m, n) \quad (11.2.41)$$

where

$$G_x(m, n) = \frac{Z_0}{jk_0} \iint_S T_{11}^x(x', y') G_0(\mathbf{r}_{mn}^x, \mathbf{r}') dS' \quad (11.2.42)$$

$$G_y(m, n) = \frac{Z_0}{jk_0} \iint_S T_{11}^y(x', y') G_0(\mathbf{r}_{mn}^y, \mathbf{r}') dS'. \quad (11.2.43)$$

An approximate evaluation of these integrals gives

$$G_x(1, 1) = G_y(1, 1) = \frac{Z_0}{jk_0} \left(\frac{a}{2} - \frac{jk_0 a^2}{4} \right) \quad (11.2.44)$$

$$G_x(m, n) = G_y(m, n) = \frac{Z_0}{jk_0} \frac{e^{-jk_0 R}}{4\pi R} \Delta x \Delta y \quad m, n \neq 1 \quad (11.2.45)$$

where $a = \sqrt{\Delta x \Delta y / \pi}$ and $R = \sqrt{[(m-1)\Delta x]^2 + [(n-1)\Delta y]^2}$.

There are two approaches that one can adopt to solve for $J_{x,y}(m, n)$. One is to solve Equation 11.2.37 for $A_{x,y}(m, n)$, and then solve Equations 11.2.40 and 11.2.41 for $J_{x,y}(m, n)$. The other approach is to substitute Equations 11.2.40 and 11.2.41 into Equation 11.2.37 to obtain the system of equations for $J_{x,y}(m, n)$ and then solve this system directly for $J_{x,y}(m, n)$. In either case, the matrix–vector product can be evaluated efficiently using the FFT:

$$\{A_x\} = \mathcal{F}_D^{-1} \left\{ \tilde{G}_x^P(u, v) \circ \tilde{J}_x^P(u, v) \right\} \quad (11.2.46)$$

$$\{A_y\} = \mathcal{F}_D^{-1} \left\{ \tilde{G}_y^P(u, v) \circ \tilde{J}_y^P(u, v) \right\} \quad (11.2.47)$$

where $\tilde{G}_{x,y}^P(u, v) = \mathcal{F}_D \{G_{x,y}^P(m, n)\}$. Since $\tilde{G}_{x,y}^P(u, v)$ can be precalculated, only four FFTs (two forward and two inverse FFTs) are needed to compute a matrix–vector product, which is the same as in the previous algorithm.

To demonstrate the performance of the CG–FFT method, we consider a microstrip corporate-fed planar array depicted in Figure 11.3a, where the relative permittivity of the substrate is $\epsilon_r = 2.2$ and the substrate thickness is $h = 1.59$ mm. The radiation patterns in the two principal planes $\phi = 0^\circ$ and $\phi = 90^\circ$ are given in Figure 11.3b, which shows excellent agreement between this method and the conventional moment method. The number of unknowns used in the calculation is over 50,000 and the memory required is less than 10 MB, whereas the memory requirement for the moment method is over 600 MB.

11.2.3 Scattering by a Dielectric Object

We now consider the computation of the electric field inside an inhomogeneous dielectric body to illustrate the application of the CG–FFT method in three dimensions. The inhomogeneous body is characterized by a position-dependent permittivity ϵ and a constant permeability μ_0 . The integral equation for this problem is derived in Section 10.3.5, which can be written explicitly as

$$\mathbf{E}(\mathbf{r}) = \mathbf{E}^{\text{inc}}(\mathbf{r}) + (k_0^2 + \nabla \nabla \cdot) \mathbf{A}(\mathbf{r}) \quad (11.2.48)$$

where

$$\mathbf{A}(\mathbf{r}) = \frac{Z_0}{jk_0} \iiint_V G_0(\mathbf{r}, \mathbf{r}') \mathbf{J}_{\text{eq}}(\mathbf{r}') dV'. \quad (11.2.49)$$

As mentioned in Section 10.3.5, this is known as the *volume integral equation*, and its solution has been considered previously using the moment method [71,72]. However, because of the volume discretization, the number of unknowns increases very rapidly with the electrical size of the body. As a result, the moment method using a traditional direct

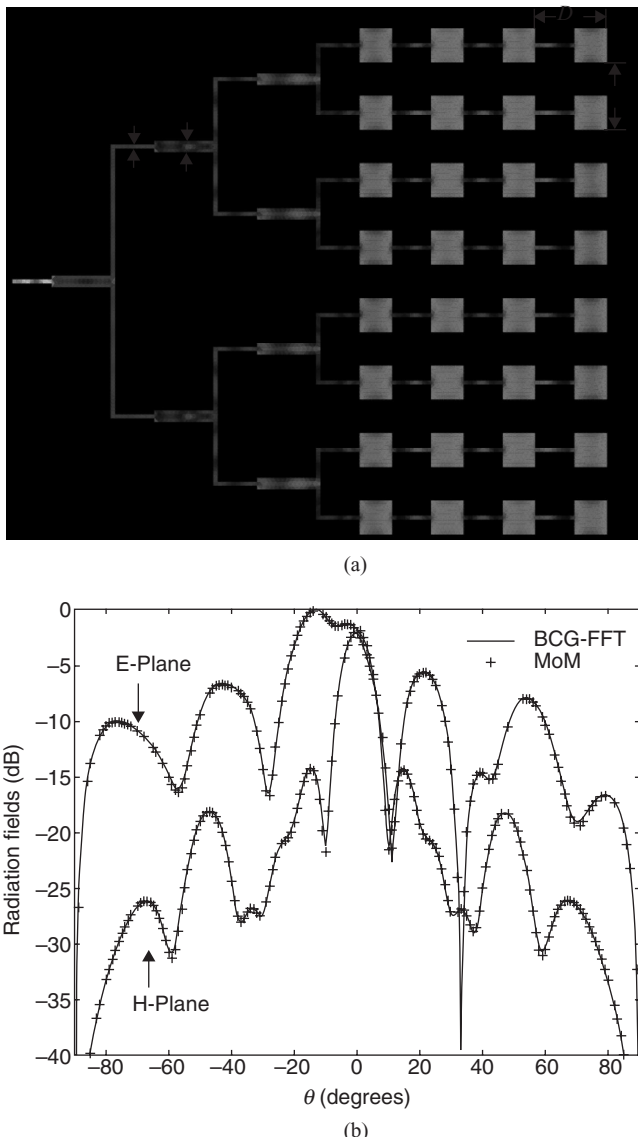


Figure 11.3 Radiation by a corporate-fed microstrip antenna array having 8×4 elements.
 (a) Geometry and current distribution. $\epsilon_r = 2.2$, $h = 1.59$ mm, $l = 10.08$ mm, $w = 11.79$ mm,
 $d_1 = 1.3$ mm, $d_2 = 3.93$ mm, $l_1 = 12.32$ mm, $l_2 = 18.48$ mm, $D_1 = 23.58$ mm, $D_2 = 22.40$ mm.
 (b) Radiation patterns at $f = 9.42$ GHz. (After Wang et al. [10], Copyright © 1998 IEEE.)

or iterative solver without any special acceleration technique has very limited use. It was the development of the CG-FFT method that made the moment-method solution of the volume integral equation useful for practical applications.

The first application of the CG-FFT method to volumetric problems can be found in the analysis of the absorption of electromagnetic power by human bodies [11]. However, the use of pulse basis functions yielded slow convergence and poor results when dealing with materials with high dielectric contrast. Better formulations were later proposed [12–17]; most of these used mixed-order (linear in one direction and constant in the other

two directions) basis functions, which are similar to the rooftop functions used earlier. Among these, the methods proposed by Zwamborn and van den Berg [14] and Gan and Chew [15] are the most accurate for materials with high dielectric contrast. These two methods are actually the extensions of the two methods discussed in the preceding subsection. To be more specific, the method of Gan and Chew is the extension of the first method, which carries out the discretization directly using the current density, whereas the method of Zwamborn and van den Berg is the extension of the second method, which simplifies the formulation by using an intermediate vector potential function. In this section, we describe only the method of Zwamborn and van den Berg since it is probably the simplest and also the most elegant formulation for this problem. For the description of the other method, the reader is referred to References [15] and [16].

To start, with the intention of solving for the electric flux density, we rewrite Equation 11.2.48 in terms of $\mathbf{D}(\mathbf{r})$ as

$$\frac{\mathbf{D}(\mathbf{r})}{\epsilon(\mathbf{r})} - (k_0^2 + \nabla \nabla \cdot) \mathbf{A}(\mathbf{r}) = \mathbf{E}^{\text{inc}}(\mathbf{r}) \quad (11.2.50)$$

where

$$\mathbf{A}(\mathbf{r}) = \frac{1}{\epsilon_0} \iiint_V G_0(\mathbf{r}, \mathbf{r}') \chi(\mathbf{r}') \mathbf{D}(\mathbf{r}') dV' \quad (11.2.51)$$

with

$$\chi(\mathbf{r}') = \frac{\epsilon(\mathbf{r}') - \epsilon_0}{\epsilon(\mathbf{r}')}. \quad (11.2.52)$$

To discretize Equation 11.2.50, we place the object in a uniform mesh with grid widths of Δx , Δy , and Δz in the x -, y -, and z -directions, respectively. Therefore, the object is modeled approximately as a collection of small volumetric rectangular cells.

To convert Equation 11.2.50 into a matrix equation, we expand the electric flux density and the vector potential as

$$\mathbf{D}(\mathbf{r}) = \epsilon_0 \sum_{q=1}^3 \sum_{m', n', k'} d^{(q)}(m', n', k') \mathbf{f}_{m', n', k'}^{(q)}(\mathbf{r}) \quad (11.2.53)$$

$$\mathbf{A}(\mathbf{r}) = \sum_{q=1}^3 \sum_{m', n', k'} A^{(q)}(m', n', k') \mathbf{f}_{m', n', k'}^{(q)}(\mathbf{r}) \quad (11.2.54)$$

where $\mathbf{f}_{m', n', k'}^{(1)}(\mathbf{r})$, $\mathbf{f}_{m', n', k'}^{(2)}(\mathbf{r})$, and $\mathbf{f}_{m', n', k'}^{(3)}(\mathbf{r})$ are vector volumetric rooftop functions in the x -, y -, and z -directions, respectively, defined as

$$\mathbf{f}_{m', n', k'}^{(1)}(\mathbf{r}) = \hat{x} \Lambda_{m'}(x) \Pi_{n'-1/2}(y) \Pi_{k'-1/2}(z) \quad (11.2.55)$$

$$\mathbf{f}_{m', n', k'}^{(2)}(\mathbf{r}) = \hat{y} \Pi_{m'-1/2}(x) \Lambda_{n'}(y) \Pi_{k'-1/2}(z) \quad (11.2.56)$$

$$\mathbf{f}_{m', n', k'}^{(3)}(\mathbf{r}) = \hat{z} \Pi_{m'-1/2}(x) \Pi_{n'-1/2}(y) \Lambda_{k'}(z). \quad (11.2.57)$$

The expansion in Equation 11.2.53 ensures the continuity of the normal component of $\mathbf{D}(\mathbf{r})$ across the rectangular cells, which might have different permittivities. We then multiply Equation 11.2.50 by $\mathbf{f}_{m, n, k}^{(p)}(\mathbf{r})$ ($p = 1, 2, 3$) and integrate over the volume to obtain

$$\left\langle \mathbf{f}_{m,n,k}^{(p)}(\mathbf{r}), \frac{\mathbf{D}(\mathbf{r})}{\varepsilon(\mathbf{r})} \right\rangle - k_0^2 \left\langle \mathbf{f}_{m,n,k}^{(p)}(\mathbf{r}), \mathbf{A}(\mathbf{r}) \right\rangle + \left\langle \nabla \cdot \mathbf{f}_{m,n,k}^{(p)}(\mathbf{r}), \nabla \cdot \mathbf{A}(\mathbf{r}) \right\rangle = \left\langle \mathbf{f}_{m,n,k}^{(p)}(\mathbf{r}), \mathbf{E}^{\text{inc}}(\mathbf{r}) \right\rangle \quad (11.2.58)$$

where $\langle \bullet \rangle$ denotes the inner product of two vector functions, defined as

$$\langle \mathbf{f}, \mathbf{g} \rangle = \iiint_V \mathbf{f} \cdot \mathbf{g} dV. \quad (11.2.59)$$

In arriving at Equation 11.2.58, we employed the divergence theorem to transfer one del operator from $\mathbf{A}(\mathbf{r})$ to $\mathbf{f}_{m,n,k}^{(p)}(\mathbf{r})$. Substituting Equations 11.2.53 and 11.2.54 into Equation 11.2.58, we obtain the following weak-form matrix equation of Equation 11.2.50:

$$\begin{aligned} & [u^{(p,q)}(m, n, k; m', n', k')] \{d^{(q)}(m', n', k')\} - [v^{(p,q)}(m, n, k; m', n', k')] \{A^{(q)}(m', n', k')\} \\ &= \{e^{\text{inc},(p)}(m, n, k)\} \end{aligned} \quad (11.2.60)$$

where $[u^{(p,q)}(m, n, k; m', n', k')]$ and $[v^{(p,q)}(m, n, k; m', n', k')]$ represent square matrices whose elements are given by

$$u^{(p,q)}(m, n, k; m', n', k') = \left\langle \mathbf{f}_{m,n,k}^{(p)}(\mathbf{r}), \frac{\varepsilon_0}{\varepsilon(\mathbf{r})} \mathbf{f}_{m',n',k'}^{(q)}(\mathbf{r}) \right\rangle \quad (11.2.61)$$

$$v^{(p,q)}(m, n, k; m', n', k') = k_0^2 \left\langle \mathbf{f}_{m,n,k}^{(p)}(\mathbf{r}), \mathbf{f}_{m',n',k'}^{(q)}(\mathbf{r}) \right\rangle - \left\langle \nabla \cdot \mathbf{f}_{m,n,k}^{(p)}(\mathbf{r}), \nabla \cdot \mathbf{f}_{m',n',k'}^{(q)}(\mathbf{r}) \right\rangle \quad (11.2.62)$$

and $\{e^{\text{inc},(p)}(m, n, k)\}$ represents the excitation vector with its elements

$$e^{\text{inc},(p)}(m, n, k) = \left\langle \mathbf{f}_{m,n,k}^{(p)}(\mathbf{r}), \mathbf{E}^{\text{inc}}(\mathbf{r}) \right\rangle. \quad (11.2.63)$$

Note that the integrals in Equations 11.2.61–11.2.63 can be evaluated easily, which are non-zero only if $\mathbf{f}_{m,n,k}^{(p)}(\mathbf{r})$ and $\mathbf{f}_{m',n',k'}^{(q)}(\mathbf{r})$ overlap with each other. Hence, $[u^{(p,q)}(m, n, k; m', n', k')]$ and $[v^{(p,q)}(m, n, k; m', n', k')]$ are sparse matrices.

In Equation 11.2.60, $\{d^{(q)}(m', n', k')\}$ and $\{A^{(q)}(m', n', k')\}$ represent the column vectors that store the expansion coefficients in Equations 11.2.53 and 11.2.54, respectively. Both are unknown, so Equation 11.2.60 cannot be solved directly. However, by using Equation 11.2.51, we can obtain a relation between $\{A^{(q)}(m', n', k')\}$ and $\{d^{(q)}(m', n', k')\}$ by substituting Equation 11.2.53 into Equation 11.2.51 and then evaluating $\mathbf{A}(\mathbf{r})$ at the point corresponding to (m, n, k) . This yields

$$A^{(q)}(m, n, k) = \sum_{m',n',k'} G^{(q)}(m, n, k; m', n', k') \chi^{(q)}(m', n', k') d^{(q)}(m', n', k') \quad (11.2.64)$$

where

$$G^{(q)}(m, n, k; m', n', k') = \iiint_V G_0(\mathbf{r}_{m,n,k}^{(q)}, \mathbf{r}') f_{m',n',k'}^{(q)}(\mathbf{r}') dV' \quad (11.2.65)$$

in which

$$\mathbf{r}_{m,n,k}^{(1)} = (m-1)\Delta x \hat{x} + (n-\frac{1}{2})\Delta y \hat{y} + (k-\frac{1}{2})\Delta z \hat{z} \quad (11.2.66)$$

$$\mathbf{r}_{m,n,k}^{(2)} = (m-\frac{1}{2})\Delta x \hat{x} + (n-1)\Delta y \hat{y} + (k-\frac{1}{2})\Delta z \hat{z} \quad (11.2.67)$$

$$\mathbf{r}_{m,n,k}^{(3)} = (m - \frac{1}{2})\Delta x \hat{x} + (n - \frac{1}{2})\Delta y \hat{y} + (k - 1)\Delta z \hat{z} \quad (11.2.68)$$

and $\chi^{(q)}(m', n', k')$ is the value of $\chi(\mathbf{r})$ at point $\mathbf{r}_{m',n',k'}^{(q)}$. The integral in Equation 11.2.65 can be approximated as

$$G^{(q)}(m, n, k; m', n', k') = \int_{-\Delta z/2}^{\Delta z/2} \int_{-\Delta y/2}^{\Delta y/2} \int_{-\Delta x/2}^{\Delta x/2} \frac{e^{-jk_0 R}}{4\pi R} dx'' dy'' dz'' \quad (11.2.69)$$

with

$$R = \sqrt{[(m - m')\Delta x + x'']^2 + [(n - n')\Delta y + y'']^2 + [(k - k')\Delta z + z'']^2}. \quad (11.2.70)$$

Equation 11.2.64 can also be written as the matrix equation

$$\{A^{(q)}(m, n, k)\} = [G^{(q)}(m, n, k; m', n', k')] \{\chi^{(q)}(m', n', k') d^{(q)}(m', n', k')\} \quad (11.2.71)$$

which can be substituted into Equation 11.2.60 to yield the final matrix equation

$$\begin{aligned} & [u^{(p,q)}(m, n, k; m', n', k')] \{d^{(q)}(m', n', k')\} - [v^{(p,q)}(m, n, k; m'', n'', k'')] \\ & \times [G^{(q)}(m'', n'', k''; m', n', k')] \{\chi^{(q)}(m', n', k') d^{(q)}(m', n', k')\} \\ & = \{e^{\text{inc.}(p)}(m, n, k)\} \end{aligned} \quad (11.2.72)$$

for the solution of $\{d^{(q)}(m', n', k')\}$.

In Equation 11.2.72, although both $[u^{(p,q)}(m, n, k; m', n', k')]$ and $[v^{(p,q)}(m, n, k; m'', n'', k'')]$ are sparse matrices, $[G^{(q)}(m, n, k; m', n', k')]$ is a fully populated matrix. Hence, the final coefficient matrix for $\{d^{(q)}(m', n', k')\}$ is fully populated. However, since $G^{(q)}(m, n, k; m', n', k')$ is a function of $m - m'$, $n - n'$, and $k - k'$, the matrix–vector product on the right-hand side of Equation 11.2.71 can be calculated by a cyclic convolution

$$\{A^{(q)}(m, n, k)\} = \{G^{(q)}(m, n, k)\} \otimes \{\chi^{(q)}(m, n, k) d^{(q)}(m, n, k)\} \quad (11.2.73)$$

where $G^{(q)}(m, n, k) = G^{(q)}(m, n, k; 1, 1, 1)$. Using a simple approximation that approximates the rectangular cell as a spherical cell of an equal volume for $m = n = k = 1$, we obtain

$$G^{(q)}(1, 1, 1) = \frac{a^2}{2} - jk_0 \frac{a^3}{3} \quad (11.2.74)$$

where $a = (3\Delta V/4\pi)^{1/3}$ with $\Delta V = \Delta x \Delta y \Delta z$. For all other cases, we can either use the mid-point approximation to find

$$G^{(q)}(m, n, k) = \frac{e^{-jk_0 R}}{4\pi R} \Delta V \quad (11.2.75)$$

where $R = \sqrt{[(m - 1)\Delta x]^2 + [(n - 1)\Delta y]^2 + [(k - 1)\Delta z]^2}$, or use a slightly more complicated evaluation [14] to find

$$G^{(q)}(m, n, k) = \frac{e^{-jk_0 R}}{R} \frac{\text{sinc}(k_0 a) - \cos(k_0 a)}{\frac{4}{3}\pi(k_0 a)^2} \Delta V \quad (11.2.76)$$

which has a better accuracy. The evaluation of Equation 11.2.73 can be accomplished through the use of the DFTs

$$\{A^{(q)}(m, n, k)\} = \mathcal{F}_D^{-1}\{\mathcal{F}_D\{G^{(q)P}(m, n, k)\} \circ \mathcal{F}_D\{\chi^{(q)P}(m, n, k)d^{(q)P}(m, n, k)\}\}. \quad (11.2.77)$$

This calculation can be carried out efficiently using six FFTs, assuming that $\mathcal{F}_D\{G^{(q)P}(m, n, k)\}$ is precalculated. The memory required is proportional to $O(N_x N_y N_z)$, where N_x , N_y , and N_z are the number of cells in the x -, y -, and z -directions, respectively, from the discretization of the rectangular box that contains the dielectric object. The computation time is proportional to $O(N_x N_y N_z \log N_x N_y N_z)$.

Although any iterative method can be employed to solve Equation 11.2.72, it was found [17] that the transpose-free quasi-minimal residual (TFQMR) algorithm [67] is a very attractive choice, because it requires only one matrix–vector product in each iteration and avoids the use of the transpose of the system matrix. To demonstrate the accuracy of this algorithm, we calculate the scattering of a plane wave from a two-layer dielectric sphere and compare the results with the Mie series solution. The incident plane wave is assumed to be polarized in the x -direction and propagates in the z -direction. The amplitude of the incident electric field is 1 V/m. Figure 11.4 shows the field in the dielectric sphere calculated using a $31 \times 31 \times 31$ grid. The number of unknowns is 92,256, and the memory used is only 16 MB.

To further demonstrate the capability of the method in treating strongly inhomogeneous dielectric objects, we consider the plane wave scattering by a human head. The construction of the electromagnetic model of the head and the material properties of the tissues of the head are described in Reference [16]. The plane wave is incident from the top, and the incident electric field is polarized in the x -direction (from the left to the right ear). The incident electric field has an amplitude of 1 V/m, and the frequency considered is 256 MHz. The results are presented in the form of specific absorption rate (SAR), defined as $SAR = \sigma |\mathbf{E}|^2 / 2\rho$, where ρ denotes the density. Figure 11.5 shows the SAR in the axial, sagittal, and coronal planes. The number of unknowns for this calculation is over 750,000, and the memory used is only 105 MB.

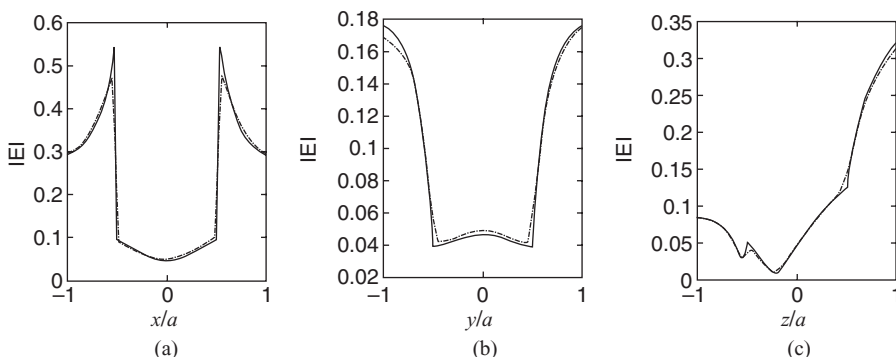


Figure 11.4 Magnitude of the total electric field inside a two-layer dielectric sphere along the x -, y -, and z -axes. The inner layer has a radius $a_1 = 7.5$ cm and $\epsilon_{1r} = 72.0 - j161.8$, the outer layer has a radius $a_2 = 15$ cm and $\epsilon_{2r} = 7.5 - j9.0$, and the frequency is 100 MHz. The solid line represents the Mie series solution, and the dash-dot line represents the numerical solution. (After Wang and Jin [17], Copyright © 1998 IEEE.)

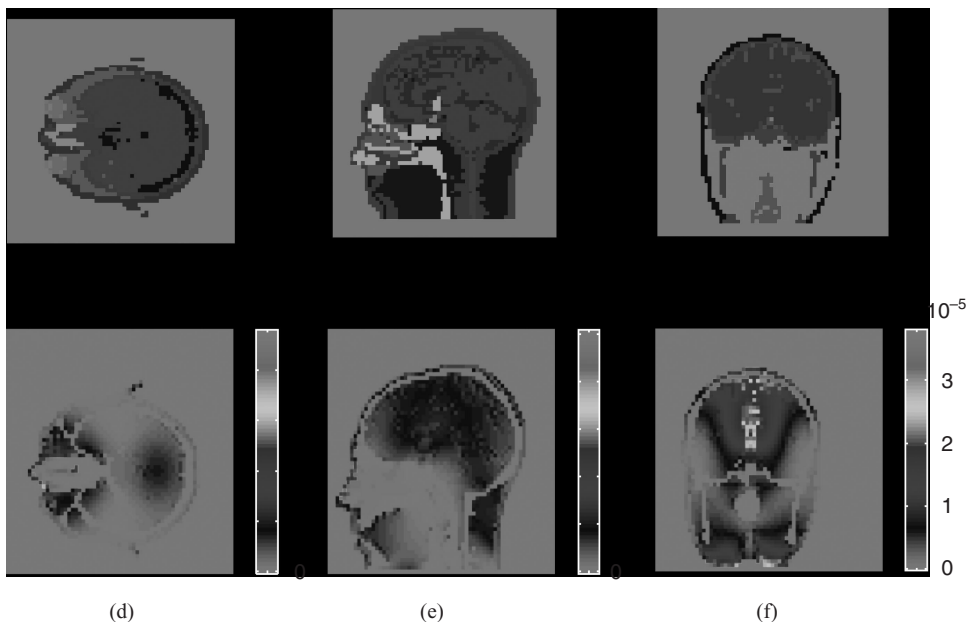


Figure 11.5 Staircase model of a human head and SAR (W/kg) at 256 MHz calculated using a $63 \times 63 \times 63$ grid under the excitation of a plane wave incident from the top. (a) Axial view. (b) Sagittal view. (c) Coronal view. (d) SAR in the axial slice. (e) SAR in the sagittal slice. (f) SAR in the coronal slice. (After Wang and Jin [17], Copyright © 1998 IEEE.) (See color insert.)

11.3 ADAPTIVE INTEGRAL METHOD

The CG-FFT method described in the preceding section requires a uniform discretization. However, modeling an arbitrary geometry with uniform rectangular grids necessitates a staircase approximation, which makes the final solution less accurate. This is often considered as the most serious drawback of the CG-FFT method. This drawback can be alleviated with the use of discretization based on triangular patches for surfaces and tetrahedral cells for volumes. However, in this case, the FFT cannot be applied directly to speed up the matrix–vector multiplication. The AIM is developed to remove this difficulty [18–22]. This method first projects the triangular or tetrahedral subdomain basis functions onto a uniform rectangular grid and then applies FFT to carry out the matrix–vector multiplication. A similar idea is also employed in the precorrected–FFT, sparse-matrix/canonical grid, and integral equation–FFT methods [23–26]. In this section, we describe the AIM using a planar and a three-dimensional example.

11.3.1 Planar Structures

Consider an arbitrarily shaped planar plate in the xy -plane, which is illuminated by an incident field $\mathbf{E}^{\text{inc}}(\mathbf{r})$. The induced current on the plate can be found by solving the integral equation in Equation 11.2.6. For this, the conducting surface is first subdivided into small triangular elements, and the current on the surface is expanded using the RWG basis function $\Lambda_n(\mathbf{r})$. Application of Galerkin’s method results in a matrix equation

$$[\mathbf{Z}]\{\mathbf{I}\} = \{\mathbf{V}\} \quad (11.3.1)$$

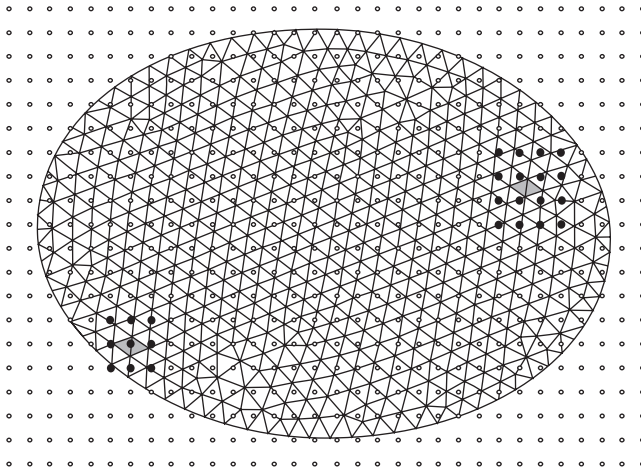


Figure 11.6 Translation of RWG basis functions on a triangular mesh to point sources on rectangular grids. The highlighted triangular basis function on the left is approximated by nine delta functions. The one on the right is approximated by 16 delta functions.

in which the impedance matrix $[Z]$ and vector $\{V\}$ have the elements given by

$$Z_{mn} = jk_0 \iiint_S \iint_S \left[\boldsymbol{\Lambda}_m \cdot \boldsymbol{\Lambda}_n - \frac{1}{k_0^2} (\nabla \cdot \boldsymbol{\Lambda}_m)(\nabla' \cdot \boldsymbol{\Lambda}_n) \right] G_0(\mathbf{r}, \mathbf{r}') dS' dS \quad (11.3.2)$$

$$V_m = \iint_S \boldsymbol{\Lambda}_m \cdot \mathbf{E}^{\text{inc}} dS. \quad (11.3.3)$$

To solve Equation 11.3.1 using the AIM, we first enclose the whole structure in a rectangular region and recursively subdivide it into small rectangular cells, as illustrated in Figure 11.6. To permit the use of FFT to perform the matrix–vector multiplication, we then translate the original triangular basis functions to rectangular grids, or in other words, approximate the original triangular basis functions by the delta functions on the uniform rectangular grids. If we denote any one of the Cartesian components of $\boldsymbol{\Lambda}_m(\mathbf{r})$ and $\nabla \cdot \boldsymbol{\Lambda}_m(\mathbf{r})$ as $\psi_m(\mathbf{r})$, the impedance matrix element of Equation 11.3.2 can be expressed as a linear combination of matrix elements in the form of

$$z_{mn} = \iint_S \iint_S \psi_m(\mathbf{r}) G_0(\mathbf{r}, \mathbf{r}') \psi_n(\mathbf{r}') dS' dS. \quad (11.3.4)$$

To calculate this efficiently, $\psi_m(\mathbf{r})$ and $\psi_n(\mathbf{r}')$ can be approximated as a combination of the Dirac delta functions on the rectangular grids:

$$\psi_m(\mathbf{r}) \approx \sum_{u=1}^{(M+1)^2} T_{mu} \delta(\mathbf{r} - \mathbf{r}_u) \quad (11.3.5)$$

$$\psi_n(\mathbf{r}') \approx \sum_{v=1}^{(M+1)^2} T_{nv} \delta(\mathbf{r}' - \mathbf{r}_v) \quad (11.3.6)$$

where T_{mu} is the expansion coefficient for the basis function $\psi_m(\mathbf{r})$, M is the expansion order, and \mathbf{r}_u is the position vector of the grid point. Once we find this translation, we can approximate the matrix element of Equation 11.3.4 as

$$\tilde{z}_{mn} = \sum_{u=1}^{(M+1)^2} \sum_{v=1}^{(M+1)^2} T_{mu} G_0(\mathbf{r}_u, \mathbf{r}_v) T_{nv}. \quad (11.3.7)$$

The accuracy of this approximation depends on the accuracy of the translation of Equations 11.3.5 and 11.3.6. Different criteria can be used to accomplish this translation. One criterion is based on the multipole moment approximation so that the translated basis function produces the same multipole moments as those of the original basis function

$$\sum_{u=1}^{(M+1)^2} (x_u - x_0)^{q_1} (y_u - y_0)^{q_2} T_{mu} = \iint_S \psi_m(x, y) (x - x_0)^{q_1} (y - y_0)^{q_2} dS$$

for $0 \leq q_1, q_2 \leq M \quad (11.3.8)$

where the reference point $\mathbf{r}_0 = (x_0, y_0)$ is chosen as the center of the basis function. This defines a set of equations, which can be solved for T_{mu} . A closed-form solution is also available [18]. Another criterion is based on the far-field approximation, so that these two basis functions produce the same far field. The derivation of the criterion is as follows. Define the residual of the far field in the direction of \mathbf{k}_l as

$$r_l = \tilde{\psi}_l - \sum_{u=1}^{(M+1)^2} T_{mu} e^{-j\mathbf{k}_l \cdot \mathbf{r}_u} \quad (11.3.9)$$

where $\tilde{\psi}_l$ is the far field, or the Fourier transform, of the original basis function $\psi_m(\mathbf{r})$ in the direction of \mathbf{k}_l . Summing the square of r_l over a set of wave directions on the unit sphere and minimizing it, we obtain a matrix equation

$$[A]\{T_m\} = \{b\} \quad (11.3.10)$$

in which the matrix $[A]$ and vector $\{b\}$ have the elements given by

$$A_{uv} = \sum_{l=1}^{2L^2} w_l \cos[\mathbf{k}_l \cdot (\mathbf{r}_u - \mathbf{r}_v)] \quad (11.3.11)$$

$$b_u = \sum_{l=1}^{2L^2} w_l \operatorname{Re}[e^{j\mathbf{k}_l \cdot \mathbf{r}_u} \tilde{\psi}_l] \quad (11.3.12)$$

where w_l is the weighting coefficient of the direction \mathbf{k}_l . The number of directions on the unit sphere is $2L^2$, which can be chosen sufficiently large to cover all the directions of interest. It was found that the far-field approximation is more accurate than the multipole moment approximation.

Using Equation 11.3.7 as the approximation of Equation 11.3.4, we obtain the corresponding approximation to Z_{mn} in Equation 11.3.2 as

$$\tilde{Z}_{mn} = jk_0 \sum_{u=1}^{(M+1)^2} \sum_{v=1}^{(M+1)^2} \left[(T_{x,mu} T_{x,nv} + T_{y,mu} T_{y,nv}) - \frac{1}{k_0^2} T_{d,mu} T_{d,nv} \right] G_0(\mathbf{r}_u, \mathbf{r}_v) \quad (11.3.13)$$

where $T_{x,mu}$, $T_{y,mu}$, and $T_{d,mu}$ denote the translation coefficients for the x -component, the y -component, and the divergence of the basis function, respectively. This expression offers a good accuracy to approximate Z_{mn} when the basis and testing functions are at a large distance. Its accuracy decreases when the basis and testing functions are close to each

other, and it eventually becomes totally erroneous when the two functions overlap. To compensate for this error and ensure the accuracy of computation, the impedance matrix can be decomposed into the near- and far-interaction components

$$[Z] = [Z^{\text{near}}] + [Z^{\text{far}}]. \quad (11.3.14)$$

Since a given basis function has only a limited number of nearby testing functions, $[Z^{\text{near}}]$ is a sparse matrix when its small entries are neglected. However, such an explicit division of near and far interactions is inconvenient for implementation. A better decomposition is

$$[Z] = [R] + [\tilde{Z}], \quad (11.3.15)$$

where \tilde{Z}_{mn} is given by Equation 11.3.13 and R_{mn} is the difference between Z_{mn} in Equation 11.3.2 and \tilde{Z}_{mn} in Equation 11.3.13. Neglecting the small matrix elements, $[R]$ is a sparse matrix like $[Z^{\text{near}}]$. From Equation 11.3.13, $[\tilde{Z}]$ can be written as

$$[\tilde{Z}] = [T_x][G][T_x]^T + [T_y][G][T_y]^T - \frac{1}{k_0^2}[T_d][G][T_d]^T \quad (11.3.16)$$

where $[T_x]$, $[T_y]$, and $[T_d]$ are sparse matrices, and $[G]$ is a matrix with the elements given by $G_{uv} = jk_0 G(\mathbf{r}_u, \mathbf{r}_v)$. The Toeplitz property of $[G]$ enables the use of FFT to accelerate the computation of the matrix–vector product. Given a known vector $\{I\}$, the matrix–vector product can be expressed as

$$\begin{aligned} [Z]\{I\} &= [R]\{I\} + [\tilde{Z}]\{I\} \\ &= [R]\{I\} + [T_x]\mathcal{F}_D^{-1}\{\mathcal{F}_D\{G^P\} \circ \mathcal{F}_D\{J_x^P\}\} + [T_y]\mathcal{F}_D^{-1}\{\mathcal{F}_D\{G^P\} \circ \mathcal{F}_D\{J_y^P\}\} \\ &\quad - \frac{1}{k_0^2}[T_d]\mathcal{F}_D^{-1}\{\mathcal{F}_D\{G^P\} \circ \mathcal{F}_D\{J_d^P\}\} \end{aligned} \quad (11.3.17)$$

where $\{J_{x,y,d}^P\}$ is expanded from $\{J_{x,y,d}\} = [T_{x,y,d}]^T\{I\}$.

From the formulation described above, we can see that a significant saving of memory due to the sparsity of matrices $[R]$ and $[T]$ and the reduction of the computation time due to the utilization of the FFT in the matrix–vector product can be achieved by the AIM. The memory consists of $[R]$ and $[T_{x,y,d}]$, which are stored in the block sparse format, and the current vector or its Fourier transform at the location of grids, which are all proportional to the total number of grid points, which is in turn proportional to $O(N)$, where N is the number of unknowns. Therefore, the total memory requirement is proportional to $O(N)$. The computation time includes the times for filling matrices $[R]$ and $[T_{x,y,d}]$ and the matrix–vector multiplication. The former grows linearly with the number of unknowns and is done only once. The latter is dominated by the FFT computation, which is proportional to $O(N \log N)$. Numerical experiments in Figures 11.7 and 11.8 verified that indeed the memory requirement is proportional to $O(N)$, the computation time of the matrix fill is proportional to $O(N)$, and the computation time per iteration is proportional to $O(N \log N)$ [19].

To demonstrate the performance of the AIM, we consider the scattering from two plates, each consisting of a triangular plate and a half-circular disk. The second plate contains a narrow slot. The monostatic radar cross-section (RCS) of each plate is computed for the HH polarization, with the incident angle θ^{inc} fixed at 80° . For the first plate, the numbers of facets and edges are 2024 and 2977, respectively. The rectangular grid has the dimension of 64×64 . The memory requirement is 7.5 MB, whereas the direct moment method needs 71 MB of memory. The information about the second plate is similar. The

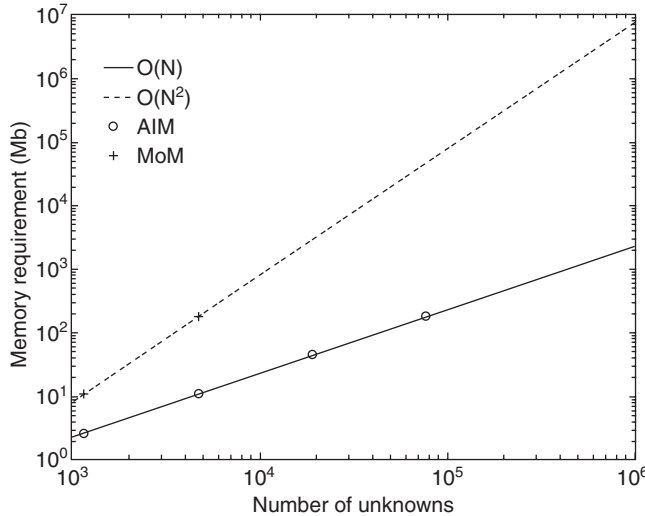


Figure 11.7 Memory requirement versus the number of unknowns. (After Ling et al. [19], Copyright © 1998 EMW Publishing.)

results are in excellent agreement with those by the conventional moment method, which can be seen from Figures 11.9 and 11.10. The AIM has also been applied to analyzing structures with small features [20] and large-scale microstrip structures [21].

11.3.2 Three-Dimensional Objects

The AIM can be extended to solve the integral equation for the problem of scattering by three-dimensional objects. Consider an arbitrarily shaped conducting object illuminated by an incident field $\mathbf{E}^{inc}(\mathbf{r})$. Its moment-method solution was already formulated in Section 10.3.3. The matrix equation obtained from the discretization of the CFIE is given by Equation 10.3.50, and the expression for its elements is given in Equation 10.3.51. The element expression can be written more explicitly as

$$\begin{aligned} Z_{mn} = & jk_0 \iint_{S_o} \iint_{S_o} \left[\Lambda_m \cdot \Lambda_n - \frac{1}{k_0^2} (\nabla \cdot \Lambda_m)(\nabla' \cdot \Lambda_n) \right] G_0 dS' dS \\ & + \frac{1}{2} \iint_{S_o} \Lambda_m \cdot \Lambda_n dS - \iint_{S_o} \Lambda_m \cdot \left[\hat{n} \times \nabla \times \iint_{S_o} \Lambda_n G_0 dS' \right] dS \end{aligned} \quad (11.3.18)$$

which can be transformed into

$$\begin{aligned} Z_{mn} = & jk_0 \iint_{S_o} \iint_{S_o} \left[\Lambda_m \cdot \Lambda_n - \frac{1}{k_0^2} (\nabla \cdot \Lambda_m)(\nabla' \cdot \Lambda_n) \right] G_0 dS' dS \\ & + \frac{1}{2} \iint_{S_o} \Lambda_m \cdot \Lambda_n dS - \iint_{S_o} \iint_{S_o} \left[\nabla \times (\hat{n} \times \Lambda_m) \right] \cdot \Lambda_n G_0 dS' dS. \end{aligned} \quad (11.3.19)$$

To enable the use of FFT, the whole object is enclosed in a rectangular box that is recursively subdivided into small boxes, so that each small box contains a few triangular elements at most. These small boxes form a uniform Cartesian grid. In order to perform the matrix–vector product using FFT, we have to translate the original triangular basis

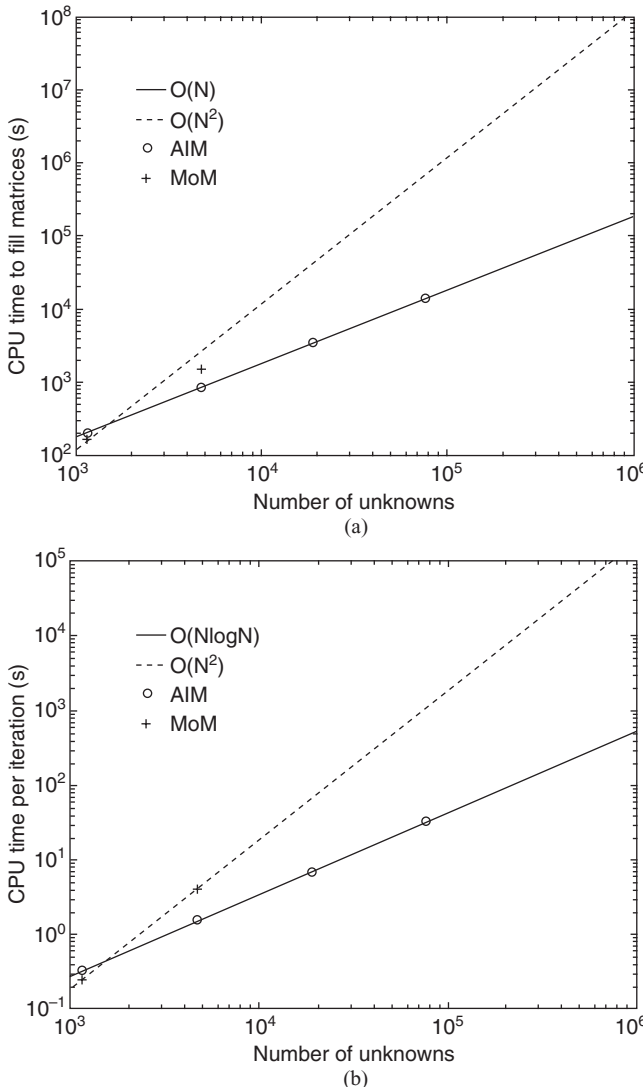


Figure 11.8 Computation time versus the number of unknowns. (a) Matrix filling. (b) Matrix solving per iteration. (After Ling et al. [19], Copyright © 1998 EMW Publishing.)

functions to the Cartesian grid, and this can be done using the basis transformation technique. Let us denote the x -, y -, and z -components of $\Lambda_m(\mathbf{r})$ as $\Lambda_m^{(1)}(\mathbf{r})$, $\Lambda_m^{(2)}(\mathbf{r})$, and $\Lambda_m^{(3)}(\mathbf{r})$ and the x -, y -, and z -components of $\nabla \times [\hat{n} \times \Lambda_m(\mathbf{r})]$ as $t_m^{(1)}(\mathbf{r})$, $t_m^{(2)}(\mathbf{r})$, and $t_m^{(3)}(\mathbf{r})$, and then define the following column vectors

$$\{\Lambda^{(k)}\} = [\Lambda_1^{(k)}(\mathbf{r}), \Lambda_2^{(k)}(\mathbf{r}), \dots, \Lambda_N^{(k)}(\mathbf{r})]^T$$

$$\{\Lambda_d\} = [\nabla \cdot \Lambda_1(\mathbf{r}), \nabla \cdot \Lambda_2(\mathbf{r}), \dots, \nabla \cdot \Lambda_N(\mathbf{r})]^T$$

$$\{t^{(k)}\} = [t_1^{(k)}(\mathbf{r}), t_2^{(k)}(\mathbf{r}), \dots, t_N^{(k)}(\mathbf{r})]^T$$

$$\{D\} = [\delta(\mathbf{r} - \mathbf{r}_1), \delta(\mathbf{r} - \mathbf{r}_2), \dots, \delta(\mathbf{r} - \mathbf{r}_{N_g})]^T$$

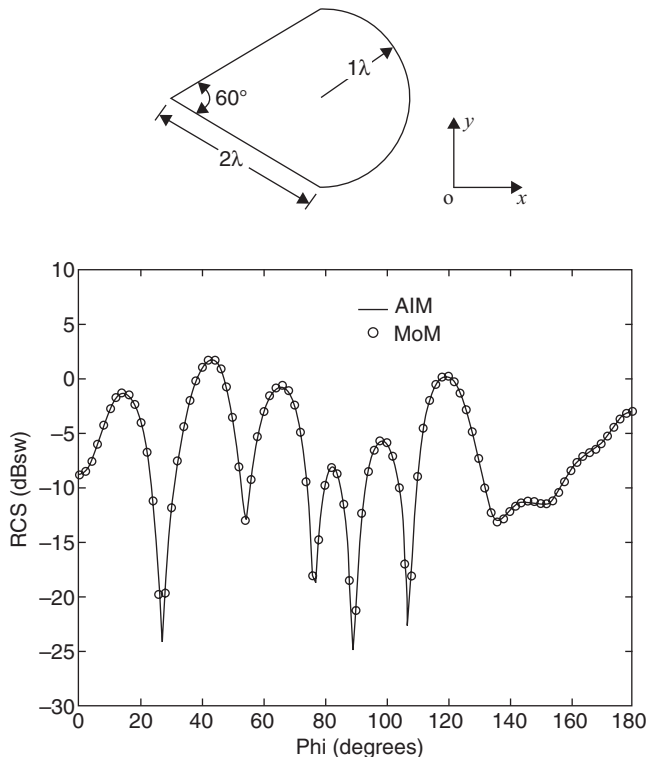


Figure 11.9 HH-polarized monostatic RCS of a triangle/half-circle combined plate at $\theta^{\text{inc}} = 80^\circ$. (After Ling et al. [19], Copyright © 1998 EMW Publishing.)

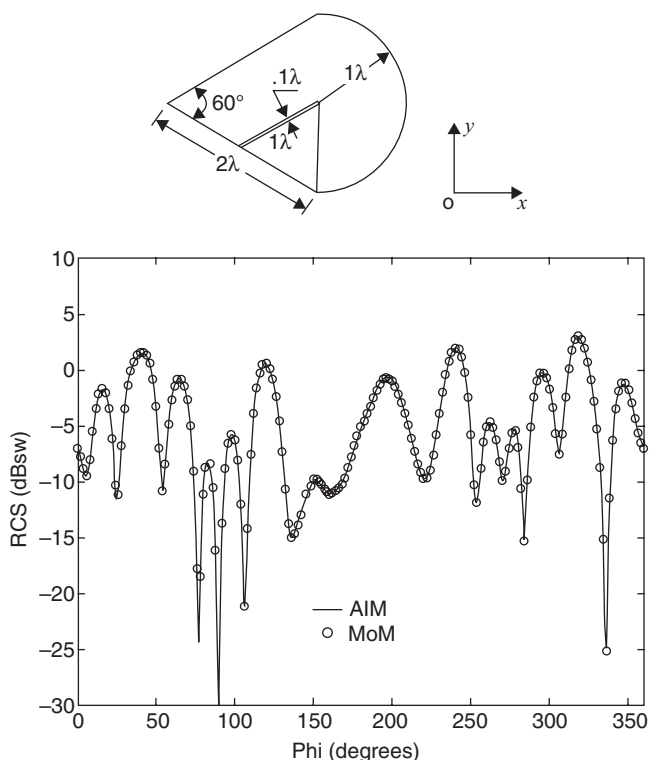


Figure 11.10 HH-polarized monostatic RCS of a triangle/half-circle combined plate having a narrow slot at $\theta^{\text{inc}} = 80^\circ$. (After Ling et al. [19], Copyright © 1998 EMW Publishing.)

where N denotes the number of unknowns, $\delta(\mathbf{r} - \mathbf{r}_u)$ is the Dirac delta function, \mathbf{r}_u is a node in the Cartesian grid, and N_g denotes the total number of nodes in the uniform Cartesian grid. By using either the multipole moment or the far-field approximation, $\{\Lambda^{(k)}\}$, $\{\Lambda_d\}$, and $\{t^{(k)}\}$ can be approximated by $\{\tilde{\Lambda}^{(k)}\}$, $\{\tilde{\Lambda}_d\}$, and $\{\tilde{t}^{(k)}\}$ on the Cartesian grid:

$$\{\tilde{\Lambda}^{(k)}\} = [T^{(k)}]\{D\}, \quad \{\tilde{\Lambda}_d\} = [T_d]\{D\}, \quad \{\tilde{t}^{(k)}\} = [T_t]\{D\} \quad (11.3.20)$$

where $[T^{(k)}]$, $[T_d]$, and $[T_t]$ are called the basis transformation matrices. They are $N \times N_g$ sparse matrices. Substituting these approximations into Equation 11.3.19, we obtain the approximation to $[Z]$ as

$$[\tilde{Z}] = \sum_{k=1}^3 [T^{(k)}][G][T^{(k)}]^T - \frac{1}{k_0^2} [T_d][G][T_d]^T + \sum_{k=1}^3 [T_t^{(k)}][G][T^{(k)}]^T \quad (11.3.21)$$

where $[G]$ is an $N_g \times N_g$ matrix with $G_{uv} = jk_0 G_0(\mathbf{r}_u, \mathbf{r}_v)$.

As in the planar structure case, \tilde{Z}_{mn} offers a good accuracy for approximating Z_{mn} when the basis and testing functions are at a large distance. To eliminate the error that occurs when the basis and testing functions are close to each other, we may decompose the impedance matrix as

$$[Z] = [R] + [\tilde{Z}] \quad (11.3.22)$$

where $[R]$ is the difference between $[Z]$ and $[\tilde{Z}]$, which is a sparse matrix after we neglect its small elements. The matrix–vector product can be expressed as

$$\begin{aligned} [Z]\{I\} &= [R]\{I\} + [\tilde{Z}]\{I\} \\ &= [R]\{I\} + \sum_{k=1}^3 ([T^{(k)}] + [T_t^{(k)}]) \mathcal{F}_D^{-1}\{\mathcal{F}_D\{G^P\} \circ \mathcal{F}_D\{J_k^P\}\} \\ &\quad - \frac{1}{k_0^2} [T_d]\mathcal{F}_D^{-1}\{\mathcal{F}_D\{G^P\} \circ \mathcal{F}_D\{J_d^P\}\} \end{aligned} \quad (11.3.23)$$

where $\{J_k^P\}$ is expanded from $\{J_k\} = [T^{(k)}]^T\{I\}$ and $\{J_d^P\}$ is expanded from $\{J_d\} = [T_d]^T\{I\}$ by zero padding.

From the formulation described above, we can see the significant saving of memory due to the sparsity of matrices $[R]$, $[T^{(k)}]$, $[T_d]$, and $[T_t]$ and the reduction of the computation time by the utilization of FFT in the matrix–vector multiplication. The memory requirements for $[R]$, $[T^{(k)}]$, $[T_d]$, $[T_t]$, and $\{G\}$ are all proportional to $O(N_g)$, which is in turn proportional to $O(N^{1.5})$ because N is the number of unknowns resulting from the surface discretization. The computation time for calculating $[R]\{I\}$ is proportional to $O(N)$, and the computation time for calculating $[\tilde{Z}]\{I\}$ is $O(N_g \log N_g)$ or $O(N^{1.5} \log N)$. Thus, the memory and computation time requirements of the formulation described above are $O(N^{1.5})$ and $O(N^{1.5} \log N)$, respectively, for calculating the matrix–vector product. A more significant reduction in the memory and computation time requirements can be achieved when the AIM is applied to the moment-method solution of volume integral equations, such as the one presented in Reference [72], for problems involving inhomogeneous objects. In that case, a volumetric discretization is required and the resulting number of unknowns is proportional to N_g . Hence, the memory and computation time requirements for calculating the matrix–vector product in an iterative solution of a volume integral equation can be reduced from $O(N^2)$ to $O(N)$ and $O(N \log N)$, respectively.

As a test case, we consider the scattering from a 1.0-m-long almond, whose detailed geometrical information is given in Reference [73]. Figure 11.11 shows the monostatic RCS of the almond at 0.3 GHz using 1560 unknowns. Figure 11.12 shows the monostatic RCS of the almond at 0.757 GHz using 6120 unknowns. These results are compared with the measured results [73,74]. As another test case, we consider the scattering from a wing having the size of $120 \times 100 \times 2.4$ inches. The discretization results in 3120 unknowns. The monostatic RCS of the wing at 0.3 GHz is given in Figure 11.13 and is compared with the result of the moment method.

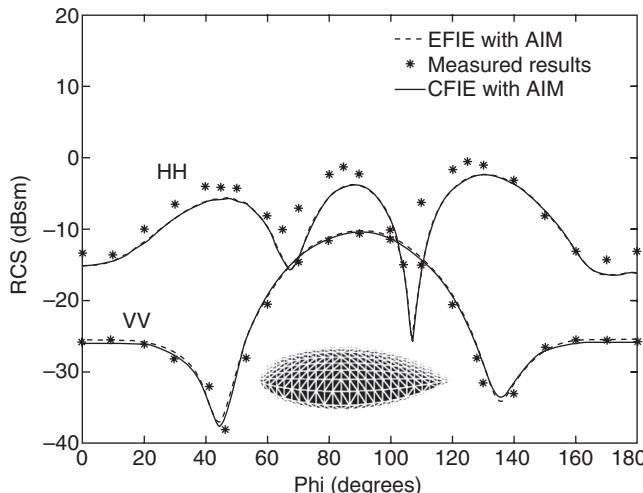


Figure 11.11 Monostatic RCS of 1.0-m-long almond at 300 MHz. (After Wang et al. [22], Copyright © 1998 Wiley.)

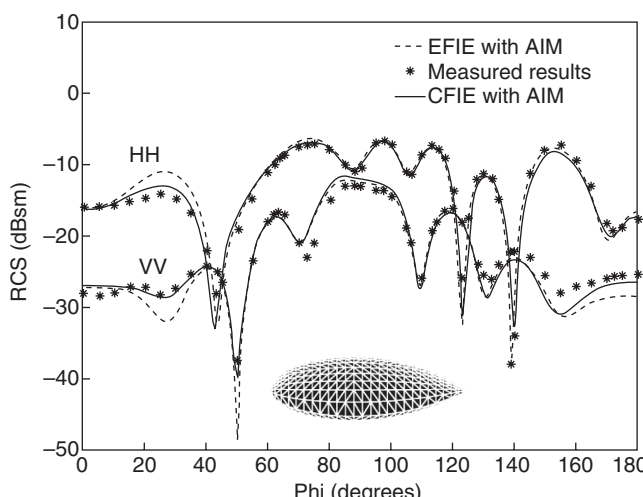


Figure 11.12 Monostatic RCS of 1.0-m-long almond at 757 MHz. (After Wang et al. [22], Copyright © 1998 Wiley.)

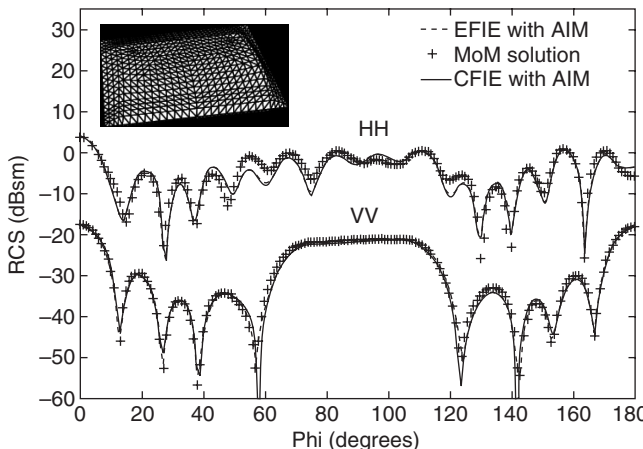


Figure 11.13 Monostatic RCS of a $304.8 \times 254 \times 6.1$ -cm wing at 300 MHz. (After Wang et al. [22], Copyright © 1998 Wiley.)

11.4 FAST MULTIPOLE METHOD

In addition to the AIM, another approach to speeding up the computation of the matrix–vector product is called the FMM, which has gained widespread use in solving a variety of electromagnetic problems, especially the scattering and radiation problems. The FMM was originally proposed by Rokhlin to evaluate particle interactions and to solve static integral equations rapidly [27,28]. It was extended to solve acoustic wave scattering problems and then to solve electromagnetic scattering problems in both two and three dimensions [29–31]. Recognizing the fact that calculating a matrix–vector product in the moment method is equivalent to calculating the self- and mutual interactions among multiple current elements—the fields radiated by each element and received by all the elements—the basic idea of the FMM is first to divide the current elements into groups by their physical locations in space—a group, hence, is a collection of current elements in close proximity to each other. The addition theorem is then used to translate the radiated fields of different current elements within a group, which emanate from different centers, to a common center. This process reduces the number of scattering centers significantly. Similarly, to calculate the fields received by each current element within a group, the fields radiated by all the other group centers are first collected or received by the group center and then redistributed to the current elements within the group. In this section, we discuss the basic ideas of the FMM and its application to two- and three-dimensional scattering analysis. We then extend the FMM to multiple levels and describe its implementation and practical applications.

11.4.1 Two-Dimensional Analysis

To illustrate the basic ideas of the FMM, we first consider the relatively simple problem of wave scattering by an infinitely long conducting cylinder. The moment-method solution of this problem was formulated in Section 10.2.2. For simplicity, we first consider the TM polarization case. The moment-method equation is given by Equation 10.2.22, with a general expression for Z_{mn} given by

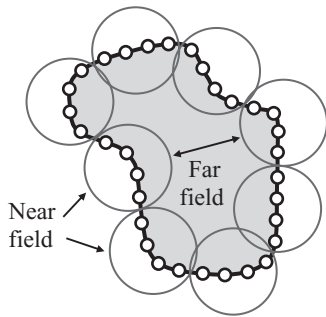


Figure 11.14 Basis functions divided into groups so that the far-field interactions can be computed rapidly, whereas the near-field interactions are calculated directly.

$$Z_{mn} = \frac{k_0 Z_0}{4} \int_{\Gamma} t_m(\mathbf{p}) \int_{\Gamma} H_0^{(2)}(k_0 |\mathbf{p} - \mathbf{p}'|) f_n(\mathbf{p}') d\Gamma' d\Gamma \quad (11.4.1)$$

where $t_m(\mathbf{p})$ denotes the testing functions and $f_n(\mathbf{p}')$ denotes the basis functions. When $t_m(\mathbf{p}) = \delta(\mathbf{p} - \mathbf{p}_m)$ and $f_n(\mathbf{p}') = 1$ for $\mathbf{p}' \in s_n$ and 0 elsewhere, Equation 11.4.1 reduces to Equation 10.2.23.

The physical meaning of Z_{mn} is the field radiated by the current element represented by the basis function $f_n(\mathbf{p}')$ and received by the current element represented by the testing function $t_m(\mathbf{p})$. Therefore, the sum on the left-hand side of Equation 10.2.22, $\sum_{n=1}^N Z_{mn} J_{z,n}$, represents the total field radiated by all the current elements $J_{z,n} f_n(\mathbf{p}')$ and received by the testing function $t_m(\mathbf{p})$. To calculate this sum directly requires N multiplications and additions, and to repeat this calculation for all the testing functions requires N^2 multiplications and additions. To speed up this calculation, we make use of the fact that when the observer is far away from a group of lighting sources, the observer sees the combined effect of all the sources instead of each individual source. The combined source can be represented by fewer parameters than those required to describe all the individual sources. Therefore, if we can divide all the basis functions into a number of groups, as illustrated in Figure 11.14, we can calculate the fields radiated by the basis functions in the far-away groups and received by the testing function $t_m(\mathbf{p})$ by first combining the radiation of those basis functions to the center of their group and then receiving the combined fields radiated by the centers of those groups. Since we need to repeat this calculation for all the testing functions, we can further speed up the calculation by letting the center of the group to which $t_m(\mathbf{p})$ belongs receive all the radiated fields from the far-away groups and then distributing the received field to each testing function in the group. The process described above is applicable only to far-field interaction calculations, whereas the fields radiated by the basis functions in the nearby groups will be calculated individually. However, since each testing function has a fixed, finite number of nearby basis functions, this direct near-field interaction calculation grows only as a linear function of N .

For the convenience of description, let us denote the group to which $f_n(\mathbf{p}')$ belongs as G_q , whose center is located at \mathbf{p}_q , and the group where $t_m(\mathbf{p})$ resides as G_p , whose center is located at \mathbf{p}_p . To perform the fast far-field interaction calculation described above, we first have to shift the effect of $f_n(\mathbf{p}')$ to its group center at \mathbf{p}_q , then translate this effect from \mathbf{p}_q to \mathbf{p}_p , and finally deliver the field received at \mathbf{p}_p to $t_m(\mathbf{p})$. These three steps can be carried out only if we can factorize the Hankel function $H_0^{(2)}(k_0 |\mathbf{p} - \mathbf{p}'|)$ in Equation 11.4.1 into a product of three functions: one containing $\mathbf{p}_q - \mathbf{p}'$, another containing $\mathbf{p}_p - \mathbf{p}_q$, and the third one containing $\mathbf{p} - \mathbf{p}_p$. For this, we use the addition theorem for the Hankel function given in Equation 6.5.32 to find

$$H_0^{(2)}(k_0|\mathbf{p} + \mathbf{d}|) = \sum_{l=-\infty}^{\infty} J_l(k_0 d) H_l^{(2)}(k_0 \rho) e^{jl(\phi_d - \pi)} \quad \rho > d \quad (11.4.2)$$

where ϕ_d denotes the angle between \mathbf{d} and the x -axis. Next, we use the integral representation of the Bessel function [75] to find

$$J_l(k_0 d) e^{-jl(\phi_d + \pi)} = \frac{1}{2\pi} \int_0^{2\pi} e^{-jk_0 d \cos(\alpha - \phi_d) - jl(\alpha + \pi/2)} d\alpha \quad (11.4.3)$$

which can also be expressed as

$$J_l(k_0 d) e^{-jl(\phi_d + \pi)} = \frac{1}{2\pi} \int_0^{2\pi} e^{-j\mathbf{k} \cdot \mathbf{d} - jl(\alpha + \pi/2)} d\alpha \quad (11.4.4)$$

where $\mathbf{k} = k_0(\hat{x} \cos \alpha + \hat{y} \sin \alpha)$. Clearly, Equation 11.4.4 can be regarded as the plane-wave expansion of a cylindrical wave. By substituting Equation 11.4.4 into Equation 11.4.2, we obtain

$$H_0^{(2)}(k_0|\mathbf{p} + \mathbf{d}|) = \frac{1}{2\pi} \sum_{l=-\infty}^{\infty} H_l^{(2)}(k_0 \rho) e^{jl\phi} \int_0^{2\pi} e^{-j\mathbf{k} \cdot \mathbf{d} - jl(\alpha + \pi/2)} d\alpha \quad \rho > d. \quad (11.4.5)$$

Now, if we express $\mathbf{p} - \mathbf{p}'$ as the sum of three vectors

$$\mathbf{p} - \mathbf{p}' = (\mathbf{p} - \mathbf{p}_p) + (\mathbf{p}_p - \mathbf{p}_q) + (\mathbf{p}_q - \mathbf{p}') = (\mathbf{p} - \mathbf{p}_p) + \mathbf{p}_{pq} + (\mathbf{p}_q - \mathbf{p}') \quad (11.4.6)$$

as illustrated in Figure 11.15, and let $\mathbf{p} = \mathbf{p}_{pq}$ and $\mathbf{d} = (\mathbf{p} - \mathbf{p}_p) + (\mathbf{p}_q - \mathbf{p}')$ in Equation 11.4.5, we obtain

$$H_0^{(2)}(k_0|\mathbf{p} - \mathbf{p}'|) = \frac{1}{2\pi} \int_0^{2\pi} e^{-j\mathbf{k} \cdot (\mathbf{p} - \mathbf{p}_p)} \tilde{\alpha}_{pq}(\alpha) e^{-j\mathbf{k} \cdot (\mathbf{p}_q - \mathbf{p}')} d\alpha$$

$$\rho_{pq} > |(\mathbf{p} - \mathbf{p}_p) + (\mathbf{p}_q - \mathbf{p}')| \quad (11.4.7)$$

where

$$\tilde{\alpha}_{pq}(\alpha) \approx \sum_{l=-L}^L H_l^{(2)}(k_0 \rho_{pq}) e^{jl(\phi_{pq} - \alpha - \pi/2)} \quad (11.4.8)$$

in which ϕ_{pq} denotes the angle that \mathbf{p}_{pq} makes with the x -axis and the infinite series is truncated. Equation 11.4.7 is the desired factorized form that can be used to implement the fast far-field calculation.

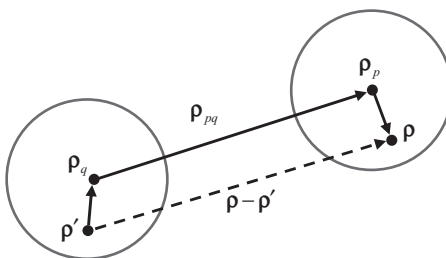


Figure 11.15 Vector $\mathbf{p} - \mathbf{p}'$ expressed as a sum of three vectors: $\mathbf{p} - \mathbf{p}_p$, $\mathbf{p}_p - \mathbf{p}_q$, and $\mathbf{p}_q - \mathbf{p}'$.

To utilize Equation 11.4.7 to speed up the calculation of the far-field interactions, we first divide altogether N basis functions into a number of groups, each containing approximately M basis functions, as illustrated in Figure 11.14. These groups can be denoted by G_p ($p = 1, 2, \dots, N/M$). If the testing function $t_m(\mathbf{p})$ belongs to the group G_p centered at \mathbf{p}_p and the basis function $f_n(\mathbf{p}')$ belongs to another group G_q centered at \mathbf{p}_q that is not an immediate neighbor of G_p (to satisfy the condition $\rho_{pq} > |(\mathbf{p} - \mathbf{p}_p) + (\mathbf{p}_q - \mathbf{p}')|$, we can substitute Equation 11.4.7 into Equation 11.4.1 to rewrite Z_{mn} as

$$Z_{mn} = \frac{k_0 Z_0}{8\pi} \int_0^{2\pi} \int_{\Gamma} t_m(\mathbf{p}) e^{-j\mathbf{k} \cdot (\mathbf{p} - \mathbf{p}_p)} d\Gamma \tilde{\alpha}_{pq}(\alpha) \int_{\Gamma} f_n(\mathbf{p}') e^{-j\mathbf{k} \cdot (\mathbf{p}_q - \mathbf{p}')} d\Gamma' d\alpha \quad (11.4.9)$$

or more concisely

$$Z_{mn} = \frac{k_0 Z_0}{8\pi} \int_0^{2\pi} \tilde{t}_{mp}(\alpha) \tilde{\alpha}_{pq}(\alpha) \tilde{f}_{qn}(\alpha) d\alpha \quad (11.4.10)$$

where

$$\tilde{t}_{mp}(\alpha) = \int_{\Gamma} t_m(\mathbf{p}) e^{-j\mathbf{k} \cdot (\mathbf{p} - \mathbf{p}_p)} d\Gamma \quad (11.4.11)$$

$$\tilde{f}_{qn}(\alpha) = \int_{\Gamma} f_n(\mathbf{p}') e^{-j\mathbf{k} \cdot (\mathbf{p}_q - \mathbf{p}')} d\Gamma'. \quad (11.4.12)$$

By using this result, the matrix–vector product or the summation in the left-hand side of Equation 10.2.22 can be written as

$$\begin{aligned} \sum_{n=1}^N Z_{mn} J_{z,n} &= \sum_{q \in B_p} \sum_{n \in G_q} Z_{mn} J_{z,n} \\ &\quad + \frac{k_0 Z_0}{8\pi} \int_0^{2\pi} \tilde{t}_{mp}(\alpha) \sum_{q \notin B_p} \tilde{\alpha}_{pq}(\alpha) \sum_{n \in G_q} \tilde{f}_{qn}(\alpha) J_{z,n} d\alpha \quad m \in G_p \end{aligned} \quad (11.4.13)$$

where B_p denotes the neighboring groups of G_p including G_p itself. Therefore, the first term in Equation 11.4.13 is the contribution from neighboring groups (near-field interactions) and is calculated directly. The second term is the contribution from all other non-neighboring groups (far-field interactions) and is calculated indirectly through three steps. By using a quadrature to evaluate the integral, Equation 11.4.13 can be replaced by

$$\begin{aligned} \sum_{n=1}^N Z_{mn} J_{z,n} &= \sum_{q \in B_p} \sum_{n \in G_q} Z_{mn} J_{z,n} \\ &\quad + \frac{k_0 Z_0}{4R} \sum_{r=1}^R \tilde{t}_{mp}(\alpha_r) \sum_{q \notin B_p} \tilde{\alpha}_{pq}(\alpha_r) \sum_{n \in G_q} \tilde{f}_{qn}(\alpha_r) J_{z,n} \quad m \in G_p \end{aligned} \quad (11.4.14)$$

where α_r denotes the quadrature points and the value of R is proportional to the size of the group (hence, is proportional to M).

Now let us count the number of operations to evaluate Equation 11.4.14 and introduce some terminologies used in the FMM. The first term (near-field interactions) can be

evaluated in $3M^2 \times N/M = 3MN$ operations. The evaluation of the second term (far-field interactions) takes three steps. The first step is to calculate the sum

$$F_{qr} = \sum_{n \in G_q} \tilde{f}_{qn}(\alpha_r) J_{z,n} \quad q = 1, 2, \dots, N/M; r = 1, 2, \dots, R \quad (11.4.15)$$

which takes $R \times M \times N/M \sim NM$ operations. This calculation is equivalent to lumping the fields radiated by the sources $f_n(\mathbf{p}') J_{z,n}$ within group G_q into the group center. This step is referred to as *aggregation*, and $\tilde{f}_{qn}(\alpha_r)$ is called the *radiation function* of $f_n(\mathbf{p}')$. The second step is to calculate the sum

$$F_{pr} = \sum_{q \notin B_p} \tilde{\alpha}_{pq}(\alpha_r) F_{qr} \quad q = 1, 2, \dots, N/M; r = 1, 2, \dots, R \quad (11.4.16)$$

which takes $R \times (N/M)^2 \sim N^2/M$. In this step, the aggregated field F_{qr} is first sent from the center of group G_q to the center of group G_p , which is accomplished by multiplying F_{qr} by $\tilde{\alpha}_{pq}(\alpha_r)$. It converts the outgoing waves from group G_q into incoming waves for group G_p . This step is called *translation*, and the summation $\sum_{q \notin B_p}$ simply collects the outgoing waves of all non-nearby groups together. The third step is to calculate the sum

$$F_{mp} = \sum_{r=1}^R \tilde{t}_{mp}(\alpha_r) F_{pr} \quad m = 1, 2, \dots, N \quad (11.4.17)$$

which takes $R \times N \sim NM$ operations. This step distributes the field received at the center of group G_p to each testing function $t_m(\mathbf{p})$ within the group. This step is called *disaggregation*, and $\tilde{t}_{mp}(\alpha_r)$ can be considered as the *receive function* of $t_m(\mathbf{p})$. Hence, the total computation time for calculating Equation 11.4.14 for all m 's or the matrix–vector product $[Z]\{J_z\}$ is

$$T = C_1 NM + C_2 \frac{N^2}{M} \quad (11.4.18)$$

where C_1 and C_2 are simply some constants. This computation time reaches a minimum of $T_{\min} = 2\sqrt{C_1 C_2} N^{3/2}$ when $M = \sqrt{C_2 N / C_1} \sim \sqrt{N}$. Hence, the computation time is reduced from $O(N^2)$ to $O(N^{3/2})$, which can be significant when N is very large. The memory required is also reduced from $O(N^2)$ to $O(N^{3/2})$.

The formulation described above can also be applied to the TE polarization case. The matrix element of the moment-method system of equations is given by

$$Z_{mn} = \frac{1}{4j} \int_{\Gamma} t_m(\mathbf{p}) \int_{\Gamma} \frac{\partial H_0^{(2)}(k_0 |\mathbf{p} - \mathbf{p}'|)}{\partial n'} f_n(\mathbf{p}') d\Gamma' d\Gamma \quad (11.4.19)$$

when $t_m(\mathbf{p})$ does not overlap with $f_n(\mathbf{p}')$. Substituting Equation 11.4.7 into this expression, we obtain

$$Z_{mn} = \frac{1}{4j} \int_0^{2\pi} \int_{\Gamma} t_m(\mathbf{p}) e^{-jk(\mathbf{p} - \mathbf{p}_p)} d\Gamma \tilde{\alpha}_{pq}(\alpha) \int_{\Gamma} f_n(\mathbf{p}') \frac{\partial e^{-jk(\mathbf{p}_q - \mathbf{p}')}}{\partial n'} d\Gamma' d\alpha \quad (11.4.20)$$

which can be used for the calculation of the far-field interactions. The entire process is identical to the TM case except that the expression of the radiation function is changed.

11.4.2 Three-Dimensional Analysis

The formulation of the FMM for two-dimensional scattering analysis can be extended to the three-dimensional case. For this, we consider the problem of wave scattering by a three-dimensional perfect conductor. Its moment-method solution using the CFIE was already formulated in Section 10.3.3. The matrix equation is given by Equation 10.3.50, and the expression for its elements is given in Equation 10.3.51. The element expression can be rewritten as

$$\begin{aligned} Z_{mn} = & jk_0 \iint_{S_o} \Lambda_m \cdot \iint_{S_o} \left(\tilde{\mathbf{I}} + \frac{1}{k_0^2} \nabla \nabla \right) \cdot \Lambda_n G_0 dS' dS \\ & + \frac{1}{2} \iint_{S_o} \Lambda_m \cdot \Lambda_n dS - \iint_{S_o} \Lambda_m \cdot \left[\hat{n} \times \nabla \times \iint_{S_o} \Lambda_n G_0 dS' \right] dS. \end{aligned} \quad (11.4.21)$$

We choose to use this form here because the FMM is used to speed up the computation when Λ_m and Λ_n are far apart. In such a case, the integrand is no longer singular; therefore, leaving two del operators on G_0 does not present any difficulty.

Again, we start with the addition theorem, now in three dimensions, which was derived in Section 7.5.1 and can be written as

$$\frac{e^{-jk_0|\mathbf{r}+\mathbf{d}|}}{|\mathbf{r}+\mathbf{d}|} = -jk_0 \sum_{l=0}^{\infty} (-1)^l (2l+1) j_l(k_0 d) h_l^{(2)}(k_0 r) P_l(\hat{d} \cdot \hat{r}) \quad r > d \quad (11.4.22)$$

where $j_l(x)$ is a spherical Bessel function of the first kind, $h_l^{(2)}(x)$ is a spherical Hankel function of the second kind, and $P_l(x)$ is a Legendre polynomial. Invoking the elementary identity [76] that expands a spherical wave into a superposition of plane waves

$$j_l(k_0 d) P_l(\hat{d} \cdot \hat{r}) = \frac{j^l}{4\pi} \iint e^{-jk\cdot\mathbf{d}} P_l(\hat{k} \cdot \hat{r}) d^2 \hat{k} \quad (11.4.23)$$

where the integral is performed over a unit sphere and $\mathbf{k} = k_0 \hat{k}$, we obtain

$$\frac{e^{-jk_0|\mathbf{r}+\mathbf{d}|}}{|\mathbf{r}+\mathbf{d}|} = -\frac{jk_0}{4\pi} \iint e^{-jk\cdot\mathbf{d}} \sum_{l=0}^{\infty} (-j)^l (2l+1) h_l^{(2)}(k_0 r) P_l(\hat{k} \cdot \hat{r}) d^2 \hat{k} \quad r > d \quad (11.4.24)$$

where the order of integration and summation has been reversed. When the infinite summation is truncated, we obtain the approximation

$$\frac{e^{-jk_0|\mathbf{r}+\mathbf{d}|}}{|\mathbf{r}+\mathbf{d}|} \approx -\frac{jk_0}{4\pi} \iint e^{-jk\cdot\mathbf{d}} T_L(\hat{k} \cdot \hat{r}) d^2 \hat{k} \quad r > d \quad (11.4.25)$$

where

$$T_L(\hat{k} \cdot \hat{r}) = \sum_{l=0}^L (-j)^l (2l+1) h_l^{(2)}(k_0 r) P_l(\hat{k} \cdot \hat{r}) \quad (11.4.26)$$

in which the infinite series has been truncated. The optimal choice of L depends on the value of the argument of the spherical Hankel function, which will be discussed later.

To use Equation 11.4.25 in the FMM, we first divide the N basis functions into a number of groups, denoted by G_p ($p = 1, 2, \dots, N/M$), each containing about M basis

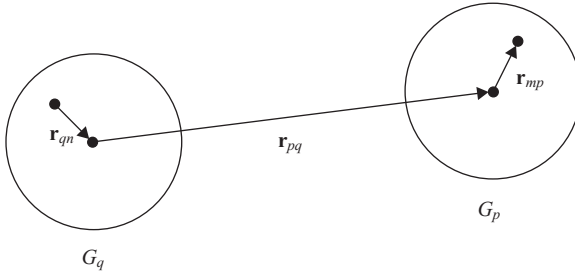


Figure 11.16 Vector $\mathbf{r} - \mathbf{r}'$ expressed as a sum of three vectors: $\mathbf{r}_{mp} = \mathbf{r} - \mathbf{r}_p$, $\mathbf{r}_{pq} = \mathbf{r}_p - \mathbf{r}_q$, and $\mathbf{r}_{qn} = \mathbf{r}_q - \mathbf{r}'$, where \mathbf{r}_p denotes the center of group G_p and \mathbf{r}_q denotes the center of group G_q .

functions. Now let \mathbf{r} be a field point in group G_p centered at \mathbf{r}_p , and \mathbf{r}' be a source point in another group G_q centered at \mathbf{r}_q (Fig. 11.16). We can decompose $\mathbf{r} - \mathbf{r}'$ into the sum of three vectors

$$\mathbf{r} - \mathbf{r}' = (\mathbf{r} - \mathbf{r}_p) + (\mathbf{r}_p - \mathbf{r}_q) + (\mathbf{r}_q - \mathbf{r}') = (\mathbf{r} - \mathbf{r}_p) + \mathbf{r}_{pq} + (\mathbf{r}_q - \mathbf{r}'). \quad (11.4.27)$$

Substituting this into Equation 11.4.25, we obtain

$$\frac{e^{-jk_0|\mathbf{r}-\mathbf{r}'|}}{|\mathbf{r}-\mathbf{r}'|} \approx -\frac{jk_0}{4\pi} \oint \oint e^{-j\mathbf{k}\cdot(\mathbf{r}-\mathbf{r}_p)} T_L(\hat{\mathbf{k}} \cdot \hat{\mathbf{r}}_{pq}) e^{-j\mathbf{k}\cdot(\mathbf{r}_q-\mathbf{r}')} d^2\hat{\mathbf{k}} \quad r_{pq} > |(\mathbf{r} - \mathbf{r}_p) + (\mathbf{r}_q - \mathbf{r}')| \quad (11.4.28)$$

or

$$G_0(\mathbf{r}, \mathbf{r}') \approx \frac{1}{jk_0} \oint \oint e^{-j\mathbf{k}\cdot(\mathbf{r}-\mathbf{r}_p)} \tilde{\alpha}_{pq}(\hat{\mathbf{k}}) e^{-j\mathbf{k}\cdot(\mathbf{r}_q-\mathbf{r}')} d^2\hat{\mathbf{k}} \quad r_{pq} > |(\mathbf{r} - \mathbf{r}_p) + (\mathbf{r}_q - \mathbf{r}')| \quad (11.4.29)$$

where

$$\tilde{\alpha}_{pq}(\hat{\mathbf{k}}) = \left(\frac{k_0}{4\pi} \right)^2 \sum_{l=0}^L (-j)^l (2l+1) h_l^{(2)}(k_0 r_{pq}) P_l(\hat{\mathbf{k}} \cdot \hat{\mathbf{r}}_{pq}). \quad (11.4.30)$$

The integral in Equation 11.4.29 can be evaluated by Gaussian quadratures using $K = 2L^2$ points. Equation 11.4.29 has the desired factorized form that can be used to formulate the FMM.

When Equation 11.4.29 is substituted into Equation 11.4.21, we obtain Z_{mn} in the form

$$Z_{mn} = \oint \oint \mathbf{V}_{mp}(\hat{\mathbf{k}}) \cdot \tilde{\alpha}_{pq}(\hat{\mathbf{k}}) \mathbf{V}_{qn}(\hat{\mathbf{k}}) d^2\hat{\mathbf{k}} \quad (11.4.31)$$

where

$$\mathbf{V}_{mp}(\hat{\mathbf{k}}) = \oint \oint_{S_o} e^{-j\mathbf{k}\cdot(\mathbf{r}-\mathbf{r}_p)} [(\tilde{\mathbf{I}} - \hat{\mathbf{k}}\hat{\mathbf{k}}) \cdot \mathbf{\Lambda}_m(\mathbf{r}) - \hat{\mathbf{k}} \times \hat{\mathbf{n}} \times \mathbf{\Lambda}_m(\mathbf{r})] dS \quad (11.4.32)$$

$$\mathbf{V}_{qn}(\hat{\mathbf{k}}) = \oint \oint_{S_o} e^{-j\mathbf{k}\cdot(\mathbf{r}_q-\mathbf{r}')} \mathbf{\Lambda}_n(\mathbf{r}') dS'. \quad (11.4.33)$$

Since the derivation above is based on the assumption that $|(\mathbf{r} - \mathbf{r}_p) + (\mathbf{r}_q - \mathbf{r}')| < r_{pq}$, Equation 11.4.31 can be used only if $\mathbf{\Lambda}_m$ and $\mathbf{\Lambda}_n$ are far apart. This condition can be satisfied

when they do not belong to the same group or neighboring groups. Using Equation 11.4.31, we can write the matrix–vector multiplication as

$$\sum_{n=1}^N Z_{mn} I_n = \sum_{q \in B_p} \sum_{n \in G_q} Z_{mn} I_n + \iint_{q \notin B_p} \mathbf{V}_{mp}(\hat{k}) \cdot \sum_{q \notin B_p} \tilde{\alpha}_{pq}(\hat{k}) \sum_{n \in G_q} \mathbf{V}_{qn}(\hat{k}) I_n d^2 \hat{k} \quad m \in G_p \quad (11.4.34)$$

where B_p denotes the neighboring groups of G_p including G_p itself. Therefore, the first term in Equation 11.4.34 is the contribution from the self and neighboring groups and is calculated directly. For this calculation, one can choose other forms, such as Equation 11.3.18, to calculate Z_{mn} . The second term is the far-field interaction to be calculated by the FMM.

As in the two-dimensional case, there are three steps in the three-dimensional FMM for calculating the far-field interaction in a matrix–vector product. The aggregation step is to calculate $\sum_{n \in G_q} \mathbf{V}_{qn}(\hat{k}) I_n$, which lumps the fields radiated by the sources $\Lambda_n I_n$ within group G_q into the group center, and $\mathbf{V}_{qn}(\hat{k})$ is referred to as the radiation function of Λ_n . The translation step is to calculate $\tilde{\alpha}_{pq}(\hat{k})$ times the aggregated field, which sends the field radiated from the center of group G_q to the center of group G_p , which is equivalent to converting the outgoing waves from group G_q into incoming waves for group G_p . The summation $\sum_{q \notin B_p}$ collects the outgoing waves of all non-nearby groups at the center of group G_p . The disaggregation step is to multiply the field received at the center of group G_p by $\mathbf{V}_{mp}(\hat{k})$, which is equivalent to distributing the received field to each testing function Λ_m within group G_p , and $\mathbf{V}_{mp}(\hat{k})$ is referred to as the receive function of Λ_m . For numerical implementation, the truncation point in Equation 11.4.26 must be chosen carefully, since including more terms beyond the optimal truncation point will actually increase the truncation error. A good choice for L in Equation 11.4.26 is $L = k_0 D + 6(k_0 D)^{1/3}$ for an accuracy around 10^{-6} , where D denotes the maximum diameter of the group [31,37]. The computational complexity analysis is similar to that for the two-dimensional FMM, which showed that when $M \sim \sqrt{N}$, the operation count for calculating Equation 11.4.34 is proportional to $O(N^{3/2})$ and the memory required is also proportional to $O(N^{3/2})$.

For a practical implementation of the FMM, the object is first placed into a cubic box, and this cubic box is then subdivided into smaller equal-sized subcubes. Each non-empty subcube defines a group. The FMM is applied to the non-nearby groups, which are the groups whose bounding subcubes do not touch each other. This ensures the satisfaction of the distance condition in Equation 11.4.29. The groups whose bounding subcubes touch each other are considered nearby groups. In the two-dimensional case, a subdivision of an arbitrary geometry into groups is illustrated in Figure 11.17, where the shaded areas represent the groups. Using groups bounded by equal-sized subcubes has an added advantage

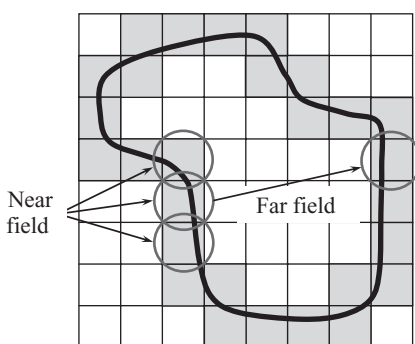


Figure 11.17 Practical subdivision of basis functions into groups and illustration of the far- and near-field interactions.

in that some groups have the same center-to-center distance r_{pq} and their transfer functions in Equation 11.4.30 are the same; hence, only one has to be calculated for these groups.

11.4.3 Multilevel Fast Multipole Algorithm

As discussed in Section 11.4.1, for a problem with N unknowns, which are divided into N/M groups, the calculation of near-field interactions, the aggregation, and the disaggregation require $O(NM)$ operations, and the calculation of the translation requires $O(N^2/M)$ operations. Using a large number of groups (i.e., small-sized groups with a small value of M) can effectively reduce the operation count for the calculation of near-field interactions, the aggregation, and the disaggregation, but it will increase the operation count required for the translation calculation. On the other hand, using a small number of groups (i.e., large-sized groups with a large value of M) can effectively reduce the operation count for the translation calculation, but it will increase the operation count for the calculation of near-field interactions, the aggregation, and the disaggregation. Therefore, the optimal choice is $M \sim \sqrt{N}$ so that the operation count in each calculation is balanced to $O(N^{3/2})$.

Since there is not much we can do with the calculation of near-field interactions, the only approach to reducing its operation count is to use small groups. If each group contains only a few basis functions, the calculation of near-field interactions will require only $O(N)$ operations, and so will the aggregation and disaggregation. To reduce the calculation of the translation, we can apply the basic idea of the FMM to the groups as we did to the basis functions. When the groups are far apart, we can aggregate the radiated fields of a few groups together into the center of a larger group, translate the field to the center of another larger group, and disaggregate the received field to the groups that reside in the second larger group. This can effectively reduce the operation count required for the translation. This idea can actually be extended to multiple levels until there are no far-apart groups among the highest-level groups. The resulting algorithm is called the *multilevel fast multipole algorithm* (MLFMA) [34–36].

The idea of the FMM and the MLFMA can be understood more easily using the example of the telephone communication network illustrated in Figure 11.18. Consider a network consisting of N telephones. Direct connections between all the telephones would need N^2 telephone lines (Fig. 11.18a). However, if we divide the telephones into groups according to their proximity to each other and connect the telephones within the same group to a single hub and then connect the hubs, the number of telephone lines can be reduced to $O(N^{3/2} \log N)$ (Fig. 11.18b). That is what we did in the standard FMM. If a second level of hubs is established, the number of telephone lines can further be reduced, as shown in Figure 11.18c. If the number of telephones is very large, we can establish multiple levels of hubs to eventually reduce the number of telephone lines to $O(N \log N)$. In a similar manner, the MLFMA can reduce the operation count and memory requirement of the FMM to $O(N \log N)$.

To implement the MLFMA in three dimensions, the entire three-dimensional object is first enclosed in a large cube, which is then divided into eight smaller cubes. Each subcube is further subdivided into eight smaller cubes, and this recursive process continues until the finest cube contains only a few basis functions or current elements. The corresponding two-dimensional picture is shown in Figure 11.19. For two current elements in the same or nearby finest cubes, their interaction is calculated in a direct manner. However, when the two elements reside in different non-nearby cubes, their interaction is calculated by the FMM, as described above. The level of cubes on which the FMM is applied depends on the distance between the two elements. The aggregation process here is to start from

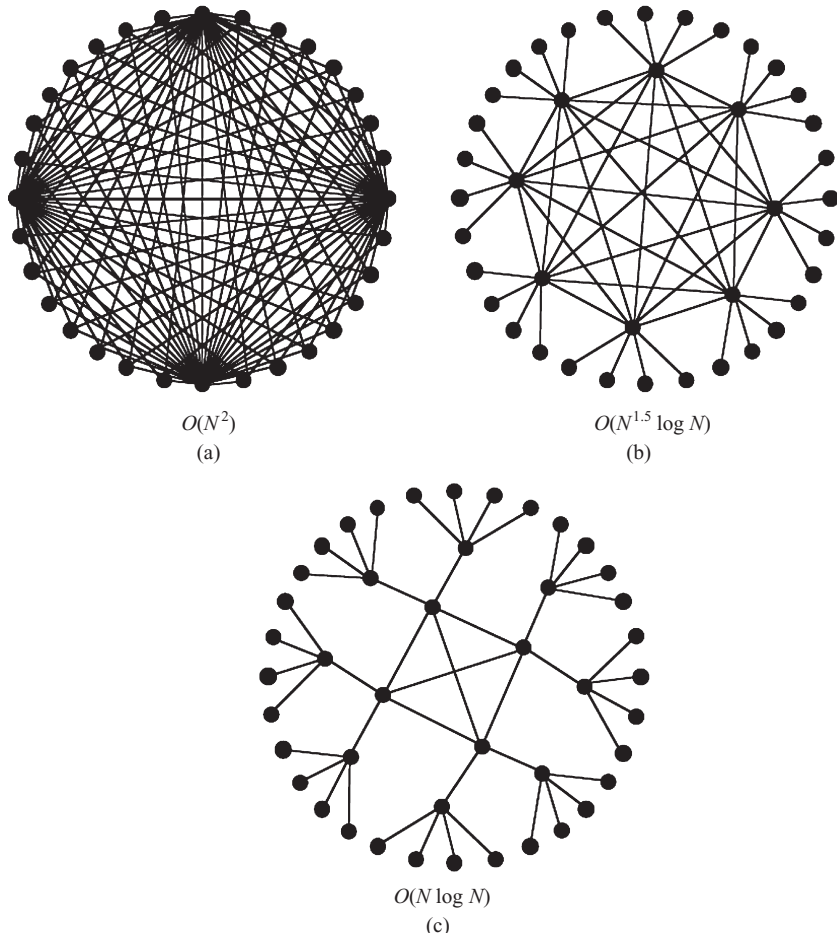


Figure 11.18 Telephone communication network. (a) Direct connections (for clarity only four telephones are connected to all other telephones). (b) Connections via hubs. (c) Connections using two layers of hubs.

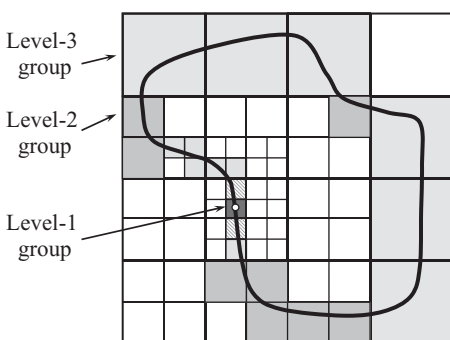


Figure 11.19 Subdivision of basis functions into multilevel groups for the implementation of the multilevel fast multipole algorithm.

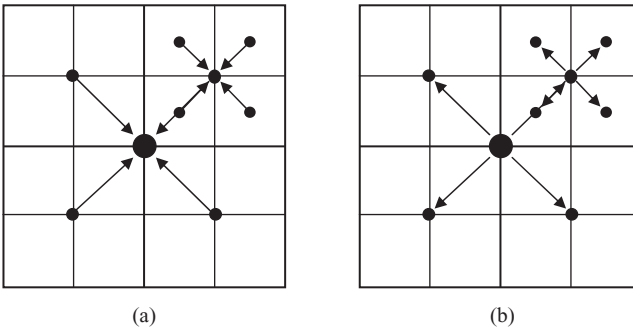


Figure 11.20 Multilevel aggregation and disaggregation processes. (a) Aggregation.
(b) Disaggregation.

the lowest level and compute the outgoing waves of the cubes at that level. These outgoing waves are then used to compute the outgoing waves of the cubes at the next higher level. This process continues until the outgoing waves at the specific level are computed. This is illustrated in Figure 11.20a. The translation then converts these outgoing waves into incoming waves for other groups at the same level. The disaggregation process converts these incoming waves at this level into incoming waves at a lower level and finally into received fields at the testing functions. This process is shown in Figure 11.20b, which simply reverses the process of aggregation.

If we denote level-1 groups by $G_q^{(1)}$, whose centers are located at $\mathbf{r}_q^{(1)}$, and level-2 groups by $G_q^{(2)}$, whose centers are located at $\mathbf{r}_q^{(2)}$, and assume that $G_q^{(1)}$ resides in $G_q^{(2)}$, then, for a basis function Λ_n residing in $G_q^{(1)}$, its radiation function for $G_q^{(2)}$ is given by

$$\mathbf{V}_{qn}^{(2)}(\hat{k}) = \oint_{S_o} e^{-jk(\mathbf{r}_q^{(2)} - \mathbf{r}')} \Lambda_n(\mathbf{r}') dS' \quad (11.4.35)$$

which can be inferred directly from Equation 11.4.33. This expression can be rewritten as

$$\begin{aligned} \mathbf{V}_{qn}^{(2)}(\hat{k}) &= e^{-jk(\mathbf{r}_q^{(2)} - \mathbf{r}_q^{(1)})} \oint_{S_o} e^{-jk(\mathbf{r}_q^{(1)} - \mathbf{r}')} \Lambda_n(\mathbf{r}') dS' \\ &= e^{-jk(\mathbf{r}_q^{(2)} - \mathbf{r}_q^{(1)})} \mathbf{V}_{qn}^{(1)}(\hat{k}) \end{aligned} \quad (11.4.36)$$

which indicates that the radiation function for level 2 can be obtained directly from that of level 1. Therefore, the aggregated field for a level-2 group can be obtained as

$$\sum_{n \in G_q^{(2)}} \mathbf{V}_{qn}^{(2)}(\hat{k}) I_n = \sum_{G_q^{(1)} \in G_q^{(2)}} e^{-jk(\mathbf{r}_q^{(2)} - \mathbf{r}_q^{(1)})} \sum_{n \in G_q^{(1)}} \mathbf{V}_{qn}^{(1)}(\hat{k}) I_n \quad (11.4.37)$$

which can be calculated efficiently from the aggregated fields for level-1 groups. In a similar manner, it can be shown easily from Equation 11.4.32 that the level-1 receive function can be obtained from the level-2 receive function as

$$\mathbf{V}_{mp}^{(1)}(\hat{k}) = e^{-jk(\mathbf{r}_p^{(1)} - \mathbf{r}_p^{(2)})} \mathbf{V}_{mp}^{(2)}(\hat{k}) \quad (11.4.38)$$

which can be used for disaggregation from an upper level to a lower level. Finally, we note that the number of quadrature points for a numerical integration in Equation 11.4.34

depends on the group size. Hence, more quadrature points are required for a higher-level group because of its larger size. This can be accomplished by interpolating the radiation function in a lower-level group when calculating the radiation function of a higher-level group in the multilevel aggregation process. Conversely, in the multilevel disaggregation process, we can down-interpolate, or *ant interpolate*, the receive function going from a higher level to a lower one. Both interpolation and ant interpolation can be performed with exponential accuracy [37].

The foregoing discussion addresses only the main ideas and some key formulas of the FMM and the MLFMA. There are many technical issues that have to be dealt with carefully to develop a fully accurate and efficient MLFMA code. The interested reader can consult recent books [37,53], which document in detail the theory, implementation, and applications of the two methods. We note that, although the formulation presented in this section used the RWG functions as the basis and testing functions, there is actually no limitation on the choice of these functions. In fact, it is rather easy to use different testing functions, which would only change the Λ_m in Equation 11.4.32, and different basis functions, which would only change the Λ_n in Equation 11.4.33. Because of higher-order convergence, the use of higher-order basis functions is particularly attractive in the FMM [38–40]. A typical convergence curve is plotted in Figure 11.21. The bistatic RCS of a conducting sphere of 72λ diameter is computed using the second-order basis functions with 537,600 unknowns, and the result is compared with the Mie series solution in Figure 11.22. The RMS error is about 0.22 dB over the entire region.

The FMM has already been applied to a variety of electromagnetic problems. These include capacitance calculations [41,42], very low-frequency simulations [43], scattering by impedance surfaces [44], scattering by homogeneous dielectric bodies [45], scattering by inhomogeneous bodies [46], scattering by buried objects [47], and layered medium problems [48–52], to name just a few. With this powerful method, very large-scale problems of unprecedented size have been solved. Figure 11.23 shows a snapshot of the surface current on a car induced by a Hertzian dipole at 1 GHz [44]. For this simulation, most parts of the car were treated as perfect electrical conductors, whereas the window glass was modeled as a thin dielectric sheet and the tires were modeled with an impedance boundary condition. Figure 11.24 displays a snapshot of the surface current on an airplane

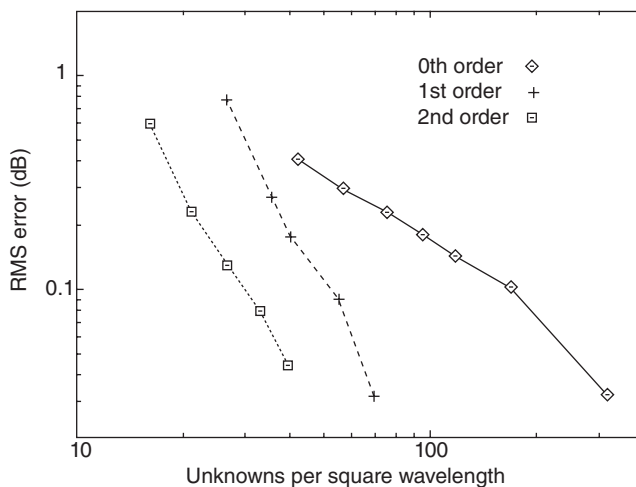


Figure 11.21 RMS error in the H-plane bistatic RCS of a 9λ -diameter sphere versus the number of unknowns per square wavelength. (After Donepudi et al. [38], Copyright © 2001 IEEE.)

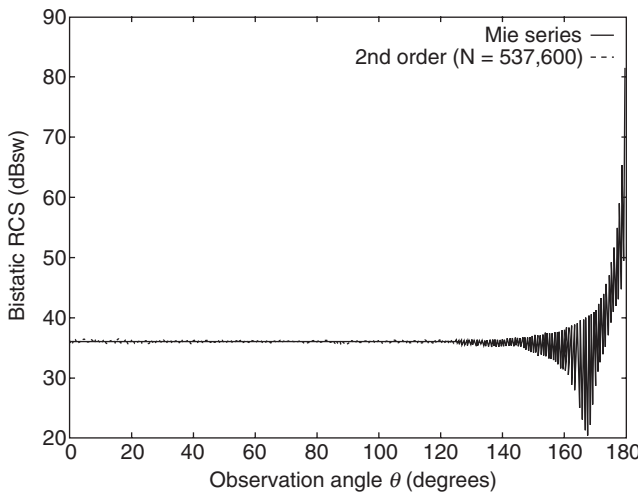


Figure 11.22 E-plane bistatic RCS pattern of a conducting sphere having a diameter of 72λ . (After Donepudi et al. [38], Copyright © 2001 IEEE.)

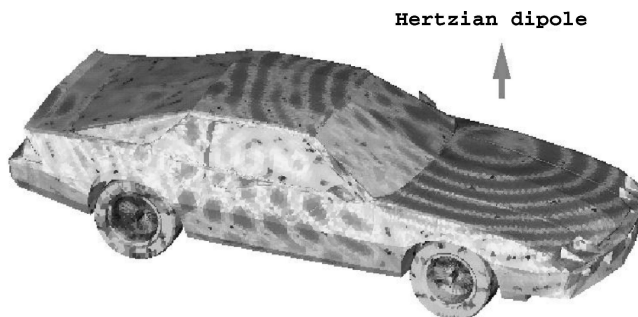


Figure 11.23 Surface current on a car induced by the radiation of a Hertzian dipole at 1.0 GHz. (After Song et al. [44], Copyright © 1998 IEEE.) (See color insert.)

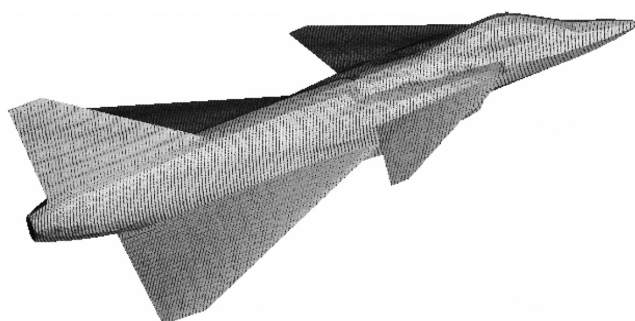


Figure 11.24 Surface current on an airplane induced by an incident plane wave at 2 GHz. The plane wave is incident 30° from the nose and is vertically polarized. (After Song et al. [44], Copyright © 1998 IEEE.) (See color insert.)

induced by an incident plane wave at 2GHz [44]. The plane wave is incident 30° from the nose and is vertically polarized. At 2GHz, the airplane is longer than 100λ . Its surface discretization resulted in nearly one million unknowns. It would take 8TB of memory to store the corresponding full moment-method matrix. This memory requirement was reduced to 2.5GB with the use of the MLFMA. Later, the same airplane was simulated at 8GHz using nearly 10 million unknowns [37].

11.5 ADAPTIVE CROSS-APPROXIMATION ALGORITHM

In the preceding three sections, we discussed three fast methods—the CG–FFT method, the AIM, and the FMM—for solving integral equations. These methods are called *physics-based* or *kernel-based* fast methods, because their formulations, implementations, and performances depend on the specific integral kernels and an explicit decomposition of integral operators. Despite their remarkable power of solving large problems involving millions of unknowns, the kernel-based methods share one common drawback: their formulations and implementations change with the inherent kernels when applied to different problems (e.g., layered medium problems). Besides the kernel-based fast methods, there is another class of fast methods, such as the ACA algorithm [54–57] and the multilevel matrix decomposition method [77–79], which are purely *algebra based* and *kernel independent*. These methods work on the moment-method matrix directly and achieve their computational speed-up solely through linear-algebra manipulations. Therefore, their formulations and implementations do not depend on the specific integral kernels and thus can be applied to the moment-method solution of different problems. In this section, we discuss the ACA method, which has been applied to the analysis of electromagnetic problems [58,59].

11.5.1 Low-Rank Matrix

Like many other fast solvers, the ACA method takes advantage of the rank-deficient nature of off-diagonal subblocks in the moment-method matrix. As we know, entries in the moment-method matrix represent the interactions between the sources represented by basis and testing functions. The diagonal entries represent self-interactions, and the off-diagonal entries represent mutual interactions, which become weaker when the distance between the basis and testing functions increases. Now consider a group of basis functions and a group of testing functions. Their interactions are represented by a subblock matrix in the moment-method matrix. When the two groups are close to each other, one group sees the other group clearly, down to small features (each individual basis and testing functions). As the distance between the two groups increases, one group sees the combined effect of the other group rather than the fine details. Therefore, even though the corresponding subblock matrix is still fully populated, not as much information is contained in this matrix as in the matrix for two nearby groups. In other words, the subblock matrix for two far-apart groups can be represented by fewer parameters. This matrix is called *rank-deficient* or *low-rank*, in contrast to a *full-rank* matrix, which represents interactions between nearby groups.

To illustrate the nature of a rank-deficient matrix, consider a subblock matrix $[z]_{M \times M}$, whose elements are given by

$$z_{mn} = \iint_S \iint_S \psi_m(\mathbf{r}) g(\mathbf{r}, \mathbf{r}') \psi_n(\mathbf{r}') dS' dS \quad m, n = 1, 2, \dots, M. \quad (11.5.1)$$

This matrix represents the interaction between a group of M testing functions $\psi_m(\mathbf{r})$ and a group of M basis functions $\psi_n(\mathbf{r}')$. If $g(\mathbf{r}, \mathbf{r}')$ can be approximated by the product of two functions such that

$$g(\mathbf{r}, \mathbf{r}') = f(\mathbf{r})h(\mathbf{r}') + e(\mathbf{r}, \mathbf{r}') \quad (11.5.2)$$

where $e(\mathbf{r}, \mathbf{r}')$ denotes the error function, z_{mn} can be written as $z_{mn} = u_m v_n + e_{mn}$, where

$$u_m = \iint_S \psi_m(\mathbf{r})f(\mathbf{r})dS \quad m = 1, 2, \dots, M \quad (11.5.3)$$

$$v_n = \iint_S \psi_n(\mathbf{r}')h(\mathbf{r}')dS' \quad n = 1, 2, \dots, M \quad (11.5.4)$$

$$e_{mn} = \iint_S \iint_S \psi_m(\mathbf{r})e(\mathbf{r}, \mathbf{r}')\psi_n(\mathbf{r}')dS'dS \quad m, n = 1, 2, \dots, M. \quad (11.5.5)$$

The matrix $[z]_{M \times M}$ can then be written as

$$[z]_{M \times M} = \{u\}_{M \times 1} \{v\}_{1 \times M} + [e]_{M \times M}. \quad (11.5.6)$$

The matrix formed by $\{u\}_{M \times 1} \{v\}_{1 \times M}$ is called a *rank-1 matrix*, which can be represented by $2M$ numbers instead of M^2 numbers.

For most problems, it is difficult to expand $g(\mathbf{r}, \mathbf{r}')$ in the form of Equation 11.5.2 with good accuracy. Instead, multiple product terms are needed to achieve a good accuracy and reduce the error function. The expansion of $g(\mathbf{r}, \mathbf{r}')$ then becomes

$$g(\mathbf{r}, \mathbf{r}') = \sum_{r=1}^R f_r(\mathbf{r})h_r(\mathbf{r}') + e(\mathbf{r}, \mathbf{r}'). \quad (11.5.7)$$

With this, z_{mn} can be written as

$$z_{mn} = \sum_{r=1}^R u_{mr}v_{rn} + e_{mn} \quad (11.5.8)$$

where

$$u_{mr} = \iint_S \psi_m(\mathbf{r})f_r(\mathbf{r})dS \quad m = 1, 2, \dots, M; r = 1, 2, \dots, R \quad (11.5.9)$$

$$v_m = \iint_S \psi_n(\mathbf{r}')h_r(\mathbf{r}')dS' \quad n = 1, 2, \dots, M; r = 1, 2, \dots, R. \quad (11.5.10)$$

The matrix $[z]_{M \times M}$ can then be written as

$$[z]_{M \times M} = [u]_{M \times R} [v]_{R \times M} + [e]_{M \times M}. \quad (11.5.11)$$

This matrix is called a rank- R matrix, which can be represented by $2RM$ numbers instead of M^2 numbers. Its multiplication with a vector can be evaluated in $2RM$ operations instead of M^2 operations. When R is much smaller than M , the multiplication can be evaluated with many fewer operations, compared to the direct multiplication.

From discussions above, it is evident that as long as we can factorize Green's functions in the form of Equation 11.5.7 with a small value of R , we can accelerate the evaluation of the matrix–vector product. That is exactly what we did in the FMM. Equation 11.4.7 is the explicit factorization of the two-dimensional Green's function, and Equation

11.4.29 is the explicit factorization of the three-dimensional Green's function for wave scattering analysis. Alternatively, we can directly calculate $[u]_{M \times R}$ and $[v]_{R \times M}$ from $[z]_{M \times M}$ and then use $[u]_{M \times R}$ and $[v]_{R \times M}$ to calculate the matrix–vector multiplication efficiently. This alternative approach has the advantage that there is no need for the explicit factorization of the Green's function. This advantage is important for problems in which the explicit factorization of the Green's function is difficult.

The well-established approach to calculating $[u]_{M \times R}$ and $[v]_{R \times M}$ from $[z]_{M \times M}$ is to employ the singular-value decomposition (SVD) method [80]. According to this method, any matrix can be decomposed into the product of three matrices:

$$[z]_{M \times M} = [U]_{M \times M} [\Sigma]_{M \times M} [V^*]_{M \times M} \quad (11.5.12)$$

where $[U]$ and $[V]$ are unitary matrices and $[\Sigma]$ is a diagonal matrix whose entries are the singular values of $[z]_{M \times M}$. Since the singular values of a rank-deficient matrix decrease exponentially, only a few large singular values contribute significantly to $[z]_{M \times M}$. If we keep the first R significant singular values and ignore the remaining small values, Equation 11.5.12 can be approximated as $[z]_{M \times M} \approx [u]_{M \times R} [v]_{R \times M}$, as we hoped for. Unfortunately, the SVD is expensive and requires the calculation of the matrix. The ACA algorithm [54–57] is developed to obtain the compressed representation at a lower cost and without the calculation of the full matrix, as it requires only a few selected rows and columns of the matrix.

11.5.2 Adaptive Cross-Approximation

The ACA algorithm is based on the *cross-approximation* or *skeleton approximation* of a rank-deficient matrix. In the cross-approximation, $[u]_{M \times R}$ and $[v]_{R \times M}$ are constructed by minimizing the error matrix

$$[e]_{M \times M} = [z]_{M \times M} - [u]_{M \times R} [v]_{R \times M} \quad (11.5.13)$$

through iterations until $\|e\| < \varepsilon \|z\|$, where ε denotes the given tolerance and $\|e\|$ and $\|z\|$ denote the Frobenius norms of $[e]_{M \times M}$ and $[z]_{M \times M}$, respectively, which are defined by

$$\|e\| = \sqrt{\sum_{m=1}^M \sum_{n=1}^M |e_{mn}|^2}. \quad (11.5.14)$$

This iterative process can be expressed as

$$[e]_{M \times M}^{(k)} = [z]_{M \times M} - [u]_{M \times k} [v]_{k \times M} \quad k = 0, 1, 2, \dots, R. \quad (11.5.15)$$

For $k = 0$, we have $[e]_{M \times M}^{(0)} = [z]_{M \times M}$. We then search through the entire $[e]_{M \times M}^{(0)}$ and find the entry that has the largest absolute value. Denoting this entry as $e^{(0)}(I_1, J_1)$, we then let

$$u(:, 1) = \frac{e^{(0)}(:, J_1)}{e^{(0)}(I_1, J_1)} \quad (11.5.16)$$

$$v(1, :) = e^{(0)}(I_1, :). \quad (11.5.17)$$

It can be shown easily that $u(:, 1)v(1, :)$ reproduces exactly the I_1 th row and J_1 th column of $[e]_{M \times M}^{(0)}$. Hence, the entries of the I_1 th row and the J_1 th column of the new error matrix $[e]_{M \times M}^{(1)} = [e]_{M \times M}^{(0)} - u(:, 1)v(1, :) = [z]_{M \times M} - [u]_{M \times 1} [v]_{1 \times M}$ have been completely eliminated

(i.e., have the value of zero). Next, we search through the entire $[e]_{M \times M}^{(1)}$ and find the entry that has the largest absolute value. Denoting this entry as $e^{(1)}(I_2, J_2)$, we then let

$$u(:, 2) = \frac{e^{(1)}(:, J_2)}{e^{(1)}(I_2, J_2)} \quad (11.5.18)$$

$$v(2, :) = e^{(1)}(I_2, :). \quad (11.5.19)$$

It can be shown easily that $u(:, 2)v(2, :)$ reproduces exactly the I_2 th row and J_2 th column of $[e]_{M \times M}^{(1)}$. However, the zero entries in the I_1 th row and the J_1 th column remain intact. Hence, the entries of the I_1 th and I_2 th rows and the J_1 th and J_2 th columns of the new error matrix $[e]_{M \times M}^{(2)} = [e]_{M \times M}^{(1)} - u(:, 2)v(2, :) = [z]_{M \times M} - [u]_{M \times 2}[v]_{2 \times M}$ have been completely eliminated (i.e., have the value of zero). This process continues. For the k th iteration, we search through the entire $[e]_{M \times M}^{(k-1)}$ for the entry that has the largest absolute value. Denoting this entry as $e^{(k-1)}(I_k, J_k)$, we then let

$$u(:, k) = \frac{e^{(k-1)}(:, J_k)}{e^{(k-1)}(I_k, J_k)} \quad (11.5.20)$$

$$v(k, :) = e^{(k-1)}(I_k, :). \quad (11.5.21)$$

The matrix formed by the product $[u]_{M \times k}[v]_{k \times M}$ would eliminate all the entries in the rows (I_1, I_2, \dots, I_k) and columns (J_1, J_2, \dots, J_k) in the new error matrix $[e]_{M \times M}^{(k)} = [z]_{M \times M} - [u]_{M \times k}[v]_{k \times M}$. In each iteration, the Frobenius norm of $[e]_{M \times M}^{(k)}$ is calculated and compared to the Frobenius norm of $[z]_{M \times M}$. The iteration continues until $\|e^{(R)}\| < \epsilon \|z\|$.

The cross-approximation described above is very similar to the *LU* decomposition with full pivoting. In fact, if the iteration continues until the end (i.e., $R = M$), $[u]_{M \times R}$ and $[v]_{R \times M}$ can be rearranged into an upper and lower triangular matrix through row and column permutations. Unfortunately, even though the cross-approximation process yields $[u]_{M \times R}$ and $[v]_{R \times M}$ successfully, it requires a full knowledge of the original matrix $[z]_{M \times M}$ in order to search for its largest entries and to calculate $\|z\|$, and it requires an update of the error matrix in each iteration. Therefore, the entire process is computationally very expensive. The ACA algorithm modifies the process to eliminate these disadvantages.

In ACA, we first pick an arbitrary row such as $I_1 = 1$ or $I_1 = M/2$, calculate $z(I_1, :)$, and let $v(1, :) = z(I_1, :)$. We then find the column number J_1 of the largest entry in $v(1, :)$. We next calculate $z(:, J_1)$ and set $u(:, 1) = z(:, J_1)/v(1, J_1)$. This completes the first iteration. To proceed to the next iteration, we first find the row number I_2 of the largest entry in $u(:, 1)$, calculate $z(I_2, :)$, and let $v(2, :) = z(I_2, :) - u(I_2, 1)v(1, :)$. We then find the column number J_2 of the largest entry in $v(2, :)$, calculate $z(:, J_2)$, and set $u(:, 2) = [z(:, 2) - u(:, 1)v(1, J_1)]/v(2, J_2)$. This completes the second iteration. For the k th iteration, we first find the row number I_k of the largest entry in $u(:, k-1)$, calculate $z(I_k, :)$, and let

$$v(k, :) = z(I_k, :) - \sum_{i=1}^{k-1} u(I_k, i)v(i, :). \quad (11.5.22)$$

We then find the column number J_k of the largest entry in $v(k, :)$, calculate $z(:, J_k)$, and set

$$u(:, k) = \frac{1}{v(k, J_k)} \left[z(:, J_k) - \sum_{j=1}^{k-1} u(:, j)v(j, J_k) \right]. \quad (11.5.23)$$

To terminate iteration, we need to calculate $\|e^{(k)}\|$ and compare it with $\|z\|$. Since in the ACA, $[e]_{M \times M}^{(k)}$ and $[z]_{M \times M}$ are not computed explicitly, we can first approximate $\|e^{(k)}\|$ by its largest contribution that has just been eliminated, which is the contribution from $u(:, k)$ and $v(k, :)$; that is, $\|e^{(k)}\| \approx \|u(:, k)\| \cdot \|v(k, :)\|$. We can also approximate $\|z\|$ by the Frobenius norm of the approximated matrix $[z]_{M \times M}^{(k)} = [u]_{M \times k} [v]_{k \times M}$; that is, $\|z\| \approx \|z^{(k)}\| = \|[[u]_{M \times k} [v]_{k \times M}]\|$. The values of $\|z^{(k)}\|$ can be calculated recursively by

$$\|z^{(k)}\|^2 = \|z^{(k-1)}\|^2 + 2 \sum_{j=1}^{k-1} |u^T(:, j)u(:, k)| \cdot |v(j, :)v^T(k, :)| + \|u(:, k)\|^2 + \|v(k, :)\|^2. \quad (11.5.24)$$

Once the termination criterion $\|e^{(k)}\| < \epsilon \|z^{(k)}\|$ is satisfied, the iteration stops.

From the description of the ACA, it is obvious that this algorithm requires only partial knowledge of the original matrix to find its approximation. The iterative process is adaptive and error-controllable in the sense that it stops when the error bound requirement is achieved. The algorithm will eventually converge to the original matrix itself if there is no rank approximation or compression. The calculation of Equations 11.5.22 and 11.5.23 in the k th iteration requires $O(kM)$ operations. Therefore, the entire process requires $O(R^2M)$ operations to generate an approximate low-rank matrix of rank R with a memory usage of $O(RM)$. However, once the approximation is generated, the matrix–vector multiplication can be evaluated using $O(RM)$ operations.

11.5.3 Application to the Moment-Method Solution

To apply the ACA algorithm to the solution of the moment-method matrix, we first divide the unknowns in the moment-method problem into groups in a multilevel fashion similar to the multilevel subdivision used in the MLFMA. With this, the moment-method matrix is implicitly divided into many subblocks of various sizes. For subblocks that represent distant interactions, we apply the ACA algorithm to compress them and store them with a reduced memory requirement. For subblocks that represent self- and nearby interactions, they are generated explicitly. When we solve the moment-method matrix iteratively, the matrix–vector product can then be computed efficiently by using the compressed representations to calculate the contribution of the distant interactions, whereas the self- and nearby interactions are calculated directly.

The ACA algorithm is ideally suited to static and low-frequency electromagnetic problems, where the integral kernel is asymptotically smooth [57]. The performance of the algorithm has also been studied for its application to electromagnetic scattering problems, where the integral kernel remains oscillatory even for a large distance [58]. One example used for the study is wave scattering by a perfectly conducting sphere of radius of 1 m. For this example, two discretizations are considered. One fixes the frequency at 30 MHz and reduces the discretization size h from $\lambda/130$ to $\lambda/520$. The other fixes the discretization size at $h/\lambda = 1/7$ and increases the frequency from 600 MHz to 2.4 GHz. Figure 11.25 shows the maximum rank of the submatrices with a fixed multilevel subdivision in the moment-method matrix computed using the ACA algorithm with a termination criterion $\epsilon = 10^{-3}$ [58]. The results show that when the frequency is fixed, the electrical size of the object is fixed. Consequently, the maximum rank remains constant, even though the discretization density is increased. On the other hand, when the frequency is increased, the electrical size of the object is increased and the maximum rank increases as well. The increase in the maximum rank is found to be proportional to \sqrt{N} . These two observations can be understood from Equation 11.5.7, which can be obtained by interpolating the integral

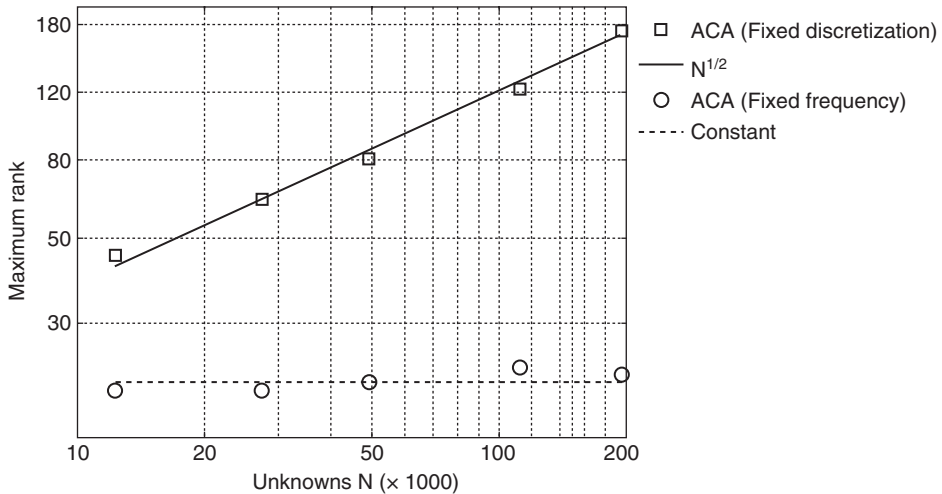


Figure 11.25 Maximum rank of the submatrices in the moment-method matrix for a conducting sphere. (After Zhao et al. [58], Copyright © 2005 IEEE.)

kernel in the direction of $\mathbf{r} - \mathbf{r}'$ when \mathbf{r} and \mathbf{r}' are far apart. Because of the oscillation in $e^{-jk_0|\mathbf{r}-\mathbf{r}'|}$, the number of points to interpolate the kernel over an object of size D is proportional to $k_0 D$. In the case of fixed frequency, $k_0 D$ is a constant; hence, the maximum rank tends to be a constant regardless of the discretization density. In the case of fixed discretization, $N \sim (k_0 D)^2$; it follows that the maximum rank should be proportional to \sqrt{N} . Figure 11.26 shows the memory and computation time used to generate the cross-approximation of the moment-method matrix for both fixed-frequency and fixed-discretization cases [58]. For the case of fixed frequency, the memory requirement and computation time scale as $O(N \log N)$, which indicates that the ACA is highly efficient for static and low-frequency applications. For the case of fixed discretization, the memory requirement and computation time scale as $O(N^{4/3} \log N)$ because many submatrices have a numerical rank much smaller than \sqrt{M} due to the termination at $\epsilon = 10^{-3}$.

Since the ACA algorithm works directly on the moment-method matrix, it can be applied to the moment-method solution of other integral equations easily. To demonstrate this capability, we consider the moment-method solution of the PMCHWT integral equations formulated in Section 10.3.4 for scattering by a dielectric object. Figure 11.27 shows the memory usage, the computation time used to generate the low-rank approximation, and the computation time used to perform a matrix–vector multiplication for a dielectric sphere with radius 0.5λ , 1.0λ , and 2.0λ , respectively, and a relative permittivity of 4. The discretization size is fixed at $h/\lambda = 1/10$; thus, the number of unknowns increases by four times as the radius doubles. In all the cases, the memory requirements and computation times scale as $O(N^{4/3} \log N)$. Figure 11.28 shows the error in the calculation of the bistatic RCS of the sphere with a radius of 1.0λ . Two numerical results are presented: one obtained with the standard moment method without any approximation to its matrix (labeled as N^2) and the other obtained using the ACA. The error is calculated using the Mie series solution as reference data. It can be seen from the figure that the loss of accuracy in the solution of the ACA is around 0.1 dB, which is negligible for most practical applications.

The ACA algorithm has also been used to implement an *LU*-decomposition-based direct solution of the moment-method matrix, which is especially attractive for applications with multiple right-hand sides such as monostatic RCS calculations [59]. The direct

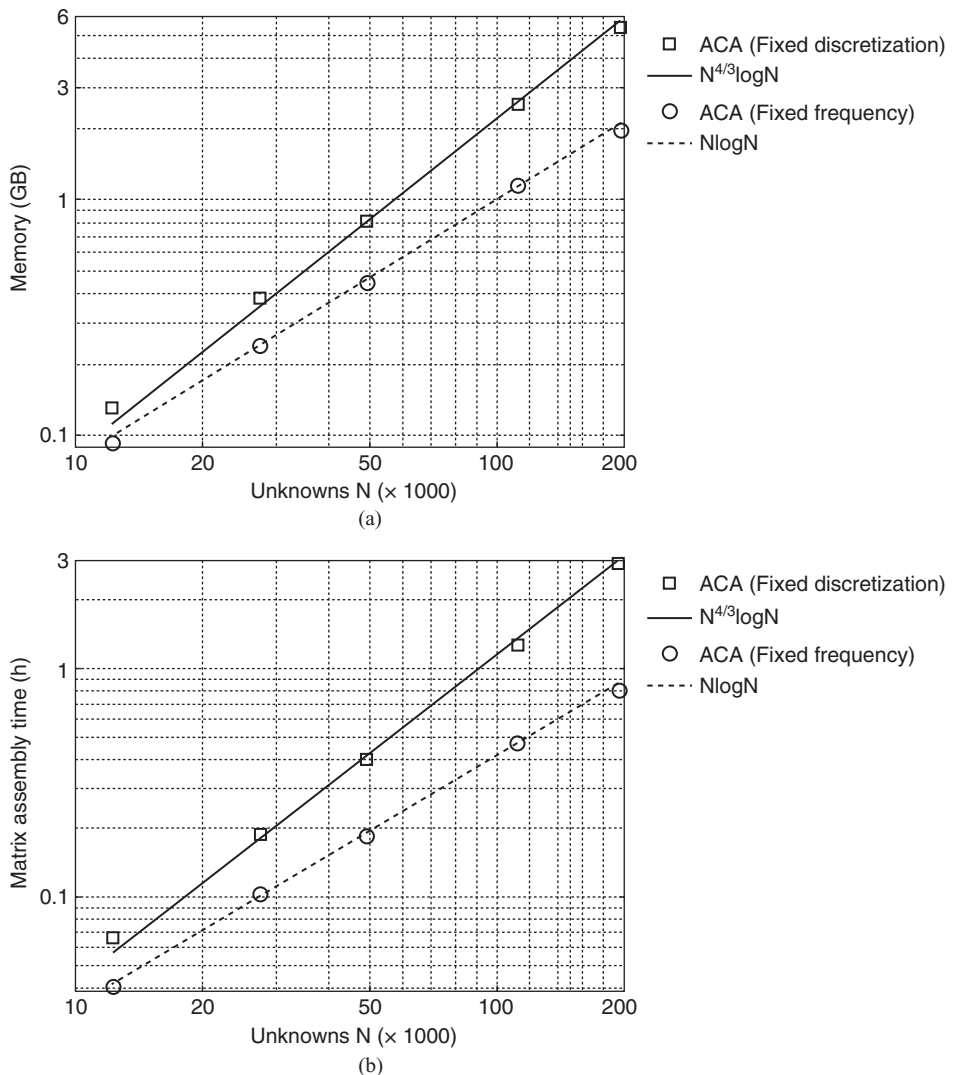


Figure 11.26 Computational complexity of the ACA algorithm applied to the moment-method matrix for a conducting sphere. (a) Memory requirement. (b) Computation time. (After Zhao et al. [58], Copyright © 2005 IEEE.)

solver is based on the fact that when unknowns are spatially grouped, not only are the subblocks of the moment-method matrix of low rank, but the subblocks of the *LU*-decomposed matrix are also of low rank and thus can be compressed. Furthermore, the subblocks of the right-hand-side matrix for monostatic RCS calculations as well as the final solution blocks are of low rank and can be compressed using the ACA algorithm. Therefore, recursive formulas can be designed to compute the *LU* subblocks in a compressed form from the low-rank approximation of the moment-method matrix subblocks [59]. Numerical examples showed that, overall, the moment-method matrix and its *LU* decomposition can be compressed over 90%, the right-hand-side matrix can be compressed over 95%, and the final solution matrix can be compressed over 85%. As a result, scattering problems modeled with over one million unknowns can be solved with a desktop personal computer.

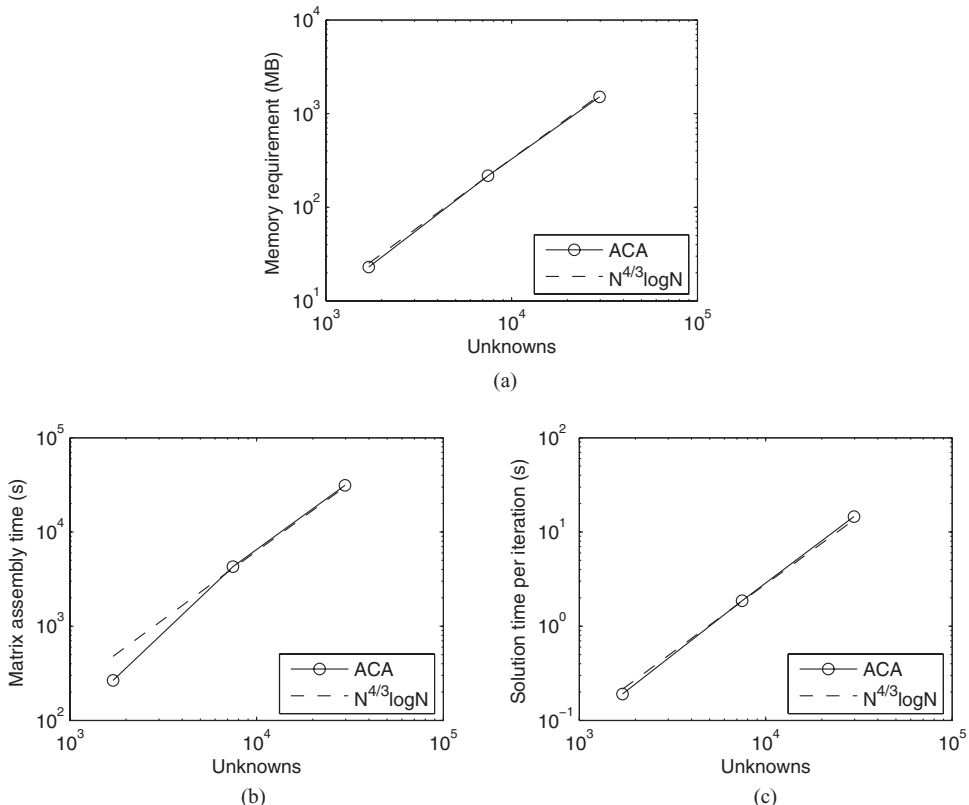


Figure 11.27 Computation time and memory requirements versus the number of unknowns in the ACA algorithm applied to dielectric spheres with radius from 0.5λ to 2.0λ . (a) Memory requirement. (b) Matrix assembly time. (c) Solution time per iteration.

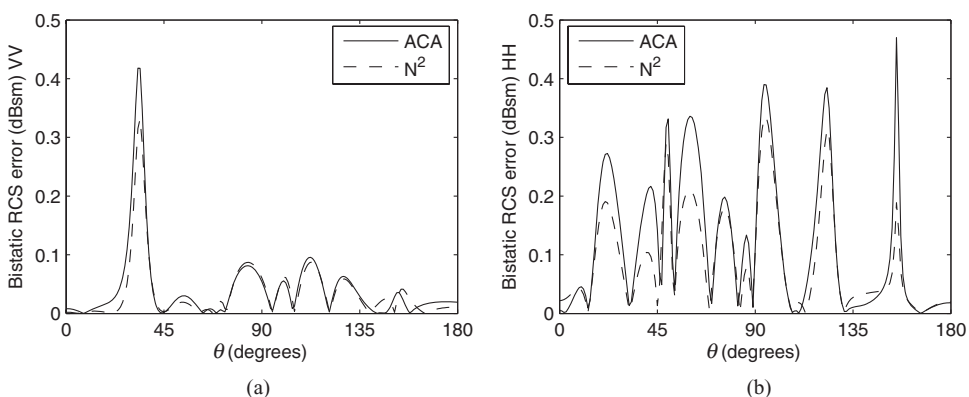


Figure 11.28 Comparison of the errors in the bistatic RCS calculations using the direct moment method and the ACA algorithm for a dielectric sphere with radius 1.0λ . (a) VV polarization. (b) HH polarization.

11.6 INTRODUCTION TO HYBRID TECHNIQUES

The finite difference method, the finite element method, and the method of moments discussed in the preceding chapters represent three major numerical techniques for modeling and analysis of electromagnetic problems. Other numerical methods, such as the transmission-line method, the finite integration technique, the finite volume method, and the boundary element method, can be identified as either variations or equivalents of one or another of these three methods. Among the three methods, the finite difference method is the simplest for calculating electromagnetic fields on a rectangular grid. Its time-domain version, the FDTD method based on Yee's algorithm, is particularly powerful for electrodynamic problems since it discretizes Maxwell's equations in such a manner that the physics of the interplay between the electric and magnetic fields is modeled correctly. The method can easily handle material anisotropy and inhomogeneity. The FDTD method is highly efficient because it does not involve any matrix solutions. As a method that solves partial differential equations directly, the FDTD method requires a grid discretization of a computational domain to compute the fields inside the domain. If the solution domain extends to infinity in an unbounded problem, the solution domain must be truncated and treated carefully so that the truncated computational domain mimics the original open space. This was a major disadvantage that limited the accuracy and use of the method. The later development of perfectly matched layers for grid truncation has successfully removed this bottleneck. The other major challenge for the finite difference method is the incapability of accurate modeling of complex geometrical structures by using a rectangular grid. This challenge can be partially resolved by the use of conformal grids or subgridding techniques (that refine the rectangular grids when found necessary); however, the resulting numerical schemes become either more complicated or less efficient.

The finite element method, on the other hand, has an unmatched capability for modeling both complex structures and materials. By using unstructured meshes with curvilinear triangular and tetrahedral elements, the method can accurately model curved surfaces, fine structures, and complex materials. Although the finite element method requires solving a large matrix equation, the associated matrix is very sparse and often symmetrical, and its solution can be obtained efficiently by using advanced sparse solvers. The finite element analysis can be carried out in either the frequency or the time domain, and its time-domain analysis can be formulated to be unconditionally stable so that the time-step size does not have to be reduced for problems containing very small finite elements. Like the FDTD method, the finite element method solves partial differential equations directly. As such, it also requires the discretization of an entire computational domain and, if this domain is unbounded, the truncation of an open domain into a finite domain. Proper treatment of the mesh truncation has been one of the major research subjects for the finite element analysis of open-region electromagnetic problems. The other major obstacle that has made the finite element method a less popular choice is the necessity for complicated mesh generation, and this obstacle is being alleviated with tremendous ongoing activities in the development of highly robust mesh generators.

In contrast to the finite difference and finite element methods, the method of moments is based on the formulation of integral equations in terms of Green's functions as the fundamental solution to Maxwell's equations. As such, the Sommerfeld radiation condition, which has to be satisfied by radiated and scattered fields, is built into the moment-method formulation automatically through the use of an appropriate Green's function; therefore, it requires no special treatment. The moment method is ideally suited

for modeling metallic objects because, by the use of a surface integral equation, the computational domain is confined to the metallic surfaces. It is also highly efficient for problems consisting of layered substrates or those comprising bulk homogeneous dielectrics, because for these cases, the effect of the dielectrics can either be accounted for by a special Green's function or be modeled by equivalent electric and magnetic surface currents. However, the capability of the moment method is challenged when one attempts to model complex structures with complex materials that may be anisotropic and inhomogeneous. Moreover, because of the use of Green's functions, the moment method generates a fully populated matrix, whose computation and solution are associated with a high degree of computational complexity. Therefore, the traditional moment method becomes very time-consuming and memory-intensive for the analysis of large problems, which are often modeled with millions of unknowns. This challenge has largely been alleviated by the development of a variety of fast solvers, such as those discussed earlier in this chapter.

From the discussions above, it can be seen clearly that the three methods have their unique strengths and weaknesses. No single method is superior to the other two for every application. The FDTD method does not require a solution of a matrix equation and thus is highly efficient. Its implementation of perfectly matched layers for grid truncation has been well developed and is highly robust. The finite element method models complex geometries and materials accurately, it yields highly sparse matrices, and its time-domain version can be made unconditionally stable. The moment method models free space accurately and requires only a surface discretization; thus, it is an attractive choice for modeling large metallic surfaces and homogeneous objects. With these observations, one naturally asks: Is it possible to use the strengths of one method to compensate for the weaknesses of the other method, or is it possible to combine the strengths of these methods and eliminate their weaknesses? The answer is affirmative with the development of hybrid techniques that combine different methods based on either numerical algebra or physical principles. In the remainder of this chapter, we describe two hybrid techniques as the examples to show how such techniques are developed as well as their enhanced capabilities. The first technique combines the *finite element time-domain* (FETD) method with the FDTD method, and the second example combines the finite element method with the moment method.

11.7 HYBRID FINITE DIFFERENCE–FINITE ELEMENT METHOD

The first example for the development of a hybrid technique is the hybridization of the FETD and FDTD methods. For many practical problems, we have to model large computational domains that contain very complex structures and also large homogeneous regions. One example is the modeling of radiation by antennas and another example is the modeling of scattering by complex targets. When an absorbing boundary condition (ABC) or a perfectly matched layer (PML) is adopted to terminate the computational domain, we have to place them some distance away from the object to be modeled. This creates a large free-space region surrounding the object that has to be modeled as well. If we use the FETD to model the fields in the free-space region, we will end up with a much larger finite element matrix that has to be solved in each time step. However, if we can employ the FDTD to model the fields in this region and let the FETD model the fields in the irregular

region close to or inside the object of interest, we can greatly improve the efficiency of the computation, since the FDTD can compute the fields directly without solving any matrix equations. In addition, the implementation of PML in the FDTD algorithm has been very well established and widely used and has been found to be very robust. When the FDTD is used to model the fields in the surrounding free space, the PML truncation can be directly applied to the FDTD. On the other hand, since the FETD can be formulated to be unconditionally stable, we can use very small finite elements to model fine features in the object of interest without negatively affecting the stability of the solution. All these observations indicate that if the FETD can be combined with the FDTD in an accurate and stable fashion, the resulting hybrid technique can be very useful for many practical applications. As a result, much effort has been devoted to the development of such a technique [81–92]. In this section, we describe a stable version that is developed based on the underlying equivalence between the FETD and the FDTD formulations [87–91].

11.7.1 Relation between FETD and FDTD

As mentioned earlier, the hybridization of the FETD and FDTD depends on a specific relation between the two methods. To reveal this relation, we consider the two-dimensional TE case and derive the FETD and FDTD time-marching equations for the electric field. For this, we consider the configuration consisting of two rectangular elements shown in Figure 11.29 and attempt to derive the time-marching equation for \mathcal{E}_4 .

The scalar components of Maxwell's equations for the TE fields in a lossless and source-free region are given by

$$\frac{\partial \mathcal{E}_y}{\partial x} - \frac{\partial \mathcal{E}_x}{\partial y} = -\mu \frac{\partial \mathcal{H}_z}{\partial t} \quad (11.7.1)$$

$$\frac{\partial \mathcal{H}_z}{\partial y} = \epsilon \frac{\partial \mathcal{E}_x}{\partial t} \quad (11.7.2)$$

$$\frac{\partial \mathcal{H}_z}{\partial x} = -\epsilon \frac{\partial \mathcal{E}_y}{\partial t}. \quad (11.7.3)$$

Applying Yee's FDTD scheme to Equations 11.7.3 and 11.7.1, respectively, we obtain

$$\mathcal{E}_4^{n+1} = \mathcal{E}_4^n - \frac{\Delta t}{\epsilon \Delta x} [\mathcal{H}_2^{n+1/2} - \mathcal{H}_1^{n+1/2}] \quad (11.7.4)$$

$$\mathcal{H}_1^{n+1/2} = \mathcal{H}_1^{n-1/2} - \frac{\Delta t}{\mu \Delta x} [\mathcal{E}_4^n - \mathcal{E}_3^n] + \frac{\Delta t}{\mu \Delta y} [\mathcal{E}_1^n - \mathcal{E}_6^n] \quad (11.7.5)$$

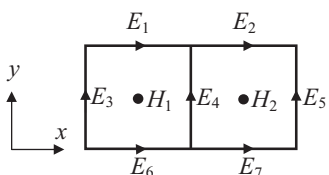


Figure 11.29 Two rectangular elements with electric fields assigned at the edges and the magnetic fields assigned at the centers.

$$\mathcal{H}_2^{n+1/2} = \mathcal{H}_2^{n-1/2} - \frac{\Delta t}{\mu \Delta x} [\mathcal{E}_5^n - \mathcal{E}_4^n] + \frac{\Delta t}{\mu \Delta y} [\mathcal{E}_2^n - \mathcal{E}_7^n]. \quad (11.7.6)$$

Equations 11.7.5 and 11.7.6 can be used to eliminate the magnetic field in Equation 11.7.4, yielding the time-marching equation for \mathcal{E}_4 as

$$\mathcal{E}_4^{n+1} = 2\mathcal{E}_4^n - \mathcal{E}_4^{n-1} - \left(\frac{c \Delta t}{\Delta x} \right)^2 [2\mathcal{E}_4^n - \mathcal{E}_3^n - \mathcal{E}_5^n] - \frac{(c \Delta t)^2}{\Delta x \Delta y} [\mathcal{E}_2^n + \mathcal{E}_6^n - \mathcal{E}_1^n - \mathcal{E}_7^n] \quad (11.7.7)$$

where $c = 1/\sqrt{\mu \epsilon}$ denotes the speed of light in the medium.

Now we consider the FETD formulation. Based on the properties of vector basis functions, we can easily write down the first-order vector basis functions for \mathcal{E}_1 , \mathcal{E}_4 , and \mathcal{E}_7 as

$$\mathbf{N}_1 = \begin{cases} \hat{x} \left(1 - \frac{y_1 - y}{\Delta y} \right) & \text{in element 1} \\ 0 & \text{in element 2} \end{cases} \quad (11.7.8)$$

$$\mathbf{N}_4 = \begin{cases} \hat{y} \left(1 - \frac{x_4 - x}{\Delta x} \right) & \text{in element 1} \\ \hat{y} \left(1 - \frac{x - x_4}{\Delta x} \right) & \text{in element 2} \end{cases} \quad (11.7.9)$$

$$\mathbf{N}_7 = \begin{cases} 0 & \text{in element 1} \\ \hat{x} \left(1 - \frac{y - y_7}{\Delta y} \right) & \text{in element 2} \end{cases} \quad (11.7.10)$$

where element 1 is the one on the left and element 2 is the other one on the right. The basis functions for other edges have similar forms. After the finite element discretization, the equation for \mathcal{E}_4 is

$$\sum_{j=1}^7 T_{ij} \frac{d^2 \mathcal{E}_j}{dt^2} + \sum_{j=1}^7 S_{ij} \mathcal{E}_j = 0 \quad i = 4 \quad (11.7.11)$$

where T_{ij} and S_{ij} are given by Equations 9.4.9 and 9.4.11, respectively. Now, instead of evaluating the integral in Equation 9.4.9 analytically or accurately using a high-order quadrature, if we adopt the trapezoidal integration

$$\int_{x_1}^{x_2} f(x) dx = \frac{x_2 - x_1}{2} [f(x_1) + f(x_2)] \quad (11.7.12)$$

we have $T_{ij} = 0$ ($i \neq j$) and $T_{44} = \epsilon \Delta x \Delta y$. The integral in Equation 9.4.11 can be evaluated easily since its integrand is a constant. With the evaluation of T_{ij} and S_{ij} , Equation 11.7.11 becomes

$$\epsilon \Delta x \Delta y \frac{d^2 \mathcal{E}_4}{dt^2} + \frac{\Delta y}{\mu \Delta x} [2\mathcal{E}_4 - \mathcal{E}_3 - \mathcal{E}_5] + \frac{1}{\mu} [\mathcal{E}_2 + \mathcal{E}_6 - \mathcal{E}_1 - \mathcal{E}_7] = 0. \quad (11.7.13)$$

Applying the central difference, instead of the Newmark-beta method, to discretize the time, we obtain

$$\mathcal{E}_4^{n+1} = 2\mathcal{E}_4^n - \mathcal{E}_4^{n-1} - \left(\frac{c\Delta t}{\Delta x} \right)^2 [2\mathcal{E}_4^n - \mathcal{E}_3^n - \mathcal{E}_5^n] - \frac{(c\Delta t)^2}{\Delta x \Delta y} [\mathcal{E}_2^n + \mathcal{E}_6^n - \mathcal{E}_1^n - \mathcal{E}_7^n] \quad (11.7.14)$$

which is exactly the same as the FDTD time-marching equation in Equation 11.7.7. Therefore, when the FETD method is applied to a rectangular mesh using the first-order vector basis functions and the trapezoidal integration to evaluate the mass matrix, and when the central difference is employed for the temporal discretization, the FETD is equivalent to the FDTD obtained with Yee's discretization scheme [93,94]. In three dimensions, the integrand in S_{ij} is no longer a constant, and the integral should be evaluated using the trapezoidal integration as well to make the FETD equivalent to the FDTD [94]. The equivalence between the FETD and FDTD allows us to formulate a numerical solution using the FETD and then replace a part of the FETD with the FDTD.

11.7.2 Hybridization of FETD and FDTD

With the establishment of the equivalence between the FETD and FDTD, we are now ready to formulate the hybrid FETD–FDTD solution. For this, consider the two-dimensional problem illustrated in Figure 11.30, where the entire solution region is discretized using a combination of an unstructured triangular mesh to conform to the geometry to be modeled and a structured rectangular mesh to discretize the surrounding uniform region. For the sake of brevity, we assume that the entire region is lossless and the source is confined inside the triangular mesh. The spatial discretization via the finite elements yields the second-order ordinary differential equation in Equation 9.4.8, which for this case can be written as

$$[T] \frac{d^2 \{\mathcal{E}\}}{dt^2} + [S] \{\mathcal{E}\} = \{\mathcal{J}\} \quad (11.7.15)$$

where the entries of $[T]$ and $[S]$ are given by Equations 9.4.9 and 9.4.11. To evaluate T_{ij} , we use exact integration for triangular elements and trapezoidal integration for rectangular elements.

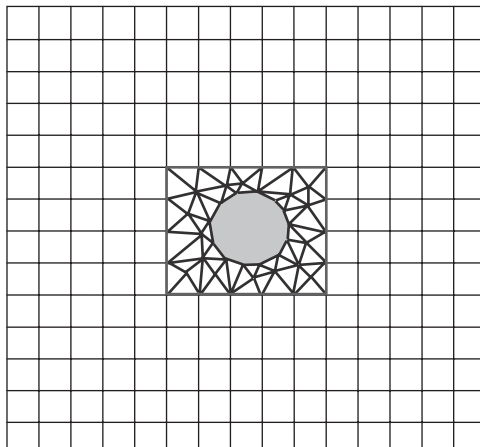


Figure 11.30 Directly interfacing a conformal unstructured mesh with a uniform rectangular mesh.

Now, we split the unknowns in $\{\mathcal{E}\}$ into two groups. The first group, denoted by $\{\mathcal{E}_1\}$, consists of all the unknowns associated with the triangular mesh (represented by thick edges in Figure 11.30), including those at the interface between the triangular and rectangular meshes. The second group, denoted by $\{\mathcal{E}_2\}$, consists of all the unknowns associated with the rectangular mesh (represented by thin edges in Figure 11.30), excluding those at the interface. Equation 11.7.15 can then be partitioned as

$$\begin{bmatrix} T_{11} & T_{12} \\ T_{21} & T_{22} \end{bmatrix} \frac{d^2}{dt^2} \begin{Bmatrix} \mathcal{E}_1 \\ \mathcal{E}_2 \end{Bmatrix} + \begin{bmatrix} S_{11} & S_{12} \\ S_{21} & S_{22} \end{bmatrix} \begin{Bmatrix} \mathcal{E}_1 \\ \mathcal{E}_2 \end{Bmatrix} = \begin{Bmatrix} \mathcal{J}_1 \\ 0 \end{Bmatrix}. \quad (11.7.16)$$

Because of certain orthogonality between the vector basis functions for rectangular elements, and because of the use of trapezoidal integration for the non-orthogonal ones, $[T_{12}] = [T_{21}] = 0$ and $[T_{22}]$ is a diagonal matrix. Hence, Equation 11.7.16 can be split into two equations

$$[T_{11}] \frac{d^2 \{\mathcal{E}_1\}}{dt^2} + [S_{11}] \{\mathcal{E}_1\} = \{\mathcal{J}_1\} - [S_{12}] \{\mathcal{E}_2\} \quad (11.7.17)$$

$$\varepsilon \Delta x \Delta y \frac{d^2 \{\mathcal{E}_2\}}{dt^2} + [S_{22}] \{\mathcal{E}_2\} = -[S_{21}] \{\mathcal{E}_1\}. \quad (11.7.18)$$

For temporal discretization, we apply the Newmark-beta method to Equation 11.7.17 with $\beta = 1/4$ and the central-difference method to Equation 11.7.18. This yields the final time-marching equations as

$$\begin{aligned} \left\{ \frac{1}{(\Delta t)^2} [T_{11}] + \frac{1}{4} [S_{11}] \right\} \{\mathcal{E}_1\}^{n+1} &= \left\{ \frac{2}{(\Delta t)^2} [T_{11}] - \frac{1}{2} [S_{11}] \right\} \{\mathcal{E}_1\}^n \\ &\quad - \left\{ \frac{1}{(\Delta t)^2} [T_{11}] + \frac{1}{4} [S_{11}] \right\} \{\mathcal{E}_1\}^{n-1} + \frac{1}{4} \{\mathcal{J}_1\}^{n+1} + \frac{1}{2} \{\mathcal{J}_1\}^n \\ &\quad + \frac{1}{4} \{\mathcal{J}_1\}^{n-1} - [S_{12}] \left(\frac{1}{4} \{\mathcal{E}_2\}^{n+1} + \frac{1}{2} \{\mathcal{E}_2\}^n + \frac{1}{4} \{\mathcal{E}_2\}^{n-1} \right) \end{aligned} \quad (11.7.19)$$

$$\{\mathcal{E}_2\}^{n+1} = 2 \{\mathcal{E}_2\}^n - \{\mathcal{E}_2\}^{n-1} - \frac{(\Delta t)^2}{\varepsilon \Delta x \Delta y} ([S_{12}] \{\mathcal{E}_1\}^n + [S_{22}] \{\mathcal{E}_2\}^n). \quad (11.7.20)$$

It is seen that although $\{\mathcal{E}_2\}^{n+1}$ appears in Equation 11.7.19, $\{\mathcal{E}_1\}^{n+1}$ does not appear in Equation 11.7.20. Therefore, given $\{\mathcal{E}\}^{n-1}$ and $\{\mathcal{E}\}^n$, we can use Equation 11.7.20 to calculate $\{\mathcal{E}_2\}^{n+1}$ explicitly, and then use the calculated $\{\mathcal{E}_2\}^{n+1}$ in Equation 11.7.19 together with $\{\mathcal{E}\}^{n-1}$ and $\{\mathcal{E}\}^n$ to calculate $\{\mathcal{E}_1\}^{n+1}$ implicitly by solving a matrix equation. Furthermore, since Equation 11.7.20 is equivalent to the original Yee's FDTD equations, which update electric and magnetic fields in a leapfrog fashion, we can use the FDTD equations to replace the calculation of Equation 11.7.20. In that case, $\{\mathcal{H}_2\}^{n+1/2}$ can be calculated from $\{\mathcal{E}\}^{n-1}$ and $\{\mathcal{E}\}^n$, which can then be used to calculate $\{\mathcal{E}_2\}^{n+1}$. Once both $\{\mathcal{E}_1\}^{n+1}$ and $\{\mathcal{E}_2\}^{n+1}$ are calculated, we can calculate $\{\mathcal{H}_2\}^{n+3/2}$ to continue the time-marching process.

Whereas the time-marching based on Equation 11.7.19 is unconditionally stable, the time-marching based on Equation 11.7.20 is conditionally stable. The stability condition

is given by Equation 8.3.5 for two-dimensional calculations and Equation 8.4.23 for three-dimensional calculations. However, because of the unconditional stability of Equation 11.7.19, we can use finite elements as small as necessary in the unstructured mesh to model fine details of the geometry without impacting the overall stability of the solution. This is a highly desirable feature of the hybrid FETD–FDTD method. Moreover, since the standard FDTD can be used to update the fields in the structured region, we can use the well-established, highly robust PML implementation formulated in Section 8.5.3 to model PML for mesh truncation. This is another highly desirable feature of this hybrid method. Obviously, because of the explicit time-marching in the structured region, the overall computation can be very efficient if the structured region is large relative to the unstructured region.

11.7.3 Application Example

The hybrid FETD–FDTD technique can be applied to three-dimensional problems in a straightforward manner [87–92]. The formulation is nearly identical to that described above except that $\Delta x \Delta y$ has to be replaced by $\Delta x \Delta y \Delta z$. The only additional requirement occurs in the transition from the unstructured tetrahedral mesh to the structured rectangular brick mesh. This transition requires the use of pyramidal elements, whose vector basis functions are now available [95–97]. Figure 11.31 shows the transition and interfacing between the FETD and FDTD solutions.

As an application example, we consider the problem of plane wave scattering by a metallic double ogive whose geometry is shown in Figure 11.32a, which is the same as

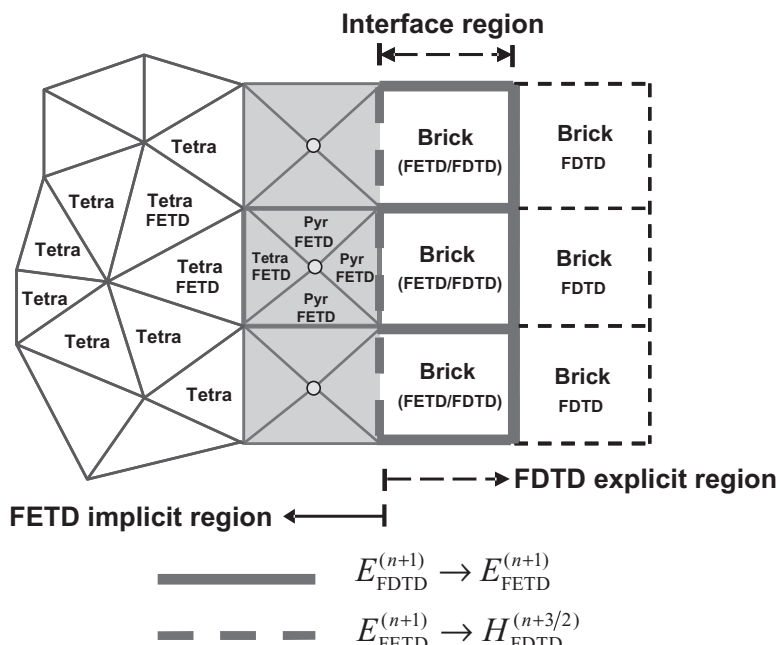


Figure 11.31 Interface between an explicit and structured FDTD grid and an implicit and unstructured FETD grid. Data exchange from the FDTD grid to the FETD grid occurs on the thick solid line, whereas data exchange from the FETD grid to the FDTD grid occurs on the thick dashed lines. (Modified after Jin and Riley [92], Copyright © 2009 Wiley.)

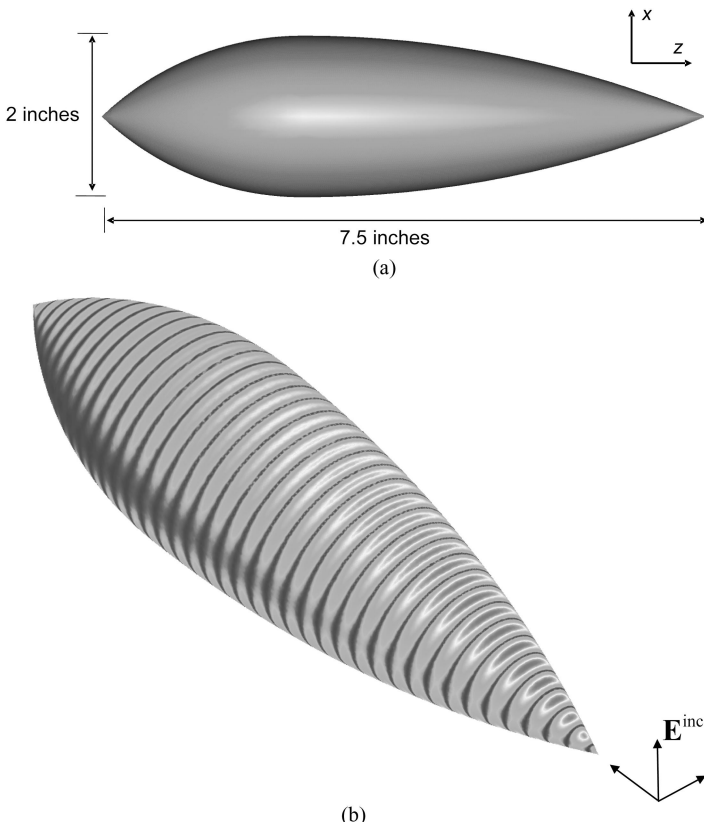


Figure 11.32 Metallic double ogive. (a) Geometry. (b) Surface current density for a sinusoidal plane wave excitation at 30GHz. (After Jin and Riley [92], Copyright © 2009 Wiley.) (See color insert.)

that in Figure 9.24. The double ogive is modeled here by first-order tetrahedral elements within the conformal FETD region, whereas the surrounding space is modeled by the FDTD technique with a PML grid termination. The surface current density due to a plane wave incident on the smaller angled tip is shown in Figure 11.32b, where the plane wave has a sinusoidal profile with a frequency of 30GHz. At 30GHz, the double ogive has an electrical length of 19.05 wavelengths. Measurements [98] and predictions for the monostatic RCS of the double ogive in the xz -plane at 9GHz are shown in Figure 11.33, which shows a very good agreement. Such kind of accuracy would be difficult to achieve without the accurate geometrical modeling, especially around the tips, afforded by finite elements.

11.8 HYBRID FINITE ELEMENT-BOUNDARY INTEGRAL METHOD

As illustrated in Chapter 9, the finite element method has a great capability for modeling complex geometries and materials. However, it has to employ an ABC or a PML to truncate the computational domain when we deal with unbounded electromagnetic problems

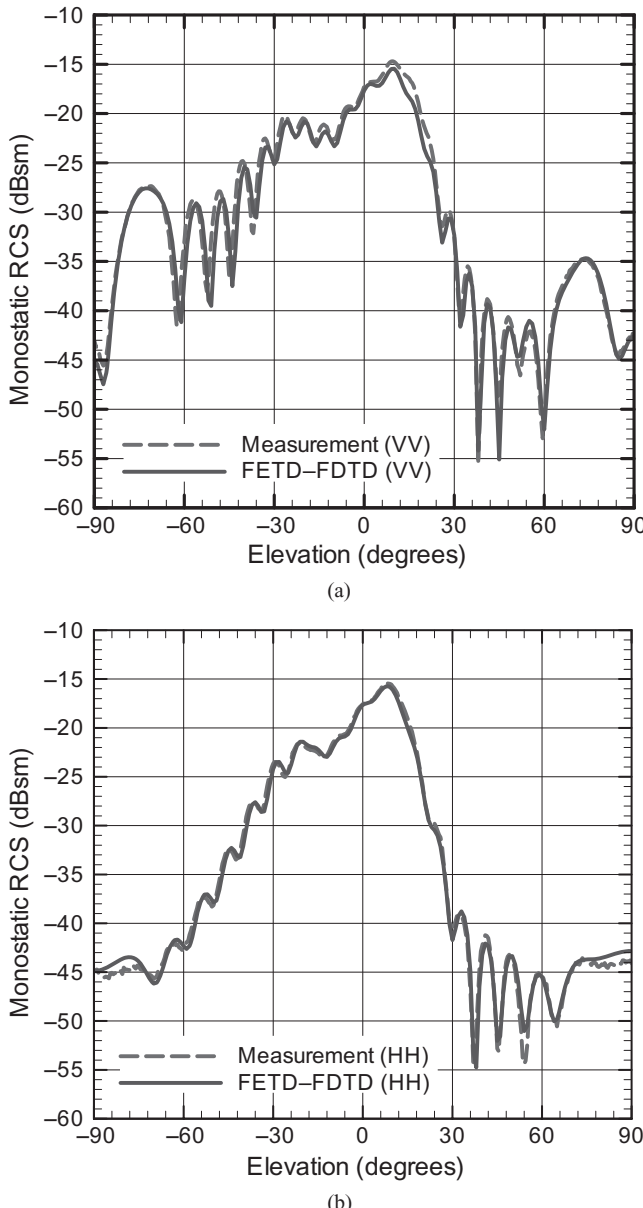


Figure 11.33 Monostatic RCS of the metallic double ogive at 9 GHz. (a) VV polarization. (b) HH polarization. (After Jin and Riley [92], Copyright © 2009 Wiley.)

such as in the case of a scattering or a radiation analysis. Because of the lack of perfect absorption, the ABC or the PML has to be placed a certain distance away from the object to be analyzed to reduce the artificial reflection error. On the other hand, the moment method described in Chapter 10 is very well suited for analyzing open-region radiation and scattering problems because it models wave propagation into free space accurately via the use of an appropriate Green's function. However, the moment method becomes less efficient when handling complex geometries and materials. The individual strengths

of the finite element and moment methods can be combined to compensate for their weaknesses, which would then permit an accurate analysis of highly complicated electromagnetic problems. This combination can be realized through the development of a hybrid technique, known as the *finite element–boundary integral* (FE–BI) method [99–106].

The basic principle of the FE–BI method is to employ an arbitrary surface to truncate the finite element mesh. This surface can be placed very closely to the object to be analyzed to minimize the computational domain. Interior to the artificial surface, the finite element discretization is applied to formulate the fields. Exterior to the surface, the fields are represented by boundary integral equations. The fields in the two regions are then coupled at the surface via field continuity conditions, which results in a coupled system for the interior and boundary fields. In the following, we describe two formulations of the FE–BI method.

11.8.1 Traditional Formulation

Consider the problem of electromagnetic radiation and scattering by an inhomogeneous object immersed in free space, as illustrated in Figure 11.34. As a radiator (antenna), the object may contain an internal source \mathbf{J}_{imp} , and as a scatterer, the object may be illuminated by an external incident wave (\mathbf{E}^{inc} , \mathbf{H}^{inc}). To use the FE–BI method to deal with this problem, we first introduce a surface S_o to truncate the computational domain. This truncation surface can be placed very close to or directly on the surface of the object. With the introduction of this surface, the entire problem is decomposed into an interior and an exterior problem, where the fields can be formulated using the finite element and boundary integral methods, respectively.

We start with the formulation of the internal field. In the interior region enclosed by S_o , the field satisfies the vector wave equation

$$\nabla \times \left(\frac{1}{\mu_r} \nabla \times \mathbf{E} \right) - k_0^2 \epsilon_r \mathbf{E} = -jk_0 Z_0 \mathbf{J}_{\text{imp}} \quad \mathbf{r} \in V_o \quad (11.8.1)$$

and the boundary conditions specific for the object. On the truncation surface, the boundary condition is unknown. However, since the field satisfies Maxwell's equations there, we can postulate a Neumann boundary condition with an unknown right-hand side:

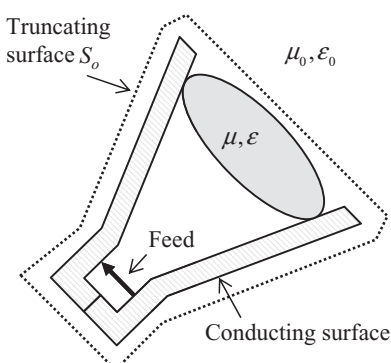


Figure 11.34 Computational domain truncated by a surface that tightly encloses the object to be analyzed. (After Jin and Riley [92], Copyright © 2009 Wiley.)

$$\hat{n} \times \left(\frac{1}{\mu_r} \nabla \times \mathbf{E} \right) = -jk_0 \hat{n} \times \bar{\mathbf{H}} \quad \mathbf{r} \in S_o \quad (11.8.2)$$

where $\bar{\mathbf{H}} = Z_0 \mathbf{H}$ and \hat{n} denotes an outward-pointing unit vector normal to S_o . Based on the finite element analysis described in Section 9.3, we can formulate the weak-form solution of the boundary-value problem defined by Equations 11.8.1 and 11.8.2 as

$$\begin{aligned} & \iiint_{V_o} \left[\frac{1}{\mu_r} (\nabla \times \mathbf{W}_i) \cdot (\nabla \times \mathbf{E}) - k_0^2 \epsilon_r \mathbf{W}_i \cdot \mathbf{E} \right] dV + jk_0 \oint_{S_o} \hat{n} \cdot (\mathbf{W}_i \times \bar{\mathbf{H}}) dS \\ &= -jk_0 Z_0 \iiint_{V_o} \mathbf{W}_i \cdot \mathbf{J}_{\text{imp}} dV. \end{aligned} \quad (11.8.3)$$

Next, we expand the electric field \mathbf{E} according to Equation 9.3.15 and use a similar expansion for the surface magnetic field,

$$\mathbf{E} = \sum_{j=1}^{N_I} \mathbf{N}_j^I E_j^I + \sum_{j=1}^{N_S} \mathbf{N}_j^S E_j^S \quad (11.8.4)$$

$$\bar{\mathbf{H}} = \sum_{j=1}^{N_S} \mathbf{N}_j^S \bar{H}_j^S \quad (11.8.5)$$

where N_I denotes the total number of edges inside S_o , N_S denotes the total number of edges on S_o , E_j^I and E_j^S denote the tangential components of \mathbf{E} at the j th edge inside S_o and on S_o , respectively, and \mathbf{N}_j^I and \mathbf{N}_j^S are the corresponding vector basis functions. Furthermore, \bar{H}_j^S denotes the tangential component of $\bar{\mathbf{H}}$ at the j th edge on S_o . Note that \mathbf{N}_j^I and \mathbf{N}_j^S are the same edge-based vector basis functions discussed in Section 9.3.2 and the superscripts are used simply to indicate whether their associated edges are inside or on S_o . By substituting Equations 11.8.4 and 11.8.5 into Equation 11.8.3 and using \mathbf{N}_i^I and \mathbf{N}_i^S as the weighting function \mathbf{W}_i , we can convert Equation 11.8.3 into the matrix equation

$$\begin{bmatrix} K^{II} & K^{IS} & 0 \\ K^{SI} & K^{SS} & B \end{bmatrix} \begin{Bmatrix} E^I \\ E^S \\ \bar{H}^S \end{Bmatrix} = \begin{Bmatrix} b^I \\ b^S \\ \bar{b}^S \end{Bmatrix}. \quad (11.8.6)$$

In Equation 11.8.6, $\{E^I\}$ represents the discrete electric field inside S_o , $\{E^S\}$ the discrete tangential electric field on S_o , and $\{\bar{H}^S\}$ the discrete tangential magnetic field on S_o . The matrix and right-hand-side vector elements are given by

$$K_{ij}^{II} = \iiint_{V_o} \left[\frac{1}{\mu_r} (\nabla \times \mathbf{N}_i^I) \cdot (\nabla \times \mathbf{N}_j^I) - k_0^2 \epsilon_r \mathbf{N}_i^I \cdot \mathbf{N}_j^I \right] dV \quad (11.8.7)$$

$$K_{ij}^{IS} = \iiint_{V_o} \left[\frac{1}{\mu_r} (\nabla \times \mathbf{N}_i^I) \cdot (\nabla \times \mathbf{N}_j^S) - k_0^2 \epsilon_r \mathbf{N}_i^I \cdot \mathbf{N}_j^S \right] dV \quad (11.8.8)$$

$$K_{ij}^{SI} = \iiint_{V_o} \left[\frac{1}{\mu_r} (\nabla \times \mathbf{N}_i^S) \cdot (\nabla \times \mathbf{N}_j^I) - k_0^2 \epsilon_r \mathbf{N}_i^S \cdot \mathbf{N}_j^I \right] dV \quad (11.8.9)$$

$$K_{ij}^{SS} = \iiint_{V_o} \left[\frac{1}{\mu_r} (\nabla \times \mathbf{N}_i^S) \cdot (\nabla \times \mathbf{N}_j^S) - k_0^2 \epsilon_r \mathbf{N}_i^S \cdot \mathbf{N}_j^S \right] dV \quad (11.8.10)$$

$$B_{ij} = jk_0 \oint_{S_o} \hat{n} \cdot (\mathbf{N}_i^S \times \mathbf{N}_j^S) dS \quad (11.8.11)$$

$$b_i^I = -jk_0 Z_0 \iiint_{V_o} \mathbf{N}_i^I \cdot \mathbf{J}_{\text{imp}} dV \quad (11.8.12)$$

$$b_i^S = -jk_0 Z_0 \iiint_{V_o} \mathbf{N}_i^S \cdot \mathbf{J}_{\text{imp}} dV. \quad (11.8.13)$$

Equation 11.8.6 is formulated based on Maxwell's equations for the interior fields. It is apparent that this equation is not sufficient for the solution of $\{E^I\}$, $\{E^S\}$, and $\{\bar{H}^S\}$, since Maxwell's equations for the exterior fields have not been considered yet. In other words, the equation has to be complemented with an additional relationship between $\{E^S\}$, and $\{\bar{H}^S\}$ from the formulation of the exterior field. Based on discussions in Section 10.3, the exterior fields satisfy the CFIE given in Equation 10.3.68, which is repeated here as

$$\begin{aligned} & \frac{1}{2} \bar{\mathbf{J}}_s(\mathbf{r}) + \hat{n} \times \mathcal{L}(\mathbf{M}_s) + \hat{n} \times \tilde{\mathcal{K}}(\bar{\mathbf{J}}_s) + \hat{n} \times \left[\frac{1}{2} \mathbf{M}_s(\mathbf{r}) - \hat{n} \times \mathcal{L}(\bar{\mathbf{J}}_s) + \hat{n} \times \tilde{\mathcal{K}}(\mathbf{M}_s) \right] \\ &= \hat{n} \times \bar{\mathbf{H}}^{\text{inc}}(\mathbf{r}) - \hat{n} \times \left[\hat{n} \times \mathbf{E}^{\text{inc}}(\mathbf{r}) \right] \quad \mathbf{r} \in S_o \end{aligned} \quad (11.8.14)$$

where $\bar{\mathbf{J}}_s = \hat{n} \times \bar{\mathbf{H}}$ and $\mathbf{M}_s = \mathbf{E} \times \hat{n}$. By adopting the same finite element expansions that were used for \mathbf{E} and $\bar{\mathbf{H}}$, we can write the expansions for $\bar{\mathbf{J}}_s$ and \mathbf{M}_s as

$$\bar{\mathbf{J}}_s(\mathbf{r}') = \hat{n}' \times \bar{\mathbf{H}}(\mathbf{r}') = \sum_{j=1}^{N_s} \boldsymbol{\Lambda}_j(\mathbf{r}') \bar{H}_j^S \quad (11.8.15)$$

$$\mathbf{M}_s(\mathbf{r}') = \mathbf{E}(\mathbf{r}') \times \hat{n}' = - \sum_{j=1}^{N_s} \boldsymbol{\Lambda}_j(\mathbf{r}') E_j^S \quad (11.8.16)$$

where $\boldsymbol{\Lambda}_j(\mathbf{r}') = \hat{n}' \times \mathbf{N}_j^S(\mathbf{r}')$ with \mathbf{N}_j^S denoting the vector basis functions used to expand \mathbf{E} and $\bar{\mathbf{H}}$ on the surface S_o . Substituting Equations 11.8.15 and 11.8.16 into Equation 11.8.14 and using $\mathbf{t}_i = \boldsymbol{\Lambda}_i + \hat{n} \times \boldsymbol{\Lambda}_i$ as the testing function for the reason discussed in Section 10.3.4, we can convert Equation 11.8.14 into the matrix equation

$$[P]\{E^S\} + [Q]\{\bar{H}^S\} = \{b^{\text{inc}}\} \quad (11.8.17)$$

where $[P]$ and $[Q]$ represent two full matrices with elements given by

$$P_{ij} = \iint_{S_o} [\hat{n} \times \mathbf{t}_i(\mathbf{r})] \cdot \left[\frac{1}{2} \boldsymbol{\Lambda}_j + \mathcal{L}(\boldsymbol{\Lambda}_j) + \hat{n} \times \tilde{\mathcal{K}}(\boldsymbol{\Lambda}_j) \right] dS \quad (11.8.18)$$

$$Q_{ij} = \iint_{S_o} \mathbf{t}_i(\mathbf{r}) \cdot \left[\frac{1}{2} \boldsymbol{\Lambda}_j + \mathcal{L}(\boldsymbol{\Lambda}_j) + \hat{n} \times \tilde{\mathcal{K}}(\boldsymbol{\Lambda}_j) \right] dS \quad (11.8.19)$$

and the elements of $\{b^{\text{inc}}\}$ are given by

$$b_i^{\text{inc}} = \oint_{S_o} [\hat{n} \times \mathbf{t}_i(\mathbf{r})] \cdot [\hat{n} \times \mathbf{E}^{\text{inc}}(\mathbf{r}) - \bar{\mathbf{H}}^{\text{inc}}(\mathbf{r})] dS. \quad (11.8.20)$$

In arriving at Equations 11.8.18 and 11.8.19, we have applied vector identities and used the fact that $\mathbf{t}_i(\mathbf{r})$ is tangential to S_o . We can now combine Equation 11.8.17 with Equation 11.8.6 to form a complete, coupled system

$$\begin{bmatrix} K^{II} & K^{IS} & 0 \\ K^{SI} & K^{SS} & B \\ 0 & P & Q \end{bmatrix} \begin{Bmatrix} E^I \\ E^S \\ \bar{H}^S \end{Bmatrix} = \begin{Bmatrix} b^I \\ b^S \\ b^{\text{inc}} \end{Bmatrix} \quad (11.8.21)$$

for the solution of $\{E^I\}$, $\{E^S\}$, and $\{\bar{H}^S\}$. The coefficient matrix in Equation 11.8.21 is a partly sparse and partly full matrix. It can be solved using a direct solver, which can exploit the sparsity of the matrix to improve the solution efficiency. For large problems involving many thousands of unknowns, an iterative solution is more efficient in both computation time and memory requirements. The iterative solution can be greatly accelerated by using a robust preconditioning technique [104].

11.8.2 Symmetric Formulation

The formulation described above yields an overall asymmetric matrix, even though the finite element part of the matrix is symmetric. In the following, we describe an alternative approach that makes use of the EFIE and MFIE separately on the truncation surface to yield a completely symmetric FE-BI matrix [106]. First, we substitute the MFIE in Equation 10.3.30 into Equation 11.8.3 to obtain

$$\begin{aligned} & \iiint_{V_o} \left[\frac{1}{\mu_r} (\nabla \times \mathbf{W}_i) \cdot (\nabla \times \mathbf{E}) - k_0^2 \epsilon_r \mathbf{W}_i \cdot \mathbf{E} \right] dV - jk_0 \oint_{S_o} (\hat{n} \times \mathbf{W}_i) \cdot [\mathcal{L}(\mathbf{M}_s) + \mathcal{K}(\bar{\mathbf{J}}_s)] dS \\ &= -jk_0 Z_0 \iiint_{V_o} \mathbf{W}_i \cdot \mathbf{J}_{\text{imp}} dV + jk_0 \oint_{S_o} \mathbf{W}_i \cdot (\hat{n} \times \bar{\mathbf{H}}^{\text{inc}}) dS. \end{aligned} \quad (11.8.23)$$

Next, we test the EFIE in Equation 10.3.29 with $\hat{n} \times \mathbf{W}_i$ and scale it with jk_0 to find another equation

$$-jk_0 \oint_{S_o} (\hat{n} \times \mathbf{W}_i) \cdot [\hat{n} \times \mathbf{M}_s + \mathcal{L}(\bar{\mathbf{J}}_s) - \mathcal{K}(\mathbf{M}_s)] dS = jk_0 \oint_{S_o} \mathbf{W}_i \cdot (\hat{n} \times \mathbf{E}^{\text{inc}}) dS \quad (11.8.24)$$

which complements Equation 11.8.23 and yields a complete system for the solution of \mathbf{E} , $\bar{\mathbf{J}}_s$, and \mathbf{M}_s . The finite element discretization of these two equations yields

$$\begin{bmatrix} K^{II} & K^{IS} & 0 \\ K^{SI} & K^{SS} + U^M & V^M \\ 0 & V^E & U^E \end{bmatrix} \begin{Bmatrix} E^I \\ E^S \\ \bar{H}^S \end{Bmatrix} = \begin{Bmatrix} b^I \\ b^S + b^M \\ b^E \end{Bmatrix} \quad (11.8.25)$$

where $[K^{II}]$, $[K^{IS}]$, $[K^{SI}]$, $[K^{SS}]$, $\{b^I\}$, and $\{b^S\}$ are the same as those given in Equations 11.8.7–11.8.13, and the elements of the other matrices and vectors are given by

$$U_{ij}^M = jk_0 \oint_{S_o} \boldsymbol{\Lambda}_i \cdot \mathcal{L}(\boldsymbol{\Lambda}_j) dS \quad (11.8.26)$$

$$U_{ij}^E = -jk_0 \oint_{S_o} \boldsymbol{\Lambda}_i \cdot \mathcal{L}(\boldsymbol{\Lambda}_j) dS \quad (11.8.27)$$

$$\begin{aligned} V_{ij}^M &= -jk_0 \oint_{S_o} \boldsymbol{\Lambda}_i \cdot \mathcal{K}(\boldsymbol{\Lambda}_j) dS \\ &= \frac{jk_0}{2} \oint_{S_o} (\hat{n} \times \boldsymbol{\Lambda}_i) \cdot \boldsymbol{\Lambda}_j dS - jk_0 \oint_{S_o} \boldsymbol{\Lambda}_i \cdot \tilde{\mathcal{K}}(\boldsymbol{\Lambda}_j) dS \end{aligned} \quad (11.8.28)$$

$$\begin{aligned} V_{ij}^E &= jk_0 \oint_{S_o} \boldsymbol{\Lambda}_i \cdot (\hat{n} \times \boldsymbol{\Lambda}_j) dS - jk_0 \oint_{S_o} \boldsymbol{\Lambda}_i \cdot \mathcal{K}(\boldsymbol{\Lambda}_j) dS \\ &= \frac{jk_0}{2} \oint_{S_o} \boldsymbol{\Lambda}_i \cdot (\hat{n} \times \boldsymbol{\Lambda}_j) dS - jk_0 \oint_{S_o} \boldsymbol{\Lambda}_i \cdot \tilde{\mathcal{K}}(\boldsymbol{\Lambda}_j) dS \end{aligned} \quad (11.8.29)$$

$$b_i^M = jk_0 \oint_{S_o} \boldsymbol{\Lambda}_i \cdot (\hat{n} \times \bar{\mathbf{H}}^{\text{inc}}) dS \quad (11.8.30)$$

$$b_i^E = jk_0 \oint_{S_o} \boldsymbol{\Lambda}_i \cdot (\hat{n} \times \mathbf{E}^{\text{inc}}) dS. \quad (11.8.31)$$

By using the definitions of the operators \mathcal{L} and \mathcal{K} in Equations 10.3.20 and 10.3.21, it can be shown that both $[U^M]$ and $[U^E]$ are symmetric and $[V^M]$ and $[V^E]$ are transpose to each other. Hence, the coefficient matrix in Equation 11.8.25 is completely symmetric and can be solved using symmetric matrix solvers.

Following the same approach or invoking the duality principle, we can derive symmetric formulations for solving the interior magnetic field and the surface electric and magnetic fields. In this case, the vector wave equation is

$$\nabla \times \left(\frac{1}{\epsilon_r} \nabla \times \bar{\mathbf{H}} \right) - k_0^2 \mu_r \bar{\mathbf{H}} = Z_0 \nabla \times \left(\frac{\mathbf{J}_{\text{imp}}}{\epsilon_r} \right) \quad \mathbf{r} \in V_o \quad (11.8.32)$$

and the corresponding weak-form representation is

$$\begin{aligned} \iiint_{V_o} \left[\frac{1}{\epsilon_r} (\nabla \times \mathbf{W}_i) \cdot (\nabla \times \mathbf{H}) - k_0^2 \mu_r \mathbf{W}_i \cdot \mathbf{H} \right] dV - jk_0 \oint_{S_o} \hat{n} \cdot (\mathbf{W}_i \times \mathbf{E}) dS \\ = Z_0 \iiint_{V_o} \mathbf{W}_i \cdot \left(\nabla \times \frac{\mathbf{J}_{\text{imp}}}{\epsilon_r} \right) dV. \end{aligned} \quad (11.8.33)$$

Substituting the EFIE in Equation 10.3.29 into this equation yields

$$\begin{aligned} \iiint_{V_o} \left[\frac{1}{\epsilon_r} (\nabla \times \mathbf{W}_i) \cdot (\nabla \times \bar{\mathbf{H}}) - k_0^2 \mu_r \mathbf{W}_i \cdot \bar{\mathbf{H}} \right] dV + jk_0 \oint_{S_o} (\hat{n} \times \mathbf{W}_i) \cdot [\mathcal{L}(\bar{\mathbf{J}}_s) - \mathcal{K}(\mathbf{M}_s)] dS \\ = Z_0 \iiint_{V_o} \mathbf{W}_i \cdot \left(\nabla \times \frac{\mathbf{J}_{\text{imp}}}{\epsilon_r} \right) dV - jk_0 \oint_{S_o} \mathbf{W}_i \cdot (\hat{n} \times \mathbf{E}^{\text{inc}}) dS. \end{aligned} \quad (11.8.34)$$

This equation can be solved together with the MFIE in Equation 10.3.30, whose weighted form can be written as

$$jk_0 \iint_{S_o} (\hat{n} \times \mathbf{W}_i) \cdot [\hat{n} \times \bar{\mathbf{J}}_s - \mathcal{L}(\mathbf{M}_s) - \mathcal{K}(\bar{\mathbf{J}}_s)] dS = jk_0 \iint_{S_o} \mathbf{W}_i \cdot (\hat{n} \times \bar{\mathbf{H}}^{\text{inc}}) dS. \quad (11.8.35)$$

The finite element discretization of Equations 11.8.34 and 11.8.35 yields the matrix equation

$$\begin{bmatrix} \bar{K}^{II} & \bar{K}^{IS} & 0 \\ \bar{K}^{SI} & \bar{K}^{SS} + U^M & -V^M \\ 0 & -V^E & U^E \end{bmatrix} \begin{Bmatrix} \bar{H}^I \\ \bar{H}^S \\ E^S \end{Bmatrix} = \begin{Bmatrix} \bar{b}^I \\ \bar{b}^S - b^E \\ -b^M \end{Bmatrix} \quad (11.8.36)$$

where

$$\bar{K}_{ij}^{II} = \iiint_{V_o} \left[\frac{1}{\epsilon_r} (\nabla \times \mathbf{N}_i^I) \cdot (\nabla \times \mathbf{N}_j^I) - k_0^2 \mu_r \mathbf{N}_i^I \cdot \mathbf{N}_j^I \right] dV \quad (11.8.37)$$

$$\bar{K}_{ij}^{IS} = \iiint_{V_o} \left[\frac{1}{\epsilon_r} (\nabla \times \mathbf{N}_i^I) \cdot (\nabla \times \mathbf{N}_j^S) - k_0^2 \mu_r \mathbf{N}_i^I \cdot \mathbf{N}_j^S \right] dV \quad (11.8.38)$$

$$\bar{K}_{ij}^{SI} = \iiint_{V_o} \left[\frac{1}{\epsilon_r} (\nabla \times \mathbf{N}_i^S) \cdot (\nabla \times \mathbf{N}_j^I) - k_0^2 \mu_r \mathbf{N}_i^S \cdot \mathbf{N}_j^I \right] dV \quad (11.8.39)$$

$$\bar{K}_{ij}^{SS} = \iiint_{V_o} \left[\frac{1}{\epsilon_r} (\nabla \times \mathbf{N}_i^S) \cdot (\nabla \times \mathbf{N}_j^S) - k_0^2 \mu_r \mathbf{N}_i^S \cdot \mathbf{N}_j^S \right] dV \quad (11.8.40)$$

$$\bar{b}_i^I = Z_0 \iiint_{V_o} \mathbf{N}_i^I \cdot \left(\nabla \times \frac{\mathbf{J}_{\text{imp}}}{\epsilon_r} \right) dV \quad (11.8.41)$$

$$\bar{b}_i^S = Z_0 \iiint_{V_o} \mathbf{N}_i^S \cdot \left(\nabla \times \frac{\mathbf{J}_{\text{imp}}}{\epsilon_r} \right) dV \quad (11.8.42)$$

and the elements of $[U^E]$, $[U^M]$, $[V^E]$, $[V^M]$, $\{b^E\}$, and $\{b^M\}$ are the same as those defined in Equations 11.8.26–11.8.31. It is evident that the coefficient matrix in Equation 11.8.36 is also symmetric.

In the two formulations described above, we either solve Equation 11.8.25 for $\{E'\}$, $\{E^S\}$, and $\{\bar{H}^S\}$ or solve Equation 11.8.36 for $\{\bar{H}'\}$, $\{\bar{H}^S\}$, and $\{E^S\}$. However, we can combine these two equations and solve for both $\{E'\}$, $\{E^S\}$ and $\{\bar{H}'\}$, $\{\bar{H}^S\}$. By subtracting the third set of equations in Equation 11.8.25 from the second set of equations in Equation 11.8.36 and similarly subtracting the third set of equations in Equation 11.8.36 from the second set of equations in Equation 11.8.25 and recombining the resultant equations, we obtain

$$\begin{bmatrix} K^{II} & K^{IS} & 0 & 0 \\ K^{SI} & K^{SS} + U & 0 & V \\ 0 & 0 & -\bar{K}^{II} & -\bar{K}^{IS} \\ 0 & V & -\bar{K}^{SI} & -\bar{K}^{SS} - U \end{bmatrix} \begin{Bmatrix} E' \\ E^S \\ \bar{H}' \\ \bar{H}^S \end{Bmatrix} = \begin{Bmatrix} b^I \\ b^S + 2b^M \\ -\bar{b}^I \\ -\bar{b}^S + 2b^E \end{Bmatrix} \quad (11.8.43)$$

where $[U] = [U^M] - [U^E]$ and $[V] = [V^M] + [V^E]$. From Equations 11.8.26–11.8.29, we have

$$U_{ij} = 2jk_0 \iint_{S_o} \boldsymbol{\Lambda}_i \cdot \mathcal{L}(\boldsymbol{\Lambda}_j) dS \quad (11.8.44)$$

$$V_{ij} = -2jk_0 \iint_{S_o} \boldsymbol{\Lambda}_i \cdot \tilde{\mathcal{K}}(\boldsymbol{\Lambda}_j) dS. \quad (11.8.45)$$

Equation 11.8.43 is still symmetric, since both $[U]$ and $[V]$ are symmetric. Although the number of unknowns involved in Equation 11.8.43 is much higher than those in Equations 11.8.25 and 11.8.36, the increase in memory requirements and computation time for an iterative solution is insignificant [106].

11.8.3 Numerical Examples

The hybridization of the finite element method with the boundary integral method can be achieved in the time domain as well. The corresponding formulation can be obtained by applying the Laplace transform to the frequency-domain formulation [107,108]. In contrast to the ABC and PML, the boundary conditions derived from the boundary integral equations are exact. This allows the truncation surface to be placed conformal to the object to be analyzed. However, this accuracy is achieved at the cost of an increased computational burden, because the boundary integrals produce full matrices for the boundary unknowns, which are computationally much more expensive than the sparse matrices produced by the ABC and PML. To this end, fast algorithms such as the AIM and FMM can be employed to speed up the computation.

We present three examples to demonstrate the capabilities of the hybrid FE–BI method. The first example is the scattering by the object sketched in Figure 11.35a, which consists of a circular conducting cylinder having a radius of 0.5 m and a height of 0.5 m sitting on a circular dielectric cylinder of the same size with $\epsilon_r = 3.0 - j4.0$. Both cylinders are then coated with a 0.1-m-thick dielectric layer with $\epsilon_r = 4.5 - j9.0$. Figure 11.35b displays the $\theta\theta$ -polarized monostatic RCS at 0.3 GHz [40,106]. The FE–BI solution is compared with the moment-method solution, which shows an excellent agreement over the entire range.

The second example consists of a thin trapezoidal conducting plate (Fig. 11.36) with its sides coated by a lossy dielectric material with $\epsilon_r = 4.5 - j9.0$. The dimensions of the conducting plate and the thickness of the coating are displayed in Figure 11.36. The monostatic RCS patterns for the VV and HH polarizations at 1.0 GHz are computed in the xy -plane and are shown in Figure 11.37. Good agreement is observed between the FE–BI and moment-method solutions [40,104]. Because of the relatively large electrical size of the object, both the FE–BI and moment-method computations are accelerated using the MLFMA. With the aid of this fast algorithm, computations were also carried out at 2.0 and 3.0 GHz [104], which represent much larger problems.

The last example is scattering by a $5\text{ m} \times 5\text{ m} \times 10\text{ m}$ conducting cavity, as shown in Figure 11.38, whose interior surface is coated with a dielectric material having $\epsilon_r = 6.0 - j8.0$ and a thickness of 0.1 m. The cavity's conducting walls have a thickness of 0.1 m, and its front side is open. The monostatic RCS patterns of the cavity with and without the coating are calculated at 0.3 GHz, and the FE–BI solutions are compared again with the moment-method results in Figure 11.39 [40]. Again, the MLFMA is used to accelerate both the FE–BI and moment-method computations and a good agreement is observed between the two results. Scattering by a large, deep, and open cavity is a numerically challenging problem that has found some important applications in radar scattering and target identification [109–111].

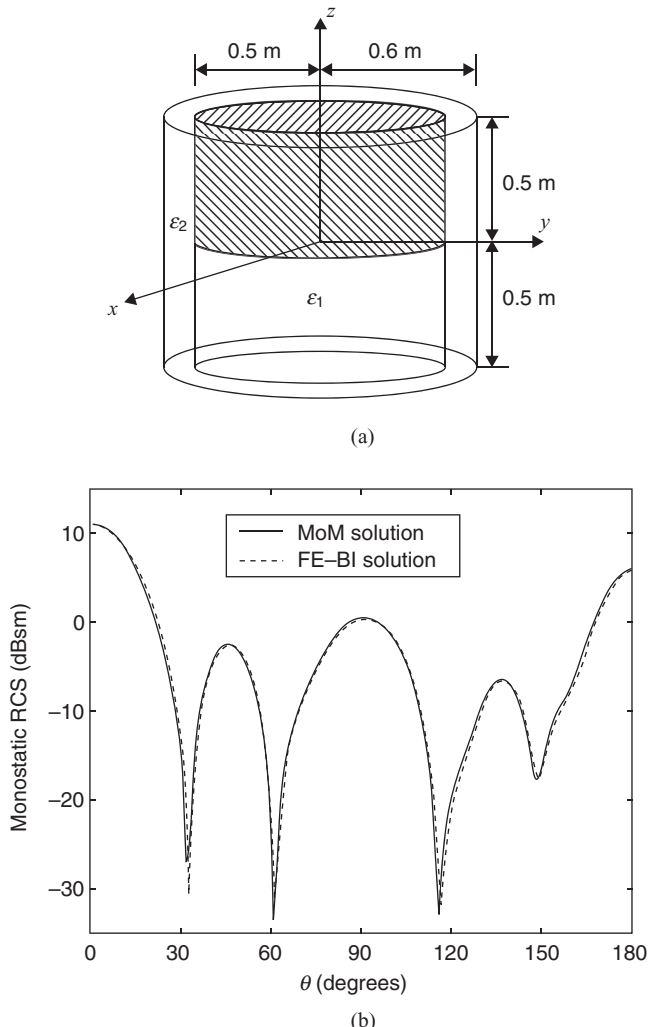


Figure 11.35 Monostatic RCS of a cylinder consisting of a conductor and two different dielectric materials. (a) Geometry. (b) $\theta\theta$ -polarized RCS at 0.3 GHz. (After Donepudi et al. [40], Copyright © 2003 IEEE.)

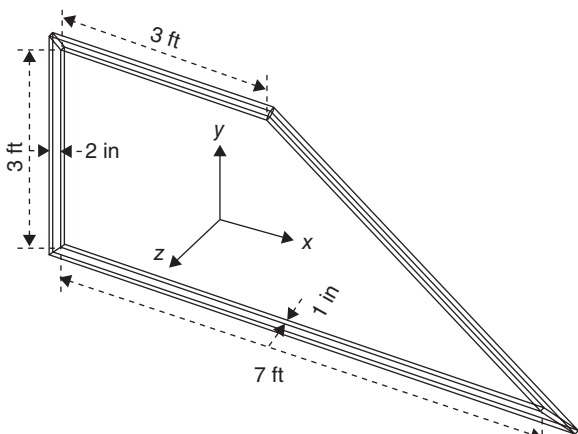


Figure 11.36 1.0-inch-thick trapezoidal conducting plate with its edges coated by 2.0-inch-wide lossy dielectric having $\epsilon_r = 4.5 - j9.0$. (After Donepudi et al. [40], Copyright © 2003 IEEE.)

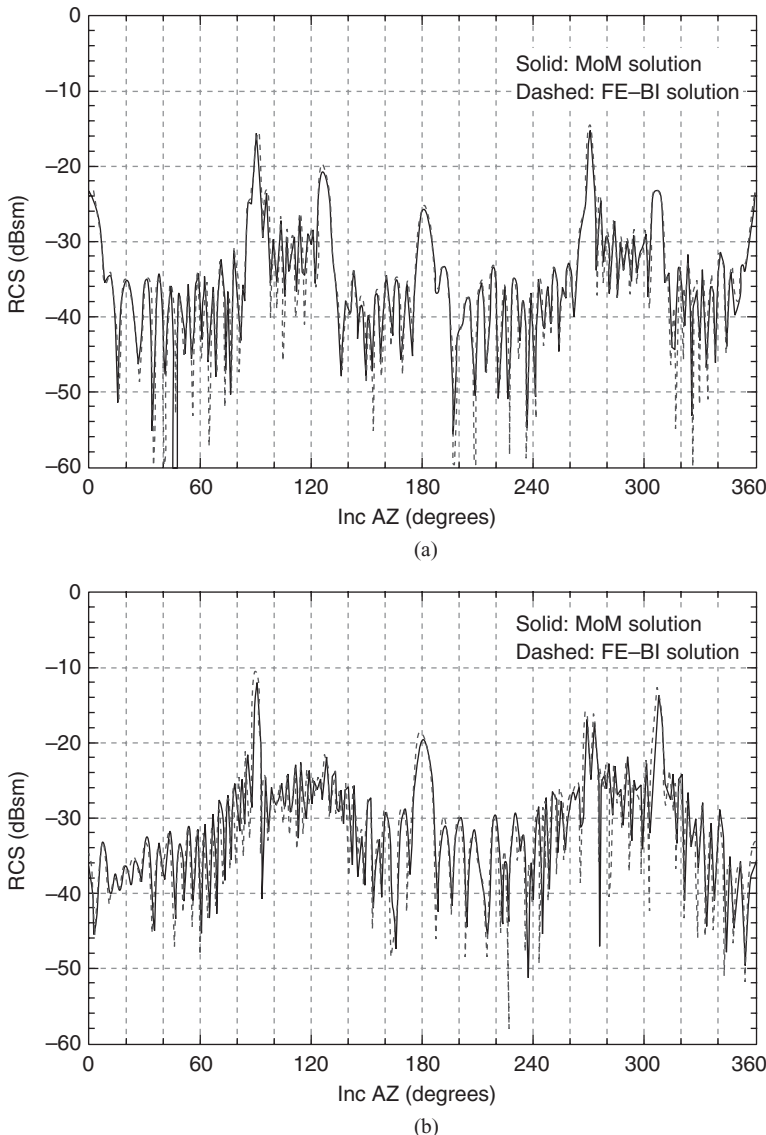


Figure 11.37 Monostatic RCS of the coated trapezoidal plate in the xy -plane at 1.0GHz.
(a) VV polarization. (b) HH polarization. (After Donepudi et al. [40], Copyright © 2003 IEEE.)

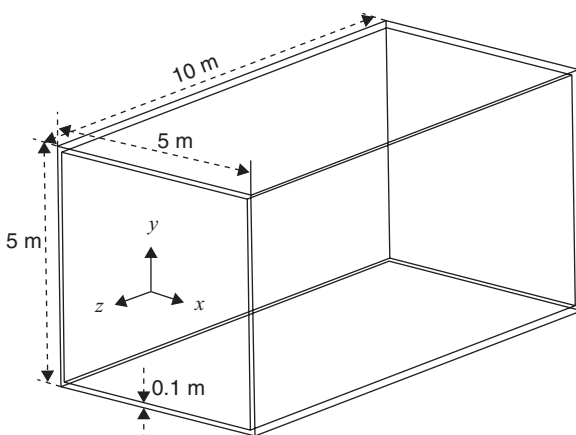


Figure 11.38 Open conducting cavity of dimension $5 \text{ m} \times 5 \text{ m} \times 10 \text{ m}$ made of 0.1-m-thick conductors with its interior surface coated by a 0.1-m-thick lossy dielectric with $\epsilon_r = 6.0 - j8.0$. Shown in the figure is the thickness of the conducting wall; the thickness of the coating is not shown for the sake of clarity.
(After Donepudi et al. [40], Copyright © 2003 IEEE.)

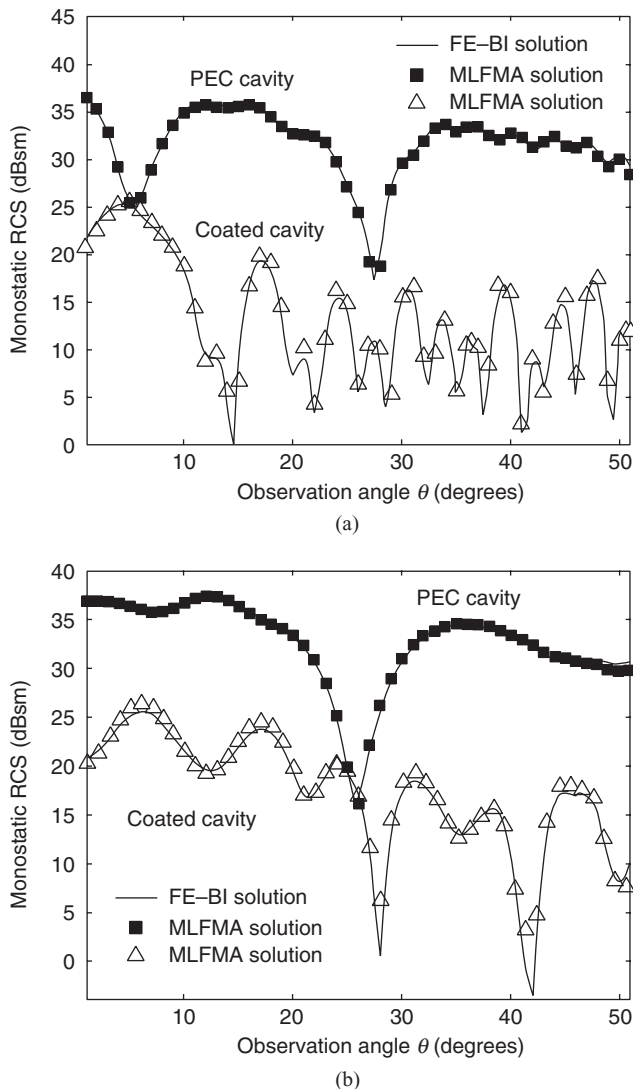


Figure 11.39 Monostatic RCS of the coated rectangular cavity in the xz -plane at 0.3 GHz. (a) $\theta\theta$ polarization. (b) $\phi\phi$ polarization. (After Donepudi et al. [40], Copyright © 2003 IEEE.)

11.9 SUMMARY

In this chapter, we discussed the development of fast algorithms to accelerate the moment-method solution of integral equations and the development of hybrid techniques that combine different numerical methods to deal with complicated electromagnetic problems. Both developments represent some of the most important progresses in computational electromagnetics during the past two decades. We should point out that the fast algorithms and hybrid techniques covered in this chapter are only the ones that have been most widely used so far. There are many other fast algorithms and hybrid techniques that were left uncovered because of the necessary limitation on the scope of this textbook. Among the fast algorithms, the most notable ones that are not covered here are the various fast time-

domain integral-equation (TDIE) solvers. In fact, many fast algorithms developed for the frequency-domain analysis can be extended into the time domain. Successful examples include the time-domain AIM (TD-AIM) and the plane wave time-domain (PWTD) method. The latter can be considered as the time-domain version of the multilevel FMM. Among the hybrid techniques, the most notable ones that are not covered here are the ones that combine a numerical method such as the moment method or the finite element method with an asymptotic technique for the analysis of scattering and radiation problems that involve relatively small features (such as antennas, gaps, and slots) on a very large platform (such as an airplane or ship). These hybrid techniques, although they are designed to solve a special class of problems, can provide a practical solution to large and complex problems that cannot be dealt with otherwise, even with today's most powerful computational techniques.

NOTES

1. The computational complexity of an algorithm for solving a matrix equation is defined as the required operation count and memory usage in terms of the dimension of the matrix.
2. Any Krylov subspace method, such as the biconjugate gradient (BCG), conjugate gradient squared (CGS), biconjugate gradient stabilized (BCGSTAB),

generalized minimal residual (GMRES), quasi-minimal residual (QMR), and transpose-free quasi-minimal residual (TFQMR) methods [62–70], can be used in conjunction with the FFT. In some cases, these methods have a better efficiency than the CG method.

REFERENCES

- [1] N. N. BOJARSKI, *k*-space formulation of the electromagnetic scattering problem, Air Force Avionics Lab. Technical Report AFAL-TR-71-75, 1971.
- [2] T. K. SARKAR, E. ARVAS, and S. M. RAO, Application of FFT and the conjugate gradient method for the solution of electromagnetic radiation from electrically large and small conducting bodies, *IEEE Trans. Antennas Propagat.*, 34(5): 635–640, 1986.
- [3] T. J. PETERS and J. L. VOLAKIS, Application of a conjugate gradient FFT method to scattering from thin planar material plates, *IEEE Trans. Antennas Propagat.*, 36(4): 518–526, 1988.
- [4] C. Y. SHEN, K. J. GLOVER, M. I. SANCER, and A. D. VARVATSIS, The discrete Fourier transform method of solving differential-integral equations in scattering theory, *IEEE Trans. Antennas Propagat.*, 37(8): 1032–1041, 1989.
- [5] K. BARKESHLI and J. L. VOLAKIS, On the implementation of the conjugate gradient Fourier transform method for scattering by planar plates, *IEEE Antennas Propagat. Mag.*, 32(2): 20–26, 1990.
- [6] M. F. CATEDRA, J. G. CUEVAS, and L. NUNO, A scheme to analyze conducting plates of resonant size using the conjugate gradient method and fast Fourier transform, *IEEE Trans. Antennas Propagat.*, 36(12): 1744–1752, 1988.
- [7] A. P. M. ZWAMBORN and P. M. van den BERG, A weak form of the conjugate gradient FFT method for plate problems, *IEEE Trans. Antennas Propagat.*, 39(2): 224–228, 1991.
- [8] J. M. JIN and J. L. VOLAKIS, A biconjugate gradient FFT solution for scattering by planar plates, *Electromagn.*, 12: 105–119, 1992.
- [9] Y. ZHUANG, K. WU, C. WU, and J. LITVA, A combined full-wave CG-FFT method for rigorous analysis of large microstrip antenna array, *IEEE Trans. Antennas Propagat.*, 44(1): 102–109, 1996.
- [10] C. F. WANG, F. LING, and J. M. JIN, A fast full-wave analysis of scattering and radiation from large finite arrays of microstrip antennas, *IEEE Trans. Antennas Propagat.*, 46(10): 1467–1474, 1998.
- [11] D. T. BORUP and O. P. GANDHI, Fast-Fourier transform method for calculation of SAR distributions in finely discretized inhomogeneous models of biological bodies, *IEEE Trans. Microwave Theory Tech.*, 32(2): 355–360, 1984.
- [12] M. F. CATEDRA, E. GAGO, and L. NUNO, A numerical scheme to obtain the RCS of three-dimensional bodies of resonant size using the conjugate gradient method and the fast Fourier transform, *IEEE Trans. Antennas Propagat.*, 37(5): 528–537, 1989.
- [13] A. P. M. ZWAMBORN, P. M. van den BERG, J. MOOBROEK, and F. T. C. KOENIS, Computation of three-dimensional electromagnetic fields distributions in a human body using the weak form of the CGFFT method, *ACES J.*, 7: 26–42, 1992.
- [14] A. P. M. ZWAMBORN and P. M. van der BERG, Computation of electromagnetic fields inside strongly inhomogeneous objects by the weak-conjugate-

- gradient fast-Fourier-transform method, *J. Opt. Soc. Am. A*, 11: 1414–1420, 1994.
- [15] H. GAN and W. C. CHEW, A discrete BCG-FFT algorithm for solving 3D inhomogeneous scattering problems, *J. Electromagn. Waves Appl.*, 9: 1339–1357, 1995.
- [16] J. M. JIN, J. CHEN, H. GAN, W. C. CHEW, R. L. MAGIN, and P. J. DIMBYLOW, Computation of electromagnetic fields for high-frequency magnetic resonance imaging applications, *Phys. Med. Biol.*, 41: 2719–2738, 1996.
- [17] C. F. WANG and J. M. JIN, Simple and efficient computation of electromagnetic fields in arbitrarily-shaped, inhomogeneous dielectric bodies using transpose-free QMR and FFT, *IEEE Trans. Microwave Theory Tech.*, 46(5): 553–558, 1998.
- [18] E. BLESZYNSKI, M. BLESZYNSKI, and T. JAROSZEWICZ, AIM: Adaptive integral method for solving large-scale electromagnetic scattering and radiation problems, *Radio Sci.*, 31: 1225–1251, 1996.
- [19] F. LING, C. F. WANG, and J. M. JIN, Application of adaptive integral method to scattering and radiation analysis of arbitrarily shaped planar structures, *J. Electromagn. Waves Appl.*, 12: 1021–1038, 1998.
- [20] S. S. BINDIGANAVALE, J. L. VOLAKIS, and H. ANASTASSIU, Scattering from structures containing small features using the adaptive integral method (AIM), *IEEE Trans. Antennas Propagat.*, 46(12): 1867–1878, 1998.
- [21] F. LING, C. F. WANG, and J. M. JIN, An efficient algorithm for analyzing large-scale microstrip structures using adaptive integral method combined with discrete complex image method, *IEEE Trans. Microwave Theory Tech.*, 48(5): 832–839, 2000.
- [22] C. F. WANG, F. LING, J. M. SONG, and J. M. JIN, Adaptive integral solution of combined field integral equation, *Microw. Opt. Tech. Lett.*, 19(5): 321–328, 1998.
- [23] J. R. PHILLIPS and J. K. WHITE, A precorrected-FFT method for electrostatic analysis of complicated 3D structures, *IEEE Trans. Comput. Aided Des.*, 16(10): 1059–1072, 1997.
- [24] X. C. NIE, L. W. LI, N. YUAN, T. S. YEO, and Y. B. GAN, Precorrected-FFT solution of the volume integral equation for 3-D inhomogeneous dielectric objects, *IEEE Trans. Antennas Propagat.*, 53(1): 313–320, 2005.
- [25] C. H. CHAN, C. M. LIN, L. TSANG, and Y. F. LEUNG, A sparse-matrix/canonical grid method for analyzing microstrip structures, *IEICE Trans. Electron.*, E80C: 1354–1359, 1997.
- [26] S. M. SEO and J. F. LEE, A fast IE-FFT algorithm for solving PEC scattering problems, *IEEE Trans. Magn.*, 41(5): 1476–1479, 2005.
- [27] V. ROKHLIN, Rapid solution of integral equations of classical potential theory, *J. Comput. Phys.*, 60: 187–207, 1985.
- [28] L. GREENGARD and V. ROKHLIN, A fast algorithm for particle simulations, *J. Comput. Phys.*, 73: 325–348, 1987.
- [29] V. ROKHLIN, Rapid solution of integral equations of scattering theory in two dimensions, *J. Comput. Phys.*, 86: 414–439, 1990.
- [30] R. COIFMAN, V. ROKHLIN, and S. WANDZURA, The fast multipole method for the wave equation: A pedestrian prescription, *IEEE Antennas Propagat. Mag.*, 35(3): 7–12, 1993.
- [31] V. ROKHLIN, Sparse diagonal forms for translation operators for the Helmholtz equation in two dimensions, Research Report 1095, Department of Computer Science, Yale University, 1995.
- [32] C. C. LU and W. C. CHEW, Fast algorithm for solving hybrid integral equations, *IEE Proc.-H*, 140: 455–460, 1993.
- [33] J. M. SONG and W. C. CHEW, Fast multipole method solution using parametric geometry, *Microw. Opt. Tech. Lett.*, 7(16): 760–765, 1994.
- [34] J. M. SONG and W. C. CHEW, Multilevel fast-multipole algorithm for solving combined field integral equations of electromagnetic scattering, *Microw. Opt. Tech. Lett.*, 10(1): 14–19, 1995.
- [35] B. DEMBART and E. YIP, A 3D fast multipole method for electromagnetics with multiple levels, *11th Ann. Rev. Progress Appl. Computat. Electromagn.*, vol. 1. Monterey, CA, 1995, pp. 621–628.
- [36] J. M. SONG, C. C. LU, and W. C. CHEW, MLFMA for electromagnetic scattering by large complex objects, *IEEE Trans. Antennas Propagat.*, 45(10): 1488–1493, 1997.
- [37] W. C. Chew, J. M. Jin, E. Michielssen, and J. M. Song, Eds., *Fast and Efficient Algorithms in Computational Electromagnetics*. Norwood, MA: Artech House, 2001.
- [38] K. C. DONEPUDI, J. M. JIN, S. VELAMPARAMBIL, J. M. SONG, and W. C. CHEW, A higher-order parallelized multilevel fast multipole algorithm for 3D scattering, *IEEE Trans. Antennas Propagat.*, 49(7): 1069–1078, 2001.
- [39] K. C. DONEPUDI, J. M. SONG, J. M. JIN, G. KANG, and W. C. CHEW, A novel implementation of multi-level fast multipole algorithm for higher-order Galerkin's method, *IEEE Trans. Antennas Propagat.*, 48(8): 1192–1197, 2000.
- [40] K. DONEPUDI, J. M. JIN, and W. C. CHEW, A higher-order multilevel fast multipole algorithm for scattering from mixed conducting/dielectric bodies, *IEEE Trans. Antennas Propagat.*, 51(10): 2814–2821, 2003.
- [41] K. NABORS and J. WHITE, Fastcap: A multipole-accelerated 3D capacitance extraction program, *IEEE Trans. Comput. Aided Des.*, 10(11): 1447–1459, 1991.
- [42] K. NABORS and J. WHITE, Multipole-accelerated capacitance extraction for 3D structures with multi-layer dielectrics, *IEEE Trans. Circ. Syst.*, 39(11): 946–954, 1992.
- [43] J. ZHAO and W. C. CHEW, Multilevel fast multipole algorithm at very low frequencies. *Fast and Efficient Algorithms in Computational Electromagnetics*, edited by W. C. Chew, J. M. Jin, E. Michielssen, and

- J. M. Song. Norwood, MA: Artech House, 2001, pp. 151–202.
- [44] J. M. SONG, C. C. LU, W. C. CHEW, and S. W. LEE, Fast Illinois solver code (FISC), *IEEE Antennas Propag. Mag.*, 40(3): 27–34, 1998.
- [45] X. Q. SHENG, J. M. JIN, J. M. SONG, W. C. CHEW, and C. C. LU, Solution of combined-field integral equation using multilevel fast multipole method for scattering by homogeneous bodies, *IEEE Trans. Antennas Propagat.*, 46(11): 1718–1726, 1998.
- [46] C. C. LU, Volume–surface integral equation. *Fast and Efficient Algorithms in Computational Electromagnetics*, edited by W. C. Chew, J. M. Jin, E. Michielssen, and J. M. Song. Norwood, MA: Artech House, 2001.
- [47] N. GENG, A. SULLIVAN, and L. CARIN, Multilevel fast multipole algorithm for scattering from conducting targets above or embedded in a lossy half space, *IEEE Trans. Geosci. Remote Sensing*, 38(4): 1561–1573, 2000.
- [48] V. JANDHYALA, E. MICHELISSEN, and R. MITTRA, Multipole-accelerated capacitance computation for 3D structures in a stratified dielectric medium using in a closed form Green’s function, *Int. J. Microwave Millimeter Wave Comput. Aided Eng.*, 5: 68–78, 1995.
- [49] L. GUREL and M. I. AKSUN, Electromagnetic scattering solution of conducting strips in layered media using the fast multipole method, *IEEE Microwave Guided Wave Lett.*, 6: 277–279, 1996.
- [50] P. A. MACDONALD and T. ITOH, Fast simulation of microstrip structures using the fast multipole method, *Int. J. Numer. Model. Electron. Network. Dev. Field.*, 9: 345–357, 1996.
- [51] J. S. ZHAO, W. C. CHEW, C. C. LU, E. MICHELISSEN, and J.M. SONG, Thin-stratified medium fast-multipole algorithm for solving microstrip structures, *IEEE Trans. Microwave Theory Tech.*, 46(4): 395–403, 1998.
- [52] F. LING, J. M. SONG, and J. M. JIN, Multilevel fast multipole algorithm for analysis of large-scale microstrip structures, *IEEE Microwave Guided Wave Lett.*, 9: 508–510, 1999.
- [53] W. C. GIBSON, *The Method of Moments in Electromagnetics*. Boca Raton, FL: Chapman & Hall/CRC, 2008.
- [54] M. BEBENDORF, Approximation of boundary element matrices, *Numer. Math.*, 86: 565–589, 2000.
- [55] S. A. GOREINOV, E. E. TYRTYSHNIKOV, and N. L. ZAMARASHKIN, A theory of pseudoskeleton approximations, *Linear Algebra Appl.*, 261: 1–21, 1997.
- [56] S. A. GOREINOV, N. L. ZAMARASHKIN, and E. E. TYRTYSHNIKOV, Pseudo-skeleton approximations by matrices of maximal volume, *Mat. Zametki*, 62(4): 619–623, 1997.
- [57] S. KURZ, O. RAIN, and S. RIJASNOW, The adaptive cross-approximation technique for the 3-D boundary-element method, *IEEE Trans. Magn.*, 38(2): 421–424, 2002.
- [58] K. ZHAO, M. N. VOUVAKIS, and J.-F. LEE, The adaptive cross approximation algorithm for accelerated method of moments computations of EMC problems, *IEEE Trans. Electromagn. Compat.*, 47(4): 763–773, 2005.
- [59] J. SHAFFER, Direct solve of electrically large integral equations for problem sizes to 1M unknowns, *IEEE Trans. Antennas Propagat.*, 56(8): 2306–2313, 2008.
- [60] M. R. HESTENES and E. STIEFEL, Method of conjugate gradients for solving linear systems, *J. Res. Nat. Bur. Standards*, 49: 409–435, 1952.
- [61] R. FLETCHER, Conjugate gradient methods for indefinite systems. *Proc. Dundee Conf. Numer. Anal. Syst.*, vol. 506. New York: Springer, 1975.
- [62] C. LANCZOS, Solution of systems of linear equations by minimized iterations, *J. Res. Nat. Bur. Standards*, 49: 33–53, 1952.
- [63] P. SONNEVELD, CGS: A fast Lanczos-type solver for nonsymmetric linear systems, *SIAM J. Sci. Statist. Comput.*, 10: 36–52, 1989.
- [64] H. A. van Der VORST, BI-CGSTAB: A fast and smoothly converging variant of BI-CG for the solution of nonsymmetric linear systems, *SIAM J. Sci. Statist. Comput.*, 13: 631–644, 1992.
- [65] Y. SAAD, GMRES: A generalized minimal residual algorithm for solving nonsymmetric linear systems, *SIAM J. Sci. Statist. Comput.*, 7: 856–869, 1986.
- [66] R. W. FREUND and N. M. NACHTIGAL, QMR: A quasi-minimal residual method for non-Hermitian linear systems, *Numer. Math.*, 60: 315–339, 1991.
- [67] R. W. FREUND, A transpose-free quasi-minimal residual algorithm for non-Hermitian linear systems, *SIAM J. Sci. Comput.*, 14: 470–482, 1993.
- [68] R. BARRET, *Templates for the Solution of Linear Systems*. Philadelphia: SIAM, 1993.
- [69] Y. SAAD, *Iterative Method for Sparse Linear Systems*. New York: PWS Publishing Company, 1995.
- [70] A. GREENBAUM, *Iterative Methods for Solving Linear Systems*. Philadelphia: SIAM, 1997.
- [71] D. E. LIVESAY and K. M. CHEN, Electromagnetic fields induced inside arbitrarily shaped biological bodies, *IEEE Trans. Microwave Theory Tech.*, 22(12): 1273–1280, 1974.
- [72] D. H. SCHAUERT, D. R. WILTON, and A. W. GLISSON, A tetrahedral modeling method for electromagnetic scattering by arbitrarily shaped inhomogeneous dielectric bodies, *IEEE Trans. Antennas Propagat.*, 32(1): 77–85, 1984.
- [73] A. C. WOO, H. T. G. WANG, M. J. SCHUH, and M. L. SANDERS, Benchmark radar targets for the validation of computational electromagnetics programs, *IEEE Antennas Propagat. Mag.*, 35(1): 84–89, 1993.
- [74] J. M. PUTNAM and M. B. GEDERA, CARLOS-3DTM: A general-purpose three dimensional method-of-moments scattering code, *IEEE Antennas Propagat. Mag.*, 35(2): 69–71, 1993.
- [75] M. Abramowitz and I. A. Stegun, Eds. *Handbook of Mathematical Functions*. New York: Dover, 1965.
- [76] J. A. STRATTON, *Electromagnetic Theory*. New York: McGraw-Hill, 1941.

- [77] E. MICHELSSEN and A. BOAG, A multilevel matrix decomposition algorithm for analyzing scattering from large structures, *IEEE Trans. Antennas Propagat.*, 44(8): 1086–1093, 1996.
- [78] J. M. RIUS, J. PARRON, E. UBEDA, and J. R. MOSIG, Multilevel matrix decomposition for analysis of electrically large electromagnetic problems in 3-D, *Microw. Opt. Tech. Lett.*, 22: 177–182, 1999.
- [79] J. PARRON, J. M. RIUS, and J. R. MOSIG, Application of the multilevel matrix decomposition algorithm for the frequency analysis of large microstrip antenna array, *IEEE Trans. Magn.*, 38(2): 721–724, 2002.
- [80] G. H. GOLUB and C. F. VAN LOAN, *Matrix Computations*. Baltimore, MD: The John Hopkins Univ. Press, 1996.
- [81] D. J. RILEY and C. D. TURNER, Interfacing unstructured tetrahedron grids to structured-grid FDTD, *IEEE Microwave Guided Wave Lett.*, 5(9): 284–286, 1995.
- [82] D. J. RILEY and C. D. TURNER, VOLMAX: A solid-model-based, transient, volumetric Maxwell solver using hybrid grids, *IEEE Antennas Propagat. Mag.*, 39(1): 20–33, 1997.
- [83] R. B. WU and T. ITOH, Hybridizing FDTD analysis with unconditionally stable FEM for objects of curved boundary, *IEEE MTT-S Int. Microwave Symp. Dig.*, 2: 833–836, 1995.
- [84] R. B. WU and T. ITOH, Hybrid finite-difference time-domain modeling of curved surfaces using tetrahedral edge elements, *IEEE Trans. Antennas Propagat.*, 45(8): 1302–1309, 1997.
- [85] M. FELIZIANI and F. MARADEI, Mixed finite-difference/Whitney-elements time domain (FD/WE-TD) method, *IEEE Trans. Magn.*, 34(5): 3222–3227, 1998.
- [86] D. J. RILEY, Transient finite elements for computational electromagnetics: Hybridization with finite differences, modeling thin wire and thin slots, and parallel processing. *Proc. 17th Ann. Review Progress Appl. Comp. Electromagn. (ACES)*. Monterey, CA, 2001, pp. 128–138.
- [87] T. RYLANDER and A. BONDESON, Stable FDTD-FEM hybrid method for Maxwell's equations, *Comput. Phys. Comm.*, 125: 75–82, 2000.
- [88] T. RYLANDER and A. BONDESON, Stability of explicit-implicit hybrid time-stepping schemes for Maxwell's equations, *J. Comput. Phys.*, 179: 426–438, 2002.
- [89] T. RYLANDER, Stable FDTD-FEM hybrid method for Maxwell's equations, Ph.D. thesis, Department of Electromagnetics, Chalmers University of Technology, Gothenburg, Sweden, 2002.
- [90] F. EDELVIK, Hybrid solvers for the Maxwell equations in time-domain, Ph.D. thesis, Department of Information Technology, Scientific Computing, Uppsala University, Uppsala, Sweden, 2002.
- [91] T. RYLANDER, F. EDELVIK, A. BONDESON, and D. RILEY, Advances in hybrid FDTD-FE techniques. *Computational Electrodynamics: The Finite-Difference Time-Domain Method* (3rd edition), edited by A. Taflove and S. C. Hagness. Norwood, MA: Artech House, 2005, pp. 907–953.
- [92] J. M. JIN and D. J. RILEY, *Finite Element Analysis of Antennas and Arrays*. Hoboken, NJ: Wiley, 2009.
- [93] G. COHEN and P. MONK, Gauss point mass lumping schemes for Maxwell's equations, *Numer. Meth. Part. Diff. Eq.*, 14: 63–88, 1998.
- [94] R. LEE, A note on mass lumping in the finite element time domain method, *IEEE Trans. Antenna Propagat.*, 54(2): 760–762, 2006.
- [95] F.-X. ZGAINSKI, J.-L. COULOMB, Y. MARECHAL, F. CLAEYSSEN, and X. BRUNOTTE, A new family of finite elements: The pyramidal elements, *IEEE Trans. Magn.*, 32(3): 1393–1396, 1996.
- [96] J.-L. COULOMB, F.-X. ZGAINSKI, and Y. MARECHAL, A pyramidal element to link hexahedral, prismatic and tetrahedral edge finite elements, *IEEE Trans. Magn.*, 33(2): 1362–1365, 1997.
- [97] R. D. GRAGLIA and I.-L. GHEORMA, Higher order interpolatory vector bases on pyramidal elements, *IEEE Trans. Antennas Propagat.*, 47(5): 775–782, 1999.
- [98] A. C. WOO, H. T. G. WANG, M. J. SCHUH, and M. L. SANDERS, Benchmark radar targets for the validation of computational electromagnetics programs, *IEEE Antennas Propagat. Mag.*, 35(1): 84–89, 1993.
- [99] J. M. JIN and V. V. LIEPA, Application of a hybrid finite element method to electromagnetic scattering from coated cylinders, *IEEE Trans. Antennas Propagat.*, 36(1): 50–54, 1988.
- [100] X. YUAN, Three-dimensional electromagnetic scattering from inhomogeneous objects by the hybrid moment and finite element method, *IEEE Trans. Microwave Theory Tech.*, 38(8): 1053–1058, 1990.
- [101] T. EIBERT and V. HANSEN, Calculation of unbounded field problems in free space by a 3D FEM/BEM-hybrid approach, *J. Electromagn. Waves Appl.*, 10(1): 61–78, 1996.
- [102] X. Q. SHENG, J. M. JIN, J. M. SONG, C. C. LU, and W. C. CHEW, On the formulation of hybrid finite-element and boundary-integral method for 3D scattering, *IEEE Trans. Antennas Propagat.*, 46(3): 303–311, 1998.
- [103] J. LIU and J. M. JIN, A novel hybridization of higher order finite element and boundary integral methods for electromagnetic scattering and radiation problems, *IEEE Trans. Antennas Propagat.*, 49(12): 1794–1806, 2001.
- [104] J. LIU and J. M. JIN, A highly effective preconditioner for solving the finite element-boundary integral matrix equation of 3-D scattering, *IEEE Trans. Antennas Propagat.*, 50(9): 1212–1221, 2002.
- [105] M. N. VOUVAKIS, S.-C. LEE, K. ZHAO, and J.-F. LEE, A symmetric FEM-IE formulation with a single-level IE-QR algorithm for solving electromagnetic radiation and scattering problems, *IEEE Trans. Antennas Propagat.*, 52(11): 3060–3070, 2004.
- [106] M. M. BOTHA and J. M. JIN, On the variational formulation of hybrid finite element-boundary integral techniques for electromagnetic analysis, *IEEE Trans. Antennas Propagat.*, 52(11): 3037–3047, 2004.

- [107] D. JIAO, A. ERGIN, B. SHANKER, E. MICHELSSEN, and J. M. JIN, A fast time-domain higher-order finite element-boundary integral method for 3-D electromagnetic scattering analysis, *IEEE Trans. Antennas Propagat.*, 50(9): 1192–1202, 2002.
- [108] A. E. YILMAZ, Z. LOU, E. MICHELSSEN, and J. M. JIN, A single-boundary, implicit, and FFT-accelerated time-domain finite element-boundary integral solver, *IEEE Trans. Antennas Propagat.*, 55(5): 1382–1397, 2007.
- [109] J. LIU and J. M. JIN, A special higher-order finite element method for scattering by deep cavities, *IEEE Trans. Antennas Propagat.*, 48(5): 494–703, 2000.
- [110] J. LIU and J. M. JIN, Scattering analysis of a large body with deep cavities, *IEEE Trans. Antennas Propagat.*, 51(6): 157–1167, 2003.
- [111] J. M. JIN, J. LIU, Z. LOU, and C. S. LIANG, A fully high-order finite element simulation of scattering by deep cavities, *IEEE Trans. Antennas Propagat.*, 51(9): 2420–2429, 2003.

PROBLEMS

- 11.1.** Consider the problem of electromagnetic wave scattering by an inhomogeneous dielectric cylinder. For the TM case, the electric field satisfies the scalar wave equation

$$\nabla^2 E_z(\rho) + k_0^2 \epsilon_r(\rho) E_z(\rho) = 0 \quad \rho \in \Omega_o$$

where Ω_o denotes the cross-sectional area of the cylinder. (1) Formulate a volume integral equation for solving for the scattered or total field when the cylinder is illuminated by an external incident field $E_z^{inc}(\rho)$. (2) Formulate the moment-method solution by subdividing Ω_o into small elements and expanding the field inside using piecewise constant basis functions. (3) Formulate the CG-FFT solution to the moment-method equation obtained using a staircase approximation of Ω_o .

- 11.2.** The AIM can be formulated by interpolating the Green's function on a Cartesian grid using the Lagrange interpolation polynomials [26], instead of projecting the basis and testing functions onto the Cartesian grid. Describe a detailed procedure to calculate the matrix-vector product based on this approach.
- 11.3.** Starting from the inhomogeneous Helmholtz equation in Equation 10.2.3, derive the following plane wave expansion

$$H_0^{(2)}(k_0 |\rho - \rho'|) = \frac{1}{2\pi} \int_{-\infty}^{\infty} \frac{e^{-jk_x(x-x') \mp jk_y(y-y')}}{k_y} dk_x \quad \begin{cases} y > y' \\ y < y' \end{cases}$$

where $k_y = \sqrt{k_0^2 - k_x^2}$. This expression can be written as

$$H_0^{(2)}(k_0 |\rho - \rho'|) = \frac{1}{2\pi} \int_{-\infty}^{\infty} \frac{1}{k_y} e^{-j\mathbf{k}(\rho - \rho_p)} e^{-j\mathbf{k}(\rho_p - \rho_q)} e^{-j\mathbf{k}(\rho_q - \rho')} dk_x.$$

By using this expression, design a fast multipole algorithm for solving integral equations of two-dimensional wave scattering.

- 11.4.** The volume integral equations for scattering by an inhomogeneous dielectric object are formulated in Section 10.3.5. Describe a three-dimensional fast multipole algorithm for a fast solution of these equations.
- 11.5.** By using Lagrange interpolation, the free-space Green's function can be factorized in the form of Equation 11.5.7. Design an algorithm for a fast calculation of the product between the moment-method matrix and a vector. Analyze the computational complexity of the algorithm for a static Green's function and a dynamic Green's function and compare the two cases.
- 11.6.** Implement the two-dimensional hybrid FETD-FDTD method described in Section 11.7 and test the algorithm on a few simple examples. Study the stability and accuracy of the solutions.

- 11.7.** Design a simple problem that consists of four brick elements and show that the FDTD equations obtained using Yee's scheme are identical to the FETD equations obtained using the first-order vector basis functions with both the mass and stiffness matrices evaluated using trapezoidal integration and using central differencing for temporal discretization. (To simplify the equations, consider the lossless and source-free case.)
- 11.8.** Consider the problem of TM wave scattering by an inhomogeneous dielectric cylinder.
(1) Formulate the EFIE, MFIE, and CFIE that can be applied to the surface of the cylinder.
(2) Formulate the traditional FE-BI method that is parallel to the three-dimensional version described in Section 11.8.1. (3) Formulate the symmetric FE-BI method that is parallel to the three-dimensional version described in Section 11.8.2. ■

CONCLUDING REMARKS ON COMPUTATIONAL ELECTROMAGNETICS

Since its beginning in the early 1960s, research on computational electromagnetics has seen a history of nearly five decades. Due to the effort of numerous researchers, many computational techniques have been developed for solving a variety of electromagnetic problems. In Chapters 8 to 11, we have covered a few most important and popular computational methods. In this chapter, we present a general overview of computational electromagnetics, including an overview of many computational methods that are left uncovered so far, practical applications of computational electromagnetics to demonstrate its importance, and finally potential challenges in the research of computational electromagnetics.

12.1 OVERVIEW OF COMPUTATIONAL ELECTROMAGNETICS

As illustrated in Figure 12.1, all computational methods for electromagnetic analysis can be divided into two groups: time-domain and frequency-domain methods, which are related to each other by the Fourier transform. Methods for solving electrostatic and magnetostatic problems belong to the group of frequency-domain methods with frequency set to zero. Among frequency-domain methods, there is a subgroup that consists of *high-frequency asymptotic methods*, which are based on ray and diffraction optics and can deal with electrically large problems very efficiently. The other subgroup is composed of *first-principle numerical methods*, which solve Maxwell's equations directly and can deal with any complicated problems at the cost of requiring more extensive computing resources.

12.1.1 Frequency- versus Time-Domain Analysis

The time-dependent Maxwell's equations represent a mathematical problem in four dimensions: three spatial dimensions plus the time dimension. Usually, the complexity of a problem grows exponentially with its dimensions (the number of independent variables). To reduce the number of dimensions, we can apply the Fourier transform to convert Maxwell's equations into the frequency domain, which eliminates the time dependence and reduces the dimensionality to three. Once the solution in the frequency domain is

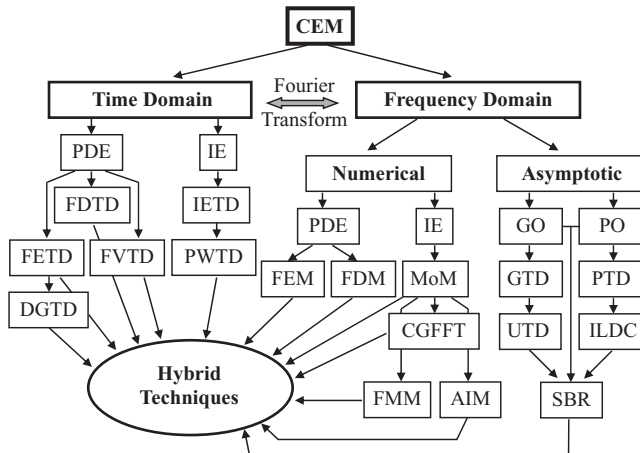


Figure 12.1 Because of the large variety of electromagnetic-related engineering problems, a large number of numerical and asymptotic methods have been developed to solve Maxwell's equations.

obtained, the time-dependent response can be obtained by using the inverse Fourier transform. The price to pay is to repeat the frequency-domain solutions at many frequencies. This was discussed clearly in Chapter 1.

Since Maxwell's equations can be solved in either the time or the frequency domain, two groups of methods have been developed in the past to deal with electromagnetic problems: frequency- and time-domain methods. However, since the solution processes in the two domains are different, the two solutions possess different strengths. For example, when a frequency-domain numerical method is employed to solve Maxwell's equations, we have to solve a system of linear equations (matrix equation) for each frequency. However, the system matrix is usually independent of excitations. Once this matrix is inverted or factorized, it can be used to obtain solutions to all excitations. This feature makes the frequency-domain methods attractive for problems where we have to consider many excitations (such as in a monostatic scattering analysis). Furthermore, since the frequency-domain methods solve Maxwell's equations at each frequency, they can deal with dispersive media easily. On the other hand, when a time-domain numerical method is adopted to solve Maxwell's equations, we have to seek a solution by time marching for each excitation. Once the solution in the time domain is obtained, we can find the solution over a wide band of frequencies using the inverse Fourier transform. However, the solution process must be repeated for every new excitation. Therefore, the time-domain methods are ideally suited for broadband problems where one seeks for a solution over a broad frequency band with only a few excitations (such as in a broadband antenna or device analysis). Because the time-domain methods solve Maxwell's equations step by step in time, they can deal effectively with non-linear problems, where the electromagnetic properties of the computational domain change with the field strengths.

12.1.2 High-Frequency Asymptotic Techniques

When the object of interest is large compared with the wavelength and does not contain small features, the problem of electromagnetic scattering by such an object or radiation in the presence of such an object can be analyzed using high-frequency asymptotic

techniques. There are two families of asymptotic techniques. One starts from *geometrical optics* [1], which is established based on the fact that at a high frequency, electromagnetic waves propagate as optical rays, which are governed by Snell's laws derived in Chapter 4. Therefore, the wave propagation problem can be analyzed with ray tracing, and during ray tracing the amplitude of the field can be determined based on the shape of the wave-front surface. It is evident that with geometrical optics, the field in the shadow region vanishes completely, whereas the field in the illuminated or lit region consists of either the incident field alone or the sum of the incident and reflected fields. The fields diffracted by the edges and wedges of the object are completely neglected, and the total field contains two non-physical discontinuities: one at the boundary between the lit and shadow regions (called the incident shadow boundary [ISB]) and the other at the boundary between the reflected region and the region that is not reached by reflection (called the reflection shadow boundary [RSB]). Obviously, the accuracy of a geometrical optics solution can be improved by first including the diffracted fields into the solution. This led to the development of the *geometrical theory of diffraction* (GTD) [2–4]. In the GTD, an approximate asymptotic solution for the diffracted field by a straight edge at normal incidence is first obtained and then extended to oblique incidences and curved edges. This solution is then added to the solution by geometrical optics. Although the new solution has a considerably better accuracy, the fields at the ISB and RSB are still discontinuous. These discontinuities can be compensated by a transition function, which can be obtained by a more accurate evaluation of the diffracted field. The result is the well-known *uniform theory of diffraction* (UTD) [5–7]. In addition to the UTD, other methods to remedy the problems in the GTD include the *uniform asymptotic theory* (UAT) [8,9] and the *spectral theory of diffraction* (STD) [10,11].

Another family of high-frequency asymptotic techniques starts from *physical optics* (PO), discussed in Chapter 3. This method approximates the induced current density on a large conducting surface in the lit region as $\mathbf{J}_s = \hat{n} \times \mathbf{H} \approx 2\hat{n} \times \mathbf{H}^{\text{inc}}$ and in the shadow region as $\mathbf{J}_s = \hat{n} \times \mathbf{H} \approx 0$. The fields radiated by these currents can then be obtained using the free-space field–source relations, which involve an integral over the currents (which is often referred to as the radiation integral or the PO integral), as discussed in Chapter 2. This approach has been used widely for the evaluation of radiation patterns of reflector antennas. Obviously, the PO approximation neglects the effect of geometrical discontinuities such as edges on the induced currents, and the approximated induced current can have a discontinuity at the boundary between the lit and shadow surfaces, although the true solution does not contain any such discontinuities. The accuracy of this approximation can be improved by adding non-uniform fringe currents to the induced currents to account for the effect of geometrical discontinuities such as edges. This led to the development of the *physical theory of diffraction* (PTD) [12–14]. Besides using non-uniform fringe currents, the effects of geometrical discontinuities can also be modeled by *incremental length diffraction coefficients* (ILDC) [15,16] and *equivalent edge currents* (EEC) [17,18]. Compared with the GTD and its improved versions, PO and the PTD are easier to use, but they require an evaluation of radiation integrals over the surface currents, which can be time-consuming when they have to be evaluated for many observation angles. However, this evaluation can be accelerated using fast algorithms similar to the fast multipole method [19,20].

The geometrical and physical optics methods can be combined to develop a highly powerful technique for computing electromagnetic scattering from large and complex objects. This hybrid technique is called the *shooting- and bouncing-ray* (SBR) method [21]. In this method, the incident wave from a source is represented by a grid of rays shooting toward the object. Each ray (its associated amplitude and phase) is traced as it

bounces around the object, and the bounces are governed by geometrical optics. At each and every intersection point of the ray with the object, a PO type of integration is performed to determine its contribution to the scattered or the radiated field. The final solution is the summation of the contributions from all rays. This hybrid technique has been implemented into a computer code [22], which has been used widely to compute radar signatures. Similar computer codes have also been developed to compute antenna radiation patterns in the presence of large platforms [23] and wave propagation in complex urban environments [24]. The effect of edge diffraction can be included in the SBR computations using the approach based on the incremental length diffraction coefficients.

In addition to their high efficiency, high-frequency asymptotic techniques also provide valuable physical insights into scattering and diffraction mechanisms, which are difficult to gain with other numerical methods. The subject of asymptotic techniques is not covered in this book simply because it is beyond the scope of this book, which is intended to serve as a textbook for graduate courses on electromagnetic theory and computational electromagnetics. The importance of high-frequency asymptotic techniques warrants another graduate course, and the material on the subject [25,26] is certainly more than enough for such a course.

12.1.3 First-Principle Numerical Methods

When electromagnetic problems are more complicated than scattering and radiation by large objects (such as analysis of microwave devices and high-frequency circuits) or when the accuracy desired is beyond the reach of asymptotic techniques, the solution can only be obtained by solving Maxwell's equations using one of several numerical methods. As with asymptotic techniques, there are also two families of numerical methods. One family of methods solves Maxwell's equations or their weak-form representations directly. This family includes the finite difference method discussed in Chapter 8 and the finite element method discussed in Chapter 9. In mathematics, they are called partial differential equation (PDE) methods. Since in the frequency domain, the finite difference method has the same computational complexity as the finite element method has (both have to solve a large, sparse matrix equation), there is little advantage to using the finite difference method. As a result, the finite element method, given its flexibility on geometrical modeling, is often preferred to the finite difference method. A method that is closely related to the finite element method is the *meshless* or *mesh-free method*, which has received much attention recently [27–32]. This method solves a PDE based on a number of discrete points in the computational domain without explicitly forming a finite element mesh. Therefore, it removes the requirement of mesh generation, which is often considered an obstacle in the application of the finite element method.

Since the formulation, application, and advantages of the finite difference and the finite element methods have been discussed in detail in Chapters 8 and 9, we do not intend to discuss them further except to mention two points. First, Maxwell's equations for static fields represent an elliptic-type PDE, and their finite difference or finite element discretization yields a positive definite matrix. Such a matrix equation can be solved iteratively in a finite number of iterations. On the other hand, Maxwell's equations for time-harmonic fields represent a hyperbolic-type PDE, and their finite difference or finite element discretization yields an indefinite matrix. The convergence of an iterative solution for such a matrix equation is usually slow; consequently, a preconditioner, such as one that is based on an incomplete *LU* decomposition, is often used to speed up the iterative convergence. Second, as shown in both Chapters 8 and 9, when the finite difference or the finite element method is applied to wave equations, the simulated wave propagates at a speed that is

slightly different from the exact value. Consequently, there is a numerical error in the phase of the solution, called dispersion error. When the first-order basis functions are employed, the phase error per wavelength is proportional to $O[(h/\lambda)^2]$, where h denotes the elemental size and λ denotes the wavelength. Since the phase error is cumulative, the error in the final solution is proportional to the electrical length that the wave travels. Therefore, the finite difference grid or finite element mesh density has to be increased to obtain a desired accuracy if the problem size becomes larger or the frequency becomes higher. A better alternative is to employ higher-order basis functions because these basis functions can reduce the phase error exponentially.

The other family of numerical methods solves Maxwell's equations indirectly by dealing with an integral equation formulated using the fundamental solution to a point source, which is known as a Green's function. The most well-known method in this family is the moment method discussed in Chapter 10. For problems involving impenetrable or piecewise homogeneous regions, we can formulate an integral equation that involves only surface integrals. This kind of integral equation is called *surface integral equation* (SIE). For problems involving inhomogeneous regions for which the Green's function is not explicitly available, the integral equation will contain volume integrals. This kind of integral equation is called *volume integral equation* (VIE). Since the number of unknowns resulting from a surface discretization is significantly smaller than that from a volume discretization, the moment method is much more efficient when it deals with an SIE. The SIEs that we have encountered so far can be classified into the *Fredholm integral equation of the first kind*, such as the electric-field integral equations (EFIE) in Equations 10.2.21 and 10.3.45, and the *Fredholm integral equation of the second kind*, such as the magnetic-field integral equations (MFIE) in Equations 10.2.30 and 10.3.46. The Fredholm integral equation of the first kind can usually be solved very accurately, but its iterative solution converges very slowly. In contrast, the iterative solution of the Fredholm integral equation of the second kind converges rapidly; however, its solution has a rather poor accuracy. Therefore, it is important to develop an effective preconditioner for the Fredholm integral equation of the first kind. In fact, many such preconditioners have been developed so far, some of which are purely algebra-based and some are physics-based. One of the physics-based preconditioners is based on the Calderon identity [33], which indicates that when the EFIE operator is applied to itself, the resulting operator yields a well-preconditioned matrix, which can be solved in a few iterations [34–37]. The more challenging cases are the combined-field integral equation (CFIE) in Equation 10.3.47 and the EFIE and MFIE for dielectric objects such as Equations 10.3.29 and 10.3.30, which contain both the EFIE and MFIE operators. So far, most preconditioners for these equations are algebra-based such as the block diagonal and near-neighbor preconditioners [38].

Unlike the PDE methods, the integral equation methods use an exact wave propagator, Green's function, to effect wave propagation. As a result, these methods do not have the problem of grid dispersion. However, they yield fully populated matrices, which are expensive to generate, store, and solve. Many fast algorithms have been developed to solve this type of matrix efficiently. We have discussed four such fast algorithms in Chapter 11: the conjugate gradient–fast Fourier transform (FFT), adaptive integral, fast multipole, and adaptive cross-approximation methods. Other fast algorithms include the precorrected–FFT [39], sparse matrix/canonical grid [40], panel clustering [41], multilevel matrix decomposition [42], hierarchical-matrix [43,44], tree clustering [45,46], matrix compression based on singular-value decomposition [47], non-uniform grid [48,49], accelerated Cartesian expansion [50], and some other fast multipole algorithms [51–60]. It should be noted that developing a fast algorithm for a wave problem is significantly more difficult than developing one for a static or quasi-static problem. The reason is that the integral

kernel for a wave problem is highly oscillatory, and, consequently, there is a minimum in the number of points for its interpolation no matter how far the wave propagates. In contrast, the integral kernel for a static problem is smooth and can be interpolated with fewer and fewer points as the distance between the source and field points increases. We have observed this clearly in the adaptive cross-approximation method. The same phenomenon can be observed in some other fast algorithms.

Among the integral equation methods other than the moment method, a method that deserves to be mentioned here explicitly is the *partial element equivalent circuit* (PEEC) method [61–65]. This method solves the surface-based EFIE for circuit geometries. Mathematically, it can be regarded as being equivalent to the moment method. However, it is formulated in terms of circuit terminologies by first discretizing the conductors in a circuit geometry into small cells with equivalent circuit parameters and then interpreting the EFIE as Kirchhoff's voltage law applied to the equivalent circuits. This equivalent-circuit-based formulation can easily include lumped circuit elements into the analysis and interface with other well-established circuit simulators [63]. The initial development of the method included only the effect of inductance [61], but the later developments included the effect of capacitance as well as the modeling of dielectrics [62]. Because of separate expansions of currents and charges, the method can be formulated such that it can perform analysis at very low frequencies, down to dc [65]. The frequency-domain formulation can also be extended to the time domain by modeling the retardation effect as a time delay [64]. This method is expected to become more popular as the need to incorporate electromagnetic effects into the design of high-frequency circuits increases.

12.1.4 Time-Domain Simulation Methods

Like their frequency-domain counterparts, the first-principle time-domain numerical methods can also be divided into two groups. One group of methods solves time-dependent Maxwell's equations or the vector wave equation directly. This group includes the well-known finite difference time-domain (FDTD) method discussed in Chapter 8 and the finite element time-domain (FETD) method discussed in Section 9.4. In addition to these two methods, other approaches include the *transmission-line matrix* (TLM) method, the *finite integration technique* (FIT), the *finite volume time-domain* (FVTD) method, the *pseudo-spectral time-domain* (PSTD) method, the *multiresolution time-domain* (MRTD) method, and the *discontinuous Galerkin time-domain* (DGTD) method. A brief description of each of these methods is given below.

The TLM method [66–69] models a three-dimensional computational domain using three sets of orthogonal, interconnected transmission lines, whose characteristic impedances depend on the properties of the surrounding medium. Huygens' principle is then used to establish a set of equations linking the voltages on each segment of the transmission lines with those of neighboring segments. These equations can then be solved in the time domain to obtain the time profiles of the voltages over the entire computational domain. Although the formulation is unique and original, the geometrical modeling capability and limitation of the TLM method are similar to those of the FDTD method. Furthermore, since the voltages are related directly to the electric fields and Huygens' principle can also be related to Maxwell's equations, the equations established using the TLM method can be derived by finite differencing [70]. Special techniques such as absorbing boundary conditions, perfectly matched layers, and dispersive and non-linear material modeling can also be implemented in the TLM method [71–73].

The FIT [74–76] discretizes the spatial variations in Maxwell's equations in integral form on a dual set of staggered grids. The method can be used for both the time- and

frequency-domain analyses. For orthogonal grids, the method yields a numerical system equivalent to that of Yee's algorithm. Therefore, the numerical characteristics of the FIT are similar to those of Yee's FDTD method. However, the methodology can be applied to non-orthogonal grids, which permits an accurate modeling of more complex geometries [77]. This modification can also be made on the FDTD method, allowing a similar geometrical modeling capability [78–80]. In view of certain equivalences between the finite difference and finite element equations, discussed in Section 11.7.1, one can also expect to observe certain equivalences between the finite integration technique and the finite element method.

The FVTD method [81–85] is a method originated for numerical analysis of problems in fluid dynamics and later adapted for electromagnetic analysis. It computes electromagnetic fields by first discretizing the computational domain into very small volumes and then integrating Maxwell's equations in differential form over each of the volumes. As such, the method can be applied to unstructured meshes and thus enjoys the same geometrical modeling flexibility as the finite element method does. The field in each volume is then coupled to the fields in the adjacent volumes through the fluxes at the interfaces, whose values can be evaluated by interpolation or extrapolation of the averages over the volumes. In particular, the flux at an interface can be split into two components that propagate in opposite directions. In addition to scattering analysis, the method has been applied to the analysis of microwave devices [86–89]. In general, the FVTD method, although free of grid dispersion, is numerically dissipative, which may cause non-physical attenuation to waves propagating over a large distance.

The PSTD method [90,91] is a variation of the FDTD method, where the spatial derivatives are evaluated in the spectral domain using either the discrete Fourier or the Chebyshev transform. This more accurate evaluation reduces the grid dispersion error in the FDTD method. However, the treatment of boundaries and interfaces becomes more complicated, as can be expected, because of the possible field discontinuities. The MRTD method [92–101] is also closely related to the FDTD method. The method employs multiresolution wavelets as basis functions to expand the electric and magnetic fields. Because of the more accurate field expansion, the grid density can be reduced in an MRTD simulation, allowing a more efficient calculation. Furthermore, wavelets can be added and subtracted dynamically during simulation, which makes it possible to design an adaptive algorithm that tailors its computational requirements to the variation of the fields.

The DGTD method [102] can be considered the extension of the finite element method and the FVTD method. It adopts the idea of expanding fields in terms of basis functions and testing the governing equation with weighting functions from the finite element method and the idea of integrating over each element instead of the entire computational domain and then coupling all the elements through fluxes at the interfaces between the elements from the FVTD method. As such, the DGTD method can use higher-order basis functions to achieve a higher-order spatial discretization in a straightforward manner. On the other hand, since the spatial discretization is based on each individual element, there are no requirements that the expansion of the fields have to be the same at the interface between two neighboring elements or that the faces of each element have to match perfectly those of the neighboring elements. More important, the method does not form a global system of equations, which has to be solved in each time step. This important feature can significantly improve the efficiency of the DGTD method. By coupling the fields in the neighboring elements through fluxes, the method can use more robust schemes, such as higher-order Runge–Kutta methods, for the temporal discretization. The DGTD method has recently been adapted to solve the time-dependent Maxwell's equations using either scalar or vector basis functions for spatial discretization [103–108]. The method

discretizes the first-order Maxwell's equations directly and calculates both the electric and magnetic fields either simultaneously or in a leapfrogging manner. An interesting alternative has also been proposed [109] that discretizes the second-order wave equation, calculates the electric and magnetic fields in a leapfrogging manner, and couples the elements based on the surface equivalence principle. This method is obtained by applying a novel domain decomposition algorithm [110] to the FETD method at the element level. It has a computation cost comparable to that of the DGTD method.

As with the frequency-domain methods, the second group of time-domain methods solves *time-domain integral equations* (TDIEs), which can be obtained from their frequency-domain counterparts by the application of the Laplace transform. This topic was covered in Chapter 10 rather briefly, where the TDIEs were solved by the *marching-on-in-time* method. It was seen from Equation 10.6.12 that the most time-consuming part of the solution process is the calculation of the right-hand side in each time step, which involves a series of matrix–vector products. Like what has been done in the frequency domain, this calculation can be accelerated by a fast algorithm with a reduced computational complexity. As mentioned in Chapter 11, many fast algorithms developed for the frequency-domain analysis can be extended into the time domain. Successful examples include the *time-domain adaptive integral method* (TD-AIM) [111–116] and the *plane-wave time-domain* (PWTD) method [117–122]. The latter can be considered the time-domain version of the multilevel fast multipole method. In addition to the marching-on-in-time method, which employs local basis functions to expand the temporal variation, one can also use global basis functions such as the Laguerre polynomials to expand the temporal variation [123–125]. By applying Galerkin testing in the time domain and making use of the orthogonality of the Laguerre polynomials, a *marching-on-in-degree* algorithm can be designed such that the expansion coefficients associated with the lowest degree of the Laguerre polynomials are calculated first, which are then used to calculate the coefficients associated with the next higher degree.

12.1.5 Hybrid Techniques

As illustrated in Figure 12.1, in addition to all the numerical and asymptotic methods, there is a group of methods called *hybrid techniques* that combine two or more different methods to deal with complicated electromagnetic problems. The motivation to develop hybrid techniques is discussed in Chapter 11, along with the development of two specific techniques to demonstrate their enhanced capabilities. Among the hybrid techniques, the early development focused on the hybridization of a numerical method such as the moment method or the finite element method with an asymptotic technique for the analysis of scattering and radiation problems that involve relatively small features (such as antennas, gaps, and slots) on a very large platform (such as an airplane or a ship) [126–132]. These hybrid techniques have achieved great success in providing practical solutions to large and complex engineering problems that cannot be dealt with otherwise even with today's most powerful computational techniques.

12.2 APPLICATIONS OF COMPUTATIONAL ELECTROMAGNETICS

Because electromagnetic phenomena are so pervasive in modern sciences and technologies, computational electromagnetics has an extremely wide range of applications. As mentioned in Chapter 8, the widespread application of computational electromagnetics is

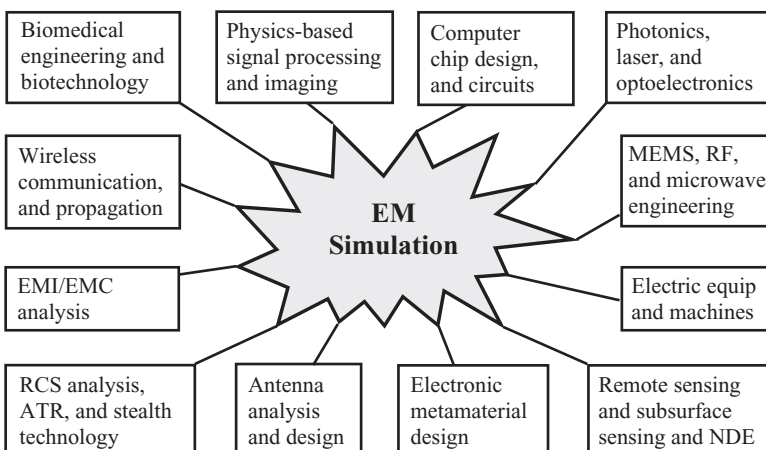


Figure 12.2 Because of the predictive power of Maxwell's equations and the pervasiveness of electromagnetic phenomena in modern technologies, computational electromagnetics can impact many scientific and technological areas. (Expanded from Chew et al. [38].)

mainly due to the predictive power of Maxwell's equations. With the aid of numerical simulations, we can analyze new problems to gain physical insights, evaluate new designs to shorten the design cycle significantly, and characterize complex systems to obtain parameters that are difficult and expensive to measure directly. Figure 12.2 lists some common applications of computational electromagnetics. In the following, we elaborate a few of them.

One of the first applications of numerical analysis in electromagnetics is the analysis of electromagnetic wave scattering by various objects because of its direct relevance to the important technology of radar. Since different objects have different scattering properties, the radar cross-section (RCS) that characterizes the scattering properties is also referred to as the *radar signature*. However, direct measurement of radar signatures of realistic targets such as airplanes is not only difficult but also very time-consuming. Numerical prediction provides a much more practical solution. The dominant methods are the high-frequency asymptotic methods, such as the shooting-and-bouncing-ray method, and the fast integral equation methods. Figure 12.3 shows the range profile, which is related to the time-domain backscattered radar signal, of a rather simple aircraft model [113]. As can be seen clearly, the variation of the range profile correlates closely with the shape of the aircraft and hence can be used to characterize the aircraft. When the range profile is taken at many directions, the data can be used to form a so-called inverse synthetic aperture radar (ISAR) image [133]. Figure 12.4 displays the calculated and measured ISAR images of the airplane shown in Figure 11.24. Such images can be used to identify targets, which is the main objective in research on automatic target recognition (ATR) [134]. Another important application of radar signature prediction is found in the design of low-observable “stealth” airplanes, where the objective is to reduce the return of radar signals, or the backscattered field of electromagnetic waves, of an airplane by modifying the shape of the airplane and applying radar-absorbing materials to its surface. In this case, a highly accurate RCS prediction tool that is capable of modeling fine details of the airplane is vital because of the high requirement for the accuracy of the prediction.

Another early application of numerical analysis in electromagnetics is antenna analysis and design. Antennas play a critical role in wireless communication, remote

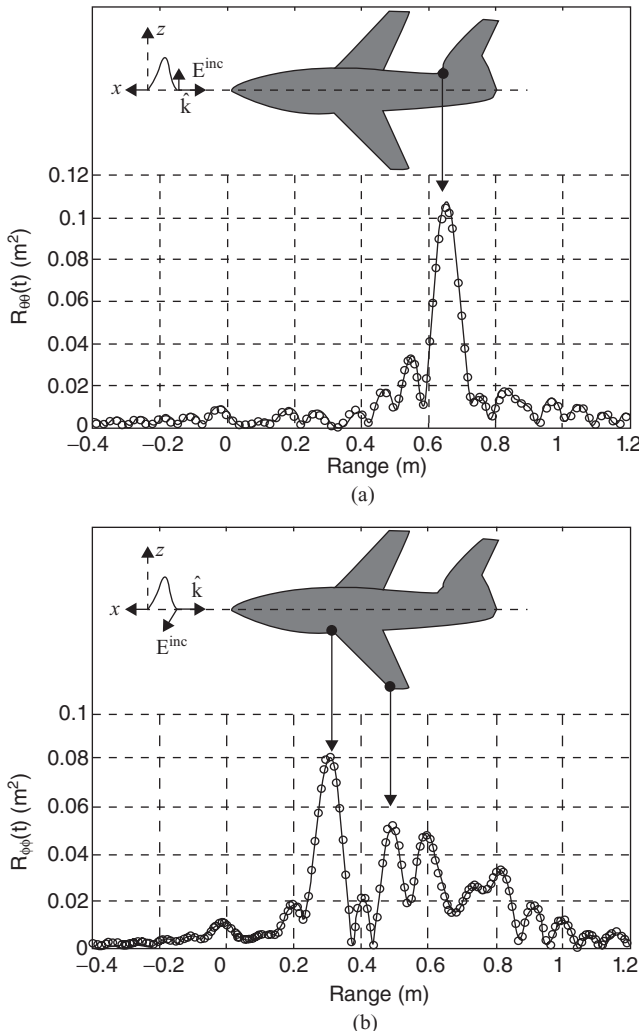


Figure 12.3 Range profile of an aircraft. (a) VV polarization. (b) HH polarization. (After Yilmaz et al. [113], Copyright © 2004 IEEE.)

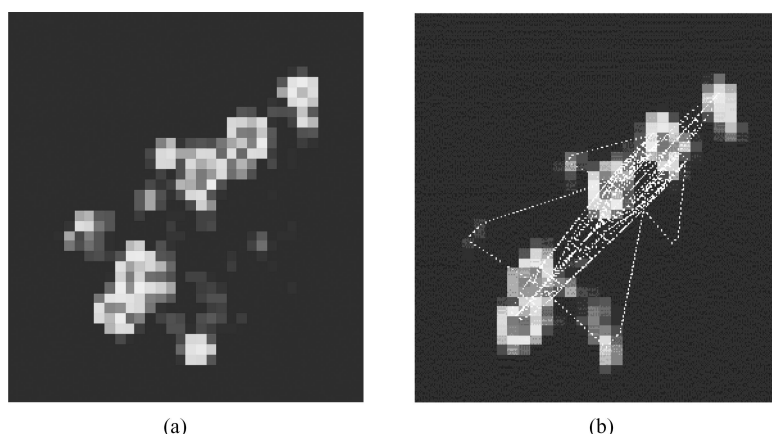


Figure 12.4 Inverse synthetic aperture radar image of an aircraft at 130° from nose-on. (a) Calculation. (b) Measurement. (After Wang and Ling [133], Copyright © 2002 IEEE.) (See color insert.)

sensing, space exploration, defense, electronic warfare, and many other electronic systems. Quantitative antenna analysis is important to the design and optimization of antennas, especially complex antennas that are not easily designed by intuitive approaches. In a typical antenna analysis, the goal is to predict radiation patterns and input impedances. In the case of multiple antennas, such as antenna arrays, it is also important to quantify the mutual coupling between antennas, which can be characterized by either a mutual impedance matrix or a scattering matrix. The prediction of radiation patterns, input impedances, and scattering matrices requires solving Maxwell's equations subject to certain boundary conditions determined by antenna configurations—a typical computational electromagnetics problem. There is a vast amount of research effort dedicated to this problem. Consequently, numerous examples have been published on using numerical methods for antenna analysis. The dominant methods are the asymptotic methods such as PO for reflector antennas that are typically many wavelengths in size; the moment method for wire antennas and microstrip antennas; and the finite element method for more complicated antennas designed with complex materials. A recent book has demonstrated the use of the finite element method for the analysis of a variety of complicated antennas and phased arrays [135].

Modeling and simulation of microwave devices started in the 1960s with numerical analysis of propagation characteristics of waveguides. The dominant methods are the finite element method for devices with a metal enclosure and the moment method for microstrip-like structures for millimeter-wave applications. Designing a microwave device to meet certain specifications is highly challenging because there are many design variables involved. Good intuition based on the understanding of electromagnetic fields is important but by itself cannot yield an optimized design. A fast numerical analysis allows the designer to search through a large design space without time-consuming cut-and-try prototyping. Consider the design of a relatively simple bandpass filter in a rectangular waveguide, as illustrated in Figure 12.5a. This design contains seven variables, which include the widths of the conducting strips and their separations. With the use of a numerical method such as the finite element method, the performance of a specific design can be simulated on a desktop computer in a few seconds. Such a fast simulation allows the designer to examine a large number of designs within a short time and select the best

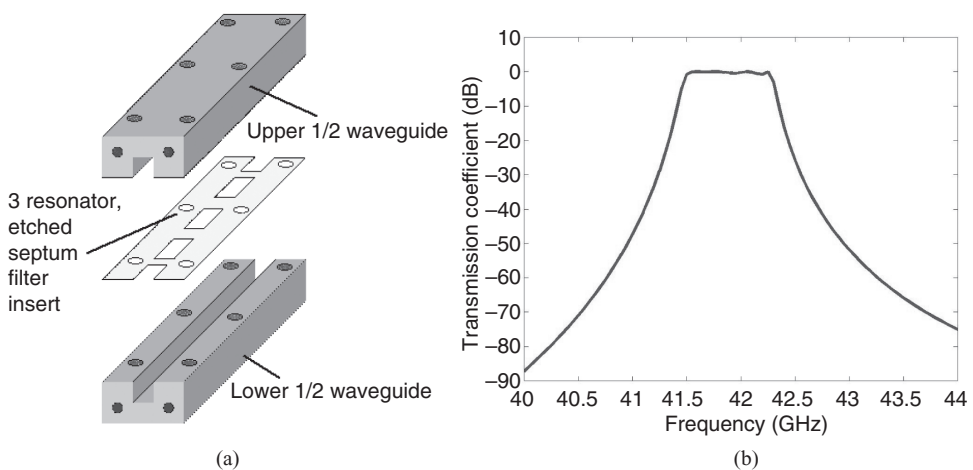


Figure 12.5 Bandpass rectangular waveguide filter. (a) Geometry. (b) Transmission frequency response.

design. It can also be incorporated into an optimization algorithm such as those based on simulated annealing or genetic algorithms to search the design space systematically for a globally optimal design. The performance of one design is shown in Figure 12.5b, where the transmission coefficient is extracted from the solution of the electric field inside the waveguide. In addition to the calculation of the desired parameters, the computed electric and magnetic fields can be visualized using a computer visualization tool. Such field visualization provides valuable insight that cannot be obtained by experiment and points the designer to the direction of better designs. Figure 12.6 shows the distribution of the electric field intensity at several frequencies and the effect of the filter insert on the electric field. As mentioned earlier, this filter has a rather simple structure. Many microwave devices are much more complicated and contain many more design variables, which can be optimized only with a computer-aided design tool based on fast simulation of electromagnetic fields.

A more recent application of computational electromagnetics is the numerical analysis of electromagnetic interference (EMI) and electromagnetic compatibility (EMC) problems [136–138]. Any electronic device will inevitably emit unintended electromagnetic fields that can potentially interfere with other devices, threatening their proper functioning. A component in an electronic device can also interfere undesirably with other components in the same device and affect the overall performance of the device. In such cases, it is critical to determine the source of the interference and eliminate or reduce the interference level. When undesirable interference is unavoidable, such as a high-level electromagnetic pulse generated by lightning or nuclear explosion, electronic systems have to be designed or hardened to withstand the undesired interference. All these problems are typically very complicated because of the high complexity of electronic devices and systems, and for many years they have been dealt with primarily by experiment. With the recent rapid increase in the simulation capability of computational electromagnetics methods in dealing with large, complex problems, numerical analysis has been attempted for the EMI/EMC problems—to evaluate the coupling of an external field into the internal components of

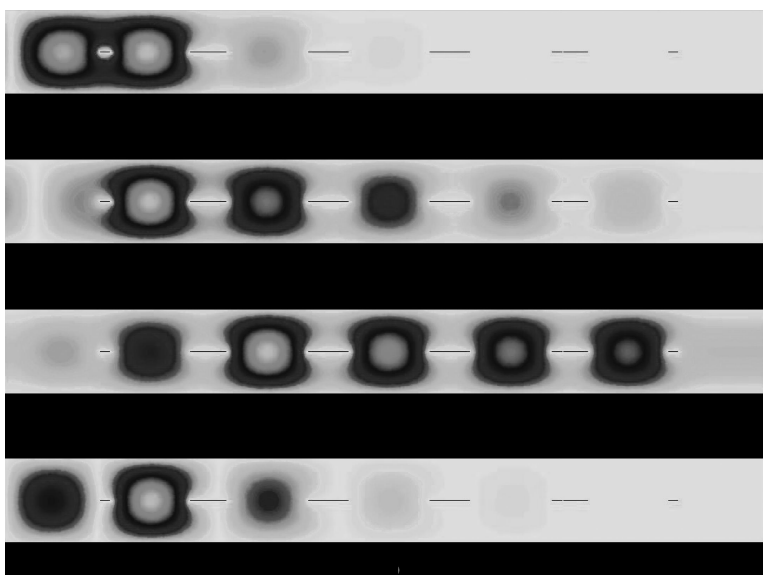


Figure 12.6 Field distribution in a waveguide filter at a few frequencies. (a) 41 GHz.
(b) 41.4 GHz. (c) 42 GHz. (d) 43 GHz. (See color insert.)

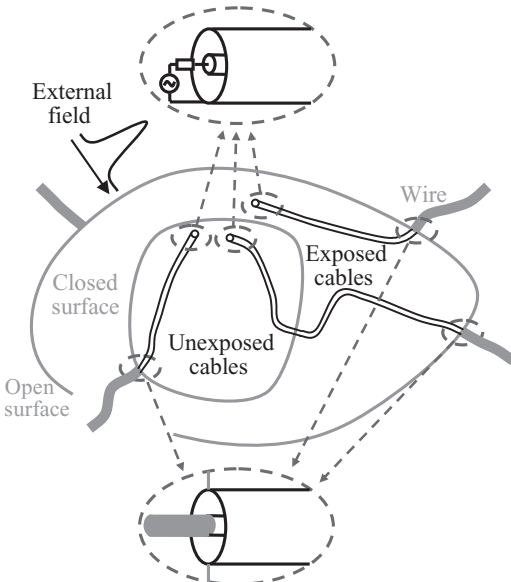


Figure 12.7 Typical electromagnetic compatibility problem: coupling of external field into an interior system.

an electronic system or the mutual coupling between different components of an electronic system, to determine the sources of unwanted electromagnetic emission, to analyze the effectiveness of shielding enclosures, and to gauge the immunity of electronic systems to high-power microwave pulses. Figure 12.7 shows a typical configuration corresponding to the coupling of an external field into the interior of an electronic system through cable connections and apertures on the shielding enclosure. Obviously, to analyze such a problem, the numerical simulation has to be able to compute electromagnetic fields over a broad frequency range on composite structures including electrically large platforms, possibly installed with antennas, shielding enclosures (possibly with apertures), printed circuit boards that support electronic components, and cables that connect various electronic systems. An excellent example based on the finite element analysis can be found in Reference [135]. Another good example [115] concerns the mutual coupling between two antennas mounted on an aircraft, whose surface mesh model is shown in Figure 12.8a. The first antenna is an eight-element log-periodic monopole array trailing the right wing of the aircraft and is connected to an unexposed modulated cable network embedded in the closed wing cavity. The second antenna is a single monopole mounted on the top of the fuselage and is connected to a feed circuit at its base. When this monopole antenna is excited by a voltage source, the radiation will be coupled to the log-periodic array, causing the undesired mutual coupling. This problem was simulated using the moment method in both the frequency and time domains. The computation was accelerated using the adaptive integral method. Figure 12.8b shows the ratio of the power coupled to the log-periodic array to the power input to the monopole antenna. The prediction of the mutual coupling level is useful to the design of the entire system.

Numerical analysis and modeling have long been applied to the analysis of optical problems, such as wave propagation in optical waveguides [139,140]. A more recent problem that has received intense attention is related to the analysis, design, and application of photonic crystals. Photonic crystals are dielectric materials with periodicity in one or more dimensions, which prevents the propagation of optical waves in a certain frequency region called the band gap [141]. This ability to control optical wave propagation can be exploited to design novel optical devices. Numerical analysis is critical for the

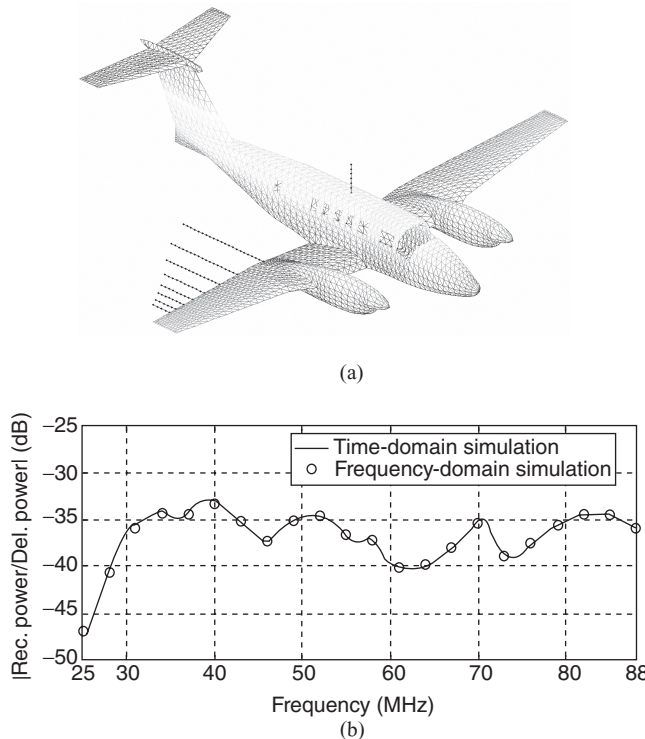


Figure 12.8 Mutual coupling between antennas. (a) Geometrical model of an airplane with an eight-element log-periodic monopole array mounted on the wing and a single monopole antenna mounted on the fuselage. (b) Ratio of the power received by the array to the power delivered to the monopole antenna. (After Bagci et al. [115], Copyright © 2007 IEEE.)

calculation of the band diagram and the characterization of wave propagation and interaction with photonic crystal structures. A two-dimensional photonic crystal is often composed of air holes drilled in a dielectric slab in a hexagonal fashion because it can be fabricated relatively easily. An optical cavity can be created by introducing a point defect (such as removing a unit cell) in a photonic crystal. By confining the energy with distributed Bragg reflection in the lateral direction and total internal reflection in the vertical direction, a high quality factor can be achieved for such a cavity [142,143]. As a basic optical component, such a cavity can in turn be used for the design of various optical devices, especially when coupled to the phenomenon of spontaneous emission. For example, by placing active media inside photonic crystal cavities with a high quality factor, one can obtain a vertical-cavity surface-emission laser (VCSEL) with a strong output power and a narrow line width [144]. However, the design of photonic crystal cavities requires a fast and robust full-wave solution of Maxwell's equations to explore the range of the design space fully. To give an example, when a photonic crystal cavity is formed by removing a single unit cell in a hexagonal lattice, the numerical analysis shows that the cavity supports only degenerate dipole modes in the photonic band gap, whose quality factors are on the order of only a few hundred. However, by reducing the size of the six surrounding holes and shifting them away from the center of the cavity, the cavity can support more cavity modes with much higher quality factors [143]. Figure 12.9a shows one such configuration, where a unit cell without a hole is surrounded by four layers of unit cells with holes with the six neighboring holes modified. For this configuration, there

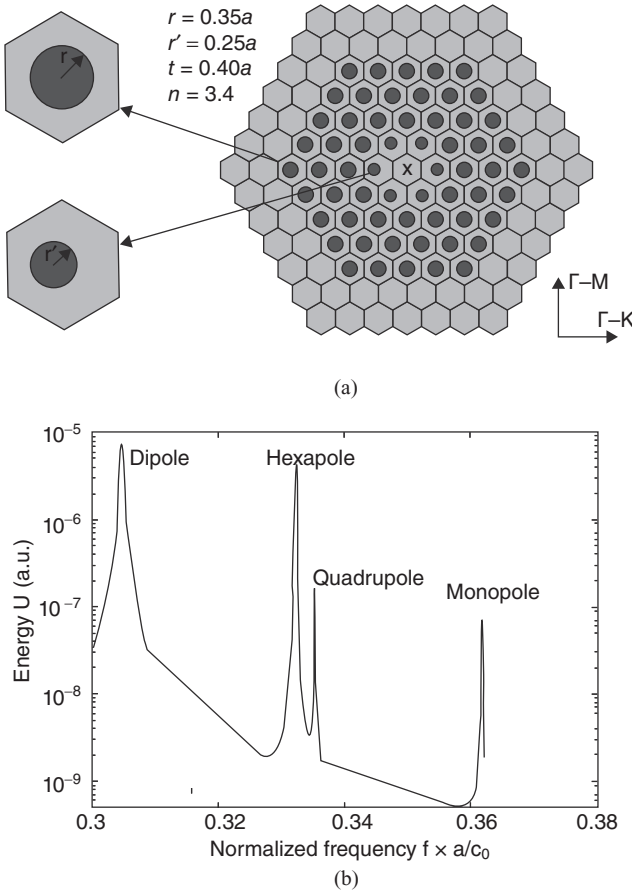


Figure 12.9 Photonic crystal cavity with nine holes in the Γ -K direction. (a) Geometry. The dielectric slab has a refractive index of $n = 3.4$ and a thickness of $t = 0.4a$, where a denotes the lattice constant. The regular holes have a radius of $r = 0.35a$, and the modified holes have a radius of $r' = 0.25a$. (b) Energy stored in the cavity. The locations of the energy peaks correspond to the resonant frequencies of the resonant modes. (After Li and Jin [147], Copyright © 2008 Wiley.)

is a transverse electric (TE_z) band gap, which can be utilized to trap the light in the defect region, thus forming a cavity in the band gap. Figure 12.9b shows the energy stored in the cavity as a function of frequency, which reveals four different types of resonant modes. In addition to the doubly degenerate dipole modes, the other three modes are identified as the doubly degenerate quadrupole modes and non-degenerate hexapole and monopole modes. The field distributions of these modes are displayed in Figure 12.10, where a null is observed for both hexapole and monopole modes at the center of the cavity. The existence of this null significantly decreases the out-of-plane radiation loss and hence increases their quality factors [145]. In fact, when the number of layers of the surrounding unit cells is further increased, the quality factor of the hexapole mode can reach the value of 100,000. Apparently, a numerical analysis tool is useful here to find the optimal values for the radii and offset of the neighboring holes as well as to understand the characteristics of the resonant modes. The calculations shown here were performed using the finite element method in conjunction with a domain decomposition technique [146,147]. Similar results can also be obtained with the FDTD method [143]. In addition to forming a cavity, one

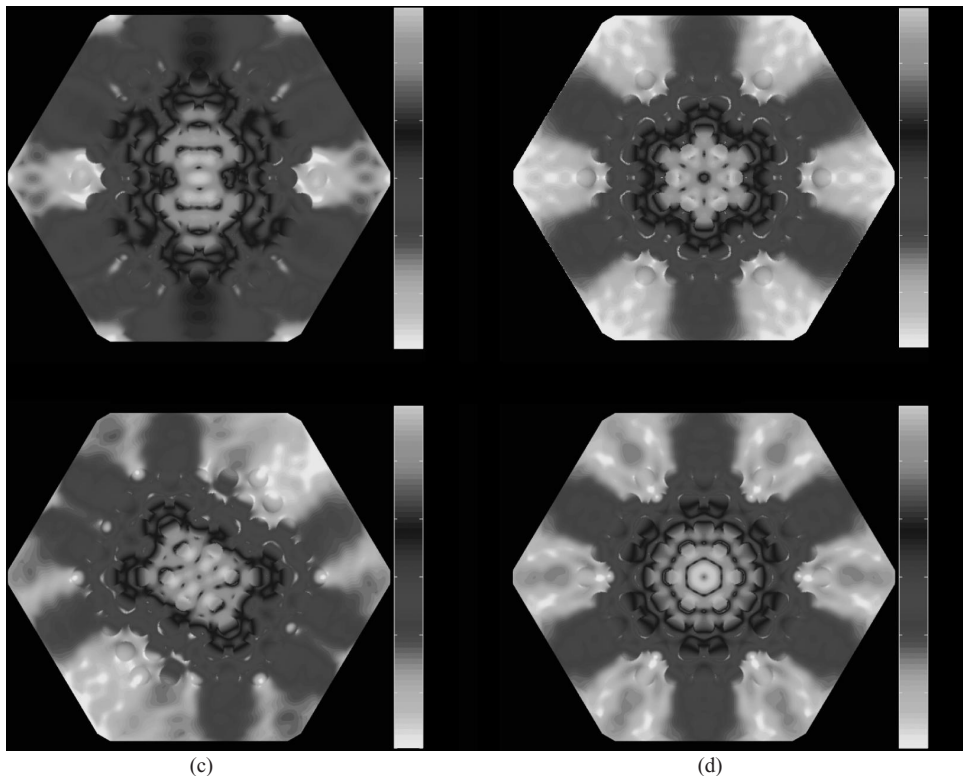


Figure 12.10 Normalized magnitude of the electric field at the midplane. (a) Doubly degenerate dipole modes. (b) Non-degenerate hexapole mode. (c) Doubly degenerate quadrupole modes. (d) Non-degenerate monopole mode. (After Li and Jin [147], Copyright © 2008 Wiley.) (See color insert.)

can also make an optical waveguide by removing a line of unit cells, as illustrated in Figure 12.11.

Computational electromagnetics has also been applied to biomedical engineering because electromagnetic fields are involved in several biomedical technologies such as magnetic resonance imaging (MRI) [148–152], non-invasive microwave imaging [153–155], and electromagnetic hyperthermia [156–160]. A typical MRI system consists of three main components that are all related to electromagnetics. The first component is a main magnet, whose goal is to produce a very strong static magnetic field that has to be extremely uniform (with a deviation on the order of a few parts per million). A stronger static field provides a higher signal-to-noise ratio (SNR) for MRI images, and a better uniformity improves the spatial resolution of the images. The second component is a set of gradient coils, whose goal is to produce three static magnetic fields, in the same direction as the main static field, with linear variation in their intensities in the x -, y -, and z -directions, respectively. When superimposed upon the main static field, they can provide a spatial resolution to the MRI signals. These gradient fields have to be able to switch on and off rapidly. The third component is a radio-frequency (RF) resonator, commonly called an RF coil, which is to produce an RF magnetic field, in the direction transverse to the direction of the main static field, to excite the nuclei in the object to be imaged, and then to receive the MRI signals emitted by the nuclei. This RF field has to be relatively uniform such that the intensity of the received MRI signal can correlate closely with the density of the excited nuclei. The frequency of the RF field is linearly proportional to the

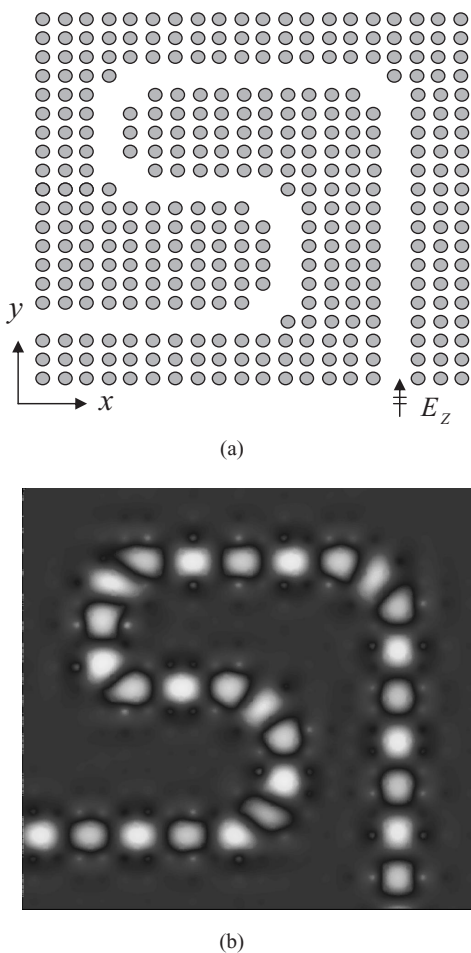


Figure 12.11 Photonic crystal waveguide.
 (a) Top view of the geometry. (b) A snapshot of the field distribution. (After Li and Jin [146], Copyright © 2007 OSA.)
 (See color insert.)

strength of the main static field; hence, the stronger the static field, the higher the frequency of the RF field and the higher the SNR of the MRI signals. However, a higher-frequency RF field interacts strongly with the imaging object such as the human body, making it difficult to design an RF coil to generate a uniform RF field in the volume of interest. Numerical techniques such as the finite element method and the FDTD method have been used extensively to study the interaction of the RF field with imaging objects [150–152]. The analysis can provide critical information such as the RF field inhomogeneity, RF field penetration depth, SNR, and level of specific absorption rate (SAR). The information can be used to design better and safer RF coils or develop imaging schemes that can compensate for the unavoidable field inhomogeneity. Figures 8.14, 8.15, and 9.8 show a few calculated examples related to the RF field interaction with a human head for MRI applications. In non-invasive microwave imaging, the goal is to produce an image of an object comprising different dielectrics by utilizing their different scattering and absorption properties. This technology has a number of applications such as non-destructive evaluation of structures and early detection of breast cancer. The recent development of ultrawide-band microwave technology has shown promise for practical applications since it provides vastly much more information than any single-frequency technologies. In this research, numerical analysis by the FDTD method has been used extensively to build numerical

models and test the feasibility of the technology [153–155]. In electromagnetic hyperthermia, the goal is to use electromagnetic fields to deliberately heat a designated spot in a patient as a therapeutic modality for cancer. This goal is technically very difficult to achieve because for an electromagnetic field to penetrate deeply into the human body its frequency has to be relatively low (around 100 MHz). However, at such a low frequency, it is difficult to focus electromagnetic energy at a designated spot because of its complex interactions with the human body, and to achieve a focus, one has to use multiple radiation elements (applicators) with adjustable amplitude and phase [156]. This difficulty is further complicated by the difficulty of measuring the electromagnetic power and the temperature inside the human body. The only realistic solution is to solve Maxwell's equations numerically to obtain the distribution of electromagnetic power and then solve the bio-heat transfer equation to obtain the temperature variations [157–160]. With such a numerical simulation capability, one can then design an electromagnetic applicator array and optimize the amplitude and phase of the input to each applicator to heat a designated spot. Figure 12.12 shows a numerical example of electromagnetic hyperthermia using an annular

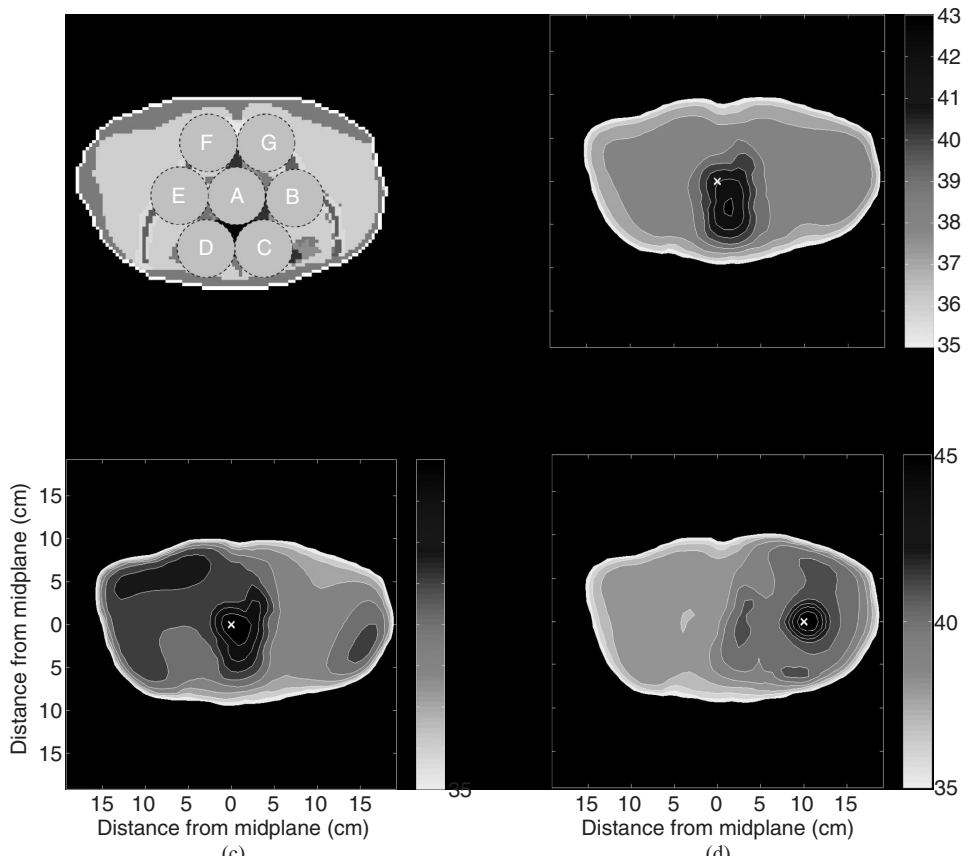


Figure 12.12 Electromagnetic hyperthermia using an annular phased array of applicators at 85 MHz. (a) Cross-section of the human trunk with seven targeted regions. (b) Steady-state temperature optimized based on the specific absorption rate for region A. (c) Steady-state temperature optimized based on the temperature for region A. (d) Steady-state temperature optimized based on the temperature for region B. (After Kowalski and Jin [158], Copyright © 2000 IEEE.) (See color insert.)

phased array of applicators at 85 MHz [158]. In particular, Figure 12.12a shows the cross-section of the human trunk with seven targeted regions. The electromagnetic deposited power measured in terms of the SAR is first calculated by solving Maxwell's equations for the boundary-value problem. This solution is then fed into a feedback control algorithm to optimize the amplitude and phase of each applicator to focus the deposited power at a targeted region. Figure 12.12b shows the temperature distribution optimized based on the SAR for region A. Since the temperature distribution does not coincide exactly with the SAR, the heated spot is not obtained at the targeted region. This problem can be alleviated by solving the bio-heat transfer equation using the deposited power as the input and then optimizing the amplitude and phase of each applicator based on the calculated temperature. The result is shown in Figure 12.12c. Figure 12.12d shows a similar result when the elevated temperature is targeted at region B.

12.3 CHALLENGES IN COMPUTATIONAL ELECTROMAGNETICS

Given an electromagnetic-related problem encountered in practical applications, to seek its numerical solution, we first have to describe the problem mathematically by defining the equivalent boundary-value problem consisting of governing PDEs and boundary conditions. Our knowledge of electromagnetic physics helps us on this first step. Then we need to examine this mathematical problem and develop an effective numerical method for solving the problem. This requires us to have a broad knowledge of numerical methods and their advantages and disadvantages so that we can either choose an existing method or develop a new approach. Once we have formulated the numerical method, we have to implement it into an efficient computer code. Implementation of a numerical method requires a good knowledge of computer programming and linear algebra. Different implementations can have very different efficiencies in terms of computation time and memory usage, although the method being implemented is the same. Once the computer code is developed and fully tested and validated, we can use it to deal with the specific boundary-value problem at hand. This involves the construction of a geometrical model and specification of the electrical properties (permittivity, permeability, and conductivity) for the entire model. This model can then be discretized geometrically and the discrete fields can be computed using the computer code developed. Once the discrete fields are computed, we can calculate the quantities of interest, such as radar cross-sections in a scattering analysis, input impedances and radiation patterns in an antenna analysis, or scattering parameters in a microwave circuit analysis, based on the definition of these quantities and their relation with the computed fields. The entire process of developing a numerical method to solve a practical engineering problem is illustrated in Figure 12.13. From the

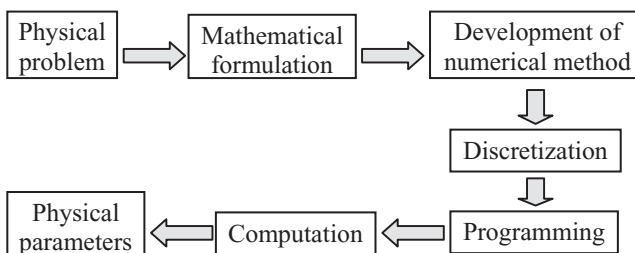


Figure 12.13 Basic steps to solving a practical engineering problem by numerical analysis.

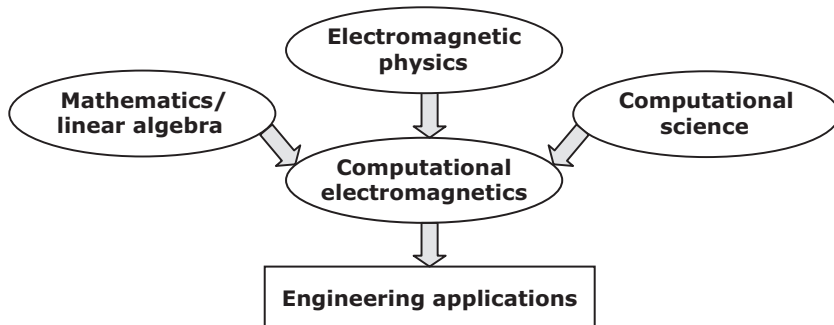


Figure 12.14 Computational electromagnetics is a highly interdisciplinary field that combines physics, mathematics, and computer science to support advanced engineering applications.

chart, we can see clearly that to deal with a numerical analysis of electromagnetic problems, we have to build a solid foundation in electromagnetic physics, mathematics (including linear algebra and functional analysis), and computational science. Of course, to deal with practical engineering problems, we have to understand advanced engineering applications and related issues, such as: What are the important problems that can benefit from a numerical analysis? What are the challenges that we have to tackle to carry out the numerical analysis? How should the verification and validation of the numerical analysis be carried out? It is therefore evident that computational electromagnetics is a highly interdisciplinary field that combines physics, mathematics, and computer science to support advanced engineering applications (Fig. 12.14).

Although computational electromagnetics has a history of nearly a half-century, and, consequently, many numerical methods have been developed during this period and many electromagnetic problems can now be simulated numerically, the field is far from mature. The broad range of applications of electromagnetic fields brings together a broad range of challenges, which include ultra large-scale, multiscale, and multiphysics modeling and simulation. Development of novel and robust numerical methods that can apply effectively across spatial, temporal, and frequency scales of several orders of magnitude and interface seamlessly with the modeling and simulation of other physical phenomena, such as acoustic, circuit, heat transfer, charge transport, and quantum phenomena, is expected to be highly challenging. These challenges will, in turn, open up new opportunities for computational electromagnetics and attract new researchers worldwide to this fascinating field.

REFERENCES

- [1] M. KLINE and I. KAY, *Electromagnetic Theory and Geometrical Optics*. New York: Wiley Interscience, 1965.
- [2] J. B. KELLER, Diffraction by an aperture, *J. Appl. Phys.*, 28(4): 116–130, 1957.
- [3] J. B. KELLER, Geometrical theory of diffraction, *J. Opt. Soc. Am.*, 52(2): 116–130, 1962.
- [4] G. L. JAMES, *Geometrical Theory of Diffraction for Electromagnetic Waves* (3rd edition, revised). London: Peregrinus, 1986.
- [5] R. G. KOYOUMJIAN and P. H. PATHAK, A uniform geometrical theory of diffraction for an edge in a perfectly conducting surface, *Proc. IEEE*, 62(11): 1448–1461, 1974.
- [6] P. H. PATHAK and R. G. KOYOUMJIAN, An analysis of the radiation from aperture on curved surfaces by the geometrical theory of diffraction, *Proc. IEEE*, 62(11): 1438–1447, 1974.
- [7] P. H. PATHAK, Techniques for high frequency problems. *Antenna Handbook, Theory, Application and Design*, edited by Y. T. LO and S. W. LEE. New York: Van Nostrand Reinhold, 1988.
- [8] D. S. AHLUWALIA, R. M. LEWIS, and J. BOERSMA, Uniform asymptotic theory of diffraction by a plane screen, *SIAM J. Appl. Math.*, 16: 783–807, 1968.
- [9] S. W. LEE and G. A. DESCHAMPS, A uniform asymptotic theory of electromagnetic diffraction by a curved

- wedge, *IEEE Trans. Antennas Propagat.*, 24(1): 25–34, 1976.
- [10] R. MITTRA, Y. RAHMAT-SAMII, and W. L. KO, Spectral theory of diffraction, *Appl. Phys.*, 10(1): 1–13, 1976.
- [11] D. P. BOUCHE, F. A. MOLINET, and R. MITTRA, Asymptotic and hybrid techniques for electromagnetic scattering, *Proc. IEEE*, 81(12): 1658–1684, 1993.
- [12] P. Y. UFIMTSEV, Method of edge waves in the physical theory of diffraction, *Izd-Vo Sov. Radio*, 1–243, 1962. Translated by U.S. Air Force Foreign Technology Division, Wright-Patterson AFB, OH, September 1971.
- [13] P. Y. UFIMTSEV, Elementary edge waves and the physical theory of diffraction, *Electromagn.*, 11(2): 125–160, 1991.
- [14] P. Y. UFIMTSEV, *Fundamentals of the Physical Theory of Diffraction*. Piscataway, NJ: IEEE Press, 2007.
- [15] K. M. MITZNER, Incremental length diffraction coefficients. Tech. Rep. AFAL-TR-73-296, Aircraft Division, Northrop Corporation, Los Angeles, CA, 1974.
- [16] R. A. SHORE and A. D. YAGHJIAN, Incremental diffraction coefficients for planar surfaces, *IEEE Trans. Antennas Propagat.*, 34(1): 55–70, 1988.
- [17] A. MICHAELI, Equivalent edge currents for arbitrary aspects of observation, *IEEE Trans. Antennas Propagat.*, 32(3): 252–258, 1984.
- [18] A. MICHAELI, Elimination of infinities in equivalent edge currents *IEEE Trans. Antennas Propagat.*, 34(7): 912–918, 1986; 34(8): 1034–1037, 1986.
- [19] A. BOAG, A fast physical optics (FPO) algorithm for high frequency scattering, *IEEE Trans. Antenna Propagat.*, 52(1): 197–204, 2004.
- [20] A. BOAG and E. MICHIELSEN, A fast physical optics (FPO) algorithm for double-bounce scattering, *IEEE Trans. Antennas Propagat.*, 52(1): 205–212, 2004.
- [21] H. LING, R. CHOU, and S. W. LEE, Shooting and bouncing rays: Calculating the RCS of an arbitrarily shaped cavity, *IEEE Trans. Antennas Propagat.*, 37(2): 194–205, 1989.
- [22] D. ANDRESH, M. HAZLETT, S. W. LEE, D. D. REEVES, D. P. SULLIVAN, and Y. CHU, XPATCH: A high-frequency electromagnetic-scattering prediction code and environment for complex three-dimensional objects, *IEEE Antennas Propagat. Magn.*, 36(1): 65–69, 1994.
- [23] AntFarmTM Antenna Simulation Toolkit, SAIC-DEMCO, Champaign, IL, <http://www.saic.com/products/software/antfarm/>.
- [24] G. LIANG and H. L. BERTONI, Review of ray modeling techniques for site specific propagation prediction. *Wireless Communications: TDMA versus CDMA*, edited by S. G. GLISIC and P. A. LEPPANEN. Norwell, MA: Kluwer, 1997, pp. 323–343.
- [25] A. K. BHATTACHARYYA, *High-Frequency Electromagnetic Techniques*. New York: Wiley, 1995.
- [26] D. BOUCHE, F. MOLINET, and R. MITTRA, *Asymptotic Methods in Electromagnetics*. Berlin, Germany: Springer-Verlag, 1997.
- [27] T. BELYTSCHKO, Y. Y. LU, and L. GU, Element-free Galerkin methods, *Int. J. Numer. Meth. Eng.*, 37(2): 229–256, 1994.
- [28] J. M. MELENK and I. BABUSKA, The partition of unity finite element method: Basic theory and applications, *Comput. Meth. Appl. Mech. Eng.*, 139: 289–314, 1996.
- [29] T. STROUBOULIS, I. BABUSKA, and R. HIDAJAT, The generalized finite element method for Helmholtz equation: Theory, computation, and open problems, *Comput. Meth. Appl. Mech. Eng.*, 195: 4711–4731, 2006.
- [30] L. PROEKT and I. TSUKERMAN, Method of overlapping patches for electromagnetic computation, *IEEE Trans. Magn.*, 38(2): 741–744, 2002.
- [31] C. LU and B. SHANKER, Generalized finite element method for vector electromagnetic problems, *IEEE Trans. Antennas Propagat.*, 55(5): 1369–1381, 2007.
- [32] O. TUNCER, C. LU, N. V. NAIR, B. SHANKER, and L. C. KEMPEL, Further development of vector generalized finite element method and its hybridization with boundary integrals, *IEEE Trans. Antennas Propagat.*, 58(3): 887–899, 2010.
- [33] G. C. HSIAO and R. E. KLEINMAN, Mathematical foundations for error estimation in numerical solutions of integral equations in electromagnetics, *IEEE Trans. Antennas Propagat.*, 45(3): 316–328, 1997.
- [34] S. H. CHRISTIANSEN and J.-C. NÉDÉLEC, A preconditioner for the electric field integral equation based on Calderon formulas, *SIAM J. Numer. Anal.*, 40(3): 1100–1135, 2002.
- [35] R. J. ADAMS, Physical and analytical properties of a stabilized electric field integral equation, *IEEE Trans. Antennas Propagat.*, 52(2): 362–372, 2004.
- [36] R. J. ADAMS and N. J. CHAMPAGNE, II, A numerical implementation of a modified form of the electric field integral equation, *IEEE Trans. Antennas Propagat.*, 52(9): 2262–2266, 2004.
- [37] F. P. ANDRIULLI, K. COOLS, H. BAGCI, F. OLYSLAGER, A. BUFFA, S. CHRISTIANSEN, and E. MICHIELSEN, A multiplicative Calderon preconditioner for the electric field integral equation, *IEEE Trans. Antennas Propagat.*, 56(8): 2398–2412, 2008.
- [38] W. C. CHEW, J. M. JIN, E. MICHIELSEN, and J. M. SONG, Eds., *Fast and Efficient Algorithms in Computational Electromagnetics*. Norwood, MA: Artech House, 2001.
- [39] J. R. PHILLIPS and J. K. WHITE, A precorrected-FFT method for electrostatic analysis of complicated 3D structures, *IEEE Trans. Comput. Aided Des.*, 16: 1059–1072, 1997.
- [40] S.-Q. LI, Y. YU, C. H. CHAN, K. F. CHAN, and L. TSANG, A sparse-matrix/canonical grid method for analyzing densely packed interconnects, *IEEE Trans. Microwave Theory Tech.*, 49(7): 1221–1228, 2001.
- [41] W. HACKBUSCH and Z. P. NOWAK, On the fast matrix multiplication in the boundary element method

- by panel clustering, *Numer. Math.*, 54: 463–491, 1989.
- [42] E. MICHELSSEN and A. BOAG, A multilevel matrix decomposition algorithm for analyzing scattering from large structures, *IEEE Trans. Antennas Propagat.*, 44(8): 1086–1093, 1996.
- [43] W. HACKBUSCH, A sparse matrix arithmetic based on H-matrices, Part I: Introduction to H-matrices, *Computing*, 62: 89–108, 1999.
- [44] W. HACKBUSCH and B. N. KHOROMSKIJ, A sparse H-matrix arithmetic, Part II: Application to multidimensional problems, *Computing*, 64: 21–47, 2000.
- [45] J. BARNES and P. HUT, A hierarchical $O(n \log n)$ force calculation algorithm, *Nature*, 324: 446–449, 1986.
- [46] D. GOPE and V. JANDHYALA, Oct-tree-based multi-level low-rank decomposition algorithm for rapid 3-D parasitic extraction, *IEEE Trans. Comput. Aided Design Integr. Circuits Syst.*, 23(11): 1575–1580, 2004.
- [47] S. KAPUR and D. E. LONG, IES³: A fast integral equation solver for efficient 3-dimensional extraction, *Proc. 37th IEEE/ACM Int. Conf. Computer-Aided Design*, November 1997, pp. 448–455.
- [48] A. BOAG, E. MICHELSSEN, and A. BRANDT, Non-uniform polar grid algorithm for fast field evaluation, *IEEE Antennas Wireless Propagat. Lett.*, 1(7): 142–145, 2002.
- [49] A. BOAG and B. LIVSHITZ, Adaptive non-uniform grid (NG) algorithm for fast capacitance extraction, *IEEE Trans. Microwave Theory Tech.*, 54(9): 3565–3570, 2006.
- [50] B. SHANKER and H. HUANG, Accelerated Cartesian expansions—A fast method for computing of potentials of the form R^{-v} for all real v , *J. Comput. Phys.*, 226: 732–753, 2007.
- [51] L. GREENGARD, J. HUANG, V. ROKHLIN, and S. WANDZURA, Accelerating fast multipole methods for the Helmholtz equation at low frequencies, *IEEE Comput. Sci. Eng.*, 5: 32–38, 1998.
- [52] B. DEMBART and E. YIP, The accuracy of fast multipole methods for Maxwell's equations, *IEEE Comput. Sci. Eng.*, 5: 48–56, 1998.
- [53] H. CHENG, L. GREENGARD, and V. ROKHLIN, A fast adaptive multipole algorithm in three dimensions, *J. Comput. Phys.*, 155: 468–498, 1999.
- [54] T. J. CUI and W. C. CHEW, Fast algorithm for electromagnetic scattering by buried conducting plates of large size, *IEEE Trans. Antennas Propagat.*, 47(6): 1116–1118, 1999.
- [55] B. HU, W. C. CHEW, E. MICHELSSEN, and J. ZHAO, An improved fast steepest descent algorithm for the fast analysis of two-dimensional scattering problems, *Radio Sci.*, 34: 759–772, 1999.
- [56] J. S. ZHAO and W. C. CHEW, Three-dimensional multilevel fast multipole algorithm from static to electrodynamic, *Microw. Opt. Tech. Lett.*, 26: 43–48, 2000.
- [57] B. HU and W. C. CHEW, Fast inhomogenous plane wave algorithm for scattering from objects above the multilayered medium, *IEEE Trans. Geosci. Remote Sensing*, 39(5): 1028–1038, 2001.
- [58] E. DARVE and P. HAVE, Efficient fast multipole method for low-frequency scattering, *J. Comput. Phys.*, 197: 341–363, 2004.
- [59] H. CHENG, W. Y. CRUTCHFIELD, Z. GIMBUTAS, L. F. GREENGARD, J. F. ETHRIDGE, J. HUANG, V. ROKHLIN, and N. YARVIN, and J. ZHAO, A wideband fast multipole method for the Helmholtz equation in three dimensions, *J. Comput. Phys.*, 216: 300–325, 2006.
- [60] M. VIKRAM and B. SHANKER, An incomplete review of fast multipole methods—from static to wideband—as applied to problems in computational electromagnetics, *Appl. Comput. Electromagn. Soc. J.*, 24(2): 79–108, 2009.
- [61] A. RUEHLI, Equivalent circuit models for three-dimensional multiconductor systems, *IEEE Trans. Microwave Theory Tech.*, 22(3): 216–221, 1974.
- [62] A. RUEHLI and H. HEEB, Circuit models for three-dimensional geometries including dielectrics, *IEEE Trans. Microwave Theory Tech.*, 40(7): 1507–1516, 1992.
- [63] C. WOLLENBERG and A. GURISCH, Analysis of 3-D interconnect structures with PEEC using SPICE, *IEEE Trans. Electromagn. Compatibility*, 41(4): 412–417, 1999.
- [64] A. E. RUEHLI, G. ANTONINI, J. ESCH, J. EKMAN, A. MAYO, and A. ORLANDI, Nonorthogonal PEEC formulation for time- and frequency-domain EM and circuit modeling, *IEEE Trans. Electromagn. Compatibility*, 45(2): 167–176, 2003.
- [65] D. GOPE, A. RUEHLI, and V. JANDHYALA, Solving low-frequency EM-CKT problems using the PEEC method, *IEEE Trans. Adv. Packaging*, 30(2): 313–320, 2007.
- [66] P. B. JOHNS and R. L. BEURLE, Numerical solution of 2-dimensional scattering problems using a transmission-line matrix, *Proc. Inst. Elec. Eng.*, 118(9): 1203–1208, 1971.
- [67] P. B. JOHNS, A symmetrical condensed node for the TLM method, *IEEE Trans. Microwave Theory Tech.*, 35(4): 370–377, 1987.
- [68] W. J. R. HOEFER, The transmission-line matrix method—Theory and applications, *IEEE Trans. Microwave Theory Tech.*, 33(10): 882–893, 1985.
- [69] C. CHRISTOPOULOS, *The Transmission-Line Modeling Method: TLM*. Piscataway, NJ: IEEE Press, 1995.
- [70] H. JIN and R. VAHLDIECK, Direct derivations of TLM symmetrical condensed node and hybrid symmetrical condensed node from Maxwell's equations using centered differencing and averaging, *IEEE Trans. Microwave Theory Tech.*, 42(12): 2554–2561, 1994.
- [71] Z. CHEN, M. M. NEY, and W. J. R. HOEFER, Absorbing and connecting boundary conditions for the TLM method, *IEEE Trans. Microwave Theory Tech.*, 41(11): 2016–2024, 1993.
- [72] N. PENA and M. M. NEY, Absorbing boundary conditions using perfectly matched layer (PML) technique for three-dimensional TLM simulations, *IEEE Trans. Microwave Theory Tech.*, 45(10): 1749–1755, 1997.

- [73] J. PAUL, C. CHRISTOPOULOS, and D. W. P. THOMAS, Generalized material models in TLM, *IEEE Trans. Antennas Propagat.*, 47(10): 1528–1542, 1999; 50(7): 997–1004, 2002.
- [74] T. WEILAND, A discretization method for the solution of Maxwell's equations for six-component fields, *Arch. Elek. Übertragung.*, 31(3): 116–120, 1977.
- [75] T. WEILAND, Time domain electromagnetic field computation with finite difference methods, *Int. J. Numer. Model. Electron. Network Dev. Field.*, 9: 295–319, 1996.
- [76] M. CLEMENS and T. WEILAND, Discrete electromagnetism with the finite integration technique, *Prog. Electromagn. Res.*, 32: 65–87, 2001.
- [77] R. SCHUHMANN and T. WEILAND, The nonorthogonal finite integration technique applied to 2D- and 3D-eigenvalue problems, *IEEE Trans. Magn.*, 36(4): 897–901, 2000.
- [78] S. DEY and R. MITTRA, A locally conformal finite-difference time-domain (FDTD) algorithm for modeling three-dimensional perfectly conducting objects, *IEEE Microwave Guided Wave Lett.*, 7(9): 273–275, 1997.
- [79] W. YU and R. MITTRA, A conformal finite difference time domain technique for modeling curved dielectric surfaces, *IEEE Microwave Guided Wave Lett.*, 11(1): 25–27, 2001.
- [80] I. A. ZAGORODNOV, R. SCHUHMANN, and T. WEILAND, A uniformly stable conformal FDTD-method in Cartesian grids, *Int. J. Numer. Model. Electron. Network Dev. Field.*, 16: 127–141, 2003.
- [81] V. SHANKAR, A. H. MOHAMMADIAN, and W. F. HALL, A time-domain finite-volume treatment for the Maxwell's equations, *Electromagn.*, 10(1): 127–145, 1990.
- [82] N. MADSEN and R. ZIOLKOWSKI, A three-dimensional modified finite volume technique for Maxwell's equations, *Electromagn.*, 10(1): 147–161, 1990.
- [83] R. HOLLAND, V. P. CABLE, and L. C. WILSON, Finite-volume time-domain (FVT) techniques for EM scattering, *IEEE Trans. Electromagn. Compat.*, 33(4): 281–294, 1991.
- [84] J. S. SHANG, Characteristic-based algorithms for solving the Maxwell equations in the time-domain, *IEEE Antennas Propagat. Mag.*, 37(3): 15–25, 1995.
- [85] N. MADSEN, Divergence preserving discrete surface integral methods for Maxwell's equations using non-orthogonal unstructured grids, *J. Comput. Phys.*, 119: 34–45, 1995.
- [86] C. FUMEAX, D. BAUMANN, and R. VAHLDIECK, Advanced FVT simulations of dielectric resonator antennas and feed structures, *J. Appl. Comput. Electromagn. Soc.*, 19: 155–164, 2004.
- [87] D. BAUMANN, C. FUMEAX, P. LEUCHTMANN, and R. VAHLDIECK, Finite-volume time-domain (FVT) modeling of a broad-band double-ridged horn antenna, *Int. J. Numer. Model. Electron. Network Dev. Field.*, 17(3): 285–298, 2004.
- [88] C. FUMEAX, D. BAUMANN, P. LEUCHTMANN, and R. VAHLDIECK, A generalized local time-step scheme for efficient FVT simulations in strongly inhomogeneous meshes, *IEEE Trans. Microwave Theory Tech.*, 52(3): 1067–1076, 2004.
- [89] D. BAUMANN, C. FUMEAX, and R. VAHLDIECK, Field-based scattering-matrix extraction scheme for the FVT method exploiting a flux-splitting algorithm, *IEEE Trans. Microwave Theory Tech.*, 53(11): 3595–3605, 2005.
- [90] Q. H. LIU, and G. ZHAO, Review of PSTD methods for transient electromagnetics, *Int. J. Numer. Model. Electron. Network Dev. Field.*, 22(17): 299–323, 2004.
- [91] Q. H. LIU and G. ZHAO, Advances in PSTD techniques. *Computational Electrodynamics: The Finite-Difference Time-Domain Method*, edited by A. TAFLOVE and S. HAGNESS. Boston, MA: Artech House, 2005, pp. 847–882.
- [92] M. KRUMPHOLZ and L. P. B. KATEHI, New time domain schemes based on multiresolution analysis, *IEEE Trans. Microwave Theory Tech.*, 44(4): 555–561, 1996.
- [93] E. TENTZERIS, R. L. ROBERTSON, J. F. HARVEY, and L. P. B. KATEHI, Stability and dispersion analysis of Battle-Lemarie-Based MRTD schemes, *IEEE Trans. Microwave Theory Tech.*, 47(7): 1004–1013, 1999.
- [94] G. CARAT, R. GILLARD, J. CITERNE, and J. WIART, An efficient analysis of planar microwave circuits using a DWT-based Haar MRTD scheme, *IEEE Trans. Microwave Theory Tech.*, 48(12): 2261–2270, 2000.
- [95] T. DOGARU and L. CARIN, Multiresolution time-domain using CDF biorthogonal wavelets, *IEEE Trans. Microwave Theory Tech.*, 49(5): 902–912, 2001.
- [96] T. DOGARU and L. CARIN, Application of Haar-wavelet-based multiresolution time-domain schemes to electromagnetic scattering problems, *IEEE Trans. Antennas Propagat.*, 50(6): 774–784, 2002.
- [97] C. SARRIS and L. P. B. KATEHI, Fundamental gridding-related dispersion effects in multiresolution time-domain schemes, *IEEE Trans. Microwave Theory Tech.*, 49(12): 2248–2257, 2001.
- [98] N. BUSHYAGER, J. PAPAPOLYMEROU, and M. M. TENTZERIS, A composite cell multiresolution time-domain technique for the design of antenna systems including electromagnetic band gap and via-array structures, *IEEE Trans. Antennas Propagat.*, 53(8): 2700–2710, 2005.
- [99] E. M. TENTZERIS, A. CANGELLARIS, L. P. B. KATEHI, and J. HARVEY, Multiresolution time-domain (MRTD) adaptive schemes using arbitrary resolutions of wavelets, *IEEE Trans. Microwave Theory Tech.*, 50(2): 501–516, 2002.
- [100] N. A. BUSHYAGER and M. M. TENTZERIS, *MRTD (Multiresolution Time Domain) Method in Electromagnetics*. San Rafael, CA: Morgan & Claypool, 2005.
- [101] Y. C. CHEN, Q. S. CAO, and R. MITTRA, *Multiresolution Time Domain Scheme for Electromagnetic Engineering*. Hoboken, NJ: Wiley, 2005.

- [102] B. COCKBURN, G. E. KARNIADAKIS, and C.-W. SHU, *Discontinuous Galerkin Methods: Theory, Computation and Applications*, vol. 11. Berlin, Germany: Springer-Verlag, 2000.
- [103] J. S. HESTHAVEN and T. WARBURTON, Nodal high-order methods on unstructured grids—I. Time-domain solution of Maxwell's equations, *J. Comput. Phys.*, 181(1): 186–211, 2002.
- [104] T. LU, P. ZHANG, and W. CAI, Discontinuous Galerkin method for dispersive and lossy Maxwell's equations and PML boundary conditions, *J. Comput. Phys.*, 200(2): 549–580, 2004.
- [105] T. XIAO and Q. H. LIU, Three-dimensional unstructured-grid discontinuous Galerkin method for Maxwell's equations with well-posed perfectly matched layer, *Microw. Opt. Tech. Lett.*, 46(5): 459–463, 2005.
- [106] S. GEDNEY, C. LUO, B. GUERNSEY, J. A. RODEN, R. CRAWFORD, and J. A. MILLER, The discontinuous Galerkin finite-element time-domain method (DGFETD): A high order, globally-explicit method for parallel computation, *IEEE Int. Symp. Electromagn. Compat.*, Honolulu, HI, pp. 1–3, July 2007.
- [107] S. D. GEDNEY, C. LUO, J. A. RODEN, R. D. CRAWFORD, B. GUERNSEY, J. A. MILLER, and E. W. LUCAS, A discontinuous Galerkin finite element time domain method with PML, *IEEE Antennas Propagat. Soc. Int. Symp.*, San Diego, CA, July 2008.
- [108] N. GODEL, S. LANGE, and M. CLEMENS, Time domain discontinuous Galerkin method with efficient modeling of boundary conditions for simulations of electromagnetic wave propagation, *Asia-Pacific Symp. Electromagn. Compat.*, Singapore, pp. 594–597, May 2008.
- [109] Z. LOU and J. M. JIN, A new explicit time-domain finite-element method based on element-level decomposition, *IEEE Trans. Antennas Propagat.*, 54(10): 2990–2999, 2006.
- [110] Z. LOU and J. M. JIN, A novel dual-field time-domain finite-element domain-decomposition method for computational electromagnetics, *IEEE Trans. Antennas Propagat.*, 54(6): 1850–1862, 2006.
- [111] A. E. YILMAZ, D. S. WEILE, J. M. JIN, and E. MICHIELSEN, A fast Fourier transform accelerated marching-on-in-time algorithm (MOT-FFT) for electromagnetic analysis, *Electromagnetics*, 21(3): 181–197, 2001.
- [112] A. E. YILMAZ, D. S. WEILE, J. M. JIN, and E. MICHIELSEN, A hierarchical FFT algorithm (HIL-FFT) for the fast analysis of transient electromagnetic scattering, *IEEE Trans. Antennas Propagat.*, 50(7): 971–982, 2002.
- [113] A. E. YILMAZ, J. M. JIN, and E. MICHIELSEN, Time-domain adaptive integral method for surface integral equations, *IEEE Trans. Antennas Propagat.*, 52(10): 2692–2708, 2004.
- [114] A. E. YILMAZ, J. M. JIN, and E. MICHIELSEN, Analysis of low-frequency electromagnetic transients by an extended time-domain adaptive integral method, *IEEE Trans. Adv. Packaging (TADVP)*, 30(2): 301–312, 2007.
- [115] H. BAGCI, A. E. YILMAZ, J. M. JIN, and E. MICHIELSEN, Fast and rigorous analysis of EMC/EMI phenomena of electrically large and complex cable-loaded structures, *IEEE Trans. Electromagn. Compat.*, 49(2): 361–381, 2007.
- [116] H. BAGCI, A. E. YILMAZ, J. M. JIN, and E. MICHIELSEN, Time domain adaptive integral method for surface integral equations. *Modeling and Computations in Electromagnetics*, edited by H. AMMARI. Berlin: Springer-Verlag, 2007, pp. 65–104.
- [117] A. A. ERGIN, B. SHANKER, and E. MICHIELSEN, Fast transient analysis of acoustic wave scattering from rigid bodies using a two-level plane wave time domain algorithm, *J. Acoust. Soc. Am.*, 106: 2405–2416, 1999.
- [118] A. A. ERGIN, B. SHANKER, and E. MICHIELSEN, The plane-wave time-domain algorithm for the past analysis of transient wave phenomena, *IEEE Antennas Propagat. Magn.*, 41(1): 39–52, 1999.
- [119] A. A. ERGIN, B. SHANKER, and E. MICHIELSEN, Fast analysis of transient acoustic wave scattering from rigid bodies using the multilevel plane wave time domain algorithm, *J. Acoust. Soc. Am.*, 107: 1168–1178, 2000.
- [120] B. SHANKER, A. A. ERGIN, K. AYGUN, and E. MICHIELSEN, Analysis of transient electromagnetic scattering phenomena using a two-level plane wave time-domain algorithm, *IEEE Trans. Antennas Propagat.*, 48(4): 510–523, 2000.
- [121] B. SHANKER, A. A. ERGIN, and E. MICHIELSEN, Plane-wave-time-domain-enhanced marching-on-in-time scheme for analyzing scattering from homogeneous dielectric structures, *J. Opt. Soc. Am. A*, 19: 716–726, 2002.
- [122] B. SHANKER, A. A. ERGIN, M. Y. LU, and E. MICHIELSEN, Fast analysis of transient electromagnetic scattering phenomena using the multilevel plane wave time domain algorithm, *IEEE Trans. Antennas Propagat.*, 51(3): 628–641, 2003.
- [123] Y. S. CHUNG, T. K. SARKAR, B. H. JUNG, M. SALAZAR-PALMA, Z. JI, S. JANG, and K. KIM, Solution of time domain electric field integral equation using the Laguerre polynomials, *IEEE Trans. Antennas Propagat.*, 52(9): 2319–2328, 2004.
- [124] B. JUNG, T. K. SARKAR, Y. CHUNG, M. SALAZAR-PALMA, Z. JI, S. JANG, and K. KIM, Transient electromagnetic scattering from dielectric objects using the electric field integral equation with Laguerre polynomials as temporal basis functions, *IEEE Trans. Antennas Propagat.*, 52(9): 2329–2340, 2004.
- [125] Z. JI, T. K. SARKAR, B. H. JUNG, Y. S. CHUNG, M. SALAZAR-PALMA, and M. YUAN, A stable solution of time domain electric field integral equation for thin-wire antennas using the Laguerre polynomials, *IEEE Trans. Antennas Propagat.*, 52(10): 2641–2649, Oct. 2004.
- [126] W. D. BURNSIDE, C. L. YU, and R. J. MARHEFKA, A technique to combine the geometrical theory of

- diffraction and the moment method, *IEEE Trans. Antennas Propagat.*, 23(4): 551–558, 1975.
- [127] G. A. THIELE and T. H. NEWHOUSE, A hybrid technique for combining moment methods with the geometrical theory of diffraction, *IEEE Trans. Antennas Propagat.*, 23(1): 62–69, 1975.
- [128] G. A. THIELE, Overview of selected hybrid methods in radiating system analysis, *Proc. IEEE*, 80(1): 66–78, 1992.
- [129] J. M. JIN, F. LING, S. T. CAROLAN, J. M. SONG, W. C. GIBSON, W. C. CHEW, C. C. LU, and R. KIPP, A hybrid SBR/MoM technique for analysis of scattering from small protrusions on a large conducting body, *IEEE Trans. Antennas Propagat.*, 46(9): 1349–1356, 1998.
- [130] A. D. GREENWOOD, S. S. NI, J. M. JIN, and S. W. LEE, Hybrid FEM/SBR method to compute the radiation pattern from a microstrip patch antenna in a complex geometry, *Microw. Opt. Tech. Lett.*, 13(2): 84–87, 1996.
- [131] M. ALAYDRUS, V. HANSEN, and T. F. EIBERT, Hybrid²: Combining the three-dimensional hybrid finite element–boundary integral technique for planar multilayered media with the uniform geometrical theory of diffraction, *IEEE Trans. Antennas Propagat.*, 50(1): 67–74, 2002.
- [132] R. FERNANDEZ-RECIO, L. E. GARCIA-CASTILLO, I. GOMEZ-REVUELTO, and M. SALAZAR-PALMA, Fully coupled multi-hybrid FEM-PO/PTD-UTD method for the analysis of radiation problems, *IEEE Trans. Magn.*, 43(4): 1341–1344, 2007.
- [133] Y. WANG and H. LING, Efficient radar signature prediction using a frequency-aspect interpolation technique based on adaptive feature extraction, *IEEE Trans. Antennas Propagat.*, 50(2): 122–131, 2002.
- [134] A. W. RIHACZEK and S. J. HERSHKOWITZ, *Theory and Practice of Radar Target Identification*. Norwood, MA: Artech House, 2000.
- [135] J.-M. JIN and D. J. RILEY, *Finite Element Analysis of Antennas and Arrays*. Hoboken, NJ: Wiley, 2008.
- [136] C. R. PAUL, *Introduction to Electromagnetic Compatibility* (2nd edition). Hoboken, NJ: Wiley, 2006.
- [137] D. POLJAK, *Advanced Modeling in Computational Electromagnetic Compatibility*. Hoboken, NJ: Wiley, 2007.
- [138] H. W. OTT, *Electromagnetic Compatibility Engineering*. Hoboken, NJ: Wiley, 2009.
- [139] M. KOSHIBA, *Optical Waveguide Theory by the Finite Element Method*. Tokyo, Japan: KTK Scientific Publishers, 1992.
- [140] F. A. FERNANDEZ and Y. LU, *Microwave and Optical Waveguide Analysis by the Finite Element Method*. New York: Wiley, 1996.
- [141] J. D. JOANNOPoulos, S. G. JOHNSON, J. N. WINN, and R. D. MEADE, *Photonic Crystals: Molding the Flow of Light* (2nd edition). Princeton, NJ: Princeton University Press, 2008.
- [142] O. PAINTER, R. K. LEE, A. SCHERER, A. YARIV, J. D. O'BRIEN, P. D. DAPKUS, and I. KIM, Two-dimensional photonic band-gap defect mode laser, *Sci.*, 284: 1819–1821, 1999.
- [143] H. Y. RYU, H. G. PARK, and Y. H. LEE, Two-dimensional photonic crystal semiconductor lasers: computational design, fabrication and characterization, *IEEE J. Sel. Top. Quantum Electron.*, 8: 891–908, 2002.
- [144] J. L. JEWELL, J. P. HARBISON, A. SCHERER, Y. H. LEE, and L. T. FLOREZ, Vertical-cavity surface-emitting lasers: Design, growth, fabrication, characterization, *IEEE J. Quantum Electron.*, 27: 1332–1346, 1996.
- [145] S. G. JOHNSON, S. FAN, A. MEKIS, and J. D. JOANNOPoulos, Multipole-cancellation mechanism for high-*Q* cavities in the absence of a complete photonic band gap, *Appl. Phys. Lett.*, 78: 3388–3390, 2001.
- [146] Y. J. LI and J. M. JIN, A fast full-wave analysis of large-scale three-dimensional photonic crystal devices, *J. Opt. Soc. Am. B.*, 24(9): 2406–2415, 2007.
- [147] Y. J. LI and J. M. JIN, Simulation of photonic crystal nanocavity using the FETI-DPEM method, *Microw. Opt. Tech. Lett.*, 50(8): 2083–2086, 2008.
- [148] J. M. JIN, *Electromagnetic Analysis and Design in Magnetic Resonance Imaging*. Boca Raton, FL: CRC Press, 1998.
- [149] P. M. ROBITAILLE and L. J. BERLINER, *Ultra High Field Magnetic Resonance Imaging*. New York: Springer, 2006.
- [150] O. P. GANDHI and X. B. CHEN, Specific absorption rates and induced current densities for an anatomy-based model of the human for exposure to time-varying magnetic fields of MRI, *Magn. Reson. Med.*, 41: 816–823, 1999.
- [151] B. K. LI, F. LIU, and S. CROZIER, High-field magnetic resonance imaging with reduced field/tissue RF artifacts—A modeling study using hybrid MoM/FEM and FDTD technique, *IEEE Trans. Electromagn. Compat.*, 48(4): 628–633, 2006.
- [152] M. KOWALSKI, J. M. JIN, and J. CHEN, Computation of the signal-to-noise ratio of high-frequency magnetic resonance imagers, *IEEE Trans. Biomed. Eng.*, 47(11): 1525–1533, 2000.
- [153] S. C. HAGNESS, A. TAFLOVE, and J. E. BRIDGES, Three-dimensional FDTD analysis of a pulsed microwave confocal system for breast cancer detection: Design of an antenna-array element, *IEEE Trans. Antennas Propagat.*, 47(5): 783–791, 1999.
- [154] E. J. BOND, X. LI, S. C. HAGNESS, and B. D. VAN VEEN, Microwave imaging via space-time beamforming for early detection of breast cancer, *IEEE Trans. Antennas Propagat.*, 51(8): 1690–1705, 2003.
- [155] X. LI, S. K. DAVIS, S. C. HAGNESS, D. W. van der WEIDE, and B. D. VAN VEEN, Microwave imaging via space-time beamforming: experimental investigation of tumor detection in multilayer breast phantoms, *IEEE Trans. Microwave Theory Tech.*, 52(8): 1856–1865, 2004.

- [156] P. F. TURNER, Regional hyperthermia with an annular phased array, *IEEE Trans. Biomed. Eng.*, 31(1): 106–113, 1984.
- [157] J.-Y. CHEN and O. P. GANDHI, Numerical simulation of annular-phased arrays of dipoles for hyperthermia of deep-seated tumors, *IEEE Trans. Biomed. Eng.*, 39(2): 209–216, 1992.
- [158] M. E. KOWALSKI and J. M. JIN, Determination of electromagnetic phased array driving signals for hyperthermia based on a steady-state temperature criterion, *IEEE Trans. Microwave Theory Tech.*, 48(11): 1864–1873, 2000.
- [159] M. E. KOWALSKI, B. BABAK, J. M. JIN, and A. G. WEBB, Optimization of electromagnetic phased-arrays for hyperthermia using magnetic resonance temperature estimation, *IEEE Trans. Biomed. Eng.*, 49(11): 1229–1241, 2002.
- [160] M. E. KOWALSKI and J. M. JIN, A temperature-based feedback control system for electromagnetic phased-array hyperthermia: Theory and simulation, *Phys. Med. Biol.*, 48: 633–651, 2003.

APPENDIX

VECTOR IDENTITIES

$$\mathbf{a} \cdot (\mathbf{b} \times \mathbf{c}) = \mathbf{b} \cdot (\mathbf{c} \times \mathbf{a}) = \mathbf{c} \cdot (\mathbf{a} \times \mathbf{b})$$

$$\mathbf{a} \times (\mathbf{b} \times \mathbf{c}) = (\mathbf{a} \cdot \mathbf{c})\mathbf{b} - (\mathbf{a} \cdot \mathbf{b})\mathbf{c}$$

$$\nabla(ab) = a\nabla b + b\nabla a$$

$$\nabla \cdot (a\mathbf{b}) = a\nabla \cdot \mathbf{b} + \mathbf{b} \cdot \nabla a$$

$$\nabla \times (a\mathbf{b}) = a\nabla \times \mathbf{b} - \mathbf{b} \times \nabla a$$

$$\nabla(\mathbf{a} \cdot \mathbf{b}) = \mathbf{a} \times \nabla \times \mathbf{b} + \mathbf{b} \times \nabla \times \mathbf{a} + (\mathbf{a} \cdot \nabla)\mathbf{b} + (\mathbf{b} \cdot \nabla)\mathbf{a}$$

$$\nabla \cdot (\mathbf{a} \times \mathbf{b}) = \mathbf{b} \cdot \nabla \times \mathbf{a} - \mathbf{a} \cdot \nabla \times \mathbf{b}$$

$$\nabla \times (\mathbf{a} \times \mathbf{b}) = \mathbf{a} \nabla \cdot \mathbf{b} - \mathbf{b} \nabla \cdot \mathbf{a} - (\mathbf{a} \cdot \nabla)\mathbf{b} + (\mathbf{b} \cdot \nabla)\mathbf{a}$$

$$\nabla \cdot (\nabla a) = \nabla^2 a$$

$$\nabla \times (\nabla \times \mathbf{a}) = \nabla(\nabla \cdot \mathbf{a}) - \nabla^2 \mathbf{a}$$

$$\nabla \times (\nabla a) = 0$$

$$\nabla \cdot (\nabla \times \mathbf{a}) = 0$$

INTEGRAL THEOREMS

$$\text{Gauss' theorem: } \iiint_V \nabla \cdot \mathbf{f} \, dV = \iint_S \mathbf{f} \cdot d\mathbf{S}$$

$$\text{Stokes' theorem: } \iint_S (\nabla \times \mathbf{f}) \cdot d\mathbf{S} = \oint_C \mathbf{f} \cdot d\mathbf{l}$$

COORDINATE TRANSFORMATION

$$\hat{\rho} = \hat{x} \cos \phi + \hat{y} \sin \phi,$$

$$\hat{x} = \hat{\rho} \cos \phi - \hat{\phi} \sin \phi$$

$$\hat{\phi} = -\hat{x} \sin \phi + \hat{y} \cos \phi,$$

$$\hat{y} = \hat{\rho} \sin \phi + \hat{\phi} \cos \phi$$

$$\hat{r} = \hat{x} \sin \theta \cos \phi + \hat{y} \sin \theta \sin \phi + \hat{z} \cos \theta, \quad \hat{x} = \hat{r} \sin \theta \cos \phi + \hat{\theta} \cos \theta \cos \phi - \hat{\phi} \sin \phi$$

$$\hat{\theta} = \hat{x} \cos \theta \cos \phi + \hat{y} \cos \theta \sin \phi - \hat{z} \sin \theta, \quad \hat{y} = \hat{r} \sin \theta \sin \phi + \hat{\theta} \cos \theta \sin \phi + \hat{\phi} \cos \phi$$

$$\hat{\phi} = -\hat{x} \sin \phi + \hat{y} \cos \phi,$$

$$\hat{z} = \hat{r} \cos \theta - \hat{\theta} \sin \theta$$

INDEX

- A posteriori error estimation, 393
- ABC. *See* Absorbing boundary condition
- Absorbing boundary condition (ABC), 298
- Engquist–Majda, 317
- first-order, 316, 383
- in finite difference method, 314–318
- in finite element method, 379–390
- one-dimensional, 314–315
- perfectly matched layers, 318–328, 386–390
- second-order, 317, 381, 385
- three-dimensional, 383–385
- two-dimensional, 316–318, 380–383
- Accelerated Cartesian expansion, 537
- Adaptive cross-approximation (ACA) method, 463
- algorithm for, 502–504
- application to moment-method solution, 504–507
- low-rank matrix, 500–502
- Adaptive finite element analysis, 393
- Adaptive integral method (AIM), 463
- planar structures, 478–482
- three-dimensional structures, 482–486
- time-domain, 527, 540
- Addition theorem
- for Bessel and Hankel functions, 238, 488
- for spherical wave functions, 281–283, 492
- Advancing front, 391
- Aggregation, step in fast multipole method, 491, 494
- Ampère, André-Marie, 9, 10
- Ampère's law, 12
- Anisotropic medium, 20
- Wave propagation in, 137–145
- Annular phased array, 550–551
- Antenna
- analysis and design of, 541, 543
- aperture, 101–102
- biconical, 259–264
- complementary, 101–102
- finite electric dipole, 57–59
- infinitesimal electric dipole, 55–57
- logarithmic spiral, 378, 380
- microstrip patch, 378
- phased array, 65–69
- radiation pattern, 85, 453, 473
- wire, 421–425
- Anterpolation, 498
- Aperture
- antenna, 96–98
- radiation through, 96–99
- scattering, 99
- Array factor, 67
- Assembly, in finite element analysis, 352–354, 363–364
- Associated Legendre function, 249
- special property, 250, 251
- Associated Legendre polynomial, 251
- Atom, structure of, 15–16
- Attenuation constant, 110
- in waveguides, 167–170
- Automatic target recognition (ATR), 541
- Auxiliar differential equations
- FDTD implementation of PML, 325–327
- FDTD modeling of dispersive media, 331–332
- Auxiliary potential functions
- reasons for use, 51–52
- Babinet's principle
- electromagnetic version of, 99–101
- Backscatter radar cross-section.
- See* Monostatic radar cross-section
- Backward differencing formula, 298
- Bandgap, 125, 545
- Basic electromagnetic theory, 3–42
- Basis functions, 343, 400
- entire-domain, 400
- first-order, 414
- hierarchical, 392
- higher-order, 392
- interpolatory, 392
- pulse, 402
- RWG, 427, 446, 454
- subdomain or subsectional, 344, 400
- triangular, 421
- triangular rooftop, 426
- two-dimensional, 350
- vector, 361–362
- Basis transformation matrices, 485
- Bessel equation
- cylindrical, 201
- spherical, 249
- Bessel functions
- addition theorem for, 238
- cylindrical, 201
- first-order, 62
- integral representation, 192, 223, 445
- large-argument approximation, 203–204

- Bessel functions (*Continued*)
modified, 215
of the first kind, 192, 201,
202
of the second kind, 201,
202
recursive relation, 221
small-argument
approximation, 202
spherical, 249
Wronskian relation, 229
- Bianisotropic medium, 20
- Biaxial medium, 20
- Biconical antenna
finite, 262–264
infinitely long, 259–261
- Bi-isotropic medium, 20,
145–146
- Birefringence, 140, 142, 146
- Bistatic radar cross-section
defined, 271
of conducting sphere, 272,
372–373, 498–499
of dielectric sphere, 276,
278, 507
- Bistatic scattering width, 227,
411
- Block-circulant matrix, 442
- Born approximation
first-order, 94
- Boundary conditions, 24–26
Dirichlet, 301, 348, 360
mixed, 360, 371
Neumann, 301, 348
on PEC surface, 26
relation to Maxwell's
equations, 24
third kind, 315
- Boundary-value problem, 343
one-dimensional, 344
scalar, 347–348
time domain, 373
vector, 359–360
weak-form representation,
351, 360, 374, 376
weak-form solution, 351,
360, 385
- Brewster angle, 132
- Bragg diffraction, 440
- Broadband antenna, 102
- Calderon identity, 537
- Capacitance calculation
by moment method, 400–404
- Cauchy's residue theorem, 113,
115
- Causality condition, 36
- Causality in Fourier transform,
31
- Cavity
cylindrical, 212–213
spherical, 255–258
uniform, 170–179
- Central differencing formula,
298
- Chain rule
symbolic vector method,
6–7
- Characteristic equations, 162
- Characteristic impedance, 109,
261
- Characteristic values, 162
- Charge
conservation of, 15
magnetic, 22
- Chiral medium, 145–146
- Circular current loop, 61–63
- Circular conducting cylinder,
224–227, 238–241, 410
- Circular dielectric cylinder,
227–230
multilayer, 230–234
- Circular dielectric waveguide,
213–214
analysis of hybrid modes,
214–217
characteristics of hybrid
modes, 217–222
- Circular polarization, 123
- Circular waveguide, 205–208
- Clockwise circularly polarized.
See Right-hand circularly
polarized
- Coaxial waveguide, 208–212
- Collocation
point, 403
subdomain, 403
- Combined-field integral
equation (CFIE), 426,
537
- Complementary antenna,
101–102
- Complex-frequency-shifted
(CFS) perfectly matched
layer, 328
- Computational complexity,
463–465
defined, 527
- of a direct method, 463
of an iterative method, 464
- Computational electromagnetics
applications of, 540–551
challenges in, 551–552
defined, 297
fast algorithms, 463–507,
537–538
finite difference method,
297–339
finite element method,
342–394
hybrid techniques, 508–526,
540
- method of moments,
399–458
overview of, 533–540
- Conditionally stable, 303
- Conduction current, 19
- Conductivity, 19
classification of media based
on, 21
- Conductor loss, 167–169
- Conjugate gradient–fast Fourier
transform (CG-FFT)
method, 463, 465–478
- radiation from microstrip
array, 473
- scattering by conducting
plate, 466–472
- scattering by conducting strip
or wire, 466
- scattering by dielectric object,
472–478
- Conservation of charges, 15
- Conservation of energy, 27
for time-harmonic fields,
32–34
- Constitutive relations, 15–22
for electric field, 17
for magnetic field, 19
- Continuity of currents, 15
free charges and currents, 23
- Convolution, 21, 329, 376
- Coulomb gauge condition,
45
- Counterclockwise circularly
polarized. *See* Left-hand
circularly polarized
- Critical angle, 133, 186
- Cross-approximation, 502
- Curl, 4
symbolic vector method, 6
- Curl theorem, 8

- Current
 conduction, 19
 continuity of, 15, 23
 impressed, 27
 infinitely long, 234–243, 355
 line, 234–236
 magnetic, 22
 sheet, 125–127
 surface, 24, 236–243,
 283–291
- Current continuity equation, 15
 free charges and currents, 23
- Current density, 24
 surface, 24
- Current loop
 equivalent to magnetic dipole,
 63
 radiation in free space, 61,
 286
 radiation in presence of cone,
 290
 radiation in presence of
 sphere, 288
- Curvilinear element, 393
- Cutoff
 for closed waveguide, 157
 for open waveguide, 184
 frequency, 157, 163, 185
 wavelength, 157, 163
 wavenumber, 157, 163, 222
- Cyclic convolution, 466, 476
- Cylindrical Bessel functions.
See Bessel functions
- Cylindrical cavity, 212–213
- Cylindrical coordinates
 curl in, 4
 divergence in, 4
 fields and waves in, 200–247
 gradient in, 5
 Helmholtz equation in, 200
 Laplacian in, 6
- Cylindrical wave functions,
 200, 203–204
- Debye medium, 330
- Delaunay criterion, 391
- Delta family, 48
- Delta function
 and Green's function, 48–49
 Dirac, 48, 405
- Diamagnetic medium, 22
- Dielectric
 defined, 16
 perfect, 21
- Dielectric loss, 167, 169–170
- Dielectric slab
 as waveguide, 178,
 183–187
 grounded, dipoles above,
 196–197
- Dielectric waveguide
 circular, 199–207
 slab, 178, 183–187
- Diffraction
 theories of, 535
- Diffusion equation, 300
 solution by finite difference
 method, 300–301
- Dipole moment
 electric, 16
 magnetic, 17
- Dirac delta function, 48, 405,
 479
- Direct solver, matrix, 392
- Dirichlet boundary condition,
 301, 348, 360
- Disaggregation, step in fast
 multipole method, 491,
 494
- Discontinuous Galerkin time-
 domain (DGTD) method,
 538, 539–540
- Discrete complex image method
 (DCIM), 447–451
- Discrete body of revolution
 (DBOR), 441
 scattering by, 441–442
- Discrete Fourier transform
 (DFT), 439, 466
- Dispersion
 for controlling group velocity,
 121
 numerical, 305
- Dispersion error, 537
- Dispersion relation, 118
- Dispersive medium, 21
 FDTD modeling of, 329–333
 FETD modeling of, 376–378
- Divergence, 3
 symbolic vector method, 6
- Divergence theorem, 4
- Drude medium, 330
- Dual expression, 94
- Duality principle, 94–95
- Dyad, 53–54
- Dyadic Green's functions,
 52–54
 electric, 53, 81
- free-space, 53
- half-space, 81
- magnetic, 53, 81
- E-plane, 270
- Echo width, 227
- Edge, 241–244
- Edge element, 361
- Edge singularity, 242
- EH mode, 178, 182, 187
 in circular dielectric
 waveguide, 218–222
- Eigenfunction expansion, 114
 for wave equation, 112–115
- Electric charge. *See* Charge
- Electric conduction, 19
- Electric current density, 11
- Electric dipole
 finite, 57–59
 horizontal, 191
 infinitesimal, 55–57
 vertical, 191
- Electric dyadic Green's function
 free-space, 53
 half-space, 81
- Electric energy, 28
- Electric-field integral equation
 (EFIE), 408, 421, 431,
 537
- Electric field intensity, 11
- Electric flux density, 17
- Electric loss tangent, 36
- Electric polarization, 15–17
- Electric scalar potential, 44
- Electric susceptibility, 17
- Electric vector potential, 47
- Electromagnetic compatibility
 (EMC), 544–545
- Electromagnetic field
 dependence of media
 properties on, 21
 effect of medium, 15–22
 excitation in waveguides,
 187–191
 in cylindrical coordinates,
 200–245
 in planar layered media,
 191–197
 in rectangular cavity,
 173–175
 in rectangular coordinates,
 152–197
 in rectangular waveguides,
 160–170

- Electromagnetic field
(Continued)
- plane waves, 125–127, 137–146
 - reflection, 127–137
 - relationship with energy and power, 26–29
 - static, 44–45
 - time-harmonic, 29–36, 45–47
 - transmission, 127–137
 - transmission line theory, 107–115
 - wave equations, 115–125
- Electromagnetic hyperthermia, 550–551
- Electromagnetic interference (EMI), 544–545
- Electromagnetic radiation in free space, 43–72
- Electromagnetic theory
- basic, 3–42
 - theorems and principles, 73–106
- Electromagnetic wave. *See* Wave
- Element radiated field, 67
- Elliptical polarization, 123, 145
- Energy
- conservation of, 28, 33
 - electric, 27
 - magnetic, 28
- Energy velocity
- in waveguide, 158
 - on a transmission line, 109
 - uniform plane wave, 119
- Engquist–Majda absorbing boundary condition, 317
- Entire-domain basis function, 400
- Equivalence principle
- surface, 85–92, 419
 - volume, 92–94, 434–435
- Equivalent edge current (EEC), 535
- Equivalent electric current, 93, 434
- Equivalent magnetic current, 93, 434
- Equivalent problem, 86
- Equivalent surface current, 86, 419
- Excitation of waveguide by general volumetric current, 189–190
- by planar surface current, 187–189
- Expansion functions, 350
- Extraordinary wave, 139
- general, 142
- Far field, 57
- Far-field approximation, 59–61
- Faraday, Michael, 9, 10
- Faraday rotation, 144, 146
- Faraday's induction law. *See* Faraday's law
- Faraday's law, 12
- for free charges and currents, 22–23
 - for time-harmonic fields, 28
- Fast algorithms, 463–507, 537–538
- adaptive
 - cross-approximation, 500–507
 - adaptive integral method, 478–487
 - algebra-based, 500
 - conjugate gradient–fast Fourier transform, 465–478
 - defined, 463
 - fast multipole method, 487–500
 - introduction, 463–465
 - kernel-based, 500
 - kernel-independent, 500
 - physics-based, 500
- Fast Fourier transform (FFT), 439, 463
- Krylov subspace methods with, 527
- Fast multipole method (FMM), 463
- multilevel, 495–500
 - three-dimensional, 492–495
 - two-dimensional, 487–491
- Fast solver, 465
- Ferrite, 22
- Ferromagnetic medium, 22
- Field. *See* Electromagnetic field; Far field
- Field singularity problem, 242–244, 290–291
- Field–source relation
- free-space, 52–53
 - half-space, 80–82
- Finite difference–finite element method, 509
- application, 514–515
- hybridization of FETD and FDTD, 512–514
- relation between FETD and FDTD, 510–512
- Finite difference method, 297–341, 508, 536
- absorbing boundary conditions, 314–318
 - diffusion equation, 300–301
 - finite differencing formulas, 298–300
 - near-to-far-field (NTF) transformation, 337–338
 - numerical dispersion analysis, 305–306
 - one-dimensional, 300–306
 - stability analysis, 302–304
 - three-dimensional, 311–314
 - two-dimensional, 206–311
 - wave excitation, 334–337
 - wave equation, 302, 306–308
 - Yee's FDTD scheme, 309–314
- Finite difference time domain (FDTD) method, 298
- dispersive media, 329–333
 - hybridization with FETD method, 512–514
 - perfectly matched layers in, 318–328
 - relation to FETD method, 510–512
 - wave excitation, 334–337
 - Yee's, 309–314
- Finite differencing formulas, 298–300
- Finite electric dipole, 57–59
- Finite elements, 344, 348
- Finite element analysis
- field in birdcage coil, 356–357
 - homogeneous waveguide, 354–355
 - in time domain, 372–379
 - inhomogeneous waveguide, 365–366
 - microwave device, 366–370
 - of scalar fields, 347–359
 - of vector fields, 359–372
 - one-dimensional, 344–347

- scattering by 2D object, 357–358
 scattering by 3D object, 370–372, 386, 390–391
 waveguide-fed horn, 358–359
- Finite element–boundary integral (FE–BI) method,** 515–517
examples, 523–526
frequency domain, 517–523
symmetric formulation, 520–523
time domain, 523
traditional formulation, 517–520
- Finite element method (FEM),** 342, 509, 517, 536–537
absorbing boundary conditions, 379–390
adaptive, 393
curvilinear elements, 393
edge element, 361
frequency domain, 359–372
general principle, 343–344
higher-order basis functions, 347, 392, 537
isoparametric element, 393
matrix solver, 391–392
mesh generation, 391
node, 344
one-dimensional example, 344–347
perfectly matched layers, 386–390
scalar fields, 347–359
subparametric element, 393
superparametric element, 393
time domain, 372–379
vector element, 361
vector fields, 359–372
- Finite element time-domain (FETD) method,** 509
formulation, 511–512
hybridization with FDTD method, 512–514
relation to FDTD method, 510–512
- Finite integration technique (FIT),** 538–539
- Finite volume time-domain (FVTD) method,** 538–539
- First-order absorbing boundary condition,** 316, 380–381
- First-order Born approximation,** 94
- First-principle numerical methods,** 533, 536–538
- Floquet's theorem,** 436
- Flux density**
 electric, 17
 magnetic, 11
- Forward differencing formula,** 298
- Fourier transform,** 30
- Fredholm integral equation,** 537
- Free space**
 defined, 43, 69
 dyadic Green's function in, 52–54
 field–source relations in, 50–51
 Green's function in, 49–50
 radiation in, 55–63
 solution of vector potentials in, 47–55
- Free-space permeability,** 12
- Free-space permittivity,** 12
- Frequency**
 dependence of media properties on, 21
- Frequency domain**
 defined, 31
 finite difference method in, 308–309
 finite element–boundary integral method in, 517–523
 finite element method, 359–372
 first-principle numerical methods, 533, 536–538
 high-frequency asymptotic methods, 533, 534–536
 method of moments in, 404–452
 relationship to time domain, 533–534
- Frequency-domain finite element method (FD-FEM),** 378
- Frobenius norm,** 502
- Full-rank matrix,** 500
- Galerkin's formulation,** 422
- Galerkin's method,** 343, 345, 351
- Gauge condition**
 Coulomb, 45
 for spherical modes, 254–255
 Lorenz, 47, 254
- Gauss, Carl Friedrich,** 10
- Gauss' law,** 13, 14
 free charges and currents, 17, 22
 magnetic, 13, 22, 30
 time-harmonic fields, 30
- Gauss–Seidel method,** 309
- Gauss' theorem,** 4, 350, 360.
See Divergence theorem
- generalized,** 7
- Gaussian pulse,** 336
- General extraordinary wave,** 142
- Generalized eigenvalue problem,** 355, 365
- Generalized function,** 48
- Generalized pencil of function (GPOF) method,** 448
- Geometrical optics,** 535
- Geometrical theory of diffraction (GTD),** 535
- Gibbs, J. Willard,** 4
- Good conductor,** 121
- Good dielectric,** 121
- Gradient,** 5
 symbolic vector method, 6
- Green's function,** 48, 399
 evaluation of, 446–451
 free-space dyadic, 53–54
 free-space scalar, 50
 free-space spectral, 191
 half-space dyadic, 81
 in free space, 49, 114–115
 on transmission line, 112–113
 spectral representation, 114
- Green's theorems,** 9
 first scalar, 9, 159
 first vector, 9
 scalar–vector, 9, 417
 second scalar, 9, 159, 405
 second vector, 9
- Group velocity,** 120–121
 in waveguide, 157
- Guided wavelength,** 157
- Gyrotropic media**
 plane waves in, 142–145
- H-plane,** 270
- Hadamard product,** 466

- Hankel functions, 203–204
 addition theorem for, 238
 large-argument
 approximation, 204, 227, 235
 small-argument
 approximation, 235, 407
 spherical, 251
 zeroth-order second kind, 405
- HE mode, 178, 182, 187
 in circular dielectric waveguide, 218–222
- Heaviside, Oliver, 10, 11
- Helmholtz decomposition theorem, 8–9
- Helmholtz equation. *See also*
 Wave equation
 in cylindrical coordinates, 200
 in rectangular coordinates, 116
 in spherical coordinates, 248
 scalar, 47, 116
 solution by finite element method, 344–347
 solution by method of moments, 404–416
 vector, 47, 116
- Hertz, Heinrich, 10, 11
- Heterogeneous medium. *See*
 Inhomogeneous medium
- Hierarchical basis functions, 392
- Hierarchical matrix method, 537
- High-frequency asymptotic methods, 533, 534–536
- Homogeneous medium, 20
- Horizontal electric dipole (HED), 191
 above layered medium, 194–196
- Human head
 modeling with CG–FFT, 477–478
 modeling with FDTD and PML, 328
 modeling with FEM, 356–357
- Huygens' principle, 87, 406
- Huygens' surface, 335
- Hybrid modes, 178, 182
 finite element method, 365–366
- in circular dielectric waveguide, 214–222
- Hybrid techniques, 508–526, 540
 defined, 463
 finite difference–finite element, 509–515
 finite element–boundary integral, 515–526
 motivations for, 508–509
- Hyperbolic partial differential equation, 302
- Identity dyad, 54
- Image, of dipole, 77–78
- Image theory, 75–82
- Impedance matrix, 479, 481, 485
- Incident field, 88, 93, 418, 435
- Incident plane wave, 225, 266
- Incident shadow boundary (ISB), 535
- Incremental length diffraction coefficients (ILDC), 535
- Induction theorem, 89
- Infinitesimal electric dipole, 55–57
- Infinitesimal magnetic dipole, 62
- Inhomogeneous medium, 20
- Input impedance
 of biconical antenna, 261
 of logarithmic spiral antenna, 380
 of microstrip antenna, 378–379
- Insulator
 defined, 21
- Integral equations
 boundary, 463, 516, 523
 combined-field, 426, 431, 537
 electric-field, 408, 421, 431, 537
 Fredholm, 537
 in time domain, 421–423
 magnetic-field, 409, 421, 537
 mixed-potential, 446
 surface, 537
 volume, 93, 435, 472, 537
- Interior resonance, 426
- Interpolating functions, 349
- Interpolatory basis functions, 392
- Intrinsic impedance, 118
- Inverse synthetic aperture radar (ISAR), 541
- Irrational vector, 8
- Isoparametric element, 393
- Isotropic medium, 20
- Iterative solver, matrix, 392
- Kirchhoff's laws, 107
- Kramers–Krönig's relations, 36
- Laplacian, 5–6
- Layered medium
 field excitation in, 191–197
 Green's function, 443–446
- Leapfrog time integration, 311
- Left-hand circularly polarized (LHCP) field, 123
- Left-handed medium, 125
 transmission into, 135–136
- Legendre functions, 249
- Legendre polynomial, 251
 orthogonal relation, 265, 285
- Legendre's equation, 249
- Linear medium, 21
- Linear polarization, 122
- Lorentz force law, 15
- Lorentz medium, 330
- Lorentz reciprocity theorem, 83
- Lorenz gauge condition, 47, 254
 time-harmonic fields and, 45–47
- Loss, in waveguide, 167–170
- Lossy medium, 21
- Low-rank matrix, 500–502
- MKS unit system, 12
- Magnetic dipole, radiation from, 62
- Magnetic dipole moment, 17
- Magnetic dyadic Green's function, 53
 half-space, 81
- Magnetic energy, 28
- Magnetic-field integral equation (MFIE), 409, 421, 537
- Magnetic field intensity, 18
- Magnetic flux density, 11
- Magnetic frill current, 423
- Magnetic loss tangent, 36
- Magnetic resonance imaging (MRI), 356, 548–549

- Magnetic susceptibility, 19
 Magnetic vector potential, 44–45
 Magnetization, 17–19
 intensity, 18
 vector, 18
 Marching on in degree, 540
 Marching on in time (MOT), 456, 540
 solution of TDIE by, 454–457, 540
 Matrix
 basis transformation, 485
 block-circulant, 442
 full-rank, 500
 impedance, 479, 481, 485
 low-rank, 500
 preconditioner for, 391, 536
 rank-1, 500
 rank-deficient, 500
 solvers for, 391–392
 storage of, 391
 subblock, 500
 system, 402, 404
 Toeplitz, 466
 Maxwell, James Clerk, 9, 10
 Maxwell–Ampère law, 12
 free charges and currents, 19, 22
 in terms of free electric current, 18–19
 time-harmonic fields, 30
 Maxwell’s equations
 differential form, 14
 free charges and currents, 22–23
 integral form, 11–13
 plane wave, 118, 137
 relationship to boundary conditions, 24
 stretched coordinates, 319–320
 symmetries in, 94–95
 time-harmonic, 30, 43
 total charges and currents, 9–15
 uniqueness of solution to, 73–75
 Medium
 anisotropic, 20, 137–145
 bianisotropic, 20
 biaxial, 20
 bi-isotropic, 20, 145–146
 chiral, 145–146
 classification of, 19–22
 diamagnetic, 22
 dispersion relation of, 118
 dispersive, 21, 329–333, 376–378
 ferromagnetic, 22
 gyrotrropic, 142–145
 heterogeneous, 20
 homogeneous, 20
 inhomogeneous, 20
 interfaces between, 24–26
 intrinsic impedance of, 118
 isotropic, 20
 layered, 191–197
 left-handed, 125, 135–136
 lossy, 21
 non-dispersive, 21
 non-magnetic, 19, 22
 non-reciprocal, 20, 83
 non-stationary, 20
 paramagnetic, 22
 reciprocal, 20
 stationary, 20
 uniaxial, 20, 137–142
 Mesh-free method, 536
 Mesh generation, in finite element analysis, 391
 Meshless method, 536
 Metamaterial
 wave propagation in, 124
 Method of moments (MoM), 399, 504, 537
 analysis of microstrip antennas and circuits, 443–452
 analysis of periodic structures, 436–442
 application of ACA to solution of, 504–507
 basic steps, 404
 capacitance calculation, 399–404
 formulation of integral equations, 404–407, 416–421, 443–446, 453–454
 in frequency domain, 404–452
 in time domain, 452–458
 introduction, 399–404
 scattering by conducting body, 425–430
 scattering by conducting cylinder, 407–411
 scattering by conducting strip, 411–415
 scattering by dielectric body, 430–435
 scattering by dielectric cylinder, 415–416
 three-dimensional, 416–407
 two-dimensional, 404–416
 wire antenna, 421–425
 Microstrip antenna
 analysis by method of moments, 443–452
 corporate-fed array, 473
 evaluation of Green’s functions, 446–451
 far-field calculation, 451–452
 formulation of integral equations, 443–446
 moment-method solution, 446
 patch antenna, 378
 series-fed array, 453
 Microwave devices, 543–544
 finite element analysis, 366–370
 Microwave imaging, 548–549
 Mie series solution, 270
 Mixed boundary condition, 360, 371
 Mixed-potential integral equation (MPIE), 446
 Mode
 degenerate, 159
 EH, 178, 182, 187, 220
 hybrid, 178, 182, 217–222
 HE, 178, 182, 187, 220
 transverse electric (TE), 154, 161–164, 211, 260
 transverse electromagnetic (TEM), 155, 212, 261
 transverse magnetic (TM), 154, 161–164, 208, 260
 Modified Bessel function, 215
 small-argument approximation, 219
 Modulated Gaussian pulse, 336
 Molecule, 16
 non-polar, 16
 polar, 16
 Moment method. *See* Method of moments

- Monostatic radar cross-section
defined, 273
of coated conducting/
dielectric cylinder, 524
of coated trapezoidal plate,
525
of conducting sphere, 273
of dielectric sphere, 278
of metallic almond, 430, 486
of metallic cube, 386
of metallic ogive, 391, 516
of metallic plate, 484
of metallic wing, 487
of open cavity, 526
Müller formulation, 432, 462
Multilevel fast multipole
algorithm (MLFMA),
495–500
Multilevel matrix decomposition
method, 500, 537
Multiresolution time domain
(MRTD) method, 538, 539
- Near-to-far-field (NTF)
transformation, 337–338
Neumann boundary condition,
301, 348
Neumann pulse, 336
Newmark-beta integration
method, 375–376, 377,
511, 513
Nodal element, 361
Nodes, in finite element
analysis, 344
Non-dispersive medium, 21
Non-invasive microwave
imaging, 548–549
Non-linear medium, 21
Non-magnetic material, 19, 22
Non-polar molecule, 16
Non-reciprocal medium, 20, 83
Non-stationary medium, 20
Non-uniform grid method, 537
Non-uniform plane wave, 117,
135
Numerical dispersion, 305
in finite difference method,
305–306
in finite element method,
346–347
Numerical phase error, 305,
537
in one-dimensional FDTD,
305
- in three-dimensional FDTD,
314
in two-dimensional FDTD,
308
with first-order elements, 347
with higher-order elements,
392
- Open circuit, 111
Optical fiber, 214. *See also*
Circular dielectric
waveguide
Optical region, 273
Optics
geometrical, 535
physical, 88, 132, 535
Ordinary wave, 138, 141, 145
Orthogonality
cavity modes, 172
waveguide modes, 158–160,
179, 368
- Panel clustering method, 537
Parabolic partial differential
equation, 300
Parallel polarization, 129,
131–132
Paramagnetic medium, 22
Partial differential equation
hyperbolic, 302
parabolic, 300
Partial differential equation
(PDE) methods, 536. *See
also* Finite difference
method, Finite element
method, Mesh-free method
Partial element equivalent
circuit (PEEC) method,
538
Perfect dielectric
defined, 21
Perfect electrical conductor
(PEC)
defined, 21
interface with, 26
Perfect magnetic conductor
(PMC), 26
Perfectly matched interface, 322
Perfectly matched layer (PML),
318–328
anisotropic absorbing
medium, 387–390
complex-frequency-shifted
(CFS), 328
- conductor-backed, 322–323
coordinate-stretched,
320–322
finite element analysis,
386–390
implementation in FDTD,
323–328
second-order, 328
- Permeability
classification of media based
on, 21–22
complex, 36
negative, 124–125
of free-space, 12
of material, 19
tensor, 20
- Permittivity
complex, 36
dielectric, 17
negative, 124–125
of free-space, 12
tensor, 20
- Perpendicular polarization,
129–131
- Perturbational method, 169
- Phase constant, 108
- Phase error. *See* Numerical
phase error
- Phase matching, 131, 322
- Phase velocity, 108
in waveguide, 157
plane wave, 119
- Phased array, 65
array factor, 67
element radiated field, 67
radiation from, 65–69
- Phasor
defined, 29
Poynting's theorem for,
34
- Photonic crystals, 545–548
- Physical equivalent, 88
- Physical optics (PO), 535
- Physical optics approximation,
89, 132, 411
- Physical theory of diffraction
(PTD), 535
- Plane of incidence, 129
- Plane wave, 117
characteristics of, 117–119
generated by current sheet,
125–127
in anisotropic media,
137–145

- in bi-isotropic media, 145–146
 polarization, 121–124
 propagation in metamaterials, 124, 135–137
 reflection, 127–135
 transformation to cylindrical waves, 223
 transformation to spherical waves, 264–269
 transmission, 127–136
 velocities, 119–121
 versus transmission line, 137
- Plane wave time-domain (PWTD) method, 527, 540
- PMCHWT formulation, 432
 moment-method and ACA solutions, 505–507
- Point matching, 403
- Point collocation, 403
- Poisson’s equation, 44, 348
- Polar molecule, 16
- Polarization, 121
 circular, 123
 electric, 15–17
 elliptical, 123, 145
 intensity, 16
 linear, 122
 of electromagnetic waves, 121–124
 parallel, 129, 131–132
 perpendicular, 129–131
 vector, 16
- Polaroid, 139
- Potentials
 electric vector, 47
 electric scalar, 44
 magnetic vector, 44–45
 retarded, 51
 scalar and vector, 43–47
- Power
 complex exiting, 34
 complex supplied, 34
 dissipated in volume, 28
 in metamaterials, 125
 passing through surface, 27
 reactive, 35
 supplied by source, 28
 time-average dissipated, 34
 uniform plane wave, 117–121
- Poynting vector, 29
 complex, 32
 time average of, 32
- Poynting’s theorem, 28
 for complex phasors, 34
- Preconditioner, 392
- Precorrected–FF method, 537
- Problem of interior resonance, 426, 431–432
- Prony method, 448
- Propagation constant, 108
- Pseudo-spectral time-domain (PSTD) method, 538, 539
- Pulse basis function, 402
- Quality factor
 photonic crystal cavity, 546–547
 rectangular cavity, 174
 resonant cavity, 172
- Quarter-wave plate, 140
- Radar cross-section (RCS), 541
 backscatter, 273
 bistatic, 271. *Also see*
 Bistatic radar cross-section
 monostatic, 273. *Also see*
 Monostatic radar
 cross-section
- Radar signature, 541
- Radiation
 by biconical antenna, 265
 by finite current, 243–245
 by infinitely long current, 234–243
 by line current, 234–236
 by phased arrays, 65–68
 by surface currents, 63–65, 236–243, 283–290
 from horn antenna, 358–359
 from microstrip array, 453, 473
 from wire antenna, 421–425
 in free space, 55–63
 in presence of conducting cylinder, 238–240
 in presence of conducting wedge, 241–243
 in presence of cone, 288–291
 in presence of sphere, 286–288
 Sommerfeld conditions, 61
 through aperture, 95–97
- Radition condition, 405, 417.
Also see Sommerfeld
 radation condition
- Radiation function, 491, 494, 497–498
- Range profile, 541
- Rank-1 matrix, 501
- Rank-deficient matrix, 500
- Rao–Wilton–Glisson (RWG) function, 426
- Ray tracing, 535
- Rayleigh scattering, 273, 276
- Rayleigh–Carson reciprocity theorem, 83–85
- Reaction, of field on source, 84
- Reactive power, 35
- Receive function, 491, 494, 497–498
- Reciprocal medium, 20
- Reciprocity theorem
 for far-field calculation, 451
 general, 82–83
 in differential form, 82
 in integral form, 83
- Lorentz, 83
- Rayleigh–Carson, 83–85
- Rectangular coordinates
 curl in, 4
 divergence in, 4
 fields and waves in, 152–197
 gradient in, 5
 Laplacian in, 6
- Recursive convolution
 FDTD modeling of dispersive media, 329–331
 FETD modeling of dispersive media, 377–378
- Recursive relation for Bessel function, 221
- Reflection
 normal incidence, 127–129
 oblique incidence, 129–132
 Snell’s law of, 131
 total, 133
 transmission line, 110–111
 uniform plane wave, 127–135
 zero, 132
- Reflection shadow boundary (RSB), 535
- Refraction
 Snell’s law of, 131
- Resonance, 170
- Resonance region, 273
- Resonant cavity. *See* Cavity

- Resonant frequency, 171
 cylindrical cavity, 213
 rectangular cavity, 173–174
 spherical cavity, 257–258
- Resonant mode
 cavity, 171
- Retarded potentials, 51
- Riccati–Bessel functions, 255
 governing equation, 268
 small-argument
 approximation, 276, 290
 Wronskian relation for, 275
- Riccati–Hankel functions, 259
 large-argument
 approximation, 270
- Right-hand circularly polarized (RCHP) field, 123
- Rooftop function, 439
- Scalar fields
 finite element analysis, 347–359
 moment-method analysis, 404–416
- Scalar Helmholtz equation, 47, 116, 200, 248
- Scattered field, 88, 225, 334
- Scattered-field formulation
 for FDTD analysis, 334
 for finite element analysis, 357, 371
- Scattered wave, 406
- Scattering
 by aperture, 95–102
 by conducting cylinder, 224–227, 407–411, 487–492
 by conducting object, 87–90, 425–430, 482–487, 492–495
 by conducting plate, 466–472, 478–484
 by conducting sphere, 269–274, 499, 505
 by conducting strip, 411–415, 466
 by conducting wire, 421–425, 466
 by dielectric cylinder, 227–234, 415–416
 by dielectric object, 90–94, 430–435, 472–478
 by dielectric sphere, 274–281, 456, 477, 505–507
- by discrete body of revolution, 441–442
- by multilayer dielectric cylinder, 230–234
- by multilayer dielectric sphere, 276–281
- by periodic conducting patch array, 436–441
 Rayleigh, 273, 276, 278
- Scattering width, 226
 bistatic, 227, 230, 413
- Second-order absorbing boundary condition, 317, 381, 385
- Separation of variables, 116–117, 200–201, 248–251
- Shooting- and bouncing-ray (SBR) method, 535
- Short circuit, 111
- Signal-to-noise ratio (SNR), 548–549
- Singular-value decomposition (SVD), 502
- Singularity of field
 at conducting edge, 243–244, 412
 at tip of cone, 290–291
- Singularity in integral, 406–407, 419–420, 427–428
- Skeleton approximation, of rank-deficient matrix, 502
- Slow wave, 121, 135
- Smith, Walter Fox, 12, 13
- Snell’s laws, 131
- Solenoidal vector, 8
- Sommerfeld identity, 192, 447
- Sommerfeld integrals, 197, 445
- Sommerfeld radiation
 conditions, 59–61, 236, 357, 371, 417
- Source vector, 402
- Sparse matrix/canonical grid
 method, 537
- Sparse solver, 352
- Specific absorption rate (SAR), 328, 477, 549
- Spectral domain. *See* Frequency domain
- Spectral theory of diffraction (STD), 535
- Spherical Bessel functions, 249
 large-argument
 approximation, 252
- small-argument
 approximation, 266
 Wronskian relation for, 282
- Spherical cavity, 255–258
- Spherical coordinates
 curl in, 4
 divergence in, 4
 fields and waves in, 248–291
 gradient in, 5
 Helmholtz equation in, 248
 Laplacian in, 6
- Spherical Hankel functions, 251
 asymptotic form, 252
- Spherical wave functions, 248, 251–253
- Spin, 18
- Stability condition of FDTD
 for diffusive equation, 303
 for wave equation, 304
 in three dimensions, 313
 in two dimensions, 307
- Standing wave, 128
- Standing wave ratio (SWR), 129
- Static fields, 44, 44–45
 finite element analysis, 348–354
 moment-method analysis, 400–403
- Stationary medium, 20
 “Stealth” airplanes, 541
- Stokes’ theorem, 5
 derivation from curl theorem, 8
- Stopband, 125
- Structured mesh, 391
- Subblock matrix, 500
- Subdomain basis function, 344, 400
- Subdomain collocation, 403
- Subparametric element, 393
- Subsectional basis function, 400
- Superparametric element, 393
- Surface current, 24
 radiation by, 63–65, 236–243, 283–290
- Surface equivalence principle, 85–87
 scattering by conducting object, 87–90
 scattering by dielectric object, 90–92
- Surface integral equation (SIE), 537

- Susceptibility
 electric, 17
 magnetic, 19
- Symbolic function, 48
- Symbolic vector method, 6–8
- System matrix, 402, 404
- Tensor
 defined, 54
 permeability, 20
 permittivity, 20
- Testing function, 402
- Theorem
 addition, 238, 488, 281–283, 492
 Cauchy's residue, 113, 115
 curl, 7
 divergence, 4
 Floquet's, 436
 Gauss', 4
 Green's, 9
 Helmholtz decomposition, 8–9
 induction, 89
 Poynting's, 28, 34
 reciprocity, 82–85
 Stokes', 5, 8
 uniqueness, 73–75
- Thin-wire approximation, 422
- Time domain
 defined, 31
 adaptive integral method, 527, 540
 finite difference method in, 306–308
 finite element-boundary integral method in, 523
 finite element method in, 372–379
 method of moments in, 452–458
 relationship to frequency domain, 533–534
- Time-domain adaptive integral method (TD-AIM), 527, 540
- Time-domain finite element method (TD-FEM), 378
- Time-domain integral equation (TDIE), 454, 540
 solution by marching on in time, 454–457, 540
 solvers, 527
- Time-domain simulation
 methods, 538–540
- Time-harmonic fields, 29–36
 and Lorenz gauge condition, 45–47
 complex permittivity and permeability, 36
 complex power, 32–35
 Fourier transforms, 30–32
 Maxwell's equations, 30, 43
 relation to arbitrary time-varying fields, 31
 relation to static fields, 43
- Time marching, 301, 375
- Time stepping, 301, 375
 leapfrog time integration, 311
- Time-stepping formula, 301, 375
- Time-varying fields
 relation to time-harmonic fields, 31
- Toeplitz matrix, 466
- Total- and scattered-field decomposition method, 335–336
- Total reflection, 133–134, 186
- Total transmission, 132
- Translation, step in fast multipole method, 491, 494
- Transmission
 into left-handed medium, 135–136
 normal incidence, 127–129
 oblique incidence, 129–132
 on transmission line, 110–111
 total, 132–133
 uniform plane wave, 127–137
- Transmission line differential equations, 107–110
 Green's function, 111–113
 reflection, 110–111
 transmission, 110–111
 versus plane wave, 137
- Transmission line matrix (TLM) method, 538
- Transpose-free quasi-minimal residual (TFQMR) algorithm, 477, 527
- Transverse electric (TE) mode, 154
 finite element analysis, 355
 in biconical antenna, 259–261
 in circular cavity, 212–213
 in circular dielectric waveguide, 218
 in circular waveguide, 206–208
 in coaxial waveguide, 208–211
 in cylindrical cavity, 171
 in cylindrical coordinates, 204–205
 in dielectric slab waveguide, 183–186
 in rectangular cavity, 173–174
 in rectangular coordinates, 161
 in rectangular waveguide, 162–167
 in spherical cavity, 255–257
 in spherical coordinates, 253–255
- Transverse electromagnetic (TEM) mode, 155
 in biconic antenna, 261
 in coaxial waveguide, 212
- Transverse magnetic (TM) mode, 154
 finite element analysis, 354
 in biconical antenna, 259–261
 in circular cavity, 212–213
 in circular dielectric waveguide, 218
 in circular waveguide, 206–208
 in coaxial waveguide, 208–211
 in cylindrical cavity, 171
 in cylindrical coordinates, 204–205
 in dielectric slab waveguide, 183–186
 in rectangular cavity, 173–174
 in rectangular coordinates, 161
 in rectangular waveguide, 162–167
 in spherical cavity, 255–257
 in spherical coordinates, 253–255

- Transverse magnetic (TM) mode
(Continued)
 in spherical coordinates,
 253–255
- Triangle function, 345
- Triangular rooftop function,
 439
- Uniaxial medium, 20
 wave propagation in,
 137–142
- Uniform asymptotic theory
 (UAT), 535
- Uniform cavity, 170–177
 general theory, 171–173
 perturbation of geometry,
 176–177
 perturbation of material,
 175–176
 rectangular, 173–174
 uniform plane wave, 117
- Uniform theory of diffraction
 (UTD), 535
- Uniform waveguide, 152
 analysis, 152–156
 characteristics, 156–160
 losses in, 167–170
 rectangular, 160–167
- Uniqueness theorem, 73–75
- Unit dyad, 54
- Unstructured mesh, 391
- Vector
 irrotational, 7
 magnetization, 18
 polarization, 16
 Poynting, 29
 solenoidal, 8
 symbolic, 6
- Vector analysis
 review of, 3–9
- Vector basis function, 361
- Vector element, 361
- Vector fields
 finite element analysis,
 359–364
- Vector function
 defined, 3
- Vector Helmholtz equation, 47,
 116
- Vector potential
 advantages of use, 51–52
- electric, 47
 magnetic, 44–45
 solution of, in free space,
 47–55
- Vector wave equation,
 373
- Vertical-cavity surface-emission
 laser (VCSEL), 546
- Vertical electric dipole (VED),
 191
 above layered medium,
 192–194
- Volume equivalence principle,
 92–94
- Volume integral equation (VIE),
 93, 435, 472, 537
- Wave
 excitation in FDTD, 334–
 337
 extraordinary, 139
 generated by current sheet,
 125–127
 in anisotropic media,
 137–145
 in bi-isotropic media,
 145–146
 ordinary, 138
 plane, 117–146
 polarization, 121–124, 129,
 145
 propagation in metamaterials,
 124–125
 reflection, 127–136
 standing, 128
 transmission, 127–136
 velocities, 119–121
- Wave equation. *See also*
 Helmholtz equation,
 Hyperbolic partial
 differential equation
 in cylindrical coordinates,
 200–204
 in rectangular coordinates,
 115–125
 in spherical coordinates,
 248–253
 solution by finite difference
 method, 302, 308–309
 solution by separation of
 variables, 116–117, 200–
 203, 248–251
- Wave function
 cylindrical, 200, 203–204
 spherical, 248, 251–253
- Wave impedance, 118
 for parallel polarization,
 132
 for perpendicular polarization,
 131
 for waveguide, 158
- Wave transformation
 cylindrical, 222–224
 spherical, 264–266
- Waveguide, 152
 circular, 205–208
 circular dielectric, 213–222
 coaxial, 208–212
 dielectric slab, 183–187
 field excitation in,
 187–191
 finite element analysis, 354–
 355, 365–366
 partially filled, 180–183
 rectangular waveguide,
 160–167
 uniform, 152–170
- Waveguide port boundary
 condition, 368
- Wavenumber, 108
- Weak-form representation, of
 boundary-value problem,
 351, 360, 374, 376
- Weak-form solution, of
 boundary-value problem,
 351, 360, 385, 518
- Weighted residual method, 343,
 402. *See also* Method of
 moments
- Weighting function, 343,
 402
- Wronskian relation
 for Bessel functions,
 229
 for Riccati–Bessel functions,
 275
 for spherical Bessel functions,
 282
- Yee’s FDTD scheme
 three-dimensional, 311–314
 two-dimensional, 309–311
- Zero reflection, 132

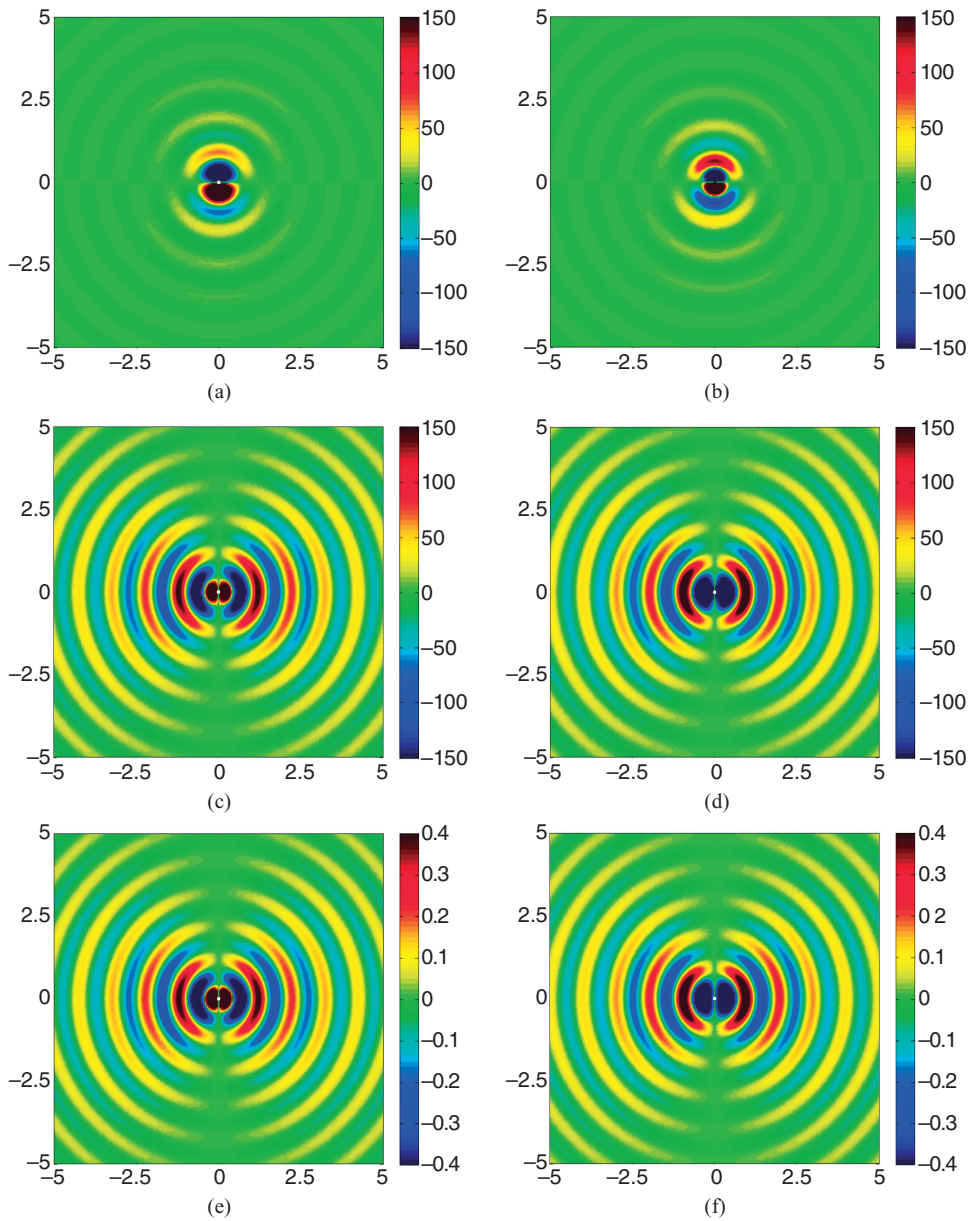


Figure 2.3 Field radiated by an infinitesimal dipole ($Il = 1 \text{ A} \cdot \text{m}$) in a $10\lambda \times 10\lambda$ region.
 (a) Real part of E_r (V/m). (b) Imaginary part of E_r (V/m). (c) Real part of E_θ (V/m).
 (d) Imaginary part of E_θ (V/m). (e) Real part of H_ϕ (A/m). (f) Imaginary part of H_ϕ (A/m).

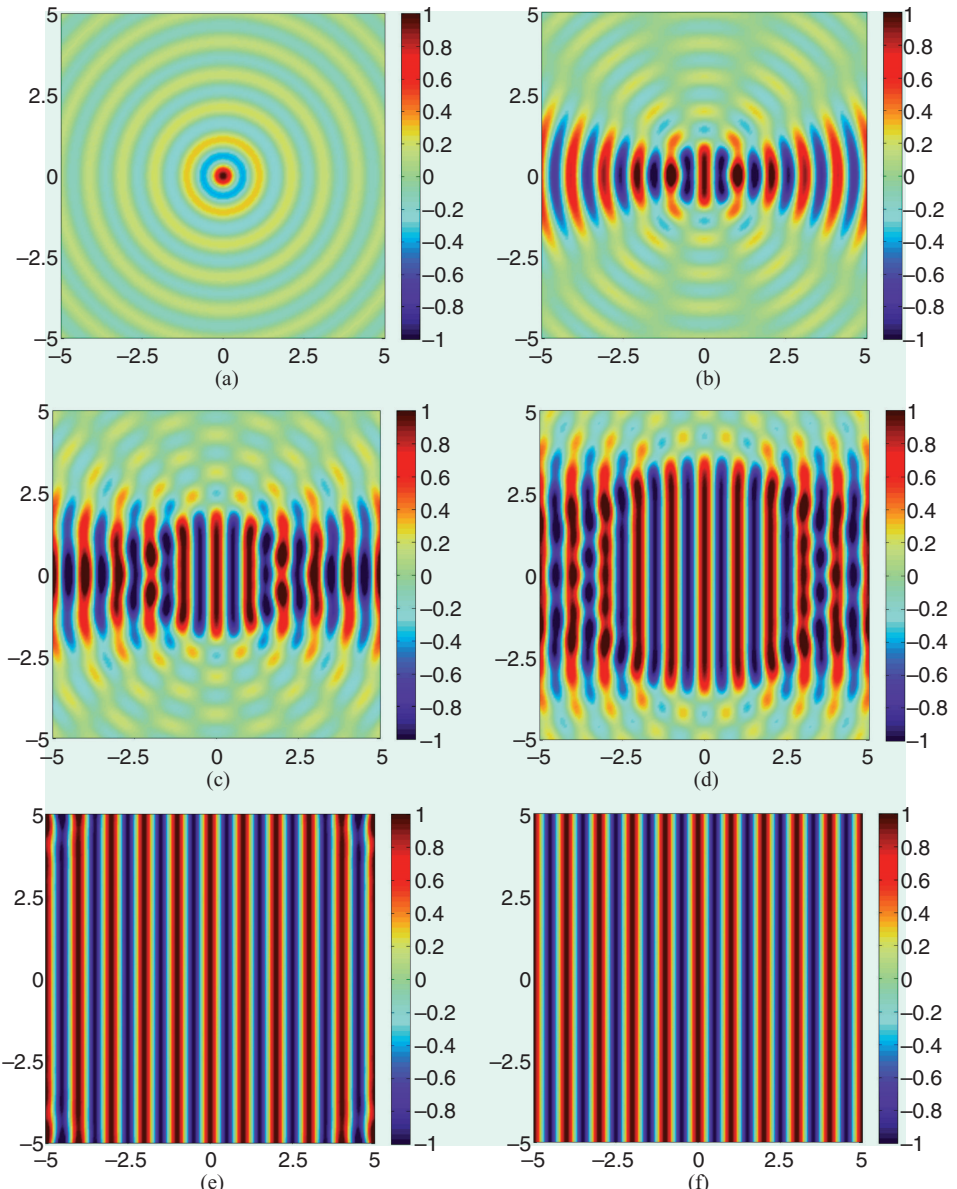


Figure 6.9 Illustration of the cylindrical wave transformation. The plots show the real part of the right-hand side of Equation 6.4.6 when the summation is evaluated from $n=-M$ to M . Clearly, a plane wave is formed in a $10\lambda \times 10\lambda$ region by increasing the number of terms in the summation. (a) $M=1$. (b) $M=5$. (c) $M=10$. (d) $M=20$. (e) $M=40$. (f) $M=80$.

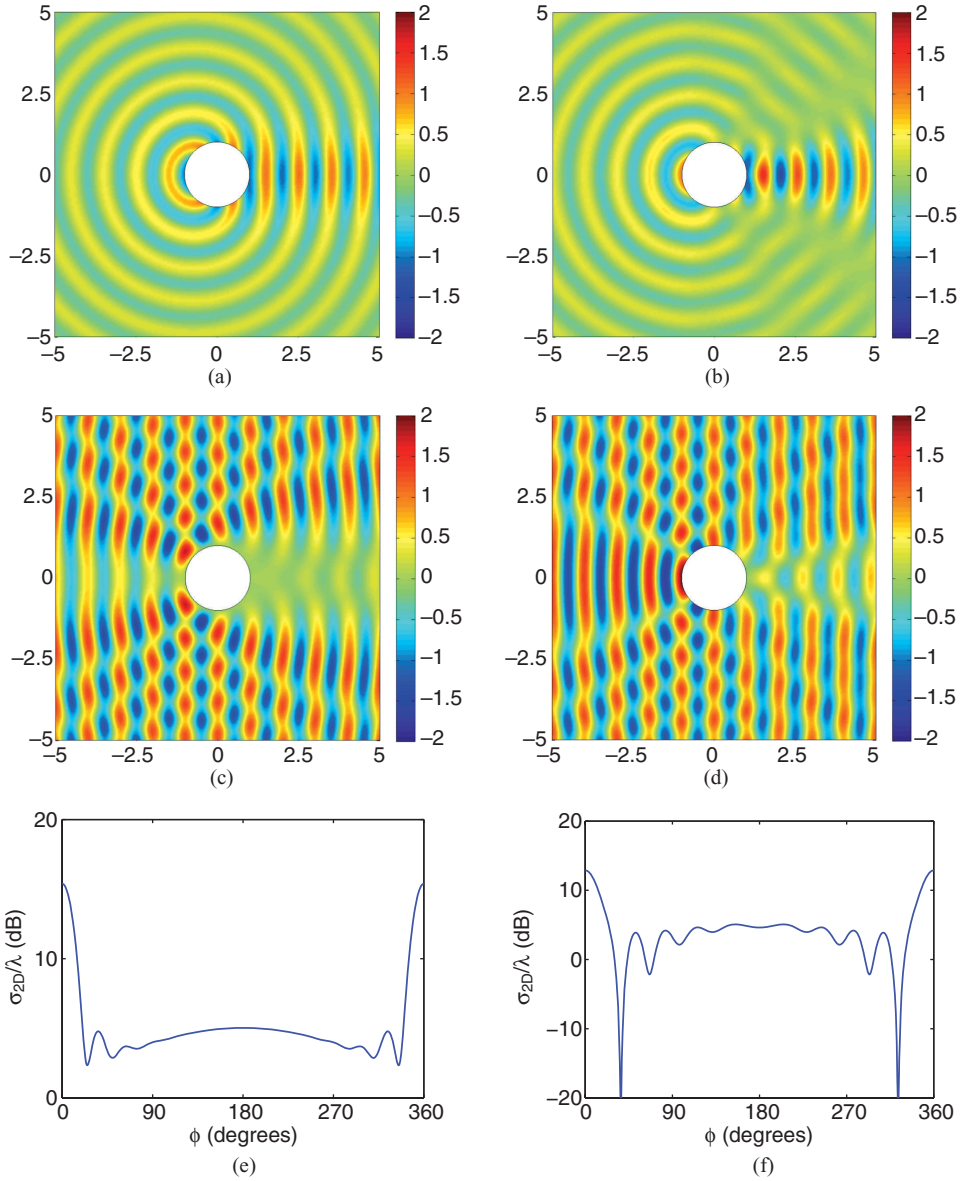


Figure 6.12 Scattering by a circular conducting cylinder with a radius of 1λ . (a) Snapshot of the scattered field E_z^{sc} . (b) Snapshot of the scattered field H_z^{sc} . (c) Snapshot of the total field E_z . (d) Snapshot of the total field H_z . (e) Scattering width for the TM case. (f) Scattering width for the TE case. The values of the fields are normalized by the magnitude of their respective incident fields.

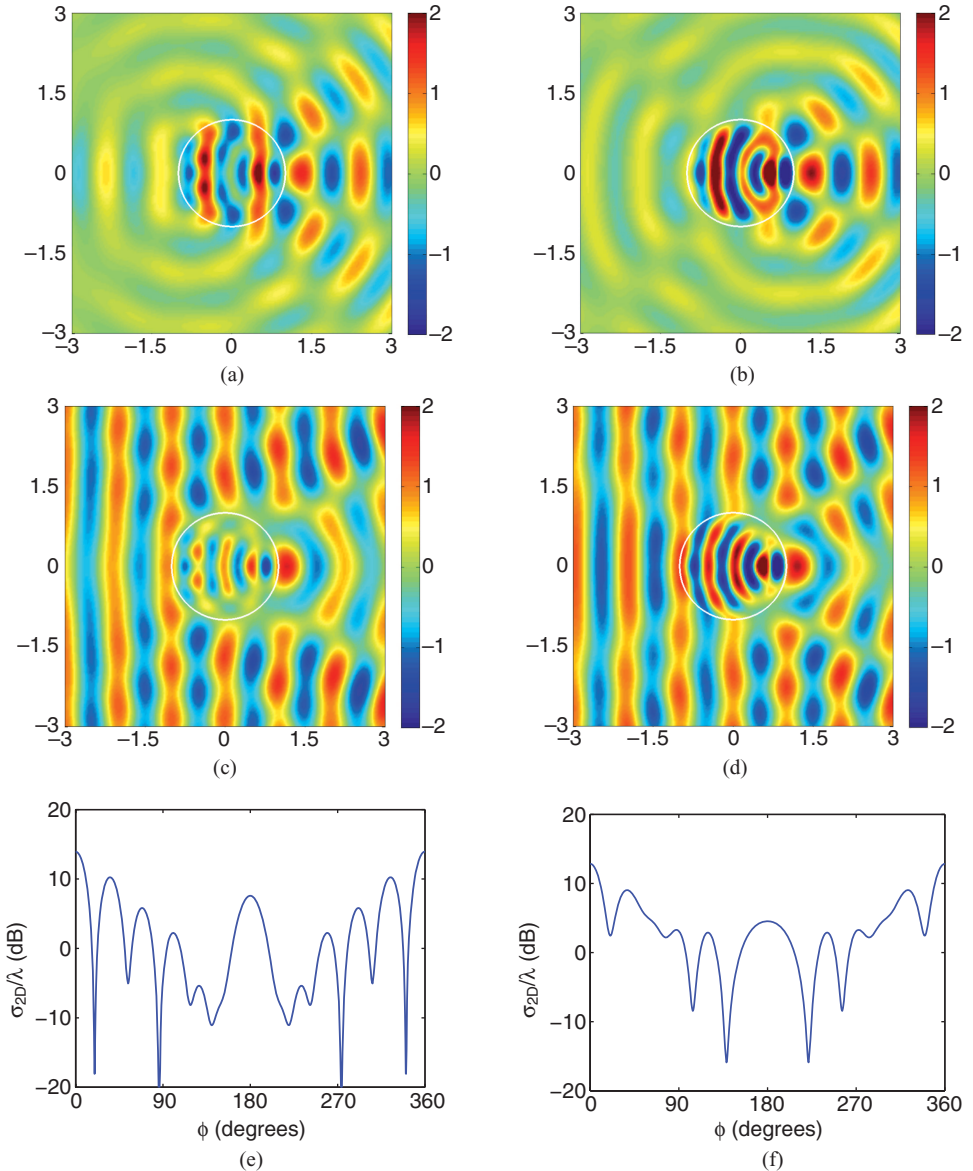


Figure 6.14 Scattering by a circular dielectric cylinder with a radius of 1λ and a relative permittivity of 4.0. (a) Snapshot of the scattered field E_z^{sc} . (b) Snapshot of the scattered field H_z^{sc} . (c) Snapshot of the total field E_z . (d) Snapshot of the total field H_z . (e) Scattering width for the TM case. (f) Scattering width for the TE case. The values of the fields are normalized by the magnitude of their respective incident fields.

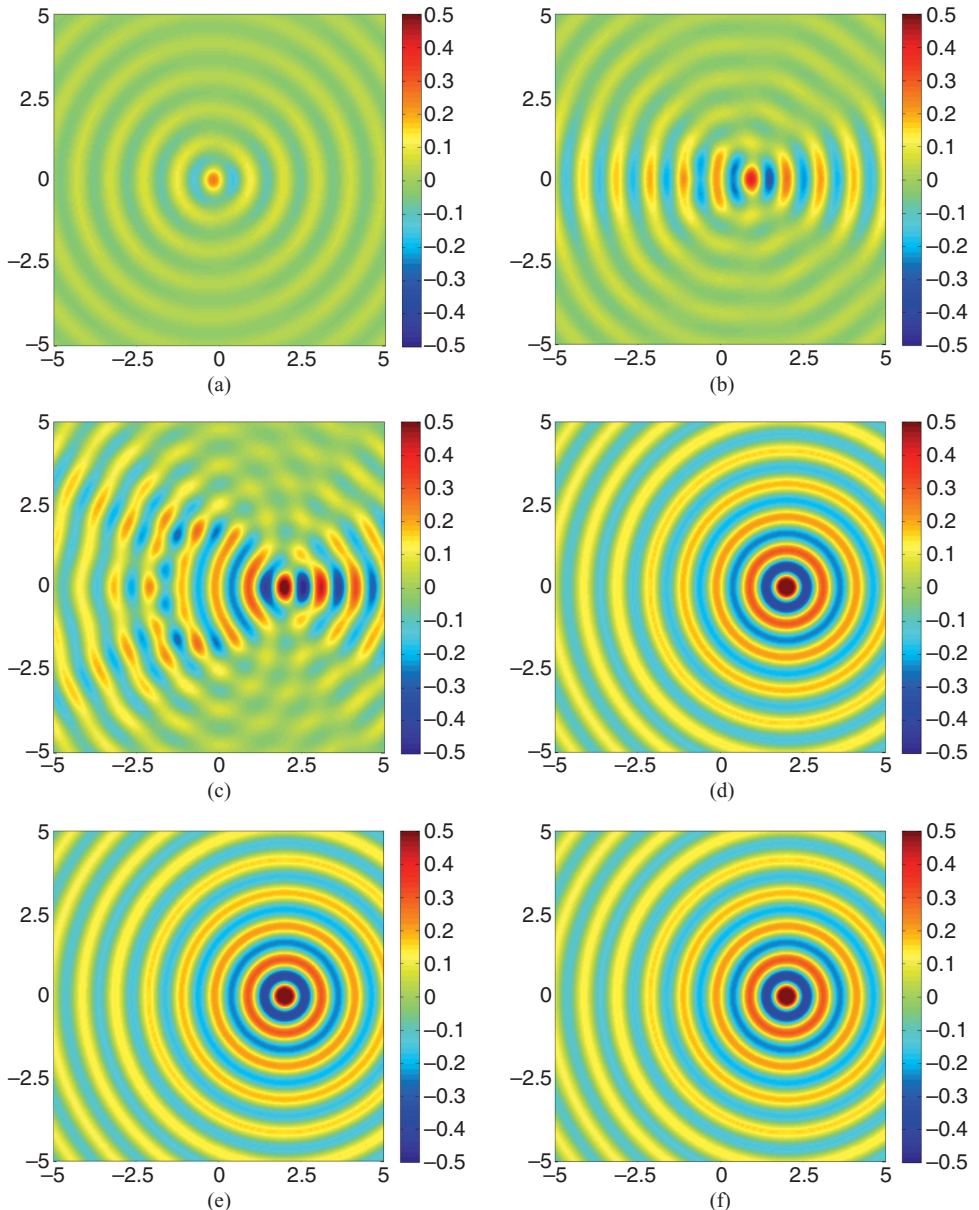


Figure 6.19 Illustration of the addition theorem for the Hankel function. The plots show the real part of the right-hand side of Equation 6.5.32 in a $10\lambda \times 10\lambda$ region when the summation is evaluated from $n=-M$ to M . Clearly, an off-centered cylindrical wave is formed by increasing the number of terms in the summation. (a) $M=1$. (b) $M=5$. (c) $M=10$. (d) $M=15$. (e) $M=20$. (f) $M=40$.

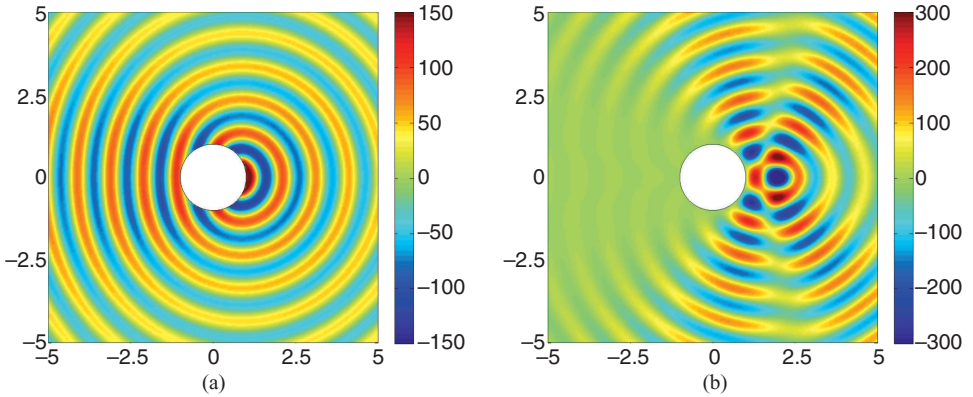


Figure 6.22 Radiation of an electric line current ($I=1\text{ A}$) placed 1λ away from a conducting cylinder with a radius of 1λ . (a) Snapshot of the scattered field E_z^{sc} (V/m). (b) Snapshot of the total field E_z (V/m).

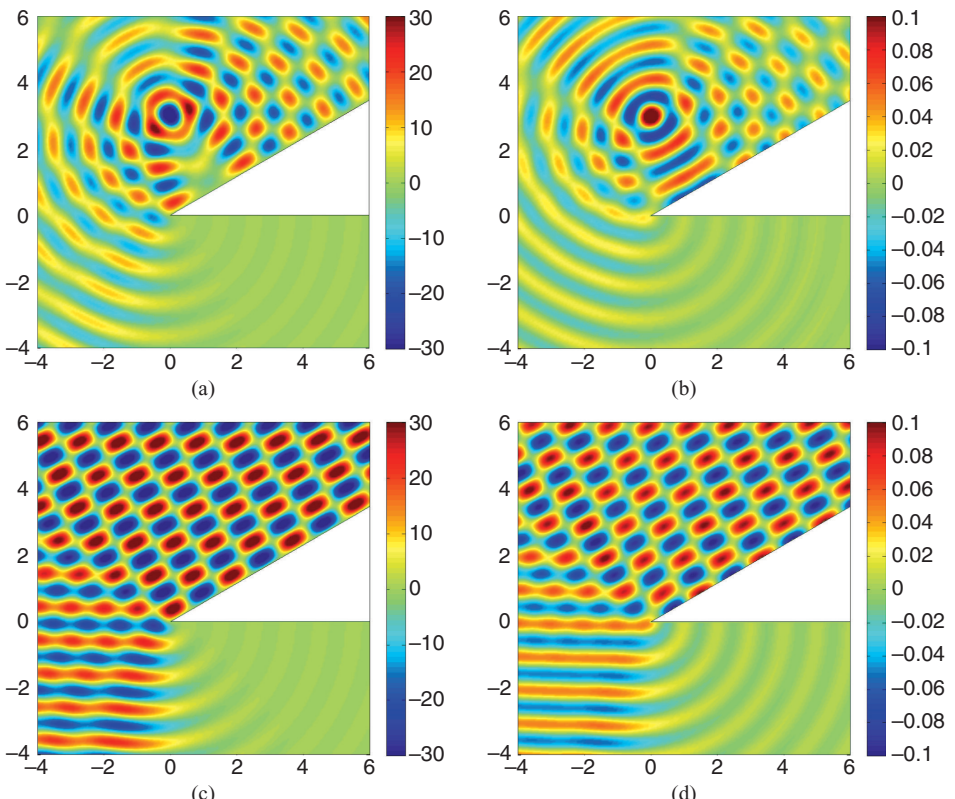


Figure 6.24 Snapshots of the field radiated by a line current in the presence of a 30° -angled conducting wedge. (a) E_z (V/m) produced by an electric current ($I=0.1\text{ A}$) placed 3λ above the wedge. (b) H_z (A/m) produced by a magnetic current ($K=37.7\text{ V}$) placed 3λ above the wedge. (c) E_z (V/m) produced by an electric current ($I=1\text{ A}$) placed 100λ above the wedge. (d) H_z (A/m) produced by a magnetic current ($K=377\text{ V}$) placed 100λ above the wedge.

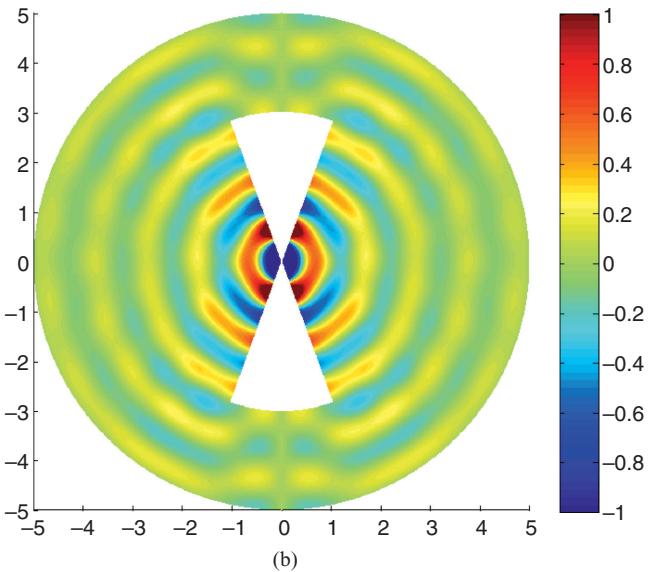
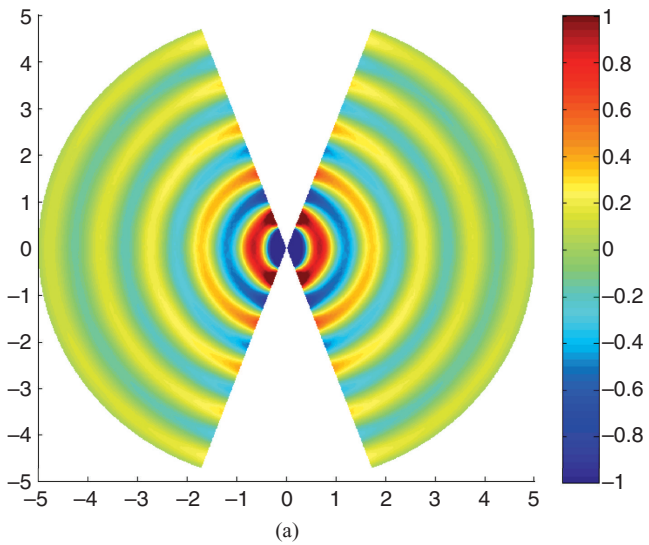


Figure 7.6 Radiation by a biconical antenna with an internal half-angle of $\theta_0 = 20^\circ$ in a region with a radius of 5λ . (a) Snapshot of the magnetic field H_ϕ of the TEM mode radiated by an infinitely long biconical antenna. (b) Snapshot of the magnetic field H_ϕ radiated by a truncated finite biconical antenna with $L = 3\lambda$.

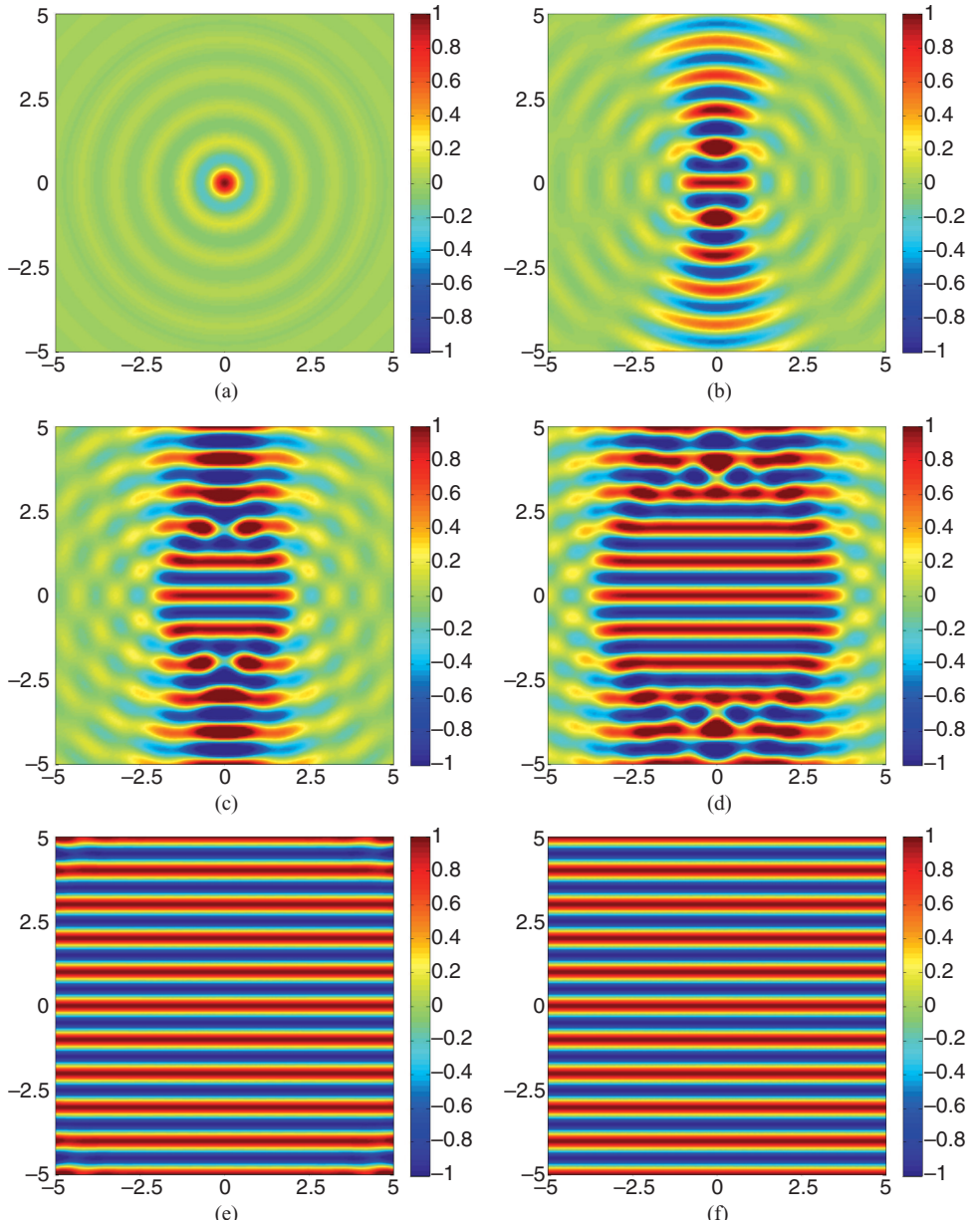


Figure 7.7 Illustration of the spherical wave transformation. The plots show the real part of the right-hand side of Equation 7.4.11 when the summation is evaluated from $n = 0$ to M . Clearly, a plane wave in a $10\lambda \times 10\lambda$ region is formed by increasing the number of terms in the summation. (a) $M = 1$. (b) $M = 5$. (c) $M = 10$. (d) $M = 20$. (e) $M = 40$. (f) $M = 80$.

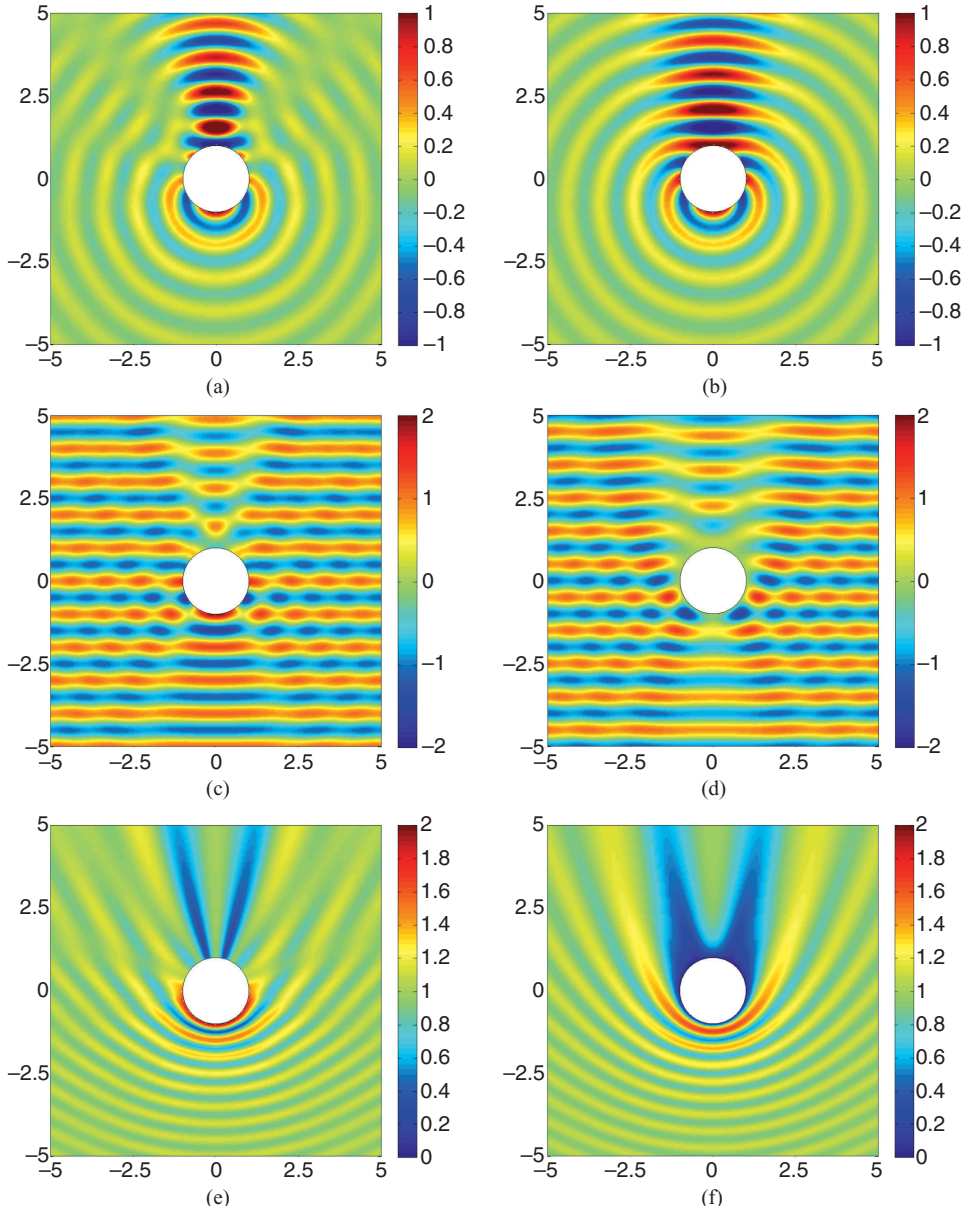


Figure 7.9 Scattering by a conducting sphere with a radius of 1λ . (a) Snapshot of the scattered magnetic field ηH_ϕ^{sc} in the E-plane. (b) Snapshot of the scattered electric field E_ϕ^{sc} in the H-plane. (c) Snapshot of the total magnetic field ηH_ϕ in the E-plane. (d) Snapshot of the total electric field E_ϕ in the H-plane. (e) Magnitude of the total magnetic field ηH_ϕ in the E-plane. (f) Magnitude of the total electric field E_ϕ in the H-plane. The values of the fields are normalized by the magnitude of the incident electric field.

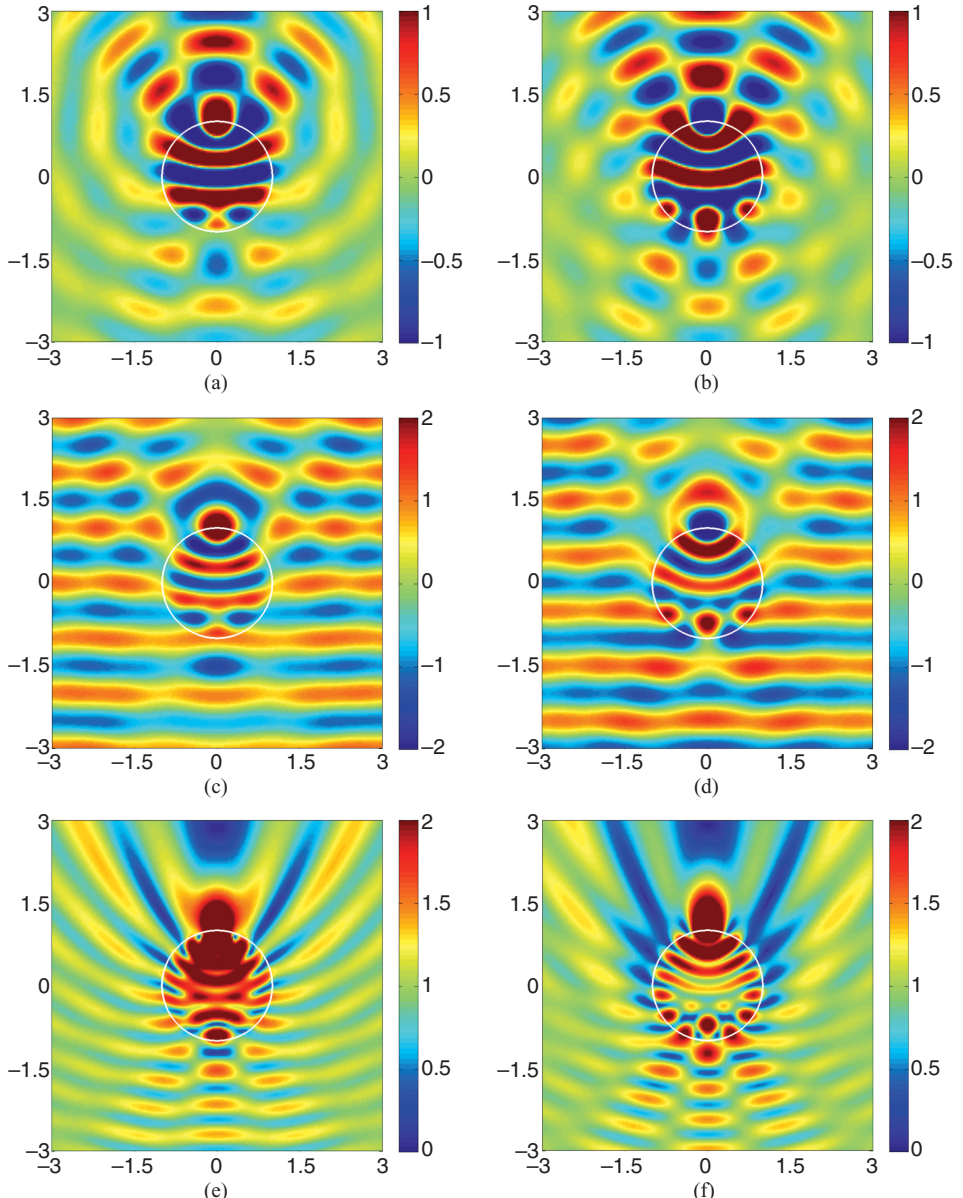


Figure 7.13 Scattering by a dielectric sphere with a radius of 1λ and a relative permittivity of 2.56. (a) Snapshot of the scattered magnetic field ηH_ϕ^{sc} in the E-plane. (b) Snapshot of the scattered electric field E_ϕ^{sc} in the H-plane. (c) Snapshot of the total magnetic field ηH_ϕ in the E-plane. (d) Snapshot of the total electric field E_ϕ in the H-plane. (e) Magnitude of the total magnetic field ηH_ϕ in the E-plane. (f) Magnitude of the total electric field E_ϕ in the H-plane. The values of the fields are normalized by the magnitude of the incident electric field.

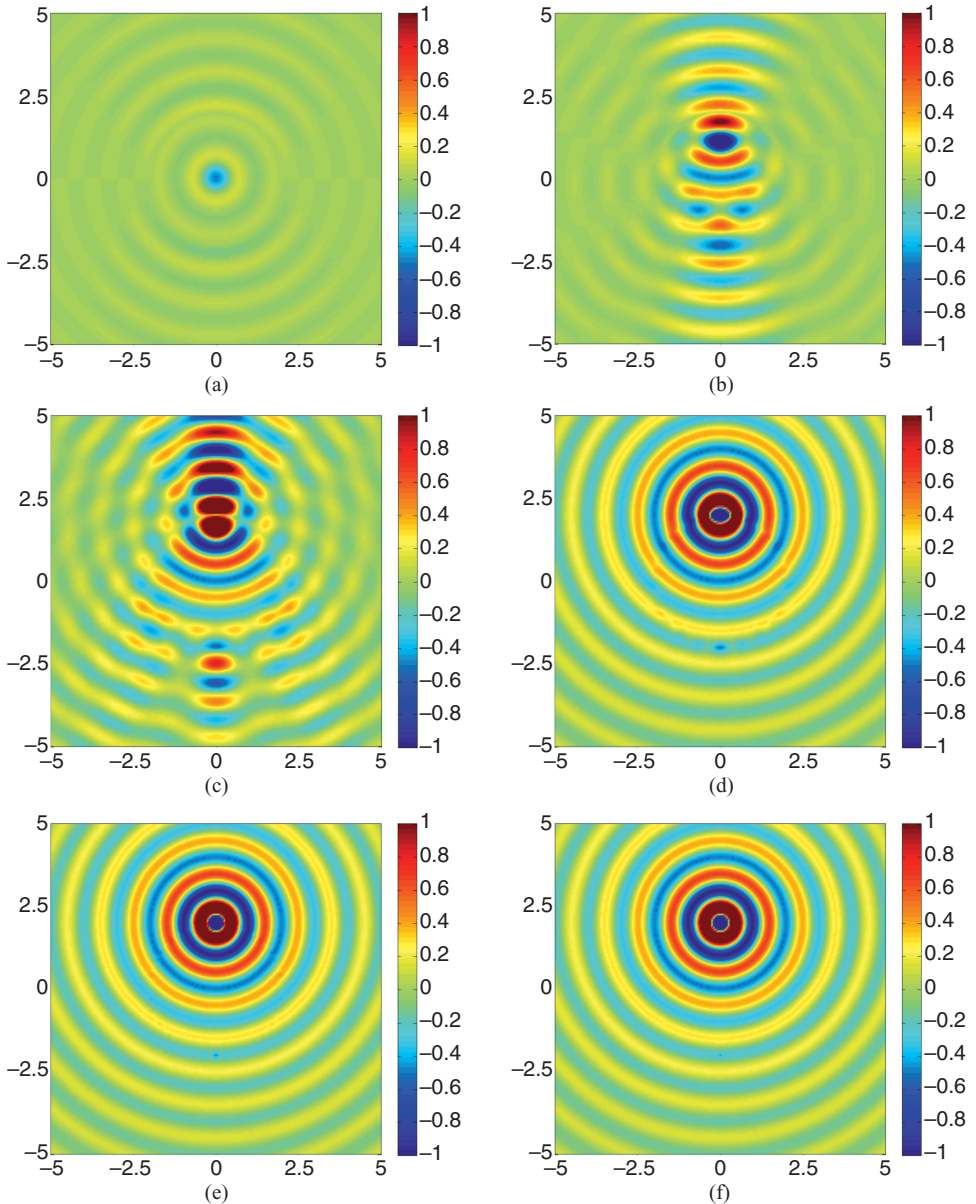


Figure 7.19 Illustration of the addition theorem for the spherical Hankel function. The plots show the real part of the right-hand side of Equation 7.5.14 in a $10\lambda \times 10\lambda$ region when the summation is evaluated from $n = 0$ to M . Clearly, an off-centered spherical wave is formed by increasing the number of terms in the summation. (a) $M = 1$. (b) $M = 5$. (c) $M = 10$. (d) $M = 20$. (e) $M = 40$. (f) $M = 80$.

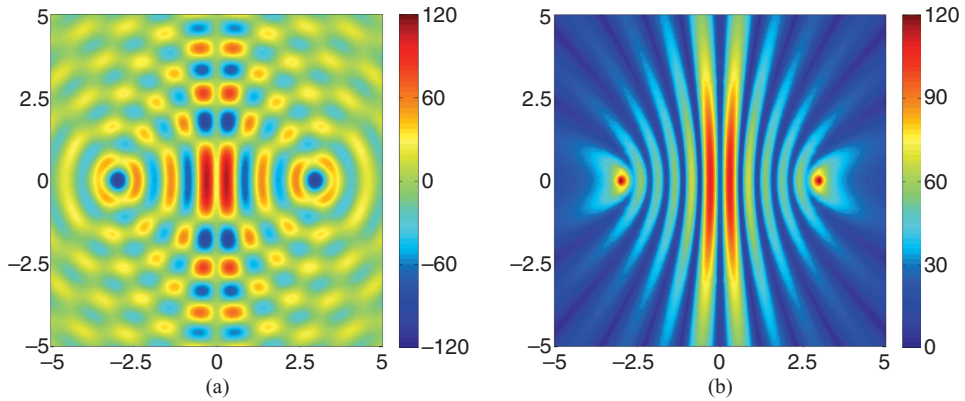


Figure 7.21 Field radiated by a circular current loop having a uniform current of 1 A and a radius of 3λ . (a) Snapshot of E_ϕ . (b) Magnitude of E_ϕ .

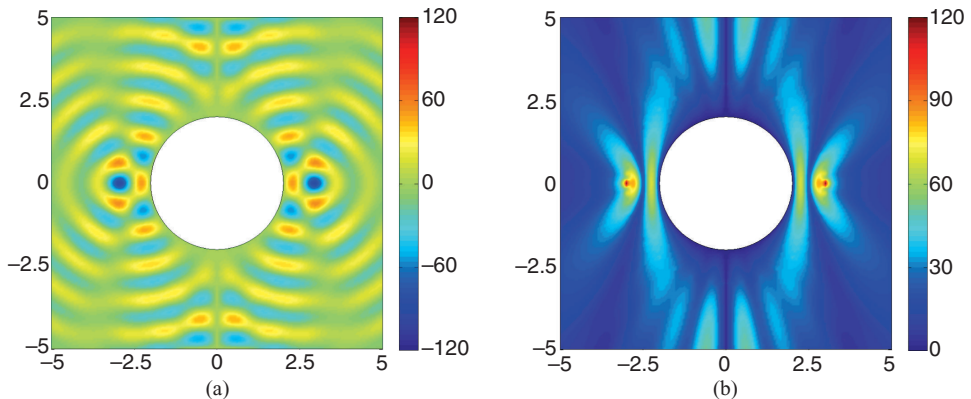


Figure 7.23 Field radiated by a circular current loop having a uniform current of 1 A and a radius of 3λ in the presence of a conducting sphere with a radius of 2λ . (a) Snapshot of E_ϕ . (b) Magnitude of E_ϕ .

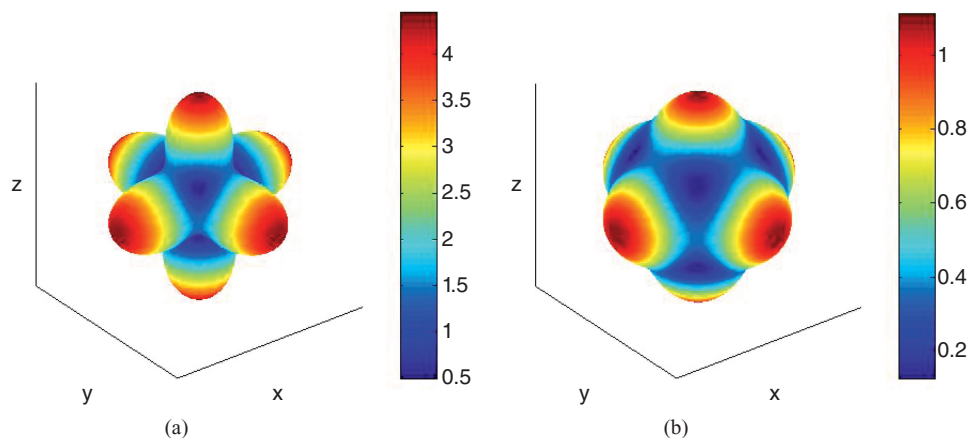


Figure 8.7 Variation of the numerical phase error in degrees per wavelength for (a) $\lambda/h = 10$ and (b) $\lambda/h = 20$.

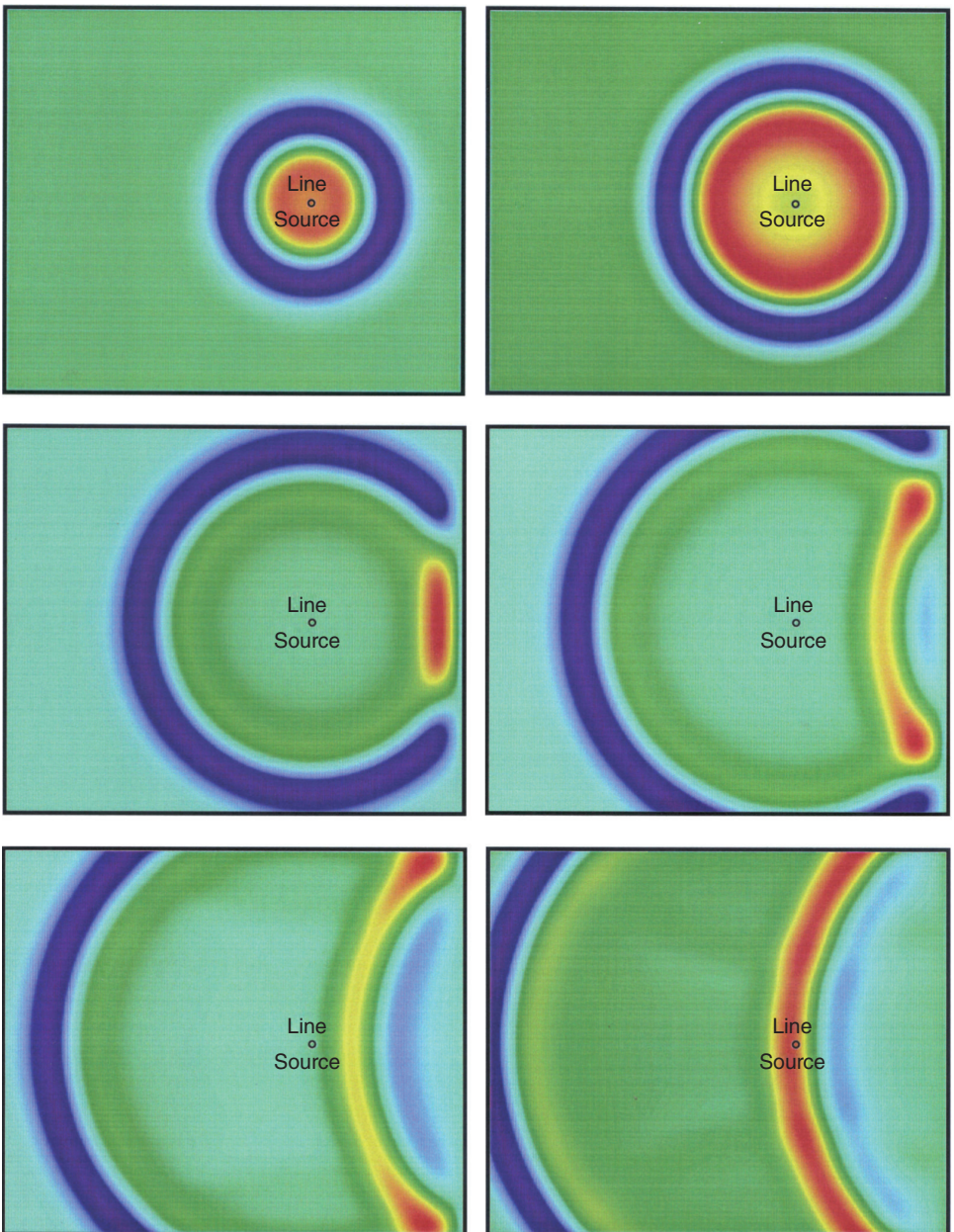


Figure 8.10 Snapshots of the electric field radiated by the line current in front of an infinitely large conducting plane.

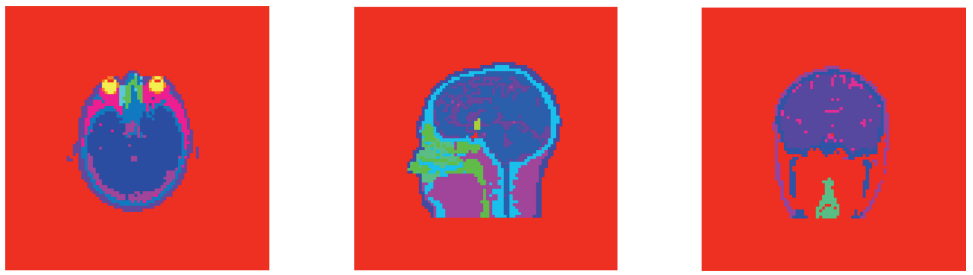


Figure 8.13 Axial, sagittal, and coronal slices of the head model used in the FDTD calculation. (After Chen et al. [12], Copyright © 1998 IEEE.)

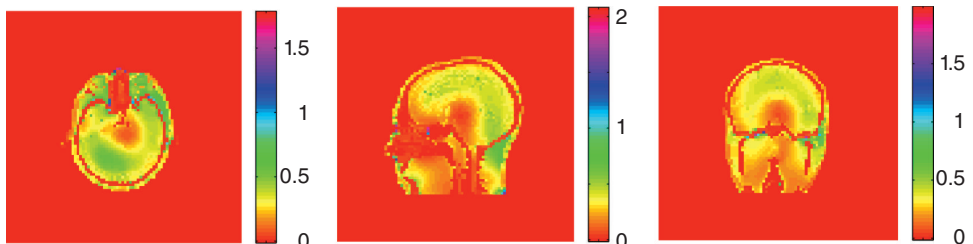


Figure 8.14 SAR (W/kg) distribution in the axial, sagittal, and coronal slices at 256 MHz. (After Chen et al. [12], © 1998 IEEE.)

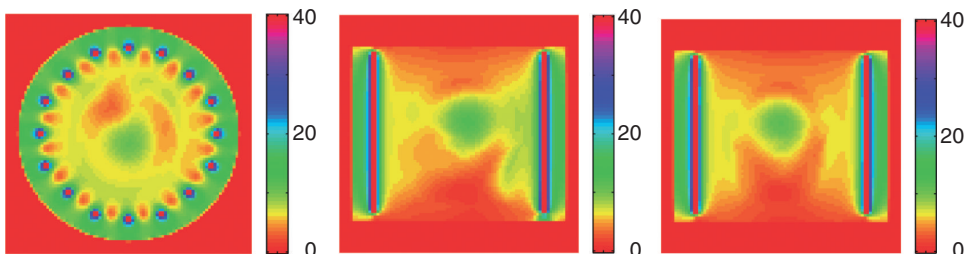


Figure 8.15 Magnetic field (A/m) distribution in the axial, sagittal, and coronal slices at 256 MHz. (After Chen et al. [12], © 1998 IEEE.)

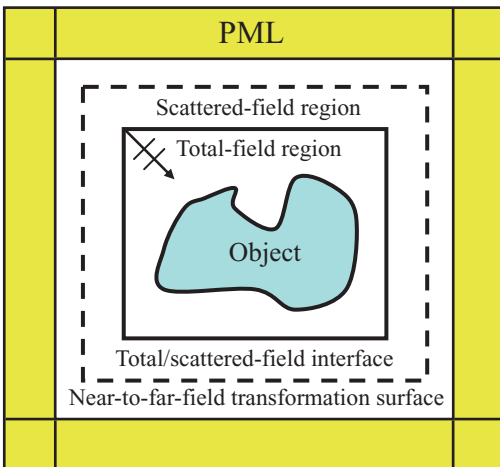


Figure 8.16 Typical setup for FDTD simulation of scattering problems. A total/scattered-field interface is introduced as a Huygens' surface to excite the incident field in the total-field region. A near-to-far-field transformation is employed to calculate far fields based on the near fields on the surface.

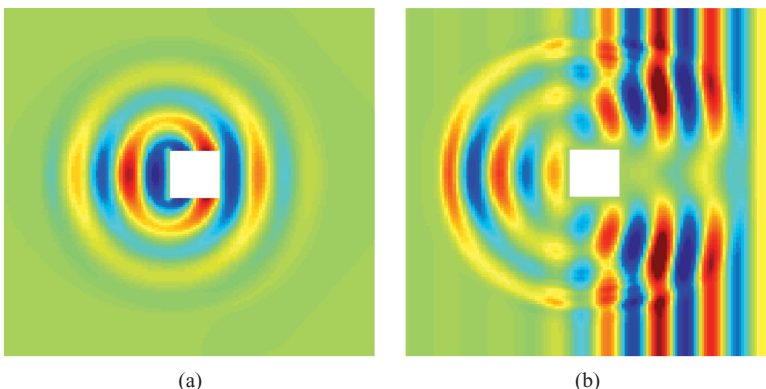


Figure 8.17 Scattering of a TM-polarized, modulated Gaussian pulse by a square conducting cylinder. (a) Snapshot of the scattered electric field. (b) Snapshot of the total electric field.

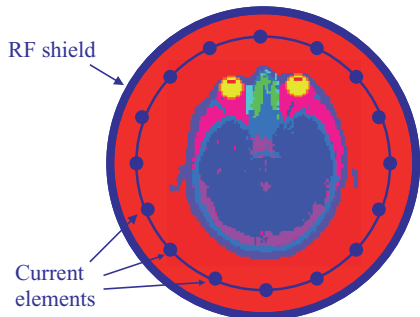


Figure 9.7 Two-dimensional model of a shielded 16-element birdcage coil loaded with the human head.

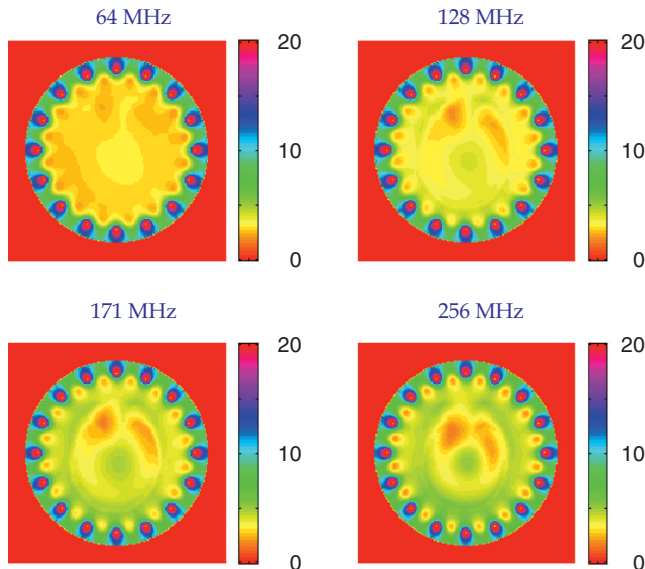


Figure 9.8 Magnitude of the magnetic field inside the loaded birdcage coil at four different frequencies. (After Jin and Chen [10], Copyright © 1997 ISMRM.)

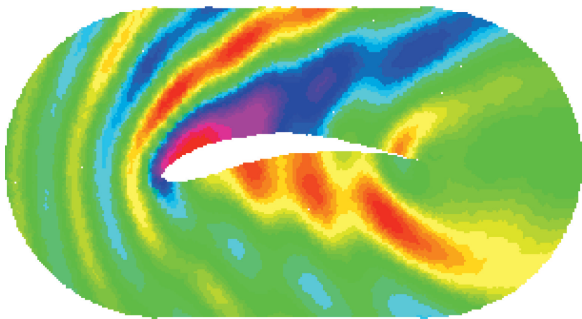


Figure 9.9 Magnitude of the magnetic field for a plane wave incident from the left to right and scattered by a conducting airfoil.

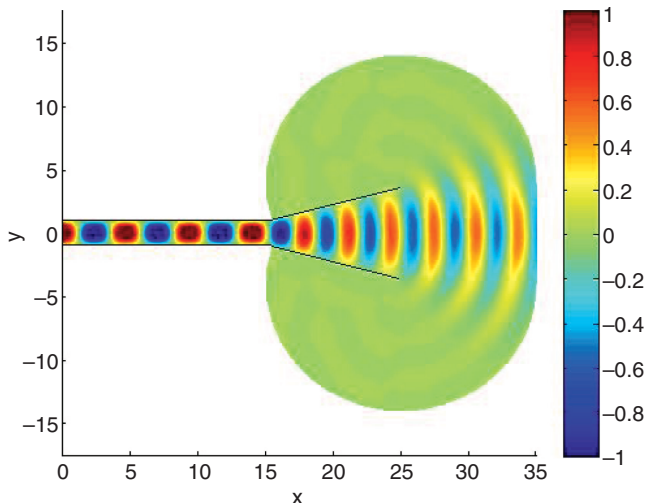


Figure 9.10 Snapshot of the radiated field E_z by a two-dimensional waveguide-fed horn antenna excited by the first TM_z mode.

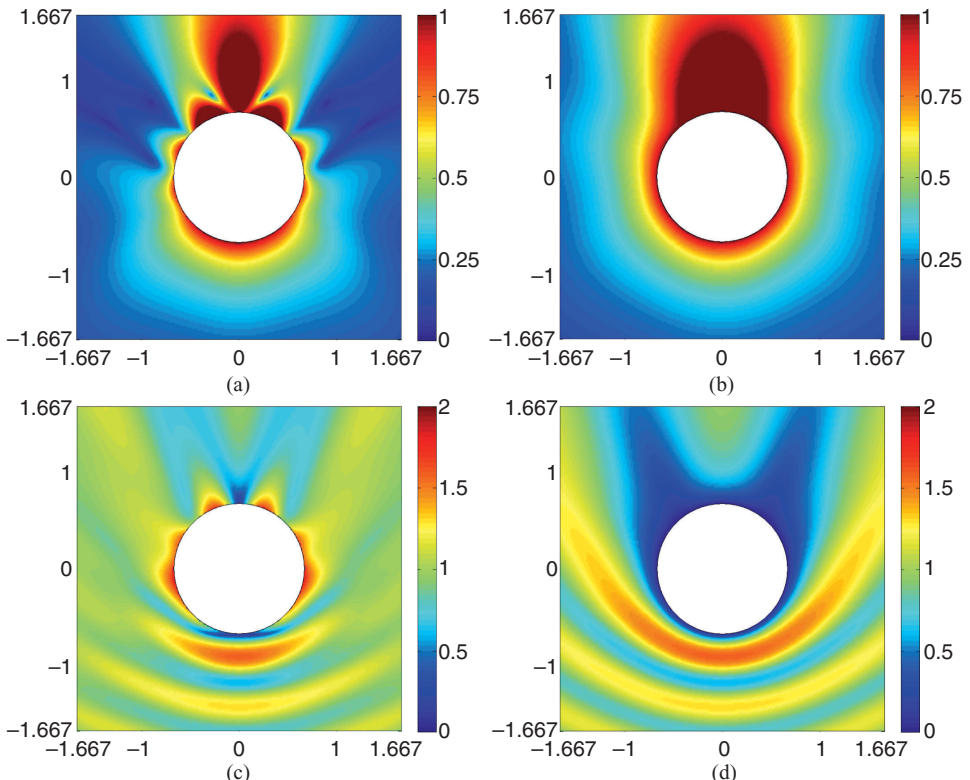


Figure 9.17 Scattering by a metallic sphere having a radius of 0.667λ . (a) Magnitude of the scattered electric field in the E-plane. (b) Magnitude of the scattered electric field in the H-plane. (c) Magnitude of the total electric field in the E-plane. (d) Magnitude of the total electric field in the H-plane. The values of the fields are normalized by the magnitude of the incident electric field.

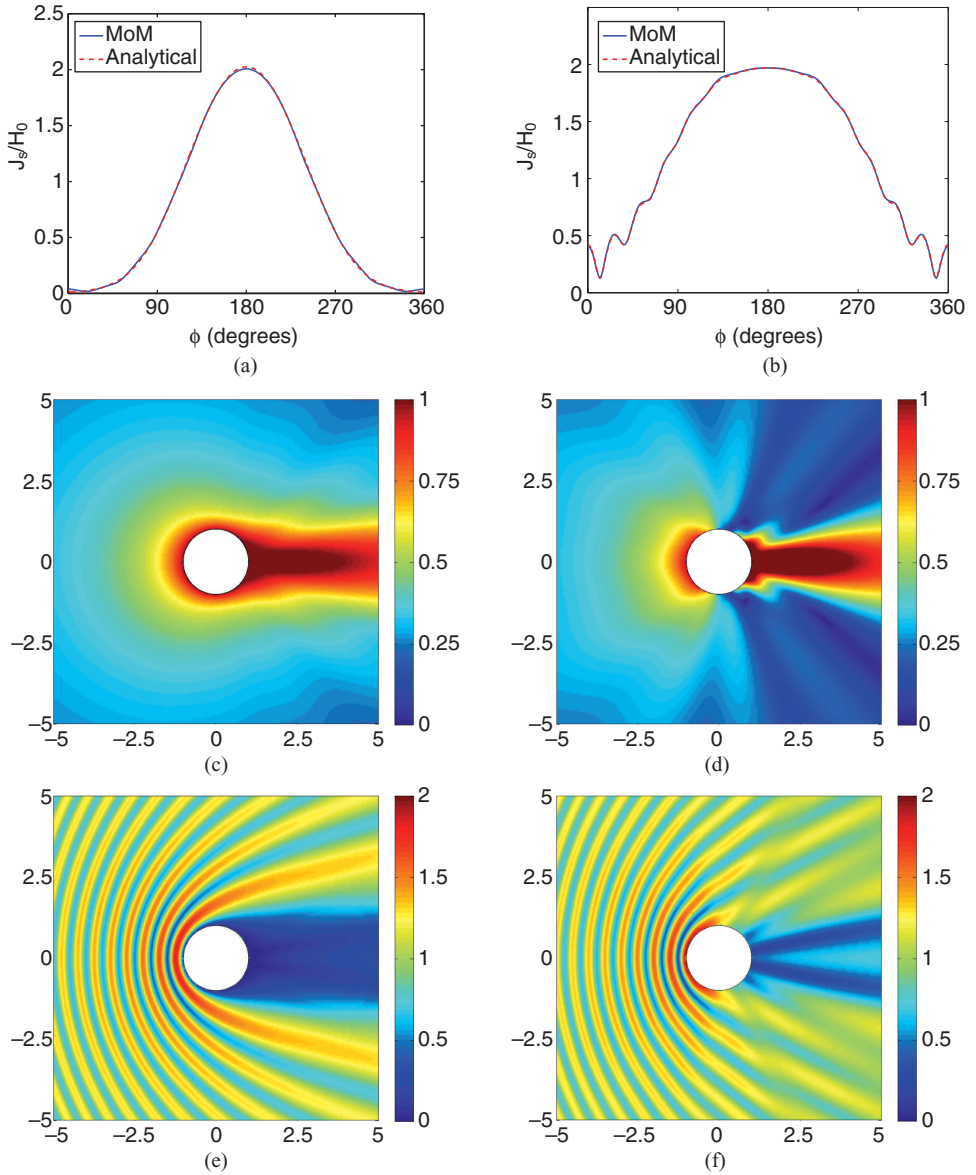


Figure 10.5 Scattering by a circular conducting cylinder with a radius of 1λ . The incident wave propagates from the left to right. The left and right columns show the results for the TM and TE polarizations, respectively. (a) Magnitude of the induced surface current density $J_{s,z}$. (b) Magnitude of the induced surface current density $J_{s,t}$. (c) Magnitude of the scattered field E_z^{sc} . (d) Magnitude of the scattered field H_z^{sc} . (e) Magnitude of the total field E_z . (f) Magnitude of the total field H_z . The values of the fields are normalized by the magnitude of their respective incident fields.

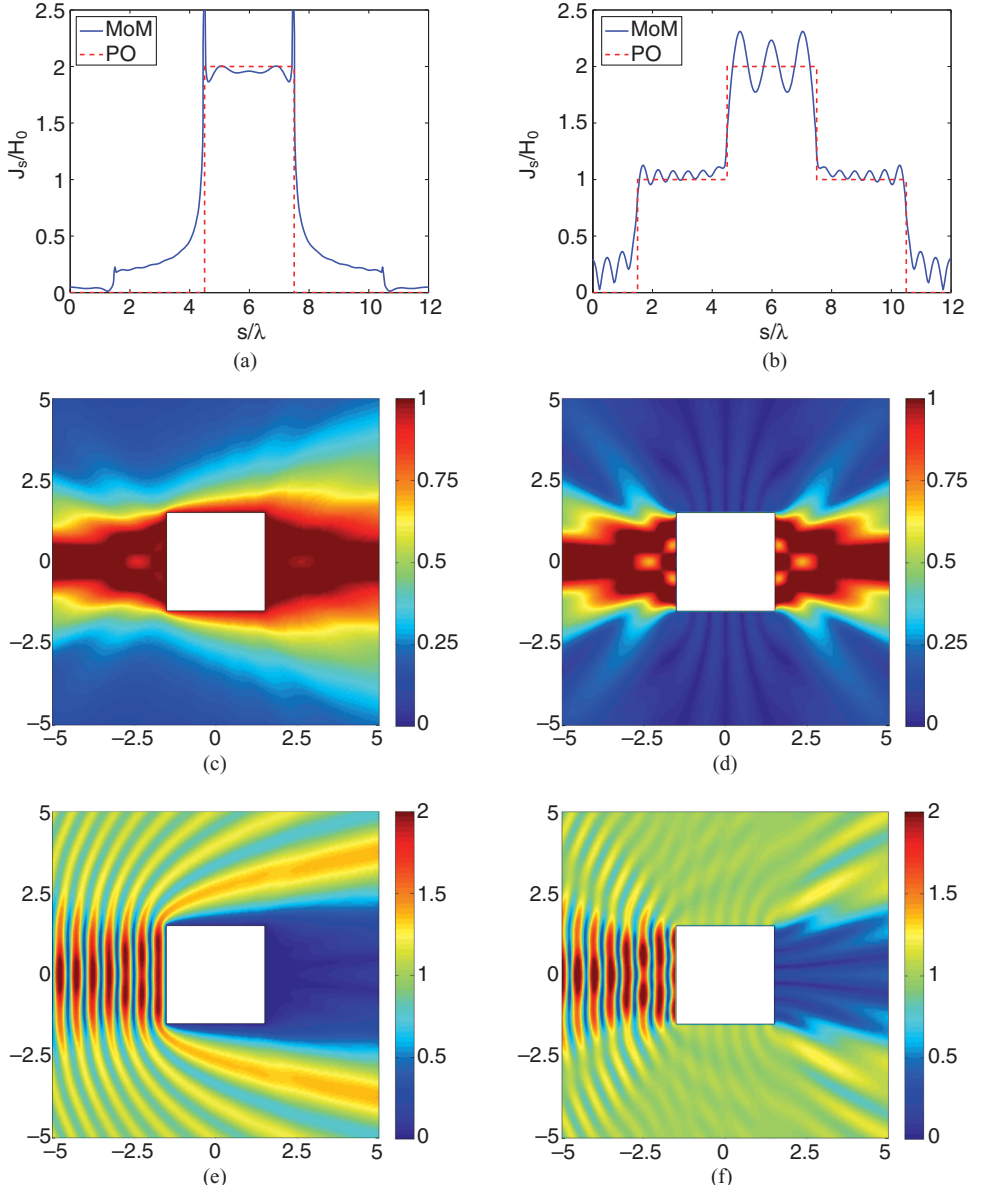


Figure 10.6 Scattering by a square conducting cylinder with a cross-section of $3\lambda \times 3\lambda$. The incident wave propagates from the left to right. The left and right columns show the results for the TM and TE polarizations, respectively. (a) Magnitude of the induced surface current density $J_{s,r}/H_0$. (b) Magnitude of the induced surface current density $J_{s,i}/H_0$. (c) Magnitude of the scattered field E_z^{sc} . (d) Magnitude of the scattered field H_z^{sc} . (e) Magnitude of the total field E_z . (f) Magnitude of the total field H_z . The values of the fields are normalized by the magnitude of their respective incident fields.

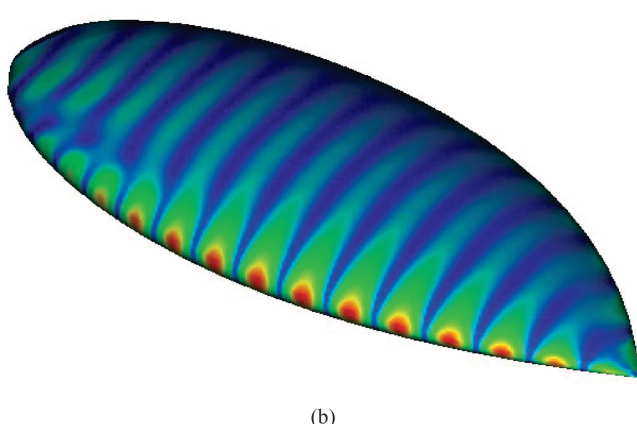
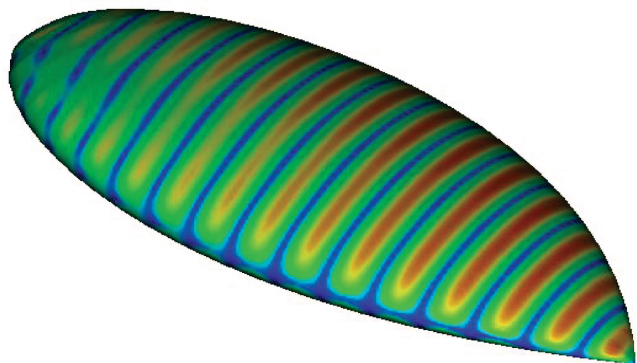


Figure 10.19 Snapshot of the induced surface electric current density on a 9.936-inch-long conducting almond with a 10-GHz plane wave incident horizontally from an azimuth angle of 30° away from the tip. (a) Vertical polarization. (b) Horizontal polarization.

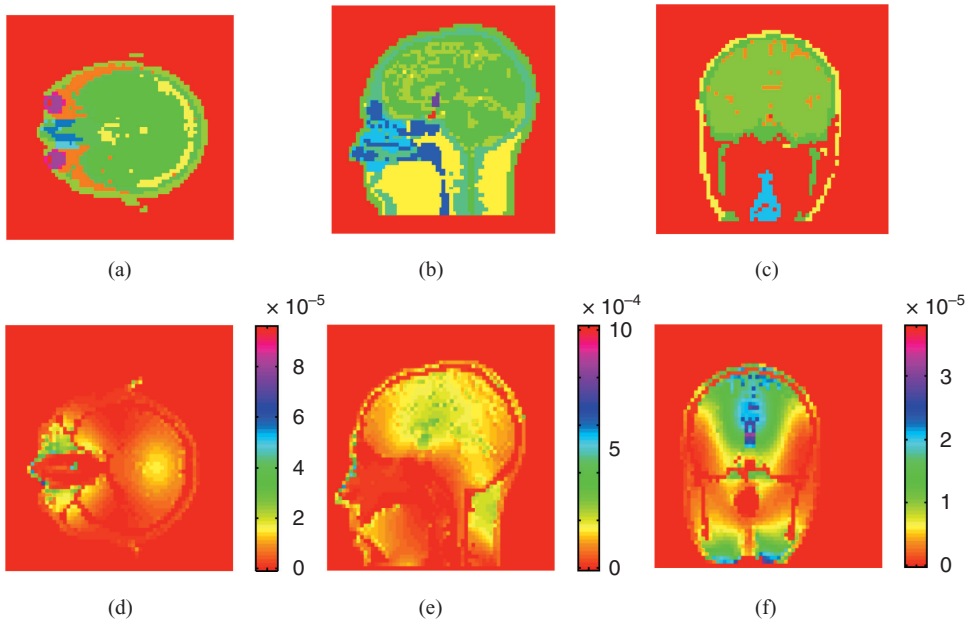


Figure 11.5 Staircase model of a human head and SAR (W/kg) at 256 MHz calculated using a $63 \times 63 \times 63$ grid under the excitation of a plane wave incident from the top. (a) Axial view. (b) Sagittal view. (c) Coronal view. (d) SAR in the axial slice. (e) SAR in the sagittal slice. (f) SAR in the coronal slice. (After Wang and Jin [17], Copyright © 1998 IEEE.)

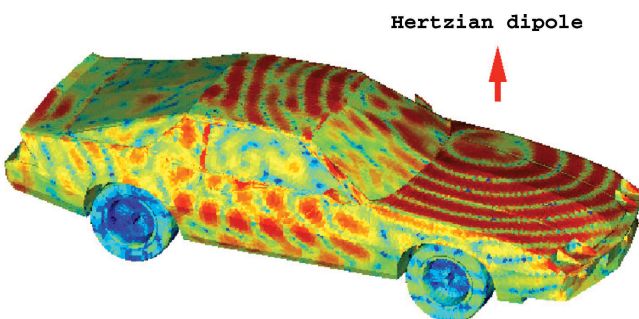


Figure 11.23 Surface current on a car induced by the radiation of a Hertzian dipole at 1.0 GHz.
(After Song et al. [44], Copyright © 1998 IEEE.)

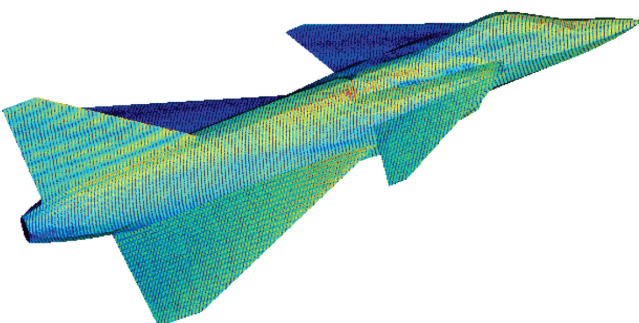


Figure 11.24 Surface current on an airplane induced by an incident plane wave at 2 GHz. The plane wave is incident 30° from the nose and is vertically polarized. (After Song et al. [44], Copyright © 1998 IEEE.)

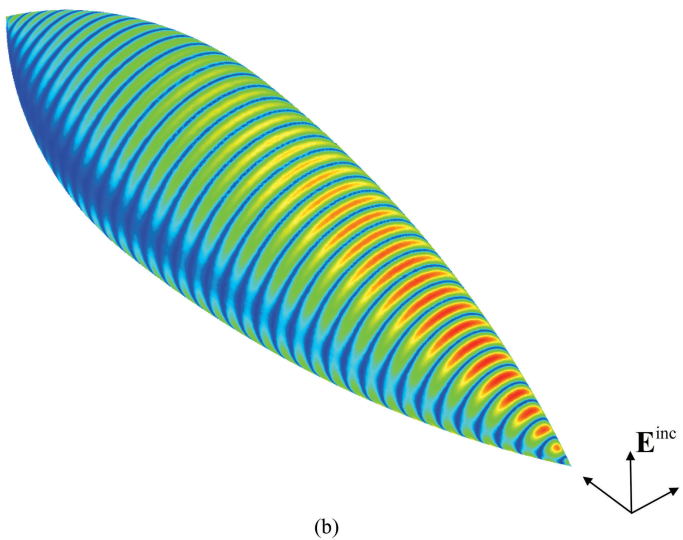
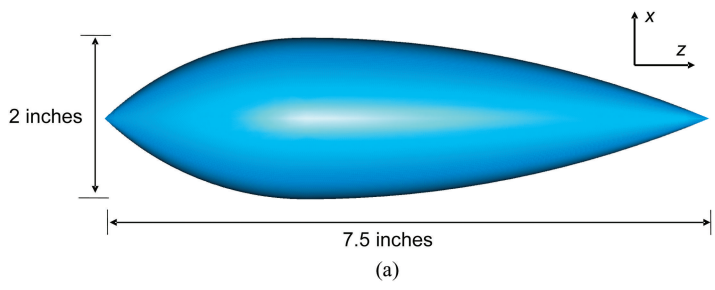


Figure 11.32 Metallic double ogive. (a) Geometry. (b) Surface current density for a sinusoidal plane wave excitation at 30GHz. (After Jin and Riley [92], Copyright © 2009 Wiley.)

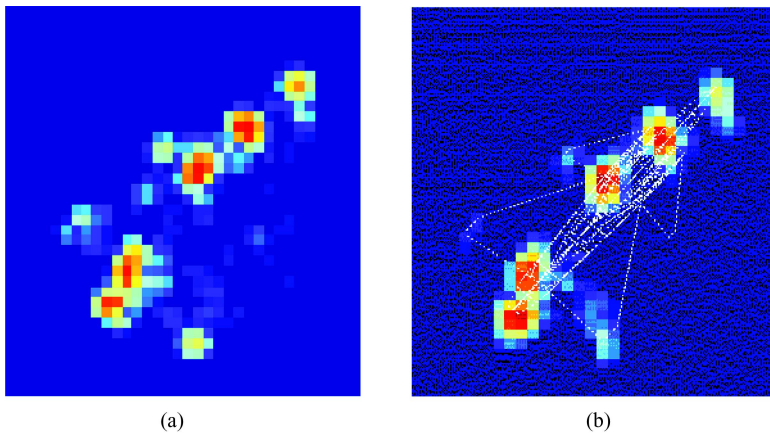


Figure 12.4 Inverse synthetic aperture radar image of an aircraft at 130° from nose-on.
 (a) Calculation. (b) Measurement. (After Wang and Ling [133], Copyright © 2002 IEEE.)

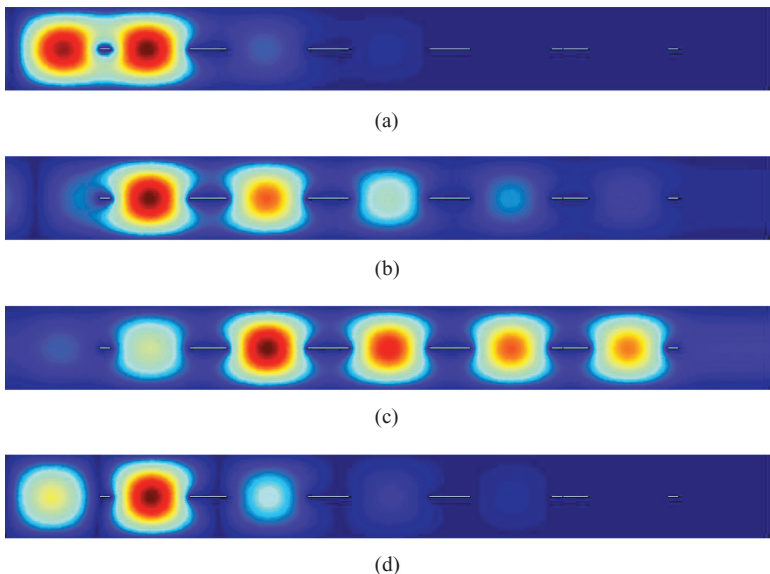


Figure 12.6 Field distribution in a waveguide filter at a few frequencies. (a) 41 GHz.
 (b) 41.4 GHz. (c) 42 GHz. (d) 43 GHz.

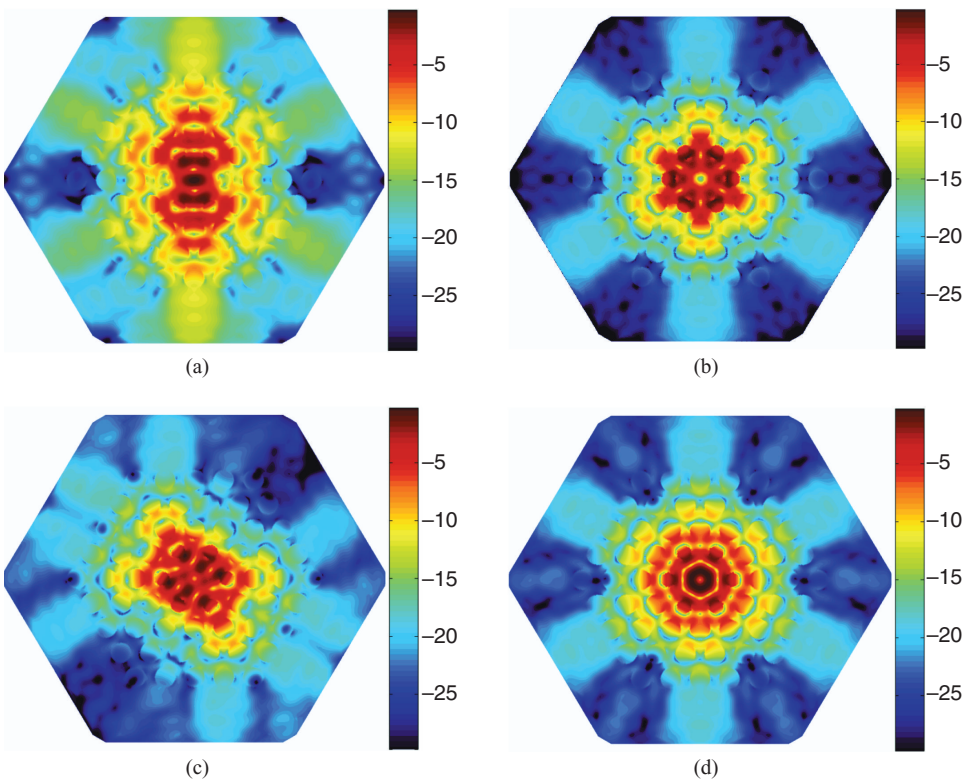
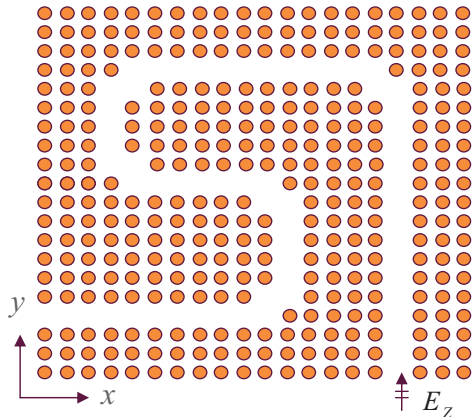
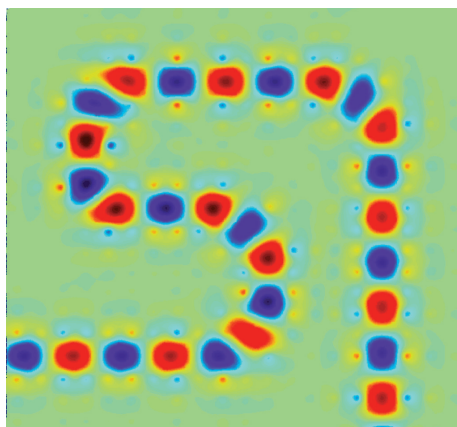


Figure 12.10 Normalized magnitude of the electric field at the midplane. (a) Doubly degenerate dipole modes. (b) Non-degenerate hexapole mode. (c) Doubly degenerate quadrupole modes. (d) Non-degenerate monopole mode. (After Li and Jin [147], Copyright © 2008 Wiley.)



(a)



(b)

Figure 12.11 Photonic crystal waveguide. (a) Top view of the geometry. (b) A snapshot of the field distribution. (After Li and Jin [146], Copyright © 2007 OSA.)

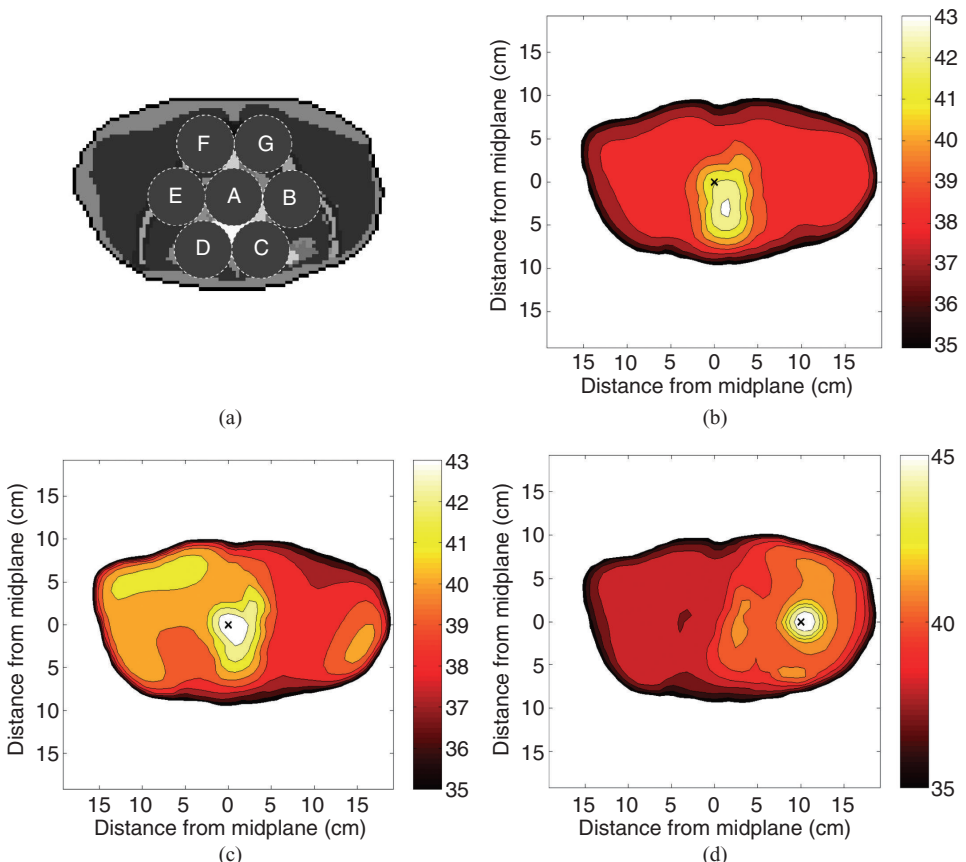


Figure 12.12 Electromagnetic hyperthermia using an annular phased array of applicators at 85 MHz. (a) Cross-section of the human trunk with seven targeted regions. (b) Steady-state temperature optimized based on the specific absorption rate for region A. (c) Steady-state temperature optimized based on the temperature for region A. (d) Steady-state temperature optimized based on the temperature for region B. (After Kowalski and Jin [158], Copyright © 2000 IEEE.)